Transactions of the ASME®

Transactions of the ASME, Journal of Heat Transfer (ISSN 0022-1481) is published quarterly (Feb., May, Aug., Nov.) for $185.00 per year by The American Society of Mechanical Engineers, 345 East 47th Street, New York, NY 10017. Second class postage paid at New York, NY and additional mailing offices. POSTMASTER: Send address changes to Transactions of the ASME, Journal of Heat Transfer, c/o THE AMERICAN SOCIETY OF MECHANICAL ENGINEERS, 22 Law Drive, Box 2300, Fairfield, NJ 07007-2300.
CHANGES OF ADDRESS must be received at Society headquarters seven weeks before they are to be effective. Please send old label and new address.
PRICES: To members, $40.00, annually: to nonmembers, $185.00. Add $30.00 for postage to countries outside the United States and Canada.
STATEMENT from By-Laws. The Society shall not be responsible for statements or opinions advanced in papers or . . . printed in its publications (B7.1, para. 3).

INDEXED by Applied Mechanics Reviews and Engineering Information, Inc.
Canadian Goods & Services Tax Registration #126148048.

Journal of Heat Transfer

Published Quarterly by The American Society of Mechanical Engineers

VOLUME 116 • NUMBER 3 • AUGUST 1994

TECHNICAL PAPERS

Contents (continued)

Invited Review Paper

On the Wave Theory in Heat Conduction

M. N. Özişik
Department of Mechanical and Aerospace Engineering, North Carolina State University, Raleigh, NC 27695

D. Y. Tzou
Department of Mechanical Engineering, The University of New Mexico, Albuquerque, NM 87131
Mem. ASME

This work contains three major components: a thorough review on the research emphasizing engineering applications of the thermal wave theory, special features in thermal wave propagation, and the thermal wave model in relation to the microscopic two-step model. For the sake of convenience, the research works are classified according to their individual emphases. Special features in thermal wave propagation include the sharp wavefront and rate effects, the thermal shock phenomenon, the thermal resonance phenomenon, and reflections and refractions of thermal waves across a material interface. By employing the dual-phase-lag concept, we show that the energy equation may be reduced to that governing the heat transport through the metal lattice in the microscopic two-step model. The dual-phase-lag concept can thus capture the microscopic mechanisms in some limiting cases.

Introduction

An equilibrium state in thermodynamic transition, in reality, needs time to establish. For a physical process occurring in a much shorter time interval than that required for attaining equilibrium, the equilibrium concept becomes an approximate description of the physical process. It is intriguing for simplifying the analysis but may not yield satisfactory results. Fourier's law in heat conduction is an example in hand. When applied to the problem involving reflectivity change resulting from short-pulse laser heating on gold films (Qiu and Tien, 1992), the diffusion theory, assuming an instantaneous response and a quasi-equilibrium thermodynamic transition, predicts a *reversed trend* for the surface reflectivity when compared to the experimental data. The response time in the type of problem is on the order of picoseconds, comparable to the phonon-electron thermal relaxation time. The metal lattice and the hot electron gas simply cannot reach thermodynamic equilibrium in such a short period of time, which is the main cause for the failure of the diffusion theory. The diffusion theory leads to ambiguous results even for simple problems like heat propagation in a semi-infinite, one-dimensional solid. As shown by Baumeister and Hamill (1969, 1971), the heat flux at the driving end needs to be *infinitely* large to maintain a diffusion behavior in the solid. Although Fourier's law may still be sufficiently accurate for engineering problems under regular conditions, the fundamental assumptions behind the model need to be carefully examined when extended to problems involving high-rate change of temperature.

A nonequilibrium description for the thermodynamic transition is the most important issue to be resolved in high-rate heat transfer. Since *heat flux* is a natural consequence for a nonequilibrium state, it has been accommodated in the fundamental state variables defining the irreversibility in thermodynamic transition (Jou et al., 1988; Tzou, 1993a). The entropy (s) in a material volume for example, is a function of internal energy (e), specific volume (v) (tranditional state variables for quasi-equilibrium), and heat flux ($\mathbf{q}$). Mathematically, $s \equiv s(e, v, \mathbf{q})$. Then the resulting entropy production rate has the following form:

$$\Sigma = \mathbf{q} \cdot \left[-\frac{\nabla T}{T^2} - \frac{\beta_T \dot{\mathbf{q}}}{T} \right], \tag{1}$$

with β_T being a positive constant ($\partial s/\partial \mathbf{q} = -\nu\beta_T \mathbf{q}/T$) and T measured in an absolute scale. To guarantee a positive-definite value for Σ, a restriction to be followed for any physically admissible process, a *sufficient* (but not necessary) condition is

$$\left[-\frac{\nabla T}{T^2} - \frac{\beta_T \dot{\mathbf{q}}}{T} \right] = \frac{\mathbf{q}}{A}, \tag{2}$$

with A being positive. The entropy production rate, consequently, is simply $|\mathbf{q}|^2/A$, which is positive definite. Alternately, Eq. (2) can be re-arranged to give

$$\mathbf{q} + \tau \dot{\mathbf{q}} = -k \nabla T, \text{ with } k = \frac{A}{T^2} \text{ and } \tau = \frac{A\beta_T}{T}. \tag{3}$$

The nonequilibrium effect lies in the coefficient of β_T. In the case of $\beta_T = 0$ ($\partial s/\partial \mathbf{q} = 0$), heat flux is dropped from the state variables and Eq. (3) is reduced to Fourier's law of heat conduction. Entropy degenerates into a function of internal energy and specific volume alone and Eq. (1) for the entropy production rate is reduced to the equilibrium version. Note that the $1/T^2$ behavior of thermal conductivity, and hence the $1/T$ behavior of the relaxation time shown in Eq. (3), are special cases resulting from the sufficient but not necessary condition, Eq. (2). Should a more complicated functional relationship be selected in Eq. (2) that also guarantees the positive-definiteness of the entropy production rate, a more complicated functional dependency of the thermal conductivity or the relaxation time on temperature may result. The special result for thermal conductivity derived in Eq. (3), however, corresponds to that for pure metals (Eckert and Drake, 1972).

Accounting for the lagging response in time between the heat flux vector and the temperature gradient, alternatively, Tzou (1992a) provided a macroscopic formulation to describe the nonequilibrium thermodynamic transition. Mathematically, this can be expressed by

$$\mathbf{q}(\mathbf{r}, t+\tau) = -k \nabla T(\mathbf{r}, t), \tag{4}$$

Contributed by the Heat Transfer Division for publication in the JOURNAL OF HEAT TRANSFER. Manuscript received by the Heat Transfer Division October 1993; revision received March 1994. Keywords: Conduction, Reviews, Transient and Unsteady Heat Transfer. Associate Technical Editor: Y. Bayazitoglu.

with τ being the phase-lag in time, an intrinsic thermal property of the medium. Equation (4) shows that the temperature gradient established at time t results in a heat flux vector at a *later* time $t+\tau$ due to insufficient time of response. In combining with the energy equation,

$$-\nabla\cdot\mathbf{q}(\mathbf{r},\ t)+S(\mathbf{r},\ t)=C_p\frac{\partial T(\mathbf{r},\ t)}{\partial t}, \tag{5}$$

the physical quantities involved in Eq. (4) must be at the same instant of time. For this purpose, Taylor's series expansion is applied to Eq. (4) with respect to τ, which gives

$$\mathbf{q}(\mathbf{r},\ t+\tau)=\mathbf{q}(\mathbf{r},\ t)+\tau\frac{\partial\mathbf{q}(\mathbf{r},\ t)}{\partial t}+o(\tau^2)=-k\nabla T(\mathbf{r},\ t). \tag{6}$$

Assuming that the phase-lag in time (τ) is so small that the second and higher order terms can be neglected, Eq. (6) is approximated by

$$\mathbf{q}(\mathbf{r},\ t)+\tau\frac{\partial\mathbf{q}(\mathbf{r},\ t)}{\partial t}\cong-k\nabla T(\mathbf{r},\ t) \tag{7}$$

which is identical to Eq. (3) derived from the nonequilibrium entropy production rate. The phase-lag in time is thus an alternative view for the functional dependence of a physical state on the heat flux vector in nonequilibrium thermodynamic transition.

Eliminating $\mathbf{q}$ from Eqs. (5) and (7), we obtain

$$\nabla\cdot k\nabla T(\mathbf{r},\ t)+\left[S(\mathbf{r},\ t)+\tau\frac{\partial S(\mathbf{r},\ t)}{\partial t}\right]=C_p\left[\frac{\partial T(\mathbf{r},\ t)}{\partial t}+\tau\frac{\partial^2 T(\mathbf{r},\ t)}{\partial t^2}\right]. \tag{8a}$$

For constant thermal conductivity, Eq. (8*a*) is further reduced to

$$\nabla^2 T(\mathbf{r},\ t)+\frac{1}{k}\left[S\ (\mathbf{r},\ t)+\tau\frac{\partial S(\mathbf{r},\ t)}{\partial t}\right]=\frac{1}{\alpha}\left[\frac{\partial T(\mathbf{r},\ t)}{\partial t}+\tau\frac{\partial^2 T(\mathbf{t},\ t)}{\partial t^2}\right]. \tag{8b}$$

where α is the thermal diffusivity. In absence of body heating ($S = 0$). Eq. (8*b*) is the energy equation postulated by Maxwell (1867), Cattaneo (1958), Morse and Feshbach (1953), and Vernotte (1958, 1961). Equation (8*b*) when compared to the diffusion equation, includes a *wave* term represented by $(\tau/\alpha)\ \partial^2 T/\partial t^2$. Approaching from the collision theory of molecules, moreover, Chester (1963) related the ratio of τ/α to the thermal wave speed

$$C^2=\frac{\alpha}{\tau}. \tag{9}$$

A finite value for the thermal wave speed, therefore, is a direct consequence of the lagging response, which is a characteristic in nonequilibrium in thermodynamic transition. Several investigators, including Nettleton (1960), Chester (1963), Maurer (1969), and Francis (1972), made attempts to estimate the magnitude of the *relaxation* parameter τ for engineering materials. It appears that the magnitude of τ ranges from 10^{-10} s for gases at standard conditions to 10^{-14} s for metals, with values of τ for liquids and insulators falling in between. The thermal wave speed in metals, consequently, is on the order of 10^5 m/s from a sole material point of view. This is the threshold value of the Fermi velocity.

In addition to the *apparent* heat source term in Eq. (8), the time-derivative of the real heat source due to the effect of finite speed of heat propagation (Frankel, 1985), another special feature in the modified heat flux law (Eq. (7)) is better envisioned by a direct integration:

$$\mathbf{q}(\mathbf{r},\ t)=-\left(\frac{k}{\tau}\right)\exp\left(-\frac{t}{\tau}\right)\int_0^t\exp\left(\frac{\eta}{\tau}\right)\nabla T(\mathbf{r},\ \eta)d\eta. \tag{10}$$

According to this equation, the heat flux $\mathbf{q}$ at a certain time t depends on the *entire* history of the temperature gradient established from 0 to t. The thermal wave theory, therefore, presents a strong path dependency (Tzou, 1992a) of the temperature gradient rather than the point value (∇T at t) depicted by Fourier's law.

An Overview of the Research

Like other constitutive models in engineering, modifications on Fourier's law are motivated by its deficiencies in advanced applications. Especially in interdisciplinary research areas where not only the temperature but also its gradient and time-rate change are needed as an entirety, a slight ambiguity in heat conduction may result in significant deviations in the coupled field response.

Maxwell's research on the kinetic theory of gases (1867) has had great influence on the development of the thermal wave theory. Morse and Feshbach (1953) hypothesized, and Cattaneo (1958) and Vernotte (1958, 1961) argued for, the instantaneous propagation of thermal signals in solids. A finite

Nomenclature

A = positive constant, WK/m
C = thermal wave speed, m/s
$C_{e,\,l,\,p}$ = volumetric heat capacity, kJ/m^{3}K
G = coupling factor of phonon–electron interactions, W/m^{3}K
f = critical frequency = C^2/α
h = Planck's constant, Js
k = thermal conductivity, W/m K
K = Boltzmann constant, J/K
M = thermal Mach number = v/C
n = number density, 1/m^3
$\mathbf{q}$ = heat flux vector, W/m^2
Q = volumetric laser heat source, W/m^3
r = distance away from the moving heat source or crack tip, m
T = temperature, K
t = physical time, s
S = volumetric heat generation rate, W/m^3
s = entropy, kJ/kg K
v = speed, m/s
α = thermal diffusivity, m^2/s
β = dimensionless time = $C^2t/2\alpha$
δ = dimensional distance = $Cx/2\alpha$
θ = dimensionless temperature = $(T-T_0)/(T_w-T_0)$
ρ = mass density, kg/m^3
Σ = entropy production rate, kJ/kg K s
τ = relaxation time, s
Ω = oscillating frequency of heat source, 1/s
ω = modal frequency, 1/s
∇ = gradient operator

Subscripts and Superscripts

0 = initial value or room temperature
a = atoms
D = Debye temperature
e = electrons
l = metal lattice
M = thermal Mach angle
q = heat flux
s = sound
T = temperature
$\bullet$ = $\partial/\partial t$ = rate change in time
I, II = media I and II

wave speed was suggested on a more physical ground. Since then, the deficiencies in the diffusion model for heat conduction and the need for a wave model accounting for the finite speed of heat propagation have been examined from various physical points of view. They are summarized in the following categories.

1 Molecular Collision Models Established on the Basis of Quantum Mechanical and Statistical Mechanics. Typical research in this category is that by Klemens (1958), Grad (1958), Ziman (1960), Chester (1963), Prohofsky and Krumhansl (1964), Maurer (1969), Bubnov (1976), Berkovsky and Bashtovoi (1977), and Cheng (1989). In this approach, the kinetic Boltzmann transport equation is used to extract macroscopic quantities such as temperature from the distribution of molecules. It characterizes the macrosocpic properties such as thermal diffusivity and thermal wave speed through the velocity and frequency of molecular collisions.

2 The Irreversible and Nonequilibrium Thermodynamics. As expected, the thermodynamic consideration for the wave behavior in heat conduction is a major branch of research. Advances being made include the extensions based on classical Onsager thermodynamics (Nettleton, 1960; Kaliski, 1965; Luikov and Berkovsky, 1974), examinations on the inequality of the nonequilibrium entropy flow (Müller, 1967a; Meixner, 1970; Green and Laws, 1972; Coleman et al., 1982; Lebon et al., 1982), the evolution and stability of thermodynamic equilibrium (Lebon and Casas-Vazquez, 1976; Bhattacharya, 1983; Coleman et al., 1986) and introductions of additional state variables for describing irreversible, thermodynamic transitions (Müller, 1967b; Lambermont and Lebon, 1973; Gyarmati, 1977; Casas-Vazquez et al., 1984; Jou et al., 1988; Ferrer and Jou, 1991, Tzou, 1993a). The special feature of fading memory in the history of thermal wave propagation was intensively discussed by Coleman (1964), Gurtin and Pipkin (1968), Nunziato (1971), and recently by Tzou (1989a, b, 1992a, 1993a) for a more rigorous engineering assessment.

3 Causality Restrictions by the Special Theory of Relativity. The fact that any speed of a moving object, including the thermal wave, must be less than the speed of light was examined by Kelly (1968) for diffusion. By using the covariant form of the Boltzmann transport equation, he showed that a finite value of the thermal diffusivity cannot co-exist with an infinite value of the thermal wave speed based on the same velocity of molecular collisions. A similar argument on the finiteness of the thermal wave speed was made by Van Kampen (1970). Within the mainframe of the relativistic general formulation for heat conduction, the energy equation is far more complicated than the linear theory initiated by Vernotte, Cattaneo, and Morse and Feshbach. Addition of a wave term in the classical diffusion only appears as a special case.

4 Analogy to the Random Walk Process for Discontinuous Diffusion. Goldstein (1951) proposed the random walk model with correlation for diffusion. Treating the diffusion problem in the formalism of the random walk process, Weymann (1967) showed that the infinite propagation velocity in heat conduction results from neglecting the atomistic struture of matters. The modified form of the heat equation accounting for such an effect gives the same hyperbolic equation for temperature waves. Taitel's work (1972) extended the random walk concept and proposed a discrete formulation for incorporating the wave effect. The main purpose is to remove the overshooting phenomenon of temperature upon impingement by the thermal wavefront.

5 Implications From Microscale Heat Transfer. When the characteristic dimension of a medium shrinks to the threshold of the mean free path of phonons, as indicated by Flik and Tien (1990) and Flik et al. (1991), the microscopic behavior of phonon scattering significantly influences the thermal behavior in heat conduction. Majumdar (1993), based on the Boltzmann transport theory, developed an equation of phonon radiative transfer (EPRT), which happens to be of the same form as the equation of radiative transfer (ERT) for participating media. Hence, well-documented mathematical techniques such those of Özişik, (1973) and Siegel and Howell (1982) can be used for their solutions. It is also shown that the hyperbolic heat conduction equation can be derived from EPRT only in the acoustically thick limit. Application of the hyperbolic heat conduction equation to thin-film superconductors was made by Bai and Lavine (1991). Also, as summarized later in this paper, interrelations between the microscopic two-step model (Qiu and Tien, 1992) and the macroscopic thermal wave model with a nonlocal response (Tzou and Özişik, 1992) and a dual-phase-lag (Tzou and Li, 1993a) have been established. For metals, in addition to the macroscopic properties such as thermal conductivity and heat capacity, the thermal wave speed also depends on the microscopic quantities such as the number densities of free electrons and atoms in metal lattice.

6 Thermal Wave Propagation. Since the relaxation behavior is a special response in time, its physical essence has been extensively explored by considering one-dimensional problems in space. Baumeister and Hamill (1969, 1971) studied the temperature wave in a semi-infinite solid subjected to a suddenly applied temperature at the wall. Fauske (1973) and Kazimi and Erdman (1975) investigated the interface temperature for two suddenly contacting media. Maurer and Thompson (1973) emphasized the importance of the wave effect in response to a high heat flux irradiation. Chen (1969), Amos and Chen (1970), and Bogy and Naghdi (1970) studied the rate-dependent response in temperature waves. The effect of time-rate change of the thermal wave speed was incorporated in the model by Luikov et al. (1976). The temperature wave across thin-film media was studied by Letcher (1969) and Kao (1977). Wiggert (1977) studied the characteristic lines in thermal wave propagation and Carey and Tsai (1982) made an attempt for the finite difference formulation. Lindsay and Straughan (1976, 1978) considered the same problem as Chen's (1969) but retrieved the nonlinearity omitted in the linearized formulation. Cylindrical waves were considered by Wilhelm and Choi (1975) in metals. The finite signal speed in heat propagation was shown admissible within the general E^3 invariant constitutive equation for energy flux by DeFacio (1975). Joseph and Preziosi (1989, 1990) introduced notions of an effective thermal conductivity and an effective heat capacity to interpret the relaxation behavior of heat and energy. The research by Özişik and his colleagues (Vick and Özişik, 1983; Özişik, and Vick, 1984) predicts the growth and decay of a thermal pulse in one-dimensional solid. The temperature ripple propagating with a finite speed has finite height and width, which is similar to that observed experimentally by Bertman and Sandiford (1970). Penetration and reflection of thermal waves by interfaces in composite media were studied (Frankel et al., 1986, 1987). Also, Frankel et al. (1985) demonstrated that the flux-formulation in the thermal wave theory is more convenient to use for problems involving flux-special boundary conditions. The effect of temperature-dependent thermal conductivity on the propagation of thermal waves was studied for a semi-infinite region $0 \leq x \leq \infty$ under different boundary conditions at $x = 0$ as well as for a pulsed energy source by Glass et al. (1986). The propagation of thermal waves in an absorbing and emitting medium was also studied (Glass et al., 1987b). The non-Fourier response of a solid subjected to an oscillatory surface flux corresponds to the practical situation of irradiation of a solid by a pulse laser. Results show that non-Fourier effect is quite significant (Human, 1986; Glass et al., 1987c) and furthermore

the non-Fourier conduction effect can be important even at a "long time" after the initial transient if the thermal disturbance is oscillatory with the period of oscillation of the same order of magnitude as the thermal relaxation time (Yuen and Lee, 1989). The Stefan problem with a moving boundary and in thermal wave formulation was analyzed by Sadd and Didlake (1977), DeSocio and Gualtieri (1983), Showalter and Walkington (1987), and Glass et al. (1987a, 1990). A two-dimensional hyperbolic heat conduction due to axisymmetric continous or pulsed surface heat sources was studied by Kim et al. (1990). The thermal wave characteristics in multidimensional media were initiated by Tzou. The thermal shock formation around a fast-moving heat source (Tzou, 1989a, b, 1990c, 1991a) and a rapidly propagating crack tip (Tzou, 1990a, b) provides similar situations to those in the high-speed aerodynamics. Subsonic, transonic, and supersonic temperature waves exist in transition of the thermal Mach number. For the dynamic crack propagation, several salient features in the transonic and supersonic waves have been observed in a recent experiment by Zehnder and Rosakis (1991). The thermal resonance phenomenon under frequency excitations (Tzou, 1991b, c, 1992d, e) simply cannot be depicted by the diffusion behavior in heat conduction.

7 Constitutive Equations for the Thermal Wave Behavior. Constitutions between the heat flux vector and the temperature gradient are another major effort made in the development of the thermal wave theory. Including the rate form of the Jeffreys type and the Guyer and Krumhansl model for second sound propagation in dielectric materials, the articles by Joseph and Preziosi (1989, 1990) provide a thorough review for the broad research made in this direction.

8 The Coupling Behavior. Coupling of the thermal relaxation behavior with the mass and momentum transfer in fluidlike structures has been studied. Typical examples are the works by Choi and Wilhelm (1976) for fully ionized electron-ion in plasma. Lindsay and Straughan (1978) for perfect fluids, and Sieniutycz (1977, 1979, 1981) and Roetman (1975) for mass transport. For deformation in one-dimensional solids, the thermoelastic formulation coupled with the thermal wave effect inlcude the works by Ward and Wilks (1952), Lord and Shulman (1967), Popov (1967), Achenbach (1968), Norwood and Warren (1969), Nayfeh and Nemat-Nasser (1971, 1972a, b), Adnan and Nayfeh (1972), Atkins et al. (1975), Kao (1976), Nayfeh (1977), and Ignaczak (1978). Two-dimensional problems with emphasis on the effects of thermal shock waves were advanced by Tzou (1989c, d, 1992a, b) and Tzou and Li (1993b, c).

Special Features in Thermal Wave Propagation

A general criterion for the dominance of wave behavior over diffusion was proposed by Tzou (1989a, b, 1992a):

$$\frac{\partial T}{\partial t} >> \left(\frac{T_0 C^2}{2\alpha} \exp\left(\frac{C^2 t}{\alpha}\right)\right) \tag{11}$$

with T_0 being the reference temperature. This criterion includes the combined effect of thermal properties (α and C), the thermal loading and response conditions ($\partial T/\partial t$ and T_0) and the transient time (t) in the physical process. For heat transfer occurring in an extremely short period of time (small value of t) or that with an extremely high rate of temperature increase (large value of $\partial T/\partial t$), the wave behavior may become pronounced regardless of the value of T_0. In this section we summarize the existing solutions to distinguish the nonequilibrium (predicted by the wave theory) from the equilibrium (predicted by the diffusion model) temperatures. The differences between the two models, indeed, reveal the physical phenomena to be expected should the temperature rate continue to increase in real applications.

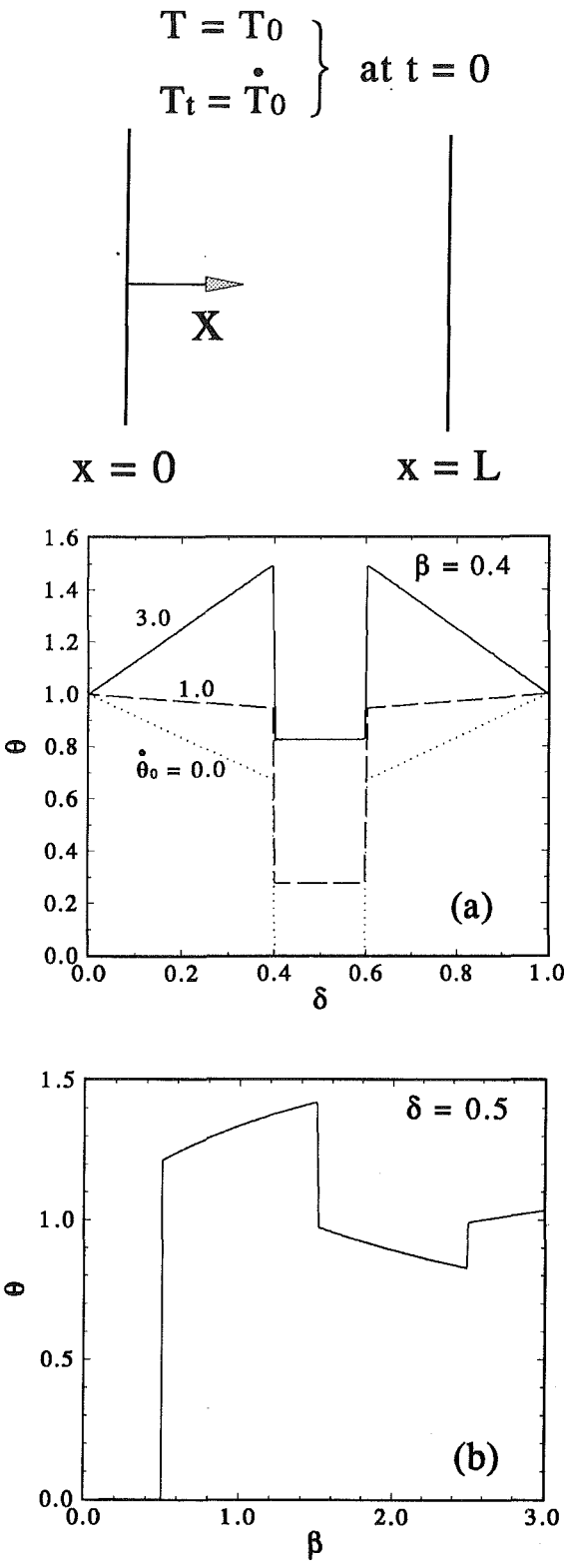

Fig. 1 Thermal waves propagating in a one-dimensional solid bounded by $x = 0$ and L: (*a*) effect of initial temperature rate on the thermal wave patterns at $\beta = 0.4$; (*b*) temperature response at the middle point of the solid ($\delta = 0.5$) for $0 < \beta < 3$. Dimensionless variables: $\delta = Cx/2\alpha$, $\beta = Ct^2/2\alpha$, $\theta = (T - T_0)/(T_w - T_0)$, and $\dot{\theta}_0 = 2\alpha \dot{T}_0/C^2(T_w - T_0)$.

(*a*) **Sharp Wavefront and Rate Effect.** A sharp wavefront is a special feature in thermal wave propagation. Figure 1 illustrates this behavior by considering a one-dimensional medium carrying two thermal waves emanating from the boundaries at $x = 0$ and L. The sharp wavefront is located at $x =$

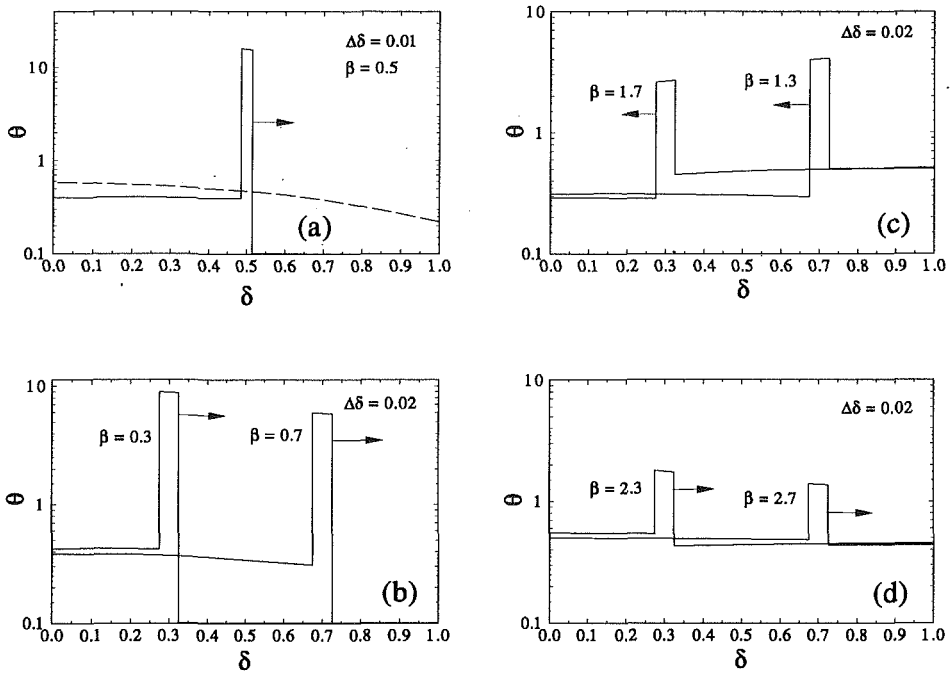

Fig. 2 Propagation of wave packets resulting from an energy pulse with a finite width: (*a*) case with $\Delta\delta$ = 0.01 at β = 0.5. Transmitted and reflected patterns at (*b*) β = 0.3 and 0.7, (*c*) β = 1.3 and 1.7, and (*d*) β = 2.3 and 2.7. $\Delta\delta = C(\Delta d)/2\alpha$ with Δd being the width of the energy pulse.

Ct or $\delta = \beta$. For $\beta = 0.4$, a representative instant of time, the two wavefronts are located at $\delta = 0.4$ (emanating from the left wall) and $\delta = 0.6$ (from the right wall). The dotted curve with a zero initial rate of temperature ($\dot{\theta}_0$) is Taitel's solution (1972). When the temperature rate increases, the temperature level increases and may exceed the wall temperature as exemplified by the curve with $\dot{\theta}_0 = 3$ as shown in Fig. 1(*a*). The two wavefronts meet at the middle point at $\delta = \beta = 0.5$. Impingement of two wavefronts induces a high temperature rate $\dot{\theta}$ of approximately 42. Owing to such high-rate heating, temperature (θ) at the middle point shoots up to 1.2 at β = 0.5 as shown by Fig. 1(*b*). Since then the two wavefronts travel back and forth in the solid and meet subsequently at β = 1.5, 2.5, etc. The temperature rate changes sign at β = 1.5 to negative (cooling) and switches to heating again at β = 2.5. The overall shooting behavior to temperature argued by Taitel, indeed, results from the effect of temperature rate, which is admissible within the framework of the thermal wave model. Such a rate effect is pertinent to the wave theory because the diffusion model cannot allow a specification on the time rate change of temperature.

Wave packets resulting from a finite-width pulse were studied by Vick and Özişik (1983). The finite width of a pulse induces a more localized temperature with a large gradient in the neighborhood of the thermal wavefront, as shown by Fig. 2(*a*) for $\Delta\delta$ = 0.01. This localized phenomenon in heat propagation was observed in the experiment by Peshkov (1944), which cannot be pictured by diffusion. For a wider energy pulse with $\Delta\delta$ = 0.02 (Özişik and Vick, 1984), Figs. 2(*b*) to 2(*d*) show the continuous patterns of transmitting and reflected thermal waves between the two boundaries at δ = 0 and 1. The arrows represent the directions of wave propagation at different instants of time. Intensity of the thermal wave decays due to the effect of diffusion.

(*b*) Thermal Shock Formation. The thermal energy tends to accumulate in a *preferential* direction around a rapidly moving heat source (Tzou, 1989a, b). Characterizing by the thermal Mach number M ($= v/C$), temperature contours surrounding the heat source are shown by Figs. 3(*b*) (for diffusion with $C \to \infty$ and M $\to$ 0) to 3(*e*) for M = 2. The heat source is located at (0, 0), origin of the material coordinates (X_1, X_2). While temperature contours in the subsonic region (M = 0.5 in Fig. 3(*c*)) bear some resemblance to those in diffusion (Fig. 3(*b*)), normal and oblique *shock* waves, respectively, exist at the transonic (M = 1, Fig. 3(*d*)) and in the supersonic (M = 2, Fig. 3(*e*)) region. For M $\geq$ 1, the shock surface is located at at angle of $\theta_M = \sin^{-1}(1/M)$ measuring from the trailing edge of the heat source. For M = 2, for example, the thermal shock angle is 30 deg. When the shock surface is approached from the heat affected zone, as shown by Fig. 3(*d*) for M = 1, and θ_M = 90 deg and 3(*e*) for M = 2 and θ_M = 30 deg, the isotherms collapse together, which induces a large temperature gradient in the neighborhood of the thermal shock waves. This motivates the research on the thermoelastic failure around an intensified fast-moving energy source (Tzou, 1989d, 1992b).

Thermal shock formation around a rapidly propagating crack tip has a similar structure (Tzou, 1990a, b). The thermal shock angle, for example, is $\sin^{-1}(1/M)$ measuring from the trailing edge of the crack tip. In transition from the heat-affected zone to the thermally undisturbed zone across the shock surface, however, a *finite* jump of temperature of $4(T)_0$ results. At the transonic and in the supersonic regions with M $\geq$ 1, moreover, singularity of the temperature gradient (Tzou, 1991d–f) *vanishes* at the crack tip. Comparisons of transonic and supersonic temperatures waves with experimental observations were summarized in a series of recent papers by Tzou (1992c, f, g).

(*c*) Thermal Resonance. Similar to displacement waves in mechanical vibrations, the wave amplitude of temperature may display a resonance phenomenon under proper conditions. For a one-dimensional solid subjected to the excitation of an externally applied heat source oscillating at a frequency Ω, this spacial behavior has been analytically demonstrated by Tzou (1991b, c, 1992d, e). The resonance frequency of temperature depends on the wave mode being excited. For the wave mode with modal frequency of $\omega = 5f$, $7(f)$, and $10f$, exemplified

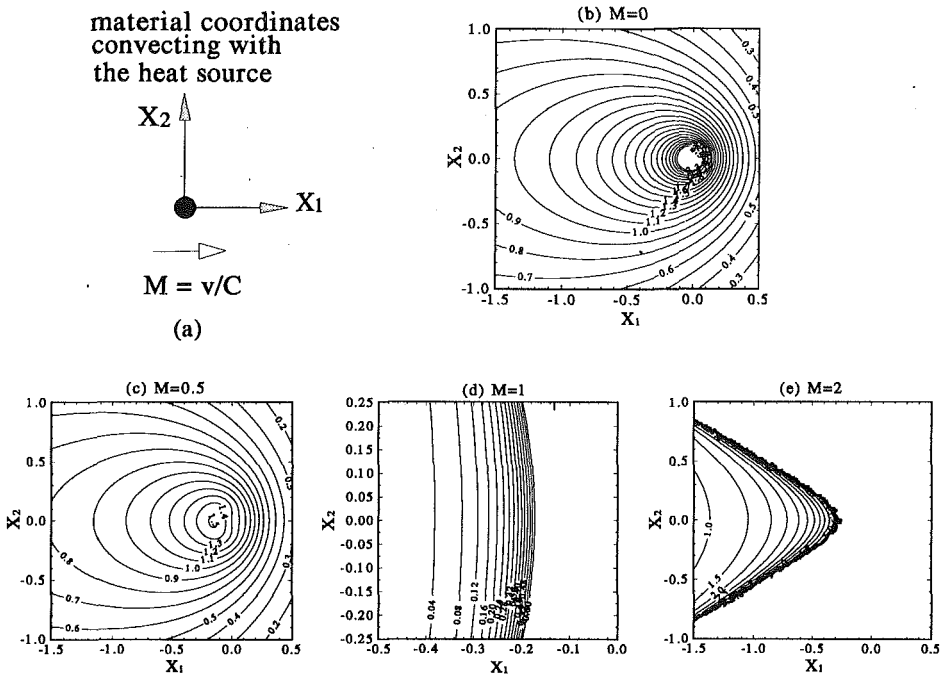

Fig. 3 (*a*) The material coordinates (X_1, X_2) convecting with the heat source. $X_1 = \nu\xi_1/2\alpha$ and $X_2 = \nu\xi_2/2\alpha$ with (ξ_1, ξ_2) being the material coordinates with dimensions. Temperature contour pattern around a moving heat source for (*b*) M = 0 (diffusion theory), (*c*) M = 0.5 (subsonic), (*d*) M = 1 (transonic), and (*e*) M = 2 (supersonic). The heat source is located at (0, 0).

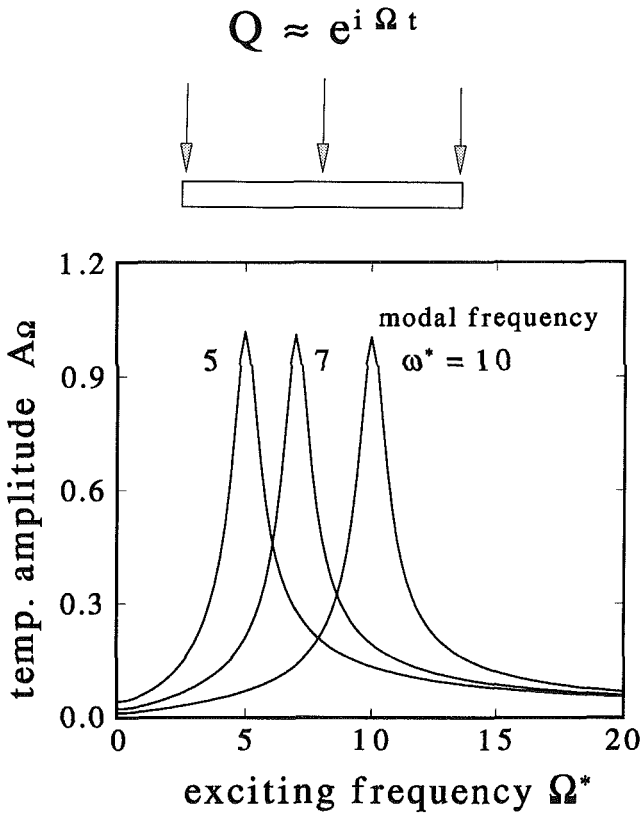

Fig. 4 Thermal resonance in a one-dimensional solid subject to the excitation of an oscillatory body heat source. The resonance curves for $\omega^* = 5$, 7, and 10. $[\omega^*, \Omega^*] = [\omega, \Omega]/f$ with $f = C^2/\alpha$.

respectively in Fig. 4, the amplitudes of temperature waves reach maximum values at particular values of Ω. Unlike the other waves, however, the temperature wave is highly dispersive due to the effect of diffusion. Only the wave mode with a modal frequency larger than the critical value of $0.64359f$ can be excited to resonate. The wave modes lower than this critical mode consume all the externally supplied energy by diffusion and no resonance could occur. Should the resonance phenomenon be produced in the laboratory and the resonance frequency be measured experimentally, most importantly, the thermal wave speed can be calculated analytically. Since such a frequency approach does not rely on the fast response of thermal devices recording arrival of the thermal wavefront, it could be used as an alternative in determining the thermal wave speed for engineering materials.

(*d*) Reflection, Refraction and Transmission of Thermal Waves. Wave behavior may disappear when transmitting across an interface between dissimilar materials (Tzou, 1993b). For a thermal shock wave emanating from a rapidly moving heat source in medium II, as shown in Fig. 5, the wave behavior can be retained only in the shaded area where $M^{(II)2} - M^{(I)2} < 1$. $M^{(I)}$ and $M^{(II)}$ here, respectively, refer to the thermal Mach number in medium I and medium II. Mathematically, $M^{(i)} = \nu/C^{(i)}$ for i = I, II. This condition implies that $C^{(I)}$ (the thermal wave speed in medium (I)) must be greater than $C^{(II)}$ (the thermal wave speed in medium (II)) to maintain the wave behavior after refraction. The thermal energy transmitted to the interface from medium II, in other words, must be carried away at a faster rate in medium I otherwise diffusion would take place as a result of energy accumulation.

Interrelations With the Microscopic Two-Step Model

When the response time becomes extremely short, say comparable to the phonon-electron relaxation time, heat transfer through the microstructures must be taken into account. The microscopic two-step model (Anisimov et al., 1974; Fujimoto et al., 1984; Brorson et al., 1987, 1990; Elsayed-Ali et al., 1987; Elsayed-Ali, 1991; Qiu and Tien, 1992), for example, considers the excitation of electron gas and the metal-lattice heating by phonon-electron interactions as a two-step process. The two processes are coupled through the phonon-electron coupling factor. Mathematically, they are described by

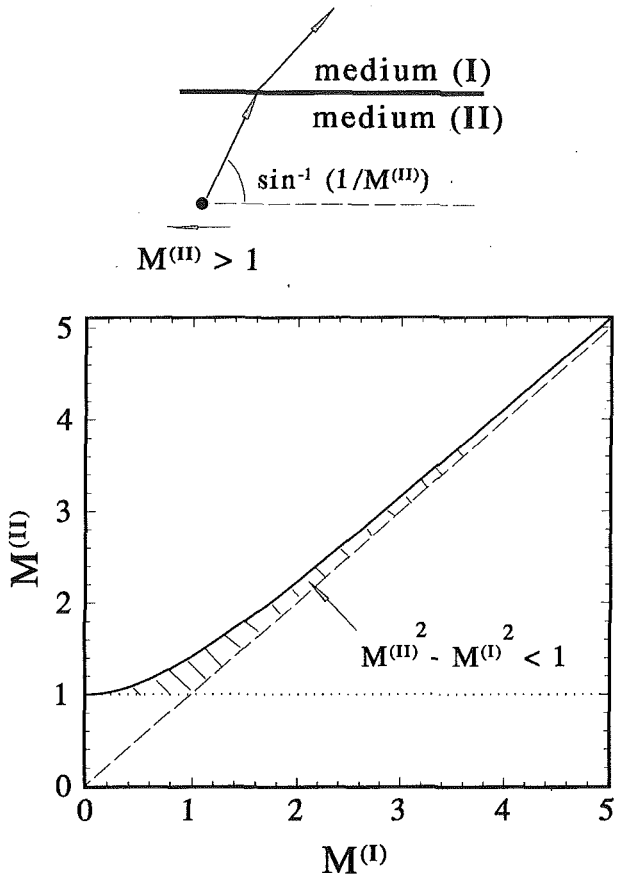

Fig. 5 Penetration of thermal shock waves through a material interface and retainment of the wave behavior after refraction (the shaded area in the state space of $M^{(I)}$ and $M^{(II)}$)

$$C_e \frac{\partial T_e}{\partial t} = \nabla \cdot (k \nabla T_e) - G(T_e - T_l) \tag{12}$$

$$C_l \frac{\partial T_l}{\partial t} = G(T_e - T_l). \tag{13}$$

Note that diffusion is assumed for heat conduction in the electron gas. The coupling factor G, within the limit of Wiedljemann–Frenz's approximations, is given by (Qiu and Tien, 1992)

$$G = \frac{\pi^4 (n_e \nu_s K)^2}{k} \text{ with } \nu_s = \frac{K}{2\pi h} (6\pi^2 n_a)^{-1/3} T_D. \tag{14}$$

In Eq. (15), ν_s is the speed of sound and h is Planck's constant. Since temperature of the metal lattice is of primary concern to practical engineers, we may eliminate the temperature of the electron gas (T_e) from Eqs. (12) and (13). Assuming constant thermal properties,[1] this results in (Tzou and Li, 1993a)

$$\nabla^2 T_l + \frac{\alpha_e}{C^2} \frac{\partial}{\partial t} (\nabla^2 T_l) = \frac{1}{\alpha} \frac{\partial T_l}{\partial t} + \frac{1}{C^2} \frac{\partial^2 T_l}{\partial t^2} \tag{15}$$

where

$$\alpha = \frac{k}{C_e + C_l} \text{ and } C = \sqrt{\frac{kG}{C_e C_l}} \tag{16}$$

are the *equivalent* thermal diffusivity (α) and thermal wave speed (C). They are expressed in terms of microscopic properties such as the number densities of free electrons and atoms in the metal lattice. In addition to a *wave* term, clearly, the phonon–electron interaction introduces a mixed-derivative term, which *dominates* over the wave behavior and diffusion.

Equation (15) is derived on a microscopic basis, which may be somewhat difficult for practical engineers to follow. An immediate question thus arises: Does a *macroscopic* description exist that correlates to the *microscopic* effect of phonon–electron interactions? Bearing in mind the wave term in Eq. (15), a possible way is to introduce the *dual-phase-lag* concept in the generalized thermal wave theory (Tzou and Li, 1993a):

$$\mathbf{q}(\mathbf{r}, t + \tau_q) = -k \nabla T(\mathbf{r}, t + \tau_T). \tag{17}$$

Expanding Eq. (17) with respect to t and retaining only the first-order terms in $\tau s'$, we have

$$\mathbf{q}(\mathbf{r}, t) + \tau_q \frac{\partial \mathbf{q}(\mathbf{r}, t)}{\partial t} \cong -k \left[\nabla T(\mathbf{r}, t) + \tau_T \frac{\partial}{\partial t} \nabla T(\mathbf{r}, t) \right] \tag{18}$$

It is the corresponding expression to Eq. (7) employing a single phase-lag (τ_q). When combined with Eq. (5) (the energy equation) and eliminating the heat-flux vector $\mathbf{q}$, a single equation results:

$$\nabla^2 T + \tau_T \frac{\partial}{\partial t} (\nabla^2 T) = \frac{1}{\alpha} \frac{\partial T}{\partial t} + \frac{\tau_q}{\alpha} \frac{\partial^2 T}{\partial t^2}. \tag{19}$$

With T representing the macroscopic lattice temperature, a direct comparison of Eqs. (15) and (19) yields

$$\tau_T = \frac{C_l}{G} \text{ and } \tau_q = \frac{1}{G} \left[\frac{1}{C_e} + \frac{1}{C_l} \right]^{-1}. \tag{20}$$

In the absence of body heating and assuming constant thermal properties, therefore, the microscopic two-step model lies within the framework of the generalized thermal wave theory employing the dual-phase-lag concept. More rigorous approaches are currently ongoing to establish a general correlation between the two models. The wave theory employing the concept of nonlocality (Özişik and Tzou, 1992; Tzou and Li, 1993a), for example, is another possibility.

The Experimental Evidence for the Wave Behavior

A rigorous, direct experimental evidence for the thermal wave behavior at room or elevated temperature is not available yet. In detecting the rise time of the surface reflectivity at the back surface of a gold thin film subjected to the irradiation of a short-pulse laser from the front surface, however, the pump-and-probe experimental technique has shown that the average heat-transport velocity of the *electron gas* in pure metals in on the order of 10^6 m/s (Figs. 2 and 3 in the work of Brorson et al., 1987). Since the temperature of the *metal lattice* remains undisturbed in this time frame of picoseconds, the thermal wave speed for heat transport through the metal lattice seems to be *lower than* the threshold value of 10^6 m/s. A precise value for such a *macroscopic* thermal wave speed among the metal lattice, unfortunately, is impossible at this stage due to insufficient information in the existing experimental results emphasizing the two-step process of heat transport. It is informative, however, that the impurities existing among the metal lattices would further slow down the thermal wave speed.

Short-pulse laser processing on thin-film structures reveals another possibility for the activation of the thermal wave behavior under regular conditions. For a protecting layer coated onto the surface of a silicon steel sheet (Li, 1992; Li et al., 1993) subject to the irradiation of a laser beam with pulse duration of 100 ns, for example, the early surface burn-out and the *one-third-of-thickness* thermal penetration depth are two special features observed in their experiment. According to the diffusion theory, however, the surface temperature is far lower than the melting temperature of the coating layer,

[1] Heat capacity of the electron gas increases with temperature in reality. A constant value is assumed here for establishing the interrelations with the generalized thermal wave theory in the simplest case.

while the thermal penetration depth predicted by diffusion is approximately 0.7 percent of the thickness. These results significantly contradict those observed experimentally. Employing the thermal wave theory, on the other hand, the surface temperature is on the order of 10^2 to 10^3°C for the transient response in microseconds, which explains the observed phenomenon of early surface burn-out. The qualitative, one-dimensional analysis (Li et al., 1993) also showed that the reflection and transmission of thermal waves across the interface between the coating layer and the silicon steel substrate is the main cause for the much deeper penetration depth.

Conclusion

Transition from diffusion to wave behavior in heat conduction involves more than a simple switch from a parabolic to a hyperbolic equation. The nonequilibrium temperature resulting from the phase-lag effect (thermal relaxation behavior) has many salient features that the diffusion model assuming equilibrium cannot describe. The sharp wavefront in thermal wave propagation, the thermal shock formation, and the temperature resonance under frequency excitations, for example, are pertinent to the wave theory. The traditional thermal wave model is believed to be suitable for capturing small-scale response in time. Through the correlation to the microscopic two-step model, Eqs. (15), (16), (19), and (20), we see that the dual-phase-lag concept in Eq. (17) or (18) might capture some small-scale response in *space* as well. While high-rate heating gradually becomes a major concern in modern industries, this finding is fairly encouraging for the continuous development of such a generalized phase-lag concept. At this point, unfortunately, there exists no precise criterion dictating which model should be intrigued under what time rate of temperature increase. Roughly speaking in the time frame, it seems that diffusion behavior comes first, the wave behavior follows and then the phonon–electron interaction comes into the picture should the response time continuously decrease. In the absence of a quantitative criterion, various research emphasizing different aspects of the thermal wave behavior is to reveal the physical phenomena to be expected should the heating-rate continue to increase.

Within the framework of the thermal wave theory, full expansions into the nonlinear regimes of τ (refer to Eqs. (7) and (18)) are possible. However, it is our opinion that finding the engineering environment in which the thermal wave behavior is illuminative by the linear theory and searching for more experimental evidences for the wave behavior in heat conduction are the two most important challenges to the researchers in the field. A significant breakthrough, for example, would be the establishment of an engineering table for the thermal wave speed in engineering materials. The resonance frequency in relation to the thermal wave speed and the thermal shock angle in relation to the permanent damage induced in solids reflect this attempt well.

References

Achenbach, J. D., 1968, "The Influence of Heat Conduction on Propagation of Stress Jumps," *Journal of Mechanics and the Physics of Solids*, Vol. 16, pp. 273–282.

Adnan, H., and Nayfeh, H., 1972, "Transient Thermo-Elastic Waves in a Half-Space With Thermal Relaxation," *Journal of Applied Mathematics and Physics*, Vol. 23, pp. 50–67.

Amos, D. E., and Chen, P. J., 1970, "Transient Heat Conduction With Finite Wave Speeds," ASME JOURNAL OF HEAT TRANSFER, Vol. 37, pp. 1145–1146.

Anisimov, S. I., Kapeliovich, B. L., and Perel'man, T. L., 1974, "Electron Emission From Metal Surfaces Exposed to Ultra-short Laser Pulses," *Soviet Physics JETP*, Vol. 39, pp. 375–377.

Atklins, R. J., Fox, N., and Vasey, M. W., 1975, "A Continuum Approach to the Second-Sound Effect," *Journal of Elasticity*, Vol. 5, pp. 237–248.

Bai, C., and Lavine, A. S., 1991, "Hyperbolic Heat Conduction in a Superconducting Film," presented at the ASME/JSME Thermal Engineering Joint Conference, Reno, NV.

Baumeister, K. J., and Hamill, T. D., 1969, "Hyperbolic Heat Conduction Equation—A Solution for the Semi-infinite Body Problem," ASME JOURNAL OF HEAT TRANSFER, Vol. 91, pp. 543–548.

Baumeister, K. J., and Hamill, T. D., 1971, "Hyberbolic Heat Conduction Equation—A Solution for the Semi-Infinite Body Problem," ASME JOURNAL OF HEAT TRANSFER, Vol. 93, pp. 126–128.

Berkovsky, B. M., and Bashtovoi, V. G., 1977, "The Finite Velocity of Heat Propagation From the Viewpoint of Kinetic Theory," *International Journal of Heat and Mass Transfer*, Vol. 20, pp. 621–626.

Bertman, B., and Sandiford, D. J., 1970, "Second Sound in Solid Helium," *Scientific American*, Vol. 222, pp. 92–101.

Bhattacharya, D. K., 1983, "On the Problem of Evolution Criterion for Thermodynamical Waves," *Acta Mechanica*, Vol. 47, pp. 87–94.

Bogy, D. B., and Naghdi, P. M., 1970, "On Heat Conduction and Wave Propagation in Rigid Solids," *Journal of Mathematical Physics*, Vol. 11, pp. 917–923.

Brorson, S. D., Fuijmoto, J. G., and Ippen, E. P., 1987, "Femtosecond Electron Heat-Transport Dynamics in Thin Gold Film," *Physical Review Letters*, Vol. 59, pp. 1962–1965.

Brorson, S. D., Kazeroonian, A., Moodera, J. S., Face, D. W., Cheng, T. K., Ippen, E. P., Dresselhaus, M. S., Dresselhaus, G., 1990, "Femtosecond Room Temperature Measurement of the Electron-Phonon Coupling Constant in Metallic Superconductors," *Physical Review Letters*, Vol. 64, pp. 2174–2175.

Bubnov, V. A., 1976, "Wave Concepts in the Theory of Heat," *International Journal of Heat and Mass Transfer*, Vol. 19, pp. 175–184.

Carey, G. F., and Tsai, M., 1982, *Journal of Numerical Heat Transfer*, Vol. 5, pp. 309–314.

Casas-Vazquez, J., Jou, D., and Lebon, G., eds., 1984, *Recent Developments in Nonequilibrium Thermodynamics*, Springer, Berlin.

Cattaneo, C., 1958, "A Form of Heat Conduction Equation Which Eliminates the Paradox of Instantaneous Propagation," *Compute Rendus*, Vol. 247, pp. 431–433.

Chen, P. J., 1969, "On the Growth and Decay of Temperature-Rate Waves of Arbitrary Form," *Zeitschrift für Angewandte Mathematik und Physik*, Vol. 20, pp. 448–453.

Cheng, K. J., 1989, "Wave Characteristics of Heat Conduction Using a Discrete Microscopic Model," ASME JOURNAL OF HEAT TRANSFER, Vol. 111, pp. 225–231.

Chester, M., 1963, "Second Sound in Solids," *Physical Review*, Vol. 131, pp 2013–2015.

Choi, S. H., and Wilhelm, H. E., 1976, "Similarity Transformation for Explosions in Two-Components Plasma With Thermal Energy and Heat-Flux Relaxation," *Physical Review A*, Vol. 14, pp. 1825–1834.

Coleman, B. D., 1964, "Thermodynamics of Materials With Memory," *Archive for Rational Mechanics and Mechanics*, Vol. 17, pp. 1–46.

Coleman, B. D., Fabrizio, M., and Owen, D. R., 1982, "On the Thermodynamics of Second Sound in Dielectric Crystals," *Archive for Rational Mechanics and Analysis*, Vol. 80, pp. 135–158.

Coleman, B. D., Hrusa, W. J., and Owen, D. R., 1986, "Stability of Equilibrium for a Nonlinear Hyperbolic System Describing Heat Propagation by Second Sound in Solids," *Archive for Rational Mechanics and Analysis*, Vol. 94, pp. 267–289.

DeFacio, B., 1975, "Heat Conduction Model With Finite Signal Speed," *Journal of Mathematical Physics*, Vol. 16, pp. 971–974.

DeSocio, I. M., and Gualtieri, G., 1983, "A Hyperbolic Stefan Problem," *Quarterly Journal of Applied Mathematics*, Vol. 41, pp. 253–259.

Eckert, E. R. G., and Drake, R. M., Jr., *Analysis of Heat and Mass Transfer*, McGraw-Hill, New York, p. 59.

Elsayed-Ali, H. E., Norris, T. B., Pessot, M. A., and Mourou, G. A., 1987, "Time-Resolved Observation of Electron-Phonon Relaxation in Copper," *Physical Review Letters*, Vol. 58, pp.1212–1215.

Elsayed-Ali, H. E., 1991, "Femtosecond Thermoreflectivity and Thermotransmissivity of Polycrystalline and Single-Crystalline Gold Films," *Physical Review B*, Vol. 43, pp. 4488–4491.

Fauske, H. K., 1973, "On the Mechanism of Uranium Dioxide Sodium Explosive Interactions," *Journal of Nuclear Science and Engineering*, Vol. 51, pp. 95–101.

Ferrer, M., and Jou, D., 1991, "Higher-Order Fluxes and the Speed of Thermal Waves," *International Journal of Heat and Mass Transfer*, Vol. 34, pp. 3055–3060.

Flik, M. I., and Tien, C. L., 1990, "Size Effect on the Thermal Conductivity of High-T_c Thin-Film Superconductors," ASME JOURNAL OF HEAT TRANSFER, Vol. 112, pp. 872–881.

Flik, M. I., Choi, B. I., and Goodson, K. E., 1991, "Heat Transfer Regimes in Microstroctures," presented at the ASME Winter Annual Meeting, Atlanta, GA.

Francis, H. P., 1972, "Thermo-Mechanical Effects in Elastic Wave Propagation: A Survey," *Journal of Sound and Vibration*, Vol. 21, pp. 181–192.

Frankel, J. I., Vick, B., and Özisik, M. N., 1985, "Flux Formulation of Hyperbolic Heat Conduction," *Journal of Applied Physics*, Vol. 58, pp. 3340–3345.

Frankel, J. I., Vick, B., and Öziski, M. N., 1986, "Hyperbolic Heat Conduction in Composite Regions," presented at the *Eighth International Heat Transfer Conference*, San Francisco, CA.

Frankel, J. I., Vick, B., and Özisik, M. N., 1987, "General Formulation and Analysis of Hyperbolic Heat Conduction in Composite Media," *International Journal of Heat and Mass Transfer*, Vol. 30, pp. 1293–1305.

Fujimoto, J. G., Liu, J. M., and Ippen, E. P., 1984, "Femtosecond Laser Interaction With Metallic Tungsten and Nonequilibrium Electron and Lattice Temperature," *Physical Review Letters*, Vol. 53, pp. 1837–1840.

Glass, D. E., Özişik, M. N., and Vick, B., 1986, "Hyperbolic Heat Conduction With Temperature-Dependent Thermal Conductivity," *Journal of Applied Physics*, Vol. 59, pp. 1881–1885.

Glass, D. E., Özişik, M. N., and Kim, W. S., 1987a, "Formulation and Solution of Hyperbolic Stefan Problem," *Journal of Applied Physics*, Vol. 70, pp. 1190–1197.

Glass, D. E., Özişik, M. N., and McRae, D. S., 1987b, "Hyberbolic Heat Conduction With Radiation in an Absorbing and Emitting Medium," *Numerical Heat Transfer*, Vol. 12, pp. 321–333.

Glass, D. E., Özişik, M. N., and Vick, B., 1987c, "Non-Fourier Effect on Transient Temperature Resulting From On-Off Heat Flux," *International Journal of Heat and Mass Transfer*, Vol. 30, pp. 1623–1631.

Glass, D. E., Özişik, M. N., and Kim, W. S., 1990, "Hyberbolic Stefan Problem With Applied Heat Flux and Temperature Dependent Thermal Conductivity," *Numerical Heat Transfer*, Vol. 18, pp. 503–516.

Goldstein, S., 1951, "On Diffusion by Discontinuous Movements, and on the Telegraph Equations," *Quarterly Journal of Mechanics and Applied Mathematics*, Vol. IV(2), pp. 129–156.

Grad, H., 1958, Kinetic Theory of Gases," in: *Handbuch der Physik*, S. Flügge, ed., Springer-Verlag, Berlin, Vol. XII, p. 271.

Green, A. E., and Laws, N., 1972, "On the Entropy Production Inequality," *Archive for Rational Mechanics and Analysis*, Vol. 45, pp. 47–53.

Gurtin, M. E., and Pipkin, A. C., 1968, "A General Theory of Heat Conduction With Finite Wave Speed," *Archives of the Rational Mechanics and Analysis*, Vol. 31, pp. 113–126.

Gyarmati, I., 1977, "On Wave Approach of Thermodynamics and Some Problems of Nonlinear Theories," *Journal of Nonequilibrium Thermodyanmics*, Vol. 2, pp. 233–267.

Human, M., 1986, "Non-Fourier Heat Transfer in Laser Heated Metal Surfaces," *Heat Transfer: Korea–U. S. A. Seminar*, J. E. Kim et al., eds. pp. 521–533.

Iganczaik, J., 1978, "Domain of Influence Theorem in Linear Themoelasticity," *International Journal of Engineering Science*, Vol. 16, pp. 139–145.

Joseph, D. D., and Preziosi, L., 1989, "Heat Waves," *Reviews of Modern Physics*, Vol. 61, pp. 41–73.

Joseph, D. D., and Preziosi, L., 1990, "Addendum to the Paper on Heat Waves," *Review of Modern Physics*, Vol. 62, pp. 375–391.

Jou, D., Casas-Vázquez, J., and Lebon, G., 1988, "Extended Irreversible Thermodynamics," *Report of the Progress in Physics*, Vol. 51, pp. 1105–1179.

Kaliski, S., 1965, "Wave Equation of Heat Conduction," *Bulletin de l'Academie Polonaise des Sciences, Série des Sciences Techniques*, Vol. XIII, pp. 211–219.

Kao, T. T., 1976, "On Thermally Induced Non-Fourier Stress Waves in a Semi-finite Medium," *AIAA Journal*, Vol. 14, pp. 818–820.

Kao, T. T., 1977, "Non-Fourier Heat Conduction in Thin Surface Layers," ASME JOURNAL OF HEAT TRANSFER, Vol. 99, pp. 343–345.

Kazimi, M. S., and Erdman, C. A., 1975, "On the Interface Temperature of Two Suddenly Contacting Materials," ASME JOURNAL OF HEAT TRANSFER, Vol. 97, pp. 615–617.

Kelly, D. C., 1968, "Diffusion: A Relativistic Appraisal," *American Journal of Physics*, Vol. 36, pp. 585–591.

Kim, W. S., Hector, L. G., and Özişik, M. N., 1990, "Hyperbolic Heat Conduction Due to Axisymmetric Continuous or Pulsed Surface Heat Source," *Journal of Applied Physics*, Vol. 68, pp. 5478–5485.

Klemens, P. G., 1958, "Thermal Conductivity and Lattice Vibrational Modes," in: *Solid State Physics*, F. Seitz and D. Turnbull, eds., Academic Press, New York.

Lambermont, J., and Lebon, G., 1973, "On a Generalization of the Gibbs Equation for Heat Conduction," *Physics Letters*, Vol. 42A, pp. 499–500.

Lebon, G., and Cases-Vazquez, J., 1976, "On the Stability Conditions for Heat Conduction With Finite Wave Speed," *Physics Letters*, Vol. 55A, pp. 393–394.

Lebon, G., and Casas-Vazquez, J., and Jou, D., 1982, "On the Definition of Non-equilibrium Entropy," *Journal of Physics: A Mathematical and General*, Vol. 15, pp. L565–L567.

Letcher, J. S., 1969, "An Improved Theory for Heat Conduction in Thin Layers," ASME JOURNAL OF HEAT TRANSFER, Vol. 91, pp. 585–587.

Li, J. D., 1992, "Reduction of Core Loss in Solicon Steel Sheets by Laser Processing," Ph.D. Dissertation, Tsinghua University, Beijing, People's Republic of China.

Li, J. D., Gu, Y., and Guo, Z., Y., 1993, "The Thermal Wave Phenomena and Analyses in the Pulse-Laser Processing for the Reduction of Core Loss in Silicon Steels," presented at 4th National Conference of Thermophysics, Hongzhou, People's Republic of China [in Chinese].

Lindsay, K. A., and Straughan, B., 1976, "Temperature Waves in a Rigid Heat Conductor," *Journal of Applied Mathematics and Physics*, Vol. 27, pp. 653–662.

Lindsay, K. A., Straughan, B., 1978, "Acceleration Waves and Second Sound in a Perfect Fluid," *Archive for Rational Mechanics and Analysis*, Vol. 68, pp. 53–87.

Lord, H. W., and Shulman, Y., 1967, "A Generalized Dynamical Theory of Thermoelasticity," *Journal of Mechanics and the Physics of Solids*, Vol. 15, pp. 299–309.

Luikov, A. V., and Berkovsky, B. M., 1974, *Convection and Thermal Waves*, Izd. Energiya, Moscow.

Luikov, A. V., Bubnov, V. A., and Soloviev, I. A., 1976, "On Wave Solutions of Heat-Conduction Equation," *International Journal of Heat and Mass Transfer*, Vol. 19, pp. 245–248.

Majumdar, A., 1993, "Microscale Heat Conduction in Dielectric Thin Films," ASME JOURNAL OF HEAT TRANSFER, Vol. 115, pp. 7–16.

Maurer, M. J., 1969, "Relaxation Model for Heat Conduction in Metals," *Journal of Applied Physics*, Vol. 40, pp. 5123–5130.

Maurer, M. J., and Thompson, H. A., 1973, "Non-Fourier Effects at High Heat Flux," ASME JOURNAL OF HEAT TRANSFER, Vol. 95, pp. 284–286.

Maxwell, J. C., 1967, "On the Dynamic Theory of Gases," *Philosophical Transactions London*, Vol. 157, pp. 49–88.

Meixner, J., 1970, "On the Linear Theory of Heat Conduction," *Archive for Rational Mechanics and Analysis*, Vol. 39, pp. 108–130.

Morse, P. M., and Feshbach, H., 1953, *Methods of Theoretical Physics*, Vol. 1, McGraw-Hill, New York.

Müller, I., 1967a, "On the Entropy Inequality," *Archive for Rational Mechanics and Analysis*, Vol. 26, pp. 118–141.

Müller, I., 1967b, "Zum Paradoxn der Wärmeleitungstheorie," *Zeitschrift für Physik*, Vol. 198, pp. 329–344.

Nayfeh, A. H., and Nemat-Nasser, S., 1971, "Thermoelastic Waves in Solids With Thermal Relaxation," *Acta Mechanica*, Vol. 12, pp. 53–69.

Nayfeh, A. H., and Nemat-Nassar, S., 1972a, "Transient Thermoelastic Waves in a Half-Space With Thermal Relaxation," *Journal of Applied Mathematics and Physics*, Vol. 23, pp. 50–67.

Nayfeh, A. H., and Nemat-Nassar, S., 1972b, "Electromagneto-Thermoelastic Plane Waves in Solids With Thermal Relaxation," ASME *Journal of Applied Mechanics*, Vol. 39, pp. 108–113.

Nayfeh, A. H., 1977, "Propagation of Thermoelastic Disturbances in Non-Fourier Solids," *AIAA Journal*, Vol. 15, pp. 957–960.

Nettleton, R. E., 1960, "Relaxation Theory of Thermal Conduction in Liquids," *Physics of Fluids*, Vol. 3, pp. 216–225.

Norwood, F. R., and Warren, W. E., 1969, "Wave Propagation in the Generalized Dynamical Theory of Thermoelasticity," *Quarterly Journal of Mechanics and Applied Mathematics*, Vol. 19, pp. 283–290.

Nunziato, J. W., 1971, "On Heat Conduction in Materials With Memory," *Quarterly Journal of Applied Mathematics*, Vol. XXIX, pp. 187–204.

Özişik, M. N., 1973, *Radiative Transfer and Interactions With Conduction and Convection*, Wiley, New York.

Özişki, M. N., and Vick, B., 1984, "Propagation and Reflection of Thermal Waves in a Finite Medium," *International Journal of Heat and Mass Transfer*, Vol. 27, pp. 1845–1854.

Özişik, M. N., and Tzou, D. Y., 1992, "On the Wave Theory in Heat Conduction," *Fundamental Issues in Small-Scale Heat Transfer*, ASME HTD-Vol. 227, pp. 13–27.

Peshkov, V., 1944, "Second Sound in Helium II," *Journal of Physics, USSR*, Vol. VIII, pp. 381.

Popov, E. B., 1967, "Dynamic Coupled Problem of Thermoelasticity for a Half-Space Taking Into Account of the Finiteness of the Heat Propagation Velocity," *Journal of Applied Mathematics and Mechanics* (*PMM*), Vol. 31, pp. 349–356.

Prohofsky, E. W., and Krumhansl, J. A., 1964, "Second-Sound Propagation in Dielectric Solids," *Physical Review A*, Vol. 133, pp. 1403–1410.

Qiu, T. Q., and Tien, C. L., 1992, "Short-Pulse Laser Heating on Metals," *International Journal of Heat and Mass Transfer*, Vol. 35, pp. 719–726.

Roetman, E. L., 1975, "Heat Conduction With Finite Signal Time," *International Journal of Engineering Science*, Vol. 13, pp. 699–701.

Sadd, M. H., and Didlake, J. E., 1977, "Non-Fourier Melting of a Semi-infinite Solid," ASME JOURNAL OF HEAT TRANSFER, Vol. 99, pp. 25–28.

Showalter, R. E., and Walkington, N. J., 1987, "A Hyperbolic Stefan Problem," Vol. XLV, pp. 769–781.

Siegel, R., and Howell, J. R., 1982, *Thermal Radiation Heat Transfer*, 2nd ed., Hemisphere Publishing Co., New York.

Sieniutycz, S., 1977, "The Variational Principles of Classical Type for Noncoupled Nonstationary Irreversible Transport Processes With Convective Motion and Relaxation," *International Journal of Heat and Mass Transfer*, Vol. 20, pp. 1221–1231.

Sieniutycz, S., 1979, "The Wave Equations for Simultaneous Heat and Mass Transfer in Moving Media—Structure Testing, Time-Space Transformations and Variational Approach," *International Journal of Heat and Mass Transfer*, Vol. 22, pp. 585–599.

Sieniutycz, S., 1981, "The Thermodynamic Stability of Coupled Heat and Mass Transfer Described by Linear Wave Equations," *International Journal of Engineering Science*, Vol. 36, pp. 621–624.

Taitel, Y., 1972, "On the Parabolic, Hyperbolic and Discrete Formulations of the Heat Conduction Equation," *International Journal of Heat and Mass Transfer*, Vol. 15, pp. 369–371.

Tzou, D. Y., 1989b, "Shock Wave Formation Around a Moving Heat Source in a Solid With Finite Speed of Heat Propagation," *International Journal of Heat and Mass Transfer*, Vol. 32, pp. 1979–1987.

Tzou, D. Y., 1989c, "Thermoelastic Fracture Induced by the Thermal Shock Waves Around a Moving Heat Source," *Heat Transfer in Manufacturing and Materials Processing*, ASME HTD-Vol. 113, pp. 11–17.

Tzou, D. Y., 1989d, "The Effects of Thermal Shock Waves on the Crack Initiation Around a Moving Heat Source," *Journal of Engineering Fracture Mechanics*, Vol. 34, pp. 1909–1118.

Tzou, D. Y., 1990a, "Thermal Shock Waves Induced by a Moving Crack," ASME JOURNAL OF HEAT TRANSFER, Vol. 112, pp. 21–27.

Tzou, D. Y., 1990b, "Thermal Shock Waves Induced by a Moving Crack—A Heat Flux Formulation," *International Journal of Heat and Mass Transfer*, Vol. 33, pp. 877–885.

Tzou, D. Y., 1990c, "The-Dimensional Structures of the Thermal Shock Waves Around a Rapidly Moving Heat Source," *International Journal of Engineering Science*, Vol. 28, pp. 1003–1017.

Tzou, D. Y., 1991a, "Thermal Shock Formation in a Three Dimensional Solid Due to a Rapidly Moving Heat Source," ASME JOURNAL OF HEAT TRANSFER, Vol. 113, pp. 242–244.

Tzou, D. Y., 1991b, "The Resonance Phenomenon in Thermal Waves," *International Journal of Engineering Science*, Vol. 29, pp. 1167–1177.

Tzou, D. Y., 1991c, "Resonance of Thermal Waves Under Frequency Excitations," *Fundamental in Conduction*, ASME HTD-Vol. 173, pp. 11–27.

Tzou, D. Y., 1991d, "The Singular Behavior of the Temperature Gradient in the Vicinity of a Macrocrack Tip," *International Journal of Heat and Mass Transfer*, Vol. 33, pp. 2625–2630.

Tzou, D. Y., 1991e, "The Effect of Thermal Conductivity on the Singular Behavior of the Near-Tip Temperature Gradient," ASME JOURNAL OF HEAT TRANSFER, Vol. 113, pp. 806–813.

Tzou, D. Y., 1991f, "On the Use of Node-Shifting Techniques for the Intensity Factor of Temperature Gradient at a Macrocrack Tip," *Journal of Numerical Heat Transfer*, Vol. 19(A), pp. 237–253.

Tzou, D. Y., 1992a, "Thermal Shock Phenomena Under High-Rate Response in Solids," in: *Annual Review of Heat Transfer*, Chang-Lin Tine, ed., Hemisphere Publishing Inc., Washington, DC, Chap. 3, pp. 111–185.

Tzou, D. Y., 1992b, "Fracture Path Emanating From a Rapidly Moving Heat Source—The Effects of Thermal Shock Waves Under High Rate Response," *Journal of Engineering Fracture Mechanics*, Vol. 41, pp. 111–125.

Tzou, D. Y., 1992c, "An Experimental Evidence for the Temperature Waves Around a Rapidly Propagating Crack Tip," ASME JOURNAL OF HEAT TRANSFER, Vol. 114, pp. 1042–1045.

Tzou, D. Y., 1992d, "Thermal Resonance Under Frequency Excitations," ASME JOURNAL OF HEAT TRANSFER, Vol. 114, pp. 310–316.

Tzou, D. Y., 1992e, "Damping and Resonance Phenomena of Thermal Waves," ASME *Journal of Applied Mechanics*, Vol. 59, pp. 862–867.

Tzou, D. Y. 1992f, "The Thermal Shock Phenomena Around a Rapidly Propagating Crack Tip: An Experimental Evidence," *International Journal of Heat and Mass Transfer*, Vol. 35, pp. 2347–2356.

Tzou, D. Y., 1992g, "The Transonic Wave Solution in the Vicinity of a Rapidly Propagating Crack Tip in 4340 Steel," *International Journal of Engineering Science*, Vol. 30, pp. 757–769.

Tzou, D. Y., and Özisik, M. N., 1992, "Interrelations Between the Microscopic Two-Step Model and the Macroscopic Thermal Wave Model," *International Journal of Heat and Mass Transfer*, submitted for publication.

Tzou, D. Y., 1993a, "An Engineering Assessment to the Relaxation Time in Thermal Waves," *International Journal of Heat and Mass Transfer*, Vol. 36, pp. 1845–1851.

Tzou, D. Y., 1993b, "Reflection and Refraction of Thermal Waves From a Surface or an Interface Between Dissimilar Materials," *International Journal of Heat and Mass Transfer*, Vol. 36, pp. 401–410.

Tzou, D. Y., and Li, J., 1993b, "Thermal Waves Emanating From a Fast-Moving Heat Source With a Finite Dimension," ASME JOURNAL OF HEAT TRANSFER, Vol. 115, pp. 526–532.

Tzou, D. Y., and Li, J., 1993c, "Local Heating Induced by a Nonhomogeneously Distributed Heat Source," *International Journal of Heat and Mass Transfer*, Vol. 36, pp. 3487–3496.

Van Kampen, N. G., 1970, "A Model for Relativistic Heat Transfer," *Physica*, Vol. 46, pp. 315–332.

Vernotte, P., 1958, "Les Paradoxes de la Théorie Continue de l'Equation de La Chaleur," *Compute Rendus*, Vol. 246, pp. 3154–3155.

Vernotte, P., 1961, "Some Possible Complications in the Phenomena of Thermal Conduction," *Compute Rendus*, Vol. 252, pp. 2190–2191.

Vick, B., Özisik, M. N., 1983, "Growth and Decay of a Thermal Pulse Predicted by the Hyperbolic Heat Conduction Equation," ASME JOURNAL OF HEAT TRANSFER, Vol. 105, pp. 902–907.

Ward, J. D., and Wilks, J., 1952, "On the Sound and the Thermo-mechanical Effect," *Philosophical Magazine*, Vol. 43, pp. 314–316.

Weymann, H. D., 1967, "Finite Speed of Propagation in Heat Conduction, Diffusion, and Viscous Shear Motion," *American Journal of Physics*, Vol. 35, pp. 488–496.

Wiggert, D. C., 1977, "Analysis of Early-Time Transient Heat Conduction by Method of Characteristics," ASME JOURNAL OF HEAT TRANSFER, Vol. 19, pp. 245–248.

Wilheim, H. E., and Choi, S. H., 1975, "Nonlinear Hyperbolic Theory of Thermal Waves in Metals," *The Journal of Chemical Physics*, Vol. 63, pp. 2119–2123.

Yuen, W. W., and Lee, S. C., 1989, "Non-Fourier Conduction in a Semi-infinite Solid Subject to Oscillatory Surface Thermal Disturbances," ASME JOURNAL OF HEAT TRANSFER, Vol. 111, pp. 178–181.

Zehnder, A. T., and Rosakis, A. J., 1991, "On the Temperature Distribution at the Vicinity of Dynamically Propagation Cracks in 4340 Steel," *Journal of The Mechanics and Physics of Solids*, Vol. 39, pp. 385–415.

Ziman, J. M., 1960, *Electrons and Phonons*, Clarendon Press, Oxford University Press, London, United Kingdom.

Application of a Complex Nusselt Number to Heat Transfer During Compression and Expansion

A. A. Kornhauser
Department of Mechanical Engineering,
Virginia Polytechnic Institute
and State University,
Blacksburg, VA 24061
Mem. ASME

J. L. Smith, Jr.
Department of Mechanical Engineering,
Massachusetts Institute of Technology,
Cambridge, MA 02139
Mem. ASME

Heat transfer during compression and expansion can be out of phase with bulk gas-wall temperature difference. An ordinary convective heat transfer model is incapable of predicting this phenomenon. Expressions for compression/expansion heat transfer developed from simple conduction models use a complex heat transfer coefficient. Thus, heat flux consists of one part proportional to temperature difference plus a second part proportional to rate of change of temperature. Surface-averaged heat flux was calculated from experimental pressure-volume data for piston-cylinder gas springs over a range of speeds, pressures, gases, and geometries. The complex Nusselt number model proved capable of correlating both magnitude and phase of the measured heat transfer as functions of an oscillation Peclet number.

Introduction

An understanding of in-cylinder heat transfer is essential to accurate performance predictions for internal combustion engines, compressors, and other reciprocating machines. These heat transfer processes have been studied since the 1920s, and the complexity and sophistication of their modeling has steadily increased. Modern heat transfer models account for many details of fluid motion, flame propagation, and cylinder geometry. Almost all models, however, base the convective part of the heat transfer on Newton's law of convection, which states that heat flux is proportional to bulk gas-wall temperature difference. What is often overlooked is that Newton's law is an engineering approximation, good for typical convective heat transfer situations where the temperature gradient at the wall is proportional to the bulk gas-wall temperature difference.

During compression and expansion this proportionality no longer holds. An example is easy to visualize: When an engine piston is at top center position the center gas is very hot, while the gas in the boundary layer is cooled to near wall temperature. As the piston moves down, work is extracted from all the gas, including the boundary layer gas. Early in the expansion the center gas is still much hotter than the wall, while the gas in the boundary layer is cooler than the wall. The temperature gradient at the wall is in the opposite direction from the bulk gas-wall temperature difference. Similar apparent anomalies occur elsewhere in the cycle.

Measurements of heat transfer out of phase with the bulk gas-wall temperature difference are evidence of this behavior. As a consequence of this phase shift, the conventional Nusselt number assumes zero, negative, and infinite values. Such experimental results have been known for more than 25 years, but they have been largely ignored. All widely used in-cylinder heat transfer models assume that heat transfer follows Newton's law.

One possible reason that this flaw in Newton's law has been ignored is that there has been no adequate alternate formulation. This paper describes an extension of the law that allows modeling of phase shift between heat transfer and bulk gas-wall temperature difference.

Contributed by the Heat Transfer Division, this paper is a revised version of one presented as part of the International Symposium on Flows in Reciprocating IC Engines at the ASME Winter Annual Meeting, Chicago, Illinois, Nov. 28–Dec. 2, 1989. Manuscript received by the Heat Transfer Division October 1992; revision received November 1993. Keywords: Transient and Unsteady Heat Transfer. Associate Technical Editor: R. J. Simoneau.

Background

As far as the authors are aware, the first attempt to address this problem was the theoretical work of Pfriem (1943). Pfriem modeled the cylinder space with a one-dimensional energy equation in which convection was neglected:

$$\frac{\partial T}{\partial t} = \alpha \frac{\partial^2 T}{\partial x^2} + \frac{1}{\rho c_p} \frac{\partial p}{\partial t} \tag{1}$$

The equation was solved with the distance between walls constant and α constant (i.e., density variations neglected) for a sinusoidal pressure variation. In order to account for the effects of turbulent convection, the space was divided into two regions: a boundary layer near the wall where convection was entirely neglected and a turbulent core where mixing was assumed to result in uniform temperature. The method of complex temperature, often used in periodic conduction problems, was used to solve the equation. The driving function was a complex pressure rather than a complex temperature or heat flux. The result was an expression for a complex heat transfer coefficient, the ratio of complex heat flux to complex temperature difference:

$$\mathrm{Nu}_c = D_h \psi \frac{1 - e^{-2\delta\psi} + s\psi(1 + e^{-2\delta\psi})}{(1 - e^{-\delta\psi})^2 + s\psi(1 - e^{-2\delta\psi})}, \tag{2}$$

where

Nu_c = complex Nusselt number based on D_h
δ = laminar boundary layer thickness
s = volume/area (1/4 D_h) turbulent core
ψ = $(1+i)\sqrt{2\mathrm{Pe}_\omega}/D_h$
Pe_ω = oscillation Peclet number = $\omega D_h^2/4\alpha$.

This complex Nusselt number was based on the difference between the wall temperature and the turbulent core temperature rather than gas mixed mean temperature.

Pfriem's analysis predicted that at small Pe_ω heat transfer would be in phase with bulk gas-wall temperature difference, while at large Pe_ω it would lead that temperature difference by 45 deg. At large Pe_ω the real and imaginary parts of Nu_c were equal and proportional to $\mathrm{Pe}_\omega^{1/2}$. No experimental data were presented to support the analysis, and the use of Nu_c in predicting in-cylinder heat transfer was not made clear.

Overbye et al. (1961) presented results of surface thermocouple heat flux measurements on fired and unfired spark-ignition engines. These tests confirmed Pfriem's prediction that heat transfer would be out of phase with bulk gas-wall temperature difference. Ordinary heat transfer coefficient took on

zero, negative, and infinite values. In order to explain these findings, Newton's law was abandoned. Heat flux was correlated as a function of gas properties, pressure, velocity, geometry, and intake manifold conditions. It was shown that the resulting expression could not be reduced to the form of Newton's law.

Wendland (1968) made surface thermocouple heat flux measurements in a gas spring apparatus. These results, too, showed heat transfer phase shift and the inapplicability of Newton's law. The system was modeled by solving a one-dimensional energy equation similar to Eq. (1) numerically, omitting turbulent convection but including the density and position variations that Pfriem had neglected. The resulting computer program qualitatively predicted Wendland's experimental results as well as those of Overbye et al.

Annand and Pinfold (1980) reported surface thermocouple heat flux measurements in a motored compression-ignition engine. Heat transfer was found to be out of phase with bulk gas-wall temperature difference. Newton's law was not abandoned, but rather was modified by correlating Nu not only as a function of Re, but as a function of ΔT and dT/dt as well. The result was

$$\mathrm{Nu} = 0.3\ \mathrm{Re}^{0.7}\left(1 + 0.27\,\frac{D}{v\Delta T}\,\frac{dT}{dt}\right). \tag{3}$$

Here v was the local instantaneous velocity and Re was based on v. The diameter used in the expression and in the nondimensional variables was cylinder diameter. The correlation did not very accurately predict the observed data over the full range of conditions, but it did predict the phase shift effect.

Lee (1983) published the result of an analysis similar to that of Pfriem. He solved Eq. (1) with the same simplifying assumptions, but proposed that turbulence be modeled by using a turbulent thermal diffusivity in Pe_ω. The resulting complex Nusselt number was

$$\mathrm{Nu}_c = \sqrt{2\mathrm{Pe}_\omega}\,\frac{(1+i)\tanh z}{1-\tanh z/z}, \tag{4}$$

where

$$z = (1+i)\sqrt{\mathrm{Pe}_\omega/8}$$

This Nu, unlike Pfriem's, was based on the difference between wall temperature and gas mixed mean temperature. As in Pfriem's study, heat transfer was found to lead bulk gas-wall temperature difference by 45 deg at high Pe_ω. The result was used to predict heat transfer related hysteresis loss for a gas spring, but its application to prediction of instantaneous heat transfer was not explained.

The authors (Kornhauser and Smith, 1987) made measurements of gas-spring hysteresis loss and used the results to compare in-cylinder heat transfer expressions. While numerical solutions based on Newton's law correlations did not match the data, the expression developed by Lee predicted most results well. The success of Lee's expression in predicting hysteresis loss led to an interest in how a complex heat transfer expression could be applied. The upshot was this study.

Application of the Complex Nusselt Number

Newton's law of convection may be written with complex temperature, heat transfer, and Nusselt number:

$$\dot{q}_c'' = \frac{k}{D_h}\,\mathrm{Nu}_c\,(T_c - T_w)$$

$$= \frac{k}{D_h}\,(\mathrm{Nu}_r + i\,\mathrm{Nu}_i)\,[\Re(T_c - T_w) + i\Im(T_c - T_w)] \tag{5}$$

Here the wall temperature is assumed constant, so it has no imaginary part. The real part of the heat transfer is

$$\Re(\dot{q}_c'') = \frac{k}{D_h}\,\{\mathrm{Nu}_r[\Re(T_c) - T_w] - \mathrm{Nu}_i\Im(T_c)\}. \tag{6}$$

For a sinusoidal temperature variation about a constant temperature T_0:

$$T_c = \Re(T_c) + i\Im(T_c) = T_0 + T_a\cos\omega t + iT_a\sin\omega t, \tag{7}$$

and

$$\frac{dT_c}{dt} = -\omega T_a\sin\omega t + i\omega T_a\cos\omega t. \tag{8}$$

Thus

$$\Im(T_c) = -\frac{1}{\omega}\,\Re\left(\frac{dT_c}{dt}\right) = -\frac{1}{\omega}\,\frac{d\Re(T_c)}{dt}, \tag{9}$$

$$\dot{q}'' \equiv \Re(\dot{q}_c'') = \frac{k}{D_h}\left\{\mathrm{Nu}_r[\Re(T_c) - T_w] + \frac{\mathrm{Nu}_i}{\omega}\,\frac{d\Re(T_c)}{dt}\right\}, \tag{10}$$

and

$$\dot{q}'' = \frac{k}{D_h}\left[\mathrm{Nu}_r\,(T - T_w) + \frac{\mathrm{Nu}_i}{\omega}\,\frac{dT}{dt}\right], \tag{11}$$

where $T = \Re(T_c)$.

Considering that compression and expansion do work directly on the fluid in contact with the wall, it is reasonable

Nomenclature

C_p = specific heat at constant pressure
D = cylinder diameter
D_h = hydraulic diameter $= 4 \times$ volume/area
$\Im(\,)$ = imaginary part of complex number
i = $\sqrt{-1}$
k = thermal conductivity
L = stroke
Nu = Nusselt number based on cylinder diameter
Nu_c = complex Nusselt number based on hydraulic diameter
Nu_i = imaginary part of complex Nusselt number
Nu_r = real part of complex Nusselt number
p = pressure
Pe_ω = oscillation Peclet number $= \omega D_h^2/4\alpha$
q'' = heat flux
$\dot{q}_c''$ = complex heat flux
r_v = volume ratio = maximum volume/minimum volume
$\Re(\,)$ = real part of complex number
Re = Reynolds number = $\rho v D/\mu$
s = volume/area turbulent core in Pfriem theory
T = mixed mean gas temperature
T_a = amplitude of sinusoidal temperature variation
T_c = mixed mean complex gas temperature
T_o = mean of sinusoidal temperature variation
T_w = wall temperature
ΔT = $T - T_w$
t = time
v = velocity
x = distance from wall
z = $(1+i)(\mathrm{Pe}_\omega/8)^{1/2}$
α = thermal diffusivity
δ = laminar boundary layer thickness
μ = absolute viscosity
ρ = density
σ = standard deviation
ψ = $(1+i)(2\mathrm{Pe}_\omega)^{1/2}/D_h$
ω = angular velocity

that the heat flux should be a function of rate of change of temperature as well as temperature difference. Since a complex number can be specified either by real part and imaginary part or by magnitude and phase, this formulation should be capable of describing heat transfer out of phase with bulk gas-wall temperature difference.

This heat transfer formulation was developed from conduction theory, but it is consistent with the semi-empirical convective model of Annand and Pinfold, which can be put in the form

$$\dot{q}'' = 0.3 \frac{k}{D} \mathrm{Re}^{0.7}(T - T_w) + 0.081 \frac{k}{v} \mathrm{Re}^{0.7} \frac{dT}{dt}. \qquad (12)$$

It would not make sense to suppose that heat transfer in a highly turbulent fluid could be predicted from a pure conduction model. It may be, however, that the complex Nusselt number model will provide a better means of correlating experimental data on heat transfer during compression and expansion than the ordinary Newton's law model.

Description of Experiments

The apparatus used in these experiments was a modification and extension of that used by the authors previously (Kornhauser and Smith, 1987, 1993). The apparatus was constructed by building a gas-spring test section on top of an existing compressor base, the cylinder of the compressor acting as a crosshead. The test section consisted of a piston and cylinder with an adjustable flat head. The adjustable head made possible various volume ratios. Two compressor bases, with different strokes, and two test sections, with different bores, were used. By combining the various bases and test sections, different bore/stroke ratios could be obtained.

For some experiments the working space was provided with extended heat transfer surface in the form of evenly spaced, interlocking, concentric fins. Experiments were done with no fins, with one fin (on the piston), with three fins (one on the piston, two on the head), and with seven fins (four on the piston, three on the head). Fin length was such that the fins were almost fully engaged at top center position and slightly disengaged at bottom center position.

Pressure was measured with a semiconductor strain gage pressure transducer mounted essentially flush with the cylinder head. Volume was calculated from the crank angle signal provided by a 1200 count-per-turn optical encoder. During each cycle 150 pressure-volume data points were collected.

Measurements were recorded as soon after apparatus startup as both speed and mean pressure became steady. The constant value of cyclic mean pressure indicated that the thermodynamic processes within the gas had reached cyclic equilibrium. The cylinder walls, however, had a much larger thermal time constant than the gas and were therefore still essentially uniformly at ambient temperature. (This was demonstrated by Faulkner (1983) in a similar apparatus equipped with wall thermocouples.)

Instantaneous surface-averaged heat transfer and mixed mean gas temperature were calculated from the pressure, volume, and time data. First, mixed-mean temperature and internal energy were calculated from the data and the gas equation of state. Work was calculated directly from pressure and volume, and heat transfer rate was then calculated from work, internal energy, time, and the first law of thermodynamics. The differentiation necessary to calculate heat transfer was done with a linear least-squares fit over five data points. Although data were collected for three cycles, all calculations were made from single-cycle data rather than from data averaged over the three cycles. Comparison of results for adjacent cycles showed that cycle-to-cycle variations were negligible. For the calculation of Nusselt number, walls and fins were assumed to be at ambient temperature.

Originally the ideal gas equation with constant specific heat was used, but it gave some clearly erroneous results: On certain runs using nitrogen and argon temperature–entropy diagrams of the cycle showed higher entropy at top center than at bottom center. Examination showed that this anomaly was due to the inaccuracy of the ideal gas assumption. A two-coefficient virial equation of state, with constants selected to provide a good fit to tabulated data (Hilsenrath et al., 1960) for the range of experimental conditions, was then used. Specific heat was evaluated from a quadratic fit to tabulated data. This equation of state was found to give results significantly different from the ideal gas law for all gases except helium.

The baseline operating condition was with helium at bore/stroke = 0.67, no fins, and volume ratio 2.0. At this baseline condition runs were made at speeds ranging from 0.034 Hz to 16.8 Hz and mean pressures ranging from 100 kPa to 1800 kPa. From the baseline case, the adjustable parameters were varied one at a time as follows:

Gas: helium (baseline), hydrogen, nitrogen, and argon
Fins: 0 (baseline), 1, 3, and 7
Bore/stroke: 0.67 (baseline), 0.42, and 1.23
Volume ratio: 2.0 (baseline), 4.0, and 8.0.

In each of these cases speed and pressure were varied over the widest range possible within the capabilities of the apparatus and instrumentation. The overall range of Pe_ω based on hydraulic diameter was roughly 0.06 to 40,000.

Sources of error were examined. One important error source was in the calculated temperature and was due to the inaccuracy of the pressure measurements. The transducer used for the lowest pressure runs had an uncertainty (2σ from best-fit quadratic) of 0.59 kPa. This corresponded to a temperature error of 1.8 K for the lowest mean cycle pressure. Since the most nearly isothermal run had a measured temperature swing of only 1.7 K, this error was large enough to make the data from this run very unreliable. For higher mean pressures and wider temperature swings, however, the accuracy was adequate: For the highest pressure, largest temperature swing case the uncertainty amounted to 0.31 K over a temperature swing of 230 K. The results of the runs with the smallest temperature swings have been discarded; the lowest temperature swing of any run reported here is 16 K.

Another important error source was in the surface area used for heat flux calculations. In calculating heat flux, the surface area of the "top land crevice" (the gap between the cylinder wall, the piston sidewall, and the seal) was neglected. The length of this crevice was made equal to the stroke in order to avoid frictional heating of the cylinder wall, so its surface area was large. For most operating conditions the neglect of this area was justified because the mass of gas within the crevice was small compared to the total mass, and this gas could be assumed to remain uniformly at wall temperature. For the worst baseline case, assuming that the open cylinder space was adiabatic and the crevice was isothermal, the gap contained 1.36 percent of the gas at top center. At high volume ratios, however, the neglect was not well justified. For the worst r_v = 8.0 case the crevice contained 12.6 percent of the gas at top center. It is clear that the effect of the crevice must be considered when evaluating the data at high r_v.

A potentially important error source was phase lag between the pressure and volume measurements, since it is heat transfer that causes the pressure change to lead the volume change. The lags, however, in pressure transducers, shaft position transducer, and electronics totaled less than 1/10 degree of crank angle at maximum speed, small enough that they did not affect results appreciably.

The number of data points per cycle, 150, was lower than usual for internal combustion engine work, but because there was no combustion pressure changes were much less rapid. Simulations showed that the error in heat transfer rate intro-

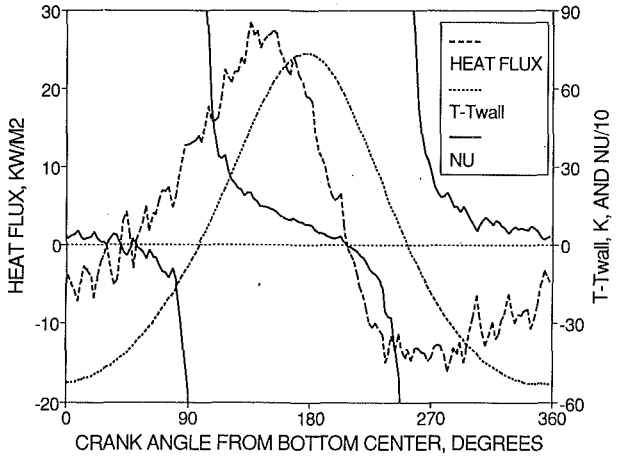

Fig. 1 $\dot{q}''$, ΔT, and Nu versus crank angle. Baseline conditions, ω = 3.37 Hz, p_{mean} = 1821 kPa, Pe_ω = 954.

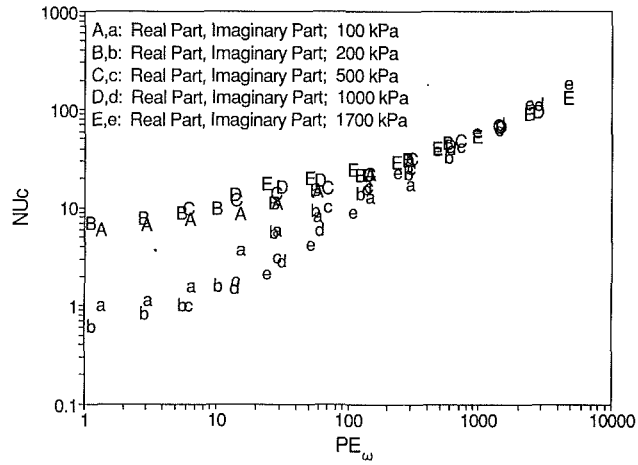

Fig. 2 Nu_c versus Pe_ω, baseline conditions. Approximate mean pressure shown, $\omega \sim$ 0.8–17 Hz at each pressure.

duced by numerical differentiation ranged from 0.2 percent of maximum rate for the most nearly isothermal baseline case to 4 percent of maximum rate for the most nearly adiabatic baseline case.

The use of pressure-volume measurements to calculate cylinder heat transfer had advantages relative to the traditional method based on surface temperature measurement. The surface temperature method is the only useful one for a fired engine, since the mass of gas, the gas properties, and the heat release rate during combustion are not precisely known. It has the disadvantage, for our purposes, of measuring only local heat fluxes, which may not be representative of the heat transfer over the entire cylinder and piston surface, and are much more subject to cycle-to-cycle variations. From pressure and volume measurements the only assumptions needed to calculate overall heat transfer are that pressure is uniform over the space, that the gas equation of state is correct, and that gas internal energy is approximately linear with temperature. These are certainly as valid as the assumptions associated with the surface temperature method.

One disadvantage of the pressure-volume method of heat transfer measurement was its sensitivity to instrument noise. To calculate the heat transfer it was necessary to differentiate the pressure and volume signals, thus magnifying any noise. In addition, at high oscillation Peclet number the heat transfer was a small difference between two large numbers (the work and the change in internal energy), causing further noise magnification. In designing the instrumentation, care was taken to minimize noise. While many runs showed relatively low noise, the high-speed runs with low heat transfer, such as the one shown in Fig. 1, displayed considerable noise.

Results

Measurements confirmed that heat transfer was out of phase with bulk gas-wall temperature difference and that Newton's law of convection was therefore inapplicable. Figure 1 shows the result of applying it to a typical run. As previous investigators found, Nusselt number became negative and infinite at various places in the cycle.

Since Newton's law was inapplicable, the heat transfer data were correlated based on the complex Nusselt number as used in Eq. (11). Nu_r and Nu_i based on hydraulic diameter were plotted against Pe_ω, the independent variable suggested by both Pfriem's and Lee's work. Since at least two $\dot{q}'' - \Delta T - dT/dt$ points are needed to determine Nu_c for a given Pe_ω, the following procedure was used: For each run a least-squares technique was used to determine an Nu_c, constant over the run, which would best fit the data for that run. This Nu_c was then plotted against mean Pe_ω for the run (based on time mean pressure, time mean volume, and hydraulic diameter at time-mean volume).

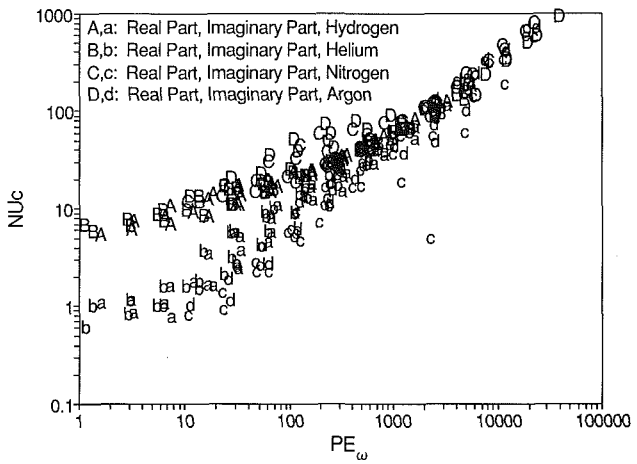

Fig. 3 Nu_c versus Pe_ω, gas comparison. H_2, He, N_2, and Ar; r_v = 2.0, D/L = 0.67, no fins.

Figure 2 shows the results at baseline conditions. The nondimensional variables correlated the results well. At high Pe_ω the real and imaginary parts of Nu_c were equal, indicating heat flux leading ΔT by 45 deg. At low Pe_ω the real part was much larger than the imaginary part, indicating that heat flux was almost in phase with ΔT. These results were as expected from the conduction-based theories. In the range $10 < Pe_\omega < 100$ the correlation broke down somewhat. High-pressure, low-speed runs showed a larger real part and a smaller imaginary part than low-pressure, high-speed runs at the same Pe_ω. The high-pressure, low-speed runs thus had a smaller heat transfer phase shift. In measurements of gas spring hysteresis loss, the authors (Kornhauser and Smith, 1987, 1993) found that their loss correlation broke down in the same region.

Figure 3 compares the results of runs made with various gases. The results for the four gases are the same at high and low Pe_ω, but at intermediate Pe_ω the heavier gases show a much larger correlation breakdown. This may indicate that the breakdown is a compressibility effect.

The results of runs made with various internal extended surfaces are compared in Fig. 4. The results for different geometries correlated well, indicating that the use of Pe_ω based on D_h was effective in accounting for shape change. The break-

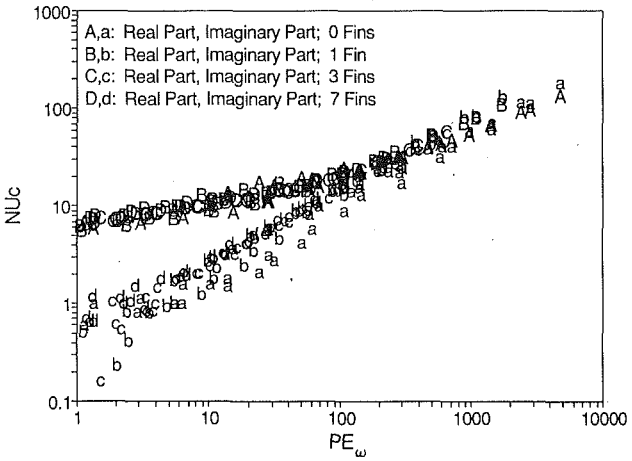

Fig. 4 Nu_c versus Pe_ω, fin comparison. 0, 1, 3, and 7 fins; helium, r_v = 2.0, D/L = 0.67.

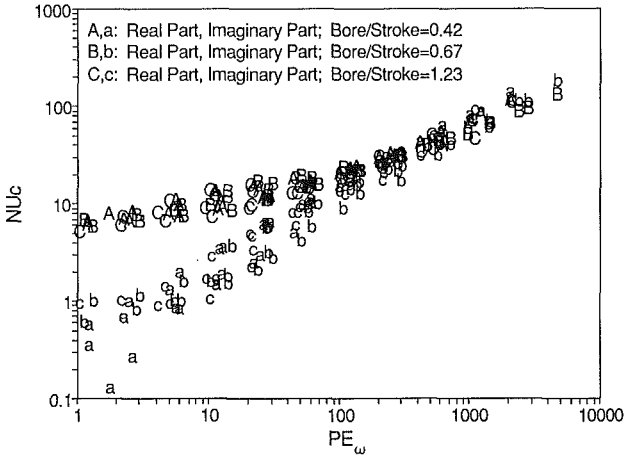

Fig. 5 Nu_c versus Pe_ω, bore/stroke comparison. D/L = 0.42, 0.67, and 1.23; helium, r_v = 2.0, no fins.

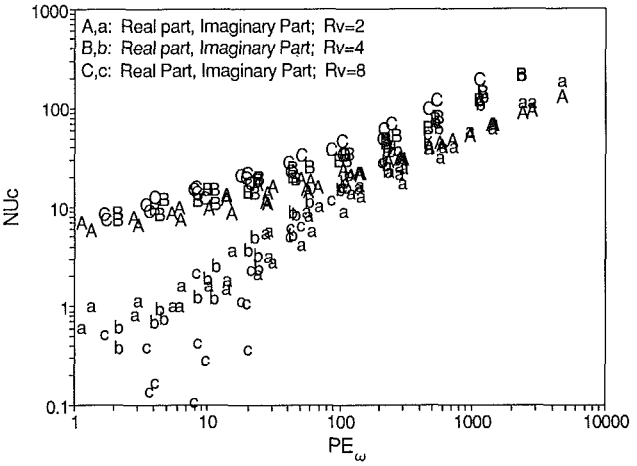

Fig. 6 Nu_c versus Pe_ω, volume ratio comparison. r_v = 2.0, 4.0, and 8.0; helium, D/L = 0.67, no fins.

down effect became smaller with one fin and disappeared altogether with three and seven. This may indicate that it is the result of a large-scale flow pattern, which the fins suppress.

Figure 5 compares the results of runs made with different bore/stroke ratios. The nondimensional variables correlated the data well. The use of Pe_ω based on D_h was effective in accounting for the change in geometry. There appeared to be no significant difference between the correlated data for the various ratios.

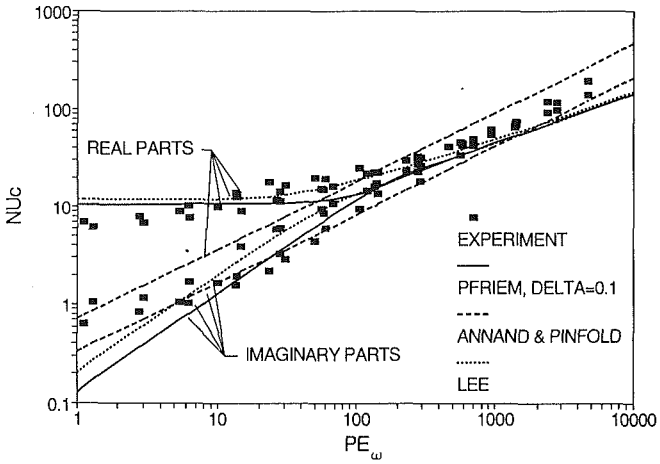

Fig. 7 Nu_c versus Pe_ω, baseline conditions. Compared with Pfreim, Annand and Pinfold, and Lee expressions.

The results of runs with different volume ratios are compared in Fig. 6. The correlation appeared to fail, especially at high Pe_ω. This was initially attributed to the effect of the top land crevice at high volume ratio. The data were then re-analyzed assuming a worst-case crevice (gas in crevice at wall temperature, gas entering crevice at cylinder mixed mean temperature). This analysis gave results that were very little different from the one that neglected the crevice area. There is evidently some effect related to volume ratio that is not accounted for in the correlation. Since only three volume ratios were tested and the basic physical reasons for the volume ratio effect were not understood, no effort was made to quantify the effect of volume ratio on complex Nusselt number.

The data presented in Figs. 2–6 are presented in tabular form, with all relevant parameters, by Kornhauser (1989). The complete pressure-volume data set (some 225,000 data points) is available from the authors on magnetic media.

Prediction of Complex Nusselt Number

The data for the baseline case are compared with the predictions of Pfriem, Annand and Pinfold, and Lee in Fig. 7.

Pfriem's ψ, s, and δ were evaluated based on the cylinder geometry at midstroke and a laminar layer thickness $\delta = 0.1D_h$. The resulting curve fit the experimental data well qualitatively and fairly well quantitatively. Experimentation with different values of δ made it evident that varying δ as a function of Pe_ω (which seems reasonable from theory) could improve the fit at low Pe_ω, but not at high.

In order to compare the Annand and Pinfold expression, approximations had to be made. Annand and Pinfold had used instantaneous mean gas density and local velocity for Re and v in Eq. (12); here time-mean density and mean piston velocity were used. Annand and Pinfold used a real heat transfer expression; it was converted to a complex expression by the same technique shown in Eqs. (5)-(11). The result was

$$Nu_c = 0.3\ Re^{0.7} + \left(0.25\frac{D}{L}\ Re^{0.7}\right) i. \tag{13}$$

Here both Re and Nu_c were based on cylinder, rather than hydraulic, diameter. This was corrected for in converting from Re to Pe_ω for plotting the figure.

Annand and Pinfold's expression was fairly close to the experimental data at high Pe_ω, but did not predict the decrease in heat transfer phase shift as Pe_ω decreased.

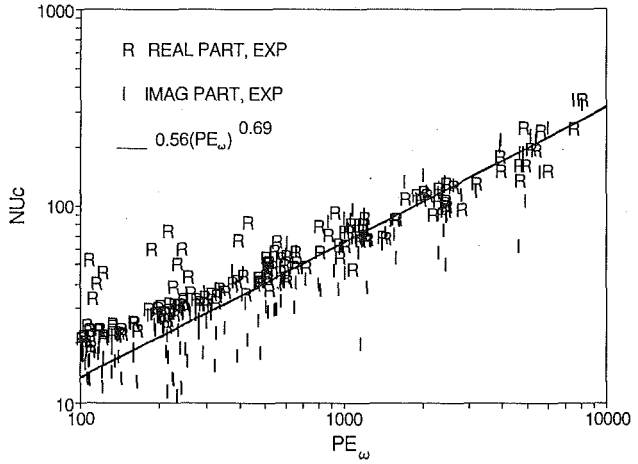

Fig. 8 Nu_c versus Pe_ω. All data at $r_v = 2.0$, $Pe_\omega > 100$, and best fit power law.

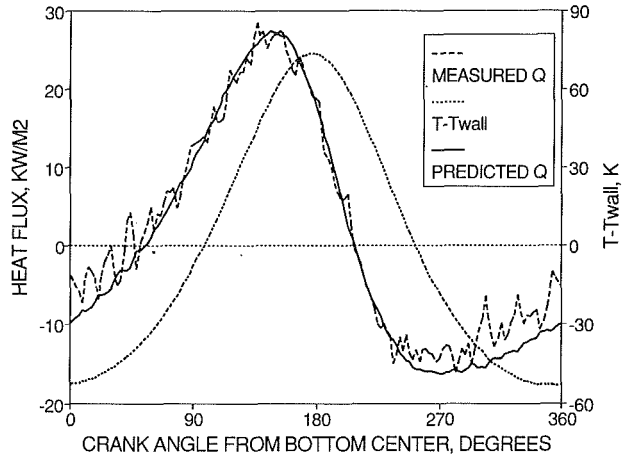

Fig. 9 $\dot{q}''$ measured, ΔT, and $\dot{q}''$ predicted versus crank angle. Baseline conditions, $\omega = 3.37$ Hz, $p_{mean} = 1821$ kPa, $Pe_\omega = 954$.

In the plot of Lee's expression no turbulent correction was made to the thermal diffusivity. Lee's expression fell closer to the data than that of Pfriem, but was inaccurate at high and low Pe_ω. The effect of introducing a turbulent thermal diffusivity would be to shift the predicted curve to the right, which would make the fit worse.

Most reciprocating machines operate in the high Pe_ω region. There, according to both these experiments and theory, the real and imaginary parts of Nu_c are approximately equal and have a power law relationship with Pe_ω. In an effort to obtain a useful expression for Nu_c, the data for $Pe_\omega > 100$ for all cases at volume ratio 2.0 were plotted in Fig. 8. A least-squares fit, assuming $Nu_r = Nu_i$, was made to all the data on that plot, although at the low-Pe_ω end $Nu_r > Nu_i$ was evident. The result was

$$Nu_r = Nu_i = 0.56(Pe_\omega)^{0.69}. \quad (14)$$

The fitted line is shown in the figure. It represents the asymptotic value of both real and imaginary parts of Nu_c at high Pe_ω.

Since the experimental data at volume ratio 2.0 are predicted by analyses based on volume ratio approaching 1, one might deduce that the correlation given in Eq. (14) is good over the range $1 < r_v < 2$. Additional experiments are desirable to verify this. Since only three volume ratios were tested and the physical reasons for the volume ratio effect were not understood, no effort was made to correlate the effect of volume ratio on complex Nusselt number at $r_v > 2$.

The use of expression (14) is demonstrated in Fig. 9. Although the Pe_ω dependence was developed for cyclic mean values, here it was used to give instantaneous Nu_c from instantaneous Pe_ω (using instantaneous density and cyclic mean D_h). Heat flux is predicted well both in magnitude and in phase.

Summary and Conclusions

For the simple heat transfer situation in this experimental apparatus, where dT/dt is entirely due to compression and expansion and p and T are approximately sinusoidal:

1 Heat transfer during compression and expansion is out of phase with bulk gas-wall temperature difference. Newton's law of convection is inadequate to describe this phenomenon.
2 Heat transfer out of phase with temperature difference can be described using a complex Nusselt number. Heat transfer is then expressed as the sum of one part proportional to temperature difference and another part proportional to rate of change of temperature (Eq. (11)).
3 Nu_c based on hydraulic diameter can be effectively correlated against Pe_ω based on hydraulic diameter. This correlation works over a wide range of conditions, but breaks down for open cylinders in the range $10 < Pe_\omega < 100$ and fails as volume ratio becomes large.
4 Heat transfer models based on conduction alone predict Nu_c qualitatively.
5 At high Pe_ω, the experimental data are predicted fairly well by a power law expression. For $r_v = 2.0$ this relationship is given by Eq. (14).

The use of a complex Nusselt number extends Newton's law of convection into areas where it was not valid with a real Nusselt number. To those familiar with the presentation of periodic functions on the complex plane, its use gives a good grasp of the phase relationship between heat transfer and temperature. It would be possible to express the same information in terms of a real Nusselt number that is a function of ΔT and dT/dt, as in Eq. (3). The usefulness, however, of a Nusselt number or heat transfer coefficient is that it expresses the geometric and fluid mechanical aspects of a problem while the temperatures remain separate. The approach of Eq. (3) discards this separation. In addition, the attempt to express the results in terms of a real Nusselt number masks the physics of the problem: Heat transfer during compression and expansion is *not* proportional to bulk gas-wall temperature difference. Work is done on fluid directly in contact with the wall, so a part of the heat transfer is in phase with the work, or dT/dt, rather than ΔT.

All physical constants are real valued, but the use of complex variables for representing periodic physical phenomena is an old and widely accepted branch of applied mathematics. The analyses of Pfriem (1943) and Lee (1983) both make use of complex arithmetic in deriving expressions for in-cylinder heat transfer. The work presented here shows how, for nearly sinusoidal fluctuations, a real Eq. (11) can be used to predict heat transfer in terms of a complex Nusselt number. For more complicated transient conditions it may be both possible and desirable to perform analyses entirely in the complex plane, much as is now done in the analysis of AC circuits, control systems, acoustic waves, and electromagnetic waves.

The complex Nusselt number heat transfer expression was developed based on conduction theory and tested with a simple one-node model, but it is not suggested that neglect of convection or of complex flow and turbulence effects is appropriate to describing in-cylinder heat transfer. What is proposed is that sophisticated in-cylinder heat transfer models should attempt to predict heat transfer in the complex Nusselt number format, rather than in the ordinary Newton's law format.

References

Annand, W. J. D., and Pinfold, D., 1980, "Heat Transfer in the Cylinder of a Motored Reciprocating Engine," SAE Paper No. 800457.

Faulkner, H. B., 1983, "An Investigation of Instantaneous Heat Transfer During Compression and Expansion in Reciprocating Gas Handling Equipment," Ph.D. Thesis, M.I.T., Cambridge, MA.

Hilsenrath, J., et al., 1960, *Tables of Thermodynamic and Transport Properties*, Pergamon Press, p. 290.

Kornhauser, A. A., and Smith, J. L., Jr., 1987, "A Comparison of Cylinder Heat Transfer Expressions Based on Prediction of Gas Spring Hysteresis Loss," *Fluid Flow and Heat Transfer in Reciprocating Machinery*, ASME, New York, pp. 89–96.

Kornhauser, A. A., 1989, "Gas-Wall Heat Transfer During Compression and Expansion," Sc.D. Thesis, M.I.T., Cambridge, MA.

Kornhauser, A. A., and Smith, J. L., Jr., 1993, "The Effects of Heat Transfer on Gas Spring Performance," ASME *Journal of Energy Resources Technology*, Vol. 115, pp. 70–75.

Lee, K. P., 1983, "A Simplistic Model of Cyclic Heat Transfer Phenomena in Closed Spaces," *Proc. 18th IECEC*, pp. 720–723.

Overbye, V. D., Bennethum, J. E., Uyehara, O. A., and Myers, P. S., 1961, "Unsteady Heat Transfer in Engines," *SAE Trans.*, Vol. 69, pp. 461–493.

Pfriem, H., 1943, "Periodic Heat Transfer at Small Pressure Fluctuations," NACA TM-1048.

Wendland, D. W., 1968, "The Effect of Periodic Pressure and Temperature Fluctuations on Unsteady Heat Transfer in a Closed System," NASA CR-72323.

Analysis of Heat Transfer and Fluid Flow Through a Spirally Fluted Tube Using a Porous Substrate Approach

Vijayaragham Srinivasan[1]

Kambiz Vafai
Professor.
Fellow ASME

Richard N. Christensen
Professor.

Department of Mechanical Engineering,
The Ohio State University,
Columbus, OH 43210

An innovative approach was opted for modeling the flow and heat transfer through spirally fluted tubes. The model divided the flow domain into two regions. The flutes were modeled as a porous substrate with direction-dependent permeabilities. This enabled modeling the swirl component in the fluted tube. The properties of the porous substrate such as its thickness, porosity, and ratio of the direction-dependent permeabilities were obtained from the geometry of the fluted tube. Experimental data on laminar Nusselt numbers and friction factors for different types of fluted tubes representing a broad range of flute geometry were available. Experimental data from a few of the tubes tested were used to propose a relationship between the permeability of the porous substrate and the flute parameters, particularly the flute spacing. The governing equations were discretized using the Finite Element Method. The model was verified and applied to the other tubes in the test matrix. Very good agreement was found between the numerical predictions and the experimental data.

1 Introduction

The design of high-performance thermal systems has stimulated considerable interest in developing techniques to improve heat transfer in heat exchanger systems. Incorporation of these techniques can substantially improve the performance of conventional heat exchangers resulting in energy and material savings. Augmentation methods that do not require external power are classified as passive schemes (Bergles, 1985). The passive schemes include techniques such as the use of artificially roughened surfaces, extended surfaces, swirl flow devices, inlet vortex generators, etc.

In the recent past, attention has been given to heat transfer augmentation by means of spirally fluted tubes. These tubes enhance convective heat transfer by introducing swirl into the bulk flow and by disrupting the boundary layer at the tube surface due to repeated changes in the surface geometry. A picture of the spirally fluted tube used in the present work is shown in Fig. 1. The parameters that are necessary to define a spirally fluted geometry are the bore diameter, envelope diameter, flute depth, pitch, and the helix angle (which is related to the number of flute starts). These parameters are also shown in Fig. 1. A change in any of these dimensions affects the flow and heat transfer characteristics of the tube.

It is generally known that numerical methods are not as readily used as are the experimental methods for predicting the heat transfer and pressure drop performance for enhanced heat exchanger tubes. There are only a limited number of investigations in this area since the flow modeling becomes extremely complex and limited due to multiple disruptions in the geometry. The problem of fully developed, laminar and turbulent, uniform property flow in a tube containing a twisted tape was studied by Date (1974). The partial differential equations of momentum and heat transfer were solved by Date by adapting the numerical procedure of Gosman and Ideriah (1972). Further, Date used a coordinate system in which the angular coordinate was always measured from the surface of the twisted tape, that is a rotating cylindrical polar coordinate system. The computational results showed that significant sec-

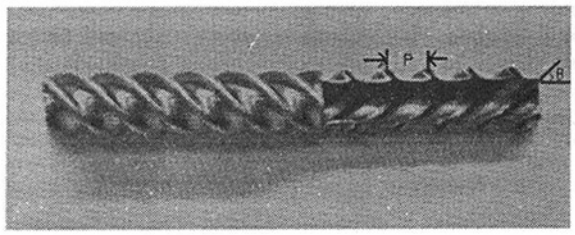

Flute Pitch, P and Helix Angle, θ

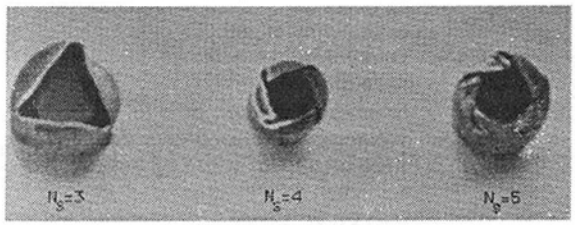

Number of Starts, N_s

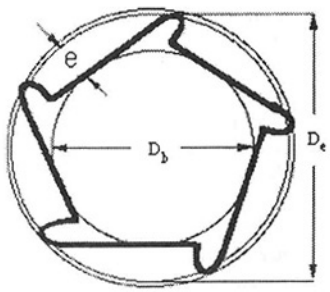

Flute Depth, e , Bore Diameter, D_b and Envelope Diameter, D_e

Fig. 1 Spirally fluted tube; geometry definition

[1]Present address: Process and Systems R&D, Praxair, Inc., Tonawanda, NY 14151.

Contributed by the Heat Transfer Division for publication in the JOURNAL OF HEAT TRANSFER. Manuscript received by the Heat Transfer Division December 1992; revision received August 1993. Keywords: Augmentation and Enhancement, Modeling and Scaling, Porous Media. Associate Technical Editor: Y. K. Dhir.

ondary velocities existed in the twisted duct, enhancing friction and heat transfer.

Barba (1984) studied the fully developed laminar and turbulent flow inside spirally fluted tubes evolved by GA Technologies. The flute geometry is considerably different in these tubes compared to the one shown in Fig. 1. Barba presented the results to optimize the flute geometry: the number of starts, size, angle, and profile of the tube. However, there was poor agreement between the predicted results and experimental data. Another important contribution in the area of numerical modeling came from the work of Arman and Rabas (1991) in which pressure drops in heat exchanger tubes with transverse ribs were predicted. In these geometries the flow is characterized by boundary layer separation at the rib location and its subsequent reattachment downstream of the rib. The study placed particular emphasis on the turbulence modeling of this type of flow. Agreement with the experimental results was found to be good for a limited set of data.

These studies suggest that numerical methods have not been as successful as are the experimental methods in the prediction of heat transfer and pressure drop enhancement. Furthermore, these numerical models are quite tedious in implementation and the required CPU time limits their applicability. As cited earlier, numerical models for predicting friction and heat transfer in enhanced surface used in most of the previous studies have relied on turbulence models (K-ϵ model) or the algebraic stress models. The past numerical results were also quite different from the experimental results. However, numerical modeling is definitely needed to predict heat transfer and pressure drop in enhanced tube geometries. In particular, experimental methods for enhanced tubes are costly and time consuming since the number of independent parameters that impact the flow field is rather extensive. The present method models the flute geometry using a porous substrate and derives in a consistent fashion the constitutive relationship for permeability of the porous substrate based on just few experimental data.

2 Modeling Theory

It is easy to imagine the complexity involved in modeling the flow field inside a spirally fluted tube. The nature of the tube side flow was indicated to some extent by flow visualization studies carried out by Srinivasan (1993). It was inferred that the spiral flutes combine the function of a swirl flow device and that of a roughness element (or a turbulence promoter). The flutes introduce a swirling motion in the near-wall region of the flow. This swirl component is carried into the core region of the flow. Also the flutes can be imagined to be a series of small cavities and large-scale fluctuations in the core region of the flow can lead to ejection of the fluid from the cavities contributing to an increased level of turbulence. This was observed in the flow visualization studies as periodic bursts of fluid from the flute region into the core region.

The present approach divides the flow through the fluted tubes into two principal domains: the flow through the flutes and flow through the open region of the tube. The flow region covered by the flutes is approximated by a porous layer. The porous layer will simulate the flow through the flute region by impacting the flow field in the open region in the same manner as the flutes do. The premise upon which this concept is based is presented below.

Heat transfer and fluid flow over surfaces with an attached porous substrate has been studied in depth by Vafai and Thiyagaraja (1987) and Vafai and Kim (1990). A complete investigation of the interface interactions between a fluid region and a saturated porous medium was provided by Vafai and Thiyagaraja (1987). The intricacies of the boundary layer in-

Nomenclature

A_f = cross-sectional flow area through fluted section of the tube as defined in Eq. (1), m^2
D = tube diameter, m
Da = Darcy number = K/R^2
D_b = bore diameter, m
D_e = envelope diameter, m
D_v = volume-based fluted tube diameter, m
e = flute depth (or height of the roughness element), m
e_f = friction factor enhancement = f_a/f_s
e_h = heat transfer enhancement = $\mathrm{Nu}_a/\mathrm{Nu}_s$
e^* = nondimensional flute depth = e/D_v
F = a function used in expressing the inertial effects
F_B = body force term
f = friction factor = $2\Delta P D_v/\rho V^2 L$
h = heat transfer coefficient, $W/(m^2K)$
K = permeability tensor for the porous medium
k = thermal conductivity, W/(mK)
L = tube length, m
ΔT_{lm} = log-mean temperature difference, K
$\dot{m}$ = mass flow rate, kg/s
N_s = number of flute starts
Nu = Nusselt number = $h D_v/k$
p = flute pitch, m
p^* = nondimensional flute pitch = p/D_v
p_e^* = nondimensional flute pitch = p/D_e
Pr = Prandtl number = $\mu C_p/k$
r, θ, z = cylindrical polar coordinates
R = radius of the porous tube, m
Re = Reynolds number = $\rho V D_v/\mu$
s = dimensionless radius of the open region (radius = sR)
T = temperature, K or °C
T_m = bulk mean temperature at a flow cross section, K
T_w = tube wall temperature, K
t_w = tube wall thickness, m
$[U_r]$, $[U_\theta]$, $[U_z]$ = column vectors of velocity-element nodal point unknowns
V = flow velocity, m/s
$\mathbf{V}$ = vector velocity
V_r, V_θ, V_z = velocities in the r, θ, and z direction, m/s
δ = porosity of the porous substrate
θ = flute helix angle = $\tan^{-1}(\pi D_{vo}/N_s p)$, deg
θ^* = nondimensional flute helix angle = $\theta/90$ deg
μ = dynamic viscosity, N s/m^2
ρ = density, kg/m^3
ΔP = pressure drop, Pa
ΔT = temperature difference, K

Subscripts

a = annulus, annulus-side, augmented
eff = effective
o = outside
s = smooth, solid
t = tube, tube-side
w = tube wall

Others

$\langle\ \rangle$ = denotes the local volume average of a quantity

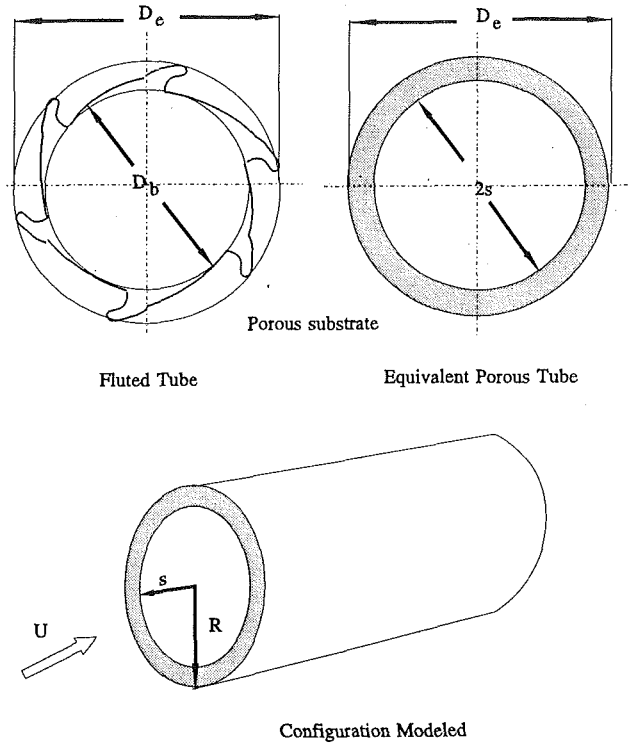

Fig. 2 Porous tube equivalent of a fluted tube

teractions at the interface on both the velocity and temperature fields were discussed in detail and theoretical solutions were obtained for the velocity and temperature distributions as well as the interface velocity and temperature. Studies by Vafai and Kim (1990) have revealed that porous substrates act as enhancement elements. The cross mixing of the fluid inside the pores in the media is responsible for this enhancement. Thus if some property of the porous matrix could give rise to a swirl component of velocity, the flow through spirally fluted tubes can be simulated. Indeed, this action is possible by specifying direction-dependent permeabilities (θ and z) in the porous substrate. Figure 2 provides a sketch of a multistart fluted tube cross section and its equivalent tube with a porous substrate. The following steps further illustrate the procedure for modeling a spirally fluted tube as a tube with a porous substrate:

- Bore diameter (D_b): The bore diameter of the fluted tube that represents the clear flow area is related to the diameter of the open region of the tube with porous wall.
- Envelope diameter (D_e): The envelope diameter of the spiral flutes is taken as the diameter of the porous tube ($2R$).
- Flow area through the fluted tube: The total cross-sectional flow area through the fluted tube is given by:

$$A_f = \frac{\pi}{4} D_v^2 \tag{1}$$

where the volume-based diameter D_v is based on the actual volume measurement inside the fluted tube. Thus, the diameter D_v can be considered as an equivalent smooth tube diameter with a flow cross-sectional area as that of the fluted tube. Therefore, the flow area through flute region is calculated as:

$$A_{fl} = A_f - \frac{\pi}{4} D_b^2 \tag{2}$$

The porosity δ of the porous substrate is then calculated as:

$$\delta = \frac{A_{fl}}{\frac{\pi}{4}(D_e^2 - D_b^2)} \tag{3}$$

- Helix angle (θ): The helix angle of the flute that determines the swirl velocity is related to the ratio of the porous substrate permeabilities in the angular and axial directions. Physically it is quite logical to relate the helix angle directly to the ratio of the porous substrate permeabilities:

$$\theta = \tan^{-1}\left(\frac{K_\theta}{K_z}\right) \tag{4}$$

In addition, the velocity vector at the interface (porous and open region) is made to coincide with the flute helix angle. This point is discussed later.

- Pitch (p): The flute pitch p largely determines the overall resistance to flow. Thus, it is appropriate to relate the pitch to the permeability of the porous substrate. The correlation between the pitch and the permeability is determined from the experimental data. Part of this correlation can be inferred from previous correlations between the permeability and particle diameter, as discussed by Vafai (1984).

3 Mathematical Formulation

In Fig. 2, a schematic diagram of the circular tube of radius R with porous walls is shown. The surface of the tube facing outside is impermeable. It is maintained at constant temperature T_w in order to simulate the experimental conditions. The fluid flow inside the tube is divided between the porous substrate and the open (or the core) region. Hence, there is an intricate coupling between the flow and temperature fields in the two regions. The flow field in the channel is assumed to be fully developed. This assumption is more justified in enhanced surfaces than it is in smooth tubes, for it has been shown by Ravigururajan and Bergles (1991) that the hydrodynamic entry length is shorter for these tubes. The fluid enters the tube with uniform temperature as it does under the experimental conditions.

The governing conservation equations for flow and temperature fields are written separately for the fluid and the porous region. For steady, incompressible flow in the fluid region the conservation of mass, momentum, and energy equations are given by

Fluid Region

$$\nabla \cdot V = 0 \tag{5}$$

$$\rho V \cdot \nabla V = -\nabla P + \mu \nabla^2 V + F_B \tag{6}$$

$$V \cdot \nabla T = \frac{k}{\rho c_p} \nabla^2 T \tag{7}$$

Porous Region. The conservation equations for the porous region are based on the generalized flow model, which includes the effects of flow inertia as well as friction caused by macroscopic shear. These equations are described in rigorous detail by Vafai and Tien (1980, 1981) as well as by Tien and Vafai (1990). This generalized flow model is also known as the Brinkman-Forchheimer-Darcy model. This model satisfies the physically real no-slip condition on a solid boundary. The governing equations for the porous layer are (Vafai and Tien, 1980; Vafai, 1984):

$$\nabla \cdot \langle V \rangle = 0 \tag{8}$$

$$\rho \langle V \rangle \cdot \nabla \langle V \rangle = -\nabla \langle P \rangle + \mu_{\text{eff}} \nabla^2 \langle V \rangle - \frac{\mu}{K} \langle V \rangle - \frac{F\delta}{\sqrt{K}} |\langle V \rangle| \langle V \rangle + F_B \tag{9}$$

$$\langle V \rangle \cdot \nabla \langle T \rangle = \frac{k_{\text{eff}}}{\rho c_p} \nabla^2 \langle T \rangle \tag{10}$$

In the above equations k_{eff}, μ_{eff} are the effective thermal conductivity and viscosity of the porous medium. Taking $\mu_{\text{eff}} = \mu$ has been found to provide good agreement with experimental data (Vafai and Thiyagaraja, 1987). The thermal conductivity

k_{eff} is related to fluid and solid matrix properties by the following:

$$k_{\text{eff}} = \delta k + (1-\delta)k_s \tag{11}$$

where the subscript s refers to the solid matrix properties. It should be noted that the variables $\langle V \rangle$ and $\langle T \rangle$ are both volume-averaged quantities as described by Vafai and Tien (1981). Note also that the thermal dispersion term has been neglected in the energy equation, based on inference from the results of Sözen and Vafai (1993).

Equations in the r–θ–z Coordinate System. The flow field is analyzed over the region shown in Fig. 2. This represents a longitudinal part of the tube's cross section above the tube centerline. Flow is symmetric about the centerline. The solution domain is bounded on the outer surface by the tube wall. Thus, for this geometry it is convenient to use cylindrical polar coordinates (r, θ, z); the corresponding velocity components are then denoted by (V_r, V_θ, V_z). Assuming all quantities are independent of θ (but velocity components V_θ, V_z are nonzero) then the generalized equations within the porous substrate region, Eqs. (8)–(10) for fully developed flow ($V_r = 0$) reduce to Eqs. (12)–(16). For convenience, the symbol $\langle\ \rangle$ is dropped from the following equations.

Continuity

$$\frac{\partial V_z}{\partial z} = 0 \tag{12}$$

Radial Momentum (r-direction)

$$\frac{\rho V_\theta^2}{r} = \frac{\partial P}{\partial r} \tag{13}$$

Axial Momentum (z-direction)

$$\mu_{\text{eff}}\left(\frac{\partial^2 V_z}{\partial r^2} + \frac{1}{r}\frac{\partial V_z}{\partial r}\right) - \frac{\mu}{K_z} V_z - \frac{F\delta}{\sqrt{K_z}} |V| V_z = \frac{\partial P}{\partial z} \tag{14}$$

Angular Momentum (θ-direction)

$$\mu_{\text{eff}}\left(\frac{\partial^2 V_\theta}{\partial r^2} + \frac{1}{r}\frac{\partial V_\theta}{\partial r} - \frac{V_\theta}{r^2}\right) - \frac{\mu}{K_\theta} V_\theta - \frac{F\delta}{\sqrt{K_\theta}} |V| V_\theta + F_\theta = 0 \tag{15}$$

It should be noted that the forcing function F_θ is included in the θ-momentum equation to cause the porous layer/fluid core interface velocity vector to be in the θ direction. The magnitude of F_θ is determined iteratively and it depends on the helix angle of the flute and the permeability (K_θ) in the θ direction.

Energy. Neglecting conduction in the axial direction, the energy equation is reduced to:

$$\rho c_p V_z \frac{\partial T}{\partial z} = k_{\text{eff}}\left(\frac{1}{r}\frac{\partial}{\partial r}\left(r\frac{\partial T}{\partial r}\right)\right) \tag{16}$$

As already noted, the equations above were written for the porous region using locally volume-averaged quantities. Note that, under fully developed conditions, these equations also apply for the fluid region, using the following limiting values:

$$K_z = \infty$$

$$K_\theta = \infty$$

$$\mu_{\text{eff}} = \mu \tag{17}$$

for $0 \le r \le s$ where s is the radius of the open (core region) of the tube.

Boundary Conditions. The no-slip condition implies that the velocity vanishes on the wall and the temperature is constant on the wall. The velocity and temperature gradients vanish at the centerline of the channel. Thus, the boundary conditions necessary to complete the problem formulation are:

$$\text{at } r = R \rightarrow V_z,\quad V_\theta,\quad V_r = 0 \text{ and } T = T_w \tag{18}$$

$$\text{at } r = 0 \rightarrow \frac{\partial T}{\partial r} = 0,\quad \frac{\partial V_z}{\partial r} = 0,\quad V_\theta = 0 \tag{19}$$

In addition to the boundary conditions given by Eqs. (18) and (19) the equations in the fluid and porous regions are coupled at the porous/fluid interface by the continuity requirements for the velocity, temperature, heat flux, and shear stress. This results in the following conditions:

$$(T)_{r=s^-} = (T)_{r=s^+}$$

$$\left(k\frac{\partial T}{\partial r}\right)_{r=s^-} = \left(k_{\text{eff}}\frac{\partial T}{\partial r}\right)_{r=s^+} \tag{20}$$

$$(V_z,\ V_\theta)_{r=s^-} = (V_z,\ V_\theta)_{r=s^+}$$

$$\left(\mu\frac{\partial V_z}{\partial r}\right)_{r=s^-} = \left(\mu_{\text{eff}}\frac{\partial V_z}{\partial r}\right)_{r=s^+}$$

$$\left(\mu\frac{\partial V_\theta}{\partial r}\right)_{r=s^+} = \left(\mu_{\text{eff}}\frac{\partial V_\theta}{\partial r}\right)_{r=s^+} \tag{21}$$

In the derivation of the equations above it may be worth noting the following points: The porosity of the matrix was assumed to be constant and the buoyancy effects were neglected since the present study deals with forced convection in a tube with a porous substrate.

4 Numerical Solution

The mass, momentum, and energy equations in the fluid and porous regions were solved using the Galerkin-based Finite Element Method. The application of this scheme in the finite element program used in the present study is well documented (FIDAP, 1991). A brief description is provided here.

Discretization. The objective of the Finite Element Method as in the Finite Difference Method is to reduce the system of governing equations into a discretized set of algebraic equations. The procedure begins with the division of the continuum region of interest into a number of simply shaped regions called elements. Within each element, the velocity, pressure, and temperature fields are approximated by the following equations:

$$V_r = \varphi^T[U_r]$$

$$V_z = \varphi^T[U_z]$$

$$V_\theta = \varphi^T[U_\theta]$$

$$P = \Psi^T[P]$$

$$T = \Theta^T[T] \tag{22}$$

where φ, Ψ, Θ are the interpolation functions for velocity, pressure, and temperature, respectively, and are local functions of nodal coordinates for the element as well as the independent variables. The vectors $[U_r]$, $[U_\theta]$, $[U_z]$, $[P]$, and $[T]$ consist of the values of the respective variables at the nodes of the element. However, the same basis functions are employed for all components of the velocity and temperature.

Substitution of these approximations into the field equations for continuity, momentum, and energy yields a set of equations for the residual error as given below:

$$f_1(\varphi,\ U_r,\ U_\theta,\ U_z) = R_1$$

$$f_2(\varphi,\ \Psi,\ \Theta,\ U_z,\ U_\theta,\ P,\ T) = R_2$$

$$f_3(\varphi,\ \Theta,\ U_r,\ U_\theta,\ U_z,\ T) = R_3 \tag{23}$$

where R_1, R_2, and R_3 are the residuals (errors) resulting from the use of the finite element approximations. The Galerkin form of the method of weighted residuals seeks to reduce these

errors to zero, in a weighted sense, by making the residuals orthogonal to the interpolation functions of each element (i.e., φ, Ψ, Θ). These orthogonality conditions are expressed by the following inner products:

$$\int_s \varphi \cdot R_1 dS = \int_s \varphi \cdot f_1 dS = 0$$

$$\int_s \Psi \cdot R_2 dS = \int_s \Psi \cdot f_2 dS = 0$$

$$\int_s \Theta \cdot R_3 dS = \int_s \Theta \cdot f_3 dS = 0 \quad (24)$$

The manipulation of the above integrals results in matrix equations for each element with the elemental nodal point unknowns forming the column vector. The resulting matrix equation takes the following form:

$$\overline{M}\dot{V} + \overline{K}V = \overline{F} \quad (25)$$

Here V represents the column vector of the unknown variables, $\overline{M}$ the mass terms in the field equations; $\overline{K}$ represents the diffusive terms for the momentum and the energy equations; and F vector provides the forcing function for the system in terms of volume forces and surface forces (traction, heat flux). The matrix equations represent the discrete analog of the governing equations for an individual fluid element. The discrete representation of the entire continuum region of interest is obtained through an assemblage of elements such that interelement continuity of velocity and temperature is enforced.

Solution Procedure. The solution of the discretized equations, Eq. (15), involves a nonlinear matrix system of equations. Typically, the application of the Galerkin procedure to the steady-state Navier–Stokes equation results in a set of nonlinear algebraic equations that may be represented in matrix form as:

$$\overline{K}(V)V = \overline{F} \quad (26)$$

where $\overline{K}$ is the global system matrix, V is the global vector of unknowns (velocities, temperatures, and pressures) and $\overline{F}$ is a vector that includes the effects of boundary conditions and body forces. Since, in the present problem, the buoyancy term in the momentum equation is not present, the momentum equation can be solved independently of the energy equation to obtain the velocity field. With this information in hand, the temperature field can be obtained from the energy equation. For large Reynolds numbers, the convective term in the energy equation becomes important and therefore the nonlinear character of the equation assumes greater significance. This dictates the use of an iterative procedure to obtain a solution. The quasi-Newton method, which has been used extensively (Engleman et al., 1981) for two-dimensional problems, was used for the present case. This method yielded convergence for all the cases studied within prescribed errors (± 0.005 for velocity). The linear solution (without the heat transfer convective terms) was used as the initial guess in the iterative process.

The momentum equation was solved using a variable grid structure for accurate resolution of the porous substrate as well as the porous/fluid interface region. In particular the "compound interest grid" method in which each interval is a constant multiple of the preceding one was used. A factor of 1.02 in the radial direction yielded finer mesh in the porous/fluid interface and the porous substrate region. Since the problem also took into account the thermal entry length (in order to simulate the experimental conditions) a variable grid was used in the axial direction of the tube similar to the one used in the radial direction, resulting in a very fine mesh near the channel entrance. This proved beneficial to capture the steep changes in the temperature field near the entrance. As the flow away from the entrance approaches the fully developed condition, a coarser grid was used downstream, saving computational time.

5 Results and Discussion

Validity of the Numerical Scheme. The basic aspects of the numerical scheme discussed above were verified in several ways. First, our results were compared with those for the fully open tube and fully plugged (porous) tube (Bejan, 1984; Vafai and Tien, 1981) by varying the thickness of the porous substrate from zero to $D_e/2$. Identical results were found between our results and the standard ones in the literature (Bejan, 1984; Vafai and Tien, 1981). Next, the results of Poulikakos and Kazmierczak (1987) for flow through tubes partially filled with porous substrate were used for refinement of our comparisons. Among the important variables that affect the flow and temperature field for this comparison are the thickness of the porous region, the Darcy number, which is related to the permeability of the porous medium, and the ratio of the effective thermal conductivity of the porous matrix to the thermal conductivity of the fluid medium. It was mentioned earlier that these variables are intimately connected with the geometric parameters of the flute that is being modeled.

The effect of Darcy number on the flow field is illustrated in Fig. 3(*a*). These results correspond to the case where the thickness of the porous region near the wall equals 20 percent of the tube outer radius, i.e., $s = 0.8$. As seen in the figure the presence of porous matrix decreases the flow in the porous region. For Darcy numbers less than 10^{-5} there is negligible flow in the porous region. The figure also demonstrates the influence of Darcy number in affecting the flow through the open region (or core region) of the tube. The velocity profiles shown in Fig. 3(*a*) match quite well with the results of Poulikakos and Kazmierczak (1987).

The effect of the thickness of the porous region on the velocity profile is shown in Fig. 3(*b*). For these cases the Darcy number is fixed at 0.001. The thickness of the porous region is seen to have a strong influence on the velocity field in both the porous and open spaces. The results obtained from this study once again match very well with the results of Poulikakos and Kazmierczak (1987) with the differences being less than 1 percent.

Our numerical experimentation had demonstrated that the presence and the properties of porous matrix have a significant effect on the velocity field inside the tube. Since the heat transfer process is intimately connected with the velocity field, the Nusselt numbers are also expected to change. In addition, the effective thermal conductivity of the porous matrix, which can be presented as a weighted average (with porosity) of the thermal conductivity of the solid and fluid medium, is also expected to influence heat transfer.

The dependence of Nusselt number on the Darcy number for a tube partially filled with porous medium is shown in Fig. 4. This has been done for a fixed value of the porous layer thickness, namely $s = 0.8$. As the Darcy number increases, i.e., as the permeability increases, the flow in the tube approaches that of a plain tube. This is because at large permeabilities, the presence of porous matrix becomes less dominant and therefore the value of the Nusselt number approaches that of a plain tube. The results shown in Fig. 4 match quite well with the results of Poulikakos and Kazmierczak (1987). Table 1 depicts the dependence of Nusselt number on the porous layer thickness at a fixed value of $Da = 0.01$ for the case of constant wall temperature. Nusselt number is found to decrease with an increase in the porous layer thickness for a fixed pressure gradient along the tube. This is because an increase in the porous layer thickness decreases the flow through the tube. As the flow in the tube decreases, the temperature of the fluid near the tube wall increases. This results in decreasing the temperature gradient and consequently the heat flux at the tube wall. Since the Nusselt number is defined as the ratio of the heat flux at the tube wall to the mean temperature difference, it is found to decrease. Once again the results obtained

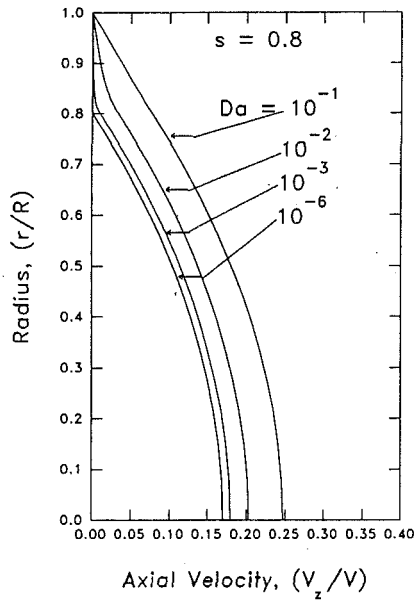

Fig. 3(*a*) Velocity profiles for s = 0.8 at different values of Darcy numbers

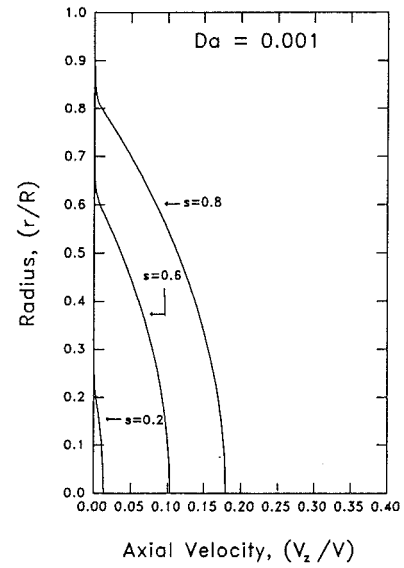

Fig. 3(*b*) Velocity profiles for Da = 0.001 at different values of s (relative thickness of the open region)

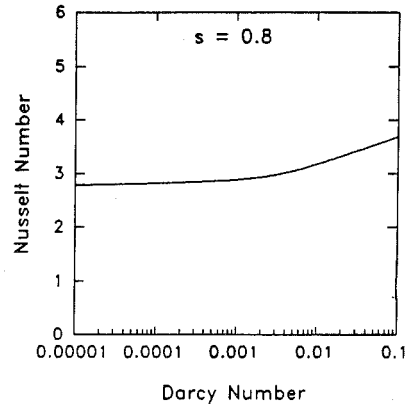

Fig. 4 Nu versus Darcy number for the constant wall temperature case, s = 0.8 and k_{eff}/k = 1

Table 1 Nu versus s for a fixed value of Da = 0.01 and k_{eff}/k = 1

s	Nu (Present Model)	Nu (Poulikakos and Kazmierczak, 1987)
0.5	2.405	2.4
0.6	2.555	2.5
0.8	3.173	3.2

Table 2 Tubes used in the experimental investigation

Tube	$D_e x 10^3$	$D_b x 10^3$	$D_v x 10^3$	$p x 10^3$	$e x 10^3$	θ
1	20.29	14.83	15.67	23.44	2.735	37.35
2	18.52	14.96	15.75	15.24	1.786	41.49
3	26.64	14.20	14.78	60.96	6.223	39.87
4	13.41	8.46	9.45	13.26	2.483	38.97

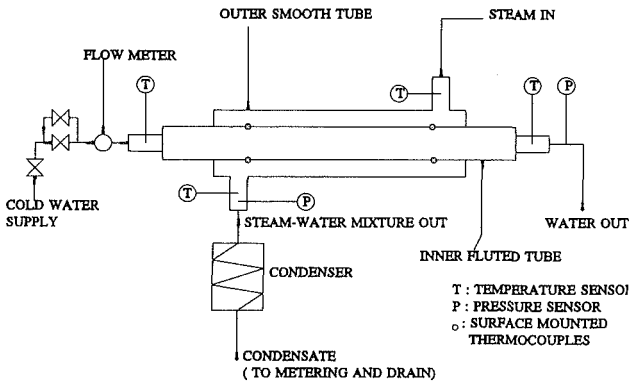

Fig. 5 Schematic of test section

are in close agreement with Poulikakos and Kazmierczak (1987). Finally, all of the numerical results obtained in the present investigation were rigorously shown to be independent of the number and type of elements.

Experimental Data. Detailed experimental investigations (Srinivasan, 1993) to obtain friction factors and Nusselt numbers were made on four fluted tubes listed in Table 2. The schematic of the test section is shown in Fig. 5. The test section for heat transfer tests, which was originally used by Garimella and Christensen (1993), was modified to include a desuperheating section and an after-condenser. Facilities were incorporated to switch steam or hot water as the heating medium on the annulus side. The experiments were done with water as a fluid medium. The friction factor tests were done under isothermal conditions. The measured pressure drop data and flow rates were reduced to their corresponding friction factors and Reynolds number using the volume-based diameter as the characteristic length. The heat transfer experiments were done using steam as a heating medium. This ensured a constant wall temperature on the fluted tube surface. More details of the experiments and the errors associated with the experimental data can be found from Srinivasan (1993).

The correlation between the flute parameters, particularly the pitch and the permeability of the porous substrate, was derived by performing parametric studies on a selected number of fluted tubes from the test matrix (Table 2). The applicability of this correlation is then checked for other tubes in the test matrix. The analysis involves the following steps:

1 Select a Reynolds number in the laminar regime. It should be noted that the experimental data consist of the Reynolds numbers based on the volume-based diameter of the tube selected for analysis. In order to provide a common ground for comparison between the numerical results and the experimental data, the same definition of Reynolds number will be used. It is calculated using the following expression:

$$\mathrm{Re} = \frac{\rho V D_v}{\mu} \tag{27}$$

Table 3 Porous layer permeability derived from the porous substrate model

Tube	e*	p*	θ	Re	δ	$K_z \times 10^{-9}$	$K_\theta \times 10^{-9}$
1	0.175	1.495	37	534.1	0.288	510.9	390.2
2	0.113	0.968	41	431.6	0.413	92.9	82.1
3	0.421	4.124	40	475.5	0.101	706.1	592.7

2 Using the standard analytical expressions, predict the plain tube pressure drop and friction factor for the above Reynolds number. Note that the friction factor is defined as:

$$f_a = 2\frac{\Delta P D_v}{\rho V^2 L} \tag{28}$$

In Eqs. (27) and (28), the velocity V is an average value based on the volume-based diameter.

3 Model the flutes as an equivalent porous layer using the procedure stated previously. The thickness and porosity of the porous substrate, the diameter of the open region, and the ratio of the direction-dependent permeabilities are defined based on Fig. 2 and Eqs. (3) and (4).

4 Select the value of the permeability so that the predicted pressure drop and friction factor using the porous substrate model is equal to the experimental value for the selected Re. It should be noted once again that this Re is based on D_v.

5 Concurrent with step (4), also select the value of the external force term in the θ-momentum equation, such that the direction of the velocity vector at the porous/fluid interface is the same as that of the flute helix angle.

6 With the known velocity profile, solve the energy equation assuming uniform temperature at the inlet. Calculate the Nusselt number, averaged over the entire tube length as in the experimental case.

Fluted tubes 1, 2, and 3 were selected for this analysis. These tubes represent a large range in the variation of the pitch parameter. The analysis yields the values for the porous substrate properties given in Table 3.

Solution of the momentum equation at various other Reynolds numbers for tubes 1 and 2 using the values of porous parameters in Table 3 are shown in Figs. 6 and 7. The friction factor predicted by the porous substrate model matches remarkably well with the experimental results. From the experimental results it is seen that the friction factor enhancement is more pronounced at lower values of the Reynolds number. This is due to the increased circumferential stress encountered by the flow at low Reynolds numbers. Compared to flow at high Reynolds number the flow at low Reynolds numbers undergoes more rotations within the tube causing increased circumferential drag. It is interesting to note that our model is able to predict correctly the friction enhancement mechanism reflected in the experimental data.

Extension of the numerical model to other tubes in the test matrix as well as to tubes not covered by the experiments will require an expression that relates the flute parameters (pitch and porosity) to the permeability of the porous substrate. Similar to the procedure described by Vafai and Tien (1980) and Vafai (1984), the permeability can be related to the flute pitch and porosity using the following constitutive functional form:

$$\mathrm{Da} = f(p_e^*)\frac{\delta^3}{(1-\delta)^2} \tag{29}$$

Based on the permeability obtained for tubes 1, 2, and 3, the following constitutive function is found to best correlate the nondimensional pitch with Darcy number:

$$\mathrm{Da} = (0.2795 p_e^{*3} - 0.2337)\frac{\delta^3}{(1-\delta)^2} \tag{30}$$

In the expression above, it should be noted that both the permeability (Darcy number) and the flute pitch are nondimensionalized with respect to the envelope diameter (D_e). This was done mainly to conform the Darcy number in the above expression to the porous media literature. Using Eq. (30), the permeability K_z for tube 4 was determined as 5.11×10^{-8} m^2. Analysis of tube 4 with the numerical model yielded results as shown in Fig. 8. The predictions of the porous substrate model are in very good agreement with the experimental data. This further confirms the appropriateness of the present model.

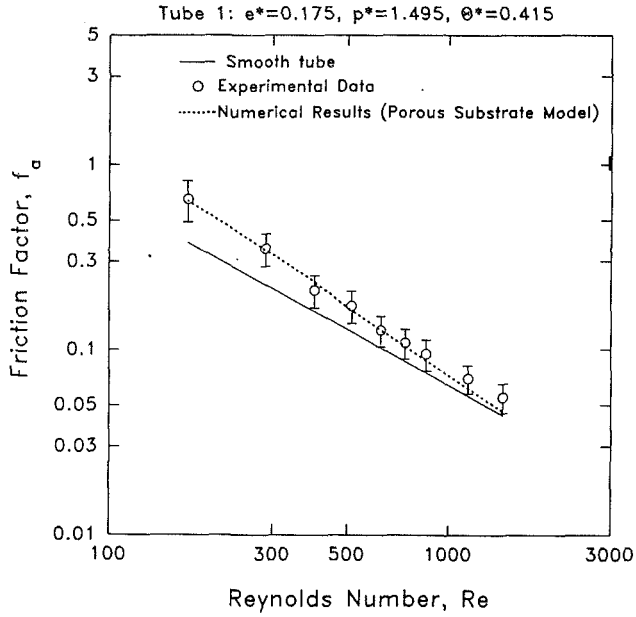

Fig. 6 Prediction of friction factor for tube 1 using porous substrate model

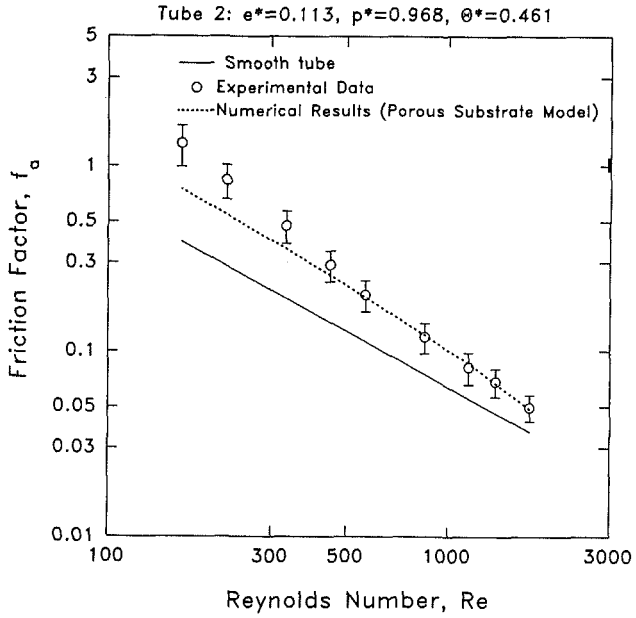

Fig. 7 Prediction of friction factor for tube 2 using porous substrate model

Typical velocity profiles in the z and θ directions are shown in Figs. 9 and 10. These profiles are for tube 2 but are representative of the velocity distributions for all of the tubes. The presence of porous layer is seen to affect flow velocities both in the porous as well as in the open regions. The θ component of velocity in Fig. 10 shows that the fluid core is in a solid body rotation. Note that at the interface the direction of the velocity vector coincides with that of the flute helix angle. The value of V_θ reaches a maximum within the porous substrate due to the no-slip condition at the wall, which introduces both axial and circumferential shear stress. Thus, the proposed numerical model is capable of capturing the main features of the flow structure.

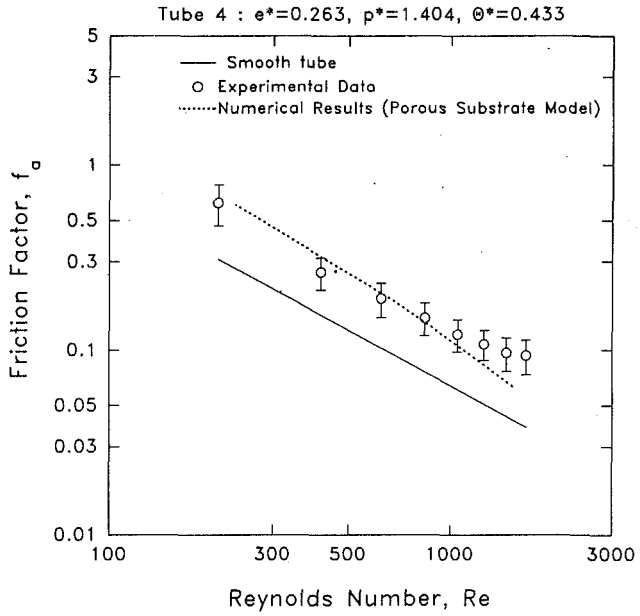

Fig. 8 Prediction of friction factor for tube 4 using porous substrate model

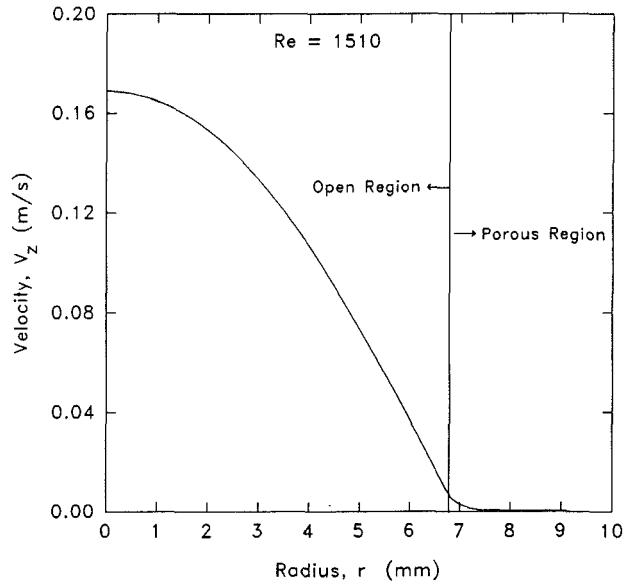

Fig. 9 Typical axial velocity profile (V_z) predicted by porous substrate model

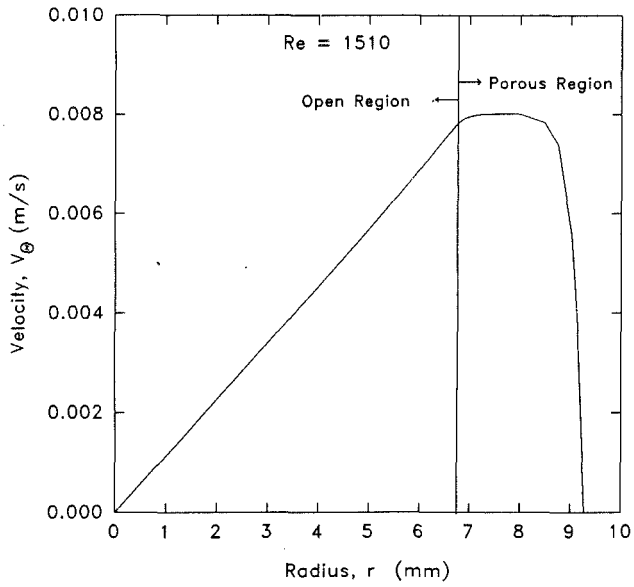

Fig. 10 Typical circumferential velocity profile (V_θ) predicted by porous substrate model

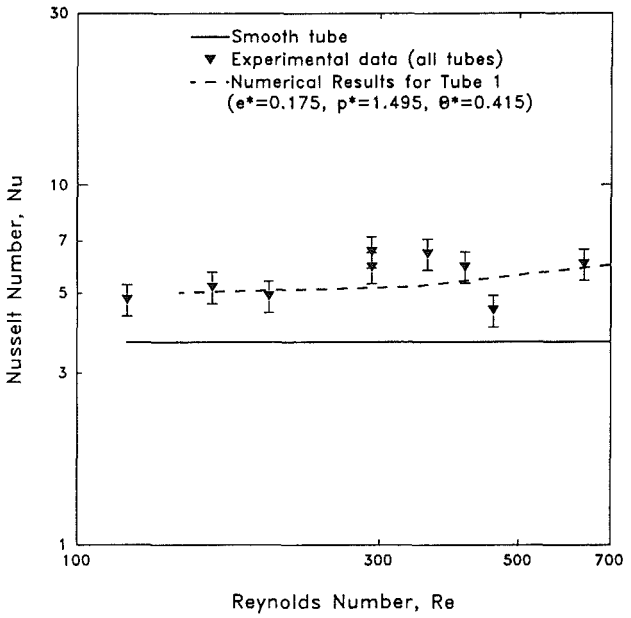

Fig. 11 Prediction of Nusselt number for tube 1 using porous substrate model

Solution of the energy equation for tubes 1 and 2 yields Nusselt numbers as shown in Figs. 11 and 12. In the same figures experimental laminar Nusselt numbers for the corresponding tubes were also plotted. The standard error was within 10 to 15 percent. The presence of porous substrate shows enhancement in Nusselt number compared to a plain tube. In the experiments, the higher flute depth (assuming same flute profile) enables a larger fraction of the flow in swirling mode. The centrifuging action enhances heat transfer. Likewise, for flutes with higher depth the porous substrate thickness is higher, resulting in a higher Nusselt number.

The effect of large k_{eff}/k in the porous matrix is seen in the temperature distribution presented in Fig. 13. Note the negligible temperature drop in the porous matrix. For Reynolds numbers below 500 the predictions are in good agreement with the experimental data. At higher Re, the porous model has underpredicted the Nusselt numbers. This is because the transition is initiated at a lower Reynolds number during heating. The transition Reynolds number obtained from the flow visualization tests as well as the friction factor tests were based on isothermal conditions. The studies of Yampolsky et al. (1984) had shown that under heated conditions the density gradients in the near-wall region could be destabilizing, thus initiating early transition. The jump in the Nusselt number as soon as transition sets in is significant. Since the numerical model is based on the assumption that the flow is laminar it is not expected to predict Nusselt number in the transition regime. Therefore we need a turbulent model to predict the Nusselt numbers in the turbulent range. In the turbulent range the predictions also need to be improved by considering the dispersion effects. It is also possible that the swirling motion in the presence of density gradients (arising out of temperature variation in the radial direction) promotes convection in the radial direction. This is an additional (even though not a significant) enhancement mechanism reflected in the experimental data that causes the experimental data to lie above the model

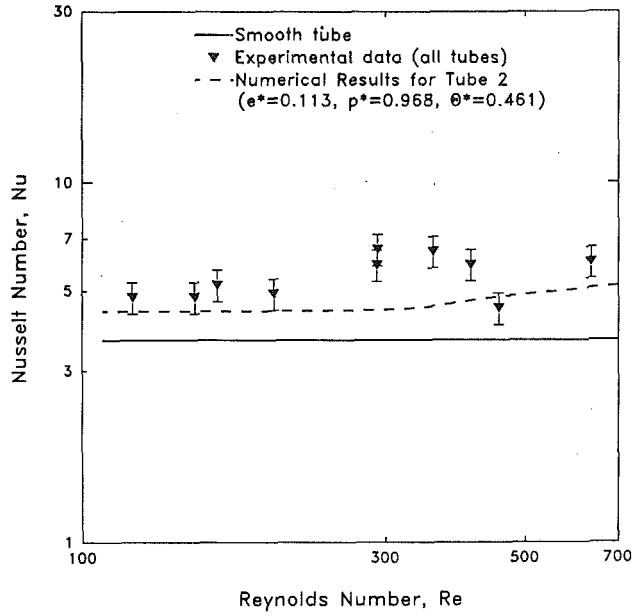

Fig. 12 Prediction of Nusselt number for tube 2 using porous substrate model

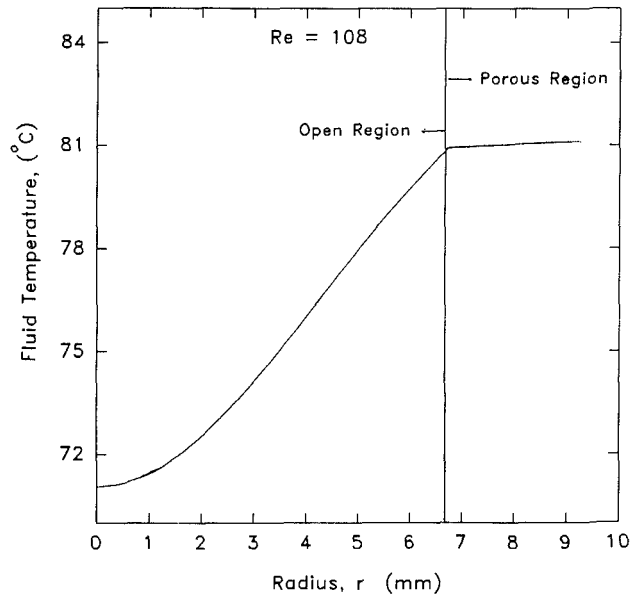

Fig. 13 Typical temperature distribution in the fully developed region predicted by the porous substrate model

predictions. Table 4 displays a sample of experimental data for both the friction factor and heat transfer enhancements for different Reynolds numbers and different tubes.

6 Conclusions

An innovative model for predicting the friction factor and heat transfer in spirally fluted tubes was presented. In this approach the flute region was modeled as a porous substrate with direction-dependent permeabilities. The modeling approach adopted in the present study enabled the porous substrate to influence the flow field in much the same manner as the spiral flutes. The application of the numerical model even to some of the tubes not covered in the Darcy number constitutive relationship gave very good agreement with the experimental results. The model presented in this work shows great promise and paves the way for future refinements and improvements to encompass various augmented tube configurations.

Table 4 Samples of experimental and numerical comparison of friction factor and heat transfer enhancement factors at different Reynolds numbers and for different tubes

Tube No.	Re	e_f		Re	e_h	
		Experiment	PSM		Experiment	PSM
1	169	1.72	1.68	120	1.3	1.37
1	300	1.6	1.6	163	1.42	1.39
1	628	1.25	1.25	200	1.34	1.4
1	1446	1.24	1.05	292	1.61	1.42
2	332	2.47	1.85	130	1.4	1.3
2	1151	1.48	1.55	170	1.42	1.32
4	207	2.02	2.22	200	1.34	1.4
4	621	1.84	1.90	220	1.35	1.4

PSM = Porous Substrate Model
e_f = Friction Factor Enhancement
e_h = Heat Transfer Enhancement

References

Arman, B., and Rabas, T. J., 1991, "Prediction of the Pressure Drop in Transverse Repeated Rib Tubes With Numerical Modeling," *Fouling and Enhancement Interactions*, ASME HTD-Vol. 164, pp. 85–92.

Barba, A., 1984, "The Prediction of Convective Heat Transfer in Spirally Fluted Tubes," Ph.D. Thesis, Victoria University of Manchester, Manchester, United Kingdom.

Bejan, A., 1984, *Convection Heat Transfer*, Wiley Interscience, New York.

Bergles, A. E., 1985, "Techniques to Augment Heat Transfer," in: *Handbook of Heat Transfer Applications*, W. M. Rohsenow, J. P. Hartnett, and E. N. Ganic, eds., McGraw-Hill, New York, pp. 3-1–3-80.

Date, A. W., 1974, "Prediction of Fully Developed Flow in a Tube Containing a Twisted Tape," *Int. J. Heat Mass Transfer*, Vol. 17, pp. 845–859.

Engleman, M. S., Strang, G., and Bathe, K. J., 1981, "The Application of Quasi-Newton Methods in Fluid Mechanics," *Int. J. Numerical Methods Eng.*, Vol. 17, pp. 707–718.

FIDAP, 1991, *Theoretical Manual*, Fluid Dynamics International Evanston, IL.

Garimella, S., and Christensen, R. N., 1993, "Experimental Investigation of Heat Transfer Characteristics of Annuli With Spirally Fluted Inner Tubes," presented at the ASME Winter Annual Meeting, New Orleans, LA.

Gosman, A. D., and Ideriah, F. J. K., 1972, "TEACH-T: A General Computer Program for Two-Dimensional, Turbulent, Recirculating Flows," Imperial College, Mech. Eng. Dept., London, United Kingdom.

Poulikakos, D., and Kazmierczak, M., 1987, "Forced Convection in a Duct Partially Filled With a Porous Material," ASME JOURNAL OF HEAT TRANSFER, Vol. 109, pp. 653–662.

Ravigururajan, T. S., and Bergles, A. E., 1991, "Visualization of Flow Phenomenon Near Enhanced Surfaces," *Fouling and Enhancement Interactions*, ASME HTD-Vol. 164, pp. 71–75.

Sözen, M., and Vafai, K., 1993, "Longitudinal Heat Dispersion in Packed Beds With Real Gas Flow," *AIAA J. Thermophysics and Heat Transfer*, in press.

Srinivasan, V., 1993, "Experimental and Numerical Investigation of Heat Transfer and Pressure Drop in Flow Through Spirally Fluted Tubes," Ph.D. Dissertation, The Ohio State University, Columbus, OH.

Tien, C. L., and Vafai, K., 1990, "Convective and Radiative Heat Transfer in Porous Media, Advances in Applied Mechanics," *Advances in Heat Transfer*, Vol. 27, Academic Press, pp. 225–281.

Vafai, K., and Tien, C. L., 1980, "Boundary and Inertia Effects on Convective Mass Transfer in Porous Media," *Int. J. Heat Mass Transfer*, Vol. 25, No. 8, pp. 1183–1190.

Vafai, K., and Tien, C. L., 1981, "Boundary and Inertia Effects on Flow and Heat Transfer in Porous Media," *Int. J. Heat Mass Transfer*, Vol. 24, pp. 195–203.

Vafai, K., 1984, "Convective Flow and Heat Transfer in Variable-Porosity Media," *J. Fluid Mech.*, Vol. 147, pp. 233–259.

Vafai, K., and Thiyagaraja, R., 1987, "Analysis of Flow Heat Transfer at the Interface Region of a Porous Medium," *Int. J. Heat Mass Transfer*, Vol. 30, No. 7, pp. 1391–1405.

Vafai, K., and Kim, S. J., 1990, "Analysis of Surface Enhancement by a Porous Substrate," ASME JOURNAL OF HEAT TRANSFER, Vol. 112, pp. 700–706.

Yampolsky, J. S., Libby, P. A., Launder, B. E., and LaRue, J. C., 1984, "Fluid Mechanics and Heat Transfer: Spiral Fluted Tubing," GA Technologies Report No. GA-A17833.

Effect of Flow Angle-of-Attack on the Local Heat/Mass Transfer From a Wall-Mounted Cube

V. Natarajan

M. K. Chyu

Department of Mechanical Engineering,
Carnegie Mellon University,
Pittsburgh, PA 15213

An experimental study of the local mass transfer over the entire surface of a wall-mounted cube is performed with a particular emphasis on the effects of flow angles-of-attack ($0 \text{ deg} \leq \alpha \leq 45 \text{ deg}$). Invoking an analogy between heat transfer and mass transfer, the presently obtained mass transfer results can be transformed into their heat transfer counterparts. Reynolds number based on the cube height and mean free-stream velocity varies between 3.1×10^4 and 1.1×10^5. To substantiate the mass transfer results, streakline patterns are visualized on the cube surfaces as well as the endwall using the oil-graphite technique. Significantly different flow regimes and local mass transfer characteristics are identified as the angle-of-attack varies. The overall convective transport is dominated by three-dimensional flow separation that includes multiple horseshoe vortex systems and an arch-shaped vortex wrapping around the rear portion of the cube. In addition to the local study, power correlations between the surface-resolved mass transfer Sherwood number and the Reynolds number are presented for all α values studied. Mass transfer averaged over the entire cube is compared with that of its two-dimensional counterpart with crossflow around a tall prism.

Introduction

Convective heat transfer over sharp-edged bluff bodies represents one of the most challenging research issues involving flow separation. Such a problem is often encountered in many prominent engineering applications. For example, three-dimensional roughness elements in the shapes of cube, diamond, and pyramid have long been considered for augmenting heat transfer from a heat-exchanger surface (Mantle, 1966). Similar transport phenomena may exist in cooling of electronic packages and wind aerodynamics around buildings, although the approaching flow characteristics may vary. Since the mid-1980s, significant research efforts have focused on flow features and thermal transport from a two-dimensional, square, bluff body. Near the midsection of a tall prism (two-dimensional regime), in the absence of endwall effects, Igarashi (1985, 1986) has systematically studied the heat transfer from the surface under different flow and geometric conditions, including the effects of different flow angle-of-attack (α, see Fig. 1). Goldstein et al. (1990) obtained mass transfer distributions both in the midsection and near the prism-endwall region (three-dimensional regime). Recently, heat transfer with three-dimensional flow separation induced by a wall-mounted cubical obstacle has attracted significant interest. Olsen et al. (1989), Roeller et al. (1991), and Chyu and Natarajan (1991) have experimentally examined the heat transfer characteristics around solitary cubical structures of normal orientation; i.e., $\alpha = 0$ deg relative to the mainstream direction. Due to the presence of the separated shear layer near the top of the cube, these results are significantly different from those in the two-dimensional case. According to Chyu and Natarajan (1991), for $3.1 \times 10^4 \leq \text{Re} \leq 1.1 \times 10^5$, heat transfer values from the front wall, the sidewalls, and the top wall are comparable to one another and are approximately 30 percent higher than that from the rear wall. As a contrast, heat transfer from the rear wall is the highest among all the surfaces of a two-dimensional square prism. Such a feature is due to vigorous vortex shedding behind the obstacle (Igarashi, 1985, 1986; Goldstein et al., 1990).

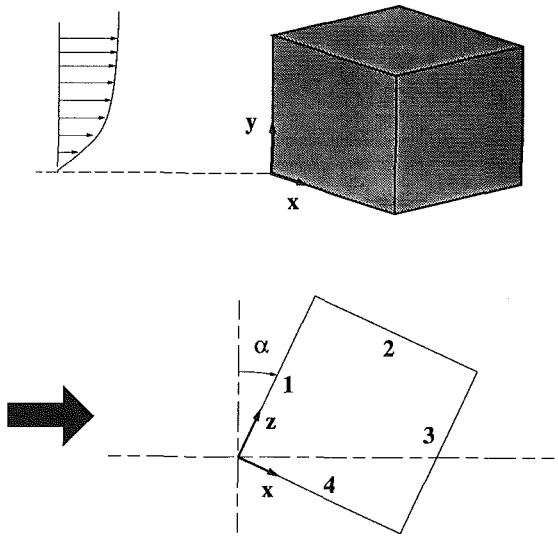

Fig. 1 Cube coordinate system

Previous studies of the effects of flow angle-of-attack on the transport phenomena around a sharp-edged bluff body are few, and the information available is mostly limited to two-dimensional situations. Based on the flow nature near surface 4 (see Fig. 1), Igarashi (1986) classified the flow patterns around the midsection of a tall prism into four different regimes. In his classification, "perfect separation" implies that the flow separating at the upstream-most edge of the prism does not reattach on any of the surfaces and the side surfaces are completely engulfed in recirculating fluid. Depending on the angle-of-attack, the separated flow may either be symmetric or asymmetric. If the separated flow reattaches on surface 4, the flow falls in the "reattachment flow" regime. Further, for large angles-of-attack, "wedge-flow" prevails with the flow literally gripping the entire front surfaces completely devoid of separation at the upstream-most edge. The four flow regimes are:

(*i*) Perfect separation and symmetric flow, 0 deg $\leq \alpha \leq 5$ deg

Contributed by the Heat Transfer Division for publication in the JOURNAL OF HEAT TRANSFER. Manuscript received by the Heat Transfer Division February 1993; revision received September 1993. Keywords: Analog Techniques, Flow Separation, Forced Convection. Associate Technical Editor: T. W. Simon.

(*ii*) Perfect separation and asymmetric flow, 5 deg $< \alpha \leq 13$ deg
(*iii*) Reattachment flow, 13 deg $< \alpha \leq 35$ deg
(*iv*) Wedge flow, 35 deg $< \alpha \leq 45$ deg

Each of these regimes has revealed distinct and profound features regarding the heat transfer from the prism surfaces. With this the case for two-dimensional regimes, it is speculated that the effects of flow angle-of-attack will also be significant for three-dimensional regimes where the body-endwall interaction is the dominating feature. To affirm such a speculation, the present study investigates the heat transfer from a wall-mounted cube with various orientations relative to the mainstream.

Since the complexity of the flow around a wall-mounted cube is expected to induce highly nonuniform surface heat transfer, resolution using conventional thermal measurement techniques may be insufficient. Therefore the present study employs a mass transfer system using the naphthalene sublimation technique. By invoking an analogy between heat transfer and mass transfer, the mass transfer results may be transformed into their heat transfer counterparts (Eckert, 1976). As suggested by Goldstein et al. (1985), a local study is much more complex and difficult to perform than its area-averaged counterparts. It generally requires a large number of data points, rapid data acquisition rate, and accurate positioning capability. To fulfill these requirements, the present study uses a computer-controlled, naphthalene surface profile measurement system similar to that developed earlier by Chyu (1986). In addition to the local study, correlations for the surface-averaged mass transfer with Reynolds number and Schmidt number are presented for various flow angles-of-attack. To corroborate the mass transfer experiments, near-wall streakline patterns are studied using the oil–graphite flow visualization technique.

Heat and Mass Transfer Analogy

The conventional heat transfer coefficient is defined as:

$$h = q/(T_w - T_\infty) \tag{1}$$

The corresponding mass transfer coefficient is given by:

$$h_m = m/(\rho_{v,w} - \rho_\infty) \tag{2}$$

By analogy between heat transfer and mass transfer, the driving potential for heat transfer, $(T_w - T_\infty)$, is equivalent to that of the naphthalene concentration difference between the surface and the free stream, $(\rho_{v,w} - \rho_\infty)$. Since naphthalene vapor concentration in the free stream is zero for the present case, Eq. (2) simplifies to

$$h_m = m\Delta t/\rho_{v,w} \tag{3}$$

The value of $\rho_{v,w}$ is evaluated using the naphthalene vapor pressure and temperature at the wall in conjunction with the ideal gas law. To determine the naphthalene vapor pressure at the wall, a third-degree correlation with Chebyshev polynomial interpolation as a function of temperature, as proposed by Ambrose et al. (1975), is used. Since the entire experimental system is maintained virtually isothermal, the naphthalene vapor concentration at the wall is uniform. To account for the minor fluctuations in the wall temperature during a test run, $\rho_{v,w}$ is determined by time-averaging the naphthalene concentration values at the surface. Details of the measurement procedures have been described by Goldstein et al. (1985) and Chyu (1986).

The magnitude of mass transfer rate per unit area, m, in Eq. (3) is determined from measuring the change of surface elevation due to sublimation. The magnitude of m is related to the change of naphthalene surface elevation (Δy) during a test run-time (Δt); i.e.,

$$m = \Delta y \rho_s / \Delta t \tag{4}$$

where ρ_s is the density of solid naphthalene. Combining Eqs. (3) and (4) leads to

$$h_m = (\rho_s \Delta y)/(\rho_{v,w} \Delta t) \tag{5}$$

The local mass transfer coefficient can further be transformed to its dimensionless counterpart, Sherwood number (Sh), defined as

$$\mathrm{Sh} = h_m D/K \tag{6}$$

By analogy, the Sherwood number is related to the Nusselt number (Nu) of heat transfer,

$$(\mathrm{Nu}/\mathrm{Sh}) = (\mathrm{Pr}/\mathrm{Sc})^n \tag{7}$$

According to Igarashi (1986), the power index n is approximately 1/3.

Experimental Setup

The experiments are performed in an open-loop, suction-mode, wind tunnel with a test section 1.22 m long and 0.31 m square in cross section. A motor speed-controller permits continuous air-speed variation up to approximately 70 m/s through the test section. Near the tunnel inlet, there are a series of filters, honeycombs, and a 16:1 contraction section for flow conditioning. An exhaust system guides the tunnel discharge out of the laboratory, ensuring the tunnel inlet air free of naphthalene. The test includes ten flow angles-of-attack: from 0 deg to 45 deg, with a 5 deg increment. Change of angle is actually done by varying the cube orientation relative to the axial air stream direction in the wind tunnel. For each angle-

Nomenclature

C_1 = correlation coefficient, see Table 1
C_2 = correlation power index, see Table 1
D = cube height
h = heat transfer coefficient, Eq. (1)
h_m = naphthalene mass transfer coefficient, Eq. (2)
m = mass transfer flux of naphthalene from surface
K = naphthalene–air diffusion coefficient
k = thermal conductivity
n = power index
Nu = Nusselt number = hD/k
Pr = Prandtl number
q = heat flux from wall
Re = Reynolds number = UD/υ
Sc = naphthalene–air Schmidt number = υ/D
Sh = naphthalene mass transfer Sherwood number = $h_m D/K$
$\overline{\mathrm{Sh}}$ = surface-resolved average Sherwood number
$\overline{\overline{Sh}}$ = overall cube Sherwood number
T_w = temperature of wall
T_∞ = temperature of free stream
t = time
U = velocity of free stream
x, y, z = coordinate system, see Fig. 1
α = flow angle-of-attack, see Fig. 1
Δ = finite difference operator
υ = kinematic viscosity of air
$\rho_{v,w}$ = vapor mass concentration or density of naphthalene at the wall
ρ_∞ = vapor mass concentration or density of naphthalene in free stream, zero in the present study
ρ_s = density of solid naphthalene

of-attack, four different Reynolds numbers, based on the cube height (D = 51 mm) and the free stream velocity, are studied: 3.1×10^4, 6.1×10^4, 8.2×10^4, and 1.04×10^5. The turbulent boundary layer is tripped by a 3-mm steel wire located at the inlet of the test section. The upstream-most edge, i.e., the common edge of surfaces 1 and 4 of the test cube, is located approximately 0.48 m from the trip wire. The boundary layer thickness at this location, without the cube, is approximately 12 to 15 mm (about $1/5 \sim 1/4$ of cube height) for all the Reynolds numbers studied. Under the same conditions, the free stream turbulence intensity determined by a hot wire anemometer is about 0.3 percent.

The cube, measured at 51 mm (2 in.) each side, is an assembly of six aluminum plates. Each plate is 6.4 mm thick. Five of these plates are exposed to the free stream and are coated with naphthalene; the sixth plate forms the mounting base. Several L-shaped brackets mounted inside the hollow cube are used to connect adjacent plates and ensure a tight fit. Two copper-constantan thermocouples for measuring the naphthalene surface temperature are also routed through the cube inside. Except very near the edge, an approximately 3 mm recess is provided on each of the surfaces to facilitate coating of naphthalene. Near the edge on each of the surfaces, a 0.8-mm-wide aluminum strip is maintained. The purpose of maintaining these metallic edges is twofold. First, they provide reference points that are essential for the local mass transfer measurements (Goldstein et al., 1985). Second, a metallic edge helps to retain a perfect cube configuration unaffected by the high naphthalene sublimation rate near the corners. The trade-off is that the metallic section is mass transfer inactive, so the mass transfer boundary is not perfectly continuous over the entire cube. However, this effect is considered to be insignificant since the edge width is less than 2 percent of the cube dimension.

The present local mass transfer measurement uses a 21 × 21 uniform grid of measurement points on each surface, which gives about 2 mm spacing between any two adjacent measurement points. In essence, each grid is equivalent to a heat flux gage on an isothermal surface. Prior to a profile measurement, all the surfaces are weighed individually on a high-precision electronic balance (Sartorius 4001 MP), which has an accuracy of 1 microgram. This enables cross verification by comparison with the integral of the local data with the surface-resolved, average mass transfer. The agreement is within 7 percent, which assures the quality of the present experimental system. The mass transfer active cube is exposed to the wind tunnel airstream for a period of 30 minutes during which thermocouple readings are recorded every three minutes. At the completion of the test, the cube is disassembled and the plates are weighed. This is followed by the post-test surface profile measurement. The difference of the two surface profiles measured before and after the wind exposure gives the local mass transfer distribution over a surface. Typical sublimation depth over the 30-minute test duration is in the order of 0.1 mm. Based on the method of Kline and McClintock (1953), estimated uncertainty of the local Sherwood number is approximately 5 percent.

For flow visualization, a solid aluminum cube is used instead of the hollow cube. Oil mixed with fine graphite powder is brushed on white glossy paper sheets, which are affixed to the cube surfaces. The flow arranges a spatial variation of black-to-white contrast, representing different levels of wall shear stress and near-wall flow directions. A dark region where graphite powder accumulates typically implies low-speed zone or the existence of flow separation and recirculation. On the contrary, in a bright region, flow speed is relatively high or the flow may be reattaching. Since important flow features are often altered or destroyed as the cube is removed from the wind tunnel, post-run photos can be very misleading. Therefore sketches of streaklines based on in-tunnel observation are presented.

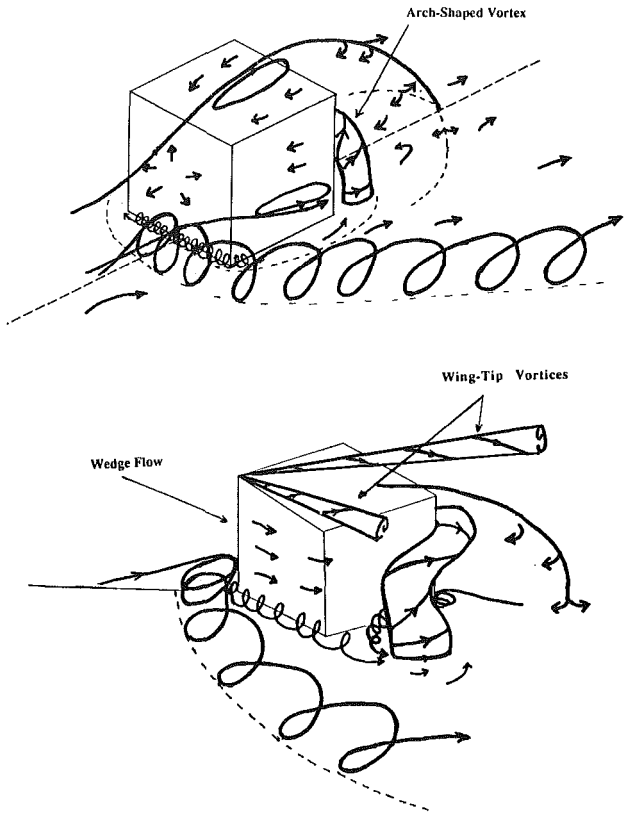

Fig. 2 Projected flowfield around a cube: (*a*) α = 0 deg; (*b*) α = 45 deg

Results and Discussion

Within the present test range, the trend of local mass transfer distributions as well as the flow characteristics is somewhat insensitive to the Reynolds number. Hence, to describe the local results and flow patterns, only the case of Re = 8.2×10^4 is reported. In addition, to illustrate the effects of flow angle-of-attack on transport phenomena, four representative cases; i.e., α = 0 deg, 10 deg, 25 deg, and 45 deg are used. Figure 1 shows the coordinate system chosen for presentation. Note that the principal axes are aligned with the individual surfaces of the cube and each of the five cube surfaces are designated as 1, 2, 3, 4, and top surface.

Flow Characteristics. Figure 2 reveals qualitative flow patterns around a cube for orientations 0 deg and 45 deg, the only two symmetric cases of this study. The sketches are based on collective evidence from streakline patterns visualized on both the cube surface (Fig. 3) and the endwall (Fig. 4). There are two common flow features observed for both orientations: (1) multiple horseshoe vortices wrapping around the base region, and (2) an "arch-shaped" vortex in the wake region behind a cube. These common features are expected to prevail for all cube orientations, since 0 deg and 45 deg are the two extreme cases in terms of α variation. The endwall flow patterns, to be discussed later, in Fig. 4 clearly confirm this expectation. Because of the asymmetric nature and the lack of conclusive information for flow away from the wall, flow schematics similar to those shown in Fig. 2 are not attempted for the two intermediate cases, α = 10 and 25 deg.

Further examination of flow sketches in Fig. 2 shows that the flow features atop the cube and around the sidewalls are significantly different between α = 0 deg and α = 45 deg. For α = 0 deg, the top surface is virtually engulfed in a separation bubble, which was initiated near the surface leading edge, whereas twin delta-wing-type vortices with spanwise helical motions are formed for α = 45 deg. The latter vortices are similar to those around airfoils with their leading edges

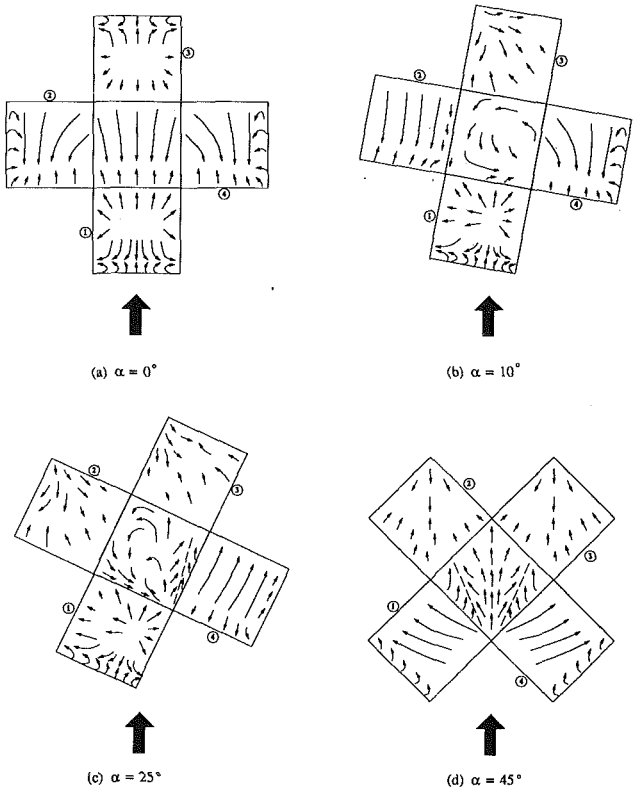

Fig. 3 Near-wall streakline patterns on cube surfaces: (*a*) α = 0 deg; (*b*) α = 10 deg; (*c*) α = 25 deg; (*d*) α = 45 deg

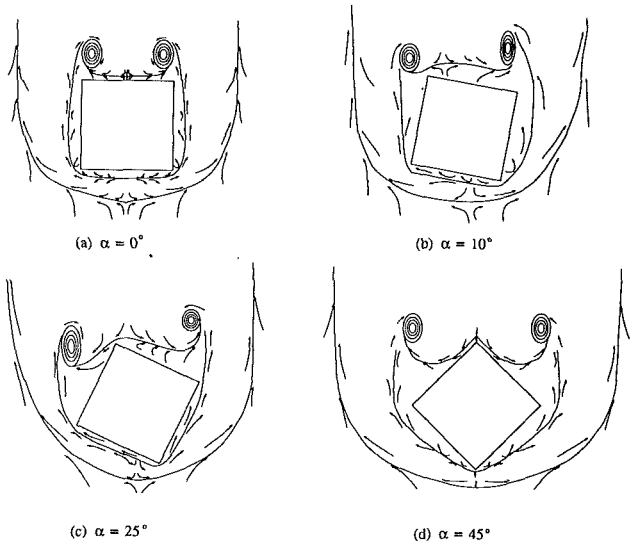

Fig. 4 Streakline patterns on endwall: (*a*) α = 0 deg; (*b*) α = 10 deg; (*c*) α = 25 deg; (*d*) α = 45 deg

inclined to the flow direction. Such flow features near the cube top agree well with those reported by Castro and Robins (1977) and Ogawa et al. (1983). Around the cube sidewalls, the majority of the surfaces are enclosed in a reverse flow for α = 0 deg. An intriguing phenomenon observed during the actual flow visualization is a strong unsteadiness with periodic burstings occurring near the lower upstream corner where the inner horseshoe vortex experiences a severe turn. The bursting frequency, which appears to increase with the Reynolds number, is about 1 to 2 hertz. As a sharp contrast, flow near the side surfaces for α = 45 deg is primarily steady and moves strictly forward, without separation.

As mentioned earlier, Igarashi (1985) has classified different flow regimes around a two-dimensional square prism, based on the specific flow features adjacent to surface 4. Following the same approach, the three-dimensional effects expected to dominate in the present cube-endwall system can be realized by looking at the corresponding two-dimensional results. According to the present flow visualization, the four distinctly different flow regimes are:

(*i*) Perfect separation and symmetric flow, $\alpha = 0$ deg
(*ii*) Perfect separation and symmetric flow, 0 deg $< \alpha \leq 14$ deg
(*iii*) Reattachment flow, 14 deg $< \alpha \leq 40$ deg
(*iv*) Wedge flow, 40 deg $< \alpha \leq 45$ deg

An interesting finding is that the transition between the flow regimes (*ii*) and (*iii*) seems to occur at nearly the same values of α as seen for the two-dimensional case. However, the two classifications are substantially different for small flow angles-of-attack and the transition from regime (*i*) to (*ii*). According to Igarashi (1985), perfect separation with symmetry prevails for 0 deg $\leq \alpha \leq$ 5 deg for the two-dimensional situation; whereas a slight angle deviation from the normal orientation (α = 0 deg) drastically destroys the flow symmetry around a cube. Part of the asymmetry is attributable to helical vorticity manifested atop the cube, which is nonexistent in its two-dimensional counterpart. Such an asymmetric flow feature can be observed from the streakline patterns for α = 10 and 25 deg, shown in Figs. 3(*b*) and 3(*c*). Evidence of asymmetry is also revealed in Figs. 4(*b*) and 4(*c*) as the separation line of the inner horseshoe vortex is skewed around the cube base. When 15 deg $\leq \alpha \leq$ 40 deg, besides asymmetry, flow separated from the upstream edge of surface 4 appears to reattach on the same surface downstream, hence the name "reattachment flow." A further increase in α, 40 deg $< \alpha \leq$ 45 deg, reveals a wedge-type behavior of the flow and the disappearance of separation from the common edge of surfaces 1 and 4. Flow adjacent to surface 4 moves steadfastly downstream showing typical wall-attached boundary layer characteristics.

It is worthy of mentioning that the nature of the flow patterns around a wall-mounted cube may vary substantially with different approaching-flow conditions; e.g., boundary layer thickness, level of free-stream turbulence, Reynolds number, etc. With the boundary layer thickness much greater than the cube size, which is typical for environmental flow around buildings, Paterka et al. (1985) reported that the reattachment flow regime prevails, even for the normal orientation α = 0 deg. Hence the present flow classification may only be valid for situations with relatively thin boundary layers, as the boundary layer thickness measured in the wind tunnel is about 1/4 to 1/3 of the cube height.

Local Mass Transfer Distributions. The local mass transfer results, shown by contour plots of local Sherwood number (Sh) in Fig. 5, display features highly accordant with the near-wall flow patterns. Since the influence of Reynolds number on the general trend of mass transfer distributions on all surfaces is found to be rather insignificant within the present test range, only the case of Re = 8.2×10^4 is presented here.

(1) $\alpha = 0$ deg. Mass transfer around a cube positioned at the normal orientation, α = 0 deg, was studied earlier by the present authors (Chyu and Natarajan, 1991). Virtually the same results have been obtained in the present tests, which provides confidence in the present data. For surface 1 (front wall), the radially outward moving streakline pattern revealed in Fig. 3(*a*) implies that a high pressure stagnation zone exists near the upper central region of the surface. The mass transfer in the stagnation zone is quite uniform and relatively low compared to the outer regions, as shown in Fig. 5(*a*). The stagnant flow accelerates radially out of this central zone and

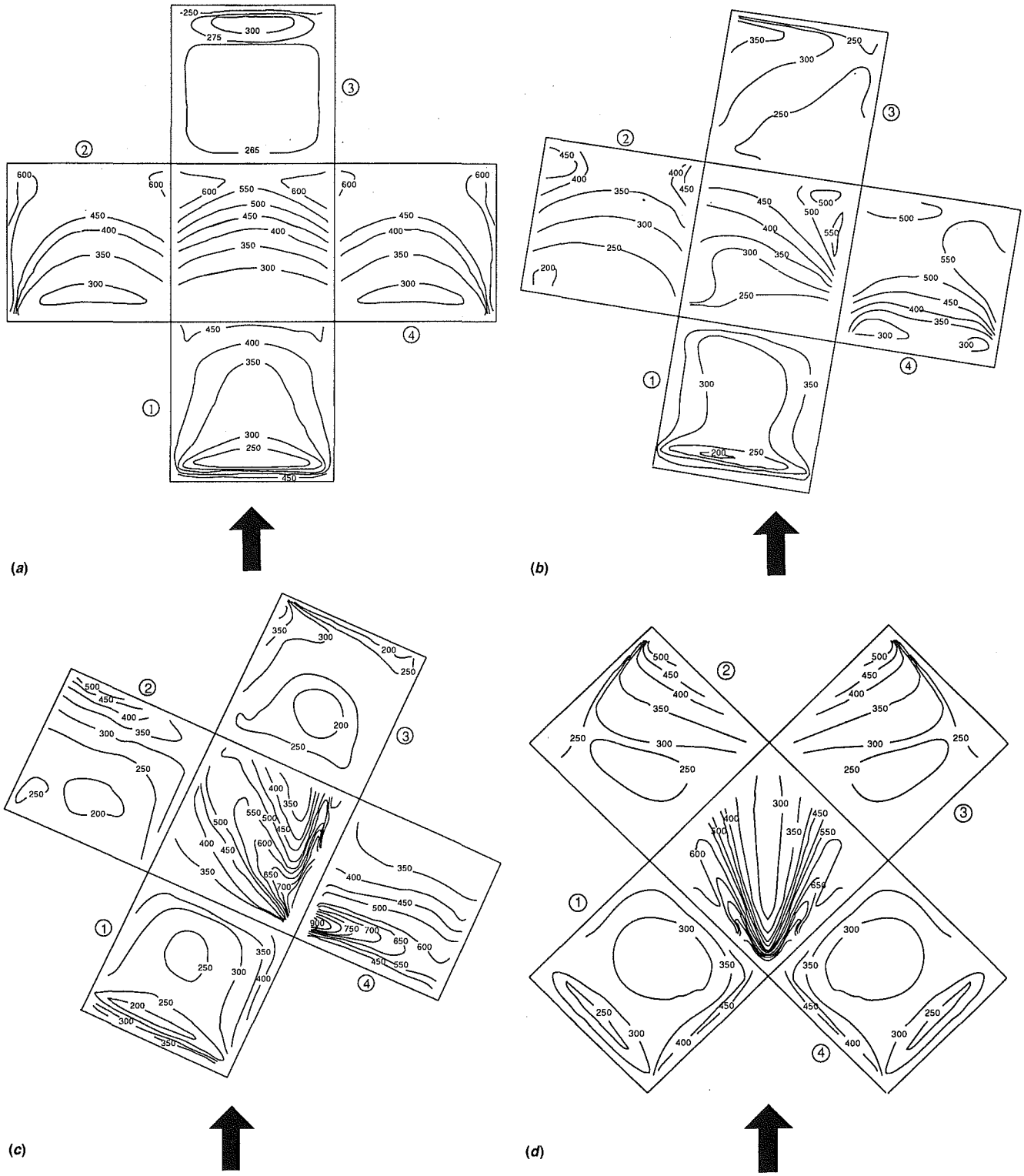

Fig. 5 Local Sherwood number contours on cube surfaces: (*a*) α = 0 deg; (*b*) α = 10 deg; (*c*) α = 25 deg; (*d*) α = 45 deg

produces a substantial increase in mass transfer towards the edges. Below the central zone, the local mass transfer reaches a minimum at approximately $y/D = 0.1$ to 0.15. Farther below this local minimum, mass transfer rises sharply again toward the lower corner immediately adjacent to the endwall junction. According to Chyu and Natarajan (1991), this elevated mass transfer is attributable to a secondary, but intense, corner vortex embedded underneath the primary vortex. A similar effect has also been reported for wall-mounted cylinders (Chyu and Natarajan, 1991) and square prisms (Goldstein et al., 1990). In the present study, such a multiple-vortex system seems to always exist for all the angles examined.

Except for the region near the leading edge, most of the side surfaces are engulfed in a recirculation zone with the result that the mass transfer increases toward the downstream edges. Due to symmetry, the mass transfer contours for the surface 4 are virtually identical to those of surface 2. An important finding is that very high mass transfer exists near the upstream lower corner where the flow, as described earlier, exhibits periodic unsteadiness with low-frequency bursting. In addi-

tion, according to flow visualization, the intense vortex responsible for the mass transfer rise near the lower corner of the front wall turns sharply into this region. The presence of such a vortex may also contribute to the elevation of mass transfer here. The Sh distribution on the top surface displays perfect symmetry with respect to the mainstream direction (x axis). The mass transfer varies little across the surface span (z direction). As a contrast, the magnitude of Sh increases continuously along the streamwise direction. Such a trend is consistent with the flow visualization, which shows that the entire top surface is engulfed by separated flow.

Transport phenomena behind the cube, i.e., near surface 3, are strongly influenced by the arch-shaped vortex that is sketched in Figs. 2(a) and 4(a). Although the wake region is expected to suffer a significant momentum deficit, highly turbulent mixing prevails, which results in fairly uniform mass transfer over the surface. The relatively slow-moving fluid present in the vicinity induces lower Sh magnitudes than those of the other surfaces. It is important to recognize that, for $\alpha = 0$ deg, the domain of influence of the arch-shaped vortex appears to lie only on the rear surface 3, whereas this is not the case when $\alpha \neq 0$ deg. Evidence to be presented later reveals that the arch-shaped vortex may expand its domain of influence to both surfaces 2 and 3.

(2) $\alpha = 10$ deg. As illustrated in Fig. 3(b), the surface streakline pattern for $\alpha = 10$ deg is asymmetric. On surface 1, this asymmetry occurs because the stagnant region due to impingement shifts slightly toward the upper right-hand corner (near junction of surface 1 and 4). Accordingly, the mass transfer Sh contours tilt slightly off the symmetric pattern, as shown in Fig. 5(b). The highest mass transfer over the entire surface 1 occurs near the upper right-hand corner near the most upstream part of the entire cube. Similar to the case of $\alpha = 0$ deg, a local minimum in Sh occurs at approximately $y/D = 0.1$ to 0.15 near the lower corner. However, its actual local location shifts slightly toward the left-hand side near the junction of surfaces 1 and 2. Based on the values of Sh contours, the case with $\alpha = 10$ deg apparently has a lower mass transfer averaged over the entire surface 1 than $\alpha = 0$ deg.

On the cube sidewalls, i.e., surfaces 2 and 4, one of the most significant features of the $\alpha = 10$ deg flow is that mass transfer near the upstream lower corner is much lower than that of $\alpha = 0$ deg. The periodic burst phenomenon that causes high mass transfer for $\alpha = 0$ deg is hardly noted in the flow visualization. According to Fig. 5(b), a 10-deg tilt produces an overall mass transfer decrease on surface 2 and, as a contrast, an increases on surface 4. This agrees well with the general behavior of heat or mass transfer with a boundary layer developing on an inclined wall. Other than this, the general trend of local mass transfer distribution on both surfaces is quite similar to that of the $\alpha = 0$ deg case. The value of Sh generally increases along the x direction, revealing the characteristics of recirculating flow adjacent to the surface. Also, Sh varies little across the height of the cube.

Locating the cube at 10 deg off symmetry drastically alters transport behind the cube. As shown in Fig. 3(b), streakline patterns on surface 3 exhibit a distorted, arch-shaped vortex. The inclined upwash from the lower edge between surfaces 2 and 3 colliding with the inclined downwash from the upper edge between the surfaces 3 and 4 implies a separation zone oriented diagonally across the surface. As a result, the surface mass transfer contours, shown in Fig. 5(b), also display a pattern of diagonal variation. However, the vortex-enhanced mixing behind the cube dominates, so that the values of Sh vary little over most of the surface. The evidence of a distorted arch-shaped vortex on the endwall can be seen in Fig. 4(b). Note that the vortex extends its domain of influence to the region downstream of surface 2 which, in essence, is one of the two sidewalls. Further examination of the four different endwall flow patterns exhibited in Figs. 4(a) to 4(d) suggests that this increasing trend of domain of influence continues as α increases.

Similar to other surfaces, the 10 deg asymmetry greatly affects the transport features atop the cube. On the top surface, the inclination of the side-edge adjacent to surface 4 impels a helical, streamwise vortex superimposed on a shear layer, which has separated at the leading edge adjacent to surface 1. The downstream edge, which is mildly skewed, is also expected to induce a weak streamwise vortex. This combined vortex flow yields streakline pattern of counterclockwise rotation as viewed from the top of the cube, sketched in Fig. 3(b). The streamwise vortex generated near the common edge with surface 4 appears to be one of the primary sources for such a secondary flow pattern. The helical motion is expected to promote higher turbulence and entrain into the boundary layer atop the cube mainstream air, which is either free of, or less concentrated with, naphthalene. Consequently, mass transfer along the path of vortex development will be higher than that of other locations. The maximum Sh over the entire top surface exists near the downstream corner, leaning to the side of surface 4 where the vortex motion appears to reach the strongest level, as illustrated in Fig. 5(b). Overall, the magnitudes of Sh on the top surface are quite similar to those of surfaces 2 and 4.

(3) $\alpha = 25$ deg. Among the four cases reported, the cube with a 25 deg angle-of-attack induces the most pronounced asymmetry in flow pattern, Fig. 3(c), and mass transfer, Fig. 5(c). The extent of asymmetry is much more distinct for surfaces 2 and 4 and the top surface. The transport features on these surfaces are substantially different from their respective counterparts of the $\alpha = 10$ deg case. On the other hand, surfaces 1 and 3 exhibit a relatively mild variation. Near the central portion of surface 1, a stagnant zone with somewhat uniform mass transfer remains evident. However, its location shifts more toward the upstream corner near the common edge adjacent to surface 4. In the lower part of the surface near the endwall junction, the effect of interaction of the corner vortex with impingement-induced downwash dominates. This results in a significant mass transfer variation in the region.

Similar to the case of $\alpha = 10$ deg, transport features behind the cube are dominated by the asymmetric or distorted arch-shaped vortex. As revealed in Fig. 4(c), the distortion is so severe that the tracks of the two arch-columns down the endwall are notably different in size and are asymmetric. Comparing the endwall streakline patterns, illustrated in Fig. 4, shows that an increase in α tends to move the arch-shaped vortex away from the cube. Hence its influence on the mass transfer from the nearby surfaces is expected to be lessened. However, even with such a diminishing effect, mass transfer on surface 3 still reveals a significant influence of the distorted vortex. A diagonal separation zone is formed due to a collision between an inclined upwash and an inclined downwash from two diagonally opposite corners. However, the separation appears to shift more toward the lower edge of surfaces 2 and 3, as compared to the $\alpha = 10$ deg case.

The mass transfer characteristics on surface 4 and the top surface show features that are distinctly from those of $\alpha = 0$ or 10 deg. The effect of reattachment on the mass transfer from surface 4 is clearly evidenced by the sharp rise in mass transfer near its upstream edge. Following reattachment, the mass transfer decreases monotonically downstream. As a direct result of the flow complexity, the Sh contours on the cube top surface display an unusual pattern. The oil streak flow visualization reveals that the flow pattern atop the cube is a combination of two different flow structures. The first is comprised of a recirculation bubble, which is typical for the $\alpha = 0$ deg case and is shown in Fig. 2(a). The second is a helical flow motion driven by a delta-wing tip vortex, as displayed in Fig. 2(b) for $\alpha = 45$ deg. The local mass transfer distributions shown in Fig. 5(c) clearly indicate that this vortex aligns its helical path very close to the joint edge with surface 4. The

existence of such delta wing-tip vortices is expected to promote more effective mixing, hence the top surface overall has a higher mass transfer than all other surfaces.

(4) $\alpha = 45$ deg. As given in Fig. 5(*d*), the Sh contours display an excellent symmetry over all the five surfaces. On surfaces 1 and 4, the two "front" surfaces, mass transfer measurements reveal a dominance of the wedge-flow behavior without flow reattachment. Accordingly, the local Sh attains its maximum near the upstream-most edge and then decreases in magnitude toward the downstream. However, such a decreasing trend ceases near the central portion of the surface where Sh reaches virtually a constant value (≈ 300). This, in principle, agrees well with the notion that surface inclination in a windward fashion flattens the boundary layer and inhibits variation in transport along the streamwise direction. Similar behavior is observed for surface 4 at $\alpha = 10$ deg. The local heat transfer reported for a two-dimensional prism (Igarashi, 1985) also demonstrates such characteristics. Another significant finding is that a relatively inactive mass transfer region exists in the lower part of the surface near the endwall junction. This is in a sharp contrast to the case of $\alpha = 0$ deg, where the presence of a set of counterrotating, horseshoe vortices heightens the mass transfer in the corner region. Based on the endwall streakline pattern shown in Fig. 4(*d*), the horseshoe vortices have their paths moved relatively away from the cube and thereby are less influential in the cube vicinity as compared to the other cases. Near the endwall junction, both surfaces 1 and 4 have a local minimum in mass transfer located near $y/D \approx 0.10$ and $x/D \approx 0.5$. Although the exact location may vary, this feature of minimum mass transfer is common to all the cases studied.

Mass transfer on surface 2 and 3, both the "rear" surfaces for this case, is dominated by the arch-shaped or inverted "*U*" vortex. Nevertheless, this vortex now conforms to the shape of a "*W*," as viewed from the top, shown in Fig. 4(*d*). The variation of mass transfer across the height of these surfaces becomes very prominent near the downstream-most edge of the cube. The Sherwood number generally increases from the upper corner of the upstream edge to the lower corner of the downstream edge, exhibiting a diagonally increasing trend. Note that the maximum mass transfer occurs at the lower part of the downstream edge where the *W*-shaped vortex appears to be in close contact with the cube surface.

On the top surface, two symmetric bands of high mass transfer emanate from the upstream-most corner and spread downstream. Compared to the streakline trace shown in 3(*d*), this phenomenon apparently is caused by the two delta wing-tip vortices. As portrayed in Fig. 2(*b*), these vortices, accompanied with helical motions, promote more effective mixing and enhanced mass transfer along their paths. According to Fig. 5(*d*), the maximum Sh over the entire surface exists near the upstream-most, leading corner, where the gradient of mass transfer variation is also the greatest. On the other hand, the lowest mass transfer occurs near the downstream-most corner. Based on the values of Sh contours, the top surface apparently has the highest mass transfer overall of the five exposed faces.

Face-Averaged Mass Transfer. Figure 6 reveals the variation of surface-averaged Sherwood number ($\overline{Sh}$), normalized by the value of $Sc^{1/3}$, with angle-of-attack at $Re = 8.2 \times 10^4$. Note that the value of α lies between 0 and 45 deg with 5 deg increments. Among the five participating surfaces, surface 4 appears to have the strongest dependence of average mass transfer on the magnitude of α. This unique characteristic makes surface 4 the most rational site to characterize the flow regime around a cube for different flow angles-of-attack. Here, the value of Sh increases initially from $\alpha = 0$ to 15 deg and then drops consistently from 15 to 45 deg. Note that the maximum $\overline{Sh}$ at $\alpha = 15$ deg coincides with the onset of the "reattachment flow" regime (i.e., 15 deg $\leq \alpha \leq$ 40 deg), as

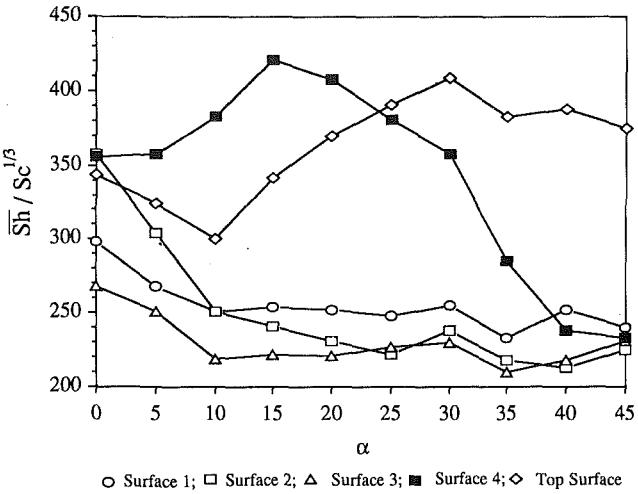

Fig. 6 Face-resolved mass transfer with angle-of-attack

categorized earlier. Reattachment is apparently responsible for such a mass transfer boost. Although the actual range of "reattachment flow" regime varies, similar observations have been reported for a two-dimensional prism (Igarashi, 1986).

As a sharp contrast to surface 4, $\overline{Sh}$ for surface 1 and 3 is less sensitive to variation in angles-of-attack. On surface 1, this insensitivity is because the flow near the surface has similar features (viz., stagnation zone, horseshoe vortices) for the cases of various α. For surface 3, it is the persistent domination of the arch-shaped vortex over the entire range of α that is responsible for the lack of sensitivity to α. In general, the average mass transfer rates for surfaces 1, 2, and 3 show a similar trend as α increases: A maximum $\overline{Sh}$ occurs at $\alpha = 0$ deg, followed by a sharp decrease for 0 deg $< \alpha \leq 10$ deg, and then levels off when 10 deg $< \alpha \leq 45$ deg. Among these three surfaces, surface 2 has the highest maximum $\overline{Sh}$ at $\alpha = 0$ deg and the most severe drop thereafter. This phenomenon can be closely linked to the fact that the unsteady bursting visualized near the upstream lower-corner diminishes with an increase in α.

According to Fig. 6, $\overline{Sh}$ on the top surface also decreases for 0 deg $< \alpha \leq 10$ deg. However, distinictly different from surfaces 1 to 3, the drop ceases at $\alpha = 10$ deg and then increases monotonically with α until reaching a maximum at $\alpha \approx 30$ deg. With a further increase in α, the magnitude of $\overline{Sh}$ levels off showing a minor decreasing trend. The minimum near $\alpha = 10$ deg represents the onset influence of the delta-wing tip vortex which develops atop the cube. With this special flow feature, the value of $\overline{Sh}$ on the top surface surpasses those of the other surfaces when $\alpha \geq 25$ deg. On the other hand, it is surface 4 that has the highest mass transfer among all the participating surfaces when $\alpha < 25$ deg. Surfaces 1 to 3 generally have lower mass transfer rates than surface 4 and the top surface.

As is usually the case, the dependence of surface average mass transfer on the Reynolds number can be represented as a power-law correlation: i.e., $\overline{Sh}/Sc^{1/3} = C_1 Re^{C_2}$. By analogy, the left-hand side of the correlation equals $\overline{Nu}/Pr^{1/3}$ in heat transfer. Table 1 lists the values of C_1 and C_2 for the participating surfaces. A positive power index, C_2, implies that the extent of mass transfer as well as heat transfer increases with Reynolds number. According to the tabulated data, all faces have the weakest dependency (lowest C_2) on the Reynolds number at $\alpha = 10$ deg. In addition, among all five participating surfaces, surface 1 (front wall) has the weakest Re dependency. Despite difference in separated flowfields, this finding agrees favorably with its two-dimensional counterpart. Using a square prism in crossflow with $5.6 \times 10^3 \leq Re \leq 5.6 \times 10^4$, Igarashi (1985) reported that the corresponding value for C_2 is 1/2 for

Table 1 Average mass transfer correlations for cube surfaces

Angle	$\alpha = 0°$		$\alpha = 10°$		$\alpha = 25°$		$\alpha = 45°$	
Constants / Surfaces	C_1	C_2	C_1	C_2	C_1	C_2	C_1	C_2
1	0.705	0.538	0.795	0.511	0.222	0.616	0.177	0.637
2	0.200	0.666	0.227	0.623	0.028	0.791	0.027	0.799
3	0.159	0.661	0.272	0.596	0.026	0.794	0.028	0.797
4	0.226	0.652	0.403	0.607	0.052	0.781	0.168	0.643
Top	0.200	0.657	0.314	0.609	0.046	0.789	0.082	0.745
Overall	0.278	0.626	0.385	0.585	0.050	0.760	0.077	0.719

surface 1 and 2/3 for the remaining surfaces. Also, these values remain unaltered as α varies.

Extrapolating Igarashi's two-dimensional correlations to the present range of Reynolds number indicates that, except for surface 3, the cube generally has a higher surface-averaged mass (heat) transfer than the corresponding tall prism by approximately 30 percent. The three-dimensional flowfield induced by the cube-endwall interaction apparently is the main cause for such a transport enhancement. This trend is completely reversed from that of the mass transfer on surface 3, which is the rear surface when $\alpha = 0$ deg, where a higher value is recorded for the prism. The difference is also about 30 percent for all the attack angles. According to earlier studies by Igarashi (1985, 1986) and Goldstein et al. (1990), this is because of enhanced turbulent mixing accompanied by strong vortex shedding behind the obstacle. In fact, surface 3 always has the highest magnitude of surface-averaged transfer coefficient over the midsection of a tall prism. As illustrated in Fig. 6 and discussed earlier, it is surface 4 or the top surface that produces the highest mass transfer in the present case. This sharp contrast highlights one of the most significant differences in transport mechanisms between the two-dimensional and the three-dimensional flow separation induced by obstacles with a square cross section.

Overall Average Mass Transfer. Correlated coefficient (C_1) and power index (C_2) for the mass transfer averaged over the entire cube surface with different angles-of-attack are given in Table 1. Since the case with $\alpha = 10$ deg has the smallest C_2 value, its overall mass transfer average is the least Reynolds number dependent. Compared to the extrapolated Igarashi's correlations (1985) for two-dimensional flow regime with a prism, the cube clearly has higher overall transfer coefficients than those of the prism for relatively small flow attack angles, say $\alpha = 0$ and 10 deg. The difference is approximately 10 to 20 percent. On the contrary, this trend reverses for $\alpha = 25$ and 45 deg. However, the difference is much less insignificant than that with a smaller α.

Figure 7 reveals the variation of the overall mass transfer with angle-of-attack. The cube data shown here is a sample results for $Re = 8.2 \times 10^4$, while the Reynolds number for the two-dimensional case (Igarashi, 1985) is 3.7×10^4. Therefore, to facilitate a rational comparison, each set of data is normalized by its corresponding values at $\alpha = 0$ deg. While each case, as discussed earlier, inherits distinctly different flow and transport characteristics around the obstacle, the overall trends disclosed in Fig. 7 are quite similar. For the cube, a local minimum exists at $\alpha = 10$ deg, and the corresponding local minimum for the two-dimensional prism is at approximately the same orientation. Following this minimum, the overall transfer coefficient for both cases increases with α and reaches a local maximum at approximately $\alpha = 25$ deg, before it declines again. For the two-dimensional case with a prism, such a local maximum at $\alpha = 25$ deg is actually the absolute

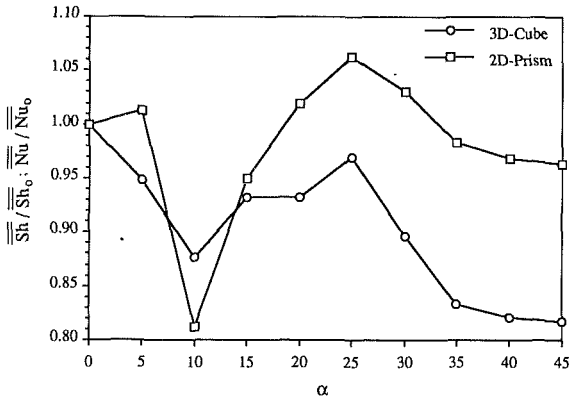

Fig. 7 Overall mass transfer variation with angle-of-attack

maximum over the entire spectrum of α. On the other hand, the corresponding absolute maximum for the cube occurs when $\alpha = 0$ deg. Note that the overall average transfer coefficient is much less sensitive to the variation of α for the three-dimensional cube case than its two-dimensional counterpart.

Conclusions

The combined effects of angle-of-attack (0 deg $\leq \alpha \leq$ 45 deg) and Reynolds number ($3.1 \times 10^4 \leq Re \leq 1.1 \times 10^5$) on both the local and the average mass transfer from a wall-mounted cube are experimentally studied using the naphthalene sublimation technique. By analogy, the mass transfer results obtained here can be readily transformed to their heat transfer counterparts. In addition to the mass transfer study, important flow features are also visualized using the oil–graphite technique. The main findings lead to the following conclusions:

1 According to the present flow visualization, there are four different flow regimes depending on the flow angle-of-attack: perfect separation and symmetric flow ($\alpha = 0$ deg), perfect separation and asymmetric flow (0 deg $\leq \alpha \leq$ 14 deg), reattachment flow (14 deg $< \alpha \leq$ 40 deg), and wedge flow (40 deg $< \alpha \leq$ 45 deg). Compared to its two-dimensional counterpart with crossflow around a tall prism, the asymmetric flow regime for the present case with three-dimensional separated flow appears to initiate at a smaller α value.

2 Mass transfer from a surface is greatly affected by the flow in its vicinity. While details may vary with α, the following two common flow features are evident: the multiple horseshoe vortices around the cube base, and the arch-shaped vortex behind the cube. The latter generally implies uniform mixing and lower transfer coefficient. As the degree of asymmetry elevates with increasing α, a pair of wing-tip vortices develops atop the cube. Underneath these vortices on the top wall is a zone of very high mass transfer. Behind the cube, asymmetry distorts the arch-shaped vortex, which, in turn, produces a diagonal zone of high mass transfer rate over the leeward surfaces. Further, asymmetry also leads to shear layer reattachment on one sidewall. As expected, the reattachment promotes heat or mass transfer in the region.

3 The values of Sherwood number averaged over each participating surface, or over the entire cube, increase with the Reynolds number. Depending on the angle-of-attack, either the top wall or one of the sidewalls subjected to a potential flow reattachment (surface 4) has the highest face-averaged mass transfer. This is in a sharp contrast to the two-dimensional case with a tall prism, where the back surface has the highest transfer coefficient. Compared to the remaining surfaces, the levels of mass transfer on these two faces are also the most sensitive to variations in α.

4 Within the present testing range, the average mass transfer over the entire cube varies strongly with the flow angle-of-

attack. The overall average Sherwood number reaches a local minimum near $\alpha = 10$ deg, where a substantial level of asymmetry initiates the development of wing-tip type vortices atop the cube. Despite very different flowfield and transport mechanisms, such a minimum also occurs in the two-dimensional case. For small flow attack angles, say $\alpha \leq 10$ deg, overall average mass transfer from the entire cube is approximately 10 to 20 percent higher than that of its two-dimensional counterpart. For $\alpha \geq 25$ deg, this trend is reversed; the difference, however, is rather insignificant.

References

Ambrose, D., Lawrenson, I. J., and Sparke, C. H. S., 1975, "The Vapor Pressure of Naphthalene," *J. Chem. Thermodynamics*, Vol. 7, pp. 1173-1176.

Castro, I. P., and Robins, A. G., 1977, "The Flow Around a Surface-Mounted Cube in Uniform and Turbulent Streams," *J. Fluid Mech.*, Vol. 79, pp. 307-335.

Chen, P. H., 1988, "Measurement of Local Mass Transfer From a Gas Turbine Blade," Ph.D. Thesis, University of Minnesota.

Chyu, M. K., 1986, "Influence of Roughness Elements on Local Mass Transfer From a Flat Surface," Ph.D Thesis, University of Minnesota.

Chyu, M. K., and Natarajan, V., 1991, "Local Heat/Mass Transfer Distributions on Surface of a Wall-Mounted Cube," ASME JOURNAL OF HEAT TRANSFER, Vol. 113, pp. 851-857.

Eckert, E. R. G., 1975, "Analogies to Heat Transfer Processes," *Measurements in Heat Transfer*, E. R. G. Eckert and R. J. Goldstein, eds., Hemisphere Publication, Washington, DC.

Goldstein, R. J., Chyu, M. K., and Hain, R. C., 1985, "Measurement of Local Mass Transfer in the Region of the Base of a Protruding Cylinder With a Computer-Controlled Data Acquisition System," *International Journal of Heat and Mass Transfer*, Vol. 28, pp. 977-985.

Goldstein, R. J., Yoo, S. Y., and Chung, M. K., 1990, "Convective Mass Transfer From a Square Cylinder and Its Base Plateau," *International Journal of Heat and Mass Transfer*, Vol. 33, pp. 9-18.

Hunt, J. C. R., Abell, C. J., Peterka, J. A., and Woo, H. G. C., 1978, "Kinematical Studies of the Flows Around Free or Surface-Mounted Obstacles; Applying Topology to Flow Visualization," *J. Fluid Mech.*, Vol. 86, pp. 179-200.

Igarashi, T., 1985, "Heat Transfer From a Square Prism to an Air Stream," *International Journal of Heat and Mass Transfer*, Vol. 28, pp. 175-181.

Igarashi, T., 1986, "Local Heat Transfer From a Square Prism to an Airstream," *International Journal of Heat and Mass Transfer*, Vol. 29, pp. 777-784.

Mantle, P. L., 1966, "A New Type of Roughened Heat Transfer Surface Selected by Flow Visualization Technique," *Proc. 3rd International Heat Transfer Conference*, Vol. 1, pp. 45-55.

Ogawa, Y., Oikawa, S., and Uehara, K., 1983, "Field and Wind Tunnel Study of the Flow and Diffusion Around a Model Cube—II. Nearfield and Cube Surface Flow and Concentration Patterns," *Atmospheric Environment*, Vol. 17, No. 6, pp. 1161-1171.

Olsen, J., Webb, B. W., and Queiroz, M., 1989, "Local Three-Dimensional Heat Transfer From a Heated Cube," presented at the ASME Winter Annual Meeting, San Francisco, CA.

Peterka, J. A., Meroney, R. H., and Kothari, K. M., 1985, "Wind Flow Patterns About Buildings," *J. Wing Engg. and Ind. Aero*, Vol. 21, pp. 21-38.

Roeller, P. T., Stevens, J., and Webb, B. W., 1991, "Heat Transfer and Turbulent Flow Characteristics of Isolated Three-Dimensional Protrusions in Channels," ASME JOURNAL OF HEAT TRANSFER, Vol. 113, pp. 597-603.

Leading Edge Film Cooling Heat Transfer Through One Row of Inclined Film Slots and Holes Including Mainstream Turbulence Effects

Shichuan Ou[1]
Research Assistant.

J. C. Han
HTRI Professor.
Fellow ASME

Turbine Heat Transfer Laboratory,
Mechanical Engineering Department,
Texas A&M University,
College Station, TX 77843

The effects of film opening shape and mainstream turbulence on the leading edge heat transfer coefficient and film effectiveness were experimentally investigated. The experiments were performed using test models with a semi-cylindrical leading edge and a flat afterbody. A bar grid (Tu = 5.07 percent) and a passive grid (Tu = 9.67 percent) produced two levels of mainstream turbulence. Two separate cases of one-row injection through film slots or holes located only at ±15 deg or only at ±40 deg from the stagnation line were studied for three blowing ratios of 0.4, 0.8, and 1.2 at the Reynolds number (Re_D) of 100,000. The slots in each row were spaced three cross-sectional slot lengths ($P = 3\ell$) apart, while the holes were spaced four holes diameters ($P = 4d$) apart. Both geometries had equal cross-sectional area and pitch. The results show that the leading edge heat transfer coefficient increases and the film effectiveness decreases with increasing blowing ratio; however, B = 0.8 provides the highest film effectiveness for the film hole with ±40 deg injection. The heat transfer coefficient increases and the film effectiveness decreases with increasing mainstream turbulence level. However, the mainstream turbulence effect on the film effectiveness is reduced as the blowing ratio is increased. Slot geometry provides better film cooling performance than the hole geometry for all test cases at the lowest blowing ratio of 0.4. However, at higher blowing ratios of 0.8 and 1.2, the reverse is true for ±40 deg injection at mainstream turbulence of 0.75 and 9.67 percent.

Introduction

Gas turbine engine performance is strongly influenced by turbine inlet temperature from a thermodynamic analysis. To obtain higher thermal efficiency, modern gas turbine engines are designed to operate at turbine inlet temperatures of 1400°–1500°C, which are far above the melting points of metals. Therefore, highly sophisticated cooling techniques such as film cooling must be applied to maintain acceptable life and safety requirements. In film cooling, a cooler fluid is ejected onto the airfoil surface and forms a protective layer between the surface and hot mainstream gases.

A gas turbine airfoil without film cooling is shown in Fig. 1. The local convective heat flux without film holes, q_o'', is given by

$$q_o'' = h_o(T_\infty - T_w) \tag{1}$$

The local heat transfer coefficient without coolant injection is h_o and can be found by performing the heat transfer test without the film opening experiment.

A gas turbine airfoil with film cooling is also shown in Fig. 1. The local heat flux (q'') is related to the local heat transfer coefficient(h) and local wall temperature (T_w) by

$$q'' = h(T_f - T_w) \tag{2}$$

where T_f is the local film temperature (mixing temperature between hot mainstream gas and injected coolant). The local heat transfer coefficient can be provided by performing the heat transfer test with film injection experiment. The film temperature is provided by a separate film cooling test experiment where local adiabatic film effectiveness (η) is determined. The local adiabatic film effectiveness is a nondimensional film temperature as shown below:

$$\eta = \frac{T_\infty - T_f}{T_\infty - T_c} \tag{3}$$

where, depending on real gas turbine engine conditions, the hot mainstream (T_∞) and coolant (T_c) temperatures are given. The local film temperature T_f is readily obtained from Eq. (3) if the local adiabatic film effectiveness has been found from the film cooling test. The local heat flux with coolant injection can then be evaluated by substituting T_f into Eq. (2).

The purpose of film cooling is to reduce heat transfer to the turbine airfoil compared with the non-film cooling case. It is necessary to compare the heat load with film cooling to that without film cooling. The heat load ratio is the ratio of local heat flux with film cooling to that without film holes. From Eqs. (1) and (2), the local heat load ratio is obtained as

$$\frac{q''}{q_o''} = \frac{h}{h_o}\left(\frac{T_f - T_w}{T_\infty - T_w}\right) \tag{4}$$

With film cooling, the heat transfer coefficient increases due to the enhancement of turbulence intensity caused by the interaction between the mainstream and coolant flow. In Eq. (4), h is greater than h_o; however, $(T_f - T_w)$ for the film injection case is expected to be smaller than $(T_\infty - T_w)$ for the non-film injection case because the film temperature is lower than the

[1]Current address: Aero Propulsion and Power Directorate, Wright Patterson Air Force Base, OH 45433.

Contributed by the Heat Transfer Division for publication in the JOURNAL OF HEAT TRANSFER. Manuscript received by the Heat Transfer Division August 26, 1991; revision received Aug. 17, 1993. Keywords: Forced Convection, Jets, Turbines. Associate Technical Editor: R. J. Simoneau.

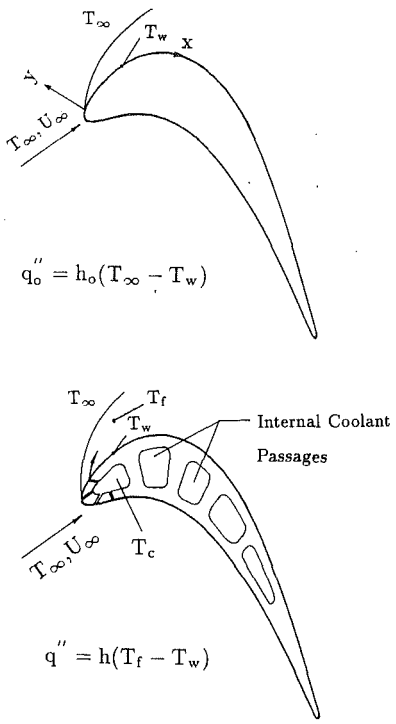

Fig. 1 Film cooling concepts

mainstream temperature. Therefore, one can expect a smaller local heat flux with film injection (q'') than without film holes (q_o''). In other words, q''/q_o'' is expected to be less than unity, which means that the heat load is reduced due to film injection. This also implies that better film cooling performance is shown by a lower heat load ratio.

There have been many investigations on the heat transfer coefficient and/or film effectiveness on a circular cylinder at low mainstream turbulence intensities. Sasaki et al. (1976) studied film coolant in the stagnation region of a circular cylinder with two rows of spanwise angled holes, one row at 15 deg and the other 45 deg from the stagnation line. They found that adiabatic film effectiveness downstream from the second row of holes increased with increasing blowing ratio until it reached optimum values of 0.5 to 0.6. They also reported that film effectiveness continually decreased as they further increased the blowing ratio.

Luckey and L'Ecuyer (1981) and Bonnice and L'Ecuyer (1983) used a circular cylinder with one to five rows of spanwise injection holes with various blowing ratios of 0–2.0. For a low mainstream turbulence intensity of about 0.5 percent and Reynolds number of 90,000, they found the surface heat flux varied in both spanwise and streamwise directions depending on the blowing ratio and injection geometry.

Mick and Mayle (1988) used a blunt body with a semicircular leading edge and a flat afterbody to study the film effectiveness and heat transfer coefficient for secondary air through two rows of inclined holes into the stagnation region of an incident mainstream flow. They found film effectiveness near the injection holes was 0.7–0.8 and the heat transfer coefficients with film injection were three times higher than those without film holes. They also reported that blowing ratios of 0.38 and 0.64 reduced the surface heat load while a blowing ratio of 0.97 increased the heat load within the injection region.

Karni and Goldstein (1990) used the naphthalene sublimation technique to study the effect of surface injection from a circular cylinder with one row of inclined holes on local mass transfer at a low mainstream turbulence intensity of 0.45 percent. They showed that the mass transfer distribution is extremely sensitive to small changes in the injection hole location compared with stagnation for spanwise injection.

Ou and Han (1992) studied the effect of high mainstream turbulence on leading edge film cooling and heat transfer through two rows of inclined film slots. They studied three blowing ratios of 0.4, 0.8, and 1.2 under high mainstream turbulence levels of 5.07–9.67 percent and at a Reynolds number of 100,000. Their results showed that the heat transfer coefficient increased with increasing blowing ratio. The intermediate blowing ratio of 0.8 provided the highest film effectiveness for both low (Tu = 0.75 percent) and high (Tu and

Nomenclature

b = width of passive grid tubes
B = blowing ratio (coolant-to-mainstream mass flux ratio) = $\rho_c U_c/(\rho_\infty U_\infty)$
d = film hole diameter
D = leading edge (cylinder) diameter
h = local convective heat transfer coefficient with film injection
h_o ($\bar{h}_o$) = local (spanwise-averaged) convective heat transfer coefficient without film holes
L_e^u = dissipation length scale
ℓ = cross-sectional length of film slot
$\overline{\mathrm{Nu}}_D$ = spanwise-averaged Nusselt number based on leading edge diameter (D)
P = pitch of film slots/holes in a row in the spanwise direction
q'' ($\bar{q}''$) = local (spanwise-averaged) convective heat flux with film injection
q''_{cond} = conduction heat loss flux with film injection
q''_{gen} = generated surface heat flux with film injection
q''_{rad} = radiation heat loss flux with film injection
$q_o''(\bar{q}_o)$ = local (spanwise-averaged) convective heat flux without film holes
$q''_{o,\mathrm{cond}}$ = conduction heat loss flux without film holes
$q''_{o,\mathrm{gen}}$ = generated surface heat flux without film holes
$q''_{o,rad}$ = radiation heat loss flux without film holes
Re_D = Reynolds number based on U_∞ and D
T_{aw} = adiabatic wall temperature
T_c = coolant temperature (injection flow temperature)
T_f = film temperature
Tu = streamwise turbulence intensity = $((\overline{u})^2)^{1/2}/\overline{U}$
T_w = local surface temperature
T_∞ = mainstream or incident air temperature
$\overline{U}$ = local time-mean streamwise velocity
U_∞ = incident mainstream velocity at X/b = 20 with no grid
U_c = velocity of coolant (injection) flow
u' = local streamwise fluctuating velocity
w = cross-sectional width of film slot
X = axial distance measured from grid
x = streamwise distance around test model circumference measured from the stagnation line
z = spanwise distance
η ($\bar{\eta}$) = local (spanwise-averaged) adiabatic film effectiveness
ρ_∞ = density of mainstream flow
ρ_c = density of coolant flow
ϕ = overall cooling effectiveness = $(T_\infty - T_w)/(T_\infty - T_c)$

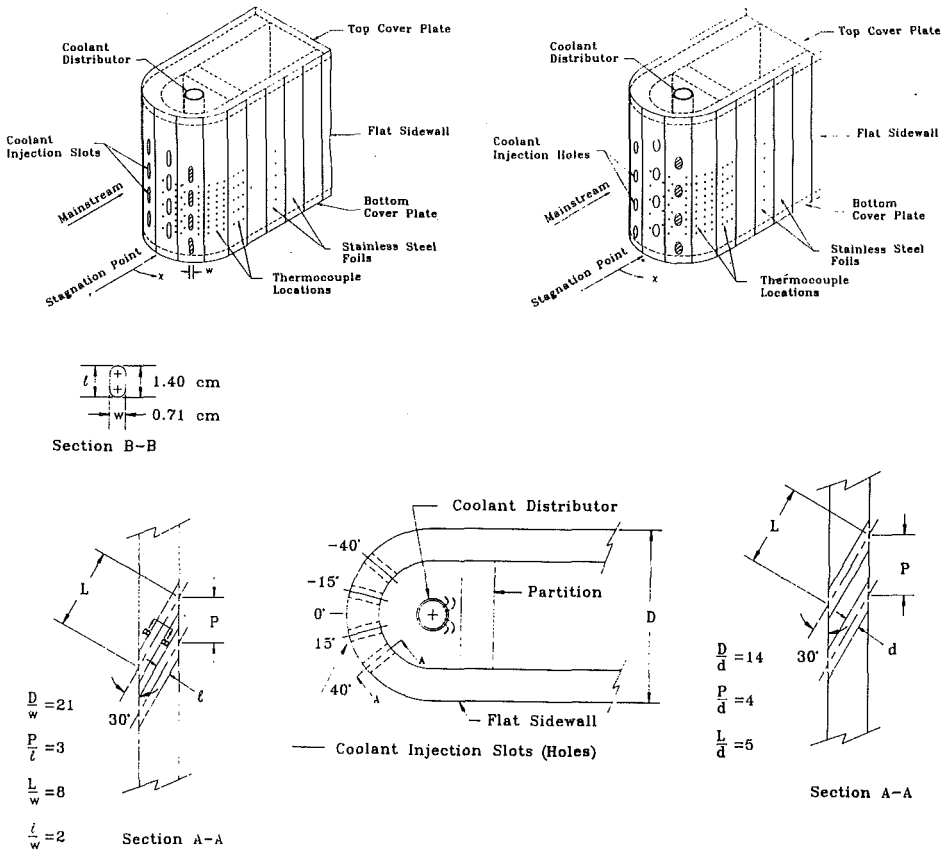

Fig. 2 Schematic of the leading edges with film slots and film holes and thermocouples

9.67 percent) mainstream turbulence conditions. The leading edge heat transfer coefficient increased film effectiveness decreased with increasing mainstream turbulence level for the low blowing ratio; however, the mainstream turbulence effect reduced for the high blowing ratio.

This study focused on the effects of film opening shape (slot and hole) and mainstream turbulence on leading edge heat transfer coefficient and film effectiveness for flow over a blunt body with a semi-cylindrical leading edge and a flat afterbody. High mainstream turbulence was produced by a bar grid or passive grid. The main concerns were to: (1) find the effect of film opening shape on the heat transfer coefficient and film effectiveness distributions for injection openings located only at ± 15 deg or only at ± 40 deg from the stagnation line and (2) compare the film cooling performance between these two geometries.

Test Apparatus and Instrumentation

The low-speed wind tunnel and turbulence grids in the present study were shown and described by Ou (1991) and Ou and Han (1992). Figure 2 shows the test models of film slots and film holes, which simulate the leading edge of a gas turbine vane. Each test model was a blunt body with a semi-cylindrical leading edge and flat afterbody. The test model was made of wood to reduce the conduction effect. The semi-cylinder was 15.2 cm in diameter and 25.4 cm in height. For ease of fabrication, the film slots were designed so that in cross section each slot had a semicircle at both ends and a rectangle between. The cross-sectional slot length-to-width ratio (1.4 cm/0.71 cm) was two. The hole diameter was 1.07 cm. There were four slots or holes in each row. Each slot was spaced three cross-sectional slot lengths apart and each hole was spaced four hole diameters apart in the spanwise direction. Both geometries had the same pitch and flow cross-sectional area, which implied that an equal amount of coolant was ejected for the same blowing ratio. Two separate cases of film injection were studied. (1) film slots (holes) only at ± 15 deg or (2) film slots (holes) only at ± 40 deg. All the slots or holes were inclined 30 and 90 deg to the surface in the spanwise and streamwise directions, respectively. The incident mainstream Reynolds number based on the cylinder diameter was about 100,000. The test models and thin foil-thermocouple technique are shown by Ou (1991) and Ou and Han (1992) for studies of two rows of film holes and slots, respectively. For tests of one-row injection at ± 15 deg the film slots or holes at ± 40 deg were plugged with silicon caulk and the surfaces made smooth and flush with the foil surface. The slots or holes at ± 15 deg were treated in a similar way for the ± 40 deg injection tests.

The output of all thermocouples was read with a Fluke 2280A data logger. The measured temperatures were recorded by an IBM personal computer that interfaced with the Fluke data logger. An auto-transformer provided constant heat flux generation in the foils by maintaining constant voltage in the circuit. A Beckman digital multimeter and a Beckman AC current clamp measured circuit voltage and current, respectively.

A pitot probe connected to a micromanometer set the desired leading edge Reynolds number and constantly monitored the mainstream velocity during the experiment. The injection flow temperature was measured by averaging the readings of two thermocouples located in the plenum. A calibrated orifice meter in front of the heater measured the mass flow rate of injection flow.

The measurements of streamwise velocity and turbulence intensity distributions using a calibrated, single hot-wire anemometer TSI IFA 100/200 were described in detail by Ou (1991) and Ou and Han (1992).

Test Conditions

Before conducting heat transfer or film cooling tests, the flow symmetry was first confirmed by measuring the corresponding mainstream velocities on both sides of the test model. This ensured that the test model was centrally located in the test duct. The mainstream turbulence decay along the centerline for the no grid, bar grid, and passive grid was then found at Re_D = 100,000. The distributions of mainstream turbulence were measured with a single hot-wire anemometer downstream for each grid. The minimum value of the turbulence intensity curve for each grid was quoted as the reference turbulence intensity for that particular grid. The reference turbulence intensities for the no grid, bar grid, and passive grid were 0.75, 5.07, and 9.67 percent, respectively. All heat transfer and film cooling tests were performed under these reference turbulence intensities for the nominal blowing ratios of 0.4, 0.8, and 1.2. The injection mass flux was found by the incident mainstream velocity (U_∞) and the desired blowing ratio. The required injection flow rate was obtained based on the total cross-sectional area of the film openings. The turbulence intensities at the film slots exit were 4–5, 6–9, and 22–30 percent for B = 0.4, 0.8, and 1.2, respectively. They were 3–5, 7–12, and 25–30 percent for the film hole case.

The temperature of the injection flow for the heat transfer tests was about the same as that of the mainstream (24°C). The ejected hot air was maintained at 49°C for the film heating tests. The density ratio of coolant to mainstream was 0.9 due to this temperature difference. The density ratio plays an important role in affecting the film cooling performance. This study focused on the effect of high mainstream turbulence at a constant density ratio.

Data Analysis

Heat transfer tests for no film holes (smooth surface) were performed by supplying power to the thin foils to generate electric heat. The mainstream temperature was maintained at 24°C. This resulted in a higher local wall temperature than the mainstream temperature ($T_w > T_\infty$). The local heat transfer coefficient was calculated as follows by considering the conduction and radiation heat loss fluxes in the test model:

$$h_o = \frac{q''_o}{T_w - T_\infty} = \frac{q''_{o,\text{gen}} - q''_{o,\text{cond}} - q''_{o,\text{rad}}}{T_w - T_\infty} \tag{5}$$

The heat flux generated by non-film holes was about 960 W/m^2. Heat loss tests were performed separately to find total heat loss flux from the test model for a no-mainstream-flow condition. The heat loss calibration was conducted by supplying power to the test model until steady state. This was done for several different power inputs to obtain the relationship between the total heat loss flux and the foil temperature. Local radiation heat loss flux was estimated using a foil emissivity of 0.22 at 45°C. The conduction heat loss flux could be estimated by knowing the total heat loss and radiation heat loss fluxes. The conduction heat loss flux to the surroundings was about 3 percent of the generated surface heat flux, while the radiation heat loss flux to the duct walls was about 10 percent of the generated heat flux. Small heat conduction losses through the thin foil and tiny thermocouples were neglected in the calculations.

A similar procedure was applied to the heat transfer tests with film injection. However, the injection flow temperature was maintained the same as that of the mainstream ($T_f = T_\infty$). The local heat transfer coefficient was calculated as

$$h = \frac{q''}{T_w - T_\infty} = \frac{q''_{\text{gen}} - q''_{\text{cond}} - q''_{\text{rad}}}{T_w - T_\infty} \tag{6}$$

Similar heat loss tests were performed for the heat transfer tests with film injection to find total heat loss flux from the test model with film openings.

A constant heat flux existed everywhere except on the foils with film openings. It was easy to calculate the uniform q''_{gen} for those foils without film openings. The surface heat flux generated for foils with film openings was nonuniform in both spanwise and streamwise directions. A detailed discussion about estimating this nonuniform heat flux was given by Mehendale and Han (1992). This method was also used by Mick and Mayle (1988).

Film heating tests were performed by injecting hot air at 49°C. The mainstream temperature was maintained at 24°C. This resulted in higher injection flow and film temperatures than the mainstream temperature ($T_c > T_\infty$, $T_f > T_\infty$). The test surface is initially assumed to be adiabatic since it is difficult to find the film temperature. Under this assumption there is no heat transfer at the surface and the local film temperature must be equal to the local adiabatic wall temperature ($T_f = T_{aw}$).

Since the test surface was not perfectly adiabatic, some corrections had to be applied to the measured wall temperature, T_w, to obtain the adiabatic film effectiveness. These corrections included the effect of heat transfer by conduction through the wood model (q''_{cond}), heat loss by radiation to the test duct walls, and the local heat transfer coefficient h with film injection calculated in Eq. (6) from the corresponding heat transfer tests.

The film tests in the present study had heat conduction from inside the test model to the outer test surface for the locations in the leading edge region. In other words, there was a conduction heat gain to be considered. This heat gain was evaluated based on a one-dimensional conduction model. Note that thermocouple locations near the film openings received additional conduction gain from the hot air passing through the film openings. The values of these two conduction heat gains were used to estimate the total conduction heat gain for

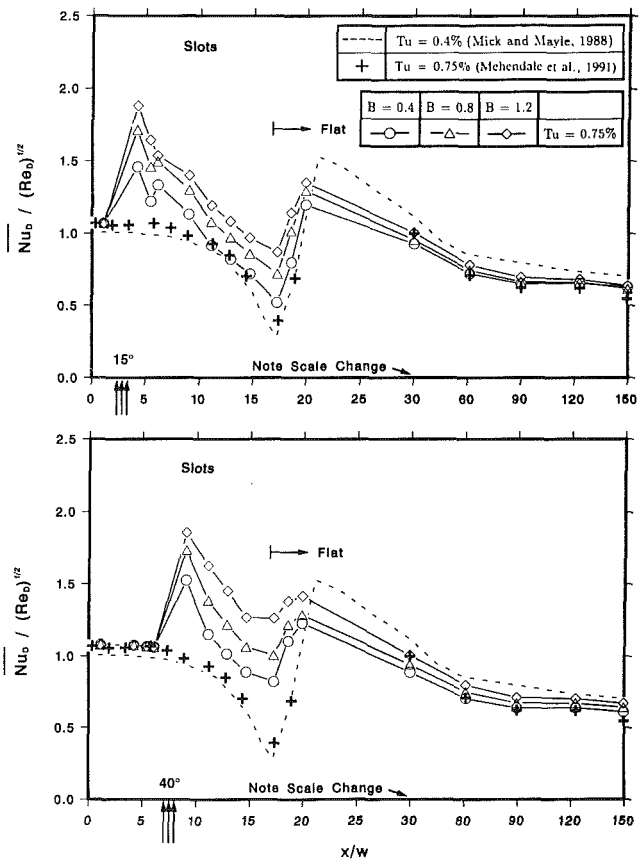

Fig. 3 Effect of blowing ratio on spanwise-averaged distributions of Nusselt number through one row of film slots at (*a*) ±15 deg and (*b*) ±40 deg for *Tu* = 0.75 percent

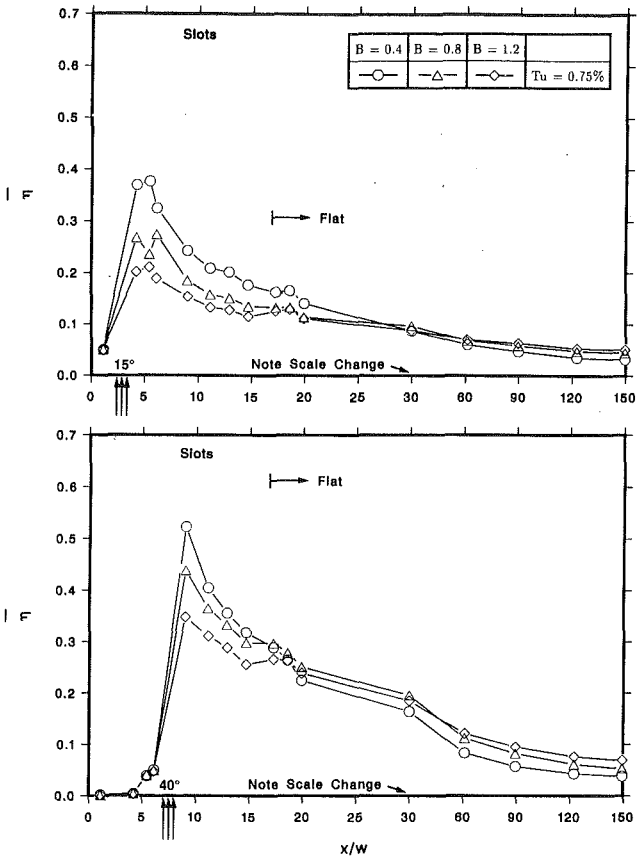

Fig. 4 Effect of blowing ratio on spanwise-averaged distributions of film effectiveness through one row of film slots at (*a*) ±15 deg and (*b*) ±40 deg for Tu = 0.75 percent

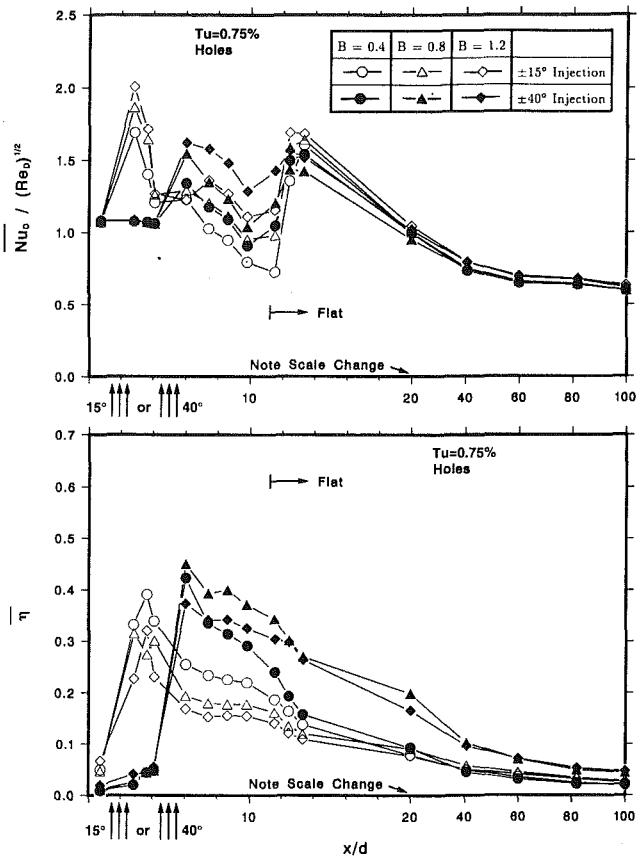

Fig. 5 Effect of blowing ratio on spanwise-averaged distributions of (*a*) Nusselt number and (*b*) film effectiveness through one row of film holes at ±15 deg or ±40 deg for Tu = 0.75 percent

the thermocouple locations near the film openings. The local adiabatic film effectiveness was then calculated by

$$\eta = \frac{T_f - T_\infty}{T_c - T_\infty} = \frac{T_{aw} - T_\infty}{T_c - T_\infty} = \frac{T_w - T_\infty}{T_c - T_\infty} + \frac{q''_{\text{rad}} - q''_{\text{cond}}}{h(T_c - T_\infty)} \tag{7}$$

The local film effectiveness and heat load ratio q''/q''_o were obtained as in Eqs. (3) and (4), respectively. Solving for T_f from Eq. (3) and substituting into Eq. (4), one obtains the local heat load ratio as

$$\frac{q''}{q''_o} = \frac{h}{h_o}\left[\frac{T_\infty - T_w}{T_\infty - T_w} - \frac{\eta(T_\infty - T_c)}{(T_\infty - T_w)}\right] = \frac{h}{h_o}\left[1 - \frac{\eta}{\phi}\right] \tag{8}$$

where $\phi = (T_\infty - T_w)/(T_\infty - T_c)$ is the overall cooling effectiveness. Both the local heat transfer coefficient and adiabatic film effectiveness depend on streamwise and spanwise locations (x, z). With a constant value of the overall cooling effectiveness, ϕ, spanwise-averaged heat load ratio $\overline{q}''(x)/\overline{q}''_o(x)$ can be calculated using

$$\frac{\overline{q}''(x)}{\overline{q}''_o(x)} = \frac{1}{n}\sum_{i=1}^{n}\left[\frac{h(x, z_i)}{h_o(x, z_i)}\right]\left[1 - \frac{\eta(x, z_i)}{\phi}\right] \tag{9}$$

where n is the number of thermocouples in a row to obtain the spanwise-averaged heat transfer coefficient and film effectiveness. The value of ϕ was about 0.5–0.6 for gas turbine components. By using T_∞ = 1371°C, T_w = 927°C, and T_c = 649°C, the overall cooling effectiveness in advanced gas turbine engines was estimated to be 0.61. T_∞ = 24°C, T_w = 37.8°C, and T_c = 49°C was used for our test conditions and the overall cooling effectiveness estimate was 0.55. A value of 0.6 was used in the present study. The best film cooling design should minimize heat load as compared to the non-film heat transfer case. In other words, the spanwise-averaged heat load ratio should be less than unity and as small as possible.

An uncertainty analysis based on the method of Kline and McClintock (1953) was carried out for both heat transfer coefficients with film injection and film effectiveness. Based on 95 percent confidence levels and primarily due to the q''_{gen} estimate, the maximum uncertainty of the heat transfer coefficient was about 15 percent around the film openings and less than 5 percent far downstream of the last thermocouple location on the flat side wall. The maximum uncertainty of the adiabatic film effectiveness is about 8 percent near the film openings and less than 5 percent far downstream of the flat side wall.

Results and Discussions

Non-film heat transfer tests were conducted on a smooth leading edge model to find h_o for the evaluation of heat load ratio. Detailed non-film heat transfer data were shown by Mehendale et al. (1991).

The local streamwise mean velocity and turbulence intensity distributions along the centerline and right-side line for three mainstream turbulence conditions were shown and described by Ou (1991) and Ou and Han (1992). The dissipation length scales range from 0.6–1.0 cm for the bar grid and 1.3–1.5 cm for the passive grid along the centerline down to the location of minimum turbulence, where the reference turbulence intensities were quoted. The length scales were determined based on the method proposed by Hancock and Bradshaw (1983) and were calculated from the local streamwise mean and fluctuating velocity measurements as $L_e^u = -(\overline{u}'^2)^{3/2}/(\overline{U}\cdot d(\overline{u}')^2/dX)$.

Figure 3 shows the heat transfer coefficient data for the low mainstream turbulence case (Tu = 0.75 percent) through one row of film slots at either ±15 deg or ±40 deg. Also shown for reference are the non-film data from the Mehendale et al. (1991) investigation and the published results of Mick and Mayle (1988). The three-arrow symbol represents the stream-

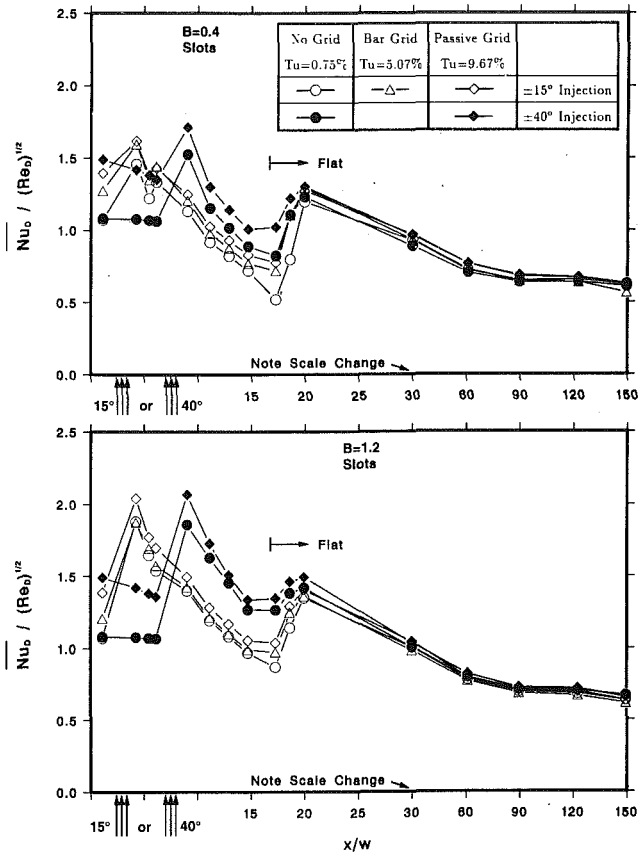

Fig. 6 Effect of mainstream turbulence on spanwise-averaged distributions of Nusselt number through one row of film slots for (*a*) $B = 0.4$ and (*b*) $B = 1.2$

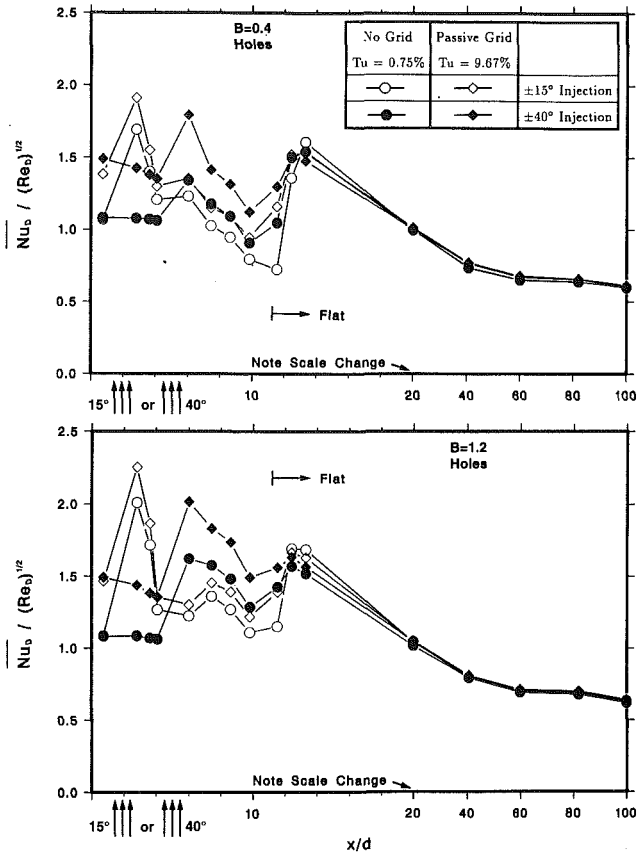

Fig. 7 Effect of mainstream turbulence on spanwise-averaged distributions of Nusselt number through one row of film holes for (*a*) $B = 0.4$ and (*b*) $B = 12$

wise location of injection slots. The spanwise-averaged heat transfer coefficients have been converted into the spanwise-averaged Nusselt numbers normalized by a square root of the Reynolds number. The non-film heat transfer coefficient data of this study follow the published results for the no grid case. The non-film heat transfer coefficient decreases from the stagnation line due to laminar boundary layer formation. It reaches a minimum at flow separation ($x/w \approx 17$) and a maximum at flow reattachment ($x/w \approx 20$). Figure 3 suggests that the heat transfer coefficient increases with increasing blowing ratio for both injection cases. This is because a higher blowing ratio causes more interaction between injection flow and mainstream flow, which creates higher jet turbulence at the exit of the film slots as described earlier. The increase in the heat transfer coefficient is most severe immediately downstream from the row of film slots (peak region at $x/w \approx 4$ for ± 15 deg injection and 9 for ± 40 deg injection). The heat transfer coefficients then decrease with x for all blowing ratios because the coolant is diluted by the mainstream.

Figure 4 presents the spanwise-averaged film effectiveness data with one row of film slots for ± 15 deg and one for ± 40 deg for the no grid ($Tu = 0.75$ percent). A higher blowing ratio under low mainstream turbulence conditions causes more penetration of injection flow into the mainstream and thus results in lower leading edge film effectiveness for one-row injection cases. The leading edge film effectiveness from ± 15 deg injection is obviously much lower than from ± 40 deg injection for the region downstream of ± 40 deg row of slots. This is because the injection flow from the ± 15 deg row has been diluted by the mainstream. Further comparison, which is based on the equal distance from the center of each row of slots in the streamwise direction, shows that the film effectiveness distributions from the ± 40 deg slots are higher than those from the ± 15 deg. This is due to the growth of the mainstream boundary layer. The potential-flow velocity increases with the streamwise distance x from the stagnation line. The mainstream velocity at ± 40 deg is greater than that at ± 15 deg. Thus, the higher mainstream velocity at ± 40 deg readily deflects the injection flow back along the surface and arrests the injection flow from penetrating into the mainstream.

Figure 5 shows the results of heat transfer coefficient and film effectiveness for the film holes under low mainstream turbulence conditions. Note that the two three-arrow symbols do not mean simultaneous two-row injection at ± 15 deg and ± 40 deg. The first three-arrow symbol represents ± 15 deg injection and the second one ± 40 deg injection. This will also apply to the subsequent figures. The trend for a higher blowing ratio resulting in a higher heat transfer coefficient is similar to the slot geometry. However, the film effectiveness reaches the maximum value at $B = 0.8$ and the minimum value at $B = 0.4$. This is probably due to geometry effect.

The effect of mainstream turbulence on heat transfer coefficient for the slot at ± 15 deg or ± 40 deg for $B = 0.4$ and $B = 1.2$ is plotted in Fig. 6. As expected, both injections show the heat transfer coefficient increasing with increasing mainstream turbulence level. Figure 7 shows the results of heat transfer coefficient data for the film hole geometry at $B = 0.4$ and $B = 1.2$. The figure also shows that, like the film slots, an increase in mainstream turbulence level increases the heat transfer coefficient for one row injection cases.

Figure 8 shows the effect of mainstream turbulence on film effectiveness distributions through one row of film slots at ± 15 deg or ± 40 deg for $B = 0.4$ and $B = 1.2$. Unlike the heat transfer coefficient, the film effectiveness decreases with increasing mainstream turbulence level for the lowest blowing

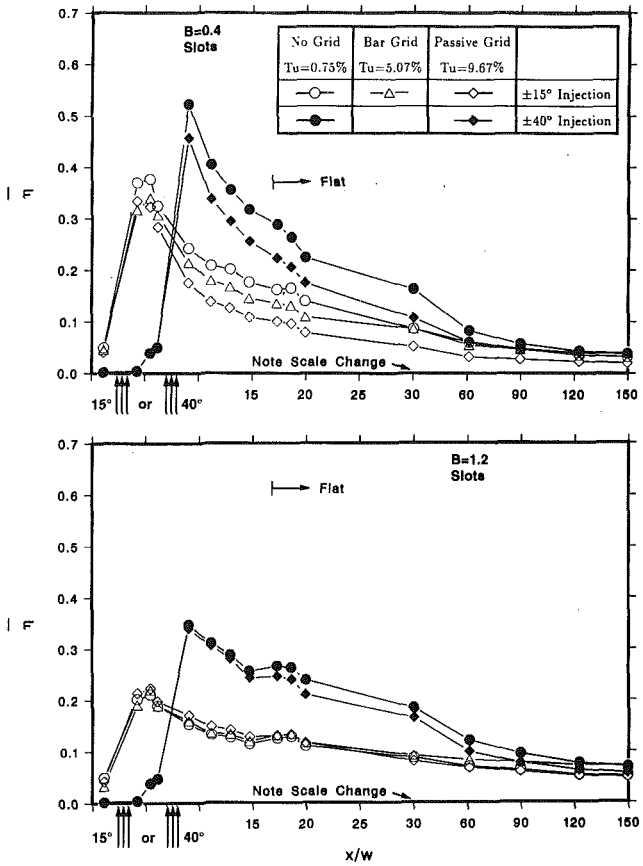

Fig. 8 Effect of mainstream turbulence on spanwise-averaged distributions of film effectiveness through one row of film slots for (*a*) B = 0.4 and (*b*) B = 1.2

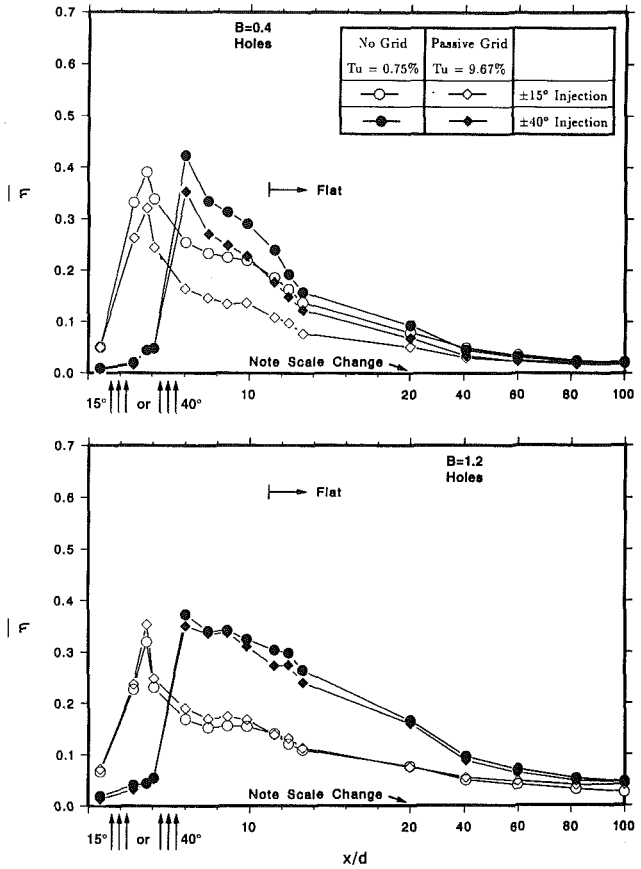

Fig. 9 Effect of mainstream turbulence on spanwise-averaged distributions of film effectiveness through one row of film holes for (*a*) B = 0.4 and (*b*) B = 1.2

ratio of B = 0.4. As described earlier, the turbulence created by the injection flow at the exit of the film slots is 4–5 percent and 22–30 percent for blowing ratios B = 0.4 and B = 1/2, respectively. As a result, the higher mainstream turbulence disturbs the film layer and destroys the film coverage for the lowest blowing ratio of B = 0.4. However, the injection turbulence dominates the flow field at the highest blowing ratio of 1.2 and diminishes the effect of mainstream turbulence. This behavior has been shown by Ou and Han (1992) with the aid of liquid crystal thermal visualization.

Figure 9 presents the film effectiveness data results for the film hole geometry at B = 0.4 and B = 1.2. The hole geometry shows similar effects of mainstream turbulence compared with the slot geometry for the corresponding injection case. Again, an increase in mainstream turbulence decreases the film effectiveness at the lowest blowing ratio of 0.4. The mainstream turbulence effect diminishes considerably as the blowing ratio is increased to 1.2.

Figure 10 shows a comparison of the spanwise-averaged heat load ratio between two geometries with one row of film openings for the low mainstream turbulence. The film cooling performance for both geometries for the ±15 deg injection decreases as the blowing ratio is increased. The 3ℓ slot performs better than the 4d hole at B = 0.4. The 4d hole gives better film cooling performance up to $x/w \approx 8.5$ at B = 0.8 and 1.2. However, the reverse is true after that location. Unlike B = 0.4 and 0.8, the blowing ratio of 1.2 is not able to reduce heat load because q''/q_o'' is greater than unity in several regions. Wadia and Nealy (1988) observed this phenomenon where heat load ratios greater than unity suggest equivalence by a negative Stanton number reduction parameter for blowing ratio greater than 1.0. The 3ℓ slot for the ±40 deg injection performs best at B = 0.4 but occurs at B = 0.8 for the 4d hole. The 4d-hole reduces more heat loads than the 3ℓ slot at B = 0.8 and 1.2. It is reversed at B = 0.4. The 1.2 blowing ratio shows its capability in heat load reduction because higher mainstream velocity can deflect the injection flow and prevent excessive penetration into the mainstream.

The results of the comparison of heat load ratio for the high mainstream turbulence are shown in Fig. 11. It shows that the differences of heat load ratio for all three blowing ratios decrease under high mainstream turbulence conditions. This is because the denominator $\bar{q}_o''$ (the spanwise-averaged heat flux without film openings) is larger at higher mainstream turbulence levels. It also shows that the heat load ratios at high mainstream turbulence are less than unity over most of the test surface, and that film cooling causes a significant reduction in the heat load ratio at the flow reattachment point for all blowing ratios and both injection cases. The 3ℓ slot configuration for the ±15 deg injection performs better in the leading edge regions than the 4d hole at B = 0.4. Like the low mainstream turbulence case, the 4d hole reduces more heat loads up to the $x/w \approx 8.5$ than the 3ℓ slot at B = 0.8 and 1.2. The reverse is true after that location. B = 0.4 provides the best performance for the 3ℓ slot ±40 deg injection. However, B = 0.8 performs best for the 4d hole. The 3ℓ slot performs better than the 4d hole at B = 0.4 but is reversed at B = 1.2. All three blowing ratios can reduce the heat load.

Table 1 shows the effect of mainstream turbulence on leading edge local heat transfer coefficient of 3ℓ slot and 4d hole's ±15 deg injection for B = 0.4. It is seen that high mainstream turbulence causes higher values of heat transfer coefficient at all locations. The 4d hole produces higher heat transfer coefficients than the 3ℓ slot. No significant differences of variations

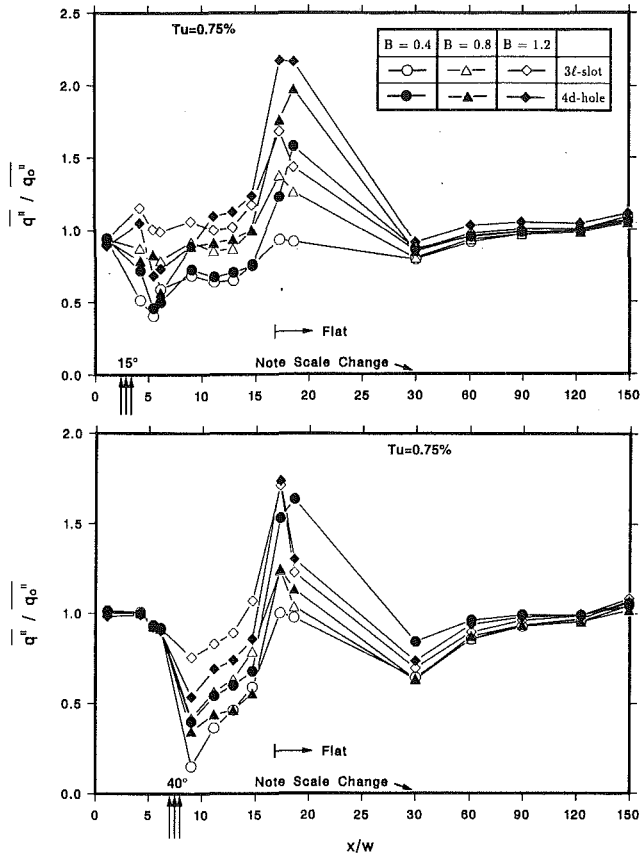

Fig. 10 Comparison of surface heat load ratio between 3ℓ slot and $4d$ hole for (*a*) ±15 injection and (*b*) ±40 deg injection at Tu = 0.75 percent, for ϕ = 0.6

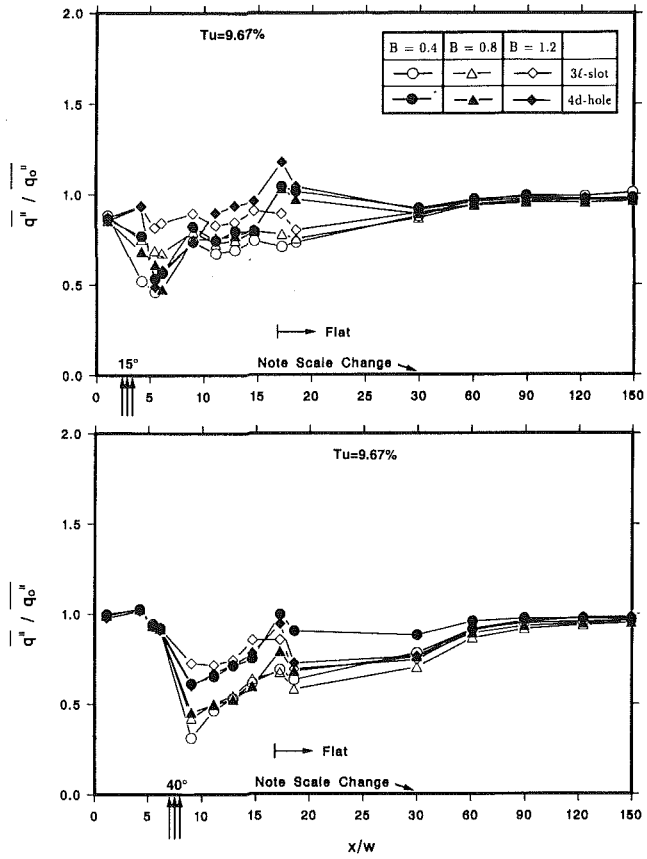

Fig. 11 Comparison of surface heat load ratio between 3ℓ slot and $4d$ hole for (*a*) ±15 deg injection and (*b*) ±40 deg injection at Tu = 9.67 percent, for ϕ = 0.6

Table 1 Local $Nu_D / (Re_D)^{1/2}$ of 3ℓ slot and $4d$ hole at ±15 deg injection and blowing ratio of B = 0.4 for the no grid and passive grid

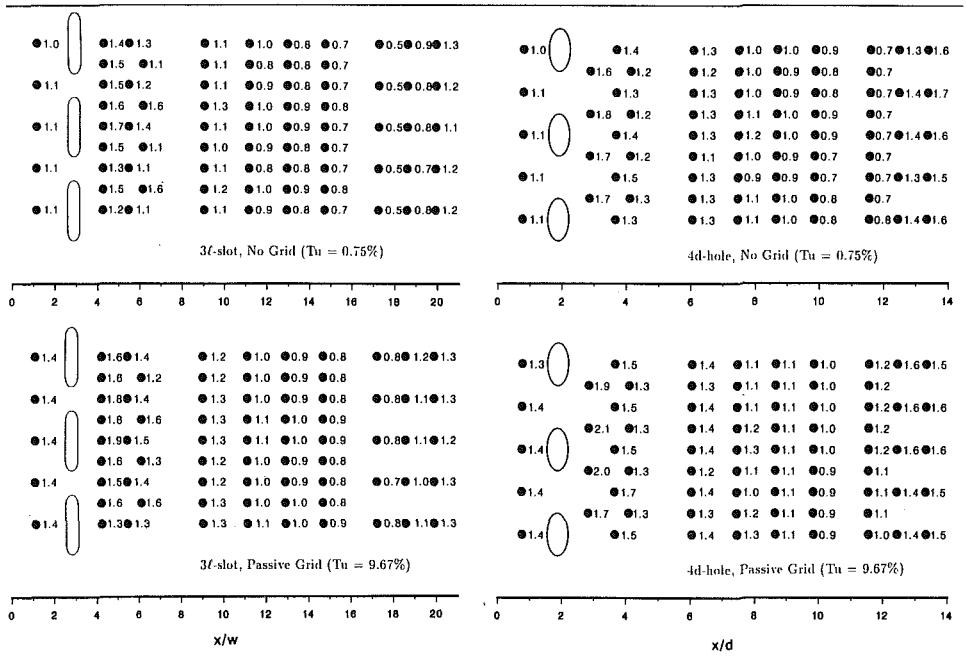

in the spanwise direction is found for either geometry at low and high mainstream turbulence levels (Tu = 0.75 and 9.67 percent).

Table 2 shows the effect of mainstream turbulence on leading edge local film effectiveness of both geometries' ±15 deg injection for B = 0.4. As described earlier, high mainstream turbulence, unlike the heat transfer coefficient, results in lower local film effectiveness at every location. The variations in the streamwise and spanwise directions are significant for both geometries and mainstream turbulence levels.

Table 2 Local film effectiveness of 3ℓ slot and $4d$ hole at ± 15 deg injection and blowing ratio of $B = 0.4$ for the no grid and passive grid

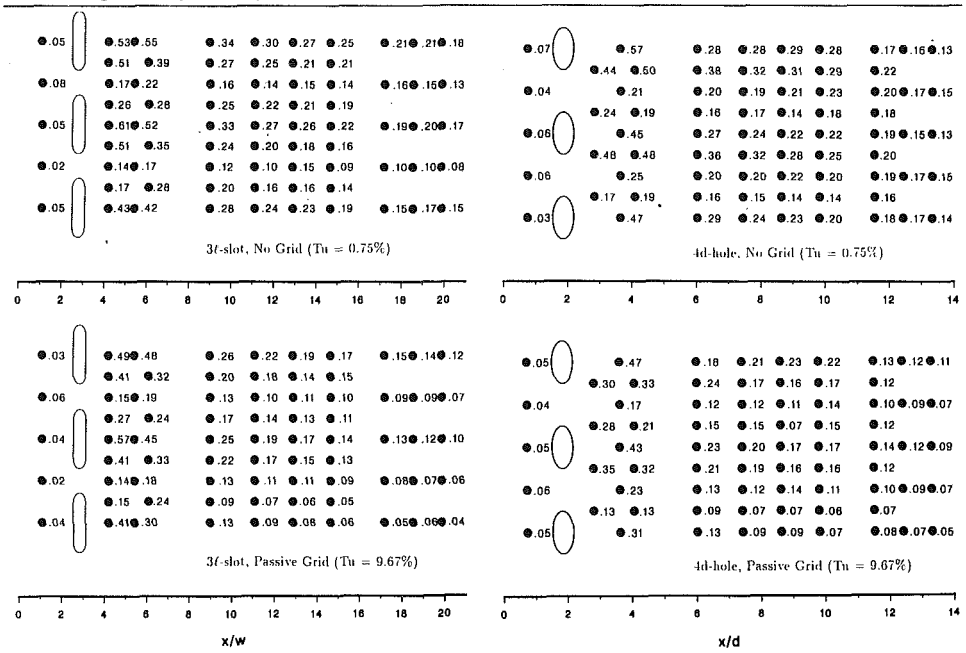

Concluding Remarks

The heat transfer coefficient and film effectiveness with ± 15 deg or ± 40 injection for film slots and film holes have been experimentally studied for flow over a blunt body with a semicylinder and flat afterbody. The tests were conducted for three blowing ratios of 0.4, 0.8, and 1.2 at the incident mainstream Reynolds number of 100,000 for three mainstream turbulence intensities of 0.75, 5.07, and 9.67 percent. The major findings are:

1 In general, the heat transfer coefficient increases and the film effectiveness decreases with increasing blowing ratio for all cases studied except that film effectiveness reaches the maximum at $B = 0.8$ for the ± 40 deg injection of film hole geometry.
2 The heat transfer coefficient increases with increasing mainstream turbulence level for all test cases at three studied blowing ratios.
3 The film effectiveness decreases with increasing mainstream turbulence level at the lowest blowing ratio of 0.4; however, the mainstream turbulence effect is reduced at the highest blowing ratio of 1.2.
4 The 3ℓ slot geometry provides more heat load reduction than $4d$ hole geometry for all test cases at a blowing ratio of 0.4. However, at the higher blowing ratios of 0.8 and 1.2, the reverse is true for ± 40 deg injection at mainstream turbulences of 0.75 and 9.67 percent.

Acknowledgments

This project was supported by Textron Lycoming through contract #H164150. Their support is greatly appreciated.

References

Bonnice, M. A., and L'Ecuyer, W. R., 1983, "Stagnation Region Gas Cooling—Effects of Dimensionless Coolant Temperature," NASA CR-168197.

Hancock, P. E., and Bradshaw, P., 1983, "The Effect of Free-Stream Turbulence on Turbulent Boundary Layers," ASME *Journal of Fluids Engineering*, Vol. 105, pp. 284–289.

Karni, J., and Goldstein, R. J., 1990, "Surface Injection Effect on Mass Transfer From a Cylinder in Crossflow: A Simulation of Film Cooling in the Leading Edge Region of a Turbine Blade," ASME *Journal of Turbomachinery*, Vol. 112, pp. 418–427.

Kline, S. J., and McClintock, F. A., 1953, "Describing Uncertainties in Single-Sample Experiments," *Mechanical Engineering*, Vol. 75, Jan., pp. 3–8.

Luckey, D. W., and L'Ecuyer, M. R., 1981, "Stagnation Region Gas Film Cooling—Spanwise Angled Injection From Multiple Rows of Holes," NASA CR-165333.

Mehendale, A. B., Han, J. C., and Ou, S., 1991, "Influence of High Mainstream Turbulence on Leading Edge Heat Transfer," ASME JOURNAL OF HEAT TRANSFER, Vol. 113, pp. 843–850.

Mehendale, A. B., and Han, J. C., 1992, "Influence of High Mainstream Turbulence on Leading Edge Film Cooling Heat Transfer," ASME *Journal of Turbomachinery*, Vol. 114, pp. 707–715.

Mick, W. J., and Mayle, R. E., 1988, "Stagnation Film Cooling and Heat Transfer, Including Its Effect Within the Hole Pattern," ASME *Journal of Turbomachinery*, Vol. 110, pp. 66–72.

Ou, S., 1991, "Leading Edge Film Cooling Heat Transfer Including the Effect of Mainstream Turbulence," Ph.D. Dissertation, Texas A&M University, College Station, TX.

Ou, S., Mehendale, A. B., and Han, J. C., 1992, "Influence of High Mainstream Turbulence on Leading Edge Film Cooling Heat Transfer: Effect of Film Hole Row Location," ASME *Journal of Turbomachinery*, Vol. 114, pp. 716–723.

Ou, S., and Han, J. C., 1992, "Influence of Mainstream Turbulence on Leading Edge Film Cooling Heat Transfer Through Two Rows of Inclined Film Slots," ASME *Journal of Turbomachinery*, Vol. 114, pp. 724–733.

Sasaki, M., Takahara, K., Sakata, K., and Kumagai, T., 1976, "Study on Film Cooling of Turbine Blades," *Bulletin of the JSME*, Vol. 19, No. 137, pp. 1344–1352.

Wadia, A. R., and Nealy, D. A., 1988, "Experimental Simulation of Turbine Airfoil Leading Edge Film Cooling," ASME *Journal of Turbomachinery*, Vol. 110, pp. 226–232.

Convective Heat Transfer to a Confined Impinging Array of Air Jets With Spent Air Exits

A. M. Huber

R. Viskanta

Heat Transfer Laboratory,
School of Mechanical Engineering,
Purdue University,
West Lafayette, IN 47907

This investigation has examined the influence of spent air exits located between the jets on the magnitude and uniformity of the local heat transfer coefficient for a confined 3 × 3 square array of axisymmetric air jets impinging normally to a heated surface. The heat transfer coefficient was measured using a 0.025-mm-thick stainless steel impingement surface coated with liquid crystals. The temperature distribution along the surface was determined by measuring the reflected wavelength of light from the liquid crystal with the use of bandpass filters and an electronic digitizer board. The effect of small nozzle-to-plate spacings (0.25 and 1.0 diameters) commonly used in material processing applications was also considered. Average Nusselt numbers are presented for a Reynolds number range of 3500 to 20,400 along with radial distributions of the local Nusselt number. The local Nusselt number distributions illustrate the uniformity of the convective heat transfer coefficient and contribute to understanding the variations in the magnitude of the average Nusselt number. Results have shown that the addition of spent air exits increased the convective heat transfer coefficient and changed the location of the optimal separation distance. In addition, significant enhancement of the uniformity and magnitude of the heat transfer coefficient was observed at the 0.25 and 1.0 jet diameter nozzle-to-plate spacings when compared to a 6.0 diameter spacing.

Introduction

The heat transfer during materials processing and manufacturing is enhanced through jet impingement for many different applications, including the tempering and shaping of glass, the annealing of metal and plastic sheets, the cooling of turbine blades, and the drying of textiles, veneer, paper, and film materials. Rapid and uniform heating or cooling of the material is necessary to ensure material quality. The high heat and/or mass transfer rates that occur in the impingement regions of the jets result in high local transport coefficients. However, a disadvantage of impingement heating or cooling can be the nonuniformity of the heat flux distribution. Crossflow and adjacent jet interaction cause variations in the heat transfer performance of individual jets in an array, which can affect the quality and/or performance of the product (Martin, 1977; Viskanta, 1993). Metzger and Korstad (1972), Obot and Trabold (1987) and others have shown that crossflow caused by the spent air exiting radially outward from the edges of the array decrease the magnitude and the uniformity of the heat transfer coefficient. The crossflow and adjacent jet interference degradation of the heat transfer coefficient can be minimized by having the spent air exit through openings in the orifice plate, and the uniformity and magnitude of the convective coefficient are enhanced for the entire array. With the possibility of a very large number of jet orifices in each array, the geometry of the spent air exit significantly affects the performance of the impinging jet array. To help ensure product quality and performance through large and uniform heat transfer coefficients, it is important to understand the heat transfer and fluid flow characteristics of impinging gaseous jet systems.

Research during the past four decades on impinging gas jet heat transfer has led to a large body of literature. This literature has been reviewed by Livingood and Hrycak (1973), Martin (1977), Downs and James (1987), Jambunathan et al. (1992), and Viskanta (1993). However, the majority of the publications deal with cool turbulent air jets impinging normally onto a heated flat plate at large nozzle-to-plate spacings ($H/D > 1$) with or without crossflow. The available literature for axisymmetric impinging gas jet systems that is relevant to materials processing and manufacturing and not to gas turbine blade or electronic cooling is limited, with no known literature addressing the issue of axisymmetric air jet arrays with spent air exits located between the jets and/or nozzle-to-plate spacings smaller than 0.5 diameters. However, Hollworth and Dagan (1980) did examine arrays of impinging jets with spent air removal through the impingement surface. They found that for arrays with staggered (not lined up with the jet orifices) spent air exit holes the heat transfer rates were 20 to 30 percent larger than for arrays with a crossflow spent air exit geometry. However, for many material processing and manufacturing applications it is not possible to have the spent air exit through the impingement surface. Thus, spent air removal through the jet orifice plate is required to avoid crossflow degradation of the heat transfer coefficient. Also, most laboratory investigations have utilized unconfined jet systems. Confinement can and does affect the heat transfer relative to unconfined jets through entrainment of ambient air and a different pressure distribution. Saad et al. (1992) recently examined confined slot jet arrays at large separation distances ($H \geq 4$ slot widths) with spent air exits located in the confinement surface relative to the drying of paper. They commented that heat transfer data obtained with unconfined jets cannot be used reliably for design of confined jet systems, and, if spent air exits are not located between the nozzles in the confinement surface, crossflow of spent air will have an adverse effect on impingement heat transfer.

This paper examines the effect of the separation distance ($H/D = 6$, 1, 0.25), Reynolds number (3500–20,400), and the presence of spent air exits located between the jet orifices in the jet orifice plate on the local Nusselt number distributions for an axisymmetric confined air jet array. As previously mentioned, the geometry of the spent air exit significantly affects both the uniformity and magnitude of the local heat transfer

Contributed by the Heat Transfer Division and presented at the National Heat Transfer Conference, Atlanta, Georgia, August 8–11, 1993. Manuscript received by the Heat Transfer Division March 1993; revision received September 1993. Keywords: Forced Convection, Jets, Materials Processing and Manufacturing Processes. Associate Technical Editor: W. Simon.

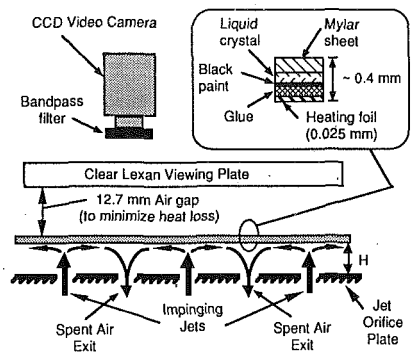

Fig. 1 Schematic diagram of orifice plate with spent air exits and impingement surface

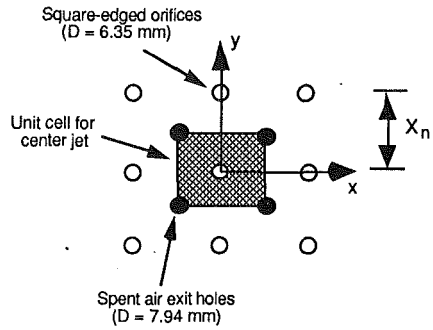

Fig. 2 Top view of the jet array orifice plate

coefficient, which, in turn, affects the product quality and performance. The knowledge gained from the local Nusselt number distributions is then used to understand the behavior of the observed average Nusselt numbers. The experimental data were also compared to the results of other investigators.

Experimental Apparatus

A thermochromatic liquid crystal technique was used to visualize and measure isotherms on the impingement surface. Ferguson (1968) discusses liquid crystals and their use in testing. Several researchers (den Ouden and Hoogendoorn, 1974; Goldstein and Timmers, 1982; Akino et al., 1989; Baughn et al., 1991) have used liquid crystals to determine the convective heat transfer coefficients for various flow geometries. den Ouden and Hoogendoorn, Goldstein and Timmers, and Baughn et al. selectively used a specific color to determine the surface temperature with human color sensation for jet impingement studies. This method involves a large amount of manual labor and relies on human color sensation, which varies between individuals. Therefore, it is subject to error and limited reproducibility. Akino et al. (1989) eliminated the uncertainty involved with human color sensation by using bandpass filters and a video imaging system to select specific wavelengths of reflected light and thus determine the surface temperature for flow along a flat plate with a short attached cylinder. This basic technique was adapted for use with the available equipment and employed to obtain the experimental data presented in this paper.

The experimental apparatus (Fig. 1) was constructed to enable a wide range of conditions and geometries to be examined. Before entering the experimental apparatus, the air is dried and filtered, while a combination of two turbine flow meters permits measurement of a large range of flow rates (i.e., Reynolds numbers). Then, after passing through the regulator, turbine flow meters, and heater, the dry air flows into the rectangular plenum chamber (25.4 cm wide, 25.4 cm deep, and 36.2 cm high) and is calmed. About 100 mm from the top of the plenum the air flows through a stainless steel mesh screen and a 51-mm-thick honeycomb flow straightener, which helps to ensure uniform flow from the jet orifices. The orifices are square-edged with a 1.5 l/D ratio and diameter of 6.35 mm. The inlet of each orifice was slightly rounded to ensure similar entrance conditions for each orifice. The orifice plate is 9.5 mm thick and 254 mm square. Thermocouples inside the plenum monitor the air temperature. Because of the low Mach number (0.14 maximum) the plenum air temperature is virtually identical to the jet exit temperature ($T/T_o = 0.9961$ for isentropic flow at Mach = 0.14). Thus, the average plenum air temperature is used for the jet exit temperature. However, this assumption is one reason the uncertainty in the jet exit temperature is the largest source of uncertainty in the Nusselt number.

An impingement surface similar to that shown in Fig. 1 was constructed to observe and measure the distribution of the convective heat transfer coefficient over the entire area of the surface for single and multiple isothermal jets. The impingement surface was held in tension by compressed springs over a Lexan frame. The temperature measurements using liquid crystals provides information of the heat transfer coefficient distribution as well as its magnitude. Without the use of the liquid crystal it would be very difficult to obtain even rough estimates of the local heat transfer coefficient over an area of any substantial size.

The jet orifice plate and plenum shown in Fig. 1 were mounted on a stand, which allowed vertical movement. To change the separation distance, the locking bolts were loosened and the plenum and orifice plate moved upward or downward with an attached screw jack. To ensure accurate spacing, aluminum blocks were machined to within a ± 0.012 mm tolerance and used to check the spacing between the jet orifice plate and the impingement surface.

For this study a 3×3 square isothermal jet array was used with a jet-to-jet spacing of six diameters ($X_n/D = 6$). This jet spacing was recommended by Freidman and Mueller (1951) to reduce adjacent jet interference and maximize heat transfer over the surface. Martin (1977) also presents an optimum value of roughly 7 diameters for $H/D = 5.4$. Figure 2 illustrates the arrangement of the orifices and spent air exit holes on the

Nomenclature

A_f = jet exit area to heat transfer area ratio $= (\pi/4)(D/X_n)^2$
D = jet diameter, m
G = factor in Martin (1977) correlation
H = distance from jet exit to impingement surface, m
K = factor in Martin (1977) correlation
k = thermal conductivity of air at jet exit, W/m-K
l = thickness of the orifice plate, m
M = mass flow rate of air, kg/s
Nu_D = Nusselt number based on jet diameter $= hD/k$
q_{conv} = convective heat flux, W/m^2
Re_D = Reynolds number based on jet diameter $= 4M/(\pi D\mu)$
r = radial distance from stagnation point of jet, m
T_{jet} = jet exit temperature, K
T_w = liquid crystal (impingement surface) temperature, K
X_n = spacing between jets in a square array, m
μ = air viscosity at jet orifice exit, N-s/m^2

orifice plate. The impingement surface and orifice plate are of sufficient size to eliminate end effects, and are open to the atmosphere on all four sides. Thus, when the spent air exit holes are closed, the spent air exits in a crossflow geometry from the four sides of the impingement surface. The spent air exit holes in the orifice plate access rectangular channels (9.5 mm by 6.3 mm) machined through the length of the orifice plate. These channels vent the spent air to the atmosphere through the sides of the orifice plate. The unit cell (38.1 mm square) for the center jet is also shown. This unit cell is the total impingement surface area cooled by the center jet, and the ratio of the jet exit area to this surface area is the dimensionless open area, A_f. The experimental measurements were taken over the area of this unit cell for the center jet. The center jet is representative of each individual jet in an array without crossflow, which is not located on the edge of the array. Jets located on the boundary or edge of an array do not have adjacent jet interference on all sides and thus exhibit slightly different behavior. Measurements indicated that the average Nusselt numbers for the center jet unit cell and the average values for a boundary jet unit cell varied by less than 10 percent.

Experimental Procedure

Before the experimental tests were conducted, the flow meters and bandpass filters were calibrated. The bandpass filters were calibrated by placing the liquid crystal assembly on a flat aluminum plate instrumented with thermocouples embedded near the surface 12.7 mm apart. A constant-temperature cold plate was placed at each end of the aluminum plate and the plate was insulated. The temperature at each end of the aluminum plate was then varied to establish a linear temperature gradient along the length of the plate and the stainless steel impingement surface within the working temperature range of the liquid crystal. The liquid crystal surface was viewed through the clear Lexan plate with the bandpass filters. Then the location of the isotherm indicated by the bandpass filter was matched with the temperature on the impingement surface recorded by the thermocouples. This eliminated errors in measuring the impingement surface temperature from the backside and resulted in a less than 0.1 °C uncertainty in the impingement surface temperature. This small uncertainty was achieved using the bandpass filters and a liquid crystal sheet with a narrow one degree Celsius working range. The typical temperature difference between the impingement surface temperature and the jet exit temperature was about 13 °C. In addition, because the stainless steel impingement surface was very thin (0.0254 mm) a simple numerical estimation of the impingement assembly showed that the heat transfer could be modeled as one dimensional through the stainless steel heater and liquid crystal layer.

The heat transfer measurements were made by recording the isotherm indicated by a bandpass filter with a video camera. Simultaneously the electrically imposed heat flux (voltage drop times the current across the heater), air flow rate, jet exit temperature, and ambient temperature were measured. Approximately 20 isotherms were recorded for every 25.4 mm distance. The recorded isotherms were then digitized with an EPIX, Inc. (Northbrook, IL) digitizing board and software and a PC computer using 80 pixels per 25.4 mm in the horizontal direction. The individual digitized images were processed, and the intensity value of each pixel depicting the location of the isotherm was set equal to the calculated local Nusselt number. The local Nusselt number for each isotherm was determined from

$$\mathrm{Nu}_D = \frac{q_{\mathrm{conv}} D}{(T_w - T_{\mathrm{jet}})k} \tag{1}$$

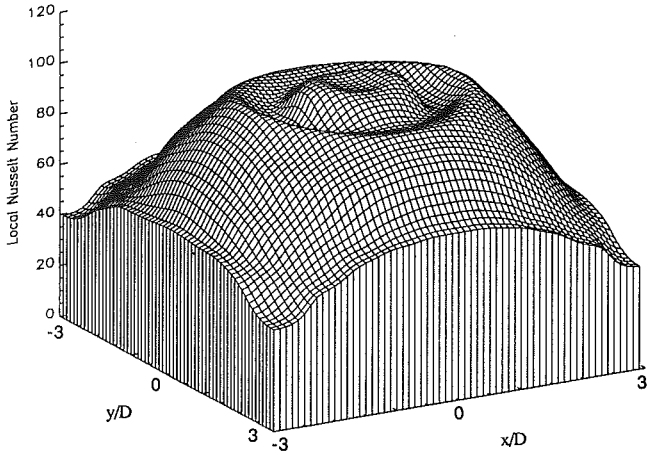

Fig. 3 Local Nusselt number distribution for $H/D = 1.0$ and $\mathrm{Re}_D = 17{,}100$

The jet exit temperature was used in defining the Nusselt number rather than the adiabatic wall temperature (Goldstein et al., 1990) for several reasons. One, because the jet exit temperature was approximately equal to the ambient air temperature, which minimized entrainment effects; two, the Reynolds numbers used in this study were low enough to avoid significant compressibility effects (maximum Mach number of 0.14); and three, for design purposes the jet exit temperature is a more convenient temperature with which to work. The convective heat flux was determined from the total electric power input rate minus the estimated heat losses. The heat losses were a combination of radiation from the heater surface and conduction losses through the top of the impingement surface assembly. Tests were conducted in the absence of jet impingement (no air flow) to obtain an estimate of the heat losses. These tests involved natural convection, radiation from the impingement surface, and conduction losses through the impingement surface assembly. The tests indicated that the heat losses during jet impingement were less than 3 percent of the total electric power input.

Using a 95 percent confidence level, the uncertainty in the Nusselt and Reynolds numbers was determined with a root-sum-square method (Moffat, 1988). The Nusselt number calculation had an uncertainty range of 4 to 9 percent, while the uncertainty in the Reynolds number calculation was estimated to be 3.2 percent. The results were reproducible within these uncertainty ranges.

After each individual isotherm image had been processed, the individual images were superimposed to create a surface map of the isotherms. Using commercial computer software (PV-WAVE produced by Precision Visuals Inc., Boulder, CO) the surface isotherm map was converted to a uniform two-dimensional array of local Nusselt numbers, with each pixel from the isothermal image (7200 pixels for the unit cell) corresponding to one array entry. Various plots and slices of the data were then obtained to gain understanding of the local heat transfer coefficient over the entire unit cell surface.

Results and Discussion

Local Heat Transfer. Since the $X_n/D = 6$ value was used to minimize the adjacent jet interaction as discussed previously, the local heat transfer coefficient is fairly symmetric around the stagnation point. Thus, two-dimensional plots of the radial Nusselt number distributions can be used for comparison. The three-dimensional plot, Fig. 3, illustrates the symmetry of the local heat transfer coefficient around the stagnation point for the unit cell area. This figure is for a separation distance of one diameter ($H/D = 1$), which Metzger et al. (1969), Hrycak

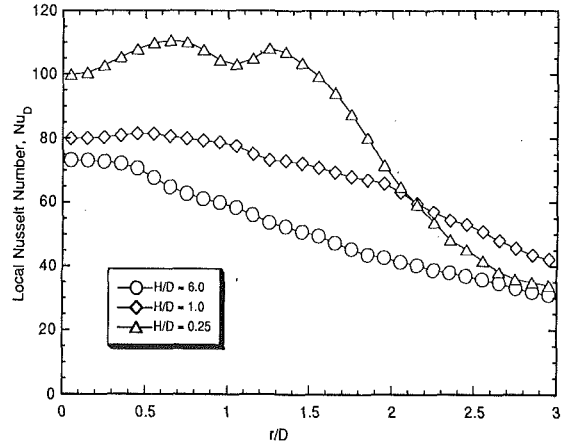

Fig. 4 Effect of separation distance on local Nusselt number distributions for $Re_D = 10,300$

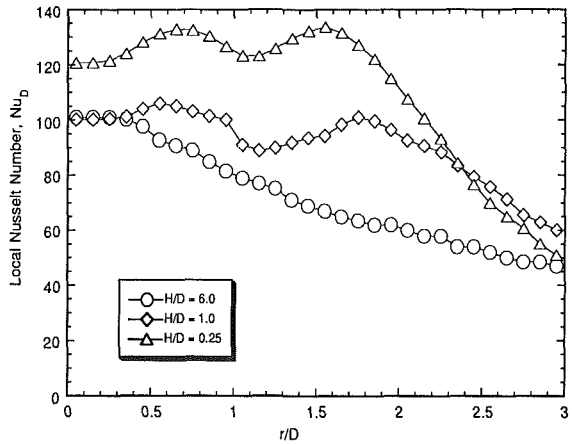

Fig. 5 Effect of separation distance on local Nusselt number distributions for $Re_D = 17,100$

(1981), and Ichimiya and Okuyama (1991) have reported is the approximate distance for the maximum average heat transfer coefficient with an array of axisymmetric air jets ($H/D < 0.5$ distances were not examined by these investigators). Examination of the local Nusselt numbers plotted in Fig. 3 clearly shows the presence of secondary peaks and indicate that these secondary peaks increase the average convection coefficient. Their effect on the average values will be discussed in the following sections.

Effect of Separation Distance (H/D). Figures 4 and 5 show the effect of the separation distance on the local Nusselt number profiles. At a separation distance of six diameters, roughly equal to the length of the potential core, the Nusselt number is maximum at the stagnation point and decreases as r/D increases, for both Reynolds numbers. However, as the separation distance is decreased to one diameter, secondary peaks occur in the profile, and the maximum Nusselt number no longer occurs at the stagnation point. These peaks occur at $r/D \approx 0.5$ and $r/D \approx 1.7$ and are more pronounced for $Re_D = 17,100$ than for $Re_D = 10,300$. At the separation distance of 0.25 diameters these secondary peaks are clearly present, with the location of the second peak decreasing to $r/D \approx 1.5$.

Prior researchers have discussed and provided explanations for the occurrence of these secondary peaks with single unconfined jets. Lytle and Webb (1991) used an unconfined fully developed pipe flow nozzle to study these secondary maxima at low separation distances. While their nozzle geometry and flow conditions differ from those of this study, the location of the secondary peaks reported by Lytle and Webb, and the location of the secondary peaks measured in this study correspond very well. The inner peak, which occurred at $r/D \approx 0.5$, is attributed to both the fluid accelerating out of the stagnation region that thins the local boundary layer and the influence of the shear-layer generated turbulence around the circumference of the jet noticed by various investigators (Huber, 1993). As the Reynolds number increased, the acceleration and shear-layer turbulence effect increased, and the inner peak becomes more pronounced. There is agreement among several authors (Gardon and Akfirat, 1965; den Ouden and Hoogendoorn, 1974; Obot et al., 1979; Lytle and Webb, 1991) that the inner secondary peak becomes less pronounced as the Reynolds number is reduced and the separation distance is increased. However, due to the differing nozzle geometry and flow conditions, the separation distance where the peak disappeared varied among the studies.

The outer secondary peak was observed by Lytle and Webb (1991) to be caused by the transition to turbulent flow in the boundary layer. They showed from turbulence and heat transfer measurements that the outer secondary peak in the heat transfer coefficient correlates well with a peak in the turbulence intensity of the radial velocity component. This was also shown by den Ouden and Hoogendoorn (1974). Thus, similar to the inner peak, Figs. 4 and 5 reveal that as the Reynolds number was increased from 10,300 to 17,100, the effect of the boundary layer transition increased, and the outer peak in the local Nusselt number became more pronounced. A decrease in the Reynolds number or the separation distance appears to promote an earlier boundary layer transition, because the location of the outer peak moves toward the stagnation point when either of these two parameters are varied appropriately. This is consistent with the findings of Lytle and Webb (1991) who found an almost equal dependence of the location of the outer secondary peak on the Reynolds number and separation distance.

Figures 4 and 5 also exhibit crossover points for the $H/D = 1.0$ and 0.25 distributions. Between $r/D = 2$ and 2.5 the local Nusselt numbers for $H/D = 0.25$ drop below the local values for $H/D = 1.0$. This crossover is probably due to the fact that the boundary layer flow for $H/D = 0.25$ becomes turbulent earlier than for the $H/D = 1.0$ arrangement. The turbulent flow then consumes more momentum and slows down faster for the latter geometry. This tends to decrease the convective heat transfer coefficient with increasing r/D faster for the $H/D = 0.25$ arrangement. Also, for this case the local coefficients are higher, which will slightly raise the temperature of the fluid as it transports more energy away from the surface than with the $H/D = 1.0$ geometry. This will tend to decrease the temperature difference and slightly lower the convective coefficient, since the temperature difference is assumed to be constant.

Effect of Reynolds Number. Figure 6 details the dependence of the local Nusselt number profiles on the Reynolds number for a separation distance of one jet diameter. One of the major differences between the profiles is in the magnitudes and locations of the secondary peaks. As mentioned, the secondary peaks exhibit a strong dependence on the Reynolds number, separation distance, and nozzle geometry. At a Reynolds number of 3500 there is no evidence of the secondary peaks, and the profile is very similar to those obtained at $H/D = 6.0$ for all the examined Reynolds numbers. As the Reynolds number is increased to 6900, the profile shape has not changed significantly but there is a faint indication of an inner secondary peak. At a Reynolds number of 10,300 the secondary peaks are clearly discernible but still not pronounced. But, when the Reynolds number is increased to 13,700 the secondary peaks are now clearly evident. As the Reynolds number is further increased to 17,100 and then 20,400, the secondary peaks become more pronounced.

While the inner secondary peak remains fixed as the Reyn-

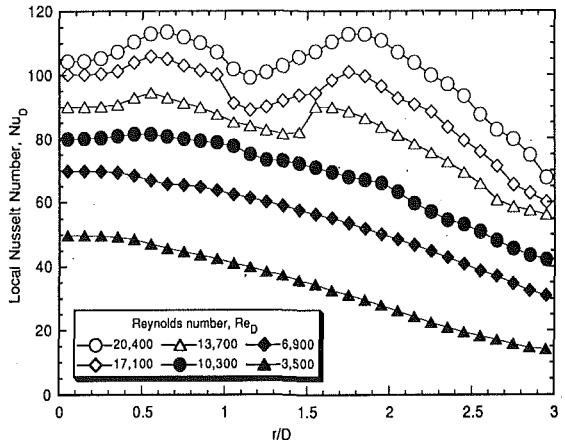

Fig. 6 Effect of Reynolds number on local Nusselt number distributions for $H/D = 1.0$

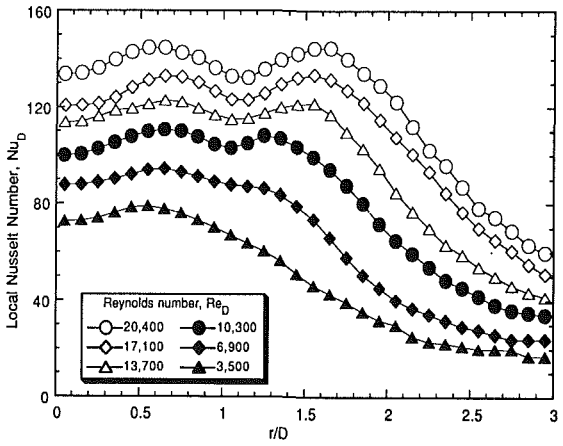

Fig. 7 Effect of Reynolds number on local Nusselt number distributions for $H/D = 0.25$

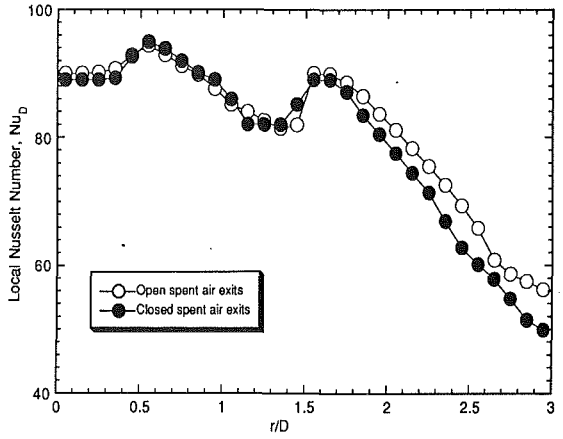

Fig. 8 Local Nusselt numbers with and without spent air exits for $H/D = 1$ and $Re_D = 13{,}700$

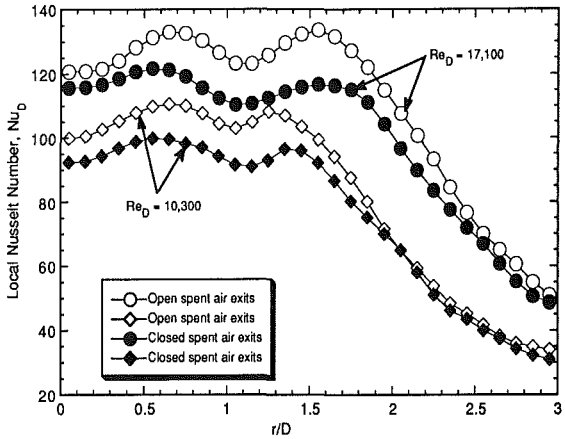

Fig. 9 Local Nusselt numbers with and without spent air exits for $H/D = 0.25$

olds number changes, the outer peak moves outward with increasing Reynolds number. As mentioned previously, this effect was also documented by Lytle and Webb (1991) for their single unconfined jet with a fully developed profile. Gardon and Akfirat (1965) and Ichimiya and Okuyama (1991) also observed this trend, while den Ouden and Hoogendoorn (1974) found that the turbulence level at the jet exit affected the location of the outer peak. An increasing turbulence level at the jet exit influences the radial velocity component, which promotes earlier transition to a turbulent boundary layer. Turbulence intensity was not measured in this experimental work, but the jets are considered fully turbulent based on Polat et al. (1989) who state that for $Re_D \geq 3000$ a jet is fully turbulent. Measured heat transfer results from this study have also shown negligible differences as the turbulence level at the jet exit was varied by removing the screens and flow straighteners from the plenum.

Figure 7 shows these same trends with the outer secondary peak closer to the stagnation point for $H/D = 0.25$. The outer peaks have moved inward when compared to Fig. 6, because the boundary layer transition occurs earlier at the smaller separation distance. Also, because of the smaller separation distance, the secondary peaks are present at all of the lower Reynolds numbers.

Effect of Spent Air Exits. From Fig. 8 it is clear that for a separation distance of one jet diameter the presence of spent air exits has no effect on the local Nusselt number distribution. This is because the gap between the impingement surface and confining jet orifice plate is large enough to channel the flow outward without a significant pressure drop. Also, because the jet used for the measurements is the center jet of the 3×3 array, all of the flow is radially outward and thus, even with the spent air exits blocked, there is no crossflow to degrade the convective coefficient. In a large array, crossflow and flow channeling can have a significant effect on both the uniformity and magnitude of the heat transfer coefficient (Krötzsch, 1968; Metzger and Korstad, 1972; Livingood and Hrycak, 1973; Downs and James, 1987; Obot and Trabold, 1987). These effects should be minimized by placing spent air exits between the jet orifices in the jet orifice plate; however, the small array used in this study does not experience crossflow and flow channeling. Thus, for a large array a difference in the heat transfer coefficients for the closed and open spent air exits would be expected at $H/D \geq 1$.

When the separation distance is decreased to 0.25 jet diameters, there is a clear difference between the Nusselt numbers with and without the spent air exits. This is shown in Fig. 9 for two Reynolds numbers. The narrower gap between the impingement surface and the confining jet orifice plate results in a resistance to the flow, which, with no spent air exits, must exit radially outward. This resistance to the flow and the resulting higher pressure in the stagnation region degrade the heat transfer coefficient. With no spent air exits, the boundary layer transition also appears to be delayed as the outer secondary peak occurs at a larger r/D value for the case of no spent air exits than with spent air exits. Once again, the presence of crossflow would have degraded the convective coefficient for the arrangement with no spent air exits and increased the difference between the two cases.

Figure 9 depicts the importance of spent air exits with small

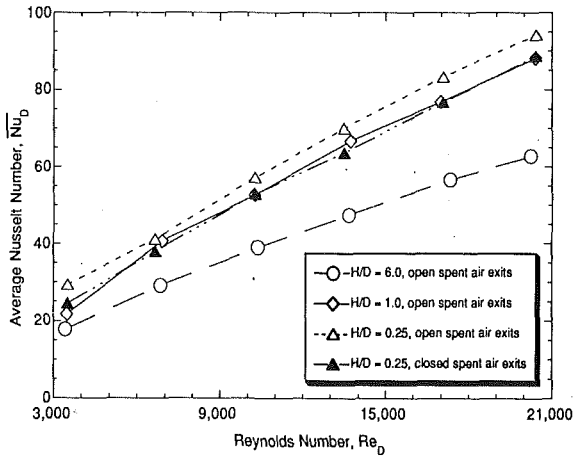

Fig. 10 Effect of separation distance on average Nusselt numbers

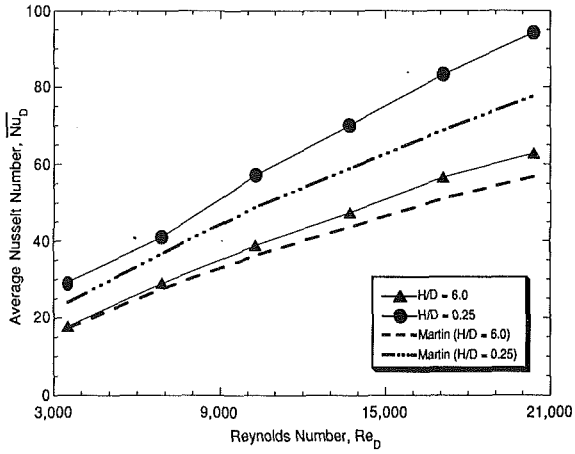

Fig. 11 Comparison of average Nusselt numbers with Martin (1977) correlation

separation distances. The additional elimination of crossflow heat transfer coefficient degradation means that a significant enhancement of the convective coefficient can occur through the use of spent air exits. The uniformity of the convective coefficient across the array would also be improved as each individual jet's unit cell has identical flow conditions and Nusselt number distributions. Uniformity of the local heat transfer coefficient is important for the material processing applications for which arrays of this type are used.

Average Nusselt Number. The three-dimensional plots of the local Nusselt number were averaged over the square unit cell area. In an array, the local Nusselt number distribution should be identical for each unit cell; therefore, the average Nusselt number for the unit cell is the average for the entire array. Figure 10 illustrates the average Nusselt number for various separation distances and Reynolds numbers. As expected, increasing the Reynolds number and/or decreasing the separation distance increases the average Nusselt number.

The average Nusselt number for $H/D=6.0$, which is at the end of the potential core region, has the lowest average Nusselt numbers for a given Reynolds number. For this separation distance, the local maximum Nusselt number occurs in the stagnation point region, which occupies a small fraction of the total area. However, when the separation distance is decreased to $H/D=1.0$, there is a considerable enhancement of the average Nusselt number. This is due to the secondary maximum peaks in the local Nusselt number. These secondary peaks occur as rings, which significantly increase the surface area where the local Nusselt numbers are high. The dependence on the Reynolds number is also strengthened because of the relationship between the secondary peaks and the Reynolds number. At the low Reynolds number of 3500 the difference between the average Nusselt number for $H/D=6.0$ and 1.0 is small, because the secondary peaks are virtually nonexistent at this value. But, as the Reynolds number is increased, the secondary peaks appear and become more pronounced for $H/D=1.0$. Thus, the average Nusselt number becomes significantly higher than for $H/D=6.0$.

The Nusselt numbers for $H/D=0.25$ with the open spent air exits exhibit the same trends seen with $H/D=1.0$. The smaller separation distance further enhances the heat transfer coefficient, when compared to the one-diameter spacing, by affecting the strength of the secondary peaks. However, both $H/D=0.25$ and 1.0 separation distances exhibit a similar dependence on the Reynolds number as shown by the relative equivalent slopes.

The figure also illustrates enhancement of the convective coefficient due to the spent air exits. The average Nusselt numbers for $H/D=0.25$ with closed spent air exits are almost identical to the average Nusselt number values for $H/D=1.0$, and significantly lower than the values for $H/D=0.25$ with open spent air exits. Thus, without spent air exits located between the jet nozzles, the enhancement of the convective heat transfer coefficient by the smaller separation distance ($H/D=0.25$) is offset by the degrading effects of the spent air exiting radially outward. The heat transfer coefficient degradation due to crossflow enforces the observation that without spent air exits it is not beneficial to decrease the separation distance below H/D = 1.0. From the local Nusselt number distributions and the average values presented in Fig. 10, the importance of properly designed spent air exits is apparent to obtain high convective coefficients and maintain uniformity across the jet array. A big advantage of the spent air exits is the elimination of crossflow degradation, which helps to ensure fairly uniform heating or cooling over the entire surface covered by an impinging jet array.

The average Nusselt numbers reported in this paper are compared to the correlation presented by Martin (1977) in Fig. 11. This correlation has been shown to predict average Nusselt numbers accurately for many jet impingement systems that have minimal or no crossflow (Martin, 1977; Ichimiya and Okuyama, 1991). The correlation was obtained by modifying the equation for a single round orifice, and thus Martin (1977) comments that it is valid for arrays with good outlet flow conditions. He further states that when the spent air is forced to flow laterally over the width of the material (crossflow) the outlet stream may significantly influence the flow and temperature fields. Because the experimental data has spent air exits and no crossflow, the correlation from Martin (1977) presented below should be applicable:

$$\overline{Nu}_D = 0.5KG\mathrm{Re}_D^{0.667}\mathrm{Pr}^{0.42} \tag{2}$$

where

$$K=\left\{1+\left(\frac{(H/D)\sqrt{A_f}}{0.6}\right)^6\right\}^{-0.05} \tag{3}$$

and

$$G=2\sqrt{A_f}\,\frac{1-2.2\sqrt{A_f}}{1+0.2(H/D-6)\sqrt{A_f}} \tag{4}$$

The range of validity given for this correlation is: $2000\le \mathrm{Re}_D\le 100{,}000$, $0.004\le A_f\le 0.04$, and $2\le H/D\le 12$. Figure 11 reveals the good agreement between the correlation and the experimental data for $H/D=6.0$, as the correlation underpredicts the experimental data by less than 10 percent. The differences between the experimental data and the empirical correlation predictions are probably due to variations

in nozzle geometry and flow conditions (i.e., turbulence level, plenum design), which have a large influence on impingement heat transfer. For example, Obot et al. (1979) observed that measured impingement heat transfer coefficients were larger for orifices than for converging nozzles. The Martin (1977) correlation is based on results for round nozzles. Thus, the orifices used for this study would be expected to yield higher heat transfer coefficients than the values predicted by the Martin correlation.

At $H/D=0.25$, which is outside the range of its validity, the correlation underpredicts the experimental data by about 18 percent. The $H/D=1.0$ data also differed from the correlation by about 14 percent. Since the correlation is not valid below $H/D=2.0$, the K and G factors that correct for the influence of the separation distance do not account for the presence of the secondary peaks. Thus, the difference between the present experimental data and the values predicted by the correlation increases as the secondary peaks become more pronounced.

Conclusions

This paper has reported a study on local heat transfer to confined isothermal impinging gas jets to gain understanding of the physical mechanisms that affect the average heat transfer coefficient and the uniformity of the local heat transfer coefficient. It was found that at small separation distances ($H/D\leq 1.0$) secondary maxima occur in the local convective coefficient for a jet in an array similar to a single jet. These secondary maxima enhance the average convective heat transfer coefficients. Also, at small separation distances ($H/D\leq 1.0$), degradation of the Nusselt number by adjacent jet interference before impingement is minimized.

Without spent air exits located between the jet orifices in the jet orifice plate, the heat transfer enhancement is lost as the radially outward flow of spent air degrades the convective coefficient. With spent air exits the surface area heated or cooled by each jet in an array experiences similar conditions and thus will exhibit similar performance. Therefore, the spent air exits are important in maintaining uniform heat transfer over the entire surface covered by a jet array.

References

Akino, N., Kunugi, T., Ichimiya, K., Mitsushiro, K., and Ueda, M., 1989, "Improved Liquid-Crystal Thermometry Excluding Human Color Sensation," ASME JOURNAL OF HEAT TRANSFER, Vol. 111, pp. 558–565.

Baughn, J. W., Hechanova, A. E., and Yan, X., 1991, "An Experimental Study of Entrainment Effects on the Heat Transfer From a Flat Surface to a Heated Circular Impinging Jet," ASME JOURNAL OF HEAT TRANSFER, Vol. 113, pp. 1023–1025.

den Ouden, C., and Hoogendoorn, C. J., 1974, "Local Convective Heat Transfer Coefficients for Jets Impinging on a Plate: Experiments Using a Liquid Crystal Technique," *Proceedings of the 5th Heat Transfer Conference*, Vol. 5, AIChE, New York, pp. 293–297.

Downs, S. J., and James, E. H., 1987, "Jet Impingement Heat Transfer—A Literature Survey," ASME Paper No. 87-HT-35.

Ferguson, J. L., 1968, "Liquid Crystals in Non-destructive Testing," *Journal of Applied Optics*, Vol. 7, pp. 1729–1737.

Freidman, S. J., and Mueller, A. C., 1951, "Heat Transfer to Flat Surfaces," *Proceedings of the General Discussion on Heat Transfer*, Institute of Mechanical Engineers, pp. 138–142.

Gardon, R., and Akfirat, J. C., 1965, "The Role of Turbulence in Determining the Heat Transfer Characteristics of Impinging Jets," *International Journal of Heat and Mass Transfer*, Vol. 8, pp. 1261–1272.

Goldstein, R. J., and Timmers, J. F., 1982, "Visualization of Heat Transfer From Arrays of Impinging Jets," *International Journal of Heat and Mass Transfer*, Vol. 25, pp. 1857–1868.

Goldstein, R. J., Sobolik, K. A., and Seol, W. S., 1990, "Effect of Entrainment on the Heat Transfer to a Heated Circular Air Jet Impinging on a Flat Surface," ASME JOURNAL OF HEAT TRANSFER, Vol. 112, pp. 608–611.

Hollworth, B. R., and Dagan, L., 1980, "Arrays of Impinging Jets With Spent Fluid Removal Through Vent Holes on the Target Surface—Part 1: Average Heat Transfer," ASME *Journal of Engineering for Power*, Vol. 102, pp. 994–999.

Hrycak, P., 1981, "Heat Transfer From a Row of Impinging Jets to Concave Cylindrical Surfaces," *International Journal of Heat and Mass Transfer*, Vol. 24, pp. 407–418.

Huber, A. M., 1993, "Heat Transfer With Impinging Gaseous Jet Systems," Ph.D. thesis, Mechanical Engineering Department, Purdue University.

Ichimiya, K., and Okuyama, K., 1991, "Characteristics of Impingement Heat Transfer Caused by Circular Jets With Confined Wall," *Proceedings of the 3rd International Cold Regions Heat Transfer Conference*, J. P. Zarling, ed., University of Alaska—Fairbanks, AK, pp. 523–532.

Jambunathan, K., Lai, E., Moss, M. A., and Button, B. L., 1992, "A Review of Heat Transfer Data for Single Circular Jet Impingement," *International Journal of Heat and Fluid Flow*, Vol. 13, pp. 106–115.

Krötzsch, P., 1968, "Heat and Material Transfer on Impact Streaming From Fields of Nozzles and Orifices," *Chemie Ingenieur Technik*, Vol. 40, p. 339.

Livingood, J. N. B., and Hrycak, P., 1973, "Impingement Heat Transfer From Turbulent Air Jets to Flat Plates—A Literature Survey," NASA TM X-2778.

Lytle, D., and Webb, B. W., 1991, "Secondary Heat Transfer Maxima for Air Jet Impingement at Low Nozzle-to-Plate Spacings," *Experimental Heat Transfer, Fluid Mechanics, and Thermodynamics*, J. F. Keffer, R. K. Shah, and E. N. Gánic, eds., Elsevier Science Publishing Co., New York, pp. 776–783.

Martin, H., 1977, "Heat and Mass Transfer Between Impinging Gas Jets and Solid Surfaces," *Advances in Heat Transfer*, T. Irvine and J. P. Harnett, eds., Vol. 13, Academic Press, New York, pp. 1–60.

Metzger, D. E., Yamashita, T., and Jenkins, C. W., 1969, "Improvement Cooling of Concave Surfaces With Lines of Circular Air Jets," ASME *Journal of Engineering for Power*, Vol. 91, pp. 149–158.

Metzger, D. E., and Korstad, R. J., 1972, "Effects of Crossflow on Impingement Heat Transfer," ASME *Journal of Engineering for Power*, Vol. 94, pp. 35–42.

Moffat, R., 1988, "Describing the Uncertainties in Experimental Results," *Experimental Thermal and Fluid Science*, Vol. 1, pp. 3–17.

Obot, N. T., Mujumdar, A. S., and Douglas, W. J. M., 1979, "The Effect of Nozzle Geometry on Impingement Heat Transfer Under a Round Turbulent Jet," ASME Paper No. 79-WA/HT-53.

Obot, N. T., and Trabold, T. A., 1987, "Impingement Heat Transfer Within Arrays of Circular Jets: Part 1—Effects of Minimum, Intermediate, and Complete Crossflow for Small and Large Spacings," ASME JOURNAL OF HEAT TRANSFER, Vol. 109, pp. 872–879.

Polat, S., Huang, B., Mujumbar, A. S., and Douglas, W. J. M., 1989, "Numerical Flow and Heat Transfer Under Impinging Jets: A Review," *Annual Review of Numerical Fluid Mechanics and Heat Transfer*, C. L. Tien, ed., Hemisphere Publishing Corp., Vol. 2, pp. 157–197.

Saad, N. R., Polat, S., and Douglas, W. J. M., 1992, "Confined Multiple Impinging Slot Jets Without Crossflow Effects," *International Journal of Heat and Fluid Flow*, Vol. 13, No. 1, pp. 2–14.

Viskanta, R., 1993, "Heat Transfer to Impinging Isothermal Gas and Flame Jets," *Experimental Thermal and Fluid Science*, Vol. 6, pp. 111–134.

Turbulent Heat Transfer Between a Series of Parallel Plates With Surface-Mounted Discrete Heat Sources

S. H. Kim[1]
Graduate Research Assistant.

N. K. Anand
Associate Professor.
Mem. ASME

Department of Mechanical Engineering,
Texas A&M University,
College Station, TX 77843

Two-dimensional turbulent heat transfer between a series of parallel plates with surface mounted discrete block heat sources was studied numerically. The computational domain was subjected to periodic conditions in the streamwise direction and repeated conditions in the cross-stream direction (Double Cyclic). The second source term was included in the energy equation to facilitate the correct prediction of a periodically fully developed temperature field. These channels resemble cooling passages in electronic equipment. The k–ϵ model was used for turbulent closure and calculations were made for a wide range of independent parameters (Re, K_s/K_f, s/w, d/w, and h/w). The governing equations were solved by using a finite volume technique. The numerical procedure and implementation of the k–ϵ model was validated by comparing numerical predictions with published experimental data (Wirtz and Chen, 1991; Sparrow et al., 1982) for a single channel with several surface mounted blocks. Computations were performed for a wide range of Reynolds numbers (5×10^4–4×10^5) and geometric parameters and for $Pr = 0.7$. Substrate conduction was found to reduce the block temperature by redistributing the heat flux and to reduce the overall thermal resistance of the module. It was also found that the increase in the Reynolds number decreased the thermal resistance. The study showed that the substrate conduction can be an important parameter in the design and analysis of cooling channels of electronic equipment. Finally, correlations for the friction factor (f) and average thermal resistance (R) in terms of independent parameters were developed.

Introduction

The continuing emphasis on miniaturization of electronic components and increasing power density has led to special considerations of thermal management in their design. Heat generated per unit volume of a device must be dissipated to the cooling fluid in order to maintain the operating temperature limit and its peak performance. Heat transfer analysis in such channels continues to play an important role in thermal control of electronic components. A number of thermal management strategies for electronic equipment are discussed by Nakayama (1987) and Incropera (1988). Forced convection is one of the common ways to cool channels with surface-mounted chips. Heat transfer analysis in channels between circuit boards is challenging because of the complex geometry, heating condition, and interaction between convection and conduction. A typical piece of electronic equipment consists of a stack of circuit boards containing surface-mounted heat-generating chips. The coolant is forced through the channel formed between two adjacent circuit boards to remove heat. Heat generated by the chips is removed in part by forced convection and the rest is conducted to the substrate/circuit board, which is eventually dissipated by forced convection in an adjacent channel or in the same channel. In this work, heat transfer in such channels is studied with the help of a simplified two-dimensional model, as shown in Fig. 1(*a*). Surface-mounted volumetric heat sources simulate an electronic package and the plates on which these heat sources are mounted will represent the circuit board/substrate. Plates are considered to be conducting so that the channels are thermally linked to each other. Since heat sources are considered to have the same strength and position in the streamwise direction, the thermal characteristics start from the developing flow at the channel inlet and eventually attain the condition of periodically fully developed flow (PDF) and heat transfer. The condition of periodically fully developed heat transfer is very important from the design point of view since heat transfer and friction in the PDF form the lower bound.

The objective of this work is to study numerically the periodically fully developed flow (PDF) and heat transfer between a series of parallel plates with surface-mounted heat sources. Consideration will be given to the turbulent flow and heat transfer with substrate conduction.

A small number of earlier investigations have employed a fairly simple model, consisting of a single parallel plate channel mounted with a series of blocks on one side, with either isothermal or isoflux heating conditions. Asako and Faghri (1991) numerically predicted turbulent flow in channels with three-dimensional blocks using the k–ϵ model, while Knight and Crawford (1988) studied two-dimensional heat transfer and fluid flow in channels with blocks. A low-Reynolds-number k–ϵ model was used to obtain closure of the turbulence model.

Experimental studies were carried out using a mass transfer technique by Sparrow et al. (1982). Heat transfer techniques were used by Lehmann and Wirtz (1985), Moffat et al. (1985), Sridhar et al. (1990), and Wirtz and Chen (1991) to study turbulent heat transfer with surface mounted blocks in a single channel. However, all of the previous results represented the thermal characteristics of such channels, where walls were

[1]Presently with the Department of Mechanical Engineering, Kei Myung University, Taegu, Korea.

Contributed by the Heat Transfer Division and presented at the ASME Winter Annual Meeting, Anaheim, California, November 8–13, 1992. Manuscript received by the Heat Transfer Division May 1993; revision received November 1993. Keywords: Conjugate Heat Transfer, Electronic Equipment, Numerical Methods. Associate Technical Editor: Y. Jaluria.

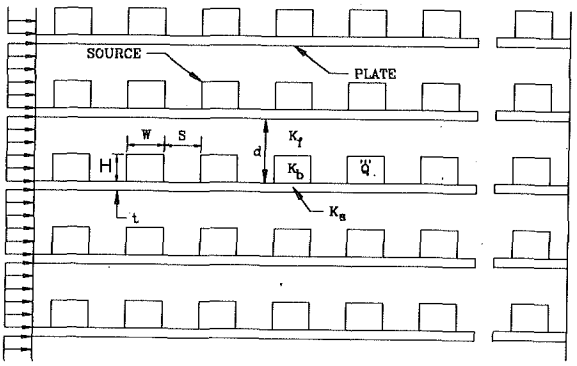

Fig. 1(*a*) Typical arrays of cooling channels in electronic equipment

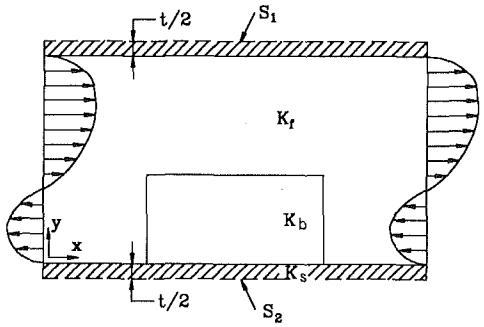

Fig. 1(*b*) Computational domain for PDF

Fig. 1 Two-dimensional model

heated by subjecting them to uniform wall temperatures or uniform heat flux conditions along the entire length of the channel or in part.

As pointed out by Incropera (1988), Sathe and Joshi (1990), and Peterson and Ortega (1990), conjugate effects play a very important role for the heat transfer analysis in electronic packaging. Several investigations have been reported in the literature highlighting conjugate effects in rectangular channels (Ramadhyani et al., 1985; Incropera et al., 1986; Davalath and Bayzitoglu, 1987; Sathe and Joshi, 1990; Nigen and Amon, 1991). Therefore, as stated earlier, the objective of this work is to study numerically periodically fully developed flow and heat transfer between a series of conducting parallel plates with surface-mounted volumetric heat sources. The model development, solution technique, experimental validation of the solution technique, and representative results will be discussed in the following sections.

Model Development

Consideration will be given to steady two-dimensional turbulent heat transfer in channels formed between adjacent plates (Fig. 1*a*). Thermophysical properties of the fluid and solid are assumed to remain constant. The plate thickness is assumed to be relatively thin compared to the channel width. Far from the channel entrance flow and heat transfer will be periodically fully developed (Patankar et al., 1977) because of periodic positioning of the blocks. Temperatures in the channel walls are not known *a priori* and must be determined as part of the solution. To solve for the temperature field proper boundary conditions should be imposed. In the interior of the stack, the temperature field within the channel and including the channel wall is subjected to a repeated condition (Kim et al., 1991). This implies that the temperature and heat flux at a given streamwise location on the channel walls are identical as long as these locations are separated by a distance equal to the sum of the channel width and the wall thickness ($d + t$). In this light a computational domain for PDF problems can be isolated as shown in Fig. 1(*b*). Thus the problem considered in

Nomenclature

C_1, C_2, C_μ, σ_k, σ_ϵ = turbulent modeling constants
c_p = specific heat
d = channel width (Fig. 1*a*)
E = integration constant
f = friction factor
h = heat transfer coefficient or block height
H = block height (Fig. 1*a*)
K = thermal conductivity
k = turbulent kinetic energy
l = module length = $w + s$
Nu = Nusselt number = $h\,(2d)/K_f$
p = effective pressure or p function
P_k = production of kinetic energy
Pr, Pr_t = laminar and turbulent Prandtl numbers
R = overall thermal resistance for block
R_t = dimensional thermal resistance
Re = Reynolds number = $\rho u_b\,(2d)/\mu$
Q''' = heat source per unit volume
q'' = heat flux
s = block spacing (Fig. 1*a*)
S = source term
S_1, S_2 = top and bottom surfaces of the computational domain (Fig. 1*b*)
T = temperature
t = substrate thickness (Fig. 1*a*)
u, v = velocities
U_f, U_s = fluid and solid conductance
u_p = velocity parallel to the wall
w = block width (Fig. 1*a*)
x, y = streamwise and cross-stream coordinates
y_p^+ = nondimensional distance measured from the wall = $y_p\,k_p^{1/2}\,C_\mu^{1/4}\,\rho/\mu$
z = distance along the block-fluid interface
β = global pressure drop per module
Γ = diffusion coefficient
η = normal to wall
θ = nondimensional temperature = $(T - T_b)/(Q'''\,wH/k_f)$
μ = dynamic viscosity
ρ = density
σ = global temperature rise per module
τ = shear stress
ϕ = general variable

Subscripts

b = block or bulk property
eff = effective
i = interface
s = substrate or solid
t = turbulent
w = wall

Superscripts

$\hat{}$ = periodic property
$\bar{}$ = average property

this study is subjected to "Double Cyclic Condition" and to the best of the author's knowledge this is the first attempt to study such a class of problems.

Surface-mounted blocks create a number of recirculation pockets and the recirculation pockets preclude the possibility of using a simple mixing length model as turbulence closure. Generally, a two-equation model (k–ϵ) is reported to perform well for two-dimensional recirculation flows.

Flow Field. Based on the foregoing discussion, the equation for a general variable (ϕ) transported by convection and diffusion in turbulent flow is given by:

$$\frac{\partial}{\partial x}(\rho u\phi)+\frac{\partial}{\partial y}(\rho v\phi)=\frac{\partial}{\partial x}\left(\Gamma_\phi\frac{\partial\phi}{\partial x}\right)+\frac{\partial}{\partial y}\left(\Gamma_\phi\frac{\partial\phi}{\partial y}\right)+S_\phi \quad (1)$$

In this equation, the general variable (ϕ) represents u, v, T, k, and ϵ. Γ_ϕ and S_ϕ represent appropriate transport coefficients and source terms.

Far from the entrance, the flow and the temperature field will be periodically fully developed. As explained by Patankar et al. (1977), the pressure p and T in a periodically fully developed flow can be divided into the global and local terms:

$$p(x, y)=-\beta x+\hat{p}(x, y) \quad (2)$$

$$T(x, y)=\sigma x+\hat{T}(x, y) \quad (3)$$

In these equations, β can be interpreted as a global pressure drop per module and σ as a global temperature rise per module. Therefore, $\hat{p}$ and $\hat{T}$ have periodic characteristics, which are repeated module to module. The global pressure drop and temperature rise per module can be represented as:

$$\beta=(p(x, y)-p(x+l, y))/l \quad (4)$$

$$\sigma=(T(x+l, y)-T(x, y))/l \quad (5)$$

It should be noted that Eqs. (3) and (5) are applicable only when heat addition per module is constant. Although Patankar et al. (1977) derived the equations for a constant heat flux case, this concept can be extended to a constant heat source per module since the resultant temperature rise per module would be constant as in a uniform heat flux case. An energy balance per module yields,

$$\sigma=(Q'''Hw)/(\rho u_b c_p dl) \quad (6)$$

where:

$$u_b=\frac{1}{d}\int_0^d u dy \quad (7)$$

Substituting these periodic quantities into the conservation equations, one is able to obtain a set of conservation equations in terms of the periodic variables of $\hat{p}$ and $\hat{T}$ with additional source terms (S_{pdf}). The source term (S_{pdf}), as a result of PDF, is also included in Table 1, which shows a particular variable of ϕ, S_ϕ and S_{pdf} for a periodic turbulent flow field. It should be noted that the last source term in the energy equation (Table 1) should be included when conducting solid blockages are present in the channels for a correct prediction of the temperature field (Kim and Anand, 1992). Moreover, Γ_{eff} is not expected to be a constant inside the flow field in the turbulent flow. Accordingly, this source term was retained in this work.

Thermal Field in the Solid. It should be noted that the energy equation in Table 1 is applicable to the fluid region. The energy equation in the solid region in terms of periodic quantities can be written as

$$\frac{\partial}{\partial x}\left(K\frac{\partial\hat{T}}{\partial x}\right)+\frac{\partial}{\partial y}\left(K\frac{\partial\hat{T}}{\partial y}\right)+Q'''\delta=0 \quad (8)$$

where δ equals unity inside the block sources and zero in other parts. However, it is our intention to use one general form of the energy equation to obtain the temperature distribution in both solid and fluid regions. With the convective terms being absent in the energy equation for the solid with a proper heat flux continuity at the interface, the energy equation, Eq. (8), can have a general form of conservation equation, Eq. (1), with the following modifications:

$$\Gamma=(\mu/\text{Pr})(K/K_f) \text{ and } S_\phi=Q'''/c_p \text{ and } S_{pdf}=0 \quad (9)$$

In this equation, K/K_f represents the thermal conductivity ratio of either the block (K_b/K_f) or the substrate (K_s/K_f) to the fluid. In addition, S_ϕ is Q'''/c_p in the block and zero in the substrate. Note that heat generation in the block is assumed to be uniform. The thermal contact resistance between heat-generating components and the substrate might exist. However, in this study it is neglected.

Table 1 General variables and corresponding diffusion coefficients and sources

ϕ	Γ	S_ϕ	S_{pdf}
1	0	0	0
u	μ_{eff}	$-\partial\hat{p}/\partial x+S_u$	β
v	μ_{eff}	$-\partial\hat{p}/\partial y+S_v$	0
T	$\mu/Pr+\mu_t/Pr_t$	0	$-\rho u\sigma+\partial(\Gamma_{\text{eff}}\sigma)/\partial x$
K	$\mu+\mu_t/\sigma_k$	$P_k-\rho\varepsilon$	0
ε	$\mu+\mu_t/\sigma_\epsilon$	$(C_1P_k\varepsilon-C_2\rho\epsilon^2)/k$	0

Constants:
$C_1=1.44$, $C_2=1.92$, $C_\mu=0.09$, $\sigma_k=1.0$, $\sigma_\epsilon=1.22$, and $Pr_t=0.9$

where:

$$\mu_{\text{eff}}=\mu+\mu_t$$

$$\mu_t=C_\mu\rho k^2/\epsilon$$

$$S_u=\frac{\partial}{\partial x}\left(\mu_{\text{eff}}\frac{\partial u}{\partial x}\right)+\frac{\partial}{\partial y}\left(\mu_{\text{eff}}\frac{\partial v}{\partial x}\right)$$

$$S_v=\frac{\partial}{\partial x}\left(\mu_{\text{eff}}\frac{\partial u}{\partial y}\right)+\frac{\partial}{\partial y}\left(\mu_{\text{eff}}\frac{\partial v}{\partial y}\right)$$

$$P_k=\mu_t\left[2\left\{\left(\frac{\partial u}{\partial x}\right)^2+\left(\frac{\partial v}{\partial y}\right)^2\right\}\right]+\mu_t\left(\frac{\partial u}{\partial y}+\frac{\partial v}{\partial x}\right)^2$$

Boundary Conditions. Based on these discussions, periodic conditions for all unknowns in the streamwise direction can be stated as

$$\hat{\phi}(0, y)=\hat{\phi}(l, y) \quad (10)$$

For completion of the problem formulation, the wall function method is employed near the wall. Since a finite volume method is used, the boundary condition should be specified in terms of wall fluxes between the wall and the adjacent grid point (denoted by subscript p). For the velocities parallel to the wall, wall shear stress is calculated from the universal velocity profile and equilibrium condition,

$$\tau_w=\rho\kappa C_\mu^{1/4}k_p^{1/2}u_p/\ln(Ey^+) \text{ for } y_p^+>11.5 \quad (11a)$$

$$\tau_w=\mu u_p/y_p \text{ for } y_p^+<11.5 \quad (11b)$$

All flux variables (u, v, p, and k) normal to the wall are set to zero. The equilibrium assumption is also applied to approximate the turbulent kinetic energy near the wall. The production and dissipation of kinetic energy is calculated from

$$P_k\simeq\tau_w\frac{\partial u}{\partial y}=\frac{\tau_w^2}{\rho y_p k_p^{1/2}C_\mu^{1/4}\kappa} \text{ and } \bar{\epsilon}=C_\mu^{3/4}\frac{k_p^{3/2}}{\kappa y_p} \quad (12)$$

It should be noted that the dissipation rate of ϵ in the ϵ equation is also employed to prescribe the value near the wall control volume (dissipation term in Eq. (12)). Generally, the wall function described above is based on the equilibrium as-

sumption near the wall. Therefore, the current wall treatment may have some deficiency because the equilibrium condition is no longer valid for the recirculation flow. However, as discussed later, the predicted values of the average heat transfer coefficient and fluid friction factor using this approach compare very well with the published experimental data.

Interface Condition. Unlike the flow field, the temperature field in the fluid is coupled with the temperature in the solid region and a special treatment is needed at the solid and fluid interface. The wall function for the energy equation and the harmonic mean method were employed to calculate the diffusion coefficient near the wall control volume. The wall temperature can be obtained from

$$T_p^+ = \frac{(T_w - T_p)\rho c_p C_\mu^{1/4} k_p^{1/2}}{q_w''} = \mathrm{Pr}_t \left(\frac{1}{\kappa} \ln (E y_p^+) + P \right) \quad (13)$$

where the empirical P function of Jayetilleke (1969) is given by

$$P = 9.24 \left[\left(\frac{\mathrm{Pr}}{\mathrm{Pr}_t} \right)^{3/4} - 1 \right] \left[1 + 0.28 \exp \left(-0.007 \frac{\mathrm{Pr}}{\mathrm{Pr}_t} \right) \right] \quad (14)$$

The relation between the heat flux and temperature at the wall surface is given as

$$q_w'' = U_f (T_w - T_p) = U_s (T_s - T_w) \quad (15)$$

where U_f is the conductance in the fluid between the wall and the position P while U_s is the conductance in the solid. Therefore, conductances of fluid and solid can be rearranged as follows:

$$U_f = \frac{\rho C_p C_\mu^{1/4} k_p^{1/2}}{\mathrm{Pr}_t \left(\frac{1}{\kappa} \ln (E y_p^+) + P \right)} \text{ if } y^+ > 11.5$$

$$\text{and } U_f = \frac{\rho C_p \mu}{\mathrm{Pr}\, y_p} \text{ if } y^+ < 11.5 \quad (16a)$$

and

$$U_s = \frac{K_s}{y_s} \quad (16b)$$

The diffusion coefficient at the interface is given by

$$\Gamma_i = \frac{1}{C_p} \left(\frac{U_s U_f}{U_s + U_f} \right) \quad (17)$$

The value of the diffusion coefficient (Γ) depends on y^+. Due to the coupled nature of the heat transfer problem the temperature of the solid is also a function of y^+. In some parts of the block the distance (y^+) of the near-wall point (p) could be less than 11.5 and in some parts y^+ could be greater than 11.5. This will result in a physically unrealistic temperature distribution within the solid, since heat generated per block is considered to be constant. To avoid this problem the Reynolds number for this study was chosen so the distance (y^+) of the near wall point p was always greater than 11.5.

Attention is now given to the temperature boundary conditions in the cross-stream direction. To simulate the circuit board arrangement, a series of plates are stacked parallel to one another. Temperature distribution in these plates is not known *a priori* and must be determined as a part of the solution procedure. If there are multiple channels somewhere in the interior of this stack, the thermally "repeated condition" could be established (Kim et al., 1991). The implication of the repeated boundary condition in the cross-stream direction is that the temperature and heat flux at any point on the surface S_1 will be the same as on the corresponding point on the surface S_2. It should be noted that the location of the S_1 surface is arbitrary. However, once S_1 is fixed, S_2 has to be fixed along a corresponding cross-stream location in the adjacent channel. For convenience, a channel with a wall formed by half the thickness of two adjacent plates (i.e., bottom half of the upper plate and top half of the lower plate) is considered. The repeated condition can be mathematically stated as

$$T(x, -t/2) = T(x, d + t/2) \quad (18a)$$

$$\left(\frac{\partial T}{\partial y} \right)_{(x, -t/2)} = \left(\frac{\partial T}{\partial y} \right)_{(x, d + t/2)} \quad (18b)$$

Solution Technique

The set of governing equations with the associated boundary conditions was solved by using a finite volume technique. Velocity and pressure variables were stored at the staggered locations and were coupled by the SIMPLER algorithm (Patankar, 1980). Convection and diffusion terms were linked by the method suggested by Amano (1984). This method is a combination of hybrid and exponential schemes. In the flow field, wall diffusion flux was calculated using Eq. (11). These flux terms are manifested as source terms in x and y momentum equations. To facilitate this prescription, the coefficients linking the variable (ϕ) at the node adjacent to the wall was set to zero. The solid and fluid regions were assigned appropriate thermal conductivity values; however, the interface diffusion coefficient was represented by the harmonic mean of the solid and fluid thermal conductances (Eq. (17)). A set of discretization equations for each variable was solved by the line-by-line procedure, which is the combination of the Tri-Diagonal Matrix Algorithm (TDMA) and the Gauss–Seidel technique. Due to the periodic conditions in the streamwise direction, the Cyclic Tri-Diagonal Matrix Algorithm (CTDMA) was used to sweep in the streamwise direction to calculate the flow field. On the other hand, CTDMA was used to sweep in both the cross-stream and the streamwise directions to calculate the temperature field. Since the pressure gradient (β) and the flow Reynolds number (Re) have a one-to-one relation, calculations for required Re values were made as follows: an initial guess for β was made and the corresponding Re was calculated. This procedure was repeated with a modified value of β until the required value of Re was achieved. Convergence was declared when relative values of each of the variables (u, v, k, ϵ, and T) ceased to vary by more than 10^{-5} between two successive iterations.

Grid-Independent Solution. Grid independence was established by examining the cross-stream velocity and temperature distributions at the middle of the cavity with periodically fully developed flow and heat transfer. Henceforth, the phrase "cavity" will be used to describe the space between two adjacent block heat sources. For the purpose of the grid independence study, the Re was chosen to be 10^5. Three different uniformly spaced grid sizes (24 × 24, 38 × 38, and 42 × 42) were used. In addition, an expansion factor of 1.1 far from the wall and a contraction coefficient of 0.95 toward the wall was used, so that a finer grid spacing was formed near the wall. The velocity and temperature distributions for various grid sizes are shown in Fig. 2. Grid independence was declared when maximum changes in velocity and temperature distributions were less than 3 percent. Accordingly, for a range of geometric parameters examined in this study 30, 34, and 36 grid lines were used in the x direction and 26, 32, and 40 grid lines were used in the y direction. Shear stress and Nusselt number distributions along the bottom wall of the PDF module were also examined for grid independence (shown in Kim, 1993) and these two variables did satisfy the same 3 percent criterion.

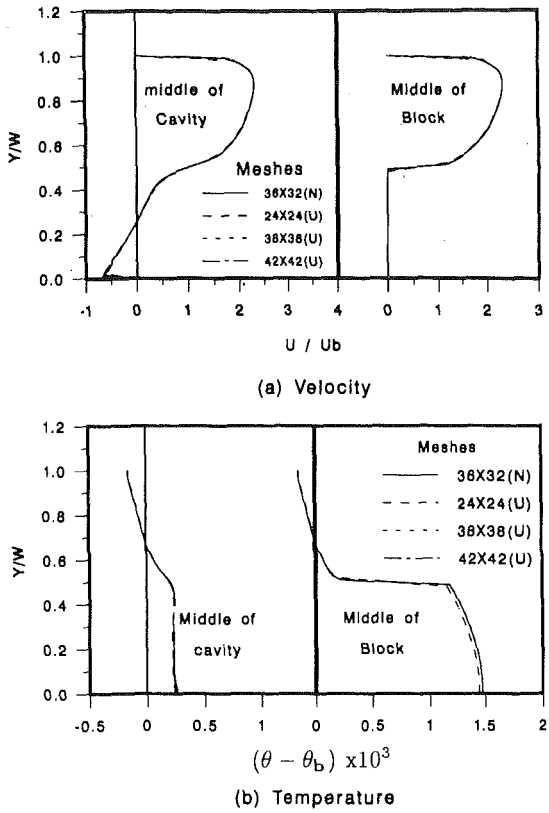

Fig. 2 Effect of grid size on velocity and temperature distributions: s/w = 1, d/w = 1, h/w = 5, Re = 1 × 10^5

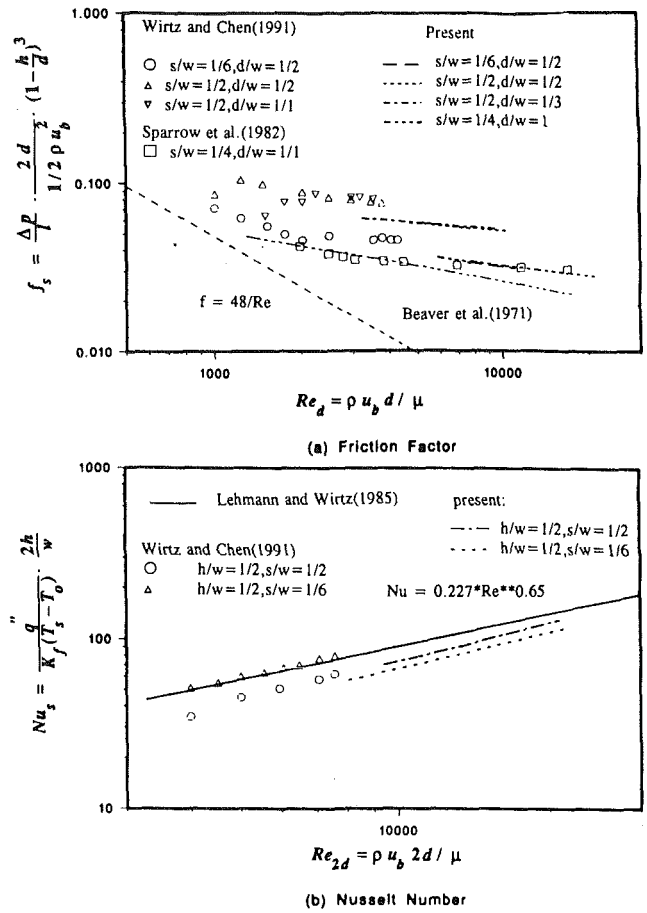

Fig. 3 Comparison of prediction with the experimental data for fully developed flow in parallel plate channel with surface-mounted blocks

Validation of the Solution Technique

The solution technique for the turbulent periodically fully developed flow along with the numerical implementation of the k-ϵ model was validated by comparing predictions with the experimental data for the flow and heat transfer between the parallel plates (Kim, 1993). However, the focus of this work is the periodically fully developed heat transfer in channels formed between a series of parallel plates with surface-mounted discrete heat sources. Absence of experimental data for the temperature field in the present geometry prevents a direct comparison. Therefore, the solution technique was also validated by comparing numerical predictions with the experimental data for fully developed flow and heat transfer in channels formed between two parallel plates with surface-mounted blocks in Fig. 3. In Fig. 3(a), the numerically predicted friction factor is compared with the experimental data of Wirtz and Chen (1991) and Sparrow et al. (1982). The data of Wirtz and Chen (1991) are for the parallel-plate channel with two-dimensional flow and that of Sparrow et al. (1982) is for three-dimensional flow. Also, Fig. 3(a) shows the experimentally measured friction factor for smooth parallel plate channels (Beavers et al., 1971) without blocks. It is evident from Fig. 3(a) that the predicted friction factor values are in good agreement with the experimental data. The maximum difference between the predicted and experimental data not considering the experimental uncertainty is 30 percent and the numerical model underpredicts the experimental data for the friction factor. Figure 3(b) shows the comparison of the numerically predicted and experimentally determined Nusselt number distribution for the same geometry discussed in Fig. 3(a). Wirtz and Chen (1991), in their heat transfer experiments, considered thirteen blocks of which only one was heated at the top surface during each experiment. Hence, our numerical predictions were made for hydrodynamically fully developed, but thermally developing flow (Graetz problem), for the purpose of comparison. Again, the numerical predictions underpredict the experimental data and the maximum difference not considering the experimental uncertainty is 15 percent. This degree of agreement between the model prediction and the experimental data is considered good for turbulent flow and heat transfer. It should be noted that the qualitative trends of model predictions are in very good agreement with the experimental data.

Results and Discussion

In this section governing independent parameters are identified and representative results for velocity and temperature fields are discussed. Finally, thermal performance of these cooling channels is discussed in terms of Nusselt number and thermal resistance.

Independent Parameters. A careful examination of the governing equations reveals that the independent parameters are Reynolds number (Re) based on hydraulic diameter of the channel ($2d$), Prandtl number (Pr), thermal conductivity ratio (K_b/K_f and K_s/K_f), and geometric parameters. The independent geometric parameters are the ratio of the block height to block width (H/w), the ratio of the block spacing to block width (s/w), the ratio of channel height to the block width (d/w), and the ratio of the substrate thickness to block width (t/w). A range of thermophysical parameters was chosen such that they corresponded to the ones used in actual practice. Typically, a fluid such as air (K_f = 0.025 W/m°C, Pr = 0.7) is used. A typical substrate is made up of a combination of epoxy-glass, copper, or ceramic laminate with an effective

Table 2 Parametric ranges in present study

Parameters	Range
Re	5×10^4-4×10^5
Pr	0.7
k_b/k_f	500
k_s/k_f	0.1, 1, 10, 20, 50, 100
s/w	0.5, 0.75, 1
h/w	0.25, 0.5
d/w	0.5, 1, 1.5
t/w	0.1

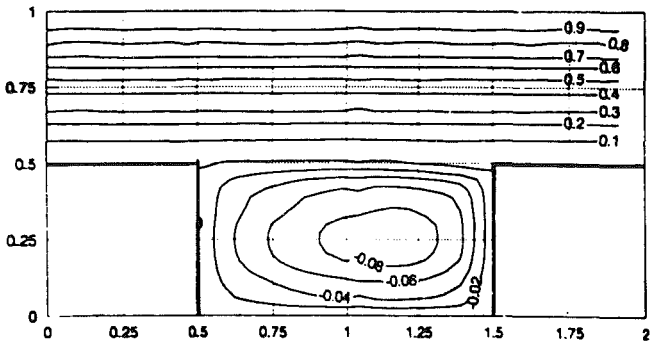

(a) Streamline

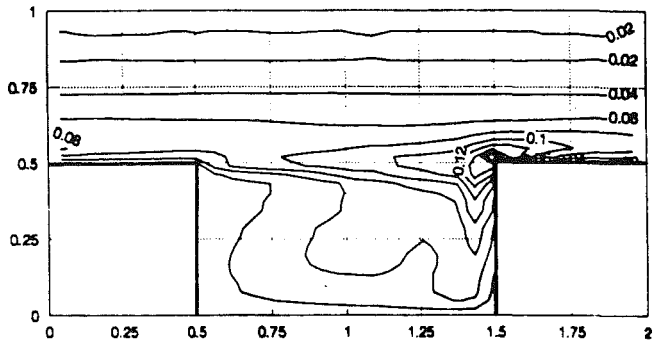

(b) Turbulent Kinetic Energy

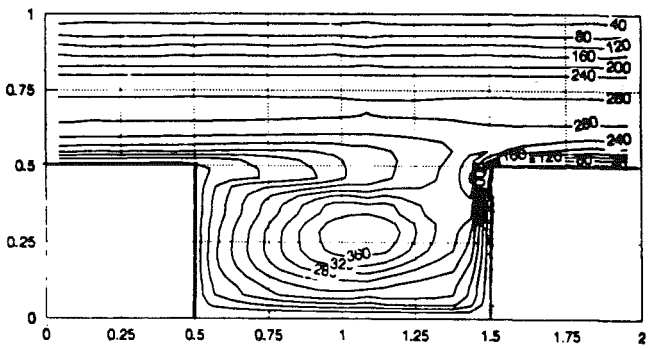

(c) Ratio of μ_t to μ

Fig. 4 Contours of isolines for flow field: Re = 1 × 10^5, l/w = 2, d/w = 1, h/w = 0.5, and s/w = 1

thermal conductivity of 0.2–0.6 W/m°C (Sathe and Joshi, 1990; Incropera et al., 1986). Electronic packages have a wide range of conductivity due to the varying amounts of different material components and this conductivity is generally higher compared to that of air. However, in order to focus on the

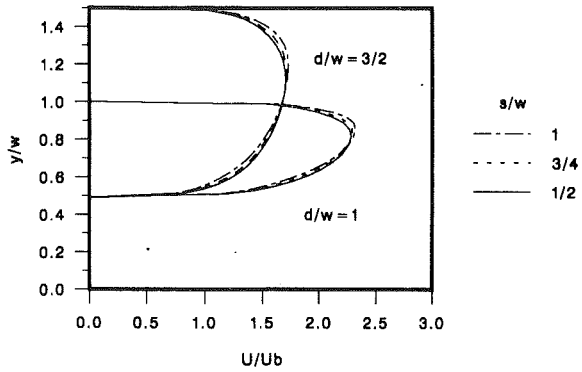

Fig. 5(*a*) Velocity distributions at the middle of block

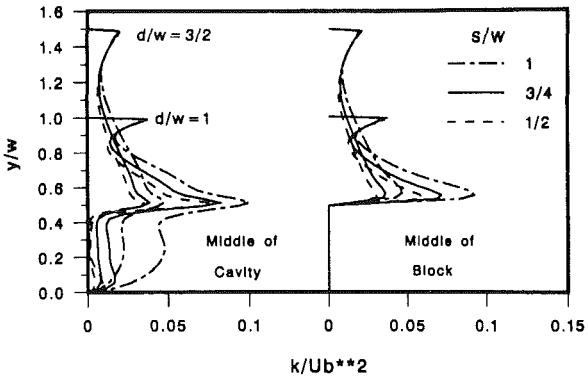

Fig. 5(*b*) Turbulent kinetic energy distributions at the middle of cavity and block

Fig. 5 Flow field: Re = 1 × 10^5, h/w = 0.5

substrate effect, the conductivity ratio of block to air is set to 500 in this study. Based on the aforementioned discussion, the range of independent parameters were chosen and are presented in Table 2.

Representative flow field results are shown in Fig. 4. For the purpose of clarity, the computational module was chosen such that it included a rear half and a front half of two adjacent blocks in the periodically fully developed region. The rear half of the block represents the downstream part and the front half represents the upstream part of a single block, respectively. Figure 4(*a*) shows the streamline distribution. As shown, the flow can be divided into the main bypass flow over the blocks and recirculation flow between the blocks. As expected, the streamline strength of the cavity is comparably lower than that of the main flow. The same flow pattern was found for other geometric parameters. The strength of the recirculation flow increases as does the Reynolds number, the block spacing, and the block height. Also, the recirculation strength increases as the channel height decreases. Figures 4(*b*) and 4(*c*) show the isolines for nondimensional kinetic energy (k/u_b^2) and the ratio of the turbulent viscosity to the dynamic viscosity (μ_t/μ), respectively. The hydrodynamic and thermal boundaries are periodically interrupted on the top surface of the blocks so that free shear flow and shear flow are repeated. This results in a higher value of k along the line coinciding with the top of the block. The maximum value of k occurs near the top upstream corner of the block. The higher value of effective k near the top of the block shifts the maximum point of the streamwise velocity profile toward the top surface in order to maintain momentum conservation. Figure 4(*b*) shows well the transport of k downstream and into the cavity. It should be reiterated that not only turbulent kinetic energy but also the dissipation energy maintains the maximum values at the front top corner

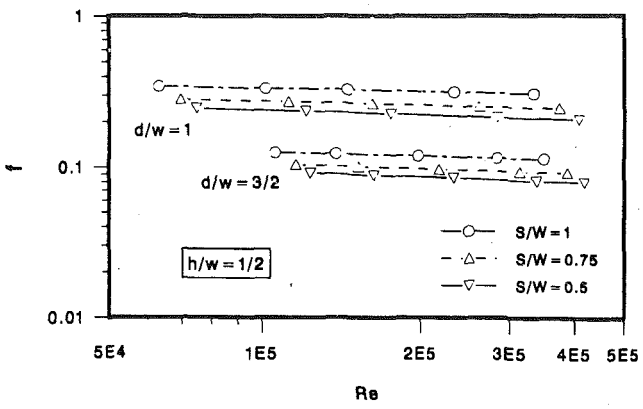

(a) Tall Block

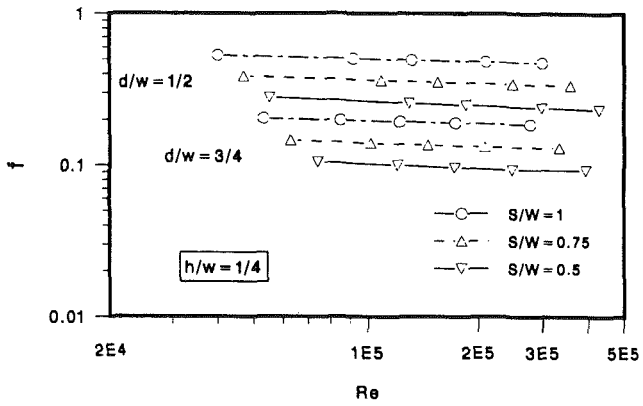

(b) Flat Block

Fig. 6 Friction factor as a function of Reynolds number and geometric parameters

and the line co-incident with the block surface. This is why the contours are shown with a family of sharp convex curves downstream of the rear top corner of the block. As a result the location of the maximum (μ_t/μ) moves into the cavity (Fig. 4*c*). As Reynolds number increases the turbulent viscosity also increases. The distributions of (μ_t/μ) are very important to understand the thermal field since (μ_t/μ) directly affects the eddy thermal diffusivity.

Figure 5 shows the parametric effects on the flow field for tall blocks ($h/w = 1/2$). Figure 5(*a*) shows the velocity distribution at the middle of the block for Re = 10^5. Calculations were made for both tall ($h/w = 1/2$) and flat ($h/w = 1/4$) blocks (Kim, 1993), but only the case of a tall block is considered for the purpose of discussion in this paper. It is clear that the velocity profile is shifted to the top wall more in a narrow channel and the effect of block spacing (s/w) on velocity distribution is more pronounced in a narrow channel than in a wider channel. This is due to the fact that the value of k is higher in narrow channels ($d/w = 1$) than in wider channels ($d/w = 3/2$) and higher in larger block spacings than in small block spacings (refer to Fig. 5*b*). Figure 5(*b*) shows the nondimensional kinetic energy distribution (k/u_b^2) for narrow and wider channels. Each profile shows a maximum in the k value at the top surface of the block while the value of k at the top wall remains nearly constant. This maximum value of k increases with increase in channel width and has a larger value in a narrow channel than in a wider channel. There is a qualitative agreement of the k distribution with experimental measurements obtained within the cavity (Garimella and Eibeck, 1990) and over the block (Wirtz and Chen, 1991). Similar trends were observed for the case of flat blocks.

Figure 6 shows the variation of the turbulent friction factor with the Reynolds number for different geometric parameters. The friction factor in this study is defined in Eq. (19):

$$f=\frac{\Delta p}{l}\frac{2d}{\rho u_b^2/2}=\frac{\beta(2d)}{\rho u_b^2/2} \tag{19}$$

In general the friction factor for a smaller channel width and larger block spacing is higher for the entire range of Reynolds number considered in this study. The effect of block spacing is more pronounced for channels with flat blocks. The same trend for the effect of block spacing was observed by Wirtz and Chen (1991) from their experimental results. For a given area of the main bypass flow ($(d - h)/w$), it can be seen that the friction factors of the channels with flat blocks are smaller since the effective turbulent kinetic energy in these channels are smaller. For all of the different geometries examined, as a part of this study, the friction factors are nearly constant or decrease slightly in the entire range of Reynolds number. Since channels with blocks can be regarded as a roughened channel, the present results are consistent with the fact that the friction factors are independent of Reynolds number for fully developed turbulent flow.

Temperature Field. For the purpose of studying the temperature field, a PDF module was chosen such that it includes one complete block and a half cavity on either side of the block. In this study the nondimensional temperature (θ) is defined as

$$\theta=(T-T_b)/Q'''wH/K_f \tag{20}$$

In this equation, the bulk temperature (T_b) is calculated at the inlet of the PDF module and is given by

$$T_b=\frac{\int_0^d |u|Tdy}{\int_0^d |u|dy} \tag{21}$$

Here, θ represents the nondimensional temperature difference between local absolute temperature and the bulk temperature. Physically this represents the temperature rise due to self heating without the effect of temperature rise induced by upstream modules. Therefore, it can be positive or negative.

Figure 7 shows representative nondimensional isotherms with different substrate conductivities. Figures 7(*a*) and 7(*b*) represent the adiabatic case ($K_s/K_f = 0$) and highly conducting substrate ($K_s/K_f = 100$), respectively. When the substrate is adiabatic the maximum temperature occurs at the downstream bottom corner of the block. As the value of K_s/K_f increases, a part of the heat from the block is transferred by conduction and eventually to the neighboring channel. Thus, the maximum temperature decreases within the block and its location also shifts toward the top surface of the block. As expected, the temperature gradient is mostly large near the block surface for both cases. Another large temperature gradient occurs at the top wall for the conducting substrate. It should be recalled that the top and bottom surfaces (S_1 and S_2) are subjected to the repeated boundary condition. Figure 7(*a*) shows that there is no heat flow from the block to the adjacent channel via substrate (zero gradient). For this reason, there is no cluster of isotherms near the top wall. At high values of substrate conductivity $K_s/K_f = 100$ the isotherms inside the substrate are arranged vertically. This represents that the energy from the bottom of the block is spreading well so that not only transverse conduction but also the axial conduction is increased. In general, temperatures over the block decreased with increases in Reynolds number and substrate conductivity. Also, at the high values of substrate conductivity a significant portion of the heat from the block is transported to the adjacent chan-

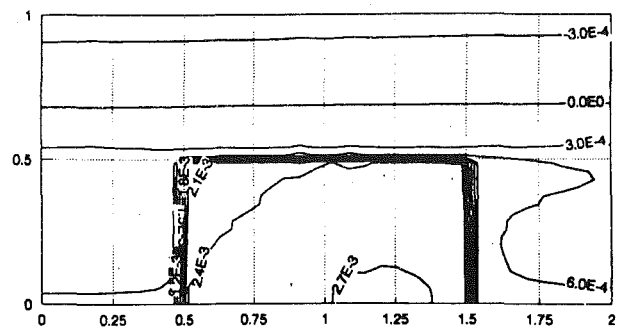

(a) $K_s/K_f=0$

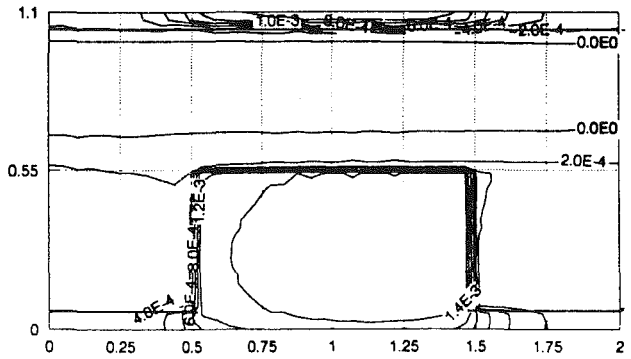

(b) $K_s/K_f=100$

Fig. 7 Nondimensional isotherms for different substrate conductivities: Re = 1 × 10^5, *s/w* = 1, *d/w* = 1, *h/w* = 0.5, *t/w* = 0.1

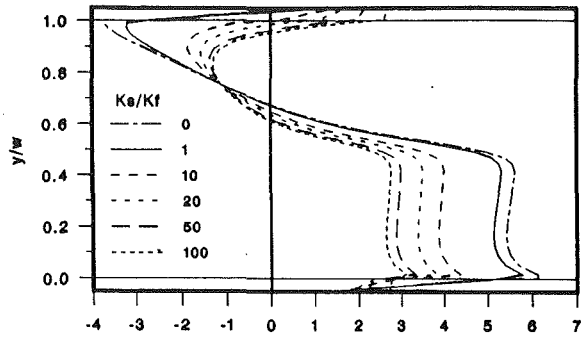

(a) Middle of Cavity

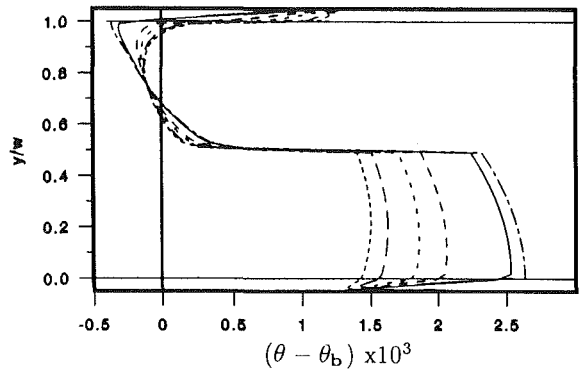

(b) Middle of Block

Fig. 8 Nondimensional temperature distributions in the transverse direction for different substrate conductivities: Re = 1 × 10^5, *s/w* = 1, *d/w* = 1, *h/w* = 0.5, *t/w* = 0.1

nel via the substrate conduction. This is reflected as densely packed isotherms near the top wall in Fig. 7(*b*). This can be shown more obviously in Fig. 8, which shows the effect of substrate conduction on temperature distribution in the middle of the cavity and in the middle of the block. As a consequence, the repeated condition temperatures at S_1 and S_2 surfaces for the given streamwise location are exactly same. The temperature inside the block is the maximum for the case of adiabatic substrate and the temperature inside the block monotonically decreases with an increase in substrate conductivity. Due to the repeated condition on S_1 and S_2, the temperature at the top wall increases with an increase in substrate conductivity. It is important to examine the temperature rise at the top wall and the temperature drop in the cavity and inside the block. The block benefits the most by lowering its maximum temperature.

From Figs. 5 and 8 it is clear that the location of the maximum velocity ($\partial u/\partial y = 0$) is not the location of the zero temperature gradient ($\partial\theta/\partial y = 0$). In this light, the simulation of the repeated boundary condition by Davalath and Bayazitoglu (1987) is only applicable to high Peclet number laminar flows. However, the procedure adapted in this study is universal for simulating the repeated boundary condition (Kim et al., 1991). Details of the local temperature and solid-fluid interface heat flux distributions can be found elsewhere (Kim, 1993).

Nusselt Number for Block Surface. The local Nusselt number (Nu_b) for the block surface exposed to the fluid is defined as

$$Nu_b = hw/K_f = \frac{1}{(\theta_w - \theta_b)} \frac{\partial\theta}{\partial n} \tag{22}$$

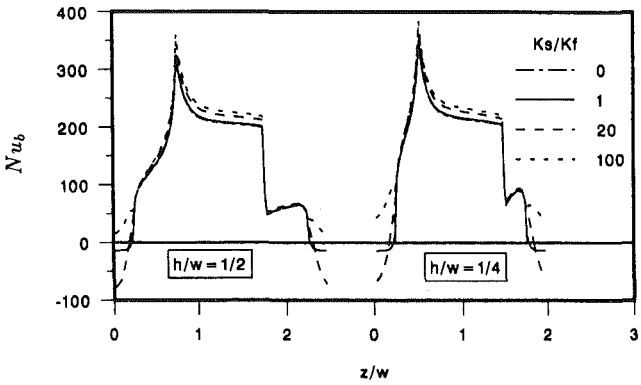

Fig. 9 Local Nusselt number distribution over the block

Figure 9 shows the typical distributions of local Nusselt numbers along the block surface for different substrate conductivities for tall and flat blocks. Generally, the local Nusselt number has a distribution similar to that of the heat flux. Nusselt number is maximum at the top upstream corner of the block and decreases along the downstream and rear and front surfaces. It should be reiterated that the temperature distribution along the block surface is nearly constant. As shown in Fig. 9, an increase in the substrate conduction results in a slight increase in the Nusselt number. This slight increase in Nu_b was found for other block spacings and all other geometric parameters studied here. Substrate conduction decreases both the heat flux and the surface temperature. However, the ratio of the heat flux to the temperature increases with an increase in the substrate conduction, thus resulting in an increase in

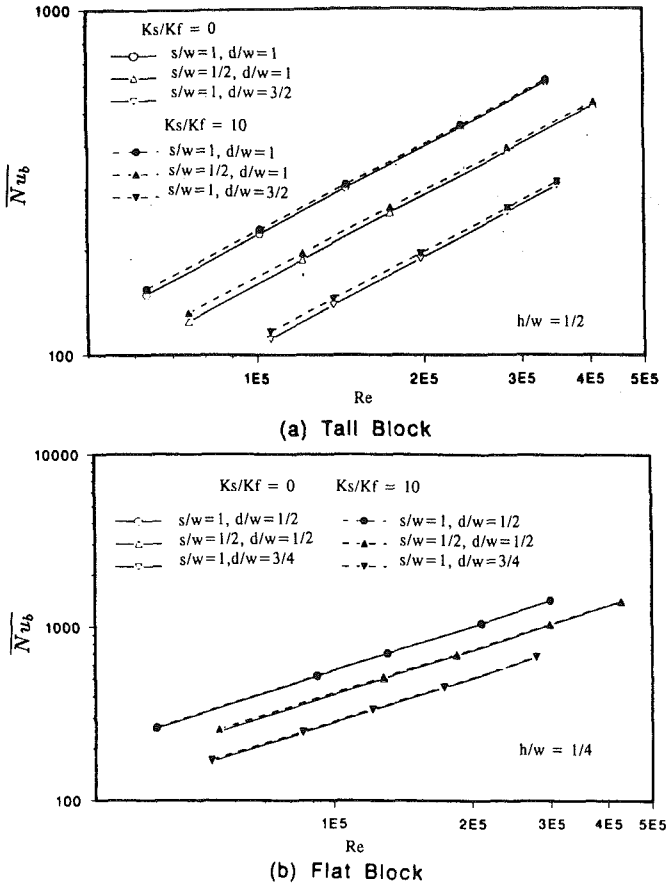

Fig. 10 Distribution of average Nusselt number for different Reynolds numbers and geometric parameters

Nu_b. This is quite contrary to the results of Ramadhyani et al. (1985) and Incropera et al. (1986). In their conjugate heat transfer studies small isothermal heat sources with a large substrate were considered both in laminar and in turbulent flows. Results showed substrate conduction decreased the Nusselt number over the source. Since isothermal heat sources were considered, substrate conduction reduced the heat flux to the fluid from the source while the temperature remained the same, which resulted in a decrease in the local Nusselt number. However, this study shows substrate conduction reduces not only the heat flux to the fluid from the source, but also the temperature of the block source so that the Nusselt number increases with an increase in the substrate conduction.

Overall Thermal Performance. Based on the local Nusselt number, the average Nusselt number for the block ($\overline{Nu_b}$) is defined as

$$\overline{Nu_b} = \frac{1}{1+\frac{2h}{w}} \int_0^{1+\frac{2h}{w}} Nu_b d\left(\frac{z}{w}\right) \tag{23}$$

Figures 10(*a*) and 10(*b*) show average Nusselt numbers for different K_s/K_f, s/w, and d/w values as a function of Re for tall block and flat blocks, respectively. The average Nusselt number generally increases with an increase in Re and block spacing, and with a decrease in the channel width (d/w). The linear increase of an average Nusselt number (on a log-log scale) with respect to Re, and the strong dependency on the channel width was also found in the experiments of Garimella and Eibeck (1990). In this investigation the average Nusselt number was found to be proportional to $Re^{0.82}$. Anderson and Moffat (1990) experimentally showed that the average Nusselt number is proportional to $Re^{0.8}$. Wirtz and Chen (1991) experimentally showed that the average Nusselt number is proportional to $Re^{0.65}$ as a lower bound. Thus our numerical predictions are consistent with the experimental results of other investigators. Substrate conduction increases the average Nusselt number slightly and the effect remains almost the same in the whole Re range. This behavior exists in the range of geometric parameters examined.

The impact of substrate conduction is less for flat blocks compared to that of tall blocks. As seen in the average Nusselt number distribution, however, it is only an indicator of the thermal performance of the block, which is exposed to the fluid. Considering the fact that the module has multiple paths for convective, conductive, and/or cooling modes, thermal performance in an electronic cooling area is often specified in terms of its overall resistance. Thermal resistance per unit length (thermal resistance) in this study is defined as the temperature difference between maximum temperature inside the block and the bulk temperature. It should be noted that the resistance of the convective cooling is the reciprocal of the Nusselt number. Nondimensional overall thermal resistance is given by

$$R = R_t K_f = (\theta_{\max} - \theta_b) \tag{24}$$

where R_t is the dimensional resistance and is defined as $R_t = (T_{\max} - T_b)/Q''' wH$.

Figure 11 shows the overall thermal resistance variation with Re and K_s/K_f for tall and flat blocks. It is shown that the thermal resistance decreases with increase in Reynolds number and the substrate conductivity. A larger block spacing and smaller channel height contribute in reducing the thermal resistance. Most of the decrease in thermal resistance occurs in the conductivity range of 0 to 20; however, it continues to decrease when substrate conductivity increases further. The same trend can be found for the effect of Reynolds number such that the thermal resistance decreases quite linearly as the Reynolds number increases. The impact of Reynolds number is more pronounced for lower substrate conductivity while the impact of substrate conduction is more pronounced for lower Reynolds numbers. The increase in Reynolds number and the substrate conductivity continues to contribute to the decrease in thermal resistance in turbulent flow. Between the two ways to reduce thermal resistance, it might be better to increase the substrate conductivity while holding Re constant since there is no additional pressure drop penalty. It should be recalled that this conclusion is based on the simplifying assumption that the thermal contact resistance between heat-generating components and the substrate is neglected. Although consideration of thermal contact resistance would reduce the quantity of substrate conduction, it will not mitigate the importance of substrate conduction.

Correlations for Friction Factor and Overall Thermal Resistance. The least-square method was used to develop correlations for the friction factor (f) and the overall thermal resistance (R) using the numerically established data. The correlations for thermal resistance are presented in two different equations in order to emphasize the effect of substrate conduction. The correlations for average Nusselt number over the block surface are presented in terms of the same parameters in Kim (1993).

The correlation equations for f and R are as follows:

$$f = 0.042\ \mathrm{Re}^{-0.085}\left(1-\frac{h}{d}\right)^{-2.75}\left(1+\frac{s}{w}\right)^{1.73}\left(\frac{d}{w}\right)^{-0.416} \tag{25}$$

For $K_s/K_f = 0$,

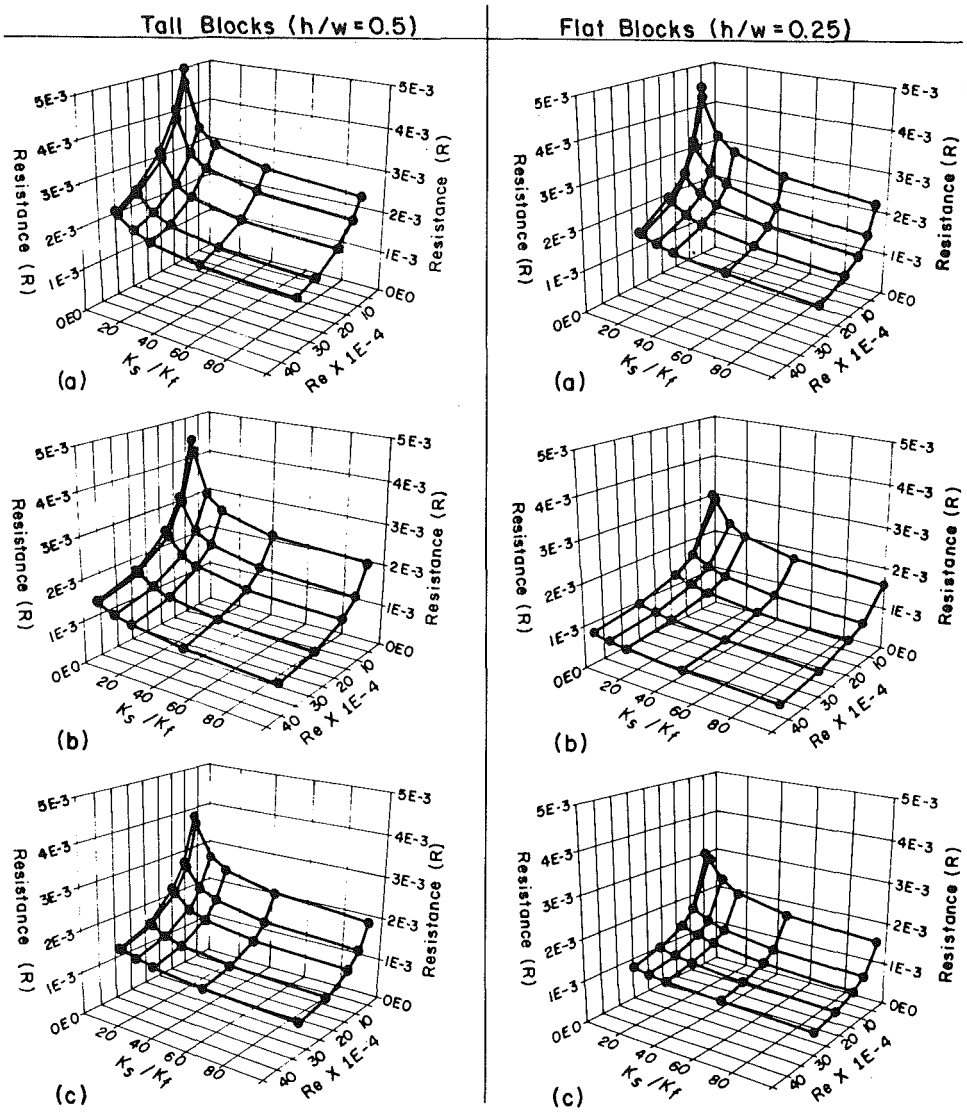

Fig. 11 Variation of overall thermal resistance of a turbulent PDF module with respect to Reynolds number and substrate conductivity: (*a*) *h/d* = 1/3, *s/w* = 1, (*b*) *h/d* = 1/2, *s/w* = 0.5, (*c*) *h/d* = 1/2, *s/w* = 1

$$R = 30.915\ (\mathrm{Re})^{-0.701}\left(1-\frac{h}{d}\right)^{0.916}\left(1+\frac{s}{w}\right)^{-0.879}(d/w)^{0.814} \tag{26}$$

For $K_s/K_f \neq 0$,

$$R = 26.136\ (\mathrm{Re})^{-0.633}\left(1-\frac{h}{d}\right)^{-1.183}\left(1+\frac{s}{w}\right)^{-0.708} \times (d/w)^{2.167}\left(\frac{t}{h}\right)^{1.44}\left(\frac{K_s}{K_f}\right)^{-0.083} \tag{27}$$

Coefficients of determination for friction factor, thermal resistance for $K_s/K_f = 0$, and $K_s/K_f \neq 0$ are 0.985, 0.998, and 0.978, respectively. These correlations are not only useful to design engineers but also reveal the impact of independent parameters on the overall thermal resistance and friction factor for the PDF modules.

Summary

Turbulent heat transfer and fluid flow between a series of parallel plates with surface-mounted heat generating blocks was studied numerically. A periodically fully developed flow (PDF) module was isolated for the purpose of computation. Repeated boundary conditions were imposed in cross-stream directions to simulate the presence of a series of channels. Governing equations for two-dimensional PDF modules were solved by a finite volume technique. The k–ϵ model was used for turbulent closure. The solution technique was validated by comparing the experimental data for a single parallel plate channel and single channels with surface-mounted blocks (Sparrow et al., 1982; Wirtz and Chen, 1991). In addition, numerical predictions were found to be qualitatively consistent with the experimental results of Garimella and Eibeck (1990) and Wirtz and Chen (1991) under limiting conditions. Calculations were performed for a wide range of independent parameters (Re, K_s/K_f, s/w, d/w, and h/w). The key findings are as follows:

1 A double cyclic problem is defined for considering periodically fully developed flow and heat transfer in the streamwise direction and repeated condition in the transverse direction. Results are successfully obtained for turbulent PDF module with/without the substrate conduction.

2 The presence of the block directly affects the increase in the kinetic energy near the top surface of the block, which plays a major role in determining the flow characteristics. Any parameter that increases the effective kinetic energy contributes to an increase in the friction factor. The friction factor decreases slightly or stays nearly constant with an increase in the

Reynolds number. However, it increases with a decrease in the channel width and an increase in block spacing. The friction factor is shown to be higher than that of the parallel plate channel with the same height. Parametric effects on the friction factor are generalized with a correlation (Eq. (25)).

3 The temperature of the block surface can be reduced with an increase in Reynolds number and substrate conduction. The distributions of $\overline{Nu}_b$ and R are reflected from the temperature and heat flux at the block surface. However, it seems that the thermal resistance is a better indicator to measure the cooling performance in presence of multiple modes of cooling. The Nusselt number increases with an increase in the Reynolds number and increases slightly with an increase in the substrate conductivity. The opposite trend is found for the thermal resistance. The substrate conduction effect is very apparent in the graph showing the variation of thermal resistance with the independent parameters. It decreases with an increase in block spacing and with a decrease in channel width. Also, flat blocks have less thermal resistance than tall blocks with the same geometric parameters and Re.

4 Consideration of the substrate conduction is critically important in the design and analysis of electronic component cooling. Absence of the substrate conduction is shown to be detrimental to the cooling performance of the channel for a given amount of heat generation. On the other hand, by considering the substrate conduction effect, a more compact and efficient design can be achieved for the cooling channel.

Acknowledgments

The initial stage of the code development was in part supported by the Texas State Energy Research in Applications Program (ERAP, contract # 3121-70340). The supercomputer time (Cray-YMP) was made available through a grant from the Texas A&M University Super Computer Center.

References

Amano, R. S., 1984, "Development of a Turbulence Near-Wall Model and Its Application to Separated and Reattached Flows," *Numerical Heat Transfer*, Vol. 7, pp. 59–75.

Anderson, A. M., and Moffat, R. J., 1990, "A New Type of Correlation for Air Cooling of Regular Arrays of Electronic Components," *Thermal Modeling and Design of Electronic System Devices*, ASME HTD-Vol. 153, pp. 27–39.

Asako, Y., and Faghri, M., 1988, "Three Dimensional Heat Transfer and Fluid Flow Analysis of Arrays of Square Blocks Encountered in Electronic Equipment," *Numerical Heat Transfer*, Vol. 13, pp. 481–498.

Asako, Y., and Faghri, M., 1989, "Three Dimensional Heat Transfer Analysis of Arrays of Heated Square Blocks," *International Journal of Heat and Mass Transfer*, Vol. 32, pp. 395–405.

Asako, Y., and Faghri, M., 1991, "Parametric Study Turbulent Three Dimensional Heat Transfer of Arrays of Heated Blocks Encountered in Electronic Equipment," ASME HTD-Vol. 171, pp. 135–141.

Beavers, G. S., Sparrow, E. M., and Lloyd, J. R., 1971, "Low Reynolds Number Turbulent Flow in Large Aspect Ratio Rectangular Ducts," ASME *Journal of Basic Engineering*, Vol. 93, pp. 296–299.

Davalath, J., and Bayazitoglu, Y., 1987, "Forced Convection Cooling Across Rectangular Blocks," ASME JOURNAL OF HEAT TRANSFER, Vol. 109, pp. 321–328.

Garimella, S. V., and Eibeck, P., 1990, "Onset of Transition in the Flow Over a Three-Dimensional Array of Rectangular Obstacles," ASME HTD-Vol. 153, pp. 1–6.

Incropera, F. P., Kerby, J. S., Moffat, D. F., and Ramadhyani, S., 1986, "Convection Heat Transfer From Discrete Heat Sources in a Rectangular Channel," *International Journal of Heat and Mass Transfer*, Vol. 29, pp. 1052–1058.

Incropera, F. P., 1988, "Convection Heat Transfer in Electronic Equipment Cooling," ASME JOURNAL OF HEAT TRANSFER, Vol. 110, pp. 1097–1110.

Jayatilleke, C. L. V., 1969, "The Influence of Prandtl Number and Surface Roughness on the Resistance of the Laminar Sublayer to Momentum and Heat Tranfser," *Progr. Heat Mass Transfer*, Vol. 1, pp. 193–329.

Kim, S. H., Anand, N. K., and Fletcher, L.S., 1991, "Free Convection Between Series of Vertical Parallel Plates With Embedded Line Heat Source," ASME JOURNAL OF HEAT TRANSFER, Vol. 113, pp. 108–115.

Kim, S. H., and Anand, N. K., 1992, "Periodically Fully Developed Flow in Channels With Conducting Blockages," *AIAA Journal of Thermophysics and Heat Transfer*, Vol. 6, pp. 91–97.

Kim, S. H., 1993, "A Numerical Analysis of Convective Heat Transfer in Channels Simulating Electronic Components," Ph.D. Thesis, Texas A&M University, May.

Knight, R. W., and Crawford, M.E., 1988, "Numerical Prediction of Turbulent Flow and Heat Transfer in Channels With Periodically Varying Cross Sectional Area," *Proc. 1988 National Heat Transfer Conference*, ASME, Vol. 1, pp. 669–676.

Lehmann, G. L., and Wirtz, R. A., 1985, "The Effect of Variation in Streamwise Spacing and Length on Convection From Mounted Rectangular Components," *Heat Transfer in Electronic Equipment—1985*, ASME HTD-Vol. 48, pp. 39–47.

Moffat, R. J., Arvizu, D. E., and Ortega, A., 1985, "Cooling Electronic Components: Forced Convection Experiments With an Air-Cooled Array," ASME HTD-Vol. 48, pp. 17–27.

Nakayama, W., 1987, "Survey of Design Approaches in Japanese Computer," presented at the International Symposium on Cooling Technology for Electronic Equipment, Honolulu, HI.

Nigen, J. S., and Amon, C. H., 1991, "Forced Convective Cooling Enhancement of Surface-Mounted Electronic Package Configurations Through Self-Sustained Oscillatory Flows," ASME HTD-Vol.171, pp. 39–46.

Patankar, S. V., Liu, C. H., and Sparrow, E. M., 1977, "Fully Developed Flow and Heat Transfer in Ducts Having Streamwise-Periodic Variations of Cross-Sectional Area," ASME JOURNAL OF HEAT TRANSFER, Vol. 99, pp. 180–186.

Patankar, S. V., 1980, *Numerical Heat Transfer and Fluid Flow*, Hemisphere Publishing Company, New York.

Peterson, G. P., and Ortega, A., 1990, "Thermal Control of Electronic Equipment and Devices," *Advances in Heat Transfer*, Vol. 20, pp. 181–314.

Ramadhyani, S., Moffat, D. F., and Incropera, F. P., 1985, "Conjugate Heat Transfer From Small Isothermal Heat Sources Embedded in a Large Substrate," *International Journal of Heat and Mass Transfer*, Vol. 28, pp. 1945–1952.

Sathe, S., and Joshi, Y., 1990, "Natural Convection Liquid Cooling of a Substrate-Mounted Protrusion in a Square Enclosure: Effect of Thermophysical Properties, Geometric Dimensions and Boundary Conditions," ASME HTD-Vol. 153, pp. 73–80.

Sparrow, E. M., Niethammer, J. E., and Chaboki, A., 1982, "Heat Transfer and Pressure Drop Characteristics of Arrays of Rectangular Modules Encountered in Electronic Equipment," *International Journal of Heat and Mass Transfer*, Vol. 25, pp. 961–973.

Sridhar, S., Faghri, M., Lessmann, R. C., and Schmidt, R., 1990, "Heat Transfer Behavior Including Thermal Wakes in Forced Air Cooling of Arrays of Rectangular Blocks," ASME HTD-Vol. 153, pp. 15–25.

Webb, B. W., and Ramadhyani, S., 1985, "Conjugate Heat Transfer in a Channel With Staggered Ribs," *International Journal of Heat and Mass Transfer*, Vol. 28, pp. 1679–1687.

Wirtz, R. A., and Chen, W., 1991, "Laminar-Transitional Convection From Repeated Ribs in a Channel," ASME HTD-Vol. 171, pp. 89–94.

Generation of Longitudinal Streamwise Vortices—A Device for Improving Heat Exchanger Design

G. Biswas

P. Deb

S. Biswas

Department of Mechanical Engineering,
Indian Institute of Technology,
Kanpur—208016, India

Laminar flow and heat transfer characteristics in a rectangular channel, containing built-in vortex generators of both the slender delta-wing and winglet-pair type, have been analyzed by means of solution of the full Navier–Stokes and energy equations. Each wing or winglet pair induces the creation of streamwise longitudinal vortices behind it. The spiraling flow of these vortices serves to entrain fluid from their outside into their core. These vortices also disrupt the growth of the thermal boundary layer and serve ultimately to bring about the enhancement of heat transfer between the fluid and the channel walls. The geometric configurations considered in the study are representative of single elements of either a compact gas–liquid fin-tube crossflow heat exchanger or a plate-fin crossflow heat exchanger. Physically, these vortex generators can be mounted on the flat surfaces of the above-mentioned heat exchangers by punching or embossing the flat surfaces. They can also act as spacers for the plate fins. Because of the favorable pressure gradient in the channel, the longitudinal vortices are stable and their influence persists over an area many times the area of the slender vortex generators. From a heat transfer point of view, the delta-wing generator is found to be more effective than the winglet-pair. However, most convective heat transfer processes encounter two types of loss, namely, losses due to fluid friction and those due to heat transfer across finite temperature gradient. Because these two phenomena are manifestations of irreversibility, an evaluation of the augmentation techniques is also made from a thermodynamic viewpoint. Conclusions that are drawn thus include discussion about the influence of vortex generators (wings/winglets) on irreversibility.

Introduction

Augmentation of heat transfer is of special interest in channel flows where the rate of the heat transfer between the fluid and the channel walls deteriorates as the boundary layer grows on the channel walls and the flow tends to become fully developed. Protrusions can be mounted on these channel walls in order to disrupt the growth of the boundary layer and thereby enhance the heat transfer between the flowing fluid and the channel walls. Two relevant applications using this kind of flow configuration are the heat transfer between the gas and the fin in the case of gas–liquid fin-tube crossflow heat exchangers and the heat transfer between flowing fluid and plates in the case of plate-fin heat exchangers (Fig. 1). The evolution toward a fully developed flow can be disturbed by using a multilouvered surface geometry for the plates. Investigation by Achaichia and Cowell (1988) provides detailed performance data for louvered fin surfaces. However, in using louvered fins, enhancement is obtained at the price of high pressure drop. To circumvent this difficulty, protrusions in the form of slender delta-wings or winglets can be deployed (Fig. 2). As shown, the base of the wing remains attached to the fin and the apex faces the incoming stream with an angle of attack with this configuration. The longitudinal vortices are generated along the side edge of the wing-shaped vortex generator due to the pressure difference between the front surface facing the flow and the back surface. These longitudinal vortices, generated by the vortex generators, can be made to disrupt the growth of boundary layer in a channel by exchanging the fluid from the near-wall region with the channel-core region and thus they can serve to enhance the heat transfer rate while producing less of a pressure drop. Because of these advantages, the effect of delta-wing and winglet-pair on heat transfer in a channel flow is the subject of investigation in this study.

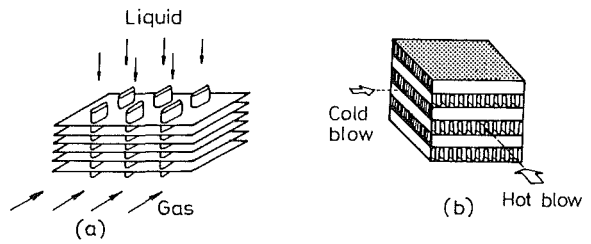

Fig. 1 Typical arrangement of heat exchanger cores: (*a*) gas–liquid fin-tube crossflow; (*b*) plate-fin (single or multipass)

The configuration used in this study closely resembles an element of a core region of the kind of heat exchangers mentioned above (Fig. 2). The wings or winglets protrude out of fins or plates, and can also serve the purpose of spacers. Use of longitudinal vortices for boundary layer control is well known (Pearcy, 1961) and the vortex generators are used in commercial airplanes for this purpose. Experimental investigations due to Fiebig et al. (1986, 1991) and Tiggelbeck et al. (1992) can be referred to in connection with augmentation of heat transfer by means of longitudinal vortices. Velocity field and heat transfer measurements were reported for slender wings embedded in a turbulent boundary layer (Eibeck and Eaton, 1987). Despite the presence of turbulent diffusion, the influence of longitudinal vortices on momentum and energy transport could be traced to a location as far downstream as 60 wing chords behind the delta winglet. Computational studies on related topics have been performed by Fiebig et al. (1989) and Biswas and Chattopadhyay (1992) for laminar flows in a delta-wing geometric configuration placed inside a channel.

Contributed by the Heat Transfer Division for publication in the JOURNAL OF HEAT TRANSFER. Manuscript received by the Heat Transfer Divison January 1992; revision received August 1993. Keywords: Augmentation and Enhancement, Heat Exchangers, Numerical Methods. Associate Technical Editor: R. J. Simoneau.

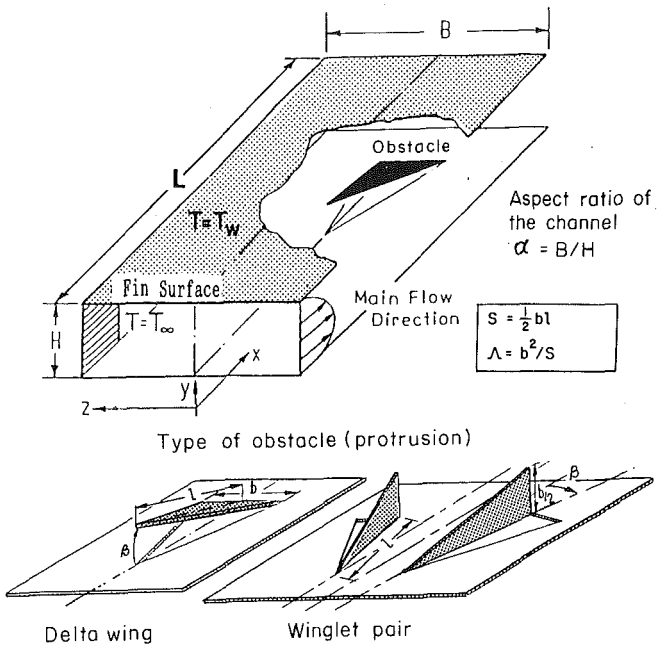

Fig. 2 Flow model for computation

Both studies discussed the influence of angle of attack and Reynolds number on velocity and temperature fields.

The present paper gives quantitative performance data for a delta-wing and winglet-pair in a channel with different angles of attack and a wide range of operating conditions. It also compares the performance of wings and winglets by taking into account two parameters: the augmentation of heat transfer and the associated flow losses. Finally, the irreversibility brought about by the heat transfer processes involving delta-wings and winglet-pairs is considered. An evaluation of the energy exchange process from this standpoint is called second-law analysis (Bejan, 1977, 1979). Based on an evaluation of the irreversibility, this study is able to draw some conclusions about the efficient use of thermal energy.

Statement of the Problem

Computation is performed in a channel formed by two neighboring fins (Fig. 2). An obstacle in the form of a delta-wing or winglet-pair (of zero thickness) is placed inside. The base of the wing is fixed on the bottom wall and the apex faces the incoming flow stream at an angle of attack. In the case of the winglet-pair, one side of each is fixed on the bottom wall and the trailing edge of each is free. Since symmetry prevails in the central vertical plane of the channel, the flow field in only half of the channel is computed. The dimensionless equations for continuity, momentum, and energy for this problem may be expressed in their conservative forms as follows:

$$D \equiv \frac{\partial U}{\partial X} + \frac{\partial V}{\partial Y} + \frac{\partial W}{\partial Z} = 0 \tag{1}$$

$$\frac{\partial U}{\partial \tau} + \frac{\partial U^2}{\partial X} + \frac{\partial UV}{\partial Y} + \frac{\partial UW}{\partial Z} = -\frac{\partial P}{\partial X} + \frac{\nabla^2 U}{\mathrm{Re}} \tag{2}$$

$$\frac{\partial V}{\partial \tau} + \frac{\partial UV}{\partial X} + \frac{\partial V^2}{\partial Y} + \frac{\partial VW}{\partial Z} = -\frac{\partial P}{\partial Y} + \frac{\nabla^2 V}{\mathrm{Re}} \tag{3}$$

$$\frac{\partial W}{\partial \tau} + \frac{\partial UW}{\partial X} + \frac{\partial VW}{\partial Y} + \frac{\partial W^2}{\partial Z} = -\frac{\partial P}{\partial Z} + \frac{\nabla^2 W}{\mathrm{Re}} \tag{4}$$

$$\frac{\partial \theta}{\partial \tau} + \frac{\partial U\theta}{\partial X} + \frac{\partial V\theta}{\partial Y} + \frac{\partial W\theta}{\partial Z} = \frac{\nabla^2 \theta}{\mathrm{Re} \cdot \mathrm{Pr}} \tag{5}$$

In the equations above, velocities have been nondimensionalized with the average incoming velocity U_{av} at the channel inlet, all lengths with channel height H, the pressure with ρU_{av}^2, and the nondimensional temperature is defined as $\theta =$

Nomenclature

B = channel width
Br = ratio of wing span to width of the channel = b/B
b = wingspan
C_f = skin friction = $[2(\partial u/\partial y)_w]/(\rho U_{av}^2)$
$\overline{C}_f$ = combined spanwise average friction coefficient, Eq. (7)
C_p = specific heat of the fluid
D = divergence of velocity vectors, Eq. (1)
Ec = Eckert number = U_{av}^2/C_pT_∞
H = channel height
h = heat transfer coefficient = $-k(\partial T/\partial y)_w/(T_w - T_b)$
j = mean Colburn factor = $\overline{\mathrm{Nu}}_c/(\mathrm{Re\ Pr}^{1/3})$
k = thermal conductivity of the fluid
Ns_3 = rate of nondimensional entropy generation per unit volume, Eq. (13)
Nu = local Nusselt number based on bulk temperature of the fluid
Nu_{xe} = local Nusselt number based on entry temperature of the fluid, Eq. (24)
$\overline{\mathrm{Nu}}$ = spanwise average Nusselt number
$\overline{\mathrm{Nu}}_c$ = average Nusselt number for the entire channel
P = nondimensional pressure = $p/\rho U_{av}^2$
p = pressure
Pr = Prandtl number = $\mu C_p/k$
q = wall heat flux
Re = Reynolds number = $U_{av}H/\nu$
r = ratio of wall temperature to ambient temperature = T_w/T_∞
S = wing area
T = temperature
$\overline{T}_b$ = average bulk temperature for the entire channel
t = time
U, V, W = axial, vertical, spanwise components of velocity
u, v, w = axial, vertical, spanwise components of velocity
X, Y, Z = axial, vertical or normal, and spanwise coordinates (normalized by H)
x, y, z = axial, vertical or normal, and spanwise dimension of coordinates
α = aspect ratio of the channel = B/H
δ_{ij} = Kronecker delta
$\overline{\theta}_b$ = average nondimensional bulk temperature for the entire channel = $(\overline{T}_b - T_\infty)/(T_w - T_\infty)$
Λ = aspect ratio of the wing
μ = dynamic viscosity of the fluid
ν = kinematic viscosity of the fluid
σ = stress tensor
τ = nondimensional time

Subscripts

av = average
b = bulk condition
sa = spanwise combination of top and bottom plate
w = wall
1 = bottom fin-plate
2 = top fin-plate

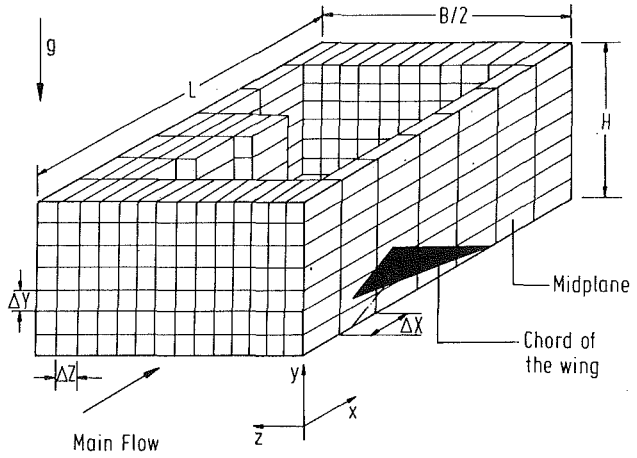

Fig. 3(*a*) Grid spacing in the computational domain and the location of the wing-type vortex generator

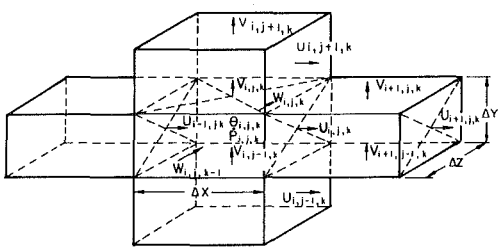

Fig. 3(*b*) Three-dimensional staggered grid showing the locations of the discretized variables

$(T - T_\infty)/(T_w - T_\infty)$. Boundary conditions of interest in this investigation are:

Top and bottom plates:

$$u = v = w = 0; \quad T = T_w$$

Side wall ($z = B/2$) and midplane ($z = 0$):

$$w = \left(\frac{\partial v}{\partial z}\right) = \left(\frac{\partial u}{\partial z}\right) = 0; \quad \left(\frac{\partial T}{\partial z}\right) = 0$$

At the channel inlet:

$$u = u(y), \; v = w = 0; \quad T = T_\infty$$

At the exit, a smooth transition through the outflow boundary is ensured by setting:

$$\frac{\partial^2 u}{\partial x^2} = \frac{\partial^2 v}{\partial x^2} = \frac{\partial^2 w}{\partial x^2} = 0; \quad \frac{\partial^2 T}{\partial x^2} = 0$$

No-slip boundary conditions for the velocities on the obstacles are used. The details of kinematic boundary condition on the surface of the vortex-generators are discussed elsewhere (Biswas et al., 1989; Biswas and Chattopadhyay, 1992). The temperature of the obstacle is considered constant and equal to T_w.

Method of Solution

A modified version of the Marker and Cell (MAC) method of Harlow and Welch (1965) and Hirt and Cook (1972) is used to obtain the numerical solution of Eqs. (1)–(5). The computational domain is divided into a set of Cartesian cells (Fig. 3*a*). A staggered grid arrangement is used such that the velocity components are defined at the center of the cell faces to which they are normal (Fig. 3*b*). The pressure and temperature are defined at the center of the cell.

In practice, the wings can easily be manufactured by punching or embossing the wall. In some computational results, the effects due to the hole beneath the vortex generator have been taken into account. The heat exchanger core is considered to have a number of plates and on each plate the vortex generators are punched out in such a way that the holes are perfectly aligned. In our computational domain, a small part of the top and bottom boundaries are set so as to identify the punched holes. For this purpose spacewise periodic boundary conditions on the locations of the punched holes have been employed in the y direction. Such boundary conditions have already been discussed in the earlier work of Biswas and Chattopadhyay (1992). However, for plate-fin heat exchangers, no hole exists underneath the vortex-generators in order to avoid mixing of the hot and cold streams.

Twofold solutions for the velocities are obtained. First the velocity components are advanced explicitly using the previous state of the flow, having calculated accelerations caused by convection, diffusion, and pressure gradients through a time step $\delta\tau$. The explicit time increment may not necessarily lead to a velocity field with zero mass divergence in each cell. In the subsequent fold, adjustment of pressure and velocity is done by an iterative process in order to ensure mass conservation in each cell. This iterative correction of the velocity field through the "implicit" continuity equation is equivalent to the solution of Poisson's equation for pressure. The process is repeated successively in all cells until no cell has a magnitude D greater than 10^{-4}. This solution scheme is continued until a steady flow is obtained. After evaluating the correct velocities, the energy equation is solved with a successive overrelaxation technique to determine the temperature field.

The convective terms of Eqs. (2), (3), (4), and (5) are discretized by a weighted average scheme (Hirt et al., 1975), which combines upwind and central differencing to achieve the stability of the upwind method and better formal accuracy of the central differencing. The following example in conjunction with Fig. 3(*b*) illustrates the essence of this discretization scheme. The second term of the x-momentum equation $[\partial UV/\partial Y]$ is discretized as

$$\left[\frac{\partial UV}{\partial Y}\right]_{i,j,k} = \frac{1}{4\delta Y}\left[(V_{i,j,k} + V_{i+1,j,k})(U_{i,j,k} + U_{i,j+1,k})\right.$$
$$+ \alpha_p |(V_{i,j,k} + V_{i+1,j,k})| (U_{i,j,k} - U_{i,j+1,k})$$
$$- (V_{i,j-1,k} + V_{i+1,j-1,k})(U_{i,j-1,k} + U_{i,j,k})$$
$$\left. - \alpha_p |(V_{i,j-1,k} + V_{i+1,j-1,k})| (U_{i,j-1,k} - U_{i,j,k})\right]$$

The factor α_p serves to balance the upwind contribution. If $\alpha_p \to 0$, the difference equations are centered in space. In the present paper, the factor α_p was restricted between 0.2 and 0.3 so that the formulation can retain "something" of the second-order accuracy (Roache, 1972). Runchal and Wolfstein (1969) and Timin and Esmail (1983) used this discretization scheme to compute driven cavity flows. Their results compare favorably with those of the second-order schemes. However, in the present problem of a channel with a built-in delta-wing, for a grid size of $40 \times 15 \times 26$ (in the x, y and z directions, respectively) and Reynolds number of 500, the CPU time with respect to steady solution was 2 h 15 min and 36.2 s on an HP-9000/850 series computer.

An effort was undertaken to obtain grid-independent results. For Re = 500 and Pr = 0.7, in a channel ($\alpha = 2$) with a built-in delta wing ($\Lambda = 1$) at an angle of attack (β) of 26 deg, reasonable agreement between the results obtained for 15×26 and 20×30 cross-stream grids was found. It may be mentioned that for a 15×26 cross-stream grids, 60 grid nodes were taken in the x direction for a nondimensional length of 8.4. Similarly, for Re = 500 and Pr = 0.7, in the channel with a built-in winglet-pair at an angle of attack 32 deg, grid-independent results were obtained for a grid size of $(76 \times 30 \times 15)$. Grid independence was also tested for other geometric and flow

parameters. In each case, beyond a small value (±4 percent), further refinements of grid size were not computationally economical.

Evaluation of the Performance Parameters

Nusselt Number and Skin Friction. In order to have a quantitative estimation of the heat transfer performance, the combined spanwise average Nusselt number

$$\overline{\mathrm{Nu}}_{sa}=\frac{B(q_1+q_2)(H/k)}{2\int_0^{B/2}(T_{w1}(x,z)-T_b(x))dz+2\int_0^{B/2}(T_{w2}(x,z)-T_b(x))dz} \quad (6)$$

has been calculated at each longitudinal location in the channel. Similarly, for an accounting of the flow losses, the combined spanwise average friction coefficient has been calculated from:

$$\overline{C}_f=\frac{\mu\left\{2\int_0^{B/2}\left(\frac{\partial u}{\partial y}\right)_{u=0}dz+2\int_0^{B/2}\left(\frac{\partial u}{\partial y}\right)_{y=H}dz\right\}}{\frac{\rho}{2}U_{av}^2(2B)} \quad (7)$$

The average Nusselt number for the entire channel is calculated as

$$\overline{\mathrm{Nu}}_c=\frac{1}{L}\int_0^L\overline{\mathrm{Nu}}_{sa}dx \quad (8)$$

Entropy Generation. The rate of entropy generation per unit volume is given by Kirkwood and Crawford (1952) as:

$$\dot{S}_3=-\frac{1}{T^2}(q\cdot\nabla T)-\frac{1}{T}(\sigma:\Delta\overline{V}) \quad (9)$$

The first term on the right-hand side of Eq. (9) may be written as:

$$-\frac{1}{T^2}(q\cdot\nabla T)=\frac{k}{T^2}\left[\left(\frac{\partial T}{\partial x}\right)^2+\left(\frac{\partial T}{\partial y}\right)^2+\left(\frac{\partial T}{\partial z}\right)^2\right] \quad (10)$$

The second term on the right-hand side of Eq. (9) is expanded as

$$(\sigma:\nabla\overline{V})=\left(p+\frac{2}{3}\mu\Delta\right)\delta_{ij}\left(\frac{\partial u_i}{\partial x_j}\right)-\mu\left(\frac{\partial u_i}{\partial x_j}+\frac{\partial u_j}{\partial x_i}\right)\frac{\partial u_i}{\partial x_j} \quad (11)$$

After invoking the incompressibility condition, Eq. (11) can be written as:

$$-\frac{(\sigma:\nabla\overline{V})}{T}=\frac{\mu}{T}\left[2\left\{\left(\frac{\partial u}{\partial x}\right)^2+\left(\frac{\partial v}{\partial y}\right)^2+\left(\frac{\partial w}{\partial z}\right)^2\right\}+\left(\frac{\partial u}{\partial y}+\frac{\partial v}{\partial x}\right)^2+\left(\frac{\partial v}{\partial z}+\frac{\partial w}{\partial y}\right)^2+\left(\frac{\partial u}{\partial z}+\frac{\partial w}{\partial x}\right)^2\right] \quad (12)$$

Use of Eqs. (10) and (12) in Eq. (9) and nondimensionalization yields:

$$Ns_3=\frac{\dot{S}_3H^2}{k}=\frac{(r-1)^2}{[\theta(r-1)+1]^2}\cdot\left[\left(\frac{\partial\theta}{\partial X}\right)^2+\left(\frac{\partial\theta}{\partial Y}\right)^2+\left(\frac{\partial\theta}{\partial Z}\right)^2\right]+\frac{\mathrm{Ec}\cdot\mathrm{Pr}}{[\theta(r-1)+1]}\cdot\left[2\left\{\left(\frac{\partial U}{\partial X}\right)^2+\left(\frac{\partial V}{\partial Y}\right)^2+\left(\frac{\partial W}{\partial Z}\right)^2\right\}+\left(\frac{\partial U}{\partial Y}+\frac{\partial V}{\partial X}\right)^2+\left(\frac{\partial V}{\partial Z}+\frac{\partial W}{\partial Y}\right)^2+\left(\frac{\partial U}{\partial Z}+\frac{\partial W}{\partial X}\right)^2\right] \quad (13)$$

After evaluating this quantity, we integrate Ns_3 over the entire volume to get total nondimensional volumetric entropy generation in the channel as:

$$Ns=\int\int\int Ns_3\,dXdYdZ \quad (14)$$

Merit Function. If Q is the total rate of heat transfer, then $Q=\overline{h}_c(T_w-\overline{T}_b)\,2BL$, or

$$Q=2(B/H)\,\overline{\mathrm{Nu}}_c\,kL\,(T_w-\overline{T}_b) \quad (15)$$

Equation (15) can be rearranged as:

$$Q=2(B/H)\quad kL\,\overline{\mathrm{Nu}}_c\,T_w\left(1-\frac{1}{r}\right)(\theta_w-\overline{\theta}_b) \quad (16)$$

The rate of exergy transfer accompanying energy transfer at a rate of Q is given by Moran (1982) as

$$Q_a=Q\left[1-\frac{T_a}{T_w}\right]=Q\left[1-\frac{1}{r}\right] \quad (17)$$

where T_a, the exergy reference environment temperature, has been considered as the ambient temperature T_∞. The wall temperature T_w has been considered as a suitable temperature at the surface where heat transfer takes place. If $\dot{S}$ is the total rate of entropy generation (dimensional), the destruction of exergy is

$$I=T_a\dot{S}=\frac{1}{r}T_w\dot{S} \quad (18)$$

As such, the total rate of entropy generation, $\dot{S}$, may be written as

$$\dot{S}=\frac{k}{H^2}\int\int\int Ns_3\,d(HX)d(HY)d(HZ) \quad (19)$$

Invoking Eq. (14) in Eq. (19), we obtain

$$\dot{S}=HkNs \quad (20)$$

Finally, Eqs. (18) and (20) will yield

$$I=\frac{1}{r}T_w\,H\,k\,Ns \quad (21)$$

A merit function is defined as the ratio of exergy transferred to the sum of exergy transferred and exergy destroyed

$$M=\frac{Q_a}{Q_a+I} \quad (22)$$

Substituting for Q_a from Eq. (16) and I from Eq. (21), we obtain

$$M=\frac{2(B/H)(r-1)^2\,\overline{\mathrm{Nu}}_c(\theta_w-\overline{\theta}_b)}{2(B/H)(r-1)^2\,\overline{\mathrm{Nu}}_c(\theta_w-\overline{\theta}_b)+\frac{rH}{L}Ns} \quad (23)$$

This merit function is now evaluated for various flow parameters in a channel using delta wing or winglet pairs as vortex generators. However, it might be observed that Eq. (23) is another form of second-law efficiency (Moran, 1982).

Results and Discussion

A number of computations have been performed with a delta-wing or a winglet-pair as vortex generator. When we envision a wing moving in an infinite medium, the wake grows

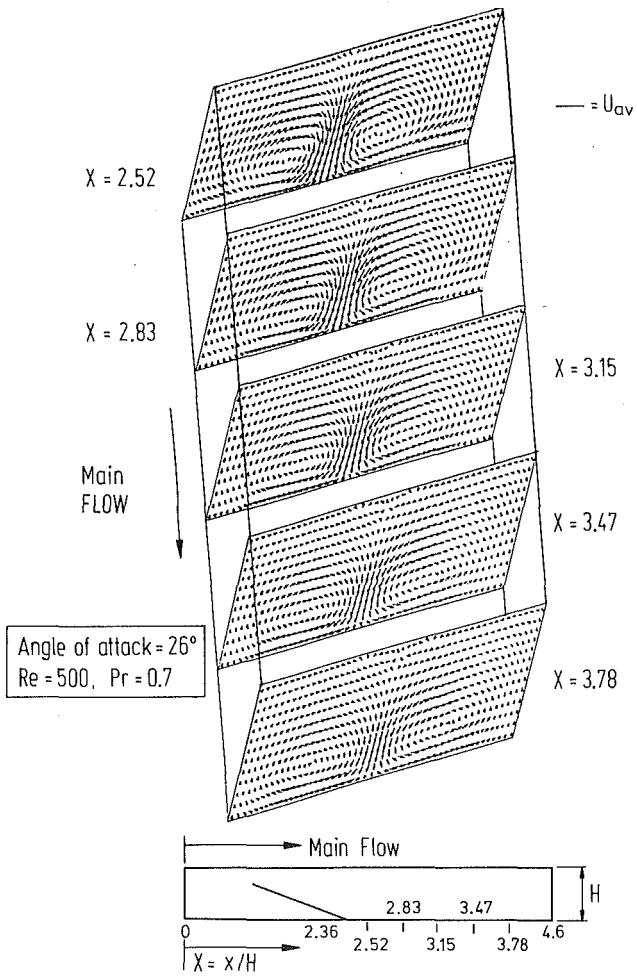

Fig. 4 Cross-stream velocity vectors at different axial locations behind the wing showing generation and deformation of vortices in the channel

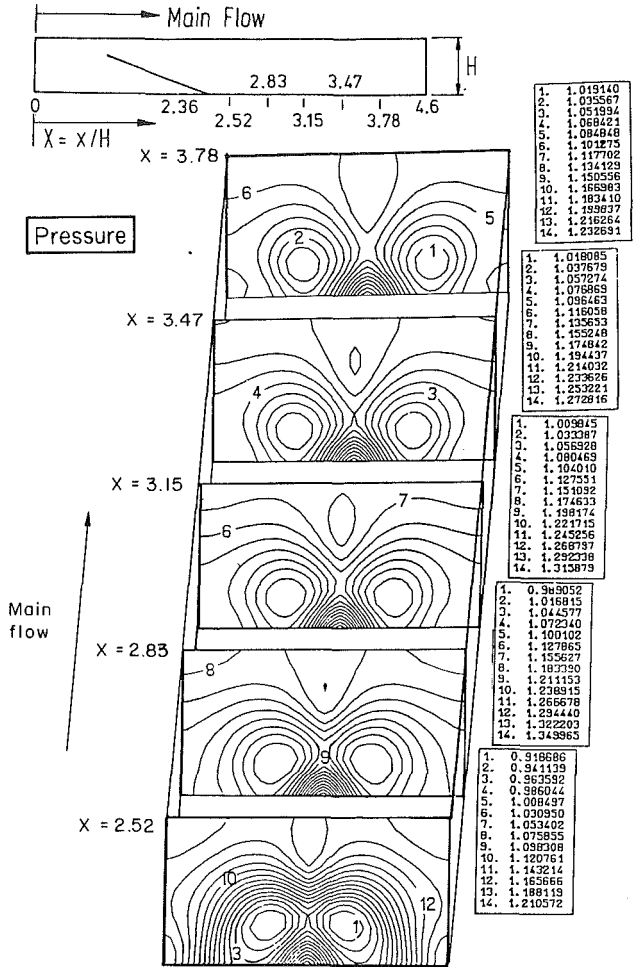

Fig. 5 Static pressure distribution at different axial locations behind the delta wing

longer and basically becomes a swirling flow supported by trailing vortices. However, the flow in a channel with an attached delta-wing shows no trailing edge vortices. Figure 4 shows the generation of vortices and their deformation as they move along the channel in presence of a delta-wing. Deformation takes place due to the reduction in strength of the vortices, which is brought about by the viscous resistance of the walls. The cross-stream velocity vectors at different axial locations can be seen in this figure. Figure 5 illustrates the static pressure distribution on the cross planes at the same axial locations and for the same geometric and flow parameters as those of Fig. 4. The nondimensional static pressure ($p/\rho U_{av}^2$) contours follow the same qualitative trends as those observed in experiments conducted by Hummel (1978).

Figure 6 shows the isotherms over eight cross planes located at eight different axial locations in a channel for Re = 1500 and Pr = 0.7. It is seen that as the fluid stream moves from an axial distance $X = 1.268$ to $X = 5.706$, the value of the isotherms in the core region increases and consequently the bulk temperature keeps on rising. The relative location of the wing has been shown clearly in this figure. Due to the spiraling structure of the flow behind the wing, there is a mixing of the cooler stream of the core with the hot fluid from the wall and thus, as can be seen, the core temperature rises in the downstream.

The influence of angle of attack of the wing-type vortex generators on heat transfer and the effect of Reynolds number on heat transfer in a channel with built-in wing-type vortex generators have been discussed in detail, in the work of Biswas and Chattopadhyay (1992). In their study, a fully developed velocity profile was considered at the inlet of the channel. For a developing flow, the effect of flow development in the channel and the effect of vortex generators on the flow field are superimposed downstream. In the earlier study, in order to distinguish the effect of vortex generators (to eliminate the effect of flow development), a fully developed velocity profile at the inlet was deployed. However, here we shall include the effect of developing flow and the influence of punched holes beneath the vortex generators on the heat transfer performance. Figure 7 shows the comparison of cross-stream velocity vectors at different axial locations from the inlet of the channel for the cases without and with stamping on the solid walls. Due to the stamping on the walls, a velocity field normal to the vortex motion is induced in the downstream direction. This induced downward normal velocity field reduces the strength of the vortex flow and, as compared with the case where there is no stamping, a decayed circulatory flow pattern is observed at the same axial location. Figure 8 shows the heat transfer performance in a channel for a simultaneously developing flow (Kakac et al., 1987) in presence of a delta-wing. Figure 8 also compares the heat transfer on the channel walls for the cases with and without stamping. For the case without stamping, in the region of the wing (from $X = 2.92$ to $X = 3.79$), the combined spanwise average Nusselt number rises to a high value of 10 and then takes a plunge. A small dead water zone exists in the immediate neighborhood behind the wing-wall junction, which causes poor heat transfer at that location. However, downstream of the wing, heat transfer is increased

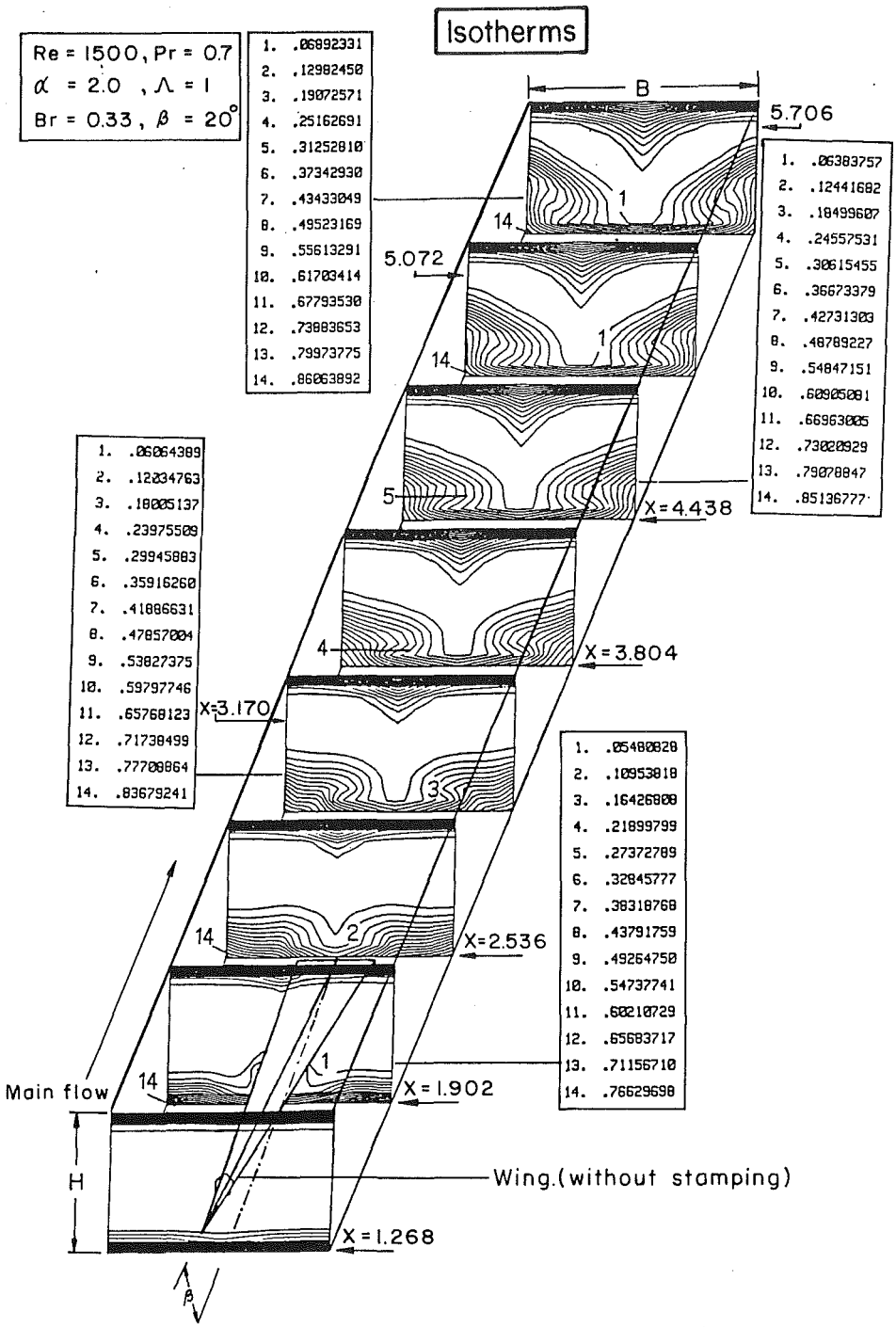

Fig. 6 Isotherms at different cross planes in the channel in presence of built-in delta wing

remarkably as compared with the plane channel flow. As such, even for a very long channel ($X = 10.28$), enhancement of the heat transfer at the exit of the channel is more than 46 percent. The enhancement is not so pronounced when the effect of a punched hole beneath the wing is taken into account. Due to the downward normal stream at the cross planes (as shown in Fig. 7), the strength of longitudinal vortices is reduced to a great extent although a spiraling flow pattern still exists. The improvement in the heat transfer coefficient is relatively less than that of the case without any punched hole (about 29 percent over the plane channel at the exit plane).

Figure 9 illustrates the relative heat transfer performance of delta-wing and winglet-pair configurations with other geometric and flow parameters unchanged. The main difference between the wing and winglet is that the winglet has a free trailing edge, whereas the wing has no trailing edge (wing-span is attached to the plate). However, delta-wing produces streamwise vortices with higher strength, which brings about better improvement in heat transfer as compared with built-in winglet pair. In a moderately long channel ($X = 8.4$), the enhancement in combined spanwise Nusselt number for a built-in delta-wing ($\beta = 26$ deg, $\Lambda = 1$, and $Br = 0.42$) at the exit of the channel is more than 34 percent than that of a plane channel. This enhancement for the winglet-pair at the same location is about 14 percent. Therefore, from a heat transfer point of view, the delta-wing is found to be more effective than the winglet-pair.

Figure 10 shows the influence of angle of attack of the winglet-pair on combined spanwise average Nusselt number in

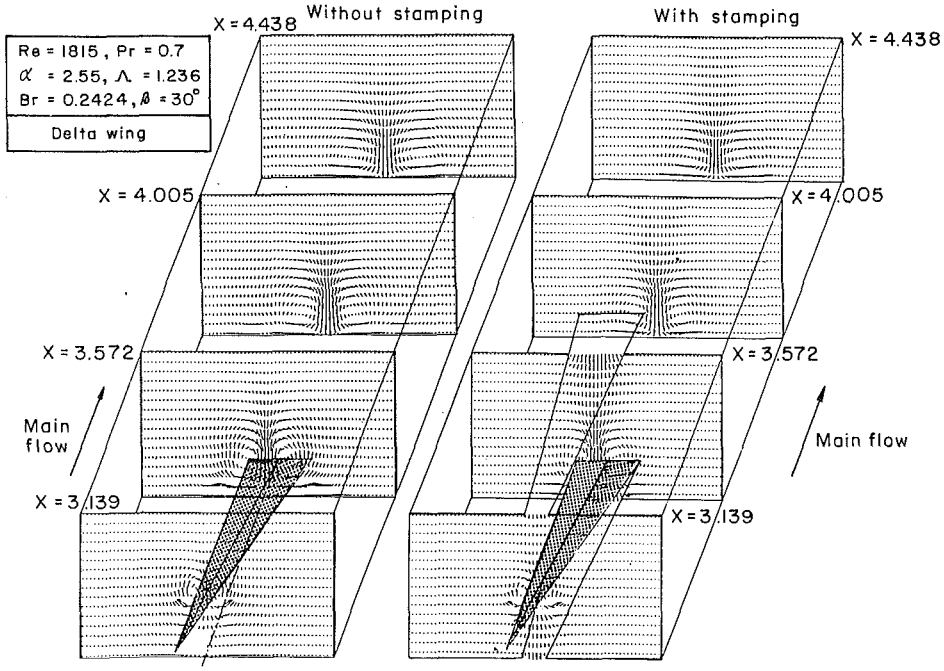

Fig. 7 Effect of stamping on cross-stream velocity vectors at different axial locations in the channel with delta wing as the obstacle

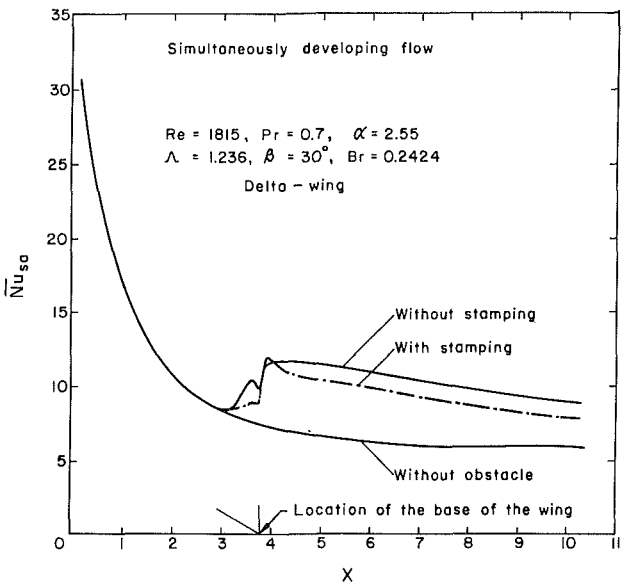

Fig. 8 Effect of stamping on the distribution of combined spanwise average Nusselt number in the channel; simultaneously developing flow

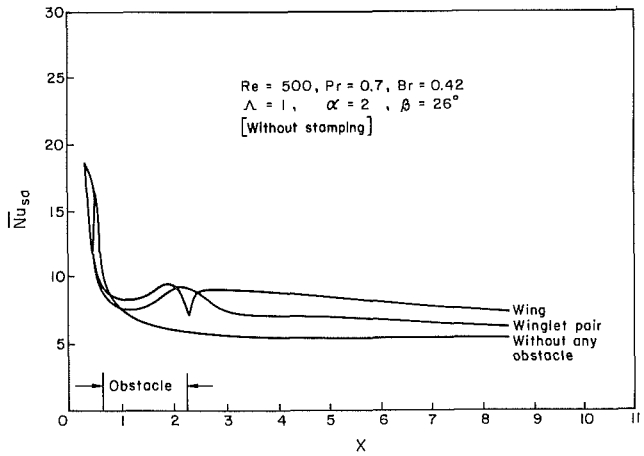

Fig. 9 Effect of type of obstacle on the distribution of combined spanwise average Nusselt number in the channel; developed profile at the inlet

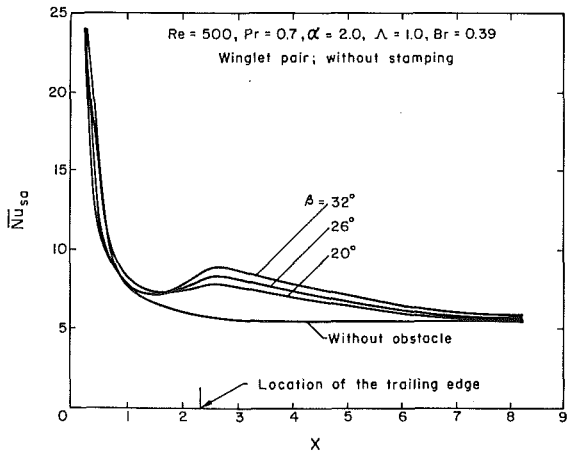

Fig. 10 Effect of angle of attack of winglet pair on the distribution of combined spanwise average Nusselt number in the channel; developed profile at the inlet

the channel. At a nondimensional distance of 4 from the inlet, for an angle of attack of 20 deg, we observe an enhancement of 30 percent in the combined spanwise average Nusselt number over the case of a plane channel. Now, at the same location, for an angle of attack of 26 deg, an improvement of about 6 percent in $\overline{Nu}_{sa}$ over the case of the 20 deg angle of attack is obtained. However, at the same location, an improvement of 12 percent over the case of 20 deg angle of attack is discerned for $\beta = 32$ deg. The winglets with higher angle of attack produce vortices with higher strength, which in turn results in improved heat transfer.

Figure 11 shows the distribution of combined spanwise average friction coefficient ($\overline{C}_f \times \mathrm{Re}$, Eq. (7)) for three different cases. The plot clearly shows the effect of stamping on the distribution of ($\overline{C}_f \times \mathrm{Re}$). Here we have considered a simultaneously developing flow. For a long channel, at the exit ($X = 10.28$), the increase in ($\overline{C}_f \times \mathrm{Re}$) for the case with a built-

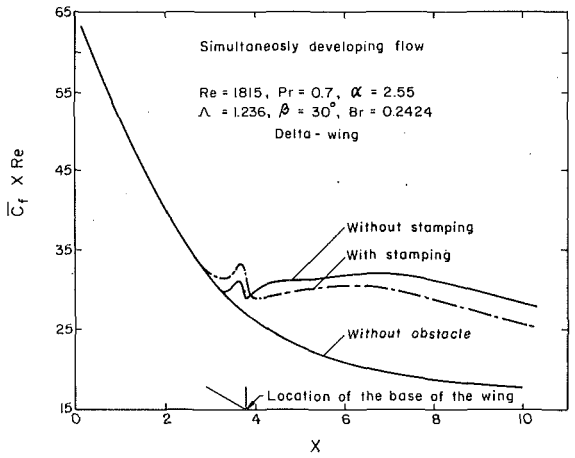

Fig. 11 Effect of stamping on the distribution of combined spanwise average friction coefficient in the channel; simultaneously developing flow

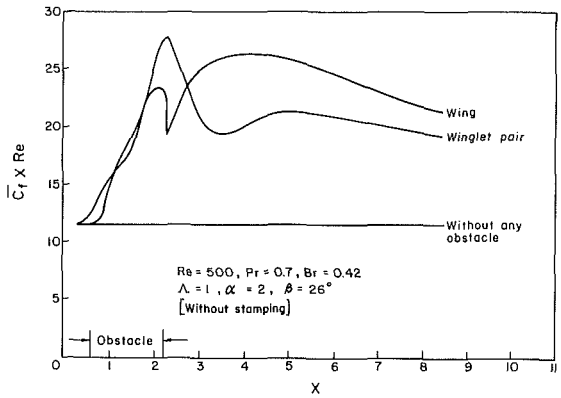

Fig. 12 Effect of type of obstacle on the distribution of combined spanwise average friction coefficient in the channel; developed profile at the inlet

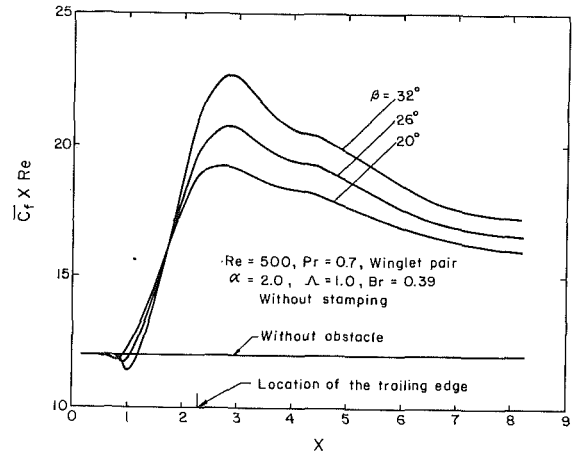

Fig. 13 Effect of angle of attack of the winglet pair on the distribution of combined spanwise average skin friction coefficient in the channel; developed profile at the inlet

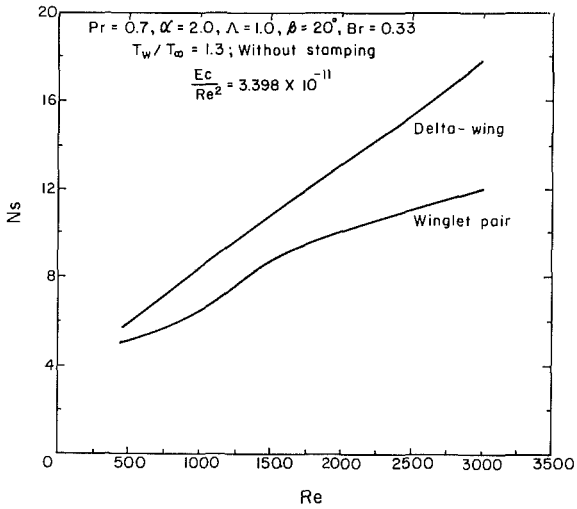

Fig. 14 Effect of type of obstacle on the variation of volumetric entropy generation with Reynolds number

in vortex-generator (without stamping) over that for a plane channel is about 64 percent. On the other hand it was noted that the value of friction coefficient ($\overline{C}_f \times$ Re) is 49 percent more for this case than the plane channel value when the effect of the punched hole under the wing is taken into account. The reason for this reduction in friction coefficient is attributed to the spiraling flow with relatively less vortex strength. This last fact is also evident from Fig. 7.

Figure 12 shows the distribution of combined spanwise average friction coefficient ($\overline{C}_f \times$ Re) in the channel for the wing and winglet-pair and compares them with the distribution of ($\overline{C}_f \times$ Re) in a plane channel. As mentioned earlier, delta-wing generates streamwise vortices with higher strengths. Increased frictional losses are due to steeper velocity gradients at the walls. These losses rise with vortex strength, and as a consequence, ($\overline{C}_f \times$ Re) is higher for vortices with higher strength. At the channel exit ($X = 8.4$), ($\overline{C}_f \times$ Re) for a delta-wing is about 79 percent more than for the plane channel flow. For winglet-pair, the increase in ($\overline{C}_f \times$ Re) at the same location, over the case of a plane channel flow, is nearly 65 percent.

Figure 13 shows the effect of varying the angle of attack of the vortex generators on ($\overline{C}_f \times$ Re) while keeping the size constant. Increasing the angle of attack has the effect of increasing vortex strength, which in turn increases resistance and consequently a higher value of combined spanwise average friction coefficient is obtained.

Figure 14 shows the total entropy generation in the channel at various Reynolds numbers (in the range of 500–3000) for two different cases, namely, with a built-in delta-wing and winglet-pair. It is evident that for all the Reynolds numbers, the entropy generation in the case of a built-in delta-wing is much more than that of a delta winglet-pair. With increasing Reynolds number, the delta-wing generates vortices of higher strengths. This culminates in steeper velocity gradients at the wall. As a result, frictional losses become high and consequently, the total generation of entropy becomes much more pronounced.

Figure 15 shows the variation of merit function, M, with Reynolds number (in the range of 500–3000) for the built-in delta-wing and winglet-pair. The delta winglet-pair shows better performance than delta-wing with regard to merit function. For the case of heat transfer in a channel with a built-in wing-pair, the increase in irreversibility associated with the increase in exergy transfer occurs at a relatively lower rate as compared to the case of a built-in delta-wing. Although with regard to augmentation of heat transfer in the channel, the built-in delta-wing shows better performance, it can be certainly argued that the built-in winglet-pair is more effective with respect to efficient use of energy.

Comparison With Experiments

The model validation was performed through comparison with some published experimental results. Local Nusselt numbers along the centerline of the bottom plate with a delta-wing at an angle of attack of 20 deg were calculated. Reynolds and

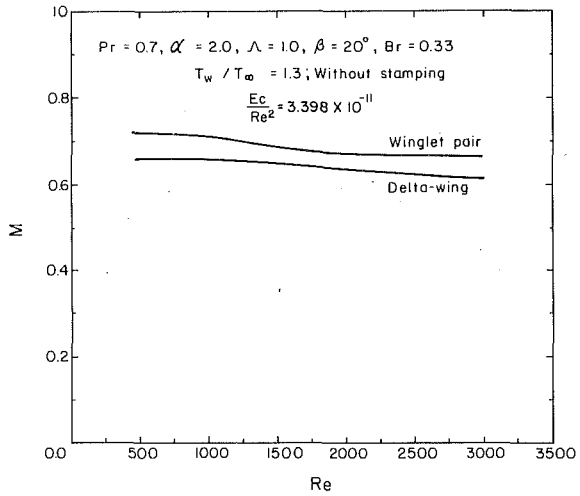

Fig. 15 Effect of type of obstacle on the variation of merit function with Reynolds number

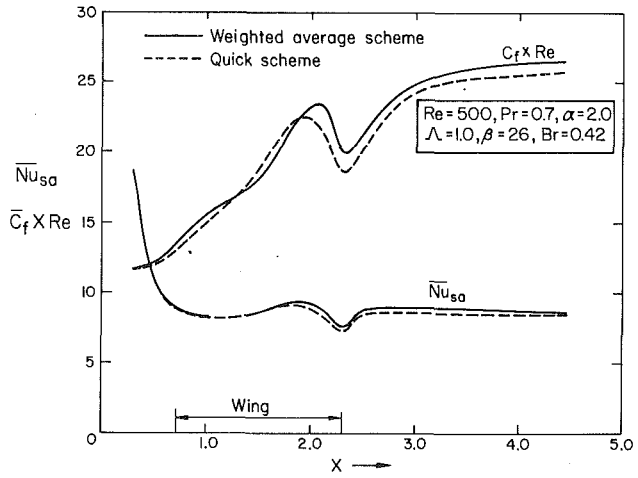

Fig. 17 Comparison of weighted average scheme with QUICK

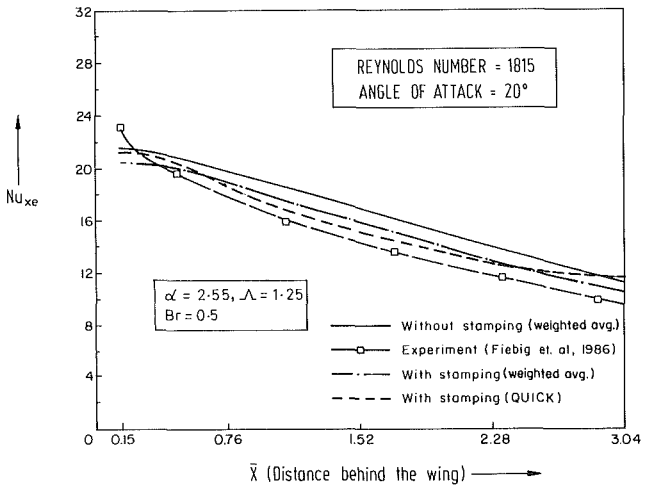

Fig. 16 Comparison of computed results with experimental observation

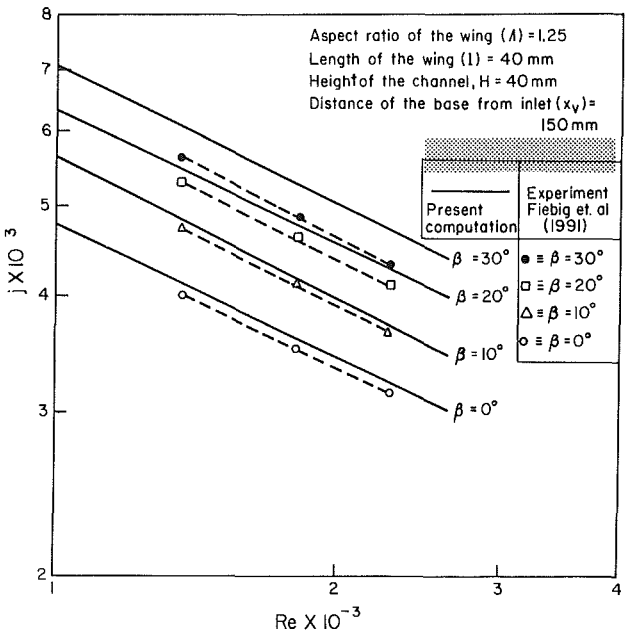

Fig. 18 Comparison between computational and experimental results for Colburn factor as a function of Reynolds number at different angles of attack

Prandtl numbers for this computation are 1815 and 0.7, respectively. Here local Nusselt number values are evaluated on the basis of entry temperature of the incoming stream as

$$Nu_{xe} = \frac{-k\left[\left(\frac{\partial T}{\partial y}\right)_{y=0,z=0}\right]_x (H/k)}{[T_{wl}(x) - T_\infty]_{y=0,z=0}} \quad (24)$$

Figure 16 shows that the computed values of local Nusselt numbers (with weighted average scheme) compare favorably with the experimental results of Fiebig et al. (1986). In the experiment, the channel walls had punched holes on them and the experimental results are closer to the computed results for the case with stamping. Computational results due to QUICK discretization scheme (Leonard, 1979), have also agreed closely with the experiment, except near the exit of the channel. The local heat transfer coefficients were determined by unsteady liquid crystal thermography. Measurement error is indeed minimal in this process. The RSS uncertainty described by Moffat (1987) was below 4.3 percent for local heat transfer coefficients. However, the small discrepancy between the experimental and numerical results could be attributed to physical boundary condition on the channel walls. It was not possible to maintain a perfect isothermal condition on the channel walls.

We may mention that we have also compared the results due to our weighted average scheme of discretization with those due to the QUICK discretization scheme (Leonard, 1979), which is formally more accurate. The comparison is shown in Fig. 17. The maximum discrepancy in Nusselt number is found to be less than 3 percent.

Overall heat transfer performance data are validated through comparison with respect to the mean Colburn factor (j) using delta-wing for three different angles of attack. The experimental results were obtained from Fiebig et al. (1991). In the experiment, the reference plate-fin area started from the location of the base of the wing; its longitudinal extent was 7.5 wing chord lengths and its lateral extent was four times the wing span. Identifying this zone on the bottom plate as the reference area, experiments were conducted in a plane channel and in a channel with a built-in delta wing at different angles of attack. Figure 18 shows the mean Colburn factor (j) versus Reynolds number of a delta-wing of aspect ratio 1.25 at various angles of attack. The numerical model and the experiment corroborate with each other reasonably well. The curves can be represented by $j = C_n$, Re^n, where n and C are constants.

Concluding Remarks

With the above-mentioned events in mind, we are now in a position to consider the practical application of this augmentation technique. The flow configuration resembles closely a single element of a cascade in fin-tube or plate-fin crossflow heat exchanger with a row of vortex generators. In practice, for such an exchanger the channel may not be allowed to be so long ($X \geq 8.0$), i.e., another row of vortex generators may be punched out or mounted before this length is reached in the downstream direction. In that event, at about $X = 4$ (refer to Fig. 9), augmentation of heat transfer due to winglet-pair is also quite substantial. Moreover, in the case of winglets, separation bubbles are not formed near the wing-plate junction. It has also been seen that the flow loss (corresponding to the combined spanwise average friction coefficient) due to the winglet-pair is less than that due to the wing. Besides, due to formation of trailing edge vortices for the free trailing edge of winglet, the small zone of poor heat transfer as it is observed with the wing can be avoided. Thus, based on this and a comparative study of second-law efficiency, the use of winglets appears to be a more attractive augmentation technique.

Acknowledgments

We are grateful to the referees for valuable comments. Help and encouragement received from Dr. Robert J. Simoneau of NASA-Lewis and Prof. David A. Blank of US Naval Academy are gratefully acknowledged.

References

Achaichia, A., and Cowell, T. W., 1988, "Heat Transfer and Pressure Drop Characteristics of Flat Tube and Louvered Plate Fin Surfaces," *Experimental Thermal and Fluid Science*, Vol. 1, pp. 147–157.

Bejan, A., 1977, "The Concept of Irreversibility in Heat Exchanger Design," ASME JOURNAL OF HEAT TRANSFER, Vol. 99.

Bejan, A., 1979, "A Study of Entropy Generation in Fundamental Convective Heat Transfer," ASME JOURNAL OF HEAT TRANSFER, Vol. 101, pp. 718–725.

Biswas, G., Mitra, N. K., and Fiebig, M., 1989, "Computation of Laminar Mixed Convection Flow in a Channel With Wing Type Built-in Obstacles," *AIAA Journal of Thermophysics and Heat Transfer*, Vol. 3, pp. 447–453.

Biswas, G., and Chattopadhyay, H., 1992, "Heat Transfer in a Channel With Built-in Wing-Type Vortex Generators," *International Journal of Heat and Mass Transfer*, Vol. 35, pp. 803–814.

Eibeck, P. A., and Eaton, J. K., 1987, "Heat Transfer Effects of a Longitudinal Vortex Embedded in a Turbulent Shear Flow," ASME JOURNAL OF HEAT TRANSFER, Vol. 109, pp. 16–24.

Fiebig, M., Kallweit, P., and Mitra, N. K., 1986, "Wing Type Vortex Generators for Heat Transfer Enhancement," *Proceedings of the Eighth International Heat Transfer Conference*, San Francisco, Vol. 6, pp. 2909–2913.

Fiebig, M., Brockmeier, U., Mitra, N. K., and Güntermann, T., 1989, "Structure of Velocity and Temperature Fields in Laminar Channel Flows With Longitudinal Vortex Generators," *Numerical Heat Transfer—Part A*, Vol. 15, pp. 281–302.

Fiebig, M., Kallweit, P., Mitra, N. K., and Tiggelbeck, S., 1991, "Heat Transfer Enhancement and Drag by Longitudinal Vortex Generators in Channel Flow," *Experimental Thermal and Fluid Science*, Vol. 4, pp. 103–114.

Harlow, F. W., and Welch, J. E., 1965, "Numerical Calculation of Time Dependent Viscous Incompressible Flow of Fluid With Free Surface," *The Physics of Fluids*, Vol. 8, pp. 2182–2188.

Hirt, C. W., and Cook, J. L., 1972, "Calculating Three Dimensional Flows Around Structures and Over Rough Terrain," *J. Comp. Phys.*, Vol. 10, pp. 324–340.

Hirt, C. W., Nichols, B. D., and Romero, N. C., 1975, "SOLA—A Numerical Solution Algorithm for Transient Fluid Flows," Los Alamos Scientific Lab Report LA-5652.

Hummel, D., 1978, "On the Vortex Formation Over a Slender Wing at Large Angles of Incidence," Advisory Group on Aerospace Research and Development Rept. AGARD-CCP-247.

Kakac, S., Shah, R. K., and Aung, W., 1987, *Handbook of Single Phase Convective Heat Transfer*, Wiley, New York, p. 4.55.

Kirkwood, J. G., and Crawford, B., Jr., 1952, "The Macroscopic Equations of Transport," *Journal of Physical Chemistry*, Vol. 56, pp. 1048–1051.

Leonard, B. P., 1979, "A Stable and Accurate Modelling Procedure Based on Quadratic Upstream Interpolation," *Comp. Methods Appl. Mech. Eng.*, Vol. 19, pp. 59–98.

Moffat, R. J., 1987, "Describing the Uncertainties in Experimental Results," *Experimental Thermal and Fluid Science*, Vol. 1, pp. 3–17.

Moran, M. J., 1982, *Availability Analysis: A Guide to Efficient Energy Use*, Prentice Hall, Englewood Cliffs, NJ, pp. 58, 85.

Pearcy, H. H., 1961, *Shock-Induced Separations in Boundary Layers and Flow Control*, Vol. 2, Pergamon Press, New York.

Roache, P. J., 1972, *Computational Fluid Dynamics*, Hermosa, Albuquerque, NM.

Runchal, A. K., and Wolfstein, M., 1969, "Numerical Investigation Procedure for the Steady State Navier-Stokes Equations," *J. Mech. Eng. Sci.*, Vol. 11, pp. 445–452.

Tiggelbeck, S., Mitra, N. K., and Fiebig, M., 1992, "Flow Structure and Heat Transfer in a Channel With Multiple Longitudinal Vortex-Generators," *Experimental Thermal and Fluid Science*, Vol. 5, pp. 425–436.

Timin, T., and Esmail, N., 1983, "A Comparative Study of Central and Upwind Difference Schemes Using the Primitive Variables," *Int. J. Numer. Methods in Fluids*, Vol. 3, pp. 295–305.

Heat Transfer Enhancement Under Various Orientations Resulting From Attraction Mode Induction Electrohydrodynamic Pumping

B. D. Margo

J. Seyed-Yagoobi

Department of Mechanical Engineering,
Texas A&M University,
College Station, TX 77843-3123

An induction electrohydrodynamic (EHD) pump in an axisymmetric configuration was designed and built to examine the heat transfer enhancement that accompanies fluid pumping. The apparatus was operated at several tilt angles between 0 (horizontal) and 90 while the augmentation of heat transfer was measured and compared to typical forced pumping and natural circulation. The increase in the overall conductance value for EHD pumping compared to typical forced pumping under turbulent flow conditions was as high as 71 percent. This corresponds to a much higher increase in the inside convection coefficient, which is the only resistance to heat transfer being affected by induction pumping.

EHD Pumping

Electrodynamic (EHD) pumping is produced by the interaction of electric fields and free charges in a dielectric fluid medium. Pumping is achieved when electric fields push or pull charges through the fluid in a given direction. Therefore, the two basic requirements of EHD pumping are the presence of free charges in the fluid and the existence of electric fields to interact with the free charges.

One method of creating free charges in a dielectric fluid is based on the establishment of an electrical conductivity gradient perpendicular to the desired direction of fluid motion. The resulting variation of the electric field requires a net charge inside the medium. These charges then interact with a traveling electric wave that is created along the walls of the pump, propelling the charges through the fluid and setting the fluid in motion. This results in an induction EHD pump.

The electrical conductivity gradient can be obtained by several means. One method is based on the fact that electrical conductivity in dielectric fluids is often a strong function of temperature. Thus, if a temperature gradient exists, a conductivity gradient will also exist.

In an induction EHD pump, the charges in the fluid come from the dissociation of molecules into positive and negative ions. Therefore, there are local regions of positive or negative charge, but the net electric charge in the fluid is zero. This differs from ion-drag EHD pumping, which has a net charge imbalance due to generation of charges at the electrode–fluid interface.

When the walls of the pumping section are cooled, the thermal gradient results in a negative electrical conductivity gradient in the radial direction. This produces a variation in the electric field, which in turn results in a net charge inside the fluid medium. These charges are then attracted to electrodes imbedded in and along the wall of the pump. While the charges are delayed due to the thermal gradient, the voltage distribution on the electrodes is varied to create a traveling wave, which moves along the pump wall. The ions opposite the electrodes are attracted to the new voltage location, so that they tend to follow the wave, dragging the surrounding fluid with them and generating axial pumping. This is the basis for attraction type induction EHD pumping in which the fluid and the electric wave travel in the same direction.

If the walls are heated, the exact opposite takes place, with the formation of a positive electrical conductivity gradient in the radial direction. Fluid movement in the axial direction is then due to the repulsion of charges by the moving electric field. This is the basis for repulsion-type induction EHD pumping in which the fluid and electric wave travel in opposite directions.

The basic theory for thermal induction pumping was developed by Melcher (1966). He verified his results with a small working model and considered using EHD to study fluid properties as well as pumping.

Forced convection cooling of underground power cables using EHD pumping was investigated by Crowley et al. (1983). Kuo (1982) applied finite element techniques to induction pumping and suggested that EHD pumps could be a feasible alternative to mechanical pumps where dielectric fluids require both heat transfer and circulation.

Seyed-Yagoobi et al. (1989a, 1989b) examined EHD pumping theoretically and experimentally in a vertical axisymmetric configuration. The theoretical model included the effects of entrance conditions, buoyancy effects, and secondary flow, and was found to predict experimental velocities accurately in both the attraction and repulsion modes. The external pressure load on the pump was found to play a significant role in pumping performance, possibly resulting in two-directional flow. It was also observed that the pumping performance depends heavily on the temperature profile entering the pump as well as the electrical conductivity level of the fluid.

Washabaugh et al. (1989) examined induction EHD pumping of several fluids using a six-phase traveling wave. Two different pumping phenomena were discussed: ion migration pumping and charge relaxation pumping. It was found that each pumping mode has a characteristic time, and the pumping method that first comes into play is the one with the shorter characteristic time. Also, theoretical and experimental results showed that when charge relaxation pumping is predominant, the fluid flow direction can be altered. Reverse pumping, opposite to the direction of the traveling wave, occurs when the voltage to frequency ratio is small but switches to forward pumping when the ratio is large.

Contributed by the Heat Transfer Division and presented at the National Heat Transfer Conference, Atlanta, Georgia, August 8-11, 1993. Manuscript received by the Heat Transfer Division March 1993; revision received September 1993. Keywords: Augmentation and Enhancement, Forced Convection, Heat Exchangers. Associate Technical Editor: Y. Bayazitoglu.

Bohinsky and Seyed-Yagoobi (1990) investigated the performance of a cylindrical wire electrode induction EHD pump using several working fluids in order to find the optimum pumping conditions for these different fluids. Several of the fluids tested produced high velocities especially when the fluids were doped to electrical conductivity levels between 1×10^{-10} to 1×10^{-9} S/m.

The nonmechanical nature of EHD pumps, with no moving parts and no need for external pressure, makes them well suited for many applications such as circulating oil through heat exchangers. Low maintenance also makes them well suited for use with high-power underground cables, which normally require mechanical pumps at regular intervals along the cable route to cool the cables and increase power transfer. EHD pumping could also be used to increase the maximum heat capacity of heat pipes by increasing fluid flow through the capillary structure. More importantly, the light weight, low maintenance, and lack of vibration of EHD pumps make them promising for future outer space use.

EHD Assisted Heat Transfer

There has been no reported work that specifically covers the heat transfer enhancement that accompanies induction EHD pumping. Therefore, this section examines general EHD-assisted heat transfer.

Heat transfer enhancement techniques are classified in two separate categories. Passive methods require no direct application of external power. Extended surfaces, rough surfaces to promote turbulence, and swirl-flow devices to create secondary velocities are all examples of passive techniques.

Active methods of heat transfer enhancement require some amount of external power to operate. This technique includes mechanical stirring of the fluid, fluid vibration, and the use of electrostatic fields to disturb fluid flow.

Both active and passive methods are widely used to enhance heat transfer. Unfortunately, the increased pressure drop across a heat exchanger associated with most of these methods results in increased pumping power. EHD pumping, however, supplies both the pumping power and the method of heat transfer enhancement.

In the area of EHD-assisted heat transfer, most of the work has been done in examining heat transfer enhancement produced by using EHD effects to create secondary velocities in the fluid flow. Recently, Atten et al. (1989) examined the effects of electroconvection on heat transfer in a cylindrical pipe using a wire electrode along the axis of the cylinder. Results showed that the pressure drop along the pipe and the heat transfer from the liquid to the pipe were strongly affected by the turbulent agitation of the fluid by the electric field.

Nelson and Shaughnessy (1989) numerically studied a different class of electrically driven flows in which the fluid motion derives from buoyant forces resulting from Joule heating of the fluid. Their results indicated that the resulting flow depended upon four dimensionless quantities: the Grashof and Reynolds numbers and two newly defined dimensionless groups that characterized the degree of space-charge perturbation of the electric field and the rate of energy dissipation within the fluid.

Sato et al. (1991) examined an EHD pump using a ring-shaped electrode and a square-shaped electrode to study fluid flow due to dielectrophoretic force, suggesting that heat transfer would be augmented between the fluid and the pump walls. Flow rates of 10 cm/s were achieved with one set of electrodes.

Humidity, temperature, and pressure effects on corona discharge in a tube were studied experimentally by Ohadi et al. (1991). It was found that higher working fluid temperatures resulted in larger corona currents and higher corresponding heat transfer enhancements. The effect of humidity on heat transfer enhancement was found to depend also on the Reynolds number.

A flat plate heat transfer arrangement was investigated by Tada et al. (1991) using two flat heating plates with electrode wires running midway between the plates parallel to the fluid flow direction to promote secondary velocities. This arrangement proved to be beneficial to heat transfer between the fluid and the plates.

Similar experiments were conducted by Ishiguro et al. (1991) using parallel plates and wire electrodes close to each of the plate surfaces. The use of electric fields between the wires and the plates to disturb the flow along the wall was found to increase the rate of heat transfer.

Heat transfer enhancement using an EHD liquid jet was studied by Yabe (1991) by applying a high voltage across a ring and plate electrode system. Due to the flow ejected through the ring from the plate, the convective heat transfer from the plate was increased by a factor of 100.

Although electrohydrodynamcis and its use in heat transfer enhancement have been widely studied, no work has been reported that investigates the resulting heat transfer enhancement caused by induction EHD pumping of single-phase liquids. This paper examines experimentally the heat transfer enhancement that accompanies pumping in an induction EHD pump operated at various tilt angles. The main difference between this study and other work in EHD heat transfer enhancement is that the induction EHD pump is the only source of pumping as well as the basis for heat transfer enhancement.

Experimental Apparatus

The experimental apparatus for attraction mode induction pumping in a vertical configuration is shown in Fig. 1(*a*). The pumping section was constructed with two concentric tubes. An inner pumping tube with electrodes imbedded in the inner wall contained the pumping fluid, and an outer tube contained the cooling fluid, as shown in Fig. 1(*b*). A Lexan tube with a 2.5 cm inner diameter and 3 mm wall thickness was used for the pumping tube. It consisted of 78 electrodes spaced 1.0 cm apart with a total heat transfer length of 80 cm. The electrodes were constructed of 18 gage tin-copper wire press fit into grooves in the inner surface of the tube. A hole through the pumping tube wall in each groove allowed the electrodes to be connected to bus lines in the annulus section. The exposed electrode ends sticking out of the pumping tube in the annulus section were connected to three tin-copper bus lines placed 120 apart around the pumping tube to carry the three-phase traveling wave.

The outer Plexiglas tube was 7.6 cm in diameter and formed an annulus section through which cooling fluid flowed while the pump was operated in the attraction mode. The cooling fluid also served to insulate the exposed bus lines electrically. Two polyethylene flanges sealed the ends of the cooling section. This prevented any mixing between the pumping and cooling sections. The bus lines were attached to female banana plugs outside the outer tube to allow connection to the power supply,

The flanges on the pumping section allowed it to be bolted to the rest of the pumping loop, which was constructed with an inner diameter of 3.8 cm to minimize the pressure load on the induction pump. The heating section consisted of a copper pipe 55 cm long. A heating tape wrapped around the pipe supplied the necessary heat, and a 120–140 volt 10 amp variac was used to control the heating tape. Insulation around the heating tape was used to minimize heat loss to the surroundings. The heating section was located at one end of the straight section of the pumping loop in order to maximize the flow produced by natural convection when the pumping loop was tilted.

PVC pipe and fittings were used to construct the curved and remaining straight sections of the loop. Threaded fittings at

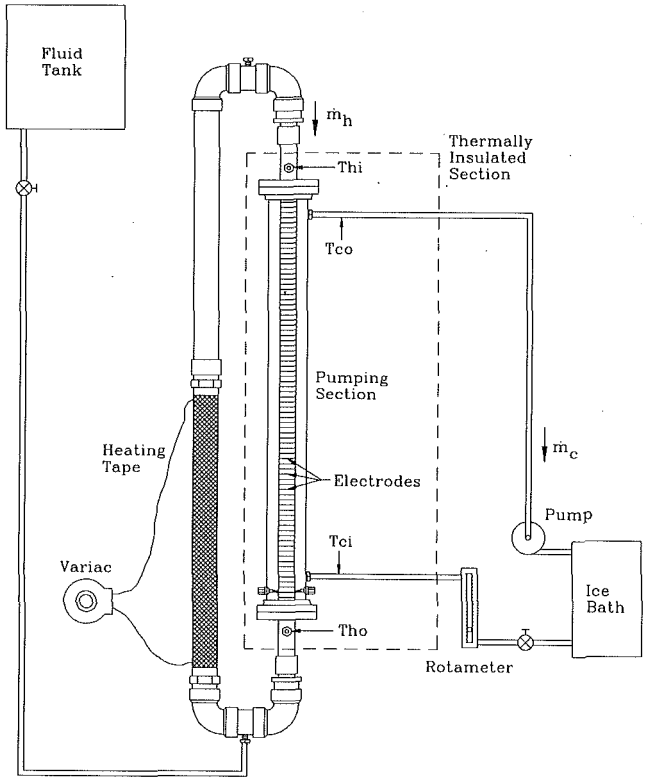

Fig. 1(*a*) Schematic of induction pumping apparatus in a vertical (90 deg tilt) configuration

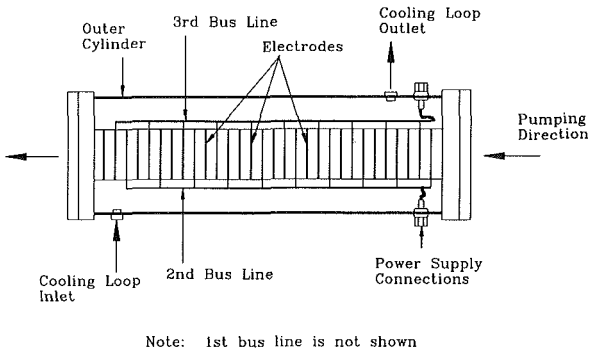

Note: 1st bus line is not shown

Fig. 1(*b*) Schematic of pumping section (not to scale)

either end of the curved sections allowed disassembly when necessary. The entire pumping and cooling sections were wrapped in several layers of fiberglass pipe insulation to minimize heat transfer from the surroundings.

The high-voltage, three-phase power supply used in the experiments was capable of generating sine, square, or triangle type waveforms at voltages of 0–12 kV, zero to peak, and frequencies between 0–13 Hz. Details of the power supply were described by Bohinsky (1991).

Two K-type thermocouples were mounted on brass rods, which could be lowered into the pumping tube on either side of the pumping section to obtain radial temperature profiles at the entrance and exit, ($T_{h,i}$ and $T_{h,0}$). A thermocouple thermometer was used to measure these temperatures. Two thermistor probes and a thermistor thermometer were used to measure the inlet and outlet temperatures of the cooling section, ($T_{c,i}$ and $T_{c,0}$). A rotameter was calibrated for the pumping fluid and operating temperatures and used to obtain accurate flow rates in the cooling loop.

The fluid used in the experiments was *n*-hexane, an aromatic

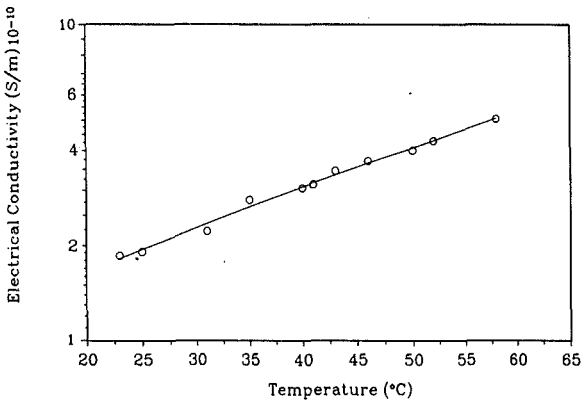

Fig. 2 Electrical conductivity of *n*-hexane as a function of temperature

fluid shown by Bohinsky (1991) to produce high pumping velocities. The electrical conductivity of the fluid was altered by doping it with overbased calcium sulfonate to the level that produced the highest pumping velocities. The resulting electrical conductivity as a function of temperature is shown in Fig. 2. Other details of the fluid properties were discussed by Margo (1992).

First, for each tilt angle that was investigated, tests were run using the induction pump to pump the fluid through the loop. The induction pump was operated in the attraction mode, where the walls of the pumping section were cooled with the external cooling loop. The frequency and peak voltage were varied over the desired range, and the inlet and outlet temperatures of the pumping and cooling sections were measured, as well as the cooling loop flow rate, power supply settings, and peak current.

In the second mode of operation, the pumping loop was monitored without energizing the induction pump to examine the effect of natural circulation on heat transfer. The heating and cooling sections were operated in the same manner as for induction pumping to keep the inlet temperatures relatively the same. This supplied the necessary natural convection to move the fluid through the loop (at angles other than 0). Again, the appropriate temperature and flow rate measurements were then taken in this configuration.

The third mode of operation was that of forced convection. The pumping loop had to be modified for these experiments by removing the curved PVC section at the end of the loop that was lowest when the loop was tilted. A mechanical centrifugal pump was then connected to the end of the loop to circulate the fluid. Without operating the induction pump, the fluid was then pumped at flow rates similar to those achieved with induction pumping. The necessary measurements were again taken at each flow rate.

The same procedures described below were used to calculate the heat transfer in the pumping section for each mode of operation. The most important heat transfer characteristic of interest was the total conductance of the pumping section, *UA*. In order to calculate the *UA* value, inlet and outlet temperatures of the cooling section and pumping section had to be known, as well as the cooling loop flow rate. Due to the existence of temperature profiles at the entrance and exit of the pumping section, bulk temperatures had to be calculated. This was accomplished by weighing each temperature measured across the radial direction based on the corresponding horizontal slice of the total cross-sectional area. This method assumed a uniform flow field or a constant velocity over the entire cross section at the entrance and exit of the pumping section, as well as a temperature gradient solely in the radial direction. Typical operating conditions for the experiments are shown in Table 1.

Table 1 Typical operating conditions

Voltage (zero to peak)	10.0 kV
Frequency	1.0 - 12.0 Hz
Waveform	sinusoidal
Wavelength	3.0 cm
Pumping Section Entrance Bulk Temperature	38 - 42 C
Cooling Loop Entrance Temperature	10 - 12 C
Cooling Loop Flow Rate	4.08×10^{-5} kg/s
Ambient Temperature	22 - 24 C

The heat transfer rate between the cooling fluid in the annulus and the pumping fluid in the inner tube was calculated from the cooling loop temperatures and flow rate as follows:

$$q = \dot{m}_c c_p (T_{c,o} - T_{c,i}) \tag{1}$$

This heat transfer rate could then be used to calculate the overall conductance value, UA, for the pumping section based on a logarithmic mean temperature difference relation for a concentric tube counterflow heat exchanger configuration

$$UA = \frac{q}{\Delta T_{LMTD}} \tag{2}$$

where

$$\Delta T_{LMTD} = \frac{(T_{h,i} - T_{c,o}) - (T_{h,o} - T_{c,i})}{\ln \dfrac{(T_{h,i} - T_{c,o})}{(T_{h,o} - T_{c,i})}} \tag{3}$$

The overall conductance of the pumping section including both convection along the tube walls and conductance through the tube wall could be calculated in the equation

$$\frac{1}{UA} = \frac{1}{A_i h_i} + \frac{\ln(D_o/D_i)}{2\pi kL} + \frac{1}{A_o h_o} \tag{4}$$

where h_i and h_o are the inside and outside convection coefficients, respectively, D_i is the inside diameter of the pumping tube, and D_o is the outside diameter. L is the length of the heat transfer section of the pumping tube, and k is the thermal conductivity of the Lexan tube. From the UA value, the overall heat transfer coefficient, U, could be calculated by dividing the overall conductance value by the surface area of the pumping section. Due to the thin wall of the pumping section, the outer surface area was used, where A is 0.0719 m^2. Note that because of the geometry of the pumping section, only the UA values were calculated rather than the inside convection coefficient. This was due to the complicated conduction taking place in the wall of the pumping tube as well as difficulties in calculating the outside convection coefficient. The bus lines tended to act as fins, and the annulus flow with respect to the inner tube was a combination of crossflow and parallel flow. This made it difficult to calculate the individual convection coefficients for both the pumping and cooling sections. In addition, the presence of the electrodes embedded in the wall further complicated the conduction taking place in the tube wall.

After calculating the heat transfer rate, the mass flow rate of the pumping section could be calculated based on the pumping section entrance and exit bulk temperatures by

$$\dot{m}_h = \frac{q}{c_p (T_{h,i} - T_{h,o})} \tag{5}$$

Experimental Results

The mass flow rates achieved with induction EHD pumping using n-hexane are shown in Fig. 3 for tilt angles of 0, 30, 60, and 90 deg. The mass flow rate for each angle reached a peak between 6.0 and 9.0 Hz and dropped as the frequency was changed from this optimum. Varying the frequency of the electric wave corresponds to changing the speed of the traveling wave along the walls of the pumping section. Thus, as the frequency and wave speed increase, the pumping velocity increases as the charges in the fluid follow the wave. However, beyond a certain point, the wave moves too fast for the charges to keep up, and the fluid velocity again drops. The highest flow rate achieved was 0.167 kg/s, corresponding to a velocity of 49 cm/s or a Reynolds number of 31,800, reached at 8.0 Hz with a 90 tilt configuration. The lowest peak flow rate occurred at a 30 deg tilt angle, where a mass flow rate of 0.065 kg/s was reached, corresponding to a velocity of 20 cm/s or a Reynolds number of 12,400. The performance of the temperature-induced EHD pump is dependent on the temperature profiles within the pumping section. The temperature distributions are different under different tilt angles due to the interaction of induction EHD pumping and natural circulation. This results in mass flow rates that are dependent on tilt angle.

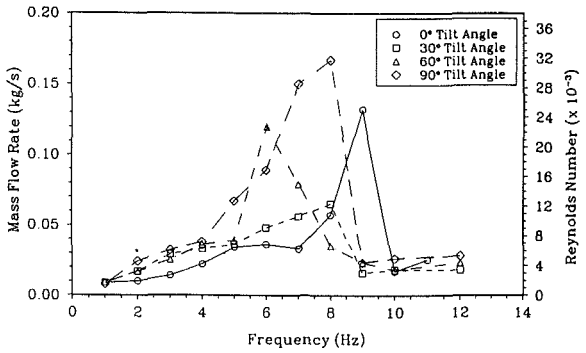

Fig. 3 Mass flow rate and Reynolds number as a function of frequency for induction pumping at all tilt angles

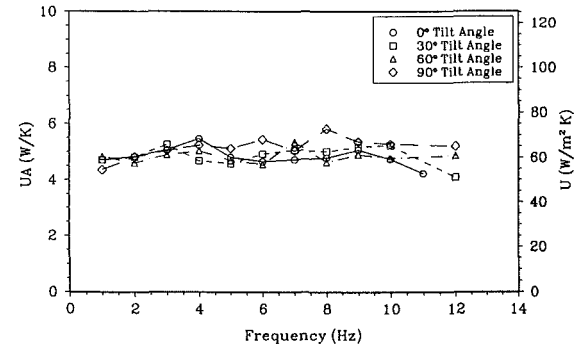

Fig. 4 UA and U values as a function of frequency for induction pumping at all tilt angles

The corresponding UA values for the four angles are shown in Fig. 4. No predominant peaks were seen for the UA values such as those seen in the mass flow rate. All UA values were in the range of 4.0 and 5.8 W/K, with peak UA values occurring between 5.26 and 5.82 W/K.

In comparing these induction pumping UA values to those for forced pumping and natural circulation, the highest UA values for a given induction pumping flow rate were used. This was a result of several slightly different UA values being possible for a given flow rate, since the flow rate is frequency dependent. Otherwise, the UA values remained relatively constant at all mass flow rates. The resulting UA values for induction pumping, forced pumping, and natural circulation at all tilt angles are shown in Figs. 5–8. The UA values corresponding to forced pumping ranged mainly from 3.0 to 4.0 W/K at all angles, while the UA values for natural circulation ranged from 3.0 to 3.5 W/K. These UA values for natural circulation were very close to those for forced pumping at the

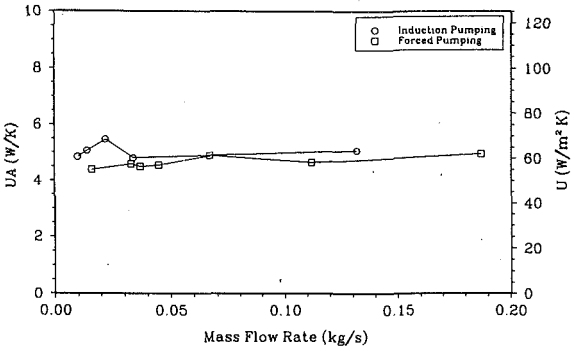

Fig. 5 Comparison of *UA* and *U* values for induction pumping, forced pumping, and natural circulation at 0 deg tilt

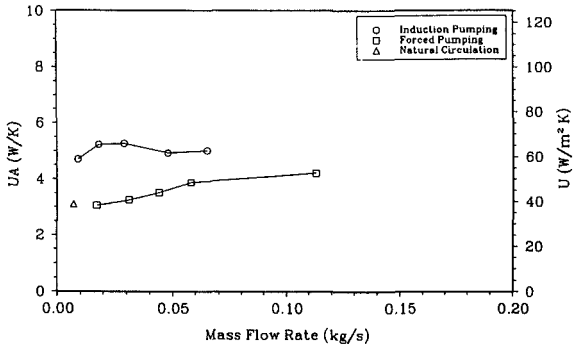

Fig. 6 Comparison of *UA* and *U* values for induction pumping, forced pumping, and natural circulation at 30 deg tilt

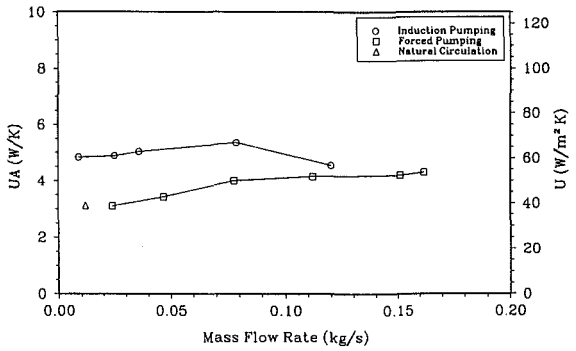

Fig. 7 Comparison of *UA* and *U* values for induction pumping, forced pumping, and natural circulation at 60 deg tilt

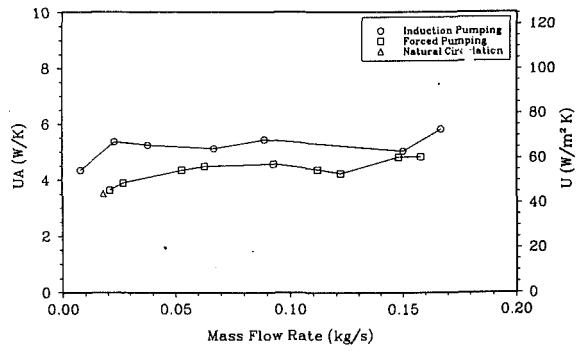

Fig. 8 Comparison of *UA* and *U* values for induction pumping, forced pumping, and natural circulation at 90 deg tilt

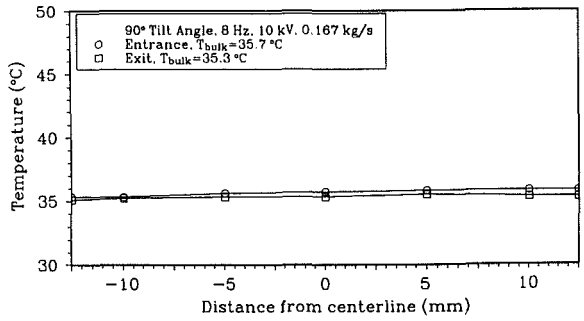

Fig. 9 Pumping section entrance and exit temperature profiles for peak flow rate induction pumping at 90 deg tilt

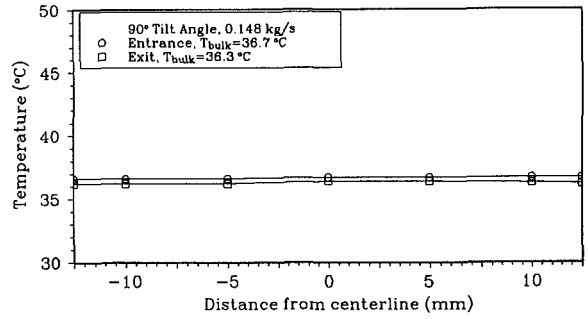

Fig. 10 Pumping section entrance and exit temperature profiles for forced pumping at 90 deg tilt

same low flow rates. This is expected since the flow through the pumping section due to natural circulation should be very similar to that of forced pumping at a similar flow rate. Only with induction pumping are secondary velocities highly affected.

In the horizontal or 0 deg tilt configuration, there was very little difference between the *UA* values for induction pumping and forced pumping. The highest *UA* value with induction pumping was 23 percent higher than that for forced pumping at a similar flow rate, but at other flow rates the difference was much less significant.

In the 30 deg tilt configuration, induction pumping increased the overall conductance by 28 to 71 percent as compared to forced pumping. The corresponding increase over natural circulation was 51 percent at a similar flow rate or 71 percent when compared to the peak *UA* value for induction pumping.

At 60 deg tilt, the overall *UA* value was increased by 10 to 58 percent over forced pumping at similar flow rates. The increase over natural circulation was 55 percent for a similar flow rate or 71 percent for the peak *UA* value with induction pumping.

In the vertical or 90 deg tilt configuration the overall conductance value was increased by 14 to 48 percent over forced pumping. The increase in *UA* value over natural circulation was 42 percent when compared to induction pumping at a similar flow rate or 66 percent when compared to the peak *UA* value.

The dependence of *UA* value on tilt angle was not consistent. This was due to the interaction of free convection and the radial and axial pumping motion. In particular, the pumping motion was due to temperature profiles, which are in turn affected by the tilt angle.

Since comparisons were made between *UA* values rather than individual convection coefficients, the actual increase in the inside convection coefficient was much greater than the values given here. This was due to the fact that both the outside convection coefficient and the conduction through the walls of the pump are included in the *UA* value.

Typical pumping section entrance and exit temperature profiles for induction pumping and forced pumping are shown in Figs. 9 and 10. As a result of the turbulent flow, the temper-

ature profiles were relatively uniform at both the entrance and exit of the pumping section. Thus the method of evaluating the bulk temperatures based on a uniform flow field was acceptable. Despite the fact that no visible thermal boundary layer formed during forced pumping, which could be broken up with induction pumping, higher UA values were achieved with induction pumping at most angles compared to forced pumping. This suggests that induction pumping with n-hexane produces even more mixing in the pumping section than normal turbulent flow, resulting in higher overall conductance values. The small radial temperature gradient present was still enough to result in significant pumping.

The repeatability of the experiments resulted in a precision uncertainty of approximately 7.5 percent in the UA value and 14 percent in the mass flow rate. Throughout the experiments, the electrical conductivity of the fluid was monitored to ensure that no changes occurred. The electrical conductivity of n-hexane monitored at 23°C remained in the range of 1.1×10^{-10} to 1.5×10^{-10} S/m. Although similar variations were seen at different temperatures, the shape of the conductivity curve remained the same.

To achieve significant heat transfer enhancement with an induction EHD pump, the fluid properties that play a critical role are electrical conductivity and viscosity, as shown by Bohinsky and Seyed-Yagoobi (1990). If a given fluid with an electrical conductivity less than 10^{-10} S/m were doped using an additive to bring the conductivity into the range of 10^{-10} to 10^{-9} S/m, significant pumping may be achieved also resulting in heat transfer enhancement.

Conclusions

For EHD pumping to be considered for use in heat transfer applications such as heat exchangers, a better understanding of the heat transfer enhancement resulting from such pumping was necessary. The induction EHD pump, which was designed and built for these heat transfer experiments, was capable of pumping n-hexane at velocities as high as 49 cm/s, corresponding to a Reynolds number of 31,800 and a mass flow rate of 0.167 kg/s. This pumping mechanism was also a method of active heat transfer enhancement, increasing the overall conductance of the heat transfer section by as much as 71 percent when comparing induction pumping to forced pumping at a similar flow rate. A similar increase of 71 percent in the overall conductance value was seen when comparing the peak UA value with induction pumping to that of natural convection. Due to the turbulent flow conditions, the operating frequency of the induction pump was found to have a significant effect on the mass flow rate but little influence on the heat transfer enhancement.

Additional work has been done by Seyed-Yagoobi et al. (1994) to examine the enhancement of heat transfer resulting from induction pumping under laminar flow conditions using dodecylbenzene, a synthetic petroleum fluid, as the working fluid. The overall conductance value was increased by as much as 122 percent. This was due to the mixing that occurred with induction pumping, which would impede the development of a thermal boundary layer. Due to the laminar flow in this case, the operating frequency did have an effect on the peak UA value.

The heat transfer enhancement seen in these experiments was significant, especially considering the fact that the increase in the inside convection coefficient alone was much higher than the increase in the measured UA value.

Acknowledgments

This work was supported in part by the McDonnell Douglas Space Division Company and the NASA Center for Space Power at Texas A&M University.

References

Atten, P., Elouadie, L., and Malraison, B., 1989, "Electroconvection in a Wire-Cylinder Geometry With Forced Flow and Its Effect on Heat Transfer," *Proceedings, IEEE-IAS Annual Meeting*, San Diego, CA, pp. 2078–2083.

Bohinsky, B. J., and Seyed-Yagoobi, J., 1990, "Induction Electrohydrodynamic Pumping—Selecting an Optimum Working Fluid," *Proceedings, IEEE-IAS Annual Meeting*, Seattle, WA, pp. 795–801.

Bohinsky, B. J., 1991, "An Experimental Study of Induction Electrohydrodynamic Pumping in a Horizontal Axisymmetric Configuration," Master of Science Thesis, Department of Mechanical Engineering, Texas A&M University.

Crowley, J. M., Chato, J. C., Abdulhadi, R., Kelly, D. P., Kervin, D. J., Krein, P. T., Kuo, B. S., Ochs, H., and Seyed-Yagoobi, J., 1983, "Electrohydrodynamic Pumping in Cable Pipes," EPRI EL-2834, Project 7871-1, Final Report, February.

Crowley, J. M., Wright, G., and Chato, J. C., 1990, "Selecting a Working Fluid to Increase the Efficiency and Flow Rate of an EHD Pump," *IEEE Transactions on Industry Applications*, Vol. 26, pp. 42–49.

Ishiguro, H., Nagata, S., Yabe, A., and Nariai, H., 1991, "Augmentation of Forced-Convection Heat Transfer by Applying Electric Fields to Disturb Flow Near a Wall," *Proceedings, ASME/JSME Thermal Engineering Conference*, Vol. 3, pp. 25–31.

Kuo, B. S., 1982, "Flow Characteristics and Heat Transfer for Pressure and Electric Field Driven Laminar Flow With Temperature-Dependent Properties in a Pipe With Irregular Cross Section," Ph.D. Thesis, Department of Mechanical and Industrial Engineering, University of Illinois at Urbana-Champaign.

Margo, B. D., 1992, "Heat Transfer Enhancement Resulting From Induction Electrohydrodynamic Pumping," Master of Science Thesis, Department of Mechanical Engineering, Texas A&M University.

Melcher, J. R., 1966, "Traveling-Wave Induced Electroconvection," *Physics of Fluids*, Vol. 9, pp. 1548–1555.

Nelson, D. A., and Shaughnessy, E. J., 1989, "An Exact Solution for Electrically Driven Convection Between Vertical Electrodes," *Proceedings, IEEE-IAS Annual Meeting*, San Diego, CA, pp. 2084–2089.

Ohadi, M. M., Weber, J. M., Kim, S. W., and Whipple, R. L., 1991, "Effect of Humidity, Temperature, and Pressure on Corona Discharge Characteristics and Heat Transfer Enhancements in a Tube," *Proceedings, ASME/JSME Thermal Engineering Conference*, Reno, NV, Vol. 3, pp. 15–24.

Sato, M., Yabe, A., and Taketani, T., 1991, "Heat Transfer Enhancement by Applying an Electro-Hydrodynamical Pump Utilizing Dielectrophoretic Force," *Proceedings, ASME/JSME Thermal Engineering*, Reno, NV, Vol. 3, pp. 3–8.

Seyed-Yagoobi, J., Chato, J. C., Crowley, J. M., and Krein, P. T., 1989a, "Induction Electrohydrodynamic Pump in a Vertical Configuration: Part 1—Theory," ASME JOURNAL OF HEAT TRANSFER, Vol. 111, pp. 664–669.

Seyed-Yagoobi, J., Chato, J. C., Crowley, J. M., and Krein, P. T., 1989b, "Induction Electrohydrodynamic Pump in a Vertical Configuration: Part 2—Experimental Study," ASME JOURNAL OF HEAT TRANSFER, Vol. 111, pp. 670–674.

Seyed-Yagoobi, J., Margo, B. D., and Bryan, J. E., 1994, "Effect of Frequency on Heat Transfer Enhancement in Temperature Induced Electrohydrodynamic Pumping," *IEEE Transactions on Dielectrics and Electrical Insulation*, Vol. 1, No. 3, pp. 468–473.

Tada, Y., Takimoto, A., and Hayashi, Y., 1991, "Heat Transfer Enhancement in a Convective Field by Applying Ionic Wind," *Proceedings, ASME/JSME Thermal Engineering Conference*, Reno, NV, Vol. 3, pp. 9–14.

Washabaugh, A. P., Zahn, M., and Melcher, J. R., 1989, "Electrohydrodynamic Traveling-Wave Pumping of Homogeneous Semi-insulating Liquids," *IEEE Transactions on Electrical Insulation*, Vol. 24, No. 5, pp. 807–834.

Yabe, A., 1991, "Active Heat Transfer Enhancement by Applying Electric Fields," *Proceedings, ASME/JSME Thermal Engineering Conference*, Reno, NV, Vol. 3, pp. xv–xxiii.

Analysis of Heat Transfer Regulation and Modification Employing Intermittently Emplaced Porous Cavities

K. Vafai
Professor.
Fellow ASME

P. C. Huang

Department of Mechanical Engineering,
The Ohio State University,
Columbus, OH 43210

The present work forms a fundamental investigation on the effects of using intermittently porous cavities for regulating and modifying the flow and temperature fields and therefore changing the skin friction and heat transfer characteristics of an external surface. A general flow model that accounts for the effects of the impermeable boundary and inertial effects is used to describe the flow inside the porous region. Solutions of the problem have been carried out using a finite-difference method through the use of a stream function-vorticity transformation. Various interesting characteristics of the flow and temperature fields in the composite layer are analyzed and discussed in detail. The effects of various governing dimensionless parameters, such as the Darcy number, Reynolds number, Prandtl number, the inertia parameter as well as the effects of pertinent geometric parameters are thoroughly explored. Furthermore, the interactive effects of the embedded porous substrates on skin friction and heat transfer characteristics of an external surface are analyzed. The configuration analyzed in this work provides an innovative approach in altering the frictional and heat transfer characteristics of an external surface.

Introduction

Forced convection heat transfer through porous media has been a major topic for various studies during the past decades due to many engineering applications such as thermal insulation engineering, water movements in geothermal reservoirs, underground spreading of chemical waste, nuclear waste repository, grain storage, and enhanced recovery of petroleum reservoirs (Tien and Vafai, 1989; De Vries, 1958). The majority of the previous investigations include flow through a semi-infinite porous medium for external boundaries, and flow through structures that are fully filled with the porous medium for internal flows. However, consideration of the interaction between the porous-saturated region and the fluid region did not form a part of most of these studies due to the difficulties in simultaneously solving the coupled momentum equations for both porous and fluid regions. There has been very little work done on these types of interactions, which can occur in various practical applications. Furthermore, many of the existing studies on convective heat transfer in porous media are based on the Darcy's law, which is found to be inadequate for the formulation of fluid flow and heat transfer problems in porous media when there is an impermeable boundary and/or the Reynolds number based on the pore size is greater than unity.

A general theory and numerical calculation techniques for flow field and heat transfer in recirculating flow without including the porous medium have been developed by Gosman (1976), and were successfully used by various investigators such as Gooray (1982) and Gooray et al. (1981, 1982). They have shown that these methods can be applied to give reasonably accurate quantitative heat transfer results for the separated forced convection behind a backstep. A few studies have been reported on forced convection in a rectangular cavity. Yamamoto et al. (1979) experimentally studied the forced convection on a heated bottom surface of a cavity situated on a duct wall. They have shown that reattachment of separated flow for shallow cavities and vortex flow for deeper ones had a large effect on the heat transfer behavior on the heated bottom surface. Sinha et al. (1981) reported the experimental results for laminar separating flow over backsteps and cavities. They found that cavities can be classified as closed, shallow open, and open depending on the range of the value of the aspect (depth-width) ratio. Aung (1983) performed an experimental investigation of separated forced convection laminar flow past two-dimensional rectangular cavities where the walls are kept at a constant temperature. He found that the temperature distribution outside of the cavity had little influence on the flow in the cavity and the local heat transfer distribution on the cavity floor attains a maximum value that is located between the midpoint of the cavity floor and the downstream wall.

Bhatti and Aung (1984) numerically examined the laminar separated forced convection in the cavities. They found that the average Nusselt number in open cavity flow is related to the Reynolds number raised to a power that depends on the aspect ratio of the cavity and that the influence of the upstream boundary layer thickness on the heat transfer in the cavity is negligible. Most of the existing related studies on convection in composite systems were focused on the problem of natural convection in an enclosure (Beckermann et al., 1988; Bejan, 1984; Sathe et al., 1988; Cheng, 1978; Poulikakos and Bejan, 1985) or forced convection in a duct (Poulikakos and Kazmierczak, 1987; Bejan, 1984), or external and internal boundaries (Vafai and Kim, 1990; Poulikakos, 1986; Bejan, 1984). However, to the best of the author's knowledge, there have not been any investigations on the forced convection over porous cavities in the open literature.

The present work constitutes one of the first analyses of the separated forced convection through porous cavities. The pre-

Contributed by the Heat Transfer Division for publication in the JOURNAL OF HEAT TRANSFER. Manuscript received by the Heat Transfer Division September 1992; revision received August 1993. Keywords: Materials Processing and Manufacturing Processes, Porous Media, Thermal Packaging. Associate Technical Editor: C. E. Hickox, Jr.

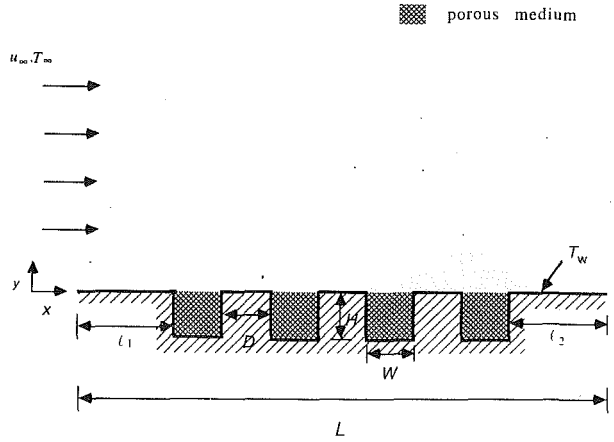

Fig. 1 Schematic diagram of flow and heat transfer over intermittently emplaced porous cavities

sent investigation provides a valuable fundamental framework for predicting heat transfer and fluid flow characteristics for other composite systems. The results and fundamental information presented here along with those analyzed by Huang and Vafai (1993) can be extended to examine various applications such as in electronic cooling and in heat exchanger design, reduction of skin friction and heat transfer enhancement or augmentation, some of the manufacturing processes, geothermal reservoirs, and oil extraction. In addition, the present work constitutes an innovative way of regulating and modifying the skin friction and heat transfer characteristics of an external surface.

Analysis and Formulation

The configuration for this problem is shown in Fig. 1. The height and width of the porous cavities are H and W, respectively, the distance between two cavities is D, the length of the wall is L, the free-stream velocity is u_∞, and the free-stream temperature is T_∞. The wall is maintained at a constant temperature T_w. It is assumed that the flow is steady, laminar, incompressible, and two dimensional. In addition, the thermophysical properties of the fluid and the porous matrix are assumed to be constant and the fluid-saturated porous medium is considered homogeneous and isotropic and in local thermodynamic equilibrium with the fluid. For the fluid region the conservation equations for mass, momentum, and energy are

$$\nabla \cdot \mathbf{v} = 0 \tag{1}$$

$$\mathbf{v} \cdot \nabla \mathbf{v} = -\frac{1}{\rho_f} \nabla P + \nu_f \nabla^2 \mathbf{v} \tag{2}$$

$$\mathbf{v} \cdot \nabla T = \alpha_f \nabla^2 T \tag{3}$$

Based on the Brinkman–Forchheimer-extended Darcy model, which accounts for the effects of the inertial and impermeable boundary, the mass, momentum and energy equations in the porous matrix (Vafai and Tien, 1981, 1982) can be expressed as

$$\nabla \cdot \mathbf{v} = 0 \tag{4}$$

$$\mathbf{v} \cdot \nabla \mathbf{v} = -\frac{1}{\rho_f} \nabla P + \nu_{\text{eff}} \nabla^2 \mathbf{v} - \left(\frac{\nu_{\text{eff}}}{K} + \frac{F\epsilon}{\sqrt{K}} |\mathbf{v}| \right) \mathbf{v} \tag{5}$$

$$\mathbf{v} \cdot \nabla T = \alpha_{\text{eff}} \nabla^2 T \tag{6}$$

where K and ϵ are the porous medium's permeability and porosity, and ν_{eff} and α_{eff} are the effective kinematic viscosity and thermal conductivity of the porous medium. It should be noted that velocity $\mathbf{v}$ and temperature T in the porous region are both volume-averaged quantities as described by Vafai and Tien (1981). The boundary conditions necessary to complete the problem formulation are

$$u = u_\infty, \quad v = 0, \quad P = P_\infty, \quad T = T_\infty \quad \text{at} \quad x = 0 \tag{7}$$

$$u = 0, \quad v = 0, \quad T = T_w \quad \text{on all solid walls} \tag{8}$$

$$u = u_\infty, \quad P = P_\infty, \quad T = T_\infty \quad \text{as } y \to \infty \tag{9}$$

In addition to these, the two sets of conservation equations are coupled by the following matching conditions at the porous/fluid interface:

$$u|_{y=H^-} = u|_{y=H^+}, \quad v|_{y=H^-} = v|_{y=H^+} \tag{10a}$$

$$P|_{y=H^-} = P|_{y=H^+}, \quad \mu_{\text{eff}} \frac{\partial v}{\partial y}\bigg|_{y=H^-} = \mu_f \frac{\partial v}{\partial y}\bigg|_{y=H^+} \tag{10b}$$

$$\mu_{\text{eff}} \left(\frac{\partial u}{\partial y} + \frac{\partial v}{\partial x} \right)\bigg|_{y=H^-} = \mu_f \left(\frac{\partial u}{\partial y} + \frac{\partial v}{\partial x} \right)\bigg|_{y=H^+} \tag{10c}$$

$$T|_{y=H^-} = T|_{y=H^+}, \quad k_{\text{eff}} \frac{\partial T}{\partial y}\bigg|_{y=H^-} = k_f \frac{\partial T}{\partial y}\bigg|_{y=H^+} \tag{10d}$$

Nomenclature

A = dimensionless geometric parameter = W^*/H^*
B = dimensionless geometric parameter = D^*/H^*
C_f = friction coefficient
D = spacing between the porous cavities, m^{-1}
Da_L = Darcy number = K/L^2
F = a function used in expressing inertia terms
h = convective heat transfer coefficient, $Wm^{-2}K^{-1}$
H = thickness of the porous medium, m
k = thermal conductivity, $Wm^{-2}K^{-1}$
K = permeability of the porous medium, m^2
ℓ_1 = length of plate upstream from the cavities, m
ℓ_2 = length of plate downstream from the cavities, m
L = length of the external boundary as shown in Fig. 1, m
N = number of cavities
Nu = Nusselt number = hx/k_f
P = pressure, Pa
Pe_L = Peclet number = $u_\infty L/\alpha$
Pr = Prandtl number = ν/α
Re = Reynolds number = $u_\infty L/\nu$
S^Φ = source term, used in Eq. (24)
T = temperature, K
u = x-component velocity, ms^{-1}
v = y-component velocity ms^{-1}
$\mathbf{v}$ = velocity vector, ms^{-1}
W = width of the porous cavity, m
x = horizontal coordinate, m
y = vertical coordinate, m
α = thermal diffusivity, m^2s^{-1}
α_{eff} = effective thermal diffusivity = $k_{\text{eff}}/\rho_f c_{p,f}$, m^2s^{-1}
ϵ = porosity of the porous medium
θ = dimensionless temperature = $(T - T_\infty)/(T_w - T_\infty)$
Λ_L = inertial parameter = $FL\epsilon/\sqrt{K}$
μ = dynamic viscosity, $kgm^{-1}s^{-1}$
ν = kinematic viscosity, m^2s^{-1}
ξ = vorticity
ρ = fluid density, kgm^{-3}
Φ = transported property; general dependent variable
ψ = stream function

Superscripts

* = dimensionless quantity

Subscripts

eff = effective
f = fluid
∞ = condition at infinity

Vorticity-Stream Function Formulation. The governing equations above are cast in terms of the vorticity-stream formulation. Introducing stream function and vorticity as

$$u=\frac{\partial\psi}{\partial y},\quad v=-\frac{\partial\psi}{\partial x} \tag{11}$$

$$\xi=\frac{\partial v}{\partial x}-\frac{\partial u}{\partial y} \tag{12}$$

the governing equations for the whole region can be expressed in dimensionless form as

$$\frac{\partial\psi^*}{\partial y^*}\frac{\partial\xi^*}{\partial x^*}-\frac{\partial\psi^*}{\partial x^*}\frac{\partial\xi^*}{\partial y^*}=\frac{1}{\mathrm{Re}_L}\nabla^2\xi^*+S^* \tag{13}$$

$$\nabla^2\psi^*=-\xi^* \tag{14}$$

$$\frac{\partial\psi^*}{\partial y^*}\frac{\partial\theta}{\partial x^*}-\frac{\partial\psi^*}{\partial x^*}\frac{\partial\theta}{\partial y^*}=\nabla\cdot\left(\frac{1}{\mathrm{Pe}_L}\nabla\theta\right) \tag{15}$$

where in the fluid region

$$\mathrm{Re}_L=\frac{u_\infty L}{\nu_f},\quad \mathrm{Pe}_L=\frac{u_\infty L}{\alpha_f},\quad S^*=0 \tag{16a}$$

and in the porous region

$$\mathrm{Pe}_L=\frac{u_\infty L}{\alpha_{\mathrm{eff}}},\quad \mathrm{Da}_L=\frac{K}{L^2},\quad \Lambda_L=\frac{FL\epsilon}{K^{1/2}} \tag{16b}$$

$$S^*=-\frac{1}{\mathrm{Re}_L\mathrm{Da}_L}\xi^*-\Lambda_L|\mathbf{v}^*|\xi^*-\Lambda_L\left(v^*\frac{\partial|\mathbf{v}^*|}{\partial x^*}-u^*\frac{\partial|\mathbf{v}^*|}{\partial y^*}\right)+\frac{u^*}{\mathrm{Re}_L}\frac{\partial}{\partial y^*}\left(\frac{1}{\mathrm{Da}_L}\right)-\frac{v^*}{\mathrm{Re}_L}\frac{\partial}{\partial x^*}\left(\frac{1}{\mathrm{Da}_L}\right)+|\mathbf{v}^*|u^*\frac{\partial}{\partial y^*}(\Lambda_L)-|\mathbf{v}^*|v^*\frac{\partial}{\partial x^*}(\Lambda_L) \tag{17}$$

the dimensionless boundary conditions thus become

$$\psi^*=y^*,\quad \xi^*=-\frac{\partial^2\psi^*}{\partial x^{*2}},\quad \theta=0,\ \text{at } x^*=0 \tag{18}$$

$$\psi^*=0,\quad \xi^*=-\frac{\partial^2\psi^*}{\partial x^{*2}},$$

$$\theta=1,\ \text{at } x^*=\begin{cases}l_1^*+(N-1)(W^*+D^*)\\ l_1^*+NW^*+(N-1)D^*\end{cases},\quad 0>y^*>-H^* \tag{19}$$

$$\psi^*=0,\quad \xi^*=-\frac{\partial^2\psi^*}{\partial y^{*2}},\quad \theta=1,$$

$$\text{at } x^*=\begin{cases}l_1^*+(N-1)(W^*+D^*)<x^*<l_1^*+NW^*+(N-1)D^*,\ y^*=-H^*\\ 0<x^*<l_1^*\\ l^*+NW^*+(N-1)D<x^*<l_1^*+NW^*+ND^*\\ (1-l_2^*)<x^*<1\end{cases},\qquad y^*=0 \tag{20}$$

$$\frac{\partial\psi^*}{\partial y^*}=1,\quad \xi^*=-\frac{\partial^2\psi^*}{\partial x^{*2}},\quad \theta=0,\ \text{as } y^*\to\infty \tag{21}$$

where N (= 1, 2, 3, 4) is the number of porous cavities. Note that the variables in the equations above are defined as follows:

$$x^*=\frac{x}{L},\quad y^*=\frac{y}{L},\quad u^*=\frac{u^*}{u_\infty},\quad v^*=\frac{v}{u_\infty},\quad \mathbf{v}^*=\sqrt{u^{*2}+v^{*2}} \tag{22a}$$

$$\psi^*=\frac{\psi}{u_\infty L},\quad \xi^*=\frac{L\xi}{u_\infty},\quad \theta=\frac{T-T_\infty}{T_w-T_\infty} \tag{22b}$$

$$H^*=\frac{H}{L},\quad l_1^*=\frac{l_1}{L},\quad l_2^*=\frac{l_2}{L},\quad D^*=\frac{D}{L},\quad W^*=\frac{W}{L} \tag{22c}$$

From the equations above, boundary conditions, and geometry arrangement of cavities given above it is seen that the present problem is governed by seven dimensionless parameters. These are Darcy, Reynolds, and Prandtl numbers, the inertia parameter, the number of cavities N, and the geometry parameters A and B, where

$$A=\frac{W^*}{H^*},\quad B=\frac{D^*}{H^*}. \tag{23}$$

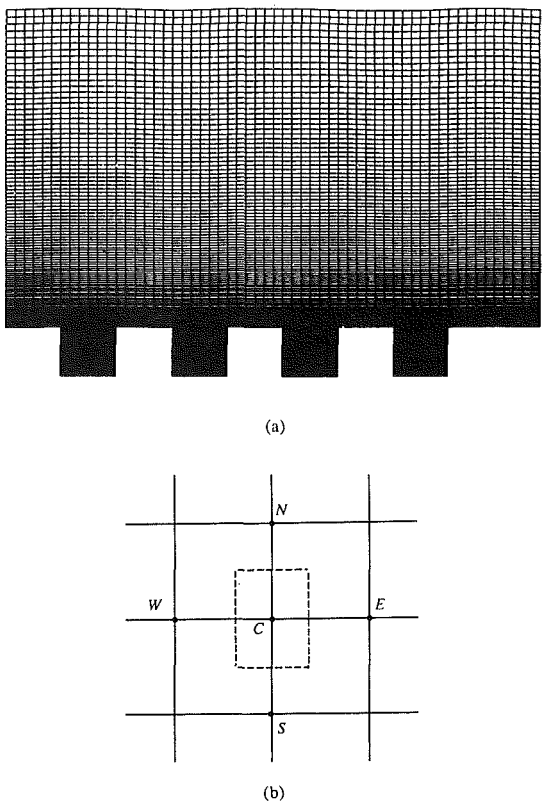

Fig. 2 *(a)* **The nonuniform grid system for the whole computational domain; (*b*) local integration cell in the computational domain**

Numerical Scheme and Stability and Accuracy Considerations

Employing a nonuniform rectangular grid system, the finite-difference form of the vorticity transport, stream function, and energy equations were derived using control-volume integration of these differential equations over discrete cells surrounding the grid points, as shown in Fig. 2. In the above discretization scheme the upwind and central-differencing formats are also introduced for the convective and diffusive terms, respectively. This results in a system of equations of the following form:

$$C_C\Phi_C=C_N\Phi_N+C_S\Phi_S+C_E\Phi_E+C_W\Phi_W+S^\Phi \tag{24}$$

where Φ stands for the transported variables, Cs are coefficients combining convective and diffusive terms, and S^Φ is the appropriate source term. The subscripts on C denote the main grid points surrounded by the four neighboring points denoted as N, S, E, and W.

To ensure the continuity of the diffusive and convective fluxes across the interface without requiring the use of an excessively fine grid structure, the harmonic mean formulation suggested by Patankar (1980) was used to handle abrupt changes in thermophysical properties, such as the permeability and the thermal conductivity, across the interface. Moreover, the source terms incorporated with the boundary and inertia effects were linearized as described by Patankar (1980). The vorticity at sharp corners requires special consideration. Seven different methods of handling this corner vorticity are discussed by Roache (1976). Here average treatment for the evaluation of vorticity suggested by Greenspan (1969) is used to model the mathematical limit of a sharp corner as appropriately as possible.

The finite difference equations thus obtained were solved by the extrapolated-Jacobi scheme. This iterative scheme is based on a double cyclic routine, which translates into a sweep of only half of the grid points at each iteration step (Adams and Ortega, 1982). In this work convergence was considered to have been achieved when the absolute value of relative error on each grid point between two successive iterations was found to be less than 10^{-6}. The iterative procedure was then terminated. To examine the independence of the results on the chosen Δx and Δy, many numerical runs with different combinations of Δx and Δy were performed. This was done by a systematic decrease in the grid size until further refinement of the grid size resulted in less than 1 percent difference in the converged results. A grid size of 162×188 was finally found to model accurately the flow field described in the results for all the considered cases. The application of the boundary condition at infinity, at a finite distance from the wall was given careful consideration. This was done through the following procedure. The length of the computational domain in the vertical direction was systematically increased until the maximum vorticity changes for two consecutive runs would become less than 1 percent. Therefore, in our investigation the computational domain is chosen to be larger than the physical domain.

Along the x direction, the computational domain starts at a distance of one-fifth of total length upstream, i.e., L, of the physical domain. This procedure eliminates the errors associated with the singular point at the leading edge of the composite system. On the other side, the computational domain is extended over a distance of two-fifths of the total length downstream from the trailing edge of the physical domain. Since the present problem has a significant parabolic character, the downstream boundary condition on the computational domain does not have much influence on the physical domain. In the y direction the computational domain is extended up to a distance sufficient enough to ensure that even for the smallest value of the Reynolds number the upper boundary lies well outside the boundary layer through the entire domain. In the present study locating the upper boundary at a distance of eight times the depth of the cavity has been found to be sufficient. Extensions beyond eight times the depth of the cavity had no effect on the solution.

To validate the numerical scheme used in the present study, initial calculations were performed for laminar flow over a flat plate (i.e., $H^* = 0$, for no porous substrate) and that over a flat plate embedded in a porous medium (i.e., $H^* \to \infty$ and $W^* \to \infty$, representing the full porous medium case). The results for $H^* = 0$ agree to better than 1 percent with boundary layer similarity solutions for velocity and temperature fields. The results for $H^* \to \infty$ and $W^* \to \infty$ agree extremely well with data reported by Vafai and Thiyagaraja (1987) and Beckermann et al. (1987).

Results and Discussion

The effects of the geometric arrangements of the porous cavities as well as the effects of different values of Ra_L, Da_L, Pr, and Λ_L on the flow and temperature fields were investigated. Table 1 displays various input parameter sets considered in this analysis. The parameter sets presented in Table 1 were only a subset of much larger set that was investigated in this work. The parameter sets presented in Table 1 were found to be most important in revealing pertinent aspects of the geometric arrangements of the porous cavities and variations in the thermophysical properties. Figures 3–12 show streamlines and isotherms over multiple porous cavities for the corresponding cases listed in Table 1. To illustrate the results of flow and temperature fields inside the porous cavity, only the portion that concentrates on the porous/fluid region and its close vicinity is presented. However, it should be noted that the computational domain included a significantly larger region than what is displayed in the subsequent figures. Furthermore, for brevity some figures are not shown here.

Table 1 Input data of governing parameters for intermittently emplaced cavities

Case #	Re_L	Da_L	Pr	Λ_L	A	B	N
1	3×10^5	8×10^{-6}	0.7	0.35	6	1	4
2	2×10^5	8×10^{-6}	0.7	0.35	6	1	4
3	3×10^5	8×10^{-6}	0.7	0.35	6	1	4
4	3×10^5	8×10^{-6}	7	0.35	6	1	4
5	3×10^5	8×10^{-6}	100	0.35	6	1	4
6	3×10^5	8×10^{-6}	0.7	1.05	6	1	4
7	3×10^5	8×10^{-6}	0.7	0.35	3	1	4
8	3×10^5	8×10^{-6}	0.7	0.35	6	0.8	4
9	3×10^5	8×10^{-6}	0.7	0.35	3	2	4
10	3×10^5	8×10^{-6}	0.7	0.35	12.5	1	2

Effect of the Reynolds Number. Figure 3 shows streamlines and isotherms over four porous cavities with $A = 6$ and $B = 1$ for the case where $\mathrm{Pr} = 0.7$, $\Lambda_L = 0.35$, $\mathrm{Da}_L = 8 \times 10^{-6}$, and $\mathrm{Re}_L = 3 \times 10^5$. It can be seen that a laminar vortex resides within each of these cavities. The strength of the eddies within each cavity decreases farther along the flow direction. These recirculating flows are formed as the primary flow impinges on the downstream cavity wall and then flows toward the bottom surface. Due to an increase in the thickness of external boundary layer along the plate, there is a reduction in the mass flow rate that penetrates into each subsequent cavity. This in turn causes a reduction in the strength of vortices within the cavities as the flow moves farther downstream. Figure 3(a) also shows that within each cavity the streamlines between the vortex center and the downstream wall of that cavity are denser than those between the vortex center and the upstream wall of the cavity. This is because the magnitude of the downstream vertical velocity is larger than the upstream one. The small fluctuations of the porous/fluid interfacial streamline are due to the macroscopic shear frictional resistance at the interface. As the Reynolds number decreases from 3×10^5 to 2×10^5, the center of the vortex for each cavity moves further to the left as seen in Fig. 4.

The reason for this trend is that the lower the Reynolds number, the lower the momentum of the flow, which in turn results in lower bulk frictional resistance for the flow. As a result the size of the vortex formed in the cavity increases. It should be noted that even though the increase in the increase in the size of the vortex is small, nevertheless, through careful examination of the results it can be clearly observed. Comparison of the isotherms in Figs. 3(b) and 4(b) indicates that at a smaller Reynolds number, due to the larger size of the vortex, the isotherms penetrate farther inside the cavity.

To evaluate the effects of the intermittent porous cavities on the shear stress and heat transfer rate at the wall, additional calculations were carried out. For the shear stress the results were cast in dimensionless form by means of the local friction coefficient as

$$C_f = \frac{\tau_{w,x}}{\rho_f u_\infty^2/2} = \frac{2}{\mathrm{Re}_L} \frac{\partial u^*}{\partial y^*}\bigg|_{y^*=0}$$

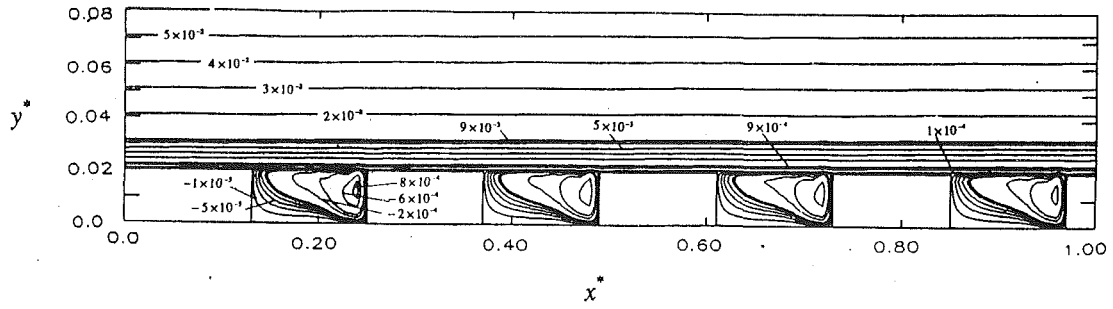

(a)

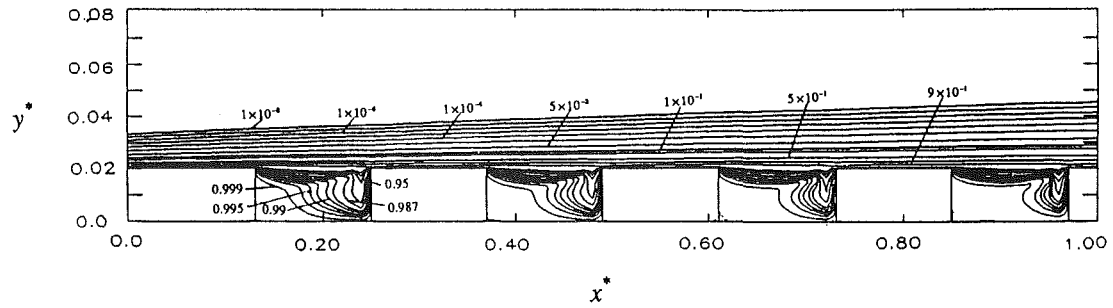

(b)

Fig. 3 (*a*) Streamlines and (*b*) isotherms for flow over four obstructing porous cavities for $Re_L = 3 \times 10^5$, $Da_L = 8 \times 10^{-6}$, $\Lambda_L = 0.35$, $Pr = 0.7$, $k_{eff}/k_f = 1.0$, $A = 6$, $B = 1$

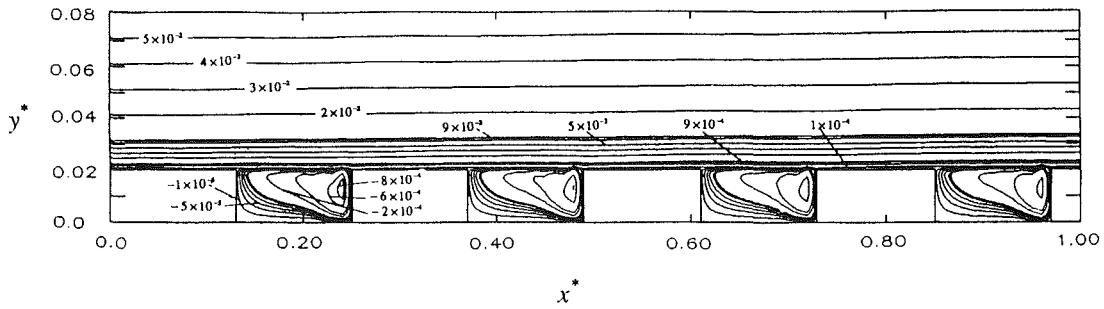

(a)

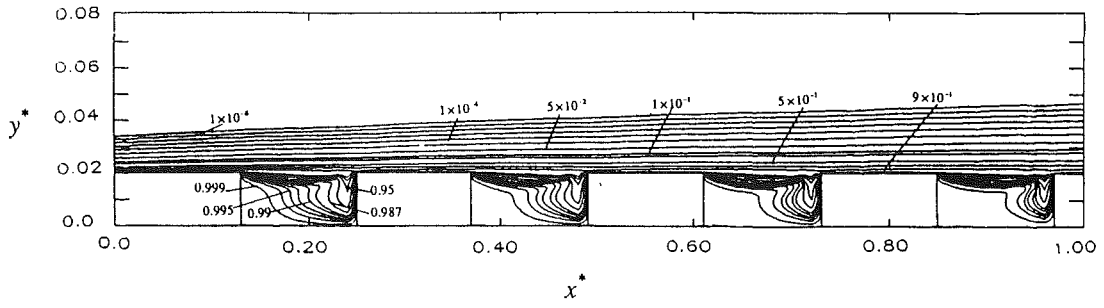

(b)

Fig. 4 (*a*) Streamlines and (*b*) isotherms for flow over four obstructing porous cavities for $Re_L = 2 \times 10^5$, $Da_L = 8 \times 10^{-6}$, $\Lambda_L = 0.35$, $Pr = 0.7$, $k_{eff}/k_f = 1.0$, $A = 6$, $B = 1$

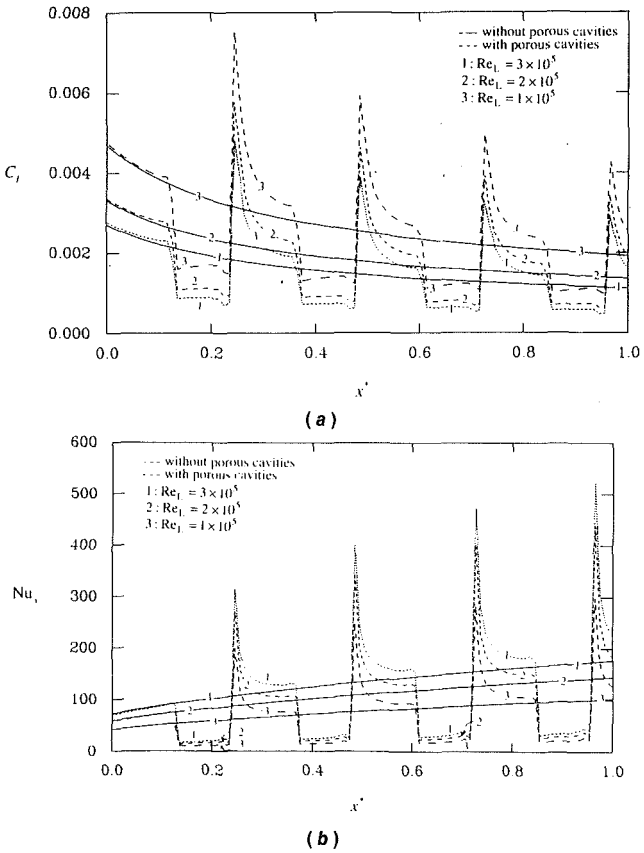

Fig. 5 Effects of the Reynolds number on (*a*) friction coefficient and (*b*) Nusselt number for flow through alternate porous cavity-block obstacles for $Da_L = 8 \times 10^{-6}$, $\Lambda_L = 0.35$, $Pr = 0.7$, $k_{eff}/k_f = 1.0$, $A = 3$, $B = 1$, $H^* = 0.02$

and for the heat transfer rate the results were presented in dimensionless form in terms of dimensionless Nusselt number

$$Nu_x = \frac{hx}{K_f} = -x^* \frac{k_e}{k_f} \frac{\partial \theta}{\partial y^*}\bigg|_{y^*=0} \tag{26}$$

This results in more meaningful comparisons for the heat flux at the external boundary between the composite system and the case where there were no porous obstacles. The effect of Reynolds number on friction coefficient along the wall ($y^* = 0$) is shown in Fig. 5(*a*). It can be seen that local friction coefficient fluctuates periodically as the streamwise coordinate increases due to the presence of the porous cavity obstacles, with a decreasing mean. This decrease in local friction coefficient is to a greater extent at the inlet of each porous cavity due to the nonzero velocity at this porous/fluid interface, which is different from the decrease at the impermeable solid wall. In addition, the peak in each cycle occurs at an x^* value corresponding to the right corner of each corner. This is due to a very steep velocity gradient in the fluid as it turns around the right corner of the cavities. Passing the right corner of the porous cavity, a secondary boundary layer begins at the leading edge of intercavity wall. The values of the C_f decrease again along the intercavity wall. As expected, as the Reynolds number increases, the friction coefficient and its fluctuation along the wall decreases.

Figure 5(*b*) shows the effect of Reynolds number on the Nusselt number distribution along the wall ($y^* = 0$). A periodically fluctuating variation of Nusselt number along the wall is observed with an increasing mean. At the inlet of each porous cavity, spacing between isotherms is large (see Figs. 3(*b*) or 4(*b*)), indicating a region of low temperature gradient. Therefore, the local Nusselt number reduces to a trough at the permeable wall. As the fluid turns around the right corner of each porous cavity, the Nusselt number reaches a peak because of the steep velocity gradient, which increases the heat transfer by convection. As can be seen in Fig. 5(*b*), the maximum and minimum values of Nu_x in each cycle increase as the Reynolds number increases. This is due to the higher velocities near the wall for larger Reynolds number, resulting in an increase in the transfer of convective energy.

Effect of the Darcy Number. The Darcy number $Da_L = K/L^2$ is directly related to the permeability of the porous medium. Figures 3 and 6 show the streamlines and isotherms for $Re_L = 3 \times 10^5$, $\Lambda_L = 0.35$, $Pr = 0.7$, $A = 6$, and $B = 1$ but with $Da_L = 8 \times 10^{-6}$ and 8×10^{-8}, respectively. Comparison of the streamlines in Figs. 3(*a*) and 6(*a*) shows that as the Darcy number decreases, the size of the vortices is reduced. This is because smaller values of Da_L translate into larger bulk frictional resistance for the flow in the porous medium. This in turn reduces the extent of penetration of the primary flow into the cavity. Comparison of the isotherms in Figs. 3(*b*) and 6(*b*) depicts that for the lower Darcy number case the isotherms penetrate deeper inside the cavity, especially in the left half section of cavity. The reason for this interesting effect is that for a lower Darcy number, heat diffusion is more significant than heat convection in the porous region. Note that in this study the conductivity of the porous medium is taken to be equal to that of the fluid, to concentrate on the effects of the geometric and thermophysical variations.

The effects of Darcy number on the variation of friction coefficient and local Nusselt number are depicted in Figs. 7(*a*) and 7(*b*), respectively. The fluctuating features for these two distributions (C_f and Nu_x) along the wall were given previously when the effects of the Reynolds number were discussed. As can be seen in Fig. 7(*a*), the values of C_f at the inlet of cavity increase with a decrease in the Darcy number. This is because of the larger bulk frictional resistance that the external flow experiences at the porous/fluid interface for a larger Darcy number. However, the peak values of C_f at the position corresponding to the right corner of each porous cavity increase as the Darcy number increases. Comparison of the Nusselt number distribution in Fig. 7(*b*) shows that at each permeable part of the wall (the inlet of cavity) the values of Nu_x decrease as the Darcy number decreases, while at the inner-cavity solid wall values of Nu_x increase as the Darcy number decreases. This is due to the lower velocity at the permeable part of wall and the higher velocity at the solid wall. These decreases and increases in the convective energy transport cause a lower temperature gradient and heat flux at the permeable wall, and a higher temperature gradient and heat flux at the solid wall, respectively.

Effect of the Prandtl Number. To study the effects of the Prandtl number on the flow and temperature fields, three different Prandtl numbers were chosen such that they will cover a wide range of thermophysical fluid properties. The numerical results are presented in Figs. 3, 8, and 9 for $Re_L = 3 \times 10^5$, $\Lambda_L = 0.35$, $Da_L = 8 \times 10^{-6}$, $A = 6$, and $B = 1$ for three different fluids with $Pr = 0.7$ (air), $Pr = 7$ (water), and $Pr = 100$ (some oil), respectively. Obviously, the Prandtl number variations have no effect on the flow field. However, as expected, the isotherms penetrate farther inside the porous cavities as Prandtl number decreases.

Inertial Effects. The inertial effects become noticeable when the Reynolds number based on the pore diameter becomes large. The effect of the inertial parameter is shown in Figs. 3 and 10 for $Re_L = 3 \times 10^5$, $Da_L = 8 \times 10^{-6}$, $Pr = 0.7$, $A = 6$, and $B = 1$ but $\Lambda_L = 0.35$ and 1.05, respectively. Comparison of the streamlines in Fig. 3(*a*) and 10(*a*) shows that as the inertial parameter increases, the strength of the vortices is reduced. This is due to the larger bulk frictional resistance for the flow,

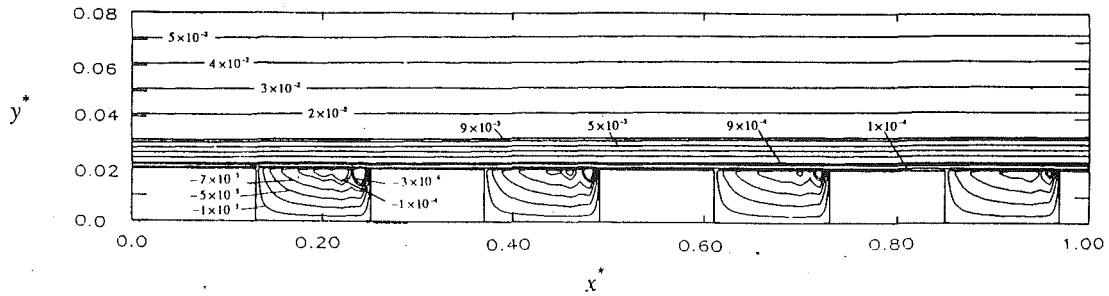

(a)

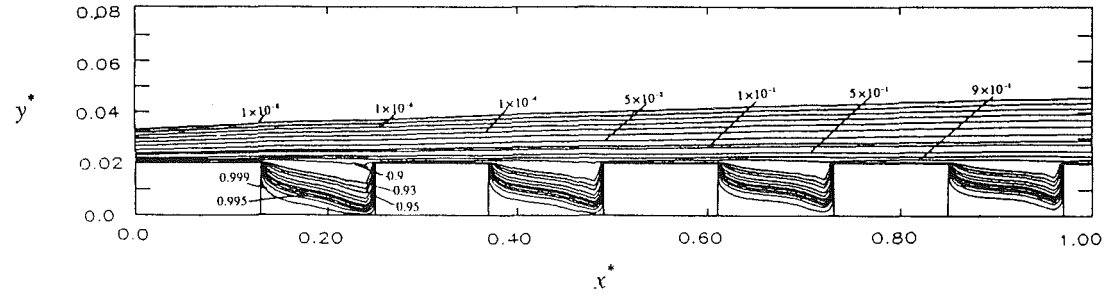

(b)

Fig. 6 (*a*) **Streamlines and** (*b*) **isotherms for flow over four obstructing porous cavities for** $Re_L = 3 \times 10^5$, $Da_L = 8 \times 10^{-6}$, $Pr = 0.7$, $k_{eff}/k_f = 1.0$, $\Lambda_L = 0.35$, $A = 6$, $B = 1$

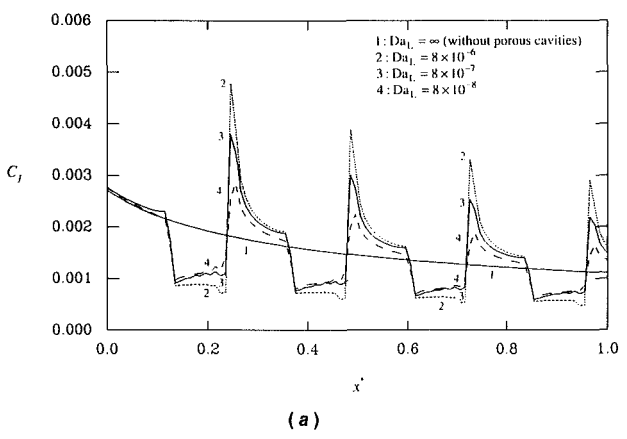

(a)

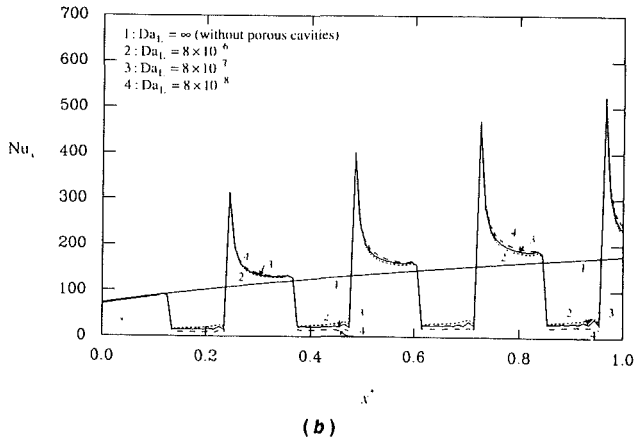

(b)

Fig. 7 Effects of the Darcy number on (*a*) **friction coefficient and** (*b*) **Nusselt number for flow through alternate porous cavity-block obstacles for** $Re_L = 3 \times 10^5$, $\Lambda_L = 0.35$, $Pr = 0.7$, $k_{eff}/k_f = 1.0$, $A = 3$, $B = 1$, $H^* = 0.02$

which the flow experiences at a larger inertial parameter. This in turn reduces the extent of penetration of the primary flow into the cavity. Comparison of the isotherms in Figs. 3(*b*) and 10(*b*) shows that for the smaller inertial parameter case the isotherms penetrate deeper into the cavity. This is owing to higher velocities for the smaller inertial parameter, which increases the transport of the convective energy. The above-described effects result in the friction coefficient and Nusselt number distributions shown in Fig. 11.

Effect of the First Geometric Parameter A. The effects of the aspect ratio (the first geometric parameter) A on the flow and temperature fields were studied for the general case of $Re_L = 3 \times 10^5$, $\Lambda_L = 0.35$, $Da_L = 8 \times 10^{-6}$, $Pr = 0.7$, and $B = 1$. The streamlines and isotherms for aspect ratios of $A = 3$ and 6 are presented in Figs. 12 and 3, respectively. As seen in Fig. 3 for $A = 6$ the flow in the cavity consists of a single laminar vortex that occupies the entire cavity. For $A = 3$ the flow is still characterized by a single vortex, but the vortex center is displaced toward the upstream cavity wall. This kind of flow situation may persist up to a certain value of A where the center of vortex just coincides with the center of cavity.

Effect of the Second Geometric Number B. The second geometric number $B = D^*/W^*$ reflects the influence of cavity array arrangement on the flow. There are two configurations considered in this analysis. The numerical runs were carried out for the general case of $Re_L = 3 \times 10^5$, $Da_L = 8 \times 10^{-6}$, $\Lambda_L = 0.35$, $Pr = 0.35$, and $A = 6$. When $A = 6$ and $B < 1$ the flow separates from the upstream top left corner of the first cavity,

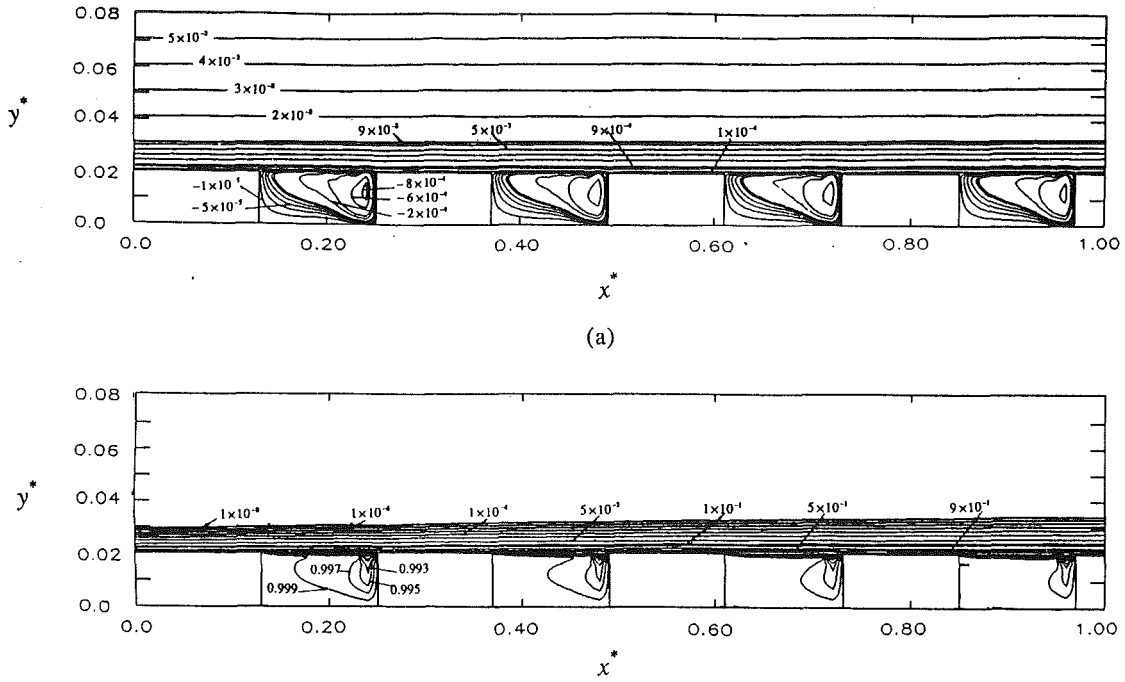

Fig. 8 *(a)* Streamlines and *(b)* isotherms for flow over four obstructing porous cavities for $Re_L = 3 \times 10^5$, $Da_L = 8 \times 10^{-8}$, $\Lambda_L = 0.35$, $Pr = 7$, $k_{eff}/k_f = 1.0$, $A = 6$, $B = 1$

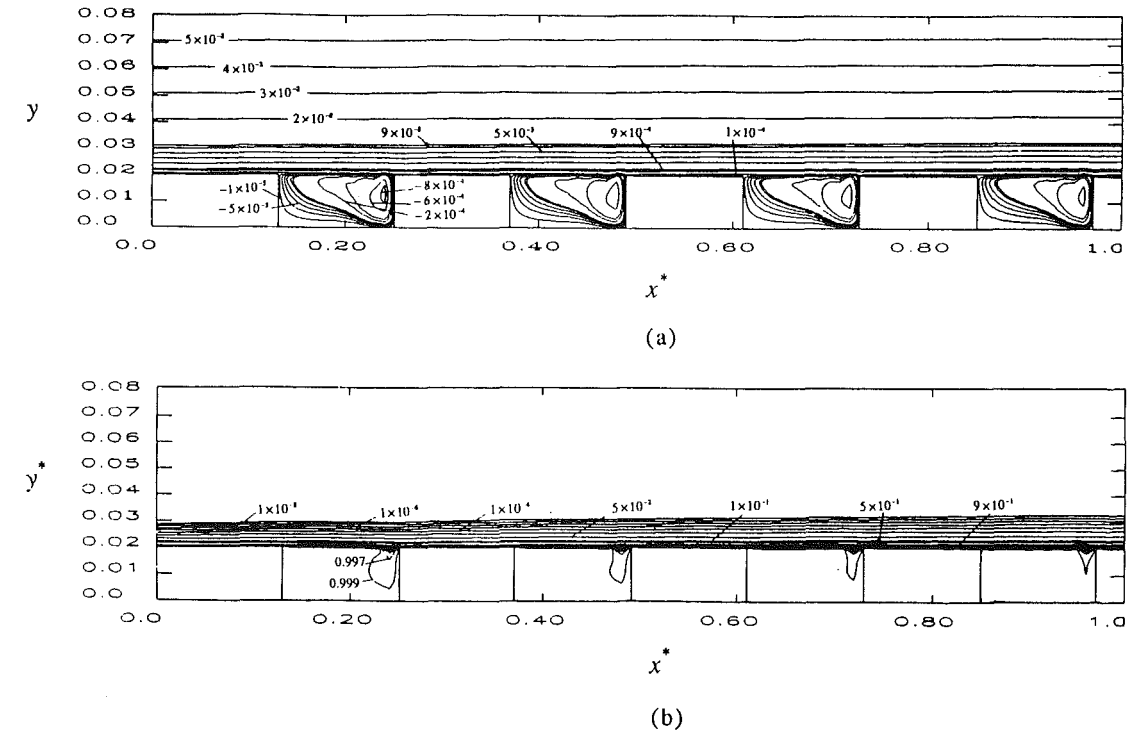

Fig. 9 *(a)* Streamlines and *(b)* isotherms for flow over four obstructing porous cavities for $Re_L = 3 \times 10^5$, $Da_L = 8 \times 10^{-6}$, $\Lambda_L = 0.35$, $Pr = 100$, $k_{eff}/k_f = 1.0$, $A = 6$, $B = 1$

reattaches on the bottom surface, and then reaches the downstream cavity wall. After passing through the first cavity the flow separates from the plate and an eddy region appears behind the separation point. This is due to a very steep velocity gradient (vorticity) in the fluid as it turns around the top right corner of the first cavity.

Under a special condition where both parameters A and B were changed, a few interesting results were found. When the value of A was decreased from 6 to 3 and B increased from 0.8 to 2, a secondary boundary layer started from the top right corner of the first cavity and was maintained over the external boundary between the first two cavities. This secondary boundary layer resulted in vortex flow inside the other three cavities. The reason for the appearance of the secondary boundary layer was that as the fluid turned around the top right corner of the first cavity, it experienced a milder velocity gradient. The ve-

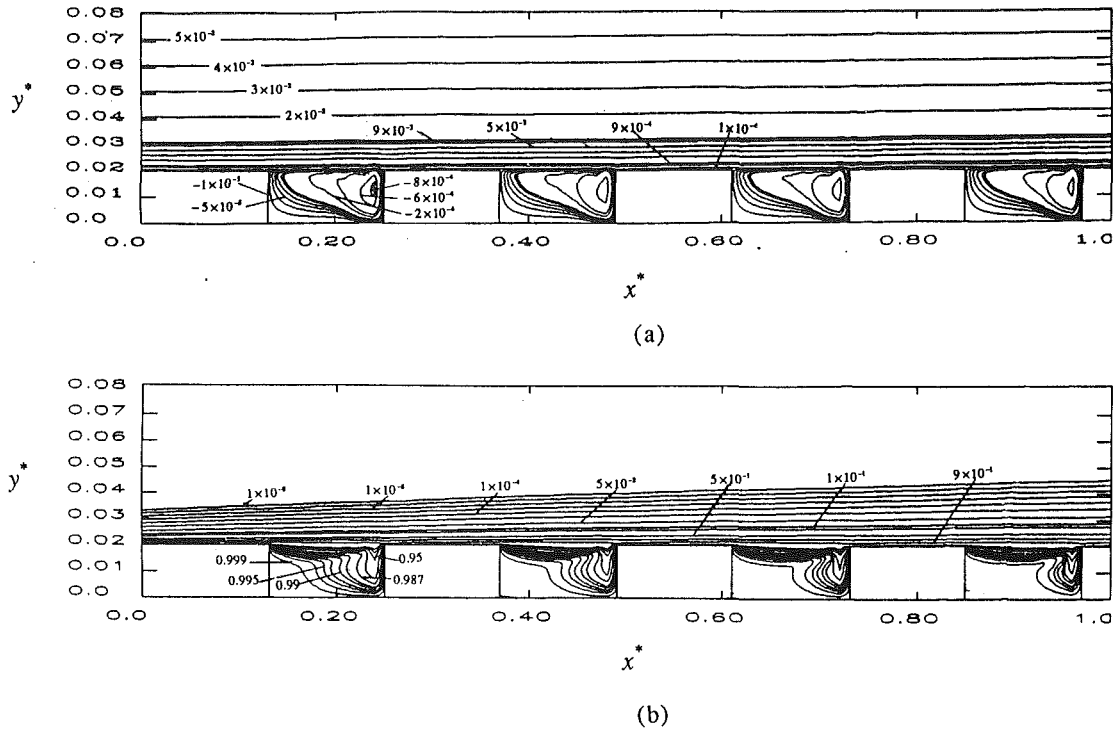

Fig. 10 (*a*) Streamlines and (*b*) isotherms for flow over four obstructing porous cavities for $Re_L = 3 \times 10^5$, $Da_L = 8 \times 10^{-6}$, $\Lambda_L = 1.05$, Pr = 0.7, $k_{eff}/k_f = 1.0$, $A = 6$, $B = 1$

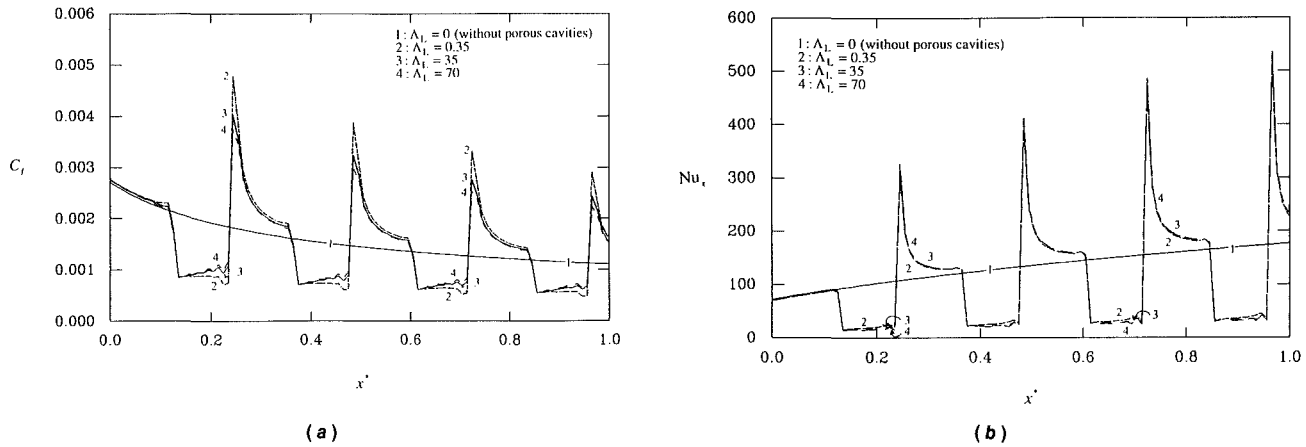

Fig. 11 The influence of the inertial parameter on (*a*) friction coefficient and (*b*) Nusselt number for flow through alternate porous cavity-block obstacles for $Re_L = 3 \times 10^5$, $Da_L = 8 \times 10^{-6}$, Pr = 0.7, $k_{eff}/k_f = 1.0$, $A = 3$, $B = 1$, $H^* = 0.02$

locity gradient was so small that the longitudinal pressure gradient was enough to reattach the flow to the wall. Comparison of the isotherms indicated that a reduction in the second geometric parameter B created a significant distortion of the isotherms. This is due to the separated and reattached flow regions, which were described previously. Finally, the streamlines and isotherms for the two-porous-cavity array were found to be very similar to those for the four-cavity array. It was found that the increase in the number of blocks has no substantial effect on the main features of the flow and temperature fields.

Conclusions

The main focus of this research is to analyze laminar forced convection over a composite porous/fluid system composed of multiple porous cavities. Since very little work has been done on external forced convection fluid flow and heat transfer in the composite systems, the objective of the present work is to study the interaction phenomena occurring in the porous medium and the fluid layer, and to analyze the effects of various parameters governing the physics of the problem under consideration. Characteristics of the flow and temperature fields in the composite layer and the effects of various governing dimensionless parameters, such as the Darcy number, Reynolds number, Prandtl number, the inertia parameter as well as the effects of pertinent geometric parameters were thoroughly analyzed and discussed. In addition, the interactive effects of the embedded porous substrates on skin friction and heat transfer characteristics of an external surface are analyzed. The fundamental information presented here can be extended to examine various applications such as in electronic cooling and in heat exchanger design, reduction of skin friction and heat transfer enhancement or augmentation, some of the manufacturing processes, geothermal reservoirs and oil extraction. The present work constitutes one of the first analyses of the laminar separated forced convection through porous cavities.

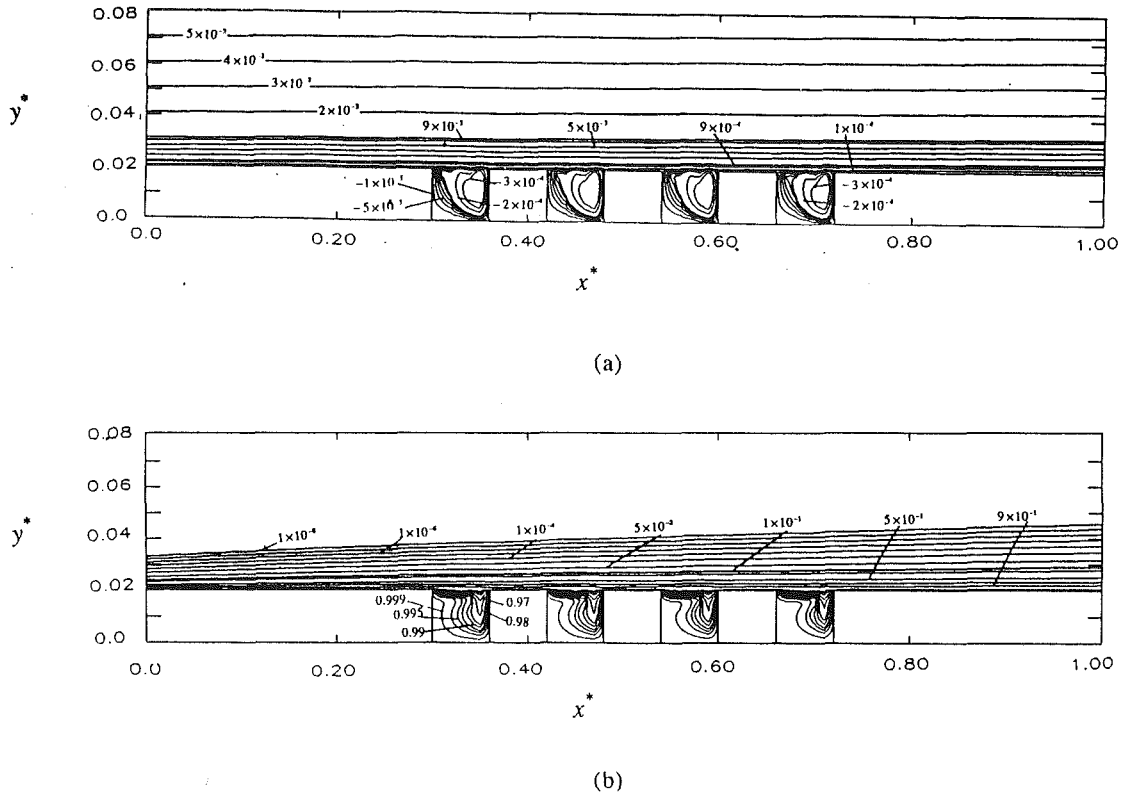

Fig. 12 (*a*) **Streamlines and** (*b*) **isotherms for flow over four obstructing porous cavities for** $Re_L = 3 \times 10^5$, $Da_L = 8 \times 10^{-6}$, $\Lambda_L = 0.35$, $Pr = 0.7$, $k_{eff}/k_f = 1.0$, $A = 3$, $B = 1$

Acknowledgments

A grant from OSC is acknowledged and appreciated.

References

Adams, J., and Ortega, J., 1982, "A Multicolor SOR Method for Parallel Computation," *Proceedings of Int. Conf. on Parallel Procession*, pp. 53–56.

Aung, W., 1983, "An Interferometric Investigation of Separated Forced Convection in Laminar Flow Past Cavities," ASME JOURNAL OF HEAT TRANSFER, Vol. 105, pp. 505–512.

Beckermann, C., Ramadhyani, S., and Viskanta, R., 1987, "Natural Convection Flow and Heat Transfer Between a Fluid Layer and a Porous Layer Inside a Rectangular Enclosure," ASME JOURNAL OF HEAT TRANSFER, Vol. 109, pp. 363–370.

Beckermann, C., Viskanta, R., and Ramadhyani, S., 1988, "Natural Convection in Vertical Enclosures Containing Simultaneously Fluid and Porous Layers," *J. Fluid Mech.*, Vol. 186, pp. 257–284.

Bejan, A., 1984, *Convection Heat Transfer*, Wiley, New York.

Bhatti, A., and Aung, W., 1984, "Finite Difference Analysis of Laminar Separated Forced Convection in Cavities," ASME JOURNAL OF HEAT TRANSFER, Vol. 106, pp. 49–54.

Cheng, P., 1978, "Heat Transfer in Geothermal System," *Adv. Heat Transfer*, Vol. 14, pp. 1–105.

De Vries, D. A., 1958, "Simultaneous Transfer of Heat and Moisture in Porous Media," *Transactions of American Geophysical Union*, Vol. 39, pp. 909–916.

Gooray, A. M., Watkins, C. B., and Aung, W., 1981, "Numerical Calculations of Turbulent Heat Transfer Downstream of a Rearward-Facing Step," *Proceedings of the 2nd International Conference on Numerical Method in Laminar and Turbulent Flow*, Venice, Italy, pp. 639–651.

Gooray, A. M., 1982, "Numerical Calculation of Turbulent Recirculating Heat Transfer Beyond Two-Dimension Backsteps and Sudden Pipe Expansion," Ph.D. Thesis, Mechanical Engineering Department, Howard University, Washington, DC.

Gooray, A. M., Watkins, C. B., and Aung, W., 1982, "K-ϵ Calculations of Heat Transfer in Redeveloping Turbulent Boundary Layers Downstream of Reattachment," ASME Paper No. 82-HT-77.

Gosman, A. D., 1976, "The TEACH-T Computer Program Structure, Flow, Heat and Mass Transfer in Turbulent Recirculating Flows—Prediction and Measurement," Lecture Notes from McGill University, Canada.

Greenspan, D., 1969, "Numerical Studies of Steady, Viscous, Incompressible Flow in a Channel With a Step," *J. Eng. Mathematics*, Vol. 3, No. 1, pp. 21–28.

Huang, P. C., and Vafai, K., 1993, "Flow and Heat Transfer Control Over an External Surface Using a Porous Block Array Arrangement," *Int. J. Heat Mass Transfer*, Vol. 36, pp. 4019–4032.

Patankar, S. V., 1980, *Numerical Heat Transfer and Fluid Flow*, Hemisphere, Washington, DC.

Poulikakos, D., and Bejan, A., 1985, "The Departure From Darcy Flow in Natural Convection in a Vertical Porous Layer," *The Physics of Fluids*, Vol. 28, pp. 3477–3484.

Poulikakos, D., 1986, "Buoyancy-Driven Convection in a Horizontal Fluid Layer Extending Over a Porous Substrate," *Phys. Fluids*, Vol. 29, pp. 3949–3957.

Poulikakos, D., and Kazmierczak, M., 1987, "Forced Convection in a Duct Partially Filled With a Porous Material," ASME JOURNAL OF HEAT TRANSFER, Vol. 109, pp. 653–662.

Roache, P. J., 1976, *Computational Fluid Dynamics*, Hermosa, Albuquerque, NM.

Sathe, S. B., Lin, W. Q., and Tong, T. W., 1988, "Natural Convection in Enclosures Containing an Insulation With a Permeable Fluid-Porous Interface," *Int. J. Heat Fluid Flow*, Vol. 9, pp. 389–395.

Sinha, S. N., Gupta, A. K., and Oberai, M. M., 1981, "Laminar Separating Flow Over Backsteps and Cavities—Part II: Cavities," *AIAA J.*, Vol. 20, No. 3, pp. 370–375.

Tien, C. L., and Vafai, K., 1989, "Convective and Radiative Heat Transfer in Porous Media," *Advances in Applied Mechanics*, Vol. 27, pp. 225–282.

Vafai, K., and Tien, C. L., 1981, "Boundary and Inertia Effects on Flow and Heat Transfer in Porous Media," *Int. J. Heat Mass Transfer*, Vol. 24, pp. 195–203.

Vafai, K., and Tien, C. L., 1982, "Boundary and Inertia Effects on Convective Mass Transfer in Porous Media," *Int. J. Heat Mass Transfer*, Vol. 25, pp. 1183–1190.

Vafai, K., and Thiyagaraja, R., 1987, "Analysis of Flow and Heat Transfer at the Interface Region of a Porous Medium," *Int. J. Heat Mass Transfer*, Vol. 30, pp. 1391–1405.

Vafai, K., and Kim, S. J., 1990, "Analysis of Surface Enhancement by a Porous Substrate," ASME JOURNAL OF HEAT TRANSFER, Vol. 112, pp. 700–705.

Yamamoto, H., Seki, N., and Fukusako, S., 1979, "Forced Convection Heat Transfer on Heated Bottom Surface of a Cavity," ASME JOURNAL OF HEAT TRANSFER, Vol. 101, pp. 475–479.

The Effect of Temperature Modulation on Natural Convection in a Horizontal Layer Heated From Below: High-Rayleigh-Number Experiments

J. Mantle
Graduate Student.

M. Kazmierczak
Assistant Professor of Mechanical Engineering. Mem. ASME

B. Hiawy
Graduate Student.

Department of Mechanical, Industrial, and Nuclear Engineering, University of Cincinnati, Cincinnati, OH 45221-0072

An experimental investigation was conducted to study the effects of wall temperature modulation in a horizontal fluid layer heated from below. A series of 45 transient experiments was performed in which the bottom wall temperature changed periodically with time in a "sawtoothlike" fashion. The amplitude of the bottom wall temperature oscillation varied from 3 to 70 percent of the enclosure's mean temperature difference, and the period of the temperature swings ranged from 43 seconds to 93 minutes. With water as the fluid in the test cell, the flow was fully turbulent at all times. The Rayleigh number of the experiments (based on the enclosure's height and on the mean temperature difference) was $0.4 \times 10^8 < Ra < 1.2 \times 10^9$. *It was found that for small changes in the bottom wall temperature, the cycle-averaged heat transfer through the layer was unchanged, independent of the period, and was equal in magnitude to the well-established steady-state value when the hot wall is evaluated at the mean temperature. However, this study shows that the cycle-averaged heat transfer increases notably, up to 12 percent as compared to the steady-state value, for the experiments with large temperature modulations. Futhermore, it was observed that the enchancement was a function of the amplitude and period of the oscillation.*

Introduction

Natural convection is a challenging and interesting phenomenon to investigate due to the coupling of the fluid flow and the energy transport. It has been extensively studied because of its importance in many engineering applications and because it is often found to be the controlling mechanism in many naturally occurring processes. An excellent overview of this important subject is given by Gebhart et al. (1988).

With regard to buoyancy-driven flow in enclosures, the field is now mature (Bejan, 1984; Ostrach, 1988). The two most common configurations studied were the horizontal cylinder and the rectangular enclosure. When dealing with internal flows in the latter geometry, a further distinction is made based on whether the enclosure is heated from below or from the side. With bottom heating, the Rayleigh number must exceed a certain critical value before flow ensues, and the final pattern achieved is markedly different from the flow pattern generated by side heating.

Deardorff (1964) and Fromm (1965) were among the first researchers who numerically solved the steady laminar two-dimensional governing equations for flow in a horizontal layer with bottom heating. Early experiments were conducted by Globe and Dropkin (1959) and O'Toole and Silveston (1961) that covered a fairly large range of Rayleigh number. Krishnamurti (1973) in an excellent paper experimentally investigated the transition to turbulence and was able to characterize the flow into five regimes based on Rayleigh and Prandtl numbers. Sparrow et al. (1970) postulated that the main physical mechanism responsible for the energy transport at moderate to high Rayleigh number is the release of thermals from the boundary layers, which was later confirmed by the experiments of Chu and Goldstein (1973) conducted in the range $3 \times 10^5 < \mathrm{Ra} < 2 \times 10^7$.

Since these works, there has been an explosion of research on the subject of natural convection in enclosures. There are far too many papers in this field to cite; however, the impetus for much of this later work was the energy crisis, which emphasized energy conservation in buildings and solar energy. For example, much of the later work centered on *discrete* boundary conditions where heating is imposed only over a portion of the driving wall. Other work focused on the *aspect ratio* of the enclosure, while still other work investigated buoyancy-driven flow in an enclosure containing *internal partitions*. The reader is referred to Yang (1987) for a more thorough discussion.

The majority of the previous works was for *steady* flows. Very few transient problems were investigated, and these mostly considered a vertical enclosure with heating from the *side*. For example, Schladow et al. (1989), and references therein, considered a sudden change in the side wall temperature, and the case where the side wall temperature varied sinusoidally with time was numerically studied by Yang et al. (1989) and Kazmierczak and Chinoda (1992). Regarding transient natural convection with *bottom* heating, the authors could only find the very early classic work of Elder (1968, 1969) who numerically and experimentally studied the early evolution of the flow in the layer when suddenly heated from below by a wall held at a hotter (constant) temperature.

This paper reports an experimental investigation of buoyancy-driven flow in a horizontal layer driven by a bottom heated surface that periodically changes temperature with time. The hot wall temperature varies about a mean value, and the temperature of the top cold wall is held fixed. The main objective of this study is to determine the effect, if any, that the oscillating surface temperature has on the heat transfer through

Contributed by the Heat Transfer Division for publication in the JOURNAL OF HEAT TRANSFER. Manuscript received by the Heat Transfer Division July 1992; revision received August 1993. Keywords: Enclosure Flows, Natural Convection, Transient and Unsteady Heat Transfer. Associate Technical Editor: J. R. Lloyd.

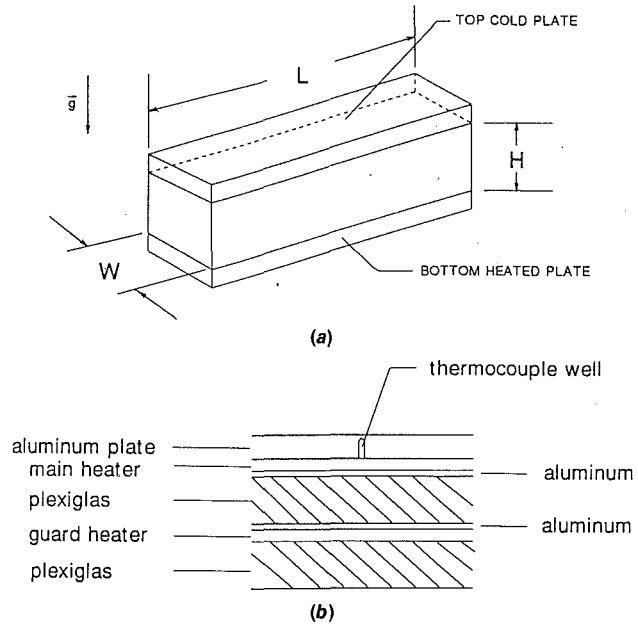

Fig. 1 Experimental apparatus: (*a*) isometric sketch, (*b*) cross section of heated bottom plate

the horizontal layer. A cyclic variation in boundary conditions is often realized in many environmental processes and engineering devices.

Experimental Apparatus

Test Cell. The experiments were performed in the rectangular vessel shown schematically in Fig. 1(*a*). The height to length aspect ratio was 1/4, and its internal dimensions measured 50.8 cm long by 12.7 cm deep and by 12.7 cm high. The vertical side walls were constructed out of 1.91-cm-thick clear plexiglas. The top and bottom horizontal walls are thick aluminum plates.

The top wall was cooled by circulating cold tap water through five large channels, which were milled lengthwise along the top plate. To insure isothermality of the top plate, the water was made to travel in opposite directions in adjacent channels and was circulated at a high flow rate. The temperature of the upper wall was measured using eight 30 gage type-T thermocouples that were embedded to a depth of 0.16 cm from the inside surface.

The bottom plate was constructed in a "sandwich" fashion. The cross section showing the different layers making up the bottom hot plate is drawn in Fig. 1(*b*). The upper layer was made from 1.3-cm-thick aluminum plate and was heated by a 13.6 ohm resistance flexible rubber main heater located directly underneath. To prevent losses from the bottom of the enclosure, a second or "guard" heater was used. The main heater and the guard heater were separated by a 2.54-cm-thick insulating plexiglass layer. Sandwiched between the heaters and the plexiglass layer were thin (0.3-cm-thick) aluminum plates to help diffuse the temperature irregularities of the heaters. In addition, highly conductive paste was placed between all layers to enhance the thermal contact. Finally, a 2.54-cm-thick plexiglass plate was added below the guard heater for insulation. Eight thermocouples were embedded in the upper aluminum plate (within 0.16 cm from inside surface) and in each of the thin aluminum plates located next to the heaters. The upper thermocouples were used to measure the bottom wall temperature, and the thermocouples in the thin aluminum plates were used to record the heater temperatures.

The test cell was mounted and leveled on a sturdy work table and was filled with distilled water. An insulation jacket made from 9.5-cm-thick sytrofoam board surrounded the vessel and insulated the top and all sides.

Main Heater Electrical Circuit. To oscillate the bottom wall temperature, the electric circuit shown in Fig. 2(*a*) was used. This circuit was designed to vary the power to the main heater periodically. The major components of the circuit included a variac, timer, an external (variable) resistor, and the primary main heater. The timer is a switch, which cyclicly opens and closes. The time period is programmable using the top tuning knob and by setting four dip switches located on the timer side and can be adjusted from 2.0 seconds to 24 hours. When the timer switch is closed, the current passes through the variable resistor but is bypassed when the timer switch opens. Thus, the voltage drop (power) across the main heater varies in a step fashion (Fig. 2*b*) as the external resistor is switched in and out of the circuit by the timer. As previously stated, the time period of the voltage oscillation is adjusted by changing the timer setting. The amplitude, or the change in voltage drop across the main heater, is adjusted by changing the resistance of the external variable resistor. Thus, using the circuit just described, the voltage (power) applied to the main heater is a square wave (Fig. 2*b*) adjustable in amplitude and in period.

Given this power variation to the main heater, the bottom wall temperature varies in a sawtoothlike fashion due to the effect of thermal storage of the bottom plate. Figure 3 shows the measured thermal boundary conditions encountered in three different runs. In each figure, the upper solid line is the instantaneous (spatial average of eight thermocouples) bottom wall temperature versus time, and the dashed line represents the mean (cycle-averaged) bottom wall temperature. The lower solid line shows the instantaneous upper cold plate temperature. Inspection of Fig. 3 shows that for short time periods and for small temperature modulations, the bottom plate temperature time distribution takes on a triangular appearance (Fig. 3*a*) but becomes distinctively sawtooth in profile for longer periods and for larger temperature amplitudes (Figs. 3*b–c*). It is worth noting that the cold plate temperature is constant with respect to time for the top two runs in Fig. 3 but fluctuates slightly with time for the run with the largest time period (Fig. 3*c*).

Nomenclature

A = area of heated surface, m^2
Amp = amplitude of temperature change, °C
g = gravitational acceleration, m/s^2
H = enclosure height, m
k = thermal conductivity, W/m °C
Nu = Nusselt number, Eq. (5)
p = dimensionless time period = $P\alpha/H^2$
P = time period of temperature oscillation, s
Q = heat transfer rate, W
Ra = Rayleigh number, Eq. (2)
T = temperature, °C
α = thermal diffusivity, m^2/s
β = coefficient of volumetric thermal expansion, K^{-1}
ν = kinematic viscosity, m^2/s
ρ = fluid density, kg/m^3

Subscripts

c = cold (top) wall
h = hot (bottom) wall
max = maximum
min = minimum

Superscript

$\overline{\ }$ = denotes a quantity averaged over time

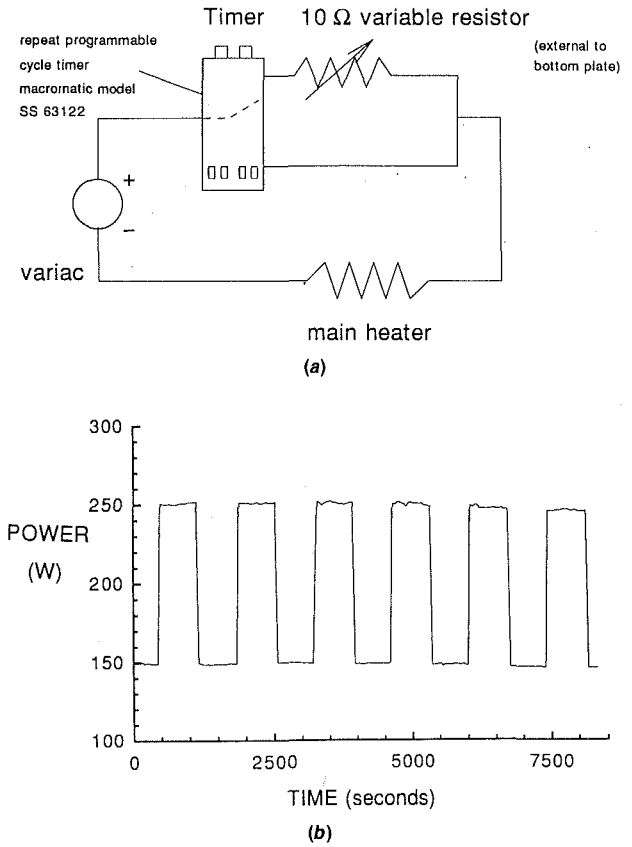

Fig. 2 Electrical circuit used to modulate the power to the main heater: (*a*) schematic wiring diagram, (*b*) measured voltage variation with time for typical experiment

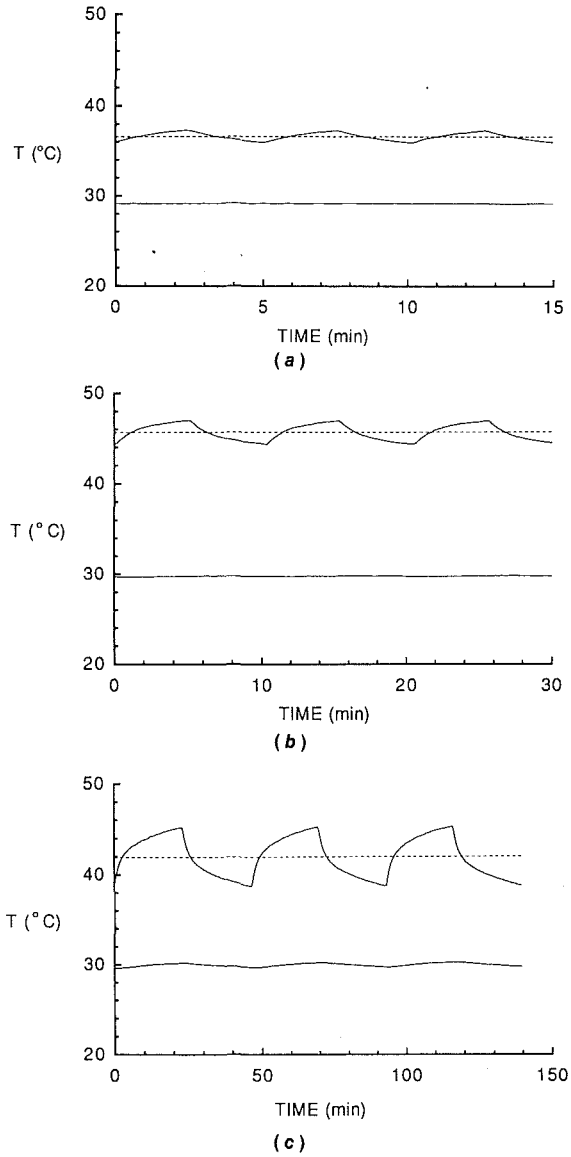

Fig. 3 Measured bottom plate temperature variation with time for typical experiments: (*a*) run 17, (*b*), run 9, (*c*) run 20

Procedure and Data Collection. The experimental procedure was as follows. The main heater circuit was turned on and the timer period and the resistance of the external resistor set. Cooling water was supplied to the cold plate and the guard heater turned on. As a rough estimate, the power to the guard heater was initially set at 5 percent of the main heater power. The system then ran for several cycles until the initial transient died and the temperature measurements began repeating itself. A check was then made of the temperature of the guard heater. Since the guard heater was powered by a separate variac with constant power output, the temperature of the guard heater was nearly constant, although the temperature of the main heater cycled. The power to the guard heater was adjusted until its temperature became equal to the minimum temperature experienced by the main heater. This reduced the heat loss through the hot plate to the minimum level and prevented the power from the guard heater from contributing to the heat gain of the apparatus. The loss through the bottom wall was calculated (using the time-averaged temperature drop data and assuming conduction heat transfer through the 2.54-cm-thick plexiglass plate) to be less than 1 percent of the energy going into the fluid layer. Note that for the steady-state baseline experiments that ran with constant power, the guard heater to main heater temperature differential could be made very small, and in fact, could be eliminated after making several fine adjustments to the guard heater. This was a very time-consuming iterative process, and instead, in many experiments only one or two adjustments were made, just enough to get fairly close to the main heater temperature, and then the power was corrected for conduction heat loss. The accuracy of this method was checked by repeating several steady-state experiments, with and without bottom wall correction, and the comparison revealed that practically identical results could be obtained without having to make the painstaking adjustments to completely eliminate the heat loss.

Once the final adjustments to the guard heater were made, the experimental data were logged. In general, the system responded rather quickly to changes made to the bottom wall, but extreme care was exercised to ensure that the periodic solution was actually measured. Typically, the experiments were run 10 to 40 cycles beyond the point where the mean main heater temperature, mean guard heater temperature, and the mean bottom plate temperature became constant before reducing the data.

The data taking was automated using a Hewlett-Packard 75000 data acquisition system driven by a 386/25 MHz personal computer running LabTech Notebook software. The raw temperature data sampled at 10 second intervals for the majority of the runs and were scanned even faster for the experiments with short time periods. The data were recorded and saved on the hard drive of the PC. A FORTRAN program then processed the data. The program calculated the mean temperature, amplitude, and the period of the driving wall. From the voltage drop data it calculated the cycle-averaged power to the mean heater and, using the guard heater and main heater temperature data, corrected for heat losses due to conduction through the

Table 1 Summary of steady-state experiments; constant bottom wall temperature

Experiment Number	Ra(x10^9)	Nu
1A	.7800	52.53
1B	.1131	58.60
1C	.4412	42.93
1D	.2456	36.15
1E	.6091	48.36
1F	.5160	45.51
1G	.3789	41.42
1H	.3167	39.19
1I	.1956	33.82
1J	.1588	31.14
1K	.1399	30.39
1L	.6908	50.33
1M	.8790	54.11
1N	.9740	55.60
1O	1.077	57.46
1P	1.672	65.34
1Q	1.520	63.25
1R	1.359	60.99

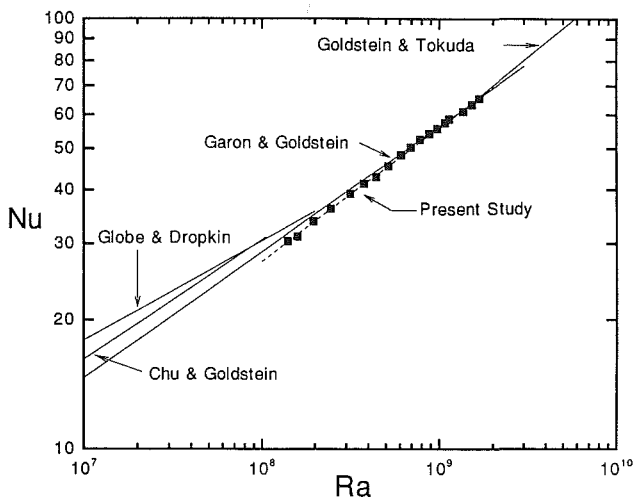

Fig. 4 Nu versus Ra: comparison of steady-state experimental data (constant bottom wall temperature experiments) with published experimental correlations

bottom plate. Finally, the Rayleigh number and the cycle-average Nusselt numbers were calculated.

Uncertainty Analysis. An uncertainty analysis was carried out following standard procedure (Coleman and Steele, 1989). For a typical experiment the total uncertainty in the temperature difference, ΔT, and the power measurements were 1.4 percent and 2.7 percent, respectively. This combined to give a maximum overall error of 4.2 percent in the reported Nusselt number. Note that this result included both bias and random errors. The sources of error for the power measurement uncertainty were errors associated with measuring the main heater voltage and resistance, while the error in the temperature difference uncertainty considered the accuracy of the thermocouple output and the error associated with converting the signal to a temperature reading by the data acquisition hardware. The random errors were computed directly from the data collected (multiple periodic solutions were obtained for each run) estimated at a 95 percent confidence interval (approximately ± two standard deviations).

Table 2 Correlation for steady-state natural convection experiments with bottom heating (Goldstein et al., 1990)

Investigators	Correlations	Range of Ra	Fluid
Globe & Dropkin	Nu = 0.440 Ra$^{0.230}$	4 x 10^6 - 2 x 10^8	Water
Chu & Goldstein	Nu = 0.183 Ra$^{0.278}$	2 x 10^5 - 1 x 10^8	Water
Garon & Goldstein	Nu = 0.130 Ra$^{0.293}$	1 x 10^7 - 3 x 10^9	Water
Goldstein & Tokuda	Nu = 0.0556 Ra$^{1/3}$	10^9 - 2 x 10^{11}	Water
Present Results	Nu = 0.087 Ra$^{0.312}$	10^8 - 2 x 10^9	Water

Results and Discussion

Steady-State Experiments. A series of 18 steady-state experiments were performed for the twofold purpose of: first, to validate the accuracy of the experimental apparatus and procedure by comparing the present data to existing correlations found in the literature; second, to obtain "baseline" data, or a reference datum, to compare with the oscillating experiments so as to determine the degree of heat transfer enhancement caused by the wall temperature oscillations.

The results of these experiments are presented in Table 1 and are graphically depicted in Fig. 4. Also plotted in Fig. 4 are previously reported correlations obtained from earlier investigators. It is found that the present data correlate well by a single equation over the range of Ra investigated. Using a least-squares fit the following equation (dashed line of Fig. 4) was obtained:

$$\mathrm{Nu} = 0.087\ \mathrm{Ra}^{0.312} \quad 10^8 < \mathrm{Ra} < 2\times 10^9 \tag{1}$$

The other correlations plotted in Fig. 4 are listed in Table 2 along with their range of applicability. Note that, of the several correlations reported, only the third equation, i.e., the Garon and Goldstein (cited by Goldstein et al., 1990) correlation, extends over the entire Rayleigh number range of the present experiment. The other correlations fit only the high or low end of the present data and, thus, represent the extreme limits of these correlations. Comparison of the present data (dashed line) to those of Garon and Goldstein (Fig. 4) shows very good agreement. Furthermore, it is interesting to note that the Rayleigh number power dependence obtained, 0.312, is the arithmetic average of the exponents of the two correlations that apply to experiments with Ra numbers an order of magnitude lower and higher, 0.293 (Garon and Goldstein) and 0.33 (Goldstein and Tokuda, cited by Goldstein et al., 1990), respectively.

Experiments With Changing Bottom Wall Temperature. Forty-five transient experiments (Table 3) were conducted to investigate the impact that modulating the bottom wall temperature has on the heat transfer through the horizontal layer. The three parameters to this problem are: the period (P) and the amplitude (Amp) of the bottom wall temperature oscillation, and the Rayleigh number of the fluid layer. The Rayleigh number used in this study was defined in the classical manner as:

$$\mathrm{Ra} = \frac{g\beta\overline{\Delta T}\,H^3}{\nu\alpha} \tag{2}$$

where the representative temperature difference was based on the mean (cycle-averaged) hot wall temperature, $\overline{T_h}$, minus the mean cycled-averaged cold wall temperature, $\overline{T_c}$:

$$\overline{\Delta T} = \overline{T_h} - \overline{T_c} \tag{3}$$

The properties appearing in Eq. (2) were evaluated at the average of the mean wall temperatures. The period, P, of the bottom wall temperature modulation is the duration of time

Table 3 Summary of experiments with oscillating bottom wall temperature

Run	p (Minutes)	p (x 10^3)	$\overline{\Delta T}$ (°C)	AMP/$\overline{\Delta T}$ (%)	Ra (x10^6)	$\overline{Nu}_{cycle}$	$\frac{\overline{Nu}}{Nu_{ss}}$
37	0.72	0.396	7.34	3.00	0.433	43.56	1.011
36	1.44	0.792	7.38	6.03	0.436	43.57	1.010
34	2.56	1.407	7.35	10.00	0.433	43.75	1.016
35	2.55	1.402	7.46	10.32	0.441	43.30	1.000
12	5.12	2.815	7.51	4.59	0.434	42.64	0.990
13	10.23	5.625	7.51	7.19	0.434	43.03	0.999
14	23.31	12.816	7.49	10.21	0.433	43.11	1.001
15	46.67	25.660	7.46	12.94	0.433	43.04	1.000
17	5.11	2.810	7.44	9.01	0.433	41.60	0.966
18	10.23	5.625	7.28	14.08	0.422	42.64	0.998
19	23.11	12.706	7.31	19.63	0.424	43.19	1.010
16	46.67	25.660	7.29	25.10	0.423	43.01	1.006
33	5.09	2.799	7.31	19.02	0.428	43.79	1.021
32	10.21	5.614	7.27	29.78	0.425	44.18	1.032
31	23.08	12.690	7.11	41.56	0.415	44.56	1.049
30	46.33	25.473	7.01	55.21	0.408	45.08	1.078
51	5.08	2.782	7.40	18.85	0.412	43.77	1.033
50	10.17	5.569	7.19	29.62	0.397	44.37	1.059
49	46.29	25.348	7.16	53.77	0.396	45.24	1.080
48	92.50	50.652	7.11	70.75	0.391	46.13	1.106
42	0.72	0.401	12.07	3.73	0.798	52.91	1.015
41	1.28	0.712	12.13	6.65	0.803	53.40	1.023
40	2.55	1.419	12.20	12.38	0.811	52.54	1.003
5	5.11	2.832	12.03	5.32	0.767	52.06	1.012
2	10.25	5.681	12.00	7.75	0.761	52.02	1.013
3	23.30	12.915	12.00	10.67	0.766	52.12	1.013
4	46.72	25.896	11.90	13.87	0.756	52.16	1.018
23	5.11	2.844	11.99	10.38	0.784	51.43	0.992
21	10.23	5.693	11.92	15.14	0.773	51.77	1.004
22	23.24	12.933	11.87	20.51	0.773	52.27	1.013
20	46.60	25.934	12.03	26.97	0.789	52.68	1.014
39	5.09	2.833	11.99	21.22	0.792	52.62	1.012
45	10.17	5.614	11.94	31.71	0.729	52.86	1.044
46	23.13	12.769	11.80	43.98	0.722	53.99	1.069
44	46.41	25.621	11.60	58.58	0.706	54.73	1.091
47	92.71	51.180	11.24	76.25	0.685	55.76	1.123
7	5.11	2.867	15.95	5.64	1.118	58.23	1.006
9	10.25	5.750	15.90	8.21	1.116	58.07	1.004
8	23.30	13.071	15.98	10.98	1.122	58.34	1.007
10	46.69	26.192	15.92	14.38	1.124	58.51	1.009
28	5.10	2.872	16.11	10.99	1.172	58.51	0.996
27	10.23	5.762	16.17	15.55	1.183	58.46	0.992
25	23.21	13.072	16.25	21.02	1.198	59.19	1.001
24	46.54	26.212	16.25	27.63	1.193	59.46	1.006
26	93.00	52.378	15.88	34.63	1.162	59.42	1.014

between successive temperature peaks. The values used for each run are reported dimensionally in column 2 of Table 3 and in nondimensional form, appropriately nondimenionalized as defined in the nomenclature, in column 3 of Table 3. The amplitude (Amp) is the final parameter and is the average of the maximum and minimum temperature deviation from the mean value, i.e.,

$$\text{Amp} = [(T_{h_{\max}} - \overline{T_h}) + (\overline{T_h} - T_{h_{\min}})]/2 \tag{4}$$

In all the runs reported, except for the cases that had very large value of amplitude, the magnitude of the fluctuation was always symmetric about the mean value in spite of the sawtooth shape appearance of the bottom wall boundary condition. The amplitude was then nondimensionalized with the representative temperature difference.

In the experiments, the focus was on the parameters related to the time-dependent boundary condition. Specifically, as shown in Table 3, experiments were conducted around three different values of Ra. For experiments at the two lower Rayleigh numbers, the period of the wall temperature oscillation varied from 0.72 minutes to 93 minutes and the dimensionless amplitude ranged from 3 to 70 percent. These parmeters varied over a slightly smaller range of values at the third (higher) Rayleigh number.

The results of the experiments is the measured heat transfer rate through the layer, which is reported in terms of a conduction-referenced Nusselt number defined as

$$\overline{\text{Nu}}_{\text{cycle}} = \frac{Q_{\text{cycle}}}{kA\ \overline{\Delta T}/H} \tag{5}$$

and listed in the seventh column of Table 3. The temperature

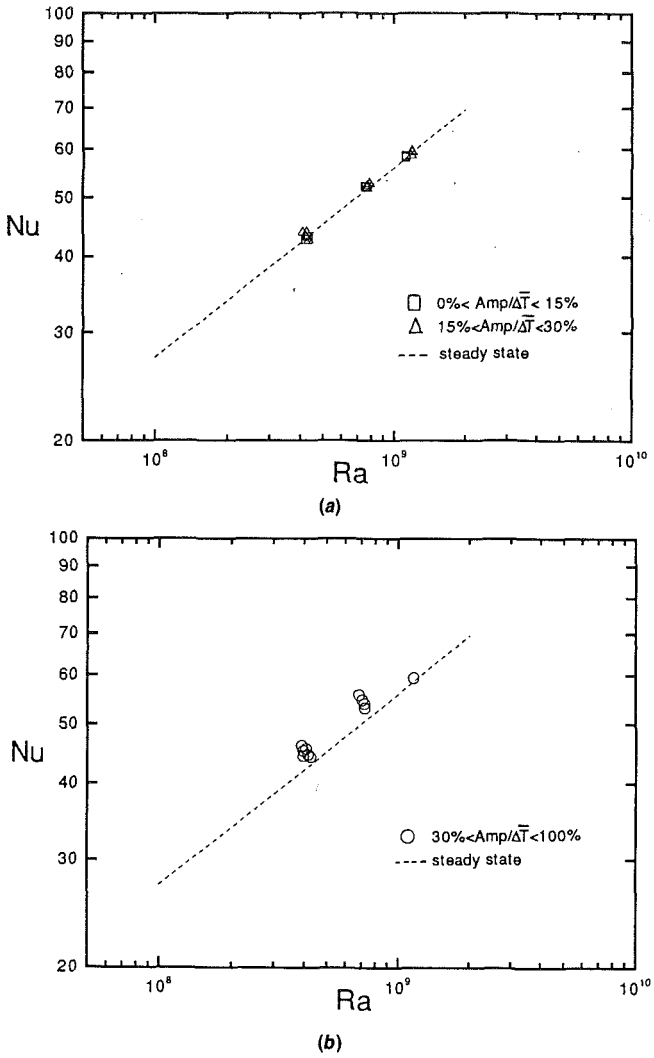

Fig. 5 Nu as a function of Rayleigh number for oscillating bottom wall temperature experiments: (*a*) low and moderate-temperature amplitude, (*b*) high-temperature amplitude

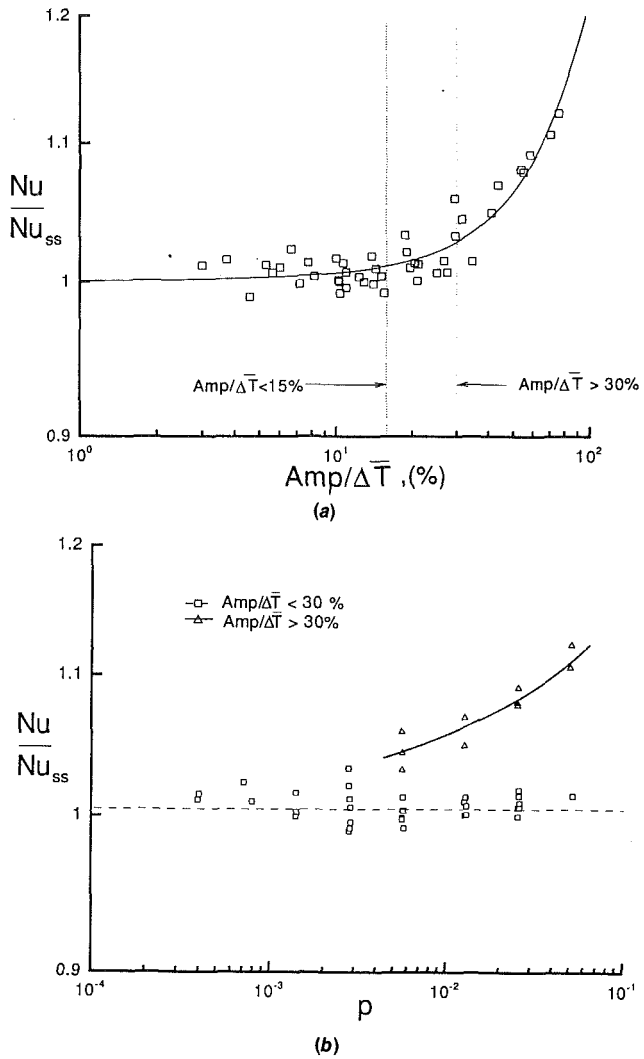

Fig. 6 Heat transfer enhancement dependence on: (*a*) dimensionless amplitude, (*b*) dimensionless period

difference used in Eq. (5) is given by Eq. (3), and all other quantities in the above equation are defined in the nomenclature. The Nusselt numbers are shown plotted versus Rayleigh number in Fig. 5. Runs having a small to moderate value of dimensionless amplitude (0 percent < Amp/$\overline{\Delta T}$ < 30 percent) are shown in Fig. 5(*a*), while runs with large dimensionless amplitude (Amp/$\overline{\Delta T}$ > 30 percent) are plotted in Fig. 5(*b*). In both figures, the dashed line represents the correlation to the steady-state experiments, Eq. (1). Inspecting Fig. 5(*a*), we conclude that low (0 percent < Amp/$\overline{\Delta T}$ < 15 percent) to moderate size (15 percent < Amp/$\overline{\Delta T}$ < 30 percent) wall temperature modulation has negligible effect upon the time-averaged heat transfer through the layer (for the given time period constraint). A closer inspection of the data in Fig. 5(*a*) reveals that the runs with moderate temperature amplitude (triangular symbols) show somewhat more scatter than the lower amplitude experiments (runs denoted by square symbols) but, in general, the data are centered over the steady-state results. It should be made clear, however, that although the cycle-averaged heat transfer for these oscillating wall temperature experiments may be numerically equal to the heat transfer for the constant wall temperature case, the instantaneous heat at the walls may be changing with time. We suspect that the heat transfer actually increases and decreases with time as a function of the bottom wall temperature, but overall, these effects balance one another when integrated over the cycle.

When the dimensionless temperature amplitude is increased above 30 percent, however, a measurable increase in the cycle-averaged heat transfer occurs, as shown by Fig. 5(*b*). Clearly, at the two lower Rayleigh numbers tested, the measured cycle-averaged heat transfer (Nu) is now higher than the steady-state constant wall temperature value (Fig. 5*b*). This finding was checked again at the lowest value of Rayleigh number by repeating experiments 30–32 and obtaining similar results (runs 49–51).

The amount of heat transfer enhancement caused by the oscillating wall temperature is shown more clearly in Fig. 6. The ratio, Nu/Nu_{ss}, tabulated in the last column of Table 3 is shown plotted against dimensionless amplitude in Fig. 6(*a*) and dimensionless period in Fig. 6(*b*). The curved lines in Fig. 6 were all obtained by fitting second-order polynominals (with least error) through *all* the data points in the top figure (Fig. 6*a*) and through points with large dimensionless temperature amplitude in the lower figure. Figure 6(*a*) shows that the heat transfer enhancement clearly depends on the dimensionless amplitude of the bottom wall temperature oscillation. Heat transfer is increased on, the order of 10 percent, if the bottom wall temperature fluctuation is large (temperature oscillation greater than 30 percent) but remains unchanged if the temperature change varies less than 15 percent. Figure 6(*b*) contains the same data as Fig. 6(*a*), but the heat transfer ratio is plotted versus dimensionless period. Figure 6(*b*) confirms the fact that

the period of the wall temperature oscillation has no influence on the heat transfer rate through the layer if the dimensionless amplitude is small, but shows that the period is important when the temperature fluctuations are large. Clearly more data are required to correlate the data properly in terms of the amplitude and period, but, nevertheless, Fig. 6 suggests that the heat transfer augmentation depends on the dimensionless amplitude and period of the wall temperature oscillation.

Before closing this section, one last remark is in order. This investigation, like so many other studies, is not an end but rather inspires more work to be done. Although this study showed that the wall temperature modulation can increase the rate of heat transfer through the layer, the experiments report only the magnitude and the conditions favorable for enhancement, but don't explain why the rate of heat transfer differs. Future work is needed to uncover the underlining physical mechanisms responsible for the increase in the heat transfer rate. One aspect of the problem not investigated in the present study, and thought to be at the heart of this matter, is the turbulent flow field within the layer. A careful and in-depth examination of the turbulent flow structure is needed, with particular attention placed on understanding the relationship between the changing wall temperature and the resulting flow patterns.

Conclusions

This paper reported the results of an experimental investigation of transient natural convection in a horizontal layer with a time-dependent boundary condition. The temperature of the bottom wall periodically changed with time, and the temperature of the top wall was held fixed. It was shown that the oscillatory surface temperature may or may not influence the time-averaged heat transfer through the cavity. If the bottom wall temperature oscillation is less than 15 percent of the mean temperature difference across the enclosure, the cycle-averaged heat transfer is unchanged and equal to the heat transfer through the layer with constant temperature walls. On the other hand, if the amplitude of the surface temperature modulation is greater than 30 percent, then the cycle-averaged heat transfer is larger than the steady-state value.

The consequence of these findings to engineering problems depends on the application in mind. This work has shown that the changing wall temperature should be considered if the surface temperature varies greatly but may be ignored for small temperature fluctuations provided that the overall heat transfer rate is the only issue.

References

Bejan, A., 1984, *Convection Heat Transfer*, Wiley, New York.

Chu, T. Y., and Goldstein, R. J., 1973, "Turbulent Convection in a Horizontal Layer of Water," *J. Fluid Mech.*, Vol. 60, Part 1, pp. 141–159.

Coleman, H. W., and Steele, W. G., 1989, *Experimentation and Uncertainty Analysis for Engineers*, Wiley, New York.

Deardorff, J. W., 1964, "A Numerical Study of Two-Dimensional Parallel-Plate Convection," *Journal of the Atmospheric Sciences*, Vol. 21, pp. 419–438.

Elder, J. W., 1968, "The Unstable Thermal Interface," *J. Fluid Mech.*, Vol. 32, Part 1, pp. 69–96.

Elder, J. W., 1969, "The Temporal Development of High Rayleigh Number Convection," *J. Fluid Mech.*, Vol. 35, Part 3, pp. 417–437.

Fromm, J. E., 1965, "Numerical Solutions of the Non-linear Equations for a Heated Fluid Layer," *Physics of Fluids*, Vol. 8, No. 10, pp. 1757–1769.

Gebhart, B., Jaluria, Y., Mahajan, R. L., and Sammakia, B., 1988, *Buoyancy-Induced Flows and Transport*, Hemisphere, New York.

Globe, S., and Dropkin, D., 1959, "Natural Convection Heat Transfer in Liquids Confined by Two Horizontal Plates and Heated From Below," ASME JOURNAL OF HEAT TRANSFER, Vol. 81, pp. pp. 24–28.

Goldstein, R. J., Chiang, H. D., and See, D. L., 1990, "High-Rayleigh Number Convection in a Horizontal Enclosure," *J. Fluid Mech.*, Vol. 213, pp. 111–126.

Kamierczak, M., and Chinoda, Z., 1992, "Buoyancy-Driven Flow in an Enclosure With Time Periodic Boundary Conditions," *Int. J. Heat Mass Transfer*, Vol. 35, No. 6, pp. 1507–1518.

Krishnamurti, R., 1973, "Some Further Studies on the Transition to Turbulent Convection," *J. Fluid Mech.*, Vol. 60, Part 2, pp. 285–303.

Ostrach, S., 1988, "Natural Convection in Enclosures," ASME JOURNAL OF HEAT TRANSFER, Vol. 110, pp. 1175–1190.

O'Toole, J. L., and Silveston, P. L., 1961, "Correlations of Convective Heat Transfer in Confined Horizontal Layers," *Chemical Engineering Program Symposium Series*, Vol. 32, Series 57, pp. 81–86.

Schladow, S. G., Patterson, J. C., and Street, R. L., 1989, "Transient Flow in a Side-Heated Cavity at High Rayleigh Number: A Numerical Study," *J. Fluid Mech.*, Vol. 200, pp. 121–148.

Sparrow, E. M., Husar, R. B., and Goldstein, R. J., 1970, "Observation and Other Characteristics of Thermals," *J. Fluid Mech.*, Vol. 41, Part 4, pp. 793–800.

Yang, K. T., 1987, "Natural Convection in Enclosures," *Handbook of Single-Phase Convective Heat Transfer*, S. Kakac, R. Shah, and W. Aung, eds., Wiley, New York, pp. 13.1–13.51.

Yang, H. Q., Yang, K. T., and Xia, Q., 1989, Periodic Laminar Convection in a Tall Vertical Cavity," *Int. J. Heat Mass Transfer*, Vol. 32, No. 11, pp. 2199–2207.

Natural Convection in a Porous, Horizontal Cylindrical Annulus

J. P. Barbosa Mota

E. Saatdjian

ENSIC,
1 Rue Grandville, B. P. 451,
54001 Nancy Cédex, France

Natural convection in a porous medium bounded by two horizontal cylinders is studied by solving the two-dimensional Boussinesq equations numerically. An accurate second-order finite difference scheme using an alternating direction method and successive underrelaxation is applied to a very fine grid. For a radius ratio above 1.7 and for Rayleigh numbers above a critical value, a closed hysteresis loop (indicating two possible solutions depending on initial conditions) is observed. For a radius ratio below 1.7 and as the Rayleigh number is increased, the number of cells in the annulus increases without bifurcation, and no hysteresis behavior is observed. Multicellular regimes and hysteresis loops have also been reported for fluid layers of same geometry but several differences between these two cases exist.

Introduction

Natural convection in a horizontal annulus has been considerably studied for a fluid layer. In 1961, the experimental work of Liu et al. showed the existence of a multicellular regime for relatively small radius ratios ($R = 1.15$). Later, Bishop and Carley (1966) provided photographs showing an oscillatory regime. Grigull and Hauf (1966) used a Mach-Zehnder interferometer and visualized different convective regimes including one where three-dimensional effects were present in the upper part of the layer. An oscillatory three-dimensional convection regime was also reported by Bishop et al. (1968) for an annular space filled with air; tobacco smoke was used to visualize the flow. Mack and Bishop (1968) used a perturbation technique to solve the steady two-dimensional equations and, although the analysis is valid only for small Rayleigh numbers, the results reveal the existence of secondary flows in the upper and lower parts of the layer for very small Prandtl numbers. Recent studies include the works of Powe et al. (1969, 1971), Kuehn and Goldstein (1976), and Rao et al. (1985). The numerical work of Fant et al. (1989) showed that at fairly high Rayleigh numbers, thermal instability for air appears as steady counterrotating cells near the top of the annulus. Perhaps their most interesting result is that the same flow exhibits a hysteresis behavior for small gap widths. In the limit $\mathrm{Pr} \to 0$, an unsteady hydrodynamic instability was demonstrated at high Grashof numbers in the middle of the annulus. Cheddadi et al. (1989) solved the same equations in primitive variables using the artificial compressibility method to obtain the pressure field. The tangential velocity component was measured using laser-Doppler anemometry in an air-filled annular space. Experimental and numerical values agree well; hysteresis behavior was also reported.

Results for a porous layer are less numerous. Caltagirone (1976a, b) visualized the thermal field using the Christiansen effect and observed a fluctuating three-dimensional regime in the upper part of the layer even though the lower part remained strictly two dimensional. Both a perturbation method and a finite difference technique were used to solve the two-dimensional Boussinesq equations. The former was based on a power series expansion of the Rayleigh number up to the third term and the latter used a 49×49 regular grid on the entire domain. Neither method predicted the instabilities observed experimentally. A local stability analysis using the Galerkin method succeeded in estimating a transitional Rayleigh number. A three-dimensional finite element simulation confirmed the existence of spiral, unsteady flows. Caltagirone's experiments have recently been reconsidered by Mojtabi et al. (1991) for the same radius ratio. Two cells of different length have been constructed; the thermal field is visualized by the Christiansen effect. The results of these experiments will be discussed in more detail later.

Rao et al. (1987, 1988) have solved the Boussinesq equations in both two and three dimensions using the Galerkin method. For a radius ratio of 2 and for Rayleigh numbers above 65, these authors obtain three possible numerical solutions depending on the initial conditions. The bifurcation point is in agreement with the value obtained experimentally by Caltagirone (1976a). The two-dimensional bifurcation phenomena of this problem have been studied, using perturbation techniques, by Himasekhar and Bau (1988) for small radius ratios. These authors considered gaps of radius ratio $2^{1/2}$, $2^{1/4}$, and $2^{1/8}$ and conclude that in all these cases, the transition to multiple cells occurs via a "perfect bifurcation"; one solution branch loses stability while another one gains it.

Recently, Arnold et al. (1991) solved the two-dimensional equations using a very fine mesh. For $R = 2$, a steady four-cell regime is seen to occur at a Rayleigh number of about 120; further increase of the Rayleigh number does not result in the appearance of more cells. However, for $R = 1.2$, a four-cell regime appears at $\mathrm{Ra} = 250$ and up to eight cells were observed on increasing the Rayleigh number.

Here, the two-dimensional equation model used by Arnold et al. (1991) is solved to study in detail the possible flow regimes in a horizontal, porous cylindrical layer. Particular attention to possible hysteresis behavior is given.

Problem Formulation and Solution

Consider a porous layer bounded between two horizontal concentric cylinders of radii R_i and R_o as shown in Fig. 1. The surfaces of the two cylinders are held at the constant temperatures T_i and T_o, respectively, with $T_i > T_o$. The saturated porous medium is treated as a fictitious fluid with heat capacity $(\rho c)_e = \epsilon(\rho c)_f + (1-\epsilon)(\rho c)_s$ and an effective thermal conductivity λ_e. The physical properties of the medium are evaluated at the average temperature $T_m = (T_i + T_o)/2$ and are assumed constant. Only the density variations with temperature are taken into account in the buoyancy terms (Boussinesq approximation) and Darcy's law is assumed valid. The governing dimensionless equations (see Caltagirone (1976a, b) or Arnold et al. (1991)) are:

Contributed by the Heat Transfer Division for publication in the JOURNAL OF HEAT TRANSFER. Manuscript received by the Heat Transfer Division June 1992; revision received September 1993. Keywords: Natural Convection, Porous Media. Associate Technical Editor: C. E. Hickox, Jr.

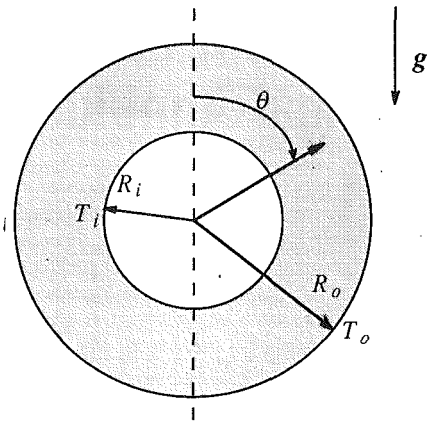

Fig. 1 Flow geometry and coordinate system

$$\frac{\partial T}{\partial t} + \mathbf{V} \cdot \nabla T = \nabla^2 T \tag{1}$$

$$\nabla^2 \psi = \mathrm{Ra}\mathbf{k}' \cdot \nabla T \tag{2}$$

where $\mathbf{k}' = \sin\theta \mathbf{e}_r + \cos\theta \mathbf{e}_\theta$. The dimensionless parameter Ra appearing above is the Rayleigh number defined as:

$$\mathrm{Ra} = \frac{(\rho c)_f \rho_o g \alpha (T_i - T_o) K R_i}{\lambda_e \mu}$$

and, assuming flow symmetry about the vertical centerline, the boundary conditions in dimensionless form are:

$$T = 1;\ \psi = 0;\ \text{for } r = 1$$

$$T = 0;\ \psi = 0;\ \text{for } r = R$$

$$\frac{\partial T}{\partial \theta} = 0;\ \psi = 0;\ \text{for } \theta = 0,\ \pi \tag{3}$$

where $R = R_o/R_i$ is the radius ratio. At low Rayleigh numbers, the assumption of flow symmetry has been verified experimentally by Caltagirone (1976a, b) for two-dimensional convection in a porous layer; Fant et al. (1989) have verified this hypothesis for a fluid layer. Although two-dimensional phenomena are not the only type that can occur in this problem, two-dimensional bifurcations are likely to precede three-dimensional ones, as stated and confirmed by Himasekhar and Bau (1988) for small radius ratios.

Since the steady-state solution for the conduction regime is:

$$T = 1 - \frac{\ln r}{\ln R}$$

an expression for the Nusselt number is easily found:

$$\mathrm{Nu} = \frac{(\partial T/\partial r)_{\text{convection}}}{(\partial T/\partial r)_{\text{conduction}}} = -r \ln R \left(\frac{\partial T}{\partial r}\right)_{\text{convection}}$$

and, in particular:

$$\mathrm{Nu}_i = -\ln R \left(\frac{\partial T}{\partial r}\right)_{r=1}$$

$$\mathrm{Nu}_o = -R \ln R \left(\frac{\partial T}{\partial r}\right)_{r=R}$$

where Nu_i and Nu_o are the local Nusselt numbers for the inner and outer cylinders, respectively. At steady state, the mean Nusselt number is given by:

$$\overline{\mathrm{Nu}} = \frac{1}{\pi}\int_0^\pi \mathrm{Nu}_i\, d\theta = \frac{1}{\pi}\int_0^\pi \mathrm{Nu}_o\, d\theta \tag{4}$$

Equations (1)–(3) were solved using second-order centered finite differences. The energy equation was solved by the implicit alternating direction method and the stream function equation was solved using successive underrelaxation. A 101×101 regularly spaced grid covering half the computational domain was employed. The local Nusselt numbers for both the inner and outer cylinders were calculated using the following third-order difference schemes:

$$\mathrm{Nu}_i = -\ln R \frac{-11T_{1,j} + 18T_{2,j} - 9T_{3,j} + 2T_{4,j}}{6\Delta r} + O(\Delta r)^3$$

$$\mathrm{Nu}_o =$$

$$-R \ln R \frac{11T_{N,j} - 18T_{N-1,j} + 9T_{N-2,j} - 2T_{N-3,j}}{6\Delta r} + O(\Delta r)^3$$

The integrals in Eq. (4) were calculated using the extended Simpson's rule and the final mean Nusselt number was taken as the average of the two calculated values.

The importance of working with a sufficiently fine grid has been discussed for a fluid layer by Rao et al. (1985) who implies that an overly coarse grid could be one of the reasons why some authors do not obtain multicellular flow regimes. Fant et al. (1989) used a 31×101 mesh for the entire annulus with nodes concentrated near the top of the layer where multicellular flow can develop. In a porous layer, Caltagirone (1976a, b) used a 49×49 grid covering the entire annulus since symmetry was not assumed a priori. Arnold et al. showed that calculations for $R = 1.2$ and $\mathrm{Ra} = 300$ yielded a two-cell regime with a 71×71 grid and a four-cell regime with a 101×101 mesh. The 101×101 grid used here for half the annulus is finer than practically all of the grids previously employed, which showed multicellular flow behavior. For $R = 2$ and Rayleigh numbers up to 150, a 120×120 grid was employed and the results were

Nomenclature

c = heat capacity
$\mathbf{e}_r$, $\mathbf{e}_\theta$ = radial and tangential unit vectors
g = gravitational acceleration
$\mathbf{k}'$ = $\sin\theta \mathbf{e}_r + \cos\theta \mathbf{e}_\theta$
K = permeability of porous medium
L = length of the cylinders
Nu = Nusselt number
Nu_i, Nu_o = Nusselt number at inner and outer cylinders, respectively
$\overline{\mathrm{Nu}}$ = mean Nusselt number
Pr = fluid Prandtl number
r = radial coordinate
R = radius ratio = R_o/R_i
R_i, R_o = inner and outer cylinder radii, respectively
Ra = Rayleigh number
t = time
T = dimensionless temperature
T_i, T_o, T_m = temperatures of inner, outer cylinder, mean temperature
TOL = tolerance value
$\mathbf{V}$ = velocity vector
α = thermal expansion coefficient
δ = relative convergence error
ϵ = porosity
θ = tangential coordinate
λ_e = effective thermal conductivity
μ = fluid viscosity
ρ, ρ_o = fluid density, density at T_o
ψ = dimensionless stream function

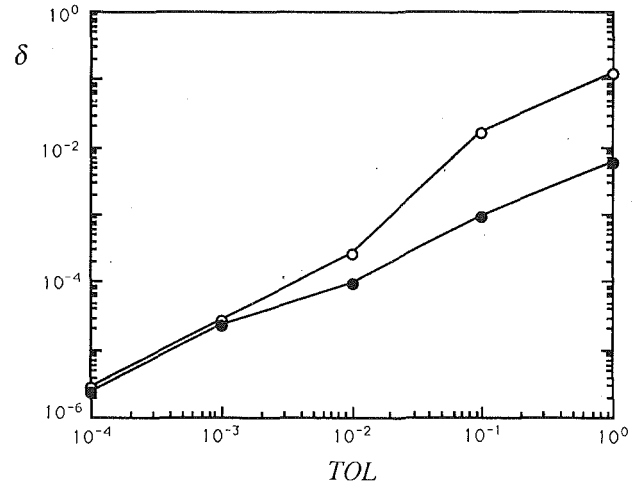

Fig. 2 Convergence error for different *TOL* values

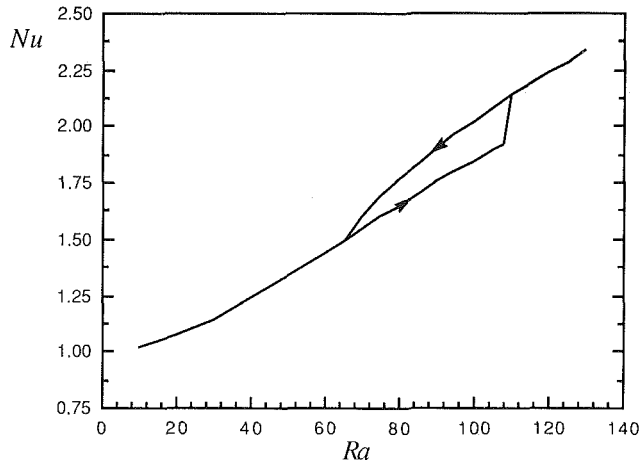

Fig. 3 $\overline{\text{NU}}$ versus Ra for $R=2$

compared to those of the 101×101 mesh. The streamline pattern and the isotherms show no visible difference and the numerical value of the Nusselt number is the same to within 0.1 percent.

The calculations were performed on a RISC workstation and the CPU time required varied from about 15 minutes to several hours depending on the Rayleigh number. For each radius ratio, the search for a possible hysteresis behavior was conducted by first determining the steady-state solutions for successively larger values of the Rayleigh number. Subsequently, calculations were then carried out in inverse order, i.e., for decreasing Rayleigh numbers. At first, the Rayleigh number is increased by intervals of 5, but near the bifurcation points and during the whole hysteresis loop, intervals of 1 were employed. In some cases, the sequence of Rayleigh numbers was increased by intervals of 0.1; this was the case for very small radius ratios and high Rayleigh numbers.

Calculations were assumed to converge when the dimensionless temperature difference between two successive time steps was smaller than a given tolerance value (TOL) for every grid point. In terms of the dimensional temperature, this can be written as:

$$\max \left| \frac{T_{i,j}^{n+1} - T_{i,j}^{n}}{T_i - T_o} \right| < \text{TOL}$$

where n and $n+1$ are any two successive time steps. For $R=2$ and $R=1.2$, a tolerance value of 10^{-4} was used, for the other

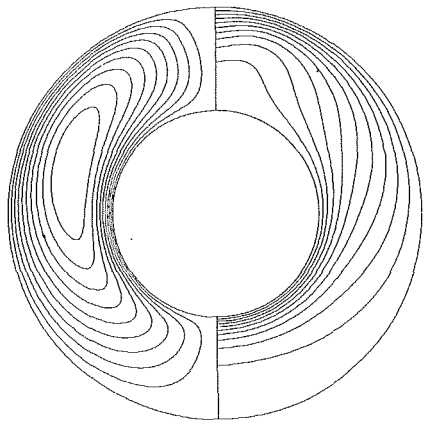

Fig. 4 Streamlines and isotherms for $R=2$, $Ra=100$

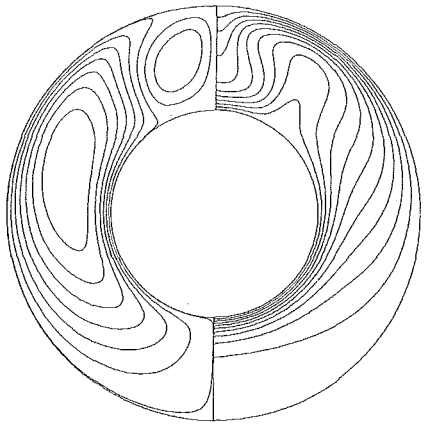

Fig. 5 Streamlines and isotherms for $R=2$, Ra = 140

values of R, a value of 10^{-3} was preferred. In order to estimate the convergence error, calculations concerning representative cases of the two-cell ($R=2$, $Ra=100$) and of the four cell ($R=2$, $Ra=150$) flow regimes were performed with different tolerance values. The results are presented in Fig. 2. The parameter δ is defined as:

$$\delta = \frac{|\overline{\text{Nu}}(\text{TOL}=10^{-8}) - \overline{\text{Nu}}|}{\overline{\text{Nu}}(\text{TOL}=10^{-8})}$$

and may be considered a good approximation to the true relative tolerance error. The calculations for Ra = 100 started from the regime of pure conduction ($Ra=0$). For Ra = 150, the initial estimate was the solution for $Ra=100$ (already in the four-cell domain). It may be concluded from Fig. 2 that tolerance values of 10^{-3} and 10^{-4} should give convergence errors for $\overline{\text{Nu}}$ less than 10^{-4}. The convergence error should not be taken as the truncation error, which is of order $(\Delta r^2 + \Delta\theta^2)$.

Results and Discussion

The calculations were first performed for $R=2$, a case for which experimental results are reported in the literature. The mean Nusselt number $\overline{\text{Nu}}$ as a function of Rayleigh number is shown in Fig. 3, a closed hysteresis loop is seen to occur. On increasing the Rayleigh number, the mean Nusselt number increases gradually along the lower branch and at Ra = 110, the flow changes from a two-cell to a four-cell regime with an abrupt rise in the curve slope. This is a consequence of more efficient fluid mixing due to the counterrotating additional cell. Isotherms and streamlines representative of both regimes are shown in Figs. 4 and 5 for Ra = 100 and Ra = 140, respec-

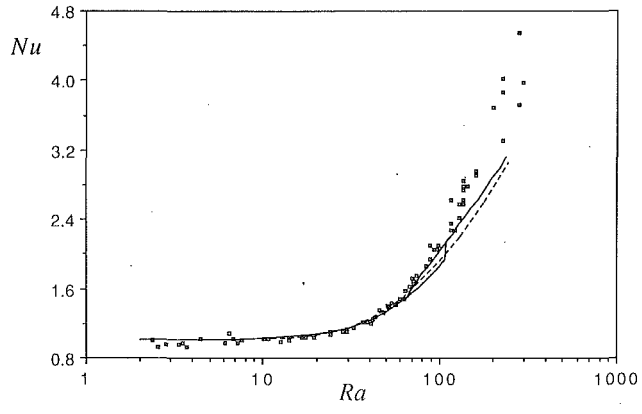

Fig. 6 $\overline{Nu}$ versus Ra for $R=2$, solid line = present simulation, dashed line = model of Caltagirone (1976a, b)

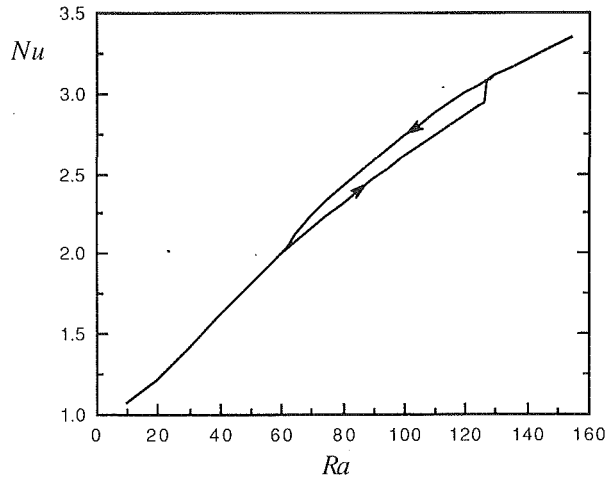

Fig. 7 $\overline{Nu}$ versus Ra for $R=2.5$

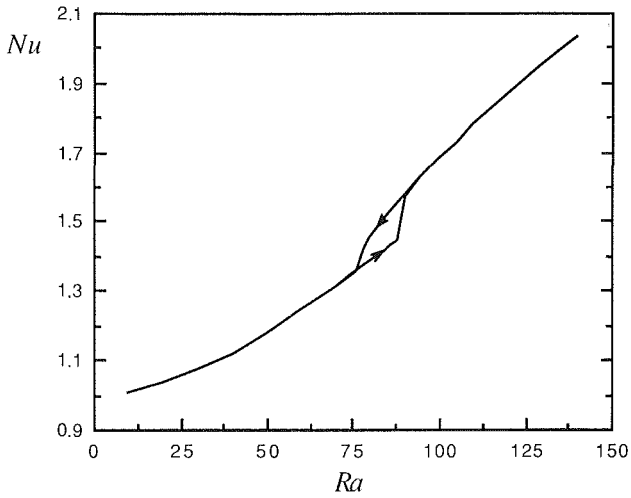

Fig. 8 $\overline{Nu}$ versus Ra for $R=1.8$

tively. When the Rayleigh number is decreased slowly past the loop's upper limit, the mean Nusselt number follows the upper path and meets the other curve at Ra = 67; at this point the streamlines change from four to two cells.

Caltagirone (1976a) obtained experimental results for the same radius ratio by a method of visualization of the thermal field using the Christiansen effect in a porous annulus with length $L=0.8$ m and inner radius $R_i=0.04$ *m*. The optical method is based on the fact that the porous medium, which was formed by transparent isotropic glass powder, has a refraction coefficient near to that of the colorless liquid (water). Thus the solid and the liquid were optically homogeneous only for the central wavelength, which owing to the differences of the dispersion curves is a function of temperature alone. The cell was illuminated by an arc lamp producing a set of spectrum lines each corresponding to a different isotherm.

For Rayleigh numbers below 65 ± 4, Caltagirone (1976a) observed the expected steady two-dimensional regime with the two-cell symmetric pattern about the vertical centerline. At higher Rayleigh numbers, the author states that fluctuating three-dimensional effects developed on top of the main two-dimensional motion in the upper part of the layer, although the lower zone remained two dimensional. Experimental Nusselt numbers were also determined based on temperature measurements of the thermal field by means of 16 thermocouples introduced in the porous layer. These data are compared, in Fig. 6, with our numerical results. The numerical predictions of Caltagirone (1976a) using a much coarser grid are also included. The loop's lower limit (Ra = 67) is in excellent agreement with the observed transitional Rayleigh number. As might be expected, the upper branch is closer to the experimental results because the instabilities, which were visible for Rayleigh numbers within the loop's limits, are better described by the four-cell flow pattern. At higher Rayleigh numbers, the mean Nusselt number measured experimentally is much above the calculated value. This implies that there is a significant heat transfer increase due to the three-dimensional effects over the length of the cylinders. The numerical values of Caltagirone (1976) are in all cases below the ones obtained here.

Recently, Mojtabi et al. (1991) have constructed two cells of radius ratio $R=2$ and visualized the thermal field using the Christiansen effect. With the longer experimental cell and on increasing the Rayleigh number these authors obtain a two-cell flow for Rayleigh numbers up to 250; at this point three-dimensional effects appear in the upper part of the cell. However, on decreasing the Rayleigh number from 338, these authors report that a steady four-cell flow is established in the layer. The flow pattern changes from four cells to two cells at Ra = 69 according to Mojtabi et al. (1991). This value is in excellent agreement with both the value of 67 obtained by our calculations and with the earlier experiments of Caltagirone (1976b). These results are particularly interesting because for a given range of Rayleigh numbers, two different two-dimensional flow patterns can be observed experimentally. The experiments do not confirm, however, the loop's upper limit of Ra = 110 obtained by our calculations. Also, the third flow pattern containing six cells and obtained numerically by both Rao et al. (1987) and Mojtabi et al. (1991) using the Galerkin method has not yet been visualized experimentally.

The influence of radius ratio on this phenomenon was also investigated with our computer simulation. For $R=2.5$, the hysteresis loop expands considerably and extends from Ra = 60 to Ra = 127 as shown in Fig. 7. For $R=1.8$, the loop narrows and is located between Ra = 75 and Ra = 90 as shown in Fig. 8. In both cases, a transition from a two to a four-cell regime occurs. Unfortunately, no experimental data is available for this case.

If the radius ratio is further decreased, the hysteresis loop disappears completely. For $R=1.5$ and $R=1.2$ four-cell regimes appear at Ra = 102 and Ra = 235, respectively. This last value is somewhat lower than that reported by Arnold et al. (1991). Here, the criterion for the appearance of a cell is based on the sign of the stream function while Arnold et al. based their criterion on a visualization of the streamlines. The method employed here is to be preferred.

For $R=1.2$ calculations were carried out up to Ra = 1400,

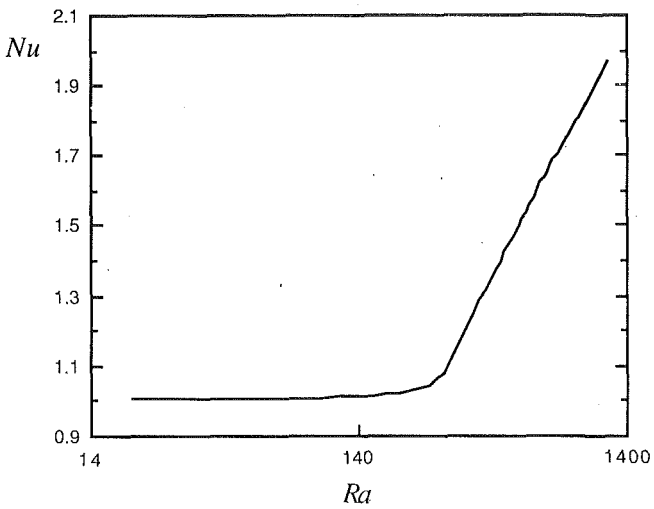

Fig. 9 $\overline{Nu}$ versus Ra for $R = 1.2$

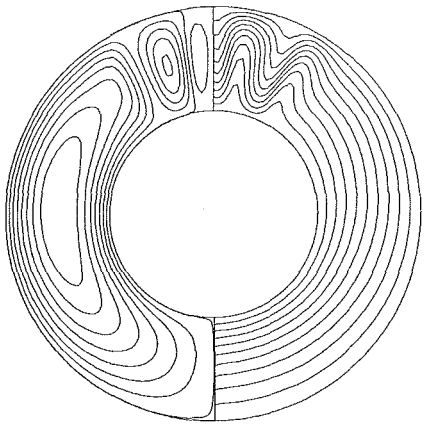

Fig. 10 Streamlines and isotherms for $R = 1.2$, $Ra = 320$

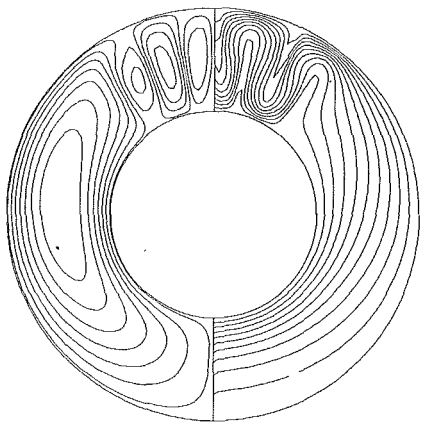

Fig. 11 Streamlines and isotherms for $R = 1.2$, $Ra = 800$

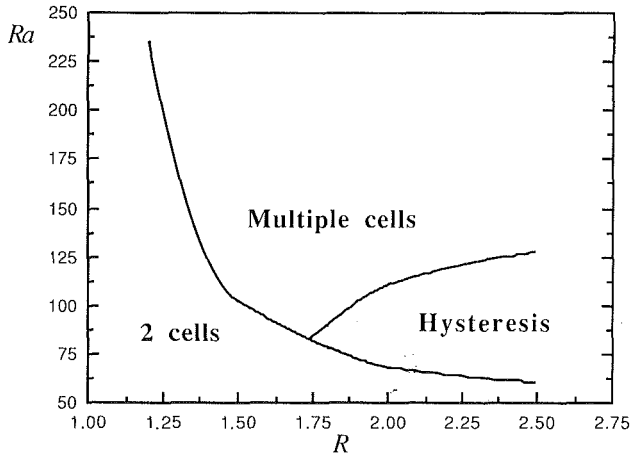

Fig. 12 Zone where multicellular flow occurs

the mean Nusselt number is given in Fig. 9. No hysteresis loop was encountered and a four-cell regime appears for $Ra = 235$. The fluid in the two-cell regime moves upward along the inner cylinder as a result of warming up on contact with the hot surface. It then falls along the outer, colder cylinder. In the four-cell regime, the two secondary cells are counterrotating. Further increase of the Rayleigh number results in the appearance of a six-cell flow regime at $280 < Ra < 290$, which is depicted in Fig. 10 for $Ra = 320$. The additional cell is generated between the other two and rotates in the same direction as the main cell, creating a zone of shear between them. An eight-cell regime appears at $340 < Ra < 350$ but further increase of the Rayleigh number does not lead to additional cells. The fourth cell appears between the two cells that are rotating in the same sense, thus eliminating the zone of shear that existed previously. Figure 11, obtained for $Ra = 800$, shows a typical eight-cell flow pattern. The results for radius ratio less than 1.7 resulting in smooth flows regime transitions agree with the results of Himasekhar and Bau (1988).

The numerical work of Fant et al. (1989) for a fluid layer shows a similar hysteresis behavior between $2.85 \times 10^5 < Ra < 3.51 \times 10^5$ for $Pr = 0.706$ (air) and $R = 1.2$. In this range, both a two and a four-cell regime can be obtained; the same abrupt change in the mean Nusselt number is observed at the loop's upper limit. For a narrower gap $R = 1.1$ and the same Prandtl number, the range obtained by these authors for a closed hysteresis behavior is $2.57 \times 10^6 < Ra < 2.84 \times 10^6$; however, the transition is now from two to six cells. The results in both a fluid and a porous layer imply that reducing the radius ratio increases flow stability. On the other hand, the observed expansion of the hysteresis loop when the gap spacing of the layer is decreased seems to contradict the results obtained here for a porous layer. This is misleading since both the loop's upper and lower limits increase as the radius ratio decreases. In fact, the ratio of the limit's Ra_{upper}/Ra_{lower} is closer to unity for $R = 1.1$ than for $R = 1.2$ suggesting that for the fluid layer, the loop will completely disappear only in the limit $R \to 1$. Figure 12 is a plot of the Rayleigh number versus radius ratio for the porous layer. Our calculations show that hysteresis loops disappear for $R < 1.7$ approximately; this is shown in Fig. 12. Zones where multicellular regimes can occur are also indicated.

Conclusions

The numerical solution of natural convection in a porous medium bounded by two horizontal isothermal cylinders shows that multicellular regime can occur. For very small radius ratio and on increasing the Rayleigh number, the steady-state regime changes from two to four to six to eight cells without exhibiting a hysteresis loop. For a radius ratio above 1.7 approximately, closed hysteresis loops between regimes containing 2 or 4 cells are obtained. Closed hysteresis loops have been reported for fluid layers but several differences between these two cases exist and have been fully explained above.

Acknowledgments

Very useful discussions with Prof. N. Midoux and Jean Claude André are acknowledged by the authors. One of the authors (J.P.B.M.) benefits from the financial support of JNICT (Portugal) through grant No. BD/1607/91-RM.

References

Arnold, F., et al., 1991 "Natural Convection in a Porous Medium Between Concentric, Horizontal Cylinders," *Numerical Methods in Thermal Problems*, Pineridge Press, Swansea, United Kingdom, Vol. 7, Part 2, pp. 1084–1091.

Bishop, E. H., and Carley, C. T., 1966, "Photographic Studies of Natural Convection Between Concentric Cylinders," *Proc. Heat Transfer Fluid Mechanics Institute*, Stanford Univ. Press, Stanford, CA, pp. 63–78.

Caltagirone, J. P., 1976a, "Instabilités Thermoconvectives en milieu poreux," Thèse d'état, Univ. Pierre et Marie Curie, Paris, VI, France.

Caltagirone, J. P., 1976b, "Thermoconvective Instabilities in a Porous Medium Bounded by Two Concentric Horizontal Cylinders," *J. Fluid Mech.*, Vol. 76, Part 2, pp. 337–362.

Cheddadi, A., Caltagirone, J. P., and Mojtabi, A., 1989, "An Experimental and Numerical Study of Natural Convection in Horizontal Cylindrical Annuli," *Numerical Methods in Laminar and Turbulent Flow*, Pineridge Press, Swansea, United Kingdom, Vol. 6, Part 2, pp. 1157–1166.

Fant, D. B., Rothmayer, A., and Prusa, J., 1989, "Natural Convective Flow Instability Between Horizontal Concentric Cylinders," *Numerical Methods in Laminar and Turbulent Flow*, Pineridge Press, Swansea, United Kingdom, Vol. 6, Part 2, pp. 1047–1065.

Grigull, U., and Hauf, W., 1966, "Natural Convection in Horizontal Cylindrical Annuli," *Proc. 3rd Int. Heat Transfer Conf.*, Vol. 2, pp. 182–195.

Himasekhar, K., and Bau, H. H., 1988, "Two-Dimensional Bifurcation Phenomena in Thermal Convection in Horizontal, Concentric Annuli Containing Saturated Porous Media," *J. Fluid Mech.*, Vol. 187, pp. 267–300.

Kuehn, T. H., and Goldstein, R. J., 1976, "An Experimental and Theoretical Study of Natural Convection in the Annulus Between Horizontal Concentric Cylinders," *J. Fluid Mech.*, Vol. 74, pp. 695–719.

Liu, C. Y., Mueller, W. K., and Landis, F., 1961, "Natural Convection Heat Transfer in Long Horizontal Cylindrical Annuli," *Int. Devl. Heat Transfer*, Vol. 5, pp. 976–984.

Mack, L. R., and Bishop, E. H., 1968, "Natural Convection Between Horizontal Concentric Cylinders for Low Rayleigh Numbers," *Quart. J. Mech. Appl. Math.*, Vol. 21, pp. 223–241.

Mojtabi, M. C., et al., 1991, "Numerical and Experimental Study of Multicellular Free Convection Flows in an Annular Porous Layer," *Int. J. Heat Mass Transfer*, Vol. 34, No. 12, pp. 3061–3074.

Powe, R. E., Carley, C. T., and Bishop, E. H., 1969, "Free Convection Flow Pattern in Cylindrical Annuli," ASME JOURNAL OF HEAT TRANSFER, Vol. 91, pp. 310–314.

Powe, R. E., Carley, C. T., and Carruth, S. T., 1971, "A Numerical Solution for Natural Convection in Cylindrical Annuli," ASME JOURNAL OF HEAT TRANSFER, Vol. 93, pp. 210–220.

Rao, Y. F., et al., 1985, "Flow Patterns of Natural Convection in Horizontal Cylindrical Annuli," *Int. J. Heat Mass Transfer*, Vol. 28, pp. 705–714.

Rao, Y. F., Fukuda, K., and Hasegawa, S., 1987, "Steady and Transient Analyses of Natural Convection in a Horizontal Porous Annulus With the Galerkin Method," ASME JOURNAL OF HEAT TRANSFER, Vol. 109, pp. 919–927.

Rao, Y. F., Fukuda, K., and Hasegawa, S., 1988, "A Numerical Study of Three-Dimensional Natural Convection in a Horizontal Porous Annulus With Galerkin Method," *Int. J. Heat Mass Transfer*, Vol. 31, No. 4, pp. 695–707.

Y. Kamotani

F.-B. Weng

S. Ostrach

Department of Mechanical and Aerospace Engineering,
Case Western Reserve University,
Cleveland, OH 44106

J. Platt

NASA Lewis Research Center,
Cleveland, OH 44135

Oscillatory Natural Convection of a Liquid Metal in Circular Cylinders

An experimental study is made of natural convection oscillations in gallium melts enclosed by right circular cylinders with differentially heated end walls. Cases heated from below are examined for angles of inclination (ϕ) ranging from 0 deg (vertical) to 75 deg with aspect ratios Ar (height/diameter) of 2, 3, and 4. Temperature measurements are made along the circumference of the cylinder to detect the oscillations, from which the oscillatory flow structures are inferred. The critical Rayleigh numbers and oscillation frequencies are determined. For $Ar=3$ and $\phi=0$ deg, 30 deg the supercritical flow structures are discussed in detail.

1 Introduction

The quality of crystals grown from melts is determined largely by their homogeneity of composition and structure. In melt growth of semiconductor crystals, for example, the electronic properties of the crystal are to a large extent determined by the compositional homogeneity of the crystal. All crystal growth processes of solidification from a melt involve temperature gradients; these temperature gradients cause density gradients, which can lead to natural convection flows when a gravity field is present. These flows can affect the transport of energy and material, which in turn can have a profound influence on the structure and quality of the resulting crystals (Hurle, 1972; Ostrach, 1983). A problem occurs when the flow is oscillatory; this can result in periodic inhomogeneities in crystals grown under such conditions (Kim et al., 1992; Müller et al., 1984).

Although material used in crystal growth span a large range of Prandtl numbers, the present study focuses on low-Prandtl-number fluids because of the importance of oscillations in such fluids. Semiconductors such as silicon and germanium are examples of materials that have low Prandtl numbers. For natural convective flow of a low Prandtl number fluid along a wall, the velocity boundary layer is thinner than the thermal boundary layer. This means that fluctuations in temperature can occur outside of the region where the resulting fluctuations in the velocity field would be damped by the viscous effects. This lack of damping makes low-Prandtl-number fluids more prone to develop unsteady flows.

The present work investigates natural convection of a liquid metal in circular cylinders with differentially heated end walls because it is a basic configuration for several crystal growth systems (e.g., vertical Bridgman technique). For most such applications the container aspect ratio (length/diameter ratio) is larger than unity, so only large-aspect-ratio containers are considered herein. The reduced-gravity environment of space has been suggested for growing better quality crystals but before expensive experiments are carried out in space, where body forces, although reduced in magnitude, can occur in any direction, the transport phenomena in melts need to be studied in the simpler case of normal gravity. For that reason the effect of container inclination angle on the melt flow is also investigated herein.

Much work has been done in the past for natural convection of low Prandtl fluids in vertical circular cylinders heated from below concerning the transition from a quiescent state to steady flow, but work on the transition from steady to oscillatory flow is limited to a few numerical (Crespo et al., 1988, 1989; Crespo and Bontoux, 1989; Fontaine et al., 1988; Neumann, 1990) and experimental (Verhoeven, 1969; Müller et al., 1984) studies. Except for the work by Verhoeven (1969) in which the oscillation frequency is reported with the container inclined 20 deg from the vertical, no work has been performed on the oscillation phenomenon in tilted cylinders. Since liquid metals are generally opaque, flow structures during oscillations have not been investigated experimentally. Therefore, the main objectives of the present work are: (1) to study the temperature field in detail during oscillation and to reconstruct the flow fluid based on the information obtained, (2) to study the oscillation phenomenon inclined cylinders.

2 Experiment Design

2.1 Important Parameters. Consider the system shown in Fig. 1. A cylinder of fluid inclined at angle ϕ to the gravity vector has constant (but different) temperature ends and insulated sides. By heating the bottom end natural convection is generated. It can be shown that the important dimensionless parameters associated with the flow are: Ra = Rayleigh number, Pr = Prandtl number, Ar = aspect ratio (L/D), and ϕ = inclination angle. In the present work we consider the situation where $\mathrm{Pr}<1$, $Ar>1$, $\mathrm{Ra}>>1$, and $0\le\phi<90$ deg.

2.2 Experimental Setup. The goal of this study is to approach a situation with constant-temperature boundaries at the ends of the cylinder and an insulated boundary along its circumference. This was accomplished by enclosing the molten gallium (Pr = 0.0207) with a copper plate on the bottom, a

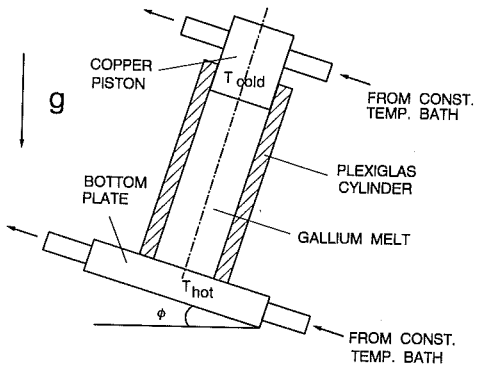

Fig. 1 Test section

Contributed by the Heat Transfer Division for publication in the JOURNAL OF HEAT TRANSFER. Manuscript received by the Heat Transfer Division June 1993; revision received September 1993. Keywords: Liquid Metals, Natural Convection, Transient and Unsteady Heat Transfer. Associate Technical Editor: J. R. Lloyd.

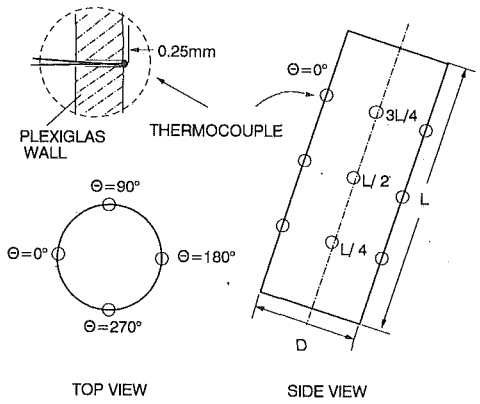

Fig. 2 Location of thermocouples

plexiglass tube along the sides, and a copper piston on top (Fig. 1). These materials were chosen for their thermal conductivities, with copper more conducting than gallium; plexiglass is much less conductive than either of these metals, making it an insulator in this situation. In order to reduce the heat loss from the side wall further the cylinder was wrapped by 1-cm-thick foam insulation. The heat loss was judged to be negligible based on the fact that when the system was heated from above in vertical orientation (stable configuration and thus no fluid motion), the temperature distribution was very linear in the axial direction and axisymmetric. Cylinders of two different diameters were used: a 1.59-cm-dia cylinder for $Ar=2$ and a 1.27-cm-dia cylinder for $Ar=2$, 3, and 4. The wall thickness of the two cylinders was 4 mm. The whole apparatus was placed on a tilt table.

The bottom plate was made of copper with an internal channel for water circulation. The top copper piston was also designed to maintain its temperature by running constant temperature water through it. Both top and bottom end temperatures were monitored by imbedded thermocouples.

Holes were drilled along the circumference of the plexiglass cylinder for thermocouples to measure temperatures in the gallium. Twelve copper-constantan thermocouples made from 0.12-mm-dia wire were used in each test section, four equally spaced around the circumference at each of the three levels: $L/4$, $L/2$, and $3L/4$, as shown in Fig. 2. These thermocouples were placed so that their beads protruded only 0.25 mm into the cylinder (Fig. 2) in order to avoid affecting the temperature oscillations. The idea of using many thermocouples arranged as described is to study the relationship among the outputs, especially their phase relations, on the basis of which one can deduce the overall convection pattern and flow structure. A similar technique was employed by Olson and Rosenberger (1979) in a similar problem but with gases and by Verhoeven (1969) in the experiment with Hg. The flow structure can be deduced uniquely only when it is relatively simple (e.g., quiescent, unicellular). The effect of those thermocouples on the flow was carefully assessed. For that purpose a test section with only one thermocouple was constructed. The critical temperature difference for the onset of oscillations and the oscillation frequency were determined with the thermocouple placed at several locations from the wall. If the protrusion distance was larger than 1 mm, the onset was delayed. On the other hand, if it was flush with the wall, it could not pick up the oscillations cleanly. Comparing the data with those taken with the test section with 12 thermocouples protruding 0.25 mm into the fluid, their difference was judged to be negligible within the experimental error.

Most of the data were gathered by an Omega OM-900 Data Acquisition System, which converts the analog signals of the thermocouples to digital temperatures with a resolution of $\pm 0.03°C$, and is capable of gathering data at a wide range of rates. For the experimental data the relatively low acquisition rate of 1 Hertz was used because of the low frequencies of oscillation that were observed.

2.3 Experimental Procedure. The procedure to fill the test section was as follows: The bottom plate and the copper piston were heated above the melting temperature of gallium, which is 29°C. Solid clean gallium pieces were placed in the test section, melted, and then stirred to remove trapped air pockets. The oxide film that formed at the melt surface was removed carefully. The copper piston was inserted so that the air trapped between the bottom of the piston and the surface of the gallium would escape through the air-expulsion holes in the plexiglass cylinder.

Typically two runs were made to find the critical temperature difference for the onset of oscillations. First a coarse run with temperature steps of about 2°C was made to get a general idea of the critical temperature difference. Then the system was returned to zero temperature difference. Following that a second run was made with temperature steps of 0.5°C. At each step about 10 minutes were allowed for the system to reach steady state before data collection. The data were then examined for oscillations. The existence or nonexistence of oscillations was usually obvious by observing the temperature traces recorded by the computer. (Oscillation in any one of the temperature traces was considered sufficient to consider the system oscillating.) A fast Fourier transform was applied to the data to calculate the frequencies of the oscillations. In a case where the existence of oscillations was questionable, another set of data was taken at the same temperature difference to check repeatability of the possible oscillations.

The experiment error in the temperature measurement is estimated to be $\pm 0.1°C$ with all the thermocouples calibrated carefully. The error in the frequency measurement is estimated to be ± 3 percent. Both values are more than adequate considering the reproducibility of the experimental data, which will be discussed later. The error in the tilt angle is estimated to be ± 0.1 deg.

3 Results and Discussion

3.1 Temperature Traces and Flow Structures. The thermocouple data give us information about convection in the fluid and based on that the flow structure is inferred qualitatively. Because of space limitation only the results for $Ar=3$ are presented.

Nomenclature

Ar = aspect ratio $= L/D$
D = container diameter
f = frequency of oscillations
f^* = dimensionless frequency $= fArL/(g\beta\Delta TL)^{1/2}$
g = gravitational acceleration
L = container length
Pr = Prandtl number $= \nu/\alpha$
Ra = Rayleigh number $= g\beta\Delta TD^3/\nu\alpha$
Ra_{cr} = critical Rayleigh number
α = fluid thermal diffusivity
β = fluid thermal expansion coefficient
ΔT = temperature difference between top and bottom ends
ΔT_{cr} = critical temperature difference
θ = azimuthal angle, Fig. 2
ν = fluid kinematic viscosity
ϕ = inclination angle, Fig. 1

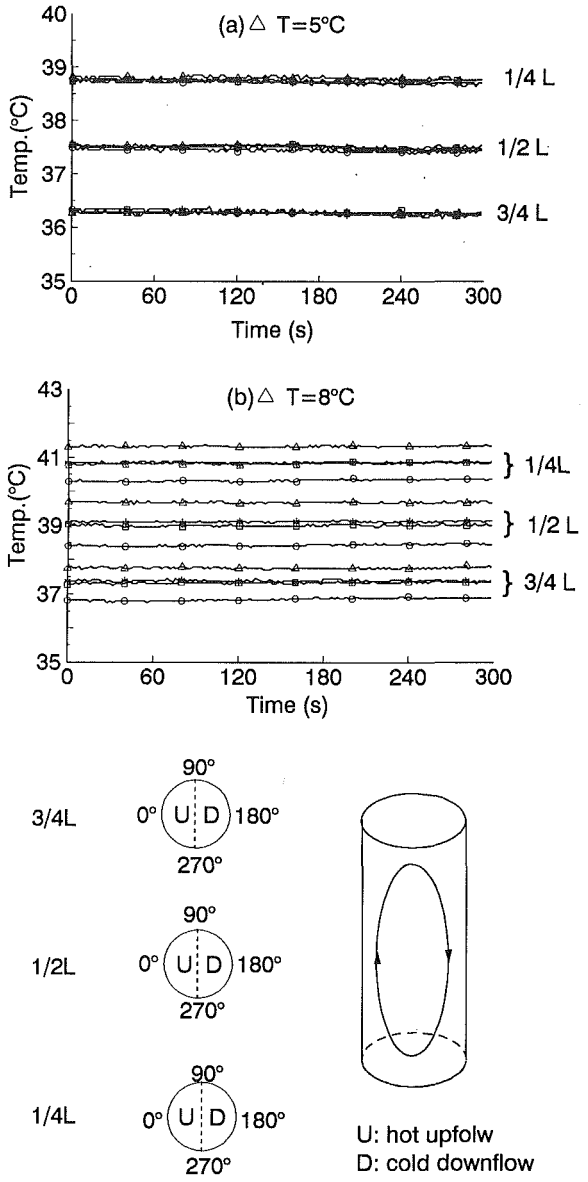

Fig. 3 Thermocouple outputs showing no flow and unicellular flow for $Ar = 3$ and $\phi = 0$ deg: Δ—$\phi = 0$ deg; □ —$\theta = 90$ deg; ○ —$\theta = 180$ deg; ∗ —$\theta = 270$ deg

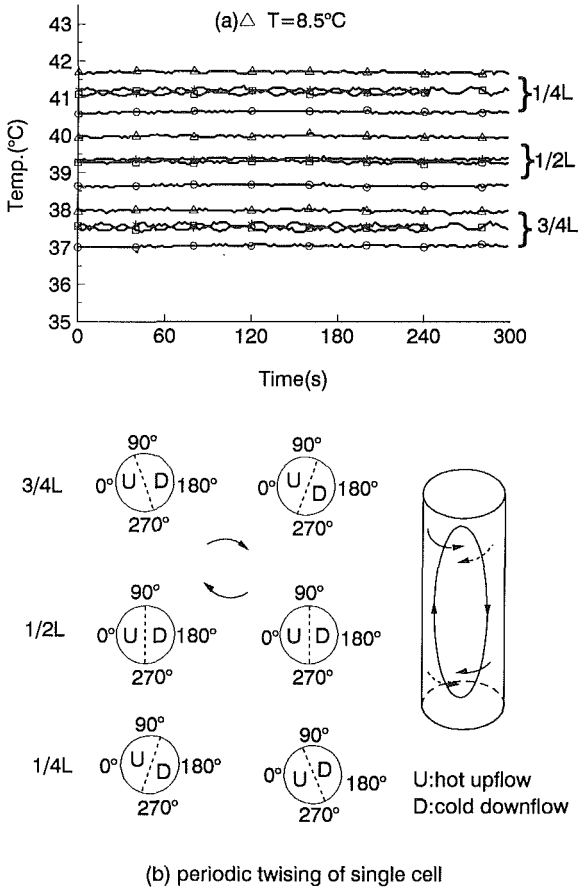

Fig. 4 Thermocouple outputs showing onset of oscillations and postulated flow pattern; see Fig. 3 for explanation of symbols

The vertical case is discussed first. The temperature recordings obtained at various ΔT values are shown in Fig. 3. Figure 3(*a*) shows the thermocouple outputs at $\Delta T = 5°C$ ($Ra = 2.7 \times 10^3$). The four outputs at each height are all close to each other. The outputs from different heights show that temperature changes linearly in the axial direction. Those facts suggest that no or very weak flow exists in the cylinder so that heat transfer is dominated by conduction.

When ΔT is increased to above 6°C, the temperature field becomes nonaxisymmetric. Around $\Delta T = 6$–7°C the temperature field changes slowly with time, but at $\Delta T = 8°C$ ($Ra = 4.3 \times 10^3$) it becomes steady (Fig. 3*b*). As seen in Fig. 3(*b*), at all heights the thermocouple located at the aximuthal angle of 0 deg shows the highest reading, while the one at 180 deg shows the lowest, and those at 90 and 270 deg are both nearly equal to the average of the above two values. The temperature distribution indicates clearly that there exists a unicellular flow with upflow centered around 0 deg and downflow around 180 deg as illustrated in Fig. 3(*c*). That transition from no flow to steady flow is a result of a well-known thermal instability. According to the analyses by Carlson and Sani (1971) and Schneider and Straub (1992) the instability occurs at $Ra = 3.7 \times 10^3$ for $Ar = 3$ and the resulting flow is unicellular. The critical Ra averaged over several runs in the present experiment is $3.2 \times 10^3 \pm 10$ percent, so it is slightly less than the prediction but it agrees well with the experimental value of 3.3×10^3 obtained by Müller et al. (1984) using gallium. The circulation direction of the unicell seems to be determined by a slight nonuniformity in the thermal boundary condition because for a given test setup the direction is, most of the time, repeatable. A slight error in the tilt angle does not seem to be an important factor in the present experiment because even if the container is rotated to a different orientation on the tilt table, the same flow direction is obtained.

At $\Delta T = 8.5°C$ ($Ra = 4.5 \times 10^3$) the temperature traces at 90 and 270 deg start to show periodic variations at the $L/4$ and $3L/4$ heights but not at the midheight (Fig. 4*a*). It is noted that in this particular run the thermocouples at 90 and 270 deg are positioned along the boundary between the upflow and downflow and those at 0 and 180 deg are near the apexes of those flows. The temperature gradient in the aximuthal direction is largest across the boundary and smallest at the apexes. Consequently, if the unicell was rotated back and forth around the cylinder axis within a small azimuthal range, the thermocouple outputs at 90 and 270 deg would show the largest temperature oscillations and they would be 180 deg out of phase from each other, while those at 0 and 180 deg would show the smallest oscillations, just as observed in the present experiment. Based also on the facts that no oscillations are found at the midheight and that the oscillation patterns at the $L/4$ and $3L/4$ heights are 180 deg out of phase from each

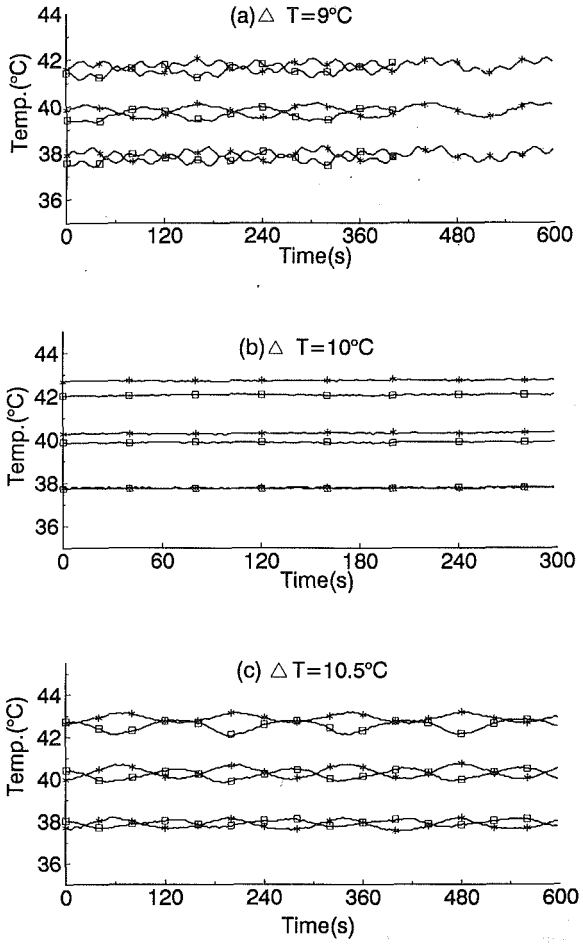

Fig. 5 Thermocouple outputs in supercritical regime; see Fig. 3 for explanation of symbols

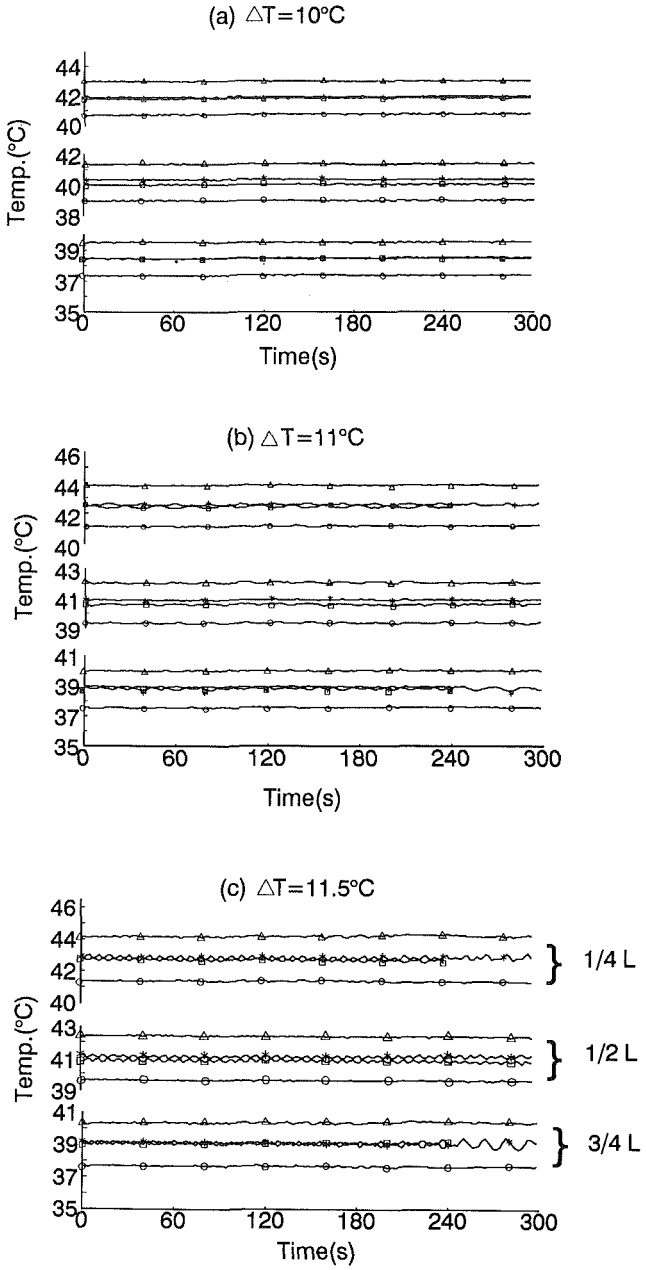

Fig. 6 Thermocouple outputs for $Ar=3$ and $\phi=30$ deg; see Fig. 3 for explanation of symbols

other, one can construct the flow structure during oscillations as illustrated in Fig. 4(*b*): The unicell is twisted back and forth at the top and bottom. The fact that the oscillation amplitude is highest near the side walls suggests that the oscillation phenomenon is associated with what is happening near the hot and cold walls. Since the events at the hot and cold ends are synchronized according to the phase measurement, they must be communicating by way of the axial convection.

The $\Delta T=9.0°C$ ($Ra=4.8\times10^3$) lower frequency oscillations appear and they are superposed on the above higher frequency ones (Fig. 5*a*). The oscillations are detected by all the thermocouples at 90 and 270 deg. At a given height the output at 90 deg is 180 deg out of phase from that at 270 deg. At both 90 and 180 deg azimuthal locations the outputs from three different heights are all in phase. Those facts suggest that the whole cell is rolled back and forth together while being twisted back and forth. In some tests, instead of the back and forth rolling, the thermocouples clearly indicate that the cell simply rotates around the center axis while it is being twisted back and forth. If ΔT is increased to $10.0°C$ ($Ra=5.3\times10^3$) oscillations completely disappear (Fig. 5*b*). Such disappearance of oscillations in a certain Ra range was also observed by Verhoeven (1969). The relations among all the outputs are not the same as those for the steady-flow before the appearance of oscillations (Fig. 3*b*). A careful examination of all the outputs reveals that the flow still has a unicellular structure but the cell is twisted.

At $\Delta T=10.5°C$ ($Ra=5.6\times10^3$) the flow becomes oscillatory again (Fig. 5*c*). The oscillation pattern is similar to the lower frequency pattern in Fig. 5(*a*), which implies that the cell is again rolled back and forth together. Increasing ΔT further beyond this point simply increases the oscillation amplitude but with increasingly distorted patterns.

The above-mentioned sequence of events was found to be repeatable, even when different test sections were used. The values of ΔT at which those events occurred were reproducible within ±10 percent. In the case of $Ar=2$ only the back and forth twisting was observed. For $Ar=4$ the initial steady straight cell got twisted first (still steady) and then the twisted cell started to roll back and forth. The thermocouple outputs in the experiment by Verhoeven (1969) for $Ar=11$ suggested also a similar back and forth motion during oscillations.

Crespo et al. (1988, 1989) computed numerically oscillatory flow for $Ar=2$ and $Pr=0.02$. The computed flow does not agree with the temperature outputs of the present experiment and the computed frequency is an order of magnitude greater than the present data.

A case with tilted cylinder is discussed next. The case of $\phi=30$ deg, $Ar=3$ is discussed in detail herein because it is

typical for all tilted cases with $\phi \geq 30$ deg. Up to $\Delta T = 10°C$ ($Ra = 5.4 \times 10^3$) the flow is in steady unicellular motion (Fig. 6*a*) with upflow at the top (0 deg) and downflow at the bottom (180 deg). At a given ΔT the temperature difference across the cylinder diameter is larger than that in the vertical case, which shows that the convection in the axial direction is stronger in the tilted case.

Starting at $\Delta T = 11.0°C$ ($Ra = 5.9 \times 10^3$) some thermocouples show oscillations (Fig. 6*b*). In Fig. 6(*b*) oscillations are detected only by the thermocouples at the $L/4$ and $3L/4$ heights. At those heights only the outputs at 90 and 270 deg (side thermocouples) show oscillations and they are 180 deg out of phase with each other. The situation is identical to the vertical case at the onset of oscillations and thus the oscillations are considered to be caused by the back and forth twisting of the basic unicellular structure at the hot and cold ends.

However, with a slight increase in ΔT to 11.5°C ($Ra = 6.2 \times 10^3$) the oscillation frequency changes to a higher frequency and all the side thermocouples show oscillations (Fig. 6*c*). At every axial location the outputs from the side thermocouples are exactly 180 deg out of phase with each other, indicating that the basic cell is still being rolled back and forth but no clear phase relations can be discerned among the outputs at different axial locations, so how the rolling propagates in the axial direction cannot be determined.

With further increase in ΔT the flow becomes increasingly chaotic. No new flow structures appear.

The situation for $0 \text{ deg} < \phi < 30$ deg is complex because it is a transition from the vertical situation to the inclined one and the data are less reproducible.

3.2 Critical Rayleigh Numbers. Critical temperature differences (ΔT_{cr}) to induce oscillations were determined from the temperature traces with increasing ΔT. A few measurements made for decreasing ΔT indicated a hysteresis effect, with ΔT_{cr} to eliminate oscillations (decreasing ΔT) about 1°C lower than ΔT_{cr} to induce oscillations (increasing ΔT).

Critical Rayleigh numbers (Ra_{cr}) based on ΔT_{cr} are shown in Fig. 7 for $Ar = 3$ and $0 \text{ deg} \leq \phi \leq 75$ deg. Ra_{cr} dropped slightly from its vertical-case value as ϕ was initially increased; it was smallest around $\phi = 10$ deg, and then as ϕ was increased further Ra_{cr} increased monotonically until ΔT_{cr} was beyond the range of temperature that the water baths could provide. The oscillations are associated with the back and forth rolling of the convection cell as discussed above. Therefore, the tendency of increasing Ra_{cr} with ϕ seems to be related to the fact that the rolling motion is increasingly suppressed by the hydrostatic pressure as the component of gravity normal to the motion increases with ϕ.

The values of Ra_{cr} for various values of Ar are presented in Fig. 8 for the vertical case. They are compared with the data taken from Müller et al. (1984) and good agreement is shown. The figure also shows the data by Verhoeven (1969) for large Ar (= 11). Ra_{cr} becomes smallest around $Ar = 3$. If Ar is larger than that, the viscous retardation effects of the side wall tend to delay the oscillations. On the other hand if Ar is smaller, the effect of confining the flow between the top and bottom walls becomes important and the appropriate parameter is then the Rayleigh number based on L as in the Rayleigh–Bénard problem.

3.3 Frequencies of Oscillations. Figure 9(*a*) shows the frequencies of oscillations for $Ar = 3$. They are divided into three groups. The medium frequency oscillations (~0.05 Hz) occur near the onset of oscillations for $\phi \leq 30$ deg. They are caused by the back and forth twisting of the basic unicellular flow at the top and bottom. If ϕ is close to 0 deg those oscillations are followed by low-frequency oscillations with increasing ΔT, which are associated with the back and forth rolling of the entire cell. If ϕ is larger than about 10 deg but

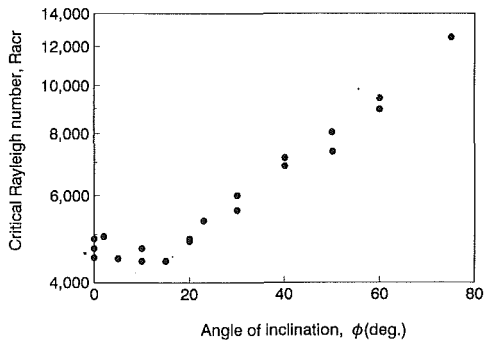

Fig. 7 Critical Rayleigh numbers for onset of oscillations versus ϕ for $Ar = 3$

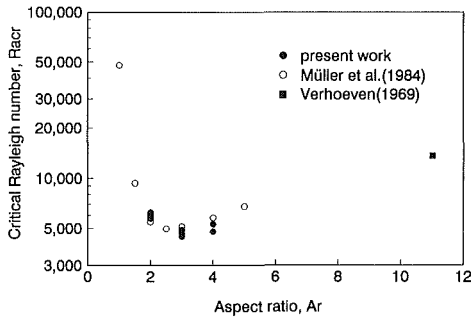

Fig. 8 Critical Rayleigh numbers for onset of oscillations versus Ar for $\phi = 0$ deg

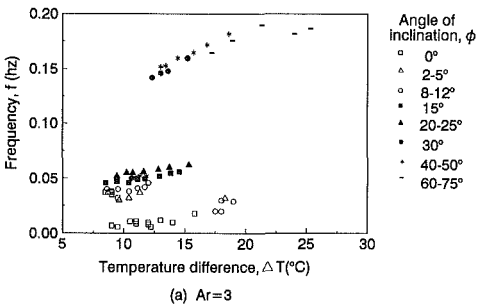

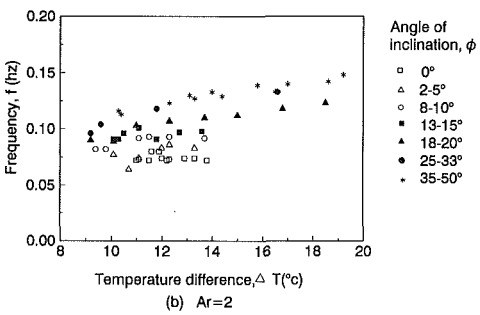

Fig. 9 Oscillation frequencies for $Ar = 2$ and 3

less than 30 deg, those medium frequency oscillations are followed by high-frequency oscillations (~0.17 Hz). If ϕ is larger than 50 deg, the oscillations start with the high frequencies. Those low-amplitude, high-frequency oscillations are associated with the localized back and forth twisting of the cell.

The oscillation frequencies for $Ar = 2$ (with $D = 1.27$ cm) are presented in Fig. 9(*b*). They stay in one group. They are all related to the back and forth twisting of the convection cell at the hot and cold ends. Generally frequency increases with ϕ.

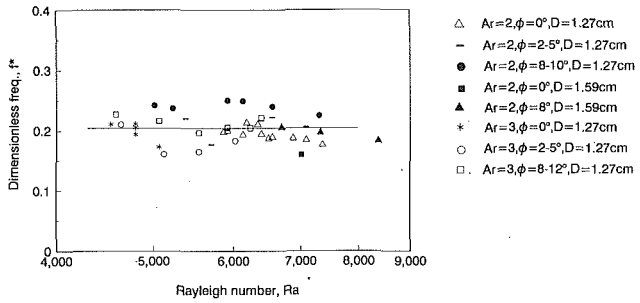

Fig. 10 Dimensionless medium oscillation frequencies for $Ar=2$ and 3

It is quite difficult to correlate all the measured frequencies because the oscillations have various modes and the basic flow changes with ϕ. Therefore, an attempt was made to correlate only the data for small ϕ (<10 deg) and only those associated with the back and forth twisting. In Fig. 10 the measured frequencies (f) for $Ar=3$ and $Ar=2$ (with $D=1.27$ and 1.59 cm) are nondimensionalized as $f^*=fArL/(g\beta\Delta TL)^{1/2}$. The dimensionless frequency puts the measured frequencies into approximately one valve, which is independent of Ra, as seen in the figure. As discussed above, the oscillation frequency of the back and forth twisting at both ends is expected to be related to the time of convection across the cylinder length. The axial convection velocity scales with $(g\beta TL)^{1/2}$ when Ar is small and that velocity divided by L is then the proper frequency scale. Comparison of that frequency scale with that used in this f^* expression shows that the convection velocity is modified as $(g\beta\Delta TL)^{1/2}/Ar$ when Ar is larger than unity to account for the side wall effect. Although the convection velocity is expected to decrease with increasing Ar, there are some other factors (Ra, flow structure, ϕ) that could influence the velocity. Therefore this expression of f^* is regarded as a first approximation and that may explain the data scatter in Fig. 10.

4 Conclusions

Conclusions drawn from the present experiment are:

1 The flow is found to become oscillatory beyond a certain Ra. The oscillations are associated with the back and forth motion of the basic unicellular structure. As a result the oscillation amplitude is largest along the interface between the warm upflow and the cold downflow.

2 In the case of vertical cylinders with $Ar=2$ and 3 the oscillations near the onset are associated with back and forth twisting of the basic convection cell at the hot and cold ends, while with $Ar=4$ they are associated with slow back and forth rolling of the entire cell. The frequency for the former case scales with the time of convection across the cylinder length.

3 In inclined cylinders ($\phi>30$ deg) with $Ar=2$ the oscillations are still associated with the cell twisting at both ends while with $Ar=3$ the oscillations start with the same twisting but they are followed by higher frequency, low-amplitude oscillations, which are associated with localized cell twisting.

The present work has identified and described some interesting buoyancy-flow phenomena associated with low-Pr fluids. The conditions for oscillations have been determined and their characteristics (flow structure, temperature field, and frequency) have been described. This information should be of value to crystal growers when they interpret their results.

References

Carlson, G. S., and Sani, R. L., 1971, "On Thermoconvective Instability in a Bounded Cylindrical Fluid Layer," *International Journal of Heat and Mass Transfer*, Vol. 14, pp. 2157–2160.

Crespo del Arco, E., Bontoux, P., Sani, R. L., Hardin, G., and Extremet, G. P., 1988, "Steady and Oscillatory Convection in Vertical Cylinders Heated From Below. Numerical Simulation of Asymmetric Flow Regimes," *Advances in Space Research*, Vol. 8, No. 12, pp. 281–292.

Crespo del Arco, E., Bontoux, P., Sani, R. L., Hardin, G., Extremet, G. P., and Chikhaoui, A., 1989, "Finite Difference Solutions for Three-Dimensional Steady and Oscillatory Convection in Vertical Cylinders—Effect of Aspect Ratio," ASME HTD-Vol. 99, pp. 67–76.

Crespo del Arco, E., and Bontoux, P., 1989, "Numerical Solution and Analysis of Asymmetric Convection in a Vertical Cylinder: An Effect of Prandtl Number," *Physics of Fluids A*, Vol. 1, No. 8, pp. 1348–1359.

Fontaine, J. P., Crespo del Arco, E., Randriamampianina, A., Extremet, G. P., and Bontoux, P., 1988, "Convective Motions in Liquid Metals for Materials Processings. Numerical Simulation of Oscillation Regimes and the Effect of Rotation," *Advances in Space Research*, Vol. 8, No. 12, pp. 265–272.

Hurle, D. T. J., 1972, "Hydrodynamics, Convection, and Crystal Growth," *Journal of Crystal Growth*, Vol. 13/14, pp. 39–43.

Kim, K. M., Witt, A. F., and Gatos, H. C., 1992, "Crystal Growth From the Melt under Destabilizing Thermal Gradients," *Journal of Electrochemical Society*, Vol. 119, pp. 1218–1226.

Müller, G., Neumann, G., and Weber, W., 1984, "Natural Convection in Vertical Bridgman Configurations," *Journal of Crystal Growth*, Vol. 70, pp. 78–93.

Neumann, G., 1990, "Three-Dimensional Numerical Simulation of Buoyancy-Driven Convection in Vertical Cylinders Heated from Below," *Journal of Fluid Mechanics*, Vol. 214, pp. 559–578.

Olson, J. M., and Rosenberger, F., 1979, "Convective Instabilities in a Closed Vertical Cylinder Heated From Below. Part 1. Monocomponent Gases," *Journal of Fluid Mechanics*, Vol. 92, pp. 609–629.

Ostrach, S., 1983, "Fluid Mechanics in Crystal Growth," *Journal of Fluids Engineering*, Vol. 105, pp. 5–20.

Schneider, S., and Straub, J., 1992, "Laminar Natural Convection in a Cylindrical Enclosure With Different End Temperatures," *International Journal of Heat and Mass Transfer*, Vol. 35, pp. 545–557.

Verhoeven, J. D., 1969, "Experimental Study of Thermal Convection in a Vertical Cylinder of Mercury Heated From Below," *Physics of Fluids A*, Vol.1 2, pp. 1733–1740.

Criteria for Predicting the Transition to Turbulence in Natural Convection Along a Vertical Surface

V. L. Vitharana

P. S. Lykoudis

School of Nuclear Engineering,
Purdue University,
West Lafayette, IN 47907

This paper evaluates the existing criteria for predicting the transition to turbulence in natural convection adjacent to a vertical surface. We have conducted an experiment that establishes the point of transition in mercury by means of both hot-film anemometry and local heat transfer measurements. These results confirm the claim of Bejan and Lage that the Grashof number correlates transition data better than the Rayleigh number. We have also concluded that the laminar-turbulent transition in liquid metals as well as regular fluids occurs in the vicinity of $Gr_x = 10^9$. Furthermore, we show that the E parameter suggested by Gebhart and his co-workers for predicting the onset of transition, when appropriately modified, yields a criterion that depends on the Grashof number alone.

Introduction

Natural convection is a commonplace occurrence in a multitude of technological applications of current interest as well as in our environment. As a consequence, there already exists an abundance of knowledge on most aspects of this particular mode of heat transfer. In spite of this scenario, a cursory glance at the literature would reveal that there is no consensus on a criterion for predicting the onset of transition in a natural convection boundary layer formed along a vertical plane.

Recently, Bejan and Lage (1990), after re-examining a number of previous works on this issue, concluded that the transition Rayleigh number has a strong Prandtl number dependence. In addition, they observed that the transition occurs approximately at a constant Grashof number (i.e., $Gr_x = 10^9$) irrespective of the fluid. The motivation, then, for the present inquiry stemmed primarily from these findings of Bejan and Lage and a need for a more critical review of literature on this phenomenon, especially in low Pr fluids. During the ensuing literature survey we discovered that the existing experimental data in liquid metals were inadequate to demarcate the elusive point of transition reasonably. Therefore, the main objectives of our effort were: (*a*) to determine the point of transition in mercury ($Pr = 0.025$) by means of hot-film anemometry as well as local heat transfer measurements, and (*b*) to assess the existing transition criteria in view of our experimental results and the previous data.

Literature Review

Let us first consider certain previous studies on natural transition to supplement the discussion given by Bejan and Lage (1990). Vitharana (1992) provides a comprehensive review of the currently available data on this subject.

Humphreys and Welty (1975) were the first to investigate flow instability in mercury using instantaneous velocity data acquired from a hot-film anemometer. Their apparatus consisted of a uniformly and symmetrically heated vertical channel of constant height having width-to-height (W/L) ratios of 0.25, 0.50, and 0.67. They also obtained local heat transfer correlations for the aspect ratios of 0.25, 0.50, 0.67, and ∞, the latter being the single plate limit, and reached a maximum Gr_x^* of 10^{11} for each configuration. However, Humphreys and Welty had not presented instantaneous velocity data for the single-plate geometry. Moreover, their heat transfer data for the single plate follow the laminar correlation in the entire Gr_x^* domain. As for the vertical channel configuration, they begin to observe velocity fluctuations at the $W/L = 0.50$ and 0.67 aspect ratios as early as $Gr_x^* = 4.0 \times 10^9$. Despite that, the velocity trace obtained from the $W/L = 0.25$ geometry is fairly stable at this stage. Not until Gr_x^* reaches 2.0×10^{10} do they detect chaotic oscillations of velocity at all channel spacings. Besides, it is obvious that the fluctuations are much more pronounced at $W/L = 0.50$ compared to those at the other two aspect ratios. However, Humphreys and Welty do not satisfactorily explain this phenomenon. In light of the observations above, we find it rather difficult to draw an unequivocal conclusion, from the study of Humphreys and Welty, regarding the point of transition in natural convection of mercury adjacent to a single vertical plate. One of the objectives of the present work, therefore, is to specifically address this issue.

Sheriff and Davies (1978) studied free convection of sodium in order to establish the validity of analytical expressions for the Nusselt number in low Pr fluids. Observing the increasing disparity between their experimental Nu_x and the laminar prediction at higher Gr_x^*, they concluded that $Bo_x^* = 1.0 \times 10^7$ marked the onset of transition in sodium. However, after examining their data Bejan and Lage (1990) argued that there is a discrepancy between the experimental Nu_x numbers and the laminar correlation, starting from $Bo_x^* = 4.0 \times 10^5$. Although there are two (Bo_x^*, Nu_x) data points in this neighborhood that lie above the laminar correlation, a closer scrutiny of Sheriff's and Davies' last eight (Bo_x^*, Nu_x) data points suggests that they more or less follow the one-third slope appropriate for turbulent convection beginning from a Bo_x^* number of around 1.0×10^6. This corresponds to a Gr_x number of 1.8×10^9 or a Ra_x number of 1.3×10^7. However, it should be pointed out here that it is extremely difficult to identify the exact point of transition from the heat transfer data, and it is quite possible to reason that transition in sodium occurs somewhere between $Bo_x^* = 4.0 \times 10^5$ and $Bo_x^* = 1.0 \times 10^6$. In any case, it appears from the heat transfer data of Sheriff and Davies that transition in

Contributed by the Heat Transfer Division for publication in the JOURNAL OF HEAT TRANSFER. Manuscript received by the Heat Transfer Division January 1993; revision received September 1993. Keywords: Flow Transition, Liquid Metals, Natural Convection. Associate Technical Editor: Y. Jaluria.

sodium (Pr = 0.007) occurs at a Ra_x number well below the traditionally accepted value of 10^9.

More recently, Uotani (1987) studied natural convection heat transfer in the Pb–Bi alloy (Pr = 0.023), in both stratified and nonstratified cases. Examining his nonstratified Nu_x versus Bo_x^* data, Bejan and Lage (1990) concluded that in Pb–Bi the transition occurs before $Bo_x^* = 2.9 \times 10^6$ since all of Uotani's (Bo_x^*, Nu_x) points lie above the laminar correlation. Although a consistent positive deviation from the laminar correlation is manifest in all his experimental Nu_x numbers, a closer look at them shows that they all follow the slope of the laminar line fairly well, except possibly for the last datum point, which is located beyond $Bo_x^* = 1.0 \times 10^8$. The most plausible argument one can put forward to account for such a consistent deviation is the existence of systematic experimental errors. The fact that Uotani's data follow the laminar trend up to a Bo_x^* number of 10^8 and that he has only one (Bo_x^*, Nu_x) point beyond this makes it rather difficult to derive any conclusion regarding the point of transition from his experiment.

Compared to the meager supply of data in liquid metals and other fluids, information concerning natural transition in air and water is rather profuse. The most extensive study on transition in air and water has been done by Gebhart and his coworkers (Godaux and Gebhart, 1974; Jaluria and Gebhart, 1974; Qureshi and Gebhart, 1978; Mahajan and Gebhart, 1979). According to their work, transition in air and water occurs almost at a constant value of $G^*/x^{2/5}$. Having demonstrated the proportionality of this variable to the fifth root of the local kinetic energy flux at a given streamwise location, they subsequently nondimensionalized it with the arbitrary factor $(\nu^2/g)^{2/15}$ to yield the new parameter $E = G^*(\nu^2/gx^3)^{2/15}$. According to Gebhart et al. (1988) velocity transition in both gases and water occurs around $E = 19.5$ while thermal transition is observed near $E = 20.5$.

Experimental Apparatus and Procedure

This experiment was conducted in a rectangular enclosure filled with mercury. A uniform heat flux was maintained over one wall of the enclosure. The opposite side was water cooled. For a detailed description of the experimental apparatus and procedure, see Vitharana (1992). Meanwhile, Fig. 1 shows a schematic elevation of this test section. The x axis lies along the heated wall while the y axis is oriented perpendicular to it. The taper in the lower portion of the water-cooled side,

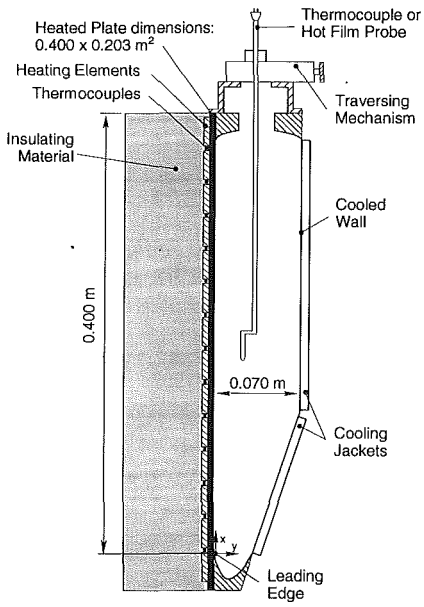

Fig. 1 Test section (not to scale)

though not relevant to the geometry of the present experiment, had been made to satisfy the requirements of another investigation, which involved the presence of a magnetic field. The bottom surface of the test section was curved in order to ensure smooth fluid circulation.

The end-effects caused by the finite geometry of the test section were dealt with as follows. The interference of the unheated side walls on the measurements taken within the boundary layer was minimized by selecting the central plane perpendicular to the heated wall for data acquisition. Furthermore, near the top and the bottom of the heated plate the flow field changes its direction. Therefore, the flow in these regions cannot be considered to simulate natural convection over a vertical plane. In fact, using the same apparatus, Tokuhiro (1991) found the Nu_x number in these areas to be considerably higher than the expected values. When he excluded about 30 percent of the total wall height each for the entrance and exit lengths based on the studies by Eckert and Carlson

Nomenclature

Bo_x = local Boussinesq number $= \dfrac{g\beta\Delta T_w x^3}{\alpha^2} = Ra_x Pr$

Bo_x^* = modified local Boussinesq number $= \dfrac{g\beta q_w'' x^4}{k\alpha^2} = Ra_x^* Pr$

E = kinetic energy flux parameter $= G^*(\nu^2/gx^3)^{2/15}$

E_{Gr} = $Gr_x^{1/15}$

g = acceleration due to gravity, ms^{-2}

G = local Grashof parameter $= 4(Gr_x/4)^{1/4}$

G^* = modified local Grashof parameter $= 5(Gr_x^*/5)^{1/5}$

Gr_x = local Grashof number $= \dfrac{g\beta\Delta T_w x^3}{\nu^2}$

Gr_x^* = modified local Grashof number $= \dfrac{g\beta q_w'' x^4}{k\nu^2}$

h = convective heat transfer coefficient, W/m^2K

k = thermal conductivity, W/mK

Nu_x = local Nusselt number $= hx/k$

Pr = Prandtl number

q_w'' = heat flux, W/m^2

Ra_x = local Rayleigh number $= \dfrac{g\beta\Delta T_w x^3}{\nu\alpha}$

Ra_x^* = modified local Rayleigh number $= \dfrac{g\beta q_w'' x^4}{k\nu\alpha}$

t_m = momentum diffusion time, s

t_f = free-fall time, s

T_w = wall temperature, K

T_∞ = temperature outside the boundary layer, K

ΔT_w = wall to bulk temperature difference, K

x, y, z = right-hand rectangular coordinates, m

α = thermal diffusivity, m^2/s

β = coefficient of thermal expansion, K^{-1}

μ = viscosity, kg/ms

ν = kinematic viscosity, m^2/s

ρ = density, kg/m^3

Subscripts

∞ = a bulk quantity

w = wall

x = a local quantity

Superscripts

$*$ = modification for constant heat flux case

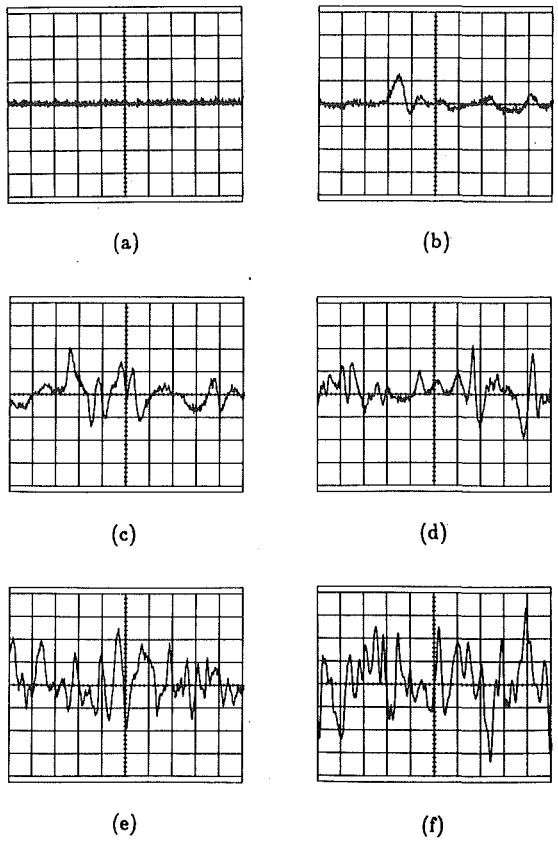

Fig. 2 Instantaneous velocity fields at $x = 0.25$ m for different heat fluxes. Vertical scale 10 mV/div. Horizontal scale 0.5 s/div. (*a*) $q''_w = 400$ W/m^2, $Gr_x = 1.2 \times 10^9$; (*b*) $q''_w = 1000$ W/m^2, $Gr_x = 2.5 \times 10^9$; (*c*) $q''_w = 1500$ W/m^2, $Gr_x = 3.5 \times 10^9$; (*d*) $q''_w = 4000$ W/m^2, $Gr_x = 8.2 \times 10^9$; (*e*) $q''_w = 8000$ W/m^2, $Gr_x = 1.3 \times 10^{10}$; (*f*) $q''_w = 16000$ W/m^2, $Gr_x = 1.9 \times 10^{10}$

(1961) and Elder (1965), it was found that the heat transfer results in the core region that lies in between were virtually unaffected by the conditions at the ends. Hence, so as to avoid these end effects all measurements were restricted to 0.15 m $\leq x \leq$ 0.25 m. Thus, the boundary layer in the vicinity of the central plane confined by 0.15 m $\leq x \leq$ 0.25 m limits can be regarded as two dimensional and representative of natural convection over a flat plate immersed in a large pool.

The *modus operandi* adhered to in the determination of the transition point in mercury is described below. For six different heat fluxes q''_w, the difference between the wall temperature T_w, and the temperature outside the boundary layer T_∞, $\Delta T_w = T_w - T_\infty$, was measured during steady state at three downstream locations x (namely $x = 0.15$ m, 0.20 m, and 0.25 m) from the leading edge of the heated plate. Then, using a hot-film anemometer and a storage oscilloscope the instantaneous velocity fields were recorded for each (q''_w, x) combination. In our experiment, the beginning of velocity fluctuations was considered to herald the velocity or hydrodynamic transition. When the hot-film probe was traversed in the y direction at all three x stations we investigated, it was found that the maximum velocity disturbance intensity was located around the same y distance from the wall (i.e., $y = 2.5$ mm) regardless of the heat flux. Hence, the hot-film probe was positioned inside the boundary layer at $y = 2.5$ mm throughout the experiment. Also, the above-mentioned maximum was fairly broad; i.e., the disturbance intensity dropped rather slowly as we moved away from this locality. Finally, using the heat transfer data acquired as described earlier, the Nu_x number was plotted against the Bo_x^* number and compared with the theoretical laminar correlation. A deviation of the experimental Nu_x number from the laminar correlation beyond

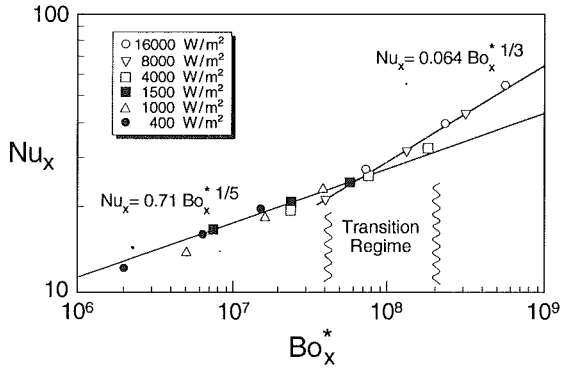

Fig. 3 Nu_x versus Bo_x^* data. (Here, $Nu_x = 0.71 Bo_x^{*1/5}$ represents the theoretical laminar correlation provided by Fujii and Fujii (1976), whereas $Nu_x = 0.064 Bo_x^{*1/3}$ correlates turbulent data. The transition regime is shown based on hot-film data.)

a certain Bo_x^* number pointed to thermal transition. Then, this piece of evidence was used to corroborate the information gathered by hot-film anemometry.

Experimental Results

Figure 2 depicts a representative collection of instantaneous velocity fields spanning all flow regimes. In this figure, oscillograms inside the boundary layer at $x = 0.25$ m are shown for all six heat fluxes. The instantaneous velocity data for the other x stations can be found from Vitharana (1992). Local heat transfer data are shown in Fig. 3. The Nu_x versus Bo_x^* format was chosen for this purpose because the modified Boussinesq number is the dimensionless parameter that accurately describes natural convection of liquid metals adjacent to a uniformly heated vertical surface. In this figure, the $Nu_x = 0.71\ Bo_x^{*1/5}$ line represents the analytical laminar heat transfer correlation for mercury provided by Fujii and Fujii (1976), while $Nu_x = 0.064\ Bo_x^{*1/3}$ correlates the turbulent data. In the meantime, reduced heat transfer data are given in Table 1. The relevant thermophysical properties have been evaluated at the film temperature. Furthermore, Figs. 4 and 5 present $Ra_{x,tr}$ versus Pr data and $Gr_{x,tr}$ versus Pr data, respectively, for mercury (as revealed from the present investigation) and other fluids (as reported by Vitharana, 1992). In Fig. 4 the $Ra_{x,tr} = 10^9$ Pr relation is shown, while the $Gr_{x,tr} = 10^9$ line is shown in Fig. 5. In both these figures, the spans of transition Rayleigh and Grashof numbers for air and water are shown by vertical straight lines. The respective symbols for air and water represent the mean values of these dimensionless numbers at transition. Also, compare Figs. 4 and 5 with the corresponding figures given by Bejan and Lage (1990).

Error Analysis

The major contributors to experimental error are the measurements of temperature, heat flux, and the distance from the leading edge. Estimated uncertainties in these measurements are listed below:

Uncertainty in temperature = ± 0.1 K

Uncertainty in heat flux = ± 5 percent

Uncertainty in distance from the leading edge = ± 0.15 cm

Taking these primary sources of error into account along with an allowance of ± 1 percent for systematic errors in each measurement, Table 2 shows the estimated errors associated with different parameters at various heat fluxes. At a certain heat flux, the error in a given quantity does not appreciably change with the streamwise location. The error associated with the Rayleigh number is comparable to that of the Grashof number.

Table 1 Reduced heat transfer data

x (m)	q_w'' (W/m^2)	E	Gr_x	Ra_x	Nu_x	Nu_x from laminar correlation
0.25		16.55	1.9×10^{10}	4.3×10^{8}	56.8	39.9
0.20	16000	15.19	1.1×10^{10}	2.4×10^{8}	40.9	33.3
0.15		13.40	4.8×10^{9}	1.1×10^{8}	28.1	26.5
0.25		14.46	1.3×10^{10}	3.0×10^{8}	42.3	35.4
0.20	8000	13.13	7.0×10^{9}	1.7×10^{8}	31.0	29.6
0.15		11.74	3.3×10^{9}	7.8×10^{7}	21.1	23.5
0.25		12.53	8.2×10^{9}	2.1×10^{8}	32.7	31.9
0.20	4000	11.45	4.2×10^{9}	1.1×10^{8}	26.1	26.7
0.15		10.24	1.8×10^{9}	4.6×10^{7}	19.6	21.2
0.25		10.20	3.5×10^{9}	9.0×10^{7}	24.5	25.3
0.20	1500	9.35	1.7×10^{9}	4.4×10^{7}	20.8	21.2
0.15		8.31	6.7×10^{8}	1.7×10^{7}	16.5	16.8
0.25		9.42	2.5×10^{9}	6.5×10^{7}	22.9	23.4
0.20	1000	8.64	1.3×10^{9}	3.3×10^{7}	18.3	19.5
0.15		7.67	5.4×10^{8}	1.4×10^{7}	13.7	15.5
0.25		7.90	1.2×10^{9}	3.0×10^{7}	19.8	19.5
0.20	400	7.17	5.9×10^{8}	1.5×10^{7}	15.9	16.3
0.15		6.39	2.5×10^{8}	6.5×10^{6}	11.9	12.9

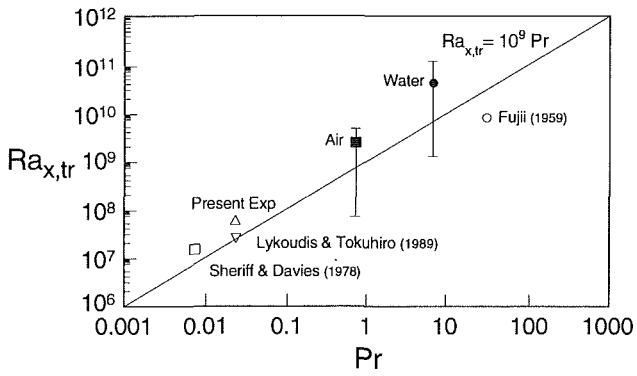

Fig. 4 Transition Ra_x number for different fluids (based on the present experiment and literature review)

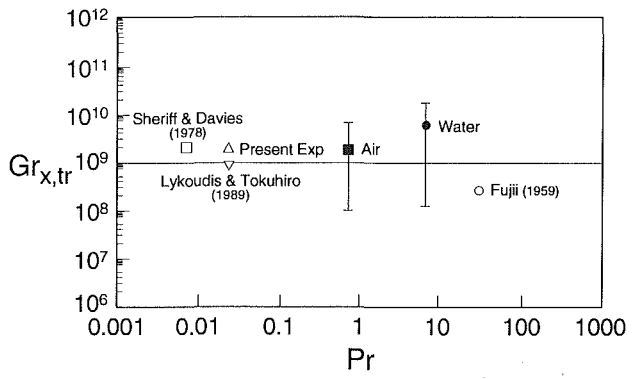

Fig. 5 Transition Gr_x number for different fluids (based on the present experiment and literature review)

Table 2 Experimental uncertainties

q_w''(W/m^2)	Error in Nu_x	Error in Gr_x	Error in E
16000	±6%	±5%	±3%
8000	±6%	±5%	±3%
4000	±7%	±6%	±3%
1500	±10%	±9%	±5%
1000	±12%	±11%	±6%
400	±24%	±23%	±11%

Table 3 Gr_x and Ra_x, and E parameter at the beginning of velocity fluctuations

x (m)	q_w''(W/m^2) at transition	Gr_x at transition	Ra_x at transition	E at transition
0.25	1000	2.5×10^{9}	6.5×10^{7}	9.42
0.20	1500	1.7×10^{9}	4.4×10^{7}	9.35
0.15	Between 1500 and 4000	Between 6.7×10^{8} and 1.8×10^{9}	Between 1.7×10^{7} and 4.6×10^{7}	Between 8.31 and 10.24

Discussion

Figures 2(*a*) through 2(*f*), corresponding to $x=0.25$ m, collectively demonstrate the development of an initially steady, laminar velocity field during the course of lengthy transition process. Similar comments can be made about the velocity traces obtained at $x=0.20$ m and $x=0.15$ m. As Fig. 2(*a*) illustrates the velocity field is very stable at $Gr_x=1.2\times10^9$ exhibiting the presence of laminar flow. Here, a comment about the small zig-zag oscillations superimposed on the signal is in order. These fluctuations were found to be present even in the anemometer output from quiescent mercury and can be attributed to electronic noise. At $Gr_x=2.5\times10^9$, random disturbances begin to appear in the velocity field, indicating the inception of transition. The flow field is characterized by turbulent fluctuations at $Gr_x=3.5\times10^9$ and 8.2×10^9 as apparent from Figs. 2(*c*) and 2(*d*). These fluctuations become fairly strong by $Gr_x=1.3\times10^{10}$ as indicated by Fig. 2(*e*). Eventually, Fig. 2(*f*) shows the presence of vigorous turbulence around $Gr_x=1.9\times10^{10}$.

Next let us consider the values of Rayleigh and Grashof numbers at the initiation of transition for all three streamwise locations. The values of the E parameter at transition are also included here for later comparison; see Table 3.

Although the transition Gr_x and Ra_x values at $x=0.25$ m and $x=0.20$ m can be directly calculated from the experimental data, the corresponding values at $x=0.15$ m could only be found to lie within the bounds shown. However, this does not seriously hamper the analysis. At $x=0.15$ m, the flow field is clearly laminar when $Gr_x=6.7\times10^8$ and turbulent by $Gr_x=1.8\times10^9$. The critical Gr_x number must then lie between these two values. In addition, according to this table the hydrodynamic transition in mercury occurs, on an average, around a Gr_x number of 2.0×10^9 or a Ra_x number of 5.0×10^7. This clearly shows that the transition Ra_x number in mercury is much lower than the widely accepted value of 10^9.

The local heat transfer data provided by Fig. 3 and Table 1 will now be discussed. As evident from Table 1, the experimental Nu_x number in the laminar regime deviates about -5 percent from the theoretical laminar correlation. As we proceed in the Bo_x^* scale, the experimental Nu_x begins to depart from

Table 4 Gr_x and Ra_x, and E at the departure of Nu_x from laminar trend

q_w'' (W/m^2)	x(m)	Gr_x	Ra_x	E
8000	0.20	7.0×10^9	1.7×10^8	13.13
16000	0.15	4.8×10^9	1.1×10^8	13.40

Table 5 Transition Gr_x and Ra_x spans for air and water

Fluid	Transition Gr_x range	Transition Ra_x range
Air	1.1×10^8 to 7.3×10^9	8.3×10^7 to 5.2×10^9
Water	1.4×10^8 to 2.0×10^{10}	1.4×10^9 to 1.3×10^{11}

the laminar trend. However, according to Table 1, the actual point of departure of the Nu_x number from the laminar behavior depends on the amount of applied heat flux. In this analysis, it is considered to begin when the experimental Nu_x number: (*a*) deviates at least about +10 percent from its laminar course, and (*b*) subsequently follows the one-third slope characteristic of turbulent convection. According to this criterion, the data follow the laminar correlation for heat fluxes 400 W/m^2, 1000 W/m^2, 1500 W/m^2, and 4000 W/m^2. The points of departure for other two heat fluxes are indicated in Table 4.

From Table 4 it can be deduced that experimental Nu_x numbers begin to depart from the laminar trend, on the average, when $Gr_x = 5.0$ to 7.0×10^9 or $Ra_x = 1.0$ to 2.0×10^8. Also, recall here that significant velocity fluctuations were initially detected around $Gr_x = 2.0\times10^9$ or $Ra_x = 5.0\times10^7$. This is quite similar to the findings of Cheesewright (1968), who detected significant velocity fluctuations in air beginning from $Gr_x = 2.0\times10^9$. However, neither the local heat transfer data nor the mean temperature profiles did relinquish their laminar characteristics until about $Gr_x = 5.0\times10^9$ during Cheesewright's experiment. Moreover, it is transparent from the present heat transfer data that the critical Grashof number and the height at which transition occurs decrease with the increasing heat flux. This comment is pertinent because at ($q_w'' = 4000$ W/m^2, $x = 0.25$ m) the Nu_x number has not still abandoned the laminar course. These trends are similar to those observed at the beginning of velocity transition.

Bearing the inferences drawn from the present experiment in mind, let us now delve into important information furnished by past studies in other fluids. From our perusal of previous publications (Vitharana, 1992) we learned that transition in air, on an average, occurs approximately at $Gr_x = 2.3\times10^9$, whereas that in water, on the average, begins near $Gr_x = 5.8\times10^9$. The corresponding transition Ra_x numbers are 1.8×10^9 and 3.8×10^{10}, respectively. Note the jump in the critical Ra_x number accompanied by the increase in Pr number from 0.7 to 7. Since the average figures provided above do not fully portray the scatter in critical Grashof and Rayleigh numbers reported by individual experimenters, their spans should be of interest too. They are given in Table 5.

The spread of the critical Rayleigh number further widens as we take into account sodium, mercury, and ethylene glycol in addition to air and water, though this does not affect the range of the critical Grashof number. At this juncture, the critical Rayleigh number can be found to lie between 10^7 and 10^{11}, whereas the critical Grashof number still remains between 10^8 and 10^{10}. Also note the distinct increase in the critical Rayleigh number when we move from low-Pr fluids to their higher counterparts. This approximately satisfies the relation $Ra_{x,tr} = 10^9$ Pr as pointed out by Bejan and Lage (1990). However, no such trend is visible in the behavior of the Grashof number; see Figs. 4 and 5. Although the variation of the critical Grashof number is considerably less than that of the critical Rayleigh number, it still spans about two orders of magnitude. Use of various criteria by individual experimenters to identify transition and the effect of external disturbances can be cited as the main reasons for this. Nonetheless, even when the same criterion is used, several experimenters (e.g., Vliet and Liu, 1969; Godaux and Gebhart, 1974; Jaluria and Gebhart, 1974; Qureshi and Gebhart, 1978; Mahajan and Gebhart, 1979) have noted that the transition Gr_x number varied with the heat flux. This observation is consistent with our results as remarked earlier.

Table 6 Values of the E parameters at the deviation of Nu_x from laminar trend for mercury, air, and water

Fluid	E	E_{Gr}
Mercury	13.27	4.49
Air	20.50	4.24
Water	19.20	4.49

Gebhart and his co-workers have studied the aforesaid phenomenon in detail in both air and water. They contend that a unique value of $E = G^*(\nu^2/gx^3)^{2/15}$ fairly well forecasts a given transition event in both gases and water. It is therefore natural to consider the values attained by the E parameter at the onset of transition in the present liquid-metal experiment. Although the transition Gr_x is decreasing with the increasing heat flux, the value of the E parameter at the beginning of velocity fluctuations seems to be very stable. The average Gr_x here is about 2.0×10^9. Its spread about the mean is about ±25 percent. The mean of E at the velocity transition is 9.35. Its spread about the mean is less than ±1 percent. Next, let us consider the value of E at the point of departure of the Nu_x from the laminar correlation. In this experiment, the mean value of Gr_x during this event is 6.0×10^9. The variation of Gr_x about the mean value is about ±20 percent. The mean value of E at the departure of Nu_x from laminar trend is 13.27. Its spread about the mean is nearly ±1 percent. Although Gebhart and his coworkers do not provide values for E at the initiation of velocity fluctuations and at the point of departure of Nu_x from the laminar trend, the latter event should occur almost simultaneously as the departure of mean temperature profile from the laminar shape. In gases and water, according to Gebhart et al. (1988), the mean temperature profile begins to depart from laminar trend when E is about 20. However, in the present experiment, the value assumed by E during this event is about 30 percent lower than this.

Now, let us recapitulate how Jaluria and Gebhart (1974) arrived at the E criterion. They first observed that transition occurred at a constant value of $G^*/x^{2/5}$. Here, recall that $G^* = 5(Gr_x^*/5)^{1/5}$. Subsequently, they nondimensionalized it with the arbitrary factor $(\nu^2/g)^{2/15}$ to yield $E = G^*(\nu^2/gx^3)^{2/15}$. However, the following analysis points out that the E parameter could eventually be interpreted solely in terms of the Grashof number. The argument is as follows:

Instead of nondimensionalizing $G^*/x^{2/5}$ with the arbitrary factor $(\nu^2/g)^{2/15}$, one could equally well use $(\nu^2/g(\Delta\rho/\rho))^{2/15}$ for this purpose. The use of the latter factor is more instructive since it shows the influence of the Grashof number on the transition as

$$G^*/x^{2/5}(\nu^2/g(\Delta\rho/\rho))^{2/15} =$$

$$G^*(1/Gr_x)^{2/15} = 5(Gr_x^*/5)^{1/5}(1/Gr_x)^{2/15}.$$

As such, the natural transition should occur at a constant value of the parameter $(Gr_x^*)^{1/5}(1/Gr_x)^{2/15}$. By noting that $Gr_x^* = Gr_x Nu_x$, it follows that the transition should occur at a constant value of $Gr_x^{1/15} Nu_x^{1/5}$. On the other hand the variation of $Nu_x^{1/5}$ with the heat flux during transition is negligibly small. Therefore, it can be argued that transition occurs at a constant value of $Gr_x^{1/15}$. For this reason we define $E_{Gr} = Gr_x^{1/15}$ as a modified E criterion[1] and proceed to compare its ability to predict transition in juxtaposition with Gebhart's E parameter. Table 6, using mercury, air, and water, which span a Prandtl number range of about three orders of magnitude, compares the values of these two parameters at the departure of the Nu_x number from the laminar trend. If we consider all three fluids at the same time, the Nu_x number deviates from its laminar course when $E = 17.65 \pm 25$ percent or $E_{Gr} = 4.40 \pm 4$ percent. Hence, it is clear that E_{Gr} predicts natural transition with an accuracy much greater than that of E when *all three fluids are taken into account*. For lack of sufficiently detailed data, other fluids cannot be used in this comparison.

Conclusions

Our experimental results indicate that velocity fluctuations begin to show up in mercury near $Gr_x = 2.0 \times 10^9$. Moreover, the local Nusselt number abandons its laminar course around $Gr_x = 6.0 \times 10^9$. These findings support the argument of Bejan and Lage (1990) that transition in low-Pr fluids takes place at Ra_x much lower than 10^9. In addition, our detailed analysis verifies their claim that Gr_x is a better predictive parameter of transition than Ra_x. Furthermore, in our discussion we did demonstrate that a minor modification of the arbitrary nondimensionalization of $G^*/x^{2/5}$ effected by Jaluria and Gebhart (1974) would yield a better transition criterion E_{Gr}, which is solely based on the Grashof number. Hence, it is worthwhile to consider the physical interpretation of the Grashof number, particularly in analogy to that of the Reynolds number. According to the interpretations of nondimensional numbers advanced by Lykoudis (1990), Grashof number is the square of the ratio of the momentum diffusion time to the free-fall time. The free-fall time is revealed from the balance of gravitational and inertial forces that exists when an object falls in an ambience of different density in the absence of dissipative forces. Following Lykoudis (1990), the free fall time $t_f \sim (L/g(\Delta\rho/\rho))^{1/2}$ and the momentum diffusion time $t_m \sim L^2/\nu$. Hence, $Gr = g(\Delta\rho/\rho)L^3/\nu^2 \sim (t_m/t_f)^2$. For forced convection, Re number can be interpreted as follows:

$$Re = \frac{UL}{\nu} = \frac{L^2/\nu}{L/U} \sim \frac{t_m}{t_c}$$

Here t_c is the time taken by a fluid particle to travel a distance L. In forced flows, the transition occurs when $t_m >> t_c$. In direct analogy, in buoyancy-driven flows, the transition takes place when $t_m >> t_f$. Although this is not a proof that a constant value of Grashof number or E_{Gr} parameter is associated with transition, it gives an intuitive feel for the role of the Grashof number in analogy to that of the Reynolds number.

[1] In Vitharana (1992), E_{Gr} has been denoted by E'.

References

Bejan, A., and Lage, J. L., 1989, Duke University, Durham, NC, private communication to P. S. Lykoudis and A. T. Tokuhiro.

Bejan, A., and Lage, J. L., 1990, "The Prandtl Number Effect on the Transition in Natural Convection Along a Vertical Surface," ASME JOURNAL OF HEAT TRANSFER, Vol. 112, pp. 787–790.

Cheesewright, R., 1968, "Turbulent Natural Convection From a Vertical Plane Surface," ASME JOURNAL OF HEAT TRANSFER, Vol. 90, pp. 1–8.

Eckert, E. R. G., and Carlson, W. O., 1961, "Natural Convection in an Air Layer Enclosed Between Two Vertical Plates With Different Temperatures," *International Journal of Heat and Mass Transfer*, Vol. 2, pp. 106–120.

Elder, J. W., 1965, "Laminar Free Convection in a Vertical Slot," *Journal of Fluid Mechanics*, Vol. 23, pp. 77–98.

Fujii, T., 1959, "Experimental Studies of Free Convection Heat Transfer," *Bulletin of JSME*, Vol. 2(8), pp. 555–558.

Fujii, T., and Fujii, M., 1976, "The Dependence of Local Nusselt Number on Prandtl Number in the Case of Free Convection Along a Vertical Surface With Uniform Heat Flux," *International Journal of Heat and Mass Transfer*, Vol. 19, pp. 121–122.

Gebhart, B., Jaluria, Y., Mahajan, R. L., and Sammakia, B., 1988, *Buoyancy-Induced Flows and Transport*, Hemisphere, New York.

Godaux, F., and Gebhart, B., 1974, "An Experimental Study of the Transition of Natural Convection Flow Adjacent to a Vertical Surface," *International Journal of Heat and Mass Transfer*, Vol. 17, pp. 93–107.

Humphreys, W. W., and Welty, J. R., 1975, "Natural Convection With Mercury in a Uniformly Heated Vertical Channel During Unstable Laminar and Transitional Flow," *AIChE Journal*, Vol. 121, pp. 268–274.

Jaluria, Y., and Gebhart, B., 1974, "On Transition Mechanisms in Vertical Natural Convection Flow," *Journal of Fluid Mechanics*, Vol. 66, pp. 309–337.

Lykoudis, P. S., 1990, "Non-dimensional Numbers as Ratios of Characteristic Times," *International Journal of Heat and Mass Transfer*, Vol. 33, pp. 1568–1570.

Mahajan, R. L., and Gebhart, B., 1979, "An Experimental Determination of Transition Limits in a Vertical Natural Convection Flow Adjacent to a Surface," *Journal of Fluid Mechanics*, Vol. 91, pp. 131–154.

Qureshi, Z. H., and Gebhart, B., 1978, "Transition and Transport in a Buoyancy Driven Flow in Water Adjacent to a Vertical Uniform Flux Surface," *International Journal of Heat and Mass Transfer*, Vol. 21, pp. 1467–1479.

Sheriff, N., and Davies, N. W., 1978, "Sodium Natural Convection From a Vertical Plate," *6th International Heat Transfer Conference*, Paper NR-23.

Tokuhiro, A. T., 1991, "Natural Convection Heat Transfer Enhancement in Mercury With Gas Injection and in the Presence of a Transverse Magnetic Field," Ph.D. Thesis, Purdue University, West Lafayette, IN.

Uotani, M., 1987, "Natural Convection Heat Transfer in a Thermally Stratified Liquid Metal," *Journal of Nuclear Science and Technology*, Vol. 24(6), pp. 442–451.

Vitharana, V. L., 1992, "Criteria for Transition to Turbulence in the Natural Convection of Mercury With and Without a Transverse Magnetic Field," M.S. Thesis, Purdue University, West Lafayette, IN.

Vliet, G. C., and Liu, C. K., 1969, "An Experimental Study of Turbulent Natural Convection Boundary Layers," ASME JOURNAL OF HEAT TRANSFER, Vol. 91, pp. 517–531.

Electromagnetic Theory Predictions of the Directional Scattering From Triangular Surfaces

R. A. Dimenna

R. O. Buckius

Department of Mechanical and Industrial Engineering, University of Illinois, 1206 West Green Street, Urbana, IL 61801

Angular predictions of directional scattering distributions for metal and dielectric surfaces with length scales of the order of the wavelength are made from rigorous electromagnetic scattering theory. The theoretical and numerical formulation of the electromagnetic scattering solution based on the extinction theorem is presented. One-dimensional triangular surface profiles are generated using a Fourier series representation for various correlation lengths, deviations, and surface peak positions. Bidirectional reflection functions and directional emissivities are calculated for the surface geometry parameters above and various optical properties. Angular enhancements in bidirectional reflection and emissivity are quantified. Angular scattering and emissivity predictions have been extended beyond those previously reported to include surfaces with equivalent correlation length and deviation.

Introduction

The directional nature of surface radiative properties is of interest in many thermal engineering applications. Consideration of the directional nature of surface properties has demonstrated the directional selectivity of such spatially contoured surfaces. For triangular surfaces, the directional enhancements of the emissivity have been quantified (Hollands, 1963) for surface lengths large compared to the wavelength. Closely related triangular surfaces also exhibit important directional results including angular enhancements (Perlmutter and Howell, 1962; Brandenberg and Clausen, 1965). Demont et al. (1982) have shown that grooving of surfaces is important when directionally enhancing emission. More recently angular emission enhancements have been quantified and analytical models based upon classical engineering approaches proposed (Hesketh et al., 1988a). The analyses in all these works consider surface structure that is large relative to the wavelength, which precludes consideration of many infrared wavelengths and/or small surface roughnesses. The results presented here quantify the directional nature of thermal radiation properties for surfaces that include such microstructures.

Rigorous qualification of the directional scattering distribution for contoured surfaces with structure on the order of the wavelength generally requires electromagnetic theory predictions to quantify surface radiative properties. Recent advances (Celli et al., 1985; Maradudin et al., 1989, 1990; Sánchez-Gil and Nieto-Vesperinas, 1991; Nieto-Vesperinas and Sánchez-Gil, 1992) in electromagnetic scattering predictions provide such solutions, based on the extinction theorem (Wolf, 1973). The directional distribution of scattered energy is a function of the material surface, through the optical constants, the wavelength and angle of incident energy, and the surface parameters including correlation length, deviation, and peak position. The geometry of the surface plays an important role in determining the magnitude of the scattered energy distribution. Typical surfaces are described by the correlation length and the deviation, but by changing the geometry of a surface with constant correlation length and deviation, the directional distribution of scattered energy is significantly altered. This work presents the effects of changing surface parameters and material optical parameters on the angular directional scattering distribution and directional emissivity from typical silicon and aluminum surfaces.

The basic radiative surface properties are the bidirectional reflection function and the bidirectional transmission function. The hemispherical radiative properties of reflection and transmission are obtained by integrating the bidirectional functions (Siegel and Howell, 1981). When an opaque surface such as silicon or aluminum is analyzed, the hemispherical emissivity from a surface is obtained from the hemispherical reflection function. Since the surface material is described by specific values of the dielectric properties, all of the radiative properties are spectral quantities.

The following sections contain the theoretical and numerical formulation of the scattering solution and directional scattering distribution results. The definitions of the radiative properties that are used for directional distributions of the scattered energy are presented. The exact integral equation solutions of the electromagnetic wave equations and the numerical representations are also developed. Results of the bidirectional reflection function and directional emissivity from various triangular surfaces follow.

Analysis for Deterministic Surface Scattering

Surface Reflection and Transmission Properties. For an electromagnetic wave incident upon a surface, scattering processes characterize the change in the directional and energy distributions of the incident wave. The phenomenon is expressed in terms of the incident power and either the scattered power or the transmitted power. The ratio of incident power and scattered power is the bidirectional reflection function, while the ratio of incident power and transmitted power is the bidirectional transmission function. From the Poynting theorem relation (Stratton, 1941), the bidirectional reflection function is expressed as π times the ratio of the reflected radiant power per unit solid angle per unit area normal to the direction of reflection to the incident radiant power (Brewster, 1992). Likewise, the bidirectional transmission function is π times the ratio of the transmitted power per unit solid angle per unit area normal to the direction of transmission to the radiant power. These functions are

$$\rho''_\lambda(\theta_o, \theta_s) = \frac{\dfrac{\pi}{\cos\theta_s}\dfrac{d\Phi_s}{d\Omega_s}}{\dfrac{d\Phi_o}{d\Omega_o}} \tag{1a}$$

Contributed by the Heat Transfer Division for publication in the JOURNAL OF HEAT TRANSFER. Manuscript received by the Heat Transfer Division July 1993; revision received November 1993. Keywords: Radiation, Radiation Interactions, Solar Energy. Associate Technical Editor: R. Viskanta.

and

$$\tau''_\lambda(\theta_o, \theta_t) = \frac{\dfrac{\pi}{\cos\theta_t}\dfrac{d\Phi_t}{d\Omega_t}}{\dfrac{d\Phi_o}{d\Omega_o}} \tag{1b}$$

where the subscripts o, s, and t denote the incident, scattered, and transmitted quantities, respectively. Hemispherical reflection and transmission from the surface are obtained by integrating Eqs. (1) over all the scattering and transmitting angles, respectively, for a given incidence angle. The other surface properties, emissivity and absorptivity, are obtained from Kirchhoff's law and conservation of energy on the surface. The directional emissivity is (Siegel and Howell, 1981)

$$\epsilon'_\lambda(\theta_o) = 1 - \rho'_\lambda(\theta_o) = 1 - \frac{1}{\pi}\int_{2\pi} \rho''_\lambda(\theta_o, \theta_s)\cos\theta_s\, d\Omega_s. \tag{2}$$

The following sections formulate exact solutions for the power functions Φ_s, Φ_t, and Φ_o for use in Eqs. (1) to determine the emissivity with Eq. (2).

Electromagnetic Theory. Rigorous exact solutions for the scattering of incident waves from surfaces are given by electromagnetic theory (Soto-Crespo and Nieto-Vesperinas, 1989; McGurn and Maradudin, 1989; Maradudin et al., 1991; Nieto-Vesperinas and Sánchez-Gil, 1990). The deterministic surface considered is shown in Fig. 1. For the one-dimensional surface varying in the x direction, scattering is considered solely in the plane of incidence. The surface interface is described by $z = \zeta(x)$, which separates a semi-infinite vacuum from a dielectric or metal material characterized by a linear, spatially uniform and isotropic, dielectric constant, ϵ. The dielectric constant is a function of the refractive index, n, and the absorption index, κ, of the surface (Brewster, 1992). The linearly polarized, monochromatic, plane electromagnetic incident wave strikes the surface at an incidence angle, θ_o, with the z axis. The components of the incident, reflected, and transmitted wave vectors are, respectively,

$$K_o = k_o(\sin\theta_o,\ 0,\ -\cos\theta_o) \tag{3a}$$

$$K_s = k_o(\sin\theta_s,\ 0,\ \cos\theta_s) \tag{3b}$$

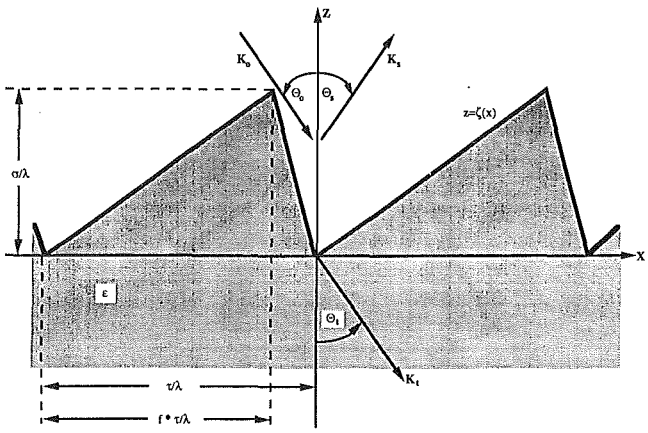

Fig. 1 Deterministic surface scattering geometry (*y* coordinate into the page)

$$K_t = \sqrt{\epsilon}k_o(\sin\theta_t,\ 0,\ -\cos\theta_t) \tag{3c}$$

where $k_o = 2\pi/\lambda$.

As shown in Fig. 1, the surface is described by the ratios of correlation length to wavelength, τ/λ, and deviation to wavelength, σ/λ. In addition, the position of the surface peak is determined by the parameter, f, which is any value between 0.0 and 1.0. There is no depolarization for either the transverse magnetic (TM) or transverse electric (TE) incident wave, since only the incidence plane is of interest. Consequently, the electric field vector for TE polarization and the magnetic field vector for TM polarization have only $\hat{\mathbf{j}}$ components ($\hat{\mathbf{j}}$ is the unit vector on the y axis).

The incident vectors are

$$\mathbf{E}(x, z) = \hat{\mathbf{j}}E_o \exp\{ik_o(x\sin\theta_o - z\cos\theta_o)\},\quad \text{TE polarized} \tag{4a}$$

$$\mathbf{H}(x, z) = \hat{\mathbf{j}}H_o \exp\{ik_o(x\sin\theta_o - z\cos\theta_o)\},\quad \text{TM polarized} \tag{4b}$$

where E_o and H_o are the complex amplitudes of the incident wave. The time-dependence factor $\exp(-i\omega t)$ is suppressed throughout. The reflected and transmitted fields are now ob-

Nomenclature

A_{mn}, B_{mn} = surface coefficient matrices
E = electric field intensity vector
f = surface peak position location
F = electric field intensity derivative
G = Green's function
H = magnetic field intensity vector
$H^{(1)}$ = Hankel function of first kind
$\hat{\mathbf{i}}, \hat{\mathbf{j}}, \hat{\mathbf{k}}$ = unit vectors
K = wave vector
L = magnetic field intensity derivative
L_x, L_y = surface lengths
M = number of surface points for numerical computations
n = surface refractive index
$\hat{\mathbf{n}}$ = surface outward normal vector
r = scattering reflection function
S = surface perimeter
t = scattering transmission function
x, y, z, x', z' = surface coordinates
δ = dirac delta function
γ = normalization constant
ϵ = emissivity, complex dielectric constant
ϵ_o = permittivity of free space
ζ = surface profile
θ = angle of energy
κ = absorption index
λ = wavelength of incidence energy
μ_o = permeability of free space
ρ'' = bidirectional reflection function
ρ' = directional reflectivity
σ = surface deviation length
τ = surface correlation length
τ'' = bidirectional transmission function
τ' = directional transmissivity
Φ = radiant power flow
ω = circular frequency of radiation
Ω = solid angle

Subscripts

o = incident
s = scattered
t = transmitted
TE = transverse electric polarization
TM = transverse magnetic polarization
ζ = surface interface
λ = spectral

Superscripts

$'$ = directional, first derivative
$''$ = bidirectional, second derivative
$<$ = below
$>$ = above

tained by solving the corresponding Helmholtz equations. Each polarization is discussed independently.

TM Polarization. For the surface, $z > \zeta(x)$, as presented in Fig. 1, the Helmholtz equations describing the magnetic field have been formulated (Stratton, 1941). **H** is considered to be polarized perpendicularly to the plane of incidence. The **H** field satisfies a continuity condition on the component tangent to the surface. By using Maxwell's equations (Stratton, 1941), the following jump conditions for the magnetic field and the derivative of the magnetic field are obtained:

$$H_y^{>}(x, z)|_{z=\zeta(x)} = H_y^{<}(x, z)|_{z=\zeta(x)} \tag{5}$$

$$\frac{\partial}{\partial n} H_y^{>}(x, z)|_{z=\zeta(x)} = \frac{1}{\epsilon}\frac{\partial}{\partial n} H_y^{<}(x, z)|_{z=\zeta(x)}. \tag{6}$$

H_y is the only component of **H** that remains after accounting for TM polarization in Eqs. (5) and (6). The derivative in Eq. (6) is taken with respect to the surface normal.

The Helmholtz equation in two dimensions is transformed by using a Green's function for a line source (Sanchez-Gil and Nieto-Vesperinas, 1991). After a coordinate transformation, the two-dimensional Green's function above and below the surface is expressed in terms of the zeroth-order Hankel function of the first kind (Morse and Feshbach, 1946).

In order to obtain the scattered power in terms of the scattering angle, θ_s, and the transmitted power in terms of the transmitting angle, θ_t, the result is integrated over the volumetric vacuum above the surface and over the volume below the surface. By use of Green's theorem, the volumetric integral of the Helmholtz equation is expressed as an integral over an arbitrary surface, S (Stratton, 1941). The volumetric integral is reduced, and the surface integral above the surface is

$$-4\pi H_y^{>}(x, z) = \int_{S^{>}} \left[H_y^{>}(x', z') \frac{\partial G_o(x, z; x', z')}{\partial n} - G_o(x, z; x', z') \frac{\partial H_y^{>}}{\partial n} \right] da', \tag{7a}$$

while the surface integral below the surface is

$$-4\pi H_y^{<}(x, z) = \int_{S^{<}} \left[H_y^{<}(x', z') \frac{\partial G_\epsilon(x, z; x', z')}{\partial n} - G_\epsilon(x, z; x', z') \frac{\partial H_y^{<}}{\partial n} \right] da'. \tag{7b}$$

Equations (7) are integrals over arbitrary surfaces, $S^{>}$ and $S^{<}$. Since the surfaces are arbitrary, the integral in Eq. (7*a*) is taken over a surface at infinity and added to an integral taken over the material surface. The integral over the surface at infinity is interpreted as the incident field (Wolf, 1973). Similarly, the integral in Eq. (7*b*) is taken over a surface extending to negative infinity and added to an integral taken over the material surface. The surface extending to negative infinity contributes nothing since there are no incoming waves passing toward the surface $z = \zeta(x)$ from negative infinity and the outgoing waves are assumed to decay exponentially. In this way, when the normal derivative is correctly assigned and Eq. (6) is substituted into Eqs. (7), the pair of coupled integral equations for the magnetic field are

$$H_y^{>}(x, z) = H_y^{>}(x)_o + \frac{1}{4\pi}\int_{-\infty}^{\infty} \left[H(x') \left(-\zeta'(x') \frac{\partial}{\partial x'} + \frac{\partial}{\partial z'} \right) \times G_o(x, z; x', z')|_{z'=\zeta(x')} - G_o(x, z; x', z') \times L(x')|_{z'=\zeta(x')} \right] dx' \tag{8a}$$

$$H_y^{>}(x, z) = -\frac{1}{4\pi}\int_{-\infty}^{\infty} \left[H(x') \left(-\zeta'(x') \frac{\partial}{\partial x'} + \frac{\partial}{\partial z'} \right) \times G_\epsilon(x, z; x', z')|_{z'=\zeta(x')} - \epsilon G_\epsilon(x, z; x', z') \times L(x')|_{z'=\zeta(x')} \right] dx' \tag{8b}$$

where G_o and G_ϵ are the Green's functions and

$$H(x') = H_y^{>}(x', z')|_{z'=\zeta(x')} \tag{9a}$$

$$L(x') = \left(-\zeta'(x') \frac{\partial}{\partial x'} + \frac{\partial}{\partial z'} \right) H_y^{>}(x', z')|_{z'=\zeta(x')}. \tag{9b}$$

The Hankel functions in G_o and G_ϵ have singularities and must be directly integrated by numerical computation (Maradudin et al., 1990; Sánchez-Gil and Nieto-Vesperinas, 1991). Equations (8) are the integral equations governing TM polarized surface scattering from a dielectric surface. With the integral representations of G_o and G_ϵ, Eqs. (8) provide the angular spectrum of the scattered field and transmitted fields (Sanchez-Gil and Nieto-Vesperians, 1991).

The total power scattered into the region above and below the material surface is calculated from the Poynting power theorem (Stratton, 1941). After evaluating the integrals of the power theorem, the power scattered into any angle is

$$\frac{d\Phi_s}{d\theta_s} = \frac{L_y}{8\epsilon_o\omega}\frac{k_o}{2\pi}|r_{TM}(\theta_s)|^2 \tag{10a}$$

and the power transmitted into any angle is

$$\frac{d\Phi_t}{d\theta_t} = \frac{L_y}{8\epsilon_o\omega\epsilon}\frac{k_o}{2\pi}|t_{TM}(\theta_t)|^2. \tag{10b}$$

The scattering reflection function, $r_{TM}(\theta_s)$, and the scattering transmission function, $t_{TM}(\theta_t)$, are given by

$$r_{TM}(\theta_s) = \int_{-\infty}^{\infty} \{\exp\{-ik_o(x\sin\theta_s + \zeta(x)\cos\theta_s)\} \times (ik_o(\zeta'(x)\sin\theta_s - \cos\theta_s)H(x) - L(x))\}dx \tag{11a}$$

and

$$t_{TM}(\theta_t) = \int_{-\infty}^{\infty} \{\exp\{-i\sqrt{\epsilon}k_o(x\sin\theta_t - \zeta(x)\cos\theta_t)\} \times (i\sqrt{\epsilon}k_o(-\zeta'(x)\sin\theta_t + \cos\theta_t)H(x) + \epsilon L(x))\}dx. \tag{11b}$$

After evaluating the magnitude of the incident power flow with the Poynting power theorem, the result and Eqs. (10) are substituted into Eqs. (1) to give the desired results for the TM polarized bidirectional reflection function

$$\rho''_{\lambda TM}(\theta_o, \theta_s) = \frac{1}{8}\frac{1}{L_x\cos\theta_s\cos\theta_c}|r_{TM}(\theta_s)|^2 \tag{12a}$$

and the TM polarized bidirectional transmission function

$$\tau''_{\lambda TM}(\theta_o, \theta_t) = \frac{1}{8}\frac{1}{\epsilon}\frac{1}{L_x\cos\theta_t\cos\theta_o}|t_{TM}(\theta_t)|^2. \tag{12b}$$

Equation (12*a*) is integrated over all scattering angles and Eq. (12*b*) is integrated over all transmitting angles to obtain the hemispherical reflectivity, $\rho'_\lambda(\theta_o)$, and the hemispherical transmissivity, $\tau'_\lambda(\theta_o)$, for TM polarization. When the dielectric medium is nonabsorbing, conservation of energy on the surface requires that the hemispherical functions sum to unity.

TE Polarization. In the case of TE polarization, the electric field vector, **E**, is perpendicular to the plane of incidence. The formulation is exactly the same as for the TM polarization, with E_y substituted for H_y in all of the equations. Using the continuity equation for the **E** field (Stratton, 1941) and reducing it by using Maxwell's equations yields the jump conditions as

$$E_y^{>}(x, z)|_{z=\zeta(x)} = E_y^{<}(x, z)|_{z=\zeta(x)} \tag{13}$$

$$\left.\frac{\partial E_y^{>}(x, z)}{\partial n}\right|_{z=\zeta(x)} = \left.\frac{\partial E_y^{<}(x, z)}{\partial n}\right|_{z=\zeta(x)}. \quad (14)$$

Equations similar to Eqs. (8) are obtained as

$$E_y^{>}(x, z) = E_y^{>}(x)_o + \frac{1}{4\pi}\int_{-\infty}^{\infty}\left[E(x')\left(-\zeta'(x')\frac{\partial}{\partial x'}+\frac{\partial}{\partial z'}\right)\right.$$
$$\times G_o(x, z; x', z')|_{z'=\zeta(x')} - G_o(x, z; x', z')$$
$$\left.\times F(x')|_{z'=\zeta(x')}\right]dx' \quad (15a)$$

$$E_y^{>}(x, z) = -\frac{1}{4\pi}\int_{-\infty}^{\infty}\left[E(x')\left(-\zeta'(x')\frac{\partial}{\partial x'}+\frac{\partial}{\partial z'}\right)\right.$$
$$\times G_\epsilon(x, z; x', z')|_{z'=\zeta(x')} - G_\epsilon(x, z; x', z')$$
$$\left.\times F(x')|_{z'=\zeta(x')}\right]dx' \quad (15b)$$

where $E(x')$ and $F(x')$ are

$$E(x') = E_y^{>}(x', z')|_{z'=\zeta(x')} \quad (16a)$$

and

$$F(x') = \left(-\zeta(x')\frac{\partial}{\partial x'}+\frac{\partial}{\partial z'}\right)E_y^{>}(x', z')|_{z'=\zeta(x')}. \quad (16b)$$

Applying the integral representation of G_o and G_ϵ to Eqs. (15) gives the angular distributions of the scattered field and the transmitted field for TE polarization, which are evaluated using the Poynting power theorem (Stratton, 1941). The power scattered and transmitted into any angle are

$$\frac{d\Phi_s}{d\theta_s} = \frac{L_y}{8\mu_o\omega}\frac{k_o}{2\pi}|r_{TE}(\theta_s)|^2 \quad (17a)$$

and

$$\frac{d\Phi_t}{d\theta_t} = \frac{L_y}{8\mu_o\omega}\frac{k_o}{2\pi}|t_{TE}(\theta_t)|^2. \quad (17b)$$

The scattering reflection function, $r_{TE}(\theta_s)$, and the transmission function, $t_{TE}(\theta_t)$, are given by

$$r_{TE}(\theta_s) = \int_{-\infty}^{\infty}\{\exp\{-ik_o(x\sin\theta_s + \zeta(x)\cos\theta_s)\}$$
$$\times(ik_o(\zeta'(x)\sin\theta_s - \cos\theta_s)E(x) - F(x))\}dx \quad (18a)$$

and

$$t_{TE}(\theta_t) = \int_{-\infty}^{\infty}\{\exp\{-i\sqrt{\epsilon}k_o(x\sin\theta_t - \zeta(x)\cos\theta_t)\}$$
$$\times(i\sqrt{\epsilon}k_o(-\zeta'(x)\sin\theta_t + \cos\theta_t)E(x) + \epsilon F(x))\}dx. \quad (18b)$$

After evaluating the magnitude of the incident power, the TE polarized bidirectional reflection function is

$$\rho''_{\lambda TE}(\theta_o, \theta_s) = \frac{1}{8}\frac{1}{L_x\cos\theta_s\cos\theta_o}|r_{TE}(\theta_s)|^2 \quad (19a)$$

and the TE polarized bidirectional transmission function is

$$\tau''_{\lambda TE}(\theta_o, \theta_t) = \frac{1}{8}\frac{1}{L_x\cos\theta_s\cos\theta_o}|t_{TE}(\theta_t)|^2. \quad (19b)$$

Equations (19) are integrated over all the scattering and transmitting angles to give the TE polarized hemispherical reflection and transmission functions. These functions must also sum to unity when the dielectric medium is nonabsorbing, to satisfy conservation of energy on the surface.

For unpolarized reflection, a simple average of Eqs. (12*a*) and (19*a*) is taken. Unpolarized transmission is an average of Eqs. (12*b*) and (19*b*). The unpolarized equations for bidirectional reflection and bidirectional transmission are integrated over all θ_s and θ_t to obtain unpolarized hemispherical reflectivity and transmissivity, which in the case of nonabsorbing mediums must be equal to unity.

Numerical Implementation. The surface scattering equations given by the electromagnetic theory formulation are solved numerically. Accurate solutions are obtained by a quadrature scheme described by Celli et al. (1985), Maradudin et al. (1989, 1990), Sánchez-Gil and Nieto-Vesperinas (1991), and Nieto-Vesperinas and Sánchez-Gil (1992).

The integral equations are discretized over the interval of interest, L_x, so that the integrals are replaced with summations. The matrix elements are provided by Maradudin et al. (1990). With the matrix elements, the discretized unknowns $H(x_n)$, $L(x_n)$, $E(x_n)$ and $F(x_n)$ are determined. Thus Eqs. (11) and (18) reduce to

$$r_{TM}(\theta_s) = \sum_{n=-M}^{M-1}\{\Delta x\{ik_o(\zeta'(x_n)\sin\theta_s - \cos\theta_s)H(x_n)$$
$$-L(x_n)\}\exp[-ik_o(x_n\sin\theta_s + \zeta(x_n)\cos\theta_s)]\} \quad (20a)$$

$$t_{TM}(\theta_t) = \sum_{n=-M}^{M-1}\{\Delta x\{i\sqrt{\epsilon}k_o(-\zeta'(x_n)\sin\theta_t + \cos\theta_t)H(x_n)$$
$$+\epsilon L(x_n)\}\exp[-i\sqrt{\epsilon}k_o(x_n\sin\theta_t - \zeta(x_n)\cos\theta_t)]\} \quad (20b)$$

and

$$r_{TE}(\theta_s) = \sum_{n=-M}^{M-1}\{\Delta x\{ik_o(\zeta'(x_n)\sin\theta_s - \cos\theta_s)E(x_n) - F(x_n)\}$$
$$\times\exp[-ik_o(x_n\sin\theta_s + \zeta(x_n)\cos\theta_s)]\} \quad (21a)$$

$$t_{TE}(\theta_t) = \sum_{n=-M}^{M-1}\{\Delta x\{i\sqrt{\epsilon}k_o(-\zeta'(x_n)\sin\theta_t + \cos\theta_t)E(x_n)$$
$$+F(x_n)\}\exp[-i\sqrt{\epsilon}k_o(x_n\sin\theta_t - \zeta(x_n)\cos\theta_t)]\}. \quad (22b)$$

These expressions are solved and used in the bidirectional reflection function equations, Eqs. (12) and (19).

All equations are programmed on a Cray Y-MP4/464 or a Convex C3880 using matrix factoring and solving routines to solve for the unknowns, $H(x_n)$, $L(x_n)$, $E(x_n)$, and $F(x_n)$. The specific routines used are CGETRF and CGETRS on the Cray, which factor the matrix into its LU decomposition and solve the matrix, respectively. On the Convex, the routines CGEFA and CGESL are used to solve the system of equations. The surfaces with longer surface lengths and larger deviations are run on the Convex. Simple polynomial approximations (Abramowitz and Stegun, 1965) are used to obtain values of the Hankel functions within the matrix elements.

The surfaces are constructed using a Fourier series representation of the surface. Since a Fourier series is not an exact representation of a surface, the number of terms in the surface series is important. The number of terms in the series must be large enough to remove any numerical inconsistencies on the order of the surface deviation. However, since the numerical solution relies on the first and second derivatives on the surface, the number of terms must be small enough to provide numerically continuous derivatives. Up to 75 terms have been included without altering the presented results. For the triangular deterministic surfaces presented, a 25-term Fourier series is used to generate the surface profiles. This series keeps continuous derivatives and removes any numerical inconsistencies associated with smaller series that may affect results.

The surface length is made as long as numerically possible to minimize the edge effects from the incident plane wave on the surface. Surface lengths are typically 30λ to 200λ depending on τ/λ. Typical surface lengths are divided into 2400 increments on the Cray and 3300 increments on the Convex. These lengths require the memory limit of each machine. Surfaces that have a large σ/λ require more increments than surfaces with small σ/λ. All results presented conserve energy to within

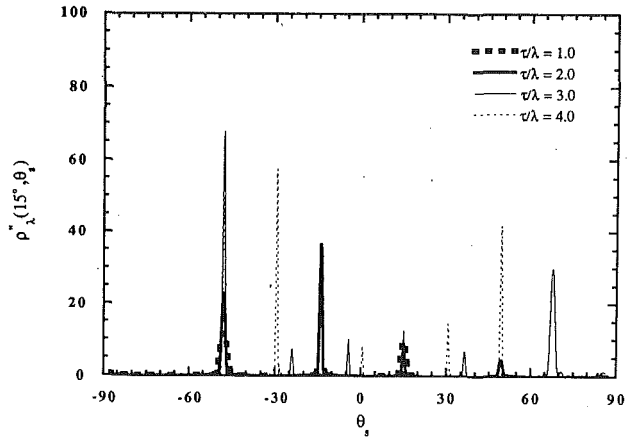

Fig. 2 Comparison of scattering solutions from silicon (n = 2.0, κ = 4.0) surfaces of varying correlation length, τ/λ, for constant deviation, σ/λ = 1.0 and constant f = 0.5, for the bidirectional reflection function at θ_o = 15 deg versus θ_s.

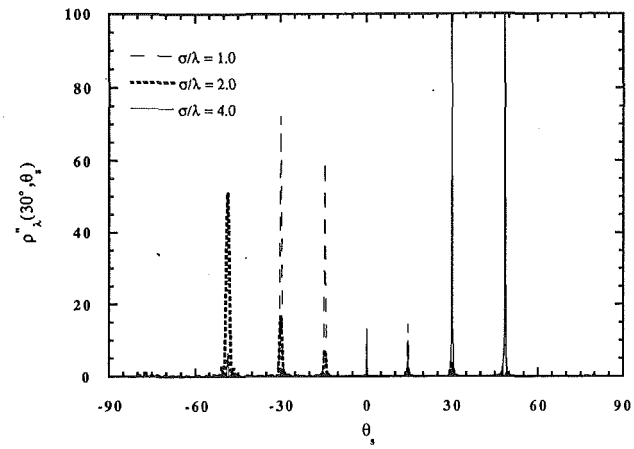

Fig. 3 Comparison of scattering solutions from silicon (n = 2.0, κ = 4.0) surfaces of varying deviation, σ/λ, for constant correlation length, τ/λ = 4.0 and constant f = 0.5, for the bidirectional reflection function at θ_o = 30 deg versus θ_s.

1 percent as evaluated by examining conservation of energy for a true dielectric surface (i.e., κ = 0.0).

Results

The directional distribution of scattered energy is affected by the surface parameters of correlation length, τ/λ, deviation, σ/λ, and surface peak location parameter, f. These parameters determine the location and the magnitude of the scattered energy for a given incident wave angle, θ_o. The magnitude of the scattered energy is also altered by changing the surface material. Magnitude variations produce significant changes in hemispherical emission from surfaces with similar parameters. The following results are from typical silicon surfaces, with dielectric constants, n = 2.0 and κ = 4.0 (Hesketh, 1988b), and from aluminum surfaces with dielectric constants, n = 1.5 and κ = 10.0 (Brewster, 1992; Palik, 1985). A plane incident wave is used for all the results. Since the surface parameters are normalized with the incident wavelength, the scattering results are general for any incident wavelength, but the dielectric properties of surfaces are typically wavelength dependent.

Figure 2 compares the bidirectional reflection function from surfaces of varying τ/λ, constant σ/λ = 1.0, and the symmetric value of f = 0.5. The bidirectional reflection function from a typical silicon surface for a wave incident at angle, θ_o = 15 deg, is presented versus the scattering angle, θ_s. As shown in Fig. 2, the correlation length significantly alters the locations and magnitudes of dominant reflection. The number of locations of reflected energy increases as the correlation length increases. For the four cases shown in Fig. 2, the reflection locations increase from 2 when τ/λ = 1.0 to 7 when τ/λ = 4.0. These locations are predicted by classical optical grating theory, which is a simple function of the correlation length and the incident angle ($\sin\theta_s = \sin\theta_o + n\lambda/\tau$; n = 0, ±1, ±2, . . . ,) (Klein and Furtak, 1986). However, grating theory fails to predict the magnitude of the scattered energy, which is important for predicting bidirectional reflection.

The magnitude of the reflected energy at a dominant scattering angle is a function of the correlation length. Figure 2 shows that at a scattering angle of θ_s = −47.8 deg, all four surfaces have scattered energy. However, the magnitudes of the reflection function are significantly different for each correlation length. When the correlation length is doubled from 1.0 to 2.0, the reflection function approximately doubles at θ_s = −47.8 deg. If the correlation length is tripled from 1.0 to 3.0, the reflection function increases by over a factor of 5. However, quadrupling τ/λ from 1.0 to 4.0 only approximately quadruples the reflection function at θ_s = −47.8 deg. Although the magnitude of the reflection function is a strong function of the correlation length, it does not follow a simple formulation analogous to grating theory and must be rigorously predicted. As shown in Fig. 2, the directional distribution of energy at θ_o = 15 deg is more distributed for τ/λ = 4.0, but the most dominant spike occurs when τ/λ = 3.0. By varying the correlation length, the directional distribution of the scattered energy is significantly altered.

In Fig. 3, the bidirectional reflection functions for silicon surfaces of varying σ/λ, constant τ/λ = 4.0, and the symmetric value of f = 0.5, are compared. The bidirectional reflection function for an incident wave of θ_o = 30 deg is plotted versus the scattering angle, θ_s. Since the correlation length does not change, the locations of reflected energy are the same for all three deviations. However, the magnitude of the reflected energy in each location changes with surface deviation. Although some reflection occurs at all of the predicted locations, only a few modes are dominant for each deviation. When σ/λ = 1.0 and σ/λ = 2.0, a significant amount of backscattering occurs. When the deviation reaches 4.0, however, the scattering is almost completely forward. This forward scattering is significantly larger than the backscattering regions for the smaller deviations. At other incident angles, the σ/λ = 1.0 and σ/λ = 2.0 surfaces have significant forward scattering and the σ/λ = 4.0 surface has backscattering. This scattering phenomenon is rigorously computed to predict the relative magnitudes of the directional distribution.

Figure 4 shows the directional contribution of surface geometry to the bidirectional reflection function by varying f for constant τ/λ = 4.0 and constant σ/λ = 1.0. The bidirectional reflection function from a silicon surface with a wave incident at θ_o = 30 deg is plotted versus θ_s. Since the correlation length does not vary, the reflection locations are the same for all three cases. The magnitudes of the reflected energy in the different locations vary for the different geometries. For a symmetric surface described by f = 0.5, significant backscattering into θ_o = −30 deg occurs. The magnitudes of the reflection peaks vary significantly. When the surface peak is skewed to f = 0.7, however, the reflection function magnitudes at all reflection peaks are of a similar order. When the peak position is almost a right angle (f = 0.9) the dominant reflection is normal to the surface. Therefore, the peak position of the surface is a significant factor in determining the magnitude of dominant modes of reflection. The distribution of scattered energy is altered by simply changing the geometry of a surface with constant surface parameters, τ/λ and σ/λ.

Figures 2, 3, and 4 show the effects of geometry and the

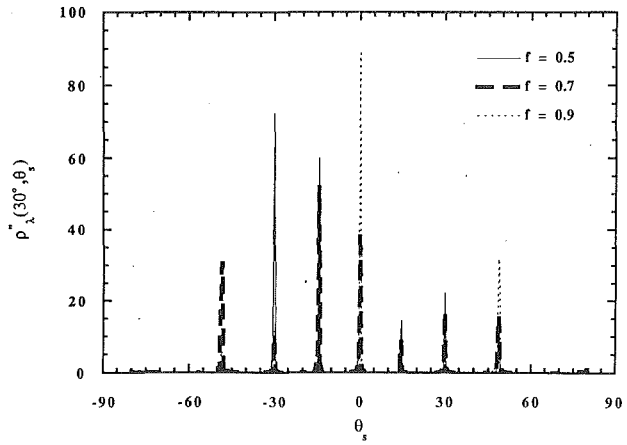

Fig. 4 Comparison of scattering solutions from silicon (n = 2.0, κ = 4.0) surfaces of varying surface peak position, f, constant correlation length, τ/λ = 4.0, for constant deviation, σ/λ = 1.0, for the bidirectional reflection function at θ_o = 30 deg versus θ_s.

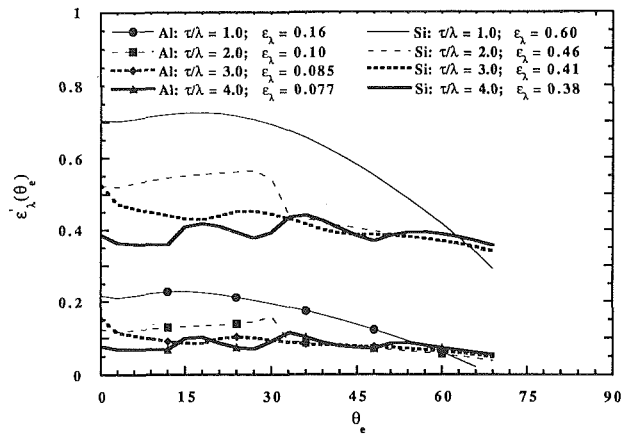

Fig. 5 Comparison of emission from silicon (n = 2.0, κ = 4.0) and aluminum (n = 1.5, κ = 10.0) surfaces of varying correlation length, τ/λ, constant deviation, σ/λ = 1.0, and constant f = 0.5.

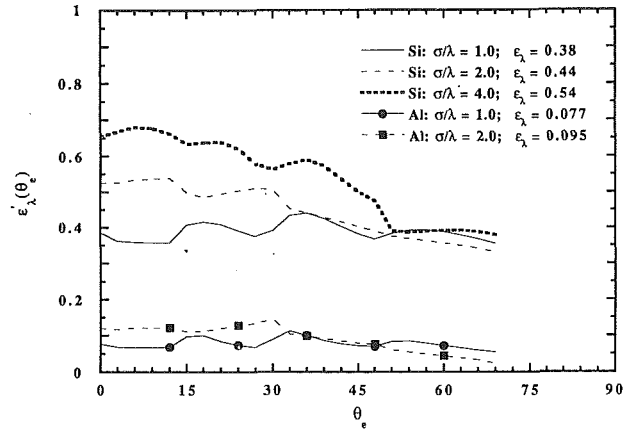

Fig. 6 Comparison of emission from silicon (n = 2.0, κ = 4.0) and aluminum (n = 1.5, κ = 10.0) surfaces of varying deviation, σ/λ, constant correlation length, τ/λ = 4.0, and constant f = 0.5.

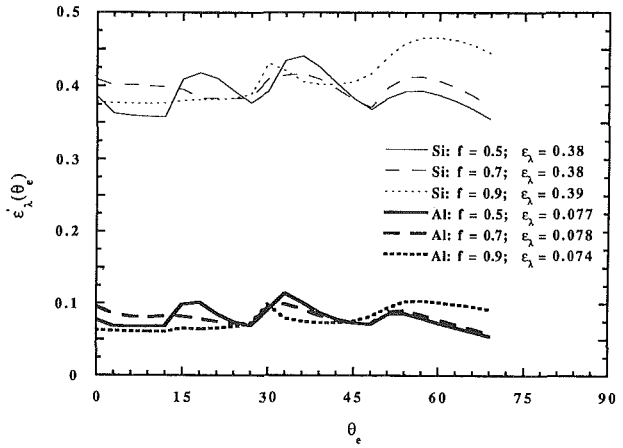

Fig. 7 Comparison of emission from silicon (n = 2.0, κ = 4.0) and aluminum (n = 1.5, κ = 10.0), surfaces of varying peak position, f, constant correlation length, τ/λ = 4.0, and constant surface deviation, σ/λ = 1.0. Angular results are the average of the positive θ_e and negative θ_e emissivities.

surface parameters on the directional distribution of the scattered energy from a surface. Varying the correlation length varies the location and the magnitude of the reflected energy, while varying the deviation and the peak position of the surface only changes the magnitude of the reflected energy. The directional distribution of reflected energy is significantly enhanced or decreased by changing any of the three surface parameters. Although the reflection results for aluminum surfaces are not presented, the only alteration in the previous results is in the magnitude of the bidirectional reflection function.

In Figs. 5, 6, and 7, emissivity from both silicon surfaces and aluminum surfaces is compared for various surface parameters. The directional spectral emissivity is presented versus emission angle, θ_e, along with the hemispherical spectral emissivity. At grazing incident angles, the directional spectral emissivity is not rigorously computed due to numerical limitations and the function is approximated to obtain hemispherical spectral emissivity. Various approximations to extend the data to 90 deg have been made, and the hemispherical spectral emissivity values are calculated to within 5 percent.

Figure 5 shows the directional spectral emissivity from silicon and aluminum surfaces with varying τ/λ, constant σ/λ = 1.0, and the symmetric value of f = 0.5. The general shapes of the emissivity curves for silicon and aluminum are similar, although the magnitude of the emissivity is larger for silicon surfaces. The surfaces with a small correlation length are more monotonic than the surfaces with longer correlation lengths. For a surface with τ/λ = 4.0 enhancements occur at approximately θ_e = 18 deg and θ_e = 36 deg. As the correlation length decreases to τ/λ = 1.0, which makes the surface deviation more prominent, these enhancements are decreased until the surface becomes monotonic. As shown in Fig. 5, the hemispherical spectral emissivity is largest for the roughest case of τ/λ = 1.0. This value decreases significantly as τ/λ is lengthened. Also, the silicon is a much better emitter than the aluminum for the properties used in these predictions.

Figure 6 compares the directional spectral emission function from silicon and aluminum surfaces for varying σ/λ, constant τ/λ = 4.0, and the symmetric value of f = 0.5. Again, the silicon is a much better emitter than the aluminum. The directional emissivity becomes more monotonic as the surface roughness increases. In addition, the magnitude of the emissivity increases as the roughness is increased. Enhancements occur for all of the emissivities shown. For the σ/λ = 1.0 emission functions, these enhancements are a significant increase over the hemispherical spectral emissivity. For silicon, the hemispherical spectral emissivity is 0.38, but the directional spectral emission function becomes approximately 0.43 at θ_e = 36 deg.

Figure 7 compares the effect of surface peak position on the directional spectral emission function. Emission from both silicon and aluminum surfaces is shown for σ/λ = 1.0 and τ/λ = 4.0. The directional emissivity at all θ_e is presented as the average of the positive and negative angle emission values. The peak position affects the shape of the directional spectral

emission function, but does not change the hemispherical spectral emissivity significantly. This occurs because the magnitudes of the various emission functions are approximately the same even though the distribution is slightly different. When the distributions are integrated, the directional phenomena are averaged, and the hemispherical emissivities are approximately the same.

Conclusions

Through recent advances in numerical approaches to electromagnetic theory, solutions for the angular scattering from very rough surfaces are presented. Geometric structure for triangular surfaces is included for length scales of the order of the wavelength. Rigorous predictions for thermal radiative properties are presented for various optical properties.

The geometric parameters of correlation length, deviation, and surface peak position significantly change the scattering distribution. The correlation length of the surface determines the possible locations of scattered energy, while the magnitude of the scattering locations is determined by all the parameters. In many instances, the surface parameters change the phenomena from complete backscattering to forward scattering. In addition, the phenomena a particular surface exhibits change with the angle of incident energy on the surface.

The surface peak location parameter also significantly affects the directional distribution of the scattered energy. By simply changing the peak position of the surface, the scattered energy distribution is changed. The locations of distributed scattered energy remain constant due to the constant correlation length, but the magnitude in each location is altered. In addition, the surface material, described by wavelength-dependent dielectric properties, changes the magnitude of the scattered distribution.

The directional emissivities for silicon and aluminum surfaces show that silicon is a much better emitter than aluminum for the dielectric properties examined. The directional emissivities show enhancements over the hemispherical emissivity at various emission angles. In some instances, these enhancements are over 10 percent. As the surface becomes rougher, the directional emissivities become more monotonic. The correlation length and the surface deviation affect the directional and hemispherical emissivity, while the surface peak position only significantly affects directional emissivity. This occurs because the directional emissivities for constant correlation length and deviation have a different directional scattering distribution of approximately the same amount of emitted energy. When these directional distributions are integrated over all of the emission angles, the directional effects are lost, and the hemispherical emissivities are approximately equal.

Acknowledgments

This research was supported, in part, by the National Center for Supercomputing Applications, Urbana, Illinois, and the McDonnell Douglas Corporation, St. Louis, Missouri.

References

Abramowitz, M., and Stegun, I. A., eds., 1965, *Handbook of Mathematical Functions*, 9th ed., Dover, New York, p. 370.

Brandenberg, W. M., and Clausen, O. W., 1965, "The Directional Spectral Emittance of Surfaces Between 200 and 600°C," in: *Symposium on Thermal Radiation of Solids*, S. Katzoff, ed., NASA SP-55, pp. 313–319.

Brewster, M. Q., 1992, *Thermal Radiative Transfer & Properties*, 1st ed., Wiley, New York, pp. 121, 502.

Celli, V., Maradudin, A. A., Marvin, A. M., and McGurn, A. R., 1985, "Some Aspects of Light Scattering From a Randomly Rough Metal Surface," *Journal of the Optical Society of America A*, Vol. 2, pp. 2225–2239.

Demont, P., Huetz-Aubert, M., and Tran N'Guyen, H., 1982, "Experimental and Theoretical Studies of the Influence of Surface Conditions on Radiative Properties of Opaque Materials," *Int. J. Thermophys.*, Vol. 3, pp. 335–364.

Hesketh, P. J., Gebhart, B., and Zemel, J. N., 1988a, "Measurements of the Spectral and Directional Emission From Microgrooved Silicon Surfaces," ASME JOURNAL OF HEAT TRANSFER, Vol. 110, pp. 680–686.

Hesketh, P. J., Zemel, J. N., and Gebhart, B., 1988b, "Polarized Spectral Emittance From Periodic Micromachined Surfaces. I. Doped Silicon: The Normal Direction; II. Doped Silicon: Angular Variations," *Physical Review B*, Vol. 37, pp. 10795–10813.

Hollands, K. G. T., 1963, "Directional Selectivity, Emittance, and Absorptance Properties of Vee Corrugated Specular Surfaces," *Solar Energy*, Vol. 7, pp. 108–116.

Klein, M. V., and Furtak, T. E., 1986, *Optics*, Wiley, New York, pp. 253–328.

Maradudin, A. A., Méndez, E. R., and Michel, T., 1989, "Backscattering Effects in the Elastic Scattering of p-Polarized Light From a Large-Amplitude Random Metallic Grating," *Optics Letters*, Vol. 14, pp. 151–153.

Maradudin, A. A., Michel, T., McGurn, A. R., and Méndez, E. R., 1990, "Enhanced Backscattering of Light From a Random Grating," *Annals of Physics*, Vol. 203, pp. 255–307.

Maradudin, A. A., Lu, J. Q., Michel, T., Gu, T. H., Dainty, J. C., Sant, A. J., Méndez, E. R., and Nieto-Vesperinas, M., 1991, "Enhanced Backscattering and Transmission of Light From Random Surfaces on Semi-infinite Substrates and Thin Films," *Waves in Random Media*, Vol. 3, pp. S129–S141.

McGurn, A. R., and Maradudin, A. A., 1989, "An Analogue of Enhanced Backscattering in the Transmission of Light Through a Thin Film With a Randomly Rough Surface," *Optics Communications*, Vol. 72, pp. 279–285.

Morse, P. M., and Feshbach, H., 1946, *Methods of Theoretical Physics*, Technology Press, Cambridge, MA, p. 155.

Nieto-Vesperinas, M., and Sánchez-Gil, J. A., 1990, "Light Transmission From a Randomly Rough Dielectric Diffuser: Theoretical and Experimental Results," *Optics Letters*, Vol. 15, pp. 1261–1263.

Nieto-Vesperinas, M., and Sánchez-Gil, J. A., 1992, "Light Scattering From a Random Rough Interface With Total Internal Reflection," *Journal of the Optical Society of America A*, Vol. 9, pp. 424–436.

Palik, E. D., ed., 1985, *Handbook of Optical Constants*, Academic Press, New York, pp. 547–568.

Perlmutter, M., and Howell, J. R., 1962, "A Strongly Directional Emitting and Absorbing Surface," ASME JOURNAL OF HEAT TRANSFER, Vol. 85, pp. 282–283.

Sánchez-Gil, J. A., and Nieto-Vesperinas, M., 1991, "Light Scattering From Random Dielectric Surfaces," *Journal of the Optical Society of America A*, Vol. 8, pp. 1270–1286.

Siegel, R., and Howell, J. R., 1981, *Thermal Radiation Heat Transfer*, Hemisphere Publishing Corp., New York, p. 64.

Soto-Crespo, J. M., and Nieto-Vesperinas, M., 1989, "Electromagnetic Scattering From Very Rough Random Surfaces and Deep Reflection Gratings," *Journal of the Optical Society of America A*, Vol. 6, pp. 367–384.

Stratton, J. A., 1941, *Electromagnetic Theory*, 1st ed., MacGraw-Hill, New York, pp. 23–131.

Torrance, K. E., and Sparrow, E. A., 1967, "Theory of Off-Specular Reflection From Roughened Surfaces," *Journal of the Optical Society of America*, Vol. 57, pp. 1105–1114.

Wolf, E., 1973, "A Generalized Extinction Theorem and Its Role in Scattering Theory," *Coherence and Quantum Optics*, E. Wolf, ed., Plenum, pp. 339–357.

Surface Radiation Effects on Flame Spread Over Thermally Thick Fuels in an Opposing Flow

J. West

S. Bhattacharjee

Department of Mechanical Engineering,
San Diego State University,
San Diego, CA 92182

R. A. Altenkirch

Department of Mechanical Engineering, and
NSF Engineering Research Center for
Computational Field Simulation,
Mississippi State University,
Mississippi State, MS 39762

A computational model of flame spread over a thermally thick solid fuel in an opposing-flow environment is presented. Unlike thermally thin fuels, for which the effect of fuel surface radiation is negligiible for high levels of opposing flow, fuel surface radiation is important for thermally thick fuels for all flow levels. This result is shown to derive from the fact that the ratio of the rate of heat transfer by re-radiation from the surface to that by conduction from the gas to the solid is proportional to the length over which heat can be conducted forward of the flame to sustain spreading. For thin fuels, this length decreases with increasing flow velocity such that while radiation is important at low flow velocities it is not at the higher velocities. For thick fuels at low flow velocities, the conduction length is determined by gas-phase processes and decreases with increasing flow velocity. But at higher flow velocities, the conduction length is determined by solid-phase processes and is rather independent of the gas-phase flow. The result is that over a wide range of flow velocities, the conduction length of importance does not change substantially as it switches from one phase to another so that the ratio of radiation to conduction is of unit order throughout that wide range of flow.

Introduction

The importance of understanding the governing mechanisms of flame spread is well established. Much experimental and analytical work has been carried out to determine flame spread mechanisms in normal and elevated convection levels for both thermally thin and thick fuels (e.g., de Ris, 1969; Frey and T'ien, 1979; Altenkirch et al., 1980; Fernandez-Pello et al., 1981; Mao et al., 1984; Olson et al., 1989; Altenkirch et al., 1983, Altenkirch and Bhattacharjee, 1990; Bhattacharjee and Altenkirch, 1990, 1991; Bhattacharjee et al., 1990, 1991). However, little has been done to investigate the behavior of thermally thick flame spread between, and including, the quiescent environment limit and moderate forced opposed convection where the effects of buoyancy are comparable to those of the forced flow.

de Ris (1969), in his analytical solution for the flame spread rate, $\hat{V}_f$, found the flame spread rate to be independent of the opposing velocity, $\hat{V}_g$, for thermally thin fuels and proportional to $\hat{V}_g$ for thermally thick fuels. The analytical solution was produced under the assumption of infinite-rate chemical kinetics and thus applies only to low levels of opposing convection and/or high levels of oxygen in the flow. The velocity field was prescribed as an Oseen flow, and assumptions were made regarding the fluid and fuel properties to allow a solution to be obtained.

Fernandez-Pello et al. (1981), in their experimental study, investigated the effect of opposing convection level and ambient oxygen concentration on the flame spread rate over thermally thick sheets of polymethylmethacrylate (PMMA). Their study confirmed the behavior of the flame spread rate as a function of opposing convection and ambient oxygen concentration as predicted by de Ris for low forced convective levels.

Previous numerical models for thermally thick fuels (Di Blasi et al., 1987, 1988) employ a constant pressure and a prescribed flow field and neglect any radiative process. Additionally results for various ambient oxgyen concentrations for a fixed heat of combustion (Di Blasi et al., 1988) resulted in flame temperatures well in excess of physically realistic and/or known levels.

Studies that include the effects of either gas and/or fuel surface radiation on thermally thin fuels were conducted by Altenkirch and Bhattacharjee (1990) and Bhattacharjee and Altenkirch (1990, 1991). The former effort produced scaling arguments about the relative importance of heat conduction to radiative heat transfer over different flame spread regimes, while the latter studies were ones in which a numerical model, including both gas-phase and fuel surface radiation, was used to obtain predictions of the near-quiescent flame spread rate over a thermally thin fuel.

Here a model, similar to previously presented numerical models (Bhattacharjee et al., 1990; Bhattacharjee and Altenkirch, 1990, 1991), that couples the gas-phase flow field to prediction of the thermally thick flame spread rate and additionally considers the effects of fuel surface radiative loss is presented. This model will be used to investigate the importance of radiative effects for flame spread over thick fuels, particularly at the low flow velocities where radiative effects affect flame spread over thin fuels. Gas-phase radiation, although potentially important at near-quiescent conditions such as those that can be obtained in the microgravity environment of spacecraft, is neglected in favor of considering the major radiative effect as a heat loss from the fuel surface to the ambient environment (Bhattacharjee and Altenkirch, 1990; Bhattacharjee et al., 1991).

Problem Formulation

The flame spread model consists of the elliptic, partial differential equations describing conservation of mass, energy, momentum, and species in the gas phase and the elliptic partial differential equation describing conservation of energy in the solid phase. The gas-phase equations are written in steady-state form for a single-step, Arrhenius reaction and solved in flame-fixed coordinates such that the flame sees an opposing, forced flow of velocity equal to the flame spread rate plus any forced opposing velocity, if present. Because the gas-phase

Contributed by the Heat Transfer Division and presented at the National Heat Transfer Conference, San Diego, California, August 9–12, 1992. Manuscript received by the Heat Transfer Division December 1992; revision received July 1993. Keywords: Fire/Flames, Microgravity Heat Transfer, Radiation Interactions. Associate Technical Editor: W. L. Grosshandler.

Table 1 Equation coefficients for the gas phase

Equation	ø	$\Gamma_ø$	$S_ø$
Continuity	1	0	0
x-momentum	$u=\hat{u}/\hat{V}_r$	μ/Pr	$-\partial P/\partial x$
y-momentum	$v=\hat{v}/\hat{V}_r$	μ/Pr	$-\partial P/\partial y$
Fuel	m_f	μ	$-Da_g\rho^2 m_{ox} m_f\, e^{-Eg/T}$
Oxygen	m_{ox}	μ	$-sDa_g\rho^2 m_{ox} m_f\, e^{-Eg/T}$
Energy	$T=\hat{T}/\hat{T}_\infty$	μ	$\Delta H_c Da_g\rho^2 m_{ox} m_f\, e^{-Eg/T}$

formulation is similar to that given elsewhere (Bhattacharjee et al., 1990), only a brief description is presented.

A velocity characteristic of the gas, $\hat{V}_r$, which is the sum of the forced convective velocity, $\hat{V}_g$, and the flame spread rate, $\hat{V}_f$, is used as the unit in which velocities are measured. This velocity is used to develop the thermal length in the gas, $\hat{L}_r = \hat{\alpha}_r/\hat{V}_r$, which is the unit in which all lengths are measured. The gas-phase thermal diffusivity is evaluated at a reference temperature, $\hat{T}_r$, which is the average of the adiabatic, stoichiometric flame temperature neglecting dissociation and the ambient temperature.

The conservation equations in the gas may be written in the same common form as in Eq. (1) where the various ϕ's, Γ_ϕ's and S_ϕ's are given in Table 1:

$$\frac{\partial(\rho u\phi)}{\partial x}+\frac{\partial(\rho v\phi)}{\partial y}=\frac{\partial}{\partial x}\left\{\Gamma_\phi\frac{\partial(\phi)}{\partial x}\right\}+\frac{\partial}{\partial y}\left\{\Gamma_\phi\frac{\partial(\phi)}{\partial y}\right\}+S_\phi \quad (1)$$

Contributions to the momentum sources due to the compressible nature of the flow were found to be negligible for this type of flow (Bhattacharjee et al., 1990), and so they are neglected.

To solve for the seven unknowns in the gas phase, i.e., u, v, P, T, ρ, m_f, and m_{ox}, the six conservation equations along with the equation of state, $\rho T = \hat{\rho}_\infty/\hat{\rho}_r$, and a square root dependence of viscosity and thermal conductivity on temperature are used. The computational domain for the gas-phase equations is a two-dimensional x-y coordinate system with origin located on the fuel surface at the rear of the computational domain. The x direction is along the fuel surface with positive x upstream and y direction is normal to the fuel surface with positive y into the gas. Boundary conditions suitable for the modeling of forced convective flows are the following:

Upstream at $x=x_{\max}$,

$$u=(v_f+v_g),\ v=0,\ m_f=0,\ m_{ox}=m_{ox,\infty},\ T=1,\ P=0$$

Downstream at $x=0$,

$$\text{all}\ \frac{\partial\phi}{\partial x}=0$$

At $y=y_{\max}$,

$$u=-(v_f+v_g),\ \frac{\partial v}{\partial y}=0,\ m_f=0,\ m_{ox}=m_{ox,\infty},\ T=1,\ P=0$$

at $y=0$,

$$u=-v_f,\ v=v_w,\ T=T_s \quad (2)$$

The quantities v_f, v_w, and T_s are obtained from the solution to the solid-phase problem, while m_f and m_{ox} at $y=0$ are obtained from an interfacial species balance, Eqs. (3) and (4), respectively. The meanings of ϕ and Γ_ϕ are given in Table 1:

$$\left(\rho v_w\phi+\Gamma_\phi\frac{\partial(\phi)}{\partial y}\right)\Bigg|_{y=0}=\rho v_w \quad (3)$$

$$\left(\rho v_w\phi+\Gamma_\phi\frac{\partial(\phi)}{\partial y}\right)_{y=0}=0 \quad (4)$$

The gas-phase length and velocity scales were used to write the solid-phase energy equation in dimensionless form:

$$-v_f\frac{\partial T_s}{\partial x}=\frac{\partial}{\partial x}\left\{\alpha_s\frac{\partial T_s}{\partial x}\right\}+\frac{\partial}{\partial y}\left\{\alpha_s\frac{\partial T_s}{\partial y}\right\} \quad (5)$$

The boundary conditions for this equation, including a surface

Nomenclature

$\hat{A}_s$ = pre-exponential factor for solid pyrolysis = 2.82×10^9 s^{-1}

$\hat{B}_g$ = frequency factor for the gas-phase reaction = 5.982×10^9 $m^3/kg\cdot s$

$\hat{C}_g$ = specific heat at constant pressure for the gas, kJ/kg·K (see Table 2)

$\hat{C}_s$ = specific heat of the solid fuel = 1.465 kJ/kg·K

Da_g = Damkohler number in the gas phase = $\hat{\rho}_r\hat{B}_g\hat{L}_r/\hat{V}_R$

E_g = dimensionless activation energy in the gas phase = $\hat{E}_g\overline{R}/\hat{T}_\infty$

$\hat{E}_g$ = gas-phase activation energy = 1.424×10^5kJ/kmol

$\hat{E}_s$ = solid-phase activation energy = 1.298×10^5kJ/kmol

$\hat{L}_r$ = reference thermal length = $\hat{\alpha}_r/(\hat{V}_g+\hat{V}_f)$, m

$\hat{L}_g$ = thermal length in the gas phase = $\hat{\alpha}_g/\hat{V}_g$ for small $\hat{V}_f$, in both x and y directions, m

$\hat{L}_{sx}$ = thermal length in the solid phase in the x direction = $\hat{\alpha}_s/\hat{V}_f$, m

L_v = dimensionless effective latent heat of evaporation = $\hat{L}_v/\hat{C}_s\hat{T}_\infty$

$\hat{L}_v$ = effective latent heat of evaporation = $\hat{L}_v^o+(\hat{C}_g-\hat{C}_s)(\hat{T}_s-\hat{T}_\infty$, kJ/kg

$\hat{L}_v^o$ = latent heat of evaporation for PMMA at 298 K, = 941 kJ/kg

$\dot{m}''$ = dimensionless mass = $\dot{\hat{m}}''/\hat{\rho}_s\hat{V}_r$

$\dot{\hat{m}}''$ = mass flux from fuel to the gas phase, $kg/m^2\cdot s$

$\hat{M}_f$ = molecular weight of PMMA = 100 kg/kmol

$\hat{M}_{ox}$ = molecular weight of oxygen = 32 kg/kmol

m_f = mass fraction of fuel in the gas phase

m_{ox} = mass fraction of oxygen in the gas phase

$m_{ox,\infty}$ = mass fraction of oxygen for ambient conditions

P = dimensionless pressure = $(\hat{P}-\hat{P}_\infty)/(\hat{\rho}_r\hat{V}2_r)$

$\hat{P}$ = pressure, N/m^2

Pr_r = reference Prandtl number for the gas = $\hat{\mu}_r\hat{C}_g/\hat{\lambda}_r$

$\hat{Q}_{gsc}$ = gas-phase to solid-phase heat conduction = $\hat{\lambda}_g(\hat{T}_f-\hat{T}_v)_g\hat{L}_g w/\hat{L}_g$, W

$\dot{\hat{q}}_{net}$ = net heat flux incoming to the fuel surface, W/m^2

$\dot{q}_{net}$ = dimensionless net heat flux to the fuel surface = $\dot{\hat{q}}_{net}/(\hat{\rho}_s\hat{C}_s\hat{T}_\infty\hat{V}_r)$

$\hat{Q}_{rad}$ = solid-phase surface radiative heat loss = $\hat{\sigma}\epsilon(\hat{T}_f^4-\hat{T}_v^4)\hat{L}_{sx}w$, W

$\overline{R}$ = universal gas constant = 8.314 kJ/kmol·K

S_c = conduction/convection parameter = $\hat{\lambda}_r/(\hat{\rho}_s\hat{L}_r\hat{V}_r\hat{C}_s)$

S_R = radiation/conduction parameter = $\epsilon\hat{\sigma}\hat{T}_\infty^3/(\hat{\rho}_s\hat{C}_s\hat{V}_r)$

S_ϕ = source term for property ϕ

s = stoichiometric ratio = $\hat{M}_{ox}\nu_{ox}/\hat{M}_f\nu f$ = 1.92

T = dimensionless gas temperature $\hat{T}/\hat{T}_\infty$

$\hat{T}$ = gas temperature, K

$\hat{T}_f$ = flame temperature used in scaling, K

$\hat{T}_r$ = reference temperature for the gas, K (see Table 2)

T_s = dimensionless solid temperature = $\hat{T}_s/\hat{T}_\infty$

$\hat{T}_s$ = solid temperature, K

$\hat{T}_v$ = pyrolysis temperature used in scaling = 700 K

$\hat{T}_\infty$ = ambient temperature = 298 K

u = dimensionless x velocity = $\hat{u}/\hat{V}_r$

radiative loss term, which is the only radiative effect considered in this model, are:

$$\text{at } x = x_{\max}: \quad T_s = 1$$

$$\text{at } x = 0: \quad \frac{\partial T_s}{\partial x} = 0$$

$$\text{at } y = y_{\min} < 0: \quad \frac{\partial T_s}{\partial y} = 0$$

$$\text{at } y = 0: \quad \dot{q}''_{\text{net}} = S_c \mu \left.\frac{\partial T}{\partial y}\right|_{y=0} - S_R\,(T_{s-1}^4) - \dot{m}'' L_v \quad (6)$$

The solid thickness and density are assumed to be constant, with the mass of the fuel evaporated considered to be negligible in comparison to the total amount of fuel available for pyrolysis. Clearly this assumption could lead to violation of mass conservation in the model. For the computations presented here the amount of fuel pyrolyzed was never more than the amount of fuel entering the computational domain. However, when the amount of fuel evaporated is on the order of the amount of fuel available, the neglect of the mass conservation equation in the solid may cause appreciable error in the energy equation as well. This situation occurred only when small fuel thicknesses were modeled, i.e., when the fuel half-thickness, $\hat{\tau}$, was equal to or less than about 0.05 cm. The neglect of solid-phase mass conservation also precluded taking into account any effect of fuel surface regression, which may become important at high opposing velocities (Altenkirch et al., 1982).

The expression for the pyrolysis mass flux of the solid fuel that is used in Eq. (6) was developed from a solution to the one-dimensional energy equation obtained by Lengelle (1970) in which the regression rate for the fuel surface was obtained from an asymptotic expansion for the solid temperature field for large activation energy of pyrolysis. The numerical values in Eq. (7) arise from an assumed residual density, $\hat{\rho}_s/\hat{\rho}_{s,\infty} = 0.01$, which allows the solution to be obtained:

$$\hat{\dot{m}}'' = \left\{\frac{\hat{\rho}\hat{T}_s^2 \hat{A}_s \hat{\lambda}_s \overline{R}}{\hat{E}_s[3.615\hat{L}_v^o + 4.605\hat{C}_s(\hat{T}_s - \hat{T}_\infty)]}\right\}^{1/2} \exp\left(\frac{-E_s}{2\overline{R}\hat{T}_s}\right) \quad (7)$$

In order to determine the two unknowns T_s and $\hat{V}_f$, another condition other than the solid surface energy balance and the boundary conditions on T_s is needed. This condition was provided by determining the flame spread rate $\hat{V}_f$ such that the flame leading edge is fixed at a certain x location near the front of the computational domain. This entailed increasing $\hat{V}_f$ if the flame started to progress ahead of this point to retard the progression and decreasing $\hat{V}_f$ if the flame started to fall behind this point. The flame leading edge was identified by a solid surface temperature of 1.2 $\hat{T}_\infty$, the eigen temperature. This choice of the eigen temperature only fixes the location of the flame in the computational domain; by changing this value, the location of the flame within the computational domain is shifted slightly, leaving all other aspects of the solution unchanged.

The heat of combustion and specific heat were defined as functions of the ambient oxygen concentration in order to approximate the effects of gas-phase chemical dissociation. The method was identical to that of West et al. (1992) and consists of determining the equilibrium product distribution and flame temperature for adiabatic, stoichiometric combustion of the solid fuel and defining the heat of combustion and constant, gas-phase specific heat to be consistent with this calculation.

The combustion process is modeled using a one-step, second-order Arrhenius reaction. The gas-phase kinetic properties, i.e., pre-exponential factor and activation energy, were selected from a range of values that appear in the literature for PMMA that also resulted in computations that matched low-oxygen, high forced convection experimental results (Fernandez-Pello

Nomenclature (cont.)

$\hat{u}$ = x velocity, m/s
$\hat{V}_f$ = absolute value of flame spread rate, m/s
$\hat{V}_g$ = absolute value of opposing gas velocity, m/s
$\hat{V}_r$ = reference velocity (= $\hat{V}_f$ in a quiescent environment), m/s
$\hat{V}_w$ = velocity at the fuel surface normal to the surface, m/s
v = dimensionless y velocity = $\hat{v}/\hat{V}_r$
$\hat{v}$ = y velocity, m/s
V_f = dimensionless spread rate = $\hat{V}_f/\hat{V}_r$
V_g = dimensionless opposing gas velocity = $\hat{V}_g/\hat{V}_r$
v_w = dimensionless velocity at the fuel surface normal to the surface = $\hat{V}_w/\hat{V}_r$
$\hat{w}$ = width of fuel sample; model is independent of this value, m
x = dimensionless coordinate parallel to fuel surface = $\hat{x}/\hat{L}_r$
$\hat{x}$ = coordinate parellel to the fuel surface, m
$x_{\min}$ = minimum x in computational domain, $x = 0$
$x_{\max}$ = maximum x in computational domain, $x = 28$
y = dimensionless coordinate normal to the fuel surface = $\hat{y}/\hat{L}_r$
$\hat{y}$ = coordinate normal to the fuel surface, m
$y_{\max}$ = maximum y in the computational domain, $y = 28$
$\hat{\alpha}_r$ = reference thermal diffusivity of the gas, m^2/s
$\hat{\alpha}_s$ = thermal diffusivity of the solid, m^2
α_s = dimensionless thermal diffusivity of the solid = $\hat{\alpha}_s/\hat{\alpha}_r$
Γ_ϕ = dimensionless viscosity = $\mathrm{Pr}_r\mu$ or μ
ΔH_c = dimensionless heat of combustion = $\Delta\hat{H}_c/\hat{C}_g\hat{T}_\infty$
$\Delta\hat{H}_c$ = heat of combustion of PMMA, kJ/kg (see Table 2)
ϵ = emittance of the fuel surface
$\hat{\lambda}_r$ = thermal conductivity of the gas, W/m·K (see Table 2)
μ = dimensionless dynamic viscosity = $\hat{\mu}/\hat{\mu}_r$
$\hat{\mu}_r$ = reference dynamic viscosity, kg/m·s (see Table 2)
ν_f = stoichiometric coefficient for fuel
ν_{ox} = stoichiometric coefficient for oxygen
ρ = dimensionless gas density = $\hat{\rho}/\hat{\rho}_r$
$\hat{\rho}_r$ = reference density for the gas, kg/m^3 (see Table 2)
ρ_s = dimensionless solid density = $\hat{\rho}_s/\hat{\rho}_{s,\infty}$
$\hat{\rho}_\infty$ = ambient gas density, kg/m^3
σ = Stefan–Boltzmann constant = 5.67×10^{-8} W/m^2·K^4
$\hat{\tau}$ = half-thickness of the fuel sheet, m
ϕ = any dimensionless dependent variable = $\hat{\phi}/\hat{\phi}_r$

Subscripts

f = fuel
g = gas
ox = oxygen
R = radiation
r = reference state
rad = radiation
s = solid
∞ = ambient

Superscripts

$\hat{}$ = dimensional quantity
$''$ = per unit area
$'$ = per unit length

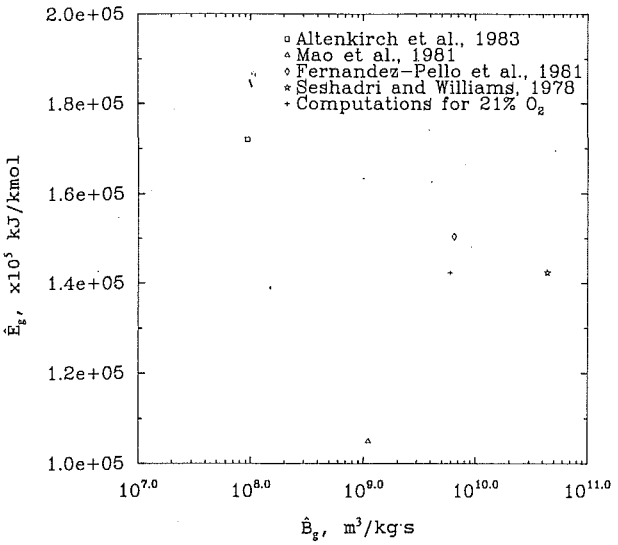

Fig. 1 Chemical kinetic properties used in modeling PMMA combustion. Also the property combination, indicated by the plus symbol, that reproduces the maximum experimental spread rate at 21 percent O_2 in N_2 and 1 atm pressure, neglecting radiation.

Table 2 Properties for the gas-phase calculations

Property	Pressure atm	Ambient O_2 21%	Ambient O_2 30%	Ambient O_2 50%
$\hat{T}_r$ (K)	any	1312	1565	1959
$\hat{\mu}_r$ (x10^5, kg/m·s)	any	4.812	5.567	6.629
$\hat{\lambda}_s$ (x10^2, W/m·K)	any	6.853	7.550	5.615
$\hat{C}_g$ (kJ/kg·K)	any	1.299	1.356	1.447
$\hat{\rho}_r$ (kg/m^3)	1.5	0.401	0.341	0.280
$\Delta\hat{H}_c$ (x10^{-3}, kJ/kg)	any	24.24	21.54	17.53

et al., 1981). The level of opposing velocity used to find the computational match to experiment was the one that produced the maximum experimental spread rate at 21 percent oxygen. This is illustrated in Fig. 1, a presentation of PMMA kinetic properties used by others along with a combination of kinetic properties that reproduces the maximum experimental spread rate at 21 percent oxygen by volume at 1 atm pressure when used in computations neglecting all radiative processes.

There are an infinite number of kinetic property combinations that reproduce the experimental results. Consequently, a combination that is both representative of values used by others for modeling PMMA combustion and which matches the activation energy from experimental results obtained by Seshadri and Williams (1979) was chosen. The values are $B_g = 5.92 \times 10^9$ m^3/kg·s and $\hat{E}_g = 1.424 \times 10^5$ kJ/kmol.

The gas-phase kinetic constants were chosen using data at 21 percent ambient oxygen concentration because no combination of constants could be found that allowed experimental spread rates to be matched at both 21 percent and the higher oxygen concentrations for the heats of combustion listed in Table 2. This difficulty can likely be traced to the fact that the spread rate for a thick fuel is sensitive to flame temperature, i.e., it depends approximately on the square of the difference between the flame and vaporization temperatures (de Ris, 1969). Accurate prediction of flame temperature is then needed over a range of oxygen concentrations in order to yield good agreement between measured and predicted spread rates over that range. While the adiabatic dissociation model used here to establish heats of combustion as a function of ambient oxygen concentration is more realistic than using a fixed heat of combustion, it does not take into account the fact that the extent of dissociation compared to the maximum for the adiabatic situation is variable because of radiative losses from the flame.

The environmental conditions for the base case are 50 percent O_2 in N_2 by mass at 1 atm pressure with an opposing velocity ranging from 1 to 80 cm/s and a fuel half-thickness of 5 cm. Unless otherwise stated, the results presented will neglect fuel surface radiative loss. Values for the gas-phase dynamic viscosity and thermal conductivity were taken from Touloukian (1970). Properties for PMMA were taken from Lengelle (1970) and are: $\hat{C}_s = 1.465$ kJ/kg·K, $\hat{L}_v^o = 941$ kJ/kg$_{fuel}$, $\hat{\rho}_s = 1190$ kg/m^3, $\hat{\lambda}_s = 0.209$ W/m·K, and $\hat{M}_f = 100$ kg/kmol.

The gas- and solid-phase equations are solved separately using a control volume algorithm (Patankar, 1980). The computational domain in the gas phase was 28 thermal lengths per side with a nonuniform 60×42 grid with the highest concentration of grid points near the leading edge of the flame. The computational domain in the solid phase was 28 gas-phase thermal lengths in the x direction with the required number of gas-phase length scales in the y direction to conform to the solid thickness being considered. The solid-phase grid size was 60×20 with the highest concentration of grid points near the fuel surface.

The computational domain was sized to insure that the flame was embedded in the boundary layer removed from the leading edge of the fuel sample where the boundary layer begins to grow. For flame spreading against a forced flow, the distance from the flame leading edge to the leading edge of the fuel plate determines the strength of the opposing flow in the boundary layer there. From a practical standpoint, the spread rate becomes relatively insensitive to this distance, although in principle it is always dependent on it. Computational experience shows that if the distance between the leading edge of the flame and the fuel bed is greater than about 8 $\hat{L}_r$ the spread rate is insensitive to this distance. As a result, for all computations presented here this distance is never less than 8 $\hat{L}_r$.

Results and Discussion

The results of the computations are shown in Figs. 2 and 3, in which the computed spread rates as a function of fuel half-thickness, $\hat{\tau}$, are shown for flows of $\hat{V}_g = 5$ cm/s and 15 cm/s, respectively. In both figures the flame spread rate for small $\hat{\tau}$ decreases with increasing fuel thickness and then reaches a thick limit where any additional thickness increase has no effect on the flame spread rate.

de Ris (1969), in his analytical solution for the flame spread rate over thermally thin fuels, found that the flame spread rate was inversely proportional to the fuel half-thickness, $\hat{\tau}$; for thick fuels, the flame spread rate is proportional to the opposing velocity, $\hat{V}_g$. Thus the predicted behavior of the computations and de Ris's analytical results agree in that in the thermally thin regime the flame spread rate is inversely proportional to the fuel thickness, while beyond a thick limit the flame spread rate is no longer dependent on the fuel thickness.

Comparison of the figures reveals that the value of the thick limit is influenced by the level of opposing flow. For a given fuel thickness, an increase in the opposing velocity causes the fuel to resemble more closely a thermally thick fuel. Likewise, reducing the level of opposing flow for a given fuel thickness causes the fuel to behave more like a thermally thin fuel.

The results of the computations for the flame spread rate as a function of forced opposing flow are shown in Fig. 4, where the flame spread rate, $\hat{V}_f$, is presented as a function of the opposing velocity, $\hat{V}_g$, with and without considering the effects of fuel surface radiation. The flame spread rate initially

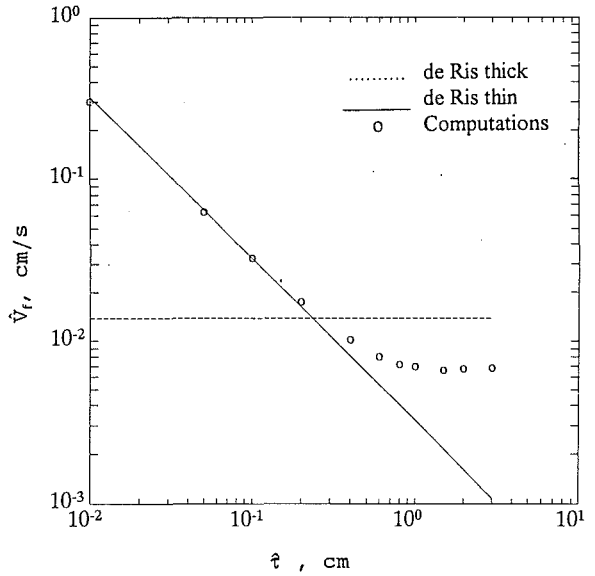

Fig. 2 Flame spread rate $\hat{V}_f$ as a function of fuel half-thickness, $\hat{\tau}$, for 50 percent O_2 in N_2 at 1 atm and opposing velocity, $\hat{V}_g$, of 5 cm/s neglecting fuel surface radiation

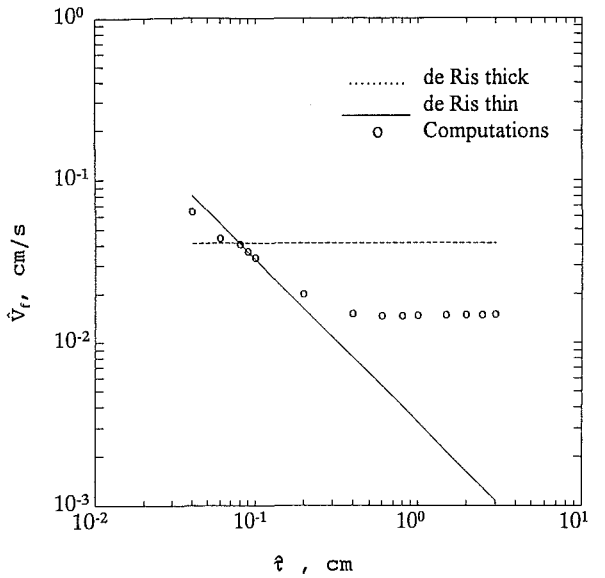

Fig. 3 Flame spread rate $\hat{V}_f$ as a function of fuel half-thickness, $\hat{\tau}$, for 50 percent O_2 in N_2 at 1 atm and opposing velocity, $\hat{V}_g$, of 15 cm/s neglecting fuel surface radiation

increases with increasing opposing flow velocity, reaches a maximum, and then decreases with increasing $\hat{V}_g$.

The initial increase of $\hat{V}_f$ is in the agreement with the de Ris result for thermally thick fuels, i.e., the flame spread rate is proportional to the opposing flow velocity. That the spread rate decreases after a limiting value of opposing flow is reached is due to the computational model's inclusion of finite-rate, gas-phase kinetics.

Figure 4 also shows that the effect of fuel surface radiation on the thermally thick flame spread rate is a net decrease in the spread rate. This net decrease does not go down with increasing opposing flow velocity as is predicted for thermally thin fuels (Altenkirch and Bhattacharjee, 1990; Bhattacharjee and Altenkirch, 1990; West et al., 1992).

Understanding of this difference may be obtained from scaling arguments similar to those of Alterkirch and Bhattacharjee (1990). There the relative importance between fuel surface radiative heat loss and gas-to-solid heat conduction for thin fuels was expressed as in Eq. (8), a ratio of heat loss from fuel

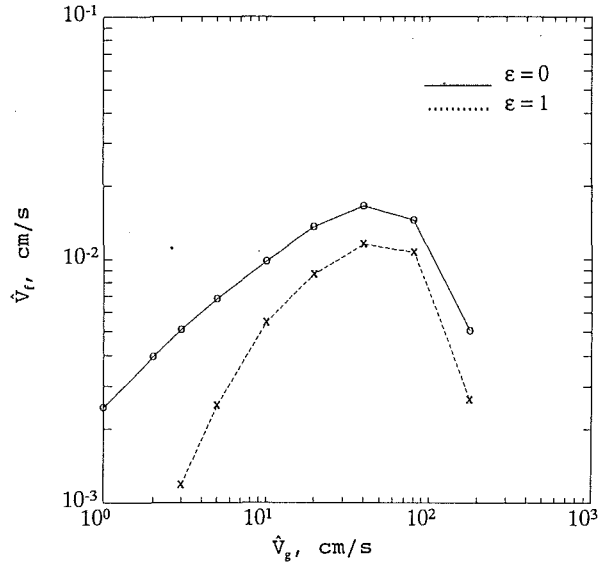

Fig. 4 Flame spread rate $\hat{V}_f$ as a function of opposing velocity, $\hat{V}_g$, for 50 percent O_2 in N_2 at 1 atm, fuel half-thickness, $\hat{\tau}$, of 5 cm with and without the effect of fuel surface radiation

surface radiation to the heat conducted from the flame to the fuel.

$$R_s = \frac{\hat{Q}_{\text{rad}}}{\hat{Q}_{gsc}} = \frac{\hat{\sigma}\epsilon(\hat{T}_v^4 - \hat{T}_\infty^4)\hat{L}_r}{\hat{\lambda}_g(\hat{T}_f - \hat{T}_v)} \tag{8}$$

For thermally thin fuels the only length scale of interest is the gas-phase length scale, $\hat{L}_g = \hat{\alpha}_g/\hat{V}_g$, therefore, $\hat{L}_r = \hat{L}_g$. Inserting this length into the above expression reveals that as the level of opposing velocity increases and $\hat{V}_f \ll \hat{V}_g$, the relative importance of fuel surface radiation decreases.

For fuels that are not thermally thin, conduction through the solid is an additional mechanism of heat transfer into the virgin fuel besides $\hat{Q}_{gsc}$. Nevertheless, the $\hat{Q}_{gsc}$ still plays a dominant role (Ito and Kashiwagi, 1986). The radiation number R_s, derived for thin fuels, should express the relative importance of surface radiation for non-thin fuels too. The only problem is to determine what is an appropriate $\hat{L}_r$ for the non-thin fuel.

For thermally thick fuels and low levels of opposing velocity, $\hat{V}_f$ is of the same order as $\hat{V}_g$ and $\hat{L}_g > \hat{L}_{sx}$ due to the density differences between the gas and solid fuel. Under these conditions the gas-phase scale is impressed upon the solid, and the problem scales with the gas phase as in the thermally thin case, $\hat{L}_r = \hat{L}_g$. Therefore, it is expected that R_s would be large enough that fuel surface radiation loss would result in an appreciable spread rate decrease.

For high levels of opposing velocity where $\hat{V}_f \ll \hat{V}_g$ and thus $\hat{L}_g < \hat{L}_{sx}$ (Altenkirch et al., 1983), the solid-phase length is dominant. This is also evident from Figs. 5 and 6, which compare the gas- and solid-phase temperature contours in the region of the flame anchor for base conditions, neglecting fuel surface radiation. The two situations shown correspond to opposing flow velocities, $\hat{V}_g$, of 5 and 80 cm/s, respectively. The flame anchor is identified as the location of maximum heat flux from the gas phase to the solid phase, $Q_{gsc,\max}$, and corresponds to $x = 0$ in the figure. In the case of Fig. 5 the greatest extent of heating in the front of the flame is accomplished in the gas phase while in Fig. 6 the greatest extent of heating ahead of the flame occurs in the solid phase.

Thus the transition of the scaling of the problem from the gas scale for small opposing velocity to the solid scale at large opposing velocity results in R_s being largely independent of opposing velocity. This nearly constant scaling for the thermally thick flame spread problem results in fuel surface ra-

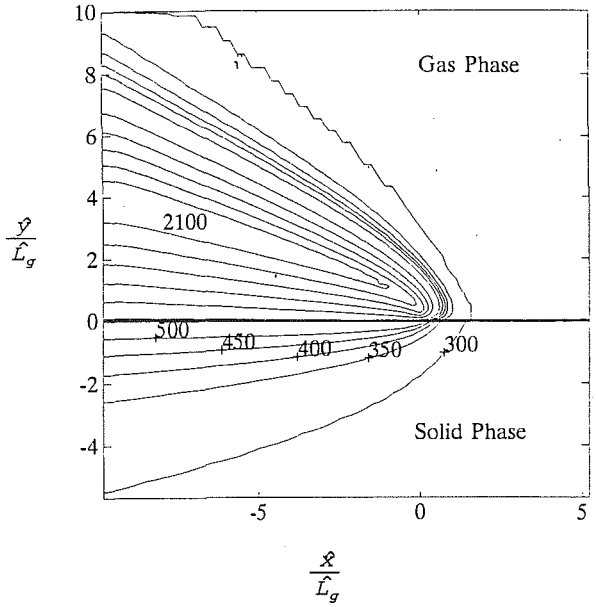

Fig. 5 Temperature contours, in K, for gas and solid phase showing greatest forward heat penetration occurring in the gas phase for an opposing flow velocity, $\hat{V}_g$, of 5 cm/s. Computation is for 50 percent O_2 in N_2 at 1 atm pressure and fuel half-thickness, $\hat{\tau}$, of 5 cm.

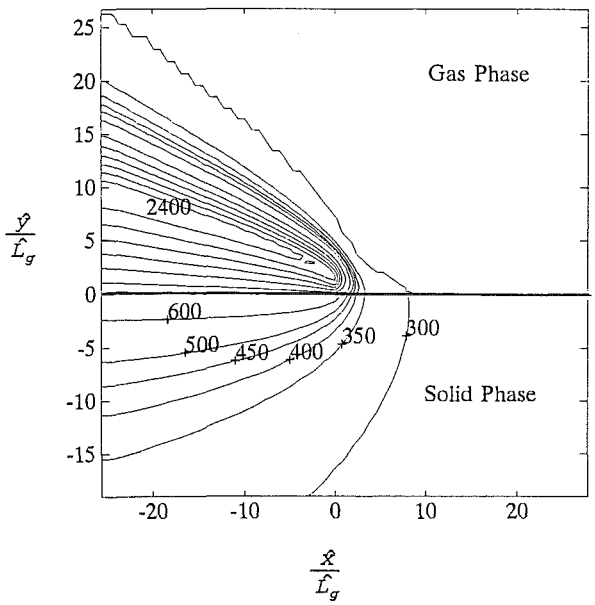

Fig. 6 Temperature contours, in K, for gas and solid phases showing greatest forward heat penetration occurring in the solid phase for an opposing flow velocity, $\hat{V}_g$, of 80 cm/s. Computation is for 50 percent O_2 in N_2 at 1 atm pressure and fuel half-thickness, $\hat{\tau}$, of 5 cm.

diation being important regardless of the level of opposing velocity.

Conclusions

In contrast to flame spread over thermally thin fuels, the effect of fuel surface radiation on the flame spread rate over thermally thick fuels is important regardless of level of opposing velocity. The effect of fuel surface radiation on the spread rate over thermally thin fuels has been found earlier to decrease with increasing opposing velocity. This difference can be explained by arguments that show that the x-direction length scale of the thermally thick problem is not markedly affected by the level of opposing velocity while the x-direction length scale of the thermally thin problem decreases with increasing opposing velocity.

Acknowledgments

Support for this work from NASA through Contracts No. NAS3-23901 and No. NCC3-221 is gratefully acknowledged. We also thank Prof. S. V. Patankar for providing to us an initial version of the gas-phase software.

References

Altenkirch, R. A., Eichhorn, R., and Shang, P. C., 1980, "Buoyancy Effects on Flame Spreading Down Thermally Thin Fuels," *Combust. Flame*, Vol. 37, pp. 71–83.

Altenkirch, R. A., Rezayat, M., Eichhorn, R., and Rizzo, F. J., 1982, "Boundary Integral Equation Method Calculations of Surface Regression Effects in Flame Spreading," ASME JOURNAL OF HEAT TRANSFER, Vol. 104, pp. 734–740.

Altenkirch, R. A., Eichhorn, R., and Rizvi, A. R., 1983, "Correlating Downward Flame Spread Rates for Thick Fuels," *Comb. Sci. Tech.*, Vol. 32, pp. 49–66.

Altenkirch, R. A., and Bhattacharjee, S., 1990, "Opposed-Flow Flame Spread With Implications for Combustion at Microgravity," *AIAA Prog. Aero. Astro.*, Vol. 130, pp. 723–740.

Bhattacharjee, S., and Altenkirch, R. A., 1990, "The Effect of Surface Radiation on Flame Spread in a Quiescent, Microgravity Environment," *Combust. Flame*, Vol. 84, pp. 160–169.

Bhattacharjee, S., Altenkirch, R. A., Srikantaiaih, N., and Vedha-Nayagam, M., 1990, "A Theoretical Description of Flame Spreading Over Solid Combustibles in a Quiescent Environment at Zero Gravity," *Comb. Sci. Tech.*, Vol. 69, pp. 1–15.

Bhattacharjee, S., and Altenkirch, R. A., 1991, "Radiation-Controlled, Opposed-Flow Flame Spread in a Microgravity Environment," *Twenty-Third Symposium (International) on Combustion*, The Combustion Institute, Pittsburgh, PA, pp. 1627–1633.

Bhattacharjee, S., Altenkirch, R. A., Olson, S., and Sotos, R. G., 1991, "Heat Transfer to a Thin Solid Combustible in Flame Spreading at Microgravity," ASME JOURNAL OF HEAT TRANSFER, Vol. 113, pp. 670–676.

de Ris, J. N., 1969, "Spread of a Laminar Diffusion Flame," *Twelfth Symposium (International) on Combustion*, The Combustion Institute, Pittsburgh, PA, pp. 241–252.

Di Blasi, C., Continillo, G., Crescitelli, S., and Russo, G., 1987, "Numerical Simulation of Opposed Flow Flame Spread Over a Thermally Thick Solid Fuel," *Combust. Sci. Tech.*, Vol. 54, pp. 25–36.

Di Blasi, C., Crescitelli, S., Russo, G., and Fernandez-Pello, A. C., 1988, "Prediction of the Dependence on the Opposed Flow Characteristics of the Flame Spread Rate Over Thick Solid Fuel," *Second International Symposium on Fire Safety Science*, Tokyo, Japan, June 13–17.

Fernandez-Pello, A. C., Ray, S. R., and Glassman, I., 1981, "Flame Spread in an Opposed Forced Flow: The Effect of Ambient Oxygen Concentration," *Eighteenth Symposium (International) on Combustion*, The Combustion Institute, Pittsburgh, PA, pp. 579–589.

Frey, A. E., and T'ien, J. S., 1979, "A Theory of Flame Spread Over a Solid Fuel Including Finite Rate Chemical Kinetics," *Combust. Flame*, Vol. 36, pp. 263–289.

Ito, A., and Kashiwagi, T., 1986, "Temperature Measurements in PMMA During Downward Flame Spread in Air Using Holographic Interferometry," *Twenty-First Symposium (International) on Combustion*, The Combustion Institute, Pittsburgh, PA, pp. 65–74.

Lengelle, G., 1970, "Thermal Degradation of Polymers," *AIAA Journal*, Vol. 8, pp. 1989–1996.

Mao, C. P., Kodoma, H., and Fernandez-Pello, A. C., 1984, "Convective Structure of a Diffusion Flame Over a Flat Combustible Surface," *Combust. Flame*, Vol. 57, pp. 209–236.

Olson, S. L., Ferkul, P. V., and T'ien, J. S., 1989, "Near Limit Flame Spread Over a Thin Solid Fuel in Microgravity," *Twenty-Second Symposium (International) on Combustion*, The Combustion Institute, Pittsburgh, PA, pp. 1213–1222.

Patankar, S. V., 1980, *Numerical Heat Transfer and Fluid Flow*, McGraw-Hill, New York.

Seshadri, K., and Williams, F. A., 1978, "Structure and Extinction of Counterflow Diffusion Flame Above Condensed Fuels: Comparison Between PMMA and Its Liquid Monomer, Both Burning in Nitrogen–Air Mixtures," *Journal of Polymer Science—Polymer Chemistry Edition*, Vol. 16, pp. 1755–1778.

Touloukian, Y. S., 1970, "Thermophysical Properties of Matter, The TPRC Data Series, IFI/Plenum.

West, J. S., Bhattacharjee, S., and Altenkirch, R. A., 1992, "A Comparison of the Roles Played by Natural and Forced Convection in Opposed-Flow Flame Spreading," *Combust. Sci. Tech.*, Vol. 83, pp. 233–244.

Radiation Heat Transfer in Fluidized Beds: A Comparison of Exact and Simplified Approaches

G. Flamant

J. D. Lu[1]

B. Variot

Institut de Science et de Génie
des Matériaux et Procédés,
C.N.R.S.,
B.P. No. 5,
Odeillo—66125—Font-Romeu Cedex, France

Radiation heat transfer at heat exchanger walls in fluidized beds has never been examined through a complete formulation of the problem. In this paper a wall-to-bed heat transfer model is proposed to account for particle convection, gas convection, and radiation exchange in a variable porosity medium. Momentum, energy, and intensity equations are solved in order to determine the velocity, temperature, radiative heat flux profiles and heat transfer coefficients. The discrete-ordinates method is used to compute the radiative intensity equation and the radiative flux divergence in the energy equation. Both the gray and the non-gray assumptions are considered, as well as dependent and independent scattering. The exact solution obtained is compared with several simplified approaches. Large differences are shown for small particles at high temperature but the simplified solutions are valid for large particle beds. The dependency of radiative contribution on controlling parameters is discussed.

Introduction

It has been well accepted that radiation plays an increasingly important role in fluidized bed heat transfer when temperature rises. Since particle convection, gas convection, and radiative transport occur simultaneously and in parallel, the heat transfer in high-temperature fluidized beds is more difficult to describe and quantitative knowledge about it is more empirical than that at ambient conditions.

On one hand a detailed review is given by Saxena et al. (1989) on the experimental techniques for the measurement of radiative and total heat transfer in high-temperature gas-solid fluidized beds. On the other hand, several theoretical models have been developed for the analysis of this heat transfer mode:

1 Szekely and Fisher (1969), Mahbod and Tabesh (1985), and Flitris et al. (1988) used the concept of unsteady state heat conduction through a single spherical particle adjacent to the wall, just as proposed by Botterill and Williams (1963), and included the radiative transport and gas convection for large particle situation ($d_p \geq 2$ mm). The alternate slab model of Kolar et al. (1979) can be linked with this group of authors who describe the particulate as a succession of wall composed either of particles or solid slab separated by gas.

2 Vedamurthy and Sastri (1974) considered that conductive and radiative heat transfer took place between the wall and the emulsion layer through a gas film. Yoshida et al. (1974), Flamant and Arnaud (1984), and Glicksman and Decker (1985) considered the emulsion phase heat transfer on the basis of the particle packet model (Mickley and Fairbanks, 1955) and used the effective thermal diffusion coefficient as the sum of conductive and radiative components. Chen and Chen (1981) proposed the two-flux model to describe the radiative flux transferred in the emulsion phase. Then two formulae for calculating the effective absorptivity and emissivity of emulsion phase were presented by Brewster (1986) with the two-flux method based on a steady-state nonisothermal layer near the wall. The two unknowns—the average particle temperature at the wall and the nonisothermal layer thickness—were offered by Flamant and Bergeron (1988) for three particle size regimes.

It can be found that most of the previous models were used for small particle beds and thus considered only simultaneous transport of the conductive and radiative fluxes. A gas film between the heat transfer wall and emulsion phase was introduced but its thickness was varied.

As a conclusion, two main approaches have been developed previously: the discrete models in which are classified the studies of group (1), and the continuous models related with group (2). In order to propose a general formulation taking into account the variation of particle convection and gas convection with particle diameter and temperature, we have chosen the latter approach, because it is more convenient for modeling the change of nonisothermal zone near the wall with solid diameter. This choice can be discussed for large particles because only one diameter depth is concerned with the temperature variation, but our measurements indicate that it is realistic even in this case (Flamant et al., 1993).

In the field of packed beds, there were some theoretical researches on the combined radiation and convection in particulate tube flow (e.g., Tabanfar and Modest, 1987) and porous media (e.g., Yoshida et al., 1990), but a detailed survey is lacking for the fluidized bed where the two-dimensional transient combined heat transfer happens in a thin layer near the walls. In order to make a systematic observation about the effect of radiation in high-temperature fluidized beds, the discrete-ordinates radiation model is combined with the pseudo-homogeneous model for particle convection and gas convection in this paper. The exact solution is used to check several simplified approaches. At the same time, the qualitative trend of the dependency of radiation on governing parameters is also discussed.

Mathematical Description

In high-temperature gas-solid fluidized beds heat is exchanged between heat transfer walls and the bed by particle convection, gas convection, and radiation when the wall contacts the emulsion phase and by gas convection and radiation when contacting with bubbles. The overall heat transfer coefficient can be written as

$$h_w = (1 - f_b)(h_{ep} + h_{eg} + h_{er}) + f_b(h_{bg} + h_{br}) \quad (1)$$

where h_{ep}, h_{eg}, and h_{er} are the contributions of the emulsion due to particle convection, gas convection, and radiation, respectively, and h_{bg} and h_{br} are the gas convection and radiation

[1] Present address: N.K.C.C.L., Dept. of Power Engineering, Huazhong Univ. of Science and Technology, Wuhan, 430074 Hubei, People's Republic of China.

Contributed by the Heat Transfer Division and presented at the National Heat Transfer Conference, San Diego, California, August 9-12, 1992. Manuscript received by the Heat Transfer Division November 1992; revision received August 1993. Keywords: Packed and Fluidized Beds, Radiation Interactions, Transient and Unsteady Heat Transfer. Associate Technical Editor: R. O. Buckius.

components of the bubble phase. All these contributions vary with particle diameter and bed temperature; the main objective of this paper is to propose a general approach for the prediction of the effect of these parameters on the bed-to-wall heat transfer coefficient.

For the period of the wall contacting the bubbles, Flamant and Menigault (1988) have described the general situation of absorbing gases including particulate. Therefore only the period of wall contacting the emulsion packets is considered here.

The heat exchanging element considered is a vertical wall with length L and a constant temperature T_w (as shown in Fig. 1). When a packet of emulsion phase with the bed bulk temperature T_B contacts the wall, a transient heat transfer process happens, which can be described by a set of volume-averaged boundary layer equations:

Momentum equation

$$\frac{\partial}{\partial y}\langle p\rangle^g - \frac{\mu_g}{\delta}\frac{\partial^2\langle v_y\rangle}{\partial x^2} + \frac{\mu_g\langle v_y\rangle}{K} + \rho_g C\langle v_y\rangle^2 \qquad (2)$$

Energy equation for the gas phase

$$\frac{\partial}{\partial t}[(\delta-\delta_{st})(\rho C_p)_g\langle T_g\rangle^g] + (\rho C_p)_g\langle v_y\rangle\frac{\partial}{\partial y}\langle T_g\rangle^g = \frac{\partial}{\partial x}\left[\lambda_{ge}\frac{\partial}{\partial x}\langle T_g\rangle^g\right] + h_{gp}S(\langle T_p\rangle^p - \langle T_g\rangle^g) \qquad (3)$$

Energy equation for the particle phase

$$\frac{\partial}{\partial t}[\delta_{st}(\rho C_p)_g + (1-\delta)(\rho C_p)_p]\langle T_p\rangle^p = \frac{\partial}{\partial x}\left[\lambda_{pe}\frac{\partial}{\partial x}\langle T_p\rangle^p\right] - \frac{\partial}{\partial x}\langle q_r\rangle - h_{gp}S[\langle T_p\rangle^p - \langle T_g\rangle^g] \qquad (4)$$

The bases of these equations are detailed by Lu et al. (1993); a summary of the discussion is presented in the following.

The heterogeneous fluid flow and heat transfer theory in porous media and the concept of variable property boundary layer are applied here, and the "local volume average technique" (Whitaker, 1969) is used, which averages the microscopic conservation equations over a representative volume including both the fluid and solid phases. The volume-averaged

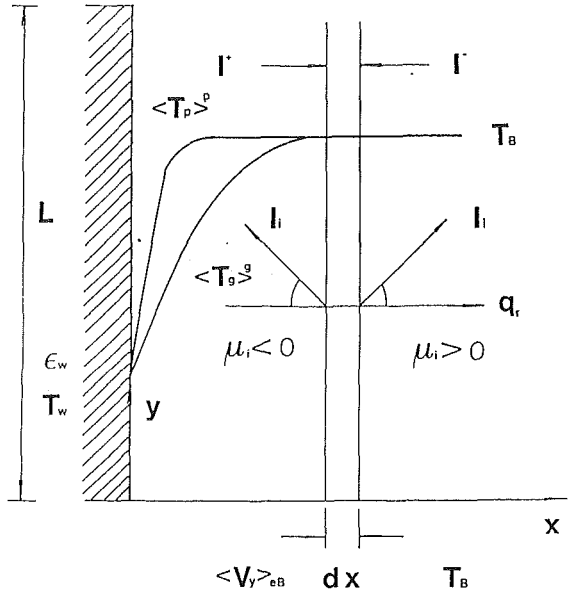

Fig. 1 Coordinates and boundary conditions for the vertical wall

quantity of a quantity associated with one phase W is defined as:

$$\langle W\rangle = \frac{1}{V}\int_{V_i} W dV = \frac{V_i}{V}\cdot\frac{1}{V_i}\int_{V_i} W dV = \delta\langle W\rangle^i \quad \text{for} \quad i=g$$

$$= (1-\delta)\langle W\rangle^i \quad \text{for} \quad i=p \qquad (5)$$

where V_i is that portion of a representative volume V, $\delta = V_g/V$ is the porosity and $\langle W\rangle^i$ is the intrinsic phase average of W. The volume-averaging procedure operating for the gas-phase momentum Eq. (2) gives the last two terms of Eq. (2), which represent the total drag force per unit volume due to the presence of particles. These equations are similar to those presented by Vafai and Sozen (1990), except for two terms: a divergence term of radiative flux, which is added in Eq. (4) to account for the radiative transfer at high temperature, and a contribution due to the stagnant part of the fluid included in

Nomenclature

a = absorption coefficient, m^{-1}
B = back-scatter fraction
C = in Eq. (2), $C = 1.75\,(1-\delta)/\Phi\, d_p\,\delta^3$
C_p = specific thermal capacity, J/(kg·K)
d = diameter, m
f_b = fraction of bubble phase
h = heat transfer coefficient, $W/(m^2K)$
I = radiation intensity or flux in two-flux method
K = in Eq. (2), $K = \Phi^2\,\delta^3\,d_p^2/[150/(1-\delta^2)]$
L = length, m
n = parameter in the Brewster model (1986) used for the estimation of the solid temperature at the wall (Appendix A)
P = particle scattering function
p = pressure, Pa
q = heat flux, W/m^2
S_r = scaling factor for the optical thickness in order to account for dependent scattering
T = temperature, K
t = time, s
t_c = contact time between wall and emulsion, s
U = superficial fluidizing velocity, m/s
V = volume m^3
v = velocity, m/s
w = weight in discrete-ordinates method
x = lateral coordinate (distance from the wall), m
y = axial coordinate of the fluidized bed, m
δ = porosity
Δ_e = depth of the nonisothermal layer at the wall in the Brewster model (1986)
ϵ = emissivity
Θ = angle between directions of propagation and observation
θ = polar angle
λ = thermal conductivity, W/(m·K)
μ = $\cos\theta$
μ_g = dynamic viscosity of gas, kg/(m·s)
ρ = density, kg/m^3
σ = Stefan-Boltzmann constant, $W/(m^2K^4)$
σ_s = scattering coefficient, m^{-1}
Φ = sphericity
φ = azimuthal angle
ω = solid angle

Subscripts and Superscripts

B = bulk of fluidized bed
b = bubble phase
e = emulsion phase
g = gas phase
i = instantaneous value
mf = minimum fluidization
p = particle phase
r = radiative transfer
st = stagnant part of gas phase
w = heat transfer wall
x = distance from the wall
y = axial direction of the fluidized bed

Eq. (4). The gas phase is divided into two parts (the flowing part and the stagnant part) to account for the fact that only a part of the gas is effective for mixing and the other part is composed of the relatively stagnant fluid fillets surrounding the contact points between adjacent particles (Dixon and Gresswell, 1979). The details of deducing these equations were given in a paper of Lu et al. (1993). The divergence of the radiative flux is introduced to account for the radiant transfer when the temperature arises. Here an assumption has been made that the gradient of radiative heat flux with respect to the x coordinate is much larger than the gradient with respect to the y coordinate ($\partial\langle q_r\rangle/\partial x \gg \partial\langle q_r\rangle/\partial y$) since the following relation exists between the second derivatives of the particle temperature: $\partial^2\langle T_p\rangle^p/\partial x^2 \gg \partial^2\langle T_p\rangle^p/\partial y^2$ in the nonisothermal region of the emulsion packet near the wall.

The initial and boundary conditions for Eqs. (2)–(4) are:

$$t=0, \quad \langle T_g\rangle^g = \langle T_p\rangle^p = T_B \tag{6}$$

$$x=0, \quad \langle T_g\rangle^g = \langle T_p\rangle^p = T_w \tag{7}$$

$$\langle v_y\rangle = 0 \tag{8}$$

$$x\to\infty, \quad \langle T_g\rangle^g = \langle T_p\rangle^p = T_B \tag{9}$$

$$\langle v_y\rangle = \langle v_y\rangle_{eB} \tag{10}$$

In some of the previous investigations (Yoshida et al., 1974; Flamant and Arnaud, 1984; Glicksman and Decker, 1985) the divergence of the radiative flux was approximated by assuming the radiative transfer to be a diffusion process with a radiative thermal diffusion coefficient. But this diffusion approximation is only valid in the case of optically thick media and is unapplicable in the region near the heat transfer wall, so a gas film or a slip temperature boundary condition should be introduced in those models. Since the nonslip temperature boundary conditions are used for both gas and particle phase in the present model, the radiative flux should be obtained from the solution of the equation of radiation transfer.

The main formulations of the problem are presented in the following:

Exact Formulation. The transfer equation for symmetric monochromatic radiation in a one-dimensional case can be given by (Chandrasekhar, 1960):

$$\mu\frac{\partial\langle I_\lambda(x,\mu)\rangle}{\partial x} = -(\sigma_{s\lambda}+a_\lambda)\langle I_\lambda(x,\mu)\rangle + a_\lambda\langle I_{b\lambda}\rangle + \frac{\sigma_{s\lambda}}{2}\int_{-1}^{1}\langle I_\lambda(x,\mu)\rangle P(\mu,\mu')d\mu' \tag{11}$$

where μ is the directional cosine with respect to coordinate x ($\mu=\cos\theta$) and P is the scattering phase function.

The radiative heat flux, which is in the x direction, can be determined by

$$\langle q_r\rangle = \int_0^\infty\int_{4\pi}\langle I_\lambda(x,\mu)\rangle\mu d\omega d\lambda \tag{12}$$

Integrating Eq. (11) over all angles yields the following equation for the divergence of the radiation flux:

$$\frac{\partial}{\partial x}\langle q_r\rangle = 4\pi\int_0^\infty a_\lambda\langle I_{b\lambda}\rangle d\lambda - a\int_0^\infty 4\pi\langle I_\lambda(x,\mu)\rangle d\omega d\lambda \tag{13}$$

The monochromatic absorption coefficient a_λ, scattering coefficient $\sigma_{s\lambda}$, and scattering phase function P in Eq. (11) should be determined in order to predict the radiation flux. For low-porosity systems like packed or fluidized beds, whether the scattering is dependent or independent is a controversial scientific subject. Brewster and Tien (1982) concluded that the independent scattering assumption is valid in packed beds and fluidized beds of large particles even for a closed-packed arrangement. They proposed the limit of $c/\lambda=0.3$ (i.e., $\delta>0.3$), where c is the average interparticle distance and λ the wavelength of radiation. Therefore, the scattering and absorption coefficients can be expressed as (Siegel and Howell, 1972):

$$\sigma_{s\lambda} = 1.5(1-\epsilon_{\lambda p})(1-\delta_e)/d_p \tag{14}$$

$$a_\lambda = 1.5\epsilon_{\lambda p}(1-\delta_e)/d_p \tag{15}$$

where the local porosity δ_e is used to account for the increase of the porosity near the wall. The phase function P is related to single-particle scattering function,

$$P(\mu,\mu') = \frac{1}{\pi}\int_0^\pi P[\Theta(\mu',\varphi'=0\to\mu,\varphi)]d\varphi \tag{16}$$

where

$$\cos\Theta = \mu\mu' + (1-\mu^2)^{1/2}(1-\mu'^2)^{1/2}\cos\varphi \tag{17}$$

and

$$P(\Theta) = \frac{8}{3\pi}(\sin\Theta - \Theta\cos\Theta) \tag{18}$$

for large, diffusely reflecting, spherical particles.

On the contrary, Singh and Kaviany's (1991) recent investigation based on a Monte-Carlo simulation of the radiation showed that the deviation from the independent theory may be significant even for high-porosity particulate ($\delta_e=0.935$) and increases with a decrease in porosity. They also showed (Singh and Kaviany, 1992), that the dependent properties for a bed of opaque spheres can be obtained from their independent properties by scaling the optical thickness while leaving the albedo and the phase function unchanged, and the scaling factor was presented in the following form:

$$S_r = 1.0 + 1.84(1-\delta_e) - 3.15(1-\delta_e)^2 + 7.20(1-\delta_e)^3 \quad \text{for} \quad \delta_e > 0.3 \tag{19}$$

In this paper, the calculation is mainly with the independent scattering theory, but the effect of dependent scattering is also checked.

Two kinds of assumptions on radiative properties of particle surfaces are applied: one is the grey body assumption and the other is the nongray assumption. For the latter, a band model is used, i.e., the radiation properties are assumed to be constant in each band. The emissivities of sand for the grey and the nongray assumptions are shown in Appendix B. A two-band model is used because a step change of ϵ_p was reported at about $\lambda=3.5$ μm (Touloukian and Dewitt, 1972).

When Eq. (13) is inserted into Eq. (4), Eqs. (2)–(4) and (11) form the governing differential-integral equations for heat transfer of emulsion phase with walls, which were not easily solved in the general situation. The discrete-ordinates method is used in this paper to approximate the equations in differential forms, which is based on the division of the azimuthally symmetric radiation flux into N discrete conical streams, $I(x,\mu_i)$, $i=1$ to N (Chandrasekhar, 1960). Therefore Eqs. (11) and (13) are replaced by a discrete set of equations for a finite number of ordinate directions and for spectral band (index k),

$$\mu_i\frac{\partial\langle I_k(x,\mu_i)\rangle}{\partial x} = -(\sigma_{sk}+a_k)\langle I_k(x,\mu_i)\rangle + a_k\langle I_{bk}\rangle + \frac{\sigma_{sk}}{2}\sum_{j=1}^{N} w_j\langle I_k(x,\mu_j)\rangle P(\mu_i,\mu_j) \tag{16}$$

$$\frac{\partial}{\partial x}\langle q_r\rangle = 4\pi\sum_{k=1}^{M} a_k\langle I_{bk}\rangle - 2\pi\sum_{k=1}^{M} a_k\sum_{j=1}^{N}\langle I_k(x,\mu_j)\rangle w_j \tag{17}$$

where integrals are replaced by quadratures summed over each ordinate; $M=1$ for grey body assumption and $M=2$ for two-band assumption. The divisions μ_i correspond to the zeroes of the Legendre polynomials $L_N(\mu)$ and the weights w_j are given by

$$w_j = \frac{1}{L_N'(\mu_j)}\int_{-1}^{1}\frac{L_N(\mu)}{\mu-\mu_j}d\mu \tag{18}$$

Calculation has been made for $N=10$ but ordinate numbers between 10 and 20 were compared. The use of large N does not increase the accuracy of the results significantly. Some differences have been observed only for very small temperature difference between the bed and the wall ($|T_w - T_g| < 50$ K).

The boundary conditions for Eq. (17) are:

$$x=0, \quad \langle I_{ki}\rangle = \epsilon_w \sigma T_w^4/\pi + 2(1-\epsilon_w)\sum_{j=1}^{N/2}\langle I_{kj}\rangle w_j|\mu_j| \quad (i=N/2+1, N) \tag{19}$$

$$\langle I_k(x, \mu_i)\rangle = \langle I_k(x, \mu_{N/2+i})\rangle \quad (i=1, N/2) \tag{20}$$

The instantaneous local radiant heat transfer coefficient is defined as

$$h_{er'i'y} = \left\{\epsilon_w \sigma T_w^4 - 2\pi\epsilon_w \sum_{k=1}^{M}\sum_{j=1}^{N/2}\langle I_{kj}\rangle w_j|\mu_j|\right\}\Big/(T_w - T_B) \tag{21}$$

Two-Flux Formulation. When the solid angles about a location are divided into just two directions, one for each hemisphere, this is the well-known two-flux method. So Eqs. (11) and (13) can be replaced by

$$\frac{1}{2}\frac{d\langle I_k^+\rangle}{dx} = -(a_k + B\sigma_{sk})\langle I_k^+\rangle + B\sigma_{sk}\langle I_k^-\rangle + \pi a_k \sigma\langle I_{bk}\rangle \tag{22}$$

$$\frac{1}{2}\frac{d\langle I_k^-\rangle}{dx} = (a_k + B\sigma_{sk})\langle I_k^-\rangle - B\sigma_{sk}\langle I_k^+\rangle - \pi a_k \sigma\langle I_{bk}\rangle \tag{23}$$

$$\frac{\partial}{\partial x}\langle q_r\rangle = \sum_{k=1}^{M}\frac{\partial}{\partial x}(\langle I_k^+\rangle - \langle I_k^-\rangle) = 4\pi\sum_{k=1}^{M} a_k\sigma\langle I_{bk}\rangle - 2\pi\sum_{k=1}^{M} a_k(\langle I_k^+\rangle + \langle I_k^-\rangle) \tag{24}$$

where the superscripts + and − refer to the forward ($\mu>0$) and backward ($\mu<0$) directions, respectively. B is the backscatter fraction defined as (Brewster and Tien, 1982),

$$B = \frac{1}{2}\int_0^1\int_{-1}^0 P(\mu, \mu')d\mu' d\mu \tag{25}$$

For large opague spheres used in a fluidized bed B is equal to 0.5 for specularly reflecting ones and 0.667 for diffusely reflecting cases (Brewster and Tien, 1982).

For the two-flux radiation Eqs. (22) and (23) the boundary conditions are

$$x=0, \quad \langle I_k^+\rangle = \epsilon_w\sigma T_w^4 + (1-\epsilon_w)\langle I_k^-\rangle \tag{26}$$

$$x\to\infty, \quad \langle I_k^-\rangle = \langle I_k^+\rangle \tag{27}$$

The instantaneous local radiant heat transfer coefficient is determined by

$$h_{er'i'y} = \sum_{k=1}^{M}(\langle I_k^+\rangle - \langle I_k^-\rangle)|_{x=0}(T_w - T_B)^{-1} \tag{28}$$

The averaged values over the resident time and length of heat transfer wall can be obtained by

$$h_{er} = \int_0^L\int_0^{t_c} h_{er'i'y}dtdy/(Lt_c) \tag{29}$$

Brewster's Formulation. Based on the theory of independent scattering, Brewster (1986) also used two-flux method and presented two formulae for the effective absorptivity and emissivity of emulsion phase with an assumption of a steady-state exponential particle temperature profile near the wall. The effective absorptivity of emulsion phase is calculated by

$$\alpha_{ke} = \left[\frac{\epsilon_{kp}}{B(1-\epsilon_{kp})}\left[\frac{\epsilon_{kp}}{B(1-\epsilon_{kp})}+2\right]\right]^{1/2} - \frac{\epsilon_{kp}}{B(1-\epsilon_{kp})} \tag{30}$$

and the formula for the effective emissivity is,

$$\epsilon_{ke} = \frac{\epsilon_{kp}}{B(1-\epsilon_{kp})}\left\{\sum_{j=0}^{4} C_j^4(\Theta-1)^j \times\left[\frac{E[1+2B(1-\epsilon_{kp})/\epsilon_{kp}]^{1/2}+j}{E+j}\right] - \Theta^4\right\} \tag{31}$$

where $E = 3(1-\delta_{eB})\{\epsilon_{kp}[2B(1-\epsilon_{kp})+\epsilon_{kp}]\}^{1/2}(\Delta_e/d_p)$ and $\Theta = T_o/T_B = 1+[(T_w/T_B-1)/n]$. The parameters Δ_e/d_p and n were estimated by Flamant and Bergeron (1988) for three particle size regions, on the basis of literature data, Vedamurthy and Sastri (1974), Decker and Glicksman (1981), Flamant and Arnaud (1984); as shown in Appendix A, the nonisothermal depth Δ_e in the emulsion is assumed to be three, one, and half particle diameter for small, medium, and large solid diameter, respectively.

The radiative heat transfer coefficient is estimated by:

$$h_{er} = \sum_{k=1}^{M}\frac{\sigma(\alpha_{ke}T_w^4 - \epsilon_{ke}T_B^4)}{\left[1+\alpha_{ke}\left[\frac{1}{\epsilon_w}-1\right]\right](T_w - T_B)} \tag{32}$$

Isothermal Approximation. The more simplified models were to consider the emulsion packet to be isothermal and just used a simple formula for the effective emissivity of emulsion phase (Borodulya et al., 1983; Flamant, 1985; Brewster, 1986). In this case, the effective emissivity of emulsion packet is equal to its effective absorptivity; thus Eq. (32) is reduced to,

$$h_{er} = \sum_{k1}^{M}\frac{\sigma(T_w^4 - T_B^4)}{\left[\frac{1}{\epsilon_{ke}}+\frac{1}{\epsilon_w}-1\right](T_w - T_B)} \tag{33}$$

Equation (31) is used in this paper to calculate the effective emissivity ϵ_e.

Results and Discussion

The model described above can be used to predict particle convective, gas convective, radiative, total emulsion phase, and overall average heat transfer coefficients for a wide range of parameters, but the main attention in this paper is paid to the calculation of radiative heat exchange rate. Since the thermal properties of material, especially for gas phase, are affected by temperature, the coefficients in the governing equations are two-dimensional functions due to the change of temperature and porosity, which should be determined by the local transient temperature. The fluidizing fluid and bed material used in the prediction are air and silica sand, whose thermal properties are given in Appendix B. Concerning the void fraction distribution, the effect of various distribution profile on velocity field and heat transfer was examined by Lu et al. (1993). Finally the analytical function proposed by Kubie and Broughton (1975) selected in this paper is:

$$\delta_e = 1-3(1-\delta_{eB})[x/d_p - 2(x/d_p)^2/3] \quad \text{for} \quad x/d_p < 1$$
$$\delta_e = \delta_{eB} \quad \text{for} \quad x/d_p \geq 1 \tag{34}$$

Numerical Solution. The governing equations for the problem considered are coupled and nonlinear, making analytical solution impossible. For this case, a numerical technique, namely the finite difference method, is required to solve the problem. In order to make the choice of Δx, Δy, and Δt independently, an implicit scheme is used. The variable grid sizes are used in the computation, with a finer grid used near the heat transfer wall and leading edge region to account for the steep velocity and temperature gradients. Backward differencing of first order is developed in the temporal derivative terms, whereas central differencing is used for the spatial derivatives, except for the convective terms for which upwind differencing is employed, along with the linearization of inertial term in the momentum equation and the source term in the energy equation for particle phase. For the radiation flux

Table 1 Comparison of emulsion phase radiative heat transfer coefficients with different theoretical approaches: $\epsilon_p = 0.6$, $\epsilon_w = 0.8$, $B = 0.667$, $\delta_{eB} = 0.45$, $M_{d\text{-}o}$: discrete ordinate, $M_{2\text{-}f}$: two-flux, M_B: Brewster's approximation, M_{iso}: isothermal approximation

	d_p (mm)	0.1		1.0		4.0	
	t(s)	0.1	1.0	0.1	1.0	0.1	1.0
T_B =1173K, T_w =373K	M_{d-o}	49.17	17.48	89.91	73.61	93.17	88.16
	M_{2-f}	45.36	15.17	88.16	70.69	91.59	86.24
	M_B	19.72		70.70		85.30	
	M_{iso}	92.40		92.40		92.40	
T_B =373K, T_w =1173K	M_{d-o}	82.09	53.61	92.65	90.54	93.00	92.69
	M_{2-f}	80.69	51.47	91.18	89.73	92.34	92.01
	M_B	78.22		91.26		92.13	
	M_{iso}	92.40		92.40		92.40	
T_B =1173K, T_w =1073K	M_{d-o}	151.9	76.71	226.0	198.5	231.3	224.2
	M_{2-f}	138.8	65.43	217.1	187.4	222.7	215.0
	M_B	113.0		198.8		216.6	
	M_{iso}	223.9		223.9		223.9	
T_B =1073K, T_w =1173K	M_{d-o}	149.0	76.02	215.4	191.8	219.8	214.1
	M_{2-f}	149.0	73.02	218.6	193.7	223.5	217.4
	M_B	127.8		204.9		218.3	
	M_{iso}	223.9		223.9		223.9	

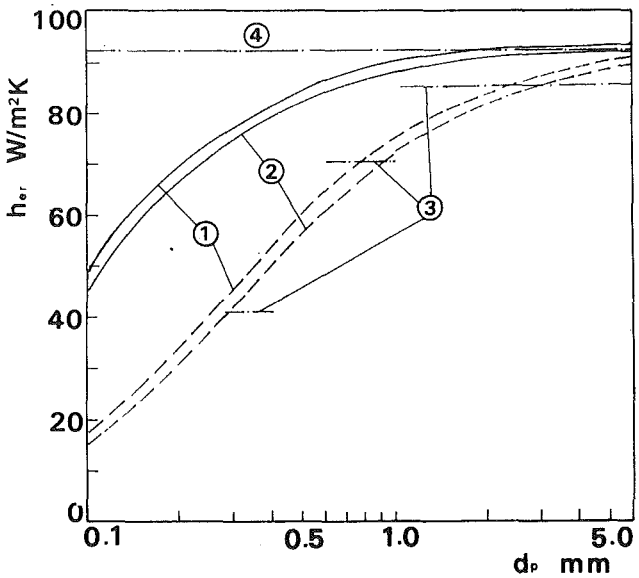

Fig. 2 Comparison of radiative heat transfer coefficients in emulsion phase as calculated using different approaches versus particle diameters: $T_B = 1173$ K, $T_w = 373$ K, $\delta_{eB} = 0.45$, $\epsilon_w = 0.8$, $\epsilon_p = 0.6$; (1) discrete-ordinates method; (2) two-flux method; —— $t_c = 0.1$ s, - - - $t_c = 1.0$ s; (3) Brewster's formula; (4) isothermal emulsion approximation

equation, the differencing direction is in agreement with the flux direction. The calculation is iterated until the solution converges. The accuracy of the finite-difference solution is tested by increasing the number of grid points and investigating some limiting cases. A 31×21 grid configuration is found to yield qualitatively and quantitatively good results and the results do not differ more than 1% from the results using a 51×31 mesh. The influence of integration time on the accuracy of the solution is also examined. Any significant difference in heat transfer coefficient is not observed when decreasing the time step (Δt) from 10^{-3} s to 10^{-4} s but small Δt is used for high-temperature calculations because the characteristic time of radiative heat transfer is much smaller than for conduction and convection.

Comparison of Different Theoretical Approaches. The discrete-ordinates method used in this model can be considered as the exact solution when the number of discrete radiant streams N is large enough (Tien, 1988). It also must be noted that the radiative flux is calculated on the basis of the transient temperature field determined by Eqs. (2)–(4). Some examples of the results are given in the paper of Lu et al. (1993). The solution procedure through such a complete formulation is complicated, but it can be used to check the validity of several approximating approaches. The two-flux method is based on a simple physical approximation that the positive-direction and negative-direction radiative intensities are each assumed isotropic. Brewster's formulae (1986) are based on an assumed steady-state exponential particle profile near the wall and the isothermal approximation considers the particle remains at the same temperature as in bed bulk when the emulsion packet contacts the wall.

Table 1 and Fig. 2 show the predicted results for four combinations of bed and wall temperatures with four theoretical approaches (grey approximation), i.e., the discrete-ordinate method with transient temperature field, two-flux method with transient temperature field, steady-state nonisothermal layer, and the isothermal assumption, respectively. The ordinate number N in the discrete-ordinates method is ten. The parameters needed for Brewster's formulae are chosen as $n = 2$ and $\Delta_e/d_p = 9$ for the $d_p = 0.1$ mm bed; note that these values were not given in the paper of Flamant and Bergeron (1988) but they were chosen from our temperature profile calculation. The emissivity for the last approach is obtained from the absorptivity formula given by Brewster (1986). It is found there is no obvious difference between the results predicted by discrete-ordinates and two-flux methods when the temperature difference between T_B and T_w is large. But when the temperature difference decreases, the deviation between the two method increases (if the temperature of bed bulk is higher than the wall temperature). For a resident time of 0.1 s, a bed and wall temperatures of 1173 K and 1073 K, respectively, the radiative heat transfer coefficients in the emulsion phase predicted by the discrete-ordinates method are 9.4 percent higher than those calculated by the two-flux method for 0.1 mm particle beds and this difference is 3.8 percent for 6.0 mm particle beds. It increases with time and reaches 17.2 percent and 4.1 percent, respectively, at $t_c = 1.0$ s. It seems the two-flux method is an acceptable approximation in general cases for engineering calculation since the relative discrepancy decreases with particle size and less computer CPU time is needed. But the discrete-ordinates method describes the radiative transport procedure that happens in emulsion packets more accurately in particular cases: high-temperature, small particles, and strong nonisotropic scattering (forward or backward) because it describes the radiative transfer phenomena more realistically.

Concerning Brewster's analytical formulations, three main domains are selected: small particles ($d_p < 400$ μm), medium-size particles ($0.6 < d_p < 1$ mm), and large particles ($d_p > 1$ mm). Because the author does not propose values for the parameters of its model Δ_e and n, the data from Flamant and Bergeron were chosen (see Appendix A). It can be observed in Fig. 2 that calculated radiative heat transfer coefficients are in rather good agreement with the results of the exact formulation, in the three ranges, for residence times of 1 s (they approach for long time limit for $T_B > T_w$ and the short-time limit for $T_B < T_w$). Attention must be paid in the small-diameter region because of large variation of h_{er} in this zone. Brewster's approximation can be used only with a change of the nonisothermal depth Δ_w with particle diameter in this region. Since the dependency of the radiative transport rate on the resident time is small for large particle bed ($d_p > 1$ mm), Brewster's formulae seem to be good approximation for these cases as long as the needed parameters are adopted.

It is interesting to note that the simplest approach based on the assumption of isothermal emulsion phases predicts the radiative transfer rate (which is the maximum with the two-flux method) with good accuracy for beds of particle larger than 2 mm. But when the particle size decreases, the error

Table 2 Comparison of emulsion phase radiative heat transfer coefficients with independent and dependent scattering theories: $\epsilon_p = 0.6$, $\epsilon_w = 0.8$, $\delta_{eB} = 0.45$

	d_p (mm)	0.1		0.5		1.0	
	t(s)	0.1	1.0	0.1	1.0	0.1	1.0
T_B =1173	M_{ind}	49.17	17.48	84.82	59.25	89.91	73.61
T_w =373K	M_{dep}	38.96	12.11	80.70	48.79	88.14	65.07
T_B =373K	M_{ind}	82.09	53.61	91.98	86.46	92.65	90.54
T_w =1173K	M_{dep}	78.13	46.59	91.56	83.40	92.52	89.29
T_B =1173K	M_{ind}	151.9	76.71	217.1	170.1	226.0	198.5
T_w =1073K	M_{dep}	132.0	62.27	209.9	149.7	223.0	182.9
T_B =1073K	M_{ind}	149.0	73.02	207.9	165.7	215.4	191.8
T_w =1173K	M_{dep}	130.3	57.77	201.8	146.7	213.0	178.0

Table 3 Calculated values of the radiative heat transfer coefficient comparison of the gray and nongray assumptions: $\epsilon_w = 0.8$, $\delta_{eB} = 0.45$, $t_c = 0.2$ s

d_p (mm)	ϵ_w grey and 2 bands	T_w / T_B	h_{er} for: 373 / 773		h_{er} for: 373 / 1173		h_{er} for: 773 / 1173		h_{er} for: 1073 / 1173	
			773	373	1173	373	1173	773	1173	1073
0.1	0.2		14.5	20.6	34.5	58.2	65.1	82.1	110	103
	0.6		16.8	26.6	38.1	75.5	75.3	103	128	126
	1.0		18.1	29.8	40.7	84.4	81.4	113	139	139
	0.2,1.0		17.9	27.3	39.7	69.0	74.4	93.6	120	115
	0.4,1.0		18.0	28.3	39.9	75.3	77.0	102	128	125
0.5	0.2		22.9	23.9	61.5	66.8	103	106	160	149
	0.6		30.1	32.6	79.6	91.2	135	144	208	200
	1.0		33.6	37.1	88.4	104	151	162	232	226
	0.2,1.0		31.6	34.1	76.2	84.6	125	130	185	176
	0.4,1.0		32.4	35.3	81.5	92.4	136	143	205	196
1.0	0.2		23.9	24.2	65.4	67.3	109	109	166	154
	0.6		32.1	33.2	87.1	92.4	146	149	221	212
	1.0		36.3	37.8	97.9	105	164	169	249	240
	0.2,1.0		33.7	34.8	82.3	85.9	133	135	195	185
	0.4,1.0		34.8	36.0	88.8	93.8	146	149	218	208
2.0	0.2		24.4	24.3	67.1	67.5	111	110	169	158
	0.6		33.1	33.4	90.7	92.8	150	151	228	217
	1.0		37.6	38.1	105	106	170	172	257	247
	0.2,1.0		34.7	35.1	85.2	86.4	137	137	200	189
	0.4,1.0		35.9	36.3	92.4	94.3	151	151	224	213
4.0	0.2		24.6	24.3	67.9	67.5	112	110	171	158
	0.6		33.5	33.5	92.5	93.0	153	152	230	220
	1.0		38.2	38.2	105	106	174	173	261	251
	0.2,1.0		35.2	35.2	86.5	86.6	139	137	202	190
	0.4,1.0		36.4	36.4	94.1	94.5	153	152	226	215

increases fast, because of cooling or heating of the particles near the wall, and at the same time it cannot predict the dependency of radiation on the direction of heat flux.

Dependent and Independent Scattering. The results predicted by independent dependent scattering theories are shown in Table 2, where the particles in fluidized beds are considered as large (geometric range) and opaque spheres. It appears in this table that the radiative heat transfer coefficients predicted by the dependent scattering theory are smaller than those calculated by independent scattering theory, especially for small size particle beds, long contact time of emulsion phase at the wall and high bed and wall temperatures, where differences as large as 20 percent are calculated. Dependent scattering is due to two effects: the far-field interference between the scattered waves and the multiple scattering inside the unit cell for which scattering and absorption characteristics of individual particles are affected by neighbors. From the theoretical study of Singh and Kaviany (1992) it seems that multiple scattering is the main reason for the reduction of radiative transfer. It can also be noticed that the differences between two groups of results are small for large particle beds ($d_p \geq 1.0$ mm), since fewer layers of particles near the wall take part in heat transfer in large particle beds than in small particle beds.

Gray and Nongray Assumptions. Figure 3 shows the radiative components predicted under the gray and the nongray assumptions for particle emissivities, where $\epsilon_p = 0.6$ is taken for the gray assumption and $\epsilon_{1p} = 0.2$ ($0 < \lambda < 3.5$ μm) and $\epsilon_{1p} = 1.0$ ($3.5 < \lambda < \infty$ μm) for the nongray assumption. It appears that the radiative heat transfer components calculated

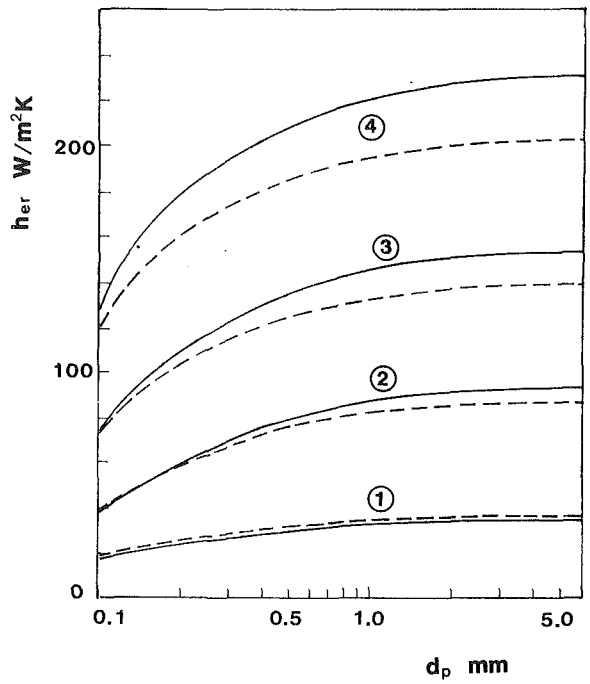

Fig. 3 Comparison of gray radiative heat transfer coefficients calculated from gray and nongray assumptions versus particle diameters: $\delta_{eB} = 0.45$, $\epsilon_w = 0.8$, $t_c = 0.2$ s; —— gray particles, - - - nongray particles; (1) $T_B = 1173$ K, $T_w = 373$ K; (2) $T_B = 373$ K, $T_w = 1173$ K; (3) $T_B = 1173$ K, $T_w = 1073$ K; (4) $T_B = 1073$ K, $T_w = 1173$ K

with the gray assumption are smaller than those predicted with the nongray assumption for only one combination, i.e., low wall temperature and large bed temperature ($T_w = 373$ K, $T_B = 1073$ K) but the situation is reversed for all the other cases, especially for large particle beds. This trend is due to the shift of the black body emission to small wavelengths when the temperature increases, i.e., to the low-emissivity region ($\epsilon_{1p} = 0.2$) in our case.

The results of numerical simulation are listed in Table 3 for five particle diameters, eight temperature combinations of the bed and the wall, and five emissivity assumptions: three with the gray assumption ($\epsilon_p = 0.2$, 0.6, and 1.0) and two with the two-band model.

The radiative heat transfer coefficient is always larger for $T_w > T_B$ than for $T_w < T_B$ except for small temperature difference between the wall and the bed (last column).

As expected, under the gray assumption, h_{er} increases with the particle emissivity and the difference between low and large emissivity situation rises with particle diameter. At high temperature the radiative component increase can reach 50 percent when ϵ_p rises from 0.2 to 1.

For the main situations of Table 3 the results for the gray assumption with $\epsilon_p = 0.6$ are very near those for the two-band calculation with $\epsilon_{1p} = 0.4$ and $\epsilon_{2p} = 1.0$; significant differences can be noticed with $\epsilon_{1p} = 0.2$. At low temperature the latter assumption gives higher radiative heat transfer coefficient than the former because of the high emissivity for larger wavelengths, but the differences are about 5 percent. For medium and high temperature, the situation reverses and the gray assumption overestimates the radiative component; the maximum difference is 15 percent.

The problem is the accurate knowledge of the particle optical properties. For example, in the case of sand, the emissivity in the first band is strongly dependent on iron oxide content.

Radiative Contribution. The relative importance of the radiative transport, which was often used in literature, is shown in Table 4 and Fig. 4, as well as the total heat transfer coefficients of the emulsion phase at the resident time of 0.2 s. It appears that the ratios of the radiative heat transfer coefficient

Table 4 Emulsion heat transfer coefficients and percentage of radiative transfer at different temperature conditions: $\epsilon_p = 0.6$, $\epsilon_w = 0.8$, $\delta_{eB} = 0.45$, $t_c = 0.2$ s

d_p (mm)	total / ratio \ T_w / T_B	373 773	373 1173	773 1173	773 1173	1073 1173	1173 1073
0.1	h_e	846 931	951 1103	1136 1204		1284 1287	
	h_{er}/h_e	1.99 2.86	4.01 6.84	6.63 8.52		9.98 9.78	
0.5	h_e	388 418	476 550	601 641		727 726	
	h_{er}/h_e	7.77 7.81	16.7 16.6	22.5 22.4		28.6 27.5	
1.0	h_e	312 311	390 409	480 495		585 578	
	h_{er}/h_e	10.3 10.7	22.3 22.6	30.3 30.1		37.9 36.6	
2.0	h_e	281 260	357 336	422 419		511 500	
	h_{er}/h_e	11.7 12.9	25.4 27.7	35.6 36.0		44.5 43.3	
4.0	h_e	284 248	357 309	404 388		483 469	
	h_{er}/h_e	11.8 13.5	25.9 30.1	37.7 39.1		47.7 46.8	

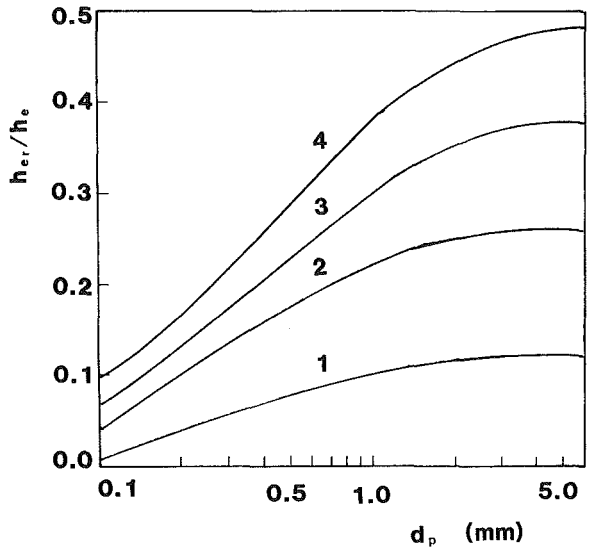

Fig. 4 Percentage of emulsion phase radiative transfer coefficient versus particle diameters: $\delta_{eB} = 0.45$, $\epsilon_w = 0.8$, $t_c = 0.2$ s, $\epsilon_p = 0.6$; (1) $T_B = 1173$ K, $T_w = 373$ K; (2) $T_B = 373$ K, $T_w = 1173$ K; (3) $T_B = 1173$ K, $T_w = 1073$ K; (4) $T_B = 1073$ K, $T_w = 1173$ K

to the total heat transfer coefficients are mainly dependent on particle size, wall temperature, and bed temperature. The larger the particle size and the higher the temperature, the more important the radiative transfer is. This is due to the variation of dominant transport modes in beds with particle size. In large particle beds the gas convection is dominant and the radiative transport plays a more and more important role as the temperature increases. On the other hand, the particle convective component is dominant in small particle beds and the radiation is less important. For the situations considered, the ratio of h_{er} versus h_e is always smaller than 10 percent even at the high-temperature conditions in the 0.1 mm particle bed, but on the opposite side it is larger than 10 percent even if the temperature of the bed or of the wall is only 773 K in the 4.0 mm particle bed. This conclusion is in agreement with Baskakov (1985); the radiative heat flux can exceed the convective heat flux in the extreme case. When the residence time of emulsion packets increases, the change of h_{er}/h_e is determined by the dependence of each component with time. In general h_{er}/h_e increases with increasing resident time, except for small particle beds when $T_B > T_w$. It should be indicated that the variation of h_{er}/h_e presented here is only for the emulsion phase, it would change with the radiation properties of particles and the wall and the fluidizing velocity. Since $(h_{ep} + h_{eg}) \gg h_{bg}$ and $h_{er} < h_{br}$, the ratio of h_r and h_w would increase with the increase of overflow velocity $(U - U_{mf})$ according to Eq. (1).

According to Fig. 4 and Table 4, radiation is a larger fraction of the total heat transfer when temperature differences are smaller. One must consider separately the radiative flux and the radiative heat transfer coefficient. As a first approximation the former is proportional to the difference $|T_e^4 - T_w^4|$, which increases with the temperature difference, but the radiative heat exchange coefficient could be written as:

$$q_{er} = h_{er} |T_e - T_w| \tag{35}$$

with $h_{er} \alpha T_e^3 + T_e^2 T_w + T_e T_w^2 + T_w^3$ (T_e is the mean emulsion temperature at the wall). The radiative heat exchange coefficient increases with temperature and when temperature difference decreases (for the same reference level for T_w or T_e). As a consequence q_{er} and h_{er} vary in the opposite direction with temperature difference $|T_e - T_w|$.

Another observation can be made from the data of Table 4. For particle size smaller than 1 mm, the total heat transfer is larger for wall temperature larger than bed temperature $(T_w > T_B)$, but the situation is reversed for large particle diameters. This trend is due to the relative importance of conduction and convection near the wall. In the former situations conduction through the stagnant gas at the wall plays an important role in the heat exchange mechanisms while convection in the flowing gas is dominant in the latter situations. These heat transfer mechanisms both increase with temperature.

Conclusions

This paper is the first to present a theoretical investigation for the radiative heat transfer in high-temperature fluidized beds using complete and simplified formulations and solution of the coupled conduction, convection, and radiation problem in the case of a gray and nongray medium.

From the comparison of different theoretical formulations, it can be found that the two-flux method can be used for the calculation of the radiative component of emulsion phase except for small particle fluidized beds at high temperatures when $T_B - T_w$ is small, as its results are in agreement with those of the discrete-ordinates method. Brewster's formulae with adequate parameters and even the isothermal emulsion approximation can be used for large particle beds, $d_p > 1$ mm for the former formulation and $d_p > 2$ mm for the latter. The predicted radiative transfer rates depend on the scattering behavior of the bed. The data obtained for the dependent scattering theory are smaller than with the independent scattering theory, and differences as high as 20 percent were calculated.

The particle optical properties, calculated from the gray and the nongray assumptions, exhibit significant differences (as large as 15 percent), depending on the bed temperature. But this example shows the importance of the knowledge of real emissivity of particles for the calculation of radiation exchange in fluidized beds.

It should be pointed out that the dependence of radiant transfer rate on governing parameters, such as bed and wall temperatures, particle size, etc., discussed above is only valid for the assumed situation, because the heat transfer in fluidized beds is a complicated function of these parameters. In order to generalize the results, heat transfer classification schemes can be proposed. Several particle classification schemes have been published by considering the hydrodynamic and thermal properties (Geldart, 1973; Jovanovic and Catipovic, 1983; Saxena and Ganzha, 1984), but they were obtained at ambient conditions. In order to check the validity of these schemes at high-temperature conditions and extend them to account for radiant transfer, more detailed theoretical and experimental researches are needed for the quantitative description.

References

Baskakov, A. P., 1985, "Heat Transfer in Fluidized Beds: Radiative Transfer in Fluidized Beds," *Fluidization*, 2nd ed., A. M. Xavier and J. F. Davison, eds., Academic Press, London, pp. 465-472.

Borodulya, V. A., and Kovensky, V. I., 1983, "Radiative Heat Transfer Between a Fluidized Bed and a Surface," *Int. J. Heat Mass Transfer*, Vol. 26, pp. 277-287.

Borodulya, V. A., Kovensky, V. I., and Makhorin, K. E., 1983, "Fluidized Bed Radiative Heat Transfer," *Fluidization*, D. Kunii and R. Toei, eds., pp. 379-387.

Botterill, J. S. M., and Williams, J. R., 1963, "The Mechanism of Heat Transfer to Gas-Fluidized Beds," *Trans. Institute of Chemical Engineering*, Vol. 41, pp. 217-230.

Brewster, M. Q., and Tien, C. L., 1982, "Radiative Transfer in Packed/Fluidized Beds," ASME JOURNAL OF HEAT TRANSFER, Vol. 104, pp. 573-579.

Brewster, M. Q., 1986, "Effective Absorptivity and Emissivity of Particulate Madia With Application to a Fluidized Bed," ASME JOURNAL OF HEAT TRANSFER, Vol. 108, pp. 710-713.

Chandrasekhar, S., 1960, *Radiative Transfer*, Dover, New York.

Chen, J. C., and Chen, K. L., 1981, "Analysis of Simultaneous Radiative and Conductive Heat Transfer in Fluidized Beds," *Chemical Engineering Communication*, Vol. 9, pp. 255-271.

Decker, N. A., and Glicksman, L. R., 1981, "Conduction Heat Transfer at the Surface of Bodies Immersed in Gas Fluidized Beds of Spherical Particles," *AIChE Symp.*, Series No. 208, Vol. 77, pp. 341-349.

Dixon, A. G., and Gresswell, D. L., 1979, "Theoretical Prediction Effective Heat Transfer Parameters in Packed Beds," *AIChE Journal*, Vol. 19, pp. 663-678.

Fatah, N., Flamant, G., Hernandez, D., Gauthier, D., and Olalde, G., 1992, "Gas and Solid Temperature Distribution Near an Immersed Wall in Fluidized Bed. An Experimental and Theoretical Contribution," *Fluidization VII*, Potter and Nicklin, eds., Engineering Foundation, New York, pp. 803-812.

Flamant, G., and Arnaud, G., 1984, "Analyse et Modelisation du Transfer de Chaleur entre une Paroi et un Lit Fluidisé à Haute Temperature," *Int. J. Heat Mass Transfer*, Vol. 27, pp. 1725-1735.

Flamant, G., 1985, "Transfert de Chaleur Couplés dans les Lits Fluidisés à Haute Temperature. Application à la Conversion Thermique de l'Energie Solaire," These de docteur Es-Science, No. 93, Institut National Polytechnique de Toulouse, France.

Flamant, G., and Menigault, T., 1988, "Combined Wall-to-Fluidized Bed Heat Transfer. Bubble and Emulsion Contributions at High Temperature," *Int. J. Heat Mass Transfer*, Vol. 30, pp. 1803-1812.

Flamant, G., and Bergeron, G., 1988, "Contribution du Rayonnement au Transfert de Chaleur Lit Fluidise-Paroi," *Entropie*, No. 145, pp. 25-34.

Flamant, G., Lu, J. D., and Variot, B., 1993, "A Generalized Model for Vertical Walls to Gas-Solid Fluidized Beds Heat Transfer. Part 2: Radiation and Temperature Effects," *Chemical Engineering*, Vol. 48, No. 13, pp. 2493-2503.

Flitris, Y., Flamant, G., and Hatzikonstantinou, P., 1988, "Wall-to-Fluidized Bed Radiative Heat Transfer Analysis Using the Particle Model," *Chemical Engineering Communication*, Vol. 72, pp. 187-199.

Geldart, D., 1973, "Type of Gas Fluidization," *Powder Technology*, No. 7, pp. 285-292.

Glicksman, L., and Decker, N. A., 1985, "Heat Transfer From an Immersed Surface to Adjacent Particles in a Fluidized Bed: the Role of Radiation and Particle Packing," *Proceedings, 8th International Conference on Fluidized-Bed Combustion*, Houston, TX, pp. 45-50.

Jovanovic, G., and Catipovic, N., 1983, "A New Approach in Classifying Solids in Bubbling Gas-Fluidized Beds," *Fluidization*, D. Kunii and R. Toei, eds., pp. 69-76.

Kolar, A. K., Grewal, N. S., and Saxena, S. C., 1979, "Investigation of Radiative Contribution in a High Temperature Fluidized Bed Using the Alternate Slab Model," *Int. J. Heat Mass Transfer*, Vol. 22, pp. 1695-1703.

Kubie, J., and Broughton, J., 1975, "A Model of Heat Transfer in Gas Fluidized Beds," *Int. J. Heat Mass Transfer*, Vol. 18, pp. 289-299.

Lu, J. D., Flamant, G., and Snabre, P., 1993, "A Generalized Model for Vertical Walls to Gas-Solid Fluidized Beds Heat Transfer. Part 1: Particle Convection and Gas Convection," *Chemical Engineering Science*, Vol. 48, No. 13, pp. 2479-2492.

Mahbod, B., and Tabesh, T., 1985, "Theoretical Prediction of Thermal Radiative Interaction With Large Particle Gas Fluidized Bed With an Immersed Horizontal Tube," *Proceeding: International Symposium on Heat Transfer*, B. X. Wang, ed., Hemisphere Publishing Corp., Beijing, pp. 526-534.

Mickley, H. S., and Fairbanks, D. F., 1955, "Mechanism of Heat Transfer to Fluidized Beds," *AIChE Journal*, Vol. 1, pp. 374-384.

Saxena, S. C., and Ganzha, V. L., 1984, "Heat Transfer to Immersed Surfaces in Gas-Fluidized Beds of Large Particles and Powder Characterization," *Powder Technology*, Vol. 39, pp. 199-208.

Saxena, S. C., Srivastava, K. K., and Vadivel, R., 1989, "Experimental Techniques for the Measurement of Radiative and Total Heat Transfer in Gas Fluidized Beds: a Review," *Experimental Thermal and Fluid Science*, Vol. 2, pp. 350-364.

Siegel, R., and Howell, R. J., 1972, *Thermal Radiation Heat Transfer*, McGraw-Hill, New York.

Singh, B. P., and Kaviany, M., 1991, "Independent Theory Versus Direct Simulation of Radiation Heat Transfer in Packed Beds," *Int. J. Heat Mass Transfer*, Vol. 34, pp. 2869-2882.

Singh, B. P., and Kaviany, M., 1992, "Modelling Radiative Heat Transfer in Packed Beds," *Int. J. Heat Mass Transfer*, Vol. 35, pp. 1397-1405.

Szekely, J., and Fisher, R. J., 1969, "Bed to Wall Radiation Heat Transfer in a Gas-Solid Fluidized Bed," *Chemical Engineering Science*, Vol. 24, pp. 833-849.

Tabanfar, S., and Modest, M. F., 1987, "Combined Radiation and Convection in Absorbing, Emitting, Nongray Gas-Particulate Tube Flow," ASME JOURNAL OF HEAT TRANSFER, Vol. 109, pp. 478-484.

Thring, R. H., 1977, "Fluidized Bed Combustion for the Stirling Engine," *Int. J. Heat Mass Transfer*, Vol. 20, pp. 911-918.

Tien, C. L., 1988, "Thermal Radiation in Packed and Fluidized Beds," ASME JOURNAL OF HEAT TRANSFER, Vol. 110, pp. 1231-1242.

Touloukian, Y. S., and Dewitt, D. P., 1972, "Thermal Radiative Properties, Nonmetallic Solids," *The TPRC Data Series*, Vol. 8, IFI Plenum, New York.

Vafai, K., and Sozen, M., 1990, "Analysis of Energy and Momentum Transport for Fluid Flow Through a Porous Bed," ASME JOURNAL OF HEAT TRANSFER, Vol. 112, pp. 690-699.

Vedamurthy, V. N., and Sastri, V. M. K., 1974, "An Analysis of Conductive and Radiative Heat Transfer to Walls of Fluidized Bed Combustors," *Int. J. Heat Mass Transfer*, Vol. 17, pp. 1-9.

Whitaker, S., 1969, "Advances in Theory of Fluid Motion in Porous Media," *Industrial and Engineering Chemistry*, Vol. 61, pp. 14-18.

Yoshida, K., Veno, T., and Kunii, D., 1974, "Mechanism of Bed-Wall Heat Transfer in a Fluidized Bed at High Temperature," *Chemical Engineering Science*, Vol. 29, pp. 77-82.

Yoshida, H., Yun, J. H., and Echigo, R., 1990, "Transient Characteristics of Combined Conduction, Convection, and Radiation Heat Transfer in Porous Media," *Int. J. Heat Mass Transfer*, Vol. 33, pp. 847-857.

APPENDIX A

Parameters Δ_e/d_p and n Estimated by Flamant and Bergeron (1988)

d_p, μm	n	Δ_e/d_p
280-400	3	3
600-1000	6	1
>1000	14	1/2

with: $T_o = T_b \pm \dfrac{T_w - T_b}{n}$

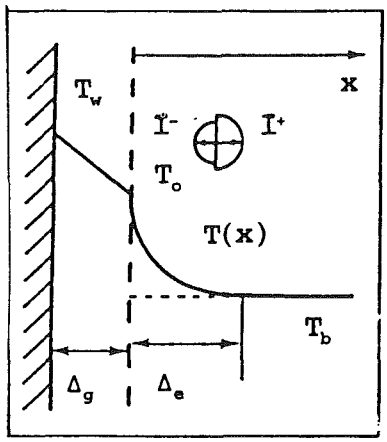

APPENDIX B

Physical Properties of Air (Flamant, 1985)

$$\rho_g = (351/T)\ \text{kg/m}^3$$
$$\lambda_g = 5.66\times10^{-3}T + 1.1\times10^{-2}\ \text{W/(m·K)}$$
$$C_{pg} = (0.99 + 1.22\times10^{-4}T - 5.68\cdot T^{-2})\times10^3\ \text{J/(kg·K)}$$
$$\mu_g = 0.42\times10^{-6}T^{2/3}\ \text{N·s/m}^2$$

Physical Properties of Silica Sand (Kubie and Broughton, 1975; Touloukian and Dewitt, 1972)

λ_g = 1.87 W/(m·K)
C_{pp} = 860 J/(kg·K)
ρ_p = 2600 kg/m^3
ϵ_p = 0.6 for gray body assumption
ϵ_{1p} = 0.2 (λ = 0-3.5 μm) and ϵ_{2p} = 1 (λ = 3.5-∞ μm) for nongray body.

R. P. Roy

V. Velidandla

Arizona State University,
Department of Mechanical and
Aerospace Engineering,
Tempe, AZ 85287-6106

S. P. Kalra

Electric Power Research Institute,
Nuclear Power Division,
Palo Alto, CA 94303

P. Peturaud

Electricité de France,
6, Quai Watier,
78401 Chatou Cedex France

Local Measurements in the Two-Phase Region of Turbulent Subcooled Boiling Flow

Local measurements of vapor phase residence time fraction, vapor bubble size distribution, bubble axial velocity, and vapor and liquid temperatures were performed in turbulent boiling flow of Refrigerant-113. The dissolved air content of the experimental fluid was minimized. Data are reported for three wall heat fluxes, two fluid mass velocities, and three subcoolings at test section inlet. Local time-averaged interfacial area concentrations were estimated. The measuring devices, viz., dual-sensor fiber-optic probe for the vapor bubble measurements and phase-compensated chromel-alumel microthermocouple for the fluid temperature measurement, provided more complete and accurate data compared with our earlier work. The data should be helpful in the development and validation of multidimensional turbulent boiling flow models. Further work is needed, however, before the local interfacial area concentration can be determined with confidence.

Introduction

Fundamental experiments are crucial to the development of mechanistic multidimensional models of turbulent boiling flow. For example, experiments that measure the spatial distributions of vapor and liquid phases, interfacial area concentration, and turbulent velocity and temperature fields are essential. Some of the experimental data can be used to develop constitutive equations for the model while others can help validate the model. These considerations motivated the experiments described in this paper.

We report the results of experiments in which some basic aspects of turbulent subcooled boiling flow were explored. This flow is characterized by discrete vapor bubbles flowing with a liquid continuum. The vapor bubbles are generated at the heated wall(s) and play important roles in the transport of thermal energy and momentum in the fluid. Partial nucleate boiling is the mode of heat transfer at the wall upon commencement of boiling. With significant vapor generation, however, fully developed nucleate boiling occurs. All the measurements reported here were performed at the latter heated wall condition.

The earliest basic experimental studies of the subcooled boiling flow field were by Jiji and Clark (1964) and Walmet and Staub (1969). In both studies, miniature thermocouples were used to measure the temperature (mean and fluctuations) distribution in a boiling layer of water adjacent to the heated wall. No effort was made to distinguish between the vapor and liquid temperatures (the thermocouples appear to have been too slow to permit this). Walmet and Staub also measured the vapor fraction distribution in their rectangular test section with one side heated by the x-ray attenuation technique, and the mean liquid axial velocity distribution by miniature total and static pressure probes. Later, Shiralkar (1970) and Dix (1971) used hot-film sensors with constant temperature anemometry (CTA) to measure vapor fraction distribution in subcooled boiling flow of Refrigerant-114. Delhaye et al. (1973) constructed a fast microthermocouple that could distinguish between vapor and liquid temperatures in subcooled boiling flow and performed measurements in water. They suggested that the local vapor fraction can be estimated from the probability density function (PDF) of the microthermocouple temperature signal. Hino and Ueda (1985a, b) studied some characteristics of wall heat transfer and flow field in subcooled flow boiling through a vertical annular channel. Spatial distributions of vapor–liquid mixture mean temperature and fluctuation intensity were measured by means of compensated chromel-constantan microthermocouples with fast response. PDFs of the local mixture temperature signals were constructed. Also reported were: the power spectra of mixture temperature fluctuations, and the distributions of bubble frequency and vapor and liquid residence time intervals. Hasan et al. (1991) measured the transverse distribution of *fluid* (i.e., the vapor–liquid mixture) mean temperature and vapor phase residence time fraction in subcooled boiling flow of Refrigerant-113 (R-113) through a vertical annular channel. The fluid temperature was measured by a chromel-constantan microthermocouple and the vapor fraction by a miniature cylindrical hot-film sensor operated in the CTA mode. The microthermocouple (time constant $\approx$ 7 ms) was not fast enough to be able to distinguish between vapor and liquid temperatures. A drawback of the vapor fraction data reported was the presence of a significant amount of dissolved air in the working fluid.

A formulation for the local, time-averaged interfacial area concentration in vapor–liquid flow was proposed by Kataoka et al. (1986). This was related to multisensor measurements in such flows and then applied to air–water bubbly and slug flows. Revankar and Ishii (1992) calculated local, time-averaged interfacial area concentration from their double-sensor probe measurement of the statistical characteristics of interfacial velocity in bubbly air–water flow.

The measurements reported in this paper were performed in turbulent subcooled boiling flow of R-113 through a vertical annular channel. Significant improvements over our previous effort (Hasan et al., 1991) were instituted in the area of measurement instrumentation. The vapor phase residence time fraction was measured by a dual-sensor fiber-optic probe. This probe also enabled measurement of vapor bubble size and axial velocity. The local, time-averaged interfacial area concentration was estimated from these measurements. The dissolved air content of R-113 was minimized so that the effect of air content on vapor fraction measurement was minimal. A phase-compensated chromel-alumel microthermocouple measured the

Contributed by the Heat Transfer Division and presented at the National Heat Transfer Conference, San Diego, California, August 9–12, 1992. Manuscript received by the Heat Transfer Division April 1993; revision received November 1993. Keywords: Boiling, Multiphase Flows. Associate Technical Editor: R. A. Nelson, Jr.

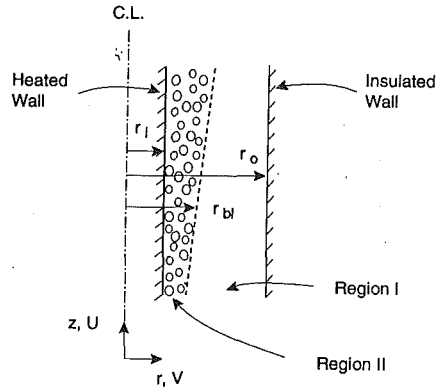

Fig. 1 Boiling layer and adjacent all-liquid region in subcooled boiling flow

local temperature in the flow. The time constant of this microthermocouple (≈ 3.4 ms) was small enough to permit separation of the vapor and liquid temperatures. Both the mean and the fluctuation intensity of liquid temperature are reported.

The data on vapor bubble size and axial velocity and the estimates of interfacial area concentration should be useful for developing constitutive relations. Data on liquid temperature fluctuation intensity will help in the formulation of a model for turbulent heat flux in the liquid phase. Data on local vapor fraction and mean liquid and vapor temperatures can be used for validation of multidimensional models of turbulent subcooled boiling flow.

The Experiments

The annular test section in which these experiments were carried out features a heated inner wall and an insulated outer wall. Subcooled boiling flow in such a channel is shown schematically in Fig. 1. Two regions are shown, a boiling fluid layer adjacent to the heated wall (region II) and an outer all-liquid region (region I). An advantage of the annular geometry is that the flow field can be studied by intrusive probes (e.g., fiber-optic probe, microthermocouple) and nonintrusive probes (e.g., laser-Doppler velocimeter) without having to disrupt the heated wall.

I The Test Section. Figure 2 shows a part of the vertical annular test section. Its inner tube is of 304 stainless steel (i.d. = 14.6 mm, o.d. = 15.9 mm) and the outer pipe of transparent pyrex glass (i.d. = 38.1 mm, o.d. = 47.0 mm) except for a 0.496 m long *measurement section*, which is made of quartz

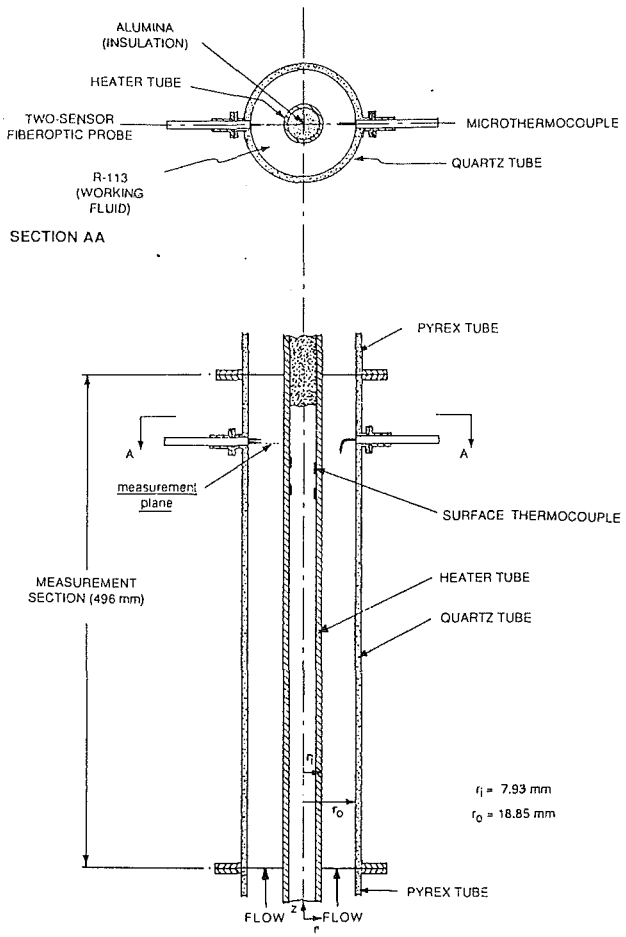

Fig. 2 Measurement section

(i.d. = 37.7 mm, o.d. = 41.7 mm).[1] The inner tube can be resistively heated by direct current, the upper 2.75 m of the 3.66 m long test section being the heated length. The lower 0.91 m serves as the hydrodynamic entrance length.

A dual-sensor fiber-optic probe and a chromel-alumel microthermocouple were installed diametrically opposite each other in the measurement section. Four surface thermocouples were installed on the inner wall of the heater tube. The tube was then filled with aluminum oxide powder insulation. The

[1] Quartz is used in view of the laser-Doppler velocimetry measurements planned for the next phase of our work.

Nomenclature

$\bar{a}_i$ = local time-averaged interfacial area concentration
D_i = diameter of ith bubble
$\overline{D}_{sm}$ = Sauter mean diameter of bubble
g = acceleration due to gravity
G = mass velocity
N_t = number of vapor bubbles that pass a point in space per second
p = pressure
p_r = partial pressure of R-113
$P_d(D)$ = cumulative probability distribution function of the diameter of detected bubbles
q''_w = wall heat flux
r = radial coordinate
r_{bl} = radius of boiling layer outer edge
r_i = annulus inner wall radius
r_o = annulus outer wall radius
R^* = nondimensional radial coordinate $\equiv (r-r_i)/(r_o-r_i)$
T = mean temperature
t' = temperature fluctuation
T_{in} = mean liquid temperature at test section inlet
$\overline{U}_g$ = time-mean vapor bubble axial velocity
$\overline{U}_s$ = time-mean interface axial velocity
z = axial coordinate
α_G = local residence time fraction of vapor
α_0 = the maximum angle between the local interface velocity and the axial coordinate
$\rho_c(x)$ = probability density function of the chord length of detected bubbles
$\rho_d(D)$ = probability density function of the diameter of detected bubbles
ρ_l, ρ_g = liquid, vapor density
σ = surface tension
σ_U^2 = variance of interface axial velocity

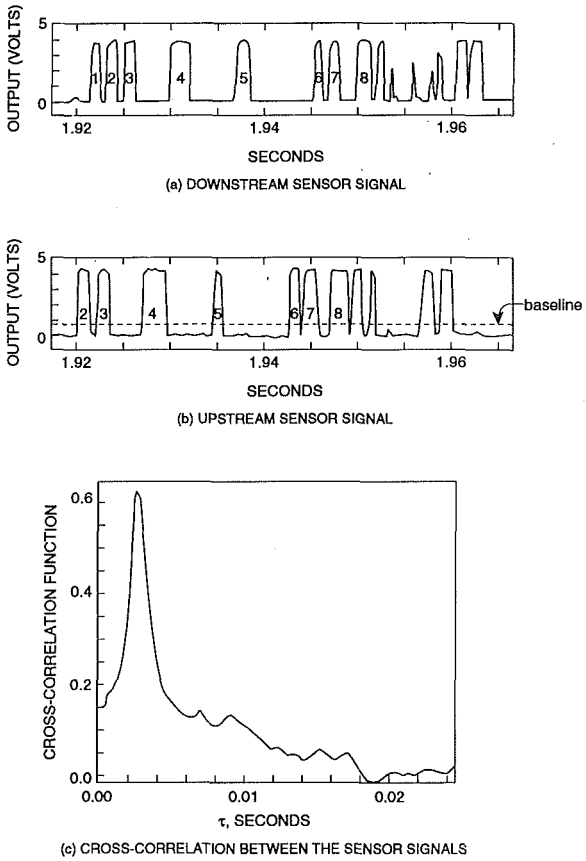

Fig. 3 Typical outputs of fiber-optic sensors and their cross-correlation

measurement plane (shown in Fig. 2) was approximately 1.94 m downstream of the beginning of the heated length.

II Measurement Instrumentation

1 Vapor Phase Residence Time Fraction, Bubble Diameter, and Bubble Axial Velocity. As mentioned earlier, these measurements were made by means of a dual-sensor fiber-optic probe. This probe (Photonetics, France) features two fiber-optic sensors, each of which acts as a guide to infrared light emitted by an LED. The active part of the fiber tip has a characteristic size of 20 μm and the two tips are 1.77 mm apart. The sensor discriminates between vapor and liquid phases because their refractive indices are different, the infrared light being totally reflected when the sensor tip is surrounded by vapor. The probe and its opto-electronic circuit provide a response time of approximately 10 μs. Performance of such probes has been characterized by Cartellier (1990).

Figures 3(*a*) and (*b*) show typical signals from the two sensors when they are placed in the boiling layer. The sampling time interval and the total record length for each of these signals were 230 μs and 4.7 s, respectively. Each voltage pulse signifies an encounter of the sensor tip with a vapor bubble; the sharp rise corresponds to an interfacial crossing from liquid to vapor and the sharp drop corresponds to an interfacial crossing from vapor to liquid. Not all the bubbles that impinge on the upstream sensor encounter the downstream sensor and vice versa. Let us consider, for example, the time interval between 1.92 s and 1.94 s in the figures. The downstream sensor encounters five bubbles (designated as numbers 1–5) during this interval while the upstream sensor detects four of these bubbles (numbers 2–5). Also, the time interval of passage of any bubble (i.e., the time between the two interfacial crossings) is not necessarily the same for the two sensors. This is because the same bubble chord lengths may not be traversed by a bubble

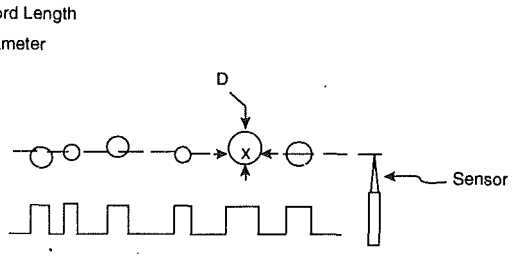

Fig. 4 Bubble chord lengths detected by fiber-optic sensor

and the bubble (i.e., its interface) may not travel with exactly the same velocity (magnitude and direction) at the two sensors. Our measurements indicate that the downstream sensor detects, on the average, a smaller number of vapor bubbles per unit time than the upstream sensor. Also, the vapor phase residence time fraction measured by the upstream sensor is always slightly higher (for example, 1 to 4 percent higher in the vapor fraction range of 5 to 35 percent). We consider the upstream sensor measurement to be more accurate since the path to it was unhindered. All vapor fraction data presented in this paper are upstream sensor measurements.

A baseline at 0.9 volt is shown in Fig. 3(*b*). A judicious choice of this voltage is important because the data analysis algorithm uses the points of intersection of the baseline with the voltage pulses to calculate the residence time of the vapor phase. The baseline voltage should be small compared to the pulse amplitude but larger than the noise level of the liquid phase signal. Consideration must also be given to the rise and fall time of the pulses.

At steady state and in the limit of very long record length, the vapor phase residence time fraction is equal to the probability of existence of vapor at the sensor location.

The cross-correlation function of the two signals is shown in Fig. 3(*c*). This function describes the general dependence of the set of data from one signal on the other signal data set. The time displacement, τ, corresponding to the sharp peak represents the most probable travel time of bubbles (i.e., their interfaces) from the upstream sensor to the downstream sensor. Since the sensor tips were juxtaposed along the axial (z) direction with a known spacing, the most probable bubble (or interface) velocity could be calculated from the most probable travel time. A distribution about the most probable velocity is expected, however, because bubbles of different sizes and shapes travel at different relative velocities with respect to the ambient liquid and because the flow is turbulent.

Generally, a vapor bubble will not be pierced by the sensor tip along its diameter. A chord length, x, will be traversed instead, Fig. 4. The PDF of the measured chord lengths, $\rho_c(x)$, can be constructed. It has been shown (Herringe and Davis, 1976) that the cumulative probability distribution function of the diameter of the detected bubbles is given by

$$P_d(D) = \int_0^D \rho_c(x)dx - \frac{1}{2} D\rho_c(x=D) \tag{1}$$

The corresponding PDF is

$$\rho_d(D) = \frac{dP_d(D)}{dD} \tag{2}$$

These relations are based on the assumptions that the vapor bubbles are spherical, the bubble axial velocity is independent of its diameter, and the sensor has equal probability of piercing any point on the projected frontal area of a bubble. As will be shown later, most bubbles were less than 2 mm in diameter. Thus, the assumption of sphericity of the bubbles is reasonable. On the other hand, the assumption that the bubble velocity is

Table 1 Range of experiments and measurement uncertainties†

	Range	Uncertainty
Wall heat flux	79,400 - 126,00 W/m^2	±200 W/m^2
Mass velocity	579, 801 kg/m^{2}s	± 3 kg/m^{2}s
R-113 partial pressure at measurement plane (sat. temp.)	269 kPa (80.1°C)	± 0.7 kPa
Mean liquid temperature at test section inlet	43.0, 50.3°C	± 0.1°C
Wall temperature	95-102°C	± 0.4°C
Vapor local residence time fraction	0-52%	± 1% for 0% < α_G < 10% ± 2% for 10% < α_G < 52%
Bubble diameter	0.1 - 2.6 mm	± 0.05 mm
Sensor radial traverse:		
fiber optic sensor	0 - 10 mm	± 30 μm
microthermocouple	0 - 9 mm	± 30 μm

† The uncertainty estimates are for 95 percent confidence.

independent of its diameter is a weak one and introduces some error in the bubble diameter PDF.

2 Liquid and Vapor Temperatures. The chromel-alumel microthermocouple used for these measurements (Beckman et al., 1993) features a disk-shaped junction, 2.5 μm thick and 0.09 mm in diameter. When operated in conjunction with an active phase-lead compensation circuit (similar in principle to Hishida and Nagano, 1978), the time constant of the microthermocouple was measured to be about 3.4 ms in turbulent flow of R-113 in the same Reynolds number range as the present experiments. This response was sufficiently fast for distinguishing vapor temperature from liquid temperature in the subcooled boiling layer.

3 Heated Wall Temperature. Four surface thermocouples (Omega, foil thickness = 0.01 mm, junction length = 0.5 mm) were baked onto the inner wall of the heater tube with a thin layer of epoxy cement. The temperature of the tube outer wall, which forms the inner wall of the annulus, was calculated from the measured inner wall temperature by a steady-state heat conduction analysis.

4 Pressure. The measurement plane (m.p.) pressure was monitored by a test gage (Omega, 0-1200 kPa range, 1.4 kPa resolution).

5 Flow Rate. The volumetric flow rate of liquid at the test section inlet was measured by a turbine flow meter (Flow Technology).

6 Heating Power Input. The power input to the test section was calculated as the product of the magnitude of direct current from a DC power supply (Rapid Power Technologies; 40 volts, 1500 A maximum) and the voltage differential across the heater tube.

Results

Table 1 contains the ranges of variables over which the measurements were performed as well as the associated measurement uncertainties.

At the outset, test section heat balance was carried out using the supplied heating power, the liquid mass flow rate, and the mixed-mean liquid temperature rise in single-phase liquid flow experiments. About 2 percent of the supplied power was found to be lost to the ambient.

Air is highly soluble in liquid R-113 and, in boiling flow experiments, the influence of dissolved air on vapor fraction and temperature can be significant. Dissolved air increases the apparent vapor fraction in boiling flow, the extent of this increase depending on the air concentration, the local pressure, and the local temperature. Furthermore, the saturation temperature is lowered. Careful degassing of the rig R-113 inventory followed by measurement of the residual dissolved air content is therefore essential prior to each experiment. Measurement of the residual dissolved air was performed by an Aire-Ometer (Seaton-Wilson). Henry's law was then invoked to calculate the partial pressure of air in the gas phase. The R-113 partial pressure was found by subtracting the air partial pressure from the measured total pressure. For the experiments reported here, the air partial pressure was typically 8 kPa out of the total pressure of 277 kPa at the measurement plane. This translates to a reduction in the R-113 saturation temperature from 81.2°C to 80.1°C. Assuming the R-113 vapor-air mixture to be a mixture of perfect gases, the volume fraction of R-113 can be calculated from the corresponding pressure fraction. For example, for a measured vapor (plus air) fraction of 0.20 (i.e., 20 percent), the R-113 vapor fraction is calculated to be 0.194 (i.e., 19.4 percent). Thus, the error due to the residual dissolved air was less than the uncertainty associated with the vapor fraction measurement (Table 1).

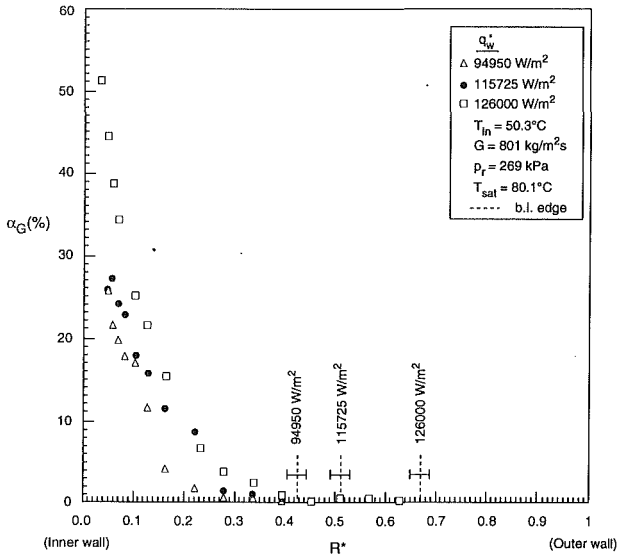

Fig. 5 Vapor fraction radial profiles at three wall heat fluxes

1 Vapor Phase Residence Time Fraction—Radial Distribution. Each measurement was repeated at least once and the average of the measured values was taken to be the local value.

Figure 5 shows vapor fraction radial profiles for three wall heat fluxes (94950, 115725, 126000 W/m^2) at the same fluid mass velocity (801 kg/m^{2}s), R-113 pressure at m.p. (269 kPa), and mean liquid temperature at test section inlet (50.3°C). The location of the boiling fluid layer (b.l.) outer edge is shown for each profile. This location was determined as follows: a best-fit curve was drawn through the data points in the vapor fraction range (0.0, 0.12) and the point of intersection of this curve with the 0.001 vapor fraction line was designated as the b.l. edge. An uncertainty estimate of the location is also shown in the figure.

It is apparent from the data that both the radial extent of the boiling fluid layer and the vapor fraction near the heated wall increase with wall heat flux. Vapor fraction data very near the heated wall were not obtained because the closest that we ventured to the wall was 0.5 mm (0.4 mm in a few experiments).

In Fig. 6, we present radial distributions of vapor fraction for two fluid mass velocities (579, 801 kg/m^{2}s) at the same wall heat flux (94950 W/m^2), R-113 pressure at m.p. (269 kPa), and mean liquid temperature at test section inlet (43.0°C). The b.l. edge locations are shown also. As expected, the boiling

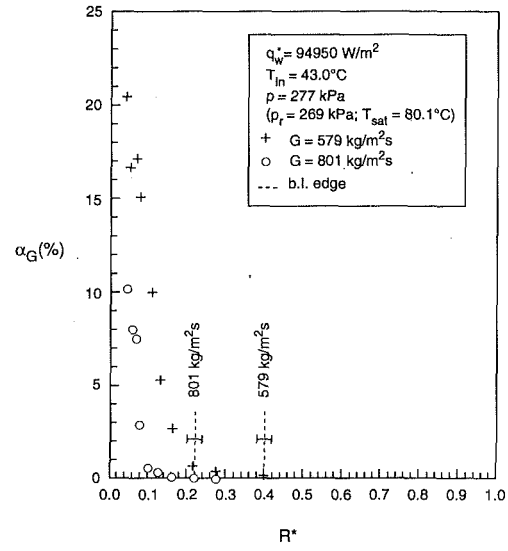

Fig. 6 Vapor fraction radial profiles at two fluid mass velocities

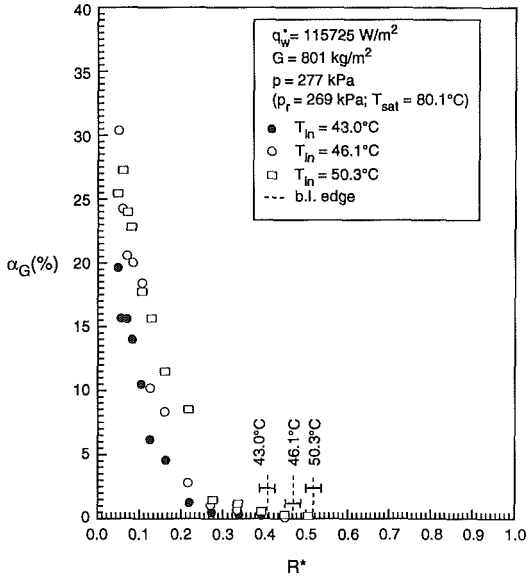

Fig. 7 Vapor fraction radial profiles at three inlet liquid subcoolings

fluid layer is thicker at the lower mass velocity. The vapor fraction near the heated wall is higher as well at the lower mass velocity.

Figure 7 shows the radial profiles of vapor fraction for three mean liquid temperatures at the test section inlet (43.0, 46.1, 50.3°C) with the same wall heat flux (115725 W/m^2), fluid mass velocity (801 kg/m^{2}s), and R-113 pressure at m.p. (269 kPa). At lower liquid subcooling, the vapor condensation rate is smaller and more vapor bubbles survive. As such, the transverse extent of the boiling fluid layer is larger as is the vapor fraction in the layer.

2 Vapor Bubbles—Size Distribution. In Figs. 8(*a*, *b*), we show the PDFs of bubble chord length and diameter, $\rho_c(x)$ and $\rho_d(D)$, respectively, at one location in the boiling fluid layer ($R^* = 0.163$) and two inlet liquid subcoolings. The vapor fraction profiles for these two conditions are given in Fig. 7. The chord length PDFs were obtained directly from the fiber-optic probe data. The diameter PDFs were then calculated by Eqs. (1) and (2). At the higher liquid subcooling ($T_{in} = 43.0$°C), the local vapor fraction is about 4 percent and the most probable bubble diameter about 1.2 mm. The largest bubble diameter

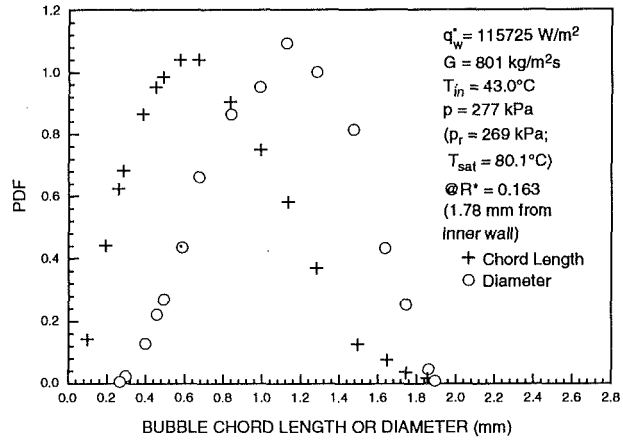

(a) At Higher Liquid Subcooling

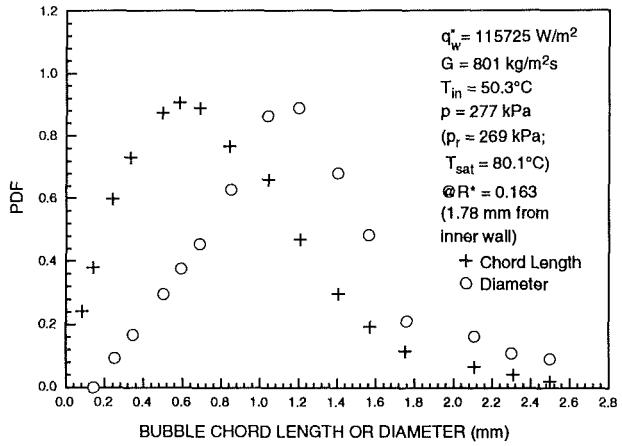

(b) At Lower Liquid Subcooling

Fig. 8 Vapor bubble size distribution at the same radial location for two inlet liquid subcoolings

is roughly 1.9 mm but such a bubble has a very small probability of existence. At the lower liquid subcooling ($T_{in} = 50.3$°C), the local vapor fraction is about 11 percent and the most probable bubble diameter about 1.2 mm. However, nonzero probability persists till larger bubble diameters (>2.5 mm). That larger vapor bubbles are found when the liquid is less subcooled is reasonable. The larger bubbles are partly responsible for the higher local vapor fraction at lower subcooling. Another contributor to higher vapor fraction is the closer packing of the bubbles as indicated by a higher rate of bubble detection by the fiber-optic probe.

The Sauter mean diameter of vapor bubbles can be calculated from the bubble diameter PDF. The Sauter mean diameter is defined as (American Society of Testing and Materials, 1988):

$$\overline{D}_{sm} \equiv \frac{\sum_i D_i^3}{\sum_i D_i^2} \tag{3}$$

where D_i is the diameter of the ith bubble. Figures 9(*a*, *b*, *c*) show the radial distributions of the most probable bubble diameter and the Sauter mean bubble diameter in the boiling fluid layer for the three experiments of Fig. 7. The corresponding bubble detection rates are also shown. Bubble diameter values could not be obtained in the outer part of the boiling layer because the bubble detection rate became rather

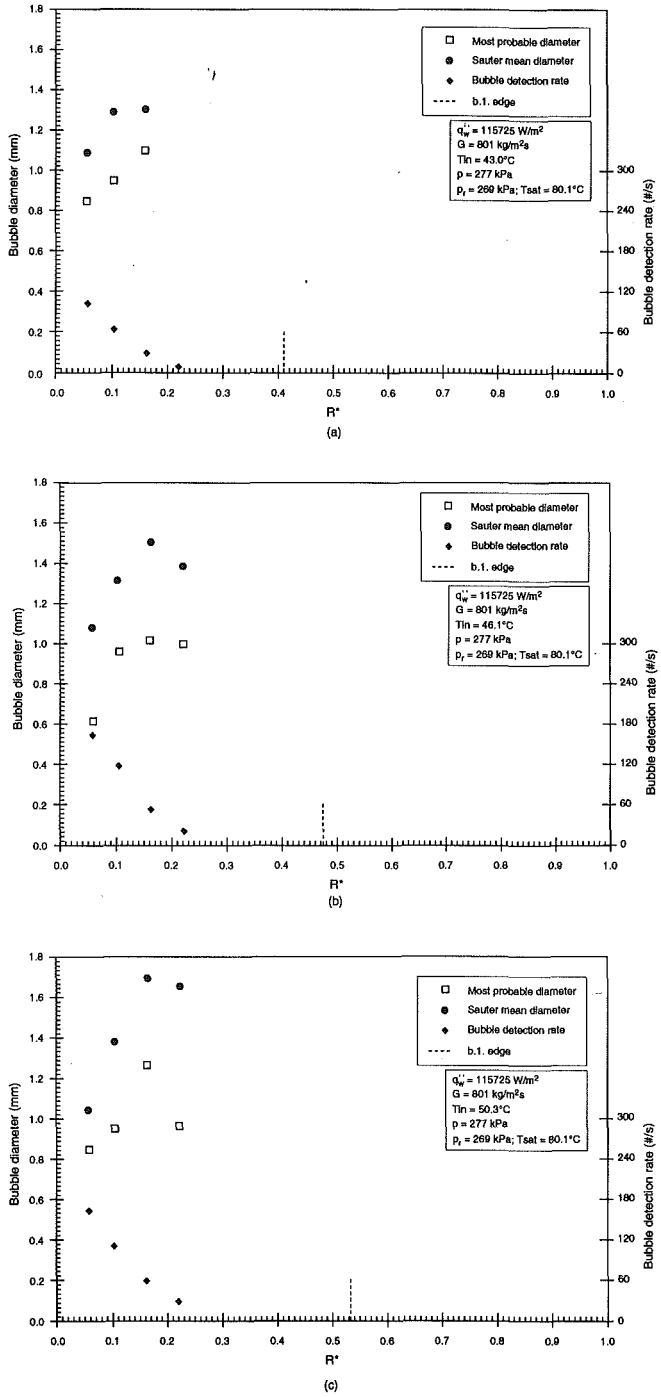

Fig. 9 Radial distributions of vapor bubble size and detection rate at three inlet liquid subcoolings

low. As such, it was not possible to construct meaningful bubble chord length PDFs.

The bubble detection rate falls significantly as we move away from the heated wall. A contributor to this decrease is the radial spreading of the boiling layer. For example, if we assume that there is no bubble coalescence and no bubble condensation, a reduction of about 20 percent can be expected in the bubble detection rate in going from $R^* = 0.058$ to $R^* = 0.221$ (the locations closest to and farthest from the heated wall in Figs. 9(*a*, *b*, *c*) detection rate data). The actual reduction in bubble detection rate is considerably more, however, suggesting occurrence of bubble coalescence and condensation.

As for the bubble diameter radial distribution, the bubbles are relatively small near the heated wall although the vapor fraction is high there. The bubble size first increases as one moves away from the wall. This is another indication of bubble coalescence. Farther from the wall, the bubble diameter decreases again. The vapor fraction is low in this region as is the bubble detection rate. An increased vapor condensation rate may be suggested as the cause of the decrease in bubble diameter. It should be noted also that the bubble size is generally larger at lower liquid subcoolings, Fig. 9(*b*, *c*).

3 Vapor Bubbles—Axial Velocity Distribution. The fiber-optic sensors detect the passages of vapor–liquid interfaces as vapor bubbles flow. The velocity measured by the sensors may thus be termed the *interface velocity*. For spherical bubbles, the interface velocity may be equated to the bubble velocity provided the bubbles neither grow nor shrink. Since the dominant flow direction in our experiments was axial and the two sensors were juxtaposed along the axial direction, the axial interface velocity was measured. The time-mean *bubble axial velocity* ($\overline{U}_g$) and *interface axial velocity* ($\overline{U}_s$) are assumed to be equal in this work.

As mentioned earlier, the cross-correlation technique was utilized for the velocity measurements. The time displacement τ corresponding to the sharp peak of the cross-correlation function (CCF) was used to calculate the most probable bubble axial velocity. Figure 10(*a*) shows the radial profile of this velocity for experiments at two wall heat fluxes (94950, 115725 W/m^2) and the same fluid mass velocity (801 kg/m^{2}s), R-113 pressure at m.p. (269 Pa), and mean liquid temperature at test section inlet (43.0°C). The vapor fraction profiles for these experiments can be found in Figs. 6 and 7. The bubble size distribution for the higher heat flux case is contained in Fig. 9(*a*). Also shown in Fig. 10(*a*) are: (*i*) a liquid mean axial velocity profile measured in single-phase flow at the same mass velocity, a lower wall heat flux, and a higher m.p. pressure, and (*ii*) the estimated liquid mean axial velocity profile in a part of the boiling fluid layer for the case of 115725 W/m^2 wall heat flux. The latter profile was obtained by estimating the local relative velocity between the vapor bubbles and the liquid, given the measured vapor fraction (Zuber and Findlay, 1965):

$$(\overline{U}_{\text{relative}}) = 1.53 \left[\frac{\sigma_g(\rho_l - \rho_v)}{\rho_l^2}\right]^{1/4} (1-\alpha_G)^{1/2} \qquad (4)$$

The data in Fig. 10(*a*) suggest that, in vertical upflow, bubbles in a higher vapor fraction boiling layer travel with a larger axial velocity than bubbles in a lower vapor fraction boiling layer. Of course, the bubbles are, on the average, larger in the former condition. A comparison of the liquid axial velocity profile in nonboiling flow with the estimated liquid axial velocity profile in the boiling layer indicates that these profiles are quite different, the liquid generally traveling faster and having a steeper velocity gradient near the heated wall in the latter condition. This is a tentative observation only since we did not measure the liquid velocity in the boiling fluid layer.

Figure 10(*b*) shows the radial profiles of the most probable bubble axial velocity for experiments at two mean liquid temperatures at the test section inlet (50.3, 43.0°C) with the same wall heat flux (94950 W/m^2), fluid mass velocity (801 kg/m^{2}s), and R-113 pressure at m.p. (269 kPa). The vapor fraction profiles for these experiments are given in Figs. 5 and 6. The data in Fig. 10(*b*) indicate that vapor bubbles travel with higher axial velocity at lower liquid subcooling. This is a reasonable trend since the boiling fluid layer at a lower liquid subcooling has, on the average, higher vapor fraction and larger bubbles.

In reality, bubbles of different sizes can be expected to travel at different velocities. This leads to a statistical distribution of the bubble (or interface) velocity at any given location in the boiling layer. It has been suggested that if the mean flow is in the axial direction and it is assumed that the probability

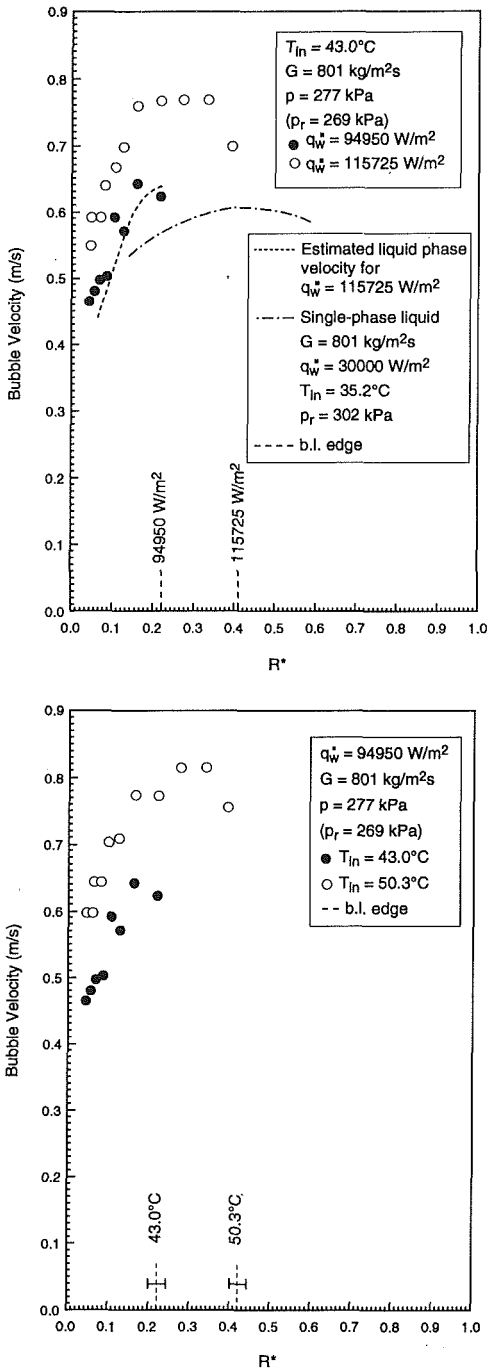

Fig. 10 (*a*) Radial distributions of most probable vapor bubble axial velocity at two wall heat fluxes; (*b*) radial distribution of most probable vapor bubble average axial velocity at two inlet liquid subcoolings

density of the flow velocity is peaked in this direction, then the mean square of the bubble axial velocity fluctuations is an important parameter in the determination of the local time-averaged interfacial area concentration $\bar{a}_i$ (Kataoka et al., 1986).

The PDF of the interface (or bubble) axial velocity can be determined directly from dual-sensor data if the distribution of the interface transit time between the two sensors can be obtained (Kataoka et al., 1986). This was not done in our study. Instead, the PDF was determined from the CCF of the two sensor signals and the auto-correlation function (ACF) of the upstream sensor signal. The procedure is as follows:

Let $x_1(t)$ and $x_2(t)$ denote the upstream and downstream sensor signals, respectively. $R_{x_1x_1}(\tau)$ is the ACF of the upstream sensor signal and $R_{x_1x_2}(\tau)$ the CCF of the two signals. We assume that

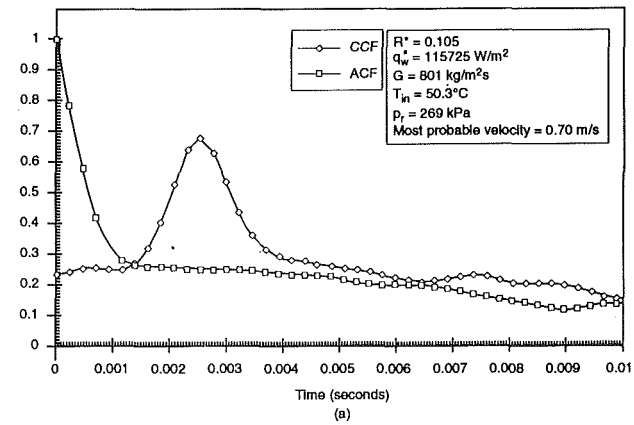

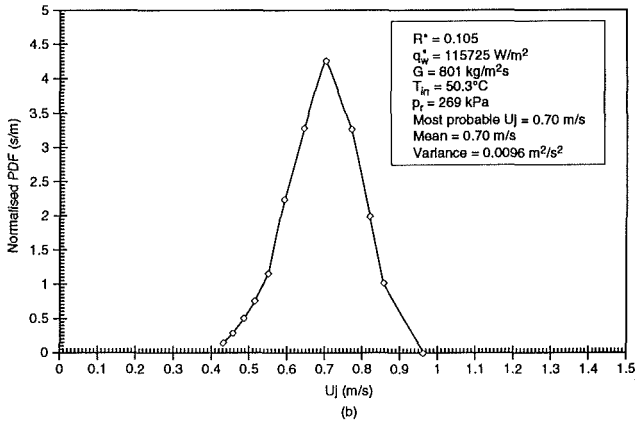

Fig. 11 (*a*) Auto- and cross-correlation functions of two sensor signals at a location in the boiling layer; (*b*) calculated probability density function of the interface (bubble) axial velocity

$$x_1(t) = x_2\left(t + \frac{d}{U_s}\right) \tag{5}$$

where d is the axial spacing between the sensors and U_s the interface axial velocity. Equation (5) implies that x_2 is identical to x_1 except for being shifted by the time interval d/U_s, where U_s may be random. The CCF is then given by

$$R_{x_1x_2}(\tau) = \int_0^\infty R_{x_1x_1}\left(\tau - \frac{d}{U_s}\right) p(U_s)\,dU_s \tag{6}$$

where $p(U_s)dU_s$ is the probability of the interface axial velocity being between U_s and $U_s + dU_s$. Equation (6) may be approximated as:

$$R_{x_1x_2}(\tau_i) \cong \sum_{j=1}^{N} R_{x_1x_1}(\tau_i - d/U_{sj})\,p(U_{sj})\,dU_{sj} \tag{7}$$

Equation set (7), $i = 1, \ldots, N$, enables determination of probability densities $p(U_{sj})$, $j = 1, \ldots, N$, and hence the PDF. The variance of the interface axial velocity, σ_U^2, can be calculated from this PDF and used in the estimation of the local time-averaged interfacial area concentration, $\bar{a}_i$.

Figure 11(*a*) shows the CCF of the sensor signals and the ACF of the upstream sensor signal at radial location $R^* = 0.105$ in the boiling fluid layer for the experiment at wall heat flux 115725 W/m², fluid mass velocity 801 kg/m²s, R-113 pressure at m.p. of 269 kPa, and mean liquid temperature of 50.3°C at the test section inlet. The most probable interface axial velocity calculated from the CCF is noted in the figure. The interface axial velocity PDF is shown in Fig. 11(*b*). The corresponding most probable interface axial velocity is noted also and is, of course, equal to the value obtained from the CCF.

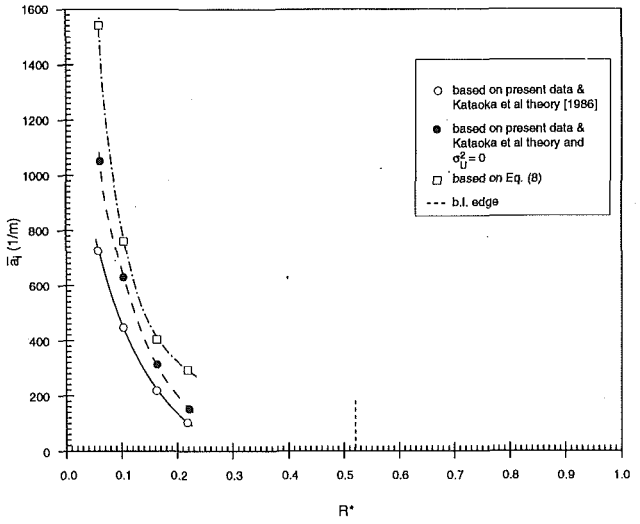

Fig. 12 Radial distribution of interfacial area concentration for an experiment

4 Local Time-Averaged Interfacial Area Concentration—Radial Distribution. The method suggested by Kataoka et al. (1986) for determining the local time-averaged interfacial area concentration, $\bar{a}_i$, involves the use of the mean and the variance of the interface axial velocity, $\overline{U}_s$ and σ_U^2, respectively, to calculate α_o, the maximum angle between the interface velocity and the axial direction. $\bar{a}_i$ is then calculated from α_o, $\overline{U}_s$, and N_t, the number of bubbles that pass through the specific location in the boiling layer per second. The radial distribution of $\bar{a}_i$ calculated by this method for the experimental condition of Fig. 11 is shown in Fig. 12. The values of α_o ranged between 19 and 24 deg.

Another method of calculating the local time-averaged interfacial area concentration uses the relation

$$\bar{a}_i = \frac{6\alpha_G}{\overline{D}_{sm}} \tag{8}$$

where $\overline{D}_{sm}$, the Sauter mean bubble diameter, is given by Eq. (3). Direct comparison of $\bar{a}_i$ calculated by Eq. (8) with that calculated by the method of Kataoka et al. would not be appropriate because inherent in our calculation of $\overline{D}_{sm}$ is the assumption that bubble axial velocity is independent of its size. A simplified way to incorporate this assumption in the method of Kataoka et al. would be to set $\sigma_U^2 = 0$, which is tantamount to setting $\alpha_o = 0$. The values of $\bar{a}_i$ based on this scenario are also plotted in Fig. 12 as are the $\bar{a}_i$ values obtained from Eq. (8). While the values of $\bar{a}_i$ from Eq. (8) are consistently higher, they are of the same order of magnitude. It is also apparent that further work is needed before $\bar{a}_i$ in bubbly boiling flow can be determined satisfactorily.

5 Liquid and Vapor Temperatures—Radial Distributions. Depending upon whether vapor or liquid surrounds the microthermocouple junction at any particular time, the microthermocouple, ideally, senses the corresponding phase temperature. Some limitations are, however, introduced into the temperature sensing process by the 3.4 ms microthermocouple time constant, as well as possible wetting of the junction and the finite time required for it to dry.

In the following, by the term *fluid* we mean *liquid* when in the all-liquid region and *liquid and vapor* when in the boiling layer. The microthermocouple signal represents the fluid temperature at any given location. When in the boiling layer, it becomes necessary to extract information about the individual phase temperatures from the fluid temperature signal. One method of doing this is to construct a PDF of the signal and then methodically separate the PDF into two PDFs, one for the liquid phase and the other for the vapor phase. We separated the PDF on the basis of the following criteria: (*i*) the mean vapor temperature should be close to the local saturation temperature and the vapor temperature PDF should be approximately symmetric[2]; (*ii*) although the liquid remains, on the average, subcooled, a thin superheated liquid layer is present around each vapor bubble (Delhaye et al., 1973) causing the liquid temperature PDF to exhibit a tail in the superheated region; and (*iii*) the ratio (area of the vapor temperature PDF)/(area of the fluid temperature PDF) should be close to the local vapor residence time fraction as measured by the fiber-optic probe (for example, within ±15 percent of the value). Once the PDFs are separated, the liquid and vapor mean temperatures and fluctuation intensities can be determined.

Figure 13(*a*) depicts the fluid, liquid, and vapor temperature PDFs at one radial location in the boiling fluid layer ($R^* = 0.07$). Figures 13(*b*, *c*) contain, respectively, the mean fluid and liquid temperature radial distributions and the corresponding temperature fluctuation intensity distribution for the experiment at wall heat flux of 115725 W/m^2, fluid mass velocity of 801 kg/m^{2}s, R-113 pressure at m.p. of 269 kPa, and mean liquid temperature of 43.0°C at test section inlet. We observe from Fig. 13(*b*) that the liquid phase remains subcooled (in the mean sense) to $R^* = 0.04$ and possibly even closer to the heated wall. The liquid temperature fluctuation intensity is seen to be substantial in the boiling fluid layer, Fig. 13(*c*). It is suggested that the intensity at any location in the boiling layer depends mainly on: (*i*) the local vapor fraction, which is proportional to the frequency of bubble (interface) passage, and (*ii*) the local liquid subcooling, which varies between a low in the thin thermal layer around the bubbles and a high away from the bubbles. The liquid temperature fluctuation intensity increases with the frequency of bubble passage. An increase in the local liquid subcooling also enhances the intensity because the range of temperature sensed is larger. We observe in Fig. 13(*c*) that the liquid temperature fluctuation intensity first increases as the heated wall is approached followed by a decrease. While the bubble passage frequency increases as the wall is approached, the liquid subcooling diminishes, the effects on the intensity being opposite. Also, except at the bubble nucleation sites, the wall temperature fluctuation intensity acts as the boundary condition for the liquid temperature fluctuation intensity. The intensity at the wall should be low due to the significant thermal inertia of the wall.

Two comments are appropriate here. First, along with the mean liquid temperature distribution in the boiling layer, data on the distribution of liquid temperature fluctuation intensity are important for turbulence modeling. A viable approach to modeling of turbulent heat flux in the liquid phase is based on two equations: One equation governs the transport of temperature fluctuation variance and the other its rate of dissipation (So et al., 1993). Second, although the present microthermocouple is significantly faster than the one used in our earlier work, it still attenuated temperature fluctuations at higher frequencies (>50 Hz) to some extent.

Figures 14(*a*, *b*) show, respectively, the mean fluid and liquid temperature radial distributions and the fluid and liquid temperature fluctuation intensity radial distributions for an experiment at the same wall heat flux, mass velocity, and pressure as the previous case but a test section inlet liquid temperature of 50.3°C. Compared to the Fig. 13(*b*) data, the liquid is less subcooled at the measurement plane, Fig. 14(*a*). The liquid temperature fluctuation intensity is lower than in the previous experiment, a trend that indicates a strong influence of the local liquid subcooling.

[2]This temperature distribution is possibly due to local pressure fluctuations, which lead to fluctuations in vapor temperature.

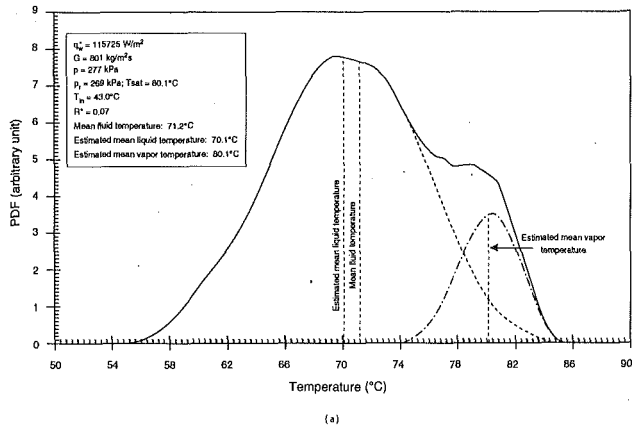

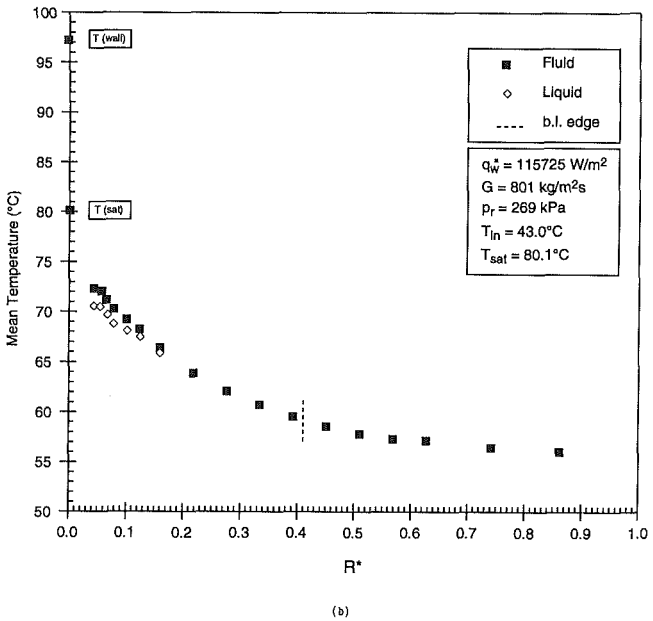

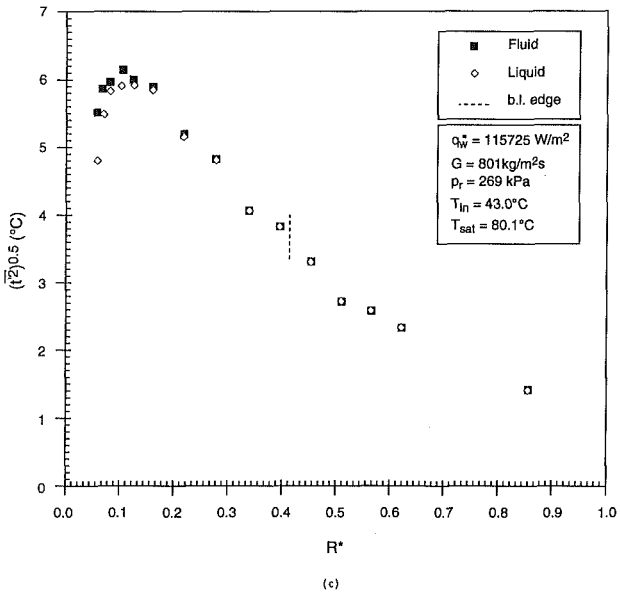

Fig. 13 (*a*) A typical fluid temperature PDF; (*b*) radial distributions of mean fluid and liquid temperatures; (*c*) radial distributions of fluid and liquid temperature fluctuation intensities

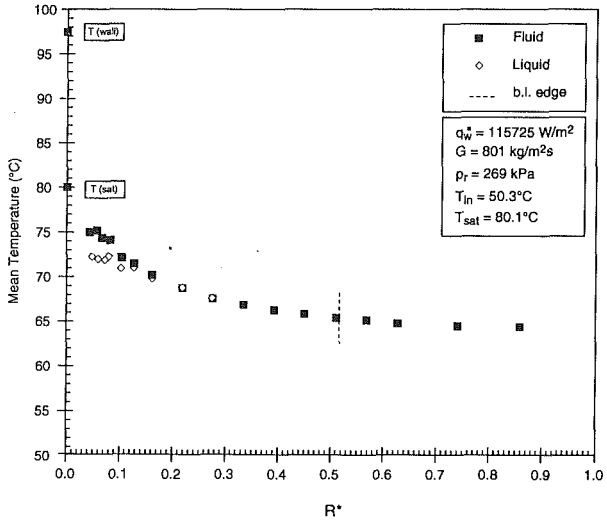

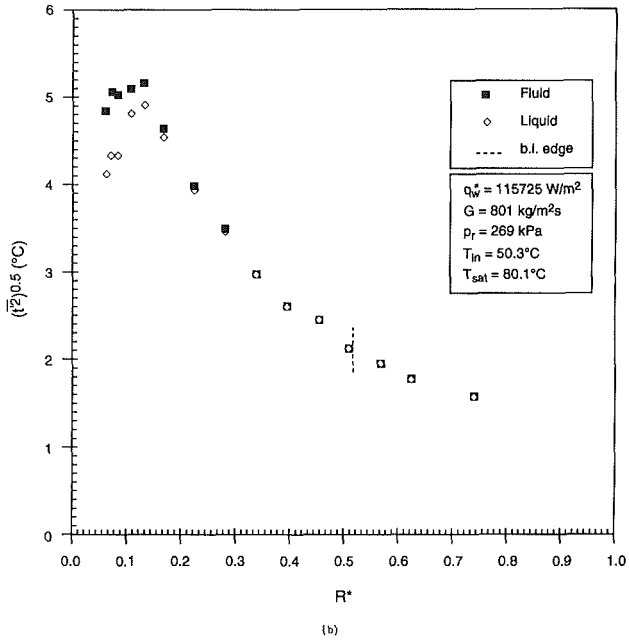

Fig. 14 (*a*) Radial distributions of mean fluid and liquid temperatures; (*b*) radial distributions of fluid and liquid temperature fluctuation intensities

Concluding Remarks

The reported measurements are results of our continuing effort to study the fundamental characteristics of turbulent subcooled boiling flow. The objective of this effort is to facilitate the development and subsequent validation of a multidimensional turbulent subcooled boiling flow model. Development of the model is in progress.

A few comments about the measurements are in order. The fiber-optic probe is among the fastest and least disruptive probes available for local vapor fraction measurement. It is possible, by means of dual-sensor fiber-optic probes, to obtain information regarding the distributions of size and velocity in the dominant flow direction of vapor bubbles. It is also possible to estimate the local time-averaged interfacial area concentration. While the assumption of spherical bubble shape is reasonable for small bubbles (for example, <2 mm diameter), a study of bubble shape by a three-dimensional imaging technique would be important. It would also be desirable to meas-

ure the transverse motion of the bubbles. A multisensor fiber-optic probe with the sensors arranged judiciously (similar in principle to the resistivity probe of Ishii and Revankar, 1992) should be useful.

The chromel-alumel microthermocouple used in these measurements is quite fast (time constant with phase-lead compensation ≈ 3.4 ms). It would, however, be important to construct microthermocouples that are inherently faster (for example, time constant without phase-lead compensation ≈ 2 ms). Caution should be exercised regarding the extent of time constant reduction by phase-lead compensation. This is to reduce the possibility of nonphysical amplification of high-frequency temperature fluctuations in the fluid by the compensation circuit.

Finally, it is imperative that the turbulence characteristics of the liquid phase velocity field be measured. We have, so far, performed some measurements only in the all-liquid region of subcooled boiling flow (Roy et al., 1993) and have just commenced measurements in the boiling layer.

Acknowledgments

This research was partially funded by the National Science Foundation, Thermal Sciences Program, Division of Chemical and Thermal Systems under Grant No. CTS-8918830. Funding from Electric Power Research Institute and Electricité de France is also gratefully acknowledged.

References

American Society for Testing and Materials, 1988, "Standard Practice for Determining Data Criteria and Processing for Liquid Drop Size Analysis," ASTM E 799-87.

Beckman, P., Roy, R. P., Whitfield, K., and Hasan, A., 1993, "A Fast-Response Microthermocouple," *Review of Scientific Instruments*, Vol. 64(10), pp. 2947-2951.

Cartellier, A., 1990, "Optical Probes for Local Void Fraction Measurements: Characterization of Performance," *Review of Scientific Instruments*, Vol. 61(2), pp. 874-886.

Delhaye, J. M., Semeria, R., and Flamand, J. C., 1973, "Void Fraction, Vapor and Liquid Temperatures; Local Measurements in Two-Phase Flow Using a Microthermocouple," ASME JOURNAL OF HEAT TRANSFER, Vol. 95, pp. 363-370.

Dix, G. E., 1971, "Vapor Void Fraction for Forced Convection With Subcooled Boiling at Low Flow Rates," General Electric Report NEDO-10491.

Hasan, A., Roy, R. P., and Kalra, S. P., 1991, "Some Measurements in Subcooled Flow Boiling of Refrigerant-113," ASME JOURNAL OF HEAT TRANSFER, Vol. 113, pp. 216-223.

Herringe, R. A., and Davis, M. R., 1976, "Structural Development of Gas-Liquid Mixture Flows," *Journal of Fluid Mechanics*, Vol. 73(1), pp. 97-123.

Hino, R., and Ueda, T., 1985a, "Studies on Heat Transfer and Flow Characteristics in Subcooled Flow Boiling—Part 1. Boiling Characteristics," *International Journal of Multiphase Flow*, Vol. 11(3), pp. 269-281.

Hino, R., and Ueda, T., 1985b, "Studies on Heat Transfer and Flow Characteristics in Subcooled Flow Boiling—Part 2. Flow Characteristics," *International Journal of Multiphase Flow*, Vol. 11(3), pp. 283-297.

Hishida, M., and Nagano, Y., 1978, "Simultaneous Measurements of Velocity and Temperature in Nonisothermal Flows," ASME JOURNAL OF HEAT TRANSFER, Vol. 100, pp. 340-345.

Ishii, M., and Revankar, S. T., 1992, "Interfacial Area and Phase Distribution Measurements in Two-Phase Flow With Four-Sensor Probe," *ANS Proceedings*, National Heat Transfer Conference, San Diego, CA, Vol. 6, pp. 85-92.

Jiji, L. M., and Clark, J. A., 1964, "Bubble Boundary Layer and Temperature Profiles for Forced Convection Boiling in Two-Phase Flow," ASME JOURNAL OF HEAT TRANSFER, Vol. 86, pp. 50-58.

Kataoka, I., Ishii, M., and Serizawa, A., 1986, "Local Formulation and Measurements of Interfacial Area Concentration in Two-Phase Flow," *International Journal of Multiphase Flow*, Vol. 12(4), pp. 505-529.

Revankar, S. T., and Ishii, M., 1992, "Local Interfacial Area Measurement in Bubble Flow," *International Journal of Heat and Mass Transfer*, Vol. 35(4), pp. 913-925.

Roy, R. P., Hasan, A., and Kalra, S. P., 1993, "Temperature and Velocity Fields in Turbulent Liquid Flow Adjacent to a Bubbly Boiling Layer," *International Journal of Multiphase Flow*, Vol. 19(5), pp. 765-795.

Shiralkar, B., 1970, "Local Void Fraction Measurements in Freon-114 With a Hot-Wire Anemometer," General Electric Report NEDE-13158.

So, R. M. C., and Sommer, T.P., 1993, "A Near-Wall Heat Transfer Turbulence Model for Different Prandtl Number Fluids," *Proceedings of Second International Symposium on Engineering Turbulence Modeling and Measurements*, Florence, Italy.

Walmet, G. E., and Staub, F. W., 1969, "Pressure, Temperature and Void Fraction Measurement in Nonequilibrium Two-Phase Flow," *Two-Phase Flow Instrumentation*, ASME, Eleventh National Heat Transfer Conference, Minneapolis, MN, pp. 89-101.

Zuber, N., and Findlay, J. A., 1965, "Average Volumetric Concentration in Two-Phase Flow Systems," ASME JOURNAL OF HEAT TRANSFER, Vol. 87, pp. 453-468.

Nucleate Pool Boiling of a TURBO-B Bundle in R-113

S. B. Memory
Department of Mechanical Engineering,
University of Miami,
Coral Gables, FL 33124

S. V. Chilman

P. J. Marto
Fellow ASME

Department of Mechanical Engineering,
Naval Postgraduate School,
Monterey, CA 93940

Heat transfer measurements were made during nucleate boiling of R-113 from a bundle of 15 electrically heated, copper TURBO-B tubes arranged in an equilateral triangular pitch, designed to simulate a portion of a flooded evaporator. Five of the tubes that were oriented in a vertical array on the centerline of the bundle were each instrumented with six wall thermocouples. For increasing heat flux, the incipient boiling wall superheat of upper tubes decreased as lower tubes were activated. In the boiling region at low heat fluxes (≈ 1 kW/m^2), the average bundle heat transfer coefficient was 4.6 times that obtained for a smooth tube bundle (under identical conditions) and 1.6 times greater than that obtained for a single TURBO-B tube; a similar bundle factor has been reported for a smooth tube bundle. At high heat fluxes (100 kW/m^2), the average bundle heat transfer coefficient was 3.6 times that of a smooth tube bundle. Furthermore, there was still a significant bundle factor (1.22), contrary to a smooth tube bundle, where all effect of lower tubes was eliminated at high heat fluxes.

Introduction

In recent years significant progress has been made in understanding nucleate boiling heat transfer and two-phase convection effects on the shell side of smooth tube bundles (Leong and Cornwell, 1979; Cornwell et al., 1980; Cornwell and Schuller, 1982; Wege and Jensen, 1984; Hwang and Yao, 1986; Cornwell and Scoones, 1988; Jensen and Hsu, 1988; Cornwell, 1989). These works observed the two-phase flow patterns and deduced that sliding bubbles from lower tubes on upper tubes, as well as liquid forced convection, could account for significant heat transfer in the top part of a bundle. This is known as bundle effect. There is much confusion in the literature regarding the use of the terms bundle *effect* and bundle *factor* and it is often not made clear which is being cited.[1] Bundle effect is defined as the ratio of the heat transfer coefficient for an upper tube in a bundle with lower tubes activated to that for the same tube activated alone in the bundle. Bundle factor is defined as the ratio of *average* heat transfer coefficient for the whole bundle to that of an isolated single tube of similar surface. In many cases, however, the data for a single isolated tube (which should ideally be taken in the same apparatus as the bundle) are not available and data taken from a single tube activated alone in the bundle are often used. Bundle factor is typically slightly lower than bundle effect and is obviously of more use to a designer who can simply use it with single tube data to estimate average bundle coefficients. For this reason, data tabulated later in this paper are presented as bundle factor.

The influence of tube position within a smooth tube bundle has also been extensively studied using R-11, R-12, R-22 and R-113 (Wallner, 1974; Fujita et al., 1986; Chan and Shoukri, 1987; Rebrov et al., 1989; Marto and Anderson, 1992). For both square and staggered tube arrangements with tube pitch-to-diameter ratios between 1.2 and 2.0, the influence of lower tubes in a bundle has been shown to increase the heat transfer significantly from upper tubes at low heat fluxes due to two-phase convection effects. At heat fluxes in the fully developed nucleate boiling region (>50 kW/m^2), the data for all tubes within the bundle merge and are representative of single tube behavior. Furthermore, these works seem to verify that heat transfer behavior at low and high heat fluxes can be predicted by interpolation formulas, combining pool boiling and forced convection contributions. Similar behavior has also been obtained for finned tube bundles (Hahne and Müller, 1983; Yilmaz and Palen, 1984; Müller, 1986).

There has been a limited amount of work on modified finned[2] and porous-coated tube bundles; the reader is referred to Jensen (1988) and Thome (1990) for good reviews in this area. For a THERMOEXCEL-E tube bundle, Arai et al. (1977) found a significant bundle factor of approximately 1.5 at low heat fluxes for three different bundle orientations. At higher heat fluxes (>30 kW/m^2) the bundle factor approached unity, the data agreeing closely with single THERMOEXCEL-E tube data; this earlier transition to single-tube behavior was attributed to domination of convection effects by nucleation at lower heat fluxes. For a porous coated surface, Czikk et al. (1970) and Fujita et al. (1986) found a bundle factor of unity over a wide range of heat fluxes (1–100 kW/m^2) and average bundle data agreed closely with single-tube data.

From the above, it is clear that two-phase interactions that occur in tube bundles during boiling can be very complex and change with heat flux level, fluid properties, tube surface, and tube bundle layout. Therefore, it is very difficult to use information from one type of bundle and fluid combination, and apply it to a different situation. Instead, a complete range of experimental data is needed in the open literature that covers various fluids, tube surfaces, bundle layouts, heat fluxes, and inlet qualities, so that theoretical models can be formulated and appropriately evaluated. This is particularly important in the refrigeration industry where new, alternative refrigerants and refrigerant-oil mixtures are being proposed.

For natural convection in bundles, the majority of published information is for air (Marsters, 1972; Sparrow and Niethammer, 1981; Sparrow and Boessneck, 1983; Tokura et al., 1983; Al-Alusi and Bushnell, 1992). Consequently, there is very little information regarding the onset of nucleate boiling in a bundle, bundle hysteresis effects, and the influence of surface history upon the incipient boiling condition. Marto and Anderson (1992) report these effects for a smooth tube bundle using pure

[1] In some cases, the present authors have had to use their judgment as to whether it is bundle factor or bundle effect that is being cited.

Contributed by the Heat Transfer Division and presented at the National Heat Transfer Conference, San Diego, California, August 9–12, 1992. Manuscript received by the Heat Transfer Division February 1993; revision received August 1993. Keywords: Boiling, Finned Surfaces, Refrigeration. Associate Technical Editor: V. K. Dhir.

[2] Modified finned tubes refer to finned tubes that have undergone some additional machining process, such as rolling, grooving, etc.

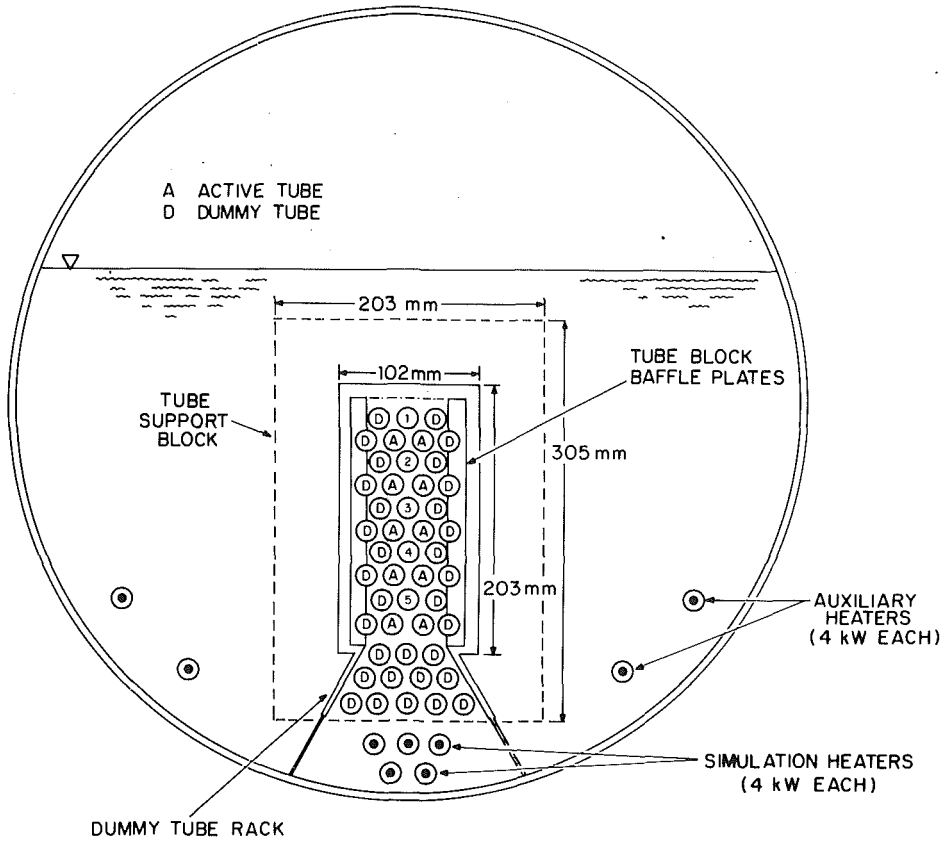

Fig. 1 Sectional view of evaporator

R-113 (pitch-to-diameter (P/D) ratio of 1.2) and found little effect of lower heated tubes on upper tubes in this region. Furthermore, the presence of heated lower tubes reduced the incipient boiling point and accompanying temperature overshoot of the upper tubes. Inagaki and Komori (1990) report natural convection data in water for a bundle of two horizontal smooth tubes for P/D ratios between 1 and 7. They obtained a maximum enhancement in the upper tube heat transfer at a P/D around 3; at a P/D of 1.2, no enhancement was found, consistent with that found by Marto and Anderson (1992). Unfortunately, no incipient boiling information is presented.

The present paper is a continuation of work started by Marto and Anderson (1992) on a smooth tube bundle. Its purpose is to shed further light on the mechanisms that affect bundle heat transfer by obtaining data from a bundle of enhanced tubes (TURBO-B) in R-113. It emphasizes the influence of tube position within the bundle in both the natural convection and boiling regions. The data are compared with the smooth tube data of Marto and Anderson (1992) and are expected to serve as reference data for comparison with other refrigerants from bundles of smooth and enhanced tubes. It should be noted that R-113 (a CFC) is not a common refrigerant and due to environmental concerns, will be completely phased out over the next few years. However, because of its convenient thermophysical properties, it has been widely used in the two-phase literature and thus provides a good basis for comparison when carrying out fundamental studies.

Experimental Apparatus

Full details of the experimental facility can be found in Marto and Anderson (1992). Essentially, it consisted of an evaporator and condenser arranged to provide reflux operation. The evaporator, shown schematically in Fig. 1, was fabricated from stainless steel plate, 0.61 m in diameter and 0.24 m long. The bundle consisted of 15 electrically heated enhanced tubes, which were cantilever-mounted from the back wall of the evaporator to permit easy viewing along the axis of the tubes through the lower of two glass windows mounted on the front. Ten of these tubes were active (marked '*A*') and contained 1 kW heaters; the remaining five were instrumented tubes (marked '1' through '5') each of which, in addition to 1 kW heaters, contained six wall thermocouples. The instrumented tubes were located along the centerline of a symmetric, staggered tube bundle as shown. Two auxiliary heaters, each capable of 4 kW, were installed on each side of the test bundle to maintain the pool at saturation conditions and to provide system pressure control. Five simulation heaters, also capable of 4 kW each, were mounted below the test bundle to simulate an additional 15 active tubes and to provide inlet vapor quality into the bottom of the test bundle. Each set of heaters (bundle, auxiliary and simulation) could be independently activated using three separate rheostat controllers.

The bundle also contained a number of unheated dummy smooth tubes (marked '*D*') that were used to guide the two-phase mixture through the bundle. Two vertical baffle plates were installed to restrict side circulation into and out of the bundle. To permit side entry of liquid into the bottom of the dummy tube rack, the area adjacent to the simulation heaters was left open. Thus, liquid circulation was vertically upward over the test tubes with no net horizontal component.

The enhanced tubes were made from commercially available TURBO-B copper tubing. The surface of the TURBO-B tube is made from a regular finned tube, which is then cross-grooved and rolled to provide a grid of rectangular flattened blocks that are wider than the original fins (see Fig. 2). The tubes are supplied in a variety of nominal diameters and (depending on the rolling process) size of flattened blocks (sometimes referred to as TURBO-B *S*, *M*, and *L*), thus providing differing gap widths to suit a particular application. The present tubes were

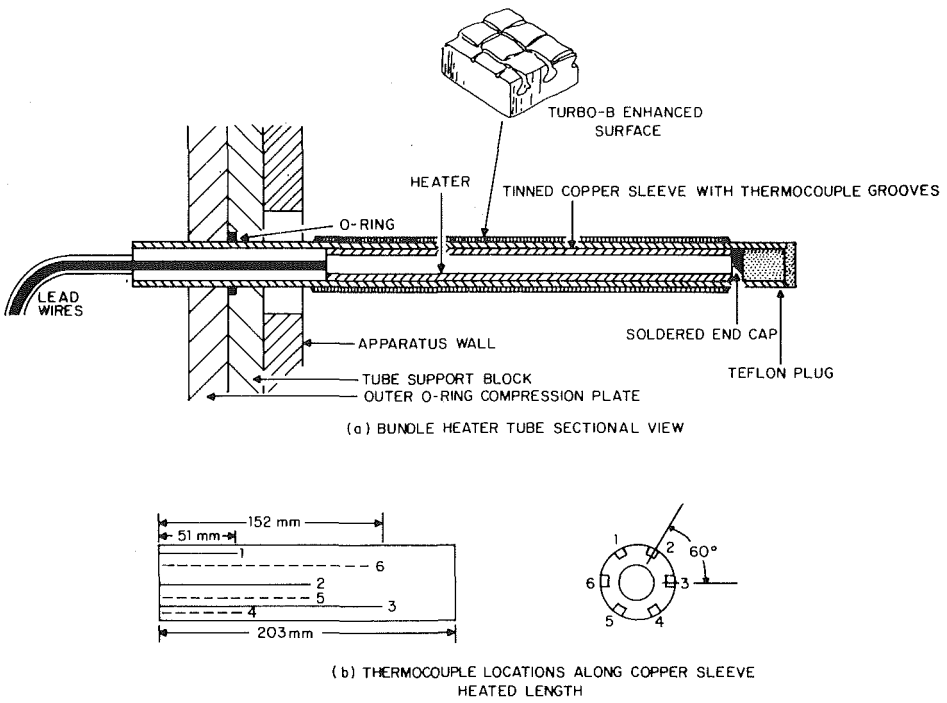

Fig. 2 Instrumented tube construction

TURBO-B *M* and had a diameter to the base of the enhancement (root diameter) of 14.2 mm. The thickness of the enhancement was 0.85 mm, giving a nominal outside diameter of 15.9 mm. When calculating heat flux, the root diameter has been used. If the surface area had been computed using the nominal outside diameter, a 12 percent decrease in heat flux would result. The 15 enhanced tubes were arranged in an equilateral triangular pitch with a centerline-to-centerline spacing of 19.1 mm, providing a pitch-to-outside diameter ratio (*P/D*) of 1.2. The heated length[3] of each tube was 190 mm.

In measuring boiling heat transfer coefficients, great care must be exercised with the cartridge heater and temperature measuring instrumentation to ensure good accuracy. Various installation techniques have been reviewed by Jung and Bergles (1989). Based upon extensive pool boiling data with R-113, they concluded that the heat transfer coefficient of a single tube in pool boiling is not sensitive to variations in the cartridge heater heat flux provided that enough thermocouples (at least four) are used to measure an average wall temperature. During this investigation, six thermocouples were used in each of the instrumented tubes. Figure 2 is a cross-sectional sketch of an instrumented tube showing the tube construction (cartridge heater, copper sleeve, and test tube) and the location of the six wall thermocouples. The fabrication procedure used for the enhanced tubes was the same as that used by Marto and Anderson (1992) for the smooth tubes; the reader is referred to Marto and Anderson for full details.

Measurements and Procedures

Vapor temperatures were measured by two thermocouples at the top of the condenser and one thermocouple near the top of the evaporator. Liquid temperatures were measured by three thermocouples, two located close to the free surface of the liquid and the third located at the bottom of the pool close to the dummy tube rack. During operation, the top two thermocouples were located in a frothy, two-phase mixture and were considered to be well representative of the saturation temperature at the free surface. All measurements were taken when all three liquid thermocouples indicated the same temperature, i.e., no subcooling in the pool. Full details of the experimental procedures are given by Marto and Anderson (1992).

The average outer wall temperature of the instrumented test tubes was obtained by averaging the six wall thermocouples in the copper sleeve and correcting for the small radial temperature drop due to conduction across the copper wall. The temperature drop across the solder joint between the copper sleeve and the test tube (estimated to be 0.05 mm) was neglected. During all the tests, the vapor pressure was kept at atmospheric and the liquid level was kept approximately 10 cm above the top row of tubes. The local saturation temperature for each tube in the bundle was then calculated using a hydrostatic pressure correction between the tube location and the free surface of the liquid (any pressure drop effects due to the two-phase flow in the bundle were neglected). For a given tube, the average heat flux was calculated by dividing the electrical power (after it was corrected for small axial losses from each end of the test tube) by the tube surface area (using the root diameter of the enhancement).

During this investigation, nucleate boiling data were obtained following two different surface aging procedures.[4] With the first procedure (surface aging *C*), the evaporator power was secured overnight. The following morning prior to taking data, the pool temperature was slowly brought up to saturation conditions using the auxiliary heaters; operation of the tubes then commenced with increasing heat flux in predetermined steps. In this way, boiling incipience and bundle start-up problems could be investigated. The second procedure (surface aging *D*) consisted of boiling the test bundle at 100 kW/m^2 for 30 minutes followed by immediate operation with decreasing heat flux in predetermined steps. Once the required heat flux in the evaporator had been fixed, the coolant flow through

[3]The heaters used were Watlow Firerod heaters, which were continuously wound with an 8 in. nominal length and a 7.5 in. actual heated length.

[4]Marto and Anderson (1992) used four different aging procedures, A, B, C, and D. Although they briefly discussed the results of procedures A and B, all the data presented by them were for procedures C and D.

the condenser was adjusted to maintain the saturation temperature corresponding to 1 atmosphere. It should be noted that the liquid recirculation pattern that existed in the evaporator prior to commencement of each experiment may have been affected by the different aging procedures. However, once the system was in operation, data were not taken until 10–15 minutes after start-up. Therefore, most of the recirculation variations would have disappeared prior to actually taking data. Nevertheless, due to possible variations in the recirculation pattern, the uncertainty of the first one or two data points taken at very low heat fluxes (following aging procedure *C*) may be larger than the uncertainties stated later in the paper.

Seven independent tests were conducted for increasing and decreasing heat flux. Tests 1 to 5 progressively activated the five instrumented enhanced tubes within the bundle (starting with only the top tube, i.e., tube 1 active) to see the effect of lower heated tubes on the performance of the upper tubes. Test number 6, in addition, looked at the effect of activating the remaining ten enhanced tubes around these instrumented tubes. All these tests were essentially carried out with zero quality entering the bottom of the bundle. Test number 7 included an inlet quality by activating the simulation heaters below the bundle. The power to these simulation heaters was varied to represent 15 additional active tubes operating at the same heat flux as the test bundle.

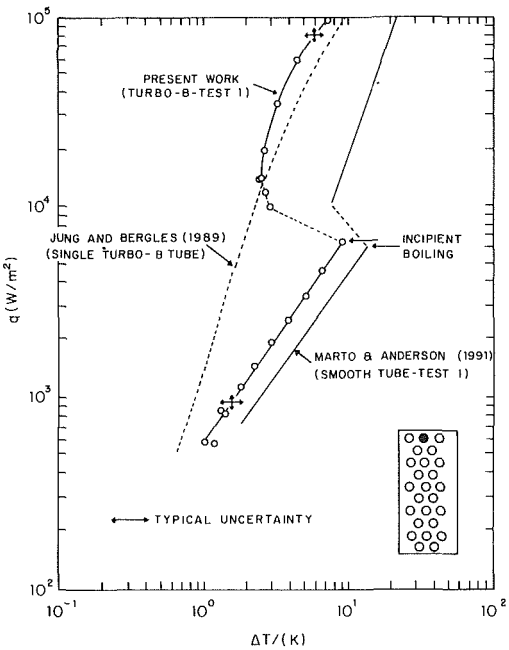

Fig. 3 Tube 1 operating alone with increasing heat flux (aging procedure *C*)

Results and Discussion

All data were obtained with R-113 at a pressure of 1 atm over a range of heat fluxes between 1 and 100 kW/m^2. During increasing heat flux runs, the onset of nucleate boiling was observed through the lower viewing window. This "point" was defined as the applied heat flux where first nucleation was observed on the instumented enhanced tubes. When heat flux is plotted versus the wall superheat (defined as the average wall temperature minus the saturation temperature), the "incipient boiling" condition is indicated by a dramatic change in slope since the heat transfer mechanism changes from single-phase convection to two-phase convection with the activation, growth, and departure of vapor bubbles.

The uncertainty in the experimental data was estimated using a propagation of error analysis. The uncertainty in the wall superheat was dominated by the uncertainty in the wall temperature measurements. At each operating point, the values of the six wall thermocouples were recorded and compared to examine variations in wall temperature caused either by nonuniformities in the cartridge heater coils or by the test tube soldering and assembly procedure. This problem has been explored in more detail by Wanniarachchi et al. (1986). The maximum variation of the six measured wall temperatures was 1.8°C at the maximum heat flux ($\approx$100 kW/m^2) and 0.4°C at the minimum heat flux ($\approx$1 kW/m^2). This variation appeared to be random and independent of thermocouple orientation and was probably caused by the tube soldering process. The uncertainty in the saturation temperature was estimated to be 0.1°C. These variations in wall temperature and saturation temperature created an estimated uncertainty in the wall superheat of $\pm$0.9°C at high heat fluxes and $\pm$0.2°C at low heat fluxes. For the heat flux, the uncertainty depends on the current and voltage measurements (which decrease relatively with increasing values) as well as the tube surface area measurement (which remains constant). The corresponding uncertainty in the measured heat flux was estimated to be 5 percent at low heat flux decreasing to 1.5 percent at high heat flux.

Throughout this investigation, the instrumented tubes located along the centerline of the tube bundle were numbered consecutively from the top downward as tubes 1, 2, 3, 4, and 5, respectively (Fig. 1). It was mentioned earlier that when using aging procedure *C*, the pool was slowly brought up to saturation conditions using the auxiliary heaters; these auxiliary heaters had to remain on throughout certain tests (with low numbers of activated tubes in the bundle) in order to maintain saturation conditions in the pool. It was found that the value at which the power to these auxiliary heaters was set significantly affected the data in the natural convection region: the higher their power setting, the higher the heat transfer. This is presumably due to the greater buoyancy-induced circulation from the auxiliary heaters enhancing the flow velocity across the tubes. Therefore, to eliminate any uncertainty due to their activation, all tests reported here were conducted with the auxiliary heaters set at 1 kW. The effect of the auxiliary heaters are discussed more fully by Memory et al. (1992) and Cerza et al. (1993).

Figure 3 shows the data for tube 1 operating alone as a single tube (test 1), during increasing heat flux (aging procedure *C*). Typical uncertainty bands for both q and ΔT are included at low and high heat fluxes; it can be seen that the uncertainty in ΔT is the more significant, especially at low heat flux. Also shown are the data of Marto and Anderson (1992) taken on the same apparatus for a smooth tube operating alone. In the natural convection region, both sets of data have the same slope, but the TURBO-B data indicate a significant increase in the heat transfer coefficient. This is probably due to the auxiliary heater settings, which were not carefully controlled in the experiments of Marto and Anderson (1992) and can significantly affect this region. The point of incipience occurs at a similar value of heat flux ($\approx$7 kW/m^2) for both types of tube and both sets of data demonstrate a significant temperature overshoot of about 7°C. In the boiling region, the TURBO-B tube yields a heat transfer coefficient three to four times that of the smooth tube, the enhancement decreasing as heat flux increases.

The increasing heat flux data of Jung and Bergles (1989) for pool boiling of a copper TURBO-B tube[5] in R-113 at 1 atm (100 mm heated length, 19.1 mm nominal outside diameter, 18 mm root diameter) are also included in Fig. 3 for comparison. Their data indicate no temperature overshoot, probably due to the different surface aging procedure used. Their tube was preboiled at a heat flux of 30 kW/m^2 for 30 minutes and

[5]The data of Jung and Bergles (1989) are also for the TURBO-B *M* tube.

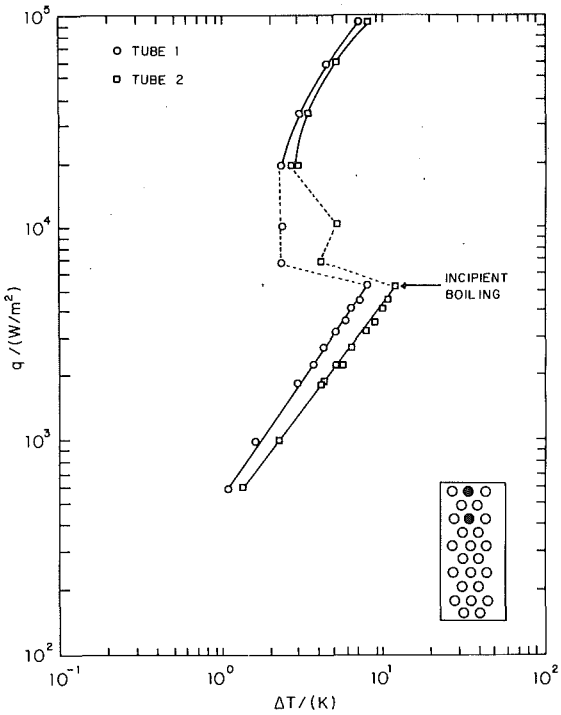

Fig. 4 Tubes 1 and 2 operating simultaneously with increasing heat flux (aging procedure *C*)

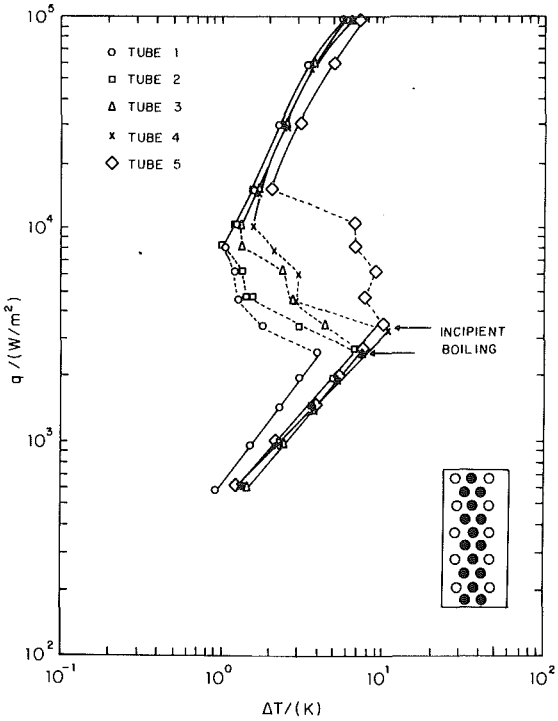

Fig. 5 Tube bundle operating with no simulation heaters with increasing heat flux (aging procedure *C*)

then deactivated until the thermocouples recorded the saturation temperature of the pool (length of time not given), indicating that the pool was not allowed to subcool overnight, in contrast to the present tests. Clearly, then, in addition to variations in local flow conditions, the incipient boiling characteristics depend upon the active site distribution on the boiling surface, which in turn depends upon the immediate past history of the heating surface and the temperature of the surrounding pool. In the fully developed nucleate boiling region, both sets of data are in reasonably good agreement. The small differences seen may be due to the presence of the closely packed bundle and the vertical baffle plates, generating a different liquid circulation pattern over tube 1.

Figure 4 shows the results for tubes 1 and 2 operating simultaneously (test 2), during increasing heat flux. The natural convection data of tube 1, compared to the data in Fig. 3 when operating as a single tube, show that there appears to be little influence of the lower heated tube (tube 2) upon the heat transfer of the upper tube (tube 1). However, the natural convection heat transfer coefficient for the lower tube is less than the upper tube. This behavior is exactly the same as that reported by Marto and Anderson (1992) for smooth tubes and may be due to expansion of the flow after it leaves the tightly packed bundle, i.e., there are differences in the velocity and temperature fields in the wake region of a heated tube within the bundle compared to those of a heated tube at the top of the bundle.

Figure 4 also shows that the incipient boiling heat flux is reduced to about 5 kW/m^2 for both tubes, although tube 2 shows an irregular nucleation process until higher heat fluxes are reached. This irregular behavior has been observed by Wanniarachchi et al. (1987) during boiling of R-114 from a single enhanced tube containing numerous nucleation sites. They attributed this behavior to incomplete nucleation along the boiling surface due to nonuniform heat flux or nonuniform cavity openings. Tube 1 displays a slightly smaller characteristic temperature overshoot (about 6°C) than shown in Fig. 3. Once fully boiling, tube 2 agrees very closely with tube 1 but with a slightly lower heat transfer coefficient.

In the natural convection region, similar behavior was also seen with three heated tubes (test 3), i.e., no apparent influence on tube 2, similar to that reported by Marto and Anderson (1992) for a smooth tube bundle. However, lower heated tubes do seem to influence the point of incipience, such that all three tubes partially nucleated at a lower heat flux (3 kW/m^2). This suggests that it is the lowest active tube in the bundle that first nucleates, which then "triggers" the tubes above, probably due to the increased activity within the pool caused by bubbles from below impinging on the upper tubes. In the fully developed nucleate boiling region, all three tubes exhibited similar behavior, with a decrease in heat transfer as one moves down the bundle. Similar results were also obtained when tubes 4 and 5 were activated (tests 4 and 5).

Figure 5 shows the behavior of tubes 1 through 5 when all 15 active tubes are heated as a bundle (test 6). In the natural convection region, tube 1 still exhibits a lower wall superheat than the other heated tubes. The main effect of having heated tubes around the five instrumented tubes is to reduce the heat flux at which incipience first occurs. The transition from natural convection to full nucleation for all five instrumented tubes occurs over a range of heat flux from 3 kW/m^2 to 16 kW/m^2 with the top tube reaching full nucleation first, followed by the other tubes in order down the bundle; however, this transition becomes more "erratic" as one moves down the bundle, i.e., lower tubes partially nucleate as they are affected by the nucleation of other tubes. In the fully developed boiling region, there is a small effect of tube position. Figure 6 shows the additional effect of including the simulation heaters below the bundle (test 7). The added inlet quality causes both the point of incipience and the temperature overshoot to decrease further for all five instrumented tubes; the top tube now starts nucleating at a heat flux of 1.5 kW/m^2 and has a temperature overshoot of only 1.5°C. Again, the data show that transition to full nucleation occurs in order down the bundle.

Due to the way in which the tubes were individually manufactured, making too many direct comparisons between data taken on different tubes can lead to misinterpretation. Of more validity is what happens to the top tube as successive tubes

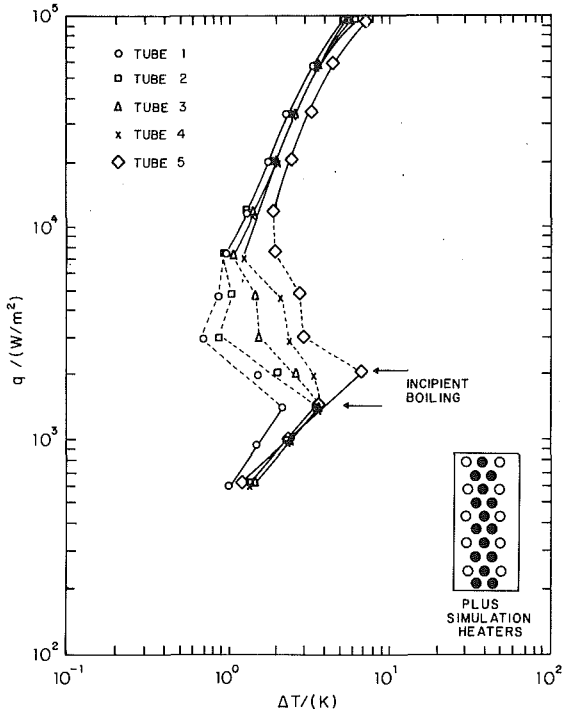

Fig. 6 Tube bundle operating with simulation heaters with increasing heat flux (aging procedure *C*)

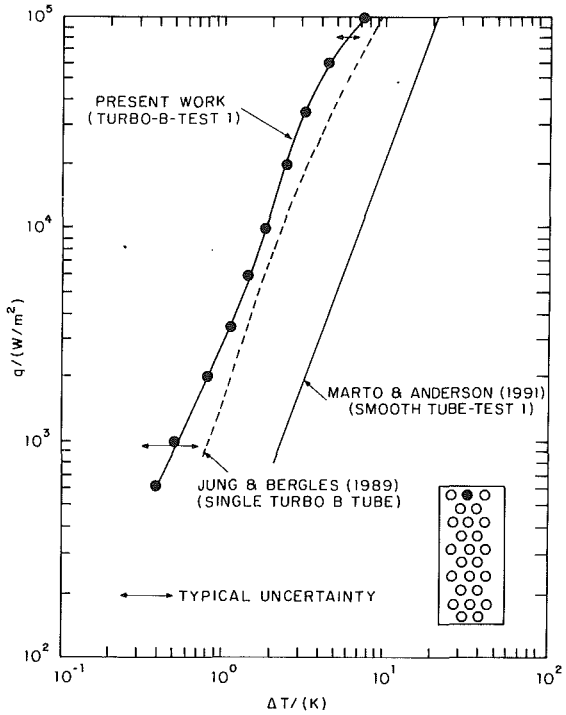

Fig. 8 Tube 1 operating alone with decreasing heat flux (aging procedure *D*)

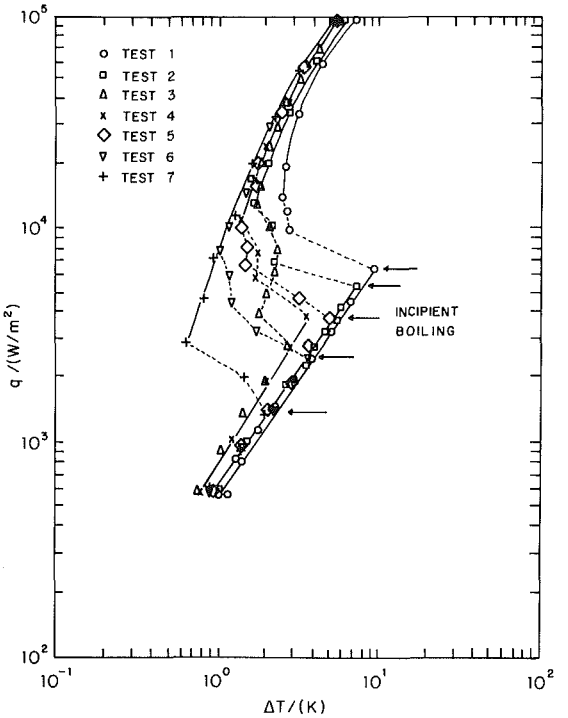

Fig. 7 Tube 1 operating for all seven tests with increasing heat flux (aging procedure *C*)

below it are activated. Figure 7 shows these data for tube 1 during all seven tests. In the natural convection region, it can be seen that the successive activation of lower tubes slightly enhances the performance of the top tube, as discussed above. There is also slight enhancement evident in the boiling region, larger than that reported by Marto and Anderson (1992) for a smooth tube bundle, indicating that the bubbles from a lower tube impacting on an upper tube still have an enhancing effect at these high heat fluxes. This is discussed in more detail below.

In the region between natural convection and fully developed nucleate boiling, Fig. 7 shows that the heat flux at which the incipient point occurs decreases steadily from 7 kW/m^2 for test 1 to 1.5 kW/m^2 for test 7. Furthermore, the temperature overshoot decreases from 7°C for test 1 to 1.5°C for test 7. These results seem to substantiate the idea that lower tubes "trigger" earlier nucleation on upper tubes. From a theoretical consideration of boiling incipience from an isolated surface (Hsu, 1962; Han and Griffith, 1965; Howell and Siegel, 1967), one may expect a lower incipient heat flux for an enhanced tube due to the high density of relatively large, uniform active cavities present on such a surface. This has been experimentally verified for single tubes by Memory and Marto (1992). However, comparison of the present work with that of Marto and Anderson (1992) shows that incipience occurs at a similar heat flux for both types of surface for all except test 7. This may be an indication that the flow velocities induced by the closely spaced tubes in the bundle are more important in the initiation of boiling than the cavity size.

For test 7, the data of Marto and Anderson (1992) show that for a smooth tube bundle, the presence of two-phase flow at the entry of the bundle (with a quality greater than zero) eliminates all evidence of temperature overshoot. This is in contrast to the present enhanced tube data, where there is still a small temperature overshoot for test 7. This difference in behavior between a smooth and enhanced tube (when both are influenced by two-phase flow at entry to the bundle) has also been found for a simple smooth and enhanced two-tube array by Memory et al. (1993). They found that for a smooth tube in natural convection, two-phase convection effects from below enhance the heat transfer to values similar to that of a nucleating smooth tube, hence eliminating all evidence of temperature overshoot. For an enhanced tube in natural convection, two-phase convection effects from below also enhance the heat transfer to values similar to that of a nucleating *smooth* tube. For decreasing heat flux, there is added heat transfer (due to the larger number of active nucleation sites) and thus temperature overshoot is never completely eliminated.

Figure 8 shows the data for tube 1 operating separately as

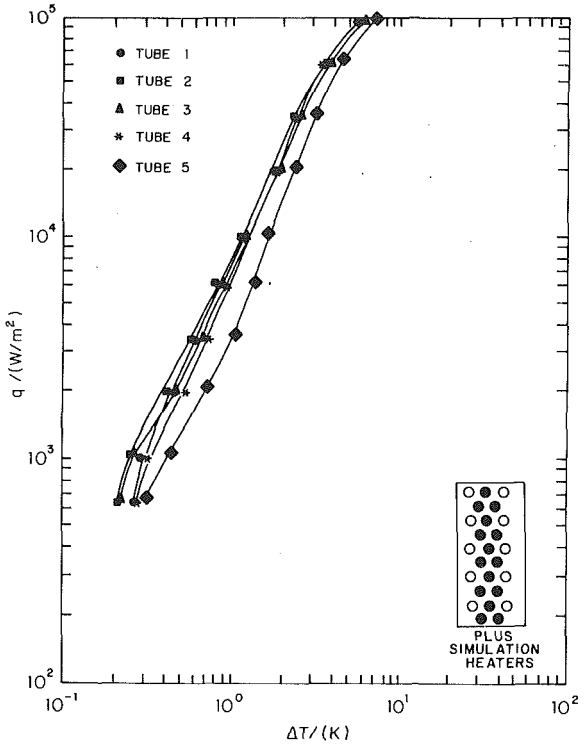

Fig. 9 Tube bundle operating with simulation heaters with decreasing heat flux (aging procedure *D*)

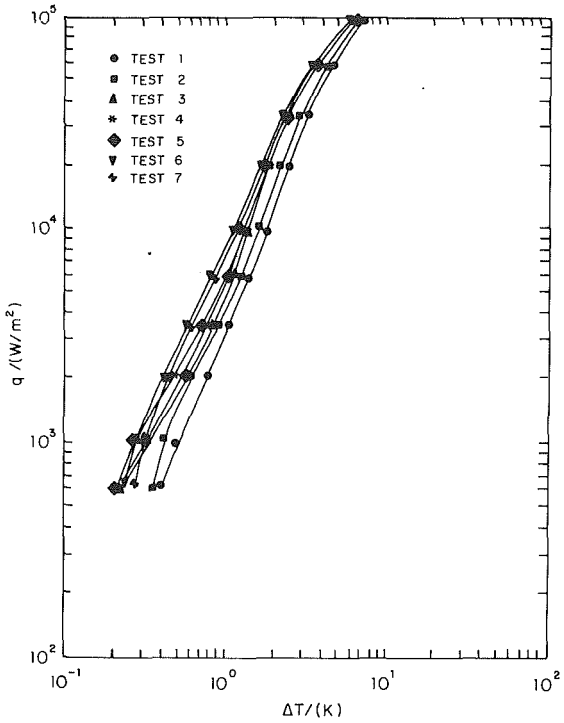

Fig. 10 Tube 1 operating for all seven tests with decreasing heat flux (aging procedure *D*)

a single tube (test 1) for decreasing heat flux (aging procedure *D*). Uncertainty bands for ΔT are again shown, indicating that care must be taken when interpreting results at low heat flux. When compared to Fig. 3 (increasing heat flux), the data show very good agreement at high heat fluxes and a definite hysteresis pattern at low heat fluxes. Also shown on Fig. 8 are the decreasing smooth tube data of Marto and Anderson (1992) for test 1 (taken on the same apparatus) and the decreasing single tube TURBO-B data of Jung and Bergles (1989). It can be seen that the two sets of TURBO-B data are in good agreement and both provide enhancements in the heat transfer coefficient of between 3 and 4 over the whole range of heat flux. For tests 2 to 5, the lowest active tube in the bundle always behaved just like tube 1 in Fig. 8 since there is no bubble impingement from below. The tubes above, however, were shifted to the left, indicating improvement in heat transfer due to the two-phase activity from below.

Figure 9 shows data for the whole bundle in operation plus the simulation heaters (test 7) for decreasing heat flux. From a comparison with Fig. 8, it is clear that the wall superheat of tube 1 has been significantly reduced by the presence of the activated bundle at all heat fluxes, improving heat transfer performance and indicating a definite bundle effect. Figure 10 shows the data for tube 1 only for all seven tests during decreasing heat flux. This figure demonstrates the bundle effect more clearly, having a value of about 1.4 at high heat fluxes, increasing to over 2 at low heat fluxes. When the data in Fig. 10 are compared to those in Fig. 7, it is clear that the decreasing heat flux data agree very well with the increasing heat flux data taken in the fully developed nucleate boiling region.

Marto and Anderson (1992) found similar bundle effects for a smooth tube bundle at low heat fluxes and attributed them to two mechanisms as postulated by Cornwell (1989). The first of these is due to local liquid forced convection, which is more important for smooth and finned tubes. The second is due to bubbles from lower tubes impinging on the upper tubes causing additional turbulence in the superheated liquid boundary layer. In addition, these bubbles can "trap" an evaporating microlayer between the heated surface and sliding bubble, creating very large heat transfer coefficients. One may expect this effect to be greater for an enhanced surface due to the higher number of active sites at low heat fluxes creating more bubble activity from below. However, this may be offset by greater nucleation from the surface itself, such that the added heat transfer from the effect of bubbles from below might be relatively small for an enhanced surface when compared to a smooth surface. A third mechanism that could further increase heat transfer when large sliding bubbles are present is secondary nucleation. Mesler and Mailen (1977) found that when a bubble bursts through a thin liquid film (such as an evaporating microlayer), many new bubbles grow from that location due to entrained vapor nuclei created from the bursting process. This mechanism would tend to be more important for an enhanced surface due to the higher active site density. It is hard to conjecture which of these mechanisms are dominant for the TURBO-B bundle at low heat fluxes, except to say that the behavior is probably bubble rather than convection related.

Table 1 summarizes the bundle factor for the smooth and TURBO-B tube bundles at three nominal heat fluxes: bundle factor here is not calculated using isolated single tube data, but single tube data taken from test 1. The average bundle heat transfer coefficient is averaged for all five instrumented tubes during test 7. The smooth tube bundle data are from Anderson (1989) taken on the same apparatus under similar conditions. It can be seen that at low heat fluxes, the TURBO-B surface provides a bundle factor of 1.61. This is very similar to the smooth and THERMOEXCEL-E tube bundle factors found respectively by Anderson (1989) and Arai et al. (1977). However, unlike these authors, who found that bundle operation gave no increase in bundle performance for heat fluxes greater that about 30 kW/m^2, the present data for TURBO-B still exhibit a bundle factor of 1.22 even at the highest heat flux of 100 kW/m^2. The present data are also contrary to the porous coated bundle data of Czikk et al. (1970) and Fujita et al. (1986) who essentially obtained a bundle factor of unity over the whole range of heat flux tested. It seems, therefore, that the mechanisms mentioned above may differ somewhat

Table 1 Comparison of TURBO-B and smooth tube bundles

	Heat-Transfer Coefficient/(W/m²K)		
Heat Flux/ (kW/m²)	1.5	10	100
Smooth Bundle			
Test 1	488	1511	4658
Test 7	790	1782	4670
Bundle Factor(a)	1.62	1.18	1.00
TURBO-B Bundle			
Test 1	2263	5279	13770
Test 7	3654	8010	16770
Bundle Factor(a)	1.61	1.52	1.22
Enhancement (Test 7)(b)	4.6	4.5	3.6

(a) Bundle factor is defined in the Introduction

(b) Enhancement is defined as ratio of the average heat-transfer coefficient of the TURBO-B bundle to that of the smooth bundle.

for the porous-coated surface when compared to other types of structured surface (THERMOEXCEL-E and TURBO-B) at low heat fluxes.

Also given in Table 1 are the average *bundle* heat transfer enhancements that are obtained if one replaces the smooth bundle with the TURBO-B bundle at the same three heat fluxes under otherwise identical conditions. It can be seen that a TURBO-B tube bundle enhances the overall heat transfer coefficient by a factor of 4.6 at low heat fluxes, dropping to 3.6 at high heat fluxes (it must be remembered that there is greater uncertainty in the data at low heat flux). If one compares these values with that for a single tube within the bundle, then at low heat fluxes, the enhancements are the same. At high heat fluxes, however, the average bundle enhancement of 3.6 is greater than the single tube enhancement (3.0), restating the fact that the effect of active tubes below is greater for the enhanced tube bundle than for the smooth tube bundle.

The present results confirm that, in general, a bundle factor should be used in the design of flooded evaporators and that the use of single tube data will be conservative. This bundle factor will, however, depend upon the type of boiling surface used, the operating heat flux and, of course, the working fluid.

Conclusions

Nucleate pool boiling data of R-113 at atmospheric pressure were obtained using a small bundle of TURBO-B copper tubes. The data were obtained for both increasing and decreasing heat flux. Based upon the results pertaining to this particular bundle and apparatus, the following conclusions may be made:

1 The effect of auxiliary heaters (to aid experimentation) can be significant in the natural convection region and must be carefully accounted for.
2 In the natural convection region, heated lower tubes do not have much influence on heat transfer from upper tubes.
3 The presence of heated lower tubes in a bundle reduces the incipient boiling heat flux and the accompanying temperature overshoot for upper tubes.
4 During nucleate boiling, the presence of heated lower tubes improves the average bundle heat transfer coefficient at all heat fluxes, from 60 percent at low heat flux to 22 percent at high heat flux. This leads to a bundle factor that should be included in the design of flooded evaporators.
5 When compared to a smooth tube bundle under similar conditions, enhancements in the average bundle heat transfer coefficient of 4.6 and 3.6 were obtained at low and high heat fluxes, respectively.

Acknowledgments

This work was funded by the Naval Surface Weapons Center, Carderock Division, Annapolis Detachment, MD. The authors would like to thank Mr. Petur Thors of Wolverine Tube Co. for supplying the TURBO-B tubes and Dr. John Thome for his useful comments.

References

Al-Alusi, T. R., and Bushnell, D. J., 1992, "An Experimental Study of Free Convection Heat Transfer From an Array of Horizontal Cylinders Parallel to a Vertical Wall," ASME JOURNAL OF HEAT TRANSFER, Vol. 114, pp. 394–400.

Anderson, C. L., 1989, "Nucleate Pool Boiling Performance of Smooth and Finned Tube Bundles in R-113 and R-114/Oil Mixtures," M.Sc. Thesis, Naval Postgraduate School, Monterey, CA.

Arai, N., Fukushima, T., Arai, A., Nakajima, T., Fujie, K., and Nakayama, Y., 1977, "Heat Transfer Tubes Enhancing Boiling and Condensation in Heat Exchangers of a Refrigerating Machine," *ASHRAE Transactions*, Vol. 83, Pt. 2, pp. 58–70.

Cerza, M., Memory, S. B., and Marto, P. J., 1993, "The Influence of Pool Circulation on Natural Convection and Pool Boiling of R-113 From a Vertical Array of Tubes," *6th Int. Symp. on Transport Phenomena (ISTP-6) in Thermal Engineering*, Seoul, Korea, Vol. 1, pp. 99–104.

Chan, A. M. C., and Shoukri, M., 1987, "Boiling Characteristics of Small Multitube Bundles," ASME JOURNAL OF HEAT TRANSFER, Vol. 109, pp. 753–760.

Cornwell, K., Duffin, N. W., and Schuller, R. B., 1980, "An Experimental Study of the Effects of Fluid Flow on Boiling Within a Kettle Reboiler Tube Bundle," ASME Paper No. 80-HT-45.

Cornwell, K., and Schuller, R. B., 1982, "A Study of Boiling Outside a Tube Bundle Using High Speed Photography," *Int. J. Heat Mass Transfer*, Vol. 25, pp. 683–690.

Cornwell, K., and Scoones, D. J., 1988, "Analysis of Low Quality Boiling on Plain and Low-Finned Tube Bundles," *Proceedings 2nd UK Heat Transfer Conf.*, Vol. 1, pp. 21–32.

Cornwell, K., 1989, "The Influence of Bubbly Flow on Boiling From a Tube in a Bundle," *Proceedings of Eurotherm Seminar No. 8, Advances in Pool Boiling Heat Transfer*, Paderborn, Germany, May 11–12, pp. 177–183.

Czikk, A. M., Gottzmann, C. F., Ragi, E. G., Withers, J. G., and Habdas, E. P., 1970, "Performance of Advanced Heat Transfer Tubes in Refrigerant-Flooded Liquid Coolers," *ASHRAE Trans.*, Vol. 76, pp. 96–109.

Fujita, Y., Ohta, H., Hidaka, S., and Nishikawa, K., 1986, "Nucleate Boiling Heat Transfer on Horizontal Tubes in Bundles," *Proceedings of 8th Int. Heat Transfer Conf.*, San Francisco, Vol. 5, pp. 2131–2136.

Hahne, E., and Müller, J., 1983, "Boiling on a Finned Tube and a Finned Tube Bundle," *Int. J. Heat Mass Transfer*, Vol. 26, pp. 849–859.

Han, C. Y., and Griffith, P., 1965, "The Mechanism of Heat Transfer in Nucleate Pool Boiling, Part I, Bubble Initiation, Growth and Departure," *Int. J. Heat Mass Transfer*, Vol. 8, No. 6, pp. 887–904.

Howell, J. R., and Siegel, R., 1967, "Activation, Growth and Detachment of Boiling Bubbles in Water From Artificial Nucleation Sites of Known Geometry and Size," NASA TN-D-4101.

Hsu, Y. Y., 1962, "On the Size Range of Active Nucleation Cavities on a Heating Surface," ASME JOURNAL OF HEAT TRANSFER, Vol. 84, No. 3, pp. 207–216.

Hwang, T. H., and Yao, S. C., 1986, "Crossflow Boiling Heat Transfer in Tube Bundles," *Int. Communication Heat and Mass Transfer*, Vol. 13, pp. 493–502.

Inagaki, T., and Komori, K., 1990, "Natural Convection Heat Transfer From Two Horizontal Cylinders in Vertical Alignment," *Trans. ISME*, Vol. 56, pp. 3050–3055 [in Japanese; translation in *Heat Transfer—Japanese Research*, Vol. 20, No. 5–6, 1991, pp. 549–559].

Jensen, M. K., 1988, "Boiling on the Shellside of Horizontal Tube Bundles," *Two-Phase Flow Heat Exchangers*, S. Kakac et al., eds., Kluwer Academic Publishers, pp. 707–746.

Jensen, M. K., and Hsu, J. T., 1988, "A Parametric Study of Boiling Heat Transfer in a Horizontal Tube Bundle," ASME JOURNAL OF HEAT TRANSFER, Vol. 110, pp. 976–981.

Jung, C. J., and Bergles, A. E., 1989, "Evaluation of Commercial Enhanced Tubes in Pool Boiling," Report DOE/ID/12772-1, Rensselaer Polytechnic Institute, Troy, NY.

Leong, L. S., and Cornwell, K., 1979, "Heat Transfer Coefficients in a Reboiler Tube Bundle," *The Chemical Engineer*, United Kingdom, April, pp. 219–221.

Marto, P. J., and Anderson, C. L., 1992, "Nucleate Boiling Characteristics

of R-113 in a Small Tube Bundle," ASME JOURNAL OF HEAT TRANSFER, Vol. 114, pp. 425–433.

Marsters, G. F., 1972, "Arrays of Heated Horizontal Cylinders in Natural Convection," *Int. J. Heat Mass Transfer*, Vol. 15, pp. 921–933.

Memory, S. B., and Marto, P. J., 1992, "The Influence of Oil on Boiling Hysteresis of R-114 From Enhanced Surfaces," *Pool and External Flow Boiling*, V. K. Dhir and A. E. Bergles, eds., ASME, pp. 63–71.

Memory, S. B., Chilman, S V., and Marto, P. J., 1992, "Nucleate Boiling Characteristics of a Small Enhanced Tube Bundle in a Pool of R-113," *Two-Phase Flow and Heat Transfer*, ASME HTD-Vol. 197, pp. 129–138.

Memory, S. B., Lake, L. R., and Marto, P. J., 1993, "The Influence of a Lower Heated Tube on Heat Transfer From an Upper Heated Tube in CFC-114," *Proc. 3rd World Conf. on Experimental Heat Transfer, Fluid Mechanics and Thermodynamics*, M. D. Kelleher et al., eds., Hawaii, Vol. 2, pp. 1197–1206.

Mesler, R., and Mailen, G., 1977, "Nucleate Boiling in Thin Liquid Films," *AIChE Journal*, Vol. 23, p. 954.

Müller, J., 1986, "Boiling Heat Transfer on Finned Tube Bundles: The Effect of Tube Position and Intertube Spacing," *Proceedings of 8th Int. Heat Transfer Conf.*, San Francisco, Vol. 5, pp. 2111–2116.

Rebrov, P. N., Bukin, V. G., and Danilova, G. N., 1989, "A Correlation for Local Coefficients of Heat Transfer in Boiling of R-12 and R-22 Refrigerants on Multirow Bundles of Smooth Tubes," *Heat Transfer—Soviet Research*, Vol. 21, No. 4, pp. 543–548.

Sparrow, E. M., and Niethammer, J. E., 1981, "Effect of Vertical Separation Distance and Cylinder-to-Cylinder Temperature Imbalance on Natural Convection for a Pair of Horizontal Cylinders," ASME JOURNAL OF HEAT TRANSFER, Vol. 103, pp. 638–644.

Sparrow, E. M., and Boessneck, D. S., 1983, "Effect of Transverse Misalignment on Natural Convection From a Pair of Parallel, Vertically Stacked, Horizontal Cylinders," ASME JOURNAL OF HEAT TRANSFER, Vol. 105, pp. 241–247.

Thome, J. R., 1990, *Enhanced Boiling Heat Transfer*, Hemisphere Publishing Corporation, Ch. 10, pp. 254–260.

Tokura, I., Saito, H., Kishinami, K., and Muramoto, K., 1983, "An Experimental Study of Free Convection Heat Transfer From a Horizontal Cylinder in a Vertical Array Set in Free Space Between Parallel Walls," ASME JOURNAL OF HEAT TRANSFER, Vol. 105, pp. 102–107.

Wallner, R., 1974, "Heat Transfer in Flooded Shell and Tube Evaporators," *Proceedings 5th Int. Heat Transfer Conf.*, Tokyo, Vol. 5, pp. 214–217.

Wanniarachchi, A. S., Marto, P. J., and Reilly, J. T., 1986, "The Effect of Oil Contamination on the Nucleate Pool Boiling Performance of R-114 From a Porous Coated Surface," *ASHRAE Trans.*, Vol. 92, Pt. 2, pp. 525–538.

Wanniarachchi, A. S., Sawyer, L. M., and Marto, P. J., 1987, "Effect of Oil on Pool Boiling Performance of R-114 From Enhanced Surfaces," *Proceedings 2nd ASME-JSME Thermal Engineering Joint Conference*, Honolulu, HI, Vol. 1, pp. 531–537.

Wege, M. E., and Jensen, M. K., 1984, "Boiling Heat Transfer From a Horizontal Tube in an Upward Flowing Two-Phase Crossflow," ASME JOURNAL OF HEAT TRANSFER, Vol. 106, pp. 849–855.

Yilmaz, S., and Palen, J. W., 1984, "Performance of Finned Tube Reboilers in Hydrocarbon Service," ASME Paper No. 84-HT-91.

P. J. Halvorson
Graduate Research Assistant,
Nuclear Engineering Program.

R. J. Carson[1]
Graduate Research Assistant,
Nuclear Engineering Program.

S. M. Jeter
Associate Professor,
Mechanical Engineering Program.

S. I. Abdel-Khalik
Southern Nuclear Distinguished Professor,
Nuclear Engineering Program.

George W. Woodruff School of
Mechanical Engineering,
Georgia Institute of Technology,
Atlanta, GA 30332

Critical Heat Flux Limits for a Heated Surface Impacted by a Stream of Liquid Droplets

An experimental apparatus has been constructed to allow investigation of heat transfer from a horizontal, upward facing, heated surface impacted by streams of monodisperse water droplets of varying size and impact frequency. Droplet diameters between 2.3 and 3.8 mm were used, with drop frequencies varying from 2 to 15 droplets per second. The droplet impact velocity was 1.3 m/s. Critical heat flux, surface superheat, droplet size, and frequency were the primary measured data. Heat fluxes as high as 325 W/cm^2 were achieved with wall superheats of only 24°C. The liquid film thickness produced upon droplet impact is shown to be a key factor in these experiments, and the importance of investigating the wetted area is highlighted. The effectiveness of droplet impact cooling using droplets with diameters on the order of millimeters is shown.

1 Introduction

Droplet impact cooling is a promising technology with potential applications in high-power solid state electronics, materials processing, aerospace flight, and energy conversion. Droplet impact cooling involves heat transfer from a thin liquid film coupled with the dynamics of formation and stability of such a film. Experimental investigation is necessary since evaporation and boiling heat transfer even under simpler conditions is incompletely understood and the introduction of droplet dynamics and the influences of the surface greatly complicate the process. The experimental research described in this paper was undertaken as a contribution toward better understanding of droplet impact cooling.

Droplet impact cooling experiments can be broadly divided into two categories: those producing a sprayed mist from a nozzle, such as an atomizer, and those producing a monodisperse stream of droplets that impact a fixed region of the heated surface one droplet at a time. Fundamentally, sprays and streams of droplets are closely related and either one can produce a thin liquid film on a heated surface. In either case, droplet diameters can range from below 40 μm (Tilton and Chow, 1987) to above 5 mm (Toda, 1974).

In an early set of studies (Toda and Uchida, 1970; Toda, 1972, 1974), experimental, analytical, and statistical studies on droplet impact cooling were conducted. Models for droplet spreading on impact and the critical film thickness below which nucleate boiling would be suppressed were developed. A model combining experimental parameters, analytical work, and statistical droplet size and velocity distributions was developed to predict the heat fluxes of spray cooling. Heat fluxes of up to 400 W/cm^2 were experimentally observed for water sprayed onto a polished metal surface.

Bonacina et al. (1975, 1979) conducted two series of experiments using water sprays. The second series used smaller droplets, thinner films, and produced higher heat fluxes (up to 215 W/cm^2). The fraction of the heated surface wetted by the spray for the highest flux was only 20 percent. A correlation to predict the wetted surface fraction was developed.

Inada et al. (1983) conducted a combined experimental and numerical investigation of post-CHF droplet impact cooling with water at various temperatures. The heat flux during the brief contact time (10 to 15 ms) with the heated surface was computed to be as high as 4000 W/cm^2. The time-averaged heat flux would be considerably lower.

Valenzuela et al. (1986, 1987) conducted experimental studies with a single stream of droplets produced by an ink jet printer head producing small, fast droplets. Heat fluxes of 320 W/cm^2 and heat transfer coefficients of 9 W/cm^2°C were found.

Tilton and Chow (1987) and Pais et al. (1989) conducted experimental investigations of droplet impact cooling, using a spray of water from a variety of nozzles. The velocity, mean diameter, and frequency of droplets impacting the surface were found to be key characteristics of droplet impact cooling. Heat fluxes of 1180 W/cm^2 were obtained at wall superheats of only 20°C. The resulting heat fluxes were compared with the much lower values reported by Bonacina et al. (1979) and Toda (1972). Pais et al. (1989) postulated that the lower heat fluxes obtained by Bonacina et al. could be due to the lower velocity and smaller droplet diameters causing a large fraction of the water droplets to be entrained by the counterflowing vapor before reaching the heated surface, resulting in the large dry surface fractions reported. The higher droplet velocity of Toda's experiments was believed to have led to a large fraction of the water rebounding away from the heated surface.

While this review demonstrates that considerable work has been accomplished in the past, most of the work has concentrated on sprays and streams of submillimeter droplets, which produce extremely thin films, or on wall temperatures above the CHF temperature. The current investigation focuses on the use of much larger liquid droplets and demonstrates the possibility of obtaining sustained, reasonably high heat fluxes with thicker films at moderate wall superheats.

2 Experimental Apparatus

An experimental apparatus was designed to examine the heat

[1]Current address: Compa Industries, Inc., 6290 Montrose Rd., Rockville, MD 20852.

Contributed by the Heat Transfer Division for publication in the JOURNAL OF HEAT TRANSFER. Manuscript received by the Heat Transfer Division April 1993; revision received August, 1993. Keywords: Evaporation, Sprays/Droplets. Associate Technical Editor: L. C. Witte.

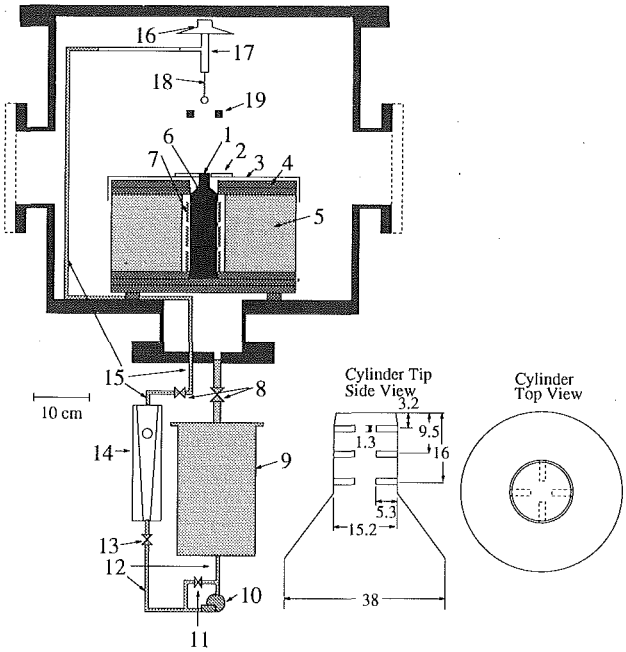

Fig. 1 Experimental setup in pressure vessel. 1: nickel surface, 2: PTFE seal, 3: stainless steel cover sheet, 4: water-resistant insulation boards, 5: high-temperature fiber insulation (with PTFE wrap), 6: copper cylinder, 7: heater rings, 8: ball valves for vacuum sealing, 9: heated fluid reservoir, 10: pump, 11: recirculation control valve, 12: heated 1/4 in. stainless steel tubing and coupled fittings, 13: flow control valve, 14: flow meter, 15: insulated 1/4 in. tubing, 16: speaker, 17: dropper assembly, 18: needle and droplet, 19: light switch (coupled LED and phototransistor). Close up of cylinder top and side view in lower right corner, dimensions in mm.

flux characteristics of droplet impact cooling at various droplet diameters and impact frequencies. The equipment can be divided into three systems: the heat transfer surface, the fluid delivery system, and the instrumentation. A schematic diagram of the experimental apparatus is shown in Fig. 1.

2.1 Heat Transfer Surface. The heat transfer surface is the nickel-plated end of a 21-cm-long, 3.8-cm-dia. heated copper cylinder (Fig. 1). The lower region of the cylinder is surrounded by ring-shaped electrical heaters. The input voltage can be varied by an autotransformer to provide power levels between 0 and 900 W. An electronic temperature controller is used to deactivate the heaters when the surface temperature exceeds a preset value. The cylinder is well insulated in the radial and downward directions so that heat would be removed from the exposed upper surface. Calorimetric tests have shown the overall performance of the insulating system to be excellent, limiting the heat loss through the insulation to 20 W for a typical experiment with 330 W power input.

The upper part of the cylinder is reduced to a 1.52 cm diameter to attain a higher heat flux at the tip for the same power input. The last 0.254 cm of the upper part tapers to the final tip diameter of 1.42 cm. The final taper provides a seal with a 0.318 cm thick polytetrafluoroethylene (PTFE) disk pressed onto the cylinder. The PTFE disk prevents water from leaking down to the sides of the copper cylinder and is bolted to a stainless steel cover sheet.

2.2 Fluid Delivery. A recirculating coolant system has been designed to allow operation as a sealed system (Fig. 1). Distilled water has been used in all experiments. Stainless steel is used for all metal components in contact with the water. The water is recirculated to the dropper by a magnetically coupled gear pump. The flow rate is controlled by means of a needle valve and is measured by a rotameter. Experiments with preheated water droplets makes use of resistance heaters surrounding the reservoir and lower sections of the piping.

Water flows out of a needle, forms a droplet, and falls to the surface 9 cm below when its weight is enough to break it free. A free fall to the heated surface below results in a droplet impact velocity of 1.3 m/s. Standard press fit stainless steel hypodermic needles 1 to 2 cm long are used. The three needles used (17, 19, and 22 gage) give a reasonably broad range of droplet diameters and corresponding film thickness after impact. Table 1 gives the dimensions of the needles used and the corresponding ranges of experimental variables.

Experimental measurements of volumetric flow and droplet frequency were used to provide calibration curves of droplet diameter as a function of droplet frequency.

In addition to the unassisted, gravity-generated droplet streams, the apparatus is designed to produce liquid droplets at higher frequencies. An audio speaker coil is mounted so that it can vertically vibrate the dropper assembly, forcibly breaking off the droplets before the weight of the droplet alone would have overcome the surface tension forces.

The falling droplets pass through a light switch, a coupled LED and phototransistor pair, and impact the heated surface below.

2.3 Instrumentation. The cylinder is instrumented to provide accurate measurements of the upward heat flow rate (i.e., average surface heat flux) and surface temperature. Measurements are also made of the fluid flow rate and droplet frequency so that the average droplet diameter can be determined. K-type thermocouples measure the copper cylinder temperature at three axial positions below the heated surface (see inset to Fig. 1). The temperature readings of three thermocouples are averaged to obtain the temperature at each of the three levels. The temperature gradient between the two levels closest to the exposed hot surface is used to determine the upward heat flow rate, and hence the surface heat flux; it is also extrapolated to determine the surface temperature. The gradient between the second and third level thermocouples was used to check the uniformity of the heat flux through the upper region of the copper cylinder, which would not be uniform if water were leaking past the PTFE seal. Both the surface heat flux and surface temperature are time and area averaged; consequently, the data could not show temperature variations during the course of a single droplet evaporation or radial temperature differences of the hot surface.

Nomenclature

Adjusted CHF = critical heat flux based on wetted area, w/cm^2
d = droplet diameter before impact, cm
D = droplet diameter after impact, cm
dps = droplets per second
Re = Reynolds number = $\rho v d/\mu$
Surf. Avg. CHF = critical heat flux based on total tip area, W/cm^2
v = droplet velocity, m/s
We = Weber number of the liquid drop = $\rho v^2 d/\sigma$
β = droplet spreading ratio = D/d
μ_{drop} = dynamic viscosity of liquid at saturation temperature, Ns/m^2
μ_{wall} = dynamic viscosity of liquid at wall temperature, Ns/m^2
ρ = liquid density, g/cm^3
σ = surface tension, g/s^2

Two thermocouples in contact with the upper and lower parts of the copper cylinder are used to calculate the heat storage term of the heat balance. The change in temperature over time, combined with each region's mass and heat capacity, was used to calculate the rate of change of internal energy for the cylinder.

The temperature at a specified radial position within the insulation is measured to allow calculation of heat losses using an experimentally determined overall heat conductance of the insulation. Power input is measured by an electromechanical wattmeter; as a backup, the power is also measured by digital meters monitoring current and voltage across the heaters.

The temperature of the feedwater is measured in the reservoir, leaving the flow meter, and at a point immediately prior to entry into the dropper assembly. The mass flow rate of the water is measured by a calibrated rotameter. For the unassisted, gravity-generated droplet streams, the droplet rate, together with the calibration curves, can be used to determine the volumetric flow rate and droplet diameter. Each droplet passes between the coupled LED and phototransistor, producing a trace on a storage oscilloscope. The uniformity of the droplet rate during the course of a test can be visually monitored, while the droplet rate itself is manually recorded.

A PC-based data acquisition system was used to collect and record the data. Temperatures can be recorded every three seconds; the recorded temperature consists of an average of 30 readings. Power input, heat storage in the cylinder, heat leakage through the insulation, and heat flow through the tip are all monitored or computed online throughout the experiment.

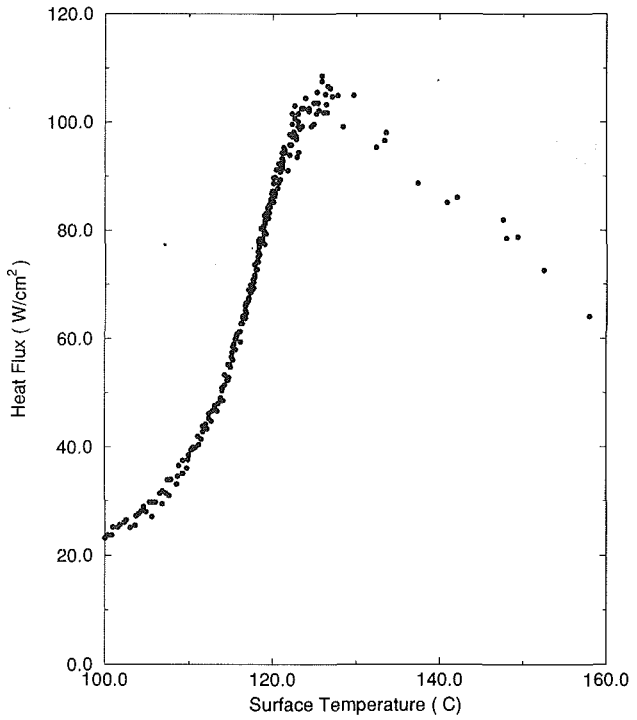

Fig. 2 Flux measurements during the course of a 19 gage, 9 drop per second test (data points correspond to 3 second intervals)

3 Experimental Procedure

In a typical experiment, a stream of droplets of controlled size and frequency impacts the hot surface as the copper cylinder is slowly allowed to heat up, resulting in gradually increasing surface temperatures and heat fluxes until CHF is reached. Typically, the pump is turned on and the flow rate is adjusted until the droplet frequency reaches the desired value for the needle size being used. The heater is then energized; power is set at a value slightly higher than the expected heat flow rate at CHF. Setting the power to match the expected CHF power allows the experiment to approach CHF slowly. The surface temperatures obtained by this procedure prior to reaching CHF have been shown to match those obtained using steady-state tests at the corresponding heat fluxes (Carson, 1991). A typical plot of heat flux versus surface temperature obtained during a test run is shown in Fig. 2.

Data collection starts when the surface temperature rises above 100°C, and proceeds at 3 second intervals. The coolant flow rate and droplet frequency are checked periodically and logged on the data acquisition computer. Given that typical wall temperatures at CHF are less than 150°C, the electronic temperature controller is set to interrupt the power to the heaters when the top level thermocouples reach 180°C. After CHF, the temperature at the surface rises to the average copper cylinder temperature, typically around 250°C. The tip can be rapidly cooled with a high-velocity jet of water, which reduces the surface temperature to around 140°C in less than a minute; at that time the jet is cut back to a stream of droplets. When the surface temperature drops below 100°C, the experimental apparatus is ready for the next run.

The primary data resulting from a single CHF run are the heat flux and temperature at the CHF condition, along with the corresponding droplet frequency and mass flow rate. The average droplet diameter is calculated from the known flow rate and frequency. The critical conditions are extracted from a plot of heat flux against wall superheat during the CHF run (Fig. 2); the highest flux value is selected as the critical heat flux.

3.1 Error Analysis. Errors in the measured temperature values are dominated by the roundoff error of the analog to digital converters. Errors of 0.1°C result from the conversion. Errors in surface temperature and heat flux are caused by errors in the measured temperatures as well as uncertainties in the thermocouple locations. The thermocouples measuring the temperature gradient are inserted into holes with a diameter of 0.127 cm. The thermocouple junctions fit snugly into the holes; the error in location is estimated to be less than one tenth the diameter, or 0.0127 cm. A constant thermal conductivity for copper at 100°C was used to calculate the heat flux. The error in conductivity should be less than 0.02 W/cm°C, based on the expected range of temperatures for the various experiments. Treating these as independent errors, the expected error in the calculated heat flux can be estimated to be ±2.9 percent by error propagation analysis. The error in tip temperature is approximately ±2°C; in both cases the error is dominated by the uncertainty of the position of the thermocouples.

The presence of the thermocouple holes causes the measured heat flux to be slightly higher than the true flux. The temperature profile is not linear due to the area restrictions caused by the thermocouple holes themselves. Ignoring conduction across the thermocouple beads, the corresponding bias in the measured heat flux values for all experiments was found to be less than 0.5 percent. Due to the small magnitude of the bias, the data were not adjusted.

The droplet rate is observed on a storage oscilloscope, to within ±3 percent accuracy. During the course of a CHF run, the droplet rate may change slightly; therefore, the final value corresponding to the drop rate during the critical heat flux transition is the one recorded.

A heat balance was conducted for all experiments. For the case shown in Fig. 2 (19 gage, 9 dps) the power input is 276 W. The calculated heat flow through the tip of the cylinder is 151 W; the rate of heat loss through the insulation is 15 W, while the rate of heat storage in the copper is 90 W. The difference between the observed power input and output, 7 percent, is on the same order as the expected error; conse-

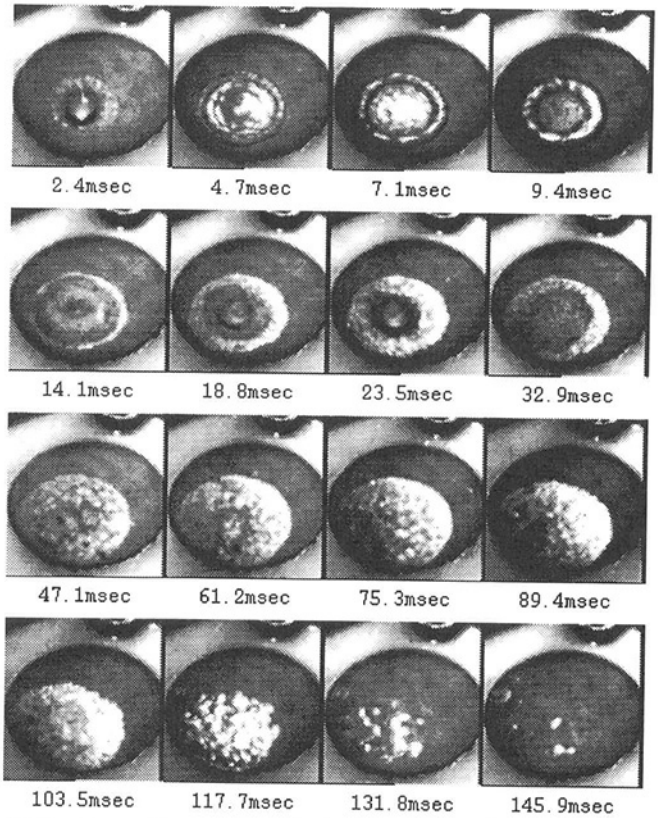

Fig. 3 Evaporation sequence of a single droplet from the 22 gage needle running at 5 *dps*

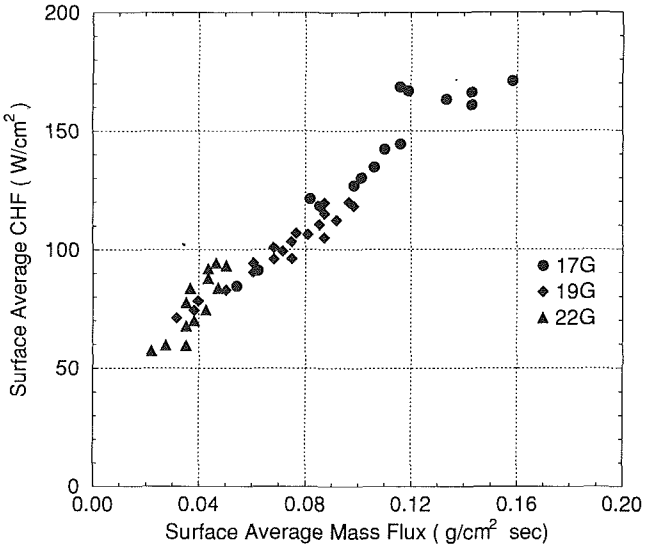

Fig. 4 Surface-averaged critical heat flux versus surface-averaged mass flux for water at 20°C using three different needle sizes

quently the error analysis and calorimetric tests were consistent.

4 Results and Discussion

Experiments were done with needles of three gages: 17, 19, and 22 gage. The 22 gage needle had the smallest diameter, producing the smallest droplets and the thinnest films. One set of experiments was performed with the 17 gage needle and water preheated to 50°C, while all others were done with water at 20°C.

During the course of a test run, the heat flux and surface temperature are gradually increased until CHF is reached. At heat fluxes well below CHF, the impacting droplet spreads uniformly over a portion of the heated surface, removing heat primarily by evaporation from the surface of the water with no signs of nucleate boiling. As the critical heat flux is approached, the center region of the liquid film becomes white in appearance, apparently due to nucleate boiling, and appears to form a thicker region at the impact site. During this same time period, the outer region of the wetted area remains as a thin liquid film, and continues with evaporation from the surface. Figure 3 contains a series of video images taken with a CCD camera at 425 frames/s, which illustrates the droplet and liquid film behavior near CHF. In transition to post-CHF, the thin film extending beyond the thicker region of the film pulls back into the center, reducing the wetted area and the region of thin film evaporation. Beyond the critical heat flux, possible film boiling under the droplet quickly separates the liquid from the solid. After this cooling crisis, the heat flux drops, surface temperature rises, and the water wanders off the edge of the hot surface without making significant contact with the heated surface.

The critical heat fluxes were found to occur at wall superheats ranging from 25 to 45°C. The wall superheats tended to increase with both droplet diameter and impact frequency. The critical heat flux was found to be almost independent of droplet size for a fixed flow rate, as shown in Fig. 4.

The raw data, as shown in Fig. 4, may not reveal the details of the heat transfer processes taking place. Radiative and convective heat transfer from the dry portions of the heated surface are small compared to the phase change heat transfer of the wetted regions of the surface; consequently the heat flux of interest is the heat flux across the actual wetted area, not the average over the entire heated surface. Visual observations show that, upon impact, droplets from the 17 gage needle spread to cover almost the entire surface, while the smaller droplets produced by the other needles do not cover the entire surface. For the 22 gage needle, the smallest diameter, as little as one third of the surface is wetted by the initial impact of the droplet. This situation dictates that the heat flux based on the wetted area should be a more useful quantity, as shown in subsequent paragraphs.

Our experiment does not measure the transient wetted area online; instead a model predicting the ratio of the diameter of the wetted area and that of the impacting droplet has been used. Kurabayashi et al. (1967) developed an equation to predict the droplet spreading ratio, β, as a function of Weber number and Reynolds number. This equation was later modified by Yang (1975), and may be expressed as follows:

$$\frac{1}{2}\,\mathrm{We}=\frac{3}{2}\,\beta^2\left[1+3\,\frac{\mathrm{We}}{\mathrm{Re}}\left(\frac{\mu_{\mathrm{drop}}}{\mu_{\mathrm{wall}}}\right)^{0.14}\left(\beta^2\ln\beta-\frac{\beta^2-1}{2}\right)\right]-6. \tag{1}$$

The spreading ratios predicted by Eq. (1) were compared to experimental measurements by Valenzuela et al. (1986), and found to be accurate. The general range of spreading ratios agrees with those of Toda (1974). The spreading ratios also agree with wetted areas observed in the high-speed video sequence of Fig. 3. The ranges of Weber numbers for the experiments conducted are given in Table 1. Visual observations indicate that for the range of variables used in this investigation, the droplets do not fragment upon impact with the heated surface.

Using Eq. (1), the heat flow rate per unit wetted area, the adjusted CHF, can be computed and the mass flow rate per unit wetted area, the adjusted mass flux, can also be determined. Assuming the droplet forms a disk after impact, an average initial film thickness can be determined.

Table 1 Ranges of the experimental variables

Needle Gauge	17	19	22
Needle ID (mm)	1.07	0.69	0.43
Needle OD (mm)	1.47	1.07	0.71
Droplet Rate (dps)	3.0 – 15.0	2.5 – 11.4	2.9 – 12.0
Droplet Diameter (mm)	3.17 – 3.81	2.96 – 3.41	2.33 – 2.85
Spreading Ratio, β	3.5 – 3.7	3.5 – 3.6	3.3 – 3.4
Initial Film Thickness (mm)	0.169 – 0.184	0.164 – 0.175	0.146 – 0.161
Weber Number	74 – 90	70 – 80	55 – 67

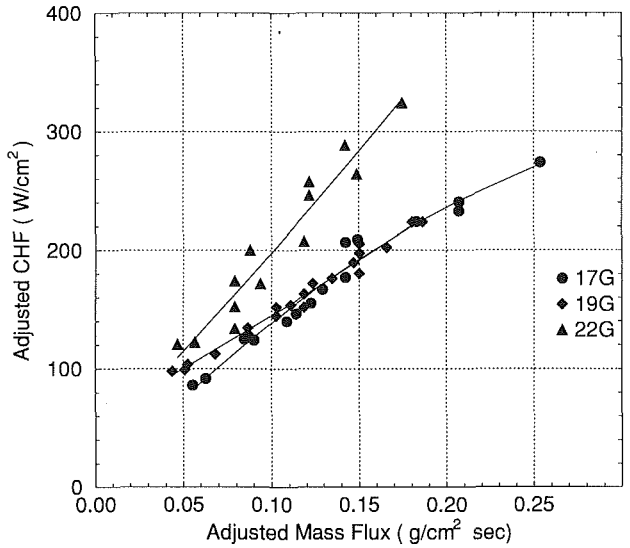

Fig. 5 Critical heat flux based on initial wetted area versus mass flux based on the same area; water at 20°C using three different needle sizes

The data adjusted and plotted in this fashion, Fig. 5, clearly show the higher heat fluxes attainable with smaller droplets. This effect is attributed to the thinner liquid film produced by impact of smaller droplets on the heated surface. This form of the data can also be extrapolated to an array of many droplet generators. Since both the heat flux and the mass flux are based on the initial wetted area, Eq. (1) could be used to determine the optimal spacing of droplet generators in large-scale applications.

In Fig. 5, the 19 gage needle CHF data are close to the 22 gage needle data at low mass flow rates, but at higher flow rates the data are closer to the 17 gage data. One possible explanation of this phenomenon is that the evaporation time quickly exceeds the droplet period. This would cause the wetted area to increase and flood the heated surface, with excess water running off without being evaporated.

Models based on conduction through a thin film predict much lower fluxes than those observed in this investigation (Rizza, 1981; Valenzuela and Drew, 1987). This difference is attributed to the presence of nucleate boiling in parts of the film. The presence of nucleate boiling is supported by three factors: the observed high heat transfer coefficients compared to those predicted by conduction models, Toda's model for the critical film thickness (Toda, 1974), and high-speed video observations of the surface.

Referring to Fig. 3, the indicated times are measured relative to the instant when the droplet is just above the surface. The heated surface was viewed in reflected light.

Nucleate boiling could cause disturbance of the surface, and breakup of the reflection; this can first be seen in the third and fourth frames. The velocity of impact can be seen to transfer to an outward radial velocity in the first three frames, an inward rebound in the next three frames, and a final outward spreading in the remaining frames. At approximately 24 ms, the center of the liquid film, where nucleate boiling appears

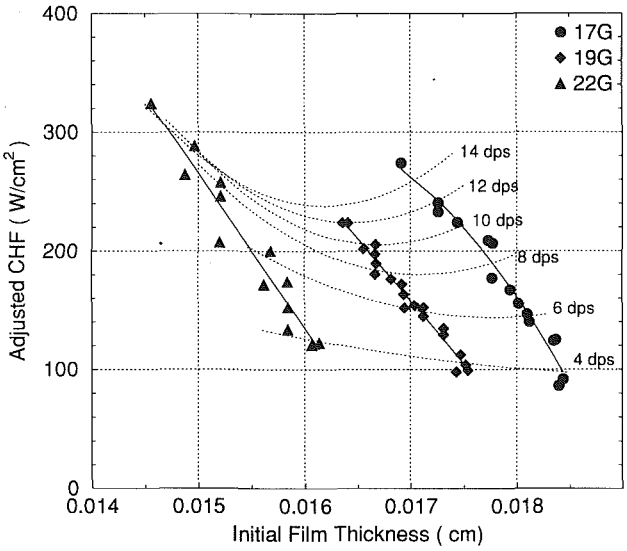

Fig. 6 Critical heat flux based on initial wetted area versus initial film thickness for water at 20°C using three different needle sizes; includes lines of constant drop rate

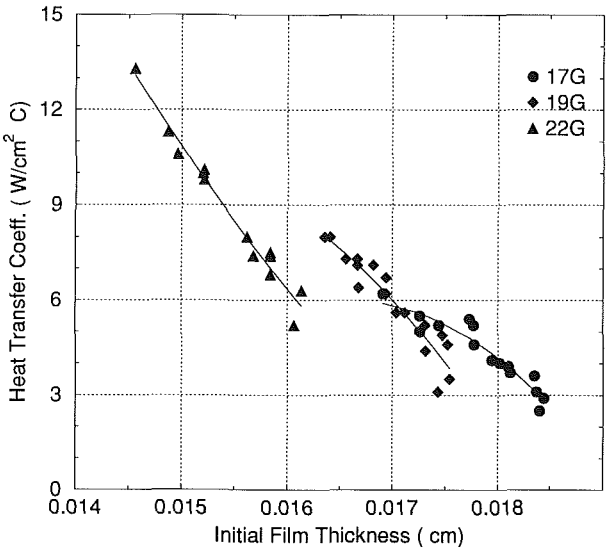

Fig. 7 Heat transfer coefficient versus initial film thickness for water at 20°C using three different needle sizes

to take place, is much thicker than the edges, which provide comparatively smooth reflections. This may indicate that boiling is suppressed in the outer region where the film is thinner. Small droplets are seen to be ejected from the film at about 24 ms. The center bulge spreads after about 30 ms, also spreading the nucleate boiling. At this point there is a long period of boiling with a nearly constant wetted area before the surface starts to dry out. In the final stages, the film becomes thin enough to suppress boiling once again (61 ms). Dry out occurs evenly across the entire surface at 117 ms, not preferentially from the edges of the film as might be expected.

Figure 6 shows the relationships between CHF, film thickness, and droplet frequency. Points at the upper end of the 17 gage data are of around the same film thickness as points at the lower end of 19 gage data. The difference in heat flux is apparently due to the higher droplet rates of the larger needle. The constant droplet frequency lines show the increase in heat flux for the 22 gage data. Increased dry time between droplets is another factor leading to lower fluxes at the lower droplet rates.

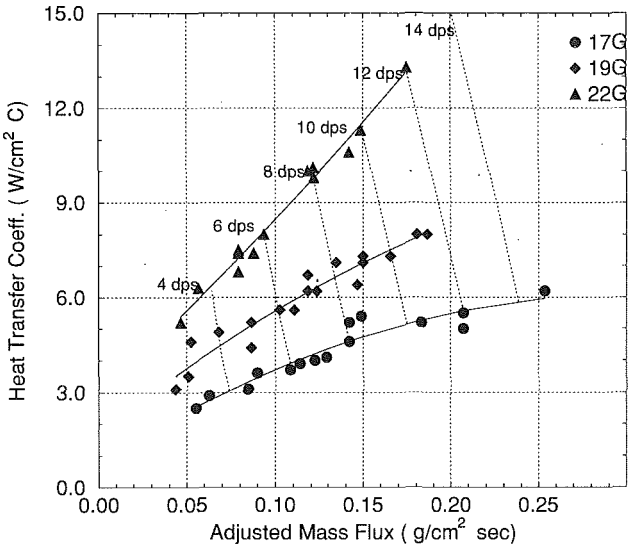

Fig. 8 Heat transfer coefficient versus mass flux based on initial wetted area for water at 20°C using three different needle sizes; includes lines of constant droplet rate

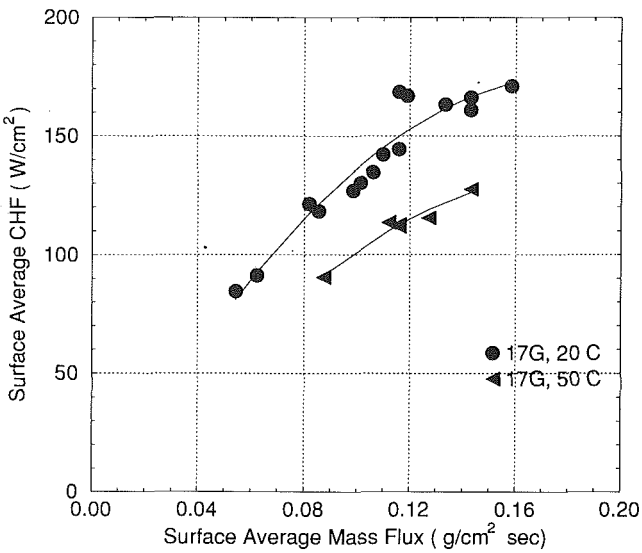

Fig. 9 Surface averaged critical heat flux versus surface averaged mass flux for water at room temperature and 50°C, using a 17 gage needle

Figure 7 shows the relationship between the calculated heat transfer coefficient at the CHF point and initial film thickness. The trend to higher heat transfer coefficients for thinner films is clearly illustrated.

Figure 8 shows the heat transfer coefficients corresponding to the heat fluxes of Fig. 5. These values are found to be comparable to those of other droplet impact cooling experiments, and higher than those of most other water-based cooling methods. These results demonstrate the effectiveness of droplet impact cooling even with relatively large droplet diameters.

In an additional investigation, the temperature of the cooling water was varied in an attempt to determine the effect of subcooling. The results, shown in Fig. 9, show a significant decrease in CHF when the cooling water is preheated to 50°C. Inada et al. (1983) performed experiments using similar droplet sizes and subcoolings. While the heat fluxes of Inada et al. were considerably higher due to their model of wetted area, they do show a similar trend for preheated water. The decrease in heat fluxes of the preheated experiments indicates that cooler water is advantageous, perhaps an indication that the cooler water is better able to maintain contact with the heated surface, or that the large temperature difference between fluid and wall causes a high flux due to conduction in the initial stages of droplet spreading.

5 Conclusions

An experimental apparatus has been constructed to allow investigation of droplet impact cooling of an upward-facing, heated surface. Measurements of the critical heat flux and surface temperature for various drop sizes and impact frequencies were made. Distilled water at either room temperature (20°C) or heated to 50°C was used as the cooling fluid. Droplet diameters ranged from 2.3 to 3.8 mm, frequency of impact ranged from 2 to 15 droplets per second, impact velocity was 1.3 m/s, and resulting film thicknesses were between 0.15 and 0.18 mm.

Unadjusted critical heat fluxes, averaged over the entire heated surface, ranging from 60 to 170 W/cm^2 were achieved with water at room temperature. For a given mass flux of coolant, the CHF was found to change very little with variations in droplet frequency and diameter. Such averaging, however, does not account for the smaller initial wetted area of smaller droplets. Modeling of droplet spreading on impact allowed the calculation of the heat flow rate per unit wetted area. These adjusted critical heat fluxes provide a more meaningful comparison since they account for the reduced wetted area of the smaller droplets. In a practical cooling system, smaller droplets would be more closely spaced than large droplets; the resulting overall average heat fluxes can then approach the adjusted flux. The adjusted CHF values were found to vary between 100 and 320 W/cm^2, and also show the increased CHF of the thinner films. Preheating the coolant from 20 to 50 °C was found to decrease the CHF by as much as 20 percent. This indicates that sensible heating of the water from its impact temperature accounts for a significant fraction of the heat removed from the heated surface. Models developed for thin films appear to greatly underpredict the effectiveness of impact cooling of the thicker films used in this investigation (Toda, 1974; Rizza, 1981; Valenzuela and Drew, 1987).

The heat fluxes attained in our droplet impact cooling experiment were found to lie between those reported for pool boiling and those of droplet impact cooling using submillimeter droplets (approximately 100 μm diameter) Lienhard et al. (1973) have shown pool boiling heat fluxes to be around 120 W/cm^2, while enhanced pool boiling can double the CHF (Bockwoldt et al., 1992). Droplet impact cooling with droplet diameters close to one millimeter may fill the gap between pool boiling, with fluxes around 120 W/cm^2, and submillimeter droplet impact cooling, with fluxes around 1000 W/cm^2, while being simpler to design and operate than submillimeter droplet impact cooling.

References

Bockwoldt, T. S., Jeter, S. M., Abdel-Khalik, S. I., and Hartley, J. G., 1992, "Induced Convective Enhancements of the Critical Heat Flux From Partially Heated Horizontal Flat Plates in Saturated Pool Boiling," ASME JOURNAL OF HEAT TRANSFER, Vol. 114, pp. 518–521.

Bonacina, C., Comini, G., and Del Giudice, S., 1975, "Evaporation of Atomized Liquids on Hot Surfaces," *Letters in Heat and Mass Transfer*, Vol. 2, pp. 401–406.

Bonacina, C., Del Giudice, S., and Comini, G., 1979, "Dropwise Evaporation," ASME JOURNAL OF HEAT TRANSFER, Vol. 101, pp. 441–446.

Carson, R. J., 1991, "Critical Heat Flux for a Heated Surface Impacted by a Stream of Liquid Droplets," M. S. thesis, Nuclear Engineering Program, Georgia Institute of Technology.

Inada, S., Miyasaka, Y., Nishida, K., and Chandratilleke, G. R., 1983, "Transient Temperature Variation of a Hot Wall Due to an Impinging Water Drop—Effect of Subcooling of the Water Drop," *ASME-JSME Thermal Engineering Joint Conference Proceedings*, pp. 173–182.

Kurabayashi, T., Karasawa, T., and Iida, K., 1967, "Impact of Liquid Droplets on a Solid Surface," JSME, *Preprint No. 175*, Sept., pp. 153–156.

Lienhard, J. H., Dhir, V. K., and Riherd, D. M., 1973, "Peak Pool Boiling

Heat Flux Measurements on Finite Horizontal Flat Plates," ASME JOURNAL OF HEAT TRANSFER, Vol. 95, pp. 477–482.

Pais, M. R., Tilton, D. E., Chow, L. C., and Mahefkey, E. T., 1989, "High Heat Flux, Low Superheat Evaporative Spray Cooling," Paper No. AIAA-89-0241.

Rizza, J. J., 1981, "A Numerical Solution to Dropwise Evaporation," ASME JOURNAL OF HEAT TRANSFER, Vol. 103, pp. 501–507.

Tilton, D. E., and Chow, L. C., 1987, "High Power Density Evaporative Cooling," Paper No. AIAA-87-1536.

Toda, S., and Uchida, H., 1970, "A Study of Mist Cooling—Thermal Behaviors of Liquid Films Formed From Mist Drop on a Heated Surface at High Temperatures and High Heat Fluxes," in: *Heat Transfer 1970—Preprints of papers presented at the Fourth International Heat Transfer Conference—Paris–Versailles*, Vol. 5.

Toda, S., 1972, "A Study of Mist Cooling (1st Report: Investigation of Mist Cooling)," *Heat Transfer—Japanese Research*, Vol. 1(3), pp. 39–50.

Toda, S., 1974, "A Study of Mist Cooling (2nd Report: Theory of Mist Cooling and Its Fundamental Experiments)," *Heat Transfer—Japanese Research*, Vol. 3(1), pp. 1–44.

Valenzuela, J. A., Jasinski, T. J., and Drew, B. C., 1986, "High Heat Flux Evaporative Cold Plate for Space Applications. Phase I. Final Report," Tech. Rept. TM–1103, Creare Inc.

Valenzuela, J. A., and Drew, B. C., 1987, "High Heat Flux Droplet Impingement Heat Transfer. Phase I. Final Report," Tech. Rept. TM–1190, Creare Inc.

Yang, W.-J., 1975, "Theory on Vaporization and Combustion of Liquid Drops of Pure Substances and Binary Mixtures on Heated Surfaces," Tech. rept. 535, Inst. Space Aero. Sci., U. Tokyo.

An Analytical Solution and Sensitivity Study of Sublimation-Dehydration Within a Porous Medium With Volumetric Heating

E. P. Scott
Department of Mechanical Engineering,
Virginia Polytechnic Institute and
State University,
Blacksburg, VA 24061-0238
Assoc. Mem. ASME

A study of sublimation-dehydration within a porous medium as a result of volumetric heating, such as that associated with microwave heating, is presented in this paper. A semi-infinite frozen porous medium with constant thermal properties subject to a sublimation-dehydration process involving a volumetric heat source is considered. One-dimensional analytical solutions for dimensionless temperature, vapor concentration, and pressure were obtained. A sensitivity study was also conducted in which the effects of the material properties inherent in these solutions were analyzed. Finally, some of the assumptions used in the formulation of the problem were analyzed, and predicted drying curves were found to compare reasonably with previously published experimental results.

Introduction

Sublimation-dehydration, which is commonly known as freeze-drying, is used as a method of removing moisture from biological materials, such as food, pharmaceutical, and biochemical products. Some of the advantages of sublimation-dehydration over evaporative drying are that the structural integrity of the material is maintained, aroma and/or flavor losses are reduced, and product degradation is minimized (Rosenberg and Bögl, 1987; Decareau, 1982; Ang et al., 1977a, b). The major disadvantage of the freeze-drying process is that it is generally slow, and consequently, the process is economically unfeasible for certain materials.

One means of alleviating this problem is through the use of microwave energy. The resulting volumetric heating effect results in mass transfer, rather than heat transfer, becoming the limiting factor in the determination of the drying time (Arsem and Ma, 1985). However, the heat and mass transfer mechanisms related to microwave-aided freeze-drying processes are not well understood; therefore, additional theoretical and experimental studies are needed. The focus of this study is on the development of an analytical solution that can be utilized to enhance the understanding of the freeze-drying process with a volumetric heat source.

Several mathematical models have been proposed to describe the freeze-drying process without microwave heating (Fey and Boles, 1987; Lin, 1981, 1982; Hill and Sunderland, 1971; McCulloch and Sunderland, 1970; Dyer and Sunderland, 1967, 1968). Most of these models were solved analytically. Only a few studies have also included a microwave heat source in the model; numerical solutions including microwave heating were presented by Ma and Peltre (1973, 1975a) and Ang et al. (1977a).

In this study, a mathematical model for sublimation-dehydration with volumetric heating is presented from which analytical solutions for dimensionless temperature, vapor concentration, and pressure were obtained for two different temperature boundary conditions. Analytical solutions can provide important insights into the mechanisms of a real process even though the assumptions used can be rather restrictive. For example, analytical solutions can provide insights into the importance of different material properties on the solution, which can aid in the development of improved mathematical models for this process. In addition, numerical solutions can have errors associated with the model and errors associated with the numerical method itself, and it is sometimes difficult to distinguish between the two types of error. Analytical solutions provide an important means of evaluating numerical schemes, which can later be used with less restrictive assumptions, if necessary, to simulate actual processes.

The importance of the material properties on the solutions was analyzed through a sensitivity study. Two factors were considered: First, the effects of the volumetric heat source on the sensitivity of temperature, vapor concentration, and pressure to changes in the various properties were determined. This is important as it is an indication of the influence of each different term in the model for a given set of process conditions. The second factor under consideration was related to the estimation of these properties. These values must be known accurately for practical use of the mathematical models; Ma and Peltre (1975b) reported that there is a need for more specific and comprehensive property data. Some methodologies exist for the simultaneous estimation of material properties inherent in a mathematical model of a given process; however, if the parameters in question are found to be correlated, they cannot be simultaneously estimated as independent values (Beck and Arnold, 1977). The second factor under consideration was, therefore, the degree of correlation between the various parameters.

An analysis of the solution was then conducted to evaluate some of the assumptions used in the analytical solution. First, the appropriateness of the assumed volumetric heating term was investigated, and then the possibility of melting occurring was addressed. The assumed freezing front location was then compared with previous theoretical and experimental results. Finally, predicted moisture content values were compared with experimental data from previous studies.

Problem Statement

A semi-infinite homogeneous frozen porous material, initially at a uniform temperature, pressure, and ice concentration, subjected to low pressure conditions and a volumetric heat source, is considered. The pressure is assumed to be below the triple point, and the pressure and vapor mass concentration

Contributed by the Heat Transfer Division and presented at the ASME Winter Annual Meeting, Anaheim, California, November 8–13, 1992. Manuscript received by the Heat Transfer Division January 1993; revision received August 1993. Keywords: Conduction, Mass Transfer, Phase-Change Phenomena. Associate Technical Editor: R. Viskanta.

are fixed at the surface. Two temperature boundary conditions are considered at the surface: a constant-temperature condition and a time-dependent heat flux condition. The volumetric heating source is assumed to be a function of time and position. A sublimation front is assumed to propagate through the material, with the interface condition governed by the Clapeyron equation and the ideal gas law. One-dimensional heat transfer is considered with conductive heat transfer in the frozen region and both conduction and convection in the dried region. No liquid is assumed to be present anywhere in the system, the mass transfer of the vapor in the dried region is assumed to be governed by both Fick's and Darcy's Laws, and the vapor mass flow rate within the dried region is assumed to be equal to that at the sublimation front at any given time. In addition, the temperature of the gas in the dried region is assumed to be in equilibrium with the dried material, and the thermophysical properties are assumed to be constant, but they may differ between the dried and frozen regions. These assumptions are consistent with those used by Fey and Boles (1987) for sublimation-dehydration without volumetric heating.

A mathematical description for temperature within the material is given below. For heat transfer in the frozen region, the temperature is given by

$$\frac{\partial^2 T_f}{\partial x^2} + G_f(x, t) = \frac{1}{\alpha_f}\frac{\partial T_f}{\partial t} \quad s(t) < x < \infty \quad t > 0 \tag{1}$$

and in the dried region, the temperature is found from

$$\frac{\partial^2 T_d}{\partial x^2} + \frac{c_{pw}\dot{W}(t)}{k_d}\frac{\partial T_d}{\partial x} + G_d(x, t) = \frac{1}{\alpha_d}\frac{\partial T_d}{\partial t} \quad 0 < x < s(t) \quad t > 0 \tag{2}$$

where, from the assumptions used, the vapor mass flow rate, $\dot{W}$, is equal to the rate of sublimation at the interface, $s(t)$:

$$\dot{W} = \omega C_i \frac{ds(t)}{dt} \tag{3}$$

where the interface position, $s(t)$, is assumed to be of the form (Fey and Boles, 1987)

$$s(t) = 2\lambda\sqrt{\alpha_d t} \tag{4}$$

where λ is a constant. The intensity of the volumetric heating is assumed to be a function of time and position in both the dried and frozen regions, which is given by

$$G_i(x, t) = \frac{A_o}{4\alpha_i t} e^{-(x/(4\alpha_i t)^{1/2} + d_i)^2} \quad i = f \text{ or } d \tag{5}$$

where d_d and d_f are arbitrary constants. Although this is an arbitrary function, it is not unreasonable since, in considering actual volumetric heating processes such as microwave-aided processes, the strength of the microwave field also decreases with distance and the absorption of the microwave energy also differs between the dried and frozen regions.

The initial temperature and the temperature as $x \to \infty$ are assumed to be constant:

$$T_d(x, 0) = T_f(\infty, t) = T_i \tag{6}$$

At $x = 0$, two different temperature boundary conditions are considered; the first is a constant-temperature condition:

$$T_d(0, t) = T_s \tag{7a}$$

and the second is an assumed heat flux of the form:

$$-k_d \left.\frac{\partial T}{\partial x}\right|_{x=0} = \frac{q}{\sqrt{4\alpha_d t}} \quad t > 0 \tag{7b}$$

(Note that Ma and Peltre (1973, 1975a) and Ang et al. (1977a) both assume convection at the surface and that Eqs. (7*a*, *b*) with $q = 0$ represent the extreme cases of convective heat transfer.)

The interface condition is determined from an energy balance at $x = s(t)$:

$$-k_d \left.\frac{\partial T_d}{\partial x}\right|_{x=s(t)} + k_f \left.\frac{\partial T_f}{\partial x}\right|_{x=s(t)} = L\dot{W}(t) \quad t > 0 \tag{8}$$

where the temperature at the interface is assumed to be constant:

$$T_f(s(t), t) = T_d(s(t), t) = T_v \tag{9}$$

It should be noted, however, that in the case of actual microwave heating, the interface temperature could vary with location and time due to the large difference in dielectric properties between the frozen and dried regions.

The governing equations and the initial, boundary, and interface conditions for the vapor mass concentration, C, and the pressure, P, are the same as those given by Fey and Boles (1987).

Problem Solution

The solution procedure is similar to that presented by Fey and Boles (1987) without volumetric heating. The nondimensional forms of Eqs. (1)–(9) were found using the similarity variable, η, and the dimensionless variables defined in the nomenclature. Using $d_d = a^+\lambda$ and $d_f = 0$ as the arbitrary constants in Eq. (5), the solutions for θ_f and θ_d with the constant-temperature boundary condition described by Eq. (7*a*) are given as

Nomenclature

A_o = volumetric heat source coefficient (Eq. (5)), °C/m²
A_o^+ = dimensionless volumetric heat source coefficient = $A_o^+/(T_s - T_i)$
a^+ = dimensionless convection coefficient = $c_{pw}\omega C_i\alpha_d/k_d$
b^+ = dimensionless constant = $C_t\alpha_d L/(T_t k_f)$
C = concentration of water vapor or ice, kg/m³
C_t' = initial dimensionless concentration of ice, $\omega C_i/C_t$
C_s' = dimensionless concentration of water vapor at surface = C_i/C_t
C_v' = dimensionless concentration of water vapor at interface = C_v/C_t
C^+ = dimensionless concentration of water vapor = $(C - C_i)/(C_v - C_s)$
c_{pw} = specific heat of water vapor, J/kg°C
d = dimensionless constant
G = volumetric heat source term, °C/m²
h = sample thickness, m
k = effective thermal conductivity, W/m°C
k_{df} = nondimensional effective thermal conductivity = k_d/k_f
L = latent heat of sublimation, J/kg
L^+ = dimensionless latent heat of sublimation = $L/R_o T_t$
Lu = Luikov moisture diffusivity = α_m/α_d
Lu_p = Luikov pressure diffusivity = α_p/α_d
P = pressure, N/m²
P_s' = dimensionless pressure at surface = P_s/P_t
P_v' = dimensionless pressure at interface = P_v/P_t
P^+ = dimensionless pressure = $(P - P_s)/(P_v - P_s)$
q = heat flux constant (in Eq. (7*b*)), W/m
q^+ = dimensionless heat flux = $q/k(T_t - T_i)$

$$\theta_f(\eta)=\left(\frac{\theta_v'-\theta_i'}{1-\theta_i'}\right)\frac{\operatorname{erfc}(\sqrt{\alpha_{df}}\eta)}{\operatorname{erfc}(\sqrt{\alpha_{df}}\lambda)}+\frac{A_o^+}{2}\left[e^{-\alpha_{df}\eta^2}-e^{-\alpha_{df}\lambda^2}\frac{\operatorname{erfc}(\sqrt{\alpha_{df}}\eta)}{\operatorname{erfc}(\sqrt{\alpha_{df}}\lambda)}\right]\quad \lambda<\eta<\infty \tag{10}$$

$$\theta_d(\eta)=\left(\frac{\theta_s'-\theta_i'}{1-\theta_i'}\right)+\left(\frac{\theta_v'-\theta_s'}{1-\theta_i'}\right)\frac{\operatorname{erf}(a^+\lambda)-\operatorname{erf}(\eta+a^+\lambda)}{\operatorname{erf}(a^+\lambda)-\operatorname{erf}(\lambda+a^+\lambda)}+\frac{A_o^+}{2}\left[e^{-(\eta+a^+\lambda)^2}-e^{-a^{+2}\lambda^2}-(e^{-(\lambda+a^+\lambda)^2}-e^{-a^{+2}\lambda^2})\times\frac{\operatorname{erf}(a^+\lambda)-\operatorname{erf}(\eta+a^+\lambda)}{\operatorname{erf}(a^+\lambda)-\operatorname{erf}(\lambda+a^+\lambda)}\right]\quad 0<\eta<\lambda \tag{11a}$$

while the solution for θ_d with the heat flux boundary condition described by Eq. (7*b*) is

$$\theta_d(\eta)=\left(\frac{\theta_v'-\theta_i'}{1-\theta_i'}\right)-\frac{q^+\sqrt{\pi}}{2}\frac{\operatorname{erf}(\eta+a^+\lambda)-\operatorname{erf}(\lambda+a^+\lambda)}{e^{-a^{+2}\lambda^2}}+\frac{A_o^+}{2}[e^{-(\eta+a^+\lambda)^2}-e^{-(\lambda+a^+\lambda)^2}+\sqrt{\pi}a^+\lambda(\operatorname{erf}(\eta+a^+\lambda)-\operatorname{erf}(\lambda+a^+\lambda))]\quad 0<\eta<\lambda \tag{11b}$$

The solution for θ_f in this case is the same as that given in Eq. (10).

The solutions for the dimensionless vapor concentration, C^+, and dimensionless pressure, P^+, in each case are the same as those given by Fey and Boles (1987):

$$C^+(\eta)=\left[1-\frac{\Delta}{\epsilon}\left(\frac{P_v'-P_s'}{C_v'-C_s'}\right)\right]\frac{\operatorname{erf}(\eta\sqrt{\epsilon/Lu})}{\operatorname{erf}(\lambda\sqrt{\epsilon/Lu})}+\frac{\Delta}{\epsilon}\left(\frac{P_v'-P_s'}{C_v'-C_s'}\right)\frac{\operatorname{erf}(\eta\sqrt{Lu_p})}{\operatorname{erf}(\lambda\sqrt{Lu_p})}\quad 0<\eta<\lambda \tag{12}$$

$$P^+(\eta)=\frac{\operatorname{erf}(\eta\sqrt{Lu_p})}{\operatorname{erf}(\lambda\sqrt{Lu_p})}\quad 0<\eta<\lambda \tag{13}$$

The interface location, λ, is found from differentiating Eqs. (10)–(13) with respect to η and substituting the resulting expressions evaluated with $\eta=\lambda$ into the interface conditions. From Eqs. (10) and (11*a*), the interface condition for the temperature boundary condition is

$$k_{df}e^{-(\lambda+a^+\lambda)^2}\left[\frac{(\theta_v'-\theta_s')/(1-\theta_i')}{\operatorname{erf}(a^+\lambda)-\operatorname{erf}(\lambda+a^+\lambda)}+\frac{A_o^+}{2}\left[\sqrt{\pi}(\lambda+a^+\lambda)+\frac{e^{-a^{+2}\lambda^2}-e^{-(\lambda+a^+\lambda)^2}}{\operatorname{erf}(a^+\lambda)-\operatorname{erf}(\lambda+a^+\lambda)}\right]\right]-\sqrt{\alpha_{df}}e^{-\lambda^2\alpha_{df}}\left[\frac{(\theta_v'-\theta_i')/(1-\theta_i')}{\operatorname{erfc}(\sqrt{\alpha_{df}}\lambda)}+\frac{A_o^+}{2}\left[\sqrt{\pi\alpha_{df}}\lambda+\frac{e^{-\alpha_{df}\lambda^2}}{\operatorname{erfc}(\sqrt{\alpha_{df}}\lambda)}\right]\right]=\frac{\sqrt{\pi}b^+C_i'\lambda}{\theta_s'-\theta_i'} \tag{14a}$$

and from Eqs. (10) and (11*b*) for the heat flux boundary condition, the interface condition is

$$\frac{\sqrt{\pi}}{2}k_{df}e^{-(\lambda+a^+\lambda)^2}\left[\frac{q^+}{e^{-a^{+2}\lambda^2}}+A_o^+\lambda\right]-\sqrt{\alpha_{df}}e^{-\lambda^2\alpha_{df}}\left[\left(\frac{\theta_v'-\theta_s'}{1-\theta_i'}\right)\frac{1}{\operatorname{erfc}(\sqrt{\alpha_{df}}\lambda)}+\frac{A_o^+}{2}\left[\sqrt{\pi\alpha_{df}}\lambda-\frac{e^{-\alpha_{df}\lambda^2}}{\operatorname{erfc}(\sqrt{\alpha_{df}}\lambda)}\right]\right]=\frac{\sqrt{\pi}b^+C_i'\lambda}{\theta_s'-\theta_i'} \tag{14b}$$

The interface condition for the vapor concentration is given by Fey and Boles (1987):

$$\frac{[(C_v'-C_s')\epsilon-(P_v'-P_s')\Delta](\sqrt{Lu/\epsilon})e^{-\epsilon\lambda^2/Lu}}{\operatorname{erf}(\lambda\sqrt{\epsilon/Lu})}+\frac{\Delta\sqrt{Lu_p}(P_v'-P_s')e^{-\lambda^2/Lu_p}}{\operatorname{erf}(\lambda/\sqrt{Lu_p})}=\sqrt{\pi}(C_i'-\epsilon C_v')\lambda \tag{15}$$

where C_v' and P_v' are found from the Clapeyron equation and the ideal gas law:

$$C_v'\theta_v'=\exp[L^+(1-1/\theta_v')] \tag{16}$$

$$P_v'=C_v'R^+\theta_v' \tag{17}$$

The unknown values for λ, θ_v', C_v', and P_v' are determined from Eqs. (13), (14*a*) for a constant-temperature boundary condition or Eq. (14*b*) for a heat flux boundary condition, and Eqs. (15)–(17).

Sensitivity Study

A sensitivity study was conducted to determine the effects of the parameters, α_{df}, Lu, Lu_p, k_{df}, Δ, ϵ, a^+, and b^+, on the mathematical solutions presented in Eqs. (10), (11*a*), (12)–(17), with and without volumetric heating. Sensitivity coefficients were used to evaluate these effects; they provide an indication of the importance of each parameter in the mathematical model, and they can also be used to determine whether

Nomenclature (cont.)

R^+ = dimensionless gas constant $= R_oC_tT_t/P_t$
R_o = ideal gas constant, J/kgK
s = location of sublimation front, m
s^+ = dimensionless sublimation front location $= s/h$
T = temperature, °C
t = time, s
$\dot{W}$ = mass flow rate of vapor, kg/s
x = position, m
X^+_{β,Y^+} = sensitivity coefficient of β associated with Y^+
Y^+ = process variable (θ, C^+, P^+)
Z = transformation variable
α = effective thermal diffusivity, m^2/s
α_{df} = nondimensional effective thermal diffusivity $= \alpha_d/\alpha_f$
α_m = mass diffusivity, m^2/s
α_p = filtration diffusivity, m^2/s
β = dimensionless material property
δ_p = filtration coefficient, s^2/m^2
Δ = nondimensional permeability $= (\epsilon\alpha_m\delta_pP_t)/(\epsilon\alpha_p-\alpha_m)C_t$
ϵ = porosity, m^3/m^3
η = similarity variable
θ = dimensionless temperature $= (T-T_i)/(T_t-T_i)$
θ_i' = initial dimensionless temperature $= T_i/T_t$
θ_s' = dimensionless surface temperature $= T_s/T_t$
θ_v' = dimensionless interface temperature $= T_v/T_t$
λ = nondimensional sublimation front location defined by Eq. (4)
ξ_i = dimensionless material property
ω = volume fraction of ice, m^3/m^3

Subscripts

avg = average value over a given region
d = dried region
f = frozen region
i = initial
s = at the surface
t = at the triple point
v = at the sublimation interface

or not the parameters are correlated, which is an important consideration in determining methodologies for the estimation of the parameters.

Sensitivity Coefficient Analysis—Magnitude. A sensitivity coefficient is defined as the change in a given variable due to a change in a specific parameter, with all other parameters remaining constant, as shown below:

$$X^+_{\beta,Y^+} \equiv \beta\left(\frac{\partial Y^+}{\partial \beta}\right)_{\xi_i \neq \beta,\text{const}} \tag{18}$$

Here, X^+_{β,Y^+} is the dimensionless sensitivity coefficient associated with the process variable Y^+ (i.e., θ, C^+, or P^+) and a specific parameter β (i.e., α_{df}, Lu, Lu_p, k_{df}, Δ, ϵ, a^+, or b^+), and $\xi_i \neq \beta$ are all parameters other than β.

In the mathematical model used in this study, all of the material properties are coupled through the interface conditions. Therefore, it was important to evaluate the sensitivity coefficients for each of the variables θ, C^+, and P^+ with respect to each of the parameter values. A sensitivity coefficient with a small magnitude (e.g., $<10^{-3}$) indicates that a given variable is insensible to changes in that specific parameter value, while a large sensitivity coefficient (~ 1) indicates that the variable is extremely sensitive to that particular parameter. This information is important in assessing the assumption of constant material properties for a given material. If the sensitivity coefficients are large, the simplifying assumption of constant property values would not be appropriate, if in actuality for a given material, the properties are thought to vary with some variable such as temperature. However, if the sensitivity coefficients are small, any actual changes in the property value would have little effect on the process variable in question, and the simplifying assumption of using constant parameter values could be justified even though these parameters might actually vary during the process.

To evaluate the sensitivity coefficients for a given parameter β associated with a given process variable Y^+, the variable was differentiated with respect to β, noting that λ and θ_v' are functions of β through the interface conditions (Eqs. (14*a*), (15)–(17)):

$$\frac{\partial Y^+(\beta, \lambda, \theta_v')}{\partial \beta} = \left(\frac{\partial Y^+(\beta, \lambda, \theta_v')}{\partial \beta}\right)_{\lambda,\theta_v',\xi_i\neq\beta,\text{const}} + \left[\left(\frac{\partial Y^+(\beta, \lambda, \theta_v')}{\partial \lambda}\right)_{\beta,\theta_v',\xi_i\neq\beta,\text{const}}\right]\frac{\partial \lambda}{\partial \beta} + \left[\left(\frac{\partial Y^+(\beta, \lambda, \theta_v')}{\partial \theta_v'}\right)_{\beta,\lambda,\xi_i\neq\beta,\text{const}}\right]\frac{\partial \theta_v'}{\partial \beta} \tag{19}$$

The partial derivative of θ_v' with respect to β was found by first solving Eq. (14*a*) for θ_v', and then differentiating with respect to a given parameter β. To find the partial of λ with respect to β, Eq. (15) was first set equal to zero. Considering this now to be a function, $f(\beta, \xi_i \neq \beta, \lambda)$, its total derivative is also equal to zero:

$$df(\beta, \xi_i\neq\beta, \lambda) = 0 = \left(\frac{\partial f}{\partial \beta}\right)_{\xi_i\neq\beta,\lambda} d\beta + \sum_{\substack{i=1\\ \xi_i\neq\beta}}^{8}\left[\left(\frac{\partial f}{\partial \xi_i}\right)_{\beta,\lambda} d\xi_i\right] + \left(\frac{\partial f}{\partial \lambda}\right)_{\beta,\xi_i\neq\beta} d\lambda \tag{20}$$

The partial of λ with respect to β was then approximated by dividing Eq. (20) by $d\beta$ and solving for $d\lambda/d\beta$, neglecting higher order terms.

The sensitivity coefficients were evaluated analytically for each variable with respect to each parameter for incremental values of the similarity variable η using $A_o^+ = 0$ and $A_o^+ = 5$.

Table 1 Orders of magnitude of the sensitivity coefficients

X^+_{β,Y^+}	$A_o^+ = 0$				$A_o^+ = 5$			
Y^+	θ		C^+	P^+	θ		C^+	P^+
β	$\eta<\lambda$	$\eta>\lambda$	$\eta<\lambda$	$\eta<\lambda$	$\eta<\lambda$	$\eta>\lambda$	$\eta<\lambda$	$\eta<\lambda$
α_{df}	10^{-1}	10^{-1}	10^{-1}	10^{-1}	10^{-1}	10^{-1}	10^{-1}	10^{-1}
k_{df}	10^{-1}	10^{-1}	1	1	10^{-4}	10^{-4}	10^{-3}	10^{-3}
a^+	10^{-2}	10^{-3}	10^{-2}	10^{-2}	10^{-1}	10^{-3}	10^{-2}	10^{-2}
b^+	10^{-4}	10^{-5}	10^{-4}	10^{-4}	10^{-4}	10^{-4}	10^{-4}	10^{-4}
ϵ	10^{-3}	10^{-3}	10^{-3}	10^{-3}	10^{-2}	10^{-2}	10^{-1}	10^{-2}
Δ	10^{-3}	10^{-3}	10^{-2}	10^{-2}	10^{-2}	10^{-2}	10^{-2}	10^{-2}
Lu	10^{-2}	10^{-2}	10^{-2}	10^{-2}	10^{-1}	10^{-1}	10^{-3}	10^{-1}
Lu_p	10^{-2}	10^{-3}	10^{-2}	10^{-2}	10^{-1}	10^{-1}	10^{-1}	10^{-2}

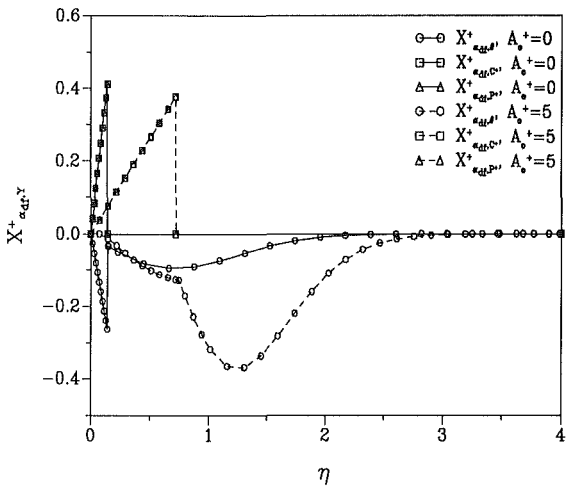

Fig. 1 Sensitivity coefficients for α_{df}

The following parameter values were used in the calculations: $\alpha_{df}=1$, $Lu=100$, $Lu_p=1000$, $k_{df}=0.1$, $\Delta=0.1$, $\epsilon=0.64$, $a^+=3$, and $b^+=3.6\times10^{-6}$. (These values are based partly on those used by Fey and Boles, 1987.)

The sensitivity coefficients for α_{df} ($X^+_{k_{df},Y^+}$) are shown in Fig. 1 for $0<\eta<4$ with $A_o^+=0$ and $A_o^+=5$. There are several characteristics evident in this figure that were also common to the sensitivity coefficients for all of the other parameters: (1) The magnitudes of the sensitivity coefficients associated with θ approach zero as $\eta\to\infty$; (2) there is a step change in the sensitivity coefficients associated with θ at the interface condition ($\eta=\lambda$); (3) the sensitivity coefficients associated with C^+ and P^+ are very similar; and (4) since there is no vapor in the frozen region, the sensitivity coefficients associated with both C^+ and P^+ are zero for $\eta>\lambda$.

As discussed previously, the order of magnitude of a sensitivity coefficient indicates the sensitivity of a given process variable to changes in a particular parameter. The orders of magnitudes of the maximum values of each sensitivity coefficient for $0<\eta<\lambda$ and $\eta>\lambda$ are given in Table 1 for $A_o^+=0$ and $A_o^+=5$. In the case where $A_o^+=0$, the maximum sensitivity coefficients for α_{df} and k_{df} were all at least on the order of 10^{-1}, indicating that θ, C^+, and P^+ are very sensitive to changes in α_{df} and k_{df}. The maximum sensitivity coefficients for ϵ and b^+ were very small ($\leq 10^{-3}$), indicating that θ, C^+, and P^+ are insensitive to changes in these parameters. As a result, the consideration of variable property values is most important for k_{df} and α_{df} while any actual variations in ϵ or b^+ would have little influence on the solutions for θ, C^+, and P^+.

The volumetric heat source coefficient (A_o^+) had the greatest effect on the maximum sensitivity coefficients for k_{df}; all of

these sensitivity coefficients ($X^+_{k_{df}\theta}$, $X^+_{k_{df}C^+}$, and $X^+_{k_{df}P^+}$) decreased three orders of magnitude for $A_o^+ = 5$ in Table 1, greatly reducing the effect of k_{df} on the solution. This has two implications for an increasing volumetric heat source term: (1) The effects of any actual variations in k_{df} decrease, and therefore, the assumption of a constant k_{df} could be justified whether or not k_{df} actually varied, and (2) the thermal diffusive effects decrease, which might lead to simplifications of the mathematical model for large values of A_o^+.

Also, with volumetric heating, the sensitivity coefficients associated with temperature for Lu, Lu_p, Δ, and ϵ increased by one to two orders of magnitude, increasing these parameters' influence on the temperature solutions. Thus, the consideration of variable property values is important for Lu, Lu_p, Δ, and ϵ with volumetric heating; if it is known that these properties are functions of temperature for a particular material, then the solution should be reformulated to include this dependence. These properties are physical in nature (i.e., associated with mass and pressure) rather than thermal; this observation, along with the observation that the influence of k_{df} decreased with an increase in A_o^+, indicates that mass and pressure diffusion are the limiting factors to the rate of drying rather than thermal diffusion with the volumetric heat source described by Eq. (5). This agrees with the observation by Arsem and Ma (1985) concerning microwave heating discussed previously.

The increase in the volumetric heat source term had no or only a small influence on the maximum sensitivity coefficients for α_{df} and b^+ and slightly increased the sensitivity of θ_f to changes in a^+. Thus, if it is found, for example, that in an actual situation α_{df} is a function of temperature, it would be important to include this in the problem formulation whether or not there is volumetric heating. However, any actual variations in b^+ would have little effect on the solutions with or without volumetric heating, and thus, any actual variations could be neglected.

Sensitivity Coefficient Analysis—Linear Dependence and Correlation Between Parameters. The material properties inherent in the solution must be known if the solution is to be practically useful. Thus, it is important to determine which parameters in the solutions can be estimated, particularly from the process variables in question. Correlation between material properties is an important consideration when developing methodologies to estimate material properties associated with a given process. In some estimation methodologies based on minimization procedures, the material parameters cannot be simultaneously estimated as independent values if they are found to be correlated (Beck and Arnold, 1977). Linearly dependent or nearly linearly dependent sensitivity coefficients for a given process variable are an indication that the parameters are correlated with respect to that process variable (Beck and Arnold, 1977). In some instances, parameters can be correlated with respect to one process variable, but not with respect to another (Saad, 1991). In this situation, the process variable resulting in the uncorrelated parameters could be used in the estimation procedure.

The sensitivity coefficients associated with θ, C^+, and P^+ for each of the parameters α_{df}, Lu, Lu_p, k_{df}, Δ, ϵ, a^+, and b^+ were compared with each other to determine linear dependence. All of the sensitivity coefficients associated with C^+ and P^+ were found to be linearly dependent, indicating that C^+ and P^+ are not appropriate variables to use in the estimation of the parameters in question. A summary of the results for the sensitivity coefficients associated with θ is given in Table 2 for $A_o^+ = 5$. A (+) sign indicates that linear dependence was found and a (−) sign indicates no linear dependence was evident. It should be noted that in some cases, the sensitivity coefficients were linearly dependent (or independent) for $\eta < \lambda$, while the opposite was true for $\eta > \lambda$. The sensitivity coefficients associated with θ for Lu, Lu_p, Δ, and ϵ were all found to be linearly dependent, indicating that these parameters cannot be simultaneously estimated as independent values from temperature measurements. Independent experiments would therefore be needed to provide estimates of these values. Any one of these values could be estimated, however, with any of the other parameters (α_{df}, k_{df}, a^+, and b^+) from data in the dried region or with α_{df} in either region. The sensitivity coefficients for k_{df} and b^+ were also found to be linearly dependent, while α_{df} and a^+ were found to be linearly independent. The parameters α_{df} and k_{df}, and α_{df} and b^+ were found to be independent only in the frozen region; however, a^+ and b^+ were found to be independent only in the dried region.

Table 2 Linear dependence of the sensitivity coefficients for θ with $A_o^+ = 5$

$X^+_{\beta,\theta}$	α_{df}	k_{df}	a^+	b^+	ε	Δ	Lu	Lu_p	
α_{df}	(+)	(-)	(-)	(-)	(-)	(-)	(-)	(-)	
k_{df}	(+)	(+)	(+)	(+)	(+)	(+)	(+)	(+)	
a^+	(-)	(-)	(+)	(+)	(+)	(+)	(+)	(+)	
b^+	(+)	(+)	(-)	(+)	(+)	(+)	(+)	(+)	$\eta>\lambda$
ε	(-)	(-)	(-)	(-)	(+)	(+)	(+)	(+)	
Δ	(-)	(-)	(-)	(-)	(+)	(+)	(+)	(+)	
Lu	(-)	(-)	(-)	(-)	(+)	(+)	(+)	(+)	
Lu_p	(-)	(-)	(-)	(-)	(+)	(+)	(+)	(+)	
	$\eta<\lambda$								

The magnitude of the sensitivity coefficients also has an effect on the estimation of the associated parameters. Large sensitivity coefficients indicate that the process variable is very sensitive to variations in the associated parameter; therefore, parameters estimated from data with large sensitivity coefficients are, in general, more accurate than parameters estimated from data with small sensitivity coefficients. Therefore, given a choice of parameters to estimate, uncorrelated parameters with the highest sensitivity coefficients should be chosen. For example, based on the temperature data in Table 1, the best parameter estimates would be found for α_{df} with or without volumetric heating, k_{df} without volumetric heating, and Lu and Lu_p with volumetric heating, while the poorest estimates would be obtained for k_{df} and b^+ with volumetric heating and b^+, ϵ, and Δ without heating. However, in comparing these results with those from Table 2, the best combination for the simultaneous estimation of independent values would be obtained from α_{df} and Lu or Lu_p with volumetric heating.

Analysis of Solution

Several aspects of the solutions presented here were analyzed. First, the appropriateness of the assumed volumetric heating was addressed, and then the validity of the assumption that no melting occurs was investigated. In addition, the assumed freezing front location was analyzed, and this and the predicted percent moisture content were compared to theoretical and experimental values found in the literature.

Volumetric Heating. The assumed volumetric heating term given in Eq. (5) was selected to reflect a decrease in the heating effect within the material as a function of distance, account for a difference in microwave absorption between the dried and frozen regions, and facilitate the analytical solution of the problem. In addition, it allows for a decrease in heating with time, which was found to provide an optimal mode of operation by Ang et al. (1978).

Table 3 Assumed dimensionless material property values for beef and assumed operating conditions

Variable	Value	Source
α_{df}	0.096	Ma and Peltre (1973)
k_{df}	0.029	Ma and Peltre (1973)
a^+	1.2	Ma and Peltre (1973, 1975b)
b^+	2.6×10^{-6}	Ma and Peltre (1973)
ε	0.75	Ma and Peltre (1973)
Δ	0.1	Assumed (based on Fey and Boles, 1987)
Lu	2.0×10^{4}	Ma and Peltre (1973)
Lu_p	300	Assumed (based on Fey and Boles, 1987)
C_i'	1.4×10^{4}	Ma and Peltre (1973)
C_s'	0.2	Assumed (based on Fey and Boles, 1973)
P_s'	0.2	Ma and Peltre (1975b)
θ_i'	0.94	Ma and Peltre (1975a)
θ_s'	1.09	Using ambient conditions (Ma and Peltre (1985))

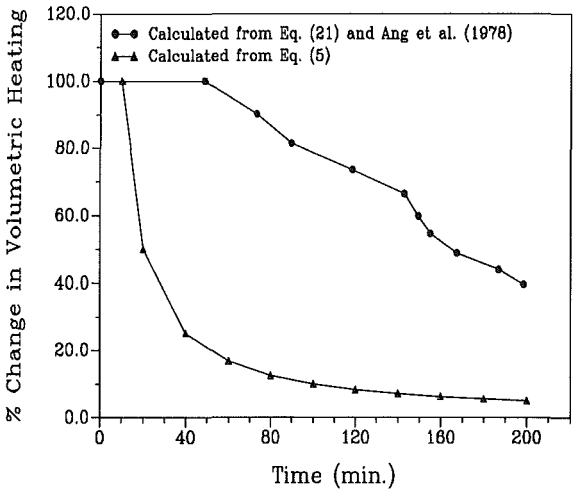

Fig. 2 Percent change in volumetric heating in the dried region from Eq. (21) and Ang et al. (1978) and from Eq. (5) using $x=0$ m and defining percent change in heating as the change from the value of the volumetric heating at 5 minutes

Ma and Peltre (1975a) describe the microwave volumetric heating for a given field strength, E, as

$$G=\frac{E^2K_i}{k_i} \quad i=d \text{ or } f \tag{21}$$

where K_i is the dissipation coefficient. The volumetric heating defined by Eq. (21) was calculated using the electrical field data from Ang et al. (1978) and the dissipation and thermal property values from Ma and Peltre (1975a). These values were compared with the volumetric heating defined by Eq. (5) at $x=0$ m in the dried region and $x=0.015$ m in the frozen region and using properties for beef from Ma and Peltre (1973, 1975a, b) (Table 3). (The sample dimensions were chosen to represent a typical experimental sample, Ma and Peltre, 1975b).

First, the percent change in the volumetric heating with time was compared. At very early times, the volumetric heating defined by Eq. (5) decreases very rapidly; however, the predicted change in volumetric heating in the dried region after 5 minutes from Eq. (5) is not unlike the change used by Ang et al. (1978) for optimal heating, as shown in Fig. 2. Note also that the time dependence is an externally adjustable variable. Next, the difference between the heating within the dried and frozen regions was investigated. The ratios of the volumetric heating for the dried and frozen regions determined from Eqs. (5) and (20) are shown in Fig. 3 as functions of time. With the exception of the early portion of the curve found using Eq. (5), both equations predict a constant ratio between the dried and frozen regions with the results from Eq. (5) about 20 percent lower than those found using Eq. (21). Therefore, based on these results, with the exception of very early times,

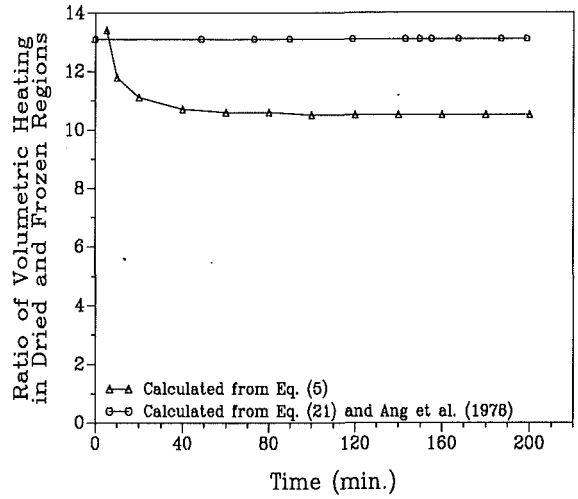

Fig. 3 Ratio of volumetric heating in the dried and frozen regions from Eq. (21) and Ang et al. (1978) and from Eq. (5) using $x=0$ m in the dried region and $x=0.015$ m in the frozen region

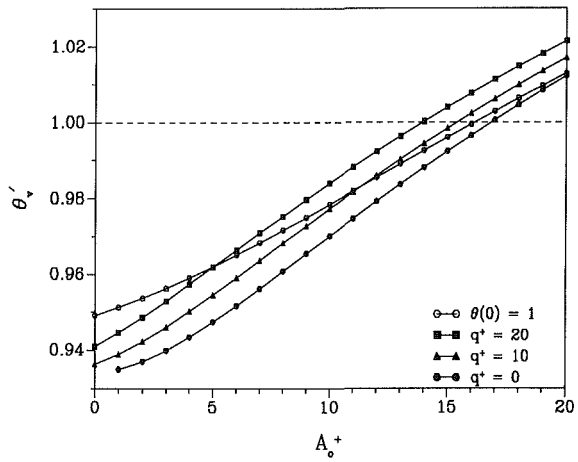

Fig. 4 Interface temperature, θ_v', as a function of dimensionless volumetric heating, A_o^+, for constant temperature ($\theta(0)=1$) and heat flux ($q^+=0$, $q^+=10$, and $q^+=20$) boundary conditions

the assumption of the volumetric heat source term in Eq. (5) is not unreasonable.

The Occurrence of Melting. The effect of the volumetric heating on the possibility of melting within the material was investigated by determining the dimensionless temperature and pressure at the interface (θ_v' and P_v'). Note that if θ_v' or P_v' is greater than one, melting will occur. The values for θ_v' and P_v' were determined using the property values in Table 3, with A_o^+ varying from 0 to 20 for both a constant-temperature boundary condition ($\theta(0)=1$) and a heat flux boundary condition with $q^+=0$, $q^+=10$, and $q^+=20$. The results are shown in Figs. 4 and 5 for θ_v' and P_v', respectively. Note that all of the solutions presented here are valid for A_o^+ at least less than 14 (with most <15) and $q^+\le 20$. Also note that the solutions for $\theta(0)=1$ and $q^+=0$ represent no and infinite resistance to heat transfer at the surface and that the two solutions converge as A_o^+ increases.

The Interface Location. The interface location is of extreme importance because it is closely associated with the drying time. The assumed interface location given in Eq. (4) was compared to experimental and theoretical results presented by Ma and Peltre (1975b); the results for the dimensionless interface condition, s^+, using the material properties in Table 3 for both a constant temperature and a heat flux boundary

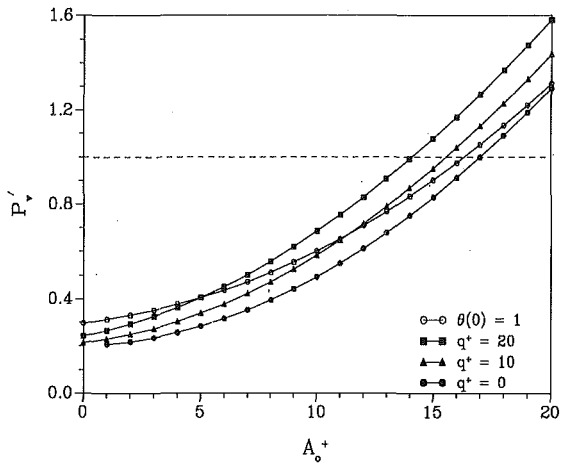

Fig. 5 Interface pressure, P'_v, as a function of dimensionless volumetric heating, A_o^+, for constant temperature ($\theta(0)=1$) and heat flux ($q^+=0$, $q^+=10$, and $q^+=20$) boundary conditions

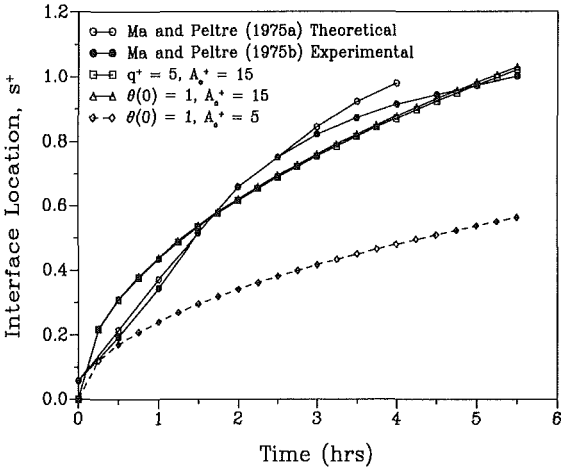

Fig. 6 Dimensionless interface position, s^+, as a function of time for constant temperature ($\theta(0)=1$) and the heat flux ($q^+=5$) boundary conditions with $A_o^+=15$ compared with theoretical and experimental results from Ma and Peltre (1975b) with $E=125$ V/cm

condition are shown along with the results from Ma and Peltre in Fig. 6. Here, s^+ is defined as s/h where h is the sample thickness (0.015 m, Ma and Peltre, 1975b).

The results using Eq. (4) and $A_o^+=15$, with $\theta(0)=1$ and $q^+=5$ are nearly identical. (Note, from Figs. 4 and 5, no melting occurs.) Both solutions provide good agreement for the prediction of the drying time for the sample ($s^+=1$); however, the velocity of the interface location is overestimated at the early drying times. This could be attributed to the assumed volumetric heating (Eq. (5)), which is very high at early times and then decreases (Fig. 3), while the actual microwave power input used by Ma and Peltre (1975b) was independent of time. Since the solution for λ is based on Eq. (5), it is expected that the velocity of the interface location would be overestimated at early times. This is evident by looking at constant-temperature boundary condition solution with $A_o^+=5$, also shown in Fig. 6; here, the interface location is better approximated at very early times; however, the interface location is greatly underpredicted at later times. It should also be noted that the theoretical results presented by Ma and Peltre (1975a) were found for an infinite slab, assuming convection on one side and insulation on the other. Their results are in close agreement with experimental results for times less than three hours; however, the overall drying time is then underestimated by over 25 percent.

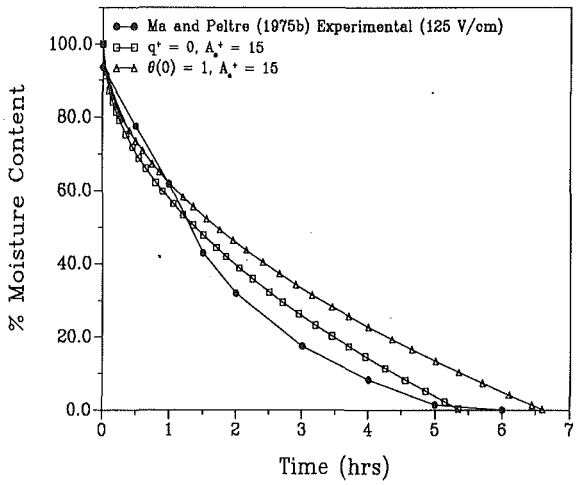

Fig. 7 Percent moisture content as a function of time for constant temperature ($\theta(0)=1$) and heat flux ($q^+=0$) boundary conditions with $A_o^+=15$ compared with experimental results from Ma and Peltre (1975b) with $E=125$ V/cm

Comparison of Drying Curves. The percent moisture content is defined as

$$\text{Percent Moisture Content} = \frac{C_{\text{avg}}(t) - C_{\text{avg},f}}{C_i - C_{\text{avg},f}} \tag{22}$$

where $C_{\text{avg}}(t)$ is the average moisture content over a thickness h at time t, $C_{\text{avg},f}$ is the averaged final moisture content at the end of drying over h, and C_i is the initial moisture content. The percent moisture content was calculated using a constant-temperature boundary condition ($\theta(0)=1$) and an insulated boundary condition ($q^+=0$), with $h=0.015$ m and $A_o^+=15$ and compared with experimental results from Ma and Peltre (1975b) with $E=125$ V/cm in Fig. 7. The total experimental drying time is in between the predicted drying times with a constant temperature and an insulated boundary condition. This is expected since the two solutions presented here represent the extreme conditions of a convective boundary condition. Once again, the drying rate is overestimated at early times for both boundary conditions; this again could be a result of the assumed time dependence of the volumetric heating in Eq. (5) compared with the time independent value used by Ma and Peltre.

Conclusions

The following conclusions were drawn from this study:

1 From the sensitivity study, the assumption of constant material properties is especially important for α_{df} with and without volumetric heating, k_{df} without volumetric heating, and Lu and Lu_p with heating.
2 Dimensionless temperature is the best process variable to use for the estimation of material properties, and temperature would provide the most information for the estimation of α_{df}, while very little information would be available for the estimation of k_{df} and b^+ with volumetric heating, and b^+, ϵ, and Δ without heating.
3 Although arbitrary, the assumed volumetric heating (Eq. (5)) is not unreasonable, if the source is allowed to vary with time.
4 The solutions presented in this paper are only appropriate for A_o^+ at least less than 14 and $q^+ \leq 20$; otherwise melting could occur.
5 The assumed sublimation front location (Eq. (4)) overestimates the drying rate at early times, while providing good agreement with the overall drying time when compared to experimental data obtained with time-independent heating.

References

Ang, T. K., Ford, J. D., and Pei, D. C. T., 1977a, "Microwave Freeze-Drying of Food: A Theoretical Investigation," *Int. J. Heat Mass Transfer*, Vol. 20, pp. 517–526.

Ang, T. K., Ford, J. D., and Pei, D. C. T., 1977b, "Microwave Freeze-Drying: An Experimental Investigation," *Chem. Eng. Sci.*, Vol. 32, pp. 1477–1489.

Ang, T. K., Ford, J. D., and Pei, D. C. T., 1978, "Optimal Modes of Operation for Microwave Freeze Drying of Food," *J. Food Sci.*, Vol. 43, pp. 648–649.

Arsem, H. B., and Ma, Y. H., 1985, "Aerosol Formation During the Microwave Freeze Dehydration of Beef," *Biotech. Progress*, Vol. 1, pp. 104–110.

Beck, J. V., and Arnold, K. J., 1977, *Parameter Estimation in Engineering and Science*, Wiley, New York.

Decareau, R. V., 1982, "Microwave Research and Development at the U.S. Army Natick Research and Development Laboratories," *J. Microwave Power*, Vol. 17, pp. 127–135.

Dyer, D. F., and Sunderland, J. E., 1967, "The Transient Temperature Distribution During Sublimation Dehydration," ASME JOURNAL OF HEAT TRANSFER, Vol. 89, pp. 109–110.

Dyer, D. F., and Sunderland, J. E., 1968, "Heat and Mass Transfer Mechanisms in Sublimation Dehydration," ASME JOURNAL OF HEAT TRANSFER, Vol. 90, pp. 379–384.

Fey, Y. C., and Boles, M. A., 1987, "An Analytical Study of the Effect of Convection Heat Transfer on the Sublimation of a Frozen Semi-infinite Porous Medium," *Int. J. Heat Mass Transfer*, Vol. 30, pp. 771–779.

Hill, J. E., and Sunderland, J. E., 1971, "Sublimation-Dehydration in the Continuum, Transition and Free-Molecule Flow Regimes," *Int. J. Heat Mass Transfer*, Vol. 14, pp. 625–638.

Lin, S., 1981, "An Exact Solution of the Sublimation Problem in a Porous Medium," ASME JOURNAL OF HEAT TRANSFER, Vol. 103, pp. 165–168.

Lin, S., 1982, "An Exact Solution of the Sublimation Problem in a Porous Medium, Part II—With an Unknown Temperature and Vapor Concentration at the Moving Sublimation Front," ASME JOURNAL OF HEAT TRANSFER, Vol. 104, pp. 808–811.

Ma, Y. H., and Peltre, P., 1973, "Mathematical Simulation of a Freeze-Drying Process Using Microwave Energy," *AIChE Symposium Series*, Vol. 132, No. 66, pp. 47–54.

Ma, Y. H., and Peltre, P., 1975a, "Freeze Dehydration by Microwave Energy: Part I. Theoretical Investigation," *AIChE Journal*, Vol. 21, No. 2, pp. 335–344.

Ma, Y. H., and Peltre, P., 1975b, "Freeze Dehydration by Microwave Energy: Part II. Experimental Study," *AIChE Journal*, Vol. 21, No. 2, pp. 344–350.

Ma, Y. H., and Peltre, P., 1985, "Application of Optimal Control Strategy to Hybrid Microwave and Radiant Heat Freeze Drying System," *Drying '85*, Hemisphere Pub. Corp., pp. 249–253.

McCulloch, J. W., and Sunderland, J. E., 1970, "Integral Techniques Applied to Sublimation Drying With Radiation Boundary Condition," *J. Food Science*, Vol. 35, pp. 834–838.

Rosenberg, U., and Bögl, W., 1987, "Microwave Thawing, Drying, and Baking in the Food Industry," *Food Technology*, Vol. 41, No. 6, pp. 85–91.

Saad, Z., 1991, "Estimation of the Kinetic Parameters of an Amine-Epoxy Resin During Cure," M.S. thesis, Dept. of Mechanical Engineering, Michigan State University, East Lansing, MI.

Transient Cooling of Hot Porous and Nonporous Ceramic Solids by Droplet Evaporation

M. Abu-Zaid[1]

A. Atreya

Combustion and Heat Transfer Laboratory,
Department of Mechanical Engineering
and Applied Mechanics,
The University of Michigan,
Ann Arbor, MI 48109-2125

This paper presents the results of an experimental investigation into transient cooling of low-thermal-conductivity porous and nonporous ceramic solids by individual water droplets. The initial surface temperature (T_S) of both solids ranged from 75 to 200°C. Both solids were instrumented with several surface and in-depth thermocouples and had the same thermal properties. This enabled investigation into the similarities and differences in the thermal behavior of porous and nonporous solids during droplet evaporation. The measured and theoretical contact temperatures, for both solids, were found to be in good agreement until they became equal to the boiling point of water (which occurs at an initial solid surface temperature of 164°C). Further increase in the initial solid surface temperature did not change the measured contact temperature. Instead, it became roughly constant at a value slightly greater than the boiling point of water. During the droplet evaporation process, surface and in-depth temperatures for the nonporous solid remain nearly constant, whereas for the porous solid there was a continuous decrease in these temperatures. A thermocouple in the porous matrix at the same location as that of the nonporous matrix cools faster under identical conditions, indicating an energy sink in the vicinity of the thermocouple. Also, evaporation time for the nonporous solid was found to be larger than that of the porous solid for the same droplet size and under the same conditions. These observations confirm that there is both in-depth and lateral penetration of water in the porous solid. The transient temperature measurements were used to determine the following quantities: (i) the recovery time (time required by the surface to recover to its initial temperature), and (ii) the size of surface and in-depth zones affected by the droplet. The instantaneous evaporation rate, and the instantaneous average evaporative heat flux for the nonporous solid, were also determined from video measurements of the droplet diameter on the solid surface and the transient temperature measurements. It was found that the average evaporative heat flux is higher for smaller droplets because of their smaller thickness on the hot surface.

1 Introduction

The study of the behavior of impinging individual droplets on a hot surface is essential for the analysis of problems involving liquid sprays. Knowledge of how the droplet impacts and evaporates will help in the understanding and prediction of the effect of sprays on cooling of hot surfaces. Such problems are encountered in a number of engineering areas: fire extinguishment, nuclear reactor safety, cooling of hot metals, cooling of turbine blades, etc. The present work is motivated by fire extinguishment, which may be divided into two parts: (*i*) extinguishment of the already burning objects; (*ii*) prevention from burning of the as-yet unburned objects. Since this work is at relatively low surface temperatures, it primarily addresses the latter part of the extinguishment problem.

A substantial portion of the combustible building materials are porous with low thermal diffusivities and water spray is the most common method used for fire extinguishment. Hence, the study of the thermal behavior of water droplet vaporization on a hot, porous, low-thermal-diffusivity solid is important for fire research. Vaporization of water droplets on such solids is expected to be different from the nonporous metallic solids. However, despite the need to address the cooling of hot porous chars and unburnt wood during a fire, the authors have been unable to find studies for a porous solid. Thus, as a first step, this paper attempts to demonstrate the similarities and differences between porous and nonporous solids during droplet evaporation.

Numerous studies of the droplet vaporization process on hot nonporous metallic solids have been reported in the literature. These studies show that the vaporization mode of a liquid droplet on a hot surface depends on many factors. These are: (*i*) initial surface temperature of the solid; (*ii*) isothermal or nonisothermal condition of the solid; (*iii*) thermal properties of the droplet and the solid; and (*iv*) the droplet momentum upon impact. Few studies have focused on in-depth cooling of the solid (which is important for predicting the rate at which fuel gases are produced), and none have reported transient in-depth temperature measurements. Surface temperature measurements have been reported by Seki et al. (1978), Makino and Michiyoshi (1979), and Michiyoshi and Makino (1978). Seki et al. demonstrated good agreement between the theoretical computation of solid–liquid contact temperature and experimental measurements.[2] Makino and Michiyoshi studied the effect of initial size of the water droplet on its evaporation time. They present a wide range of the so-called boiling curve (q versus ΔT_{sat}). This work establishes the thermal

[1]Present address: College of Engineering, Mu'Tah University, Al-Karak, Jordan.

Contributed by the Heat Transfer Division and presented at a poster session at the 22nd (International) Combustion Symposium, Seattle, Washington, August 14, 1988. Manuscript received by the Heat Transfer Division August 26, 1988. Keywords: Evaporation, Fire/Flames, Sprays/Droplets.

[2]According to the solution for a semi-infinite body with a sudden change in surface temperature (Carslaw and Jaeger, 1959), the contact temperature is given by: $T_c = T_W\gamma_W + T_S\gamma_S/\gamma_W + \gamma_S$, where $\gamma = \sqrt{\rho ck}$; ρ, c, k represent density, specific heat, and thermal conductivity, respectively, and T_S, T_W are the initial solid and droplet temperatures.

behavior of droplets during the vaporization process. Rizza's (1981) theoretical work on a nonisothermal wall is also very useful. Other works, Gottfried et al. (1966) and Bonacina et al. (1979), are of limited applicability for fire extinguishment studies.

The work most directly related to the present work is that of di Marzo and Trehan (1986). They theoretically investigated the cooling of a hot semi-infinite aluminum block and obtained isotherms and an envelope for the evaporation regime (solid surface temperature $< 164°C$) of water droplets. Evans and di Marzo(1986) also presented a model for the evaporation of a droplet in contact with high thermal conductivity and diffusivity solids. They determined that the evaporation time is in reasonable agreement with the experimental data. The model also describes the spatial and temporal behavior of the evaporation heat flux.

2 Experimental Apparatus

2.1 Requirements. An experimental study of cooling of a hot, low-thermal-diffusivity, porous solid by water droplets requires an apparatus capable of providing:

1 A heated solid that is nearly isothermal, porous, and made of a low thermal conductivity and diffusivity material. Also, the temperature of the heated solid must be controllable.
2 A heated solid instrumented with surface and in-depth thermocouples for transient temperature measurements during droplet evaporation. These measurements will be used to determine: (*i*) the recovery time, i.e., the time for the surface to recover to its initial temperature, and (*ii*) size of "surface and in-depth zones" affected by the droplet.
3 The apparatus should be capable of generating different size droplets. This apparatus must also be capable of delivering droplets on the solid surface at a specified rate and at a specified release height.

2.2 Heated Ceramic Block. To obtain a nearly isothermal solid, three different shapes of the ceramic block were considered. These were: (*i*) *hemisphere*; here, to make the flat surface isothermal, a large variation in the heat flux applied on the hemispherical surface is necessary; (*ii*) *cylinder*; it is possible to obtain a flat isothermal surface in this geometry if the cylinder is heated from below with a constant heat flux, and the cylindrical surface is kept well insulated. The primary disadvantage is that a very small cylinder height and/or a high thermal diffusivity is needed for the solid to be nearly isothermal; (*iii*) *oblate spheroidal*; this geometry was chosen because it combines the advantages of both cylindrical and spherical geometries. It also provides a natural coordinate system for the problem.

Castable porous ceramic (MgO) was used to cast a semi-oblate spheroidal solid. The measured porosity, density, specific heat, and thermal conductivity of this solid were: 33 percent, 2.05 g/cm^3, 1.08 J/g• K (at 100°C) and 0.0223 W/cm • K, respectively. It was used to simulate an isothermal semi-infinite solid. The configuration of this block along with the calculated temperatures and heat fluxes is shown in Fig. 1. The block has a major semi-axis of 8.48 cm and a minor semi-axis of 7.22 cm. Theoretical calculations described below show that this ceramic block is nearly isothermal, despite its poor thermal conductivity. For the solid shown in Fig. 1, if ξ, η, and ϕ are used to describe the orthogonal oblate-spheroidal coordinate system, then transformation from the Cartesian system is given by: $x = a \cdot \cosh \xi \cdot \cos \eta \cdot \cos \phi$, $y = a \cdot \cosh \xi \cdot \cos \eta \cdot \sin \theta$, and $z = a \cdot \sinh \xi \cdot \sin \eta$, where a is a constant and $\xi \geq 0$, $-\pi/2 \leq \eta \leq \pi/2$, $0 \leq \phi \leq 2\pi$. As shown in Fig. 1, ξ = const represents the isotherms and η = const represents the heat flux lines. As required by their definition, they are orthogonal at every point in the domain. Under steady-state conditions, the heat conduction equation reduces to the following Laplace equation:

$$\nabla^2 T = \left[\frac{1}{a^2(\sinh^2\xi + \sin^2\eta)^{1/2}\cosh\xi}\right]\frac{\partial}{\partial\xi}\left(\cosh\xi\,\frac{\partial T}{\partial\xi}\right) + \left[\frac{1}{a^2(\sinh^2\xi + \sin^2\eta)^{1/2}\cos\eta}\right]\frac{\partial}{\partial\eta}\left(\cos\eta\,\frac{\partial T}{\partial\eta}\right) + \left[\frac{1}{a^2\cosh^2\xi\cos^2\eta}\right]\frac{\partial^2 T}{\partial\phi^2} = 0 \quad (1)$$

Assuming temperature to be independent of η and ϕ, the solution of the equation above with the following boundary conditions: $T = T_1$ at $\xi = 0$ and $T = T_2$ at $\xi = 1.15$, is given by:

$$T = 2.09(T_2 - T_1)\tan^{-1}(\exp(\xi)) + 2.641T_1 - 1.641T_2; \quad \text{for} \quad \xi \leq 1.15 \quad (2)$$

and the heat flux is given by:

$$\dot{q}'' = -\frac{A}{(\sinh^2\xi + \sin^2\eta)^{1/2}}\left[\frac{\exp(\xi)}{1+\exp(2\xi)}\right] \quad (3)$$

where $A = 2.09/a\,k\,(T_2 - T_1)$.

As shown in Fig. 1, the calculated heat flux on the exposed surface between a and b is nearly constant and can be matched with the radiative and convective heat losses to the environment to obtain a constant surface temperature. This yields a maximum temperature difference across the solid of 9.01°C, which is considered to be nearly isothermal relative to the dimensions of the droplet.

Nomenclature

a = a constant
B = D/d
c = specific heat
d = diameter of droplet before impact
D = maximum diameter of droplet on surface
H = release height, i.e., the distance between the needle tip and the solid surface
k = thermal conductivity
q = heat flux
r_d = maximum radius of droplet on the surface
s = solid
T = temperature
T_e = equilibrium temperature
T_c = contact temperature
T_S = initial solid surface temperature
T_{sat} = saturation temperature
T_W = droplet temperature before impact
T_{WS} = time-averaged surface temperature
ΔT_{sat} = $T_{WS} - T_{sat}$
t = time
t^* = dimensionless time = t/τ
V = initial volume of droplet
V_i = volume of droplet influence in solid
(x, y, z) = Cartesian coordinates
w = water
γ = $\sqrt{\rho c K}$
δ^* = critical droplet thickness, i.e., droplet thickness on the nonporous solid at the time the evaporation rate starts to increase sharply
θ = $(T - T_e)/(T_S - T_e)$
(ξ, η, ϕ) = oblate spheroidal coordinates
ρ = density
τ = evaporation time of the droplet

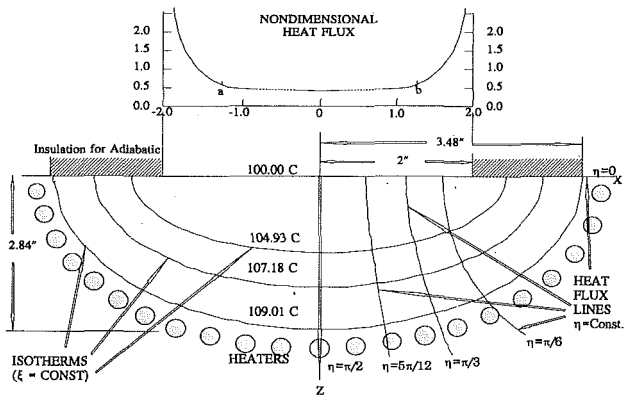

Fig. 1 Ceramic block configuration: The isotherms correspond to ξ = 0, 0.55, 0.85, and 1.15. In the range (a-b), the heat flux lost from the exposed surface by convection and radiation is equal to the heat flux arriving at this surface from the heaters. The temperature of the heaters (109°C) was calculated to achieve this balance. The range (a-b) is the usable range for water droplet experiments and is much larger than the droplet diameter.

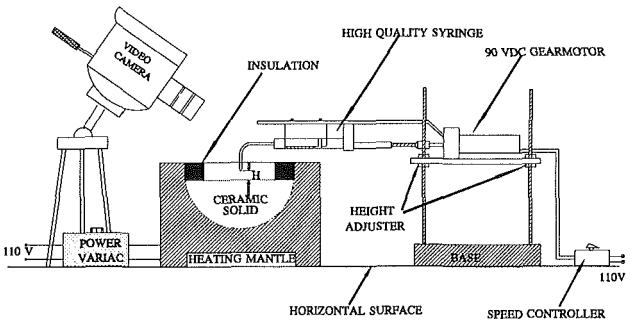

Fig. 2 Schematic of the experimental apparatus

The above-described block was instrumented with several surface and in-depth thermocouples (Chromel-Alumel 76 μm diameter). These thermocouples were flattened to a film thickness of about 15 μm. Seven surface and six in-depth thermocouples were placed inside the mold. The location of the thermocouples prior to casting was measured to within ± 0.1 mm. Due to the uncertainties introduced during the casting process and shrinkage, the thermocouple locations were evaluated by a least-squares fit to the steady-state temperatures. The thermocouple locations evaluated were very close to the measured values before casting. Attempts to determine the thermocouple locations radiographically by using x-rays were not successful.

In order to compare the results of porous and nonporous solids under the same conditions, *two identical solids were cast from the same material.* The nonporous solid was obtained by spreading a small amount of solution of very fine ceramic powder of the same material on the surface of the porous solid. This procedure closes the *surface* pores, rendering the surface nonporous. It is important to emphasize that *the thermal properties of both solids were identical, making a direct comparison possible.*

As shown in Fig. 2, the ceramic block is heated by a heating mantle. In order to achieve good contact, the heating mantle had the dimensions of the ceramic block. Furthermore, the heating mantle has been configured to deliver the heat flux to the ceramic solid according to Eq. (3). The heating mantle and therefore the temperature of the ceramic block is controlled by a power variac.

2.3 Droplet Generating System. Water droplets were generated by a high-quality motor-driven syringe. This arrangement is shown in Fig. 2. To obtain different droplet sizes, 10, 12, 15, 19, and 25 gage stainless-steel needles were used. These needles were filed to a smooth flat tip. Care was taken to keep the main body of the syringe, which contains water, at ambient temperature (25°C).

The syringe plunger was driven by a 90 V DC gear motor whose speed was controlled by a speed controller. As the syringe plunger slowly moved a droplet was formed on the tip of the needle and increased in size, until its weight becomes sufficient to detach it from the tip.

The droplet generating system was calibrated using an electronic digital scale (Mettler AE 100) with an accuracy of ± 0.1 mg. Different diameter needles were calibrated for droplet sizes at ambient temperature by individually weighing 15 droplets per droplet size. The deviation was found to be ± 2 percent from the arithmetic mean. As an example, a 30 μl droplet had a volume in the range 29.4–30.6 μl.

The motor-driven syringe system was placed on an adjustable height platform to facilitate the adjustment of the needle tip height from the hot solid surface. The adjustable range was from 0–19 cm.

3 Experimental Procedure

The experimental procedure consists of setting the variac to a fixed value to heat the ceramic block to the desired temperature and waiting for about 12 hours for the solid block to reach steady-state conditions. Water used for these experiments was double distilled, deionized, and degassed. The degassing process consists of boiling the water and cooling it under a vacuum (23 in. of mercury). Before starting the experiment, some water in the needle was ejected to ensure that the droplets were at ambient temperature (~25°C).

Tests were performed with the initial surface temperature ranging from 75–200°C. The droplet was deposited gently on the heated surface from a release height of 6–9 mm (from the tip of the needle to the hot surface). This release height was varied to achieve a constant distance between the bottom of the droplet and the surface of the solid. The transient temperature data were collected by an HP data acquisition/control unit, which was linked to a DEC 11/73 microcomputer by an IEEE interface bus.

A video camera was used to record the lifetime of the droplet on the hot surface. This recorded the droplet behavior during evaporation and provided a precise measurement of the droplet evaporation time and the droplet diameter on the hot surface.

4 Results and Discussion

Results of a typical test composed of three droplets are shown in Figs. 3 and 4. Transient surface and in-depth temperature measurements for a 30 μl droplet are shown in Figs. 3(*a*) and 3(*b*) for a nonporous solid, and in Figs. 4(*a*) and 4(*b*) for a porous solid. These figures show the repeatability of the experimental measurements during the droplet evaporation process. Figures 3(*a*) and 4(*a*) also show the uniformity of surface temperature prior to droplet impact.

Individual traces of surface and in-depth temperatures for different droplet sizes and for different initial surface temperatures were obtained and plotted in a nondimensional form. Figures 5 and 6 show plots of nondimensional surface and in-depth temperatures [$\theta = (T - T_e)/(T_S - T_e)$ versus nondimensional time [$t^* = t/\tau$] for nonporous and porous solids, respectively. The nondimensional temperature θ was chosen because θ versus t^* curves for initial solid surface temperatures (T_S) less than 164°C and droplet sizes greater than 20 μl, fall approximately on top of one another. This suggests that the almost constant surface temperature (T_e) obtained after the droplet contact and the droplet duration on the surface (τ) are important parameters for describing the droplet cooling effect

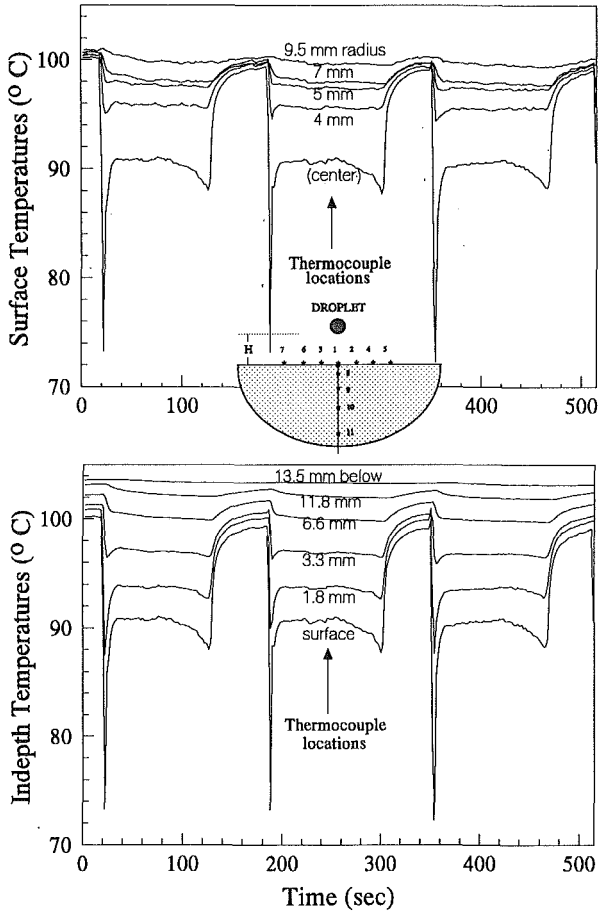

Fig. 3 Surface and in-depth temperatures for a nonporous solid at an initial surface temperature of 100°C and for a 30 μl water droplet

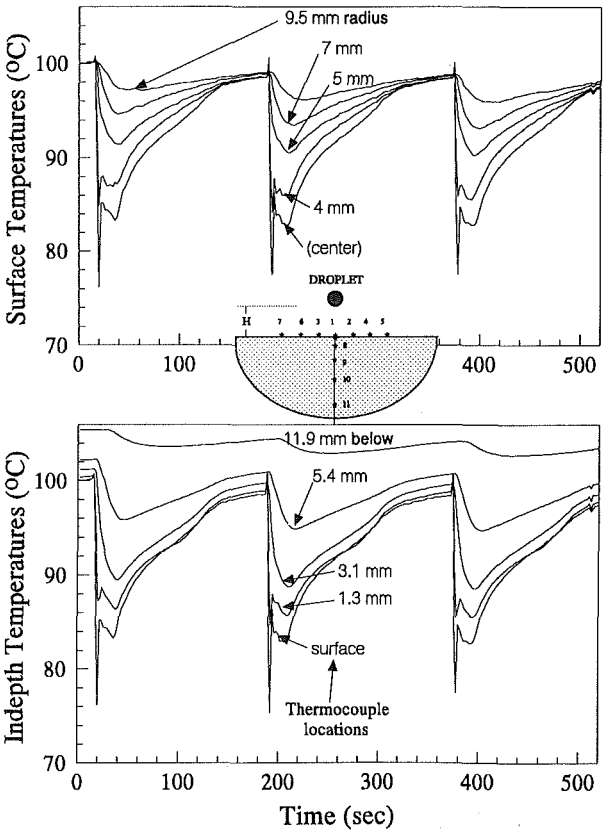

Fig. 4 Surface and in-depth temperatures for a porous solid at an initial surface temperature of 100°C and for a 30 μl water droplet

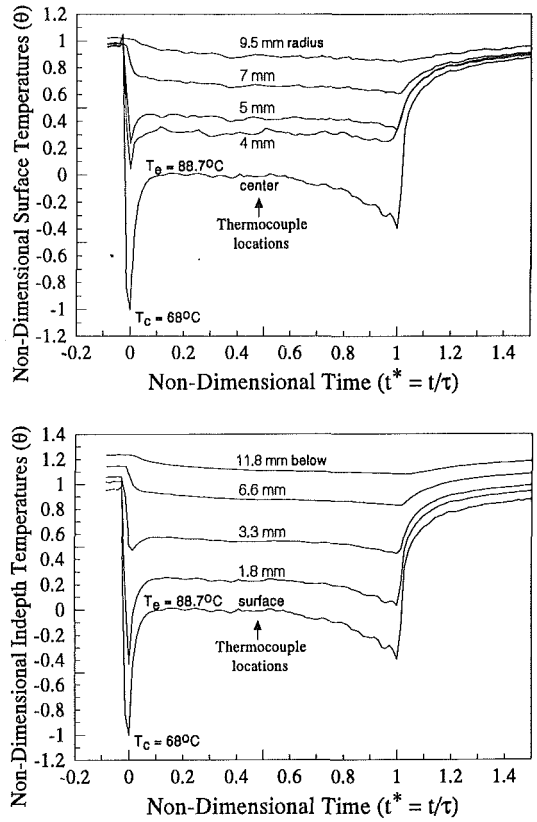

Fig. 5 Nondimensional surface and in-depth temperatures versus non-dimensional time for a nonporous solid at an initial surface temperature of 100°C and for a 51 μl water droplet

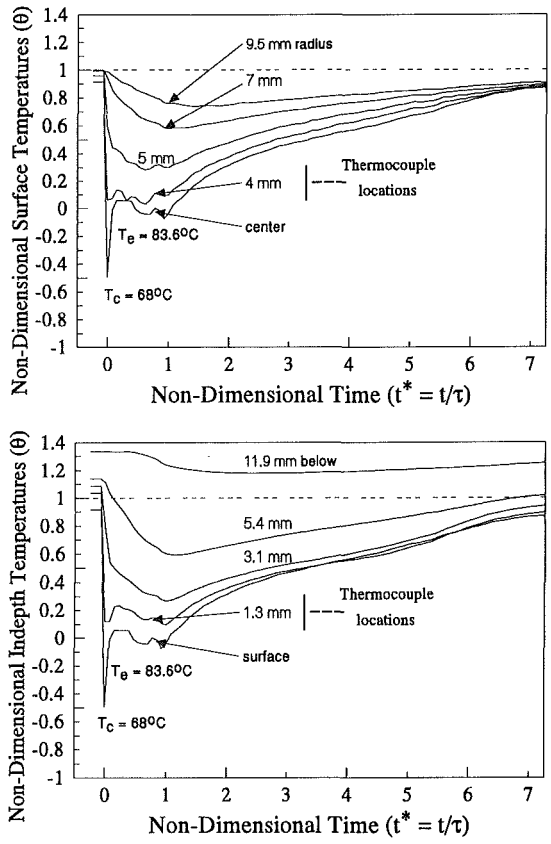

Fig. 6 Nondimensional surface and indepth temperatures versus non-dimensional time for a porous solid at an initial surface temperature of 100°C and for a 51 μl water droplet

for both nonporous and porous solids. Note that most of the cooling for the nonporous solid was accomplished in the time interval τ, but for the porous solid it took approximately seven such time intervals for the same droplet size. This is primarily because τ for the porous solid is significantly shorter. The droplet on the porous solid quickly disappears from the surface due to in-depth absorption but continues to evaporate inside the solid. It seems that τ is controlled by the droplet size and θ is a measure of the heat transfer rate. Also, for a limited range of T_S, the evaporation process is similar for different size droplets.

For both the porous and the nonporous solids at an initial surface temperature $T_S \leq 164°C$ (when the theoretical contact temperature $\leq 100°C$), the hot surface is immediately cooled to the theoretical contact temperature upon contact with the droplet. This indicates that boiling does not occur at the instant of initial contact. It also indicates that the *thermal properties of both the porous and nonporous solids are the same*. Thus, a direct comparison is possible. For $T_S > 164°C$, the measured constant temperature is approximately constant (at a value slightly greater than the saturation temperature for water at atmospheric pressure) and lower than the theoretical contact temperature. This indicates that boiling starts at the instant of initial contact. Seki et al. (1978) found that on stainless steel, the measured contact temperature increases with increase in the surface temperature up to 200°C, and was in agreement with the theoretical contact temperature. For $200 \leq T_S \leq 300°C$, they found that the measured contact temperature was less than the theoretically calculated contact temperature. The present results for the ceramic are in qualitative agreement with Seki's data except that the present data show a deviation from the theoretical value at 164°C rather than at 200°C due to the differences in the thermal properties of steel and the ceramic solid.

After achieving the contact temperature, the solid surface approaches the "equilibrium temperature" (interface temperature during evaporation). During the evaporation period the thermal behaviors of the porous and nonporous solids are different. These differences are described below.

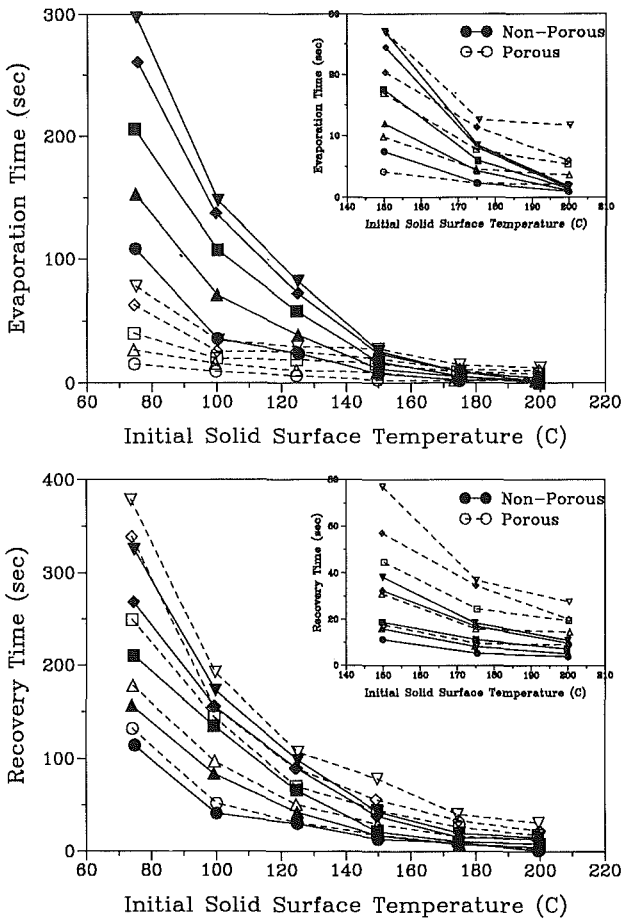

Fig. 7 Evaporation time and recovery time as a function of the initial solid surface temperature and droplet volume for porous and nonporous solids. Open symbols represent a porous solid and shaded symbols represent a nonporous solid. Symbol definitions are as follows: ▼ and ▽ —51 μl; ◆ and ◇ —43 μl; ■ and □ —30 μl; ▲ and △ —19 μl; ● and ○ —10 μl.

4.1 Nonporous Solid. Measurements show that for $T_S = 75°C$, the surface and in-depth temperatures remain nearly constant during the droplet evaporation process. This implies that the heat flux during the evaporation period is also nearly constant. For $100 \leq T_S \leq 175°C$, the interface temperature remains nearly constant until a critical droplet thickness (δ^*) is reached on the hot surface. Then, the temperature starts to decrease sharply until the droplet has completely evaporated as shown in Fig. 5(*a*). This sharp decrease in the surface temperature implies an increase in the evaporation rate. As the droplet thickness becomes small, the heat transfer through the droplet increases, allowing more evaporation to take place from the top surface of the droplet. Since water has relatively low thermal conductivity the critical droplet thickness (δ^*) is quite small. After the droplet has completely evaporated, the solid recovers *quickly* to its initial surface temperature. The time for evaporation after the droplet has achieved the critical thickness is approximately the same for different droplet sizes at a specified initial surface temperature. For initial surface temperature of 100°C, this time is approximately 25 seconds. As the initial surface temperature increases this time decreases due to higher heat flux.

For $T_S \geq 200°C$, the evaporation times are very short due to high heat transfer rates caused by high temperatures and small droplet thickness (i.e., large droplet diameter on the surface) resulting from lower surface tension. Thus, the surface temperature first drops to a temperature a few degrees above the saturation temperature of water and then it quickly recovers to its initial value.

4.2 Porous Solid. For porous materials the interface temperature never clearly attains an equilibrium value. Both the surface and the in-depth temperatures continue to decrease until the droplet vanishes from the surface (as seen in Figs. 6*a* and 6*b*). The time taken for the droplet to vanish from the surface is defined as the evaporation time. By this time a part of the droplet has already been evaporated, and the rest has penetrated in both the axial and the radial directions. The effect of the droplet penetration is clear from following two observations: (*i*) A thermocouple in the porous matrix at the same location as the nonporous matrix cools faster under otherwise identical conditions. This implies that, for the porous matrix, there must be an energy sink in the neighborhood of the thermocouple, thus confirming the in-depth penetration of moisture. (*ii*) The evaporation time for the porous case is lower than the nonporous case for the same droplet size and under the same condition. After the droplet vanishes from the surface, the porous solid recovers *slowly*, as opposed to the quick, pure conduction recovery for the nonporous solid. The porous in-depth temperature profiles during recovery are not as smooth as the nonporous solid, due to the migration of moisture inside the matrix (as can be seen from Figs. 4*b* and 6*b*). The presence of the moisture changes the effective thermal properties of the solid. This change makes the thermal recovery not only different but also longer than that of the nonporous solid.

The evaporation time for various droplet sizes versus initial solid surface temperature is shown in Fig. 7(*a*). The evaporation time is a function of the droplet size and the initial

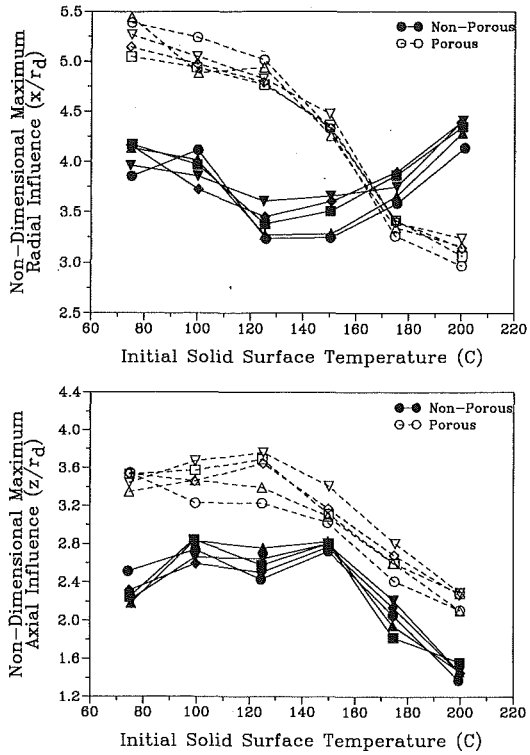

Fig. 8 Nondimensional maximum radial and axial influence distances as a function of the initial solid surface temperature and droplet volume for porous and nonporous solids. Symbol definitions are as follows: ▾ and ▿ —51 μl; ♦ and ◇ —43 μl; ■ and □ —30 μl; ▵ and ▲ —19 μl; ● and ○ —10 μl.

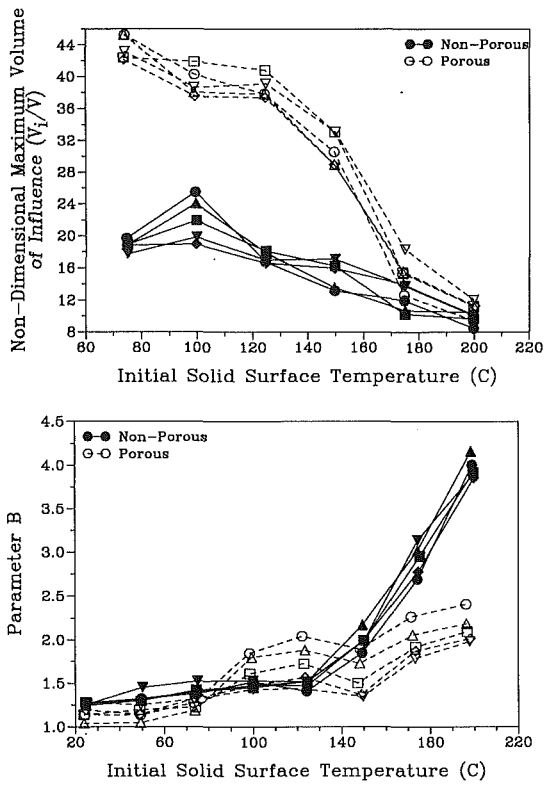

Fig. 9 Top: nondimensional maximum influence volume as a function of the initial solid surface temperature and droplet volume for porous and nonporous solids. Bottom: parameter *B* (ratio of maximum droplet diameter on the surface after impact to the droplet diameter before impact) as a function of the initial solid surface temperature and droplet volumes. Symbol definitions are as follows: ▾ and ▿ —51 μl; ♦ and ◇ —43 μl; ■ and □ —30 μl; ▲ and ▵ —19 μl; ● and ○ —10 μl.

surface temperature. As expected, the lower the initial surface temperature and the larger the droplet volume, the more time required to evaporate the droplet. For $T_S \leq 164°C$ the evaporation time of the nonporous is larger than the porous. For $T_S > 164°C$ the evaporation time for the porous solid is larger. For this range the parameter B (which is the ratio of maximum diameter of the droplet on the surface to the original droplet diameter) for the nonporous solid was larger than for the porous solid (see Fig. 9*b*). Generally, the evaporation time on the nonporous solid is larger than the porous solid for the same droplet under the same conditions. This indicates that to maintain the same surface temperature of hot porous and nonporous solids, the porous solid needs droplets at a higher frequency.

The recovery time is shown in Fig. 7(*b*). This time is defined as the time for the surface to recover to its initial temperature. This time was determined by evaluating the time it took the surface temperature to recover to 20 percent of the maximum temperature drop. The maximum temperature drop is the difference between the initial surface temperature and the equilibrium temperature of the thermocouple underneath the evaporating droplet. The nonporous solid took slightly less time to recover than the porous solid despite the fact that for the nonporous solid, the evaporation process is steady and the evaporation time is larger.

Figures 8(*a*) and 8(*b*) show the nondimensional maximum radial (x/r_d) and axial (z/r_d) influence distances of a single droplet plotted against the initial surface temperature. The influence distance encloses all locations where the temperature drop due to the droplet evaporation is at least 20 percent of the maximum temperature drop, i.e., the nondimensional temperature $\theta = 0.8$. Figures 8(*a*) and 8(*b*) show that the influence distance decreases at higher solid temperatures since more energy is available to evaporate the droplet. Also these influence distances are larger for the porous solid. Thus, while the evaporation time for the porous solid is shorter, the influence distance is larger. Hence, to maintain the same surface temperature, droplets can be spaced farther apart but need to be applied more frequently on a porous solid than on a nonporous solid. This has important implications regarding design of sprinklers for fire extinguishment.

The nondimensional maximum volume of influence (V_i/V) is shown in Fig. 9(*a*). This quantifies the cooling effect of a single droplet. The volume of influence is defined as the volume of the semi-oblate spheroid formed by the axial and radial influence distances. Due to the low thermal conductivity/diffusivity of the ceramic solid, the droplet will produce intense local cooling. Thus, the influence zone or volume is expected to be lower than for high-conductivity materials. The influence zone of the porous solid is larger than the nonporous solid due to penetration of the water into the solid matrix. This causes more cooling in both the radial and the axial directions. Figure 9(*a*) shows that the nonporous solid at $T_S < 100°C$ cools more with a 10 μl droplet than with larger droplets. This is because the evaporation process for larger droplets attains a steady state and the extra fluid in the larger droplets just increases the evaporation time. This phenomenon was not observed in porous solids because the evaporation process never quite attains a steady state.

Figure 9(*b*) shows the parameter B plotted against the initial solid surface temperature. This parameter is defined as the ratio of maximum droplet diameter during evaporation to the droplet diameter before impact. The diameter of the droplet on the surface was determined from the measured maximum wetted area. As the surface temperature increases, B tends to increase due to a decrease in the surface tension. Figure 9(*b*) shows a reversal of trend between porous and nonporous ma-

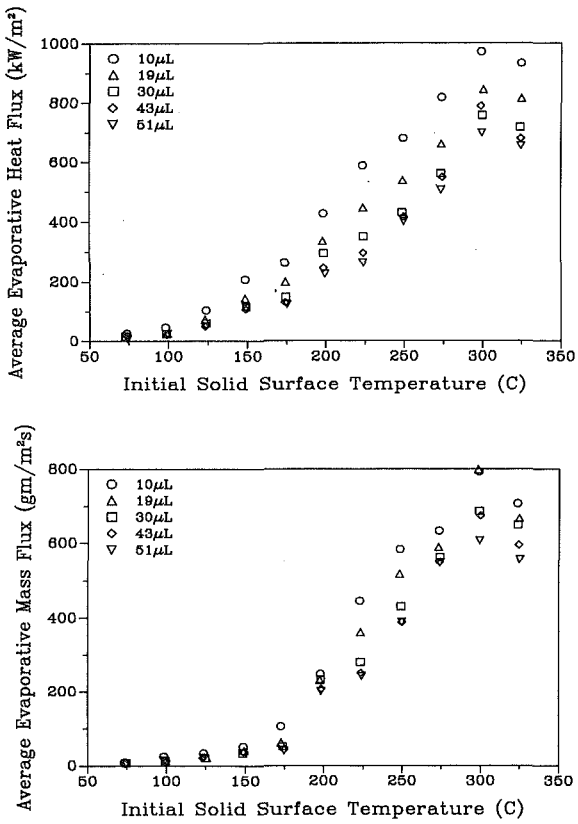

Fig. 10 Average evaporative heat flux and mass flux as a function of the initial solid surface temperatures and droplet volumes for a nonporous solid. Symbol definitions are as follows: ▽—51 μl; ◇—43 μl; □—30 μl; △—19 μl; ○—10 μl.

terials for $T_S \geq 164°C$. As indicated before, in this temperature range, boiling occurs at the instant of droplet contact with the solid surface. For the case of the nonporous solid, the droplets explode due to intense vapor formation between the droplet and the solid surface causing it to spread more than the porous case (larger B). This results in larger radial cooling (see Fig. 8*a*) and smaller evaporation time (see Fig. 7*a*). On the other hand the droplets on the porous solid did not explode due to the presence of voids in the solid, which permits part of the droplet to migrate into the solid matrix. This results in a smaller droplet diameter on the surface (smaller B), smaller radial cooling and larger evaporation time. In short, for $T_S \geq 164°C$ the droplet starts boiling at the instant of contact with the solid surface, causing a reversal between porous and nonporous material in terms of the parameter B, their evaporation time, and their radial cooling.

4.3 Heat Transfer During Droplet Evaporation. The heat transfer characteristics during the evaporation of single droplets on the nonporous solid for temperatures ranging from 75–325°C were determined from the transient measurements of surface and in-depth solid temperatures, and the droplet diameter on the solid surface.

Surface and in-depth temperature measurements during droplet evaporation show that isotherms and the heat flux lines inside the solid matrix may be approximated by an oblate spheroidal coordinate system. In such a coordinate system a temperature distribution [adapted from Keltner (1973)] is given by:

$$T(\xi, t^*) = \frac{2(T_e - T_S)}{\pi}\left(1 - 2\frac{\xi}{\delta} + \frac{\xi^2}{\delta^2}\right)\cot^{-1}\xi + T_S \qquad (4)$$

where ξ represents the isothermal lines, $t^* = \alpha t/R^2$ is the dimensionless time, α is the thermal diffusivity, R is the radius of the disk, T_S and T_e, respectively, are the solid surface temperatures before and after the step change and δ is the penetration depth. This is the solution for a step change in temperature over a disk-shaped area on the surface of a half-space. Using this equation, temperatures were evaluated at various locations and at different times. The results were in good agreement with the measured values. From Eq. (4) it can be shown that the rate at which heat arrives at the surface (Q) is given by the following equation:

$$Q = 4RK(T_e - T_S)\left(1 + \frac{\pi}{\delta}\right) \qquad (5)$$

The instantaneous average evaporative heat flux is then determined by dividing Q by the instantaneous wetted area. The instantaneous evaporation rate may also be determined from Q by dividing it by the heat of evaporation.

The average evaporative heat flux and the average evaporative mass flux were correlated with the initial solid surface temperature as shown in Figs. 10(*a*) and 10(*b*). Both quantities follow the same pattern: the higher the initial surface temperature and the smaller the droplet, the higher the average evaporative heat flux and the average evaporative mass flux. This is because at higher temperatures, more energy is available for droplet evaporation, and small droplets have larger conductance due to their smaller thickness on the hot surface. Figures 10(*a*) and 10(*b*) also show a slight decrease in both quantities for $T_S > 300°C$. Since this temperature corresponds to the maximum average evaporative heat flux and the minimum evaporative time, it is likely the beginning of the transition regime. Unfortunately, the experiments could not be continued for higher temperatures (i.e., in the transition regime), due to the burnout of the heating mantle.

5 Conclusions

The following conclusions are apparent from this study:

1 The only similarity in the thermal behavior of both porous and nonporous solids is the agreement in the experimental contact temperature. This is because it occurs during the initial contact when the droplet sees both solids as a semi-infinite body.

2 The theoretical and experimental contact temperatures are in good agreement up to the boiling point of water. They then diverge with the experimental contact temperature becoming roughly constant at a value slightly greater than the boiling point.

3 During the droplet evaporation process, surface, and in-depth temperatures for the nonporous solid remain nearly constant, whereas for the porous solid there was a continuous decrease in these temperatures.

4 The evaporation time is longer for the nonporous solid than for the porous solid for the same droplet diameter and under identical conditions. On the other hand the envelope of droplet influence was larger for the porous solid. These results confirm the in-depth cooling of the porous solid due to water penetration. These results also show that to maintain the surface temperature below a specified temperature for fire extinguishment, water droplets on a porous solid may be placed farther apart but they must be applied more frequently.

5 Smaller droplets are more efficient for cooling nonporous solids at or below 100°C. This is because the evaporation process for larger droplets attains a steady state and the extra fluid in the larger droplets just increases the evaporation time. This phenomenon was not observed in the porous solid because the evaporation process never quite attains a steady value.

6 For the nonporous solid, the instantaneous evaporation rate and the instantaneous average evaporative heat fluxes were determined from the transient measurements of surface and in-depth solid temperatures, and the droplet diameter on the

solid surface. Although the total heat transfer is more for larger droplets, the average evaporative heat flux is higher for smaller droplets. This is because small droplets have a large conductance due to their smaller thickness on the hot surface.

6 Acknowledgments

This work is supported by the Center for Fire Research, National Bureau of Standards, under Grant No. 60NANB5D0578. The authors would like to thank Dr. David D. Evans for his valuable comments and suggestions, and Professor J. V. Beck for providing the computer program for evaluating the thermal properties of the ceramic.

References

Bonacina, C., Del Giudice, S., and Comini, G., 1979, ASME JOURNAL OF HEAT TRANSFER, Vol. 101, pp. 441–446.

Carslaw, H. S., and Jaeger, J. C., 1959, *Conduction of Heat in Solids*, 2nd ed., Oxford University Press, Oxford, p. 88.

di Marzo, M., and Trehan, A. K., 1986, National Bureau of Standards Interagency Report NBS-GCR-86-516.

di Marzo, M., Wang, Z. Y., and Meng, W. H., 1987, National Bureau of Standards Report NBS-GCR-87-534.

Evans, D. D., and di Marzo, M., 1986, National Bureau of Standards Report NBSIR-86-3384.

Gottfried, B. S, Lee, C. J., and Bell, K.J., 1966, *Int. J. Heat Mass Transfer*, Vol. 9, pp. 1167–1187.

Keltner, N., 1973, ASME JOURNAL OF HEAT TRANSFER, Vol. 95, pp. 412–414.

Lee, L. Y. W., Chen, J. C., and Nelson, R. A., 1985, *Int. J. Heat Mass Transfer*, Vol. 28, pp. 1415–1423.

Makino, K., and Michiyoshi, I., 1979, *Int. J. Heat Mass Transfer*, Vol. 22, pp. 979–981.

Michiyoshi, I., and Makino, K., 1978, *Int. J. Heat Mass Transfer*, Vol. 21, pp. 605–613.

Rizza, J. J., 1981, ASME JOURNAL OF HEAT TRANSFER, Vol. 103, pp. 501–507.

Seki, M., Kawamura, H., and Sanokawa, K., 1978, ASME JOURNAL OF HEAT TRANSFER, Vol. 100, pp. 167–169.

Toda, S., 1972, *Heat Transfer Japanese Research*, Vol. 1(3), pp. 39–50.

J. V. C. Vargas
Doctoral Candidate.
Student Mem. ASME

A. Bejan
J. A. Jones Professor
of Mechanical Engineering.
Fellow ASME

Department of Mechanical Engineering and
Materials Science,
Box 90300,
Duke University,
Durham, NC 27708-0300

A. Dobrovicescu
Associate Professor,
Department of Mechanical Engineering,
Polytechnic University of Bucharest,
Bucharest 77206, Romania

The Melting of an Ice Shell on a Heated Horizontal Cylinder

This paper describes the fundamentals of melting when a shell of phase-change material rides on a heated horizontal cylinder. In the first part of the paper, contact melting theory is used to predict the history of the melting process and, in particular, the time when the remaining ice falls off the cylinder. It is shown that the melting process consists of two distinct regimes, first, an early regime when the cylinder is surrounded by ice and, second, a late regime when the cylinder cuts through the top of the ice shell. The second part describes laboratory measurements that validate the theory. The third part of the paper shows that in the complete cycle that starts with freezing the shell and ends with the contact-melting removal of the shell, there exists an optimal frozen shell thickness such that the cycle-averaged production of ice is maximized.

1 Introduction

The objective of this paper is to present the most basic features of the phenomenon in which a cylindrical shell of phase-change material melts as it rides on a heated horizontal cylinder. A common way of visualizing this phenomenon is by looking at the melting (defrosting) of the ice that forms around the horizontal evaporator tubes inside the freezer of a household refrigerator. In fact, this example is also the technological problem that triggered our interest in this phenomenon (Lim, 1992).

The formation of frost (and, later, ice) on the evaporator tubes leads to an increase in the thermal resistance between the cold space and the even colder evaporator surface. As this resistance increases, the temperature of the evaporator surface must decrease to continue to extract the appropriate refrigeration load out of the cold space. At the same time, the refrigerator works harder (i.e., less efficiently) as the compressor uses more electrical power to maintain the cold space at the prescribed temperature level. Methods of coping with the formation of ice on the evaporator surface constitute a critical technology in the development of modern domestic refrigerators and freezers (Bejan et al., 1994). The most common de-icing method consists of interrupting the refrigeration cycle after a certain interval of operation, and then heating the evaporator tubes (electrically, or by convection, or by reverse cycling) to melt the ice layer. The melting of ice on horizontal tubes is also a method of ice manufacturing, on which we focus in section 5.

In addition to the fact that it is technologically important, the melting of a shell on a horizontal cylinder represents a new phenomenon on the background of what is currently known in contact-melting heat transfer. The current state of contact-melting heat transfer research was reviewed recently (Bejan, 1994). The available studies dealt with melting inside heated capsules (e.g., Nicholas and Bayazitoglu, 1980; Bareiss and Beer, 1984; Prasad and Sengupta, 1987; Roy and Sengupta, 1987; Bahrami and Wang, 1987; Webb et al., 1987), and the movement of heated bodies through solid phase-change media (e.g., Emerman and Turcotte, 1983; Moallemi and Viskanta, 1985a, b). The melting heat transfer along plane surfaces with relative motion was studied as well (e.g., Bejan, 1989). The shell-on-cylinder configuration documented in this paper differs fundamentally from the melting around an embedded horizontal cylinder (Moallemi and Viskanta, 1985a, b) because the heated cylinder cuts through the top of the ice shell, and the shape and length of the contact melting region are time dependent.

2 The First Regime: The Cylinder Is Surrounded by Ice

Consider first the early stages of the melting process, when the cylindrical heater has not penetrated yet through the top of the ice sleeve (Fig. 1). We assume that the natural convection melting at the outer surface of the ice is negligible when compared with the melting caused by the internal heater. This

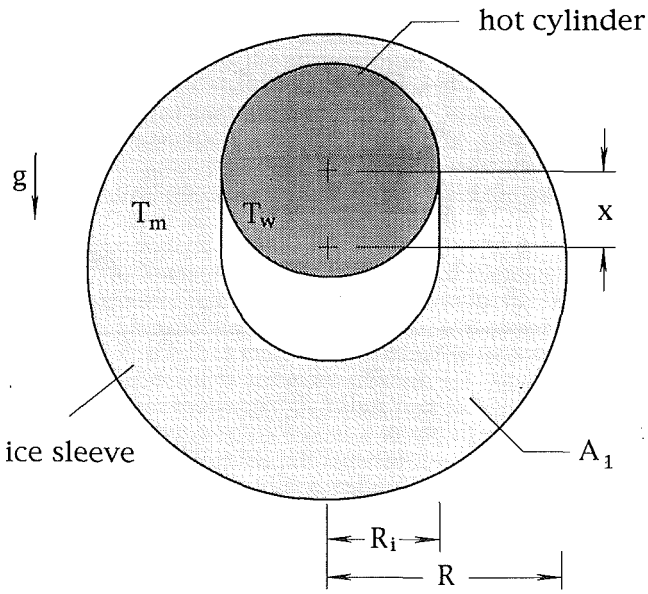

Fig. 1 Cross section through the cylinder and ice sleeve in the first regime: the ice surrounds the cylinder

Contributed by the Heat Transfer Division for publication in the JOURNAL OF HEAT TRANSFER Manuscript received by the Heat Transfer Division May 1993, revision received August 1993. Keywords: Direct-Contact Heat Transfer, Phase-Change Phenomena, Refrigeration. Associate Technical Editor: A. Faghri.

Table 1 The precision, bias, and uncertainty limits of the measurements reported in Fig. 6.

r	$\frac{P_\tau}{\tau}$	$\frac{B_\tau}{\tau}$	$\frac{U_\tau}{\tau}$	P_ξ	B_ξ	U_ξ
3	0.13	0.07	0.15	0.09	0.17	0.19
5	0.22	0.08	0.23	0.23	0.17	0.29
6.83	0.12	0.02	0.12	0.24	0.17	0.29

assumption is supported by laboratory observations of the melting process, as shown in the last paragraph of section 4.

The evolution of the melting process can be described in terms of the distance x that develops between the center of the heater cross section and the original center of the annular cross section of the ice. The assumption that the ice shell does not tilt is particularly good. It was confirmed by each of the 40 melting experiments of section 4, where we observed that the ice sample remained horizontal. Our description of the function $x(t)$ begins with the observation that the solution reported by Moallemi and Viskanta (1985a) for the steady sinking of a hot cylinder through a block of solid phase-change material can be used to deduce the instantaneous speed dx/dt in the early regime of the present configuration. Specifically, Moallemi and Viskanta's solution for $\mathrm{Ste} \ll 1$ means that

$$\frac{R_i}{\alpha}\cdot\frac{dx}{dt}=\left(\frac{5\pi g\Delta\rho R_i^3\,\mathrm{Ste}^3}{16\,\mu\alpha}\right)^{1/4} \tag{1}$$

in which the Stefan number is $\mathrm{Ste} = c(T_w - T_m)/h_{sf}$, and R_i is the radius of the hot cylinder. In Moallemi and Viskanta's analysis $\Delta\rho$ is the difference between the density of the sinking cylinder and the density of the surrounding liquid film, so that the net force with which the cylinder presses against the phase-change material is $g\Delta\rho\pi R_i^2$. The equivalent net force between the falling ice and the stationary cylinder in Fig. 1 is $g\rho_s A_1$, where ρ_s is the density of ice, R is the outer radius of the ice annulus, and A_1 is the total instantaneous area of the ice cross section,

$$A_1=\pi(R^2-R_i^2)-2R_i x \tag{2}$$

This A_1 estimate is based on the assumption that the melt water is drained axially, so that the space created under the cylinder is occupied by air. This is a very good assumption, which was confirmed in each of the 40 melting experiments described in section 4.

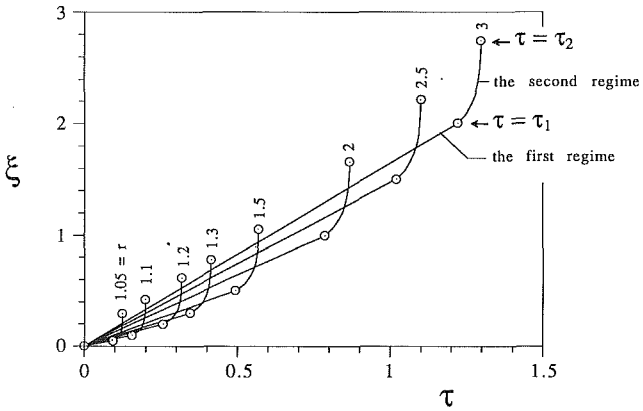

Fig. 2 The travel of the ice sleeve relative to the cylinder

We assumed further that the underside heat transfer through the crescent-shaped space filled with air is negligible, i.e., that most of the melting experienced by the ice sleeve is due to the direct contact with the upper half of the hot cylinder. This last assumption appears also in Moallemi and Viskanta's (1985a) analysis of the sinking hot cylinder, and in Emerman and Turcotte's (1983) analysis of the sinking hot sphere. Its validity was demonstrated by Moallemi and Viskanta's experiments with a cylinder sinking into solid n-octadecane.

In conclusion, we can substitute $\rho_s A_1/\pi R_i^2$ in place of $\Delta\rho$ in Eq. (1), and obtain the following equation for the instantaneous position of the ice sleeve:

$$\frac{d\xi}{d\tau}=\left(\frac{5}{16}\right)^{1/4}[\pi(r^2-1)-2\xi]^{1/4} \tag{3}$$

The new dimensionless variables are defined by writing

$$\xi=\frac{x}{R_i},\quad r=\frac{R}{R_i}>1 \tag{4}$$

$$\tau=\frac{\alpha t}{R_i^2}\left(\frac{gR_i^3}{\nu\alpha}\right)^{1/4}\left(\frac{\rho_s}{\rho}\,\mathrm{Ste}^3\right)^{1/4} \tag{5}$$

Equation (3) can be integrated from $\tau = 0$, where $\xi = 0$, to obtain

$$\xi=\frac{\pi}{2}(r^2-1)-\frac{1}{2}\left\{[\pi(r^2-1)]^{3/4}-\frac{3}{4}\,5^{1/4}\tau\right\}^{4/3} \tag{6}$$

Figure 2 shows that when described in terms of the dimen-

Nomenclature

a = dimensionless area A_2, Eq. (19)
A_1 = area, Eq. (2)
A_2 = area, Fig. 4 and Eq. (19)
B = bias limit, Table 1
B = dimensionless group, Eq. (28)
c = specific heat of water
F = dimensionless rate of ice production, Eq. (30)
g = gravitational acceleration
G = negative of the pressure gradient, Eq. (11)
h_{sf} = latent heat of melting
k = thermal conductivity of water
P = pressure
P = precision limit, Table 1
r = radius ratio = R/R_i
R = radius of the ice sleeve
R_i = radius of hot cylinder
Ra_D = Rayleigh number = $g\beta_{\mathrm{air}}(T_{\mathrm{air}} - T_m)D^3/(\alpha\nu)_{\mathrm{air}}$
Ste = Stefan number for melting = $c(T_w - T_m)/h_{sf}$
Ste_s = Stefan number for freezing = $c_s(T_m - T_c)/h_{sf}$
t = time
t_0 = freezing time
T_c = temperature of subcooled ice
T_m = melting point, freezing point
T_w = cylinder temperature
u, v = water velocity components, Fig. 4
U = uncertainty limit, Table 1
x = downward travel of the ice, Figs. 1 and 4
$\hat{x}, \hat{y}$ = curvilinear coordinates, Fig. 4
α = water thermal diffusivity
β = angular coordinate, Fig. 4
β_{air} = air coefficient of volumetric thermal expansion
δ = water film thickness, Fig. 4
θ = angle, Fig. 4 and Eq. (20)
μ = viscosity
ν = kinematic viscosity
ξ = dimensionless ice travel = x/R_i
ρ = water density
ρ_s = ice density
τ = dimensionless time, Eq. (5)
τ_1 = end of the first regime, Eq. (7)
τ_2 = end to the second regime, Eq. (22)
Φ = function, Eq. (15)
ψ = function, Eq. (18)
$( )_s$ = ice properties

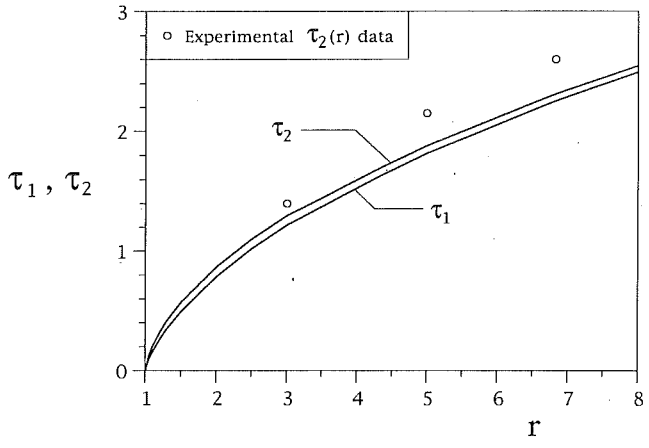

Fig. 3 The time marking the end of the first regime, τ_1, and the time when the remaining ice falls off the cylinder, τ_2. The experimental data show the time $\tau_2(r)$ measured in Fig. 6.

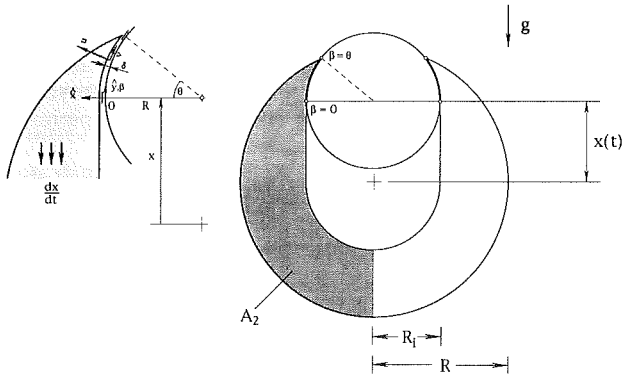

Fig. 4 Cross section through the cylinder and the hanging ice in the second regime: The cylinder is visible through the top of the ice sleeve

sionless ξ and τ, the fall of the ice sleeve depends also on the radius ratio r. The regime described by Eq. (6) and pictured in Fig. 1 is represented by the nearly straight portions of the curves drawn in Fig. 2. This first regime ends when $x = R - R_i$, or $\xi = r - 1$. This occurs at the time τ_1, which is obtained by substituting $\xi = r - 1$ in Eq. (6):

$$\tau_1 = \frac{4}{3} 5^{-1/4} \{[\pi(r^2-1)]^{3/4} - [\pi(r^2-1) - 2(r-1)]^{3/4}\} \quad (7)$$

This time is reported as τ_1 versus r in Fig. 3. As expected, τ_1 increases as the original thickness of the ice annulus increases.

3 The Second Regime: the Cylinder Cuts Through the Top of the Ice Sleeve

We now turn our attention to the accelerated fall of the ice sleeve at times τ greater than τ_1, when the hot cylinder can be seen through the top of the ice sleeve. This second regime is illustrated in Fig. 4. The angle of contact θ decreases from $\theta = \pi/2$ at $\tau = \tau_1$, to $\theta = 0$ at the τ_2 end of the contact melting process, when the remaining ice falls off the cylinder.

The travel of the ice body in the second regime can be anticipated based on contact melting theory, which is an analysis that combines the thin-film lubrication of the water layer of thickness $\delta(\hat{y})$, with the conservation of energy at the melting front represented by $\hat{x} = \delta$. The curvilinear system of coordinates $(\hat{x}, \hat{y})$ is defined on the left side of Fig. 4. One new aspect of the present contact melting phenomenon is the fact that the length $(R_i\theta)$ and shape of the contact melting region change as melting progresses.

The flow of water in the region of contact is governed by the Reynolds-type equation

$$\frac{dP}{d\hat{y}} = \mu \frac{\partial^2 v}{\partial \hat{x}^2} \quad (8)$$

in which v is the velocity component in the $\hat{y}$ (or β) direction. The $v(\hat{x}, \hat{y})$ distribution is obtained by solving Eq. (8) subject to no slip ($v = 0$) on the cylinder ($\hat{x} = 0$), and at the melting front ($\hat{x} = \delta$). The second of these conditions means that the ice velocity dx/dt is small relative to the water peripheral velocity. The resulting velocity distribution is

$$v = \frac{1}{2\mu} \frac{dP}{d\hat{y}} (\hat{x}^2 - \hat{x}\delta) \quad (9)$$

Mass conservation requires that $\partial u/\partial \hat{x} = -\partial v/\partial \hat{y}$, or that

$$\frac{\partial u}{\partial \hat{x}} = -\frac{G'}{2\mu}(\delta - \hat{x})\hat{x} - \frac{G}{2\mu}\delta'\hat{x} \quad (10)$$

where

$$G(\hat{y}) = -\frac{dP}{d\hat{y}} \text{ and } (\,)' = \frac{d}{d\hat{y}}(\,) \quad (11)$$

By integrating Eq. (10) in $\hat{x}$, and invoking the impermeable cylinder condition $u = 0$ at $\hat{x} = 0$, and the melting condition $u = -(dx/dt) \sin \beta$ at $\hat{x} = \delta$, we obtain

$$12\mu \left(\frac{dx}{dt}\right) \sin \beta = \frac{d}{d\hat{y}} (\delta^3 G) \quad (12)$$

A second relation between the ice speed and the water film thickness is the conservation of energy at the melting front,

$$\delta \frac{dx}{dt} \sin \beta = \frac{k(T_w - T_m)}{\rho h_{sf}} \quad (13)$$

This energy balance is based on the assumption that the film is thin enough so that convection in the $\hat{y}$ direction is negligible, i.e., that the temperature varies linearly across the water film. This assumption is valid when the Peclet number $\bar{v}\,\bar{\delta}/\alpha$ is smaller than 1, where $\bar{v}$ and $\bar{\delta}$ are the orders of magnitude (or average values) of v and δ. It is worth noting that the small Peclet number assumption is compatible with the Reynolds Eq. (8), which is valid when the Reynolds number $\bar{v}\,\bar{\delta}/\nu$ is smaller than 1.

Beyond this point we can replace $\hat{y}$ with $R_i\,\beta$ in Eq. (12), and eliminate δ between Eqs. (12) and (13). We integrate the resulting equation twice in β, and obtain the pressure distribution along one of the two contact regions,

$$P(\beta) - P(0) = 3\mu R_i^2 \left(\frac{dx}{dt}\right)^4 \left[\frac{\rho h_{sf}}{k(T_w - T_m)}\right]^3 \Phi(\beta, \theta) \quad (14)$$

where

$$\Phi(\beta, \theta) = \sin^4 \beta - \sin^4\theta \cdot \frac{\cos\beta(\sin^2\beta + 2) - 2}{\cos\theta(\sin^2\theta + 2) - 2} \quad (15)$$

This pressure distribution supports the weight of the ice shaded as area A_2 in Fig. 4,

$$\rho_s g A_2 = \int_0^\theta [P(\beta) - P(0)] R_i \sin\beta d\beta \quad (16)$$

In terms of the dimensionless travel ξ and time τ defined in Eqs. (4) and (5), the result of combining Eqs. (14) and (16) reads

$$\frac{d\xi}{d\tau} = \left(\frac{a}{3\psi}\right)^{1/4} \quad (17)$$

where $\psi(\theta)$ and $a(\theta, r)$ are given by

$$\psi(\theta)=\int_0^\theta \Phi(\beta,\ \theta)\sin\ \beta\ d\beta$$

$$=\frac{\sin^4\theta(1-\frac{1}{4}\sin^4\theta+\cos^2\theta-2\cos\ \theta)}{\cos\ \theta(\sin^2\theta+2)-2}$$

$$-\frac{1}{5}\sin^4\ \theta\ \cos\ \theta-\frac{4}{15}\cos\ \theta(\sin^2\theta+2)+\frac{8}{15} \tag{18}$$

$$a(\theta,\ r)=\frac{A^2}{R_i^2}=\frac{\pi}{2}\ r^2-\frac{\pi}{4}-\xi-\frac{\theta}{2}-\frac{r^2}{2}\sin^{-1}\left(\frac{\cos\ \theta}{r}\right)+\frac{\xi}{2}\cos\ \theta \tag{19}$$

The relation between ξ and θ is purely geometric,

$$\theta=\sin^{-1}\left(\frac{r^2-1-\xi^2}{2\xi}\right) \tag{20}$$

Finally, we can integrate Eq. (17) from the beginning of the second regime ($\tau = \tau_1$, when $\xi = r - 1$) by using Eqs. (18)–(20):

$$\int_{r-1}^{\xi}\left(3\frac{\psi}{a}\right)^{1/4}d\xi=\tau-\tau_1 \tag{21}$$

This integral was evaluated numerically, and plotted in Fig. 2 as the $\tau>\tau_1$ continuations of the curves obtained for the first regime. These extensions of the $\xi(\tau,\ r)$ curves show that the ice speed $d\xi/d\tau$ increases dramatically as the remaining ice falls off, i.e., as $\theta\to 0$. In the same θ limit ξ approaches $(r^2-1)^{1/2}$, and this means that the time τ_2 when the ice falls off the cylinder is given by

$$\tau_2=\tau_1+\int_{r-1}^{(r^2-1)^{1/2}}\left(3\frac{\psi}{a}\right)^{1/4}d\xi \tag{22}$$

This time was calculated numerically and plotted in Fig. 3. As expected, the ice removal time τ_2 increases as the thickness of the original ice layer increases. Important to note, however, is that the final time τ_2 is *considerably shorter* than the time that might have been estimated by extrapolating to $\xi = (r^2-1)^{1/2}$ the nearly straight portion of the ξ (τ) curve associated with the first regime. In other words, an accurate estimate of the total melting time τ_2 is possible only if the theory accounts also for the second regime. This observation is most critical when r is only slightly greater than 1, i.e., when the ice shell is relatively thin, and a larger share of the melting time is taken by the second regime.

To summarize the theoretical progress made until now, there are two distinct regimens in the melting process of Fig. 1. During the first regime the ice shell surrounds the cylinder (i.e., it is not cut yet). The first regime is analogous to Moallemi and Viskanta's (1985a) sinking cylinder problem. This is why we did not redo their analysis: We simply translated their solution into our coordinates and notation (section 2). The second regime begins when the cylinder cuts through the ice. It is the second regime that differs fundamentally from Moallemi and Viskanta's because: (*i*) The leading nose of the cylinder no longer pushes against ice, and (*ii*) the contact melting regions (one on each side) become shorter in time. To analyze the second regime we had to construct a contact melting analysis that accounted for the time dependence of the contact melting regions. The similarity between the present analysis and Moallemi and Viskanta's is that both are *contact melting theories*. There have been several contact melting analyses published during the past two decades, as shown in a recent review (Bejan, 1994).

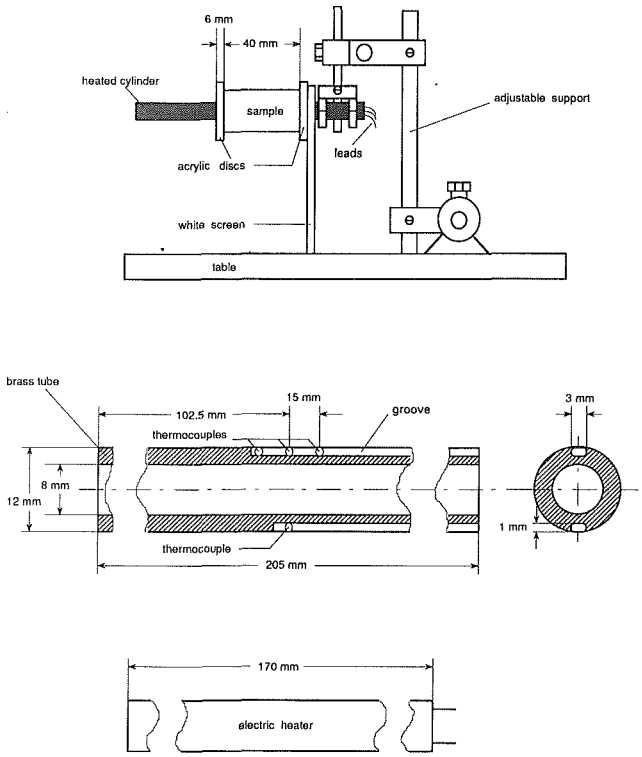

Fig. 5 The experimental apparatus (top), and the design of the heated cylinder (bottom)

4 Experiments

The theoretical melting rates and ice removal times developed above were validated through measurements made in the laboratory. The experimental apparatus is shown schematically in Fig. 5. An adjustable support structure was constructed on a horizontal table. The heated cylinder was aligned horizontally and held from one end, such that the melting of the annular ice sample could be viewed from the free end. The downward movement of the ice sample could be seen (and measured) against a vertical cardboard screen, which was painted white and covered with a square grid of size 2 mm × 2 mm.

The design of the heated cylinder is shown in the lower part of Fig. 5. The electric heater (CHROMALOX model 3618K532, maximum power 450 W at 120 V) was inserted with a tight fit inside a brass tube with an outer diameter of 12 mm. Four thermocouples [copper-constantan type TT-T-30 (special) were embedded in the outer surface of the brass tube, over the central section of the tube on which the ice sample would ride. Three thermocouples were positioned along the top of the brass tube, and the fourth was placed at the lowest point on the wetted perimeter. The thermocouple leads were buried in axial grooves, covered with high-conductivity epoxy, and taken out through the held end of the tube. The thermocouples were referenced to the ice point, and their voltages were measured with a recording multimeter. The function of the thermocouples was to measure the temperature of the contact melting surface, i.e., under the ice contact, not around the entire cylinder. We made only the measurements that were relevant to testing the theory.

The ice sample was shaped as a cylindrical shell with an inside diameter of 12 mm and axial length of 45 mm. Three different outer diameters were used, such that the radius ratio had the values $r = 3$, 5, and 6.83. Each sample was frozen in a special mold. During each melting run, the ice sample was sandwiched axially between two transparent acrylic disks, which rode with a relatively close fit on the heated cylinder. The function of these disks was to keep the axis of the ice sample

horizontal during the melting process, and to permit the viewing of the downward movement of the sample cross section.

The power input to the electric heater was held constant during each melting run. Three power settings were used (3.35 W, 12.9 W, and 29.7 W) during all the runs. The total number of runs was 40.

Two identical samples were melted one after the other during one run. The function of the first sample was to bring the temperature of the cylinder to a steady-state value, which occurred at about 1.5 minutes during its melting time. The first sample was left on the cylinder for 4 minutes, after which it was pulled out and replaced immediately with the second sample. This moment marked the start of the melting run, $t = 0$. The melting time of the second sample was 9 minutes and 35 seconds when $r = 6.83$ (29.7 W power setting), and 11 minutes and 5 seconds when $r = 3$ (3.35 W power setting).

It was assumed that during the melting of the second sample the ice was essentially isothermal at the melting point, i.e., that the subcooling of the ice during the run is negligible. This assumption is based on the fact that the second sample sat in room air more than 10 minutes before the melting run, and that the time of thermal diffusion across the sample is of the order of 1 minute. Furthermore, the ice sample was made in a mold placed in a freezer at $-8°C$. Before the melting run, the mold (with the ice sample in it) was held for 30 minutes or more in a bath of water and crushed ice, until the ice sample could be pulled out of the mold, i.e., until it could be pulled off the cylinder on which it was frozen. We were confident that when the ice sample came off it was nearly at 0°C, such that we could regard the subcooling effect as negligible.

The vertical position of the sample, and the thermocouples were read at equal time intervals (60 seconds) until the sample fell off the cylinder. The temperature readings were steady. The three upper thermocouples furnished voltage readings that agreed within 5 percent. The maximum discrepancy between the upper thermocouples and the bottom one was 10 percent: This occurred toward the end of the run, when the bottom half of the perimeter was in contact with air. For example, in the runs conducted with $r = 3$ samples (3.35 W power setting) the 5–10 percent discrepancy between the voltage readings of the two thermocouples meant that the temperature on the crest of the cylinder was 0.2°C, and at the bottom 0.22°C.

Ten runs with the same power setting and ice sample size are responsible for each of the experimental (ξ, τ) points plotted in Fig. 6. The precision and bias limits in the measurements of ξ and τ were calculated using the propagation equation of Kline and McClintock (1953) [see also Eqs. (4) and (5) in the editorial in the ASME JOURNAL OF HEAT TRANSFER, Vol. 115, p. 6]:

$$\frac{P_\tau}{\tau} = \frac{3}{4}\frac{P_{T_w}}{(T_w - T_m)} \quad \frac{B_\tau}{\tau} = \frac{3}{4}\frac{B_{T_w}}{(T_w - T_m)} \tag{23}$$

$$P_\xi = \frac{1}{R_i} P_x \quad B_\xi = \frac{1}{R_i} B_x \tag{24}$$

In the calculation of the uncertainty limits for the measured nondimensional time τ, the contributions made by the precision and bias limits of t, R_i, and the tabulated physical properties were found to be negligible relative to the precision and bias limits of T_w. The wall temperature T_w was of the order of 1°C in all the runs. The instrumented cylinder was tested by immersing it for one hour in an ice-water bath, and taking voltage readings from the thermocouples once every 10 minutes. The readings were sufficiently reproducible such that the largest deviation from 0°C was 0.01°C. Since our experimental measurements were to take place only in the close vicinity of 0°C, we regarded 0.01°C as the bias limit. The voltmeter used during this preliminary procedure and during all the runs was able to measure voltages as small as 10^{-9} V.

Similarly, in the calculation of the uncertainty limits for the measured nondimensional displacement ξ, the contributions due to the precision and bias limits of R_i were negligible relative to those of the actual displacement, x. A bias limit of ± 1 mm for x was taken as half of the distance between two horizontal grid lines on the vertical cardboard screen.

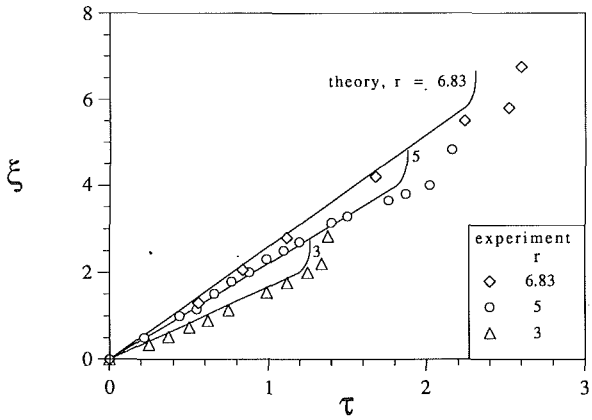

Fig. 6 Comparison between the experimental measurements and the theoretical ice movement versus time

The precision limits for both temperature and displacement were calculated as 2 times the standard deviation of each set (10 values per set) of observations for T_w and x. The uncertainty limits for τ and ξ were calculated with the following formulas, and the results are summarized in Table 1:

$$\frac{U_\tau}{\tau} = \left[\left(\frac{P_\tau}{\tau}\right)^2 + \left(\frac{B_\tau}{\tau}\right)^2\right]^{1/2} \quad U_\xi = (P_\xi^2 + B_\xi^2)^{1/2} \tag{25}$$

Figure 6 shows that there is good qualitative and quantitative agreement between the theoretical curves and the experiments data, especially during the first regime when the cylinder is surrounded by ice. The time when the ice sample fell off the cylinder is generally 15 percent longer than the theoretical time τ_2 based on Eq. (22) (see also Fig. 3). The calculated uncertainties turned out to be of the same order of magnitude as the relative mismatch between the experimental and theoretical data.

The ice samples did not break during the final moments of their ride on the cylinder. They did not even chip or crack. Every one of the 40 melting runs was smooth and continuous, as in the theory presented in section 3.

Figure 6 shows also that the melting rate is approximately constant during the run, because most of the melting time is taken by the first regime, which is quasi-steady. The second regime is considerably shorter. This is why the surface temperature was steady during the melting run.

Finally, we can show by means of a numerical example that natural convection had a negligible effect on the melting of the ice sample. This was one of the assumptions on which the theory of sections 2 and 3 was built. Consider the ice sample with $r = 3$, which had an outer diameter $D = 36$ mm. If the room air temperature is 20°C, and if the air properties are evaluated at the film temperature, we obtain $\mathrm{Ra}_D \cong 1.2 \times 10^5$, and the average heat flux $\bar{q}'' \cong 800$ W/m^2. To melt an ice shell that is 12 mm thick, this heat flux would require 1.3 hours, i.e., a time that is roughly 30 times longer than the life of the sample during the melting run.

5 Optimal Ice Sleeve Radius for Maximum Ice Production

The analytical and experimental work described until now showed that the time required by the complete removal of the ice sleeve (t_2, or τ_2 in Fig. 3) increases with the ice outer radius (R, or $r = R/R_i$). This relationship has an interesting and very

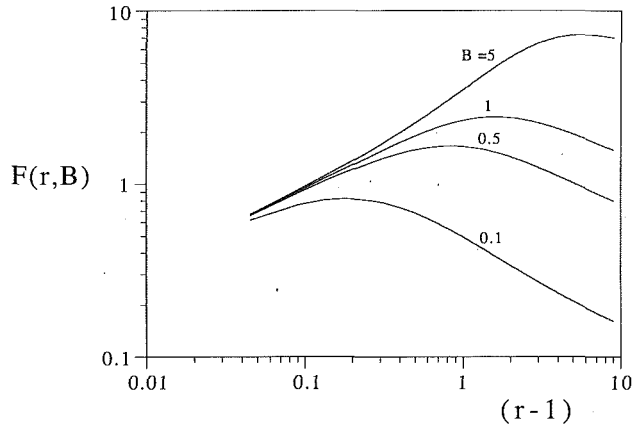

Fig. 7 The effect of the ice sleeve radius on the rate of ice production

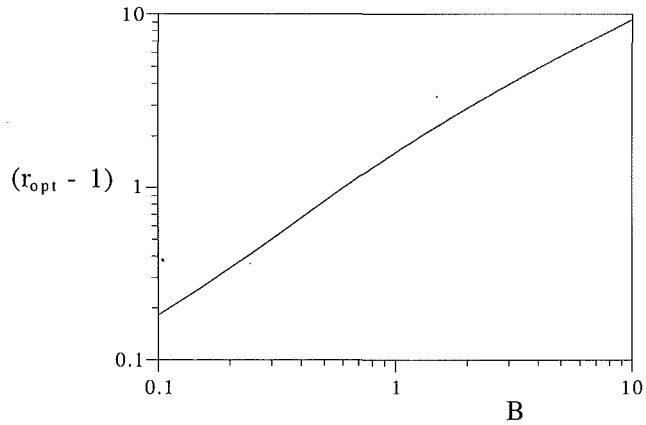

Fig. 8 The optimal ice shell radius for maximum rate of ice production

basic implication in the design of an ice manufacturing process that relies on the horizontal cylinder configuration of Fig. 1. We will show that the ice production rate averaged over time is maximum when the thickness of the ice shell has an optimal value.

One way to freeze a shell of outer radius R on a cylinder of radius R_i is by immersing the cylinder in water at the freezing point (T_m), and cooling the cylinder to a lower temperature (T_c). The latter can be accomplished by passing a refrigerant through the pipe of radius R_i. In applications involving the freezing of water, the freezing Stefan number $\text{Ste}_s = c_s(T_m - T_c)/h_{sf}$ is considerably smaller than 1. For such applications, the relationship between the time t_0 required to freeze a shell of outer radius $R = rR_i$ is given by (Carslaw and Jaeger, 1959)

$$\frac{4\ k_s(T_m - T_c)t_0}{\rho_s h_{sf} R_i^2} = 2r^2 \ln r - r^2 + 1 \tag{26}$$

The freezing time t_0 can be nondimensionalized as τ_0 in accordance with Eq. (5), so that Eq. (26) becomes

$$\tau_0 = \frac{1}{4B}(2r^2 \ln r - r^2 + 1) \tag{27}$$

The dimensionless group B represents a comparison of the properties of the ice shell during the freezing process with the properties of the water film during the melting process:

$$B = \frac{\alpha_s\ \text{Ste}_s}{\alpha\ \text{Ste}} \left(\frac{\rho}{\rho_s}\right)^{1/4} \left(\frac{\nu\alpha\ \text{Ste}}{gR_i^3}\right)^{1/4} \tag{28}$$

The total duration of a freezing and ice-removal cycle is $t_0 + t_2$, or $\tau_0 + \tau_2$. The amount of ice produced during one such cycle is proportional to the area $2A_2$ at the end of contact melting ($\theta = 0$, Fig. 4). In accordance with Eq. (19), the dimensionless quantity that is proportional to this amount of ice is

$$a(0, r) = \frac{\pi}{2}\left(r^2 - \frac{1}{2}\right) - \frac{1}{2}(r^2 - 1)^{1/2} - \frac{r^2}{2}\sin^{-1}\left(\frac{1}{r}\right) \tag{29}$$

The rate of ice production averaged over many freezing and melting cycles is proportional to the ratio

$$F(r, B) = \frac{a(0, r)}{\tau_0 + \tau_2} \tag{30}$$

which, according to Eqs. (27) and (29) and Fig. 3, is a function of r and B. The effect of the ice sleeve radius (r) on the rate of ice production (F) is illustrated in Fig. 7 by holding the B number constant. It is clear that there exists an optimal ice shell size ($R_{\text{opt}} = r_{\text{opt}}R_i$) that maximizes the rate of ice production.

Figure 8 summarizes the $r_{\text{opt}}(B)$ results obtained numerically by maximizing the function $F(r, B)$ with respect to r. The optimal ice shell is thicker when the B number is greater.

As a numerical example, consider the dimensions and melting conditions described in the experiment of section 4, namely $R_i = 6$ mm, $T_w - T_m \cong 1°\text{C}$, and the properties of water near 0°C. If we assume that during the freezing portion of the cycle the temperature difference is $T_m - T_c \cong 5°\text{C}$, and that the ice properties are nearly the same as at 0°C, from Eq. (28) we obtain $B \cong 0.14$. The optimal shell thickness read off Fig. 8 is $r_{\text{opt}} \cong 1.25$, which physically means that $R_{\text{opt}} \cong 7.5$ mm.

6 Conclusions

In this paper we documented theoretically and experimentally the fundamentals of melting when a sleeve of phase-change material (e.g., ice) rides on a heated horizontal cylinder. The key conclusions of this study are:

(*a*) The melting process consists of two distinct regimes, first, an early regime when the cylinder is surrounded by ice and, second, a late regime when the cylinder cuts through the upper portion of the ice sleeve. The falling speed of the ice in the second regime is considerably greater than in the first regime.

(*b*) The time until the ice falls off the cylinder can be predicted by using the two-parameter curve $\tau_2(r)$ shown in Fig. 3. The proper nondimensional time group has been identified in Eq. (5).

(*c*) To calculate the melting time τ_2 accurately one must take into account both regimes. This observation is critical when the original thickness of the ice shell is smaller than the cylinder radius.

(*d*) The trends and qualitative features of the theoretical solution (Fig. 2) are supported by direct observations of the melting of ice shells on a heated horizontal cylinder (Fig. 6).

(*e*) Relative to the entire cycle that begins with creating (freezing) the ice shell, and ends with heating the cylinder to remove the ice shell, there exists an optimal shell thickness such that the cycle-averaged rate of ice production is maximum (Fig. 8). The optimal outer radius of the ice shell is a function of a single nondimensional group, B, which is identified in Eq. (28).

Acknowledgments

Mr. Vargas' doctoral study at Duke University was supported by Conselho Nacional de Desenvolvimento Cientifico e Tecnologico—CNP_q (Brasil). Professor Bejan's research was sponsored by the National Science Foundation. Professor Dobrovicescu's visit at Duke University was sponsored by a grant offered to Duke University by the Denvonwood Foun-

dation. Professor Bejan acknowledges with gratitude the advice received in 1992 from Dr. J. S. Lim, Senior Research Scientist, Samsung R&D Center, Suwon, Korea, who drew his attention to the heat transfer phenomena that limit the development of modern refrigerator technology.

References

Bahrami, P. A., and Wang, T. G., 1987, "Analysis of Gravity and Conduction-Driven Melting in a Sphere," ASME JOURNAL OF HEAT TRANSFER, Vol. 109, pp. 806–809.

Bareiss, M., and Beer, H., 1984, "An Analytical Solution of the Heat Transfer Process During Melting of an Unfixed Solid Phase Change Material Inside a Horizontal Tube," *International Journal of Heat and Mass Transfer*, Vol. 27, pp. 739–746.

Bejan, A., 1989, "The Fundamentals of Sliding Contact Melting and Friction," ASME JOURNAL OF HEAT TRANSFER, Vol. 111, pp. 13–20.

Bejan, A., 1994, "Contact Melting Heat Transfer and Lubrication," *Advances in Heat Transfer*, Vol. 24, pp. 1–38.

Bejan, A., Vargas, J. V. C., and Lim, J. S., 1994, "When to Defrost a Refrigerator, and When to Remove the Scale From the Heat Exchanger of a Power Plant," *International Journal of Heat and Mass Transfer*, Vol. 37, pp. 523–532.

Carslaw, H. S., and Jaeger, J. C., 1959, *Conduction of Heat in Solids*, Oxford University Press, United Kingdom, p. 296.

Emerman, S. H., and Turcotte, D. L., 1983, "Stokes's Problem With Melting," *International Journal of Heat and Mass Transfer*, Vol. 26, pp. 1625–1630.

Kline, S. J., and McClintock, F. A., 1953, "Describing Uncertainties in Single-Sample Experiments," *Mechanical Engineering*, Vol. 75, Jan., pp. 3–8.

Lim, J. S., 1992, private communication to A. Bejan.

Moallemi, M. K., and Viskanta, R., 1985a, "Melting Around a Migrating Heat Source," ASME JOURNAL OF HEAT TRANSFER, Vol. 107, pp. 451–458.

Moallemi, M. K., and Viskanta, R., 1985b, "Experiments on Fluid Flow Induced by Melting Around a Migrating Heat Source," *Journal of Fluid Mechanics*, Vol. 157, pp. 35–51.

Nicholas, D., Bayazitoglu, Y., 1980, "Heat Transfer and Melting Front Within a Horizontal Cylinder," ASME *Journal of Solar Energy Engineering*, Vol. 102, pp. 229–232.

Prasad, A., and Sengupta, S., 1987, "Numerical Investigation of Melting Inside a Horizontal Cylinder Including the Effects of Natural Convection," ASME JOURNAL OF HEAT TRANFER, Vol. 109, pp. 803–806.

Roy, S. K., and Sengupta, S., 1987, "The Melting Process Within Spherical Enclosures," ASME JOURNAL OF HEAT TRANSFER, Vol. 109, pp. 460–462.

Webb, B. W., Moallemi, M. K., and Viskanta, R., 1987, "Experiments on Melting of Unfixed Ice in a Horizontal Cylindrical Capsule," ASME JOURNAL OF HEAT TRANSFER, Vol. 109, pp. 454–459.

A One-Dimensional Model of a Micro Heat Pipe During Steady-State Operation

J. P. Longtin
Graduate Student Researcher,
Department of Mechanical Engineering,
University of California at Berkeley,
Berkeley, CA 94720

B. Badran
Graduate Student Researcher.

F. M. Gerner
Associate Professor of
Mechanical Engineering.
Assoc. Mem. ASME

Department of Mechanical, Industrial,
and Nuclear Engineering,
University of Cincinnati,
Cincinnati, OH 45221-0072

Micro heat pipes are small structures that will be used to cool microscale devices. They function much like their conventional counterparts, with a few exceptions, most notably the absence of a wick. It is expected that water-filled micro heat pipes will be able to dissipate heat fluxes on the order of 10–15 W/cm^2 (100,000–150,000 W/m^2). This work addresses the modeling of a micro heat pipe operating under steady-state conditions. A one-dimensional model of the evaporator and adiabatic sections is developed and solved numerically to yield pressure, velocity, and film thickness information along the length of the pipe. Interfacial and vapor shear stress terms have been included in the model. Convection and body force terms have also been included in the momentum equation, although numerical experiments have shown them to be negligible. Pressure, velocity, and film thickness results are presented along with the maximum heat load dependence on pipe length and width. Both simple scaling and the model results show that the maximum heat transport capability of a micro heat pipe varies with the inverse of its length and the cube of its hydraulic diameter, implying the largest, shortest pipes possible should be used.

Introduction

The micro heat pipe is a small-scale device that uses phase change to transfer thermal energy. The hydraulic diameter of these devices is on the order of 100 μm, with a length of several centimeters. One major application for micro heat pipes is electronics cooling. As the current device density in electronic components increases, it becomes increasingly more difficult to dissipate the heat that is generated. Currently, heat fluxes on the order of 10 W/cm^2 (100,000 W/m^2) occur on the chip level. The micro heat pipe, which was first proposed by Cotter (1984) for exactly this application, combines the advantages of large latent energies associated with phase change and advanced micro-fabrication techniques. Another advantage of the micro heat pipe is that, by using phase change, a nearly uniform temperature is maintained throughout the device.

A micro heat pipe differs from a conventional heat pipe in that it is much smaller. Also it does not contain a wick, but rather uses capillary pressure due to sharp edges to return the condensate to the evaporator. A typical example with a triangular cross section is shown in Figs. 1 and 2. The evaporator section contains less liquid, has a smaller radius of curvature at the vapor–liquid interface, and hence has a depressed liquid pressure and elevated vapor pressure. This pressure difference is responsible for both the liquid and vapor flows.

Like many conventional heat pipes, the aspect ratio is very high. For the device to function properly in any orientation, the ratio of gravity forces to capillary forces, $\rho g L R_H/\sigma$, must be of order one or less. In addition, micro heat pipes have a small hydraulic diameter, just large enough to ensure that the capillary radius provides enough "pumping power" to return the condensate to the evaporator. The idea behind the micro heat pipe is that a diameter several orders of magnitude larger than the capillary radius is unnecessary. Typically the hydraulic radius is on the order of the capillary radius (Cotter, 1984; Babin et al., 1990), thus allowing their use in very small places.

Both Cotter (1984) and Babin et al. (1990) have developed models to predict the behavior of micro heat pipes; however, each has its shortcomings. Cotter's model requires knowledge of a parameter $H(L)$ a priori, which, as Babin et al. point out, behaves as a correction factor. Babin et al. present a steady-state model based, in part, on an analysis by Chi (1976); however, the profile of the liquid film is assumed to be known in computing the liquid and vapor pressure drops. Additionally, the assumption is made that the interfacial radius of curvature approaches infinity in the condenser, which is not strictly correct.

Modeling of Micro Heat Pipes

A model is developed to predict the fluid-thermal behavior of micro heat pipes, including maximum heat transfer capability, effect of pipe length, width, and working fluid, and optimum operating conditions. The model is one dimensional and considers only axial variations along the heat pipe. Equations for the conservation of mass, momentum, and energy

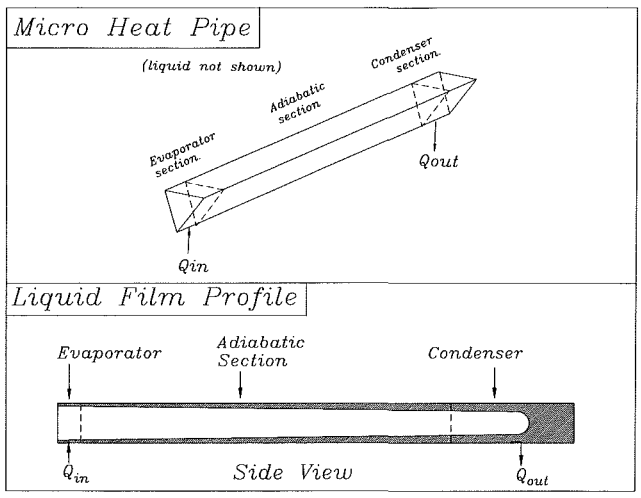

Fig. 1 The micro heat pipe (MHP)

Contributed by the Heat Transfer Division for publication in the JOURNAL OF HEAT TRANSFER. Manuscript received by the Heat Transfer Division November 1992; revision received October 1993. Keywords: Heat Pipes and Thermosyphons, Phase-Change Phenomena. Associate Technical Editor: R. Viskanta.

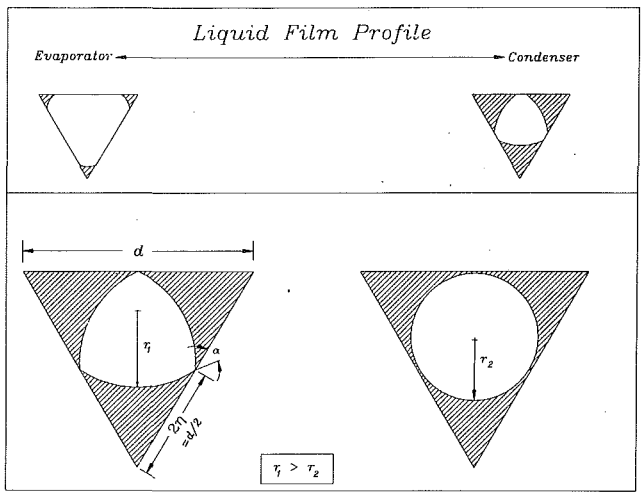

Fig. 2 Maximum radius of curvature

are developed for both the liquid and vapor. Boundary conditions and constitutive relationships for each section are then applied to close the equations. The resulting differential equations are solved numerically to yield pressure, velocity, and film thickness information for the modeled sections of the device.

The cross section of the micro heat pipe is approximated by an equilateral triangle (Fig. 1). The evaporator, adiabatic, and condenser sections are also shown in the figure. During operation, the working fluid recedes into the corners of the pipe, generating the necessary capillary driving pressure. Evaporation in the evaporator and condensation in the condenser cause the liquid to accumulate in the condenser section of the device. The amount of liquid—hence the interfacial radius of curvature—varies as a function of axial position, x, along the length of the pipe (Figs. 1 and 2). The interfacial radius of curvature, in turn, is related to the pressure difference between the liquid and vapor phases by the Laplace–Young equation,

$$P_v(x) - P_l(x) = \sigma / r(x), \tag{1}$$

or, by differentiating with respect to x,

$$\frac{dP_v}{dx} - \frac{dP_l}{dx} = -\frac{\sigma}{r^2}\frac{dr}{dx}. \tag{2}$$

The following assumptions are employed in the derivation of the governing equations:

- *Both liquid and vapor flows are incompressible.* It is expected that the Reynolds number of the liquid or vapor does not exceed about 50 (Gerner et al., 1992). Additionally, the Mach number for the vapor is $\ll 1$ for temperatures of interest ($T \sim$ 300–400 K).
- *Steady-state operation.* As a result the liquid and vapor mass flow rates are equal at any point.
- *Constant fluid properties.* During operation, the device is nearly isothermal with small pressure variations.
- *Viscous dissipation is negligible.* This is a consequence of the small velocities in both the liquid and vapor.
- *The vapor temperature T_v is constant.* This requires two criteria. First, there must not be an appreciable change in the vapor temperature from evaporator to condenser. Normally, the device transfers energy in the working fluid's liquid–vapor saturation region; thus, the vapor temperature is constant for a given pressure. Second, the pressure drop in the vapor must be small. Treating the vapor as an ideal gas, it can be seen from the Clapeyron equation (Tien, 1975) that $\Delta T \sim T_{sat}^2 \Delta P / P_{sat}$, hence a small pressure variation yields a small temperature variation.
- *The evaporator heat flux is uniform.*
- *Constant surface tension.*
- *The interfacial radius of curvature parallel to the pipe axis is much larger than that normal to the pipe axis.* This implies the mean radius of curvature is approximately equal to the radius of curvature normal to the pipe axis, $r(x)$.
- *The interfacial radius of curvature is constant at any given x location.* In practice, an extended evaporating meniscus probably forms in the evaporator that is not strictly circular (Potash and Wayner, 1972; Stephan and Busse, 1990).

The thickness of the liquid film cannot be considered negligible with respect to the hydraulic diameter of the device; thus, changes in the liquid and vapor cross sections as a function of axial position are accounted for.

It is assumed that in the evaporator and adiabatic sections the liquid interface meets the wall at a finite, constant contact angle. The contact angle is a complicated phenomenon that is affected by several factors, including the evaporation process and thickness of the evaporating film (Potash and Wayner, 1972). The model is relatively insensitive to variation in the contact angle: contact angles ranging from 0–42 deg produce less than a 20 percent change in the predicted power capacity of the device. A contact angle of 35 deg was measured for a silicon–water–air system, and this value is used for the model calculations. The portion of the wall not in contact with the liquid is assumed to be dry and adiabatic. Combined with the assumptions stated above, the cross-sectional shape of the liquid film is then well defined and can be expressed in terms of

Nomenclature

A = area
d = width of one side of equilateral pipe cross section
D_H = hydraulic diameter = $4A/P_{wet}$
f = friction factor
g = gravitational acceleration = 9.82 m/s^2
h_{fg} = latent heat of vaporization
k = friction factor coefficient
L = length
$\dot{m}$ = mass flow rate
P = pressure, perimeter
Q = total heat input into device
q'' = heat flux
r = interfacial radius of curvature
R_H = hydraulic radius = $D_H/4$
Re = Reynolds number = $\rho U D_H/\mu$
T = temperature
U = axial velocity
V = radial (phase change) velocity
w = width of pipe + space between pipes
x = axial position along pipe
α = contact angle
β = geometric coefficients
θ = angle of inclination with respect to gravity
μ = dynamic viscosity
ρ = density
σ = surface tension
τ = shear stress

Subscripts

a = adiabatic
crit = critical (initial radius of curvature)
CV = control volume
e = evaporator
i = interface
l = liquid
max = maximum
o = initial or known conditions
sat = saturated vapor
v = vapor
w = wall
wet = wetted perimeter

Table 1 Micro heat pipe parameters used in this study

Parameter	Value
d	100 μm
w	200 μm
r_{max}	59.2 μm
L_e	280 μm
L_a	20 mm
T_v	70°C
r_o	5 μm
α	35 deg

geometric constants (derived in the appendix) and the interfacial radius of curvature.

In the condenser, however, the vapor condenses on the entire pipe wall. The contact angle is no longer well defined and the shape of the liquid film cross section is not obvious. Additionally, the radius of curvature must increase monotonically from the evaporator to the condenser to avoid sign changes in the pressure gradient, as seen in Eq. (2). A continuously increasing radius of curvature results in a continuously increasing liquid cross-sectional area; however, as one progresses farther and farther into the condenser, the total mass flow *decreases*, which requires either a *decreasing* liquid cross-sectional area and/or a decreasing liquid velocity. Exactly which occurs is not obvious; however, if the liquid cross-sectional area decreases in the condenser, the device will not work, because of the requirement that the interfacial radius of curvature increase monotonically.

Furthermore, condensate that finds itself in the middle of the condenser wall must flow to one of the three corners to be returned to the evaporator. This flow process, of course, will require a pressure gradient, which must come about from a gradient in the radius of curvature of the interface. Now, since the liquid flow from the middle of the pipe wall to the corner is essentially perpendicular to the axis of the pipe, the gradient in the radius of curvature of the interface (required to generate the necessary pressure gradient for this flow) will be in a direction perpendicular to the axis. This means the flow is two dimensional, and the shape of the liquid interface, which now requires two radii of curvature to account for the condensate flow properly, is not well defined by a single radius of curvature. Recently, the thermodynamic aspects of the liquid–vapor interface in micro heat pipes have been investigated by Swanson and Peterson (1993).

Because the exact nature of the liquid film profile and the velocity distribution in the condenser are not known, the condenser section has not been included in the modeling of the heat pipe. The justification for this is that studies indicate the limiting phenomenon in micro heat pipes is the maximum pumping pressure available to overcome viscous forces in the liquid and vapor (Gerner et al., 1992; Babin et al., 1990). The bulk of the viscous losses occur in the adiabatic section due to its relatively long length. For example, in this study, the evaporator is about 0.28 mm long and the condenser is 2–3 mm in length; however, the adiabatic section is over 20 mm long. It is also assumed that the condenser section is not the limiting portion of the devices. In practice the heat pipe is a closed system, and neglecting the condenser section places some restrictions on the model, e.g., global mass conservation cannot be imposed without the condenser section.

The heat pipe is divided into a series of small control volumes (CV) of length dx for which the conservation principles are applied. Figure 11 in the appendix shows a pipe cross section with the liquid recessed into the corners. All of the following quantities are expressed in terms of the interfacial radius of curvature, $r(x)$, and geometric constants β_l, $\beta_{l,w}$, and β_i. The relevant dimensions of the micro heat pipe used in this study are listed in Table 1. The working fluid used in this study is water and its thermophysical properties are obtained from Kakaç et al. (1987).

The liquid and vapor cross-sectional areas are, respectively,

$$A_l = \beta_l r^2, \qquad A_v = \sqrt{3}d^2/4 - \beta_l r^2 \tag{3}$$

where d is the width of a side of the pipe. The liquid and vapor volumes are obtained by multiplying the appropriate area by the CV thickness, dx. The area of the wall in contact with liquid, the wall in contact with the vapor, and the area of the liquid–vapor interface are, respectively,

$$A_{l,w} = \beta_{l,w} r dx, \qquad A_{v,w} = (3d - \beta_{l,w} r)dx, \quad A_i = \beta_i r dx. \tag{4}$$

Q_{CV} is the portion of the total heat input to a pipe entering the control volume of interest. In terms of the total heat input, $Q_{CV} = Q_e dx/L_e$.

As noted above, the liquid film meets the wall at a finite, specified contact angle, where a definite distinction between solid, liquid and vapor can be made. When the two films meet, however, the two interfaces will coalesce, and the solid wall will no longer be in direct contact with the vapor (Fig. 2). Thus, in the model, a flag is included to check if the two interfaces meet. If this situation occurs in the evaporator or adiabatic section, the device will fail to operate because dr/dx changes sign. The radius of curvature at this point is called the *maximum radius of curvature*. Based on the geometry of the pipe cross section, the maximum radius of curvature is calculated to be (Figs. 2 and 11) $r_{max} = d/4 \sin(\pi/3 - \alpha)$.

A cylindrical coordinate system is used where the x axis is collinear with the geometric centerline of the pipe. The end of the evaporator is coincident with $x = 0$, and the condenser end lies at $x = L$. As a result, the vapor mass flow rate $\dot{m}_v(x) \geq 0$ and the liquid mass flow rate $\dot{m}_l(x) \leq 0$. Likewise, the interfacial phase-change velocity V_i is positive during condensation (i.e., away from centerline) and negative for evaporation. The unit vector normal to the control volume surface $\hat{\mathbf{n}}$ is positive when outward.

Conservation of Mass. During steady-state operation the time rate of change of mass in both the liquid and vapor control volumes is zero. Thus $\rho \Sigma A_k \mathbf{U}_k \cdot \hat{\mathbf{n}} = 0$ where $\mathbf{U}_k$ is the vector velocity normal to area A_k whose outward unit normal is $\hat{\mathbf{n}}$.

Referring to Fig. 3(*a*) (only one of three corners is shown) and employing Eqs. (3) and (4), the mass balance becomes

$$r\frac{dU_l}{dx} + 2U_l\frac{dr}{dx} - \frac{\beta_i}{\beta_l}V_{i_l} = 0. \tag{5}$$

The derivation for the vapor is identical to the liquid:

$$\left(\frac{\sqrt{3}}{4}d^2 - \beta_l r^2\right)\frac{dU_v}{dx} - 2\beta_l U_v r\frac{dr}{dx} + \beta_i\frac{\rho_l}{\rho_v}rV_{i_l} = 0. \tag{6}$$

Note that mass continuity across the interface, $\rho_v V_{i_v} = \rho_l V_{i_l}$, is employed in Eq. (6) to relate the liquid and vapor interface velocities.

Conservation of Energy. Since the device is nearly isothermal during operation, the film is so thin, and the Reynolds numbers are so low, conduction, convection, and viscous dissipation in the liquid may be neglected. Basically, any energy input into the CV exits by vaporizing the liquid at the interface. Recall also that the vapor temperature is assumed constant in all sections of the device, thus only the liquid phase has an expression for the conservation of energy.

Referring to Fig. 3(*b*), $q'' w = \rho_l V_{i_l} A_i h_{fg}$, or

$$V_{i_l} = \frac{q'' w}{\rho_l \beta_i r h_{fg}}. \tag{7}$$

In the adiabatic section, $q'' = 0$. Also, Eq. (7) is small enough to be substituted directly into the other equations wherever an interfacial mass velocity is required.

In practice, there will be a spatial variation in the mass flux at the interface. Near the interline, the film becomes very thin, posing little resistance to heat transfer. Likewise, the intrinsic

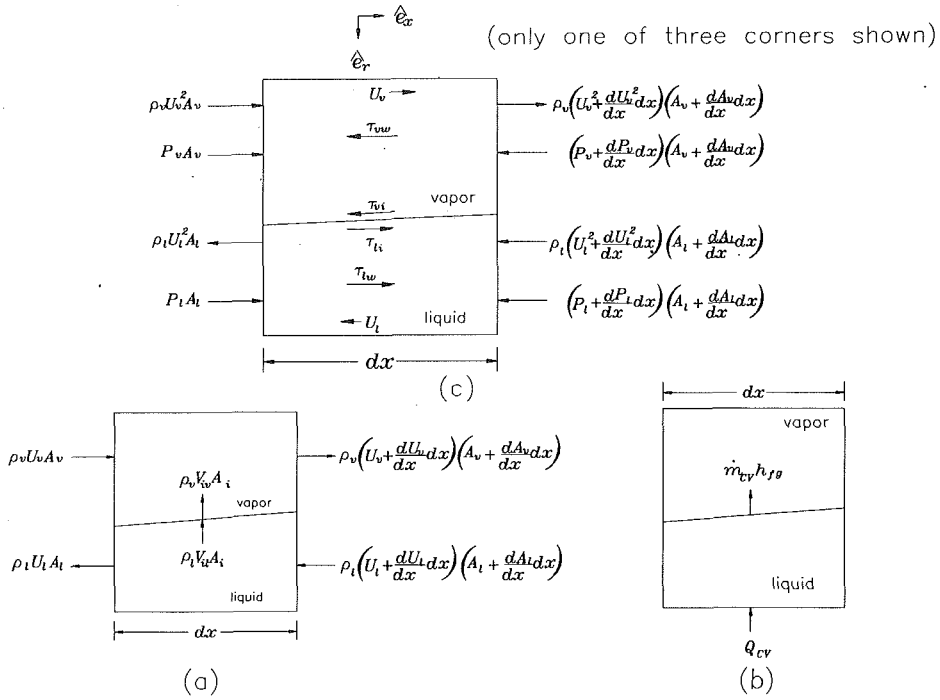

Fig. 3 *CV* **for conservation of (*a*) mass, (*b*) entropy, and (*c*) momentum**

meniscus far from the pipe walls has an abundance of fluid available for phase change. The interface mass velocity used here omits these spatial effects; hence, it represents an *averaged* interface velocity. The possibility of a dryout condition is also not captured by this formulation; however, it is expected that capillary pumping forces will be exceeded by viscous forces well before a dryout condition occurs.

Conservation of Momentum. The conservation of linear momentum for the liquid control volume consists of the following parts (White, 1986). First is the difference between the inflow and outflow of momentum into the *CV*. Referring to Fig. 3(*c*), this term becomes

$$-\rho_l\left[2A_lU_l\frac{dU_l}{dx}+U_l^2\frac{dA_l}{dx}\right]dx.$$

Note that the contribution of momentum flux due to phase change at the interface is *not* included in this term. It is accounted for as an additional component of the interfacial shear stress in the surface forces term.

The body force term (i.e., gravity) is expressed as $-\rho_l g A_l \sin\theta dx$ where θ is the inclination angle of the pipe centerline with respect to gravity. When the pipe is horizontal, $\theta = 0$.

Surface forces on the *CV* are composed of both *normal* and *tangential* surface forces. The only normal force considered is the pressure acting on the liquid cross-sectional area and is expressed as $-A_l(dP_l/dx)dx$. The tangential forces arise from shear encountered at the interface and wall. Expressions are derived for the liquid wall shear $\tau_{l,w}$, vapor wall shear $\tau_{v,w}$, and interfacial shear τ_i below. The total tangential stress for the liquid become $\tau_{l,w}A_{l,w} + \tau_iA_i$.

Combining these terms, using Eqs. (3) and (4), the liquid momentum equation becomes

$$-2\rho_l\left[rU_l\frac{dU_l}{dx}+U_l^2\frac{dr}{dx}\right]-\rho_l gr\sin\theta-r\frac{dP_l}{dx}+\tau_{l,w}\frac{\beta_{l,w}}{\beta_l}+\tau_i\frac{\beta_i}{\beta_l}=0. \quad (8)$$

The derivation for the vapor is identical to that of the liquid:

$$\rho_v\left(\frac{\sqrt{3}}{2}d^2-2\beta_l r^2\right)U_v\frac{dU_v}{dx}-2\rho_v\beta_l U_v^2 r\frac{dr}{dx}+\left(\frac{\sqrt{3}}{4}d^2-\beta_l r^2\right)\frac{dP_v}{dx}+\tau_{v,w}(3d-\beta_{l,w}r)+\tau_i\beta_i r+\rho_v g\sin\theta\left(\frac{\sqrt{3}}{4}d^2-\beta_l r^2\right)=0. \quad (9)$$

The model is one dimensional; thus, information about the radial velocity distribution within the liquid and vapor needed to compute the wall and interfacial shear stresses is unknown. To compute these shear stresses, then, both the liquid and vapor flows are assumed to be similar to fully developed duct flow, which is justified because the convective terms are small and the liquid and vapor cross-sectional areas change slowly with x. The hydraulic diameter of both the liquid and vapor is computed based on the control volume geometry discussed above. The *wetted* perimeter is used for D_H to compute the respective shear stresses. The velocity of the vapor relative to the liquid scales roughly as ρ_v/ρ_l and is on the order of 100–1000. For this reason, from the perspective of the vapor, the liquid is stationary, and can be treated as another section of the wall. The interfacial shear is thus computed for the vapor by assuming the liquid to be stationary, and, since the liquid and vapor shear stresses are equal and opposite, the liquid shear follows immediately. The equality of the liquid and vapor shear stresses follows from a simple force balance on the interface as the acceleration of the liquid and vapor is negligibly small.

For all calculations,

$$D_H=\frac{4A}{P_{\text{wet}}},\quad \text{Re}=\frac{\rho UD_H}{\mu}, \quad (10)$$

The shear stress is expressed as (Bejan, 1984)

$$\tau=\frac{1}{2}\rho U^2 f,\quad f=\frac{k}{\text{Re}}. \quad (11)$$

The constant k depends on the geometry of the duct. For the liquid, a triangular duct geometry is assumed for which k =

13.3 (Bejan, 1984). The geometry the vapor sees varies from nearly triangular in the evaporator where there is almost no liquid to approximately circular ($k = 16.0$) where the interfaces just meet (Fig. 2), hence $k = 14.7$ is used.

The shear stress at the interface has an additional component due to the momentum of the mass entering or leaving the control volume during phase change (Blangetti and Naushahi, 1980); however, scaling of both the liquid and vapor velocities indicate that the additional (phase change) term is negligible (Longtin, 1991).

Boundary Conditions. Equations (2), (5), (6), (8), and (9) constitute a set of five first-order, nonlinear, coupled ordinary differential equations in five unknowns: r, U_l, U_v, P_l, and P_v. Boundary conditions are needed at only one point for the solution to proceed. The evaporator is exposed to a constant heat flux and the adiabatic section experiences no heat transfer. The solution commences at the beginning of the evaporator and proceeds to the evaporator–adiabatic section interface where a second solution procedure begins using the boundary conditions specific to the adiabatic section. The initial conditions for the adiabatic section equations are simply taken from the solution of the evaporator section at the evaporator–adiabatic interface. The boundary conditions used at the end of the evaporator ($x = 0$) are: $U_l(0) = U_v(0) = 0$, $r(0) = r_0$, $P_v(0) = P_{sat}(T_v)$, and $P_l(0) = P_v(0) - \sigma/r_0$. Here P_v is taken to be the saturation pressure of the vapor at temperature T_v. Determining the value of the initial radius of curvature, r_0, poses some trouble because of the singularity in Eq. (1) for $r_0 = 0$. To obtain a reasonable value of r_0, the sensitivity of the solution to initial values of r_0 was investigated. For the parameters used in this study, the maximum heat transport changes by less than about 10 percent for $r_0 \leq 12\ \mu$m. (Results from the model indicate a similar trend for pipes of other lengths and widths as well.) The largest initial radius of curvature that does not have a pronounced effect on the final solution is called the *critical initial radius of curvature*, $r_{0,crit}$. In general, the larger the pipe width, the larger $r_{0,crit}$ becomes.

The next step was to determine if the actual initial radius of curvature was less than this value. The pipes are simply triangular troughs etched in a silicon wafer and covered with glass. They were charged and placed under an optical microscope that had a depth of field of only a few microns. By looking directly down upon a pipe (i.e., the lowest apex of the triangle in Fig. 2 is farthest from the observer's eye), one can focus on the midpoint the liquid–vapor interface that has receded into this apex. Next, the plane of focus was raised until the interline region comes into focus. This difference d measured on the microscope corresponds to $r(1 - \cos\phi)$ in Fig. 11. At the same time, the distance across the pipe ($=2\eta = 2r \sin\phi$) was measured. These two equations were then solved for r and ϕ. The equilibrium radius of curvature was found to be about 10 μm. Also, during operation, the film in the evaporator will become thinner than the equilibrium film distribution, reducing r_0. Based on these observations, the actual value of r_0 is immaterial as long as $r_0 \leq r_{o,crit}$.

Equations (2), (5), (6), (8), and (9) and their boundary conditions were solved numerically for the five unknowns: r, U_l, U_v, P_l, and P_v. The numerical integration method used was a fourth-order Runge–Kutta ODE solver with adaptive step size control to minimize error. The allowable error between steps in the solution procedure was always $\leq 10^{-7}$.

Results and Discussion

The model developed above can be used to predict the following:

- The maximum thermal energy a pipe of given dimensions and working fluid can transport.
- The maximum length a pipe of given cross section and working fluid can be to transfer a specified amount of heat.
- The pressure, velocity, and liquid film distribution (i.e., $r(x)$) in the pipe.
- The optimum pipe size and packing arrangement for a given application.
- Variation in MHP performance as function of variation in the operating parameters.

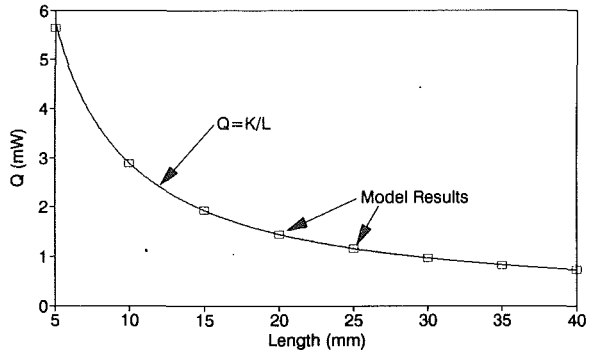

Fig. 4 Q_{max} versus L

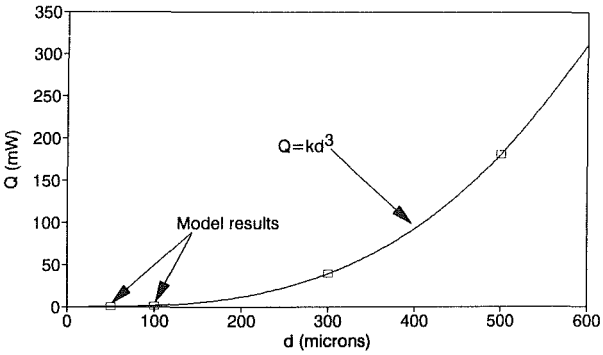

Fig. 5 Q_{max} versus d

The parameters used are those listed in Table 1 except where noted. Additionally, the initial radius of curvature, r_0, is assumed to be less than $r_{0,crit}$.

The following nondimensionalizations are employed (here D_H is for an empty pipe):

$$x^* = \frac{x}{L}, \quad r^* = \frac{r}{D_H},$$

$$U^* = \frac{U}{Q/\rho D_H^2 h_{fg}} = \frac{U}{U_{ref}}, \quad P^* = \frac{P}{\sigma/D_H} = \frac{P}{P_{ref}}. \quad (12)$$

The nondimensional pressure is derived from Eq. (1), and the nondimensional velocity is based on prior scaling results (Gerner et al., 1992).

The maximum heat transport capacity of the device is obtained iteratively. An initial guess of Q_e is made and the model is executed. If the liquid from adjacent corners meets in the adiabatic section, the device will fail to work, so Q_e is decreased. Otherwise Q_e is increased until the liquid from adjacent corners *just* meets at the end of the adiabatic section. This value of Q_e is then the reported power capacity of the device, Q_{max}. If Q_{max} is specified, other parameters (e.g., length or width) can be solved for in a similar manner.

Figures 4 and 5 show the maximum heat transfer capacity as a function of total pipe length and width, respectively. It is found from the model results as well as previous scaling (Gerner et al., 1992) that $Q_{max} \propto 1/L$ for variation in the pipe length and $Q_{max} \propto d^3$ for variation in the pipe width. The solid lines show these respective trends where the constant of proportionality, K, is computed by choosing the largest Q_{max} data

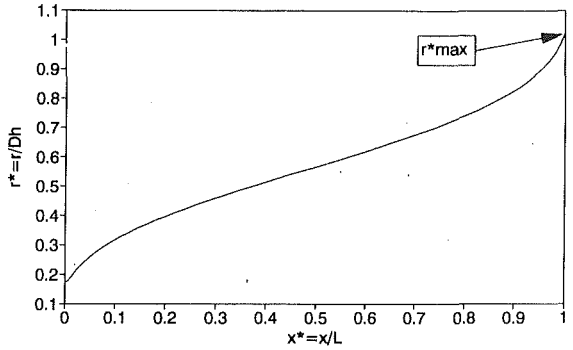

Fig. 6 r^* versus x^*

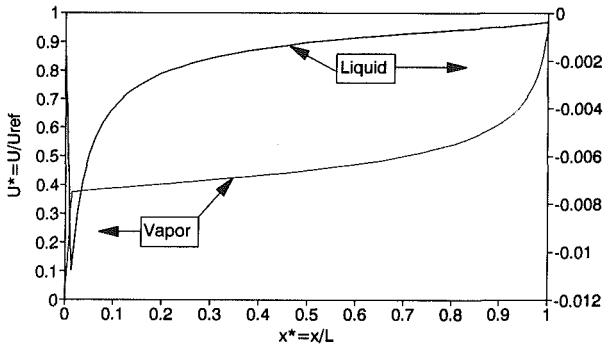

Fig. 7 U_l^* and U_v^* versus x^*

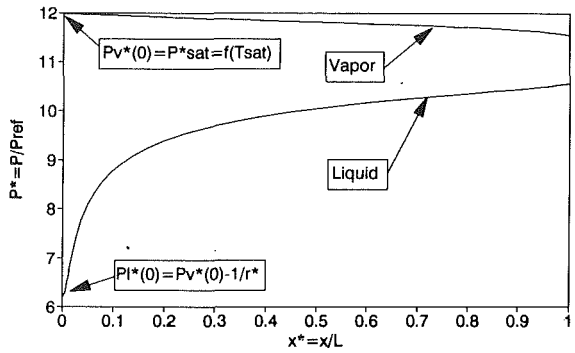

Fig. 8 P_l^* and P_v^* versus x^*

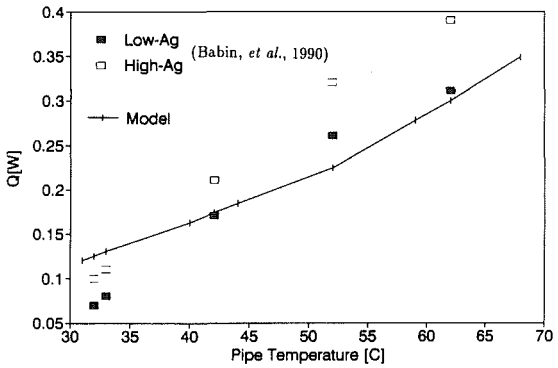

Fig. 9 Model versus silver-water experimental data (Babin et al., 1990)

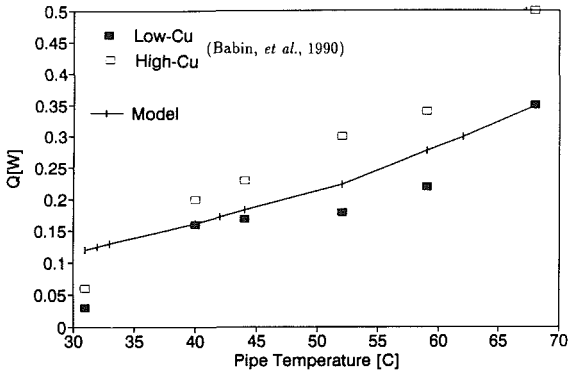

Fig. 10 Model versus copper-water experimental data (Babin et al., 1990)

point and its corresponding variable of interest from the model results (i.e., $K = [Q_{max} \cdot L]_{max}$ and $K = [Q_{max}/d^3]_{max}$, respectively). The heat transport, Q_{max}, is proportional to the fluid velocity, U. By performing a force balance on the liquid (or vapor), and scaling the capillary pressure as $\Delta P \sim \sigma/d$ and the shear stress as $\tau \sim \mu U/d$, the relationship $Q_{max} \propto d^3$ results (Gerner et al., 1992). Clearly, the maximum power capacity of a pipe is obtained for *short, wide* pipes, as long as the previous assumptions are observed.

The radius of curvature versus axial position for the evaporator and adiabatic sections is shown in Fig. 6. The rate of change of the radius of curvature dr/dx is nearly constant along the length of the pipe. The deviation of r from a linear profile comes about from the change in area of the liquid and vapor spaces. At the condenser end near $r \sim 0.8$, the vapor space begins to shrink significantly with increasing r, and mass continuity then requires a larger vapor velocity to accommodate the same mass flow. This larger vapor velocity, in turn, yields larger wall shear stresses, which require a larger radius of curvature to overcome. In a similar fashion, near the evaporator (i.e., $r \sim 0$), the liquid cross section is small, hence a large velocity is required to maintain the mass flow rate. As r increases, so does the liquid cross section, and the velocity decreases, explaining the gradual tapering off of r from $r \sim 0$ to $r \sim 0.4$.

Figure 7 shows both the liquid and vapor velocities. The vapor velocity is much higher than the liquid due to the density disparity between the two phases. The vapor velocity also increases with x because the increasing radius of curvature causes a decrease in the vapor space cross section with x, resulting in higher velocities. The liquid decelerates with x for the same reason. The variation in both liquid and vapor pressure is shown in Fig. 8. The liquid pressure drop is about an order of magnitude larger than that of the vapor.

Comparison with Experiments. Babin et al. (1990) have performed experiments with very small copper–water and silver–water heat pipes. To roughly compare the results of the model with their results, the hydraulic diameter of their device ($D_H = 0.408$ mm) was used as the hydraulic diameter for the triangular geometry in this study. It is understood that the comparison is only approximate in nature and is presented to show that the model shows both the correct trend and order of magnitude of the heat capacity of the pipe.

The model was run for the temperatures of all the data points presented in the experimental data of Babin et al. The results are shown in Figs. 9 and 10 for the silver-water and copper-water heat pipes, respectively. The agreement between the model and the experimental results is good. Also, the correct trend of increasing heat transfer with increasing operating temperature is observed, although the power capacity of the data decreases more rapidly with temperature than the model predicts.

Conclusions

This work presents the development of a one-dimensional model of a micro heat pipe during steady-state operation. A semi-integral application of the conservation of mass, mo-

mentum, and energy equations is employed, taking into account interfacial effects as well as the interfacial radius of curvature. The resulting coupled ordinary differential equations are solved numerically to yield pressure, velocity, and interfacial curvature information as a function of axial distance along the device. Only the evaporator and adiabatic sections have been modeled as previous research indicates viscous losses in the working fluid limit the maximum power capacity of the device, and the adiabatic section, due to its length, incurs most of these losses.

The model results agree with previous scaling in that the maximum power capacity of the device varies inversely with length, and to the third power of the pipe width. The model results agree in magnitude and trend with experimental data from a similar device. Model results predict an almost linear profile in the interfacial radius of curvature; deviations are explained due to the varying cross section of the liquid and vapor. The pressure drop in the liquid is also found to be about an order of magnitude larger than that of the vapor.

Acknowledgments

The authors are grateful for the funding for this work, provided in part by the National Science Foundation under contact No. CTS-8908838 and the A.F.O.S.R. under contract No. F49620-88-C-0053.

References

Babin, B. R., Peterson, G. P., and Wu, D., 1990, "Steady-State Modeling and Testing of a Micro Heat Pipe," ASME JOURNAL OF HEAT TRANSFER, Vol. 112, pp. 595-601.

Bejan, A., 1984, *Convection Heat Transfer*, Wiley, New York, pp. 77-78.

Blangetti, F., and Naushahi, M. K., 1980, "Influence of Mass Transfer on the Momentum Transfer in Condensation and Evaporation Phenomena," *Int. J. Heat Mass Transfer*, Vol. 23, pp. 1694-1695.

Chi, S. W., 1976, *Heat Pipe Theory and Practice*, McGraw-Hill, New York.

Cotter, T. P., 1984, "Principles and Prospects for Micro Heat Pipes," *Proceedings of the 5th International Heat Pipe Conference*, Tsukuba, Japan, pp. 328-335.

Gerner, F. M., Longtin, J. P., Henderson, H. T., Hsieh, W. M., Ramadas, P., and Chang, W. S., 1992, "Flow and Heat Transfer Limitations in Micro Heat Pipes," ASME HTD-Vol. 206-3, pp. 99-104.

Kakac, S., Shah, R. K., and Aung, W., 1987, *Handbook of Single-Phase Convective Heat Transfer*, Wiley, New York, pp. 22.30-22.33.

Longtin, J. P., 1991, "Analysis and Testing of Micro Heat Pipes," Masters Thesis, University of Cincinnati, Cincinnati, OH, p. 31.

Potash, M., and Wayner, P. C., 1972, "Evaporation From a Two-Dimensional Extended Meniscus," *Int. J. Heat Mass Transfer*, Vol. 15, pp. 1851-1863.

Stephan, P. C., and Busse, C. A., 1990, "Theoretical Study of an Evaporating Meniscus in a Triangular Groove," presented at the 7th International Heat Pipe Conference, Minsk, USSR.

Swanson, L. W., and Peterson, G. P., 1993, "The Interfacial Thermodynamics of the Capillary Structures in Micro Heat Pipes," *Proceedings of the 29th National Heat Transfer Conference*, Atlanta, GA, Aug. 8-11.

Tien, C. L., 1975, "Fluid Mechanics of Heat Pipes," *Annual Review of Fluid Mechanics*, Vol. 7, pp. 167-185.

White, F. M., 1986, *Fluid Mechanics*, McGraw-Hill, New York, pp. 132-141.

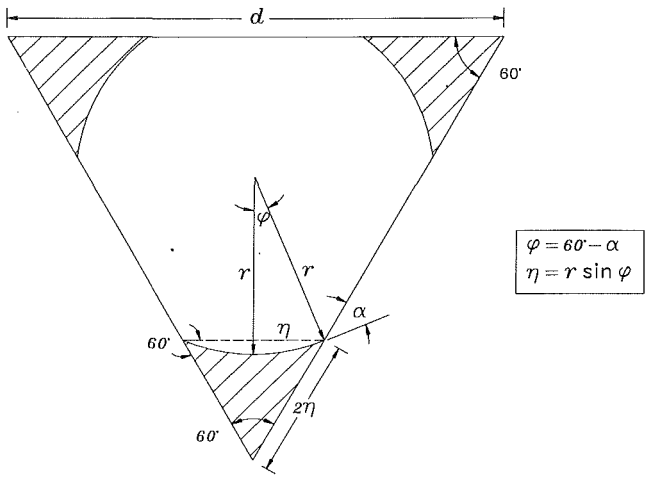

Fig. 11 Liquid film geometry

APPENDIX

Geometric Area Coefficients β_l, $\beta_{l,w}$, β_i.

Referring to Fig. 11, it can be seen that an equilateral triangle is formed by the two pipe walls and the line connecting the two interface contact points. The area occupied by the liquid, A_l, is the area of this equilateral triangle, A_{tri}, minus the area of the segment, A_{seg}, located between the liquid interface and the top of the triangle. In addition, a right triangle is formed from the radius of curvature drawn from both the interface midpoint and interface contact point and one half the top of the equilateral triangle described above. Let A_{tri2} be the area of this triangle, with included angle ϕ and opposite side $\eta = r \sin \phi$. An area $A_{\text{sector}} = \phi r^2/2$ is generated when the radius of curvature is rotated from the midpoint of the interface to the contact point through the angle ϕ. Also, by definition, the radius of curvature is normal to the interface. Thus, referring to the interface contact point at the pipe wall in the figure, ϕ and α can be related: $\phi = \pi/3 - \alpha$. The area of the equilateral triangle can now be expressed as $A_{\text{tri}} = \sqrt{3}r^2 \sin^2 (\pi/3 - \alpha)$ and the area of the segment, A_{seg}, becomes $A_{\text{seg}} = r^2[(\pi/3 - \alpha) - 0.5 \sin 2(\pi/3 - \alpha)]$ where $A_{\text{sector}} = \phi r^2/2$ and $A_{\text{tri2}} = 0.5r \sin \phi\ r \cos \phi$. The *total* area of the liquid in the pipe's triangular cross section is $A_l = \beta_l r^2$, where

$$\beta_l = 3[\sqrt{3} \sin^2 (\pi/3 - \alpha) + 0.5 \sin 2(\pi/3 - \alpha) - (\pi/3 - \alpha)].$$

Referring again to Fig. 11, it can be seen that the perimeter of the pipe wetted by the liquid for one corner is $2(2)\eta = 4\eta$. The *total* wetted perimeter (for three corners) is thus $3 \cdot 4\eta = 12\eta = 12r \sin (\pi/3 - \alpha) = \beta_{l,w} r$ where $\beta_{l,w} = 12 \sin (\pi/3 - \alpha)$. The perimeter of the interface in a corner of Fig. 11 is generated by rotating the radius of curvature through the angle 2ϕ. The *total* area of the interface becomes $A_i = 6r\phi dx = 6r(\pi/3 - \alpha)dx = \beta_i r dx$ where $\beta_i = 6(\pi/3 - \alpha)$.

Transient Two-Dimensional Gas-Loaded Heat Pipe Analysis

C. Harley

A. Faghri

Department of Mechanical and Materials Engineering, Wright State University, Dayton, OH 45435

A two-dimensional, transient mathematical model that accounts for diffusion and variable properties on the operation of a heat pipe is presented. The major advantage over previous models is that this model treats the noncondensable gas as a separate entity, which is described by mass transport phenomena. Also, the energy transport through the wall is coupled to the transient operation of the heat pipe through the use of a conjugate solution technique. The complete behavior of the heat pipe, along with the location and two-dimensional shape of the noncondensable gas front, are modeled from the initial continuum flow, liquid state startup to steady-state conditions. The proposed model predicted the existing experimental data for the operation of high-temperature heat pipes with and without noncondensable gases.

Introduction

Gas-loaded heat pipes have been applied in many diverse fields, and are useful when the temperature of a device must be held constant while a variable heat load is dissipated. However, their use is limited by the lack of a complete understanding of the performance of these devices, particularly during transient operation.

Gas-loaded heat pipes have been previously modeled with several levels of approximation. The classical flat-front analytical model of Marcus and Fleischman (1970) neglected all diffusion across the vapor-gas interface. Later studies modeled one-dimensional steady diffusion (Edwards and Marcus, 1972), and one-dimensional transient diffusion (Shukla, 1981). Rohani and Tien (1973) studied the steady-state two-dimensional diffusion process in a gas-loaded heat pipe. The importance of modeling radial diffusion in a gas-loaded heat pipe was demonstrated where the noncondensable gas tends to accumulate at the liquid-vapor interface, which retards vapor condensation. However, Rohani and Tien (1973) neglected the effect of conjugate heat transfer through the wall as well as transient effects. The transient response of a gas-loaded heat pipe was shown to be important by Shukla (1981) as transient thermal overshoots were discovered. However, this study did not include the effects of radial heat conduction in the wall or wick, nor the radial diffusion effects of the noncondensable gas.

Cao and Faghri (1990) presented a two-dimensional transient analysis of heat pipe dynamics. The analysis included the compressible vapor flow and the coupling between the heat pipe wall/wick and the vapor flow. However, the analysis was limited to the conventional heat pipe without noncondensable gas.

In the present study, the two-dimensional, transient gas-loaded heat pipe operation, including the effects of conjugate heat transfer through the wall, is modeled through a solution of the general differential conservation equations This procedure was used to simulate the high-temperature heat pipe experimentally studied by Ponnappan (1989) both with and without noncondensable gases.

Mathematical Modeling

Vapor Space. The physical configuration and coordinate system of the gas-loaded heat pipe studied is shown in Fig. 1. Gas-loaded heat pipes offer isothermal operation for varying heat loads by changing the overall thermal resistance of the heat pipe. As the heat load increases, the vapor temperature and total pressure increase in the heat pipe. This increase in total pressure compresses the noncondensable gas in the condenser, increasing the surface area available for heat transfer, which maintains a nearly constant heat flux and temperature.

The differential conservation equations for transient, compressible, two-species flow with constant viscosity are as follows (Ganic et al., 1985; Bird et al., 1960):

Mass:

$$\frac{\partial \bar{\rho}}{\partial t}+\frac{1}{r}\frac{\partial}{\partial r}(\bar{\rho} r v)+\frac{\partial}{\partial z}(\bar{\rho} w)=0 \tag{1}$$

Momentum:

$$\bar{\rho}\frac{D\mathbf{V}}{Dt}=-\nabla \bar{p}+\frac{1}{3}\bar{\mu}\nabla(\nabla\cdot\mathbf{V})+\bar{\mu}\nabla^2\mathbf{V} \tag{2}$$

Energy:

$$\overline{\rho c_p}\frac{DT}{Dt}-\nabla\cdot\bar{k}\nabla T-\nabla\cdot\left(\sum_{j=1}^{2} D_d c_{pj} T\nabla\rho_j\right)-\frac{D\bar{p}}{Dt}-\bar{\mu}\Phi=0 \tag{3}$$

where the subscript j denotes either vapor or gas.

Species:

$$\frac{D\rho_g}{Dt}-\nabla\cdot D_{gv}\nabla\rho_g=0 \tag{4}$$

where

$$\Phi=2\left[\left(\frac{\partial v}{\partial r}\right)^2+\left(\frac{v}{r}\right)^2+\left(\frac{\partial w}{\partial z}\right)^2\right]+\left(\frac{\partial v}{\partial z}+\frac{\partial w}{\partial r}\right)^2-\frac{2}{3}\left[\frac{1}{r}\frac{\partial}{\partial r}(rv)+\frac{\partial w}{\partial z}\right]^2 \tag{5}$$

where v and w are the radial and axial vapor velocities, $\bar{p}$ is the total mixture pressure, $\bar{\mu}$ is the mass-fraction-weighted mixture viscosity, $\bar{c}_p$ is the specific heat of the mixture, $\bar{k}$ is the thermal conductivity of the mixture, D_d is the self-diffusion coefficient for both the vapor and gas species, D_{gv} is the mass diffusion coefficient of the vapor-gas pair, ρ_g is the density of the noncondensable gas, and the mixture density is $\bar{\rho}=\rho_g+\rho_v$. The partial gas density is determined from the species equation and the vapor density is found from the ideal gas relation using the partial vapor pressure.

The two choices in species conservation formulation are mass and molar fraction. Molar fraction offers the possibility of a

Contributed by the Heat Transfer Division for publication in the JOURNAL OF HEAT TRANSFER. Manuscript received by the Heat Transfer Division April 1993; revision received July 1993. Keywords: Conjugate Heat Transfer, Heat Pipes and Thermosyphons, Transient and Unsteady Heat Transfer. Associate Technical Editor: R. Viskanta.

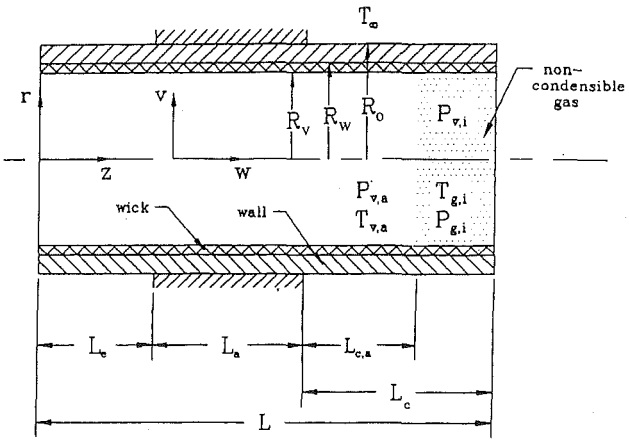

Fig. 1 NCHP configuration and coordinate system

direct simplification in the formulation by the assumption of constant molar density. This assumption is valid over a wider range of temperature and pressure than the corresponding assumption of constant mass density. However, when molar fractions are used, the momentum equation must be written in terms of molar-weighted velocities. The resulting equation cannot be written in terms of the total material derivative, and is significantly more difficult to solve.

A benefit of the general equation formulation is the allowance for variable properties. Typical of compressible gas applications, the density is related to the temperature and pressure through the equation of state

$$\bar{p} = \frac{\bar{\rho}\mathbf{R}T}{\bar{M}} \tag{6}$$

where $\bar{M}$ is the molecular weight of the vapor-gas mixture, and $\mathbf{R}$ is the universal gas constant.

In the species equation, D_{gv} is a function of pressure and temperature. For a vapor-gas mixture of sodium-argon, the relationship for D_{gv} is (Edwards et al., 1979)

$$D_{gv} = 1.3265 \times 10^{-3} T^{3/2} (\bar{p})^{-1} \tag{7}$$

where T is in degrees Kelvin, $\bar{p}$ is in N/m^2, and D_{gv} is in m^2/s. Following a similar procedure, the variable diffusion coefficient formulation for the sodium-helium pair is (Edwards et al., 1979)

$$D_{gv} = 1.2795 \times 10^{-3} T^{3/2} (\bar{p})^{-1} \tag{8}$$

The interspecies heat transfer that occurs through the vapor-gas mass diffusion was modeled with a self-diffusion model, as described by Bird et al. (1960). In the present model, however, the self-diffusion coefficient, D_d, was assumed constant at the initial temperature of the heat pipe.

Wall and Wick. In the heat pipe wall, heat transfer is described by the transient two-dimensional conduction equation

$$\rho_w c_{pw} \frac{\partial T}{\partial t} = k_w \left[\frac{1}{r} \frac{\partial}{\partial r} \left(r \frac{\partial T}{\partial r} \right) + \frac{\partial^2 T}{\partial z^2} \right] \tag{9}$$

where the subscript w denotes the heat pipe wall material. In the heat pipe wick, the model uses the conduction simplification discussed by Cao and Faghri (1990). This assumption states that, for thin wicks and working fluids with high thermal conductivities, the effect of convection due to the liquid flow in the porous wick is negligible. Therefore, heat transfer in the wick is by conduction only, as described by:

$$(\rho c_p)_{\text{eff}} \frac{\partial T}{\partial t} = k_{\text{eff}} \left[\frac{1}{r} \frac{\partial}{\partial r} \left(r \frac{\partial T}{\partial r} \right) + \frac{\partial^2 T}{\partial z^2} \right] \tag{10}$$

where $(\rho c_p)_{\text{eff}} = \varphi(\rho c_p)_l + (1-\varphi)(\rho c_p)_s$, φ is the wick porosity, and $(\rho c_p)_s$ is the heat capacity of the solid wick structure, k_{eff} is the effective thermal conductivity of the wrapped screen wick structure (Chi, 1976):

$$k_{\text{eff}} = \frac{k_l[(k_l + k_s) - (1-\varphi)(k_l - k_s)]}{[(k_l + k_s) + (1-\varphi)(k_l - k_s)]} \tag{11}$$

Boundary Conditions. At the end caps of the heat pipe,

Nomenclature

c_p = specific heat at constant pressure, J/(kg-K)
D_d = self-diffusion coefficient, m^2/s
D_{gv} = mass diffusion coefficient, m^2/s
h_{fg} = latent heat of evaporation, J/kg
k = thermal conductivity, W/(m-K)
K_p = density correction coefficient, s^2/m^2
L = length, m
m = mass, kg
$\dot{m}$ = mass flow rate, kg/s
M = molecular weight, kg/kmol
p = pressure, N/m^2
p_0 = reference pressure, N/m^2
p' = pressure correction, N/m^2
q = heat flux, W/m^2
q_{so} = heat source, W/m^2
r = radial coordinate, m
$\mathbf{R}$ = universal gas constant, N-m/(kmol-K)
R_o = outer surface radius, m
R_v = vapor space radius, m
R_w = wick-wall interface radius, m
S = surface, area, m^2
t = time, s
T = temperature, K
T_0 = reference temperature, K
v = radial velocity component, m/s
v^* = radial velocity based on guessed pressure, m/s
$\mathbf{V}$ = net velocity vector, m/s
v_δ = radial blowing/suction velocity at the wall, m/s
w = axial velocity component, m/s
w^* = axial velocity based on guessed pressure, m/s
z = axial coordinate, m
δ_w = wall thickness
ϵ = emissivity
μ = dynamic viscosity, kg/(m-s)
ρ = density, kg/m^3
ρ^* = guessed density, kg/m^3
ρ' = density correction, kg/m^3
σ = Stefan-Boltzmann constant, W/(m^3-K^4)
φ = porosity
Φ = viscous dissipation term

Subscripts

a = adiabatic or active
c = condenser
e = evaporator
eff = effective
g = gas
i = initial
l = liquid
s = wick material
sat = saturation
so = source
t = total
tr = transition quantity
v = vapor
w = wall
δ = liquid-vapor interface
0 = reference
∞ = ambient

Superscript

$\bar{}$ = mass fraction weighted quantity

the no slip-conduction for velocity, the adiabatic conduction for temperature, and the overall gas conservation conditions are imposed

$$\text{At } z=0\text{: } v=w=\frac{\partial T}{\partial z}=\frac{\partial \rho_g}{\partial z}=0 \tag{12}$$

$$\text{At } z=L\text{: } v=w=\frac{\partial T}{\partial z}=0,\ \rho_g=\rho_{g,\,BC} \tag{13}$$

where $\rho_{g,\,BC}$ is iteratively adjusted to satisfy overall conservation of noncondensable gas. This boundary condition is implemented through the calculation of the total mass of noncondensable gas in the heat pipe. If the total mass is found to be less than the mass initially present in the pipe, the boundary value is increased by 10 percent of the previous value. Conversely, if the calculated mass is larger than that initially present, the boundary value is decreased. This ensures the conservation of the overall mass to within a preset tolerance, which is 1 percent in the present formulation. The symmetry of the cylindrical heat pipe requires that the radial vapor velocity and the gradients of the axial vapor velocity, temperature, and gas density be zero at the centerline ($r=0$):

$$v=\frac{\partial w}{\partial r}=\frac{\partial T}{\partial r}=\frac{\partial \rho_g}{\partial r}=0 \tag{14}$$

The liquid–vapor interface ($r=R_v$) is impermeable to the noncondensable gas

$$\dot{m}_g=S_\delta\, AD_{gv}\nabla\ \rho_g+\rho_g\, S_\delta\, \mathbf{V}=0 \tag{15}$$

where S_δ is the surface area of the liquid–vapor interface. This formulation of $\dot{m}_g$ accounts for both convective and diffusive noncondensable gas mass fluxes at the liquid–vapor interface. To ensure saturation conditions in the evaporator section (and part of the adiabatic section since the exact transition point is determined iteratively), the Clausius–Clapeyron equation is used to determine the interface temperature as a function of pressure. The interface radial velocity is then found through the evaporation rate required to satisfy heat transfer requirements. The no-slip condition is still in effect for the axial velocity component.

At $r=R_v$ for $z\le L_e+L_a$:

$$T_{\text{sat}}=\left(\frac{1}{T_0}-\frac{\mathbf{R}}{M_v h_{fg}}\ln\frac{p_v}{p_0}\right)^{-1} \tag{16}$$

$$v_\delta=\frac{\left(k_{\text{eff}}\dfrac{\partial T_l}{\partial r}-\overline{k_\delta}\dfrac{\partial T_v}{\partial r}\right)}{(h_{fg}+\overline{c_{p\delta}}\,T_{\text{sat}})\,\overline{\rho_\delta}} \tag{17}$$

$$w=0 \tag{18}$$

where $\overline{k}_\delta$, $\overline{c}_{p\delta}$, and $\overline{\rho}_\delta$ are the vapor–gas mixture properties at the liquid–vapor interface. In Eq. (16), the saturation temperature of the vapor is found from the partial vapor pressure. A solution of the momentum equation gives the total mixture pressure, but the partial vapor pressure can be found from using the local gas density:

$$p_v=\frac{\overline{M}}{M_v}\,\overline{p}\left(1-\frac{\rho_g}{\overline{\rho}}\right) \tag{19}$$

This equation was derived assuming a mixture of ideal gases following Dalton's model for mixtures.

At the liquid–vapor interface in the active portions of the condenser section, vapor condenses and releases its latent heat energy. This process is simulated by applying a heat source at the interface grids in the condenser section. The interface velocity can be obtained through a mass balance between the evaporator and condenser section allowing for inactive sections of the condenser.

At $r=R_v$ for $z>L_e+L_a$: $q_{so}=-(h_{fg}+\overline{c_{p\delta}}\,T_\delta)(\overline{\rho}-\rho_g)v_\delta$ (20)

Due to the conjugate nature of the solution procedure, the boundary condition between the wick and the wall is automatically satisfied. In addition to the equality of temperature, this condition requires the equality of the heat fluxes into and out of the wick–wall interface ($r=R_w$):

$$k_w\frac{\partial T}{\partial r}=k_{\text{eff}}\frac{\partial T}{\partial r} \tag{21}$$

At the outer pipe wall surface, the boundary conditions depend on both the axial position and the mechanism of heat transfer being studied. In the evaporator, a constant heat flux is specified. In the condenser, a radiative boundary condition is imposed.

Evaporator:

$$k_w\left.\frac{\partial T}{\partial r}\right|_{r=R_o}=q_e \tag{22}$$

Adiabatic:

$$\left.\frac{\partial T}{\partial r}\right|_{r=R_o}=0 \tag{23}$$

Condenser:

$$-k_w\left.\frac{\partial T}{\partial r}\right|_{r=R_o}=\sigma\epsilon(T_w^4-T_\infty^4) \tag{24}$$

Initial Conditions. Since this model simulates the transient operation of a gas-loaded heat pipe, the initial physical conditions of the heat pipe are required for a solution of the problem. The initial temperature is uniform throughout the heat pipe at the start of the simulation. There is no motion of either the gas or vapor, and the noncondensable gas is evenly distributed throughout the vapor space by diffusion. The initial temperature of the heat pipe is above the free-molecular/continuum-flow transition temperature for the specific heat pipe vapor diameter (Cao and Faghri, 1993).

Numerical Methodology

The numerical procedure used in this model is the SIMPLE method (Patankar, 1980). Discretizing the differential equations resulted in a system of algebraic equations in terms of T, w, v, and ρ_g. This system of equations was solved using the Thomas or tridiagonal matrix algorithm.

The numerical procedure is as follows:

1 Input the initial conditions.
2 Initialize the pressure, temperature, gas density, and velocity fields.
3 Solve the momentum equations using the mixture density to obtain v^* and w^*, which are the vapor velocities based on the guessed pressure.
4 Solve for the new pressure field and date the previous pressure field.
5 Calculate v and w from their starred values using velocity correction formulas.
6 Solve the energy equation.
7 Solve the mass transport equation.
8 Using the mixture molecular weight, determine the new $\overline{\rho}$ from the equation of state.
9 Steps 3–8 are repeated until convergence is reached.

There are two possible methods to account for vapor compressibility. The first method is to use a density correction formulation.

$$\rho=\rho^*+\rho'=\rho^*+K_p p' \tag{25}$$

where $K_p=\partial\rho/\partial p$, and p' is the guessed pressure. The second method uses the ideal gas relationship in conjunction with an additional term in the energy equation. In this method, the pressure is chosen as the dependent variable and the vapor density is determined directly. The additional term in the energy

Table 1 Operating conditions for various cases

Case Number	Gas Pressure (torr)	Mass of Gas (kg)	Heat Load (W)	Condenser Emissivity
1	0.0	0.0	515	0.3
2	1.35	3.66×10^{-7}	451	0.56
3	1.35	3.66×10^{-7}	258 to 306	0.3
4	1.35	3.66×10^{-7}	258 to 451	0.3

Table 2 Heat pipe geometry and parameters

Parameter	
Wall	304 SS
Wick	wire mesh
Working Fluid	Sodium
Buffer Gas	Argon
L_t	2.03 m
L_e	0.375 m
L_a	0.745 m
L_c	0.91 m
R_v	0.00635 m
R_o	0.0111 m
δ_w	0.00165 m
k_{eff}	39 W/m · K
k_ℓ	70.08 W/m · K
k_w	20 W/m · K
μ_v	1.8×10^{-5} kg/m · s
ρ_v	0.003 kg/m^3
ρ_ℓ	828.1 kg/m^3
$c_{p,v}$	904 J/kg · K
h_{fg}	4.37×10^6 J/kg
φ	0.66
T_∞	300 K

equation accounts for the temperature variation caused by the high vapor velocities, and must be included when using the equation of state. In the present analysis, the ideal gas relationship resulted in better convergence characteristics. When the vapor flow was subsonic, it was found that both methods gave very similar results.

In the present study, a uniform axial grid and a nonuniform radial grid were used. The numerical simulation used 12 (radial) × 55 (axial) cells for the 2.0 m long heat pipe. The numerical model was run for several different grid distributions with less than a 3 percent maximum deviation between the solutions. The number of cells used was chosen to optimize the accuracy of the solution versus the required computer time. The physical properties at the interface are based on the harmonic average of the properties at the adjacent cells (Patankar, 1980).

Results and Discussion

Validation of the present numerical heat pipe model was accomplished by simulating four cases of experimental data of a sodium heat pipe by Ponnappan (1989), which are shown in Table 1. The heat pipe geometry and operating conditions are shown in Table 2. Vector and contour plots for Case 1 are shown in Fig. 2, where the effect of vapor compressibility can be seen. Due to the small vapor space and high heat input, the vapor velocity is very high (~330 m/s). For sodium, this velocity corresponds to a Mach number of approximately 0.5. From Fig. 2(*a*), a temperature decrease can be seen at the exit of the evaporator section, where the maximum velocity occurs. Furthermore, as the vapor velocity decreases, a temperature

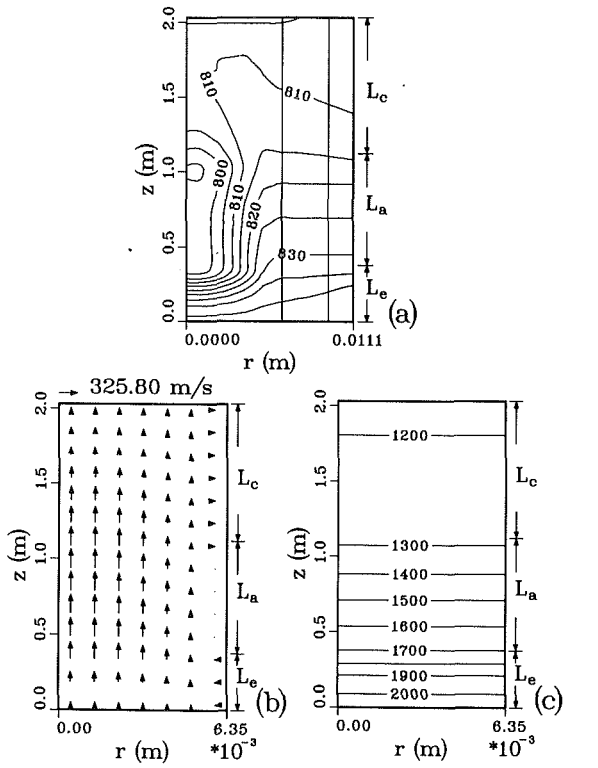

Fig. 2 Numerical simulation of the high-temperature heat pipe (Case 1): *(a)* vapor temperature contours; *(b)* vapor velocity vectors in the *r–z* plane; *(c)* vapor pressure contours

recovery can be seen in the condenser section. Also shown in Fig. 2(*a*) are the temperature drops across the wall and wick. The temperature profiles in the wall are nearly linear since the thermal conductivity of the stainless-steel pipe wall is relatively low. However, the direction of the temperature gradients in the respective sections can be seen. As expected, the temperature gradient is positive in the evaporator as heat is being added to pipe. Likewise, the temperature gradient is zero in the adiabatic section and negative in the condenser section.

The vapor velocity vectors in the *r–z* plane are shown in Fig. 2(*b*). Since the evaporator section is much shorter than the condenser section, the radial vapor velocity in the evaporator is much higher than that in the condenser. The highest vapor velocity occurs at the centerline of the heat pipe, as expected.

The vapor pressure contours are shown in Fig. 2(*c*), where the two-dimensional effects are seen to be negligible. This was expected since the vapor space diameter for this heat pipe is very small. More importantly, the vapor temperature and pressure are not dependent in the vapor space. In a heat pipe, phase change occurs only at the vapor–liquid interface, which implies that saturation conditions are seen only at the interface. In the vapor space, however, the saturation relation does not necessarily apply, where the vapor temperatures are determined from energy requirements, accounting for viscous and compressible effects. The transient axial temperature profiles for the no-gas case are shown in Fig. 3 for Case 1. From Fig. 3(*a*), the comparison with the experimental data is very good. The transient time for this heat pipe is approximately 2000 s. The vapor dynamics for this case are shown in Fig. 4.

The gas-loaded heat pipe experimentally studied by Ponnappan was simulated (Case 2), with results shown in Figs. 5 and 6. This case has a higher radiative emissivity than Case 1, which results in a decrease in the thermal resistance at the outer condenser surface. In the experiment performed by Ponnappan, the emissivity was increased when the noncondensable gas was added, so that a near-constant operating temperature

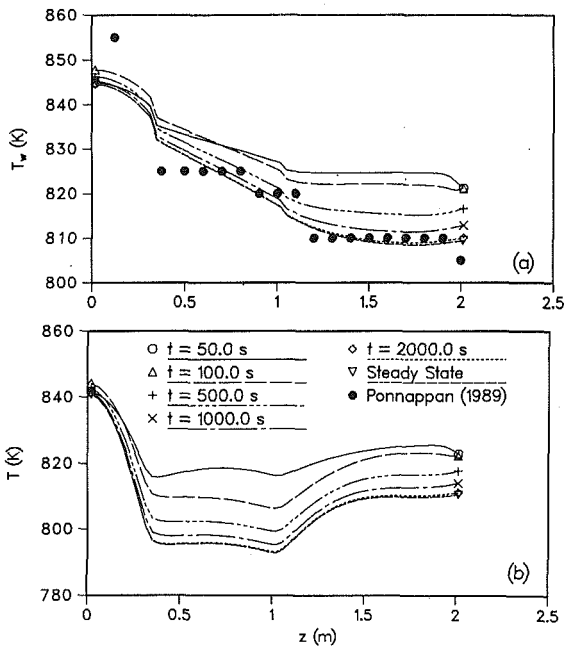

Fig. 3 *Temperature profiles for the conventional heat pipe with* $Q_{in} = 515$ W (Case 1): *(a)* transient wall temperature profile; *(b)* transient centerline temperature profile

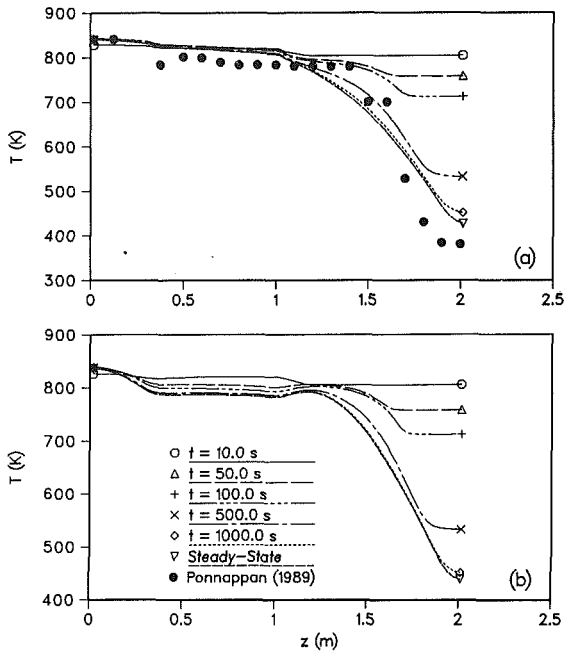

Fig. 5 Temperature profiles for the gas-loaded heat pipe with $Q_{in} = 451$ W (Case 2): *(a)* transient wall temperature profile; *(b)* transient centerline temperature profile

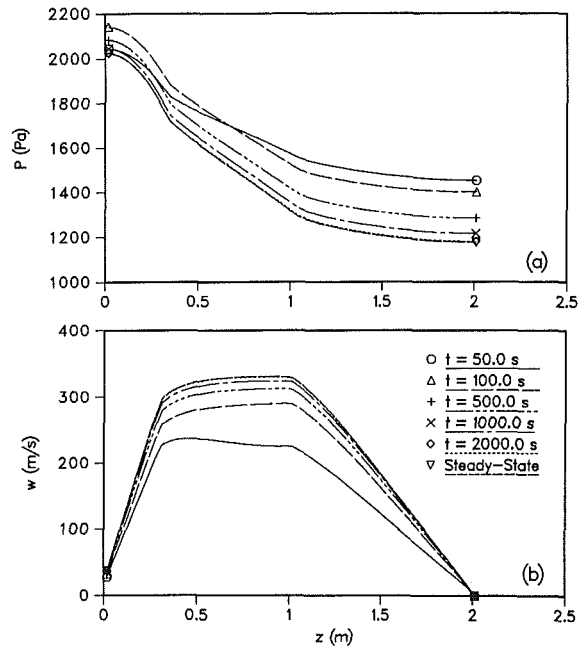

Fig. 4 Vapor flow dynamics for the conventional heat pipe with $Q_{in} = 515$ W (Case 1): *(a)* transient centerline pressure profile; *(b)* transient centerline axial velocity profile

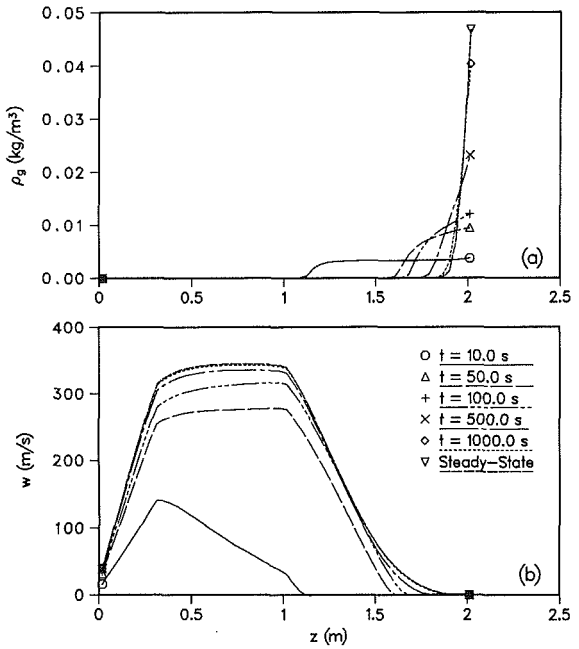

Fig. 6 Vapor-gas dynamics for the gas-loaded heat pipe with $Q_{in} = 451$ W (Case 2): *(a)* transient centerline gas density profiles; *(b)* transient centerline axial velocity profiles

(compared to Case 1) could be maintained. In Fig. 5, the wall and vapor temperatures decreased significantly in the condenser section due to the presence of the noncondensable gas. The gas density increased in the condenser during the transient operation, as shown in Fig. 6(*a*). The steady-state wall temperature is in good agreement with the data by Ponnappan.

To validate the numerical procedure further, the gas-loaded heat pipe of Ponnappan with a low radiative emissivity (Case 3) was simulated. The velocity vector and contour plots for the gas-loaded case with a low radiative emissivity (Case 3) are shown in Fig. 7. In Fig. 7(*a*), the temperature distribution for the gas-loaded case is significantly different from that of the no-gas case. As expected, there is a large temperature drop across the inactive condenser section, and the radial temperature variations in this section are relatively uniform. This is due to the low vapor velocities in this region and the resulting low convective heat transfer in the inactive condenser section.

The vapor density contours, shown in Fig. 7(*b*), are radially uniform and have a sharp axial gradient. This is a conduction-controlled heat pipe, with axial conduction through the heat pipe wall and wick as the principal heat transfer mechanism across the vapor–gas interface.

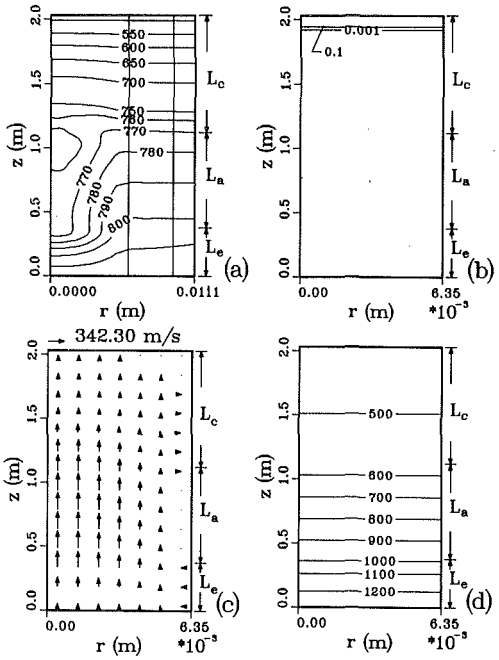

Fig. 7 Numerical simulation of the gas-loaded high-temperature heat pipe (Case 3): *(a)* temperature contours (K); *(b)* gas density isoconcentration contours (kg/m³); *(c)* vapor velocity vectors (m/s); *(d)* pressure contours (N/m²)

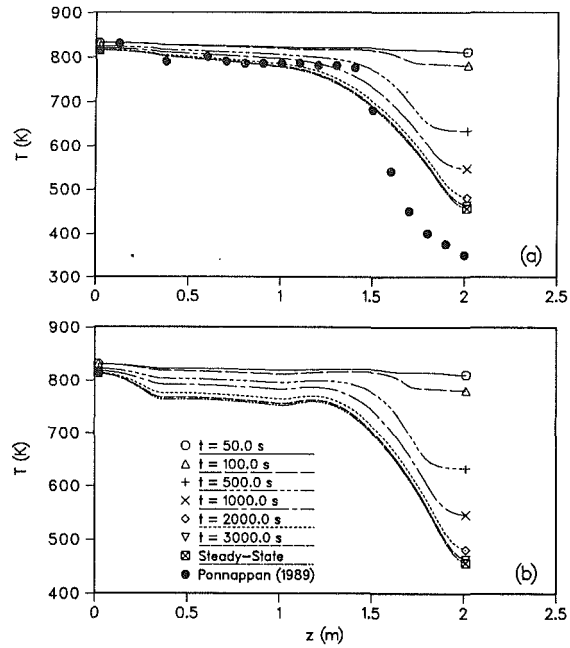

Fig. 8 Temperature profiles for the gas-loaded heat pipe with $Q_{in} = 258$ W (Case 3): *(a)* transient wall temperature profile; *(b)* transient centerline temperature profile

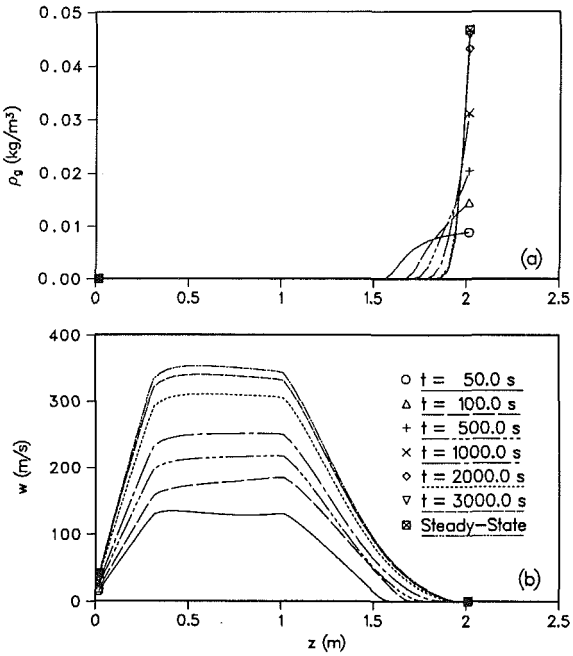

Fig. 9 Vapor-gas dynamics for the gas-loaded heat pipe with $Q_{in} = 258$ W (Case 3): *(a)* transient centerline gas density profiles; *(b)* transient centerline axial velocity profiles

The results for Case 3 with a heat input of 258 W are shown in Figs. 8 and 9. In Fig. 8(*a*), the steady-state wall temperature is compared with the experimental data by Ponnappan (1989) with reasonable agreement. In Fig. 9(*a*), the transient axial gas density profiles are given, where the importance of including conjugate heat transfer through the wall can be recognized. If the gas distribution were controlled purely by the vapor dynamics, the transient time would be on the order of 10^{-3} s (Shukla, 1981). Due to the presence and subsequent damping effect of the wall, the transient time of the noncondensable gas distribution is substantially increased. Physically, this phenomenon is controlled by temperature-dependent diffusion. At the beginning of operation, after liquid- or solid-state startup, the vapor temperature in the condenser is high. This high temperature increases the diffusive mass flux across the vapor-gas interface. However, as time increases, the vapor temperature in the condenser decreases, thus decreasing the mass flux of the noncondensable gas across the interface, and increasing the partial gas density in the reservoir. This phenomenon is reinforced by the compressible behavior of the vapor. As shown in Fig. 9(*b*), the vapor velocity is initially low. Therefore, the inertial effects of the vapor against the stationary noncondensable gas are small. As time progresses, the vapor velocity increases, which causes an increase in the inertial forces acting on the noncondensable gas, resulting in a further compression of the gas slug.

After the gas-loaded heat pipe reached steady state for a heat input of 258 W, the heat input was pulsed to 306 W, as shown in Figs. 10 and 11. The transient axial temperature profiles are shown in Fig. 10, and the transient vapor-gas dynamics are shown in Fig. 11. The curves labeled with $t = 0.0$ s correspond to steady state for $Q_{in} = 258$ W. Of primary concern in Fig. 10 is the comparison of the transient time for the 258 to 306 W heat pulse with that of the initial response to the 258 W heat input. As expected, the pulsed transient time is nearly 30 percent of the initial response time. Physically, this is due to the conduction-controlled behavior of the heat pipe. In the initial 258 W response, the heat stored in the condenser pipe wall needed to be rejected to the ambient as the noncondensable gas plug developed. However, at the application of the 258 to 306 W heat pulse, the condenser temperature was much closer to its final value, which required much less time to adjust. As the operating power changed from 258 to 306 W, the vapor pressure of the heat pipe increased. This pressure increase compressed the noncondensable gas plug, and increased the active condenser length.

The transient axial temperature results for a pulsed heat input of 258 to 451 W (Case 4) are shown in Fig. 12, and the vapor-gas dynamics are shown in Fig. 13. The main factor to be examined from this case is the initial response of the gas-

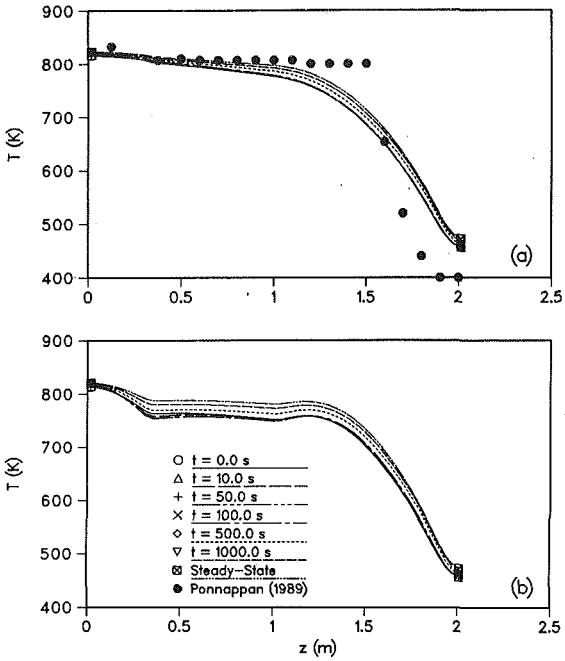

Fig. 10 Vapor-gas dynamics for the gas-loaded heat pipe with a pulsed heat input of $Q_{in} = 258$ to 306 W (Case 3): *(a)* transient wall temperature profile; *(b)* transient centerline temperature profile

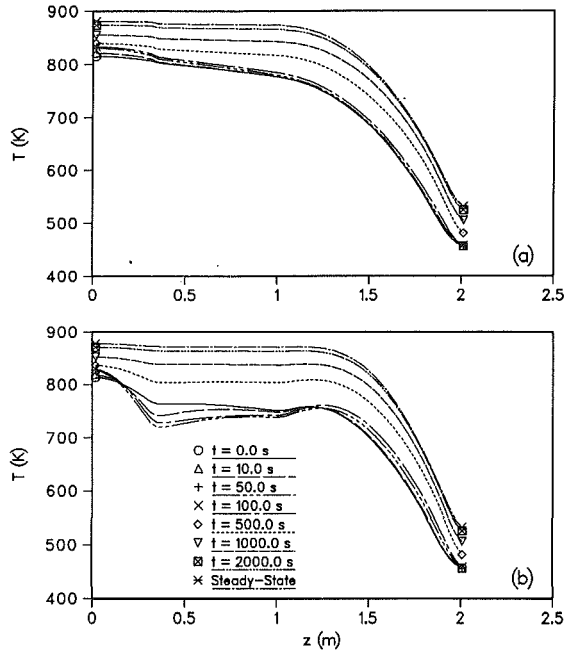

Fig. 12 Temperature profiles for the gas-loaded heat pipe with a pulsed heat input of $Q_{in} = 258$ to 451 W (Case 4): *(a)* transient wall temperature profile; *(b)* transient centerline temperature profile

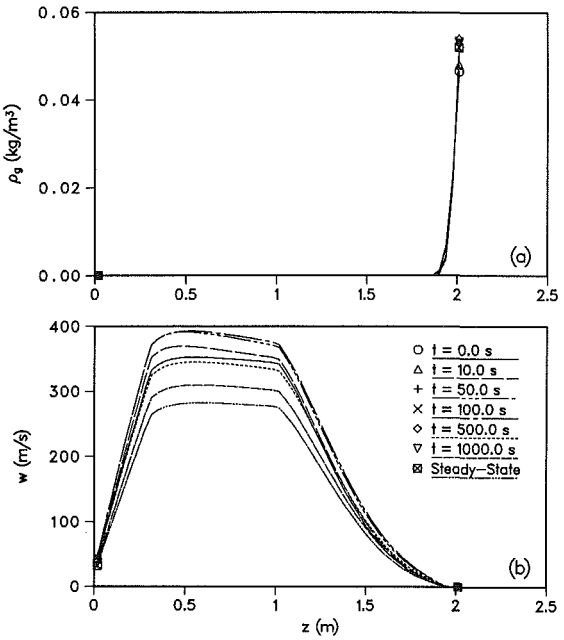

Fig. 11 Vapor-gas dynamics for the gas-loaded heat pipe with a pulsed heat input of $Q_{in} = 258$ to 306 W (Case 3): *(a)* transient centerline gas density profiles; *(b)* transient centerline axial velocity profiles

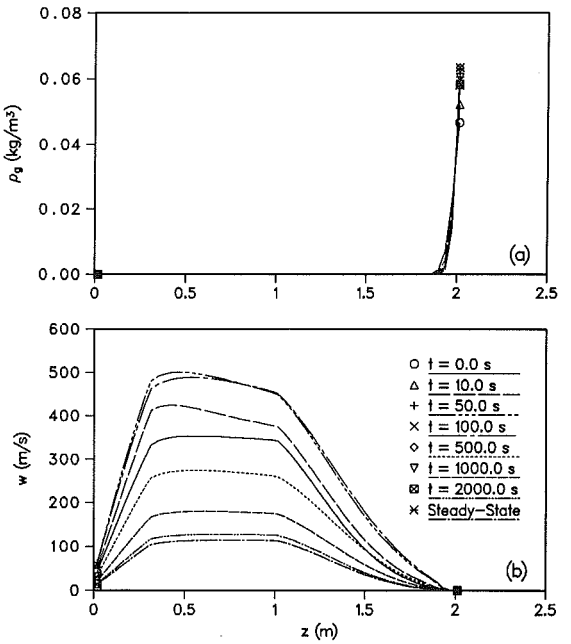

Fig. 13 Vapor-gas dynamics for the gas-loaded heat pipe with a pulsed heat input of $Q_{in} = 258$ to 451 W (Case 4): *(a)* transient centerline gas density profiles; *(b)* transient centerline axial velocity profiles

loaded heat pipe, as shown in Figs. 12(*b*) and 13(*b*). As the heat input is pulsed from 258 to 451 W, the vapor temperature initially dropped at the inlet to the adiabatic section. Similarly, the axial velocity at that point increased nearly 60 percent. These effects have been observed by Cao and Faghri (1990) and are attributed to compressibility effects.

Conclusions

A transient two-dimensional simulation of gas-loaded heat pipes has been performed. The present numerical model used a conjugate solution technique to couple the unsteady heat transfer in the wall and wick with the transient vapor flow. The boundary condition at the outer condenser pipe wall influenced the operating temperature of the heat pipe and altered the position of the vapor-gas interface. Increasing the radiant emissivity decreased the operating temperature and transient time period of the heat pipe. Steady-state gas-loaded heat pipe operation depends heavily on the mass of noncondensable gas, as this parameter affects the operating temperature and active condenser length. It was also shown that the transient time period increased when gas was added because more heat needed

to be conducted through the pipe wall to the previously active part of the condenser section. While the noncondensable gas is fundamentally one dimensional in nature, the complete problem must be solved in two dimensions accounting for conjugate heat transfer through the wall and wick.

References

Bird, R. B., Stewart, W. E., and Lightfoot, E. N., 1960, *Transport Phenomena*, Wiley, New York.

Cao, Y., and Faghri, A., 1990, "Transient Two-Dimensional Compressible Analysis for High-Temperature Heat Pipes With Pulsed Heat Input," *Numerical Heat Transfer*, Part A, Vol. 18, pp. 483–502.

Cao, Y., and Faghri, A., 1993, "A Numerical Analysis of High Temperature Heat Pipe Startup From the Frozen State," ASME JOURNAL OF HEAT TRANSFER, Vol. 115, pp. 239–246.

Chi, S. W., 1976, *Heat Pipe Theory and Practice: A Sourcebook*, Hemisphere, Washington, DC.

Edwards, D. K., Denny, V. E., and Mills, A. F.. 1979, *Transfer Processes: An Introduction to Diffusion, Convection, and Radiation*, Hemisphere, New York.

Edwards, D. K., and Marcus, B. D., 1972, "Heat and Mass Transfer in the Vicinity of the Vapor–Gas Front in the Gas-Loaded Heat Pipe," ASME JOURNAL OF HEAT TRANSFER, Vol. 94, pp. 155–162.

Ganic, E. N., Hartnett, J. P., and Rohsenow, W. M., 1985, "Basic Concepts of Heat Transfer," in: *Handbook of Heat Transfer Fundamentals*, W. M. Rohsenow et al., eds., McGraw-Hill, New York.

Marcus, B. D., and Fleishman, G. L., 1970, "Steady State and Transient Performance of Hot Reservoir Gas-Controlled Heat Pipes," ASME Paper No. 70-HT/SpT-11.

Patankar, S. V., 1980, *Numerical Heat Transfer and Fluid Flow*, Hemisphere, Washington, DC.

Ponnappan, R., 1989, "Studies on the Startup Transients and Performance of a Gas Loaded Sodium Heat Pipe," WRDC-TR-89-2046, Wright-Patterson AFB, OH.

Rohani, A. R., and Tien, C. L., 1973, "Steady Two-Dimensional Heat and Mass Transfer in the Vapor-Gas Region of a Gas-Loaded Heat Pipe," ASME JOURNAL OF HEAT TRANSFER, Vol. 95, pp. 377–382.

Shukla, K. N., 1981, "Transient Response of a Gas-Controlled Heat Pipe," *AIAA Journal*, Vol. 19, No. 8, pp. 1063–1070.

Forced Convective Heat Transfer From a Continuously Moving Heated Cylindrical Rod in Materials Processing

S. Roy Choudhury
Graduate Research Assistant.
Mem. ASME

Y. Jaluria
Professor.
Fellow ASME

Department of Mechanical and Aerospace Engineering,
Rutgers University,
New Brunswick, NJ 08903

The flow and heat transfer associated with the forced convective cooling of an infinite heated cylindrical rod moving continuously along its axis in a circular channel has been numerically investigated. Two different flow circumstances, involving uniform flow at the inlet of the cooling channel in the same as well as in the opposite direction as the movement of the cylindrical rod, are considered in this study. This problem is of interest in several manufacturing processes such as hot rolling, continuous casting, extrusion, wire drawing, and glass fiber drawing. The transport processes are time dependent at the initial stages, following the onset of motion, and usually attain steady-state conditions at large time. The temperature distribution in the solid is of particular interest in materials processing. A detailed numerical study is carried out, assuming an axisymmetric, laminar flow, transient circumstance. The governing full elliptic equations are solved, employing a finite volume method. The transport in the solid material is coupled with that in the fluid through the boundary conditions. The effects of several physical and process parameters such as rod speed, material, free-stream velocity, channel dimensions, and fluid on the temperature and the flow field are investigated. For the opposing flow circumstance, some very interesting phenomena are observed. Notable among these is the appearance of a recirculating region within the fluid adjacent to the moving solid surface, causing a reduction in the heat transfer rate as compared to the aiding forced flow case. Validation of the numerical results is carried out by comparison with earlier experimental results, indicating very good agreement.

Introduction

A circumstance that is very commonly encountered in several manufacturing processes is that of a continuously moving plate or rod subjected to heat transfer at the surface. In the extrusion of metals, plastics or food materials, for instance, the material emerges from the extruder and cools by means of convection and radiation as it moves away from the die (Fisher, 1976). Similar situations arise in hot rolling, wire drawing, glass fiber drawing, and continuous casting (Arridge and Prior, 1964; Altan et al., 1979). In most of these cases the material moves in a quiescent fluid, with the flow arising due to material motion and buoyancy. But in several instances, an externally induced forced convective mechanism is employed, in order to increase the heat transfer rate. An aiding forced flow (in the same direction as the movement of the solid material) or an opposing forced flow (in the opposite direction as the movement of the solid material) may be employed. Also as the fluid heats up, due to contact with the hot solid, thermal buoyancy effects arise. Therefore, the resulting flow and thermal fields are determined by these three mechanisms: buoyancy, externally driven forced flow, and the motion of the solid undergoing thermal processing. The present work assumes the buoyancy effects to be small as compared to the effects of external forced flow and material motion. This is valid for most important industrial processes, where the mixed convection parameter, Gr/Re^2, is very small (Jaluria, 1992).

Not much work has been done on the conjugate thermal transport from moving solids. In recent years, some work has been done on the heat transfer from a plate of finite thickness moving through a quiescent ambient medium, as reviewed by Jaluria (1992). Chida and Katto (1976) computed the flow and temperature fields for a plate, employing boundary layer approximations. Karwe and Jaluria (1988, 1991) studied, numerically, the heat transfer for this circumstance, considering temperature variation in the material. They found that the nonboundary layer effects are important near the point of emergence of the plate from the furnace or oven, and that these effects decay rapidly downstream. Kang et al. (1991) have also investigated, numerically, the conjugate transport that arises due to the continuous movement of a heated plate in a quiescent medium. The transient effects were studied in detail. In all these cases, the ambient fluid far from the flat moving surface was taken as quiescent.

In response to the need for cooling in certain applications, forced convection may be employed to enhance the heat transfer rate from the heated rod to the fluid. Abdelhafez (1985) studied, analytically, the case of a continuous flat surface moving in a parallel free stream. Kang and Jaluria (1992) studied the steady-state flow and thermal fields and computed the heat transfer rates for a flat plate moving in a channel as well as in an extensive medium with uniform forced flow.

Very little work has been done, however, on the thermal transport from a moving cylindrical rod. In materials processing, axisymmetric flow is more common than the flow over a wide flat plate, for example, in processes such as glass fiber drawing, cable coating, extrusion of cylindrical billets, wire drawing, and others. Sakiadis (1961) analyzed the boundary layer generated by a continuously moving axisymmetric rod issuing from a slot into a quiescent fluid medium, using a

Contributed by the Heat Transfer Division and presented at the ASME Winter Annual Meeting, Anaheim, California, November 8–13, 1992. Manuscript received by the Heat Transfer Division May 1993; revision received September 1993. Keywords: Forced Convection, Materials Processing and Manufacturing Processes, Moving Boundaries. Associate Technical Editor: R. Viskanta.

similarity transformation. Bourne and Elliston (1970) solved for the velocity profile and the Nusselt number for a moving circular fiber by the Karman–Pohlhausen integral technique. Chida and Katto (1976) computed the flow and temperature fields for a cylinder, employing boundary layer approximations and assuming temperature and velocity profiles in the developing region. Forced-air cooling of a moving fiber was investigated experimentally and theoretically, with an assumed heat transfer coefficient at the fiber surface, by Paek and Schroeder (1979). In none of these studies was axial or radial conduction transport included. Also none of these studies considered forced flow in a direction opposite to the movement of the rod. This configuration is employed in several industrial systems, where it is difficult to achieve the aiding flow circumstance or where it is important to minimize the loss of cooling fluid from the channel; see Kyriacou et al. (1990).

As can be seen from the literature review above, there is a strong need to study forced convective cooling in the cylindrical configuration, considering both aiding and opposing forced flow circumstances. The present study is directed at the numerical simulation of the transport from a continuously moving cylinder moving in the direction of its axis, with a uniform forced flow in the same or opposite direction as shown in Fig. 1, including the coupling of the convective transport in the fluid with the conduction within the rod. The rod is assumed to move at a uniform speed U_s. It is maintained at a given temperature T_0 far upstream of the point where it emerges from a slot, representing an extrusion die or furnace outlet. The flow field in the fluid and the temperature distributions in the solid, as well as in the flow, are studied in detail. Numerical calculations are carried out, assuming an axisymmetric, transient, laminar flow circumstance. The full elliptic equations that govern the heat transfer and the flow are solved, employing finite volume techniques. The effects of various dimensionless physical parameters such as Peclet number, Pe, the ratio K_f/K_s, of thermal conductivity of the fluid to that of the solid, the Prandtl number, Pr, as well as the effect of process parameters, such as the channel width, channel thermal conditions, and the upstream boundary conditions, are considered in detail. The results obtained lead to a better understanding of the basic physical processes and provide inputs that may be used in the design of the relevant system. They are useful, for instance, in determining the dimensions of the

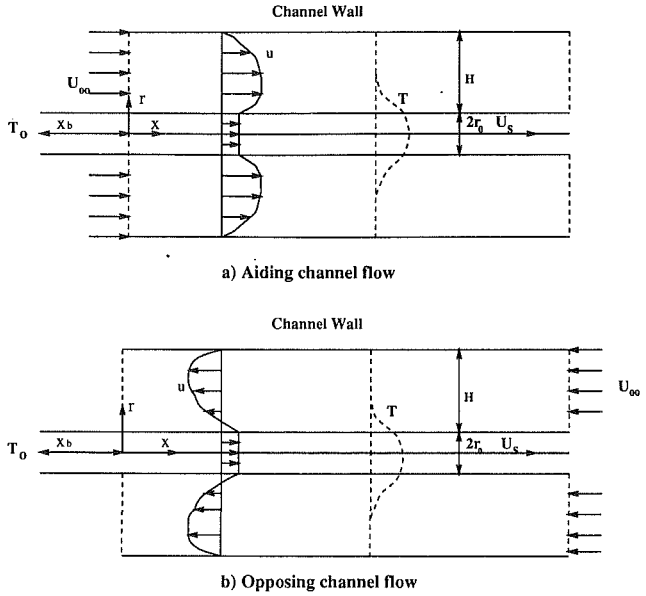

Fig. 1 Schematic of a moving axisymmetric solid in the forced flow in a channel: (*a*) aiding flow, and (*b*) opposing flow

systems needed to bring the material temperature to a desired level. Also, if the channel length is fixed, the results give an insight as to which physical or process parameters must be varied to cool the material down to the given temperature. The numerical approach is outlined and the important aspects that must be included for an accurate simulation are also discussed. Comparisons with experimental results in the literature show good agreement.

Analysis

Consider the transient, laminar flow induced by an infinitely long cylindrical rod, which is moving at a constant velocity U_s in the direction represented by its axis. The temperature of the rod is assumed to be at a uniform value of T_o at some upstream distance x_b away from the origin, $x=0$, that is, at $x=-x_b$, in order to simulate the condition of uniform temperature far

Nomenclature

B = ratio of property values for the fluid to those for the solid $=(\rho KC)_f/(\rho KC)_s$
Gr = Grashof number $=g\beta(T_0-T_\infty)r_0^3/\nu^2$
h = surface convection heat transfer coefficient $=(-K_f\ (\partial T/\partial r)_f)/(T_{surf}-T_\infty)$
H = channel gap width $=r_w-r_0$
Nu = local Nusselt number $=hr_0/K_f$
Pe = Peclet number $=U_sr_0/\alpha_s$
Pr = Prandtl number $=\nu/\alpha_f$
r_0 = radius of the moving rod
r, x = coordinate distance along the radial and axial directions, respectively
R, X = dimensionless coordinate distance along the radial and axial directions, respectively, $X=x/r_0$, $R=r/r_0$
Re = Reynolds number $=U_sr_0/\nu_f$
t, τ = physical and dimensionless time, respectively, $\tau=tU_s/r_0$
T, θ = physical and dimensionless local temperature, respectively, $\theta=(T-T_\infty)/(T_0-T_\infty)$
u, v = velocity components in x and r directions, respectively
U, V = dimensionless velocity components in x and r directions, respectively, $U=u/U_s$, $V=v/U_s$
U_∞ = free-stream velocity, positive when aiding and negative when opposing material flow
x_b, X_b = physical and dimensionless upstream penetration distance respectively, $X_b=x_b/r_0$
α = thermal diffusivity
ν = kinematic viscosity of the fluid
ξ = dimensionless coordinate distance $=x(\rho Ck)_f/U_sr_0^2\ (\rho_s^2C_s^2)$
ω, Ω = physical and dimensionless azimuthal vorticity component, respectively, $\Omega=\omega r_0/U_s$
ψ, Ψ = physical and dimensionless stream function, respectively, $\Psi=\psi/U_sr_0^2$

Subscripts

∞ = ambient medium
c, surf = center and surface of the rod, respectively
f, s = fluid and solid, i.e., rod material, respectively
w = channel wall

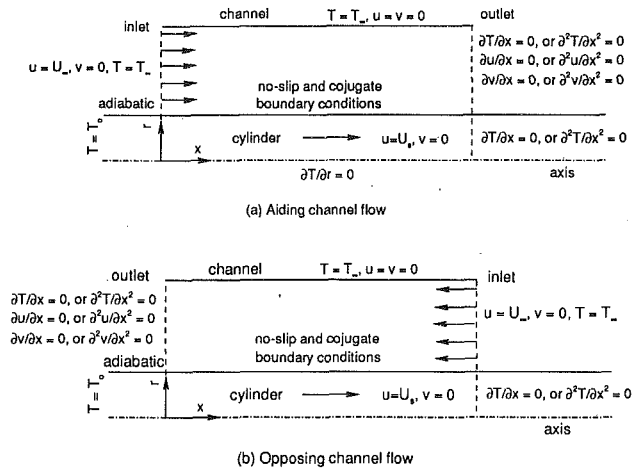

Fig. 2 Typical physical boundary conditions for a moving solid cylindrical rod in the forced flow in a channel: (*a*) aiding flow, and (*b*) opposing flow

upstream in a furnace or an oven. The flow at the inlet is assumed to be isothermal and uniform. However, it is difficult to achieve these conditions in actual practice, where the flow is usually from the periphery (Roy Choudhury and Jaluria, 1993). With an appropriate pressure difference imposed between the peripheral flow entrance and one of the flow exits, and depending on the location of the flow entrance, the flow for the most part behaves either as an aiding or an opposing flow. Far from the rod entrance into the cooling channel, the flow and the temperature develop in the case of an aiding flow. But for an opposing flow, separation may occur and the flow field cannot attain developed conditions downstream. The governing equations are solved assuming an axisymmetric flow. This approximation is satisfactory when the buoyancy effects are small or when the rod moves vertically upward or downward. The full governing equations, including the continuity, momentum, and energy equations for the fluid, and the energy equation for the solid, are given in physical terms, by Roy Choudhury and Jaluria (1992).

The boundary conditions on u, v, and T arise from the physical considerations and are shown in Fig. 2. These are the no-slip conditions at the moving surface of the rod and the channel wall, the imposed temperature at the channel wall, temperature and heat flux continuity at the fluid-solid interface, and symmetry about the axis of the solid rod. At the outlet, either developed flow and thermal condition have been used, or the second derivatives of the velocity components and temperature with respect to the axial direction are assumed to be zero. These points are considered again later.

The pressure term in the momentum equation is eliminated by taking the curl of the equation and, thus, transforming it into the vorticity transport equation, as outlined by Jaluria and Torrance (1986). The stream function ψ and the azimuthal component of vorticity ω (which is the only nonzero vorticity component for the axisymmetric circumstance) are defined as

$$u=\frac{1}{r}\frac{\partial\psi}{\partial r},\quad v=-\frac{1}{r}\frac{\partial\psi}{\partial x},\ \text{and}\ \omega=\frac{\partial v}{\partial x}-\frac{\partial u}{\partial r} \tag{1}$$

With this definition of the stream function, the continuity equation is automatically satisfied.

The governing equations are nondimensionalized by employing the following transformations:

$$X=x/r_0,\quad R=r/r_0,\quad \tau=tU_s/r_0,\quad U=u/U_s,\quad V=v/U_s,$$
$$\theta=\frac{T-T_\infty}{T_0-T_\infty}\quad \Psi=\psi/U_s r_0^2,\quad \Omega=\omega r_0/U_s,\quad \mathrm{Re}=U_s r_0/\nu_f,$$
$$\mathrm{Pe}=U_s r_0/\alpha_s,\quad \mathrm{Pr}=\nu/\alpha \tag{2}$$

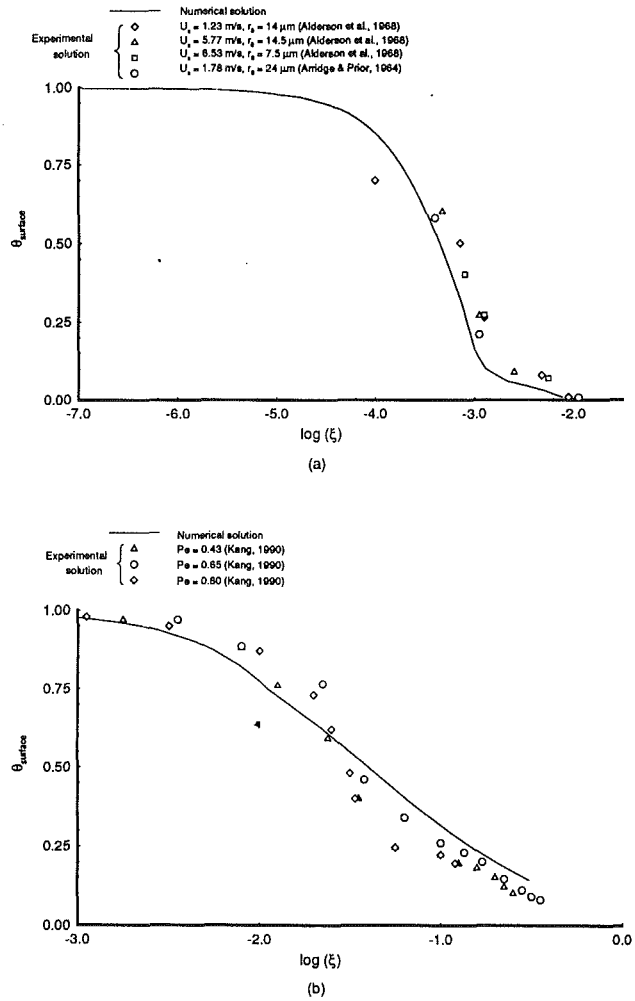

Fig. 3 Comparison of experimental data with the present numerical results: (*a*) glass rod moving in air ($B=10^{-4.8}$, $\rho_f C_f/\rho_s C_s=10^{-3.1}$, Pr = 0.7) and (*b*) aluminum rod moving downward in water ($B=0.0036$, $\rho_f C_f/\rho_s C_s=1.22$, Pr = 4.8)

The dimensionless equations thus obtained, in the vorticity-stream function formulation, are:

For the fluid

$$\frac{1}{R}\frac{\partial^2\psi}{\partial X^2}+\frac{\partial}{\partial R}\left(\frac{1}{R}\frac{\partial\psi}{\partial R}\right)=-\Omega \tag{3}$$

$$\frac{\partial\Omega}{\partial\tau}+\frac{\partial(U\Omega)}{\partial X}+\frac{\partial(V\Omega)}{\partial R}=\frac{1}{\mathrm{Re}}\left[\frac{\partial^2\Omega}{\partial X^2}+\frac{\partial}{\partial R}\left(\frac{1}{R}\frac{\partial(R\Omega)}{\partial R}\right)\right] \tag{4}$$

$$\frac{\partial\theta}{\partial\tau}+\frac{\partial(U\theta)}{\partial X}+\frac{1}{R}\frac{\partial(RV\theta)}{\partial R}=\frac{1}{\mathrm{Re}\cdot\mathrm{Pr}}\left[\frac{\partial^2\theta}{\partial X^2}+\frac{1}{R}\frac{\partial}{\partial R}\left(R\frac{\partial\theta}{\partial R}\right)\right] \tag{5}$$

The energy equation for the solid rod is

$$\frac{\partial\theta}{\partial\tau}+\frac{\partial\theta}{\partial X}=\frac{1}{\mathrm{Pe}}\left[\frac{\partial^2\theta}{\partial X^2}+\frac{1}{R}\frac{\partial}{\partial R}\left(R\frac{\partial\theta}{\partial R}\right)\right] \tag{6}$$

The initial and boundary conditions in terms of dimensionless quantities θ, Ω, and Ψ are obtained by employing the appropriate transformation of the physical boundary conditions, shown in Fig. 2. For details, see Roy Choudhury (1992). As discussed by Roache (1982), the outflow boundary condition for the stream function and vorticity can be taken as $\partial^2\Psi/\partial X^2=\partial\Omega/\partial X=0.0$. Similar treatment of outflow boundary conditions for stream function and temperature was also

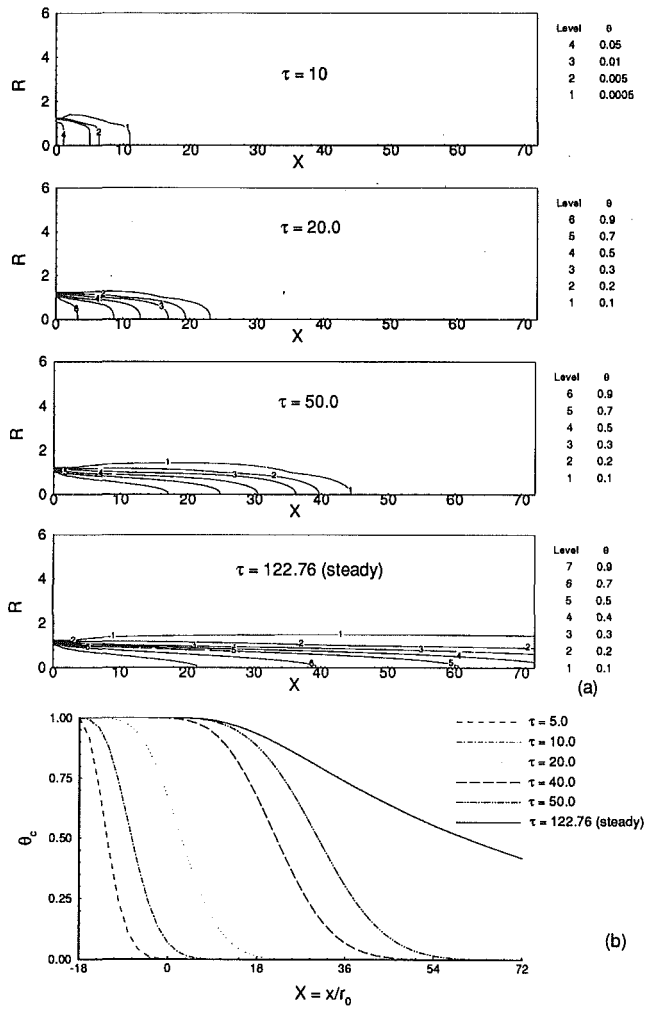

Fig. 4 Transient (*a*) isotherms and (*b*) centerline temperature variation of a teflon rod for aiding forced flow in a channel of water, with Re = 20.0, Pr = 7.0, $H/r_0 = 5.0$, $U_\infty/U_s = 2.0$

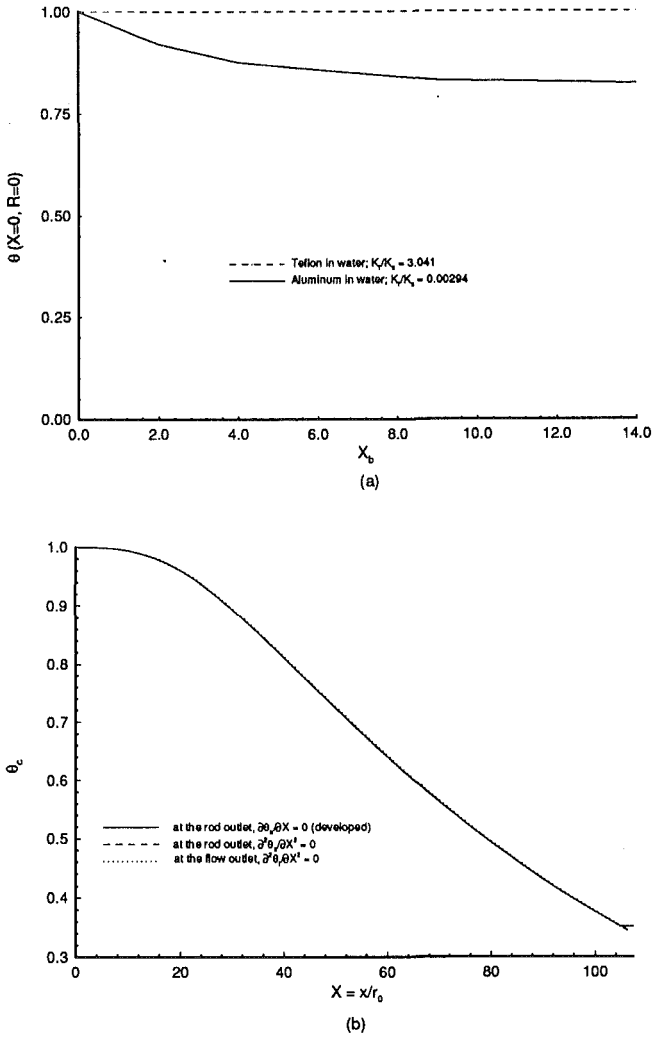

Fig. 5 (*a*) The dependence of the temperature at the channel inlet, on the upstream location $X = -X_b$ where uniform temperature $T = T_0$ is applied to simulate the uniform condition in a furnace or oven for different solid materials, with $U_\infty/U_s = 2.0$ (aiding) and (*b*) the effect of numerically imposed thermal boundary conditions at the outlet on the centerline temperature variation for a teflon rod moving in water, with $U_\infty/U_s = 2.0$ (opposing) (for both cases Re = 25, Pr = 7.0, $H/r_0 = 5.0$)

done by Vafai and Ettefagh (1990). At the channel wall and at the rod surface, the nondimensional vorticity is numerically determined, as discussed in the next section. At the rod surface, the nondimensional temperature $\theta(X, 1, \tau)$ is also numerically determined.

Numerical Scheme

Of the equations to be solved, those for the vorticity and the temperature (Eqs. (4)–(6)) are parabolic in time, elliptic in space, while the stream function equation (Eq. (3)) is elliptic. An approximation to their solution is obtained at a finite number of grid points. For a typical computational run, considering a solid aluminum rod with a length to radius ratio of 100 and moving in a channel of gap width $H = 5r_0$, a 51×11 uniform grid is used for the solid material and a 51×31 uniform grid is used for the fluid flow. These sizes are chosen by performing a grid independence study, monitoring the temperature and vorticity fields. The size of $\Delta\tau$ is limited by stability considerations.

The transient vorticity and energy equations, in conservative form for both the solid rod and the fluid, are solved using the Alternate Direction Implicit (ADI) scheme, as given by Peaceman and Rachford (1955). At each time step, after advancing the solutions for the vorticity transport and the temperature equations (for both the solid and the fluid) by the ADI scheme, the stream function equation was solved using the SOR method (Roache, 1982). The dimensionless equations are discretized using a three-point central differencing scheme (Jaluria and Torrance, 1986), except for the convection terms. To preserve the stability of the numerical scheme these nonlinear space derivatives are approximated with a donor cell scheme (Roache, 1982).

The conjugate boundary conditions at any node on the solid surface are determined in discretized form in terms of the temperature values of the adjacent nodes, by taking into account the mass and energy conservation within a control volume, lying partly within the solid and partly within the fluid (Roy Choudhury, 1992). For obtaining the value of vorticity at the rod and the channel surfaces, a Taylor series expansion of the stream function is used with a first-order approximation, which gives rise to the following boundary conditions for vorticity (Roy Choudhury and Jaluria, 1992).

At the interface between the fluid and the solid

$$\Omega(i, jn1) = \frac{1}{R_{\text{surf}}} - \frac{2[\Psi(i, jn1+1) - \Psi(i, jn1) - R_{\text{surf}}\Delta R]}{R_{\text{surf}}(\Delta R)^2} \quad (7)$$

where $jn1$ is the radial grid point on the cylinder surface, i is the axial grid point, and ΔR is the radial grid spacing. At the channel surface,

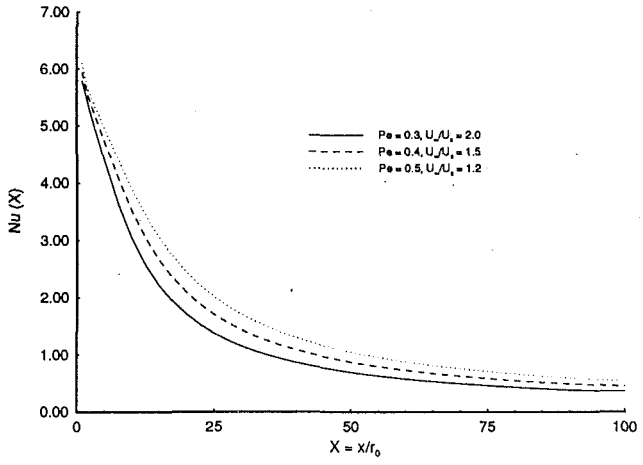

(a)

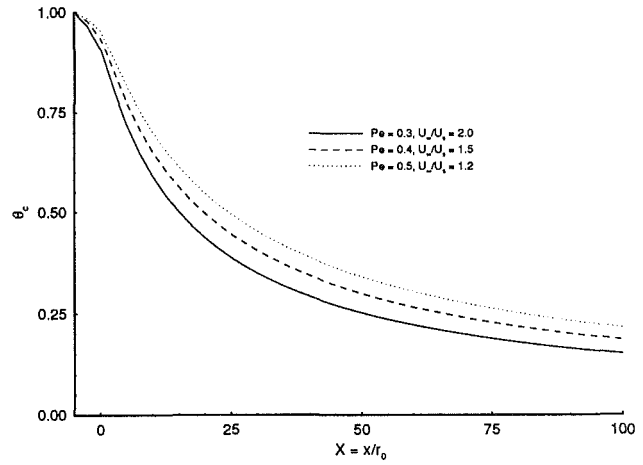

(b)

Fig. 6 Effect of the rod speed U_s (for aiding flow with given U_∞) on (*a*) local Nusselt number variation and (*b*) centerline temperature decay, for an aluminum rod moving in water, with $H/r_0 = 5.0$, $K_f/K_s = 0.0029$

$$\Omega(i, jn) = -\frac{2[\Psi(i, jn-1) - \Psi(i, jn)]}{R_w(\Delta R)^2} \tag{8}$$

where jn is the radial grid point at the channel wall, so that $R_w - R_{\text{surf}} = (jn - jn1)\cdot\Delta R$. Higher order approximations of wall vorticity gave rise to instability and, therefore, were not used.

The calculations were carried out till the maximum changes in the velocity and temperature field at all grid points satisfy a convergence criterion. The effect of the chosen convergence criteria on the steady state solution was studied, to ensure a negligible effect on the computed results.

Numerical validation of the code was carried out by running the code for a flat plate in a channel flow and comparing the results obtained with those given by Kang and Jaluria (1992). The results were found to agree very closely (Roy Choudhury, 1992). Also mass and energy fluxes across different finite volumes were calculated to ensure mass and energy conservation. Comparisons with experimental data also showed very good agreement, as shown in Fig. 3. Very few experimental data are available with a channel flow for a moving rod with forced convection. Instead the data available for quiescent flow ($U_\infty = 0$) are used for validation of the numerical scheme. A comparison of the surface temperature distributions from the present numerical results and those from the experimental data obtained by Alderson et al. (1968) and Arridge and Prior (1964) for a heated glass fiber moving in air was carried out. The results are shown in Fig. 3(*a*). Here ξ is a dimensionless co-

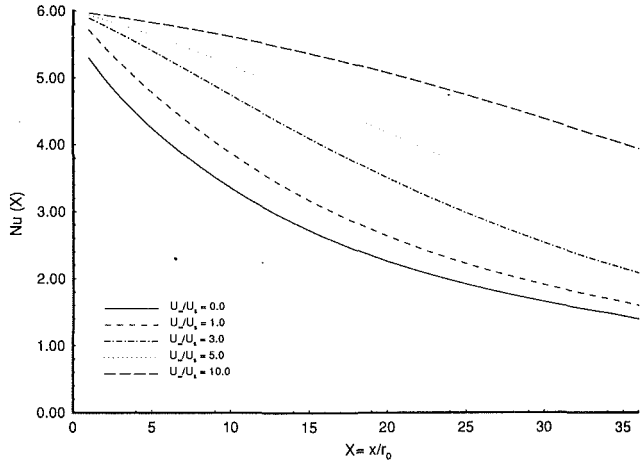

Fig. 7 Effect of the free-stream velocity for aiding flow on the local Nusselt number variation for an aluminum rod moving in water, with $H/r_0 = 5.0$, Pe = 0.6, Pr = 7.0, $K_f/K_s = 0.0029$

ordinate distance in the direction of material motion as defined by Chida and Katto (1982) as $\xi = (x(\rho CK)_f)/(U_s r_0^2(\rho_s^2 C_s^2))$. The results show very good agreement between the present numerical results and the experimental data obtained. Kang et al. (1994) performed an experiment with an aluminum cylinder moving downward in an extensive water medium. The same situation is simulated numerically and the experimental data on the surface temperature are shown in Fig. 3(*b*). Again the numerical results show very close relation to the experimental results. Also several other experimental comparisons are given by Roy Choudhury and Jaluria (1993) for an optical fiber moving in a channel with peripheral flow entrance. Again the results show very good agreement.

Numerical Results and Discussion

Numerical solutions to the vorticity, temperature, and stream function equations were obtained to study several important aspects associated with the aiding and opposing circumstances. Results were obtained over wide ranges of the governing parameters. The flow is initially transient, and reaches the steady-state condition eventually. The problem is solved as a transient problem, because the time-dependent process is important in several cases, such as during the startup process of the furnace, and because it leads to better insight and proper understanding of the physical mechanisms involved. In addition, the scheme can be used for time-varying boundary conditions for which a steady-state situation is not obtained. The transient isotherms and axial temperature distributions for a teflon rod moving in water are shown in Fig. 4. It is found from this figure that the temperature field develops gradually and does not show any overshoot or periodic behavior. The flow field also develops similarly, but develops faster than the thermal field. For the sake of brevity, no other transient results are presented here. For more detailed discussion on the transient results see Roy Choudhury (1992). Some typical steady-state results are presented here to indicate the main trends. The values of the nondimensional parameters used for these results are typical for a few important manufacturing processes, as mentioned earlier.

Effect of Boundary Conditions. Because of the upstream penetration of the effect of thermal diffusion, the relevant boundary conditions must be applied numerically at $X = -X_b$, where the value of X_b is increased till the results become essentially independent of a further increase. This is done to simulate the condition that exists upstream of the point of

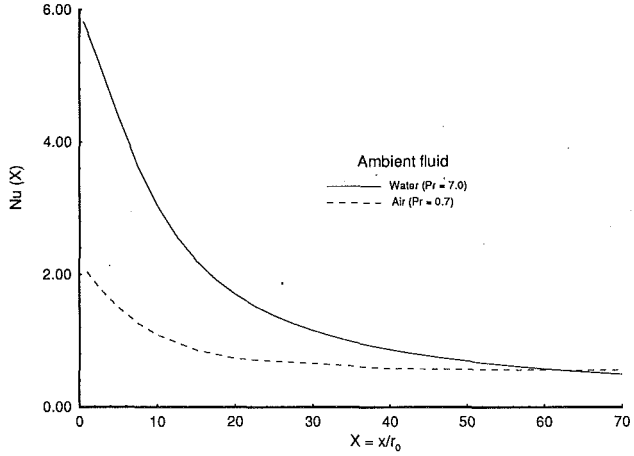

Fig. 8 The downstream variation of the local Nusselt number for an aluminum rod moving in a channel, with air or water as the fluid, for Pe = 0.3, $H/r_0 = 5.0$, $U_\infty/U_s = 2.0$ (aiding)

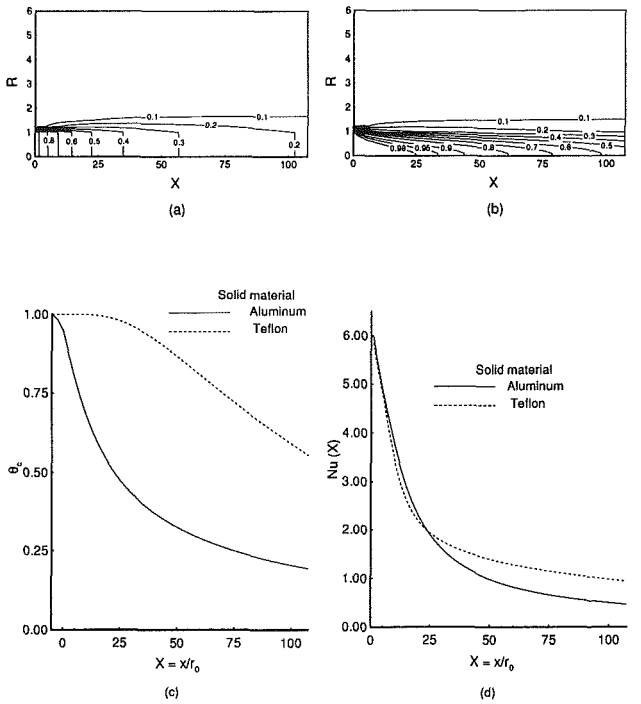

Fig. 9 Effect of the material of the moving rod on (*a*) isotherms for an aluminum rod moving in water; $K_f/K_s = 0.0029$, (*b*) isotherms for a teflon rod moving in water; $K_f/k_s = 3.041$, (*c*) centerline temperature decay, and (*d*) the variation of the local Nusselt number: Re = 40.0, Pr = 7.0, $H/r_0 = 5.0$, $U_\infty/U_s = 2.0$ (aiding)

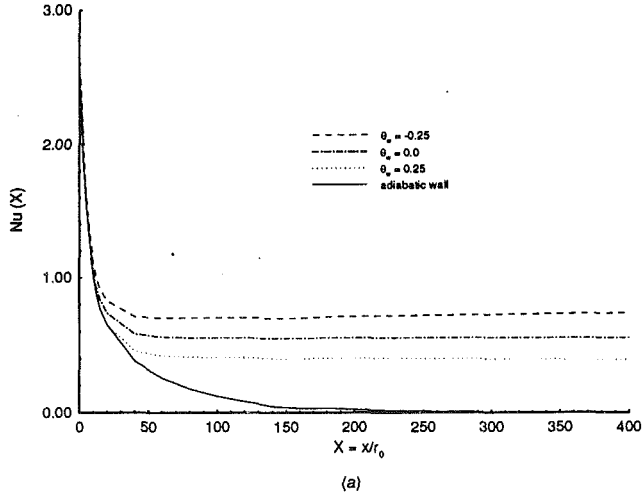

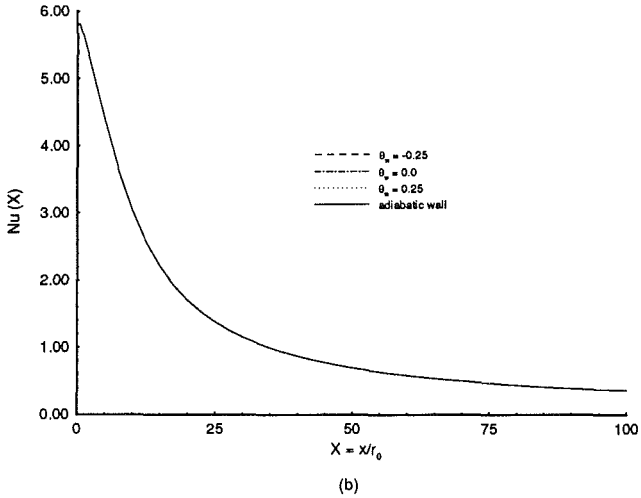

Fig. 10 Local Nusselt number variation for different thermal conditions at the channel wall for an aluminum rod: (*a*) air, Pr = 0.7, $K_f/K_s = 0.000126$, and (*b*) water, Pr = 7.0, $K_f/K_s = 0.00294$, at Pe = 0.3, $H/r_0 = 5.0$, $U_\infty/U_s = 2.0$ (aiding)

emergence from an extruder die, a furnace, or an oven. Figure 5(*a*) shows the temperature at $X = 0$ and $R = 0$ for various values of X_b, when the rod surface is assumed to be adiabatic in the region $-X_b \le X \le 0$. The value of temperature is specified at a uniform value of T_o at $X = -X_b$, or $0 \le R \le 1$. This figure indicates that the solution is dependent on the location where T_o is applied for small values of X_b. It is seen that the value of X_b has a significant effect on the computed temperature θ at $X = 0$ and $R = 0$ for a material with high thermal conductivity, such as aluminum. On the other hand the effect of upstream thermal diffusion is negligible for teflon, due to the low thermal conductivity of the material. It is also found that $X_b = 12.5$ is large enough, even for an aluminum rod, to simulate an infinitely large upstream distance, because increasing X_b further hardly affects the temperature at $X = 0$ and $R = 0$ (a cut-off criterion of less than 1 percent change in $\theta(0, 0)$ with a change of 1 in X_b is used).

The effect of different upstream boundary conditions at the surface of the rod for $-X_b \le X \le 0$ is found to be important when aluminum is the solid, but not so when the solid material is a low-conductivity one, such as teflon (Roy Choudhury and Jaluria, 1992). These results are important from the design point of view as well as the numerical simulation of the process for different materials. The type of boundary condition will influence the calculated length of the cooling trough, distance between the die and the take-up spool, etc.

The numerical imposition of the outflow boundary conditions is another difficult task. Different thermal and flow conditions have been considered at the outlet. A variation in the boundary conditions for the flow quantities, such as the velocity components, did not give rise to any significant change in the cooling of the rod, nor did it change the Nusselt numbers or the flow field. The thermal conditions, on the other hand, have to be applied very carefully at the outlet. If the channel is infinitely long, then it can be assumed that at the outflow boundary the temperature of the rod approaches the ambient temperature, i.e., $\theta \to 0$. We could say the same thing about the fluid temperature in case of an aiding flow. In case of an opposing flow, however, since the flow exit is at the point of emergence of the rod from the slot or the die, this approxi-

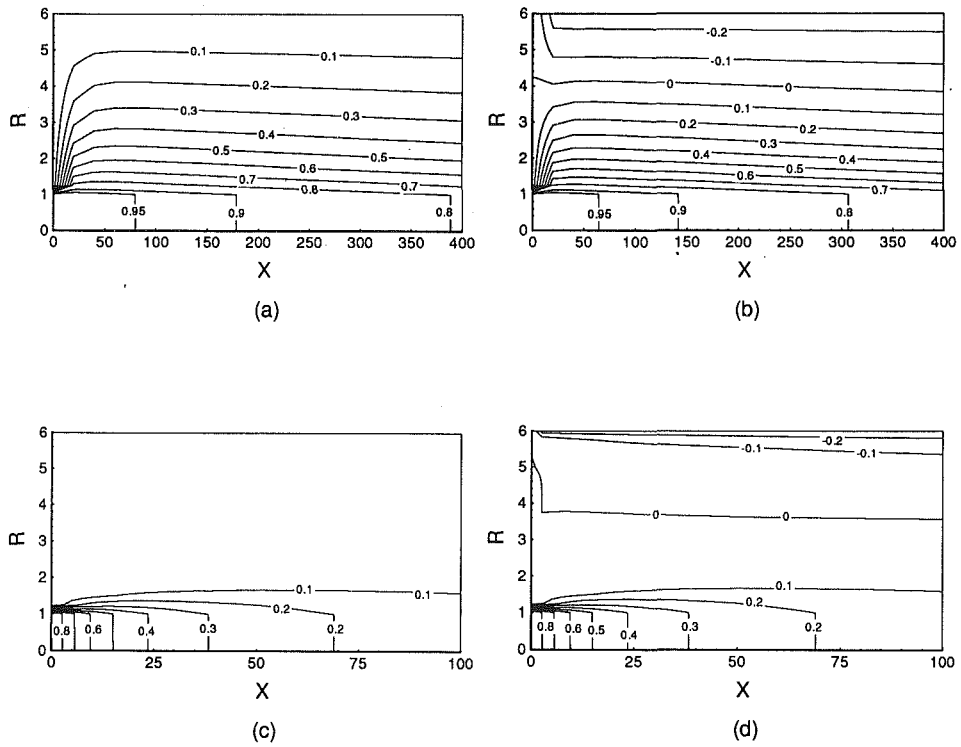

Fig. 11 Isotherms for an aluminum rod moving in different ambient fluids (aiding flow) under various thermal conditions: (*a*) air, $\theta_w = 0.0$, (*b*) air, $\theta_w = -0.25$, (*c*) water, $\theta_w = 0.0$, (*d*) water, $\theta_w = -0.25$

mation can not be made. Also, a finite length of the channel is employed in practice. Therefore, an appropriate form of the boundary conditions is necessary.

At the outflow two different thermal conditions were imposed for the fluid. In the first case, the thermal field is assumed to be developed at the outlet (i.e., $\partial\theta/\partial X = 0$). In the second instance, however, a weaker restriction is applied, which removes the requirement that the isotherms have to be parallel to the X axis. It is assumed that the isotherms are linear at the outlet, so that their slopes are constant (i.e., $\partial^2\theta/\partial X^2 = 0$). This implies that the axial diffusion is negligible. The same boundary conditions are applied for the rod at the point of exit from the channel.

Figure 5(*b*) shows the effect of boundary conditions for the opposing flow case. When the second derivative conditions is used at either the rod or the flow outlet, the conditions used at other outlet is the developed flow and temperature field assumption. It is observed that the effect of these outflow boundary conditions is small, except close to the outlet. A similar trend is observed for the aiding flow case as well; see Roy Choudhury and Jaluria (1993) for details. If the channel is a long one, these outflow boundary conditions hardly affect the flow or thermal field, because, ultimately, the second boundary condition can be used for all cases, whereas the first boundary condition should be used for a relatively long computational domain.

Aiding Flow. Several different results are obtained for the aiding flow case. For considering the effect of different physical and process parameters on the heat transfer rate and cooling, the local Nusselt number is defined as $\mathrm{Nu} = hr_0/K$, where h is the local heat transfer coefficient calculated at the surface of the rod, as defined in the nomenclature. The heat transfer coefficient h is based on the inlet temperature because it is a constant and is often known in the problems considered. Thus, the local Nusselt number can be written as

$$\mathrm{Nu} = \frac{hr_0}{K} = \frac{(-(\partial\theta/\partial R))_{R=1.0}}{\theta_{R=1.0}} \tag{9}$$

Figure 6 shows the effect of a change in the speed of the rod U_s (to maintain the forced convection velocity at the inlet constant, the ratio U_∞/U_s is varied). At a higher velocity, U_s, the heat removal rate, is larger. This is because at a higher velocity of the rod, the induced flow in the fluid increases, resulting in an increase in the local Nusselt number, as observed in Fig. 6(*a*). However, considering a finite distance through which the rod passes, even though the local Nusselt number in this region is higher for an increased rod speed, the time taken by the rod to pass through the region is smaller. This results in less thermal energy being extracted from the rod while it passes through the given region at faster speed. This can be seen from Fig. 6(*b*). Thus, in a given process, if the velocity of drawing or extrusion is increased, it is found that a larger length would be required to cool the rod to a given temperature level, despite the increase in the local heat transfer rate.

Figure 7 shows the effect of a change in the force convection velocity, U_∞, when the rod moves at a fixed speed, U_s. As expected, it is observed that the local Nusselt number and, consequently, the heat transfer rate increases with an increase in the forced convective velocity. A larger U_∞ results in a thinner boundary layer in the developing region of the channel flow, giving rise to a larger heat transfer rate, as is well known from the heat transfer literature (Burmeister, 1983).

Figure 8 shows the effect of the ambient fluid on the heat transfer rate for a given material, chosen as aluminum. The rod moves at a given velocity in a channel of given radius. The only difference is due to the fluid employed. When water ($\mathrm{Pr} = 7.0$) is the cooling medium, the heat transfer rate is much higher than when air ($\mathrm{Pr} = 0.7$) is the cooling medium at small X, because the thermal diffusion is much stronger in water than in air due to the larger thermal conductivity in the former case. However, at larger X, a crossover in Nusselt number is observed. Such a crossover in the curves is expected from the more rapid drop in the temperature in water, as compared to that in air. Many gases, like nitrogen, behave similarly to air, while some of the liquids behave like water. For the effects of

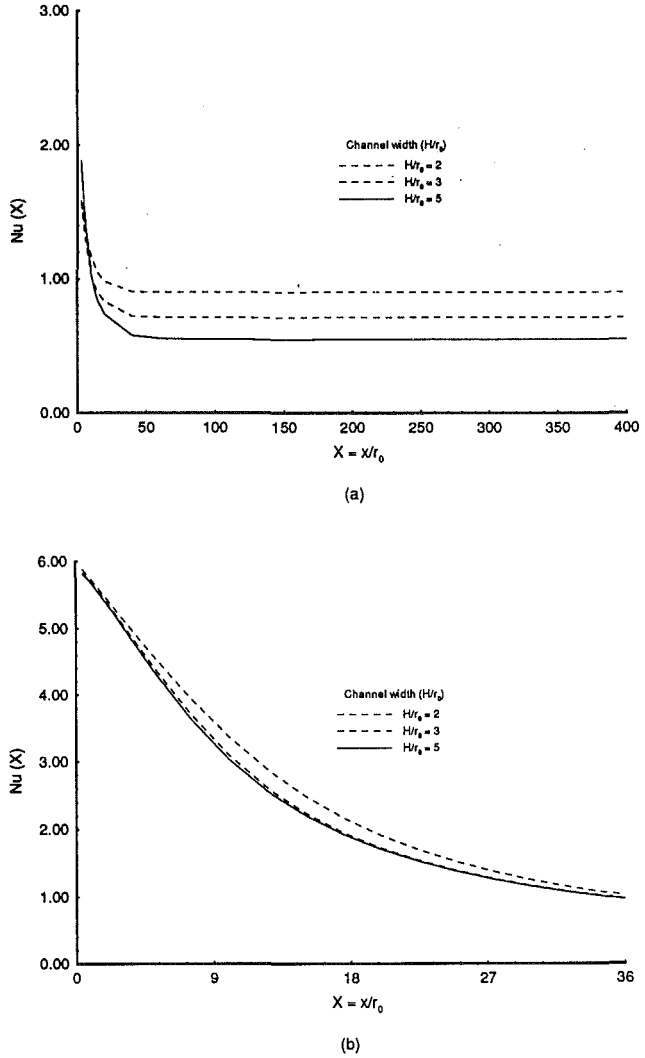

Fig. 12 The variation of the local Nusselt number with the channel gap width, H/r_0, for an aluminum rod moving in (*a*) air, Pr = 0.7, and (*b*) water, Pr = 7.0: Pe = 0.3, $U_\infty/U_s = 2.0$ (aiding)

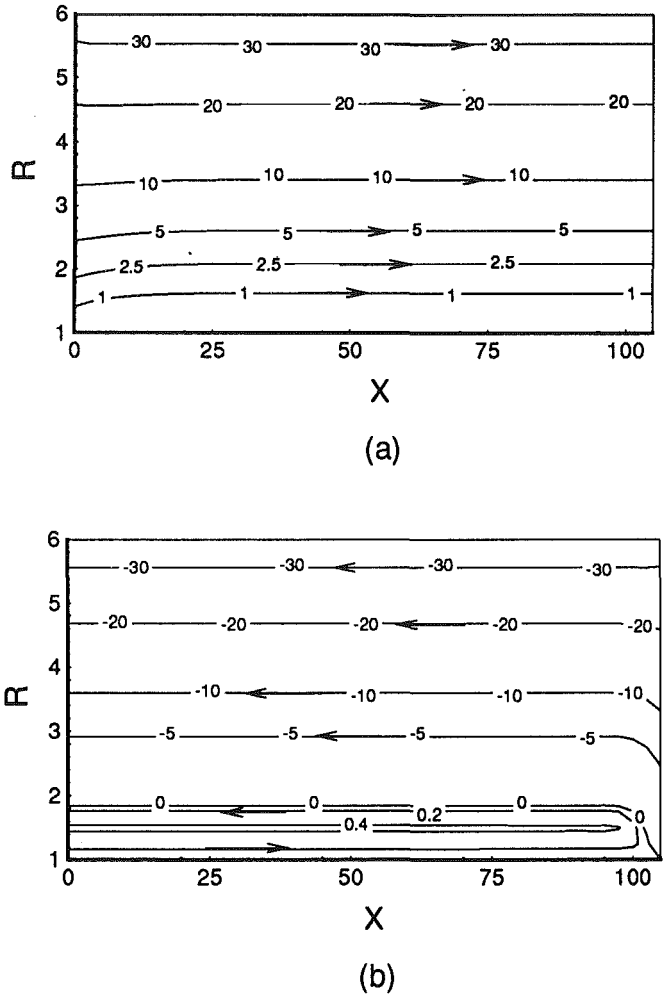

Fig. 13 Effect of flow direction on the streamlines for an aluminum rod moving in water, with Re = 40.0, Pr = 7.0, $K_f/K_s = 0.0029$, $|(U_\infty/U_s)| = 2.0$; (*a*) aiding flow, (*b*) opposing flow

different ambient fluids on the optical fiber drawing process, see Roy Choudhury and Jaluria (1993).

Figure 9 shows the isotherms, the local Nusselt number, and the centerline temperature decay for aluminum and teflon, with water as the cooling medium. The radius and speed of the rod are the same, as are the channel radius and the forced convection velocity. It is seen that within the rod there is a large variation in temperature in case of teflon, a poor conductor, while for aluminum, the temperature difference across the material is almost negligible. It can be concluded that for aluminum or any highly conducting material, the temperature can be lumped radially. It is also seen from the centerline temperature decay and the local Nusselt number distributions that there is a rapid temperature decay downstream in the case of aluminum, because of large axial diffusion. Thermal energy is, therefore, rapidly diffused downstream and then lost to the fluid at the surface. However, for teflon, there is a more gradual temperature decay downstream. Since the temperature levels are higher in the case of teflon, the temperature gradient near the rod surface is quite high, the fluid being the same (water) for both cases. This results in a larger local Nusselt number, and consequently larger heat transfer rate to the ambient, except very near the slot.

Figure 10 shows the effect of different wall thermal conditions on the heat transfer rate, when an aluminum rod moves at the same speed in air and water, with the same channel radius. In the case of air it is seen that if the wall is kept at a temperature lower than the ambient temperature ($\theta_w = -0.25$), then the rate of heat removal is larger than when the wall is maintained at the ambient temperature, as indicated by the local Nusselt number. This is due to an increase in the temperature gradient at the surface and is evident from Fig. 11(*b*) where the isotherms are seen to be closer to the surface of the rod. Similarly, the Nusselt numbers are lower when the wall temperatures are higher than the ambient temperature. The Nusselt number and, consequently, the heat transfer rate virtually vanish if the wall is maintained as adiabatic, since no heat loss occurs at the channel wall in this case.

On the other hand, for water in a channel of width $H = 5r_0$, because of higher thermal conductivity and thinner thermal boundary layer the radial drop in temperature is rapid. Therefore, the heat transfer from the rod is hardly affected by the wall boundary conditions. Again it is evident from Figs. 11(*c*) and 11(*d*) that the isotherms near the rod surface remain virtually unchanged as the wall thermal condition is changed from $\theta_w = 0$ to $\theta_w = -0.25$. Thus, it is observed from Fig. 10(*b*) that the Nusselt numbers are really unaffected by the channel wall thermal conditions, unless the channel gap width is very small. The design consideration that is worth mentioning in this context is that reducing the temperature of the wall by means of some kind of cooling jacket, when air is used as the forced convective medium, increases the heat transfer rate substan-

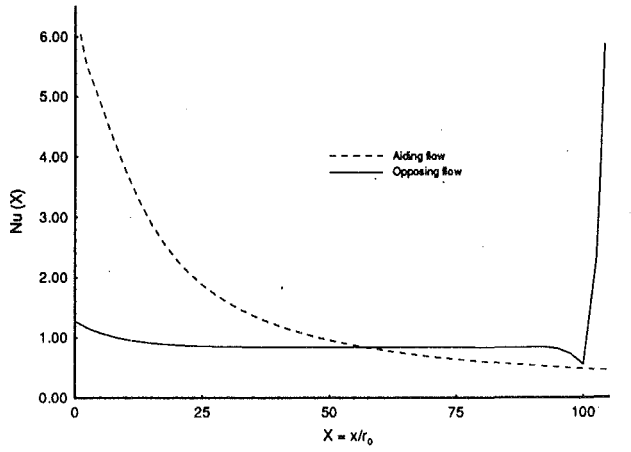

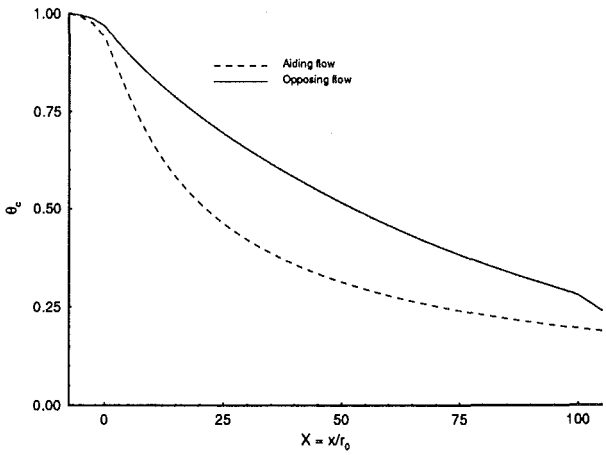

Fig. 14 Effect of flow direction on (*a*) local Nusselt number variation, and (*b*) centerline temperature decay for an aluminum rod moving in water, with Re = 40.0, Pr = 7.0, $K_f/K_s = 0.0029$, $|U_\infty/U_s| = 2.0$

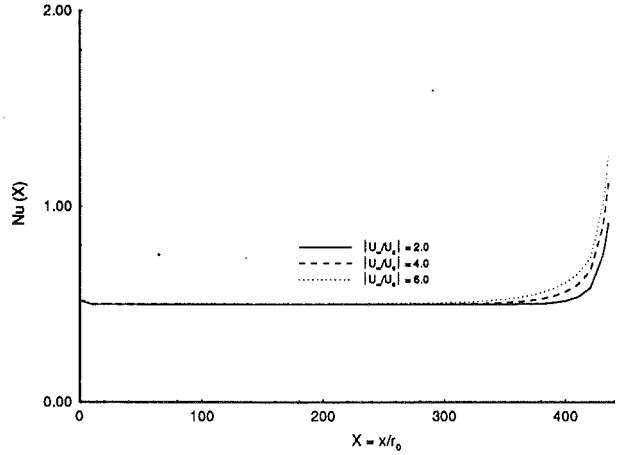

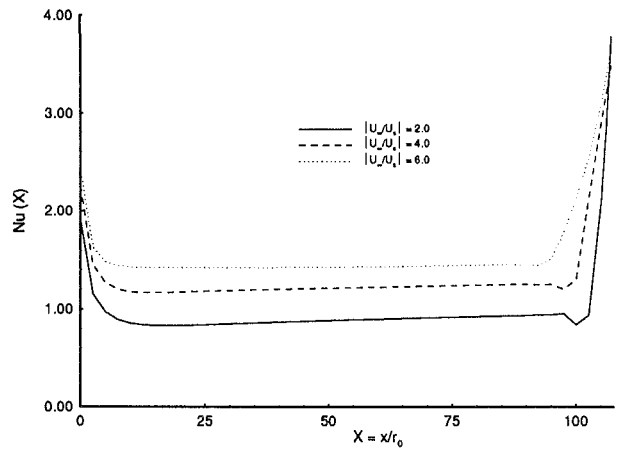

Fig. 15 Effect of the free-stream velocity on the local Nusselt number variation for (*a*) an aluminum rod moving in a channel with forced air flow in the opposite direction for Pe = 0.3, Pr = 0.7, $K_f/K_s = 0.000126$, and (*b*) a teflon rod moving in a channel with forced water flow in the opposite direction for Re = 25.0, Pr = 7.0, $K_f/K_s = 3.041$

tially. But unless the channel is very narrow, there is hardly any difference in heat transfer from the rod surface if water is used as the cooling medium.

The effect of the channel gap width on the heat transfer from the surface of the rod, for given thermal conditions, is next investigated. From Fig. 12, it can be seen that, for both air and water, with a decrease in channel width, the Nusselt number increases, as the temperature gradient at the surface increases. Comparing the Nusselt number variation for air and water, it is observed that for air the Nusselt number keeps on decreasing as the channel width is increased. But when water is used as the cooling medium, the Nusselt number hardly varies when the channel width H is more than $4r_0$. This can again be explained by the results in Fig. 11(*c*). Since most of the radial temperature drop takes place close to the surface of the rod, increasing the channel width hardly affects the heat transfer.

Opposing Flow. Figure 13 shows the effect of the forced flow direction on the flow field. It is seen from the streamlines for the opposing flow case (Fig. 13*b*) that a recirculating flow region develops near the surface of the rod. This recirculating flow region arises as a consequence of flow reversal, which occurs since the fluid near the surface of the rod tends to move along with the rod because of viscous effects. However, near the entrance of the forced flow, the fluid velocity is large enough to force the flow to take place in the same direction as the forced convection velocity. No such recirculation arises in the aiding circumstance; see Fig. 13(*a*).

Figure 14 examines the centerline temperature decay and the variation of the local Nusselt number for the opposing flow case. From Figs. 13(*b*) and 14(*a*), a direct correspondence can be established between the recirculating flows and the local Nusselt number. The Nusselt number is generally high at the inlet where the forced flow enters the channel, but as the recirculating region begins, the flow velocity near the surface of the rod becomes very small. This results in a small local heat transfer rate, and consequently the Nusselt number is relatively small as compared to that for aiding flow. A similar trend is reflected in the centerline temperature decay, which is seen to be more rapid in the case of aiding flow, as compared to opposing flow.

In most cases, the basic trends for the opposing flow are similar to those seen earlier for the aiding flow. Therefore, not all the results are shown here, to avoid redundancy. Only the response to an increase in free-stream velocity is shown. From Fig. 15(*a*) it is seen that, for air as the fluid, an increase in the forced convection velocity leads to an increase in the local Nusselt number near the flow entrance. But the Nusselt number reaches an essentially constant value away from the flow entrance. This phenomenon can also be explained in terms of the recirculating region, where the velocity is in the direction opposite to the forced convection velocity. Therefore, the surface heat transfer in this region is really independent of the

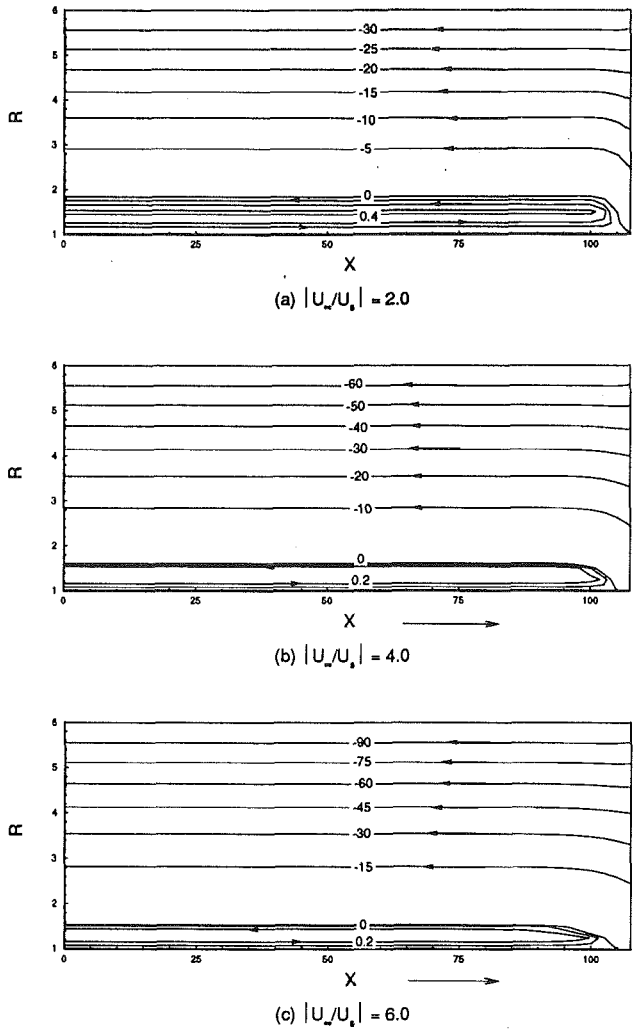

Fig. 16 The effect of free-stream velocity on the steamlines for opposing forced water flow over a teflon rod, with Re = 25.0, Pr = 7.0, $H/r_0 = 5.0$

forced convection velocity, and is principally governed by the rod movement. However, if water is the cooling medium, then changing the forced convection velocity has a more pronounced effect, as seen from Fig. 15(*b*), which shows the Nusselt number variation for a teflon rod moving in water. In this case, with an increase in the forced flow velocity the recirculating region diminishes (as seen from Fig. 16), leading to an overall increase in Nusselt number and in the consequent temperature decay.

Heat Transfer Correlations. After numerical results were obtained for many cases, some typical heat transfer correlations were also derived. The heat flux distribution in the axial direction is a very important result, but if a given length of channel is considered, the distribution of h, the heat transfer coefficient, and average h calculated from that, is very useful in determining the cylinder temperature at the exit, which is often the most useful result. Therefore, the functional dependence of Nusselt number is identified. From the discussions so far, the principal variables on which Nusselt number is found to depend are identified as the rod speed, the free-stream velocity, and the material–fluid combination, assuming the geometry (channel width and length) and wall thermal conditions to remain unchanged. Here different Nusselt number correlations are attempted for a fixed channel width and length, by first evaluating an average value of the Nusselt number over the length of the channel, and then using linear regression with the correlation asssumed to be of the form $\overline{\mathrm{Nu}} = A\mathrm{Pe}^{m_1}|U_\infty/U_s|^{m_2}$. When air is the cooling medium the length of channel considered is $l = 840r_0$, while when water is the cooling medium the length of channel considered is $l = 105r_0$. The average Nusselt number remains virtually unaffected by longer length. For all the cases, the channel width H is taken as $5r_0$. The coefficients A, $m1$, and $m2$ are given in Table 1.

Table 1 Values of the coefficients *A*, *m*1, and *m*2 for different circumstances

Type of flow	Material-fluid	A	m1	m2	Range of Pe	Range of $\lvert U_\infty/U_s\rvert$
Aiding flow	Aluminum-air	0.5866	0.0119	0.0076	0.2 - 1.5	0.5 - 10
	Aluminum-water	1.9563	0.5058	0.0899	0.2 - 1.5	0.5 - 10
	Glass-air	0.5622	0.0077	0.0029	15 - 200	0.5 - 10
Opposing flow	Aluminum-air	0.5922	0.0107	0.0173	0.2 - 1.5	0.5 - 10
	Glass-air	0.5729	0.0036	0.0056	15 - 200	0.5 - 10

It is apparent from these correlations that when water is used as the fluid, the effect of rod speed U_s is much more pronounced than the effect of the free-stream velocity U_∞. However, when air is the fluid, the Nusselt numbers reach more or less a constant value for the length of the channel considered, and depend very weakly on the rod speed or the free-stream velocity.

Conclusions

A detailed numerical study of the conjugate transport from a continuously moving infinite cylindrical rod in the forced flow in a channel has been carried out. Two different forced flow configurations, namely, one aiding and the other opposing the movement of the rod, have been considered in this study. These circumstances are of interest in several manufacturing processes, ranging from crystal growing, continuous casting, cable coating, and extrusion, to wire and glass fiber drawing. Interest lies in determining the dependence of the thermal field in the material, since this affects the thermal stresses and the quality of the product, on the physical and process variables. Such inputs are needed to design and possibly optimize the thermal system or the operating conditions associated with the processes. Also of importance and interest is the numerical simulation of the process, particularly the numerical imposition of the boundary conditions and their effect on the results.

The results obtained indicate that the penetration of the diffusion effects upstream of the point of emergence is important and must be appropriately treated in the numerical scheme. The heat transfer and the consequent temperature decay in the material undergoing thermal processing are found to depend significantly on the channel width, on the channel thermal conditions, on the fluid used, and on the rod speed. However, if the thermal conductivity of the fluid is high, then the channel width and the channel boundary conditions do not have a significant effect. For the opposing flow circumstance it is found that a recirculating region is formed near the rod surface, reducing the rate of heat transfer from the surface. As the recirculating region increases in thickness, the heat transfer from the surface is seen to decrease. Comparisons of the numerical results with experimental data available in the literature show very good agreement. A few heat transfer correlations are also derived to indicate the dependence of the Nusselt number on the important parameters in the problem.

Acknowledgments

The authors acknowledge the financial support provided by the National Science Foundation, under Grant Nos. CBT-88-03049 and DDM-92-13458, and the computing facilities provided by the NCSA and the PSC, under Grant Nos. TRA910431N and CBT920017P, for this work.

References

Abdelhafez, T. A., 1985, "Skin Friction and Heat Transfer on a Continuous Flat Surface Moving in a Parallel Free Stream," *International Journal of Heat and Mass Transfer*, Vol. 28, pp. 1234–1237.

Alderson, J.V., Caress, J. B., and Sager, R. L., 1968, "The Cooling Rate of a Glass Fibre in the Continuous Filament Process," Laboratory Report No. L.R.235 of Pilkington Bros. Ltd., Lathom, Lancashire, United Kingdom.

Altan, T., Oh, S., and Gegel, H., 1979, *Forming Fundamentals and Applications*, American Society of Metals, Metals Park, OH.

Arridge, R. G. C., and Prior, K., 1964, "Cooling Time of Silica Fibres," *Nature*, Vol. 203, pp. 386–387.

Bourne, D. E., and Elliston, D. G., 1970, "Heat Transfer Through the Axially Symmetric Boundary Layer on a Moving Circular Fibre," *International Journal of Heat and Mass Transfer*, Vol. 13, pp. 583–593.

Burmeister, L., 1983, *Convective Heat Transfer*, Wiley-Interscience Publication, New York.

Chida, K., and Katto, Y., 1976, "Conjugate Heat Transfer of Continuously Moving Surfaces," *International Journal of Heat and Mass Transfer*, Vol. 19, pp. 461–470.

Fisher, E. G., 1976, *Extrusion of Plastics*, Wiley, New York.

Jaluria, Y., and Torrance, K. E., 1986, *Computational Heat Transfer*, Hemisphere, New York.

Jaluria, Y., 1992, "Transport From Continuously Moving Materials Undergoing Thermal Processing," *Annual Review on Heat Transfer*, Vol. 4, pp. 187–245.

Kang, B. H., Karwe, M. V., and Jaluria, Y., 1991, "Numerical Simulation of Conjugate Transport From a Continuous Moving Plate in a Material Processing," *Numerical Heat Transfer*, Vol. 19, pp. 151–176.

Kang, B. H., and Jaluria, Y., 1992, "A Numerical Study of the Fluid FLow and Heat Transfer Due to a Heated Plate Moving in a Uniform Forced Flow," *Numerical Heat Transfer*, Vol. 22, pp. 143–165.

Kang, B. H., Yoo, J., and Jaluria, Y., 1994, "Experimental Study of the Convective Cooling of a Heated Continuously Moving Material," ASME JOURNAL OF HEAT TRANSFER, Vol. 116, pp. 199–208.

Karwe, M. V., and Jaluria, Y., 1988, "Fluid Flow and Mixed Convection Transport From a Plate in Rolling and Extrusion Process," ASME JOURNAL OF HEAT TRANSFER, Vol. 110, pp. 655–661.

Karwe, M. V., and Jaluria, Y., 1991, "Numerical Simulation of Thermal Transport Associated With a Continuously Moving Flat Sheet in Material Processing," ASME JOURNAL OF HEAT TRANSFER, Vol. 113, pp. 612–619.

Kyriacou, S., Polymeropoulos, C. E., and Sernas, V., 1990, "Accelerated Cooling of Optical Fiber," *Mat. Res. Soc. Proc.*, Vol. 172, p. 49.

Paek, U. C., and Schroeder, C. M., 1979, "Forced Convective Cooling of Optical Fibre in High-Speed Coating," *Journal of Applied Physics*, Vol. 50, pp. 6144–6148.

Peaceman, D. W., and Rachford, H. H., 1955, "The Numerical Solution of Parabolic and Elliptic Differential Equations," *Journal of Soc. Ind. Applied Mathematics*, Vol. 3, pp. 28–41.

Roache, P., 1982, *Computational Fluid Dynamics*, Hermosa Publishers, NM.

Roy Choudhury, S., 1992, "Numerical Study of Forced Convective Heat Transfer From a Continuously Moving Cylindrical Rod Undergoing Material Processing," M.S. Thesis, Rutgers University, New Brunswick, NJ.

Roy Choudhury, S., and Jaluria Y., 1992, "Forced Convective Heat Transfer From a Continuously Moving Cylindrical Rod Undergoing Thermal Processing," in: *Heat Transfer in Materials Processing*, ASME HTD-Vol. 224, pp. 43–50.

Roy Choudhury, S., and Jaluria, Y., 1993, "Forced Convective Cooling of an Optical Fibre During Thermal Processing," in: *Advanced Computations in Materials Processing*, ASME HTD-Vol. 241, pp. 57–71.

Sakiadis, B. C., 1961, "Boundary Layer Behavior on Continuous Solid Surfaces: I. Boundary Layer Equations for Two-Dimensional and Axisymmetric Flow," *AIChE Journal*, Vol. 7, No. 1, pp. 26–28.

Vafai, V., and Ettefagh, J., 1990, "Thermal and Fluid Flow Instabilities in Buoyancy-Driven Flows in Open-Ended Cavities," *International Journal of Heat and Mass Transfer*, Vol. 33, pp. 2329–2344.

Convective Transport Phenomena and Macrosegregation During Solidification of a Binary Metal Alloy: I—Numerical Predictions

P. J. Prescott
Department of Mechanical Engineering,
The Pennsylvania State University,
University Park, PA 16802

F. P. Incropera
Heat Transfer Laboratory,
School of Mechanical Engineering,
Purdue University,
West Lafayette, IN 47907

A continuum model is used to simulate transient convective transport phenomena numerically during solidification of a Pb–19 percent Sn alloy in an experimental test cell. Solidification occurs in an axisymmetric, annular mold of stainless steel, cooled along its outer vertical wall. Results show that, during early stages of solidification, double-diffusive convection and liquid exchange between melted and mushy zones are responsible for the formation of channels in the outer periphery of the ingot, which ultimately lead to a form of macrosegregation known as A-segregates. During intermediate stages of solidification, solutally driven natural convection spawns a cone segregate in the interior region of the ingot. The final macrosegregation pattern is characterized, in general, by increasing Sn concentration with increasing height throughout the ingot and by increasing Sn concentration with decreasing radius in the upper portion of the ingot.

Introduction

Solidification phase change is an important phenomenon in many industrial applications, as in casting, welding, energy storage, crystal growth, and food processing. While many solidification processes have evolved to be very efficient, advances have often relied, not on basic principles, but on specific empirical knowledge, which cannot be used to develop new processes to meet increasing demands for high-quality and/or special purpose materials. This paper reports the results of a model simulation aimed at obtaining a fundamental understanding of the role played by convection during the solidification of metal alloys. In a companion paper (Prescott et al., 1994), the validity of the model is assessed through a comparison with experimental results obtained for a Pb-Sn alloy.

In most alloy solidification processes, a two-phase (mushy) zone forms. The zone is comprised of solid dendrites and interdendritic liquid, and it separates fully solidified and melted regions, with which it shares solidus and liquidus interfaces, respectively. Since alloys freeze dendritically over a temperature range, the mushy zone is neither isothermal nor of uniform solid fraction. Furthermore, because dendrite arm spacings are typically of the order of 10^{-5} to 10^{-4} m, the actual solid–liquid interface within the mushy zone is macroscopically irresolvable. Hence, the mushy zone is often viewed as a porous medium with a time varying, inhomogeneous, and, perhaps, anisotropic permeability.

Convection within a solidification system can be driven by one or more of several mechanisms, including buoyancy, shrinkage, mechanical agitation, surface tension gradients, and electromagnetic body forces. This investigation specifically examines the effects of buoyancy on convection occurring during solidification of a binary metal alloy. Buoyancy-driven flow is effected by density gradients, which are established by both temperature and liquid concentration gradients. Because the dendritic array is permeable, flow may occur in the mushy zone, as well as in the melt. Temperature gradients are induced by cooling, and liquid concentration gradients arise from phase equilibrium requirements. Since the liquidus line in the equilibrium phase diagram (Fig. 1) defines the relationship between temperature and liquid concentration within the mush zone, a temperature gradient within the mushy zone is accompanied by a liquid concentration gradient, and depending upon the relative densities of the alloy constituents, solutal buoyancy forces may either augment or oppose thermal buoyancy forces.Flows in the fully melted and mushy regions are coupled and may strongly influence important properties such as the size and orientation of grains, which, in turn, determine the mechanical properties of the casting. Moreover, convection within the mushy zone is known to be responsible for macrosegregation (Flemings, 1974; Fisher, 1981), which refers to the macroscopic redistribution of alloy constituents. The formation of voids, entrapment of inclusions, and the development of residual stresses are also affected by both advective and diffusive transport phenomena.

Models that suggested a relationship between convection and macrosegregation were originally developed by Flemings and co-workers (Flemings and Nereo, 1967; Flemings et al., 1968; Mehrabian et al., 1970; Kou et al., 1978; Fujii et al., 1979). Application was, however, restricted to the mushy zone, thereby ignoring the coupling that exists between the solid, mushy, and melted regions. Szekely and Jassal (1978) and Ridder et al. (1981) accounted for coupling between the melted and mushy zones by solving a set of governing equations for each zone, subject to interfacial matching conditions. However, such multidomain models require numerical grids to be continuously remeshed in order to track the progression of the liquidus interface and are unable to predict irregular interface shapes that occur due to remelting and double-diffusive convection patterns.

The numerical calculations of this study are based on a continuum model for momentum, energy, and species transport in binary, solid–liquid phase-change systems (Bennon and Incropera, 1987a). Since the model equations apply concurrently in solid, mushy, and liquid regions, these zones are implicitly coupled, and solutions can be effected with only a

Contributed by the Heat Transfer Division for publication in the JOURNAL OF HEAT TRANSFER. Manuscript received by the Heat Transfer Division March 1993; revision received September 1993. Keywords: Double Diffusion Systems, Materials Processing and Manufacturing Processes, Phase-Change Phenomena. Associate Technical Editor: R. Viskanta.

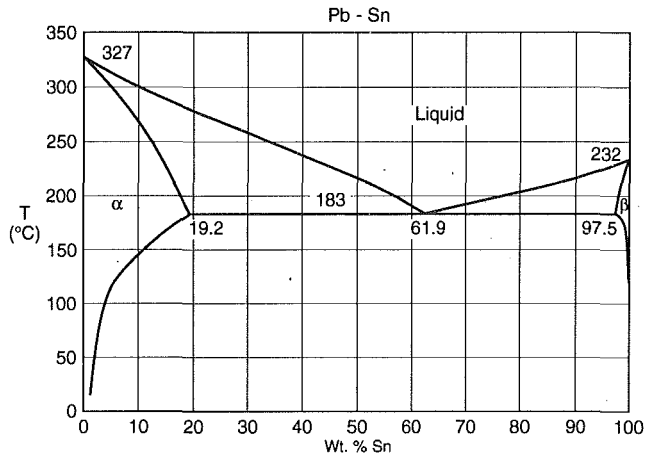

Fig. 1 Equilibrium phase diagram for the Pb–Sn system

single, fixed numerical grid and a single set of boundary conditions. In applications of the continuum model (Bennon and Incropera, 1987b,c; Christenson et al., 1989; Neilson and Incropera, 1991), features such as an irregular liquidus interface, double-diffusive convection in the melt, the channeling of interdendritic flows, and characteristic macrosegregation patterns were predicted. Similar models, which also rely on the assumption of local thermodynamic equilibrium between solid and liquid phases in the mushy zone and on Darcy's law (or extensions thereof) to accommodate interphase momentum exchange, have been developed (Voller and Prakash, 1987; Beckermann and Viskanta, 1988; Voller et al., 1989; Ganesan and Poirier, 1990; Amberg, 1991; Felicelli et al., 1991; Heinrich et al., 1991; Nandapurkar et al., 1991; Poirier et al., 1991; Xu and Li, 1991a,b), and detailed reviews of existing models have been published (Viskanta and Beckermann, 1987; Viskanta, 1990; Prescott and Incropera, 1993).

Although several studies have attempted to validate continuum models by comparing predictions with data obtained for aqueous salt solutions (Beckermann and Viskanta, 1988; Christenson et al., 1989; Neilson et al., 1990), such comparisons are almost nonexistent for metal systems. Shahani et al. (1992) studied solidification of Pb–Sn alloys in a rectangular mold, across which a nearly constant temperature difference was maintained. Using measured side wall temperatures for prescribed boundary conditions, they simulated experimental conditions and achieved reasonably good agreement between predicted and measured macrosegregation.

The objective of this study is to simulate the solidification of a Pb–19 wt pct Sn alloy in an annular test cell subjected to axisymmetric cooling along its outer vertical wall. The model and related simulations are described in this paper, while experimental results and comparisons with the predictions are presented in a companion paper (Prescott et al., 1994).

Model

A continuum model for transport phenomena in binary solid–liquid phase-change systems (Bennon and Incropera, 1987a; Prescott et al., 1991) is used, and under the assumption of axisymmetric conditions, the model transport equations are

$$\frac{\partial \rho}{\partial t} + \nabla \cdot (\rho \mathbf{V}) = 0 \tag{1}$$

$$\frac{\partial}{\partial t}(\rho u) + \nabla \cdot (\rho \mathbf{V} u) = \nabla \cdot \left(\mu_l \frac{\rho}{\rho_l} \nabla u \right) - \frac{\mu_l}{K_z} \frac{\rho}{\rho_l} (u - u_s) + \rho_l B_{lz} - \frac{\partial P}{\partial z} \tag{2}$$

$$\frac{\partial}{\partial t}(\rho v) + \nabla \cdot (\rho \mathbf{V} v) = \nabla \cdot \left(\mu_l \frac{\rho}{\rho_l} \nabla v \right) - \mu_l \frac{\rho}{\rho_l} \frac{(v - f_s v_s)}{r^2} - \frac{\mu_l}{K_r} \frac{\rho}{\rho_l} (v - v_s) - \frac{\partial P}{\partial r} \tag{3}$$

$$\frac{\partial}{\partial t}(\rho h) + \nabla \cdot (\rho \mathbf{V} h) = \nabla \cdot \left(\frac{k}{c_s^*} \nabla h \right) + \nabla \cdot \left[\frac{k}{c_s^*} \nabla (h_s^* - h) \right] - \nabla \cdot [f_s \rho (\mathbf{V} - \mathbf{V}_s)(h_l - h_s)] \tag{4}$$

and

$$\frac{\partial}{\partial t}(\rho f^{\mathrm{Sn}}) + \nabla \cdot (\rho \mathbf{V} f^{\mathrm{Sn}}) = \nabla \cdot (\rho D \nabla f^{\mathrm{Sn}}) + \nabla \cdot [\rho D \nabla (f_l^{\mathrm{Sn}} - f^{\mathrm{Sn}})] - \nabla \cdot [f_s \rho (\mathbf{V} - \mathbf{V}_s)(f_l^{\mathrm{Sn}} - f_s^{\mathrm{Sn}})] \tag{5}$$

for conservation of total mass, axial and radial momentum, energy, and species, respectively. The assumption of axial symmetry is reasonable for computational purposes, although instabilities leading to three-dimensional flow conditions may

Nomenclature

B = body force, N/kg
c = specific heat, J/kg·K
D = binary mass diffusion coefficient, m^2/s
f = mass fraction
Gr = Grashof number $= g\beta_T \Delta T L^3/\nu^2$
g = volume fraction or gravitational acceleration, m/s^2
H = height of mold cavity, m
h = enthalpy, J/kg
K = permeability, m^2
k = thermal conductivity, W/m·K
Le = Lewis number = Sc/Pr
m = slope of liquidus line on the equilibrium phase diagram, K
N = buoyancy parameter $= \beta_S/(m\beta_T)$
P = pressure, N/m^2
Pr = Prandtl number
q'' = heat flux, W/m^2
r = radius, m
Sc = Schmidt number
T = temperature, °C or K
t = time, s, or thickness, m
U = overall heat transfer coefficient, $W/m^2 \cdot K$
u, v = axial and radial velocity components, m/s
$\mathbf{V}$ = velocity, m/s
z = axial position, m
z^* = dimensionless axial coordinate $= z/H$
β_S = solutal expansion coefficient
β_T = thermal expansion coefficient, K^{-1}
μ = viscosity, $N \cdot s/m^2$
ρ = density, kg/m^3
ψ = streamfunction, kg/s·rad

Subscripts

b = bottom
c = coolant
e = eutectic
f = fusion
i = initial or inner
k = phase k
l = liquid phase
max = maximum
min = minimum
o = outer
r = radial component
s = solid phase or solutal
z = axial component

Superscripts

Sn = tin

Table 1 Physical properties of Pb, Sn, and the mold

	Properties	Pb	Sn	Mold
h_f	fusion enthalpy (J/kg)	23,020	59,020	
T_f	fusion temperature (°C)	327	232	
c_s	solid specific heat (J/kg·K)	132	243	535
c_l	liquid specific heat (J/kg·K)	159	249	
k_s	solid thermal conductivity (W/m·K)	34	62	18
k_l	liquid thermal conductivity (W/m·K)	16	51	
μ	viscosity (N·s/m^2)	2.4×10^{-3}	1.78×10^{-3}	
ρ	density (kg/m^3)	10,600	7000	7900
D_l	binary diffusion coefficient, Sn in Pb (m^2/s)	1.5×10^{-9}		
β_T	coefficient of thermal expansion (K^{-1})	1.09×10^{-4}		
β_S	solutal expansion coefficient	0.354		
K_o	permeability coefficient (m^2)	2.8×10^{-11}		

arise in the actual physical system. Furthermore, the solid that precipitates is assumed to form a stationary, coherent mushy zone, and the flow is everywhere assumed to be laminar.

The second and third terms on the right-hand sides of Eqs. (2) and (3), respectively, are Darcy damping terms, which involve permeability components K_z and K_r. In this study, permeability is assumed to be isotropic ($K_z = K_r = K$) and is evaluated from the Blake–Kozeny model (Bennon and Incopera, 1987b):

$$K = K_o\left[\frac{g_l^3}{(1-g_l)^2}\right] \tag{6}$$

where the permeability coefficient K_o, which is listed in Table 1, was determined from representative dendrite arm spacings for Pb–Sn systems (Nasser-Rafi et al., 1985). Shahani et al. (1992) used a hybrid permeability model proposed by West (1985) in their simulations of Pb–Sn solidification experiments. The effects of anisotropic permeability on solidification behavior have been studied recently by Yoo and Viskanta (1992).

The third term on the right-hand side of Eq. (2) represents the axial body force and accounts for buoyancy, which is affected by both temperature and concentration gradients in the liquid. The buoyancy term is treated in the manner described by Prescott and Incropera (1991).

The transport equations, Eqs. (1)–(5), are mutually coupled, and in this study, local thermodynamic equilibrium is assumed to exist, thereby providing closure (i.e., relationships between h, f^{Sn}, T, f_s, etc.). These relationships have been delineated previously (Prescott and Incropera, 1991), along with the manner in which they are implemented for the Pb–Sn system.

Figure 2 shows the problem domain and the numerical mesh used for its discretization. The system is patterned after an experimental apparatus (Prescott et al., 1994) for which $H = 150$ mm, $H/(r_o - r_i) = 3.15$, and $r_o/r_i = 4$. The outer and inner mold wall thicknesses are $t_o/(r_o - r_i) = 0.098$ and $t_i/(r_o - r_i) = 0.067$, respectively, and the bottom mold wall thickness is $t_b/(r_o - r_i) = 0.167$. It was determined in a previous study (Prescott and Incropera, 1991) that a 50×50 mesh of the mold cavity is suitable for resolving important physical features of the problem. Additional nodes were added to accommodate the inner and outer vertical mold walls and the mold bottom, bringing the mesh size to 54 radial nodes by 53 vertical nodes. Within the mold cavity, the grid was biased in the radial direction such that the total volume was equally distributed among all control volumes. While the mold walls do not significantly increase resistance to heat transfer, they represent approximately 20 percent of the heat capacity of the system and are

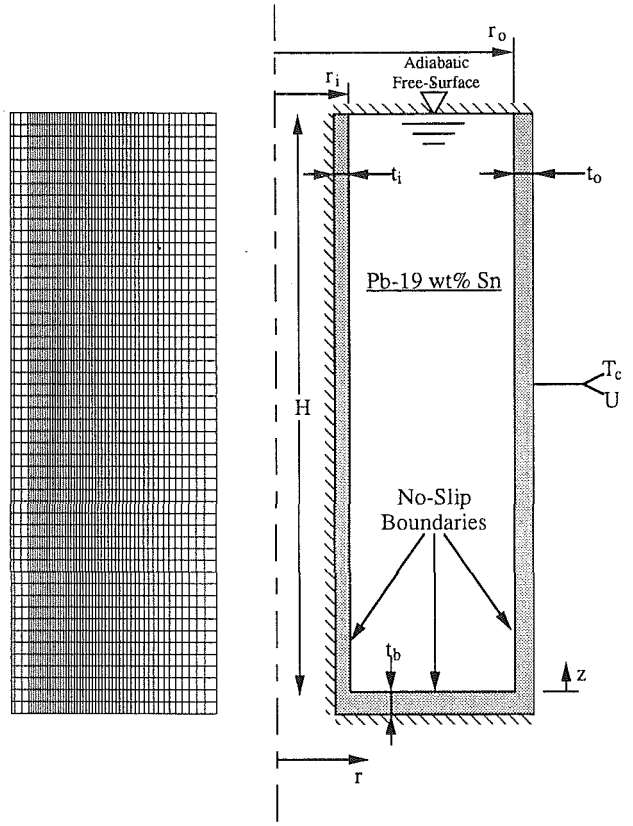

Fig. 2 The simulation system

hence included in the simulations. Control volumes associated with the mold are modeled to be unconditionally solid. Time steps of 0.25 s were used to resolve the system transients in a control-volume-based finite-difference method (Patankar, 1980), with a fully implicit time marching scheme.

Initially, both the melt and the mold are isothermal at 305°C, which is 20°C above the nominal liquidus temperature. Also, at $t = 0$ s the melt is chemically homogeneous and quiescent. Cooling occurs through the outer vertical surface of the mold, where the heat flux is assumed to obey the following relation:

$$q'' = U[T(r_o + t_o, z, t) - T_c] \tag{7}$$

The overall heat transfer coefficient, U, is set at 35 W/m^2·K (Prescott et al., 1994), which effects a cooling rate associated with large macrosegregation (Prescott and Incropera, 1991), and the chill temperature is set at $T_c = 13$°C, which is characteristic of a water-cooled mold. The top, bottom, and inner boundaries are adiabatic. Contact resistance between the mold and alloy is assumed to be negligible. The interface between the mold and the melt is modeled to be slip-free and impermeable to both Pb and Sn. It is assumed that the meniscus is shear-free and that no mass transfer occurs through the free surface.

The properties of the Pb and Sn constituents are listed in Table 1, along with properties of the stainless steel mold. Solid and liquid phase properties are found using the following linear relationships:

$$k_k = g_k^{Pb}k_k^{Pb} + g_k^{Sn}k_k^{Sn} \quad (k = s,l) \tag{8}$$

$$\mu_l = g_l^{Pb}\mu_l^{Pb} + g_l^{Sn}\mu_l^{Sn} \tag{9}$$

$$c_k = f_k^{Pb}c_k^{Pb} + f_k^{Sn}c_k^{Sn} \quad (k = s,l) \tag{10}$$

Equations (8) and (9) suggest monotonic variations of the transport properties with the volume fraction of phase constituents, while many binary solutions exhibit extrema in their transport properties at intermediate compositions. Nonetheless, Eqs. (8) and (9) are used to estimate transport properties,

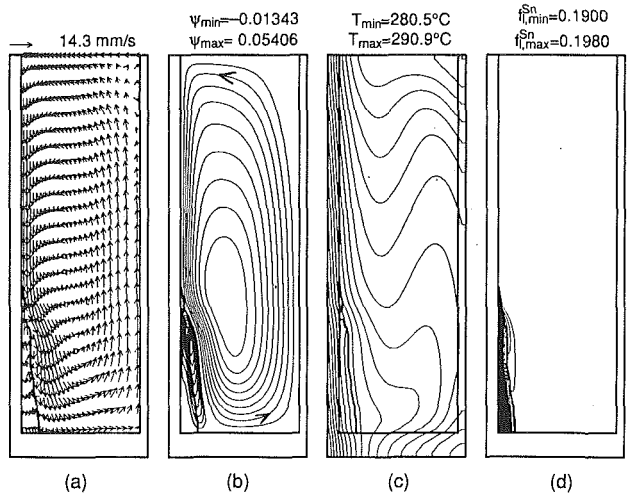

Fig. 3 Convection conditions after 140 seconds of cooling: (*a*) velocity vectors, (*b*) streamlines, (*c*) isotherms, and (*d*) liquid isocomps

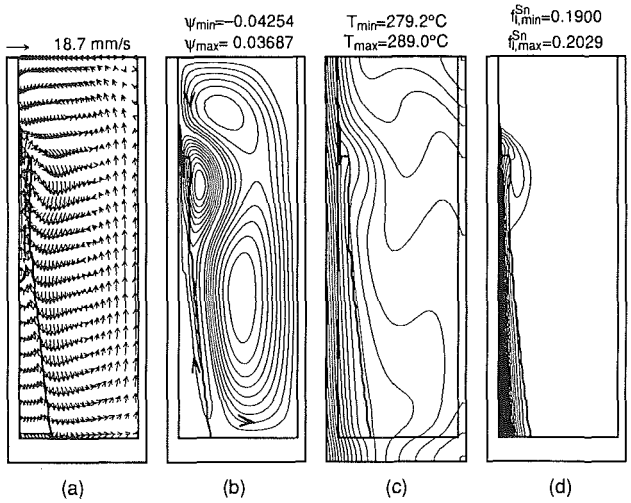

Fig. 4 Convection conditions after 155 seconds of cooling: (*a*) velocity vectors, (*b*) streamlines, (*c*) isotherms, and (*d*) liquid isocomps

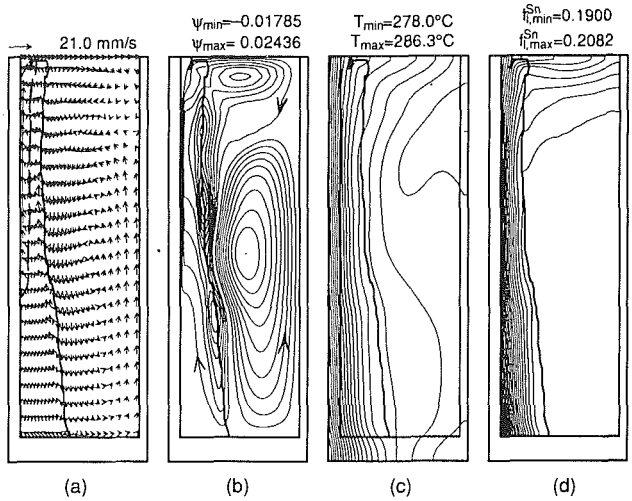

Fig. 5 Convection conditions after 175 seconds of cooling: (*a*) velocity vectors, (*b*) streamlines, (*c*) isotherms, and (*d*) liquid isocomps

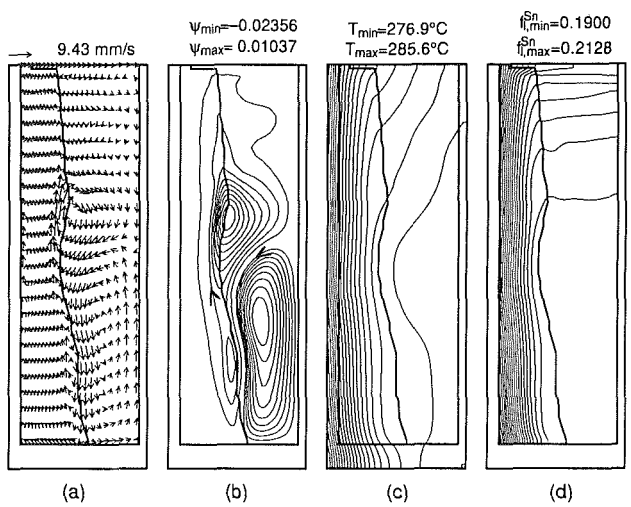

Fig. 6 Convection conditions after 195 seconds of cooling: (*a*) velocity vectors, (*b*) streamlines, (*c*) isotherms, and (*d*) liquid isocomps

since data for two-phase Pb-Sn alloys (Touloukian et al., 1970) indicate a monotonic variation in thermal conductivity with alloy composition and since the viscosity of molten Pb–Sn alloys is a linear function of constituent mole fractions (Thresh and Crawley, 1970). Since the constituent specific heats are tabulated on a unit mass basis (Table 1), Eq. (10) is written in terms of constituent mass fractions. However, Eq. (10) does not account for nonideal mixing effects.

Simulation Results

Convection conditions are represented by field plots of velocity vectors, streamlines, isotherms, and liquid isocomposition lines (liquid isocomps) in Figs. 3–6. These plots are drawn on an r–z plane, with the outer and inner radii shown, respectively, as left and right boundaries. The liquidus interface, which represents the boundary between the melt and mushy zones, is indicated by a thick line on each plot. Fully solidified regions and a solidus interface do not develop until well after convection ceases and hence do not appear in the time interval associated with the figures ($t \leq 195$ s). Velocity vectors are scaled according to the current maximum velocity, which is indicated at the top of each velocity vector plot. These velocities represent mixture velocities ($\mathbf{V}$), and since $\mathbf{V}_s = 0$, $\mathbf{V} = f_l \mathbf{V}_l$. Streamlines associated with clockwise recirculation have negative values and are plotted in ten equal increments between Ψ_{min} and 0, while counterclockwise recirculation cells have positive values, which are plotted in ten equal increments between 0 and Ψ_{max}. Isotherms are plotted in 20 equal increments between the minimum and maximum temperatures, and liquid isocomps are plotted in 20 equal increments between the minimum and maximum values of the liquid composition (expressed as mass fraction Sn). In general, the minimum temperature and maximum liquid composition are found near the outer (left) boundary of the mold cavity. In addition, macrosegregation plots, which indicate mixture (solid + liquid) composition, are presented in Fig. 7, with legends provided to facilitate interpretation.

The Prandtl number of the molten alloy is $\mathrm{Pr} = 0.016$, and the calculated Grashof number based on the hydraulic diameter of the annular cavity and a temperature difference of 5 K is $\mathrm{Gr} = 8.7 \times 10^7$. Since the process under consideration is transient, and nonisothermal boundary conditions have been imposed on the vertical mold walls, the calculated Grashof number must be interpreted with caution. The temperature difference of 5 K used to calculate the Grashof number is the approximate radial temperature difference across the bottom of the cavity during early stages of cooling, before solidification begins. In upper regions of the mold cavity, the temperature difference

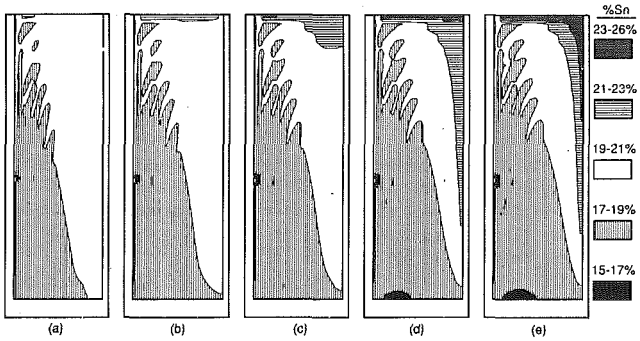

Fig. 7 Macrosegregation after (*a*) 240 seconds, (*b*) 300 seconds, (*c*) 360 seconds, (*d*) 480 seconds, and (*e*) 600 seconds

across the radial span of the mold is smaller than 5 K. Radial temperature differences in the melt become much smaller after solidification begins, and the hydraulic diameter of the molten region gradually decreases due to mushy zone growth. Conditions are further complicated during solidification by solutal buoyancy forces that arise in the mushy zone in opposition to thermal buoyancy forces.

Once cooling is initiated at the outer boundary, a thermal convection cell is established in the melt. The cell is driven by a radial temperature gradient confined within 10 mm of the mold wall, and the central portion of the melt becomes thermally stratified during the initial 90 seconds of cooling. Moreover, convective mixing reduces the temperature gradient throughout the melt, thereby delaying the onset of solidification. At $t \approx 120$ s, solid dendrites begin precipitating at the bottom of the cooled mold wall, thereby forming a two-phase (mushy) zone. As cooling continues, the mushy zone grows, with the liquidus interface moving vertically upward and radially inward, and at $t = 140$ s (Fig. 3), a thin mushy zone of nonuniform thickness is attached to the bottom one-third of the cooled mold wall.

Due to phase equilibrium requirements, the precipitation of solid is accompanied by solute (Sn) enrichment of interdendritic liquid, Fig. 3(*d*), which induces solutal buoyancy forces acting upward on the interdendritic liquid. The solutal buoyancy forces oppose thermal buoyancy forces caused by the radial temperature gradient, Fig. 3(*c*), and because the density of Sn is significantly less than Pb, the solutal forces dominate within the mushy zone ($N = -14$). Hence, solidification within the mushy zone can be regarded as providing an upward momentum source for the interdendritic liquid.

The counterclockwise, thermally driven convection cell at $t = 140$ s, Fig. 3(*b*), is enhanced by heat transfer from the bottom and inner mold walls, which possess a large thermal capacitance, Fig. 3(*c*). The interdendritic fluid that penetrates the liquidus interface at $z^* \approx 0.27$, Figs. 3(*a*) and 3(*b*), is turned downward along the liquidus interface by the momentum of the thermal convection cell, thereby confining the liquid composition gradient primarily within the mushy zone, Fig. 3(*d*). The interdendritic liquid that leaves the mushy zone is replaced with liquid from the bulk melt near the bottom of the cavity, Figs. 3(*a*) and 3(*b*).

As the mushy zone continues to grow, the influence of solutal buoyancy gradually increases, creating very dynamic convection conditions. At $t = 155$ s, Fig. 4, the mushy zone covers approximately 75 percent of the inside surface of the outer mold wall. Fluid is exchanged between the mushy and melt zones in a relatively confined region near the top of the mushy zone, Fig. 4(*b*), where a strong, solutally driven upflow, emerging from the mushy zone, interacts with thermally driven downflow in the bulk melt. The interaction turns both flows radially inward, thereby bisecting the thermal cell and returning discharged interdendritic fluid to the mush zone. Since the Pb–Sn system is characterized by a large Lewis number ($\mathrm{Le} \approx 8600$), fluid within the solutal convection cell readily exchanges energy with the bulk liquid but largely retains its composition. Hence, warm, Sn-enriched fluid from the melt is advected toward the mushy zone, establishing conditions conducive to the development of channels within the mushy zone.

A channel forms when remelting occurs due to combined thermal and solutal conditions and is, therefore, a preferred flow path for interdendritic liquid. A number of recent studies have focused on the mechanisms by which channels form in bottom chilled castings (Chen and Chen, 1991; Felicelli et al., 1991; Neilson and Incropera, 1991; Tait and Jaupart, 1992; Magirl and Incropera, 1993). A slight vertical component of the temperature gradient exists in the mushy zone, and since fluid ascending along the cooled mold wall is enriched with Sn, there is a depression in the local liquidus temperature, which is conducive to remelting. In addition, due to the advection of warm, Sn-rich fluid from the melt into the mushy zone, Figs. 4(*b*)–(*d*), remelting is enhanced, and a channel is spawned. The channel, although not fully melted, is aligned vertically and is located along the mold wall for $z^* \gtrsim 0.5$. It is delineated by a thick dashed line in Fig. 4(*a*). Actual channels are believed to be pencil-shaped regions (little pipes), which form at many discrete circumferential locations, and evidence of such channels is reported in a companion paper (Prescott et al., 1994). Since limitations of the axisymmetric model preclude the prediction of such channels, one must interpret an axisymmetric channel predicted by the model as an indication of where channels are likely to occur in the r–z plane. Furthermore, the predicted channel is not well resolved by the numerical grid, since it occupies only one radial grid point. However, due to limited computational resources, it is not presently feasible to obtain better resolution without restricting attention to the channel and its immediate surroundings.

Convection conditions at $t = 175$ s are shown in Fig. 5. The channel, which exists along the top half of the cooled mold wall, entrains Sn-enriched interdendritic fluid, Figs. 5(*b*) and 5(*d*), and fluid in the channel is accelerated toward the top of the cavity, where Sn-rich layers are formed, Figs. 5(*a*) and 5(*d*). In addition to the exchange of fluid between the mush and melt promoted by the channel, three small recirculation cells are active along the liquidus interface at $z^* \approx 0.3$, 0.6, and 0.8, Fig. 5(*b*). Such recirculations are responsible for establishing preferred flow paths of interdendritic liquid at later times. That is, channels, although not fully melted, are established by small recirculations along the liquidus interface during early solidification stages. Fluid of nominal composition enters the mushy zone at the bottom of these recirculation zones and displaces fluid of higher Sn concentration. Thus, a small Sn-depleted region, with an increased solid fraction and decreased permeability, is created. At the top of a recirculation cell, there exists an Sn-enriched zone with decreased solid fraction and increased permeability. The vertical position of these interfacial recirculation cells changes as the liquidus interface advances inward and upward, thereby creating a series of channels, which manifest themselves as A-segregates in the final casting.

The momentum associated with the thermal convection cell gradually decreases, as temperature gradients in the melt diminish and opposing solutal buoyancy forces increase. At $t = 195$ s, the thermal cell is confined to the bottom half of the fully melted zone, Fig. 6(*b*), while the solutal cell encompasses the mushy zone and the top half of the bulk melt, which has become solutally stratified, Fig. 6(*d*). The thermal cell is completely extinct by 240 seconds, beyond which a large solutally driven cell occupies the entire mold cavity and provides for the recirculation of interdendritic liquid.

Figure 7 shows the evolution of macrosegregation between the times of 240 and 600 seconds. At $t = 240$ s, macrosegregation is characterized by a pattern of A-segregates (Flemings,

1974; Fisher, 1981), Fig. 7(*a*), which formed in the outer periphery of the ingot as a result of thermosolutal convection during the early stages of solidification. The overall mass fraction solid is 10.4 percent at 240 seconds, and macrosegregation continues with time, as solidification and solutal convection in the mushy zone tend to enrich the lower and outer regions of the ingot with Pb and transport Sn to the top and downward along the inner radius. Therefore, during the intermediate stages of solidification, a large cone of Sn-rich material forms on the top and extends deep into the ingot. The development of this cone segregate is illustrated in Figs. 7(*b*)-(*e*). By 600 seconds, the overall mass fraction solid is 45.4 percent, and while the solid fraction in the top part of the cone segregate is less than 10 percent, solid fractions exceed 35 percent throughout the rest of the ingot with Pb-rich zones near the outer radius being 60 percent solidified. Hence, the permeability is sufficiently small in the cavity to inhibit fluid recirculation so that macrosegregation does not evolve significantly past 600 seconds. Finally, since discrete channels form in actual ingots and interdendritic flow patterns are, therefore, three-dimensional (Prescott et al., 1994), local composition variations may exceed those shown in Fig. 7, which are predicted for axisymmetric conditions.

Conclusions

A continuum model for momentum, energy, and species transport during binary solid–liquid phase change was used to simulate the solidification of a Pb–Sn alloy in an experimental apparatus. The effect of the stainless steel mold was included in the simulation, and the results demonstrated the importance of thermosolutal convection during solidification of a metal alloy.

Thermal convection is responsible for thermally stratifying the melt before solidification begins. Hence, a mushy region with highly nonuniform thickness forms along the bottom of the cooled mold wall, and as it grows (upward and radially inward), a solutal convection cell, driven by a radial gradient of liquid Sn concentration, develops in opposition to the thermal convection cell in the bulk melt. Thermal convection is augmented by conjugate heat transfer with bottom and inner mold walls during early stages of solidification, and the competing effects of thermal and solutal buoyancy create dynamic flow conditions and foster the development of channels in the mushy zone, which manifest themselves as A-segregates in a solidified ingot. Once a channel is formed, it entrains interdendritic liquid from warmer regions of the mushy zone. This liquid cools as it approaches a channel and precipitates Pb-rich material in the region adjacent to the channel, while the remaining Sn-rich liquid fills the channel. During intermediate stages of solidification, solutal buoyancy dominates convection conditions and provides for the recirculation of interdendritic liquid, which is responsible for the formation of a large cone segregate at the top of an ingot.

The simulation predicted a macrosegregation pattern, which is characterized, in general, by increasing Sn concentration with increasing height in the ingot and, in the upper portion of the ingot, increasing Sn concentration with decreasing radius. Furthermore, the simulation predicted large gradients in Sn concentration at locations in which channels formed during solidification.

Acknowledgments

The authors are grateful to the U.S. Department of Energy, which supported this work through Award No. DE-FG02-87ER 13759.

References

Amberg, G., 1991, "Computation of Macrosegregation in an Iron–Carbon Cast," *Int. J. Heat Mass Transfer*, Vol. 34, pp. 217–227.

Beckermann, C., and Viskanta, R., 1988, "Double-Diffusive Convection During Dendritic Solidification of a Binary Mixture," *PhysicoChem. Hydrodyn.*, Vol. 10, pp. 195–213.

Bennon, W. D., and Incropera, F. P., 1987a, "A Continuum Model for Momentum, Heat and Species Transport in Binary Solid–Liquid Phase Change Systems—I. Model Formulation," *Int. J. Heat Mass Transfer*, Vol. 30, pp. 2161–2170.

Bennon, W. D., and Incropera, F. P., 1987b, "A Continuum Model for Momentum, Heat and Species Transport in Binary Solid–Liquid Phase Change Systems—II. Application to Solidification in a Rectangular Cavity," *Int. J. Heat Mass Transfer*, Vol. 30, pp. 2171–2187.

Bennon, W. D., and Incropera, F. P., 1987c, "The Evolution of Macrosegregation in Statically Cast Binary Ingots," *Metall. Trans. B*, Vol. 18B, pp. 611–616.

Chen, C. F., and Chen, F., 1991, "Experimental Study of Directional Solidification of Aqueous Ammonium Chloride Solution," *J. Fluid Mech.*, Vol. 227, pp. 567–586.

Christenson, M. S., Bennon, W. D., and Incropera, F. P., 1989, "Solidification of an Aqueous Ammonium Chloride Solution in a Rectangular Cavity—II. Comparison of Predicted and Measured Results," *Int. J. Heat Mass Transfer*, Vol. 32, pp. 69–79.

Felicelli, S. D., Heinrich, J. C., and Poirier, D. R., 1991, "Simulation of Freckles During Vertical Solidification of Binary Alloys," *Metall. Trans. B*, Vol. 22B, pp. 847–859.

Fisher, K. M., 1981, "The Effects of Fluid Flow on the Solidification of Industrial Castings and Ingots," *PhysicoChem. Hydro.*, Vol. 2, pp. 311–326.

Flemings, M. C., and Nereo, G. E., 1967, "Macrosegregation: Part I," *Trans. Metall. Soc. AIME*, Vol. 239, pp. 1449–1461.

Flemings, M. C., Mehrabian, R., and Nereo, G. E., 1968, "Macrosegregation: Part II," *Trans. Metall. Soc. AIME*, Vol. 242, pp. 41–49.

Flemings, M. C., 1974, "Solidification Processing," *Metall. Trans.*, Vol. 5, pp. 2121–2134.

Fujii, T., Poirier, D. R., and Flemings, M. C., 1979, "Macrosegregation in a Multicomponent Low Alloy Steel," *Metall. Trans. B*, Vol. 10B, pp. 331–339.

Ganesan, S., and Poirier, D. R., 1990, "Conservation of Mass and Momentum for the Flow of Interdendritic Liquid During Solidification," *Metall. Trans. B*, Vol. 21B, pp. 173–181.

Heinrich, J. C., Felicelli, S., and Poirier, D. R., 1991, "Vertical Solidification of Dendritic Binary Alloys," *Comp. Meth. Appl. Mech. Engrg.*, Vol. 89, pp. 435–461.

Kou, S., Poirier, D. R., and Flemings, M. C., 1978, "Macrosegregation in Rotated Remelted Ingots," *Metall. Trans. B*, Vol. 9B, pp. 711–719.

Magirl, C. S., and Incropera, F. P., 1993, "Flow and Morphological Conditions Associated With Unidirectional Solidification of Aqueous Ammonium Chloride," ASME JOURNAL OF HEAT TRANSFER, Vol. 115, pp. 1036–1043.

Mehrabian, R., Keane, M., and Flemings, M. C., 1970, "Interdendritic Fluid Flow and Macrosegregation; Influence of Gravity," *Metall. Trans.*, Vol. 1, pp. 1209–1220.

Nandapurkar, P. J., Poirier, D. R., and Heinrich, J. C., 1991, "Momentum Equation for Dendritic Solidification." *Num. Heat Transfer, A*, Vol. 19, pp. 297–311.

Nasser-Rafi, R., Deshmukh, R., and Poirier, D. R., 1985, "Flow of Interdendritic Liquid and Permeability in Pb-20 wt pct Sn Alloys," *Metall. Trans A*, Vol. 16A, pp. 2263–2271.

Neilson, D. G., Incropera, F. P., and Bennon, W. D., 1990, "Numerical Simulation of Solidification in a Horizontal Cylindrical Annulus Charged With an Aqueous Salt Solution," *Int. J. Heat Mass Transfer*, Vol. 33, pp. 367–380.

Neilson, D. G., and Incropera, F. P., 1991, "Unidirectional Solidification of a Binary Alloy and the Effects of Induced Fluid Motion," *Int. J. Heat Mass Transfer*, Vol. 34, pp. 1717–1732.

Patankar, S. V., 1980, *Numerical Heat Transfer and Fluid Flow*, McGraw-Hill, New York.

Poirier, D. R., Nandapurkar, P. J., and Ganesan, S., 1991, "The Energy and Solute Conservation Equations for Dendritic Solidification," *Metall. Trans. B*, Vol. 22B, pp. 889–900.

Prescott, P. J., and Incropera, F. P., 1991, "Numerical Simulation of a Solidifying Pb–Sn Alloy: The Effects of Cooling Rate on Thermosolutal Convection and Macrosegregation," *Metall. Trans. B*, Vol. 22B, pp. 529–540.

Prescott, P. J., Incropera, F. P., and Bennon, W. D., 1991, "Modeling of Dendritic Solidification Systems: Reassessment of the Continuum Momentum Equation," *Int. J. Heat Mass Transfer*, Vol. 34, pp. 2351–2359.

Prescott, P. J., and Incropera, F. P., 1993, "Binary Solid–Liquid Phase Change With Fluid Flow," in: *Advances in Transport Processes IX*, Elsevier, Amsterdam, pp. 57–101.

Prescott, P. J., Incropera, F. P., and Gaskell, D. R., 1994, "Convective Transport Phenomena and Macrosegregation During Solidification of a Binary Metal Alloy—II. Experiments and Comparisons With Numerical Predictions," ASME JOURNAL OF HEAT TRANSFER, Vol. 116, this issue, pp. 742–749.

Ridder, S. D., Kou, S., and Mehrabian, R., 1981, "Effect of Fluid Flow on Macrosegregation in Axi-symmetric Ingots," *Metall. Trans. B.*, Vol. 12B, pp. 435–447.

Shahani, H., Amberg, G., and Fredriksson, H., 1992, "On the Formation of Macrosegregations in Unidirectionally Solidified Sn–Pb and Pb–Sn Alloys," *Metall. Trans. A*, Vol. 23A, pp. 2301–2311.

Szekely, J., and Jassal, A. S., 1978, "An Experimental and Analytical Study of the Solidification of a Binary Dendritic System," *Metall. Trans. B*, Vol. 9B, pp. 389–398.

Tait, S., and Jaupart, C., 1992, "Compositional Convection in a Reactive Crystalline Mush and Melt Differentiation," *J. Geophys. Res.*, Vol. 97, pp. 6735–6756.

Thresh, H. R., and Crawley, A. F., 1970, "The Viscosities of Lead, Tin, and Pb–Sn Alloys," *Metall. Trans.*, Vol. 1, pp. 1531–1535.

Touloukian, Y. S., Powell, R. W., Ho, C. Y., and Klemens, P. G., 1970, *Thermophysical Properties of Matter*, IFI/Plenum, New York.

Viskanta, R., and Beckermann, C., 1987, "Mathematical Modeling of Solidification," in: *Interdisciplinary Issues in Materials Processing and Manufacturing*, Samanta et al., eds., ASME, New York, pp. 501–526.

Viskanta, R., 1990, "Mathematical Modeling of Transport Processes During Solidification of Binary Systems," *JSME International Journal, Series II*, Vol. 33, pp. 409–423.

Voller, V. R., and Prakash, C., 1987, "A Fixed Grid Numerical Modelling Methodology for Convection-Diffusion Mushy Region Phase-Change Problems," *Int. J. Heat Mass Transfer*, Vol. 30, pp. 1709–1719.

Voller, V. R., Brent, A. D., and Prakash, C., 1989, "The Modelling of Heat, Mass and Solute Transport in Solidification Systems," *Int. J. Heat Mass Transfer*, Vol. 32, pp. 1718–1731.

West, R., 1985, "On the Permeability of the Two-Phase Zone During Solidification of Alloys," *Metall. Trans. A*, Vol. 16A, p. 693.

Xu, D., and Li, Q., 1991a, "Gravity- and Solidification-Shrinkage-Induced Liquid Flow in a Horizontally Solidified Alloy Ingot," *Num. Heat Transfer A*, Vol. 20, pp. 203–221.

Xu, D., and Li, Q., 1991b, "Numerical Method for Solution of Strongly Coupled Binary Alloy Solidification Problems," *Num. Heat Transfer A*, Vol. 20, pp. 181–201.

Yoo, H., and Viskanta, R., 1992, "Effect of Anisotropic Permeability on the Transport Process During Solidification of a Binary Mixture," *Int. J. Heat Mass Transfer*, Vol. 35, pp. 2335–2346.

Convective Transport Phenomena and Macrosegregation During Solidification of a Binary Metal Alloy: II—Experiments and Comparisons With Numerical Predictions

P. J. Prescott
Department of Mechanical Engineering,
The Pennsylvania State University,
University Park, PA 16802

F. P. Incropera
Heat Transfer Laboratory,
School of Mechanical Engineering.

D. R. Gaskell
School of Materials Engineering.

Purdue University,
West Lafayettte, IN 47907

Experiments involving the solidification of a Pb–19 percent Sn alloy in an axisymmetric, annular mold of stainless steel are performed, and results are compared with numerical predictions. Agreement between measured and predicted cooling curves is reasonable, although undercooling and recalescence, which occur in the experiments, are not predicted by the model. Measured temperatures also indicate that dendrite fragments are transported throughout the mold cavity during early stages of solidification, and convection patterns similar to those predicted by numerical simulation can be inferred from the measurements. While there is general agreement between measured and predicted trends for macrosegregation, the numerical simulation, which assumes axial symmetry, cannot predict the inherently three-dimensional nature of solute redistribution. Conclusions drawn from temperature and composition measurements are supported by metallographic examinations of experimental ingot specimens.

Introduction

To gain a better understanding of convective phenomena associated with the solidification of metal alloys, research has recently focused on binary solid–liquid phase change and the complex coupling of momentum, energy, and species transfer in a domain that is occupied by fully solidified, fully melted, and mushy zones whose interfaces are continually moving. The solid–liquid interface within the mushy zone is highly irregular, with characteristic length scales that render it irresolvable in the macroscopic sense, and since fluid flows through the dendritic array, it may be viewed as a porous medium with a time-varying, inhomogeneous, and anisotropic permeability. Moreover, during solidification, undercooling and other nonequilibrium effects governed by microscopic transport may be significant and dendrites can be remelted or fractured and entrained in liquid convection cells.

Despite the complex nature of binary solid–liquid phase change, significant advances have been made in obtaining solutions to mathematical models, which include convective transport phenomena (Bennon and Incropera, 1987a, b; Voller and Prakash, 1987; Beckermann and Viskanta, 1988; Voller et al., 1989). However, experimental data, to which model predictions have been compared (Beckermann and Viskanta, 1988; Christenson et al., 1989; Neilson et al., 1990), are limited and, with the exception of the recent work of Shahani et al. (1992), restricted to experiments involving aqueous analog alloys, rather than binary metal alloys.

Convection patterns in molten metals are difficult to discern experimentally, especially for buoyancy-driven flows (Stewart and Weinberg, 1969, 1971, 1972; Wolff et al., 1988), rendering numerical simulation especially attractive. However, it is imperative that numerical models be validated. In a companion paper (Prescott and Incropera, 1994), a continuum model (Bennon and Incropera, 1987a; Prescott et al., 1991) was applied to simulate the solidification of a Pb–Sn alloy in an experimental test cell. In this paper, experimental results are presented to assess the validity of the model and to obtain an improved understanding of the effects of convection on the solidification process. Temperature and composition measurements, as well as metallographic examinations, are obtained for a Pb–Sn alloy in an axisymmetric, annular mold, cooled through its outer wall. The Pb–Sn system was selected on the basis of its relatively low melting temperatures, its well-characterized equilibrium phase diagram and thermophysical properties, the large density difference between Pb and Sn, and the availability of pure grades of Pb and Sn. A specific composition of Pb–19 wt% Sn was selected because its freezing range (96°C) enhances macrosegregation, and solidification induces opposing thermal and solutal buoyancy forces. Within the mushy zone, solutal buoyancy forces are approximately 14 times larger than thermal buoyancy forces. The equilibrium phase diagram of the Pb–Sn system, as well as related thermophysical properties appear in the companion paper (Prescott and Incropera, 1994).

Shahani et al. (1992) solidified Pb–Sn alloys in a rectangular test cell, across which a horizontal temperature difference was maintained, and they measured transient mold wall temperatures and macrosegregation in solidified ingots. The measured macrosegregation patterns were compared to predictions based on simulations that used measured mold wall temperatures as thermal boundary conditions. Although reasonable agreement was found between measured and predicted macrosegregation patterns, details regarding transient convection phenomena were not revealed experimentally.

Contributed by the Heat Transfer Division for publication in the JOURNAL OF HEAT TRANSFER. Manuscript received by the Heat Transfer Division March 1993; revision received September 1993, Keywords: Double Diffusion Systems, Materials Processing and Manufacturing Processes, Phase-Change Phenomena. Associate Technical Editor: R. Viskanta.

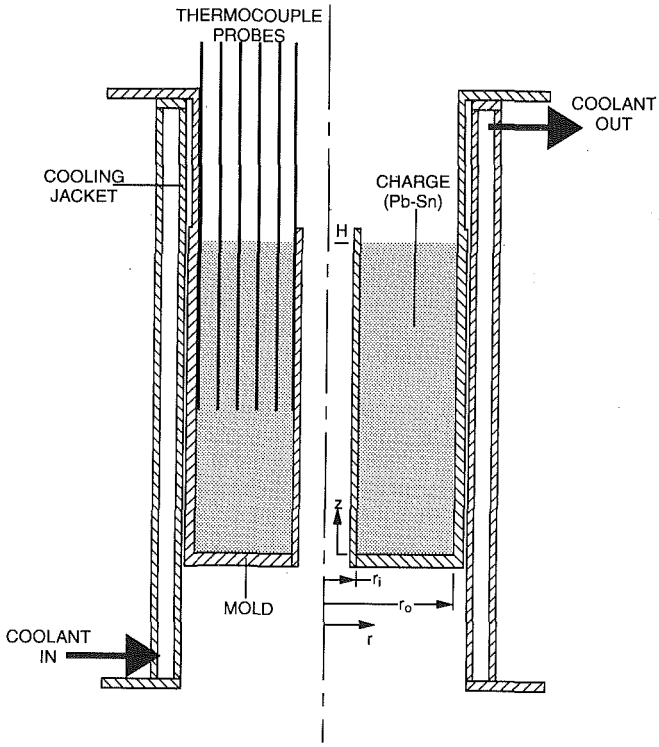

Fig. 1 Cross-sectional schematic of the experimental apparatus

Experimental Apparatus and Procedures

Test Cell. Figure 1 shows a cross-sectional schematic of the axisymmetric test cell, which includes a stainless steel mold and a cooling jacket. The mold is suspended concentrically within the cooling jacket and contains a center tube, which houses an electric heater used to melt a Pb–Sn charge. During solidification, water flows through the cooling jacket, inducing radial heat transfer from the mold. The inner and outer radii of the mold cavity are r_i = 15.9 mm and r_o = 63.5 mm, respectively, and the meniscus ($z = H$) of the melt is 150 mm above the bottom of the mold cavity. The thicknesses of the outer vertical and bottom mold walls are approximately 4 mm and 10 mm, respectively. Since the cooling jacket is quenched by direct contact with the coolant, its thermal capacitance has a negligible influence on cooling of the mold and melt.

The apparatus was designed with a small gap ($\approx$1.68 mm) between the inner surface of the cooling jacket and the outer surface of the mold, which serves as the controlling resistance to heat transfer during an experiment. Heat transfer between the outer mold wall and the inner surface of the cooling jacket occurs by conduction and radiation acting in parallel, and since the gap is small compared to the mean diameter, the two surfaces are modeled as parallel planes. The overall heat transfer coefficient between the two surfaces is then

$$U = h_{\text{cond}} + h_{\text{rad}} = \frac{k_{\text{air}}}{l} + (\epsilon/2 - \epsilon)\sigma(T_T^2 + T_c^2)(T_h + T_c) \quad (1)$$

where the total emissivities of both surfaces are assumed to be equivalent ($\epsilon_h = \epsilon_c = \epsilon$). With ϵ estimated to be 0.85, T_h = 305°C (578 K), T_c = 13°C (286 K), k_{air} = 0.034 W/m K, and l = 1.68 mm, the overall heat transfer coefficient U is 35 W/m^2·K. Auxiliary experiments were performed, and the average overall heat transfer coefficient between the mold and coolant was measured and found to be 35 W/m^2·K (±10 percent). Details of the experimental apparatus and the auxiliary experiments are documented elsewhere (Prescott, 1992).

Table 1 Radial locations of mold cavity thermocouple probes

PROBE	r (mm)	r*
1	63.5	1
2	54.0	0.8
3	44.5	0.6
4	34.9	0.4
5	25.4	0.2
6	15.9	0

Temperature Measurements. Temperature measurements were made within the mold cavity using an array of type E thermocouple probes inserted through a top lid (Fig. 1). Although the six probes could be traversed vertically, their radial locations were fixed (Table 1). Each probe contained 0.25 mm thermocouple wires, insulated with magnesium oxide (MgO) within a stainless steel sheath of 1.6 mm diameter and 305 mm length. The thermocouple junction in each probe was unexposed and grounded to the probe tip, thereby insuring protection from the alloy and an acceptable time constant (<1 s) (Prescott, 1992). Mold wall temperatures were measured at six locations corresponding to six values of the circumferential coordinate (θ = 0, 60, 120, 180, 240, 300 deg) and three values of the vertical coordinate (z^* = 0.25, 0.50, 0.75). Type E

Nomenclature

C = concentration of AAS sample solution, ppm
DAS = dendrite arm spacing, μm
H = height of mold cavity, m
h = heat transfer coefficient, W/m^2•K
k = thermal conductivity, W/m•K
K_o = permeability coefficient, m^2
l = gap width, m
Ra_d = difference Rayleigh number $= g\beta\Delta TH^4/(\nu\alpha(r_o - r_i))$
r = radius, m
r^* = dimensionless radial coordinate $= (r - r_i)/(r_o - r_i)$
T = temperature, °C or K
t = time, s, or thickness, m
U = overall heat transfer coefficient, W/m^2•K
z = axial position, m
z^* = dimensionless axial coordinate $= z/H$
ΔT_i = initial liquid superheat
Δ%Sn = difference between local and nominal wt% Sn
ϵ = emissivity
θ = circumferential coordinate, deg
σ = Stefan–Boltzmann constant $= 5.67 \times 10^{-8}$ W/m^2·K^4

Subscripts

1, 2 = primary and secondary
c = coolant or cold surface
cond = conduction
h = hot surface
i = initial or inner
o = outer
rad = radiation

Superscripts

Pb = lead
TDS = total dissolved solid

thermocouple wires (0.127 mm diameter), sheathed in 0.8 mm diameter stainless steel tubing and insulated with MgO, were tack-welded into vertical grooves (0.9 mm by 0.9 mm) on the outer mold wall. The measuring thermocouple junctions were welded to the mold at the edge of the groove, adjacent to the outer mold wall.

Thermocouple voltages were measured with a Hewlett-Packard 3054A Automatic Data Acquisition/Control Unit, which includes an HP 3497A controller, an HP 3456A digital voltmeter, and an HP 9826 computer. The HP 3456A digital voltmeter has a resolution of 100 nV, an accuracy of 5.2 μV in its d.c. mode of operation, good normal mode noise rejection, and an input impedance of 10^{10} Ω. Measurements were made by using electronic ice-point compensation with a piecewise third-order polynomial algorithm, for which results agreed with thermocouple tables to within 0.06°C over the temperature range of interest (Prescott, 1992). However, other sources of measurement error exist, and the total uncompensable, absolute error is estimated to be $\pm$1°C, with a relative (probe-to-probe) error of 0.1°C (Prescott, 1992). Since thermocouples attached to the mold wall could not be calibrated, the uncertainty in their measurements is estimated to be $\pm$2.0°C.

Macrosegregation Measurements. Post-experiment measurements were made to determine the extent of macrosegregation in the final casting. After removing the ingot from the mold, thin sections, representing r–z planes, were extracted by saw-cutting. The rough surfaces produced by the saw-cutting were removed by fly-cutting the surfaces in an end mill, using a sharp, well-rounded cutting tool. Small samples of material were than taken from specific locations by drilling 1.6 mm diameter holes approximately 3 mm into the section and collecting the ribbon of material that was generated. The mass of each sample was measured to within 0.1 mg, dissolved in nitric and hydrochloric acids, and diluted with deionized water to a known concentration of total dissolved solid (TDS).

The composition of the sample was determined by measuring the concentration of Pb in the sample solution with an atomic absorption spectrophotometer and by comparing the Pb concentration to that of TDS. It follows that the percentage of tin in the drilled sample is

$$\%\mathrm{Sn} = \frac{C^{\mathrm{TDS}} - C^{\mathrm{Pb}}}{C^{\mathrm{TDS}}} \times 100\% = (1 - C^{\mathrm{Pb}}/C^{\mathrm{TDS}}) \times 100\% \quad (2)$$

Details regarding macrosegregation measurements and their estimated uncertainties ($\pm$0.4 percent) are documented elsewhere (Prescott, 1992).

Metallography. Metallographic analysis of specimens taken from experimental ingots is an important aspect of this work, as it provides information regarding characteristics of the mushy zone during solidification. The metallurgical structure (i.e., columnar or equiaxed grains) and dendrite arm spacings are determined from macro/micrographs of polished specimens. Also, regions of high porosity or of accumulated eutectic material, which are indications of channeling of interdendritic liquid during solidification, can be identified metallographically.

After an experiment was performed, the ingot was machined to yield thin sections representing either r–z or r–θ planes. The surfaces of each section were finished by fly-cutting with a sharp, well-rounded tool, and small specimens (approximately 20 mm by 20 mm) were extracted from each section and polished in two steps on lapping wheels. The first polishing operation used 6 μm diamond abrasive on a nylon cloth, with an oil lubricant, and the second polishing wheel used 0.5 μm alumina abrasive on a soft cloth (e.g., Leco LeCloth B) for the final finish.

The metallographic structure of a polished specimen was examined under low magnifications (10× to 50×) with a metallographic microscope (Leco 300 Metallograph), equipped with a Polaroid Land camera. Polaroid type 55 film was used to record images from the microscope.

Experimental Procedure. The procedure began by heating and melting the charge in a well-insulated mold within a dry cooling jacket. After melting, the top insulating material was removed and the vertical position of the meniscus was measured from the top of the mold flange. If necessary, additional charge was added to raise the meniscus to a position of approximately 76 mm beneath the top of the mold flange. Dross was removed from the top of the melt, and the melt was stirred to insure homogeneity. The insulation was then replaced with the top lid, and the array of thermocouples was adjusted to its intended vertical position. The region at the top of the mold was purged with argon to minimize oxidation.

The melt was maintained at a temperature approximately 20°C above the intended initial condition for at least twenty minutes before cutting the power to the heater. The melt quickly became isothermal to within 2°C, as it cooled at a rate of approximately 1.3°C per minute. During this slow cooling process, the data acquisition unit scanned all of the thermocouple channels at a rate of approximately 0.4 s^{-1}, and when one of the thermocouples on the mold wall (z = 38 mm, θ = 300 deg) reached the intended initial temperature, the data logger was triggered to begin collecting and storing the measurements. The flow of cooling water was activated at t = 30 s by opening a ball valve. Initially, the coolant throttle was opened fully to maximize the cooling rate, and at t = 75 s the coolant was throttled to the desired flow rate. Data were collected for 45 minutes, before the experiment was concluded. After an experiment, coolant flow was terminated, the cooling jacket was drained, and the apparatus was readied to begin another run with the thermocouple probes in a different position. The final experiment was made with the thermocouple probes positioned above the meniscus, thereby permitting removal of the ingot from the mold.

Preliminary runs were performed before a set of final experiments, in order to insure axisymmetric cooling by adjusting the position of the mold within the coolant jacket. Cooling curves corresponding to the six thermocouples on the mold wall were examined after each run, and shimming screws on the mold flange were adjusted accordingly. A misalignment between the cooling jacket and the mold was indicated by disagreement between wall temperature measurements corresponding to the same vertical position. Typically, three to six trial runs and associated shimming adjustments were required to achieve good axial symmetry.

Experimental Results and Comparisons With Numerical Predictions

Six identical experiments (E-1 through E-6) were performed, using a Pb–19 wt pct Sn alloy with a 20°C initial superheat. Figure 2, which plots mold wall temperatures as functions of time from the final run (#4) of experiment E-1, shows that the mold is cooled axisymmetrically. Similar conditions were achieved for all runs (1–4) of experiment E-1, and good repeatability was achieved in all the experiments. The cooling rate became steady at approximately 6.6°C/min soon after the experiment began. At approximately 240 s, the rate decreased suddenly to approximately 1.6°C/min, indicating the onset of solidification, and subsequently increased gradually. At $t \approx 1200$ s, the rate became steady again at 3.7°C/min, and at $t \approx 2300$ s, an isothermal eutectic reaction occurred within the mold, temporarily halting cooling. The smaller cooling rates between 240 and 2300 s are attributed to the release of latent heat within the mushy zone, which occurred simultaneously with sensible energy changes.

Cooling curves at six different radii within the mold cavity are plotted in Fig. 3 for experiment E-1. Again, cooling is

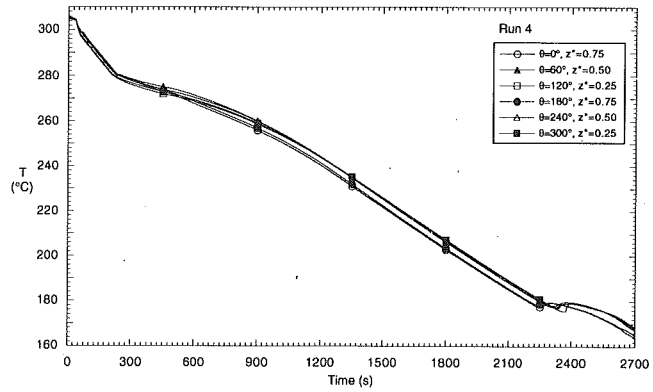

Fig. 2 Mold wall temperatures measured during run 4 of experiment E-1

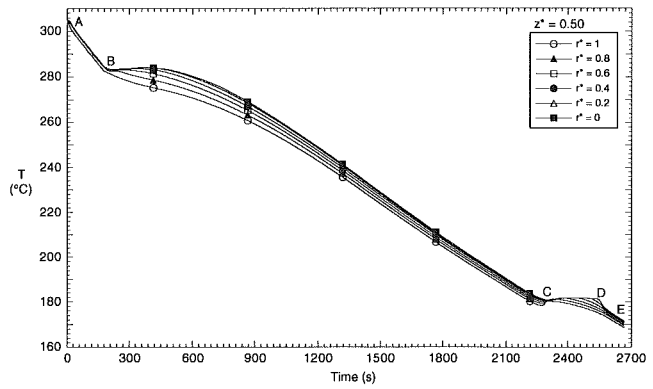

Fig. 3 Cooling curves at $z^* = 0.50$ for experiment E-1 ($0 \le t \le 2700$ s)

characterized by four stages, which begin with cooling of a superheated melt (*A*–*B*). The slopes of the cooling curves change abruptly at $t \approx 165$ s, marking the onset of solidification. The alloy solidifies continuously (*B*–*C*) as its temperature decreases by approximately 100°C, and solidification ends with an isothermal eutectic reaction (*C*–*D*) which begins at $t \approx 2300$ s. Following the eutectic reaction, the fully solidified ingot continues to cool (*D*–*E*).

Significant convection phenomena occur during the early stages of cooling ($0 < t \le 600$ s), and the effects on temperature are shown in Figs. 4(*a*)-(*c*) for $z^* = 0.083$, 0.50, and 0.83, respectively. Temperature fluctuations are pronounced before solidification begins, particularly near the bottom of the cavity and for $0.2 \le r^* \le 0.8$, Fig. 4(*a*). Such fluctuations are characteristic of natural convection in liquid metals (Hurle et al., 1974) and can be used to assess qualitatively the state of convection in solidification systems (Uhlmann et al., 1966; Vives and Perry, 1986, 1987). They are attributed to mixing caused by large eddies, which develop under unstable, but not necessarily turbulent, flow conditions (Gill, 1974; Mohamad, 1992). Gill (1974) found the onset of such instabilities to occur in liquid metals at a critical difference Rayleigh number of approximately 10^3. Although the conditions of this study are transient with nonisothermal boundary conditions, a difference Rayleigh number is estimated to be $\mathrm{Ra}_d = 1.5 \times 10^7$ for conditions prior to solidification. Following the commencement of solidification, the cooling curves become smooth as the developing dendritic array strongly dampens fluid motion and stabilizes the flow.

The cooling curves of Figs. 4(*a*)–(*c*) reveal a period of time, immediately after the commencement of solidification, during which the temperature increases for $r^* \le 0.8$. This nonequilibrium phenomenon is termed recalescence (Kurz and Fisher, 1984), and it occurs following nucleation in an undercooled

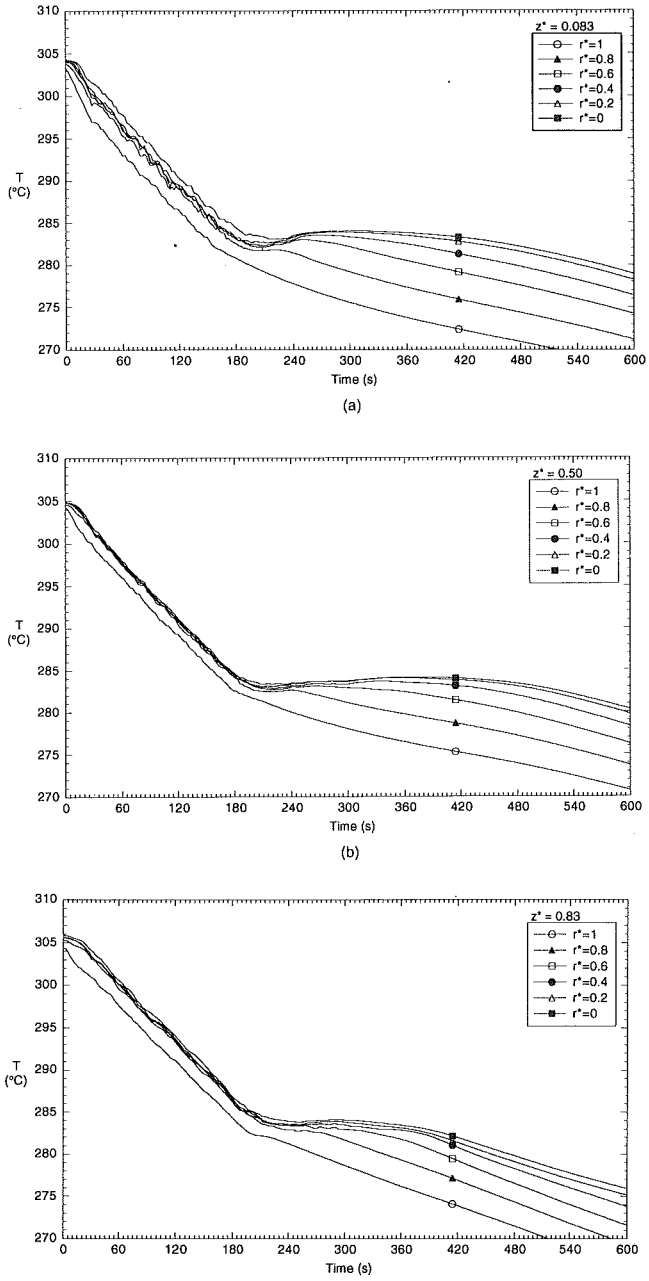

Fig. 4 Cooling curves for experiment E-1 ($0 \le t \le 600$ s): (*a*) $z^* = 0.083$ (*b*) $z^* = 0.50$, and (*c*) $z^* = 0.83$.

melt. Since undercooling provides a large thermodynamic potential for phase change, it drives a relatively rapid rate of solidification following nucleation, and the attendant release of latent heat increases the local temperature. The effect of releasing latent heat is countered by external cooling, and near the outer mold wall ($r^* = 1$), the cooling effect dominates that of latent heat release and prevents recalescence. Nonetheless, the effect of latent heat release is manifested at $r^* = 1$ by the change in slope of the corresponding cooling curves.

Small-amplitude temperature oscillations occur during recalescence for $r^* \le 0.6$, Figs. 4(*a*)–(*c*). Near the bottom of the cavity, Fig. 4(*a*), the oscillations are fully damped approximately 120 s after nucleation, while they persist for longer periods of time at the higher locations. Figs. 4(*b*) and 4(*c*). Coincident with the temperature oscillations during recalescence is a very small radial temperature gradient (nearly isothermal conditions) in the central region of the cavity, Figs.

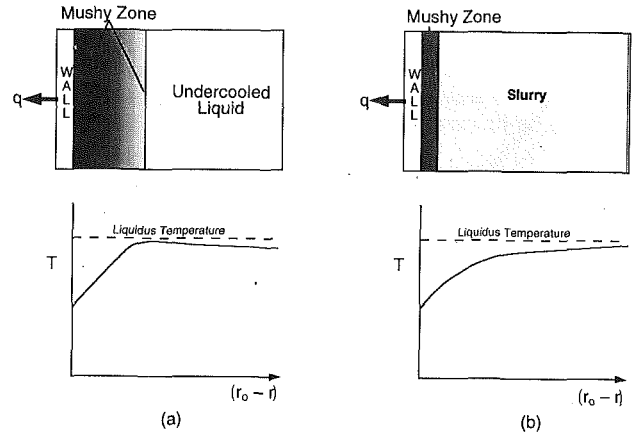

Fig. 5 Solidification in an undercooled melt: (*a*) mushy zone stays attached to the mold wall, (*b*) dendrites fracture and form a slurry with the bulk liquid

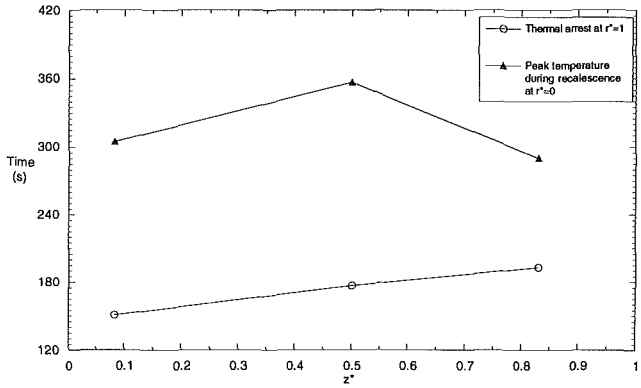

Fig. 6 Times of nucleation and peak of recalescence as functions of vertical position within the mold cavity

4(*b*) and 4(*c*). However, the radial temperature gradients remain negative throughout the period of recalescence, and their magnitudes increase as the temperature oscillations become fully damped.

The foregoing observations provide strong evidence for the existence of a convecting slurry, consisting of liquid and dendrite fragments. For transient, thermally driven flow of a low-Prandtl-number fluid, peak velocities occur near the mold wall. Hence, forces associated with the relatively large momentum of fluid in crossflow over dendrites protruding from the wall could fracture the dendrites, causing them to detach from the wall. Detached, free-floating crystals grow as they are transported through the undercooled melt, and at interior regions of the mold, where heat loss is less significant, the temperature increases due to the release of latent heat.

If free-floating crystals were not present in the undercooled melt, a different temperature distribution would characterize the data. Figure 5 illustrates two possible temperature profiles that could occur during recalescence. If the dendritic structure remains coherent and attached to the mold wall, Fig. 5(*a*), an inverted temperature profile would be observed as the mushy zone advances into an undercooled melt. That is, the release of latent heat would be confined to the mushy zone and would be most pronounced near the the advancing interface. Conversely, if solid fragments were swept into the melt by convection, Fig. 5(*b*), latent heat would be released more uniformly. Since recalescence is determined by the relative rates of latent heat release and external heat transfer, it would be more pronounced at locations further away from the cooling surface.

Figures 4(*a*)–(*c*) reveal that the times at which nucleation occurs at $r^* = 1$ and at which temperatures achieve a temporary

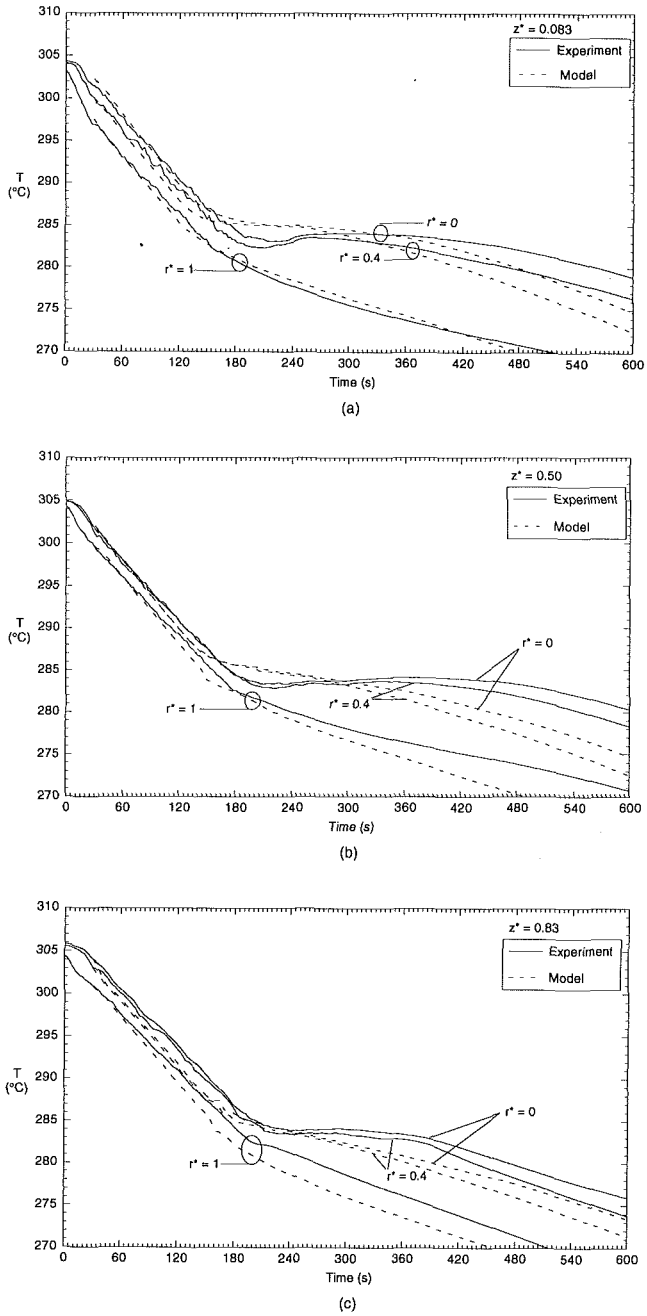

Fig. 7 Measured and predicted cooling curves at (*a*) $z^* = 0.083$, (*b*) $z^* = 0.50$, and (*c*) $z^* = 0.83$

maximum at $r^* = 0$ (during recalescence) depend on vertical position. These times are plotted as functions of z^* in Fig. 6. For a given vertical position, nucleation is assumed to occur along the outer mold wall ($r^* = 1$) at the time corresponding to the change in slope of the cooling curve (thermal arrest), Fig. 4. Since thermal convection occurs prior to the onset of solidification and is responsible for thermally stratifying the melt, nucleation first occurs at the bottom of the cooled mold wall and the point at which the nucleating isotherm intersects the mold wall ascends with time. Hence, consistent with the data of Fig. 4, the time of thermal arrest increases monotonically with z^*. However, the peak temperature during recalescence occurs first near the top and bottom of the cavity ($z^* = 0.83, 0.083$) and lastly at the intermediate elevation ($z^* = 0.50$). This trend suggests that a thermosolutal convection pattern exists in which dendrite fragments are carried radially inward near the bottom of the mold by a thermally driven convection

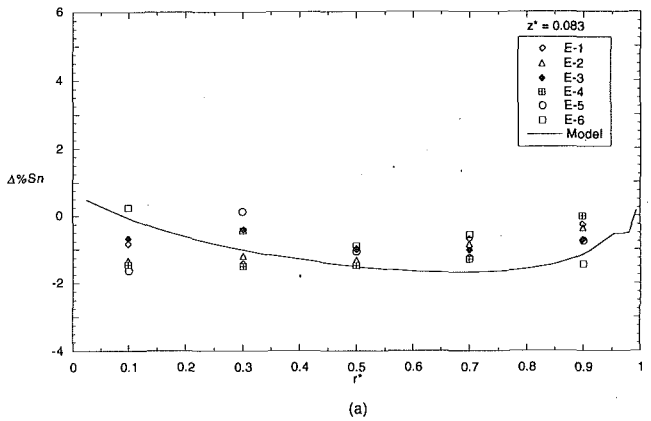

(a)

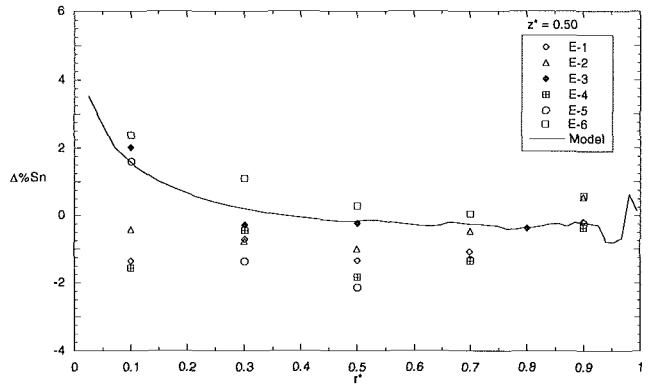

(b)

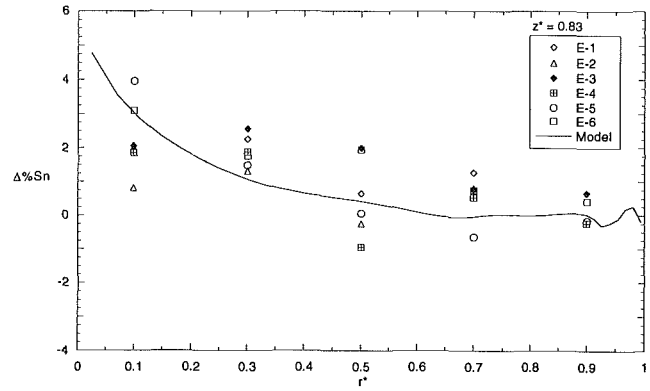

(c)

Fig. 8 Measured and predicted macrosegregation patterns at (*a*) $z^* = 0.083$, (*b*) $z^* = 0.50$, and (*c*) $z^* = 0.83$.

cell and also near the top by a solutally driven cell. The solutally driven cell develops as a result of Sn enrichment of interdendritic liquid, and thermosolutal convection patterns similar to those shown in Figs. 4(*b*), 5(*b*), and 6(*b*) of Prescott and Incropera (1994) can be inferred from the experimental cooling curves. Although the foregoing results are not conclusive, they are certainly plausible. Cooling curves and recalescence patterns from all other experiments were consistent with those of experiment E-1.

Measured temperature histories for experiment E-1 are compared with predictions based on a continuum model (Prescott and Incropera, 1994) in Figs. 7(*a*)-(*c*). Generally, the predicted cooling rate exceeds the measured cooling rate, and differences may be attributed to uncertainties in prescribed thermodynamic properties, which for example, affect the thermal capacitance of the system, to uncertainties in the heat transfer

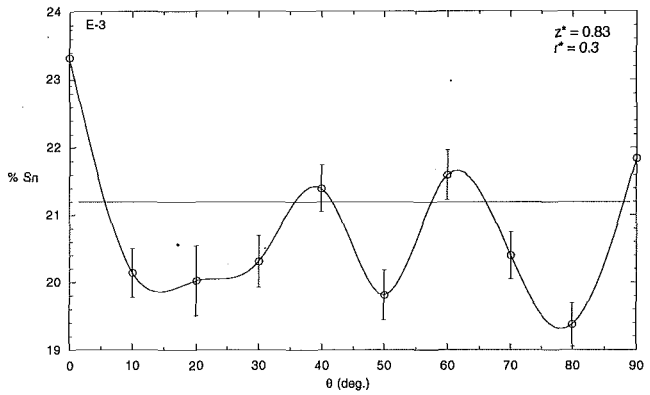

Fig. 9 Circumferential variation of measured Sn concentration at $r^* = 0.30$ and $z^* = 0.83$.

coefficient on the outer mold wall, which governs the rate of heat transfer from the system, and to the model assumption of local thermodynamic equilibrium. The overall cooling rate increases with a decrease in thermal capacitance and/or an increase in the overall heat transfer coefficient. Specific heats and densities for solid and liquid phases, as well as the latent heat of fusion, must be prescribed, and each quantity affects the thermal capacitance between liquidus and solidus temperatures. Moreover, although it is ignored in the model, irreversible mixing occurs within the actual solid and liquid phases and affects the relationship between enthalpy and temperature. Also, since temperature differences within the system are small compared to the difference between mold wall and coolant temperatures, the overall heat transfer coefficient applied on the outer mold wall has a much larger influence on heat transfer from the system than convection within the mold.

Despite the discrepancies between measured and predicted cooling rates, predicted *radial temperature differences* are in good agreement with measured data. The most conspicuous disagreement between predicted and measured cooling curves relates to the absence of undercooling and recalescence effects in the predicted cooling curves between 150 and 300 s. Because the model assumes local thermodynamic equilibrium, such phenomena cannot be predicted. This disagreement may have an important bearing on macrosegregation, since recalescence occurs during the early stages of solidification when it is believed that channels develop and much of the macrosegregation pattern is determined. It should also be noted that solid particle transport and shrinkage could also affect macrosegregation but were ignored in the model. However, because the cooling rate is controlled primarily by system thermodynamic properties and the overall heat transfer coefficient, solid particle transport and shrinkage do not significantly affect system temperatures.

The repeatability of the experiments was assessed by comparing cooling curves from experiments E-1 and E-2, between which the apparatus was completely disassembled and reassembled. More than 95 percent of the data agreed to within 0.5°C, with discrepancies attributable to small differences in the initial melt temperature and composition (Prescott, 1992).

Measured macrosegregation patterns from ingots corresponding to experiments E-1 through E-6 are compared with model predictions (Prescott and Incropera, 1994) in Figs. 8(*a*)-(*c*). Zero Δ%Sn corresponds to no macrosegregation; positive values represent Sn enrichment; and negative values represent Sn depletion. The agreement between predicted and measured macrosegregation patterns is reasonable, and although the data are scattered, they confirm general trends predicted by the model. That is, the concentration of Sn increases with increasing height and, at $z^* = 0.5$ and 0.83, with decreasing radius. However, since the uncertainty in the meas-

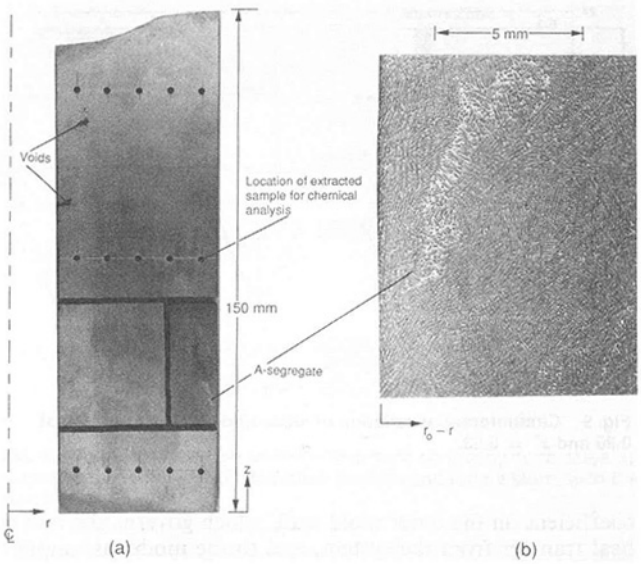

Fig. 10 Photographs of (*a*) an ingot section representing an *r–z* plane and (*b*) a portion of an A-segregate

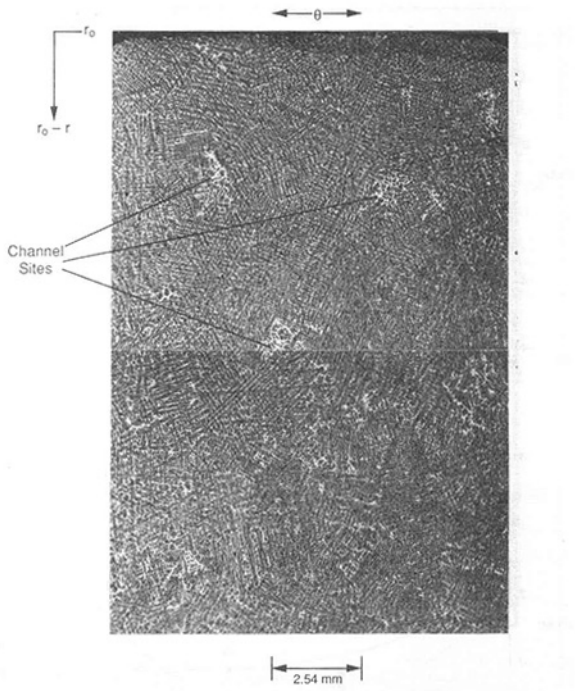

Fig. 11 Photomacrograph taken near $r^* = 1$ and $z^* = 0.50$ in the r–θ plane and showing discrete patches of eutectic (white) material

ured results is ±0.40%Sn, it does not account for the scatter, which is as large as 4 percent.

The circumferential variation of macrosegregation is plotted in Fig. 9, which shows %Sn as a function of θ at $(r^*, z^*) = (0.3, 0.83)$. All samples were taken from the ingot corresponding to experiment E-3, and the plot indicates clearly the three-dimensional nature of the macrosegregation field. If conditions were axisymmetric, the variation of %Sn with θ would be within the measurement uncertainty interval. Since the data in Fig. 8 were taken from different circumferential positions, the scatter is largely attributable to the three-dimensional macrosegregation pattern, and those locations in Figs. 8(*a*)–(*c*) that exhibit pronounced scatter are believed to be within segregated regions associated with channeling during solidification.

Discrete channel sites in the mushy zone manifest themselves as relatively large pockets of eutectic material in the soldified ingot, and evidence of their existence is provided in Figs. 10 and 11. Figure 10(*a*) shows an ingot section representing a full *r–z* plane, where the inner and outer radii are shown as left and right boundaries, respectively. A small piece, adjacent to the outer boundary at $z^* \approx 0.3$, was removed, polished and metallographically examined, Fig. 10(*b*). Eutectic material, which is Sn rich, appears white in Fig. 10(*b*), while Pb-rich dendrites appear black. The wide trail of eutectic enriched material in Fig. 10(*b*) represents part of a segregate and is indicative of channel formation during solidification. Although channel segregates are aligned primarily in the vertical direction and slant radially inward, they also tend to be oriented with a slight θ component, making it difficult to capture the full extent of a channel metallographically. A highly segregated region was also predicted to occur in the bottom half of the ingot, adjacent to the mold wall (Prescott and Incropera, 1994). In the macrograph of Fig. 11, which was taken from an *r–θ* section of an ingot, the white patches of eutectic enriched material provide further evidence of the discrete nature of channels and of the three dimensionality of the macrosegregation field.

Metallographic specimens were also used to assess the characteristics of the metallurgical structure. By examining specimens under low magnification, the structure was revealed to be largely equiaxed, and measurements from micrographs revealed average spacings of 116 (±20) μm between the centers of primary dendrites and 73 (±21) μm between the centers of secondary dendrites. These values are consistent with those (DAS_1 = 100 μm and DAS_2 = 50 μm) used to estimate the permeability coefficient K_o for the numerical simulations (Prescott and Incropera, 1994).

Conclusions

An experimental study of solidification in a binary metal alloy has been performed, and the data support several conclusions drawn from a related numerical simulation (Prescott and Incropera, 1994). Results confirm the establishment of thermal convection and stratification before solidification begins and subsequent development of a mushy zone, which forms initially at the bottom and gradually ascends along the cooled mold wall. Evidence of thermosolutal convection patterns with counterrotating convection cells was also provided experimentally, and measured macrosegregation patterns were in general agreement with predictions. Experimental observations that were not predicted by the simulations relate to the effects of undercooling, recalescence, and solid particle transport. Since undercooling and recalescence are nonequilibrium phenomena, they could not be predicted by the equilibrium continuum model, which also assumed that the mushy zone remained coherent and stationary throughout solidification (Prescott and Incropera, 1994).

Although predicted and measured macrosegregation patterns displayed many of the same trends, macrosegregation in the experimental ingots was clearly three dimensional, indicating that three-dimensional convection patterns existed during solidification. The discrete channels that formed in the mushy zone may have been due to three-dimensional flow patterns in the bulk melt before and during solidification, or, as is more likely, to flow and morphological instabilities associated with the solidification process in the mushy zone. Solidification shrinkage, which produced the pores (voids) seen in Fig. 10(*a*), also occurred but was not considered in the simulations. All experimental ingots were characterized by a significant depression of their top surfaces and by discrete and interconnected voids (pores). The extent to which discrepancies between experimental and theoretical results may be attributed to shrinkage is, as yet, unknown.

Due to its large thermal conductivity, density, and thermal

and solutal expansion coefficients, as well as its small viscosity, the Pb–Sn system experiences significant changes during early solidification stages. Numerical simulations predicted rapidly changing convection patterns during periods of transition from thermally to solutally dominated flow (Prescott and Incropera, 1994), and measured cooling curves displayed fluctuations indicative of additional complexities. In contrast, numerically predicted cooling curves were smooth, suggesting that the model was unable to predict finer details of the actual flow. Prediction of such details would necessitate waiving the assumption of axial symmetry and performing a transient, fully three-dimensional simulation of the solidification process. In addition, second-order finite-difference schemes may be necessary to achieve improved resolution of flow details.

Acknowledgments

The authors are grateful to the U.S. Department of Energy, which supported this work through Award No. DE-FG02-87ER 13759.

References

Beckermann, C., and Viskanta, R., 1988, "Double-Diffusive Convection During Dendritic Solidification of a Binary Mixture," *PhysicoChem. Hydrodyn*, Vol. 10, pp. 195–213.

Bennon, W. D., and Incropera, F. P. 1987a, "A Continuum Model for Momentum, Heat and Species Transport in Binary Solid–Liquid Phase Change Systems—I. Model Formulation," *Int. J. Heat Mass Transfer*, Vol. 30, pp. 2161–2170.

Bennon, W. D., and Incropera, F. P., 1987b, "A Continuum Model for Momentum, Heat and Species Transport in Binary Solid–Liquid Phase Change Systems—II. Application to Solidification in a Rectangular Cavity," *Int. J. Heat Mass Transfer*, Vol. 30, pp. 2171–2187.

Christenson, M. S., Bennon, W. D., and Incropera, F. P., 1989, "Solidification of an Aqueous Ammonium Chloride Solution in a Rectangular Cavity–II. Comparison of Predicted and Measured Results," *Int. J. Heat Mass Transfer*, Vol. 32, pp. 69–79.

Gill, A. E., 1974, "A Theory of Thermal Oscillations in Molten Gallium," *J. Fluid Mech.*, Vol. 64, pp. 577–588.

Hurle, D. T. J., Jakeman, E., and Johnson, C. P., 1974, "Convective Temperature Oscillations in Molten Gallium," *J. Fluid Mech.*, Vol. 64, pp. 565–576.

Kurz, W., and Fisher, D. J., 1984, *Fundamentals of Solidification*, Trans Tech Publications, Aedermannsdorf, Switzerland.

Mohamad, A. A., 1992, "Mixed Convection in Lid-Driven Shallow Cavities," Ph.D. Thesis, Purdue University, W. Lafayette, IN.

Neilson, D. G., Incropera, F. P., and Bennon, W. D., 1990, "Numerical Simulation of Solidification in a Horizontal Cylindrical Annulus Charged With an Aqueous Salt Solution," *Int. J. Heat Mass Transfer*, Vol. 33, pp. 367–380.

Prescott, P. J., Incropera, F. P., and Bennon, W. D., 1991, "Modeling of Dendritic Solidification Systems: Reassessment of the Continuum Momentum Equation," *Int. J. Heat Mass Transfer*, Vol. 34, pp. 2351–2359.

Prescott, P. J., 1992, "Convective Transport Phenomena During Solidification of Binary Metal Alloys and the Effects of Magnetic Fields," Ph.D. Thesis, Purdue University, W. Lafayette, IN.

Prescott, P. J. and Incropera, F. P., 1994, "Convective Transport Phenomena and Macrosegregation During Solidification of a Binary Metal Alloy—I. Numerical Predictions," ASME JOURNAL OF HEAT TRANSFER, Vol. 116, this issue, pp. 735–741.

Shahani, H., Amberg, G., and Fredriksson, H., 1992, "On the Formation of Macrosegregations in Unidirectionally Solidified Sn-Pb and Pb-Sn Alloys," *Metall. Trans. A.*, Vol. 23A, pp. 2301–2311.

Stewart, M. J., and Weinberg, F., 1969, "Flow of Liquid Tin in a Square Enclosure," *TMS-AIME*, Vol. 245, pp. 2108–2110.

Stewart, M. J., and Weinberg, F., 1971, "Fluid Flow in Liquid Metals: 2. Experimental Observations," *J. Crystal Growth*, Vol. 12, pp. 227–238.

Stewart, M. J., and Weinberg, F., 1972, "Fluid Flow Through a Solid–Liquid Dendritic Interface," *Metall. Trans.*, Vol. 3, pp. 333–337.

Uhlmann, D. R., Seward, T. P., III, and Chalmers, B., 1966, "The Effect of Magnetic Fields on the Structure of Metal Alloy Castings," *TMS AIME*, Vol. 236, pp. 527–531.

Vives, C., and Perry, C., 1986, "Effects of Electromagnetic Stirring During the Controlled Solidication of Tin," *Int. J. Heat Mass Transfer*, Vol. 29, pp. 21–33.

Vives, C., and Perry, C., 1987, "Effects of Magnetically Damped Convection During the Controlled Solidification of Metals and Alloys," *Int. J. Heat Mass Transport*, Vol. 30, pp. 21–33.

Voller, V. R., and Praskash, C., 1987, "A Fixed Grid Numerical Modelling Methodology for Convection-Diffusion Mushy Region Phase-Change Problems," *Int. J. Heat Mass Transfer*, Vol. 30, pp. 1709–1719.

Voller, V. R., Brent, A. D., and Prakash, C., 1989, "The Modelling of Heat, Mass and Solute Transport in Solidification Systems," *Int. J. Heat Mass Transfer*, Vol. 32, pp. 1718–1731.

Wolff, F., Beckermann, C., and Viskanta, R., 1988, "Natural Convection of Liquid Metals in Vertical Cavities," *Exp. Thermal Fluid Sci.*, Vol. 1, pp. 83–91.

Journal of Heat Transfer

Technical Notes

This section contains shorter technical papers. These shorter papers will be subjected to the same review process as that for full papers.

Study of Hyperbolic Heat Conduction With Temperature-Dependent Thermal Properties

Han-Taw Chen[1] and Jae-Yuh Lin[1]

Nomenclature

C_p = specific heat
c = propagation speed of the thermal wave
k = thermal conductivity
Q = dimensionless heat flux
R = dimensionless radiation parameter
T = temperature
t = time
x = space coordinate
α = thermal diffusivity
γ = surface absorptivity
η = dimensionless space coordinate
θ = dimensionless temperature
ξ = dimensionless time
ρ = density
σ = Stefan–Boltzmann constant

Introduction

For situations involving very low temperatures near absolute zero, very high temperature gradient, or extremely short times, heat is found to propagate at a finite speed. For these situations, the hyperbolic heat conduction (HHC) model is employed to account for the phenomena with the finite propagation speed of heat. Various analytical and numerical schemes have been developed for HHC problems with constant thermal properties. To the authors' knowledge, only Glass et al. (1986) and Kar et al. (1992) have studied temperature-dependent thermal properties. Glass et al. (1986) used MacCormack's predictor-corrector scheme to solve HHC problems in a semi-infinite slab with temperature-dependent thermal conductivity. They observed that the temperature distribution and the speed of the thermal wave are strongly affected by the temperature-dependent thermal conductivity. Kar et al. (1992) solved HHC problems with constant thermal diffusivity, but thermal conductivity, heat capacity, and density are temperature dependent. They applied the Kirchhoff transformation to linearize the nonlinear HHC equation. Afterward, separation of variables, Laplace transform techniques, and method of characteristic are respectively used to determine the analytical and numerical solutions. In fact, the major difficulty encountered in the numerical solution of HHC problems is the numerical oscillation in the vicinity of the jump discontinuity at the thermal wave front. We (Chen and Lin, 1993) have developed a powerful numerical technique with the hybrid application of the Laplace transform and control-volume methods to solve HHC problems with constant thermal properties. The present study extends this numerical scheme to solve HHC problems with temperature-dependent thermal properties. Nonlinear terms in the governing equation and boundary conditions are linearized by using Taylor's series approximation. Various examples involving a case with surface radiation are illustrated to evidence the ability of the present method for such problems.

Mathematical Formulation

To give a more reliable result for the problem considering the finite propagation speed of the thermal wave, Cattaneo (1948) and Vernotte (1958) suggested a modified heat flux model in the form of

$$\tau \frac{\partial q}{\partial t} + q = -k(T) \frac{\partial T}{\partial x} \tag{1}$$

where q is the heat flux. The relaxation time τ is defined as $\tau = \alpha_0/c_0^2 = k_0/\rho_0 C_{p0} c_0^2$. c_0 is the reference propagation speed of the thermal wave, α_0 is the reference thermal diffusivity, and k_0, ρ_0, and C_{p0} are the reference thermal conductivity, density, and specific heat, respectively. Energy conservation equation without heat source or sink in the medium can be written as

$$\rho(T) C_p(T) \frac{\partial T}{\partial t} = -\frac{\partial q}{\partial x} \tag{2}$$

Elimination of q between Eqs. (1) and (2) leads to the HHC equation as

$$\tau \frac{\partial}{\partial t}\left[\rho(T) C_p(T) \frac{\partial T}{\partial t}\right] + \rho(T) C_p(T) \frac{\partial T}{\partial t} = \frac{\partial}{\partial x}\left[k(T) \frac{\partial T}{\partial x}\right] \tag{3}$$

The product $\rho(T) C_p(T)$ and thermal conductivity $k(T)$ are assumed to vary with temperature, respectively, as

[1]Department of Mechanical Engineering, National Cheng Kung University, Tainan, Taiwan 701.

Contributed by the Heat Transfer Division of The American Society of Mechanical Engineers. Manuscript received by the Heat Transfer Division January 1993; revision received November 1993. Keywords: Conduction, Numerical Methods, Transient and Unsteady Heat Transfer. Associate Technical Editor: L. S. Fletcher.

$$\rho(T)C_p(T)=\rho_0 C_{p0}\left[1+\mathbf{A}\left(\frac{T}{T_0}\right)\right] \quad \text{and} \quad k(T)=k_0\left[1+\mathbf{B}\left(\frac{T}{T_0}\right)\right] \tag{4}$$

where T_0 is the reference temperature. **A** and **B** are arbitrary functions of temperature. For convenience of numerical analysis, the following dimensionless parameters are introduced:

$$\eta=\frac{c_0 x}{2\alpha_0}, \quad \mathrm{gj}=\frac{c_0^2 t}{2\alpha_0}, \quad Q=\frac{q}{q_r}, \quad \theta=\frac{T}{T_0},$$
$$\mathbf{D}(\theta)=\int_0^\theta \mathbf{A}(\theta')d\theta', \quad \text{and} \quad \mathbf{E}(\theta)=\int_0^\theta \mathbf{B}(\theta')d\theta' \tag{5}$$

where $q_r = \rho_0 C_{p0} c_0 T_0$ is the reference heat flux. Thus, the dimensionless form of Eqs. (1) and (3) can be written as

$$\frac{\partial Q}{\partial \xi}+2Q=-\frac{\partial}{\partial \eta}[\theta+\mathbf{E}(\theta)] \tag{6}$$

and

$$\frac{\partial^2}{\partial \xi^2}[\theta+\mathbf{D}(\theta)]+2\frac{\partial}{\partial \xi}[\theta+\mathbf{D}(\theta)]=\frac{\partial^2}{\partial \eta^2}[\theta+\mathbf{E}(\theta)] \tag{7}$$

The dimensionless initial conditions are assumed to be

$$\theta(0,\eta)=0 \quad \text{and} \quad \frac{\partial \theta}{\partial \xi}(0,\eta)=0 \tag{8}$$

Numerical Analysis

To remove ξ-dependent terms, taking the Laplace transform of Eqs. (6) and (7) gives

$$(s+2)\tilde{Q}=-\frac{d}{d\eta}[\tilde{\theta}+\tilde{\mathbf{E}}] \tag{9}$$

and

$$\frac{d^2\tilde{\theta}}{d\eta^2}-\lambda^2\tilde{\theta}+\frac{d^2\tilde{\mathbf{E}}}{d\eta^2}-\lambda^2\tilde{\mathbf{D}}=0 \tag{10}$$

where $\lambda = (s^2 + 2s)^{1/2}$ and s is the Laplace transform parameter. The Laplace transform of a function $\psi(\xi)$ is defined as

$$\tilde{\psi}(s)=\int_0^\infty e^{-s\xi}\,\psi(\xi)d\xi \tag{11}$$

The Laplace transforms of the nonlinear functions $\mathbf{D}(\theta)$ and $\mathbf{E}(\theta)$ can be approximated by using the Taylor's series approximation (Chen and Lin, 1991) and are given as

$$\tilde{\mathbf{D}}(\tilde{\theta})\approx \mathbf{A}(\bar{\theta})\tilde{\theta}+\frac{1}{s}[\mathbf{D}(\bar{\theta})-\mathbf{A}(\bar{\theta})\bar{\theta}] \tag{12a}$$

and

$$\tilde{\mathbf{E}}(\tilde{\theta})\approx \mathbf{B}(\bar{\theta})\tilde{\theta}+\frac{1}{s}[\mathbf{E}(\bar{\theta})-\mathbf{B}(\bar{\theta})\bar{\theta}] \tag{12b}$$

where $\bar{\theta}$ is the previously calculated temperature.

Due to the application of the control volume method, the integration of Eq. (10) over a typical control volume $[\eta_i - l/2, \eta_i + l/2]$ is performed, where l is the distance between two nodes. In the present study, the heat flux within this interval is assumed to be continuous. Under this assumption, the following equality can be obtained from Eq. (9):

$$\frac{d}{d\eta}[\tilde{\theta}+\tilde{\mathbf{E}}]_{\eta=\eta_i^+}=\frac{d}{d\eta}[\tilde{\theta}+\tilde{\mathbf{E}}]_{\eta=\eta_i^-} \tag{13}$$

Then, the integration of Eq. (10) in the interval $[\eta_i - l/2, \eta_i + l/2]$ is given by

$$\frac{d}{d\eta}[\tilde{\theta}+\tilde{\mathbf{E}}]_{\eta=\eta_i+l/2}-\frac{d}{d\eta}[\tilde{\theta}+\tilde{\mathbf{E}}]_{\eta=\eta_i-l/2}-\lambda^2\int_{\eta_i-l/2}^{\eta_i+l/2}[\tilde{\theta}+\tilde{\mathbf{D}}]d\eta=0 \tag{14}$$

$\tilde{\theta}(s,\eta)$ and $\bar{\theta}(\eta)$ within a control volume are approximated by shape functions in conjunction with unknown nodal temperatures and iterated values, respectively. As described in our previous work for linear HHC problems (Chen and Lin, 1993), the select of the shape function is an important step for accurately predicting the propagation of the thermal wave. The hyperbolic shape function derived from $d^2\tilde{\theta}/d\eta^2 - \lambda^2\tilde{\theta} = 0$ proved to be an excellent choice (Chen and Lin, 1993). This hyperbolic shape function is also employed in the present study. $\tilde{\theta}(s,\eta)$ within the interval $[\eta_{i-1}, \eta_{i+1}]$ is approximated by

$$\tilde{\theta}(s,\eta)=\mathbf{N}_a^-(s,\eta)\tilde{\theta}_i+\mathbf{N}_b^-(s,\eta)\tilde{\theta}_{i-1} \quad \text{for} \quad \eta\in[\eta_{i-1},\eta_i]$$
$$=\mathbf{N}_a^+(s,\eta)\tilde{\theta}_i+\mathbf{N}_b^+(s,\eta)\tilde{\theta}_{i+1} \quad \text{for} \quad \eta\in[\eta_i,\eta_{i+1}] \tag{15}$$

where $\mathbf{N}_a^-(s,\eta)$, $\mathbf{N}_b^-(s,\eta)$, $\mathbf{N}_a^+(s,\eta)$, and $\mathbf{N}_b^+(s,\eta)$ are hyperbolic shape functions and are given by

$$\mathbf{N}_a^-(s,\eta)=\frac{\sinh[\lambda(\eta-\eta_{i-1})]}{\sinh(\lambda l)}, \quad \mathbf{N}_b^-(s,\eta)=-\frac{\sinh[\lambda(\eta-\eta_i)]}{\sinh(\lambda l)}$$
$$\mathbf{N}_a^+(s,\eta)=\frac{\sinh[\lambda(\eta_{i+1}-\eta)]}{\sinh(\lambda l)}, \quad \mathbf{N}_b^+(s,\eta)=\frac{\sinh[\lambda(\eta-\eta_i)]}{\sinh(\lambda l)} \tag{16}$$

However, $\bar{\theta}(\eta)$ within the interval $[\eta_{i-1}, \eta_{i+1}]$ is approximated by

$$\bar{\theta}(\eta)=\bar{\theta}^-=\frac{\eta-\eta_{i-1}}{l}\bar{\theta}_i-\frac{\eta-\eta_i}{l}\bar{\theta}_{i-1} \quad \text{for} \quad \eta\in[\eta_{i-1},\eta_i]$$
$$=\bar{\theta}^+=\frac{\eta_{i+1}-\eta}{l}\bar{\theta}_i+\frac{\eta-\eta_i}{l}\bar{\theta}_{i+1} \quad \text{for} \quad \eta\in[\eta_i,\eta_{i+1}] \tag{17}$$

Substituting Eqs. (12), (15), and (17) into Eq. (14) yields an algebraic equation as

$$a_i\tilde{\theta}_{i-1}+b_i\tilde{\theta}_i+c_i\tilde{\theta}_{i+1}=f_i \quad i=2,3,\ldots,n-1 \tag{18}$$

where n is the total number of nodes. a_i, b_i, c_i, and f_i are

$$a_i=-\frac{d}{d\eta}\{[1+\mathbf{B}(\bar{\theta}^-)]\mathbf{N}_b^-(\eta)\}_{\eta=\eta_i-l/2}-\lambda^2\int_{\eta_i-l/2}^{\eta_i}[1+\mathbf{A}(\bar{\theta}^-)]\mathbf{N}_b^-(\eta)d\eta \tag{19a}$$

$$b_i=\frac{d}{d\eta}\{[1+\mathbf{B}(\bar{\theta}^+)]\mathbf{N}_a^+(\eta)\}_{\eta=\eta_i+l/2}-\frac{d}{d\eta}\{[1+\mathbf{B}(\bar{\theta}^-)]\mathbf{N}_a^-(\eta)\}_{\eta=\eta_i-l/2}-\lambda^2\int_{\eta_i-l/2}^{\eta_i}[1+\mathbf{A}(\bar{\theta}^-)]\mathbf{N}_a^-(\eta)d\eta-\lambda^2\int_{\eta_i}^{\eta_i+l/2}[1+\mathbf{A}(\bar{\theta}^+)]\mathbf{N}_a^+(\eta)d\eta \tag{19b}$$

$$c_i=\frac{d}{d\eta}\{[1+\mathbf{B}(\bar{\theta}^+)]\mathbf{N}_b(\eta)\}_{\eta=\eta_i+l/2}-\lambda^2\int_{\eta_i}^{\eta_i+l/2}[1+\mathbf{A}(\bar{\theta}^+)]\mathbf{N}_b(\eta)d\eta \tag{19c}$$

and

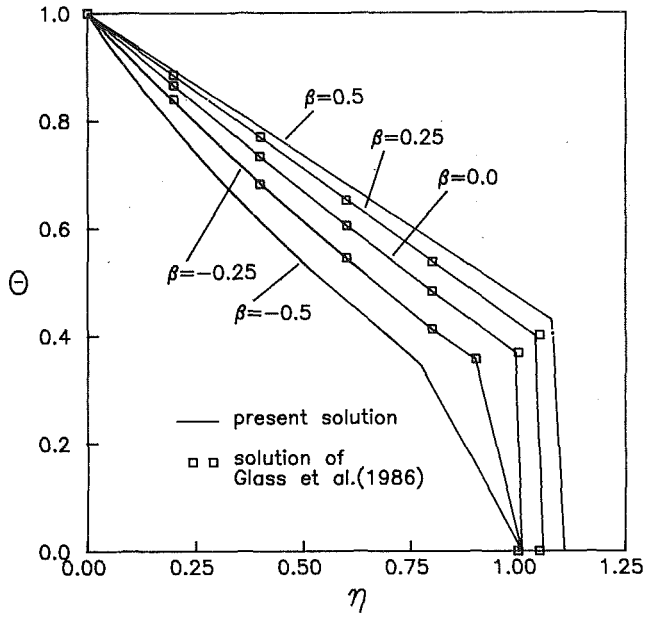

Fig. 1 Comparison of the dimensionless temperature distributions for various β values at $\xi = 1$

$$f_i=\frac{1}{s}\left\{\frac{d}{d\eta}[\mathbf{E}(\bar{\theta}^-)-\mathbf{B}(\bar{\theta}^-)\bar{\theta}^-]_{\eta=\eta_i-l/2}\right.$$
$$-\frac{d}{d\eta}[\mathbf{E}(\bar{\theta}^+)-\mathbf{B}(\bar{\theta}^+)\bar{\theta}^+]_{\eta=\eta_i+l/2}$$
$$+\lambda^2\int_{\eta_i-l/2}^{\eta_i}[\mathbf{D}(\bar{\theta}^-)-\mathbf{A}(\bar{\theta}^-)\bar{\theta}^-]d\eta$$
$$\left.+\lambda^2\int_{\eta_i}^{\eta_i+l/2}[\mathbf{D}(\bar{\theta}^+)-\mathbf{A}(\bar{\theta}^+)\bar{\theta}^+]d\eta\right\} \quad (19d)$$

The algebraic equations for nodes on the boundary surfaces can be derived in a similar way. The arrangement of the resulting algebraic equations can yield the following vector-matrix equation:

$$[\mathbf{K}]\{\tilde{\theta}\}=\{\mathbf{f}\} \quad (20)$$

where $[\mathbf{K}]$ is a band matrix, $\{\tilde{\theta}\}$ is a vector representing the unknown dimensionless temperature in the transform domain, and $\{\mathbf{f}\}$ is a vector representing the forcing term. Equation (20) is solved by iteration, which can refer to our early work (Chen and Lin, 1991). The computational procedure will not be illustrated in the present study.

Illustrative Examples

Two different examples are illustrated to validate the ability of the present numerical method for nonlinear HHC problems. All the computations are performed using the space size $l = 0.01$. All the initial guessed values for iteration are taken as zero. The tolerable value for convergence of iteration is taken as 10^{-4}. A maximum of six iterations are required for obtaining a convergent solution at a specific time.

Example 1: This example concerns a semi-infinite slab with temperature-dependent thermal conductivity, while the density and specific heat are assumed to be constant. The surface at $\eta = 0$ is kept at a fixed dimensionless temperature $\theta = 1$. The thermal conductivity $k(T)$ is assumed to be $k(T) = k_0(1+\beta\theta)$, where β is the temperature coefficient. Glass et al. (1986) have investigated this example by using the MacCormack's predictor-corrector scheme. Figure 1 shows the comparison of dimensionless temperature distributions at $\xi = 1$ for various β values. It can be seen that present numerical solutions agree well with those given by Glass et al. (1986). This implies that present numerical solutions are accurate. The effect of β on the temperature distribution is also shown in Fig. 1. Glass et al. (1986) have given a detailed discussion about this influence.

Table 1 Comparison of the dimensionless temperature for $\xi = 0.625$ and $\beta = 0.2$

η	Kar et al. (1992)	Present solution	Baumeister and Hamill (1969)	Maurer et al. (1973)
0.0	9.0	9.0	9.0	
0.15	8.5253	8.3497	8.3497	
0.3	8.0237	7.6698	7.6699	
0.45	7.4944	6.9620	6.9623	
0.6	6.9358	6.1356	6.1362	
0.75	1.0	1.0	1.0	1.0
1.8	1.0	1.0	1.0	1.0
1.95	1.2515	1.8162		1.8172
2.1	1.2973	2.0663		2.0672
2.25	1.3426	2.3369		2.3376
2.4	1.3877	2.6258		2.6263
2.5	1.4177	2.8276		2.8279

Example 2: To further evidence the accuracy of the present method, a similar problem analyzed by Kar et al. (1992) is illustrated. For this problem, the boundary surface at $\eta = 0$ is kept at $\theta = 9$ and the other boundary surface at $\eta = 2.5$ is subjected to a dimensionless surface heat flux $Q = -1.4$. $k(T) = k_0[1+\beta(\theta-1)]$ and $\rho(T)C_p(T) = \rho_0 C_{p0}[1+\beta(\theta-1)]$ are assumed. Table 1 shows a comparison of the dimensionless temperature between the present numerical solution and that given by Kar et al. (1992) for $\xi = 0.625$ and $\beta = 0.2$. It is seen from Table 1 that a great discrepancy between them is observed. Due to the application of the Kirchhoff transformation, the nonlinear problem proposed by Kar et al. (1992) can be transformed into a linear system. Thus, the analytical solutions obtained from the mathematical analyses of Baumeister and Hamill (1969) and Maurer and Thompson (1973) can be applied to compare with the present results, as shown in Table 1. This comparison shows that the analysis of Kar et al. (1992) may have some deficiencies.

Example 3: The last example investigates the thermal wave propagation in a semi-infinite slab with a radiative boundary condition that the boundary surface at $x = 0$ is subjected to a constant heat flux, $q = q_r$, and dissipates heat by radiation into the ambient at $T = 0$. $k(T)$ and $\rho(T)C_p(T)$ are assumed to be $k(T) = k_0(1+\beta_1\theta)$ and $\rho(T)C_p(T) = \rho_0 C_{p0}(1+\beta_2\theta)$, respectively. Accordingly, it is found from Eq. (6) that the dimensionless form of the boundary condition at $\eta = 0$ can be expressed as

$$-(1+\beta_1\theta)\frac{\partial\theta}{\partial\eta}=\frac{\partial}{\partial\xi}(-R\theta^4+1)$$
$$+2(-R\theta^4+1) \quad \text{at} \quad \eta=0 \quad (21)$$

where $R = \gamma\sigma\alpha_0^4 q_r^3/k_0^4 c_0^4$ represents the ratio of surface radiation to conduction. A large value of R implies strong radiation. It is evident that this example is a nonlinear problem. Thus, the Taylor's series approximation is applied to linearize Eq. (21), and then the Laplace transform of the resulting linearized equation can be obtained. Performing the integration of Eq. (10) over the interval $[0, l/2]$ in conjunction with hyperbolic shape functions can yield the following algebraic equation at node $i = 1$:

$$b_1\tilde{\theta}_1+c_1\tilde{\theta}_2=f_1 \quad (22)$$

where

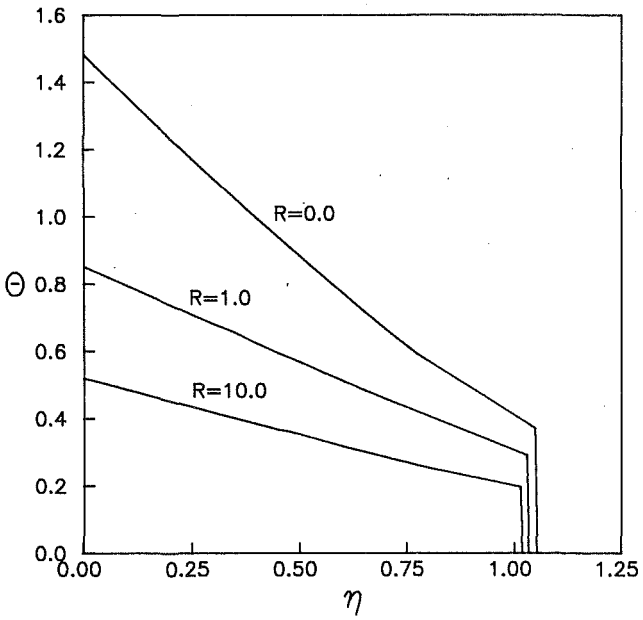

Fig. 2 Effects of R on the dimensionless temperature distribution for $\xi = 1$, $\beta_1 = 0.4$, and $\beta_2 = 0.2$

$$b_1 = \frac{d}{d\eta}\{[1+\beta_1\bar{\theta}^+]\mathbf{N}_a(\eta)\}_{\eta=l/2} - \lambda^2\int_0^{l/2}[1+\beta_2\bar{\theta}^+]\mathbf{N}_a^+(\eta)d\eta - 4R(s+2)\bar{\theta}_1^3 \quad (23a)$$

$$c_1 = \frac{d}{d\eta}\{[1+\beta_1\bar{\theta}^+]\mathbf{N}_b^+(\eta)\}_{\eta=l/2} - \lambda^2\int_0^{l/2}[1+\beta_2\bar{\theta}^+]\mathbf{N}_b^+(\eta)d\eta \quad (23b)$$

and

$$f_1 = \frac{1}{2s}\left\{\beta_1\frac{d}{d\eta}(\bar{\theta}^+)^2_{\eta=l/2} - \lambda^2\beta_2\int_0^{l/2}(\bar{\theta}^+)^2 d\eta - 2(s+2)(3R\bar{\theta}_1^4+1)\right\} \quad (23c)$$

The effects of radiation on the temperature distribution at $\xi = 1.0$, $\beta_1 = 0.4$, and $\beta_2 = 0.2$ are displayed in Fig. 2. As shown in Fig. 2, due to the dissipation of heat into the ambient, the higher surface temperature is obtained by decreasing the value of R. The wave speed for this case can be defined as $c = (\alpha/\tau)^{1/2} = c_0(1+0.4\theta/1+0.2\theta)^{1/2}$. This implies that the propagation speed of the thermal wave is faster for a higher temperature profile. Thus the smaller the value of R, the faster the propagation speed of the thermal wave.

Conclusions

Numerical solutions for various HHC problems with temperature-dependent thermal properties are proposed in the present study. Effects of some dimensionless parameters on the propagation speed of the thermal wave are also investigated. As shown in various comparative examples, the present numerical method is accurate and efficient for such problems. Although thermal properties are assumed to vary with temperature linearly in the illustrative examples, problems with other forms of temperature-dependent thermal properties can also be successfully solved in our numerical tests.

References

Baumeister, K. J., and Hamill, T. D., 1969, "Hyperbolic Heat-Conduction Equation—A Solution for the Semi-infinite Body Problem," ASME JOURNAL OF HEAT TRANSFER, Vol. 91, pp. 543–548.

Cattaneo, C., 1948, "On the Conduction of Heat," *Atti Del Seminar*, Mat. Fis. Univ., Modena, Vol. 3, p. 3.

Chen, H. T., and Lin, J. Y., 1991, "Hybrid Laplace Transform Technique for Nonlinear Transient Thermal Problems," *Int. J. Heat Mass Transfer*, Vol. 34, pp. 1301–1308.

Chen, H. T., and Lin, J. Y., 1993, "Numerical Analysis for Hyperbolic Heat Conduction," *Int. J. Heat Mass Transfer*, Vol. 36, pp. 2891–2898.

Glass, D. E., Özişik, M. N., McRae, D. S., and Vick, B., 1986, "Hyperbolic Heat Conduction With Temperature-Dependent Thermal Conductivity," *Journal of Applied Physics*, Vol. 59, pp. 1861–1865.

Kar, A., Chan, C. L., and Mazumder, J., 1992, "Comparative Studies on Nonlinear Hyperbolic and Parabolic Heat Conduction for Various Boundary Conditions: Analytic and Numerical Solutions," ASME JOURNAL OF HEAT TRANSFER, Vol. 114, pp. 14–20.

Maurer, M. J., and Thompson, H. A., 1973, "Non-Fourier Effects at High Heat Flux," ASME JOURNAL OF HEAT TRANSFER, Vol. 95, pp. 284–286.

Vernotte, M. P., 1958, "Les Paradoxes de la Theorie Continue de l'Equation de la Chaleur," *Comptes Rendus*, Vol. 246, pp. 3154–3155.

Combination of Source-and-Sink Method and Complex-Temperature Method for the Solution of Stefan Problems Imposed With Cyclic Temperature and Flux Conditions

J. G. Nyros[1] and C. K. Hsieh[1]

Nomenclature

A_0, A = temperatures
B_0, B = heat fluxes
c = specific heat
C, E, G, H, I, J, K, L, M, X, Y = special notations in Tables 1 and 2
D = thickness of slab
F = $[\omega/(2\alpha)]^{1/2}$
k = thermal conductivity
L = latent heat
R = interface position
St = Stefan number
t = time
T = temperature
x = position on x axis
α = thermal diffusivity
β_q, β_T = B_0/B, $(A_0 - T_D)/A$
γ = dimensionless thickness
Γ, Δ, Δ', Z, Θ, Θ', Λ = special angles in Tables 1 and 2
δ = Dirac delta function
θ = dimensionless temperature
ξ = dimensionless position
ρ = density, dimensionless interface position
τ = dimensionless time
ω = angular velocity

[1]Mechanical Engineering Department, University of Florida, Gainesville, FL 32611.

Contributed by the Heat Transfer Division of THE AMERICAN SOCIETY OF MECHANICAL ENGINEERS. Manuscript received by the Heat Transfer Division September 1993; revision received December 1993. Keywords: Conduction, Moving Boundaries, Phase-Change Phenomena. Associate Technical Editor: Y. Bayazitoglu.

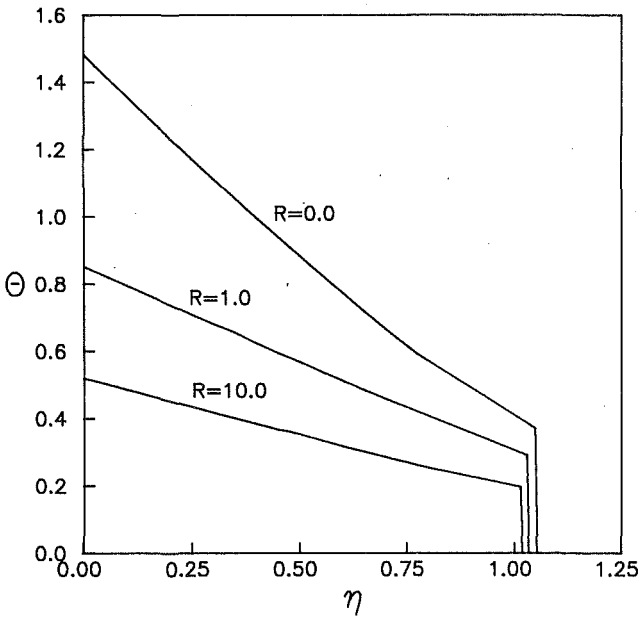

Fig. 2 Effects of R on the dimensionless temperature distribution for $\xi = 1$, $\beta_1 = 0.4$, and $\beta_2 = 0.2$

$$b_1 = \frac{d}{d\eta}\{[1+\beta_1\bar{\theta}^+]\mathbf{N}_a(\eta)\}_{\eta=l/2} - \lambda^2\int_0^{l/2}[1+\beta_2\bar{\theta}^+]\mathbf{N}_a^+(\eta)d\eta - 4R(s+2)\bar{\theta}_1^3 \quad (23a)$$

$$c_1 = \frac{d}{d\eta}\{[1+\beta_1\bar{\theta}^+]\mathbf{N}_b^+(\eta)\}_{\eta=l/2} - \lambda^2\int_0^{l/2}[1+\beta_2\bar{\theta}^+]\mathbf{N}_b^+(\eta)d\eta \quad (23b)$$

and

$$f_1 = \frac{1}{2s}\left\{\beta_1\frac{d}{d\eta}(\bar{\theta}^+)^2_{\eta=l/2} - \lambda^2\beta_2\int_0^{l/2}(\bar{\theta}^+)^2 d\eta - 2(s+2)(3R\bar{\theta}_1^4+1)\right\} \quad (23c)$$

The effects of radiation on the temperature distribution at $\xi = 1.0$, $\beta_1 = 0.4$, and $\beta_2 = 0.2$ are displayed in Fig. 2. As shown in Fig. 2, due to the dissipation of heat into the ambient, the higher surface temperature is obtained by decreasing the value of R. The wave speed for this case can be defined as $c = (\alpha/\tau)^{1/2} = c_0(1+0.4\theta/1+0.2\theta)^{1/2}$. This implies that the propagation speed of the thermal wave is faster for a higher temperature profile. Thus the smaller the value of R, the faster the propagation speed of the thermal wave.

Conclusions

Numerical solutions for various HHC problems with temperature-dependent thermal properties are proposed in the present study. Effects of some dimensionless parameters on the propagation speed of the thermal wave are also investigated. As shown in various comparative examples, the present numerical method is accurate and efficient for such problems. Although thermal properties are assumed to vary with temperature linearly in the illustrative examples, problems with other forms of temperature-dependent thermal properties can also be successfully solved in our numerical tests.

References

Baumeister, K. J., and Hamill, T. D., 1969, "Hyperbolic Heat-Conduction Equation—A Solution for the Semi-infinite Body Problem," ASME JOURNAL OF HEAT TRANSFER, Vol. 91, pp. 543–548.

Cattaneo, C., 1948, "On the Conduction of Heat," *Atti Del Seminar*, Mat. Fis. Univ., Modena, Vol. 3, p. 3.

Chen, H. T., and Lin, J. Y., 1991, "Hybrid Laplace Transform Technique for Nonlinear Transient Thermal Problems," *Int. J. Heat Mass Transfer*, Vol. 34, pp. 1301–1308.

Chen, H. T., and Lin, J. Y., 1993, "Numerical Analysis for Hyperbolic Heat Conduction," *Int. J. Heat Mass Transfer*, Vol. 36, pp. 2891–2898.

Glass, D. E., Özişik, M. N., McRae, D. S., and Vick, B., 1986, "Hyperbolic Heat Conduction With Temperature-Dependent Thermal Conductivity," *Journal of Applied Physics*, Vol. 59, pp. 1861–1865.

Kar, A., Chan, C. L., and Mazumder, J., 1992, "Comparative Studies on Nonlinear Hyperbolic and Parabolic Heat Conduction for Various Boundary Conditions: Analytic and Numerical Solutions," ASME JOURNAL OF HEAT TRANSFER, Vol. 114, pp. 14–20.

Maurer, M. J., and Thompson, H. A., 1973, "Non-Fourier Effects at High Heat Flux," ASME JOURNAL OF HEAT TRANSFER, Vol. 95, pp. 284–286.

Vernotte, M. P., 1958, "Les Paradoxes de la Theorie Continue de l'Equation de la Chaleur," *Comptes Rendus*, Vol. 246, pp. 3154–3155.

Combination of Source-and-Sink Method and Complex-Temperature Method for the Solution of Stefan Problems Imposed With Cyclic Temperature and Flux Conditions

J. G. Nyros[1] and C. K. Hsieh[1]

Nomenclature

A_0, A = temperatures
B_0, B = heat fluxes
c = specific heat
C, E, G, H, I, J, K, L, M, X, Y = special notations in Tables 1 and 2
D = thickness of slab
F = $[\omega/(2\alpha)]^{1/2}$
k = thermal conductivity
L = latent heat
R = interface position
St = Stefan number
t = time
T = temperature
x = position on x axis
α = thermal diffusivity
β_q, β_T = B_0/B, $(A_0 - T_D)/A$
γ = dimensionless thickness
Γ, Δ, Δ', Z, Θ, Θ', Λ = special angles in Tables 1 and 2
δ = Dirac delta function
θ = dimensionless temperature
ξ = dimensionless position
ρ = density, dimensionless interface position
τ = dimensionless time
ω = angular velocity

[1]Mechanical Engineering Department, University of Florida, Gainesville, FL 32611.

Contributed by the Heat Transfer Division of THE AMERICAN SOCIETY OF MECHANICAL ENGINEERS. Manuscript received by the Heat Transfer Division September 1993; revision received December 1993. Keywords: Conduction, Moving Boundaries, Phase-Change Phenomena. Associate Technical Editor: Y. Bayazitoglu.

Subscripts

D = value at $x = D$
i = initial condition
m = melting temperature
q = heat flux
T = temperature

Introduction

Approximate methods developed for the solution of Stefan problems are usually confined to those with imposed conditions that are constant or monotonically time-variant. These methods have often been tested for accuracy for phase change over a short period of time. Although a few exceptions have solutions that can be expressed in closed forms, the majority of the methods call for use of strategies that require development of special algorithms for a numerical solution (Crank, 1984; Hill, 1987; Yao and Prusa, 1989). This may cause inconvenience for use in practice. This paper is offered to present an approximate method for a closed-form solution of the Stefan problems imposed with cyclic conditions. Stefan problems with cyclic conditions have found applications in thawing and freezing of food products, material processing and treatment, and energy storage and release, among others.

Analysis

A source-and-sink method (Hsieh and Choi, 1992a, b) has been combined with a complex temperature method for the solution of a Stefan problem with a cyclic temperature or flux condition imposed on one part of the boundary and a time-invariant condition on the remainder of the boundary. The steady periodic solution is the focus of this investigation and the general methodology for the solution of this problem (see Nyros, 1993) has been applied in this paper to the solution of two examples as follows:

Governing Equation:

$$\frac{\partial^2 T}{\partial x^2} - \left(\frac{\rho L}{k}\right)\left(\frac{dx}{dt}\right)\delta(x-R) = \frac{1}{\alpha}\frac{\partial T}{\partial t}, \quad 0<x<D,\ t>0 \tag{1}$$

Initial Condition:

$$T(x,\ 0) = T_i \tag{2}$$

Boundary Conditions:

$$T(0,\ t) = A_0 + A\sin\omega t \quad \text{(Example 1)} \tag{3a}$$

$$-k\frac{\partial T(0,\ t)}{\partial x} = B_0 + B\sin\omega t \quad \text{(Example 2)} \tag{3b}$$

$$T(D,\ t) = T_D \tag{4}$$

Interface Condition:

$$T(R,\ t) = T_m \tag{5}$$

These examples are solved and the results expressed in terms of dimensionless groups defined as

$$\xi = Fx, \quad \tau = \alpha F^2 t, \quad \rho = FR, \quad \gamma = FD, \quad F = \sqrt{\frac{\omega}{2\alpha}},$$

$$\theta_T = \frac{(A_0 - T)}{A}, \quad \theta_{T,m} = \frac{(A_0 - T_m)}{A},$$

$$\beta_T = \frac{(A_0 - T_D)}{A}, \quad (\mathrm{St})_T = \frac{cA}{L},$$

$$\theta_q = \frac{(T - T_D)kF}{B}, \quad \theta_{q,m} = \frac{(T_m - T_D)kF}{B},$$

$$\beta_q = \frac{B_0}{B}, \quad (\mathrm{St})_q = \frac{cB}{LkF} \tag{6}$$

The dimensionless temperature and the interface position can be derived for the first example as

$$\theta_T(\xi,\ \tau) = \beta_T\frac{\xi}{\gamma} - \sqrt{\frac{G}{E}}\sin(2\tau - \Delta) - \frac{1}{(\mathrm{St})_T}\frac{d\rho}{d\tau}\begin{cases}\sqrt{\dfrac{C}{E}}J & \text{for } 0\le\xi\le\rho \\ \sqrt{\dfrac{G}{E}}K & \text{for } \rho\le\xi\le\gamma\end{cases} \tag{7}$$

$$\frac{d\rho}{d\tau} = \frac{(\mathrm{St})_T}{X}\left[\sqrt{\frac{E}{C}}\left(\beta_T\frac{\rho}{\gamma} - \theta_{T,m}\right) - \sin(2\tau - \Theta)\right] \tag{8}$$

They can be derived for the second example as

$$\theta_q(\xi,\ \tau) = \beta_q\gamma\left(1 - \frac{\xi}{\gamma}\right) + \sqrt{\frac{G}{2I}}\sin(2\tau - \Delta') + \frac{1}{(\mathrm{St})_q}\frac{d\rho}{d\tau}\begin{cases}\sqrt{\dfrac{C}{I}}L & \text{for } 0\le\xi\le\rho \\ \sqrt{\dfrac{G}{I}}M & \text{for } \rho\le\xi\le\gamma\end{cases} \tag{9}$$

$$\frac{d\rho}{d\tau} = \frac{(\mathrm{St})_q}{Y}\sqrt{\frac{I}{2H}}\left\{\sqrt{\frac{2I}{C}}\left[\theta_{q,m} - \beta_q\gamma\left(1 - \frac{\rho}{\gamma}\right)\right] - \sin(2\tau - \Theta')\right\} \tag{10}$$

In these equations, the specialized notations (see Nomenclature) have been defined in Tables 1 and 2. Notice that, in Eq. (8), the points of singularity are given by the relations

$$\rho = 0 \quad \text{and} \quad \tanh\rho\cot\rho\tan\Theta = 1 \tag{11}$$

whereas, in Eq. (10), the points of singularity can be found from the relation

$$\tanh\gamma\tan\gamma\tan Z = 1 \tag{12}$$

Results and Discussion

Prior to the presentation of results in dimensionless forms, sample runs are made with dimensional quantities so that the mechanism for heat transfer can be better understood. Properties of paraffin wax are used for the tests (Hsieh and Choi, 1992a). Other conditions are shown in the legend in the top chart in Figs. 1 and 2.

Equations (8) and (10) are solved by a fourth-order Runge–Kutta method to determine the liquid–solid interface position. Initial conditions are set as $t = 0$ and $R = 10^{-4}$ m (for Example 1, to avoid the singularity) or $R = 0$ (for Example 2). The steady periodic solution manifests itself well before completion of the second imposed cycle.

For tested initial values of R ranging from 10^{-5} m to 0.005 m in Example 1, initial conditions are rapidly damped, and the steady periodic solution results are totally unaffected and highly accurate (maximum position error 3.7 percent). The calculation method is also very tolerant of large and small values for time-step size. Results converge robustly. A correction method based on the energy balance equation was also developed and tested on results from Eqs. (8) and (10). The "corrected" results differed negligibly from the original, so the correction is not considered in this paper. These tests are all detailed in the work by Nyros (1993).

There are two charts for each example in Figs. 1 and 2. To facilitate viewing the interface position as related to the imposed cycles, the top chart is a composite with the imposed

Table 1 Definition of specialized notations used in Eqs. (7) and (8)

$$
\begin{aligned}
C &= [\sinh(\gamma-\rho)\cos(\gamma-\rho)]^2+[\cosh(\gamma-\rho)\sin(\gamma-\rho)]^2\\
E &= (\sinh\gamma\cos\gamma)^2+(\cosh\gamma\sin\gamma)^2\\
G &= [\sinh(\gamma-\xi)\cos(\gamma-\xi)]^2+[\cosh(\gamma-\xi)\sin(\gamma-\xi)]^2\\
J &= \sinh\xi\cos\xi\sin\Theta-\cosh\xi\sin\xi\cos\Theta\\
K &= \sinh\rho\cos\rho\sin\Delta-\cosh\rho\sin\rho\cos\Delta\\
a_\Delta &= \sinh\gamma\cos\gamma\sinh(\gamma-\xi)\cos(\gamma-\xi)\\
&\quad+\cosh\gamma\sin\gamma\cosh(\gamma-\xi)\sin(\gamma-\xi)\\
b_\Delta &= \cosh\gamma\sin\gamma\sinh(\gamma-\xi)\cos(\gamma-\xi)-\sinh\gamma\cos\gamma\cosh\\
&\quad(\gamma-\xi)\sin(\gamma-\xi)\\
c_\Delta &= (EG)^{1/2}\\
a_\theta &= \sinh\gamma\cos\gamma\sinh(\gamma-\rho)\cos(\gamma-\rho)+\cosh\gamma\sin\gamma\cosh\\
&\quad(\gamma-\rho)\sin(\gamma-\rho)\\
b_\theta &= \cosh\gamma\sin\gamma\sinh(\gamma-\rho)\cos(\gamma-\rho)-\sinh\gamma\cos\gamma\cosh\\
&\quad(\gamma-\rho)\sin(\gamma-\rho)\\
c_\theta &= (CE)^{1/2}\\
X &= \sinh\rho\cos\rho\sin\Theta-\cosh\rho\sin\rho\cos\Theta
\end{aligned}
$$

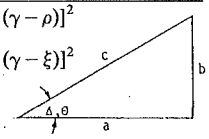

Table 2 Definition of specialized notations used in Eqs. (9) and (10)

$$
\begin{aligned}
C &= [\sinh(\gamma-\rho)\cos(\gamma-\rho)]^2+[\cosh(\gamma-\rho)\sin(\gamma-\rho)]^2\\
G &= [\sinh(\gamma-\xi)\cos(\gamma-\xi)]^2+[\cosh(\gamma-\xi)\sin(\gamma-\xi)]^2\\
H &= (\cosh\rho\cos\rho)^2+(\sinh\rho\sin\rho)^2\\
I &= (\cosh\gamma\cos\gamma)^2+(\sinh\gamma\sin\gamma)^2\\
L &= \cosh\xi\cos\xi\sin\Gamma-\sinh\xi\sin\xi\cos\Gamma\\
M &= \cosh\rho\cos\rho\sin\Lambda-\sinh\rho\sin\rho\cos\Lambda\\
a_{\Delta'} &= (\cosh\gamma\cos\gamma-\sinh\gamma\sin\gamma)\sinh(\gamma-\xi)\cos(\gamma-\xi)\\
&\quad+(\cosh\gamma\cos\gamma+\sinh\gamma\sin\gamma)\cosh(\gamma-\xi)\sin(\gamma-\xi)\\
b_{\Delta'} &= (\cosh\gamma\cos\gamma+\sinh\gamma\sin\gamma)\sinh(\gamma-\xi)\cos(\gamma-\xi)\\
&\quad-(\cosh\gamma\cos\gamma-\sinh\gamma\sin\gamma)\cosh(\gamma-\xi)\sin(\gamma-\xi)\\
c_{\Delta'} &= (2GI)^{1/2}\\
a_\Gamma &= \sinh\gamma\sin\gamma\cosh(\gamma-\rho)\sin(\gamma-\rho)\\
&\quad+\cosh\gamma\cos\gamma\sinh(\gamma-\rho)\cos(\gamma-\rho)\\
b_\Gamma &= \sinh\gamma\sin\gamma\sinh(\gamma-\rho)\cos(\gamma-\rho)\\
&\quad-\cosh\gamma\cos\gamma\cosh(\gamma-\rho)\sin(\gamma-\rho)\\
c_\Gamma &= (CI)^{1/2}\\
a_\Lambda &= \sinh\gamma\sin\gamma\cosh(\gamma-\xi)\sin(\gamma-\xi)\\
&\quad+\cosh\gamma\cos\gamma\sinh(\gamma-\xi)\cos(\gamma-\xi)\\
b_\Lambda &= \sinh\gamma\sin\gamma\sinh(\gamma-\xi)\cos(\gamma-\xi)\\
&\quad-\cosh\gamma\cos\gamma\cosh(\gamma-\xi)\sin(\gamma-\xi)\\
c_\Lambda &= (GI)^{1/2}\\
a_{\Theta'} &= (\cosh\gamma\cos\gamma-\sinh\gamma\sin\gamma)\sinh(\gamma-\rho)\cos(\gamma-\rho)\\
&\quad+(\cosh\gamma\cos\gamma+\sinh\gamma\sin\gamma)\cosh(\gamma-\rho)\sin(\gamma-\rho)\\
b_{\Theta'} &= (\cosh\gamma\cos\gamma+\sinh\gamma\sin\gamma)\sinh(\gamma-\rho)\cos(\gamma-\rho)\\
&\quad-(\cosh\gamma\cos\gamma-\sinh\gamma\sin\gamma)\cosh(\gamma-\rho)\sin(\gamma-\rho)\\
c_{\Theta'} &= (2CI)^{1/2}\\
a_Z &= \cosh\rho\cos\rho\cosh(\gamma-\rho)\sin(\gamma-\rho)\\
&\quad+\sinh\rho\sin\rho\sinh(\gamma-\rho)\cos(\gamma-\rho)\\
b_Z &= \cosh\rho\cos\rho\sinh(\gamma-\rho)\cos(\gamma-\rho)\\
&\quad-\sinh\rho\sin\rho\cosh(\gamma-\rho)\sin(\gamma-\rho)\\
c_Z &= (CH)^{1/2}\\
Y &= \sinh\gamma\sin\gamma\sin Z-\cosh\gamma\cos\gamma\cos Z
\end{aligned}
$$

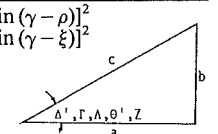

boundary cycle (normalized by the amplitude of the oscillation) placed in the top part of the chart. The bottom chart is a detailed examination of the temperature oscillation with time at different depths in the slab. In this bottom chart, the curves are lined up at temperatures equal to $A_0+(T_D-A_0)(x/D)$ for the prescribed temperature or $T_D+(B_0D/k)(1-(x/D))$ for the prescribed heat flux. In this way, the amplitude attenuation can be more easily seen in these figures.

As shown in Fig. 1, a sinusoidal temperature imposed at the boundary causes the interface position to oscillate sinusoidally with a time delay less than a quarter period. However, an imposed sinusoidal heat flux (see Fig. 2) causes the interface to oscillate with a time delay greater than a quarter period. Thus a cosine function can be inferred for the flux condition, believed to be the result of the interface position's close relationship to the local medium temperature, while the flux is the differential of the temperature.

It should be noted that the solution of the periodic steady problems given in this paper can be decomposed into two parts: one due to the boundary condition excitation without oscillation and the other strictly due to the oscillation. Then, based on the conditions imposed at the boundaries as given in Example 1, the former leads to a neutral position of the interface position located at 0.005 m. This gives rise to another phenomenon that is related to how the interface oscillates; it ranges in depth from 0.00458 m to 0.00536 m. The neutral position at 0.005 m cuts the position curve into equal areas lying between the curve and the line. All the upper lobes are fat and short while the lower lobes are slim and tall. The interface thus takes a slightly longer time to penetrate across the median line, a phenomenon in total agreement with the physics of heat penetration. However, the total period of the position oscillation remains constant at the value of the imposed cycle of excitation. The same trends are found for the imposed flux cycle as shown in the interface position chart in Fig. 2.

As for the temperature history in Figs. 1 and 2, the time delay at each depth may be found by tracking the intersection of the curves with the zero axis. In the first example (Fig. 1),

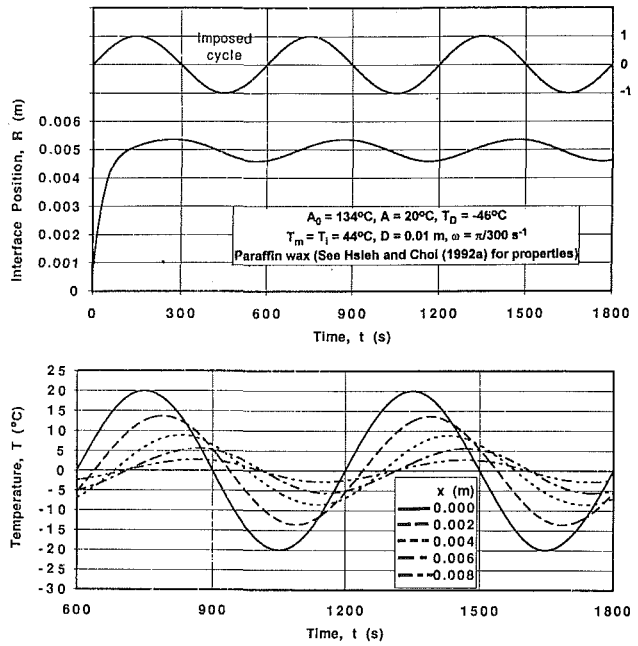

Fig. 1 Interface position and temperature histories in the slab imposed with cyclic temperature boundary condition

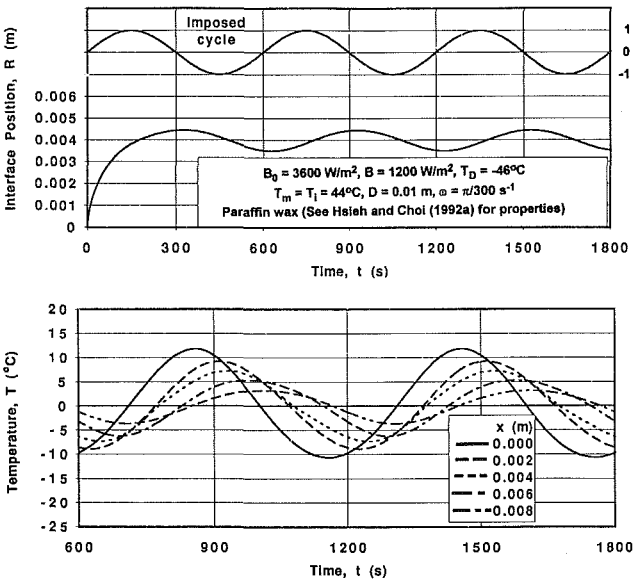

Fig. 2 Interface position and temperature histories in the slab imposed with cyclic heat flux boundary condition

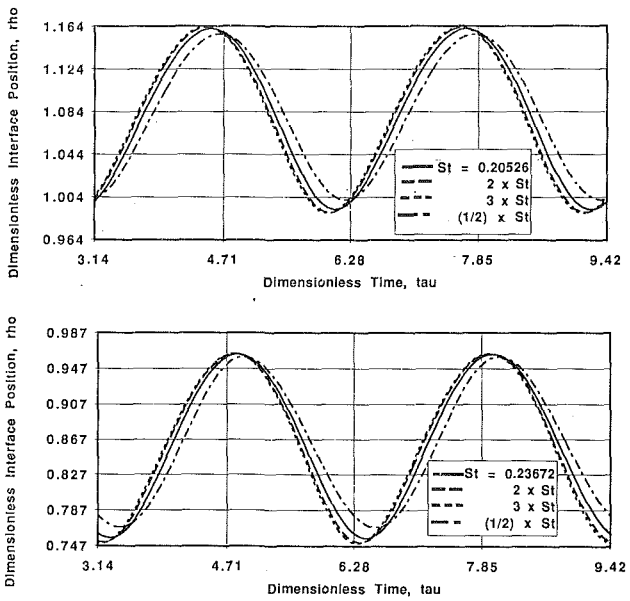

Fig. 3 Dimensionless interface position change due to Stefan number for the slab imposed with cyclic temperature and heat flux condition

delays are visible in the liquid region (small x), but are hardly noticeable in the solid region (large x). The phase-change interface thus has an effect of suppressing the time delay. For the second example (Fig. 2), the surface temperature cycle lags behind the imposed flux cycle. Notice that the interface no longer suppresses the time delay in the solid region. Discussion is complete for the dimensional plots; attention will now be directed toward the dimensionless plots.

Figure 3 shows the dimensionless interface position plotted for several Stefan numbers, one chart for each example. The Stefan number is the parameter most closely related to material properties. In the charts, a solid curve is drawn to represent the baseline established by using the conditions given in Figs. 1 and 2. The dimensionless excitation period is π, and the neutral position for ρ can be calculated to be 1.084 (for Example 1, top chart) or 0.867 (for Example 2, bottom chart). As shown for both examples, an increase of the Stefan number leads to decreased time delay and increased amplitude of oscillation of the interface. This is believed to be caused by the increase of the c/L ratio. However, such changes stabilize rapidly at large Stefan numbers, a unique feature of the cyclic excitation accompanied by phase change.

It is interesting to note that, while the dimensionless interface position is a function of the Stefan number, the dimensionless temperature is not. This is because the $(\mathrm{St})^{-1}$ in θ (Eqs. (7) and (9)) is canceled by (St) in $d\rho/d\tau$ (Eqs. (8) and (10)). Curves for dimensionless temperature look like the dimensional curves given in Figs. 1 and 2 and are thus not given in this paper. The results are presented in great detail in the work by Nyros (1993).

References

Crank, J., 1984, *Free and Moving Boundary Problems*, Clarendon, London, United Kingdom.

Hill, J. M., 1987, *One-Dimensional Stefan Problems: an Introduction*, Longman, London, United Kingdom.

Hsieh, C. K., and Choi, C.-Y., 1992a, "Solution of One- and Two-Phase Melting and Solidification Problems Imposed With Constant or Time-Variant Temperature and Flux Boundary Conditions," ASME JOURNAL OF HEAT TRANSFER, Vol. 114, pp. 524–528.

Hsieh, C. K., and Choi, C.-Y., 1992b, "A General Analysis of Phase-Change Energy Storage for Solar Energy Applications," ASME *Journal of Solar Energy Engineering*, Vol. 114, pp. 203–211.

Nyros, J. G., 1993, "Combination of Source-and-Sink Method and Complex Temperature Method for the Solution of Stefan Problems Imposed With Cyclic Temperature and Flux Conditions," M.S. Thesis, University of Florida, Gainesville, FL.

Yao, L. S., and Prusa, J., 1989, "Melting and Freezing," *Adv. Heat Transfer*, Vol. 19, pp. 1–95.

Pore Size Distribution and Apparent Gas Thermal Conductivity of Silica Aerogel

S. Q. Zeng,[1] A. J. Hunt,[1] W. Cao,[1] and R. Greif[2]

Introduction

Aerogel is an open-cell, transparent superinsulator (Kistler, 1931) whose preparation has been summarized by Hunt et al. (1991). A mixture containing water, TEOS (tetraethyl orthosilicate), alcohol (ethanol), and catalysts is mixed and poured into a mold where liquids react to form a fine silica particle suspension called an alcosol. The particles grow and interconnect to form alcogel, which is a semisolid gel containing alcohol. Alcohol is removed from the alcogel using a supercritical drying procedures, leaving aerogel. Silica aerogel is a network of short bonded chains of silica particles, which are fused together (Tewari et al., 1985). Particles of diameters 2–5 nm and pores of diameter 10–100 nm produce a solid-gas matrix in which the volume fraction of the solid can be less than 5 percent. The small pore size effectively limits the motion of gas molecules and hence reduces the apparent gas conductivity to a very low level.

The apparent gas conductivity in a confined space, K, can be expressed as follows (Kaganer, 1969):

$$K = K_g^o \Big/ \left(1 + 2\frac{2\gamma}{\gamma+1}\frac{1}{\mathrm{Pr}}\frac{2-\alpha}{\alpha}\mathrm{Kn}\right) = K_g^o/[1+(C/Pl_{ch})] \quad (1)$$

where K_g^o is the conductivity of the gas in free space, Kn is the Knudsen number defined as the ratio of the molecule mean free path, l_m ($= k_B T/\sqrt{2}\pi d^2 P$), to the characteristic dimension of the system, l_{ch}, and

$$C = 2\frac{2\gamma}{\gamma+1}\frac{1}{\mathrm{Pr}}\frac{2-\alpha}{\alpha}\frac{k_B T}{\sqrt{2}\pi d^2}; \quad (2)$$

α is the accommodation coefficient, k_B is the Boltzman constant, γ is the ratio of the specific heats, and d is the diameter of the gas molecule. Equation (1) was derived for a system that has only one length scale, but porous media usually have a range of pore or length scales. One approach for the variable pore size problem is to use Eq. (1) and simply choose the value for l_{ch} that gives the best agreement with the experimental data for the apparent gas conductivity K. Another approach uses the mean or the most probable pore size (as determined by nitrogen adsorption-desorption measurement, Fig. 1) for the characteristic length, l_{ch}, and then chooses the constant C to give the best agreement with the data. Note that the second approach explicitly relates the conductivity to the pore size.

[1] Lawrence Berkeley Laboratory, University of California, Berkeley, CA 94720.

[2] Department of Mechanical Engineering, University of California, Berkeley, CA 94720.

Contributed by the Heat Transfer Division of THE AMERICAN SOCIETY OF MECHANICAL ENGINEERS. Manuscript received by the Heat Transfer Division August 1993; revision received March 1994. Keywords: Modeling and Scaling, Porous Media, Thermophysical Properties. Associate Technical Editor: L. S. Fletcher.

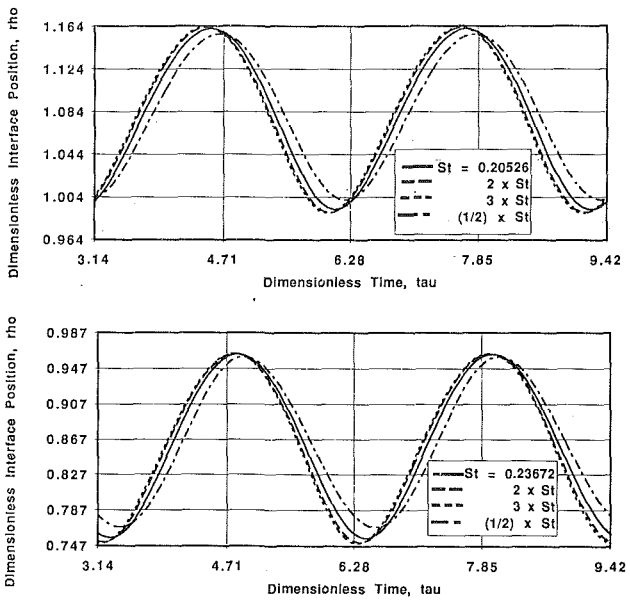

Fig. 3 Dimensionless interface position change due to Stefan number for the slab imposed with cyclic temperature and heat flux condition

delays are visible in the liquid region (small x), but are hardly noticeable in the solid region (large x). The phase-change interface thus has an effect of suppressing the time delay. For the second example (Fig. 2), the surface temperature cycle lags behind the imposed flux cycle. Notice that the interface no longer suppresses the time delay in the solid region. Discussion is complete for the dimensional plots; attention will now be directed toward the dimensionless plots.

Figure 3 shows the dimensionless interface position plotted for several Stefan numbers, one chart for each example. The Stefan number is the parameter most closely related to material properties. In the charts, a solid curve is drawn to represent the baseline established by using the conditions given in Figs. 1 and 2. The dimensionless excitation period is π, and the neutral position for ρ can be calculated to be 1.084 (for Example 1, top chart) or 0.867 (for Example 2, bottom chart). As shown for both examples, an increase of the Stefan number leads to decreased time delay and increased amplitude of oscillation of the interface. This is believed to be caused by the increase of the c/L ratio. However, such changes stabilize rapidly at large Stefan numbers, a unique feature of the cyclic excitation accompanied by phase change.

It is interesting to note that, while the dimensionless interface position is a function of the Stefan number, the dimensionless temperature is not. This is because the $(\mathrm{St})^{-1}$ in θ (Eqs. (7) and (9)) is canceled by (St) in $d\rho/d\tau$ (Eqs. (8) and (10)). Curves for dimensionless temperature look like the dimensional curves given in Figs. 1 and 2 and are thus not given in this paper. The results are presented in great detail in the work by Nyros (1993).

References

Crank, J., 1984, *Free and Moving Boundary Problems*, Clarendon, London, United Kingdom.

Hill, J. M., 1987, *One-Dimensional Stefan Problems: an Introduction*, Longman, London, United Kingdom.

Hsieh, C. K., and Choi, C.-Y., 1992a, "Solution of One- and Two-Phase Melting and Solidification Problems Imposed With Constant or Time-Variant Temperature and Flux Boundary Conditions," ASME JOURNAL OF HEAT TRANSFER, Vol. 114, pp. 524–528.

Hsieh, C. K., and Choi, C.-Y., 1992b, "A General Analysis of Phase-Change Energy Storage for Solar Energy Applications," ASME *Journal of Solar Energy Engineering*, Vol. 114, pp. 203–211.

Nyros, J. G., 1993, "Combination of Source-and-Sink Method and Complex Temperature Method for the Solution of Stefan Problems Imposed With Cyclic Temperature and Flux Conditions," M.S. Thesis, University of Florida, Gainesville, FL.

Yao, L. S., and Prusa, J., 1989, "Melting and Freezing," *Adv. Heat Transfer*, Vol. 19, pp. 1–95.

Pore Size Distribution and Apparent Gas Thermal Conductivity of Silica Aerogel

S. Q. Zeng,[1] A. J. Hunt,[1] W. Cao,[1] and R. Greif[2]

Introduction

Aerogel is an open-cell, transparent superinsulator (Kistler, 1931) whose preparation has been summarized by Hunt et al. (1991). A mixture containing water, TEOS (tetraethyl orthosilicate), alcohol (ethanol), and catalysts is mixed and poured into a mold where liquids react to form a fine silica particle suspension called an alcosol. The particles grow and interconnect to form alcogel, which is a semisolid gel containing alcohol. Alcohol is removed from the alcogel using a supercritical drying procedures, leaving aerogel. Silica aerogel is a network of short bonded chains of silica particles, which are fused together (Tewari et al., 1985). Particles of diameters 2–5 nm and pores of diameter 10–100 nm produce a solid–gas matrix in which the volume fraction of the solid can be less than 5 percent. The small pore size effectively limits the motion of gas molecules and hence reduces the apparent gas conductivity to a very low level.

The apparent gas conductivity in a confined space, K, can be expressed as follows (Kaganer, 1969):

$$K = K_g^o \Big/ \left(1 + 2\frac{2\gamma}{\gamma+1}\frac{1}{\mathrm{Pr}}\frac{2-\alpha}{\alpha}\mathrm{Kn}\right) = K_g^o/[1+(C/Pl_{ch})] \quad (1)$$

where K_g^o is the conductivity of the gas in free space, Kn is the Knudsen number defined as the ratio of the molecule mean free path, l_m ($= k_B T/\sqrt{2}\pi d^2 P$), to the characteristic dimension of the system, l_{ch}, and

$$C = 2\frac{2\gamma}{\gamma+1}\frac{1}{\mathrm{Pr}}\frac{2-\alpha}{\alpha}\frac{k_B T}{\sqrt{2}\pi d^2}; \quad (2)$$

α is the accommodation coefficient, k_B is the Boltzman constant, γ is the ratio of the specific heats, and d is the diameter of the gas molecule. Equation (1) was derived for a system that has only one length scale, but porous media usually have a range of pore or length scales. One approach for the variable pore size problem is to use Eq. (1) and simply choose the value for l_{ch} that gives the best agreement with the experimental data for the apparent gas conductivity K. Another approach uses the mean or the most probable pore size (as determined by nitrogen adsorption-desorption measurement, Fig. 1) for the characteristic length, l_{ch}, and then chooses the constant C to give the best agreement with the data. Note that the second approach explicitly relates the conductivity to the pore size.

[1] Lawrence Berkeley Laboratory, University of California, Berkeley, CA 94720.

[2] Department of Mechanical Engineering, University of California, Berkeley, CA 94720.

Contributed by the Heat Transfer Division of THE AMERICAN SOCIETY OF MECHANICAL ENGINEERS. Manuscript received by the Heat Transfer Division August 1993; revision received March 1994. Keywords: Modeling and Scaling, Porous Media, Thermophysical Properties. Associate Technical Editor: L. S. Fletcher.

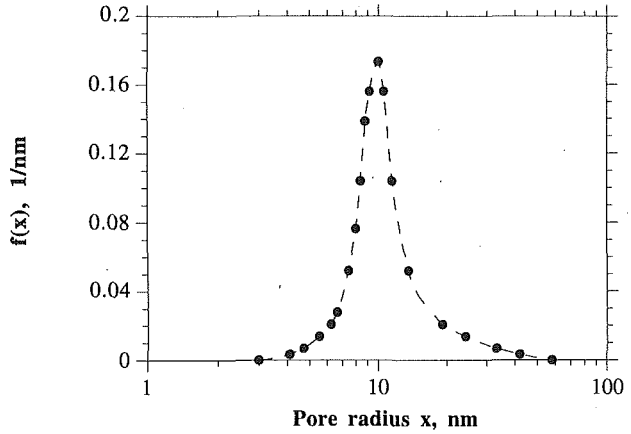

Fig. 1 Normalized pore size distribution of silica aerogel

The result for the pressure dependence of the conductivity from Eq. (1) is not in agreement with our experimental data, although it is qualitatively right for a porous medium. When the pressure is large ($Kn \ll 1$), K approaches K_g^o, and when the pressure is small ($Kn \gg 1$), K increases linearly with the pressure. To retain the main features of Eq. (1), we modify it according to

$$K = K_g^o/[1 + (C_1/P^{n_1} l_{ch})] \tag{3}$$

In this paper, we will establish a model for the determination of the apparent gas conductivity in terms of the pore sizes. We use the method of gas adsorption-desorption to determine the pore size distribution for silica aerogel. The thermal conductivity is measured by using the hot-wire technique (Morrow, 1979) and the experimental data are then used to determine the constants C_1 and n_1 in Eq. (3).

Channel Model of Apparent Gas Conductivity

The pores of an aerogel are open-type and interconnected to one another like those in a sponge. The purpose here is to find the apparent gas conductivity of an aerogel slab. The aerogel is modeled as a porous medium containing pores of various sizes, interconnected both in series and in parallel; the pores are in the form of capillaries, joined end to end in parallel, adiabatic channels that run through the material. Those assumptions are consistent with the aerogel structure in the case of one-dimensional heat transfer.

The apparent gas conductivity K_i of a channel i ($i = 1, 2, \ldots, m$) comprised of n pores of length x_j and width x_j with conductivity K_{ij} ($i = 1, 2, \ldots, m$ and $j = 1, 2, \ldots, n$) is given by (Eckert, 1959)

$$1/K_i = \sum_{j=1}^{n} x_j/K_{ij} \Big/ \sum_{j=1}^{n} x_j = \sum_{j=1}^{n} \left[x_j \Big/ \left(K_{ij} \sum_{j=1}^{n} x_j \right) \right] \tag{4}$$

The total apparent gas conductivity is equal to the sum of the conductivities of m parallel channels, i.e.,

$$K = \sum_{i=1}^{m} K_i x_i \Big/ \sum_{i=1}^{m} x_i = \sum_{i=1}^{m} \left\{ \left[x_i \Big/ \sum_{i=1}^{m} x_i \right] \Big/ \sum_{j=1}^{n} \left[x_j \Big/ \sum_{j=1}^{n} x_j K_{ij} \right] \right\} \tag{5}$$

Assuming isothermal channels in the transverse direction, instead of adiabatic channels in the direction of the temperature gradient as above, also leads to Eq. (5). K_{ij} is the apparent gas conductivity in a pore of size $x_i \times x_j$. Although Eq. (3) is difficult to use when a medium has more than one length scale, there is no restriction imposed on the size of the medium. Hence, K from Eq. (3) can be employed to calculate the apparent gas conductivity, K_{ij}, of a pore in a porous medium.

Pore Size Distribution

The quantities $x_i/\Sigma x_i$ and $x_j/\Sigma x_j$ in Eq. (5) are replaced by continuous pore size distribution functions $f(x_i)dx_i$ and $f(x_j)dx_j$, respectively:

$$K = \int_0^\infty \left\{ 1 \Big/ \int_0^\infty [1 K_{ij}] f(x_j) dx_j \right\} f(x_i) dx_i \tag{6}$$

Pore sizes x_i and x_j may be different but the pore size distributions $f(x_i)dx_i$ and $f(x_j)dx_j$ are the same; therefore, the second integral in Eq. (6) is redundant and Eq. (6) then becomes

$$K = K_g^o \Big/ \int_0^\infty (1 + C_1/P^{n_1} x) f(x) dx \tag{7}$$

The probability density function of the pore sizes, $f(x)$, can be obtained from nitrogen adsorption-desorption measurements (Gregg and Sing, 1982). At a fixed temperature, the adsorption of nitrogen by an aerogel sample is determined by the relative pressure of nitrogen vapor, which can be expressed as an adsorption isotherm $m = f(p/p_0)$ where m is the amount of adsorbed nitrogen, p is the partial pressure, and p_o is the saturation pressure of the nitrogen vapor. The Kelvin equation $x = 0.4146 \text{ nm}/\log(p_o/p)$ relates the pressure to the pore radius. The equations for m and x establish the relationship between pore size and the volume of all pores that have radii up to and including x, that is, the cumulative pore volume V_x. V_x is equal to m divided by the density of nitrogen liquid. One can plot V_x against x and pore size distribution curve is the derived curve dV_x/dx. The probability density function $f(x)$ in Eq. (7) is equal to dV_x/dx divided by the total volume of the pores V. Figure 1 shows the measured normalized pore size distribution of a silica aerogel. The most probable pore radius, x_{mp}, is about 10 nm.

Equation (7) relates the apparent gas conductivity to the pore size distribution. The apparent gas conductivities of porous media with the same mean pore size x will still be different if they have different pore size distributions $f(x)$. Consider one porous medium (1) having 50 percent of the pores with a radius 3 nm and 50 percent with radius 5 nm and another medium (2) having all pores of radius 4 nm. From Eq. (7), one obtains

$$K_{\text{medium 2}} = K_g^o/(1 + 4C_1/16P^{n_1}) > K_{\text{medium 1}} = K_g^o/(1 + 4C_1/15P^{n_1})$$

For a given mean pore size and a given total pore volume, the more uniform the pore size of a porous medium, the larger is its apparent gas conductivity. However, media with uniform pore size distributions have a smaller apparent solid and radiative conductivity. It is noted that in many applications, a porous medium is evacuated so that the gas conductivity is less important.

Equation (7) is useful for the analysis of the effects of the pore size distribution on apparent gas conductivity but it is difficult to utilize. For simplicity, using the most probable pore size, x_{mp}, in place of the pore size distribution function yields

$$K = K_g^o/(1 + C_2/P^{n_2} x_{mp}) \tag{8}$$

Thermal Conductivity Measurement

The hot-wire technique (Morrow, 1979) was used to measure the thermal conductivity of silica aerogel opacified with fine carbon particles. A schematic drawing of the experimental system is shown in Fig. 2(*a*). The equipment includes: (1) current source, capable of supplying constant current in the range from 0 to 5 A with a stability of ±0.0002 A/min; (2) shunt with a resistance 16.7 milliohms rated at 3 A; (3) digital voltmeter, five-digit resolution; (4) vacuum system, pressure ranges from 40 millitorrs to 760 torrs. The test specimen con-

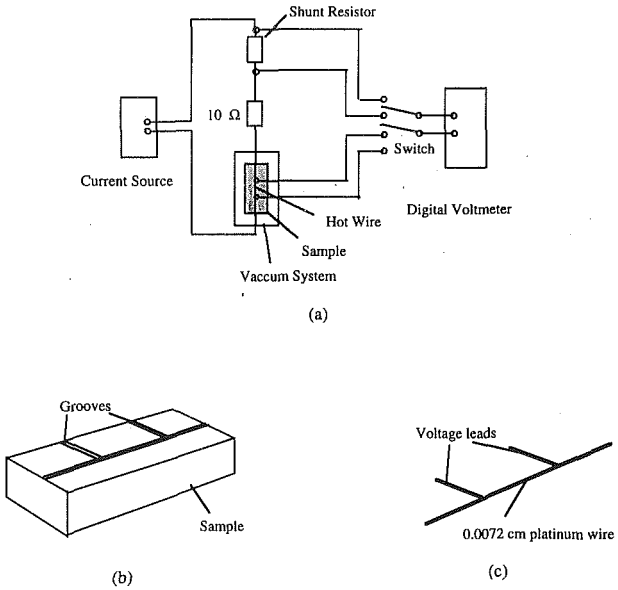

Fig. 2 Hot-wire arrangement

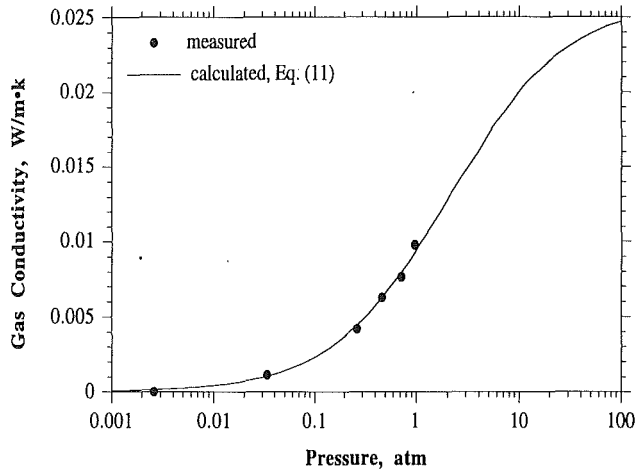

Fig. 3 Pressure dependence of the conductivity of gas in silica aerogel

sists of two $10 \times 5 \times 1.5$ cm^3 plates of aerogel containing carbon opacifier, on one of which thin grooves were cut (Fig. 2(*b*)). The hot-wire harness shown in Fig. 2(*c*) is made of pure platinum wire with a diameter 0.0072 cm. In the test, the hot-wire harness is positioned in the grooves of one specimen and the other specimen is placed on top. Two specimens are held together and placed in the vacuum system.

In the hot-wire test an electric current is passed through the hot wire imbedded in a test sample. Heat generated from the hot wire will increase the temperature of the wire. The rate at which the temperature of the hot wire increases depends on the thermal conductivity of the sample. The change of the temperature of the hot wire changes its electric resistance and the voltage drop across it.

The result for the thermal conductivity is (Morrow, 1979)

$$K = Q/[4\pi dT/d\ln(t)] = AV_wV_{sh}^2/Bd_w^2$$

where Q is the power input to the hot wire, V_w and V_{sh} are the voltage drops across the hot wire and shunt, respectively, B is the slope of the ln(time) versus V_w plot, d_w is the diameter of the hot wire, and A is a constant depending on the shunt resistance; the properties of the wire and B are measured in the experiment.

Uncertainties in the measurement are given below at the condition of a gas pressure of 0.0033 atm, when the total apparent conductivity of medium has the lowest value. The precision limit is as follows:

$$\frac{P_K}{K} = \sqrt{\left(\frac{2P_{d_w}}{d_w}\right)^2 + \left(\frac{P_{V_w}}{V_W}\right)^2 + \left(\frac{2P_{V_{sh}}}{V_{sh}}\right)^2 + \left(\frac{P_B}{B}\right)^2}$$

$$= \sqrt{\left(\frac{2\times 0.5\ \mu\text{m}}{72\ \mu\text{m}}\right)^2 + \left(\frac{0.535\ \text{mV}}{73.6\ \text{mV}}\right)^2 + \left(\frac{2\times 0.535\ \text{mV}}{73.6\ \text{mV}}\right)^2 + \left(\frac{0.0005\ \text{mV/s}}{0.01624\ \text{mV/s}}\right)^2} = 0.038$$

The bias limits B_{V_w}, $B_{V_{sh}}$, and B_B are negligible compared with B_{d_w}; therefore,

$$B_K/K = 2\times B_{d_w}/d_w = 2\times 0.5\ \mu\text{m}/72\ \mu\text{m} = 0.014$$

The overall uncertainty in the determination of K, U_K, is:

$$U_K/K = \sqrt{0.038^2 + 0.014^2} = 4.0 \text{ percent.}$$

The hot-wire technique yields the total conductivity, which includes contributions from the gas and the solid and includes radiative transfer through the gas. When the gas pressure is lower than 10^{-3} atm, the apparent gas conductivity is very small and the total conductivity essentially results from the solid and radiation contributions, which are independent of pressure. The apparent gas conductivity was obtained by subtracting the solid and radiative conductivity from the total conductivity at each pressure. The results are shown in Fig. 3.

Calculations and Discussion

Assume that the gas in the pores is air at 300 K and K_g^o is 0.026 W/m·K. The constant C expressed in Eq. (2) is found to be 0.02 N/m with the accommodation coefficient taken to be unity.

From the measured pore size distribution (Fig. 1) and the measured apparent gas conductivity (Fig. 3), the constants C_1 and n_1 in Eq. (7) and C_2 and n_2 in Eq. (8) were calculated. For each datum K from experiment corresponding to P, C/P^n was computed as a whole according to Eqs. (7) and (8), respectively. In this way, a set of data (P, C/P^n) were obtained and C and n were then obtained by curve-fitting. The following results corresponding to Eqs. (1), (7), and (8) are:

$$K = 0.026/(1 + 0.2{*}10^3/Pl_{ch}) \tag{9}$$

$$K = 0.026\Big/\left[\int_0^\infty (1 + 19.9/P^{0.768}x)f(x)dx\right] \tag{10}$$

$$K = 0.026/(1 + 17.4/P^{0.769}x_{mp}) \tag{11}$$

where l_{ch}, x, and x_{mp} are in unit nm and P in unit atm. Equation (11) is plotted in Fig. 3 along with the experimental data. The essentially equal values for n_1 (0.768) and n_2 (0.769) indicate that the pore sizes of the aerogel used in the experiment are very uniform.

By comparing Eqs. (9) and (11) at atmospheric pressure, one obtains:

$$l_{ch}/x_{mp} = 0.2{*}10^3/17.4 \approx 11.5$$

Thus, the characteristic length of the aerogel for the determination of the apparent gas conductivity is about eleven times greater than the most probable pore size. Note that the Knudsen number, $\text{Kn} = l_m/l_{ch} = 32.6\ \text{nm}/11.5 \times 10\ \text{nm} \approx 0.3$ for this condition.

Conclusions

A porous medium has a range of pore sizes and the calculation of the apparent gas conductivity should reflect this property. A channel model of the conductivity of the gas in a porous medium relates the apparent gas conductivity to a pore size distribution function, which is obtained from gas adsorption-desorption measurements. This model is used to analyze the effect of pore size distribution on the apparent gas conductivity. A simple formula for the apparent gas conductivity based on the most probable pore size is also provided. It is found that at atmospheric pressure, the characteristic length of the aerogel used for the calculation of the apparent gas conductivity is about eleven times greater than its most probable pore size and the Knudsen number is about 0.3.

Acknowledgments

This work was supported by the Assistant Secretary for Conservation and Renewable Energy, Advanced Industrial Concepts (AIC) Materials Program of the Advanced Industrial Concepts Division, Office of Industrial Technologies of the U.S. Department of Energy under Contract No. DE-AC03-76F00098.

References

Eckert, E. R. G., 1959, *Heat and Mass Transfer*, 2nd ed., McGraw-Hill, New York.

Gregg, S. I., and Sing, K. S. W., 1982, *Adsorption, Surface Area and Porosity*, 2nd ed., Academic Press, London, UK.

Hunt, A. J., Jantzen, K., and Cao, W., 1991, "Aerogel—A High Performance Insulating Material at 0.1 Bar," *Insulation Materials: Testing and Applications*, Vol. 2, ASTM STP 1116, R. S. Graves and D. C. Wysocki, eds., American Society for Testing and Materials, Philadelphia, PA, pp. 455–463.

Kaganer, M. G., 1969, *Thermal Insulation in Cryogenic Engineering*, Israel Program of Scientific Translation, Jerusalem.

Kistler, S. S., 1931, "Coherent Expanded Aerogels and Jellies," *Nature*, Vol. 127, No. 3211, p. 741.

Loeb, L. B., 1934, *The Kinetic Theory of Gases*, McGraw-Hill, New York.

Morrow, G. D., 1979, "Improved Hot Wire Thermal Conductivity Technique," *Ceramic Bulletin*, Vol. 58, No. 7, pp. 687–690.

Tewari, P. H., Hunt, A. J., Lieber, J. G., and Lofftus, K., 1985, "Microstructural Properties of Transparent Silica, Aerogels," *Aerogels, Proceedings of the First International Symposium*, J. Fricke, ed., Wuerzburg, Federal Republic of Germany, Sept. 23–25, pp. 142–147.

Corrective Solutions for Intrinsic Thermocouples Under Polynomial Substrate Loading

A. E. Segall[1]

Nomenclature

a_0–a_3 = polynomial coefficients
C_1 = dimensionless constant = $\beta/(8/\pi^2+\beta)$
C_2 = dimensionless constant = $4/(8/\pi+\beta\pi)$
C_3 = dimensionless constant = (C_1-1)
k = dimensionless thermal conductivity ratio = k_{Tc}/k_{Sb}
$R(t)$ = measured thermocouple response = $a_0+a_1t+a_2t^2+a_3t^3$
r = thermocouple wire radius
t = dimensionless time = $\alpha_{Sb}t^*/r^2$
t^* = time
α = dimensionless thermal diffusivity ratio = α_{Tc}/α_{Sb}
β = dimensionless constant = $k/\sqrt{\alpha}$
$\Delta T(t)$ = substrate temperature forcing function
$\Theta(t)$ = function defined by Eq. (7)
ξ = argument used by Eq. (9) = $C_2\sqrt{t}/|C_3|$
$\Phi(t)$ = unit step response for an ideal intrinsic thermocouple

Subscripts

Sb = substrate
Tc = thermocouple

Introduction

With the advent of general purpose finite-element and finite-difference numerical methods, the design process for high-temperature applications where all modes of heat transfer may be important and material properties often exhibit distinct temperature dependencies has become increasingly sophisticated. However, as illustrated by a number of thermal shock and fatigue studies conducted by Segall and co-workers (1991, 1992, 1993), precise temperature measurements are still required to avoid an overabundance of assumptions pertaining to the uniformity and temporal nature of the thermal state. When surface-mounted thermocouples are used for these temperature measurements, specialized techniques are required to minimize the errors associated with the junction displacement from the surface and conduction along the lead wires (Segall, 1992). Yet, even when these techniques are used, measurement errors may still permeate the data, especially when very rapid temperature changes are involved.

Although a multitude of corrective techniques have been developed for thermocouple measurements over the years, they usually required specialized numerical procedures or difficult to determine empirical constants (Quandt and Fink, 1960; Hennecke and Sparrow, 1970; Wally, 1977, to name a few). To offset these shortcomings, a number of useful analytical relationships utilizing Laplace transforms have since been derived by Keltner and Beck (1983) for intrinsic and beaded thermocouples mounted to a thick wall. Unfortunately, the difficulties associated with the inversion of these relationships have precluded use of the solutions to all but the simplest cases of measured response such as step and ramp temperature changes. Because the temperature changes and measured response associated with thermal shock are rarely step or linear functions of time, an expanded solution base is required. The purpose of this paper is therefore to expand the Laplace transform solutions to include intrinsic thermocouples with a measured response that can be approximated by an arbitrary third-order polynomial.

Analytical Considerations

All the relationships used in this analysis are based on the mathematical models derived by Keltner and Beck (1983) for the response of surface-mounted thermocouples on a thick wall or substrate. Using these relationships under the assumption of constant thermophysical properties, the principal of superposition may be used to extract the thermocouple's response $R(t)$, to an arbitrary substrate temperature loading $\Delta T(t)$, through the use of Duhamel's integral (Fodor, 1965):

$$R(t)=\frac{\partial}{\partial t}\int_0^t \Delta T(\tau)\cdot\Phi(t-\tau)\,d\tau \qquad (1)$$

where $\Phi(t)$ is the response of the thermocouple to a unit step temperature change. For an ideal intrinsic thermocouple with negligible contact resistance and lateral heat transfer to the

[1] Senior Research Associate, Center for Advanced Materials, The Pennsylvania State University, 511 Deike Building, University Park, PA 16802.

Contributed by the Heat Transfer Division of THE AMERICAN SOCIETY OF MECHANICAL ENGINEERS. Manuscript received by the Heat Transfer Division October 1993; revision received March 1994. Keywords: Conduction, Measurement Techniques, Transient and Unsteady Heat Transfer. Associate Technical Editor: L. S. Fletcher.

Conclusions

A porous medium has a range of pore sizes and the calculation of the apparent gas conductivity should reflect this property. A channel model of the conductivity of the gas in a porous medium relates the apparent gas conductivity to a pore size distribution function, which is obtained from gas adsorption-desorption measurements. This model is used to analyze the effect of pore size distribution on the apparent gas conductivity. A simple formula for the apparent gas conductivity based on the most probable pore size is also provided. It is found that at atmospheric pressure, the characteristic length of the aerogel used for the calculation of the apparent gas conductivity is about eleven times greater than its most probable pore size and the Knudsen number is about 0.3.

Acknowledgments

This work was supported by the Assistant Secretary for Conservation and Renewable Energy, Advanced Industrial Concepts (AIC) Materials Program of the Advanced Industrial Concepts Division, Office of Industrial Technologies of the U.S. Department of Energy under Contract No. DE-AC03-76F00098.

References

Eckert, E. R. G., 1959, *Heat and Mass Transfer*, 2nd ed., McGraw-Hill, New York.

Gregg, S. I., and Sing, K. S. W., 1982, *Adsorption, Surface Area and Porosity*, 2nd ed., Academic Press, London, UK.

Hunt, A. J., Jantzen, K., and Cao, W., 1991, "Aerogel—A High Performance Insulating Material at 0.1 Bar," *Insulation Materials: Testing and Applications*, Vol. 2, ASTM STP 1116, R. S. Graves and D. C. Wysocki, eds., American Society for Testing and Materials, Philadelphia, PA, pp. 455–463.

Kaganer, M. G., 1969, *Thermal Insulation in Cryogenic Engineering*, Israel Program of Scientific Translation, Jerusalem.

Kistler, S. S., 1931, "Coherent Expanded Aerogels and Jellies," *Nature*, Vol. 127, No. 3211, p. 741.

Loeb, L. B., 1934, *The Kinetic Theory of Gases*, McGraw-Hill, New York.

Morrow, G. D., 1979, "Improved Hot Wire Thermal Conductivity Technique," *Ceramic Bulletin*, Vol. 58, No. 7, pp. 687–690.

Tewari, P. H., Hunt, A. J., Lieber, J. G., and Lofftus, K., 1985, "Microstructural Properties of Transparent Silica, Aerogels," *Aerogels, Proceedings of the First International Symposium*, J. Fricke, ed., Wuerzburg, Federal Republic of Germany, Sept. 23–25, pp. 142–147.

Corrective Solutions for Intrinsic Thermocouples Under Polynomial Substrate Loading

A. E. Segall[1]

Nomenclature

a_0–a_3 = polynomial coefficients
C_1 = dimensionless constant = $\beta/(8/\pi^2+\beta)$
C_2 = dimensionless constant = $4/(8/\pi+\beta\pi)$
C_3 = dimensionless constant = (C_1-1)
k = dimensionless thermal conductivity ratio = k_{Tc}/k_{Sb}
$R(t)$ = measured thermocouple response = $a_0+a_1t+a_2t^2+a_3t^3$
r = thermocouple wire radius
t = dimensionless time = $\alpha_{Sb}t^*/r^2$
t^* = time
α = dimensionless thermal diffusivity ratio = α_{Tc}/α_{Sb}
β = dimensionless constant = $k/\sqrt{\alpha}$
$\Delta T(t)$ = substrate temperature forcing function
$\Theta(t)$ = function defined by Eq. (7)
ξ = argument used by Eq. (9) = $C_2\sqrt{t}/|C_3|$
$\Phi(t)$ = unit step response for an ideal intrinsic thermocouple

Subscripts

Sb = substrate
Tc = thermocouple

Introduction

With the advent of general purpose finite-element and finite-difference numerical methods, the design process for high-temperature applications where all modes of heat transfer may be important and material properties often exhibit distinct temperature dependencies has become increasingly sophisticated. However, as illustrated by a number of thermal shock and fatigue studies conducted by Segall and co-workers (1991, 1992, 1993), precise temperature measurements are still required to avoid an overabundance of assumptions pertaining to the uniformity and temporal nature of the thermal state. When surface-mounted thermocouples are used for these temperature measurements, specialized techniques are required to minimize the errors associated with the junction displacement from the surface and conduction along the lead wires (Segall, 1992). Yet, even when these techniques are used, measurement errors may still permeate the data, especially when very rapid temperature changes are involved.

Although a multitude of corrective techniques have been developed for thermocouple measurements over the years, they usually required specialized numerical procedures or difficult to determine empirical constants (Quandt and Fink, 1960; Hennecke and Sparrow, 1970; Wally, 1977, to name a few). To offset these shortcomings, a number of useful analytical relationships utilizing Laplace transforms have since been derived by Keltner and Beck (1983) for intrinsic and beaded thermocouples mounted to a thick wall. Unfortunately, the difficulties associated with the inversion of these relationships have precluded use of the solutions to all but the simplest cases of measured response such as step and ramp temperature changes. Because the temperature changes and measured response associated with thermal shock are rarely step or linear functions of time, an expanded solution base is required. The purpose of this paper is therefore to expand the Laplace transform solutions to include intrinsic thermocouples with a measured response that can be approximated by an arbitrary third-order polynomial.

Analytical Considerations

All the relationships used in this analysis are based on the mathematical models derived by Keltner and Beck (1983) for the response of surface-mounted thermocouples on a thick wall or substrate. Using these relationships under the assumption of constant thermophysical properties, the principal of superposition may be used to extract the thermocouple's response $R(t)$, to an arbitrary substrate temperature loading $\Delta T(t)$, through the use of Duhamel's integral (Fodor, 1965):

$$R(t)=\frac{\partial}{\partial t}\int_0^t \Delta T(\tau)\bullet\Phi(t-\tau)\,d\tau \qquad (1)$$

where $\Phi(t)$ is the response of the thermocouple to a unit step temperature change. For an ideal intrinsic thermocouple with negligible contact resistance and lateral heat transfer to the

[1] Senior Research Associate, Center for Advanced Materials, The Pennsylvania State University, 511 Deike Building, University Park, PA 16802.

Contributed by the Heat Transfer Division of THE AMERICAN SOCIETY OF MECHANICAL ENGINEERS. Manuscript received by the Heat Transfer Division October 1993; revision received March 1994. Keywords: Conduction, Measurement Techniques, Transient and Unsteady Heat Transfer. Associate Technical Editor: L. S. Fletcher.

surrounding environment, the late time ($t>0.1$) unit response is defined as:

$$\Phi(t)=1-C_1\exp(C_2^2 t)[1-\mathrm{erf}(C_2\sqrt{t})] \tag{2}$$

where

$$C_1=\beta/(8/\pi^2+\beta) \tag{3}$$

and

$$C_2=4/(8/\pi+\beta\pi). \tag{4}$$

An estimation of the actual surface temperature history may then be obtained by approximating the measured response $R(t)$, as a third-order polynomial, substituting Eq. (2) into Eq. (1), taking the Laplace transform, and rearranging terms such that:

$$\Delta T(s)=\frac{R(s)}{s\bullet\Phi(s)}=\frac{6a_3+2a_2 s+a_1 s^2+a_0 s^3}{s^4-\dfrac{C_1 s^{9/2}}{C_2+\sqrt{s}}}. \tag{5}$$

Inversion of Eq. (5) yields the following expression for a substrate surface temperature as a function of nondimensional time and the polynomial coefficients that defined the measured thermocouple response:

$$\Delta T(t)=a_0+a_1 t+a_2 t^2+a_3 t^3+\frac{C_3C_1}{C_2^2}\left[\frac{6a_3C_3^4}{C_2^4}+\frac{2a_2C_3^2}{C_2^2}+a_1\right]$$
$$+\frac{C_1}{C_2\sqrt{\pi t}}\left[\frac{6a_3C_3^6}{C_2^6}+\frac{2a_2C_3^4}{C_2^4}+\frac{a_1C_3^2}{C_2^2}+a_0\right]$$
$$+\frac{2C_1\sqrt{t}}{C_2\sqrt{\pi}}\left[\frac{6a_3C_3^4}{C_2^4}+\frac{2a_2C_3^2}{C_2^2}+a_1\right]+\frac{8C_1t^{3/2}}{C_2\sqrt{\pi}}\left[\frac{a_3C_3^2}{C_2^2}+\frac{a_2}{3}+\frac{2a_3t}{5}\right]$$
$$-\frac{C_1C_3\Theta(t)}{C_2}\left[\frac{6a_3C_3^6}{C_2^6}+\frac{2a_2C_3^4}{C_2^4}+\frac{a_1C_3^2}{C_2^2}+\frac{a_0}{C_1}(1+C_3)\right] \tag{6}$$

where

$$\Theta(t)=\frac{C_2}{C_3^2}\exp\left(\frac{C_2^2 t}{C_3^2}\right)\left[\mathrm{erf}\left(\frac{C_2\sqrt{t}}{C_3}\right)+1\right]+\frac{1}{C_3\sqrt{\pi t}} \tag{7}$$

and

$$C_3=(C_1-1). \tag{8}$$

Difficulties may arise during the evaluation of Eq. (7) for large values of dimensionless time because of the exponential term. Fortunately, evaluation of the limit of $\Theta(t)$ as t approaches infinity reveals a tendency toward zero because $C_3<0$. As an alternative, the main term in Eq. (7) may be evaluated as the exponentially scaled complementary error function and approximated by the following asymptotic series expansion (Abramowitz and Stegun, 1964):

$$\exp(\xi^2)\mathrm{erfc}(\xi)\approx\frac{1}{\xi\sqrt{\pi}}\left[1+\sum_{m=1}^{\infty}(-1)^m\frac{1\bullet3\ldots2m-1}{(2\xi^2)^m}\right] \tag{9}$$

provided

$$\xi=\frac{C_2\sqrt{t}}{|C_3|}. \tag{10}$$

Discussion and Conclusions

An evaluation of Eq. (6) was conducted using transient temperature data measured with 0.25-mm-dia. wire type-K (chromel-alumel) thermocouples mounted to a rapidly cooled silicon carbide substrate. Figure 1 shows the measured thermocouple response and cubic polynomial approximation. A typical corrective response curve calculated by Eq. (6) using the cubic polynomial coefficients is shown by Fig. 2. Interestingly, the predicted response shown in Fig. 2 appears to follow the trends

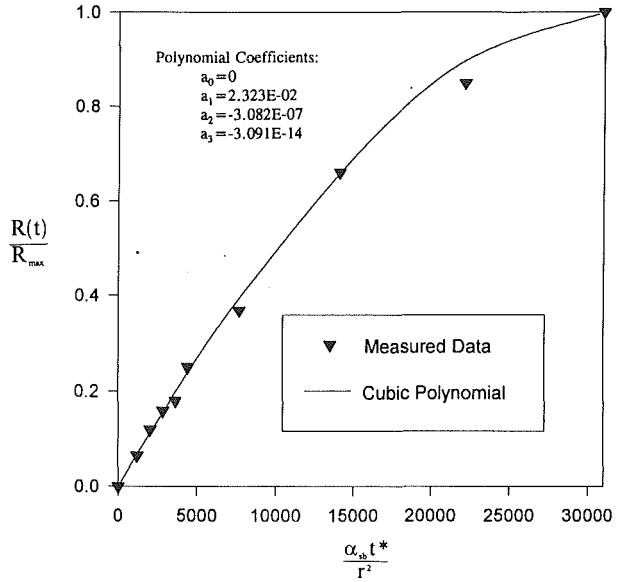

Fig. 1 Dimensionless measured response and cubic polynomial fit for a 0.25-mm-dia wire type-K thermocouple attached to a rapidly cooled silicon carbide substrate

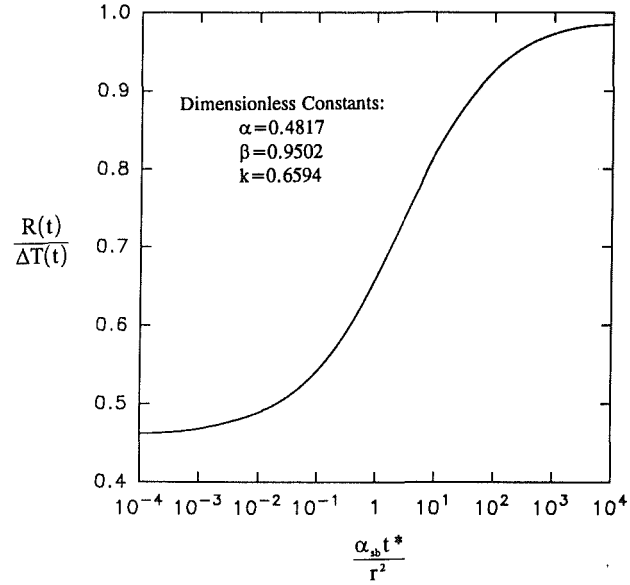

Fig. 2 Calculated response for a 0.25-mm-dia wire type-K thermocouple attached to a rapidly cooled silicon carbide substrate

predicted by Keltner and Beck (1983) for the entire time interval even though the derivations were based on the late time ($t>0.1$) response of a thermocouple subjected to a unit step temperature change. Nevertheless, it is recommended that the use of Eq. (6) should be restricted to dimensionless times greater than 0.1.

Although the inversion of Eq. (5) is exact, the ensuing algebraic expression must be considered approximate at best because of the reliance on a polynomial fit to the thermocouple response; any estimates of the accuracy of the method will be predicted on the ability of the polynomial to describe and smooth the data over the entire time interval. Hence, the polynomial should always be graphically compared to the data to ensure a goodness of fit. Higher order polynomials were specifically avoided because of their tendency to oscillate around individual data points (instability). Finally, the accuracy of the method will also be predicted on the validity of the assumptions pertaining to the lack of contact resistance and lateral heat transfer to the surrounding environment. In any case, the im-

portance of Eq. (6) is in its ability to estimate an arbitrary surface temperature history based on a measured thermocouple response described by a simple third-order polynomial. Different solutions involving combinations of constant, linear, quadratic, and cubic terms are possible by simply zeroing various coefficients.

Acknowledgments

Funding of this research by the Gas Research Institute under Contract No. 5084-238-1302 is gratefully acknowledged.

References

Abramowitz, M., and Stegun, I. A., 1964, *Handbook of Mathematical Functions*, NBS Applied Math Series, No. 55.

Foder, G., 1965, *Laplace Transforms in Engineering*, Akademiai Kiado, Budapest.

Hennecke, D. K., and Sparrow, E. M., 1970, "Local Heat Sink on a Convectively Cooled Surface—Application to Temperature Measurement Error," *Int. J. Heat Mass Trans.*, Vol. 13, pp. 287–304.

Keltner, N. R., and Beck, J. V., 1983, 'Surface Temperature Measurement Errors," ASME JOURNAL OF HEAT TRANSFER, Vol. 105, pp. 312–318.

Quandt, E. R., and Fink, E. W., 1960, "Experimental and Theoretical Analysis of the Transient Response of Surface Bonded Thermocouples," *Bettis Tech. Review*, WAPD-BT-19, Reactor Technology, pp. 31–49.

Segall, A. E., Hellmann, J. R., and Modest, M. F., 1991, "Analysis of Gas-Fired Ceramic Radiant Tubes During Transient Heating: I—Thermal Transient Modeling," *ASTM J. Testing and Evaluation*, Vol. 19, No. 6, pp. 454–460.

Segall, A. E., and Hellmann, J. R., 1992, "Analysis of Gas-Fired Ceramic Radiant Tubes During Transient Heating: II—Thermoelastic Stress Analysis," *ASTM J. Testing and Evaluation*, Vol. 20, No. 1, pp. 25–32.

Segall, A. E., 1992, "Instrumentation Techniques for Ceramic Radiant Tubes," *Exp. Tech.*, Vol. 16, No. 2, pp. 36–41.

Segall, A. E., Hellmann, J. R., and Tressler, R. E., 1993, "Thermal Shock and Fatigue Behavior of Ceramic Tubes," *Proceedings of the 10th Biennial ASME Conference on Reliability, Stress Analysis, and Failure Prevention*, New Mexico.

Wally, K., 1977, "The Transient Response of Beaded Thermocouples Mounted on the Surface of a Solid," *Proceedings of the 23rd International Instrumentation Symposium*, Instrument Society of America, pp. 127–132.

Statistical Properties of Passive Scalar and Temperature Dissipation Rates in a Turbulent Reacting Shear Layer

J. S. Shirolkar,[1] M. Queiroz,[1] and P. A. McMurtry[2]

Nomenclature

A, B = molar concentration of chemical species A or B
Ce = nondimensional heat release parameter
D = diffusion coefficient
d = diameter of the nozzle used in experimental study
k = wavenumber magnitude
L_o = length scale
r = radial direction
r_o = mean temperature peak radius
S = mixture fraction or Shvab–Zeldovich variable
T = temperature
t = time
U_o = velocity difference across the mixing layer
X = streamwise coordinate direction
Y = transverse coordinate direction used in the simulation
z = axial distance from the tip of the nozzle used in the experimental study
Z = spanwise coordinate direction used in the simulation
α = thermal diffusivity
λ = wavelength
μ = average value of the natural logarithm of temperature dissipation rate
ρ = density
ρ_o = density of the unreacted fluid
σ = rms value of the natural logarithm of temperature dissipation rate
χ = scalar dissipation rate
$$= D\left[\left(\frac{\partial S}{\partial x}\right)^2 + \left(\frac{\partial S}{\partial y}\right)^2 + \left(\frac{\partial S}{\partial z}\right)^2\right]$$
χ_t = temperature dissipation rate
$$= \alpha\left[\left(\frac{\partial T}{\partial x}\right)^2 + \left(\frac{\partial T}{\partial y}\right)^2 + \left(\frac{\partial T}{\partial z}\right)^2\right]$$

Subscripts

o = free-stream condition
t = temperature

[1]Department of Mechanical Engineering, Brigham Young University, Provo, UT 84602.

[2]Department of Mechanical Engineering, University of Utah, Salt Lake City, UT 84112.

Contributed by the Heat Transfer Division of THE AMERICAN SOCIETY OF MECHANICAL ENGINEERS. Manuscript received by the Heat Transfer Division June 1993; revision received November 1993. Keywords: Fire/Flames, Reacting Flows, Turbulence. Associate Technical Editor: W. L. Grosshandler.

Introduction

Understanding turbulent reacting flows is one of the most challenging fields of engineering science. Various theoretical models based on simplifying assumptions have been developed to predict the behavior of such flows. In some of the models proposed, the problem of modeling the mean chemical reaction rate is exchanged for the problem of describing the scalar dissipation rate. The scalar dissipation rate, which describes the destruction of the fluctuations of a passive scalar at the finest scales, is an important parameter is modeling turbulent reacting flows (Namazian et al., 1988; Effelsberg and Peters, 1988).

The application of Direct Numerical Simulation (DNS) to reacting flows has been very useful in understanding the complex interactions occurring in such flows. Givi (1989) has presented an excellent overview of the use of DNS in combustion research. However, the limitation of this technique is the range of space and time scales resolvable with the currently available supercomputer technology. Despite these limitations DNS can provide useful information, which can improve existing closures. Givi et al. (1986) used this technique to investigate the problem of local flame extinction in a time-dependent, two-dimensional mixing layer neglecting the effect of chemical heat release on the flow field. Their results indicated that the local instantaneous scalar dissipation rate evaluated at stoichiometric conditions is an important parameter in understanding the flame extinction phenomena. This was in qualitative agreement with the theoretical work of Peters (1983). McMurtry et al. (1986, 1989) performed simulations for a two and three-dimensional mixing layer with heat release using a single-step, irreversible reaction whose rate depended only on concentration. The focus of this study was on the coupling between chemical heat release and fluid dynamics. They found that the rate of chemical product formation, the thickness of mixing layer, and the amount of mass entrained into the layer all decrease with the increasing rates of heat release. Son et al. (1991) have also studied various statistical moments, proba-

portance of Eq. (6) is in its ability to estimate an arbitrary surface temperature history based on a measured thermocouple response described by a simple third-order polynomial. Different solutions involving combinations of constant, linear, quadratic, and cubic terms are possible by simply zeroing various coefficients.

Acknowledgments

Funding of this research by the Gas Research Institute under Contract No. 5084-238-1302 is gratefully acknowledged.

References

Abramowitz, M., and Stegun, I. A., 1964, *Handbook of Mathematical Functions*, NBS Applied Math Series, No. 55.

Foder, G., 1965, *Laplace Transforms in Engineering*, Akademiai Kiado, Budapest.

Hennecke, D. K., and Sparrow, E. M., 1970, "Local Heat Sink on a Convectively Cooled Surface—Application to Temperature Measurement Error," *Int. J. Heat Mass Trans.*, Vol. 13, pp. 287–304.

Keltner, N. R., and Beck, J. V., 1983, 'Surface Temperature Measurement Errors," ASME JOURNAL OF HEAT TRANSFER, Vol. 105, pp. 312–318.

Quandt, E. R., and Fink, E. W., 1960, "Experimental and Theoretical Analysis of the Transient Response of Surface Bonded Thermocouples," *Bettis Tech. Review*, WAPD-BT-19, Reactor Technology, pp. 31–49.

Segall, A. E., Hellmann, J. R., and Modest, M. F., 1991, "Analysis of Gas-Fired Ceramic Radiant Tubes During Transient Heating: I—Thermal Transient Modeling," *ASTM J. Testing and Evaluation*, Vol. 19, No. 6, pp. 454–460.

Segall, A. E., and Hellmann, J. R., 1992, "Analysis of Gas-Fired Ceramic Radiant Tubes During Transient Heating: II—Thermoelastic Stress Analysis," *ASTM J. Testing and Evaluation*, Vol. 20, No. 1, pp. 25–32.

Segall, A. E., 1992, "Instrumentation Techniques for Ceramic Radiant Tubes," *Exp. Tech.*, Vol. 16, No. 2, pp. 36–41.

Segall, A. E., Hellmann, J. R., and Tressler, R. E., 1993, "Thermal Shock and Fatigue Behavior of Ceramic Tubes," *Proceedings of the 10th Biennial ASME Conference on Reliability, Stress Analysis, and Failure Prevention*, New Mexico.

Wally, K., 1977, "The Transient Response of Beaded Thermocouples Mounted on the Surface of a Solid," *Proceedings of the 23rd International Instrumentation Symposium*, Instrument Society of America, pp. 127–132.

Statistical Properties of Passive Scalar and Temperature Dissipation Rates in a Turbulent Reacting Shear Layer

J. S. Shirolkar,[1] M. Queiroz,[1] and P. A. McMurtry[2]

Nomenclature

A, B = molar concentration of chemical species A or B
Ce = nondimensional heat release parameter
D = diffusion coefficient
d = diameter of the nozzle used in experimental study
k = wavenumber magnitude
L_o = length scale
r = radial direction
r_o = mean temperature peak radius
S = mixture fraction or Shvab–Zeldovich variable
T = temperature
t = time
U_o = velocity difference across the mixing layer
X = streamwise coordinate direction
Y = transverse coordinate direction used in the simulation
z = axial distance from the tip of the nozzle used in the experimental study
Z = spanwise coordinate direction used in the simulation
α = thermal diffusivity
λ = wavelength
μ = average value of the natural logarithm of temperature dissipation rate
ρ = density
ρ_o = density of the unreacted fluid
σ = rms value of the natural logarithm of temperature dissipation rate
χ = scalar dissipation rate
$$= D\left[\left(\frac{\partial S}{\partial x}\right)^2 + \left(\frac{\partial S}{\partial y}\right)^2 + \left(\frac{\partial S}{\partial z}\right)^2\right]$$
χ_t = temperature dissipation rate
$$= \alpha\left[\left(\frac{\partial T}{\partial x}\right)^2 + \left(\frac{\partial T}{\partial y}\right)^2 + \left(\frac{\partial T}{\partial z}\right)^2\right]$$

Subscripts

o = free-stream condition
t = temperature

[1]Department of Mechanical Engineering, Brigham Young University, Provo, UT 84602.

[2]Department of Mechanical Engineering, University of Utah, Salt Lake City, UT 84112.

Contributed by the Heat Transfer Division of THE AMERICAN SOCIETY OF MECHANICAL ENGINEERS. Manuscript received by the Heat Transfer Division June 1993; revision received November 1993. Keywords: Fire/Flames, Reacting Flows, Turbulence. Associate Technical Editor: W. L. Grosshandler.

Introduction

Understanding turbulent reacting flows is one of the most challenging fields of engineering science. Various theoretical models based on simplifying assumptions have been developed to predict the behavior of such flows. In some of the models proposed, the problem of modeling the mean chemical reaction rate is exchanged for the problem of describing the scalar dissipation rate. The scalar dissipation rate, which describes the destruction of the fluctuations of a passive scalar at the finest scales, is an important parameter is modeling turbulent reacting flows (Namazian et al., 1988; Effelsberg and Peters, 1988).

The application of Direct Numerical Simulation (DNS) to reacting flows has been very useful in understanding the complex interactions occurring in such flows. Givi (1989) has presented an excellent overview of the use of DNS in combustion research. However, the limitation of this technique is the range of space and time scales resolvable with the currently available supercomputer technology. Despite these limitations DNS can provide useful information, which can improve existing closures. Givi et al. (1986) used this technique to investigate the problem of local flame extinction in a time-dependent, two-dimensional mixing layer neglecting the effect of chemical heat release on the flow field. Their results indicated that the local instantaneous scalar dissipation rate evaluated at stoichiometric conditions is an important parameter in understanding the flame extinction phenomena. This was in qualitative agreement with the theoretical work of Peters (1983). McMurtry et al. (1986, 1989) performed simulations for a two and three-dimensional mixing layer with heat release using a single-step, irreversible reaction whose rate depended only on concentration. The focus of this study was on the coupling between chemical heat release and fluid dynamics. They found that the rate of chemical product formation, the thickness of mixing layer, and the amount of mass entrained into the layer all decrease with the increasing rates of heat release. Son et al. (1991) have also studied various statistical moments, proba-

bility density functions, power spectral densities, and autocorrelations of a conserved scalar of a reacting mixing layer generated via DNS. However, this study did not include statistics on the dissipation rate of that scalar. A review on various numerical simulations and experimental efforts made to study both reacting and nonreacting mixing layers is also presented by Son et al. (1991).

The objective of this work is to present the statistics of dissipation rate of a conserved scalar from the DNS of a turbulent reacting shear layer. Since experimental data on the statistics of temperature dissipation rate in a reacting shear layer of jet flame are readily available (Boyer and Queiroz, 1991), a comparison of this data with the DNS results will also be made.

Simulation Method

The procedure in DNS involves solving the three-dimensional, time-dependent governing equations for the detailed development of the flow field. The equations are solved using pseudospectral methods to compute spatial derivatives and second-order Adams–Bashforth time-stepping schemes to advance in time. The computational domain for the simulations presented here is chosen to be large enough to contain the most unstable mode of a hyperbolic tangent mean velocity profile and its subharmonic (as determined from linear stability theory for an incompressible flow (Michalke, 1964)). For computational convenience, the length scale L_o is chosen such that the nondimensional wavelength of the most unstable mode is 2π ($2\pi = \lambda/L_o$, where λ is the dimensional wavelength). Time is nondimensionalized by L_o/U_o, where U_o is the velocity difference across the mixing layer. Further details on the solution procedure are given by McMurtry et al. (1986).

Simulation data are presented at two nondimensional time steps ($t = 42$ and $t = 60$) and for two different values of the heat release parameter Ce: one with no heat release ($Ce = 0$); and the other giving a maximum density decrease of approximately $\rho/\rho_o = 0.5$ ($Ce = 5$). This value of the heat release parameter ($Ce = 5$) is limited by the resolution requirements. These simulations employed exactly the same initial velocity and species concentration fields. Furthermore, these simulations were performed for a binary, single-step chemical reaction occurring across a temporally developing turbulent mixing layer. The chemical reaction used is the single step, irreversible reaction:

$$A + B \rightarrow \text{Products} + \text{Heat}. \tag{1}$$

The reaction is only a function of the reactant concentration and does not depend on temperature. Although this simplified reaction mechanism neglects some important physics of flame, it still allows effects of energy release on the mixing dynamics to be studied.

The computations were performed on a $64 \times 65 \times 64$ grid. In wavenumber space this corresponds to $k_x, k_y, k_z = -32$ to 32, where k_x, k_y, k_z are the wavenumber vector components in the three coordinate directions. In this simulation, the low Mach number approximation, which filters out the acoustic waves, was used to relax the stability constraints on the numerical time step. Also, the transport coefficients were taken to be temperature independent, allowing the effects of thermal expansion to be isolated and studied in a simpler environment.

The Reynolds, Peclet, and Damkohler numbers for both the heat release and no heat release case were 500, 200, and 2, respectively. As most flows of interest occur at higher Reynolds and Damkohler numbers than those used in these simulations, it is not possible to predict precisely and reproduce quantitatively all details of a practical turbulent flow problem. However, the Reynolds number imposed in these simulations is sufficiently high so that unsteady, random motions characteristic of the large-scale motion in the flame are generated. Because a temporal mixing layer is studied here, the flow is homogeneous in the streamwise (X) and spanwise (Z) directions. Mean profiles in the transverse (Y) direction are then obtained by averaging of 64^2 data points in the X–Z plane.

Results

(a) Conserved Scalar Dissipation Rate. In many practical hydrocarbon combustion problems, the major energy releasing chemical reaction rates are high enough to justify the fast chemistry assumption. In such cases the instantaneous molecular species concentrations and temperature are functions only of a conserved scalar at that instant. The choice of the conserved scalar depends on the chemistry involved. For a reaction of the type given in Eq. (1) a conserved scalar of the Shvab–Zeldovich type is useful. The element mass fractions can be normalized to give the desired conserved scalar, namely the mixture fraction (S):

$$S = \frac{(A - B + B_o)}{(A_o + B_o)} \tag{2}$$

Shirolkar et al. (1992) studied the Probability Density Function (PDF) of mixtures fraction at $t = 42$ for the heat release (hr) and no heat release (nhr) or isothermal cases. They observed that effect of heat release is to slow the rate of development of mixing. The turbulent mixing and hence the chemical reaction was observed in a region around the center of the computational domain. They also observed that the higher moments (skewness and kurtosis) of S within the reacting zone for both the cases had nearly Gaussian values (0.0 and 3.0 respectively).

The conserved scalar approach is normally used to avoid dealing with the complex chemical production term. This is done by describing the instantaneous reaction rate in terms of the dissipation rate of the conserved scalar. Some statistical features of this scalar dissipation rate are presented below. This type of information can be useful in validating models that use the conserved scalar approach.

Figure 1 (*a*) shows the average profiles of the dissipation rate of the mixture fraction (χ) at $t = 42$ and $t = 60$ for the heat release and isothermal cases. These profiles clearly show lower dissipation rates for the heat release case. The computational domain region over which the dissipation spread is observed is larger for the isothermal case. These trends can be further explained by comparing them with the total concentration of the reactants at different times for the two different cases (Table 1). This total concentration is calculated by integrating the average concentration profiles of the reactants across the mixing layer. It is quite evident from these observations that the consumption of the reactants is related to the dissipation rate and the rate of consumption of the reactants is inhibited by the heat release. These observations are consistent with those of McMurtry et al. (1989) who studied the effect of heat release on the flow field in terms of vorticity dynamics. Their observations indicated that for heat release case the maximum amplitude of the vorticity is substantially lower compared to the isothermal case. This results in lower entrainment into the mixing region for the heat release case and hence lower reaction rates, i.e., lower rate of consumption of the reactants. From Table 1 it can be seen that at any time for the heat release case, the concentration of the reactants is higher and their consumption with time is much lower. Shirolkar et al. further showed that the reaction rate contours at the center of the spanwise location ($Z = 0$) for the heat release and isothermal cases showed the same features as the χ contours. They observed that the reaction rate field was more

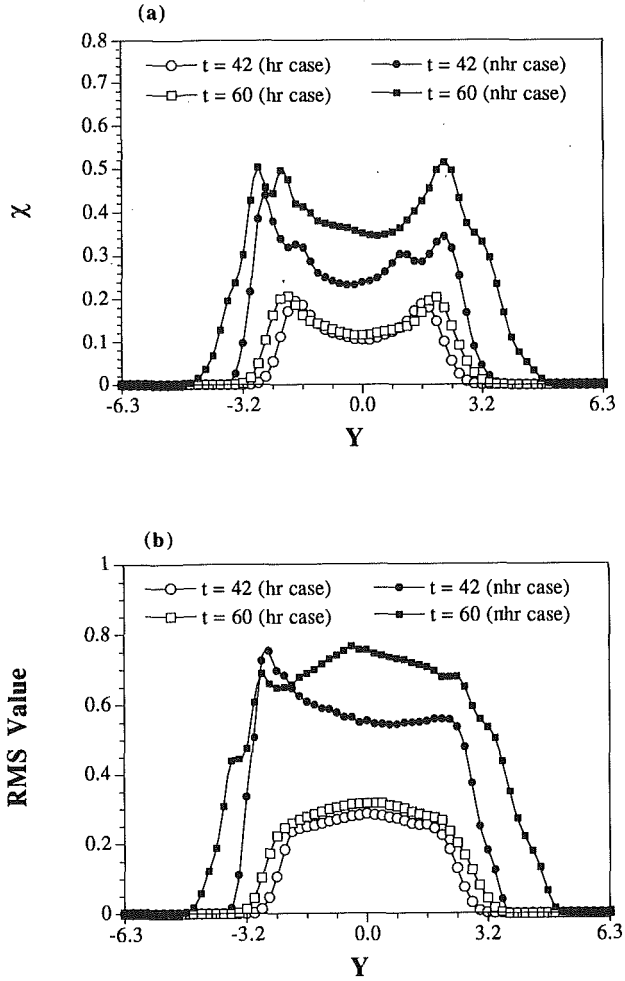

Fig. 1 (*a*) Average profiles for mixture fraction dissipation rate and (*b*) rms profiles for mixture fraction dissipation rate

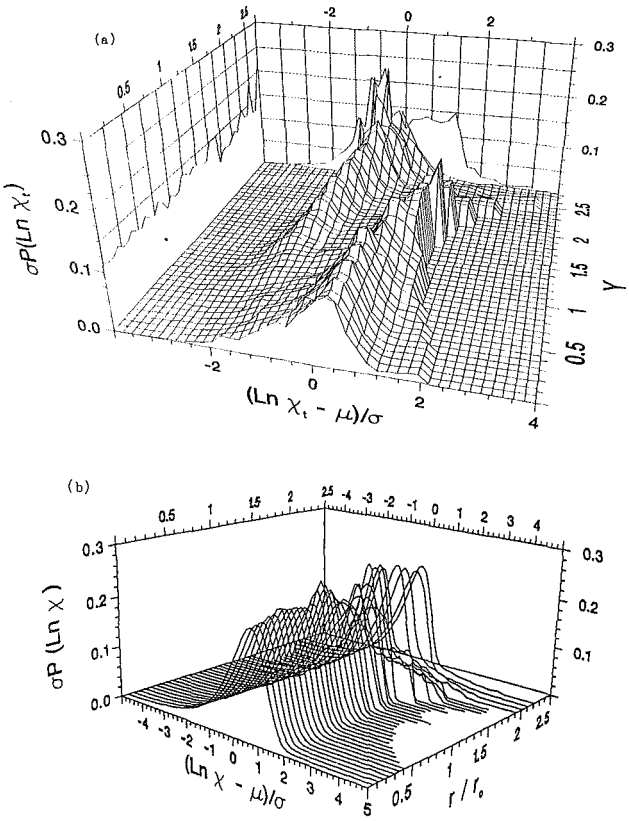

Fig. 2 (*a*) Normalized PDFs of temperature dissipation rate calculated from the DNS data for the heat release case and (*b*) normalized PDFs of temperature dissipation rate obtained from the experimental data of Boyer and Queiroz (1991)

Table 1 Reactant concentrations

CASE	TIME	TOTAL CONCENTRATION OF "A"	"B"
hr	42	5.5709	5.6084
nhr	42	5.4663	5.4663
hr	60	5.5019	5.5285
nhr	60	4.7198	4.7198

contorted with higher rates for the isothermal case as compared to the reacting case. This further substantiated the fact that heat release reduces mixing rate.

The rms profiles of χ for the two cases at $t = 42$ and $t = 60$ are presented in Fig. 1(*b*). The profiles for the isothermal case are observed to be relatively higher than those in the heat release case. This further illustrates the stabilizing effect of heat release (smaller fluctuations) on the flow field.

(*b*) Temperature Dissipation PDFs. It is in general difficult to measure experimentally the dissipation of a conserved scalar. However, it is relatively easier to measure dissipation of a nonconserved scalar such as temperature in turbulent reacting flows. Boyer and Queiroz (1991) have successfully designed a temperature probe capable of measuring spatial temperature gradients. They have conducted temperature dissipation rate measurements in a lifted turbulent nonpremixed propane flame issuing from a converging nozzle at several axial stations and along the centerline. They showed that the assumption of lognormality was a good approximation to the character of the temperature dissipation rate in the core of the flame out to the radius where the mean temperature is at a maximum (r_o). In this section the simulation results are qualitatively compared to measurements of Boyer and Queiroz.

The temperature dissipation rate statistics presented in this section are for the heat release case and are calculated in that region of the computational domain where significant mixing and hence chemical reaction have taken place (i.e., $0 \leq Y \leq 2.75$). Also for the sake of comparison, the PDFs are computed for the natural logarithm of the dissipation rate ($\ln \chi_t$). The experimental data available for comparison are at three different axial locations ($z/d = 5$, 10, 20). Furthermore, the results of Boyer and Queiroz show that the PDFs of temperature dissipation rate at all the three axial locations are similar in nature. Therefore, in order to avoid repetitiveness, the experimental data at only one axial location ($z/d = 10$) are qualitatively compared with the simulation data at the nondimensionalized time $t = 42$.

The normalized lognormal PDFs calculated from the simulation and those observed experimentally are presented in Figs. 2(*a*) and 2(*b*), respectively. The PDFs (Fig. 2 (*a*)) near the center of the computational domain ($Y = 0$) indicate that the temperature dissipation rate is lognormally distributed. This is also qualitatively observed in the data of Boyer and Queiroz (Fig. 2(*b*)) from the center of the flame out to $r/r_o = 1.5$. The discrepancies between the two results in the region farther away from the center of the computational domain could be because the heat release in the simulations is much less compared to experimental conditions. The Reynolds num-

ber specified in the simulations is also far lower than in the experiment. Furthermore, the simulations are performed for a temporally developing reacting shear layer whereas the propane flame is a spatially developing combusting shear layer. Although these two types of shear layer cannot be related exactly, there are many dynamic similarities between the two allowing for qualitative comparison. Despite these restrictions and the fact that only 64×64 grid points were available from the simulations to compute the statistics, it is evident from the PDSs (Figs. 2(*a*) and 2(*b*)) that the DNS predictions are in qualitative agreement with the data collected by Boyer and Queiroz (1991).

Concluding Remarks

The data available from a three-dimensional direct numerical simulation for a binary single-step chemical reaction in a temporally developing turbulent mixing layer were used to study the dissipation rate statistics of a conserved scalar and of temperature. In particular the effects of heat release on these statistics is considered.

The mixture fraction dissipation rate statistics showed that the effect of heat release is to slow the rate of development of mixing. As compared to the heat release case, higher dissipation rates were observed for the isothermal case, which corresponded with the relatively higher consumption of the reactants. The rms profiles of mixture fraction dissipation rate supported the fact that the heat release had a stabilizing effect on the flow field.

The temperature dissipation rate statistics were computed for the heat release case. The statistics compared qualitatively with the experiments of Boyer and Queiroz (1991). The simulation results also indicated that the temperature dissipation rate approximated the lognormal distribution in a region where there was significant mixing and hence chemical reaction. This agreement between the simulation results and experiments gives added confidence in the observations made regarding the mixture fraction dissipation rate obtained from the simulations.

References

Boyer, L., and Queiroz, M., 1991, "Temperature Dissipation Measurements in a Lifted Turbulent Diffusion Flame," *Combust. Science and Tech.*, Vol. 79, pp. 1–34.

Effelsberg, E., and Peters, N., 1988, "Scalar Dissipation Rates in Turbulent Jets and Jet Diffusion Flames," *Twenty-Second Symposium (International) on Combustion*, The Combustion Institute, Pittsburgh, PA, pp. 693–700.

Givi, P., Jou, W. -H., and Metcalfe, R. W., 1986, "Flame Extinction in a Temporally Developing Mixing Layer," *Twenty-First Symposium (International) on Combustion*, The Combustion Institute, Pittsburgh, PA, pp. 1251–1261.

Givi, P., 1989, "Model-Free Simulations of Turbulent Reactive Flows," *Prog. Energy Combust. Sci.*, Vol. 15, pp. 1–107.

McMurtry, P. A., Jou, W.-H., Riley, J. J., and Metcalfe, R. W., 1986, "Direct Numerical Simulations of a Reacting Mixing Layer With Chemical Heat Release," *AIAA J.*, Vol. 24, pp. 962–970.

McMurtry, P. A., Riley, J. J., and Metcalfe, R. W., 1989, "Effects of Heat Release on the Large-Scale Structure in Turbulent Mixing Layers," *J. Fluid Mech.*, Vol. 199, pp. 297–331.

Michalke, A., 1964, "On the Inviscid Instability of the Hyperbolic Tangent Velocity Profile," *J. Fluid Mech.*, Vol. 19, pp. 543–556.

Namazian, M., Schefer, R. W., and Kelly, J., 1988, "Scalar Dissipation Measurements in the Developing Region of a Jet," *Combustion and Flame*, Vol. 74, pp. 147–160.

Peters, N., 1983, "Local Quenching Due to Flame Stretch and Non-premixed Turbulent Combustion," *Combust. Science and Tech.*, Vol. 30, pp. 1–17.

Shirolkar, J. S., Queiroz, M., and McMurtry, P. A., 1992, "Statistical Properties of Scalar and Temperature Dissipation in a Turbulent Reacting Shear Layer," *Heat and Mass Transfer in Fire and Combustion Systems*, ASME HTD-Vol. 223.

Son, S. F., McMurtry, P. A., and Queiroz, M., 1991, "The Effect of Heat Release on Various Statistical Properties of a Reacting Shear Layer," *Combustion and Flame*, Vol. 85, pp. 51–67.

Surface Heat Transfer Coefficients of Cylindrical Food Products Cooled With Water

I. Dincer[1]

Nomenclature

- a = thermal diffusivity, m^2/s
- a_w = thermal diffusivity of water at the initial product temperature = 0.148×10^{-6} m^2/s
- Bi = Biot number
- C = cooling coefficient, 1/s
- Fo = Fourier number
- h = surface heat transfer coefficient, W/m^2K
- J_1 = lag factor
- J_0 = zeroth-order Bessel function of first kind
- k = thermal conductivity, W/mK
- L = length, m
- M = root of Bessel characteristic equation
- r = radial coordinate
- R = radius, m
- t = time, s
- T = temperature, °C or K
- W = water content, in decimal unit
- θ = dimensionless temperature
- ϕ = temperature difference, °C or K

Subscripts

- a = medium condition
- e = final
- i = initial
- n = refers to nth characteristic value
- w = water
- 1 = refers to first characteristic value

Introduction

Unsteady-state heat transfer from a solid object to any fluid medium is an important subject in many engineering-related fields and plays a role in practical processes ranging from cooling of a hot steel ball to heating and cooling of food products. As a first step to a better understanding of the heat transfer, one must carefully evaluate and understand the fluid flow, and thermophysical properties of the product. Classical explanations of the cooling phenomena are largely based on the temperature distributions and heat transfer rates. However, very limited information is available in the literature on the heat transfer coefficients in food processing applications. Most theoretical or semi-theoretical and experimental investigations of the heat transfer coefficients for geometrically shaped objects can be classified as Nusselt–Reynolds correlations. The surface heat transfer coefficients of food products subjected to cooling applications are dependent upon several parameters, e.g., the product's thermal and physical properties and environmental conditions (Dincer, 1991; Dincer et al., 1992). The well-known Nu–Re correlations may not show a realistic behavior for use in the specific application. A limited number

[1]Department of Energy Systems, TUBITAK-Marmara Research Center, P.O. Box 21, 41470, Gebze-Kocaeli, Turkey.

Contributed by the Heat Transfer Division of THE AMERICAN SOCIETY OF MECHANICAL ENGINEERS. Manuscript received by the Heat Transfer Division October 1992; revision received December 1993. Keywords: Refrigeration, Thermophysical Properties, Transient and Unsteady Heat Transfer. Associate Technical Editor: Y. Bayazitoglu.

ber specified in the simulations is also far lower than in the experiment. Furthermore, the simulations are performed for a temporally developing reacting shear layer whereas the propane flame is a spatially developing combusting shear layer. Although these two types of shear layer cannot be related exactly, there are many dynamic similarities between the two allowing for qualitative comparison. Despite these restrictions and the fact that only 64×64 grid points were available from the simulations to compute the statistics, it is evident from the PDSs (Figs. 2(*a*) and 2(*b*)) that the DNS predictions are in qualitative agreement with the data collected by Boyer and Queiroz (1991).

Concluding Remarks

The data available from a three-dimensional direct numerical simulation for a binary single-step chemical reaction in a temporally developing turbulent mixing layer were used to study the dissipation rate statistics of a conserved scalar and of temperature. In particular the effects of heat release on these statistics is considered.

The mixture fraction dissipation rate statistics showed that the effect of heat release is to slow the rate of development of mixing. As compared to the heat release case, higher dissipation rates were observed for the isothermal case, which corresponded with the relatively higher consumption of the reactants. The rms profiles of mixture fraction dissipation rate supported the fact that the heat release had a stabilizing effect on the flow field.

The temperature dissipation rate statistics were computed for the heat release case. The statistics compared qualitatively with the experiments of Boyer and Queiroz (1991). The simulation results also indicated that the temperature dissipation rate approximated the lognormal distribution in a region where there was significant mixing and hence chemical reaction. This agreement between the simulation results and experiments gives added confidence in the observations made regarding the mixture fraction dissipation rate obtained from the simulations.

References

Boyer, L., and Queiroz, M., 1991, "Temperature Dissipation Measurements in a Lifted Turbulent Diffusion Flame," *Combust. Science and Tech.*, Vol. 79, pp. 1–34.

Effelsberg, E., and Peters, N., 1988, "Scalar Dissipation Rates in Turbulent Jets and Jet Diffusion Flames," *Twenty-Second Symposium (International) on Combustion*, The Combustion Institute, Pittsburgh, PA, pp. 693–700.

Givi, P., Jou, W. -H., and Metcalfe, R. W., 1986, "Flame Extinction in a Temporally Developing Mixing Layer," *Twenty-First Symposium (International) on Combustion*, The Combustion Institute, Pittsburgh, PA, pp. 1251–1261.

Givi, P., 1989, "Model-Free Simulations of Turbulent Reactive Flows," *Prog. Energy Combust. Sci.*, Vol. 15, pp. 1–107.

McMurtry, P. A., Jou, W.-H., Riley, J. J., and Metcalfe, R. W., 1986, "Direct Numerical Simulations of a Reacting Mixing Layer With Chemical Heat Release," *AIAA J.*, Vol. 24, pp. 962–970.

McMurtry, P. A., Riley, J. J., and Metcalfe, R. W., 1989, "Effects of Heat Release on the Large-Scale Structure in Turbulent Mixing Layers," *J. Fluid Mech.*, Vol. 199, pp. 297–331.

Michalke, A., 1964, "On the Inviscid Instability of the Hyperbolic Tangent Velocity Profile," *J. Fluid Mech.*, Vol. 19, pp. 543–556.

Namazian, M., Schefer, R. W., and Kelly, J., 1988, "Scalar Dissipation Measurements in the Developing Region of a Jet," *Combustion and Flame*, Vol. 74, pp. 147–160.

Peters, N., 1983, "Local Quenching Due to Flame Stretch and Non-premixed Turbulent Combustion," *Combust. Science and Tech.*, Vol. 30, pp. 1–17.

Shirolkar, J. S., Queiroz, M., and McMurtry, P. A., 1992, "Statistical Properties of Scalar and Temperature Dissipation in a Turbulent Reacting Shear Layer," *Heat and Mass Transfer in Fire and Combustion Systems*, ASME HTD-Vol. 223.

Son, S. F., McMurtry, P. A., and Queiroz, M., 1991, "The Effect of Heat Release on Various Statistical Properties of a Reacting Shear Layer," *Combustion and Flame*, Vol. 85, pp. 51–67.

Surface Heat Transfer Coefficients of Cylindrical Food Products Cooled With Water

I. Dincer[1]

Nomenclature

- a = thermal diffusivity, m^2/s
- a_w = thermal diffusivity of water at the initial product temperature = 0.148×10^{-6} m^2/s
- Bi = Biot number
- C = cooling coefficient, 1/s
- Fo = Fourier number
- h = surface heat transfer coefficient, W/m^2K
- J_1 = lag factor
- J_0 = zeroth-order Bessel function of first kind
- k = thermal conductivity, W/mK
- L = length, m
- M = root of Bessel characteristic equation
- r = radial coordinate
- R = radius, m
- t = time, s
- T = temperature, °C or K
- W = water content, in decimal unit
- θ = dimensionless temperature
- ϕ = temperature difference, °C or K

Subscripts

- a = medium condition
- e = final
- i = initial
- n = refers to nth characteristic value
- w = water
- 1 = refers to first characteristic value

Introduction

Unsteady-state heat transfer from a solid object to any fluid medium is an important subject in many engineering-related fields and plays a role in practical processes ranging from cooling of a hot steel ball to heating and cooling of food products. As a first step to a better understanding of the heat transfer, one must carefully evaluate and understand the fluid flow, and thermophysical properties of the product. Classical explanations of the cooling phenomena are largely based on the temperature distributions and heat transfer rates. However, very limited information is available in the literature on the heat transfer coefficients in food processing applications. Most theoretical or semi-theoretical and experimental investigations of the heat transfer coefficients for geometrically shaped objects can be classified as Nusselt–Reynolds correlations. The surface heat transfer coefficients of food products subjected to cooling applications are dependent upon several parameters, e.g., the product's thermal and physical properties and environmental conditions (Dincer, 1991; Dincer et al., 1992). The well-known Nu–Re correlations may not show a realistic behavior for use in the specific application. A limited number

[1]Department of Energy Systems, TUBITAK-Marmara Research Center, P.O. Box 21, 41470, Gebze-Kocaeli, Turkey.

Contributed by the Heat Transfer Division of THE AMERICAN SOCIETY OF MECHANICAL ENGINEERS. Manuscript received by the Heat Transfer Division October 1992; revision received December 1993. Keywords: Refrigeration, Thermophysical Properties, Transient and Unsteady Heat Transfer. Associate Technical Editor: Y. Bayazitoglu.

of studies for predicting the surface heat transfer coefficients during cooling of the food products have been reported (Ranade and Narayankhedkar, 1982; Ansari, 1987; Arce and Sweat, 1980). Recently, Stewart et al. (1990) established an experimental method for estimation of the heat transfer coefficients encountered in a variety of food cooling processes by performing relatively simple experiments. Dincer (1991) developed a simple analytical model for determining the time-dependent heat transfer coefficients of several food products using the center temperature measurements of the products. But there is no study relating to the present model in the literature.

In order to ensure optimum operation conditions and energy savings in the process, an exact analysis of heat transfer is required and the surface heat transfer coefficient is an important coefficient to be determined.

The main purpose of the present study is to determine the surface heat transfer coefficients for single cylindrical products in different batches cooled in a water flow at different temperatures.

Model and Formulation

In order to ensure one-dimensional conduction so that the transient problem involves only two independent variables, it is assumed that the cylinder is infinitely long and axially symmetric. Thus, heat conduction in the cylindrical product is considered to occur in the radial direction only. Under these conditions, the heat-conduction equation in cylindrical coordinates for an infinite solid cylinder without internal heat generation is

$$[(\partial^2 T/\partial r^2) + (1/r)(\partial T/\partial r)] = (1/a)(\partial T/\partial t) \tag{1}$$

The governing equation in terms of the excess temperature $\phi = T - T_a$ is

$$[(\partial^2 \phi/\partial r^2) + (1/r)(\partial \phi/\partial r)] = (1/a)(\partial \phi/\partial t) \tag{2}$$

The initial and boundary conditions are

$$\phi(r, 0) = \phi_i = (T_i - T_a), \quad \partial\phi(0, t)/\partial r = 0,$$
$$-k\partial\phi(R, t)/\partial r = h\phi(R, t).$$

The solution of Eq. (2) in dimensionless terms for the estimation of the temperature distribution at any point of a cylindrical body may be found in the literature (Arpaci, 1966; Carslaw and Jaeger, 1959; Luikov, 1968).

The dimensionless center temperature distribution of a single cylindrical product is

$$\theta = \sum_{n=1}^{\infty} \frac{2\text{Bi}}{[M_n^2 + \text{Bi}^2]J_0(M_n)} \exp(-M_n^2 \text{Fo}) \tag{3}$$

The characteristic equation of Eq. (3) is

$$(M_n)[J_1(M_n)] + (\text{Bi})[J_0(M_n)] = 0 \tag{4}$$

where the values of M_n are roots of Eq. (4).

The solution of Eq. (4) is difficult. In this respect, a simplification has been made in the form of Eq. (5) (Pflug and Blaisdell, 1963). Thus, Eq. (4) is rewritten as

$$M_1^2 = (6\text{Bi})/(2.85 + \text{Bi}) \tag{5}$$

The following dimensionless expressions are introduced:

$$\theta = (T - T_a)/(T_i - T_a) \tag{6}$$

$$\text{Fo} = at/R^2 \tag{7}$$

$$\text{Bi} = hR/k \tag{8}$$

A simplification is introduced as Fo > 0.2 and hence, the infinite sum can be approximated by the first term of the series and may be represented by the following expression:

$$\theta = J_1 \exp(-M_1^2 \text{Fo}) \tag{9}$$

where $J_1 = [(2\text{Bi})/(M_1^2 + \text{Bi}^2)J_0(M_1)]$.

Regression analyses are carried out using the time-dimensionless temperature data in the exponential form, based on the least-squares method, as given in Eq. (10) (Dincer et al., 1992):

$$\theta = J_1 \exp(-Ct) \tag{10}$$

The following equation is obtained by combining Eqs. (9) and (10):

$$M_1^2 \text{Fo} = Ct \tag{11}$$

After making these substitutions, the following model is developed to determine the surface heat transfer coefficient for a single cylindrical product:

$$h = [(2.85kRC)/(6a - CR^2)] \tag{12}$$

The thermal conductivity (k) and thermal diffusivity (a) of the food products depend on their water content and are given as follows (Sweat, 1986; ASHRAE, 1981):

$$k = 0.148 + 0.493W \tag{13}$$

$$a = 0.08810^{-6} + (a_w - 0.08810^{-6})W \tag{14}$$

Experimental

In order to test the mathematical model employed here, an experimental investigation was performed. In this investigation, batches of 5, 10, 15, and 20 kg of three food commodities, namely, cucumbers, squash, and eggplant were weighed and prepared for the trials. The trials were repeated for varying crate loads at temperatures of 0.5, 1, and 1.5°C, respectively.

The primary elements of the hydrocooling system (Fig. 1) consisted of two major parts, namely, a conventional refrigeration unit (Tecumseh CK-99301-2 model reciprocating compressor of 9280 W capacity, a condenser cooled by dual 370 W fans, a Flica TMC 4.5 model expansion valve, and a water-cooled evaporator) and a cold water pool (test section) with inner dimensions of 2.0 × 0.8 × 0.4 m. The cold-water pool consisted of a lidded tank, insulated with glass wool, through which cooled water was pumped. The tank water level was held at 2/3 full and the water temperatures of 0.5, 1, and 1.5°C were applied for three different environmental conditions. Batches of 5, 10, 15, and 20 kg from each food commodity were placed in slatted polyethylene crates with the dimensions of 0.25 m^2 area and 0.2 m deep (the open-topped and grid-sided polyethylene cases) thermocouples were embedded at the centers of 12 products for each experiment. The crate containing the products was dipped into the cold water flow and the trial was repeated for each product batch. The water temperature was measured with three thermocouples at the inlet, just behind the crate and outlet. All 15 DCK8 Cu/Cu-Ni thermocouples were calibrated at 1°C and had wires 50 and 80 mm long and 1.2 mm in diameter to minimize conduction errors. Measurements, accurate to ±0.1°C, were continuously recorded by a calibrated CMC 821 multichannel microprocessor device (Ellab Instruments, Denmark) at 30 s intervals until all the center temperatures of the products reached the storage temperatures. Data for the 12 products were averaged for data analysis. The flow velocity of water in the tank was measured to be 0.05 m/s using a digital flowmeter (Hontzsch GmbH, Germany). The water contents of the products were determined by using a dry-matter method in the laboratory.

Individual pieces of food in the crate were arranged such that they were not piled on top of one another. They were placed in a single row. This method was applied for each type of food. For each experiment, the crate was placed 10 cm from the water inlet (as shown in Fig. 1).

A detailed description of the experimental apparatus and procedure, including schematic diagrams of the arrangements of the products, the position of the crate, and the direction of flow is given by Dincer (1991, 1992) and Dincer et al. (1992).

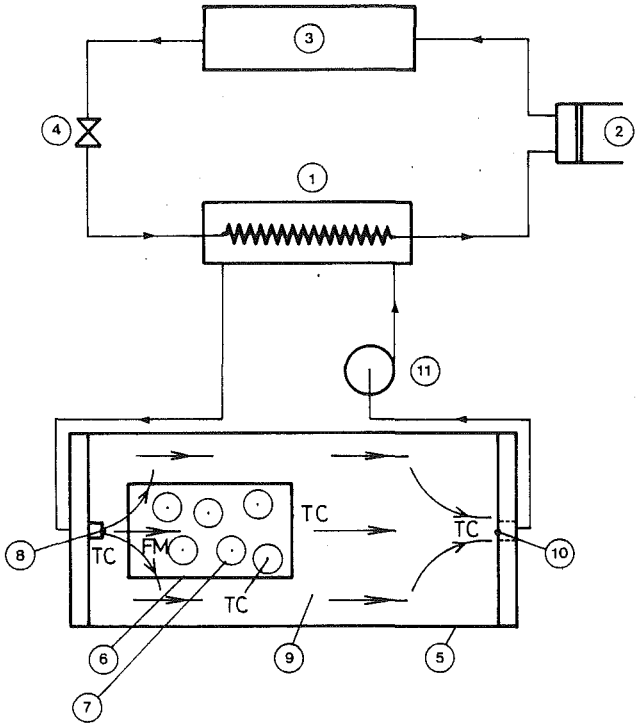

Fig. 1 Schematic drawing of the experimental apparatus: 1. evaporator, 2. compressor, 3. condenser, 4. expansion valve, 5. cold water pool, 6. crate, 7. products, 8. water inlet, 9. water flow, 10. water outlet, 11. circulation pump; TC: thermocouple, FM: flowmeter

Results and Discussion

This research was performed to determine the surface heat transfer coefficients for cylindrically shaped products so that the heat transfer mechanisms can become more predictable. Also, a better understanding will lead to better cooling effectiveness, and better operating conditions. This study involved both the mathematical model developed here and the temperature data.

First, the temperatures of 12 individual products in each batch subjected to cooling at temperatures of 0.5, 1, and 1.5°C were averaged for the analysis in order to minimize the experimental errors. These center temperatures of an individual cylindrical product were converted into dimensionless form using Eq. (6), and a regression analysis in the form of Eq. (8) was applied to the dimensionless center temperature distribution for an individual product in each batch. Then, the effective cooling parameters expressed in terms of cooling coefficient (C) and lag factor (J_1) for each batch were determined.

The determined thermal and physical properties of the cylindrically shaped products as test samples are given in Table 1.

The heat transfer results of tests performed using the cylindrically shaped products are detailed in Table 2 for cucumbers, Table 3 for squash, and Table 4 for eggplant.

The regression equations described the data well, and had very high regression coefficients of over 0.98. In the statistical evaluation, the standard deviations for all regression analyses were calculated and the minimum and maximum standard deviations were found to be 0.01528 and 0.0965. As a clearer description, it was observed that, in general, the maximum difference between the dimensionless experimental tempera-

Table 1 Properties of the test samples

Product	T_i (°C)	T_e (°C)	W (percent)	k (W/mK)	a (m^2/s)	R (cm)	L (cm)
Cucumbers	22.0 ± 0.5	4	96	0.62120	$1.456 \cdot 10^{-7}$	1.90 ± 0.05	16.0 ± 0.5
Squash	21.5 ± 0.5	7	91	0.59660	$1.426 \cdot 10^{-7}$	2.30 ± 0.05	15.5 ± 0.5
Eggplant	21.5 ± 0.5	7	93	0.60649	$1.438 \cdot 10^{-7}$	2.25 ± 0.05	14.2 ± 0.5

Table 2 Surface heat transfer coefficients obtained for cucumbers

Product	T_a (°C)	Crate load (kg)	J_1	C (1/s)	h (W/m^2K)	Regression coefficient
Cucumbers	0.5	5	1.036509	0.001684	213.24 ± 36	0.99906
		10	1.228027	0.001675	209.54 ± 34	0.99491
		15	1.221941	0.001629	191.93 ± 29	0.99537
		20	1.237056	0.001480	146.73 ± 17	0.99420
	1.0	5	1.291389	0.001602	182.52 ± 26	0.98775
		10	1.177443	0.001567	171.20 ± 23	0.99665
		15	1.210404	0.001385	124.71 ± 13	0.99627
		20	1.250717	0.001243	98.42 ± 8	0.99116
	1.5	5	1.279695	0.001604	183.19 ± 27	0.99248
		10	1.286217	0.001404	128.78 ± 14	0.99263
		15	1.266266	0.001395	126.83 ± 13	0.99070
		20	1.202154	0.001120	80.29 ± 6	0.99166

Table 3 Surface heat transfer coefficients obtained for squash

Product	T_a (°C)	Crate load (kg)	J_1	C (1/s)	h (W/m^2K)	Regression coefficient
Squash	0.5	5	1.171796	0.001272	272.26 ± 59	0.99053
		10	1.202305	0.001186	203.25 ± 33	0.98471
		15	1.192911	0.001087	151.51 ± 18	0.98710
		20	1.227165	0.001036	131.73 ± 14	0.98501
	1.0	5	1.186123	0.001188	204.54 ± 33	0.98800
		10	1.162427	0.001132	172.41 ± 24	0.98934
		15	1.193264	0.000956	106.85 ± 10	0.98751
		20	1.194586	0.000936	101.55 ± 9	0.98846
	1.5	5	1.195212	0.001118	165.50 ± 22	0.98824
		10	1.196628	0.001076	146.93 ± 17	0.98922
		15	1.188748	0.001009	122.61 ± 12	0.98589
		20	1.187695	0.000981	113.95 ± 11	0.99183

Table 4 Surface heat transfer coefficients obtained for eggplants

Product	T_a (°C)	Crate load (kg)	J_1	C (1/s)	h (W/m^{2}K)	Regression coefficient
Eggplants	0.5	5	1.195287	0.000870	80.10 ± 6	0.98757
		10	1.077374	0.000822	71.57 ± 5	0.99850
		15	1.109056	0.000794	66.99 ± 4	0.98766
		20	1.205601	0.000770	63.31 ± 4	0.98936
	1.0	5	1.194965	0.000772	63.61 ± 4	0.98977
		10	1.109408	0.000739	58.81 ± 3	0.99748
		15	1.041132	0.000692	52.51 ± 3	0.99885
		20	1.187285	0.000622	44.15 ± 2	0.99132
	1.5	5	1.165531	0.000777	64.37 ± 4	0.99316
		10	1.209623	0.000729	57.42 ± 3	0.98234
		15	1.092817	0.000656	48.07 ± 2	0.99833
		20	1.203111	0.000618	43.70 ± 2	0.99048

ture data and the dimensionless temperature values obtained by regression analyses was less than ±13 percent, except the initial value. Initially, cooling does not follow Eq. (10), which gives θ values greater than 1. At $t = 0$, the regression value for θ is the lag factor, which is a function of the thermal and physical properties (thermal conductivity, thermal diffusivity, heat transfer coefficient, and shape as well as geometry) of the product cooled in water flow.

As can be seen in Tables 2, 3, and 4, the variation in the cooling coefficient, which denotes the change in the product temperature per unit change of the cooling time for each degree temperature difference between the product and its surroundings, and especially its decrease with respect to an increase in the batch weight, strongly indicates that the flow and temperature profiles around the product were influenced by the batch weight and were different for each batch. It was found that the cooling coefficient strongly depended on the lag factor. The surface heat transfer coefficients are sensitive to the physical conditions involved among the products and their surroundings. As shown in the tables above, the surface heat transfer coefficients decrease approximately linearly, and the cooling coefficients and lag factors of each product vary unsystematically with the crate load (batch weight), probably due to changes in coolant flow around the individual cylindrical products, and thus to the heat transfer environment, depending on the loading. Increasing the crate loading from 5 to 20 kg, in loads of 5 kg, decreased the surface heat transfer coefficients by 31, 46, and 56 percent for cucumbers and by 51, 50, and 31 percent for squash, and by 21, 30, and 33 percent for eggplant at coolant temperatures of 0.5, 1, and 1.5°C. The present model was tested for individual cucumbers, squash, and eggplant in different batches. The values of the surface heat transfer coefficients obtained in this work are valid for Fourier numbers greater than 0.2, i.e., when cooling time is greater than 495 seconds for cucumbers, 741 seconds for squash, and 704 seconds for eggplant. In this experiment, the time required to reach storage temperatures for all three food commodities was greater than the time required for the analysis to be valid ($0 \approx 10^3$). These total cooling times at the water temperatures of 0.5, 1, and 1.5°C ranged between 1200 and 2010, 1050 and 1510, and 1620 and 2970 seconds for individual cucumbers, squash, and eggplant in the batches of 5, 10, 15, and 20 kg.

Different batches of food were placed in identical crates. In this way, the motion of an individual product in different batches may be different, and therefore have different effects on the surface heat transfer coefficients. The main purpose of the present study was to develop an analytical model for determining the surface heat transfer coefficients for cylindrical objects subjected to cooling and to test this model by using experimental temperature measurements for different conditions. The results of the present study showed that the surface heat transfer coefficients for the individual products may differ when applied under different experimental conditions.

This investigation indicated that this model can easily be used in order to determine the surface heat transfer coefficients as constant values for the single products.

Conclusions

A mathematical model was developed to determine the surface heat transfer coefficients for single cylindrical objects and was tested for cylindrical food products cooled in water flow at the medium temperatures of 0.5, 1, 1.5°C, respectively. In the experimental investigation, batches of 5, 10, 15, and 20 kg of product were cooled. The results of this study indicated that the surface heat transfer coefficient for an individual product decreased with an increase in batch weight and an increase in the water temperature.

Acknowledgments

The author wishes to thank the Department of Food and Refrigeration Technology, TUBITAK-Marmara Research Center for providing the experimental studies.

References

Ansari, F. A., 1987, "A Simple and Accurate Method of Measuring Surface Film Conductance for Spherical Bodies," *Int. Comm. Heat Mass Transfer*, Vol. 14(2), pp. 229-236.

Arce, J., and Sweat, V. E, 1980, "Survey of Published Heat Transfer Coefficient Encountered in Food Refrigeration Processes," *ASHRAE Transactions*, Vol. 86, pp. 235-260.

Arpaci, V. S., 1966, *Conduction Heat Transfer*, Addison-Wesley, Reading, MA.

ASHRAE, 1981, *Handbook of Fundamentals*, Atlanta, GA.

Carslaw, H. S., and Jaeger, J. C., 1959, *Conduction of Heat in Solids*, 2nd ed., Oxford University Press, London, United Kingdom.

Dincer, I., 1991, "A Simple Model for Estimation of the Film Coefficients During Cooling of Certain Spherical Foodstuffs With Water," *Int. Comm. Heat Mass Transfer*, Vol. 18(4), pp. 431-443.

Dincer, I., 1992, "Methodology to Determine Temperature Distributions in Cylindrical Products Exposed to Hydrocooling," *Int. Comm. Heat Mass Transfer*, Vol. 19(3), pp. 359-371.

Dincer, I., Yildiz, M., Loker, M., and Gun, H., 1992, "Process Parameters for Hydrocooling Apricots, Plums, and Peaches," *Int. J. Food Science Technology*, Vol. 27(3), pp. 347-352.

Luikov, A. V., 1968, *Analytical Heat Diffusion Theory*, Academic Press, New York.

Pflug, L. J., and Blaisdell, J. L., 1963, "Methods of Analysis of Precooling Data," *ASHRAE Journal*, Vol. 5, pp. 33-40.

Ranade, M. S., and Narayankhedkar, K. G., 1982, "Thermal Characteristics of Fruits and Vegetables as Applied to Hydrocooling," *Int. Inst. Refrig.*, Hamilton 1982-1, pp. 455-461.

Stewart, W. E., Becker, B. R., Greer, M. E., and Stickler, L. A., 1990, "An Experimental Method of Approximating Effective Heat Transfer Coefficients for Food Products," *ASHRAE Transactions*, Vol. 96(2), pp. 142-147.

Sweat, V. E., 1986, "Thermal Properties of Foods," in: *Engineering Properties of Foods*, M. A. Rao and S. S. H. Rizvi, eds., Marcel Dekker, Inc., New York, pp. 49-87.

Analysis of Flow and Heat Transfer Over an External Boundary Covered With a Porous Substrate

P. C. Huang[1] and K. Vafai[1,2]

Nomenclature

C_f = friction coefficient, Eq. (22)
C_T = total friction coefficient, Eq. (23)
$c_{p,f}$ = fluid heat capacity, W s kg^{-1} K^{-1}
Da_L = Darcy number = K/L^2
F = a function used in expressing inertia terms
H = thickness of the porous medium, m
k = thermal conductivity, Wm^{-1} K^{-1}
K = permeability of the porous medium, m^2
L = length of the external boundary as shown in Fig. 1(*a*), m
P = pressure, Pa
r = ratio of x-component interfacial velocity to free-stream velocity = u_I/u_∞
Pr = Prandtl number = ν/α
Re_L = Reynolds number = $u_\infty L/\nu$
T = temperature, K
u = x-component velocity, ms^{-1}
v = y-component velocity, ms^{-1}
x = horizontal coordinate, m
y = vertical coordinate, m
α = thermal diffusivity, m^2s^{-1}
α_{eff} = effective thermal diffusivity = $k_{eff}/\rho_f c_{p,f}$, m^2s^{-1}
δ = boundary-layer thickness, m
δ_t = thermal boundary-layer thickness, m
ϵ = porosity of the porous medium
Λ_L = inertial parameter = $FL\,\epsilon/\sqrt{K}$
μ = dynamic viscosity, $kgm^{-1}s^{-1}$
ν = kinematic viscosity, m^2s^{-1}
ρ = fluid density, kgm^{-3}
τ_w = wall shear stress, Nm^{-2}

Superscripts

$\bar{}$ = dimensionless quantity

Subscripts

eff = effective
f = fluid
I = interface
P = porous
t = thermal
w = condition at the wall
x = local
∞ = condition at infinity

Introduction

During the past decade there has been a renewed research interest in fluid flow and heat transfer through porous media due to its relevance in various applications such as drying processes, thermal insulation, direct contact heat exchangers, heat pipes, filtration, etc. Comprehensive reviews of the existing studies on these topics can be found in Cheng (1978) and Tien and Vafai (1989).

An important problem related to convection through porous media is flow and heat transfer through composite porous systems. The convection phenomenon in these systems is usually affected by the temperature and flow field interactions in the porous space and the open space. This type of composite system is encountered in many applications, such as some solidification problems, crude oil extraction, thermal insulation, and some geophysical systems. Due to the mathematical difficulties in simultaneously solving the coupled momentum equations for both porous and fluid regions, it is usually assumed that there is only one fluid-saturated porous region (i.e., there is no fluid region and interfacial surface) and the flow is through this infinitely extended uniform medium. Thus the interaction between the porous-saturated region and the fluid region did not form a part of most of these studies. In addition, most of the existing studies deal primarily with the mathematical formulations in the porous medium based on the use of Darcy's law, which neglects the effects of a solid boundary and inertial forces. These assumptions will easily break down since in most applications the porous medium is bounded and the fluid velocity is high.

Inertial and boundary effects on forced convection along a flat plate embedded in a porous medium were studied by Vafai and Tien (1981, 1982), and Vafai et al. (1985). Among these studies Vafai and Tien (1981) treated a fluid-saturated porous medium as a continuum, integrated the momentum equation over a local control volume, and derived a volume-averaged momentum equation, which included the flow inertia as well as the boundary effects. There have been few investigations related to porous/fluid composite systems. Poulikakos (1986) presented a detailed numerical study of the buoyancy-driven flow instability for a fluid layer extending over a porous substrate in a cavity heated from the bottom. Another related problem is that of Poulikakos and Kazmierczak (1987). In that work a fully developed forced convection in a channel that is partially filled with a porous matrix was investigated and the existence of a critical thickness of the porous layer at which the value of Nusselt number reaches a minimum was demonstrated. Kaviany (1987), Beckermann and Viskanta (1987), and Nakayama et al. (1990) evoked the boundary layer approximations and solved the generalized momentum equation presented by Vafai and Tien (1981) to investigate the same flow configuration. Vafai and Kim (1990) performed a numerical analysis of forced convection over a porous/fluid composite system, which consisted of a thin porous substrate attached to the surface of the flat plate.

The primary objective of this study is to present an analytical solution for forced convection boundary layer flow and heat transfer through a composite porous/fluid system and thereby provide a comprehensive yet extremely fast alternative as well as a comparative base for numerical solutions addressing these type of interfacial transport. The details of the interaction phenomena occurring in the porous medium and the fluid layer are systematically analyzed, revealing the effects of various parameters governing the physics of the problem under consideration. The present analysis drastically reduces typical CPU times for the interfacial simulations presented by Vafai and Kim (1990). It should be noted that the configuration considered in this work is quite generic and forms an important and fundamental geometry for a variety of applications.

Theory

The flow configuration and the coordinate system for this problem are shown in Fig. 1(*a*). In this study, we are assuming that the flow is steady, two dimensional, and that the boundary

[1]Department of Mechanical Engineering, The Ohio State University, Columbus, OH 43210.
[2]Professor, Fellow ASME.
Contributed by the Heat Transfer Division of The American Society of Mechanical Engineers. Manuscript received by the Heat Transfer Division September 1992; revision received September 1993. Keywords: Forced Convection, Materials Processing and Manufacturing Processes, Porous Media. Associate Technical Editor: C. E. Hickox, Jr.

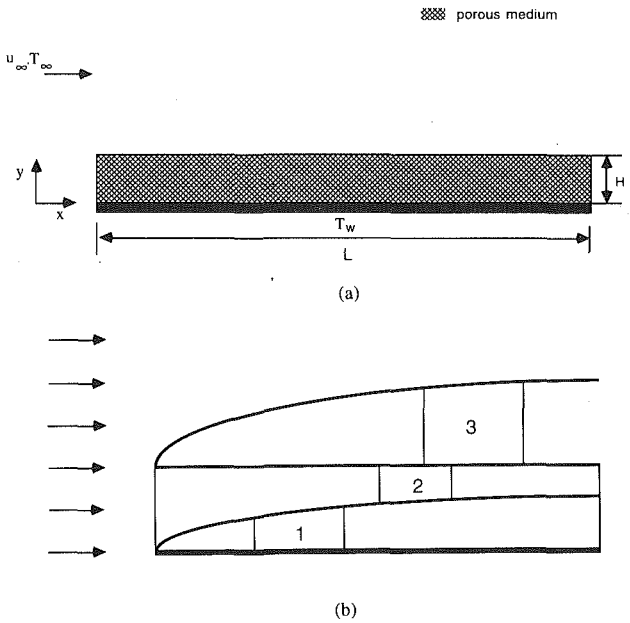

Fig. 1 (*a*) **Schematic diagram of the flow over an external boundary with an attached porous substrate;** (*b*) **control volume for integral momentum analysis of (1) porous boundary layer, (2) interfacial region between the porous and fluid layers, and (3) the fluid boundary layer**

layer approximations hold (this was established by Vafai and Kim, 1990). The conservation equations, which include the boundary and inertial effects, in the porous region can then be written as (Vafai and Tien, 1981):

$$\frac{\partial u_P}{\partial x_P}+\frac{\partial v_P}{\partial y_P}=0 \tag{1}$$

$$u_P\frac{\partial u_P}{\partial x_P}+v_P\frac{\partial v_P}{\partial y_P}=-\frac{1}{\rho}\frac{\partial P_P}{x_P}-\frac{\nu_{\text{eff}}}{K}u_P-\frac{F\epsilon}{\sqrt{K}}u_p^2+\nu_{\text{eff}}\frac{\partial^2 u_P}{\partial y_p^2} \tag{2}$$

$$u_P\frac{\partial T_P}{\partial x_P}+v_P\frac{\partial T_P}{\partial y_P}=\alpha_{\text{eff}}\frac{\partial^2 T_P}{\partial y_p^2} \tag{3}$$

where all the variables and parameters are defined in the nomenclature section. Note that variables u, v, and T are volume-averaged quantities. Since at a sufficiently large distance from the wall the flow field is uniform, the free-stream axial pressure gradient in the porous region required for maintaining the x-component interfacial velocity u_I can be expressed as

$$\frac{1}{\rho}\frac{dP}{dx_P}=-\frac{\nu_{\text{eff}}}{K}u_I-\frac{F\epsilon}{\sqrt{K}}u_I^2-u_I\frac{du_I}{dx_P} \tag{4}$$

Inserting Eq. (4) into Eq. (2), the momentum equation becomes

$$u_P\frac{\partial u_P}{\partial x_P}+v_P\frac{\partial u_P}{\partial y_P}=\frac{\nu_{\text{eff}}}{K}(u_I-u_P)+\frac{F\epsilon}{\sqrt{K}}(u_I^2-u_P^2)+\nu_{\text{eff}}\frac{\partial^2 u_P}{\partial y_P^2}+u_I\frac{du_I}{dx_P} \tag{5}$$

In the fluid region, the conservation equations for mass, momentum, and energy are

$$\frac{\partial u_f}{\partial x_f}+\frac{\partial v_f}{\partial y_f}=0 \tag{6}$$

$$u_f\frac{\partial u_f}{\partial x_f}+v_f\frac{\partial u_f}{\partial y_f}=-\frac{1}{\rho}\frac{\partial p_f}{\partial x_f}+v_f\frac{\partial^2 u_f}{\partial y_f^2} \tag{7}$$

$$u_f\frac{\partial T_f}{\partial x_f}+v_f\frac{\partial T_f}{\partial y_f}=\alpha_f\frac{\partial^2 T_f}{\partial y_f^2} \tag{8}$$

The boundary conditions are

$$x<0:\quad u=u_\infty,\quad P=P_\infty \tag{9}$$

$$x>0,\quad y=0:\quad u=v=0 \tag{10}$$

$$x>0,\quad y\to\infty:\quad u=u_\infty,\quad P=P_\infty \tag{11}$$

This implies that the free-stream flow field is not affected by the presence of the porous media. This was found to be a very good assumption based on the analysis presented by Vafai and Kim (1990). The matching conditions at the interface of the porous/fluid system are

$$u|_{y=H^-}=u|_{y=H^+},\quad v|_{y=H^-}=v|_{y=H^+} \tag{12a}$$

$$P|_{y=H^-}=P|_{y=H^+},\quad \mu_{\text{eff}}\frac{\partial v}{\partial y}\bigg|_{y=H^-}=\mu_f\frac{\partial v}{\partial y}\bigg|_{y=H^+} \tag{12b}$$

$$\mu_{\text{eff}}\left(\frac{\partial u}{\partial y}+\frac{\partial v}{\partial x}\right)\bigg|_{y=H^-}=\mu_f\left(\frac{\partial u}{\partial y}+\frac{\partial v}{\partial x}\right)\bigg|_{y=H^+} \tag{12c}$$

$$T|_{y=H^-}=T|_{y=H^+},\quad k_{\text{eff}}\frac{\partial T}{\partial y}\bigg|_{y=H^-}=k_f\frac{\partial T}{\partial y}\bigg|_{y=H^+} \tag{12d}$$

It should be noted that here we are not trying to resolve a philosophical and complex question with respect to the physical nature of the interface. In reality, a fluid-fluid or porous-fluid interface is more complicated than what has been modeled by investigators both in porous-fluid and fluid-fluid interface modeling. Here we have adopted the traditional mathematical idealization used for both fluid-fluid or porous-fluid interfaces, i.e., representing the interface by a singular surface.

Analysis

An integral analysis is applied to three different regions: the porous boundary layer region, the fluid boundary layer within the porous substrate, and the fluid boundary layer outside of the porous substrate as shown in Fig. 1(*b*).

Integral Momentum Equation for the Porous Boundary Layer. Following the Karman-Pohlhausen integral method, the parabolic velocity distribution is described as

$$\frac{u_P}{u_I}=2\frac{y_P}{\delta_P}-\left(\frac{y_P}{\delta_P}\right)^2 \tag{13}$$

where δ_P is the thickness of the momentum boundary layer in the porous region. After a lengthy analysis the integral momentum equation in dimensionless form for the porous region is derived as

$$\frac{3}{5}\bar{\delta}_P r\frac{dr}{d\bar{x}_P}+\frac{2}{15}r^2\frac{d\bar{\delta}_P}{d\bar{x}_P}=-\frac{r\bar{\delta}_P}{3\text{Re}_L\text{Da}_L}-\frac{7}{15}\Lambda_L r^2\bar{\delta}_P+\frac{2r}{\text{Re}_L\bar{\delta}_P} \tag{14}$$

where

$$\bar{x}=\frac{x}{L},\quad \bar{\delta}_P=\frac{\delta_P}{L},\quad r=\frac{u_I}{u_\infty}\text{ and }\text{Re}_L=\frac{u_\infty L}{\nu_{\text{eff}}},$$

$$\text{Da}_L=\frac{K}{L^2},\quad \Lambda_L=\frac{FL\epsilon}{\sqrt{K}}$$

This equation is subject to the following initial condition given by $\bar{\delta}_P(0)=0$, $r(0)=0$. It should be noted that $x_f=x_P$. However, we have used separate notations for x_f and x_P for the sake of consistency.

Integral Momentum Equation for the Fluid Boundary Layer Within the Porous Substrate. A lengthy integral analysis for the control volume 2 shown in Fig. 1(*b*) leads to the momentum integral equation for that region

$$-\frac{1}{\rho}\left(\delta_f\frac{\partial P}{\partial x_f}+\tau_I\right)=\frac{\partial}{\partial x_f}\int_0^{\delta_f}u_f(u_\infty-u_f)dy_f$$

$$-(1-r)u_\infty^2\left[\frac{1}{3}r\frac{d\delta_P}{dx_P}-\left(H-\frac{1}{3}\delta_P\right)\frac{dr}{dx_P}\right] \quad (15)$$

where τ_I is the shear stress in the porous/fluid interface and δ_P and δ_f are the thicknesses of porous and fluid momentum boundary layers, respectively. Assuming the following parabolic velocity distribution for the fluid boundary layer:

$$\frac{u_I}{u_\infty}=r+(2-2r)\frac{y_f}{\delta_f}-(1-r)\left(\frac{y_f}{\delta_f}\right)^2 \quad (16)$$

where the subscript f refers to fluid and $r = u_I/u_\infty$. Substituting Eq. (16) into Eq. (15) and replacing τ_I by $\nu_f(\partial u_f/\partial y_f)_{y_f=0}$, the derived integral momentum equation in dimensionless form becomes

$$\left(\frac{2}{15}+\frac{r}{15}-\frac{r^2}{5}\right)\frac{d\bar{\delta}_f}{d\bar{x}_f}+\bar{\delta}_f\left(\frac{1}{15}-\frac{2r}{5}\right)\frac{dr}{d\bar{x}_f}=(2-2r)\frac{1}{\mathrm{Re}_L\bar{\delta}_f}+(1-r)$$

$$+(1-r)\left[\frac{1}{3}r\frac{d\bar{\delta}_P}{d\bar{x}_f}+\left(\frac{\bar{\delta}_P}{3}-\bar{H}\right)\frac{dr}{d\bar{x}_f}\right] \quad (17)$$

where

$$\bar{x}_f=\frac{x_f}{L},\quad \bar{\delta}_f=\frac{\delta_f}{L},\quad \bar{\delta}_P=\frac{\delta_P}{L}\text{ and }\bar{H}=\frac{H}{L},\quad \mathrm{Re}_L=\frac{u_\infty L}{\nu_f}$$

This equation is subject to $\bar{\delta}_P(0) = 0$, $\bar{\delta}_f(0) = 0$, $r(0) = 0$.

Integral Momentum Equation for the Fluid Boundary Layer Outside of the Porous Substrate. A similar procedure for the control volume 3 in Fig. 1(*b*), which incorporates the interfacial boundary conditions, leads to the integral momentum equation for the interfacial region

$$\nu_f\frac{\partial u_f}{\partial y_f}+\nu_{\mathrm{eff}}u_I(x)[H-\delta_P(x)]+\frac{F\epsilon}{\sqrt{K}}\left(\frac{u_I}{u_\infty}\right)^2(H-\delta_P(x))=0 \quad (18)$$

Substituting the velocity distributions for both porous and fluid boundary layers into Eq. (19) gives the dimensionless form of the integral momentum equation

$$\frac{2(1-r)}{\mathrm{Re}_L\bar{\delta}_f}+\frac{(\bar{H}-\bar{\delta}_P)r}{\mathrm{Re}_L\mathrm{Da}_L}+\Lambda_L r^2(\bar{H}-\bar{\delta}_P)=0 \quad (19)$$

This equation is subject to $\bar{\delta}_P(0) = 0$, $\bar{\delta}_f(0) = 0$, $r(0) = 0$.

Integral Energy Equation. Since only one thermal boundary layer was observed in the forced convection through the porous/fluid composite system under consideration (Vafai and Kim, 1991), in this study the control volume 1 in Fig. 1(*b*) is used to derive the integral energy equation, which depends on the relative values of δ_P and δ_f. Performing an energy balance over control volume 1 and using the following parabolic temperature distribution:

$$\theta=\frac{T_P-T_w}{T_\infty-T_w}=2\frac{y_P}{\delta_t}-\left(\frac{y_P}{\delta_t}\right)^2 \quad (20)$$

the integral energy equation in dimensionless form is obtained after a very lengthy analysis for three different possible conditions as

$$\left(\frac{\bar{\delta}_t}{3}-\frac{\bar{\delta}_P}{3}+\frac{\bar{\delta}_P^2}{6\bar{\delta}_t}-\frac{\bar{\delta}_P^3}{30\bar{\delta}_t^2}\right)\frac{dr}{d\bar{x}_P}$$

$$+\frac{r}{3}\left[\left(1+\frac{\bar{\delta}_P}{10\bar{\delta}_t}-\frac{\bar{\delta}_P^2}{2\bar{\delta}_t^2}\right)\frac{d\bar{\delta}_t}{d\bar{x}_P}-\left(1-\frac{\bar{\delta}_P}{\bar{\delta}_t}+\frac{3\bar{\delta}_P^2}{10\bar{\delta}_t^2}\right)\frac{d\bar{\delta}_P}{d\bar{x}_P}\right]$$

$$\frac{d\bar{\delta}_P}{d\bar{x}_P}=\frac{2}{\mathrm{Pr}_{\mathrm{eff}}\mathrm{Re}_L}\frac{1}{\bar{\delta}_t}\quad \delta_t>\delta_P \quad (21a)$$

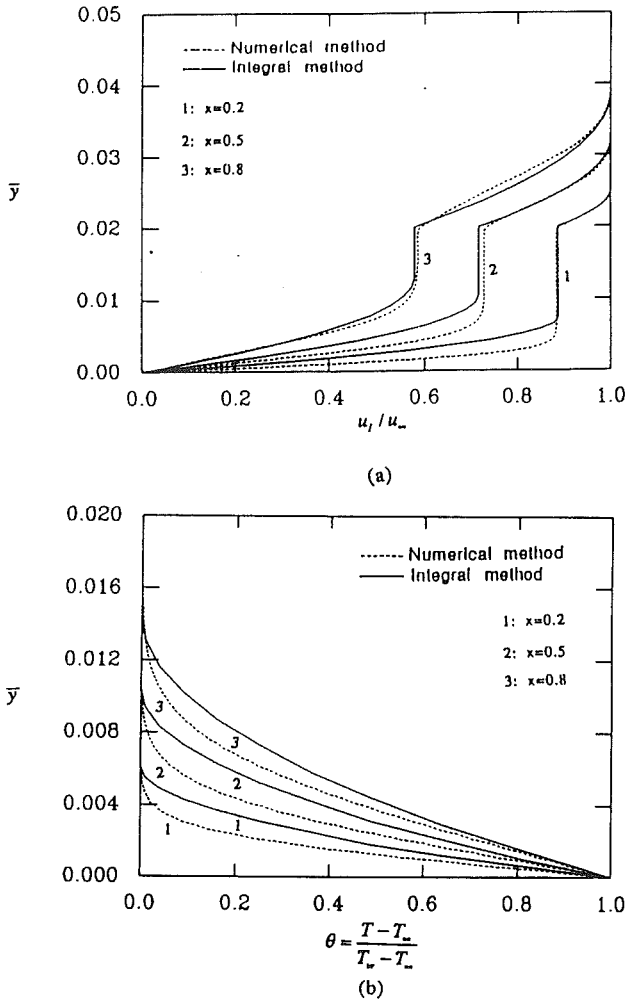

Fig. 2 (*a*) Velocity and (*b*) temperature distribution along the flat plate at three different locations, $x = 0.2$, 0.5, and 0.8, for $\mathrm{Re}_L = 3 \times 10^5$, $\Lambda_L = 0.35$, $\mathrm{Da}_L = 8 \times 10^{-6}$, $\mathrm{Pr} = 0.7$ $k_{\mathrm{eff}}/k_f = 1$, $H/L = 0.02$

$$\frac{1}{3}\left(\bar{\delta}_t\frac{dr}{d\bar{x}}+r\frac{d\bar{\delta}_t}{d\bar{x}}\right)=\frac{2}{\mathrm{Pr}_{\mathrm{eff}}\mathrm{Re}_L\bar{\delta}_t}\quad \delta_t=\delta_P \quad (21b)$$

and

$$\left(\frac{\bar{\delta}_t^2}{6\bar{\delta}_P}-\frac{\bar{\delta}_t^3}{30\bar{\delta}_P^2}\right)\frac{dr}{d\bar{x}_P}+r\left[\left(1+\frac{\bar{\delta}_t}{3\bar{d}_P}-\frac{\bar{\delta}_t^2}{10\bar{\delta}_P^2}\right)\frac{d\bar{\delta}_t}{d\bar{x}_P}\right.$$

$$\left.-\left(\frac{\bar{\delta}_P^2}{6\bar{\delta}_t^2}-\frac{\bar{\delta}_t^3}{15\bar{\delta}_P^3}\right)\frac{d\bar{\delta}_P}{d\bar{x}_P}\right]=\frac{1}{\mathrm{Pr}_{\mathrm{eff}}\mathrm{Re}_L}\frac{1}{\bar{\delta}_t}\quad \delta_t<\delta_P \quad (21c)$$

This equation is subject to $\bar{\delta}_P(0) = 0$, $\bar{\delta}_f(0) = 0$, $r(0) = 0$.

Discussion of Results and Conclusions

The combinations of Eqs. (15), (17), (19), and (21) form a set of four nonlinear simultaneous ordinary differential equations for the four unknowns δ_P, δ_f, δ_t, and r. The fourth-order Runge–Kutta method is applied to solve these equations.

As discussed earlier, the present analysis is extremely effective and expedient in showing the physics of the interfacial transport. In what follows, the solutions obtained by integral analysis are examined and compared with the velocity and temperature distributions obtained by Vafai and Kim (1990). Figure 2 shows how the boundary layer thickness, the velocity and temperature distributions are affected by the presence of a porous matrix. The results in Fig. 2 are presented for Reynolds number of $\mathrm{Re}_L = 3 \times 10^5$, Darcy number $\mathrm{Da}_L = 8 \times$

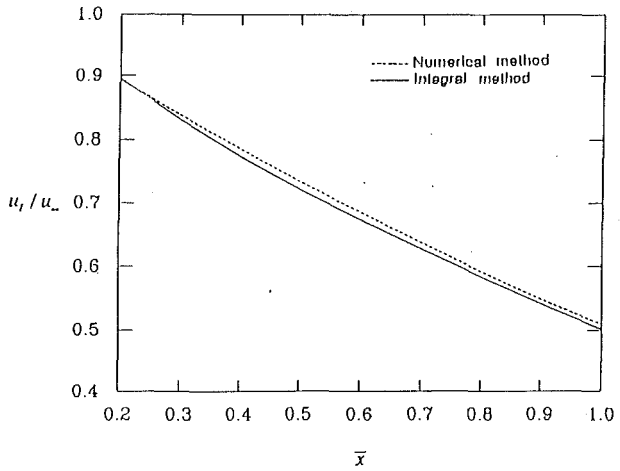

Fig. 3 Comparison of the integral solutions with numerical solutions for x-component interfacial velocity along the flat plate for $\Lambda_L = 0.35$, $Re_L = 3 \times 10^5$, $Da_L = 8 \times 10^{-6}$, $H/L = 0.02$

10^{-6}, inertial number $\Lambda_L = 0.35$, Prandtl number Pr = 0.7, effective conductivity ratio $k_{eff}/k_f = 1$, and the dimensionless thickness of the porous slab of $\bar{H} = 0.02$. As expected, there are two distinct momentum boundary layers: one in the porous region and the other one in the fluid region. Inside the porous region as the transverse coordinate increases, the velocity profile is shown to increase from zero to a constant value, which is maintained until the outer boundary layer appears. Once it crosses the porous/fluid interface, it goes through a smooth transition and approaches a free-stream value in the fluid region.

As expected, the momentum boundary layers in the porous medium as well as in the fluid region grow in the streamwise direction. Consequently, the magnitude of the interfacial velocity decreases to adapt to this growth. Figure 2(*b*) shows the temperature distribution along the flat plate at three different locations. The values of the thickness of the thermal boundary layer obtained by integral method are larger than those obtained by numerical method. This is due to the approximate expressions used for the velocity and temperature profiles in the integral analysis. Figure 3 compares the results of the numerical method and the integral method in the streamwise direction for the interfacial velocity. The results show a remarkably good agreement between the integral analysis and the full numerical solution considering the complexity and the much larger CPU requirements for the numerical simulations. It should be noted that the type of agreements found in Figs. 2(*a*), 2(*b*), and 3 are typical for a wide range of pertinent parameters but are not presented here for the sake of brevity.

The configuration considered in this work is quite generic and forms an important and fundamental geometry for a variety of applications. The results given in this work present a comprehensive yet easy comparative base for numerical solutions addressing this type of interfacial transport. The present analysis provides a rather *accurate simulation* of the interfacial transport *while drastically reducing* previously reported computational times by Vafai and Kim (1990) for this type of simulations.

References

Beckermann, C., and Viskanta, R., 1987, "Forced Convection Boundary Layer Flow and Heat Transfer Along a Flat Plate Embedded in a Porous Medium," *Int. J. Heat Mass Transfer*, Vol. 30, pp. 1547–1551.

Cheng, P., 1978, "Heat Transfer in Geothermal System," *Adv. Heat Transfer*, Vol. 14, pp. 1–105.

Kaviany, M., 1987, "Boundary Layer Treatment of Forced Convection Heat Transfer From a Semi-infinite Flat Plate Embedded in Porous Media," ASME JOURNAL OF HEAT TRANSFER, Vol. 109, pp. 345–349.

Nakayama, A., Kokudai, T., and Koyama, H., 1990, "Non-Darcian Boundary Layer Flow and Forced Convective Heat Transfer Over a Flat Plate in a Fluid-Saturated Porous Medium," ASME JOURNAL OF HEAT TRANSFER, Vol. 112, pp. 157–162.

Poulikakos, D., 1986, "Buoyancy-Driven Convection in a Horizontal Fluid Layer Extending Over a Porous Substrate," *Phys. Fluids*, Vol. 29, pp. 3949–3957.

Poulikakos, D., and Kazmierczak, M., 1987, "Forced Convection in a Duct Partially Filled With a Porous Material," ASME JOURNAL OF HEAT TRANSFER, Vol. 109, pp. 653–662.

Tien, C. L., and Vafai, K., 1989, "Convective and Radiative Heat Transfer in Porous Media," *Adv. Appl. Mech.*, Vol. 27, pp. 225–281.

Vafai, K., and Tien, C. L., 1981, "Boundary and Inertia Effects on Flow and Heat Transfer in Porous Media," *Int. J. Heat Mass Transfer*, Vol. 24, pp. 195–203.

Vafai, K., and Tien, C. L., 1982, "Boundary and Inertia Effects on Convective Mass Transfer in Porous Media," *Int. J. Heat Mass Transfer*, Vol. 25, pp. 1183–1190.

Vafai, K., Alkire, R. L., and Tien, C. L., 1985, "An Experimental Investigation Heat Transfer in Variable Porosity Media," ASME JOURNAL OF HEAT TRANSFER, Vol. 107, pp. 642–647.

Vafai, K., and Kim, S. J., 1990, "Analysis of Surface Enhancement by a Porous Substrate," ASME JOURNAL OF HEAT TRANSFER, Vol. 11, pp. 700–705.

Perturbation Solution for Laminar Convective Heat Transfer in a Helix Pipe

G. Yang[1] and M. A. Ebadian[1,2]

Introduction

Coiled pipes are used extensively in many industries. A general study of flow and heat transfer in the toroidal pipe (the coiled pipe with negligible pitch) has been reviewed by Berger et al. (1983) and Shah and Joshi (1987). It has long been recognized that the pitch of the coiled pipe will create an additional rotational force known as torsion. In a coiled pipe with considerable pitch, torsion will distort the symmetric loops of the secondary flow and twist the axial velocity contours (Wang, 1981; Germano, 1989; Kao, 1987; Tuttle, 1990). To distinguish, coiled pipes with a substantial pitch are defined as helicoidal pipes. Although numerous studies have been conducted on the toroidal pipe, a literature survey indicates that only a few papers have been published to study convection heat transfer in the helicoidal pipe (Manlapaz and Churchill, 1981; Futagami and Aoyama, 1988. In these papers, the overall heat transfer behavior has been studied by simplifying the governing equations. However, none have discussed the effects of torsion on the temperature distribution and peripheral heat transfer rate in the helicoidal pipe, which is very important information for the effective design of the compact heat exchanger and combustor. The purpose of this note is to summarize the analytical results of both thermally and hydrodynamically fully developed convective heat transfer in a helicoidal pipe subject to the (H1) boundary condition.

[1]Department of Mechanical Engineering, Florida International University, Miami, FL 33199.

[2]Fellow ASME, corresponding author.

Contributed by the Heat Transfer Division of THE AMERICAN SOCIETY OF MECHANICAL ENGINEERS. Manuscript received by the Heat Transfer Division July 1993; revision received February 1994. Keywords: Augmentation and Enhancement, Forced Convection, Heat Exchangers. Associate Technical Editor: Y. Jaluria.

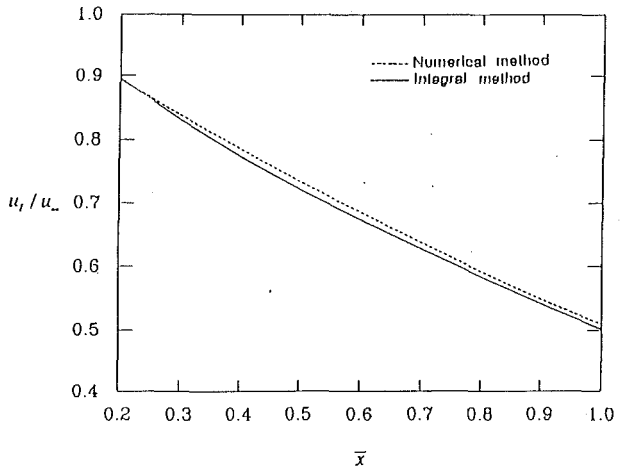

Fig. 3 Comparison of the integral solutions with numerical solutions for x-component interfacial velocity along the flat plate for $\Lambda_L = 0.35$, $Re_L = 3 \times 10^5$, $Da_L = 8 \times 10^{-6}$, $H/L = 0.02$

10^{-6}, inertial number $\Lambda_L = 0.35$, Prandtl number Pr = 0.7, effective conductivity ratio $k_{eff}/k_f = 1$, and the dimensionless thickness of the porous slab of $\bar{H} = 0.02$. As expected, there are two distinct momentum boundary layers: one in the porous region and the other one in the fluid region. Inside the porous region as the transverse coordinate increases, the velocity profile is shown to increase from zero to a constant value, which is maintained until the outer boundary layer appears. Once it crosses the porous/fluid interface, it goes through a smooth transition and approaches a free-stream value in the fluid region.

As expected, the momentum boundary layers in the porous medium as well as in the fluid region grow in the streamwise direction. Consequently, the magnitude of the interfacial velocity decreases to adapt to this growth. Figure 2(*b*) shows the temperature distribution along the flat plate at three different locations. The values of the thickness of the thermal boundary layer obtained by integral method are larger than those obtained by numerical method. This is due to the approximate expressions used for the velocity and temperature profiles in the integral analysis. Figure 3 compares the results of the numerical method and the integral method in the streamwise direction for the interfacial velocity. The results show a remarkably good agreement between the integral analysis and the full numerical solution considering the complexity and the much larger CPU requirements for the numerical simulations. It should be noted that the type of agreements found in Figs. 2(*a*), 2(*b*), and 3 are typical for a wide range of pertinent parameters but are not presented here for the sake of brevity.

The configuration considered in this work is quite generic and forms an important and fundamental geometry for a variety of applications. The results given in this work present a comprehensive yet easy comparative base for numerical solutions addressing this type of interfacial transport. The present analysis provides a rather *accurate simulation* of the interfacial transport *while drastically reducing* previously reported computational times by Vafai and Kim (1990) for this type of simulations.

References

Beckermann, C., and Viskanta, R., 1987, "Forced Convection Boundary Layer Flow and Heat Transfer Along a Flat Plate Embedded in a Porous Medium," *Int. J. Heat Mass Transfer*, Vol. 30, pp. 1547–1551.

Cheng, P., 1978, "Heat Transfer in Geothermal System," *Adv. Heat Transfer*, Vol. 14, pp. 1–105.

Kaviany, M., 1987, "Boundary Layer Treatment of Forced Convection Heat Transfer From a Semi-infinite Flat Plate Embedded in Porous Media," ASME JOURNAL OF HEAT TRANSFER, Vol. 109, pp. 345–349.

Nakayama, A., Kokudai, T., and Koyama, H., 1990, "Non-Darcian Boundary Layer Flow and Forced Convective Heat Transfer Over a Flat Plate in a Fluid-Saturated Porous Medium," ASME JOURNAL OF HEAT TRANSFER, Vol. 112, pp. 157–162.

Poulikakos, D., 1986, "Buoyancy-Driven Convection in a Horizontal Fluid Layer Extending Over a Porous Substrate," *Phys. Fluids*, Vol. 29, pp. 3949–3957.

Poulikakos, D., and Kazmierczak, M., 1987, "Forced Convection in a Duct Partially Filled With a Porous Material," ASME JOURNAL OF HEAT TRANSFER, Vol. 109, pp. 653–662.

Tien, C. L., and Vafai, K., 1989, "Convective and Radiative Heat Transfer in Porous Media," *Adv. Appl. Mech.*, Vol. 27, pp. 225–281.

Vafai, K., and Tien, C. L., 1981, "Boundary and Inertia Effects on Flow and Heat Transfer in Porous Media," *Int. J. Heat Mass Transfer*, Vol. 24, pp. 195–203.

Vafai, K., and Tien, C. L., 1982, "Boundary and Inertia Effects on Convective Mass Transfer in Porous Media," *Int. J. Heat Mass Transfer*, Vol. 25, pp. 1183–1190.

Vafai, K., Alkire, R. L., and Tien, C. L., 1985, "An Experimental Investigation Heat Transfer in Variable Porosity Media," ASME JOURNAL OF HEAT TRANSFER, Vol. 107, pp. 642–647.

Vafai, K., and Kim, S. J., 1990, "Analysis of Surface Enhancement by a Porous Substrate," ASME JOURNAL OF HEAT TRANSFER, Vol. 11, pp. 700–705.

Perturbation Solution for Laminar Convective Heat Transfer in a Helix Pipe

G. Yang[1] and M. A. Ebadian[1,2]

Introduction

Coiled pipes are used extensively in many industries. A general study of flow and heat transfer in the toroidal pipe (the coiled pipe with negligible pitch) has been reviewed by Berger et al. (1983) and Shah and Joshi (1987). It has long been recognized that the pitch of the coiled pipe will create an additional rotational force known as torsion. In a coiled pipe with considerable pitch, torsion will distort the symmetric loops of the secondary flow and twist the axial velocity contours (Wang, 1981; Germano, 1989; Kao, 1987; Tuttle, 1990). To distinguish, coiled pipes with a substantial pitch are defined as helicoidal pipes. Although numerous studies have been conducted on the toroidal pipe, a literature survey indicates that only a few papers have been published to study convection heat transfer in the helicoidal pipe (Manlapaz and Churchill, 1981; Futagami and Aoyama, 1988. In these papers, the overall heat transfer behavior has been studied by simplifying the governing equations. However, none have discussed the effects of torsion on the temperature distribution and peripheral heat transfer rate in the helicoidal pipe, which is very important information for the effective design of the compact heat exchanger and combustor. The purpose of this note is to summarize the analytical results of both thermally and hydrodynamically fully developed convective heat transfer in a helicoidal pipe subject to the (H1) boundary condition.

[1]Department of Mechanical Engineering, Florida International University, Miami, FL 33199.

[2]Fellow ASME, corresponding author.

Contributed by the Heat Transfer Division of THE AMERICAN SOCIETY OF MECHANICAL ENGINEERS. Manuscript received by the Heat Transfer Division July 1993; revision received February 1994. Keywords: Augmentation and Enhancement, Forced Convection, Heat Exchangers. Associate Technical Editor: Y. Jaluria.

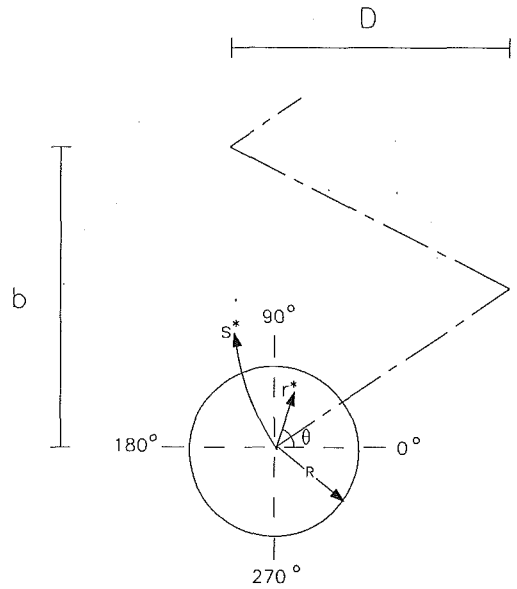

Fig. 1 Schematic representation of a helicoidal pipe

Analysis

The geometry and coordinate system under consideration are shown in Fig. 1. In this figure, D and b represent the diameter and the pitch of the helix, respectively, and R is the radius of the circular pipe. s^*, r^*, and θ are the coordinates in the axial, radial, and tangential directions, respectively. u, v, and w represent the radial, tangential, and axial velocities, respectively, and T represents the fluid temperature. The dimensionless governing equations for fully developed laminar flow and convective heat transfer can be expressed as:

$$\frac{1}{r}\frac{\partial u}{\partial \theta}+\frac{1}{r}\frac{\partial (rv)}{\partial r}+Q=0 \tag{1}$$

$$\frac{u}{r}\frac{\partial u}{\partial \theta}+\frac{v}{r}\frac{\partial (ru)}{\partial r}=\frac{2}{\mathrm{Re}}\left[-\frac{1}{r}\frac{\partial p}{\partial \theta}-\frac{u}{r^2}+\frac{1}{r}\frac{\partial u}{\partial r}+\frac{\partial^2 u}{\partial r^2}+\frac{1}{r^2}\frac{\partial v}{\partial \theta}-\frac{1}{r}\frac{\partial^2 v}{\partial r\partial \theta}-\epsilon\omega\left(\eta\cos\theta-\lambda\frac{\partial \beta}{\partial \theta}\right)\right]+\epsilon\omega\left(w^2\sin\theta+\lambda w\frac{\partial u}{\partial \theta}\right) \tag{2}$$

$$v\frac{\partial v}{\partial r}+\frac{u}{r}\frac{\partial v}{\partial \theta}=\frac{2}{\mathrm{Re}}\left[-\frac{\partial p}{\partial r}+\frac{1}{r^2}\frac{\partial^2 v}{\partial \theta^2}-\frac{1}{r^2}\frac{\partial u}{\partial \theta}-\frac{1}{r}\frac{\partial^2 u}{\partial \theta\,\partial r}-\epsilon\omega\left(\eta\sin\theta+\lambda\frac{\partial \gamma}{\partial \theta}\right)\right]+\frac{u^2}{r}-\epsilon\omega w\left[w\cos\theta-\lambda\frac{\partial v}{\partial \theta}\right] \tag{3}$$

$$v\frac{\partial w}{\partial r}+\frac{u}{r}\frac{\partial w}{\partial \theta}=\frac{2}{\mathrm{Re}}\left[4\omega+\left(\frac{1}{r}-\epsilon\omega\cos\theta\right)\frac{\partial w}{\partial r}+\frac{\partial^2 w}{\partial r^2}+\frac{\epsilon\omega}{r}\sin\theta\frac{\partial w}{\partial \theta}+\frac{1}{r^2}\frac{\partial^2 w}{\partial \theta^2}-\epsilon^2\omega^2 w-\epsilon\lambda\left(\frac{1}{r}\frac{\partial}{\partial \theta}\left(\omega\frac{\partial u}{\partial \theta}\right)+\frac{\partial}{\partial r}\left(\omega\frac{\partial v}{\partial \theta}\right)+\frac{\omega}{r}\frac{\partial v}{\partial \theta}\right)\right]-wQ \tag{4}$$

$$\frac{u}{r}\frac{\partial T}{\partial \theta}+v\frac{\partial T}{\partial r}=\frac{2\,\mathrm{Re}}{\mathrm{Pr}}\left\{\left(\frac{1}{r^2}\frac{\partial^2 T}{\partial \theta^2}+\frac{\partial^2 T}{\partial r^2}+\frac{1}{r}\frac{\partial T}{\partial r}\right)\times\epsilon\omega\left(\frac{1}{r}\frac{\partial T}{\partial \theta}\sin\theta-\frac{\partial T}{\partial r}\cos\theta\right)+\epsilon^2\omega^2\lambda^2\frac{\partial^2 T}{\partial \theta^2}\right\}-\omega w+\epsilon\omega\lambda w\frac{\partial T}{\partial \theta}, \tag{5}$$

where ϵ and λ represent the dimensionless curvature and torsion, respectively; p is the pressure of the fluid; and Pr is the Prandtl number, where

$$Q=\epsilon\omega\left(u\sin\theta-v\cos\theta-\lambda\frac{\partial w}{\partial \theta}\right) \tag{6}$$

$$\beta=\frac{1}{r}\frac{\partial w}{\partial \theta}+\epsilon\omega\left(w\sin\theta+\lambda\frac{\partial u}{\partial \theta}\right) \tag{7}$$

$$\gamma=\frac{\partial w}{\partial r}+\epsilon\omega\left(w\cos\theta-\lambda\frac{\partial v}{\partial \theta}\right) \tag{8}$$

$$\eta=\frac{\partial u}{\partial r}+\frac{u}{r}-\frac{1}{r}\frac{\partial v}{\partial \theta}. \tag{9}$$

Equations (1)–(5) are assumed hydrodynamically and thermally fully developed; therefore, u, v, w, are functions of r and θ only. The dimensionless parameters in Eqs. (1) through (5) are defined by:

$$r=\frac{r^*}{R},\ s=\frac{s^*}{R},\ u=\frac{u^*}{\overline{w}^*},\ v=\frac{v^*}{\overline{w}^*},\ w=\frac{w^*}{\overline{w}^*}$$

$$p=\frac{p^*}{\rho\nu\,\overline{w}^*/R},\ \epsilon=\frac{2D\cdot R}{D^2+\left(\frac{P}{\pi}\right)^2},\ \mathrm{Re}=\frac{2\,\overline{w}^*\cdot R}{\nu},\ \mathrm{Pr}=\frac{\nu}{\alpha}$$

$$T=\frac{T^*-T_w^*}{\frac{4R^3\overline{w}^2}{\nu^2}\frac{dT_b^*}{ds^*}},\ \overline{w}^*=\frac{R^2}{8\rho\nu}\left(-\frac{dp^*}{ds^*}\right),\ \omega=\frac{1}{1-\epsilon\cos\theta}, \tag{10}$$

$$\lambda=\frac{b}{\pi D},\ \mathrm{De}=\mathrm{Re}^2\epsilon.$$

In Eq. (10), the value with a superscript (*) indicates the dimensional value, $\overline{w}^*$ is the average velocity in the axial direction, De is the Dean number, and Re represents the Reynolds number. Therefore,

$$T_b^*=\frac{1}{\pi\overline{w}^*}\int_0^{\pi}\int_0^1 w^*\,T^*\,r^*\,dr^*d\theta. \tag{11}$$

For fully developed flow and an (H1) thermal boundary condition, the boundary conditions for Eqs. (1)–(5) will be:

$$u(\theta,1)=v(\theta,1)=w(\theta,1)=T(\theta,1)=0. \tag{12}$$

Solution Procedure

For the helicoidal pipe with a small curvature, it is natural to choose curvature, ϵ, as the perturbation parameter. The unknown variables, u, v, w, p, and T, can be written in general form:

$$\phi=\phi_0+\epsilon\phi_1+\epsilon^2\phi_2+\ldots. \tag{13}$$

In this study, only the first three terms will be considered. By substituting Eq. (13) into Eqs. (1)–(5) and collecting the terms with the same order of ϵ, one can obtain three sets of partial differential equations.

The continuity and momentum equations, Eqs. (1)–(4), can be solved independently of the energy equation, Eq. (5). A detailed explanation for the terms of u_i, v_i, and w_i can be found in the reference given by Ebadian (1993).

Temperature Distribution

By substituting the terms w_0, u_1, v_1, w_1, u_2, v_2, and w_2 from

Ebadian (1993) into each order of the energy equations and solving these equations sequentially, one can obtain the zero, first, and second-order temperature distributions. Thus,

$$T_0 = \frac{\Pr}{32\ \mathrm{Re}}\,(r^4 - 4r^2 + 3) \tag{14a}$$

$$T_1 = \left[\Pr \mathrm{Re} \sum_{i=1}^{6} (\Gamma_1)_i r^{2i-1} + \Pr^3 \mathrm{Re} \sum_{i=1}^{6} (\Gamma_2)_i r^{2i-1} + \frac{\Pr}{\mathrm{Re}} \sum_{i=1}^{6} (\Gamma_3)_i r^{2i-1}\right] \cos\theta \tag{14b}$$

$$T_2 = T_{20}(r, \Pr, \mathrm{Re}) + T_{c2}(r, \Pr, \mathrm{Re}) \cos 2\theta + T_{s1}(r, \Pr, \mathrm{Re}) \lambda \sin\theta \tag{14c}$$

In Eq. (14*b*), $(\Gamma_j)_i$ represents the coefficients in each term. Equation (14*c*) shows that the second-order solution includes three parts: the terms related to r only, T_{20}; the terms related to both r and cos 2θ, T_{c2}; and the terms related to both r and sin θ, T_{s1}. The T_{20}, T_{c2}, and T_{s1} have 48, 43, and 33 terms, respectively (cf. Ebadian, 1993).

Equation (14*a*) indicates that T_0, the temperature distribution in a straight pipe, is a function of r only. That is, the isothermal line of T_0 will be a set of concentric circles. Equation (14*b*) shows that T_1 is a function of both r and θ. However, since only the cos θ term appears in Eq. (14*b*), T_1 is symmetric to the centerline, which is connected to the innermost and outermost points. It can also be observed from Ebadian (1993) that T_1 has a positive value in the semicircle near the outer wall and a negative value near the inner wall. Equation (14*c*) indicates that T_2 has three parts. The first two parts, T_{20} and T_{c2}, are symmetric to the centerline between the inner and outer walls, while the third part, T_{s1}, is not. The series of Eqs. (14*a*), (14*b*), (14*c*) also indicate that the torsion effect appears only in the T_2 solution and links to the asymmetric terms of T_{s1} sin θ. If specifying λ equal to zero, Eq. (14) will reduce to a symmetric solution, which corresponds to the solution of the toroidal pipe. By combining T_0, T_1, and T_2, one can obtain the typical temperature distribution in a helicoidal pipe. It can be further observed from Ebadian (1993) that the high-temperature contours are not only pushed toward the outer wall, but also twisted.

The Nusselt Number

The peripheral Nusselt number is defined as:

$$\mathrm{Nu} = \frac{2}{T_b}\left(\frac{\partial T}{\partial r}\right)_{r=1}. \tag{15}$$

Substituting T into Eq. (15), one can obtain:

$$\mathrm{Nu} = \frac{2}{T_b}\left\{\frac{\Pr}{8\ \mathrm{Re}} + \epsilon\left(-\frac{29\ \Pr^2\ \mathrm{Re}}{552960} - \frac{11\ \Pr\ \mathrm{Re}}{276480} + \frac{7\ \Pr}{96\ \mathrm{Re}}\right)\cos\theta + \epsilon^2\left[-\frac{1541\ \Pr\ \mathrm{Re}^3}{33443020800} - \frac{29\ \Pr^2\ \mathrm{Re}}{1105920} - \frac{11\ \Pr\ \mathrm{Re}}{138240} + \frac{\Pr}{384\ \mathrm{Re}} + \left(-\frac{281\ \Pr^3\ \mathrm{Re}^3}{133772083200} + \frac{319\ \Pr^2\ \mathrm{Re}^3}{13934592000} + \frac{1261\ \Pr\ \mathrm{Re}^3}{133772083200} - \frac{1577\ \Pr^2\ \mathrm{Re}}{77414400} - \frac{1207\ \Pr\ \mathrm{Re}}{58060800} + \frac{7\ \Pr}{256\ \mathrm{Re}}\right)\cos 2\theta + \left(\frac{437\ \Pr^3\ \mathrm{Re}^2}{371589120} + \frac{79\ \Pr^2\ \mathrm{Re}^2}{61931520} + \frac{17\ \Pr\ \mathrm{Re}^2}{7741440} - \frac{\Pr^2}{3072} + \frac{17\ \Pr}{7680}\right)\lambda \sin\theta\right]\right\}. \tag{16}$$

Equation (16) indicates that the torsion contribution on the peripheral Nusselt number is through the sin θ terms only. Figure 2 shows that the peripheral Nusselt number changes with torsion, λ. In this figure, 0 deg and 360 deg represent the innermost point of the wall, while 180 deg indicates the outermost point of the wall. The curve of $\lambda = 0$ indicates the peripheral Nusselt number distributions in a toroidal pipe. In Fig. 2(*a*), parameters of Re = 15, Pr = 10, and $\epsilon = 0.1$ have been applied. The figure indicates that the Nusselt number is lower in the inner wall region and higher in the outer wall region. When $\lambda = 0$, Nu is symmetric to the curvature centerline. As λ increases, the peak and the valley of the curve move to one side and Nu is no longer symmetric to the centerline. Increasing λ not only causes the peak Nusselt number to deviate from the centerline, but it also slightly increases the peak values. In Fig. 2(*b*), the Prandtl number and ϵ retain the same values as those in Fig. 2(*a*); only the Reynolds number is reduced from 15 to 10. However, this figure shows a totally different Nusselt number distribution from that in Fig. 2(*a*). That is, the peripheral Nusselt number has a lower value in the outer wall region and a higher value in the inner wall region.

The Nusselt number behavior changes in Fig. 2 can be explained by analyzing Eq. (16). Equation (16) can be divided

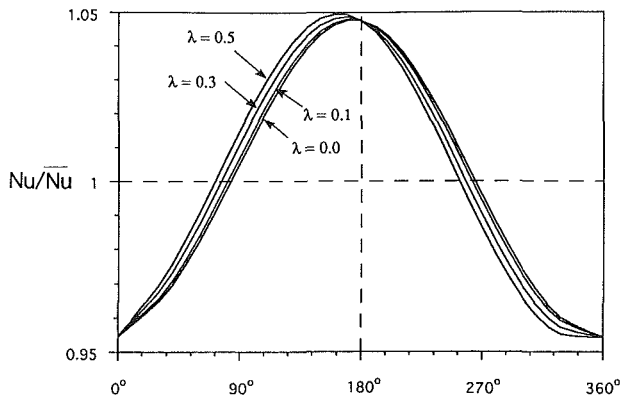

a) Re=15, Pr = 10, ε = 0.1

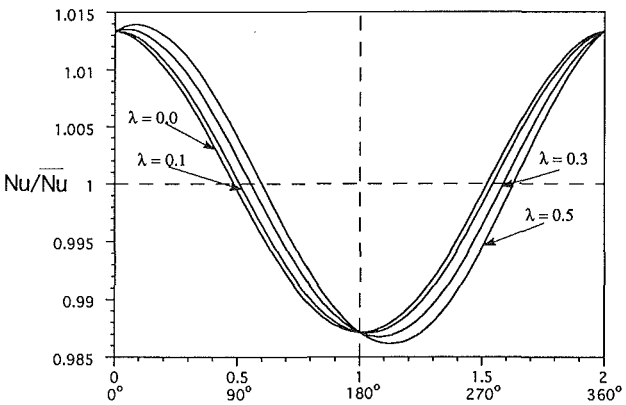

b) Re=10, Pr = 10, ε = 0.1

Fig. 2 Effect of torsion on the peripheral Nusselt number

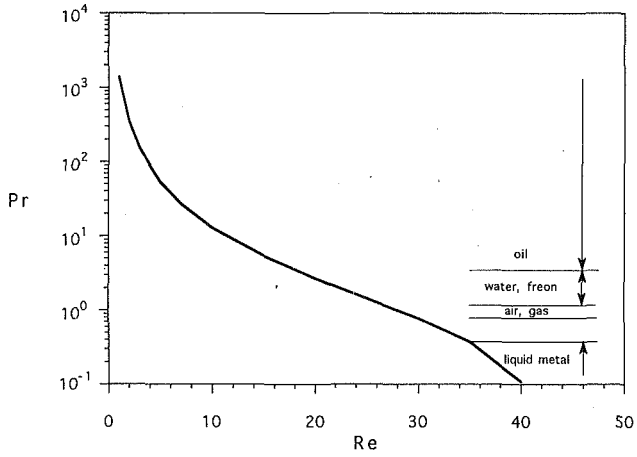

Fig. 3 The Prandt number versus the Reynolds number

into three parts: the terms not related to ϵ, the terms related to ϵ, and the terms related to ϵ^2, which reflect the contributions of T_0, T_1, and T_2, respectively. The contribution of T_0 to the Nusselt number is to provide a uniform Nusselt number along the periphery. Since the second part of Eq. (16) is one order of magnitude larger than the third part, the wave shape of the periphery is mainly determined by the T_1 contribution through $\cos\theta$. By rearranging the coefficient of $\cos\theta$ and setting it equal to zero, one gets:

$$\mathrm{Pr}=\frac{5760}{29\ \mathrm{Re}^2}\left(-\frac{11}{2880}\mathrm{Re}^2+7\right), \tag{17}$$

which is plotted as Fig. 3. In Fig. 3, in the region above the curve, the highest Nusselt number will appear in the outer wall region, while beneath this curve, the highest Nusselt number will appear in the inner wall region. It is easy to verify the behavior of the peripheral Nusselt distributions in Figs. 2(*a*) and 2(*b*), since they belong to different regions in Fig. 3. Figure 3 also indicates that the phenomenon in Fig. 2(*b*) can only occur in the case of a small Reynolds number. Physically, this phenomenon reflects that the thermal conduction surpassing thermal convection becomes the dominant heat transfer mechanism. As a result, a high temperature gradient is established near the inner wall region.

By integrating Eq. (16) along the periphery of the pipe, one can obtain the average Nusselt number $\overline{\mathrm{Nu}}$ for fully developed flow in a helicoidal pipe:

$$\overline{\mathrm{Nu}}=\frac{1}{2\pi}\int_0^{2\pi}\frac{2}{T_b}\left[\frac{\partial T}{\partial r}\right]_{r=1}d\theta=\frac{2}{T_b}\left[\frac{\mathrm{Pr}}{8\ \mathrm{Re}}+\epsilon^2\left(-\frac{1541\mathrm{PrRe}^3}{33443020800}-\frac{29\mathrm{Pr}^2\mathrm{Re}}{1105920}-\frac{11\mathrm{PrRe}}{138240}+\frac{\mathrm{Pr}}{384\ \mathrm{Re}}\right)\right]. \tag{18}$$

Equation (18) indicates that the average Nusselt number change due to curvature is contributed mainly by the T_{20} terms. The contributions of other terms (T_1, T_{s1}, and T_{c2}) on the Nu are through the bulk temperature, T_b. This is easily understood since the terms, T_1, T_{s1}, and T_{c2}, are trigonometric functions, and integration along the periphery will be zero. Table 1 shows a comparison between the present study and some previous studies on the Nusselt number. The analytical solution of Özişik and Topakoglu (1968) is based on:

$$\overline{\mathrm{Nu}}=\frac{48}{11\left[1-\left(\frac{\mathrm{De}^2\mathrm{Pr}}{1303}\right)^2\right]}. \tag{19a}$$

It can be seen that Eq. (19*a*) is only valid in a small De^2 Pr region. For example, in the case of Re = 50, ϵ = 0.01 and Pr = 5.0, the Nusselt number jumps to 54.753, since De^2 Pr/1303 is closer to 1. The correlation equation suggested by Manlapaz and Churchill (1981) is:

Table 1 Comparison of friction coefficient and Nusselt number

Re	ϵ	Nu								
		Pr = 0.7			Pr = 5			Pr = 50		
		Eq. (18)	Eq. (19a)	Eq. (19b)	Eq. (18)	Eq. (19a)	Eq. (19b)	Eq. (18)	Eq. (19a)	Eq. (19b)
10	0.05	4.364	4.364	4.388	4.364	4.364	4.442	4.372	4.573	4.267
50	0.01	4.364	4.364	4.446	4.364	4.404	4.640	5.090	6.489	5.580
30	0.05	4.365	4.366	4.491	4.369	4.498	4.817	4.933	6.438	6.154
30	0.08	4.368	4.370	4.545	4.377	4.724	5.045	6.212	7.121	6.655

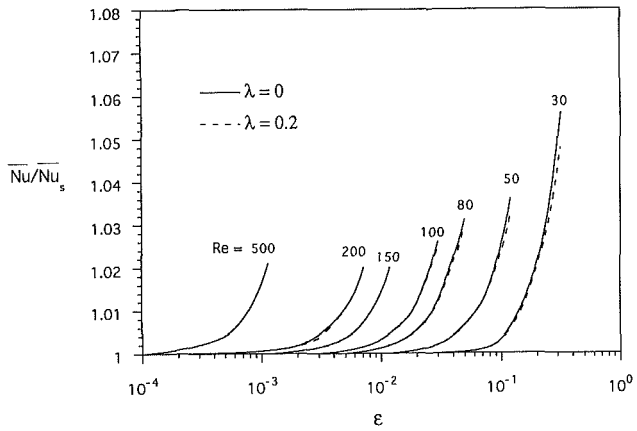

Fig. 4 Effect of curvature on the Nusselt number ratio

$$\overline{\mathrm{Nu}}=\left[\left(\frac{48}{11}+\frac{51/11}{\left(1+\frac{1342}{\mathrm{De}^2\ \mathrm{Pr}}\right)^2}\right)^3+1.816\left(\frac{\mathrm{De}}{1+\frac{1.15}{\mathrm{Pr}}}\right)^{2/3}\right]^{1/3}. \tag{19b}$$

Janssen and Hoogendoorn (1978) have correlated their test results for the toroidal pipe. The curvature ratio was changed from 0.01 to 0.083. An aqueous solution of glycerol and other oils (Pr from 27 to 440) have been used in their experimental study. For De < 20, they express the correlation equation as:

$$\overline{\mathrm{Nu}}=1.7\ \epsilon^{1/3}\ \mathrm{Re}^{2/3}\ \mathrm{Pr}^{1/6}\quad 27<\mathrm{Pr}<440. \tag{19c}$$

Table 1 indicates in the case of small Pr number (Pr = 0.7 and 5.0) the present solution is closer to the prediction by Eq. (19*a*), and in the case of Pr = 50 the present solution is closer to the prediction by Eq. (19*c*). Our prediction is always lower than the prediction by Eq. (19*b*) in all cases.

Figure 4 shows the $\overline{\mathrm{Nu}}/\overline{\mathrm{Nu}}_s$ changes with the curvature and torsion at different Reynolds number, where $\overline{\mathrm{Nu}}_s$ is the Nusselt number in a straight pipe. Pr = 5 and $\overline{\mathrm{Nu}}_s$ = 4.3636 have been used in the calculation. Figure 4 indicates that the Nusselt number increases as the curvature increases in each Reynolds number. However, torsion can only slightly reduce the Nusselt number in cases of a small Reynolds number. In the case of Re = 50, for example, the Nusselt number can be reduced by around 1 percent. When Re > 150, the torsion effect is difficult to observe.

Acknowledgments

The results presented in this paper were obtained in the course of research sponsored by the National Science Foundation (NSF).

References

Berger, S. A., Talbot, L., and Yao, L. S., 1983, "Flow in Curved Pipes," *Ann. Rev. Fluid Mech.*, Vol. 15, pp. 461–512.

Ebadian, M. A., 1993, "A Theoretical and Experimental Investigation of Viscous Flow and Convective Heat Transfer in a Helicoidal Pipe Heat Exchanger," Second Year Annual Progress Report, National Science Foundation Project, CTS-9017732, May.

Futagami, K., and Aoyama, Y., 1988, "Laminar Heat Transfer in a Helically Coiled Tube," *Int. J. Heat Mass Transfer*, Vol. 31, No. 2, pp. 387–396.

Germano, M., 1989, "The Dean Equations Extended to a Helical Pipe Flow," *J. Fluid Mech.*, Vol. 203, pp. 289–356.

Janssen, L. A. M., and Hoogendoorn, C. J., 1978, "Laminar Convective Heat Transfer in Helically Coiled Tubes," *Int. J. Heat Mass Transfer*, Vol. 21, p. 1197.

Kao, H. C., 1987, "Torsion Effect on Fully Developed Flow in a Helical Pipe," *J. Fluid Mech.*, Vol. 184, pp. 335–356.

Manalapaz, R., and Churchill, S. W., 1981, "Fully Developed Laminar Convection From a Helical Coil," *Chem. Eng. Commun.*, Vol. 9, pp. 185–200.

Özişik, M. N., and Topakoglu, H. C., 1968, "Heat Transfer for Laminar Flow in a Curved Pipe," ASME JOURNAL OF HEAT TRANSFER, Vol. 90, pp. 313–318.

Shah, R. K., and Joshi, S. D., 1987, "Convective Heat Transfer in Curved Ducts," in: *Handbook of Single-Phase Convective Heat Transfer*, Kakac et al., eds., Wiley Interscience, New York.

Tuttle, E. R., 1990, "Laminar Flow in Twisted Pipes," *J. Fluid Mech.*, Vol. 219, pp. 565–570.

Wang, C. Y., 1981, "On the Low-Reynolds-Number Flow in a Helical Pipe," *J. Fluid Mech.*, Vol. 108, pp. 185–194.

Transient Response of Crossflow Heat Exchangers With Zero Core Thermal Capacitance

F. E. Romie[1]

Steady-state behavior has been established for many years for the three basic single-pass heat exchanger configurations; counterflow, parallel flow, and crossflow with neither fluid mixed. However, only relatively recently have analyses been published on the transient response of these exchangers to variations of fluid inlet temperatures. Such transient responses have importance for system control purposes and have interest to the designer with respect to thermal stress analysis. The purpose of this note is to give the transient response of crossflow exchangers for which the thermal capacitance of the core is negligible compared to the thermal capacitances of the fluids contained in the exchanger.

An analytic solution for crossflow exchangers has been given by Spiga and Spiga (1988, 1992) for the more general case for which the ratios, V_a and V_b, of the thermal capacitances of the contained fluids to the core thermal capacitance are finite. For this note these ratios are infinite and the solution given can be regarded as a limiting case of the Spiga and Spiga solution. The advantage of the limiting case, under conditions appropriate to its use, is the simplicity of the solution and ease of numerical evaluation. Conditions appropriate to its use are examined in a following section.

The times, t_a and t_b, for fluid particles to flow through the exchanger assume special importance when the core capacitance is zero. These times, equivalently, are the times required for the resident fluids to be replaced by the incoming fluids and can be regarded as the times for information to be transmitted from one end of the exchanger to the other. For parallel flow and crossflow exchangers, the time for the exchanger to attain a new steady-state condition following a step change of either or both fluid inlet temperatures is expressible in terms of t_a and t_b when the core capacitance is zero. For parallel flow exchangers this time is the larger of t_a and t_b, as has been shown by Li (1986). For crossflow exchangers, as will be shown, this time is $t_a + t_b$. In this note t' denotes time and the dimensionless time variable, t, is chosen to be $t'/(t_a + t_b)$, which will vary from zero to unity at completion of the transient.

Differential Equations

The exchanger analyzed is defined by the following idealizations: (1) The fluid capacitance rates, $(wc)_a$ and $(wc)_b$, and the overall conductance, UA, for transfer of heat between the two fluids are uniform and constant. Any resistance to heat flow through the walls separating the fluids and any fouling resistances are included in UA. (2) No heat is conducted in the direction of fluid flow. (3) The fluids are unmixed in the exchanger. (4) The exchanger shell or casing is insulated from the fluids and does not influence their temperatures. (5) All fluid particles flow with velocities u_a or u_b; slug flow is used in the transient analysis. (6) The core thermal capacitance is negligible compared to the thermal capacitances of the contained fluids and is treated as zero.

The distance from the fluid a entrance plane is x' and the flow length is L_a; similarly, the distance from the fluid b entrance plane is y' and the flow length is L_b. The mean flow velocities are u_a and u_b and the transit times are $t_a = L_a/u_a$ and $t_b = L_b/u_b$. One can now define three variables, $x = x'/L_a$, $y = y'/L_b$, $t = t'/(t_a + t_b)$ and three parameters, $N = UA/(wc)_a$, $C = (wc)_a/(wc)_b$ and $P = t_a/(t_a + t_b)$. Energy balances using the preceding idealizations and definitions give two equations:

$$N(T_b - T_a) = P\frac{\partial T_a}{\partial t} + \frac{\partial T_a}{\partial x} \tag{1}$$

$$M(T_a - T_b) = Q\frac{\partial T_b}{\partial t} + \frac{\partial T_b}{\partial y} \tag{2}$$

To simplify notation, $M \equiv CN$ and $Q \equiv 1 - P$.

The fluid temperatures, $T_a(x, y, t)$ and $T_b(x, y, t)$ will be found with the following conditions: Initial temperatures are zero, $T_a(x, y, 0) = T_b(x, y, 0) = 0$, the uniform inlet temperature of fluid b is zero, $T_b(x, 0, t) = 0$ and the uniform inlet temperature of fluid a is a unit step function, $T_a(0, y, t) = U(t)$.

Defining the ratio $R = (hA)_b/(hA)_a$ of the conductances for transfer of heat between the fluids and wall permits computing the local wall temperature. (These conductances include any fouling resistances on the surfaces.)

$$T_w(x, y, t) = [T_a(x, y, t) + RT_b(x, y, t)]/(1 + R) \tag{3}$$

If the thermal resistance of the wall is not zero then T_w is the wall temperature at a fractional distance $R/(1 + R)$ through the wall from the fluid a surface. The local wall temperature, being simply a weighted average of the local fluid temperatures, will not be considered further.

Functions Used

The Anzelius (1926)–Schumann (1929) functions, $F_o(u, v)$

[1]Palos Verdes Estates, CA 90274.

Contributed by the Heat Transfer Division of THE AMERICAN SOCIETY OF MECHANICAL ENGINEERS. Manuscript received by the Heat Transfer Division September 1993; revision received December 1993. Keywords: Heat Exchangers, Nonequilibrium Flows, Transient and Unsteady Heat Transfer. Associate Technical Editor: W. A. Fiveland.

Acknowledgments

The results presented in this paper were obtained in the course of research sponsored by the National Science Foundation (NSF).

References

Berger, S. A., Talbot, L., and Yao, L. S., 1983, "Flow in Curved Pipes," *Ann. Rev. Fluid Mech.*, Vol. 15, pp. 461–512.

Ebadian, M. A., 1993, "A Theoretical and Experimental Investigation of Viscous Flow and Convective Heat Transfer in a Helicoidal Pipe Heat Exchanger," Second Year Annual Progress Report, National Science Foundation Project, CTS-9017732, May.

Futagami, K., and Aoyama, Y., 1988, "Laminar Heat Transfer in a Helically Coiled Tube," *Int. J. Heat Mass Transfer*, Vol. 31, No. 2, pp. 387–396.

Germano, M., 1989, "The Dean Equations Extended to a Helical Pipe Flow," *J. Fluid Mech.*, Vol. 203, pp. 289–356.

Janssen, L. A. M., and Hoogendoorn, C. J., 1978, "Laminar Convective Heat Transfer in Helically Coiled Tubes," *Int. J. Heat Mass Transfer*, Vol. 21, p. 1197.

Kao, H. C., 1987, "Torsion Effect on Fully Developed Flow in a Helical Pipe," *J. Fluid Mech.*, Vol. 184, pp. 335–356.

Manalapaz, R., and Churchill, S. W., 1981, "Fully Developed Laminar Convection From a Helical Coil," *Chem. Eng. Commun.*, Vol. 9, pp. 185–200.

Özişik, M. N., and Topakoglu, H. C., 1968, "Heat Transfer for Laminar Flow in a Curved Pipe," ASME JOURNAL OF HEAT TRANSFER, Vol. 90, pp. 313–318.

Shah, R. K., and Joshi, S. D., 1987, "Convective Heat Transfer in Curved Ducts," in: *Handbook of Single-Phase Convective Heat Transfer*, Kakac et al., eds., Wiley Interscience, New York.

Tuttle, E. R., 1990, "Laminar Flow in Twisted Pipes," *J. Fluid Mech.*, Vol. 219, pp. 565–570.

Wang, C. Y., 1981, "On the Low-Reynolds-Number Flow in a Helical Pipe," *J. Fluid Mech.*, Vol. 108, pp. 185–194.

Transient Response of Crossflow Heat Exchangers With Zero Core Thermal Capacitance

F. E. Romie[1]

Steady-state behavior has been established for many years for the three basic single-pass heat exchanger configurations; counterflow, parallel flow, and crossflow with neither fluid mixed. However, only relatively recently have analyses been published on the transient response of these exchangers to variations of fluid inlet temperatures. Such transient responses have importance for system control purposes and have interest to the designer with respect to thermal stress analysis. The purpose of this note is to give the transient response of crossflow exchangers for which the thermal capacitance of the core is negligible compared to the thermal capacitances of the fluids contained in the exchanger.

An analytic solution for crossflow exchangers has been given by Spiga and Spiga (1988, 1992) for the more general case for which the ratios, V_a and V_b, of the thermal capacitances of the contained fluids to the core thermal capacitance are finite. For this note these ratios are infinite and the solution given can be regarded as a limiting case of the Spiga and Spiga solution. The advantage of the limiting case, under conditions appropriate to its use, is the simplicity of the solution and ease of numerical evaluation. Conditions appropriate to its use are examined in a following section.

The times, t_a and t_b, for fluid particles to flow through the exchanger assume special importance when the core capacitance is zero. These times, equivalently, are the times required for the resident fluids to be replaced by the incoming fluids and can be regarded as the times for information to be transmitted from one end of the exchanger to the other. For parallel flow and crossflow exchangers, the time for the exchanger to attain a new steady-state condition following a step change of either or both fluid inlet temperatures is expressible in terms of t_a and t_b when the core capacitance is zero. For parallel flow exchangers this time is the larger of t_a and t_b, as has been shown by Li (1986). For crossflow exchangers, as will be shown, this time is $t_a + t_b$. In this note t' denotes time and the dimensionless time variable, t, is chosen to be $t'/(t_a + t_b)$, which will vary from zero to unity at completion of the transient.

Differential Equations

The exchanger analyzed is defined by the following idealizations: (1) The fluid capacitance rates, $(wc)_a$ and $(wc)_b$, and the overall conductance, UA, for transfer of heat between the two fluids are uniform and constant. Any resistance to heat flow through the walls separating the fluids and any fouling resistances are included in UA. (2) No heat is conducted in the direction of fluid flow. (3) The fluids are unmixed in the exchanger. (4) The exchanger shell or casing is insulated from the fluids and does not influence their temperatures. (5) All fluid particles flow with velocities u_a or u_b; slug flow is used in the transient analysis. (6) The core thermal capacitance is negligible compared to the thermal capacitances of the contained fluids and is treated as zero.

The distance from the fluid a entrance plane is x' and the flow length is L_a; similarly, the distance from the fluid b entrance plane is y' and the flow length is L_b. The mean flow velocities are u_a and u_b and the transit times are $t_a = L_a/u_a$ and $t_b = L_b/u_b$. One can now define three variables, $x = x'/L_a$, $y = y'/L_b$, $t = t'/(t_a + t_b)$ and three parameters, $N = UA/(wc)_a$, $C = (wc)_a/(wc)_b$ and $P = t_a/(t_a + t_b)$. Energy balances using the preceding idealizations and definitions give two equations:

$$N(T_b - T_a) = P\frac{\partial T_a}{\partial t} + \frac{\partial T_a}{\partial x} \tag{1}$$

$$M(T_a - T_b) = Q\frac{\partial T_b}{\partial t} + \frac{\partial T_b}{\partial y} \tag{2}$$

To simplify notation, $M \equiv CN$ and $Q \equiv 1 - P$.

The fluid temperatures, $T_a(x, y, t)$ and $T_b(x, y, t)$ will be found with the following conditions: Initial temperatures are zero, $T_a(x, y, 0) = T_b(x, y, 0) = 0$, the uniform inlet temperature of fluid b is zero, $T_b(x, 0, t) = 0$ and the uniform inlet temperature of fluid a is a unit step function, $T_a(0, y, t) = U(t)$.

Defining the ratio $R = (hA)_b/(hA)_a$ of the conductances for transfer of heat between the fluids and wall permits computing the local wall temperature. (These conductances include any fouling resistances on the surfaces.)

$$T_w(x, y, t) = [T_a(x, y, t) + RT_b(x, y, t)]/(1 + R) \tag{3}$$

If the thermal resistance of the wall is not zero then T_w is the wall temperature at a fractional distance $R/(1 + R)$ through the wall from the fluid a surface. The local wall temperature, being simply a weighted average of the local fluid temperatures, will not be considered further.

Functions Used

The Anzelius (1926)–Schumann (1929) functions, $F_o(u, v)$

[1]Palos Verdes Estates, CA 90274.

Contributed by the Heat Transfer Division of THE AMERICAN SOCIETY OF MECHANICAL ENGINEERS. Manuscript received by the Heat Transfer Division September 1993; revision received December 1993. Keywords: Heat Exchangers, Nonequilibrium Flows, Transient and Unsteady Heat Transfer. Associate Technical Editor: W. A. Fiveland.

and $G_o(u, v)$ and their extensions, are used to express the solution to the preceding equations. Three basic functions are:

$$F_{-1}(u, v) = \frac{\partial F_o(u, v)}{\partial v} = \exp(-u-v)\,(u/v)^{1/2} I_1(2\sqrt{uv}) \quad (4)$$

$$G_{-1}(u, v) = \frac{\partial G_o(u, v)}{\partial v} = \exp(-u-v) I_o(2\sqrt{uv}) \quad (5)$$

$$G_o(u, v) = \int_0^v G_{-1}(u, v')dv' = \exp(-u-v) \sum_1^\infty \left(\frac{v}{u}\right)^{r/2} I_r(2\sqrt{uv}) \quad (6)$$

The I_r are modified Bessel functions of the first kind rth order and u and v are positive. Series expansions of these three functions are given by Romie (1987); this paper is also the source of two recurrence equations used to evaluate F_o and F_1 in terms of F_{-1}, G_{-1}, and G_o:

$$F_o(u, v) = G_o(u, v) + G_{-1}(u, v) \quad (7)$$

$$F_1(u, v) = \int_0^v F_o(u, v')dv' = (v-u)G_o(u, v) + v(F_{-1}(u, v) + G_{-1}(u, v)) \quad (8)$$

Two additional integrals used in the following derivation are:

$$\int_0^v F_{-1}(u, v')dv' = F_o(u, v) - e^{-u} \quad (9)$$

$$\int_0^u G_o(u', v)du' = v - F_1(u, v) \quad (10)$$

Solution of Equations

The threefold Laplace transforms $T_a(p, q, s)$ $(=\tilde{T}_a)$ and $T_b(p, q, s)$ $(=\tilde{T}_b)$ of $T_a(x, y, t)$ and $T_b(x, y, t)$ are found using $x \to p$, $y \to q$, and $t \to s$. Equations (1) and (2) then give

$$N(\tilde{T}_b - \tilde{T}_a) = Ps\tilde{T}_a + p\tilde{T}_a - 1/(qs) \quad (11)$$

$$M(\tilde{T}_a - \tilde{T}_b) = Qs\tilde{T}_b + q\tilde{T}_b \quad (12)$$

These two equations are solved for $T_a(p, q, s)$ and $T_b(p, q, s)$ and the solutions are put in a form to facilitate inversion with respect to p:

$$T_a(p, q, s) = \frac{1}{sq}\left[p + Ps + \frac{N(q+Qs)}{q+M+Qs}\right]^{-1} \quad (13)$$

$$T_b(p, q, s) = \frac{M}{sq}[q+M+Qs]^{-1} \times \left[p + Ps + \frac{N(q+Qs)}{(q+M+Qs)}\right]^{-1} \quad (14)$$

Inversion with respect to $p \to x$ gives

$$T_a(x, q, s) = \frac{1}{sq} e^{-xPs} \exp\left[\frac{-xN(q+Qs)}{q+M+Qs}\right] \quad (15)$$

$$T_b(x, q, s) = \frac{Me^{-xPs}}{sq(q+M+Qs)} \exp\left[\frac{-xN(q+Qs)}{q+M+Qs}\right] \quad (16)$$

Inversion of these two equations with respect to $q \to y$ uses two Laplace transform pairs (Romie, 1987):

$$\mathcal{L}^{-1}\left[\exp\left(-\frac{uq}{q+1}\right) - e^{-u}\right] = F_{-1}(u, v) \quad (17)$$

$$\mathcal{L}^{-1}\frac{\exp\left(\frac{-uq}{q+1}\right)}{q+1} = G_{-1}(u, v) \quad (18)$$

Using these transform pairs and general properties of the Laplace transform gives

$$T_a(x, y, s) = \frac{1}{s} e^{-xPs}\left[e^{-xN} + \int_0^y Me^{-y'Qs} F_{-1}(xN, y'M)dy'\right] \quad (19)$$

$$T_b(x, y, s) = \frac{1}{s} e^{-xPs} \int_0^y Me^{-y'Qs} G_{-1}(xN, y'M)dy' \quad (20)$$

Inversion of these two equations with respect to $s \to t$ and using Eqs. (6) and (9) for the integrations gives the sought responses:

$$T_a^1(x, y, t) = U(t-xP)F_o(xN, y^*M) \quad (21)$$

$$T_b^1(x, y, t) = U(t-xP)G_o(xN, y^*M) \quad (22)$$

Here $y^* = \min(y, (t - xP)/Q)$ and the superscript 1 has been added to emphasize that these are responses to a unit step change of the fluid a entrance temperature.

For many purposes the area-mean exit temperatures, $\overline{T}_a(t)$ and $\overline{T}_b(t)$, are of special interest:

$$\overline{T}_a(t) = \int_0^1 T_a(1, y, t)dy \quad (23)$$

$$\overline{T}_b(t) = \int_0^1 T_b(x, 1, t)dx \quad (24)$$

Thus, for the unit step excitation,

$$\overline{T}_a^1(t) = U(t-P)\int_0^1 F_o(N, y^*M)dy \quad (25)$$

with $y^* = \min(y, (t - P)/Q)$, $(x = 1)$ and

$$\overline{T}_b^1(t) = \int_0^{x^*} G_o(xN, y^*M)dx \quad (26)$$

with $x^* = \min(1, t/P)$ and $y^* = \min(1, (t - Px)/Q)$, $(y = 1)$.

When $t = 1$ or greater these equations can be integrated using Eqs. (8) and (10) to give the steady-state area-mean exit temperatures.

$$\overline{T}_a^1(1) = F_1(N, M)/M \quad (27)$$

$$\overline{T}_b^1(1) = [M - F_1(N, M)]/N \quad (28)$$

Also Eqs. (21) and (22) give $T_a^1(x, y, 1) = F_o(xN, yM)$ and $T_b^1(x, y, 1) = G_o(xN, yM)$. These four steady-state solutions are attained irrespective of the values of V_a and V_b. However, if V_a and V_b are not infinite, then steady-state conditions are attained when $t' > t_a + t_b$.

When the inlet temperature of fluid a is an arbitrary function of time, $T_a(0, y, t) = \phi(t)$, the temperatures can be calculated using the usual methods of linear analysis:

$$T_\alpha(x, y, t) = \int_0^t G(t-t')T_\alpha^1(x, y, t')dt' \quad (29)$$

$$\overline{T}_\alpha(t) = \int_0^t G(t-t')\overline{T}_\alpha^1(t')dt' \quad (30)$$

Here $\alpha = a$ or b and $G(t) = d\phi/dt$.

Results and Discussion

Figure 1 shows the area-mean exit temperatures for $N = 2$, $C = 0.75$ and $P = 1/3$, $1/2$, and $2/3$. The fluid b temperature response is seen to be effectively independent of P. The fluid

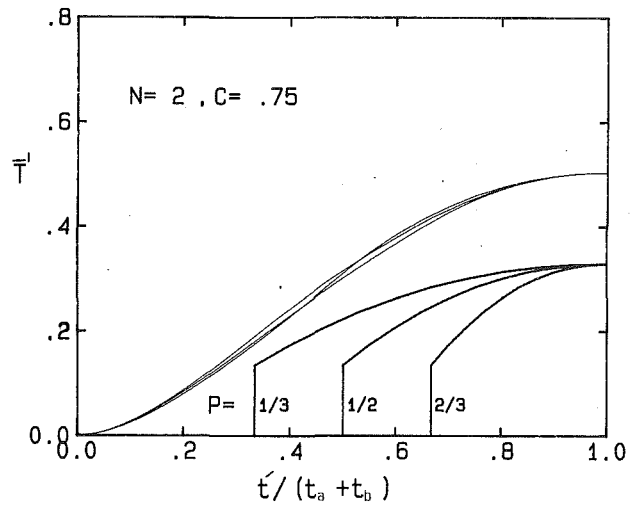

Fig. 1 Area-mean exit temperatures for fluid *a* and fluid *b* (narrow lines)

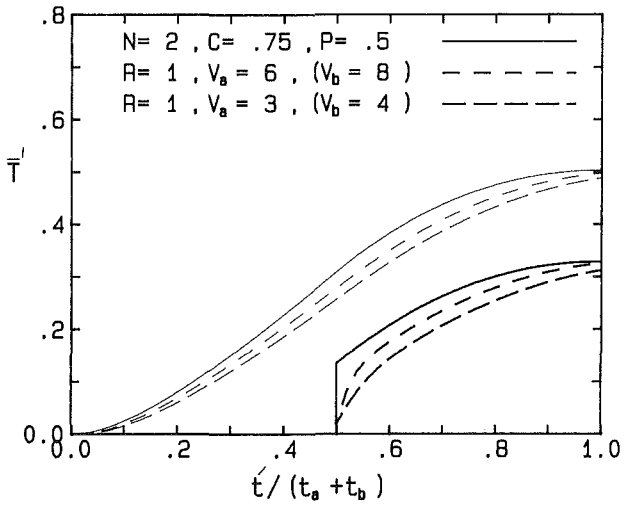

Fig. 2 Area-mean exit temperatures for fluid *a* and fluid *b* (narrow lines). Continuous lines are for zero core capacitance, broken lines for finite core capacitance.

a response exhibits a step when $t = P$ and thus $t' = t_a$. The first cross-sectional fluid *a* lamina that enters at time zero with a temperature of unity sees fluid *b* at zero temperature. (The wall is "transparent" when its thermal capacitance is zero.) This lamina therefore has a temperature of $\exp(-Nx)$. When it reaches its exit plane ($x = 1$) at time t_a its temperature is $\exp(-N)$, which is the magnitude of the jumps seen in Fig. 1.

In order to compare solutions with zero core capacitance with solutions with finite core capacitance, two additional parameters, R and V_a, must be specified. If the values of C and P are specified, then, using parameter definitions, $V_b = V_a(1/P - 1)/C$. Figure 2 gives a comparison of the Spiga and Spiga solution with the solution of this note. The comparison uses $V_a = 6$ and 3 with $N = 2$, $C = 0.75$, $R = 1$, and $P = 0.5$. It can be observed that at $t = 1$ ($t' = t_a + t_b$) the transient is effectively completed with $V_a = 6$ and almost completed with $V_a = 3$. With finite core capacitance, the first fluid *a* cross-sectional lamina sees the wall at zero temperature during its transit of the exchanger and its temperature is therefore $\exp(-N_a x)$ in which $N_a = N(1 + R)/R$. The jump at $t' = t_a$ is $\exp(-N_a)$, which, for Fig. 2, is 0.018.

The solution with zero core capacitance is much easier and faster to compute than the Spiga and Spiga solution. It is therefore of interest to estimate the upper range of V_a or V_b that is reasonable for an exchanger. Suppose that fluid *a* flows inside tubes. Then for thin wall tubes $V_a \simeq Dv/(4\Delta)$ in which D and Δ are the tube diameter and wall thickness and v is the ratio of the volummetric heat capacities of the fluid and tube materials. This ratio has the exceptionally large value of 1.7 for water and aluminum. Using this material combination gives $V_a \simeq 0.4D/\Delta$. Thus an aluminum tube with 25 mm diameter and 1 mm wall thickness gives $V_a = 10$. The parameters V_a and V_b can, of course, vary over a wide range, but this illustration indicates that the simplicity of the zero core capacitance solution can sometimes be enjoyed with acceptable accuracy.

References

Anzelius, A., 1926, "Über Erwärmung Vermittles Durchströmender Medien," *Zeitschrift für Angewandte Mathematik und Mechanik*, Vol. 6, pp. 291–294.

Li, Chung-Hsiung, 1986, "Exact Transient Solutions of Parallel-Current Transfer Processes," ASME JOURNAL OF HEAT TRANSFER, Vol. 108, pp. 365–369.

Romie, F. E., 1987, "Two Functions Used in the Analysis of Crossflow Exchangers, Regenerators and Related Equipment," ASME JOURNAL OF HEAT TRANSFER, Vol. 109, pp. 518–521.

Schumann, T. E. W., 1929, "Heat Transfer: A Liquid Flowing Through a Porous Prism," *Franklin Institute Journal*, Vol. 208, pp. 405–416.

Spiga, M., and Spiga, G., 1988, "Transient Temperature Fields in Crossflow Heat Exchangers With Finite Wall Capacitance," ASME JOURNAL OF HEAT TRANSFER, Vol. 110, pp. 49–53.

Spiga, M., and Spiga, G., 1992, "Step Response of the Crossflow Heat Exchanger With Finite Wall Capacitance," *International Journal of Heat and Mass Transfer*, Vol. 35, pp. 559–565.

Transport Correlations for Laminar Aiding Mixed Convection Over a Vertical Isothermal Surface

K. S. Manning[1] and Z. H. Qureshi[2]

Nomenclature

- $f''(0)$ = dimensionless shear stress parameter for natural convection
- $F(\mathrm{Pr})$ = Prandtl-number-dependent function in heat transfer correlations
- g = acceleration due to gravity, m/s^2
- Gr = Grashof number $= g\beta x^3(T_o - T_\infty)/\nu^2$
- h = local heat transfer coefficient, W/m^2-K
- $\bar{h}$ = surface-averaged heat transfer coefficient, W/m^2-K
- k = fluid thermal conductivity, W/m-K
- n = exponent in the mixed convection correlations
- Nu = Nusselt number $= hx/k$
- $\overline{\mathrm{Nu}}$ = Nusselt number based on average heat transfer coefficient $= \bar{h}x/k$
- Pr = Prandtl number $= \nu/\alpha$
- Re = Reynolds number $= u_\infty x/\nu$
- T = temperature, K
- u = streamwise velocity component, m/s
- x = streamwise coordinate from the leading edge, m

[1] Department of Mechanical Engineering, Norwich University, Northfield, VT 05663; Mem. ASME.

[2] Westinghouse Savannah River Company, Aiken, SC 29808; Mem. ASME.

Contributed by the Heat Transfer Division of THE AMERICAN SOCIETY OF MECHANICAL ENGINEERS. Manuscript received by the Heat Transfer Division June 1993; revision received January 1994. Keywords: Mixed Convection. Associate Technical Editor: Y. Jaluria.

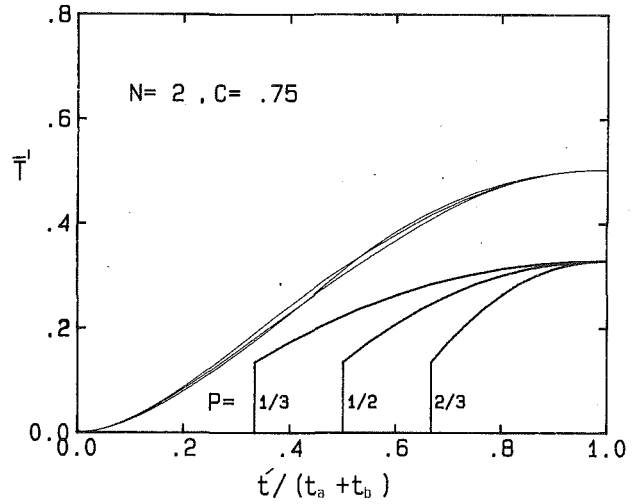

Fig. 1 Area-mean exit temperatures for fluid *a* and fluid *b* (narrow lines)

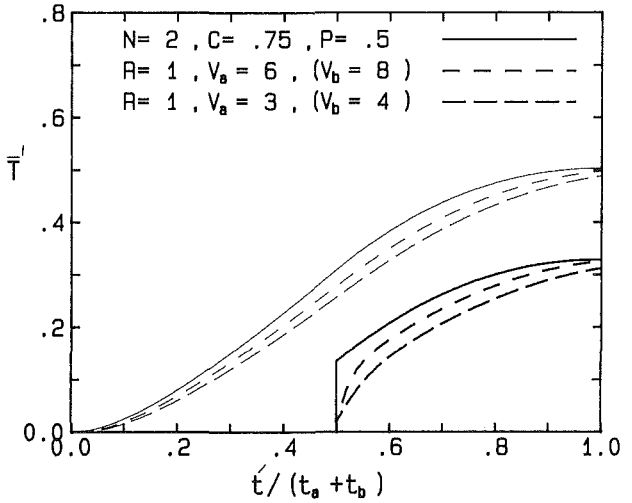

Fig. 2 Area-mean exit temperatures for fluid *a* and fluid *b* (narrow lines). Continuous lines are for zero core capacitance, broken lines for finite core capacitance.

a response exhibits a step when $t = P$ and thus $t' = t_a$. The first cross-sectional fluid *a* lamina that enters at time zero with a temperature of unity sees fluid *b* at zero temperature. (The wall is "transparent" when its thermal capacitance is zero.) This lamina therefore has a temperature of $\exp(-Nx)$. When it reaches its exit plane ($x = 1$) at time t_a its temperature is $\exp(-N)$, which is the magnitude of the jumps seen in Fig. 1.

In order to compare solutions with zero core capacitance with solutions with finite core capacitance, two additional parameters, R and V_a, must be specified. If the values of C and P are specified, then, using parameter definitions, $V_b = V_a(1/P - 1)/C$. Figure 2 gives a comparison of the Spiga and Spiga solution with the solution of this note. The comparison uses $V_a = 6$ and 3 with $N = 2$, $C = 0.75$, $R = 1$, and $P = 0.5$. It can be observed that at $t = 1$ ($t' = t_a + t_b$) the transient is effectively completed with $V_a = 6$ and almost completed with $V_a = 3$. With finite core capacitance, the first fluid *a* cross-sectional lamina sees the wall at zero temperature during its transit of the exchanger and its temperature is therefore $\exp(-N_a x)$ in which $N_a = N(1 + R)/R$. The jump at $t' = t_a$ is $\exp(-N_a)$, which, for Fig. 2, is 0.018.

The solution with zero core capacitance is much easier and faster to compute than the Spiga and Spiga solution. It is therefore of interest to estimate the upper range of V_a or V_b that is reasonable for an exchanger. Suppose that fluid *a* flows inside tubes. Then for thin wall tubes $V_a \simeq Dv/(4\Delta)$ in which D and Δ are the tube diameter and wall thickness and v is the ratio of the volummetric heat capacities of the fluid and tube materials. This ratio has the exceptionally large value of 1.7 for water and aluminum. Using this material combination gives $V_a \simeq 0.4D/\Delta$. Thus an aluminum tube with 25 mm diameter and 1 mm wall thickness gives $V_a = 10$. The parameters V_a and V_b can, of course, vary over a wide range, but this illustration indicates that the simplicity of the zero core capacitance solution can sometimes be enjoyed with acceptable accuracy.

References

Anzelius, A., 1926, "Über Erwärmung Vermittles Durchströmender Medien," *Zeitschrift für Angewandte Mathematik und Mechanik*, Vol. 6, pp. 291–294.

Li, Chung-Hsiung, 1986, "Exact Transient Solutions of Parallel-Current Transfer Processes," ASME JOURNAL OF HEAT TRANSFER, Vol. 108, pp. 365–369.

Romie, F. E., 1987, "Two Functions Used in the Analysis of Crossflow Exchangers, Regenerators and Related Equipment," ASME JOURNAL OF HEAT TRANSFER, Vol. 109, pp. 518–521.

Schumann, T. E. W., 1929, "Heat Transfer: A Liquid Flowing Through a Porous Prism," *Franklin Institute Journal*, Vol. 208, pp. 405–416.

Spiga, M., and Spiga, G., 1988, "Transient Temperature Fields in Crossflow Heat Exchangers With Finite Wall Capacitance," ASME JOURNAL OF HEAT TRANSFER, Vol. 110, pp. 49–53.

Spiga, M., and Spiga, G., 1992, "Step Response of the Crossflow Heat Exchanger With Finite Wall Capacitance," *International Journal of Heat and Mass Transfer*, Vol. 35, pp. 559–565.

Transport Correlations for Laminar Aiding Mixed Convection Over a Vertical Isothermal Surface

K. S. Manning[1] and Z. H. Qureshi[2]

Nomenclature

- $f''(0)$ = dimensionless shear stress parameter for natural convection
- $F(\mathrm{Pr})$ = Prandtl-number-dependent function in heat transfer correlations
- g = acceleration due to gravity, m/s^2
- Gr = Grashof number $= g\beta x^3(T_o - T_\infty)/\nu^2$
- h = local heat transfer coefficient, W/m^2-K
- $\bar{h}$ = surface-averaged heat transfer coefficient, W/m^2-K
- k = fluid thermal conductivity, W/m-K
- n = exponent in the mixed convection correlations
- Nu = Nusselt number $= hx/k$
- $\overline{\mathrm{Nu}}$ = Nusselt number based on average heat transfer coefficient $= \bar{h}x/k$
- Pr = Prandtl number $= \nu/\alpha$
- Re = Reynolds number $= u_\infty x/\nu$
- T = temperature, K
- u = streamwise velocity component, m/s
- x = streamwise coordinate from the leading edge, m

[1] Department of Mechanical Engineering, Norwich University, Northfield, VT 05663; Mem. ASME.

[2] Westinghouse Savannah River Company, Aiken, SC 29808; Mem. ASME.

Contributed by the Heat Transfer Division of THE AMERICAN SOCIETY OF MECHANICAL ENGINEERS. Manuscript received by the Heat Transfer Division June 1993; revision received January 1994. Keywords: Mixed Convection. Associate Technical Editor: Y. Jaluria.

y = coordinate normal to the surface, m
α = final thermal diffusivity, m^2/s
β = coefficient of thermal expansion, K^{-1}
μ = absolute viscosity, N-s/m^2
ν = kinematic viscosity, m^2/s
ξ = mixed convection parameter $= Gr/Re^2$
τ = local shear stress, N/m^2
$\bar{\tau}$ = surface-averaged shear stress, N/m^2

Subscripts

f = forced convection
m = mixed convection
n = natural convection
o = conditions at the surface
x = local value
∞ = free-stream fluid conditions

Introduction

This note focuses on the transport in aiding laminar mixed convection flow adjacent to a vertical isothermal surface. The direction of forced flow is taken to be upward for the heated surface. This situation causes the flow to be predominantly forced at the leading edge, primarily natural far downstream, and mixed in the middle. In the intermediate region of mixed convection Merkin (1969) reported a finite difference solution for $Pr = 1$. Acrivos (1966) outlined a method to analyze mixed convection based upon the limiting solutions for $Pr \to 0$ and $Pr \to \infty$. A local similarity method was employed by Lloyd and Sparrow (1970) to determine the buoyancy effects on a basic forced convection flow. This method facilitated results for relatively large values of Gr/Re^2 in the range $0.003 < Pr < 100$. However, the method was shown to be inapplicable for a free convection dominated mixed flow. An implicit difference scheme was employed by Oosthuizen and Hart (1973) to analyze the entire mixed convection regime over a vertical surface. Based upon these analyses Wilks (1976) proposed a heat transfer correlation. This correlation does not accurately predict the natural and forced convection limits. Raju et al. (1984) produced a numerical analysis of the entire mixed convection spectrum, culminating in a correlation that is very simple, but is, by their own admission, of limited (20 percent) accuracy.

Experimental investigations of mixed convection over a vertical surface in air are reported by Kliegel (1959), Oosthuizen and Bassey (1973), Gryzagoridis (1975), and Ramachandran et al. (1985).

Although an extensive effort is evidenced in the above-mentioned literature, various aspects of mixed convection from a vertical surface are either missing or not reported in an easy-to-use form. This note unifies available results and suggests correlations for local and average heat transfer rates, and for local and average shear stress over the entire spectrum of mixed convection, and for a wide range of Prandtl numbers. Additionally, the limits between natural, mixed, and forced convection are defined and mapped.

Development of the Transport Relations

Any transport correlation describing the entire mixed convection spectrum must accurately predict the forced convection regime as Gr/Re^2 approaches zero, and the natural convection regime as Gr/Re^2 approaches infinity. Furthermore, the asymptotic limits of very small and very large Prandtl number must also be approached. Before presenting the laminar transport equations a few comments on the extent of the mixed regime are in order. It has been shown by Carey and Gebhart (1983) that an aiding free stream has a stabilizing effect on the basic buoyancy-induced flow. Similarly, for a basic forced flow aiding buoyancy has been found to stabilize the flow (Mucoglu and Chen, 1978). Based upon these studies it is proposed here that, under aiding flow circumstances, the mixed flow remains laminar as long as $Re_x < 5 \times 10^5$ for forced convection, and $Gr_x Pr < 10^9$ for natural convection. These limits are well established as the limits of laminar flow.

Transport phenomena where the transport rates vary from one asymptotic behavior to another are frequently encountered in nature and in practice. Churchill and Usagi (1972) proposed a method for describing such phenomena. This method, which is used here, involves the asymptotic solutions and one additional parameter that describes the intermediate region. In the present study, this parameter is found to be Prandtl number dependent. In the following sections the heat transfer correlations will be established first, and then the shear stress correlations.

Heat Transfer Correlations. Transport correlations for pure forced or natural convection based upon similarity analyses have been substantiated with abundant experimental data.

In the forced convection limit, as $\xi \to 0$, the local heat transfer rate is given by:

$$Nu_f = \frac{h_f x}{k} = F_f \cdot Re_x^{1/2} \tag{1}$$

The Prandtl number dependent coefficient, F_f, exhibits the following asymptotic behavior (Schlichting, 1979):

$$F_f \to 0.564 Pr^{1/2} \text{ as } Pr \to 0 \tag{2}$$

and

$$F_f \to 0.339 Pr^{1/3} \text{ as } Pr \to \infty \tag{3}$$

For intermediate values of Prandtl number Schlichting (1979) has tabulated F_f. Following the method suggested by Churchill and Usagi (1972) F_f can be represented over the entire range of Prandtl number by:

$$F_f = 0.339\, Pr^{1/3} [0.100\, Pr^{-3/4} + 1]^{-2/9} \tag{4}$$

This correlation yields results very close to those tabulated by Schlichting (1979), or those calculated using the correlation of Churchill and Ozoe (1973). Disagreement with the same type of correlation presented by Chen et al. (1986) seems to be due to a misprint of the leading coefficient in that paper. Printed is 0.399 when the number should be 0.339. [Editor's Note: This coefficient has been corrected in an Errata published in the JOURNAL OF HEAT TRANSFER, Vol. 116, 1994, p. 324.]

In the natural convection limit, as $\xi \to \infty$, the local heat transfer rate is given by:

$$Nu_n = \frac{h_n n}{k} = F_n \cdot Gr_x^{1/4} \tag{5}$$

The coefficient, F_n, has the following asymptotic behavior (Ede, 1967):

$$F_n \to 0.6\, Pr^{1/2} \quad \text{as} \quad Pr \to 0 \tag{6}$$

and

$$F_n \to 0.503\, Pr^{1/4} \quad \text{as} \quad Pr \to \infty \tag{7}$$

For the entire range of Prandtl number, F_n can be represented by:

$$F_n = 0.503\, Pr^{1/4} [0.670\, Pr^{-9/16} + 1]^{-4/9} \tag{8}$$

Churchill and Usagi (1972) suggested correlations similar to those given by Eqs. (4) and (8). However, with the Prandtl number dependency built in the equations here are slightly simpler to use, yet as accurate. Values for F_f and F_n generated by Eqs. (4) and (8) are within 1 percent of those values tabulated by Schlichting (1979) and Ede (1967).

After establishing the asymptotic correlations we now present the correlation for mixed convection. Local heat transfer rates for mixed convection may be written as:

$$\frac{\mathrm{Nu}_m}{\mathrm{Re}_x^{1/2}} = [F_f^n + (F_n \xi^{1/4})^n]^{1/n} \tag{9}$$

The average heat transfer rates for mixed convection are given by:

$$\frac{\overline{\mathrm{Nu}}_m}{\mathrm{Re}_x^{1/2}} = \left[(2F_t)^n + \left(\frac{4}{3} F_n \xi^{1/4}\right)^n \right]^{1/n} \tag{10}$$

The only unknown parameter is n. It was selected here in such a way that the heat transfer results predicted by Eq. (9) agree closely with those obtained under mixed convection conditions by Merkin (1969), and Lloyd and Sparrow (1970). We found that no single value of n yielded the best agreement for all values of Prandtl number. Instead, the best value of n increases with Prandtl number. Thus, for each value of Pr the exponent, n, was determined that gave the best agreement between Eq. (9) and the available numerical results. The exponent n was found to be:

$$n = 3.5\,\mathrm{Pr}^{0.075} \tag{11}$$

Churchill (1977) proposed, and Ruckenstein (1978) confirmed (for very large Pr), a correlation similar to Eq. (9); however, the exponent n was given as equal to 3 for all Prandtl numbers. Using the exponent as found by Eq. (11) offers greater flexibility and accuracy over a broad range of Prandtl numbers.

The average Nusselt number, in Eq. (10), cannot be found by integrating the local Nusselt number from Eq. (9). Instead, it is constructed using the asymptotic average heat transfer correlations. The parameter n in Eq. (10) was determined by comparing Eq. (10) with a numerical integration of Eq. (9). The same Prandtl number dependence of n shown in Eq. (11) was found to hold for the average heat transfer correlation as well.

Shear Stress Correlations. In a fashion similar to that used to develop the heat transfer correlations, the shear stress correlations for mixed convection conditions were found using the asymptotic behavior under the pure forced and natural convection conditions.

For forced convection flow, as $\xi \to 0$, the boundary layer analysis yields the following correlation for the local shear stress, τ_f:

$$\tau_f = 0.664\,\mathrm{Re}_x^{-1/2}\left(\frac{\rho u_\infty^2}{2}\right) \tag{12}$$

Under natural convection conditions, as $\xi \to \infty$, the local shear stress can be found from the similarity solution of Gebhart (1971):

$$\tau_n = \frac{4\mu\nu}{x^2}\left(\frac{\mathrm{Gr}_x}{4}\right)^{3/4} \cdot f''(0) \tag{13}$$

where $f''(0)$ is the Prandtl number dependent dimensionless shear stress parameter. For $0.7 \le \mathrm{Pr} \le 100$ this parameter is very nicely described by a form of Hoerl's equation (Daniel and Wood, 1971):

$$f''_{(0)} = 0.6398\,\mathrm{Pr}^{-0.1783} e^{-0.00111 \cdot \mathrm{Pr}} \tag{14}$$

It is interesting to note here that the local heat transfer rate, h, under both the forced and natural convection conditions decreases in a downstream direction, as seen in Eqs. (1) and (5). However, the local shear stress behavior is different. For a forced flow it decreases as $x^{-1/2}$, whereas it increases in a buoyancy induced flow as $x^{1/4}$. The latter is due to an increasing characteristic velocity downstream.

Equations (12) and (13) may be integrated to give the average shear stress under the forced and natural convection limits. This yields

$$\bar{\tau}_f = 2\tau_f \quad \text{and} \quad \bar{\tau}_n = \frac{4}{5}\tau_n \tag{15}$$

In a similar way to that used for the heat transfer correlations the shear stress, τ_m, in a mixed convection flow may be represented in terms of τ_f and τ_n as:

$$\tau_m = [(\tau_f)^n + (\tau_n)^n]^{1/n} \tag{16}$$

The exponent, n, is determined by comparing the values for τ_m from Eq. (16) with the available values of τ_m. Only the analysis of Merkin (1969) tabulates the values of τ_m for $\mathrm{Pr} = 1$, over the entire range of the convection parameter ξ. Graphic representation of τ_m is given by Afzal and Banthiya (1977) for $\mathrm{Pr} = 0.7$ and for $0 < \xi < 40$. Based upon these analyses a value of $n = 6/5$ resulted in the best agreement. Since the results for other values of Prandtl number are not available, dependence of n on Pr could not be determined for the correlations. Using this value of n and substituting Eqs. (12), (13), and (14), the local correlation becomes

$$\frac{\tau_m}{\left(\frac{1}{2}\rho u_\infty^2\right)} \mathrm{Re}_x^{1/2} = [0.612 + (2.828 \cdot f''(0) \cdot \xi^{3/4})^{6/5}]^{5/6} \tag{17}$$

A correlation for the average shear stress under mixed convection is proposed here by combining $\bar{\tau}_f$ and $\bar{\tau}_n$ in a way similar to that used in Eq. (16). The correlation parameter, n, is determined by comparing τ_m with the values calculated by integrating Eq. (17) numerically. The final correlation for τ_m becomes:

$$\frac{\bar{\tau}_m}{\left(\frac{1}{2}\rho u_\infty^2\right)} \mathrm{Re}_x^{12} = [1.392 + (2.263 \cdot f''(0) \cdot \xi^{3/4})^{7/6}]^{6/7} \tag{18}$$

We note that these correlations approach the forced convection limits when $\xi \to 0$, and the natural convection limits when $\xi \to \infty$. The limits, shown in Eq. (15), are valid for any value of Pr. Although the best value of n in Eq. (16) is determined for the values of Prandtl number closer to unity, we believe that the shear stress correlations may be applied to other values of Pr as a first approximation.

Discussion

Values of the local heat transfer rates and shear stress rates for $\mathrm{Pr} = 1$ were reported by Merkin (1969) for $0 < \mathrm{Gr}/\mathrm{Re}^2 < \infty$. The discrepancies between these results and those obtained from the proposed correlations, Eqs. (9) and (16) are less than 3 percent over the entire mixed convection regime. For other values of Prandtl number the results are compared with the analysis of Lloyd and Sparrow (1970), whose results were shown to be in excellent agreement with Kliegel's (1959) data in air. The local heat transfer rates as predicted by Eq. (9) deviate from those of Lloyd and Sparrow (1970) by less than 1, 3, and 2 percent for $\mathrm{Pr} = 0.72$, 10, and 100, respectively. For extremely low values of $\mathrm{Pr} = 0.003$ the deviations are within 8 percent.

Agreement with results from other analyses (Oosthuizen and Hart, 1973; Afzal and Banthiya, 1977), and experimental results (Gryzagoridis, 1975) was also very good. Based upon experimentation in air, Oosthuizen and Bassey (1973) suggested a correlation for the average heat transfer rates. The discrepancy between that correlation and the proposed correlation in Eq. (10) is within 1 percent for the entire mixed convection regime. Correlations similar to those in Eqs. (9) and (10) were suggested by Churchill (1977) with a maximum discrepancy here of about 5 percent over the entire range of Pr.

We now characterize the limits between the forced, mixed, and natural convection regimes. Since the transport rates vary gradually as the flow regime changes from pure natural to pure forced convection some arbitrary criterion is needed to mark the end of one regime and the beginning of the other. The criterion for mixed convection limits used here is when the transport rates deviate by more than 5 percent from those of

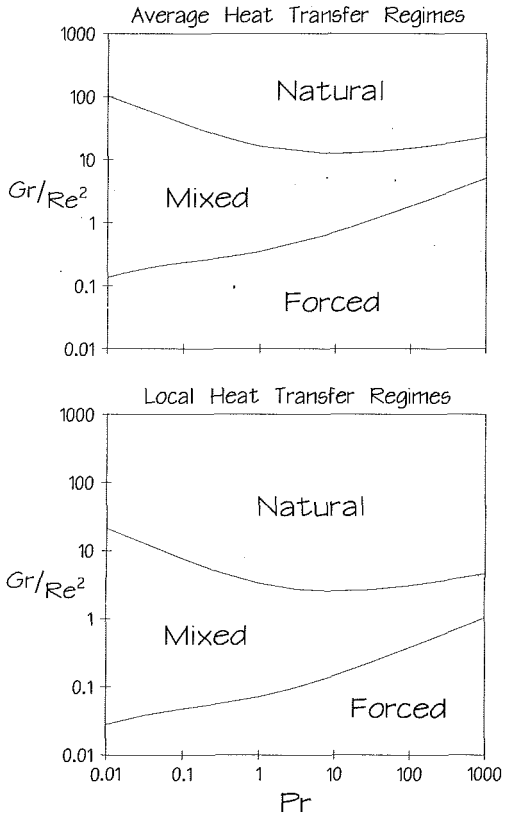

Fig. 1 Heat transfer regimes in aiding laminar mixed convection from a vertical isothermal surface based on a 5 percent limit between the pure convection and the mixed convection modes

the limiting regimes. Figure 1 shows the limits of transport regimes based on both the local and the average heat transfer rates. In both cases, values of Gr/Re^2 marking the transport regimes depend upon the value of the Prandtl number. It is also interesting to note that, in a given flow circumstance, the local transport regime at a given downstream location may become mixed while the average transport is still dominated by one of the limiting regimes, and vice versa. Thus, in practical circumstances where the total transport is of primary interest, characterization of the flow regimes based on average heat transfer is more realistic.

Since the proposed correlations are developed using their asymptotic behavior under pure natural and forced convection conditions their use is recommended for all three regimes without worrying about the presence of more than one regime present on the surface. Only the restriction of laminar aiding flow applies.

Acknowledgments

The authors acknowledge the support provided by the National Science Foundation under Grant No. MEA 82-04361.

References

Acrivos, A., 1966, "On the Combined Effect of Forced and Free Convection Heat Transfer in Laminar Boundary Flows," *Chemical Engineering Science*, Vol. 21, pp. 343-352.

Afzal, N., and Banthiya, N. K., 1977, "Mixed Convection Over a Semi-infinite Vertical Flat Plate," *Journal of Applied Mathematics and Physics (ZAMP)*, Vol. 28, pp. 993-1004.

Carey, V. P., and Gebhart, B., 1983, "The Stability and Disturbance-Amplification Characteristics of Vertical Mixed Convection Flow," *Journal of Fluid Mechanics*, Vol. 127, pp. 185-201.

Chen, T. S., Armaly, B. F., and Ramachandran, N., 1986, "Correlations for Laminar Mixed Flows on Vertical, Inclined, and Horizontal Flat Plates," ASME JOURNAL OF HEAT TRANSFER, Vol. 108, pp. 835-840.

Churchill, S. W., and Usagi, R., 1972, "A General Expression for the Correlation of Rates of Transfer and Other Phenomena," *AIChE Journal*, Vol. 18, pp. 1121-1127.

Churchill, S. W., and Ozoe, H., 1973, "Correlations for Laminar Forced Convection in Flow Over an Isothermal Flat Plate and in Developing and Fully Developed Flow in an Isothermal Tube," *Journal of Fluid Mechanics*, Aug., pp. 416-419.

Churchill, S. W., 1977, "A Comprehensive Correlating Equation for Laminar, Assisting Forced and Free Convection," *AIChE Journal*, Vol. 10, pp. 10-16.

Daniel, C., and Wood, F. S., 1971, *Fitting Equations to Data*, Wiley-Interscience, pp. 22-24.

Ede, A. J., 1967, "Advances in Free Convection," *Advances in Heat Transfer*, J. P. Hartnett and T. F. Irvine, eds., Academic Press, New York, pp. 1-64.

Gebhart, B., 1971, *Heat Transfer*, 2nd ed., McGraw-Hill, New York.

Gryzagoridis, J., 1975, "Combined Free and Forced Convection Heat Transfer From Vertical Plate," *International Journal of Heat and Mass Transfer*, Vol. 18, pp. 911-916.

Kliegel, J. R., 1959, "Laminar Free and Forced Convection Heat Transfer From a Vertical Flat Plate," Ph.D. Thesis, University of California.

Lloyd, J. R., and Sparrow, E. M., 1970, "Combined Forced and Free Convection Flow on Vertical Surface," *International Journal of Heat and Mass Transfer*, Vol. 13, pp. 434-438.

Merkin, J. H., 1969, "The Effect of Buoyancy Forces on the Boundary-Layer Flow Over a Semi-infinite Vertical Flat Plate in a Uniform Stream," *Journal of Fluid Mechanics*, Vol. 34, pp. 439-450.

Mucoglu, A., and Chen, T. S., 1978, "Wave Instability of Mixed Convection Flow Along a Vertical Flat Plate," *Numerical Heat Transfer*, Vol. 1, pp. 267-283.

Oosthuizen, P. H., and Bassey, M., 1973, "An Experimental Study of Combined Forced and Free Convective Heat Transfer From Flat Plates to Air at Low Reynolds Numbers," ASME JOURNAL OF HEAT TRANSFER, Vol. 95, pp. 120-121.

Oosthuizen, P. H., and Hart, R., 1973, "A Numerical Study of Combined Convective Flow Over Flat Plates," ASME JOURNAL OF HEAT TRANSFER, Vol. 95, pp. 60-63.

Raju, M. S., Liu, X. Q., and Law, C. K., 1984, "A Formulation of Combined Forced and Free Convection Past Horizontal and Vertical Surfaces," *International Journal of Heat and Mass Transfer*, Vol. 27, pp. 2215-2224.

Ramachandran, N., Armaly, B. F., and Chen, T. S., 1985, "Measurements and Predictions of Laminar Mixed Convection Flow Adjacent to a Vertical Surface," ASME JOURNAL OF HEAT TRANSFER, Vol. 107, pp. 636-641.

Ruckenstein, E., 1978, "Interpolating Equations Between Two Limiting Cases for the Heat Transfer Coefficient," *AIChE Journal*, Vol. 24, pp. 940-941.

Schlichting, H., 1979, *Boundary Layer Theory*, McGraw-Hill, London, United Kingdom.

Wilks, G., 1976, "Heat Transfer Coefficients for Combined Forced and Free Convection Flow About a Semi-infinite Isothermal Plate," *International Journal of Heat and Mass Transfer*, Vol. 19, pp. 951-953.

Correlations for the CHF Condition in Two-Phase Crossflow Through Multitube Bundles

M. K. Jensen[1] and H. Tang[1]

Nomenclature

A = dimensionless parameter
Bo = boiling number $= q''/Gh_{fg}$
D = tube diameter, m
G = mass flux based on minimum flow area, kg/m^{2}s

[1]Department of Mechanical Engineering, Aeronautical Engineering, and Mechanics, Rensselaer Polytechnic Institute, Troy, NY 12180-3590.

Contributed by the Heat Transfer Division of THE AMERICAN SOCIETY OF MECHANICAL ENGINEERS. Manuscript received by the Heat Transfer Division June 1993; revision received January 1994. Keywords: Boiling, Heat Exchangers, Multiphase Flows. Associate Technical Editor: L. C. Witte.

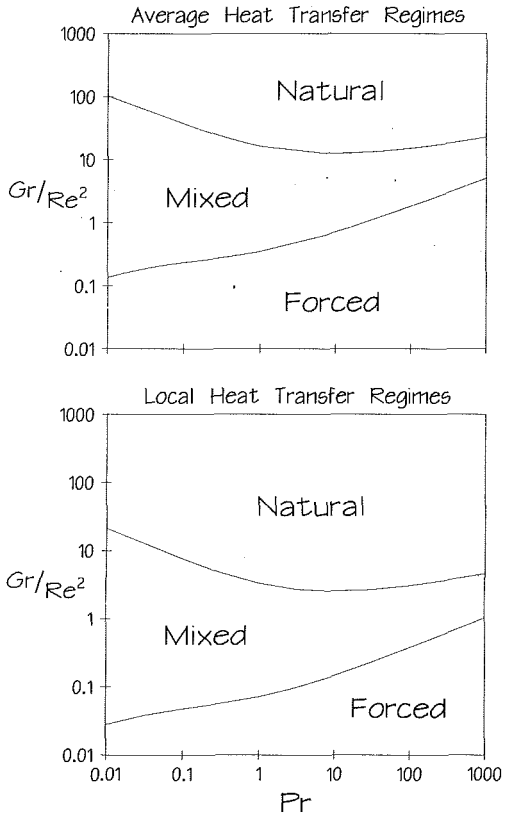

Fig. 1 Heat transfer regimes in aiding laminar mixed convection from a vertical isothermal surface based on a 5 percent limit between the pure convection and the mixed convection modes

the limiting regimes. Figure 1 shows the limits of transport regimes based on both the local and the average heat transfer rates. In both cases, values of Gr/Re^2 marking the transport regimes depend upon the value of the Prandtl number. It is also interesting to note that, in a given flow circumstance, the local transport regime at a given downstream location may become mixed while the average transport is still dominated by one of the limiting regimes, and vice versa. Thus, in practical circumstances where the total transport is of primary interest, characterization of the flow regimes based on average heat transfer is more realistic.

Since the proposed correlations are developed using their asymptotic behavior under pure natural and forced convection conditions their use is recommended for all three regimes without worrying about the presence of more than one regime present on the surface. Only the restriction of laminar aiding flow applies.

Acknowledgments

The authors acknowledge the support provided by the National Science Foundation under Grant No. MEA 82-04361.

References

Acrivos, A., 1966, "On the Combined Effect of Forced and Free Convection Heat Transfer in Laminar Boundary Flows," *Chemical Engineering Science*, Vol. 21, pp. 343-352.

Afzal, N., and Banthiya, N. K., 1977, "Mixed Convection Over a Semi-infinite Vertical Flat Plate," *Journal of Applied Mathematics and Physics (ZAMP)*, Vol. 28, pp. 993-1004.

Carey, V. P., and Gebhart, B., 1983, "The Stability and Disturbance-Amplification Characteristics of Vertical Mixed Convection Flow," *Journal of Fluid Mechanics*, Vol. 127, pp. 185-201.

Chen, T. S., Armaly, B. F., and Ramachandran, N., 1986, "Correlations for Laminar Mixed Flows on Vertical, Inclined, and Horizontal Flat Plates," ASME JOURNAL OF HEAT TRANSFER, Vol. 108, pp. 835-840.

Churchill, S. W., and Usagi, R., 1972, "A General Expression for the Correlation of Rates of Transfer and Other Phenomena," *AIChE Journal*, Vol. 18, pp. 1121-1127.

Churchill, S. W., and Ozoe, H., 1973, "Correlations for Laminar Forced Convection in Flow Over an Isothermal Flat Plate and in Developing and Fully Developed Flow in an Isothermal Tube," *Journal of Fluid Mechanics*, Aug., pp. 416-419.

Churchill, S. W., 1977, "A Comprehensive Correlating Equation for Laminar, Assisting Forced and Free Convection," *AIChE Journal*, Vol. 10, pp. 10-16.

Daniel, C., and Wood, F. S., 1971, *Fitting Equations to Data*, Wiley-Interscience, pp. 22-24.

Ede, A. J., 1967, "Advances in Free Convection," *Advances in Heat Transfer*, J. P. Hartnett and T. F. Irvine, eds., Academic Press, New York, pp. 1-64.

Gebhart, B., 1971, *Heat Transfer*, 2nd ed., McGraw-Hill, New York.

Gryzagoridis, J., 1975, "Combined Free and Forced Convection Heat Transfer From Vertical Plate," *International Journal of Heat and Mass Transfer*, Vol. 18, pp. 911-916.

Kliegel, J. R., 1959, "Laminar Free and Forced Convection Heat Transfer From a Vertical Flat Plate," Ph.D. Thesis, University of California.

Lloyd, J. R., and Sparrow, E. M., 1970, "Combined Forced and Free Convection Flow on Vertical Surface," *International Journal of Heat and Mass Transfer*, Vol. 13, pp. 434-438.

Merkin, J. H., 1969, "The Effect of Buoyancy Forces on the Boundary-Layer Flow Over a Semi-infinite Vertical Flat Plate in a Uniform Stream," *Journal of Fluid Mechanics*, Vol. 34, pp. 439-450.

Mucoglu, A., and Chen, T. S., 1978, "Wave Instability of Mixed Convection Flow Along a Vertical Flat Plate," *Numerical Heat Transfer*, Vol. 1, pp. 267-283.

Oosthuizen, P. H., and Bassey, M., 1973, "An Experimental Study of Combined Forced and Free Convective Heat Transfer From Flat Plates to Air at Low Reynolds Numbers," ASME JOURNAL OF HEAT TRANSFER, Vol. 95, pp. 120-121.

Oosthuizen, P. H., and Hart, R., 1973, "A Numerical Study of Combined Convective Flow Over Flat Plates," ASME JOURNAL OF HEAT TRANSFER, Vol. 95, pp. 60-63.

Raju, M. S., Liu, X. Q., and Law, C. K., 1984, "A Formulation of Combined Forced and Free Convection Past Horizontal and Vertical Surfaces," *International Journal of Heat and Mass Transfer*, Vol. 27, pp. 2215-2224.

Ramachandran, N., Armaly, B. F., and Chen, T. S., 1985, "Measurements and Predictions of Laminar Mixed Convection Flow Adjacent to a Vertical Surface," ASME JOURNAL OF HEAT TRANSFER, Vol. 107, pp. 636-641.

Ruckenstein, E., 1978, "Interpolating Equations Between Two Limiting Cases for the Heat Transfer Coefficient," *AIChE Journal*, Vol. 24, pp. 940-941.

Schlichting, H., 1979, *Boundary Layer Theory*, McGraw-Hill, London, United Kingdom.

Wilks, G., 1976, "Heat Transfer Coefficients for Combined Forced and Free Convection Flow About a Semi-infinite Isothermal Plate," *International Journal of Heat and Mass Transfer*, Vol. 19, pp. 951-953.

Correlations for the CHF Condition in Two-Phase Crossflow Through Multitube Bundles

M. K. Jensen[1] and H. Tang[1]

Nomenclature

A = dimensionless parameter
Bo = boiling number $= q''/Gh_{fg}$
D = tube diameter, m
G = mass flux based on minimum flow area, kg/m^{2}s

[1]Department of Mechanical Engineering, Aeronautical Engineering, and Mechanics, Rensselaer Polytechnic Institute, Troy, NY 12180-3590.

Contributed by the Heat Transfer Division of THE AMERICAN SOCIETY OF MECHANICAL ENGINEERS. Manuscript received by the Heat Transfer Division June 1993; revision received January 1994. Keywords: Boiling, Heat Exchangers, Multiphase Flows. Associate Technical Editor: L. C. Witte.

g = gravity, m/s^2
h_{fg} = enthalpy of vaporization, kJ/kg
Ku = Kutateladze number (Eq. (5))
P = transverse pitch between two tubes, m
q'' = critical heat flux, W/m^2
q_{max} = saturated liquid pool boiling critical heat flux, W/m^2
Re = Reynolds number $= GD/\mu_f$
R' = $(D/2)/(\sigma/g(\rho_f - \rho_g))^{1/2}$
x = mass quality
$_1x_2$ = transition quality between Regions 1 and 2
$_2x_3$ = transition quality between Regions 2 and 3
ρ_f, ρ_g, ρ_{TP} = saturated liquid, saturated vapor, two-phase homogeneous density, kg/m^3
σ = surface tension, N/m
ψ = defined in Eq. (7)
μ_f = liquid dynamic viscosity, Ns/m^2

Subscripts

1, 2, 3 = regions 1, 2, and 3, respectively
tr = transition

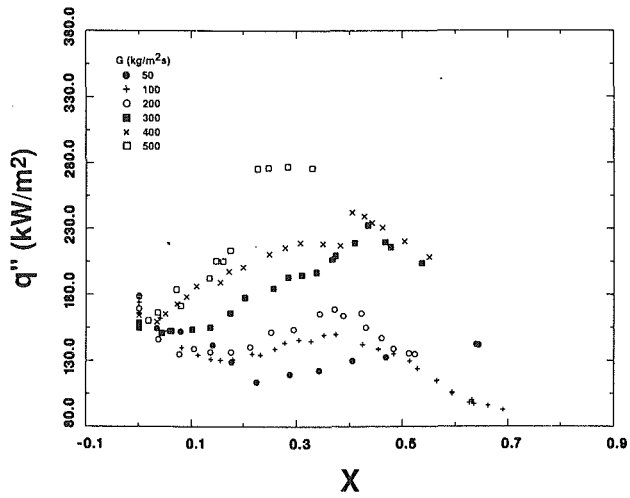

Fig. 1 Typical CHF data using R113 from in-line tube bundle, $P/D = 1.30$, 150 kPa (Dykas and Jensen, 1992)

Introduction

As found in flows inside of tubes, the critical heat flux (CHF) condition in two-phase crossflow through multitube bundles is a limiting condition that heat exchanger designers want to avoid. However, while there has been extensive study of and correlations for the CHF condition for in-tube two-phase flows, few investigations have been conducted for the CHF condition for two-phase crossflow on the shellside of horizontal tube bundles. Bundle-average CHF data and a correlation have been presented by Palen and Small (1964) and Palen et al. (1972) for large multitube bundles. Schuller and Cornwell (1984) tested a slice of a simulated 241-tube reboiler and obtained some complex and confusing behavior of the CHF condition on individual tubes. Chan and Shoukri (1987) evaluated the CHF in a small bundle (nine tubes) with natural circulation. No quality or mass flux data for individual tubes were reported in any of the above papers.

The CHF condition on individual tubes in a bundle with known mass flux and quality has been studied by Schuller and Cornwell (1984), who used a 3 column by 35 row (3×35) test section, Cumo et al. (1980) who used a 3×3 bundle, Yao and Hwang (1989) who obtained CHF data with slightly subcooled liquid, and Dykas and Jensen (1992) and Leroux and Jensen (1992) who used 5×27 bundles. Typical CHF data trends (from Dykas and Jensen, 1992) for an individual tube in a bundle are shown in Fig. 1. The zero-quality CHF varied slightly with mass flux and was lower than that of a single tube in pool boiling. At qualities greater than zero, they found that the CHF data are a complex function of mass flux, local quality, pressure level, and bundle geometry.

The only correlation in the literature for the CHF on a single tube in a multitube bundle is presented by Cumo et al. (1980), who adapted the Zuber pool boiling CHF model. The resulting correlation always predicted an increasing CHF with increasing quality. Thus, this model does not represent well all the data trends found by Cumo et al., Schuller and Cornwell, or Jensen and co-workers. Hence, it is the objective of this paper to present correlations for the CHF condition for individual tubes in two-phase crossflow in multitube bundles that do represent the observed trends.

Data Used

Only the data obtained by Dykas and Jensen (1992) and Leroux and Jensen (1992) are used in the development of the

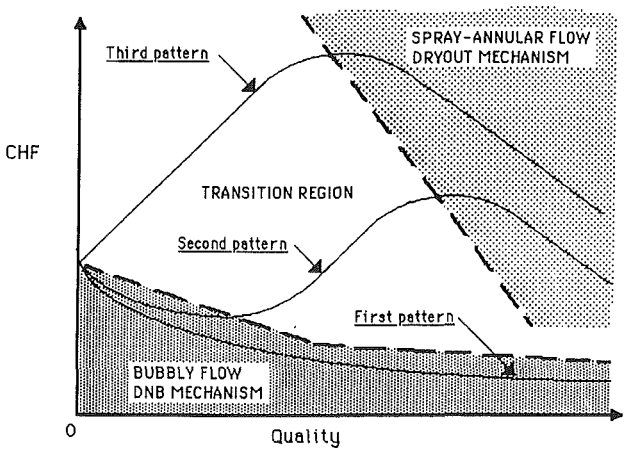

Fig. 2 Basic curve patterns observed in the data and postulated flow regimes and CHF mechanisms mapped onto typical CHF curves (Leroux and Jensen, 1992)

correlations. Except for the data of Cumo et al. (1980), the other studies do not include specific information about local quality and mass flux at the tube experiencing the CHF condition. Cumo's data were initially used in the data bank. However, attempts to reconcile those data with the data from the present experiment failed. We suspect that the difficulty lies in the definition used to identify the CHF. Leroux and Jensen (1992) defined the CHF condition as the point when there was a distinct but small rise in the slope of the resistance of the test section caused by the formation of a small, stable partial film boiling patch. Cumo et al. raised the power to test section failure and apparently used that as the CHF.

The data were obtained from two in-line square arrays (5×27) with tube pitch-to-diameter ratios of $P/D = 1.30$ and 1.70 and an equilateral triangular array (5×27) with $P/D = 1.30$. CHF data were obtained from a single tube in the center column of the 25th row from the bottom of the bundles. Tests were run with R113 at 1.5 and 5 bars for equilibrium qualities (obtained from an energy balance) ranging from 0 to 70 percent and for mass fluxes (based on the minimum flow area) of 50 to 500 kg/m^{2}s. A total of 139 staggered tube bundle data and 297 in-line tube bundle data were used.

As can be seen on Fig. 1 and from figures (not given) showing data from other test sections and at different pressures, the

data generally fall into one of three CHF curve patterns; Fig. 2 schematically shows the trends more clearly. The first pattern has a monotonically decreasing CHF with increasing quality at low mass fluxes. The flow pattern may be described as bubbly since that flow pattern typically occurs with low-velocity, low-quality flows. The second pattern initially decreases with increasing quality (similar to the first pattern) until a minimum in the curve is reached; then the curve begins to increase with quality until a maximum in the curve is attained, after which the curve again decreases with further increases in quality. Both the minimum and the maximum shift to the left with increasing mass flux; the local maximum also increases. The decreasing CHF curve at high qualities may be associated with a spray annular flow pattern. At high mass fluxes, the third pattern appears. The CHF-quality curve immediately rises from zero quality until a maximum occurs and then the curve monotonically decreases.

Leroux and Jensen (1992) speculate that the mechanism governing the CHF behavior at low mass fluxes and low to moderate qualities is a departure from nucleate boiling type (DNB) phenomena, similar to that which occurs in pool boiling. At high qualities it is believed that the CHF condition is a dryout process. For those parts of the CHF-quality curves where the slope is positive, it was assumed that this behavior reflected the transition from the low-quality to the high-quality CHF mechanisms.The flow pattern in this region can also be considered transitional.

Transition Line Correlations

The data were divided into three different regions according to the hypothesized mechanisms governing the CHF process. Region 1 was for the DNB type data. On the data figures, a straight line was drawn from about the zero quality data through the local minima exhibited in some of the data curves (the second pattern described above). All data below this line were identified as Region 1 data. This line was arbitrarily extended to high quality so that the higher quality CHF data for the pattern 1 data, described above, were excluded from Region 1, as it was assumed that the high-quality CHF data at low mass fluxes probably were governed by dryout rather than DNB. The second dividing line was drawn through the local maxima that occurred in the second and third CHF pattern curves described above. Again a straight line was used. All data above this line were placed in Region 3, which was identified with the dryout type data. Data falling between these two transition lines were placed in Region 2.

These two transition lines can be considered comparable to the transition lines used to identify charges in two-phase flow patterns and should be interpreted as indicating a region over which the transition occurs. For vertical crossflow over horizontal tube bundles only three flow patterns have consistently been observed: bubbly flow, spray-annular flow, and a transitional flow. However, no completely general flow pattern map has been proposed in the literature for shellside two-phase flow. The map given by Grant and Chisholm (1979) was developed for low pressure, air–water flows in a staggered tube bundle. The transition lines from that map did not correspond to the ones used in this study and predicted unrealistic flow patterns (e.g., bubbly flow for quality of 50 percent, mass flux of 50 kg/m^{2}s, and pressure of 1.5 bar) for certain combinations of flow conditions. Hence, that map could not be used in this study.

The two parameters that helped best to separate the different regions were quality, x, and a nondimensional group similar to that used by Taitel and Dukler (1976) for in-tube flows, $A = g\rho_{TP}(\rho_f - \rho_g)D/G^2$. This nondimensional group represents

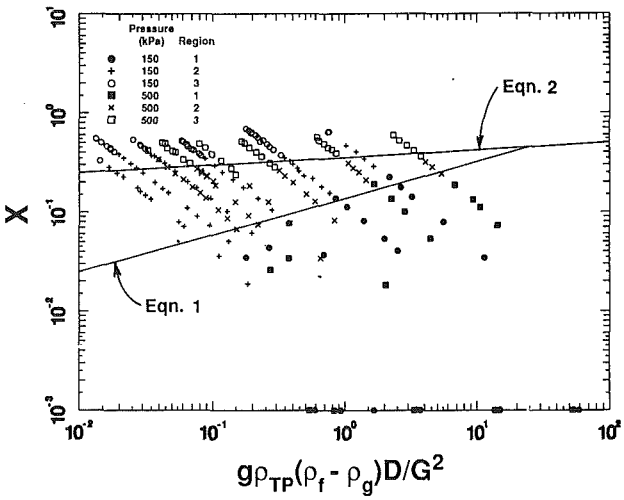

Fig. 3 CHF regions for in-line tube bundle, $P/D = 1.30$

a ratio of buoyancy to inertia forces. The data were plotted on Fig. 3 for the in-line $P/D = 1.30$ tube bundle. The in-line $P/D = 1.70$ bundle had the same transition lines. The staggered bundle data were similar. (The data along the abscissa were for very low-quality data and to have those data show up on the figure they were arbitrarily given a quality of $x = 10^{-3}$.) The resulting transition lines are given below for in-line tube bundles:

Transition line between Regions 1 and 2

$$_1x_2 = 0.137\,A^{0.369} \tag{1}$$

Transition line between Regions 2 and 3

$$_2x_3 = 0.354\,A^{0.075} \tag{2}$$

and for the staggered tube bundle:

Transition line between Regions 1 and 2

$$_1x_2 = 0.242\,A^{0.396} \tag{3}$$

Transition line between Regions 2 and 3

$$_2x_3 = 0.432\,A^{0.098} \tag{4}$$

CHF Correlations

To correlate the CHF data only the data in Regions 1 and 3 were used. We assumed that the Region 2 data could be estimated from a linear interpolation between the Region 1 and Region 3 correlations. Because of the similarity to pool boiling, Region 1 data were nondimensionalized with the Sun and Lienhard (1970) pool boiling CHF correlation (as given by Lienhard, 1988). A correlation that predicts the CHF for saturated liquid with forced convection was not used because the saturated liquid velocities used for the present data were so low as to have a negligible effect on the saturated liquid CHF. The Region 1 data were correlated using $q''/q''_{\max} = f(\psi)$ where:

$$q''_{\max} = \mathrm{Ku}\,\rho_g^{1/2} h_{fg}[\sigma g(\rho_f - \rho_g)]^{1/4} \tag{5}$$

$$\mathrm{Ku} = 0.1164 + 0.297\exp(-3.44\sqrt{R'}) \tag{6}$$

$$\psi = (\rho_{TP}/\mu_f)D(\sigma g(\rho_f - \rho_g)/\rho_f^2)^{1/4} \tag{7}$$

The quantity ψ is similar to what Haramura and Katto (1983) used for the correlation of the CHF for saturated liquid crossflow over single tubes. Region 3 data were not nondimensionalized with the pool boiling value, but were correlated using $Bo = f(A, \mathrm{Re}, P/D)$. Hence, the final correlations determined for the different test sections are:

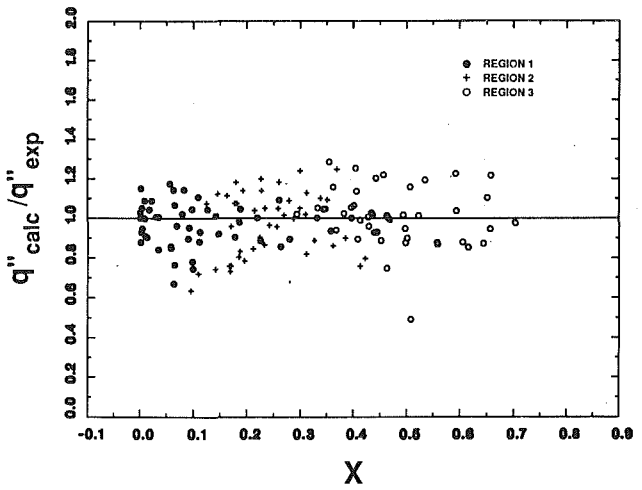

Fig. 4 Scatter plot of calculated versus experimental CHF values for staggered tube bundle

In-line Tube Bundles

Region 1

$$q''/q''_{\max} = \exp\left[\left(0.126 - \frac{1}{\psi^{0.193}}\right)(P/D)^{0.856}\right] \quad (8)$$

Region 3

$$Bo = 2.04 \times 10^{-5} A^{0.429} \mathrm{Re}^{0.0136} (P/D)^{-0.651} \quad (9)$$

Staggered Tube Bundle

Region 1

$$q''/q''_{\max} = \exp\left(-0.0322 - \frac{10.1}{\psi^{0.585}}\right) \quad (10)$$

Region 3

$$Bo = 1.97 \times 10^{-5} A^{0.165} \mathrm{Re}^{-0.0858} \quad (11)$$

Region 2 data predictions were obtained by a linear interpolation between Region 1 and Region 3 correlations. As a first step, the qualities and critical heat fluxes at which the minima in the curve pattern number 2 and the maxima in the curve pattern number 3 occur must be determined. This is accomplished by equating the transition line correlation with the corresponding CHF correlation and solving for the transition quality at a given mass flux and pressure level. For example, for an in-line bundle the minimum in the curve pattern number 2 could be found by solving Eq. (1) for the transition quality, ${}_1x_{2,tr}$, and thus, the transition critical heat flux, $q''_{1,tr}$, could be found by substituting ${}_1x_{2,tr}$ into Eq. (8). Likewise, solving Eq. (2) will produce ${}_2x_{3,tr}$ and $q''_{3,tr}$ can then be calculated from Eq. (9). To determine the CHF at some quality x, ${}_1x_{2,tr} < x < {}_2x_{3,tr}$:

$$q''_2 = q''_{1,tr} + (q''_{3,tr} - q''_{1,tr})(x - {}_1x_{2,tr})/({}_2x_{3,tr} - {}_1x_{2,tr}) \quad (12)$$

Figure 4 shows a scatter plot comparison for the calculated and experimental CHF for the staggered tube bundle; the in-line results were similar. For the 297 in-line bundle data, the average absolute deviation (AAD) between the correlated and the experimental data is 10.3 percent. All the Region 1 data were correlated with an AAD of 5.5 percent, Region 2 with 10.3 percent, and Region 3 with 14.2 percent; 75 percent of the data were correlated within ±15 percent, and 94 percent of the data were correlated within ±20 percent. For the 139 staggered bundle data, the overall AAD was 11.0 percent. For Regions 1, 2, and 3, the corresponding AAD's were 9.1, 14.0, and 10.1 percent, respectively; 75 percent of the data were correlated within ±15 percent, and 84 percent of the data were correlated within ±20 percent. The correlated data shown on Fig. 4 were generally randomly distributed with no dominant trends evident.

The data of Cumo et al. (1980) were compared against the the predictions by the correlation for the staggered tube bundle. At higher qualities their data were underpredicted consistently. Based on their definition of the CHF, this could be expected. A second possible explanation for the differences between those data and the present data is that Cumo et al. used the middle tube in a small (3 × 3) staggered bundle. Entrance effects could influence their results. However, this has not been systematically studied. In addition, their data at zero quality were generally overpredicted. This, again, could be attributable to entrance effects.

We believe the correlations to be valid for any tube row after the third or fourth row in the bundle. Hsu (1987) demonstrated that as the heat flux increased, the heat transfer coefficient was independent of position in a bundle. Because the CHF is much higher than those tested by Hsu, we can speculate that the same behavior occurs with the CHF; that is, there is small positional influence on the CHF, and the gross flow parameters set the environment for the CHF condition.

Acknowledgments

This study was sponsored by the National Science Foundation under Grant No. CBT-8704693. The NSF support is gratefully acknowledged.

References

Chan, A. M., and Shoukri, M., 1987, "Boiling Characteristics of Small Multitube Bundles," ASME JOURNAL OF HEAT TRANSFER, Vol. 109, pp. 753–760.

Cumo, M., Farello, G. E., Gasiorowski, J., Iovino, G., and Naviglio, A., 1980, "Quality Influence on the Departure From Nucleate Boiling in Cross Flows Through Bundles," *Nuclear Technology*, Vol. 49, pp. 337–346.

Dykas, S., and Jensen, M. K., 1992, "Critical Heat Flux on a Tube in a Horizontal Tube Bundle," *Experimental Thermal and Fluid Science*, Vol. 5, pp. 34–39.

Grant, I. D. R., and Chisholm, D., 1979, "Two-Phase Flow on the Shell-Side of a Segmentally Baffled Shell-and-Tube Heat Exchanger," ASME JOURNAL OF HEAT TRANSFER, Vol. 101, pp. 38–42.

Haramura, Y., and Katto, Y., 1983, "A New Hydrodynamic Model of Critical Heat Flux, Applicable Widely to Both Pool and Forced Convection Boiling on Submerged Bodies in Saturated Liquids," *International Journal of Heat and Mass Transfer*, Vol. 26, pp. 389–399.

Hsu, J.-T., 1987, "A Parametric Study of Boiling Heat Transfer in Horizontal Tube Bundles," Ph.D. Thesis, University of Wisconsin—Milwaukee, Dec.

Leroux, K. M., and Jensen, M. K., 1992, "Critical Heat Flux in Horizontal Tube Bundles in Vertical Crossflow of R113," ASME JOURNAL OF HEAT TRANSFER, Vol. 114, pp. 179–184.

Lienhard, J. H., 1988, "Burnout on Cylinders," ASME JOURNAL OF HEAT TRANSFER, Vol. 110, pp. 1271–1286.

Palen, J. W., and Small, W. M., 1964, "A New Way to Design Kettle and Internal Reboilers," *Hydrocarbon Processing*, Vol. 43, pp. 199–208.

Palen, J. W., Yarden, A., and Taborek, J., 1972, "Characteristics of Boiling Outside Large-Scale Horizontal Multi-tube Bundles," *AIChE Symposium Series No. 118*, Vol. 68, pp. 50–61.

Schuller, R. B., and Cornwell, K., 1984, "Dryout on the Shell-Side of Tube Bundles," *First U.K. National Conference on Heat Transfer*, Inst. Chem. Engineering Symposium Series No. 86, Vol. 2, pp. 795–805.

Sun, K. H., and Lienhard, J. H., 1970, "The Peak Pool Boiling Heat Flux on Horizontal Cylinders," *International Journal of Heat and Mass Transfer*, Vol. 13, pp. 1425–1439

Taitel, Y., and Dukler, A. E., 1976, "A Model for Predicting Flow Regime Transitions in Horizontal and Near Horizontal Gas-Liquid Flow," *AIChE Journal*, Vol. 22, pp. 47–55.

Yao, S. C., and Hwang, T. H., 1989, "Critical Heat Flux on Horizontal Tubes in an Upward Crossflow of Freon-113," *International Journal of Heat and Mass Transfer*, Vol. 32, pp. 95–103.

A Simplified Method for Calculating Transient Average Temperature and Heat Transfer in a Laterally Heated Cavity

F. Poujol,[1] E. Ramos,[1] and J. Rojas[1]

Nomenclature

A = aspect ratio of the cavity
C_p = heat capacity
g = gravitational acceleration
h_u = heat transfer coefficient of the partially stratified zone
h_c = heat transfer coefficient in the total stratification stage
H = height of the cavity
H_u = vertical length of the stratified zone
k = thermal conductivity
L = width of the cavity
M = mass of the fluid in the cavity
Pr = Prandtl number
q = heat flux
q_e = heat flux at the constant temperature wall (partial stratification)
Ra = Rayleigh number, defined in Eq. (3)
$\mathrm{Ra}_{\Delta Tu}$ = Rayleigh number based on $T_u - T_o$, defined in Eq. (13)
$\mathrm{Ra}_{\Delta Tc}$ = Rayleigh number based on $T - T_o$, defined in Eq. (16)
T = temperature
T' = nondimensional temperature
T_o = initial temperature and temperature of the constant-temperature wall
T_u = average temperature of the stratified zone
T^* = temperature scale defined after Eq. (26*b*)
T_s = steady-state temperature
t = time
t' = nondimensional time
V = velocity scale defined in Eq. (4)
W = depth of the cavity
x = spatial coordinate
y = spatial coordinate
z = spatial coordinate
α = thermal diffusivity
β = volumetric expansion coefficient
ΔT = average temperature increment
δ_T = boundary layer scale defined in Eq. (5)
δ_{Tc} = thickness of the boundary layer adjacent to the constant temperature wall
ν = kinematic viscosity
τ = time scale defined in Eq. (2)
τ_ν = time scale defined in Eq. (6)
τ_t = time scale for total stratification, defined in Eq. (21)

[1]Laboratorio de Energía Solar, IIM-UNAM. Ap.P. 34, 62580 Temixco, Mor. México.

Contributed by the Heat Transfer Division of The American Society of Mechanical Engineers. Manuscript received by the Heat Transfer Division December 1991; revision received November 1993. Keywords: Natural Convection, Solar Energy, Transient and Unsteady Heat Transfer. Associate Technical Editor: J. R. Lloyd.

1 Introduction and Problem Formulation

Transient natural convection in a side-heated cavity has been studied by a number of authors in the last few years. Patterson and Imberger (1980) found the relevant scales of the flow and constructed a classification of the possible regimes based on the relative values of Rayleigh and Prandtl numbers. The case studied by Patterson and Imberger involved heating and cooling by specifying a temperature difference between vertical isothermal walls and has been subsequently analyzed by other authors. The transient natural convection in a cavity with prescribed heat flux has not received much attention, although Kimura and Bejan (1984) analyzed the steady-state flow in terms of boundary layer theory and found expressions for the global Nusselt number. In this note, we study a problem similar to that described above, but considering constant heat flow on a vertical wall and a constant temperature on the other.

The geometry and boundary conditions of the problem under study in the present article are shown in Fig. 1. The height, width, and depth of the cavity are denoted by H, L, and W, respectively. Although the problem is formally stated in three dimensions, no end-effects in the z direction are considered. The cavity contains an incompressible Newtonian fluid with kinematic viscosity ν, thermal diffusivity α, thermal conductivity k, and thermal expansion coefficient β. At time $t=0$, the fluid inside the cavity is at temperature T_o and a constant and uniform heat flux q is applied at the vertical wall located at $x=L$. The opposite vertical wall is kept at temperature T_o while all other walls are thermally insulated. The equations that describe the velocity, pressure, and temperature fields as functions of position and time are the mass, momentum, and energy balance equations. The solution of such a problem has been found numerically and described in an article published elsewhere (Poujol et al., 1993). Rather than pursuing a detailed description in this paper, a simple model that displays the transient heat transfer with reasonable accuracy is presented. The model is based on the scale analysis introduced by Patterson and Imberger (1980), and adapted for the problem under consideration by Poujol et al. (1993).

2 Global Behavior Scales

The analysis is made considering fluids with Prandlt number (Pr) of order 200 and Rayleigh number based on heat flux (Ra) of order 4×10^9, which is the case studied by Poujol et al. (1993). The transient thermal behavior of the cavity can be naturally divided into three main stages: (*a*) initial heating, (*b*) partial stratification, and (*c*) total stratification.

2.1 Initial Heating. This initial stage spans the interval between the onset of flow when the fluid adjacent to the hot wall forms a thermal boundary layer that discharges hot fluid into the top region of the cavity, and the time the hot fluid reaches the constant temperature wall. The average temperature increment can be calculated according to the expression:

$$M\,C_p\,\frac{dT}{dt} = q\,H\,W \tag{1}$$

where M and C_p are the mass and the heat capacity of the working fluid, respectively, and q is the heat input per unit area. The boundary layers are completely formed at a time τ, which can be estimated from the Patterson and Imberger scale analysis as:

$$\tau \sim \frac{H^2}{\alpha}\,\mathrm{Ra}^{-2/5} \tag{2}$$

where Ra is the Rayleigh number based on the heat flux and is defined by the following expression:

$$\mathrm{Ra} = \frac{g\beta q H^4}{\alpha \nu k} \tag{3}$$

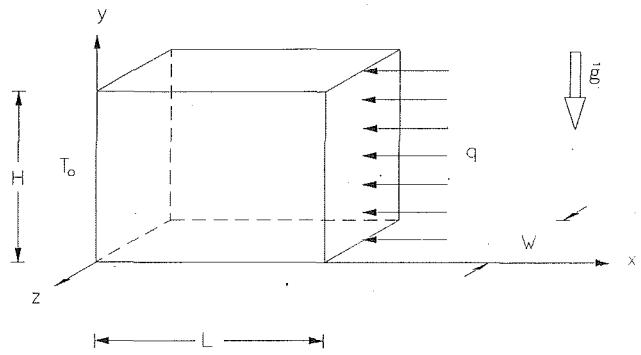

Fig. 1 Geometry of the problem analyzed

g is the acceleration due to gravity. The velocity in the thermal boundary layer and its thickness are

$$V \sim \frac{\alpha \, \mathrm{Ra}^{2/5}}{H} \tag{4}$$

and

$$\delta_T \sim \frac{H}{\mathrm{Ra}^{1/5}} \tag{5}$$

respectively.

The thermal boundary layer discharges hot fluid in the upper part of the cavity forming the intrusion layer. If $\mathrm{Pr} > \mathrm{Ra}^{25/2}$ the time taken by the intrusion layer to arrive at the constant-temperature wall is:

$$\tau_v \sim \frac{L^{5/4} H^{3/4}}{\alpha \mathrm{Ra}^{7/20}} \tag{6}$$

From this time on, the fluid in the cavity will transfer heat to the constant temperature wall.

2.2 Partial Stratification. Heat Balance in the Upper Part of the Cavity. Once the intrusion layer has reached the constant temperature wall, a thermal stratification pattern starts forming from the top of the cavity downward. The heat transferred from the fluid to the constant temperature wall is:

$$q_e = h_u \, H_u \, W (T_u - T_o) \tag{7}$$

where T_u and H_u are the average temperature and the vertical length of the stratified zone, respectively. h_u is the heat transfer coefficient. Under these conditions, the temperature rise is given by:

$$C_p \, M \frac{dT}{dt} = q \, H \, W - h_u \, H_u \, W (T_u - T_o). \tag{8}$$

In terms of T_u the average temperature T can be written as

$$T = \frac{H_u T_u + (H - H_u) T_o}{H}$$

or equivalently

$$(T_u - T_o) = \frac{H}{H_u} (T - T_o). \tag{9}$$

Upon substituting Eq. (9) into Eq. (8), the following relation is obtained:

$$C_p \, M \frac{dT}{dt} = q \, H \, W - h_u \, H \, W \, (T - T_o). \tag{10}$$

The heat transfer coefficient for the cold wall is obtained by equating the heat transferred by convection ($\sim h_u \Delta T_u$) and the heat transferred by conduction through the thermal boundary layer adjacent to the constant-temperature wall ($\sim k \Delta T_u / \delta_{Tc}$):

$$h_u \sim \frac{k}{\delta_{Tc}} \tag{11}$$

According to the Patterson and Imberger analysis, the thickness of the boundary layer adjacent to the constant temperature wall is:

$$\delta_{Tc} \sim \frac{H_u}{(Ra_{\Delta Tu})^{1/4}} \tag{12}$$

where:

$$\mathrm{Ra}_{\Delta Tu} = \frac{g \, \beta \, (T_u - T_o) H_u^3}{\alpha \nu}. \tag{13}$$

Substituting Eq. (12) into Eq. (11), the heat transfer coefficient is:

$$h_u \sim \frac{k \, (\mathrm{Ra}_{\Delta Tu})^{1/4}}{H_u}. \tag{14}$$

Using Eqs. (9) and (13), the former expression becomes:

$$h_u \sim \frac{k \, (\mathrm{Ra}_{\Delta Tc})^{1/4}}{H_u^{1/2} \, H^{1/2}}. \tag{15}$$

where $\mathrm{Ra}_{\Delta Tc}$ is defined by the expression:

$$\mathrm{Ra}_{\Delta Tc} = \frac{g \, \beta (T - T_o) H^3}{\alpha \nu}. \tag{16}$$

When $H_u = H$, Eq. (15) becomes the heat transfer coefficient for a vertical plate with length H.

The growth of H_u is due to two effects, the incoming hot fluid from the boundary layer and the heat diffusing from the upper region into the core. The first can be estimated by observing that the volume of the heated fluid ($\sim H_u \, L \, W$) is equal to the volume of fluid that has passed through the boundary layer adjacent to the heated wall ($\sim W \, \delta_T \, Vt$) while the second is $\sim (\alpha t)^{1/2}$, i.e.,

$$H_u \sim \frac{V \, \delta_T \, t}{L} + (\alpha t)^{1/2} \tag{17}$$

Substituting Eqs. (4) and (5) into Eq. (17), H_u can be expressed in terms of Ra as:

$$H_u \sim \frac{\alpha \, \mathrm{Ra}^{1/5} \, t}{L} + (\alpha t)^{1/2} \tag{18}$$

Finally, using this expression to eliminate H_u from Eq. (15), the time-dependent heat transfer coefficient for the constant temperature wall can be obtained:

$$h_u = C \frac{k \, (\mathrm{Ra}_{\Delta Tc})^{1/4}}{(A \alpha \mathrm{Ra}^{1/5} t + (H^2 \alpha t)^{1/2})^{1/2}} \tag{19}$$

where $A = H/L$ is the aspect ratio of the cavity and C is a dimensionless constant of order unity.

2.3 Total Stratification. After sufficient time has elapsed, the thermal stratification pattern covers the whole volume of the cavity. The time required is denoted by τ_t and can be estimated using Eq. (18) and assuming $H_u = H$, i.e.,

$$\tau_t \sim \frac{L \, H}{\alpha \, \mathrm{Ra}^{1/5}} \tag{20}$$

From then onward, the heat transfer coefficient is:

$$h_c = C \frac{k \, (\mathrm{Ra}_{\Delta Tc})^{1/4}}{H} \tag{21}$$

Upon substituting h_c from Eq. (21) as h_u in the heat balance equation (Eq. (10)), the following expression is obtained:

$$C_p \, M \frac{dT}{dt} = q \, H \, W - C \, k \, W \, \mathrm{Ra}_{\Delta Tc}^{1/4} (T - T_o) \tag{22}$$

The steady-state temperature can be calculated using the heat balance equation, setting $dT/dt=0$. The resulting expression for the temperature is

$$T|_{dT/dt=0}=T_s=T_o+\Delta T \tag{23a}$$

where

$$\Delta T=\frac{q^{4/5}}{k^{4/5}\left\{\frac{g\,\beta}{H\,\alpha\,\nu}\right\}^{1/5}}=T^*\ \mathrm{Ra}^{4/5} \tag{23b}$$

and

$$T^*=\frac{\alpha\,\nu}{g\beta H^3}$$

ΔT denotes the average temperature increment. Expression (23*b*) was also obtained by Kimura and Bejan (1984) as a temperature difference scale in their steady-state analysis of natural convection in a cavity with uniform heat input and output from the side. Substituting the final temperature T_s into the expression for the Rayleigh number based on the temperature difference (Eq. (16)), the following relation can be established between the steady-state Rayleigh numbers: $\mathrm{Ra}^{4/5}=\mathrm{Ra}_{\Delta Tc}$.

3 Discussion and Comparison With the Numerical Model

The theory presented in the previous sections will be discussed and compared with the results of a full numerical integration of the balance equations presented by Poujol et al. (1993).

In terms of the nondimensional variables $T'=(T-T_o)/(T_s-T_o)$ and $t'=(Wk/MC_p)\,t$, Eqs. (1), (10), and (22) are:

I Initial Heating

$$\frac{dT'}{dt'}=\mathrm{Ra}^{1/5}\qquad 0<t'<\frac{1}{A^{1/4}\mathrm{Ra}^{7/20}}$$

II Partial Stratification

$$\frac{dT'}{dt'}=\mathrm{Ra}^{1/5}\left[1-\frac{T'^{5/4}}{(t'\mathrm{Ra}^{1/5}+(t'/A)^{1/2})^{1/2}}\right]$$

$$\frac{1}{A^{1/4}\mathrm{Ra}^{7/20}}<t'<\frac{1}{\mathrm{Ra}^{1/5}}$$

III Total Stratification

$$\frac{dT'}{dt'}=\mathrm{Ra}^{1/5}\,(1-T'^{5/4})\qquad \frac{1}{\mathrm{Ra}^{1/5}}<t'$$

Comparison of the results presented above with those of the numerical solution are given in terms of an example. The numerical values of the parameters used in the example discussed below are: $A=1$, $T^*=1.01\times10^{-7}$ and $\mathrm{Ra}=4\times10^9$. In the numerical model a fluid with Prandtl number of 220 was assumed and therefore, the constraints $\mathrm{Pr}>1$ required for Eqs. (2), (4), and (5) and $\mathrm{Pr}^{25/2}>\mathrm{Ra}$ for Eq. (6) are satisfied. The numerical results were found with the PHOENICS program and using a nonuniform mesh of 81×81 volumes, which was selected after a grid independence study was carried out. Further refinement of the mesh to 101×101 volumes resulted in differences smaller than 1 percent in the temperature fields. A full discussion of the results obtained with the numerical integration can be found from Poujol et al. (1993). It is interesting to notice that due to the aspect ratio and the large value of the Rayleigh number considered, the diffusive effect in the partial stratification regime can be neglected and the corresponding heat transfer equation can be substituted by the following simpler expression:

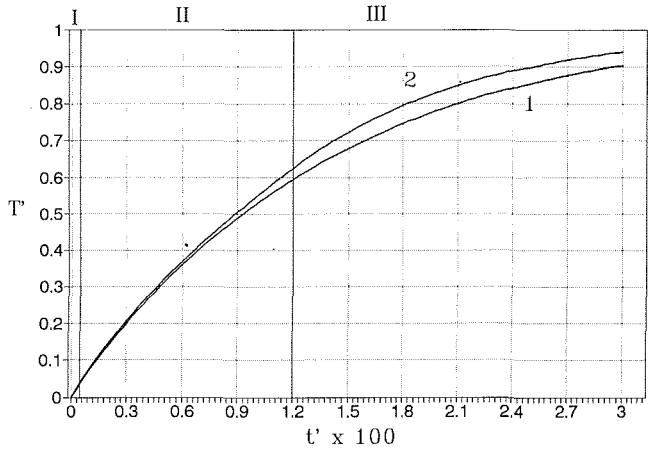

Fig. 2 Temperature as a function of time: (1) complete numerical solution of transport equations; (2) Runge-Kutta integration results from the proposed model; (I) initial heating, (II) partial stratification, (III) total stratification

$$\frac{dT'}{dt'}=\mathrm{Ra}^{1/5}-\frac{\mathrm{Ra}^{1/10}\,T'^{5/4}}{t'^{1/2}}$$

The steady-state temperature T_s obtained with the simplified model is $2.93\times10^8\ T^*$ while the numerical solution gives $T_s=3\times10^8\ T^*$. In the discussion that follows, the temperature in the model will be scaled with the steady-state value obtained in the model, while the temperature from the numerical calculation is normalized with its own steady-state value.

Figure 2 shows the temperature T' as predicted from the model (obtained with Runge-Kutta integration) as a function of t', together with the corresponding results of a complete numerical model. As it can be appreciated, a full integration and the simple theory are in qualitative agreement, although the result from the simple model overestimates the temperature by about 7 percent in the region of partial stratification. Substituting the temperature into the other expressions, it would be possible to find other properties of the flow.

4 Conclusion

A simple analytical model that predicts the time evolution of the average temperature of a cavity heated on one vertical wall has been presented. The model is based on the assumption that the flow can be separated into three stages: initial heating, partial stratification, and total stratification. The comparison of the results obtained with the model with those of a full numerical integration of the balance equations indicates that the model correctly captures the average dimensionless temperature in the enclosure during the transient time.

References

Kimura, S., and Bejan, A., 1984, "The Boundary Layer in Natural Convection Regime in a Rectangular Cavity With Uniform Heat Flow From the Side," ASME JOURNAL OF HEAT TRANSFER, Vol. 106, pp. 98-103.

Patterson, J. C., and Imberger, J., 1980, "Unsteady Natural Convection in a Rectangular Cavity," *J. Fluid Mech.*, Vol. 100, pp. 65-86.

Poujol, F., Rojas, J., and Ramos, E., 1993, "Transient Natural Convection in a Cavity With Heat Input and a Constant Temperature Wall on Opposite Sides," *Int. J. Heat Fluid Flow*, Vol. 14, No. 4, pp. 357-365.

Effects of Refractive Index and Diffuse or Specular Boundaries on a Radiating Isothermal Layer

R. Siegel[1,3] and C. M. Spuckler[2,3]

Nomenclature

a = absorption coefficient of layer, m^{-1}
c = specific heat of solid, W • s/kg • K
D = thickness of plane layer, m
$e_{\lambda b}$ = blackbody spectral emissive power, W/m^2 • μm
E_3 = exponential integral function, $E_3(\xi) = \int_0^1 \mu \exp(-\xi/\mu) d\mu$
F_m = blackbody fraction of mth spectral band
n = index of refraction
q = heat flux, W/m^2; q_λ, spectral flux, W/m^2 • μm
$q_{\lambda r1}$, $q_{\lambda r2}$ = externally incident spectral radiation fluxes, W/m^2 • μm
T_e = temperature of environment, K; $\tilde{T}_e = T_e/T_0$
T_0 = layer temperature at time $t = 0$, K
T_w = absolute temperature of layer, K; $\tilde{T}_w = T_w/T_0$
T_1, T_2 = temperatures of radiating surroundings, K
t = time, s; dimensionless time, $\tilde{t} = t\sigma T_0^3/\rho cD$
α, ϵ = absorptance and emittance of plane layer
θ = angle of incidence
ρ = reflectivity of interface; density of solid, kg/m^3
σ = Stefan-Boltzmann constant, W/m^2 • K^4
τ = transmittance of path at angle χ, $\tau = \exp(-aD/\cos\chi)$
χ = angle of refraction

Subscripts

dif = for diffuse surfaces
i, o = incoming and outgoing radiation
m = the mth spectral band
s = for specular surfaces
λ = spectral quantity
$\perp$, $\parallel$ = components for perpendicular and parallel polarization

Superscripts

i, o = at inside or outside surface of an interface

Introduction

Ceramics are under development for high-temperature applications such as in combustion chambers of high-speed aircraft. Some ceramics are reinforced with ceramic fibers, and to protect the composite from the combustion environment it is coated with another ceramic to form a laminated layer. To model these materials thermally in order to study possible radiation effects arising from their partial transparency, it is necessary to specify the nature of reflections at their interfaces. A convenient assumption is that reflections are diffuse; this may be realistic because some external surfaces and internal interfaces of ceramics are rough. Some surfaces, however, may be smooth so they are specularly reflecting. This note will examine in a simple way by considering an isothermal layer, some effects of diffuse versus specular boundary conditions. In some cases the diffuse condition yields increased temperatures due to augmented retention of incident energy by internal reflections. This is a function of the refractive index of the material. Much of the work in the literature is for glass, $n \approx 1.5$; for ceramics n can be significantly larger, thus providing increased internal radiation effects. The limiting condition is examined where there is no scattering inside the layer as this demonstrates the maximum effect of the surface condition. For specular surfaces, a small amount of scattering within the layer produces a partially diffuse behavior; for large scattering, diffuse behavior will result.

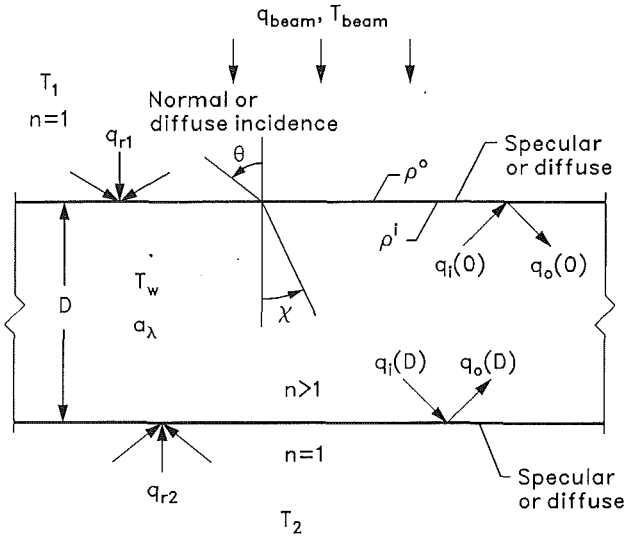

Fig. 1 Plane layer with specular or diffuse boundaries and with diffuse or normally incident radiation

Analysis

Absorptance of Layer With Specular Boundaries and No Internal Scattering. The layer in Fig. 1 with refractive index $n > 1$ has incident diffuse or beam energy. The layer partially absorbs radiation, but does not scatter internally. For specularly reflecting surfaces, radiation in each incident direction θ is refracted and internally reflected as given by Fresnel relations. The fraction of energy absorbed is given as (Siegel and Howell, 1992, p. 929): $\alpha(\theta) = [1 - \rho^o(\theta)][1 - \tau(\theta)]/[1 - \rho^o(\theta)\tau(\theta)]$ where the internal transmittance is $\tau(\theta) = \exp[-aD/\cos\chi(\theta)]$ and the angle of refraction is $\chi(\theta) = \sin^{-1}[(\sin\theta)/n]$. The reflectivity $\rho^o(\theta)$ is a function of the polarization component so $\alpha(\theta)$ has values corresponding to the perpendicular and parallel components. For diffuse incidence of unpolarized radiation, the absorptance of a layer with specular surfaces is found by integrating the absorbed energy for all incident solid angles to give

$$\alpha_s(n, aD) = \int_0^{\pi/2} [\alpha_\perp(\theta) + \alpha_\parallel(\theta)] \cos\theta \sin\theta \, d\theta \qquad (1)$$

where the ρ^o needed to obtain $\alpha_\perp$ and $\alpha_\parallel$ are

$$\rho_\perp^o(\theta) = \left[\frac{(n^2 - \sin^2\theta)^{1/2} - \cos\theta}{(n^2 - \sin^2\theta)^{1/2} + \cos\theta}\right]^2 \qquad (2a)$$

$$\rho_\parallel^o(\theta) = \left[\frac{n^2\cos\theta - (n^2 - \sin^2\theta)^{1/2}}{n^2\cos\theta + (n^2 - \sin^2\theta)^{1/2}}\right]^2 \qquad (2b)$$

[1]Senior Research Scientist; Fellow ASME.
[2]Research Scientist; Assoc. Mem. ASME.
[3]NASA Lewis Research Center, 21000 Brookpark Rd., Cleveland, OH 44135.
Contributed by the Heat Transfer Division of The American Society of Mechanical Engineers. Manuscript received by the Heat Transfer Division June 1993; revision received November 1993. Keywords: Radiation. Associate Technical Editor: M. F. Modest.

With all quantities in Eq. (1) in terms of θ, the integration is performed numerically for various n and aD. For the special case of normal incidence, $\alpha_s = (1 - \rho^o)(1 - \tau)/(1 - \rho^o\tau)$ where $\rho^o = [(n - 1)/(n + 1)]^2$ and $\tau = \exp(-aD)$.

For emission from an isothermal layer, the local internal emission is considered for each direction. Radiation internally incident on a boundary is totally reflected if it arrives at an angle larger than the critical angle for reflection, which depends on n. The formulation by Gardon (1956) for the emittance of an isothermal layer with specular boundaries provides the same result as α_s in Eq. (1); this is expected from Kirchhoff's law.

Absorptance of a Layer With Diffuse Boundaries and No Internal Scattering. The layer boundaries are now considered diffuse. For a rough surface it is assumed that incident radiation will strike surface elements at random angles so the surface reflectivity is independent of the angular distribution of the incident energy. Hence all energy incident upon and leaving a boundary is considered to behave in a diffuse manner. The diffuse reflectivity is given by the hemispherically averaged relation of the Fresnel equations (Siegel and Howell, 1992, p. 115),

$$\rho^o_{\text{dif}}(n) = \frac{1}{2} + \frac{(3n+1)(n-1)}{6(n+1)^2} + \frac{n^2(n^2-1)^2}{(n^2+1)^3}\ln\left(\frac{n-1}{n+1}\right) - \frac{2n^3(n^2+2n-1)}{(n^2+1)(n^4-1)} + \frac{8n^4(n^4+1)}{(n^2+1)(n^4-1)^2}\ln(n) \quad (3)$$

The absorptance of the layer is obtained by considering its interaction with a unit incident flux, $q_{r1} = 1$. The outgoing flux from the internal side of each diffuse boundary (see Fig. 1) is then

$$q_o(0) = 1 - \rho^o_{\text{dif}} + q_i(0)\rho^i_{\text{dif}};\ q_o(D) = q_i(D)\rho^i_{\text{dif}} \quad (4a, b)$$

where ρ^i_{dif} is at the internal side of a diffuse boundary. As a result of transmission within the layer, the fluxes at the two internal sides of the boundaries are related by (Siegel and Howell, 1992, p. 707)

$$q_i(0) = 2q_o(D)E_3(aD);\ q_i(D) = 2q_o(0)E_3(aD) \quad (5a, b)$$

Equations (4) and (5) are solved for $q_o(0)$, $q_o(D)$, $q_i(0)$, and $q_i(D)$. The fraction of incident energy that is absorbed is $\alpha_{\text{dif}} = 1 - (1 - \rho^i_{\text{dif}})[q_i(0) + q_i(D)]$, which yields

$$\alpha_{\text{dif}}(n, aD) = (1 - \rho^o_{\text{dif}})\frac{1 - 2E_3(aD)}{1 - \rho^i_{\text{dif}}2E_3(aD)} \quad (6)$$

To place α_{dif} in terms of the reflectivity ρ^o_{dif} on the outer surface of a boundary, the relation can be used that (Richmond, 1963) $\rho^i_{\text{dif}} = 1 - (1/n^2)(1 - \rho^o_{\text{dif}})$.

Heat Balance Relations for Layer Temperature With Transfer Only by Radiation. The layer absorptances are spectral quantities since the absorption coefficient depends on wavelength. Two examples are given to demonstrate effects of diffuse and specular boundaries. The first is the equilibrium temperature attained by an isothermal layer subjected to radiation incident on both boundaries and with radiation being the only means of energy transfer. The balance of absorbed and emitted energy is

$$\int_0^\infty (q_{\lambda r1} + q_{\lambda r2})\alpha_\lambda(n, a_\lambda D)d\lambda = 2\int_0^\infty \epsilon_\lambda(n, a_\lambda D)e_{\lambda b}(\lambda, T_w)d\lambda \quad (7)$$

where $\epsilon_\lambda = \alpha_\lambda$. Equation (7) is solved for the equilibrium temperature T_w.

A second example is the radiative cooling of a layer initially at temperature T_0, when placed in surroundings at $T_1 = T_2 \equiv T_e$. This is governed by the transient energy equation

$$-\rho cD\frac{\partial T_w}{\partial t} = 2\int_0^\infty \epsilon_\lambda(n, a_\lambda D)[e_{\lambda b}(\lambda, T_w) - e_{\lambda b}(\lambda, T_e)]d\lambda \quad (8)$$

For a spectrally banded calculation with M bands with each band designated by m,

$$-\rho cD\frac{\partial T_w}{\partial t} = 2\sum_{m=1}^{M}\epsilon_m(n, a_mD)[F_m(T_w)\sigma T_w^4 - F_m(T_e)\sigma T_e^4] \quad (9)$$

This is placed in dimensionless form and integrated to give

$$f(\tilde{T}_w) = \frac{1}{2}\int_{\tilde{T}_w(t)}^1 \frac{d\tilde{T}_w^*}{\sum_{m=1}^{M}\epsilon_m(n, a_mD)[F_m(\tilde{T}_w^*T_0)\tilde{T}_w^{*4} - F_m(T_e)\tilde{T}_e^4]} \quad (10)$$

Equation (10) is numerically integrated to yield cooling curves for various T_0 and T_e.

Results and Discussion

Absorptance of Layer. For specular boundaries the layer absorptance was evaluated from Eq.(1) for both diffuse and normal incidence of external radiation. Results are in Fig. 2(*a*) for refractive indices from 1 to 4 and optical thicknesses up to 4. For $a_\lambda D$ larger than 4 almost all incident energy that is not reflected is absorbed in the layer. The layer absorptance then approaches an asymptotic value of one minus the external reflectivity of the boundary. Since the boundary reflectivity is smaller for normal incidence than for diffuse, the $\alpha_{\lambda,s}$ is larger for normal incidence. For $a_\lambda D < 4$ the $\alpha_{\lambda,s}$ is influenced by the radiative path lengths within the layer. For a large n, incident diffuse energy is refracted into a small cone angle around the normal direction through the layer. Radiation within the nonscattering layer then travels along paths not much longer than the path length D for normal incidence; hence, for large n the $\alpha_{\lambda,s}$ becomes independent of normal or diffuse incidence. There are differences in $\alpha_{\lambda,s}$ when n is near 1 and refraction is therefore small. Diffuse radiation then travels along longer paths and $\alpha_{\lambda,s}$ becomes increased. This is compensated somewhat by the reflectivity of the external boundary being larger for diffuse incident radiation than for radiation incident in the normal direction.

In Fig. 2(*b*) the absorptance of a layer with diffuse boundaries is compared with that for specular boundaries; the incident radiation is diffuse. The nature of the boundary has a very significant effect when $a_\lambda D$ is less than about 3. For $n = 1$ there are no surface reflections so the results are the same for the solid and dashed curves. As n is increased the absorptance values become increasingly different, so for $n = 4$ with $a_\lambda D < 3$ there is a substantial difference in α_λ. For specular boundaries α_λ decreases as the angle of refraction becomes smaller with larger n, thus providing shorter path lengths for absorption in the layer. For diffuse boundaries the increase in α_λ with n is attributed to radiation within the layer being diffused at the boundaries into directions larger than the critical angle for reflection. This tends to retain energy within the layer and increase its absorption as radiation travels internally by multiple reflections. The effect that this can have on the layer temperature is shown by results that follow as calculated from Eqs. (7) and (10). If a layer with specular boundaries has internal scattering it will act more like a diffuse layer; the results here are without internal scattering and are expected to show the maximum possible effect of the two different types of boundaries.

Effect of Surface Condition on Layer Temperature. To illustrate how surface condition can affect the layer temper-

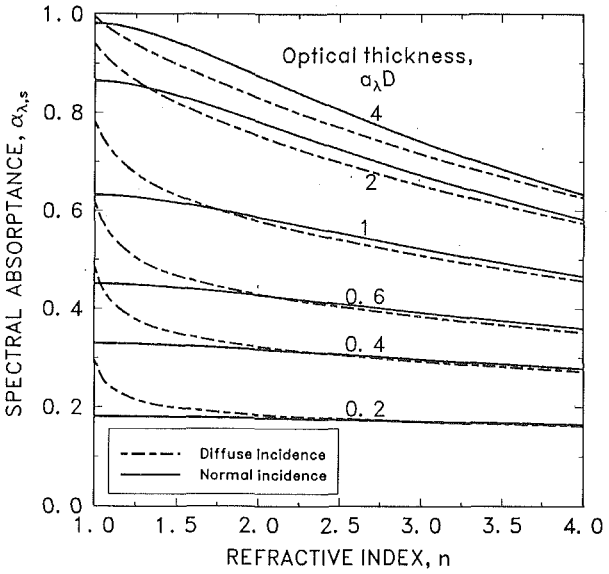

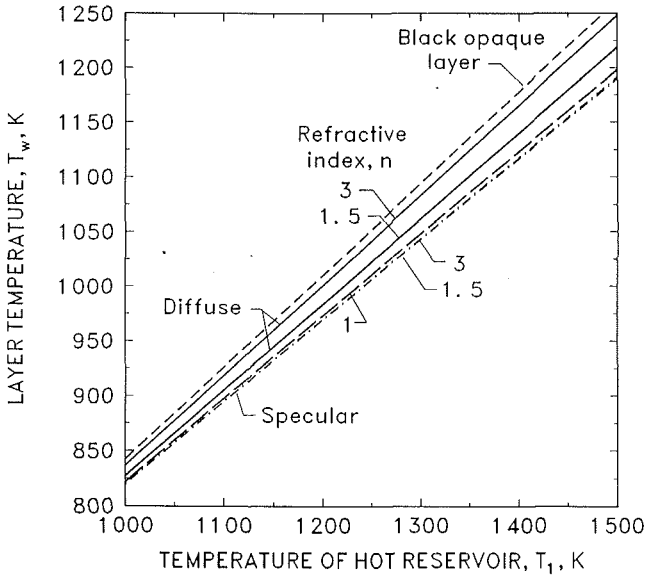

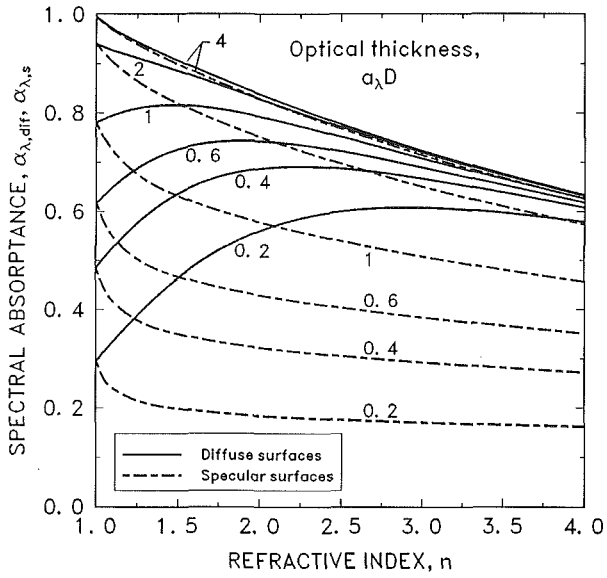

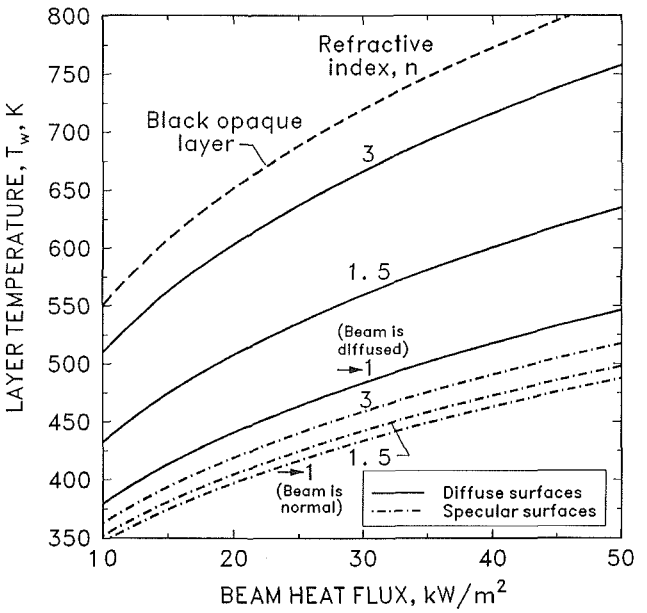

Fig. 2 The effect of diffuse or specular boundaries, and beam or diffuse incidence, on spectral absorptance (or spectral emittance) of a plane layer without internal scattering as a function of optical thickness and refractive index: (*a*) Boundaries are specular and incident external radiation is diffuse or is in the normal direction; (*b*) boundaries are diffuse, or are specular with diffuse incident radiation

Fig. 3 Effect of diffuse or specular boundaries on the equilibrium temperature of a layer with a refractive index of 1.5 or 3, and for the limiting case $n = 1$. The spectral absorption properties are similar to glass (a_λ = 0.2, 4, 100 cm^{-1} for λ = 0–2.7, 2.7–4.4, 4.4–∞ μm) and there is no internal scattering; T_2 = 300 K. (*a*) Incident radiation on one side is from a hot reservoir at T_1. (*b*) Incident radiation on one side is a beam normal to the layer with a spectral distribution like that of solar radiation.

ature, results are given for a layer with $D = 0.5$ cm and a_λ approximated as constant in each of three spectral bands, similar to the properties of glass: a_λ = 0.2, 4, 100 cm^{-1} for λ = 0–2.7, 2.7–4.4, 4.4–∞ μm. Using these properties the spectral absorptance and emittance in each band was obtained from Eqs. (1) and (6). The equilibrium temperature T_w for heat transfer only by radiation was then obtained from Eq. (7), and transient radiative cooling results were evaluated from Eq. (10).

Figures 3(*a*) and 3(*b*) show how equilibrium temperatures are affected for two different conditions of the incident radiation. As shown by Fig. 2(*b*), when $a_\lambda D$ is small the specular and diffuse boundary conditions produce significantly different α_λ. Hence for a layer without internal scattering the condition of the boundary can produce large differences in energy absorption if there is large incident energy in wavelength regions where $a_\lambda D$ is small. For a high temperature radiant source the incident energy fraction is large in the short wavelength region where semitransparent materials can have a small a_λ. The wavelength selective heat balance can then be sensitive to the specification of specular or diffuse boundary conditions. Reradiation is at longer wavelengths where $a_\lambda D$ is generally large; hence from the results in Fig. 2(*b*) the reradiated energy is not affected significantly by the boundary being specular or diffuse. For a moderate source temperature both the incident and emitted energy will be at long wavelengths where $a_\lambda D$ can be large causing α_λ to be insensitive to specular or diffuse boundaries.

In Fig. 3(*a*) the layer temperature T_w is given for radiative heating by blackbody reservoirs with T_1 given on the abscissa, and T_2 = 300 K. The T_w is given for diffuse and specular boundaries with the layer refractive index $n = 1$, 1.5, and 3. For $n = 1$ there are no surface reflections so the energy balance

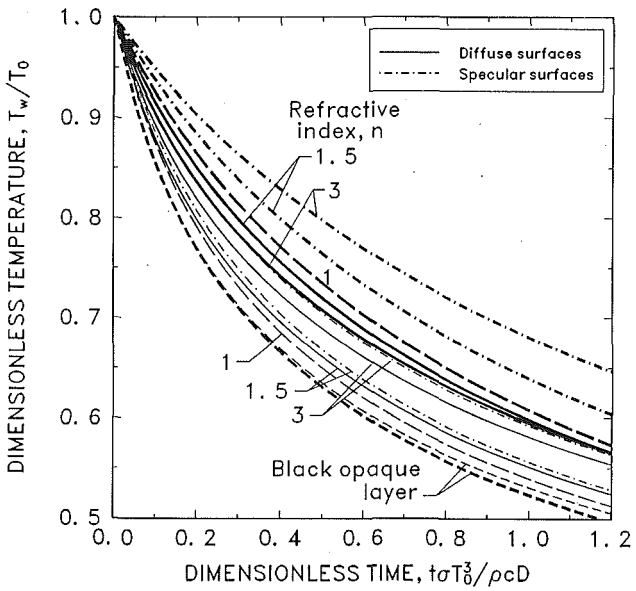

Fig. 4 Transient cooling of a layer with initial temperature T_0 = 1000 K (thin lines) or 2000 K (thick lines), T_e = 300 K, and with the same absorption properties as for Fig. 3 (a_λ = 0.2, 4, 100 cm^{-1} for λ = 0-2.7, 2.7-4.4, 4.4-∞ μm); comparisons are made for diffuse and specular boundaries with n = 1.5 and 3 (for n = 1 there are no surface reflections)

depends only on internal absorption and emission. For $n > 1$ the higher α_λ for small $a_\lambda D$ with diffuse boundaries produces increased absorption. The resulting T_w for diffuse boundaries is somewhat higher than for the specular case and the difference increases to a maximum of about 50 K as n and T_1 are increased. The temperature for an opaque black layer (or an opaque gray layer with diffuse boundaries) is shown as an upper limit. From Eq. (7) this is given by $T_w = [(T_1^4 + T_2^4)/2]^{1/4}$.

For Fig. 3(b) the nature of the incident radiation is changed on the hot side of the layer. The incident energy is a beam normal to the layer with its heat flux given on the abscissa. Two limiting cases are given for $n \to 1$; the solid curve is for the beam being diffused at the boundary, and the dot-dash curve is for the beam remaining normal to the boundary as it passes into the layer. The heat flux is high (for comparison the solar constant at earth orbit is about 1.35 kW/m^2) and has the same spectral distribution as solar energy (blackbody spectrum at 5780 K). This spectrum provides a much larger energy fraction in the short wavelength region than the hot reservoir in Fig. 3(a) and produces substantially higher T_w when the boundaries are diffuse. The upper limit is shown for a black opaque plate as given by $T_w = [(q_{\text{beam}}/\sigma + T_2^4)/2]^{1/4}$.

Effect of Surface Condition on Transient Radiative Cooling. Transient radiative cooling results from Eq. (10) are in Fig. 4 for two initial temperatures T_0 = 1000 K (thin lines) and 2000 K (thick lines), and T_e = 300 K. The absorption properties are the same as for Fig. 3. For n = 1 there are no surface reflections and hence no effect on cooling of the boundary being specular or diffuse. For T_0 = 1000 K most of the energy radiated by the layer is in the long wavelength region where $a_\lambda D$ is large for the spectral properties used here. For large $a_\lambda D$, Fig. 2(b) shows that increasing n decreases the $\alpha_\lambda = \epsilon_\lambda$ so the cooling is less rapid. The ϵ_λ is smaller for specular surfaces, which produce longer cooling times. The situation changes somewhat when T_0 is increased to 2000 K. A greater fraction of the energy is then in the short wavelength regions where $a_\lambda D$ is small. This changes the trend for the solid curves (diffuse surfaces) in Fig. 2(b) which, for small $a_\lambda D$, show ϵ_λ increasing with n to a maximum. This enhances the cooling rate with the increase in n as shown in Fig. 4 by the thick solid curves as compared with the n = 1 results (thick dashed curve). The limiting results are also shown for cooling of a black opaque layer. In this instance there is no effect of spectral selectivity and the layer with highest initial temperature T_0 cools most rapidly.

Conclusions

Equilibrium temperatures of an absorbing-emitting layer were obtained for exposure to incident radiation and with the layer boundaries either specular or diffuse. For high refractive indices the surface condition can influence the radiative heat balance if the layer optical thickness is small. Hence for a spectrally varying absorption coefficient the layer temperature is affected if there is significant radiative energy in the spectral range with a small absorption coefficient. Similar behavior was obtained for transient radiative cooling of a layer where the results are affected by the initial temperature and hence the fraction of energy radiated in the short wavelength region where the absorption coefficient is small. The results are for a layer without internal scattering. If internal scattering is significant, the radiation reaching the internal surface of a boundary is diffused and the effect of the two different surface conditions would become small.

References

Gardon, R., 1956, "The Emissivity of Transparent Materials," *Journal of the American Ceramic Society*, Vol. 39, No. 8, pp. 278-287.

Richmond, J. C., 1963, "Relation of Emittance to Other Optical Properties," *Journal of Research of the National Bureau of Standards*, Vol. 67C, No. 3, pp. 217-226.

Siegel, R., and Howell, J. R., 1992, *Thermal Radiation Heat Transfer*, 3rd ed., Hemisphere Publishing Corporation, Washington, DC.

Forced Convective Cooling of Optical Fiber During Drawing Process

S. Roy Choudhury,[1] Y. Jaluria,[1] T. Vaskopoulos,[1] and C. E. Polymeropoulos[1]

Nomenclature

h = surface convection heat transfer coefficient
H = channel width = $r_H - r_0$
K = thermal conductivity
m = fluid mass flow rate
Nu = local Nusselt number = hr_0/K_f
r, x = coordinate distances in the radial and axial directions, respectively
r_0 = radius of the moving fiber
R, X = dimensionless r and x, $R = x/r_0$, $X = x/r_0$
T = local physical temperature

[1]Department of Mechanical and Aerospace Engineering, Rutgers University, New Brunswick, NJ 08903.

Contributed by the Heat Transfer Division and presented at the National Heat Transfer Conference, Atlanta, Georgia, August 8-11, 1993. Manuscript received by the Heat Transfer Division June 1993; revision received November 1993. Keywords: Conjugate Heat Transfer, Forced Convection, Materials Processing and Manufacturing Processes. Associate Technical Editor: R. Viskenta.

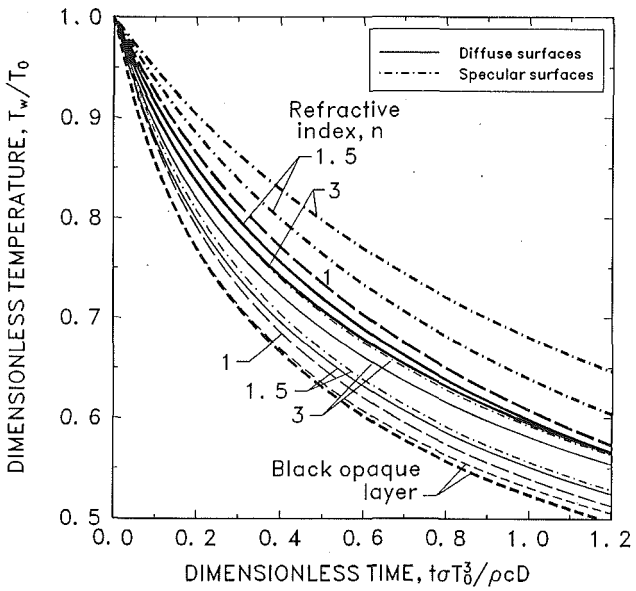

Fig. 4 Transient cooling of a layer with initial temperature T_0 = 1000 K (thin lines) or 2000 K (thick lines), T_e = 300 K, and with the same absorption properties as for Fig. 3 (a_λ = 0.2, 4, 100 cm^{-1} for λ = 0-2.7, 2.7-4.4, 4.4-∞ μm); comparisons are made for diffuse and specular boundaries with n = 1.5 and 3 (for n = 1 there are no surface reflections)

depends only on internal absorption and emission. For $n > 1$ the higher α_λ for small $a_\lambda D$ with diffuse boundaries produces increased absorption. The resulting T_w for diffuse boundaries is somewhat higher than for the specular case and the difference increases to a maximum of about 50 K as n and T_1 are increased. The temperature for an opaque black layer (or an opaque gray layer with diffuse boundaries) is shown as an upper limit. From Eq. (7) this is given by $T_w = [(T_1^4 + T_2^4)/2]^{1/4}$.

For Fig. 3(b) the nature of the incident radiation is changed on the hot side of the layer. The incident energy is a beam normal to the layer with its heat flux given on the abscissa. Two limiting cases are given for $n \to 1$; the solid curve is for the beam being diffused at the boundary, and the dot-dash curve is for the beam remaining normal to the boundary as it passes into the layer. The heat flux is high (for comparison the solar constant at earth orbit is about 1.35 kW/m^2) and has the same spectral distribution as solar energy (blackbody spectrum at 5780 K). This spectrum provides a much larger energy fraction in the short wavelength region than the hot reservoir in Fig. 3(a) and produces substantially higher T_w when the boundaries are diffuse. The upper limit is shown for a black opaque plate as given by $T_w = [(q_{\text{beam}}/\sigma + T_2^4)/2]^{1/4}$.

Effect of Surface Condition on Transient Radiative Cooling. Transient radiative cooling results from Eq. (10) are in Fig. 4 for two initial temperatures T_0 = 1000 K (thin lines) and 2000 K (thick lines), and T_e = 300 K. The absorption properties are the same as for Fig. 3. For n = 1 there are no surface reflections and hence no effect on cooling of the boundary being specular or diffuse. For T_0 = 1000 K most of the energy radiated by the layer is in the long wavelength region where $a_\lambda D$ is large for the spectral properties used here. For large $a_\lambda D$, Fig. 2(b) shows that increasing n decreases the $\alpha_\lambda = \epsilon_\lambda$ so the cooling is less rapid. The ϵ_λ is smaller for specular surfaces, which produce longer cooling times. The situation changes somewhat when T_0 is increased to 2000 K. A greater fraction of the energy is then in the short wavelength regions where $a_\lambda D$ is small. This changes the trend for the solid curves (diffuse surfaces) in Fig. 2(b) which, for small $a_\lambda D$, show ϵ_λ increasing with n to a maximum. This enhances the cooling rate with the increase in n as shown in Fig. 4 by the thick solid curves as compared with the n = 1 results (thick dashed curve). The limiting results are also shown for cooling of a black opaque layer. In this instance there is no effect of spectral selectivity and the layer with highest initial temperature T_0 cools most rapidly.

Conclusions

Equilibrium temperatures of an absorbing-emitting layer were obtained for exposure to incident radiation and with the layer boundaries either specular or diffuse. For high refractive indices the surface condition can influence the radiative heat balance if the layer optical thickness is small. Hence for a spectrally varying absorption coefficient the layer temperature is affected if there is significant radiative energy in the spectral range with a small absorption coefficient. Similar behavior was obtained for transient radiative cooling of a layer where the results are affected by the initial temperature and hence the fraction of energy radiated in the short wavelength region where the absorption coefficient is small. The results are for a layer without internal scattering. If internal scattering is significant, the radiation reaching the internal surface of a boundary is diffused and the effect of the two different surface conditions would become small.

References

Gardon, R., 1956, "The Emissivity of Transparent Materials," *Journal of the American Ceramic Society*, Vol. 39, No. 8, pp. 278-287.

Richmond, J. C., 1963, "Relation of Emittance to Other Optical Properties," *Journal of Research of the National Bureau of Standards*, Vol. 67C, No. 3, pp. 217-226.

Siegel, R., and Howell, J. R., 1992, *Thermal Radiation Heat Transfer*, 3rd ed., Hemisphere Publishing Corporation, Washington, DC.

Forced Convective Cooling of Optical Fiber During Drawing Process

S. Roy Choudhury,[1] Y. Jaluria,[1] T. Vaskopoulos,[1] and C. E. Polymeropoulos[1]

Nomenclature

h = surface convection heat transfer coefficient
H = channel width = $r_H - r_0$
K = thermal conductivity
m = fluid mass flow rate
Nu = local Nusselt number = hr_0/K_f
r, x = coordinate distances in the radial and axial directions, respectively
r_0 = radius of the moving fiber
R, X = dimensionless r and x, $R = x/r_0$, $X = x/r_0$
T = local physical temperature

[1]Department of Mechanical and Aerospace Engineering, Rutgers University, New Brunswick, NJ 08903.

Contributed by the Heat Transfer Division and presented at the National Heat Transfer Conference, Atlanta, Georgia, August 8-11, 1993. Manuscript received by the Heat Transfer Division June 1993; revision received November 1993. Keywords: Conjugate Heat Transfer, Forced Convection, Materials Processing and Manufacturing Processes. Associate Technical Editor: R. Viskenta.

T_0 = uniform temperature of fiber entering the channel
u, v = velocity components in x and r directions, respectively
U, V = dimensionless u and v, $U = u/U_s$, $V = v/U_s$
U_s = physical fiber speed
θ = dimensionless local temperature $\theta = (T - T_\infty)/(T_o - T_\infty)$

Subscripts

∞ = ambient medium
f = fluid medium
surface = fiber surface
H = channel wall
out = outlet

1 Introduction

Optical fibers are manufactured by a continuous drawing process. A solid preform rod made of silica glass is peripherally heated and softened in a furnace and then drawn along the axial direction in air and continuously wound on a drum (Fig. 1(*a*)). The rate at which fiber loses energy as it passes through the surrounding environment is of considerable practical importance. In particular, optical fibers are believed to derive their remarkably high strength from the rapid cooling as they are being formed. To preserve the pristine state of the surface and to maintain the high mechanical strength of the fiber, the newly drawn fibers have to be coated with an organic substance. The temperature at which the fiber comes out of the furnace is of the order of 1600°C, but coating cannot be applied above 200°C because of practical difficulties (Kyriacou et al., 1990). If the optical fiber is drawn at very high speed to obtain high productivity, the "natural" cooling of the fiber is not sufficient to bring the temperature of the fiber down to the desired level before it reaches the coating cup, for typical values of fiber diameter, speed, and distance between the coating cup and the furnace. Because of this limitation, very often forced convective cooling is employed to accelerate the heat transfer process. During the cooling process the buoyancy effects are small and are, therefore, neglected in this study (Roy Choudhury and Jaluria, 1994).

The basic features of the axisymmetric flow induced by a long, continuously moving cylindrical fiber in a uniform aiding, opposing, or peripheral forced flow are shown in Fig. 1. For the aiding flow, the flow is either accelerated or retarded near the fiber, depending on the fiber and flow speeds. In case of the opposing flow, however, the fiber invariably slows down the opposing external forced flow near the solid surface and, at some distance from the entrance, the flow velocity changes direction as one moves away from the fiber surface. Consequently, a recirculating flow region develops near the surface of the fiber. For the peripheral flow, depending on the point of flow entrance, the flow either aids or opposes the fiber motion.

Forced air cooling of a moving fiber has been investigated experimentally and theoretically, with an assumed heat transfer coefficient at the fiber surface, by Paek and Schroeder (1979). Forced convective cooling studies of optical fibers have also been carried out by Jochem and Ligt (1986), Kyriacou et al. (1990), and Vaskopulos et al. (1993). In their numerical study Vaskopulos et al. (1993) used the finite volume SIMPLER approach, with radial lumping of fiber temperature and assumption of negligible axial conduction in the fiber. Using constant fiber and fluid properties, they studied the effects of fiber speed, channel diameter, and the channel wall temperature on the fiber exit temperature. Recently, Roy Choudhury and Jaluria (1994) numerically studied the forced convective cooling of moving axisymmetric rods in channels. But they

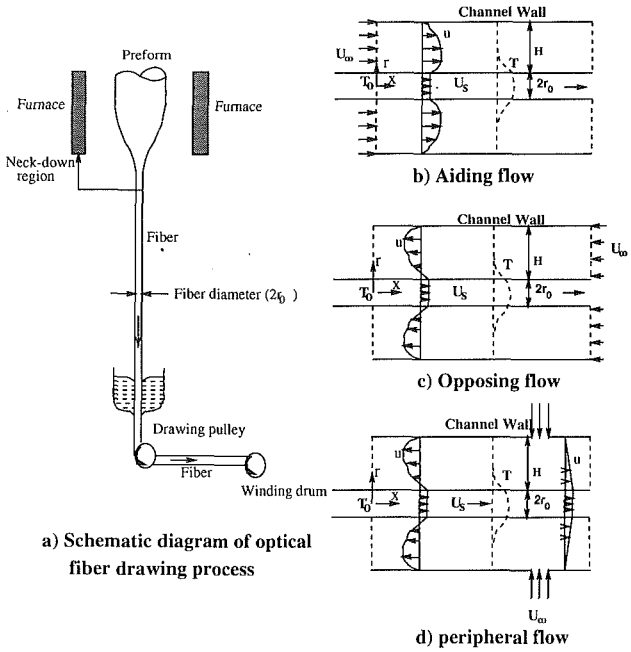

Fig. 1 (*a*) Schematic diagram of the drawing process for an optical fiber. Also shown is a moving axisymmetric solid in forced flow in a channel for (*b*) aiding flow, (*c*) opposing flow, and (*d*) peripheral flow.

used constant properties, and did not consider the more practical peripheral flow entrance situation.

The present work is directed at an experimental study with peripheral flow entrance and at a numerical simulation of the transport from a continuously moving cylindrical optical fiber. The numerical study considers coupling between the convective transport in the fluid and the conduction within the fiber. Both constant and variable properties are considered. The numerical work was motivated by some of the experimental conditions and the need to simulate the cooling process for typical configurations. Several interesting and important aspects are observed, leading to a better understanding of the underlying physical process and providing inputs that may be used in the design of the appropriate thermal system.

2 Analysis and Numerical Scheme

2.1 Constant Properties. Consider the transient, laminar flow induced by an optical fiber moving at a constant speed U_s. The temperature of the fiber is assumed to be at a uniform value of T_o at the point of entrance into the channel, that is, at $x = 0$. This temperature is fixed for a particular fiber speed and can be calculated if the distance of the cooling channel from the furnace is known. Some measured values are available in the literature (Paek and Schroeder, 1979). The flow and the temperature fields develop downstream in case of an aiding flow, but for an opposing flow separation may occur. The full governing equations, which are elliptic in nature, are solved over the entire computational domain with the relevant boundary conditions. The flow and temperature fields are assumed to be axisymmetric. This approximation is satisfactory when the buoyancy effects are small or if the fiber moves vertically. The full governing equations in axisymmetric form, assuming constant properties and neglecting buoyancy, along with the boundary conditions are given by Roy Choudhury and Jaluria (1993, 1994). A transient problem is solved, in order to investigate possible oscillations in the flow and any temperature overshoot that might arise at small times. As shown by Roy Choudhury and Jaluria (1994), the results converge smoothly to the steady-state solution at large time.

The problem is solved using the stream-function vorticity

formulation. For details of the formulation, including the nondimensionalization and initial/boundary conditions, see Roy Choudhury and Jaluria (1994). The transient vorticity and the energy equations, in conservative form for both the fiber and the fluid, are solved, using the Alternate Direction Implicit (ADI) scheme. The resulting tridiagonal matrix systems are solved using the Tridiagonal Matrix Algorithm (TDMA). At each time step, after advancing the solutions for the vorticity transport and the temperature equations (for both the solid and the fluid) by the ADI scheme, the stream function equation is solved using the SOR method. A nonuniform grid is used, with a large number of grid points near the fiber surface and the walls, to capture the large gradients near the surface accurately.

2.2 Inclusion of Variable Properties. For the optical fiber drawing process, there is a large temperature variation from the entrance to the exit of the cooling channel. Because of this temperature variation, the fluid and solid properties may change considerably. Therefore, an effect on the flow as well as on the heat transfer is expected, if the property values used are evaluated at different temperatures. For the temperature ranges employed in typical optical fiber drawing processes, the fluid density was evaluated at the smallest and the highest temperatures encountered. It was found that a negligible change occurs in the resulting temperature field (Roy Choudhury and Jaluria, 1993). Thus, for the temperature range under consideration fluid density can be assumed to be constant, considerably simplifying the analysis. But the other material properties cannot be taken as constant. If the fractional change of a material property is large, say of the order of 20 percent or larger, it is worth pursuing the variable property formulation, because of considerable difference between the results obtained for the constant and variable property cases. For details on the variable property formulation, including the dimensionless form of the vorticity transport and energy equations, see Roy Choudhury and Jaluria (1993).

When variable properties are considered, the diffusion terms in the governing differential equations become nonlinear. Therefore, the problem is solved iteratively, using the property values at the previous time step. This gives the values near the beginning of the process. At larger time, extrapolation based on previous known values is employed for improving the approximation, as outlined by Jaluria and Torrance (1986). For further details on the numerical scheme, see Roy Choudhury and Jaluria (1993).

3 Numerical Results and Discussion

Numerical solutions to the vorticity, temperature, and stream function equations were obtained to study several important aspects arising from the three configurations considered. Results were obtained over wide ranges of governing parameters. Only some typical steady-state results are presented here. All the results, unless specified otherwise, are for an optical fiber of diameter 150 μm moving at a speed of 100 m/min in a channel maintained at ambient temperature at the walls, while the average external velocity of the fluid, taken as helium, is two times the fiber speed. These are some of the commonly encountered parametric values for the fiber drawing process. Unless mentioned otherwise, the results shown are for constant fluid and fiber properties.

Figure 2 shows the effect of direction of fluid flow. For the aiding flow case (Fig. 2(*a*)), the flow field is seen to develop quickly, with the streamlines in the same direction as the flow. However, for the opposing flow (Fig. 2(*b*)), a recirculating flow region develops near the surface of the fiber. This recirculation arises because of the reversal of flow, since the fluid near the surface of the fiber tends to move along with the fiber because of viscous effects. However, near the entrance of the

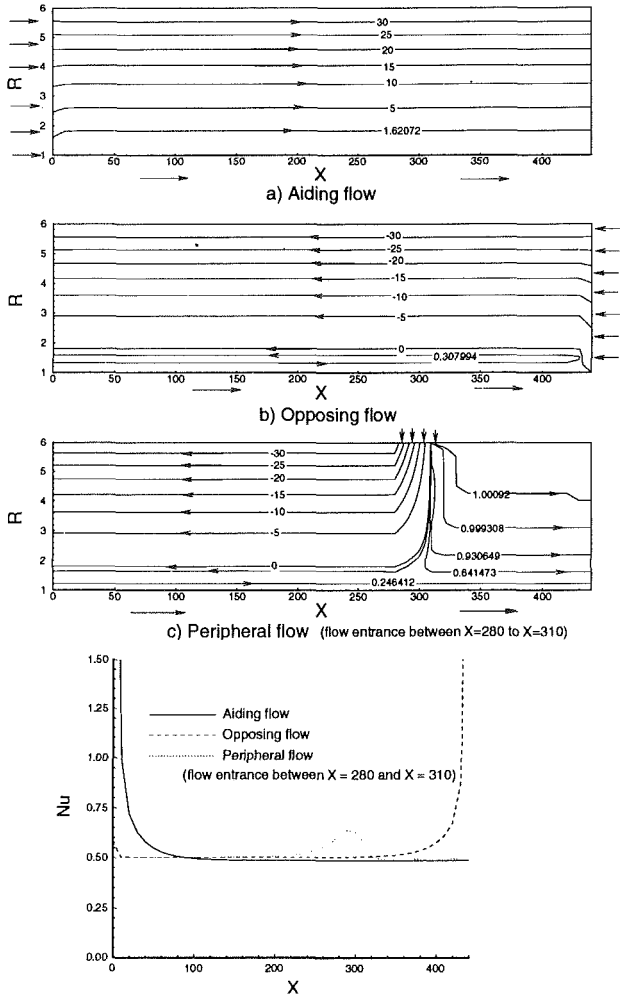

Fig. 2 Streamlines for (*a*) aiding, (*b*) opposing, and (*c*) peripheral flow; (*d*) local Nusselt number variations for different flow configurations for $H = 5r_0$

forced flow, the velocity is large enough to force the fluid to flow in the same direction as the forced convection velocity and opposite to fiber motion. Figure 2(*c*) shows the streamlines for peripheral flow entrance, which is commonly used in many industrial fiber drawing applications because it reduces the fluid loss and overcomes the difficulty, because of entrainment and heat transfer, of achieving uniform and isothermal flow at the entrance with the aiding or opposing flow cases and as before for the opposing portion of the flow, a recirculating region occurs over most of the fiber surface. Figure 2(*d*) examines the variation of the local Nusselt number Nu for different flow configurations. It is seen that the Nusselt number starts out very high at the entrance of the flow in case of aiding and opposing flow. For the peripheral flow case, the Nusselt number is not as high at the point of flow entrance, even though a "spike" can be seen there. The reason for this smaller Nusselt number can be explained from the fact that, in this case, the fluid gets heated as it reaches the fiber surface, unlike the opposing and aiding flow cases, where the cold fluid comes in contact with the fiber surface at the flow entrance. Even though the opposing flow case is like the counterflow heat exchanger, the temperature drop is not much more than the aiding flow case, which is like a parallel flow heat exchanger, because of the occurrence of the recirculating region. In fact the temperature decay over the entire length of the channel is about the same for all three flow circumstances (Roy Choudhury and Jaluria, 1993).

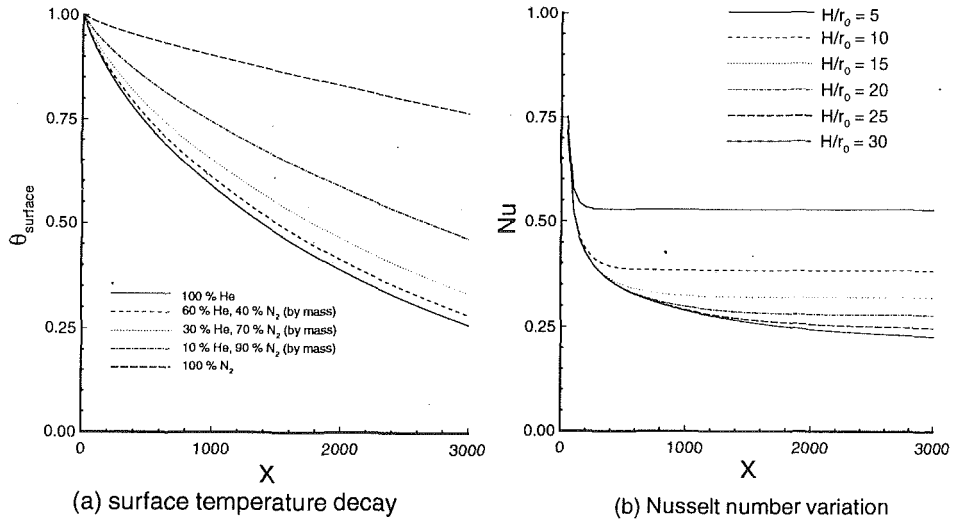

(a) surface temperature decay (b) Nusselt number variation

Fig. 3 (*a*) **Surface temperature decay for different cooling fluids for** $H = 20r_0$ **and** (*b*) **effect of channel width on the local Nusselt number distribution**

The effect of a change in fiber speed and forced convection velocity is discussed in detail by Roy Choudhury and Jaluria (1993) and is thus not presented here. In general, at higher fiber speed, a smaller amount of thermal energy can be extracted from the fiber, as the time taken by the fiber to pass through the region is smaller. As the forced convection velocity is increased, for any of three flow configurations considered, the local Nusselt number and hence the temperature decay increases.

Figure 3 shows the effect of ambient fluid and the channel width on the heat transfer from the fiber. When helium is the cooling medium, the heat transfer rate is much higher than when nitrogen is the cooling medium, because of larger thermal diffusion within the fluid for helium due to its larger thermal conductivity. A mixture of nitrogen and helium can be used to obtain intermediate levels of cooling. As seen from Fig. 3(*a*), different proportions of helium and nitrogen may be used to control the heat transfer rate and consequently the temperature decay. With a decrease in the channel width, the isotherms come closer to the surface, and the temperature gradient at the surface increases, resulting in greater Nusselt number, as seen from Fig. 3(*b*). If the channel width is large ($H > 25r_0$), then it is observed that a further increase in the channel width hardly affects the heat transfer. This is due to the fact that for such a wide channel the flow and thermal fields approach those for a uniform forced flow in an extensive medium. Thus, increasing the channel width does not significantly affect the isotherms near the fiber surface. Also it is observed from Fig. 3(*b*) that, as the channel width increases, a larger length is needed for the fluid to reach developed conditions, indicated by the local Nusselt number attaining a constant value. This is an expected result and is also observed for flow in a pipe (Burmeister, 1983).

The effect of the channel wall temperature is discussed in detail by Roy Choudhury and Jaluria (1993) and is not repeated here. In general, if the wall temperature is kept below the ambient temperature level, the cooling is better, as long as the channel is not very wide (Roy Choudhury and Jaluria, 1994).

If the property variations in the fiber are considered, keeping the fluid properties constant, it is found that, for the solid properties taken as constant at the maximum (T_o) or the minimum possible temperature (T_∞), there is hardly any effect on the temperature field (Roy Choudhary and Jaluria, 1993). So the fiber properties are taken as constant at the average temperature within the temperature range under consideration.

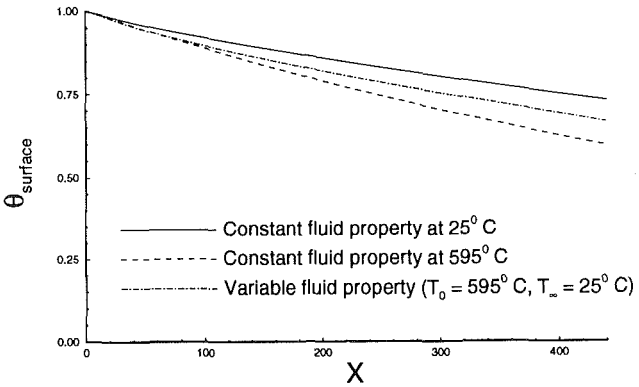

Fig. 4 Effect of fluid property variation on surface temperature decay for $H = 5r_0$

On the other hand, it is found that if fluid properties are taken as constant at the maximum or the minimum possible temperature there is considerable effect on the temperature field, as seen from Fig. 4. When the variable property formulation is used, it is observed that the initial rate of temperature decay is similar to the case when the properties of the fluid are evaluated at the maximum possible temperature, while farther downstream the temperature decays at a much slower rate. From Fig. 4 it is evident that the effect of fluid property variation on the temperature field is significant, and should be considered for an accurate numerical simulation of the fiber drawing process.

4 Comparison of Experimental Results With Numerical Predictions

Very few experimental data are available for channel flow for forced convective cooling of an optical fiber. The numerical results obtained in this study were compared with the experimental data obtained from forced fiber cooling experiments in a draw tower, with peripheral flow entrance, and the results are shown in Fig. 5. The experimental work was performed on a 6.9 m draw tower, using an aluminum cooling section consisting of a water-cooled tube 50 cm long and two plenum chambers, each 5 cm long, that were welded on either end of the tube. The optical fiber was cooled using pure helium or 50 percent (by mass) helium—nitrogen mixture. The cooling gas was introduced sideways in the lower plenum chamber of

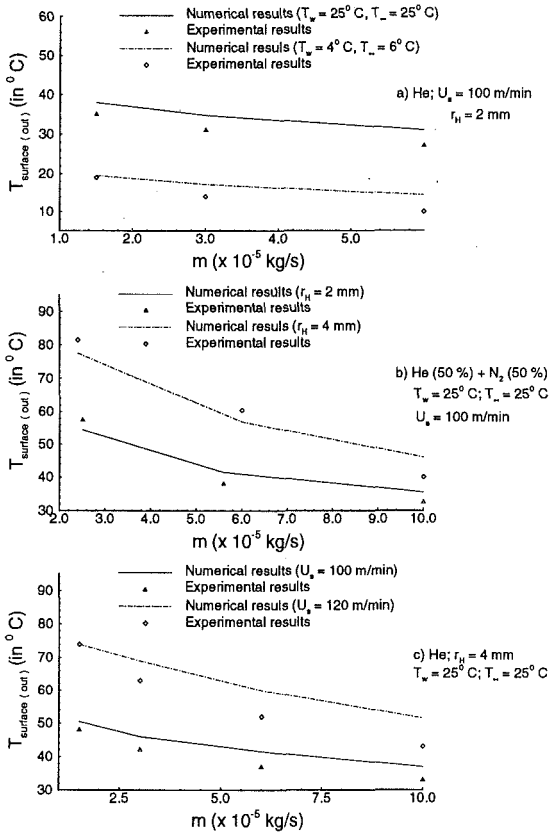

Fig. 5 Comparison of the numerical results with experimental data obtained by Vaskopulos et al. (1993) and in the present work, for different governing parameters for an optical fiber moving in a channel with peripheral flow entrance

the cooling section and through the insert tube in a direction opposite to the fiber motion. The distance between the heater exit and the upper end of the cooling section was 55 cm for all the tests. The fiber exit temperature was measured at a distance of 12 cm from the lower end of the cooling section using a commercial noncontact temperature sensor. During the experiments the fiber diameter was 150 μm and the draw speed was varied from 100 to 150 m/min. The cooling section wall temperature was controlled by a cooling jacket with circulating water and was varied between 4 and 25°C. Further details on the cooling section design, on the fiber draw tower, and on the experimental procedure can be found from Vaskopulos et al. (1993). Only a few important aspects are mentioned here for conciseness.

For most part the agreement between the experimental and numerical results is seen to be very good. The numerical model closely predicts the general trends with changes in different parameters, like channel wall temperature, channel width, and fiber speed. It is observed that at very high mass flow rates, the numerical model overpredicts the exit temperature. This may be due to the fact that under actual experimental circumstances, at high flow speeds, turbulence arises, leading to more rapid cooling.

5 Conclusions

A detailed numerical study of the conjugate transport from a continuously moving optical fiber in forced flow in a channel has been carried out. The numerical results were validated using experimental data. Three different forced flow configurations, namely, one aiding and another opposing the movement of the fiber as well as a peripheral flow, which was employed in the experiments, has been considered in this work. The heat transfer and the consequent temperature decay in the optical fiber undergoing thermal processing are found to depend significantly on the channel width, the channel thermal conditions, the fluid used, and the fiber speed. The effect of solid property variation is found to be quite insignificant. However, the effect of fluid property variations is quite substantial. For the opposing flow, it is found that a recirculating region is formed near the fiber surface. The numerical results are compared with the experimental measurements of the fiber temperature at the channel exit. Good agreement is found between the two, lending support to the numerical modeling of the fiber cooling process.

Acknowledgments

The authors acknowledge the financial support provided by the National Science Foundation, under Grant No. DDM-92-13458 and the computing facilities provided by the Pittsburgh Supercomputing Center, under Grant No. CBT920017P, for this work. The authors would also like to thank the Fiber Optics Material Research Center, Rutgers University, for providing the experimental facilities.

References

Burmeister, L., 1983, *Convective Heat Transfer*, Wiley-Interscience Publication, New York.

Jaluria, Y., and Torrance, K. E., 1986, *Computational Heat Transfer*, Hemisphere, New York.

Jochem, M. G., and Ligt, W. C., 1986, "Cooling and Bubble-Free Coating of Optical Fibers at High Drawing Rate," *Lightwave Technology*, Vol. 4, pp. 739–742.

Kyriacou, S., Polymeropoulos, C. E., and Sernas, V., 1990, "Accelerated Cooling of Optical Fiber," *Mat. Res. Soc. Symp. Proc.*, Vol. 172, pp. 49–54.

Paek, U. C., and Schroeder, C. M., 1979, "Forced Convective Cooling of Optical Fiber in High-Speed Coating," *Journal of Applied Physics*, Vol. 50, pp. 6144–6148.

Roy Choudhury, S., and Jaluria, Y., 1993, "Forced Convective Cooling of an Optical Fiber During Thermal Processing," in: *Advanced Computations in Materials Processing*, HTD-Vol. 241, pp. 57–71.

Roy Choudhury, S., and Jaluria, Y., 1994, "Forced Convective Heat Transfer From a Continuously Moving Heated Cylindrical Rod in Materials Processing," ASME JOURNAL OF HEAT TRANSFER, Vol. 116, this issue, pp. 724–734.

Vaskopulos, T., Polymeropoulos, C. E., and Zebib, X. X., 1993, "Heat Transfer From Optical Fiber During the Draw Process," *J. Mat. Proc. and Manuf. Sci.*, Vol. 1, No. 3, pp. 261–271.